



REMOTE SENSING AND DIGITAL IMAGE PROCESSING



B. Ramachandran · Christopher O. Justice · M. J. Abrams (Eds.)

Land Remote Sensing and Global Environmental Change

NASA's Earth Observing System
and the Science of ASTER and MODIS



Springer

Land Remote Sensing and Global Environmental Change

Remote Sensing and Digital Image Processing

VOLUME 11

Series Editor:

Freek D. van der Meer
*Department of Earth Systems Analysis
International Institute for
Geo-Information Science and
Earth Observation (ITC)
Enschede, The Netherlands*
&
*Department of Physical Geography
Faculty of Geosciences
Utrecht University
The Netherlands*

Editorial Advisory Board:

Michael J. Abrams
*NASA Jet Propulsion Laboratory
Pasadena, CA, U.S.A.*

Paul Curran
University of Bournemouth, U.K.

Arnold Dekker
*CSIRO, Land and Water Division
Canberra, Australia*

Steven M. de Jong
*Department of Physical Geography
Faculty of Geosciences
Utrecht University, The Netherlands*

Michael Schaepman
*Department of Geography
University of Zurich, Switzerland*

EARSeL Series Editor:

André Marçal
*Department of Applied Mathematics
Faculty of Sciences
University of Porto
Porto, Portugal*

EARSeL Editorial Advisory Board:

Mario A. Gomasasca
CNR - IREA Milan, Italy

Martti Hallikainen
*Helsinki University of Technology
Finland*

Håkan Olsson
*Swedish University
of Agricultural Sciences
Sweden*

Eberhard Parlow
*University of Basel
Switzerland*

Rainer Reuter
*University of Oldenburg
Germany*

For other titles published in this series, go to
<http://www.springer.com/series/6477>

Land Remote Sensing and Global Environmental Change

NASA's Earth Observing System
and the Science of ASTER and MODIS

Editors

Bhaskar Ramachandran

NASA LP DAAC, USGS Earth Resources Observation
and Science Center, Sioux Falls, SD 57198, USA

Christopher O. Justice

University of Maryland, College Park, MD 20742, USA

Michael J. Abrams

NASA Jet Propulsion Laboratory, Pasadena, CA 91109, USA

 Springer

Editors

Bhaskar Ramachandran
NASA LP DAAC,
USGS Earth Resources Observation
and Science Center
Sioux Falls, SD 57198, USA
bhaskar@usgs.gov

Michael J. Abrams
NASA Jet Propulsion Laboratory,
California Institute of Technology,
Pasadena, CA 91109, USA
michael.j.abrams@jpl.nasa.gov

Christopher O. Justice
Department of Geography,
University of Maryland,
College Park,
MD 20742, USA
justice@hermes.geog.umd.edu

ISBN 978-1-4419-6748-0 e-ISBN 978-1-4419-6749-7
DOI 10.1007/978-1-4419-6749-7
Springer New York Dordrecht Heidelberg London

Library of Congress Control Number: 2010936287

© Springer Science+Business Media, LLC 2011

All rights reserved. This work may not be translated or copied in whole or in part without the written permission of the publisher (Springer Science+Business Media, LLC, 233 Spring Street, New York, NY 10013, USA), except for brief excerpts in connection with reviews or scholarly analysis. Use in connection with any form of information storage and retrieval, electronic adaptation, computer software, or by similar or dissimilar methodology now known or hereafter developed is forbidden.

The use in this publication of trade names, trademarks, service marks, and similar terms, even if they are not identified as such, is not to be taken as an expression of opinion as to whether or not they are subject to proprietary rights.

Printed on acid-free paper

Springer is part of Springer Science+Business Media (www.springer.com)

This volume is dedicated to Vince Salomonson (former NASA MODIS Science Team leader) and Anne Kahle (former NASA ASTER Science Team leader) for their personal commitment and outstanding achievement in guiding the development and implementation of the MODIS and ASTER instruments and their science missions, which have exceeded all our highest expectations. This volume is also dedicated to Yoram Kaufman and Mike Barnsley (MODIS Science Team members), and Takashi Sato (ASTER Instrument Team), who are sadly no longer with us.

Prologue

Global environmental change fundamentally transforms the physical, chemical, and biological aspects of ecosystems with corresponding socioeconomic repercussions across planet Earth. These changes are largely driven by human as well as natural causes. *Global warming* and *climate change*, two near-universal terms in our everyday lexicon, increasingly symbolize environmental change globally. A closer examination reveals that land use change is perhaps the most immediate and visible type of environmental change occurring globally. A number of natural phenomena display the effects of climate change. Examples include modified growing season phenologies, melting alpine glaciers, sea ice, permafrost, and increasing frequency of extreme weather events. Perhaps, one of the more dramatic examples is *Shishmaref*, a village on Sarichef Island in the Chukchi Sea, north of the Bering Strait in Alaska. Rising temperatures have led to permafrost thawing that affects the very foundation of the village, which plans to relocate further to the south. This thawing renders its shoreline more vulnerable to further erosion, and the loss of protective sea ice leaves Shishmaref exposed to storm surges. Environmental change remains one of the most serious long-term global issues since human sustainability depends on how well our physico-ecological and socioeconomic systems function together.

Earth and environmental scientists constantly seek to better understand the processes, impacts, and projections of global change that provides the input to inform appropriate policies and management strategies. A system's approach to Earth science enables scientists to investigate and analyze complex interactions of the biophysical, geophysical, and human components germane to understanding global environmental change. The dynamics of the Earth system fosters complex spatio-temporal variations that highlight the significance of, and the need to monitor the Earth as a unified whole. Accurate, timely, and reliable data are a precursor to analyze and study several aspects of the integrated Earth system. The Earth observing satellites have helped generate unprecedented volumes of remotely sensed data that are vital to an array of Earth science investigations. Remote sensing observations have catalyzed several aspects of Earth system science by providing panoptic views and time-series measurements of the study environment in ways nearly impossible to replicate by traditional ground-based methods.

Earth observations and measurements are a vital part of the US Global Change Research Program, which provides the basis for Earth system science. NASA's Earth Observing System mission is a 15-year effort to collect and analyze a multi-sensor, multitemporal data stream across all elements of the Earth's life-support systems. NASA's EOS is a remarkably successful accomplishment in engineering a global science enterprise dedicated to advancing our understanding of global environmental change. This volume specifically focuses on the terrestrial components of change based on the scientific knowledge derived from data produced by two EOS instruments, ASTER and MODIS, which are part of the Terra and Aqua satellite missions. This volume is divided into six sections. The first three sections provide insights into the history, philosophy, and evolution of the EOS, ASTER and MODIS instrument designs and calibration mechanisms, and the data systems components used to manage and provide the science data and derived products. The latter three sections exclusively deal with ASTER and MODIS data products and their applications, and the future of these two classes of remotely sensed observations.

ASTER and MODIS instruments serve different science and application communities, though important synergies exist between the two. The ASTER mission crystallized as a synthesis of two independent efforts in the USA and Japan. JPL's Thermal Infrared Multispectral Scanner, an early EOS strawman instrument, was later refined and proposed as the Thermal Infrared Ground Emission Radiometer (TIGER) in 1988. Around the same time, Japan's Ministry of International Trade and Industry (MITI) offered to provide the Intermediate Thermal Infrared Radiometer (ITIR). NASA accepted MITI's design and called upon the TIGER team to integrate its design with that of the Japanese ITIR. This synthesis produced the ASTER instrument, a triad of sensor systems spanning from the visible to the thermal wavelengths of the electromagnetic spectrum, which produce data at Landsat-class spatial resolutions. ASTER's claim to fame derives from a number of its features. They include a VNIR stereo mapping capability and eleven spectral bands in the SWIR and TIR channels. The SWIR band selection helps map surface soil and mineral lithologies to target the phyllosilicate and carbonate absorption features. The TIR-derived emissivities not only facilitate estimating the silica content, but they help accurately determine the variable spectral emissivity of the land surface and its temperature. ASTER science applications include land surface change, geology, hydrology, soils, volcanology, glaciology, vegetation and ecosystems, and digital elevation models. Unfortunately, the SWIR sensor suffered a setback due to its anomalously high detector temperatures, which have rendered its data unusable since April 2008.

In contrast to ASTER's Landsat-class spatial resolutions, limited duty cycle, and user request-based tasking and scheduling, the MODIS instruments were designed to generate daily, continuous, global, multitemporal data that help build a holistic record of our Earth's parameters, including land, oceans, and the atmosphere. The MODIS instrument's design heritage includes the Advanced Very High Resolution Radiometer, Coastal Zone Color Scanner, High Resolution Infrared Radiation Sounder, and Landsat Thematic Mapper. The MODIS-related chapters in this vol-

ume deal exclusively with the land component. MODIS land science primarily revolves around its three product families: (1) Radiation budget variables: land surface reflectance is the most fundamental processed surface parameter for the solar reflective channels, which is used to generate the higher-level products including surface albedo; (2) Ecosystem variables: MODIS-derived data enable direct global observations of ecosystem phenology and photosynthesis, which help characterize and monitor terrestrial primary productivity essential for climate models; and (3) Land cover characteristics: human-induced land use and land cover change remain clear transformers of the land surface. MODIS products examine different aspects of these changes through its global land cover, phenology, thermal anomalies and fires, and vegetation continuous fields products. The MODIS land science mission is a clear demonstration of how satellite observations of Earth's biophysical dynamics, processes, and parameters contribute to a better understanding of our global ecosystem and their response to, and effects on global environmental change.

The first half of this volume contains chapters that articulate the data systems components embodied by the EOS Data and Information System (EOSDIS) to support both the ASTER and MODIS missions. The EOSDIS evolved considerably from its initial design. The EOS science enterprise owes its success to a large extent on the present structural components of the EOSDIS architecture. Just as the larger science community relies on advances in algorithms, analyses, and new knowledge itself, EOSDIS relies on leveraging advances in software and hardware engineering and information technologies to provide an advanced data management system infrastructure. Conceived just as the software industry was emerging from its crisis in the mid-1980s, EOSDIS provides a number of services for the larger EOS. They range from data acquisition, spacecraft command, control, and telemetry processing to data production, archival, and dissemination. EOSDIS remains one of the single largest distributed Earth science data and information management systems in the world, designed to support the larger EOS science mission to observe, analyze, and interpret global environmental change. Technology remains an integral part of virtually every aspect of the EOS mission playing key roles from building and launching the instruments, performing satellite command, control, and telemetry, and all data management aspects related to EOSDIS. Future missions stand to benefit further through advances in information technology. The Internet and the Web remain primary catalysts for information and data exchange, which facilitates data brokers and end-users to benefit from the larger science missions. Service-oriented architecture holds much promise to provide packaged functionality as interoperable Web services across different organizations.

The end of 2009 marks the 10th anniversary of the Terra platform's launch. The ASTER- and MODIS-derived land data and product suites have contributed to several biophysical, geological, and geophysical applications. These data also play a critical role as intellectual bridges connecting the pre-EOS era data and knowledge with future missions still taking shape. The next decade and beyond will witness the launch of a number of missions crucial to furthering terrestrial science. They include the Landsat Data Continuity Mission, the National Polar-orbiting Operational Environmental Satellite System mission and its preparatory precursor,

and the NASA Decadal Survey missions, namely the Hyperspectral Infrared Imager, and the Deformation Ecosystem Structure and Dynamics of Ice missions. The overall lessons learned from the EOS ASTER and MODIS missions are critical for these future missions. Emerging frameworks for coordination like the Global Earth Observing System of Systems provide additional credence and context for these future missions as well.

As global environmental change in the Anthropocene age becomes more ubiquitous, the papers presented in this volume demonstrate the value of EOS for studying the Earth's surface. The future may reflect upon the EOS era as the golden age of land remote sensing, which engendered multiple new instruments specifically designed to meet Earth science data needs. This era also saw the development of distributed data systems to generate unprecedented volumes of science quality data and an entirely new array of validated geophysical products at multiple resolutions to address major land science questions. EOS demonstrates the rich synergistic confluence of science, engineering, and technology, which can help us decipher how our terrestrial systems both contribute and respond to *global environmental change*.

Acknowledgements

Thank you to all the authors and co-authors for your contributions toward helping build our knowledge base in land remote sensing and the Earth sciences. We would like to thank the following individuals for their help in reviewing the manuscripts, which crystallized into the chapters in this volume: Mike Abrams, Pete Aniello, Rick Allen, Bryan Bailey, Mike Barnsley, Jesslyn Brown, Gyanesh Chander, Mark Chopping, Mike Crane, John Daucsavage, Chris Doescher, John Dwyer, Andy French, Alisa Gallant, Dean Gesch, Alan Gillespie, Garik Guttman, Forrest Hall, Niall Hanan, Rob Hewson, Calli Jenkerson, Lei Ji, Andy Kääb, Richard Kelly, Andrew Klein, Jim Lacasse David Landgrebe, Jon Lemig, Tom Loveland, Tom Maiersperger, Jeff Masek, David Meyer, Ron Morfitt, Rama Nemani, Bernard Pinty, Lela Prashad, Mike Ramsey, Vince Realmuto, Gabriel Senay, Gail Schmidt, Tom Sohre, Will Stefanov, Dan Steinwand, Greg Stensaas, Jim Storey, Larry Tieszen, Dan Traut, Jim VerMeer, Elizabeth Wentz, Kimberly Wickland, Mike Wimberly, Bruce Wylie, and Jane Zhang.

Several people helped both directly and indirectly throughout this project. They include Alan Gillespie, Martha Maiden, Vince Salomonson, Anne Kahle, Tom Loveland, John Dwyer, Robert Wolfe, Geoffrey Henebry, Joy Hood, Ron Beck, Hiroyuki Fujisada, Yasushi Yamaguchi, Takashi Sato, Hideyuki Toonoka, Kohei Arai, and Akira Iwasaki. We would like to thank Claire Parkinson and Sally Bensusan for their help in providing us an early graphic of the EOSDIS. We also thank John Faundeen for providing the EROS statistics.

We are grateful to NASA for support for the color plates used in this volume and in particular Jack Kaye, Woody Turner, and Ed Masuoka for their encouragement with this volume.

We thank Craig Walters for his valuable editorial support to this project, and Tom Adamson for sharing some of his editorial expertise as well. Our immense thanks and gratitude to our Springer Editors, Harry Blom and Chris Coughlin for all their help throughout this project. We also thank Ho Ying Fan and Jenny Wolkowicki at Springer, and B. Gokulnathan at SPi Global for shepherding this volume through its final stages.

Bhaskar Ramachandran
Christopher O. Justice
Michael J. Abrams

About the Editors

Bhaskar Ramachandran is a senior scientist who supports the NASA Earth Observing System (EOS) science mission at the Earth Resources and Observation Science (EROS) Center at the US Geological Survey in Sioux Falls, SD. He currently supports the MODIS science mission, and has performed similar roles for the Landsat-7 and ASTER missions in the past. His current research interests include the use of Semantic Web capabilities and building ontologies to represent geospatial science knowledge domains.

Christopher O. Justice is a Professor and Research Director at the Geography Department of the University of Maryland. He is the land discipline chair for the NASA MODIS Science Team and is responsible for the MODIS Fire Product. He is a member of the NASA NPOESS Preparatory Project (NPP) Science Team. He is the NASA LCLUC Program Scientist. He is Co-Chair of the international GOFI/GOLD-Fire Implementation Team and Co-Chair of the GEO Global Agricultural Monitoring Task. His current research is on land cover and land use change, the extent and impacts of global fire, global agricultural monitoring, and their associated information technology and decision support systems.

Michael J. Abrams received his degrees in Biology and Geology from the California Institute of Technology. Since 1973, he has worked at NASA's Jet Propulsion Laboratory in geologic remote sensing. He served on the science team for many instruments, including Skylab, HCMM, Landsat, and EO-1. Areas of specialization are mineral exploration, natural hazards, volcanology, and instrument validation. He has been on the US/Japan ASTER Science Team since 1988, and became the ASTER Science Team Leader in 2003.

Contents

Part I The Earth Observing System and the Evolution of ASTER and MODIS

| | |
|-------------------------------------------------------------------------------------------------------------------------------------------------------------------------------------------------------------------|-----------|
| 1 Evolution of NASA’s Earth Observing System and Development of the Moderate-Resolution Imaging Spectroradiometer and the Advanced Spaceborne Thermal Emission and Reflection Radiometer Instruments | 3 |
| Vincent Salomonson, Michael J. Abrams, Anne Kahle, William Barnes, Xiaoxiong Xiong, and Yasushi Yamaguchi | |
| 2 Philosophy and Architecture of the EOS Data and Information System..... | 35 |
| Martha Maiden | |
| 3 Lessons Learned from the EOSDIS Engineering Experience | 49 |
| Evelyn Nakamura | |

Part II ASTER and MODIS: Instrument Design, Radiometry, and Geometry

| | |
|--------------------------------------------------------------------------------------|------------|
| 4 Terra ASTER Instrument Design and Geometry | 59 |
| Hiroyuki Fujisada | |
| 5 ASTER VNIR and SWIR Radiometric Calibration and Atmospheric Correction..... | 83 |
| Kohei Arai, Kurtis Thome, Akira Iwasaki, and Stuart Biggar | |
| 6 ASTER TIR Radiometric Calibration and Atmospheric Correction | 117 |
| Hideyuki Tonooka | |

7 Terra and Aqua MODIS Design, Radiometry, and Geometry in Support of Land Remote Sensing 133
 Xiaoxiong Xiong, Robert Wolfe, William Barnes, Bruce Guenther, Eric Vermote, Nazmi Saleous, and Vincent Salomonson

Part III ASTER and MODIS: Data Systems

8 ASTER and MODIS Land Data Management at the Land Processes, and National Snow and Ice Data Centers 167
 John Daucsavage, Marilyn Kaminski, Bhaskar Ramachandran, Calli Jenkerson, Karla Sprenger, Ron Faust, and Tamara Rockvam

9 An Overview of the EOS Data Distribution Systems..... 183
 H.K. Ramapriyan, Robin Pfister, and Beth Weinstein

10 The Language of EOS Data: Hierarchical Data Format..... 203
 Larry Klein, Andrey Savtchenko, Abe Taaheri, Cid Praderas, and Siri Jodha Singh Khalsa

Part IV ASTER Science and Applications

11 The ASTER Data System: An Overview of the Data Products in Japan and in the United States 233
 Hiroshi Watanabe, Bryan Bailey, Kenneth Duda, Yoshiaki Kannari, Akira Miura, and Bhaskar Ramachandran

12 ASTER Applications in Volcanology..... 245
 Minoru Urai and David Pieri

13 Issues Affecting Geological Mapping with ASTER Data: A Case Study of the Mt Fitton Area, South Australia 273
 Robert Hewson and Thomas Cudahy

14 ASTER Data Use in Mining Applications..... 301
 Sandra Perry and Fred Kruse

15 ASTER Imaging and Analysis of Glacier Hazards..... 325
 Jeffrey Kargel, Roberto Furfaro, Georg Kaser, Gregory Leonard, Wolfgang Fink, Christian Huggel, Andreas Käab, Bruce Raup, John Reynolds, David Wolfe, and Marco Zapata

16 ASTER Application in Urban Heat Balance Analysis: A Case Study of Nagoya 375
 Soushi Kato and Yasushi Yamaguchi

17 Monitoring Urban Change with ASTER Data..... 397
 Maik Netzband, Elisabeth Schöpfer, and Matthias S. Möller

18 Estimation of Methane Emission from West Siberian Lowland with Subpixel Land Cover Characterization Between MODIS and ASTER..... 421
 Wataru Takeuchi, Tomoko Nakano, and Yoshifumi Yasuoka

19 ASTER Stereoscopic Data and Digital Elevation Models 439
 Thierry Toutin

20 Using ASTER Stereo Images to Quantify Surface Roughness 463
 Amit Mushkin and Alan Gillespie

21 Technoscientific Diplomacy: The Practice of International Politics in the ASTER Collaboration 483
 Dan Plafcan

Part V MODIS Science and Applications

22 MODIS Land Data Products: Generation, Quality Assurance and Validation..... 509
 Edward Masuoka, David Roy, Robert Wolfe, Jeffery Morisette, Scott Sinno, Michael Teague, Nazmi Saleous, Sadashiva Devadiga, Christopher O. Justice, and Jaime Nickeson

23 MODIS Directional Surface Reflectance Product: Method, Error Estimates and Validation..... 533
 Eric Vermote and Svetlana Kotchenova

24 Aqua and Terra MODIS Albedo and Reflectance Anisotropy Products 549
 Crystal Barker Schaaf, Jichung Liu, Feng Gao, and Alan H. Strahler

25 MODIS Land Surface Temperature and Emissivity 563
 Zhengming Wan and Zhao-Liang Li

26 MODIS Vegetation Indices..... 579
 Alfredo Huete, Kamel Didan, Willem van Leeuwen, Tomoaki Miura, and Ed Glenn

27 Leaf Area Index and Fraction of Absorbed PAR Products from Terra and Aqua MODIS Sensors: Analysis, Validation, and Refinement 603
 Ranga Myneni, Yuri Knyazikhin, and Nicolay Shabanov

28 MODIS-Derived Terrestrial Primary Production 635
 Maosheng Zhao, Steven Running, Faith Ann Heinsch,
 and Ramakrishna Nemani

29 MODIS-Derived Global Fire Products 661
 Christopher O. Justice, Louis Giglio, David Roy, Luigi Boschetti,
 Ivan Csizar, Diane Davies, Stefania Korontzi, W. Schroeder,
 Kelley O’Neal, and Jeff Morisette

**30 MODIS Snow and Ice Products, and Their Assessment
 and Applications..... 681**
 George Riggs and Dorothy Hall

**31 Characterizing Global Land Cover Type and Seasonal
 Land Cover Dynamics at Moderate Spatial Resolution
 With MODIS Data 709**
 Mark Friedl, Xiaoyang Zhang, and Alan Strahler

**32 MODIS Vegetative Cover Conversion
 and Vegetation Continuous Fields 725**
 Mark Carroll, John Townshend, Matthew Hansen,
 Charlene DiMiceli, Robert Sohlberg, and Karl Wurster

**33 Multisensor Global Retrievals of Evapotranspiration
 for Climate Studies Using the Surface Energy Budget System 747**
 Matthew McCabe, Eric Wood, Hongbo Su, Raghuvveer Vinukollu,
 Craig Ferguson, and Z. Su

Part VI The Future of Land Remote Sensing

**34 The Evolution of U.S. Moderate Resolution Optical
 Land Remote Sensing from AVHRR to VIIRS 781**
 Christopher O. Justice, Eric Vermote, Jeff Privette, and Alain Sei

35 The Future of Landsat-Class Remote Sensing 807
 Samuel Goward, Darrel Williams, Terry Arvidson, and James Irons

**36 International Coordination of Satellite Land Observations:
 Integrated Observations of the Land 835**
 John Townshend, John Latham, Christopher O. Justice,
 Anthony Janetos, Richard Conant, Olivier Arino, Roberta Balstad,
 Alan Belward, Jay Feuquay, Jiyuan Liu, Dennis Ojima, Christiana
 Schmullius, Ashbindu Singh, and Jeff Tschirley

Index..... 857

Contributors

Michael J. Abrams

NASA Jet Propulsion Laboratory, California Institute of Technology,
Pasadena, CA 91109, USA

Kohei Arai

Saga University, Honjo 1, Saga-shi, 840-8502, Japan

Olivier Arino

Earth Observation Science and Applications Department,
European Space Agency, Italy

Terry Arvidson

Lockheed Martin, NASA Goddard Space Flight Center,
Greenbelt, MD 20771, USA

G. Bryan Bailey

USGS Center for Earth Resources Observation and Science,
Sioux Falls, SD 57198, USA

Roberta Balstad

CIESIN, The Earth Institute, Columbia University,
Palisades, NY 10964, USA

William Barnes

GEST-University of Baltimore-Maryland County, and NASA
Goddard Space Flight Center (Emeritus), Greenbelt, MD 20771, USA

Alan Belward

Institute for Environment and Sustainability, Joint Research Centre,
Via E. Fermi 2749 I-21027 Ispra (VA), Italy

Stuart Biggar

Optical Sciences, University of Arizona, Meinel Building,
1630 East University, Boulevard, Tucson, AZ 85721, USA

Luigi Boschetti

Department of Geography, University of Maryland,
College Park, MD 20742, USA

Mark Carroll

Department of Geography, University of Maryland, College Park,
MD 20742, USA

Richard Conant

Natural Resource Ecology Laboratory, Colorado State University,
Fort Collins, CO 80523, USA

Tom Cudahy

CSIRO Exploration and Mining, Floreat Park Laboratories,
Private Bag, PO Wembley, WA 6014, Australia

Ivan Csiszar

Department of Geography, University of Maryland, College Park,
MD 20742, USA

John Daucsavage

SGT Inc., USGS Center for Earth Resources Observation and Science,
Sioux Falls, SD 57198, USA

Diane Davies

Department of Geography, University of Maryland, College Park,
MD 20742, USA

Sadashiva Devadiga

Terrestrial Information Systems Branch, NASA Goddard
Space Flight Center, Greenbelt, MD 20771, USA

Kamel Didan

Department Soil, Water & Environmental Science,
University of Arizona, Tucson, AZ 85721, USA

Charlene DiMiceli

Department of Geography, University of Maryland, College Park,
MD 20742, USA

Ken Duda

NASA LP DAAC, USGS Center for Earth Resources
Observation and Science, Sioux Falls, SD 57198, USA

Ron Faust

NASA LP DAAC, USGS Center for Earth Resources
Observation and Science, Sioux Falls, SD 57198, USA

Craig Ferguson

Department of Civil and Environmental Engineering,
Princeton University, Princeton, NJ 08544, USA

Jay Feuquay (deceased)

U.S. Geological Survey, Reston, VA, USA

Wolfgang Fink

Division of Physics, Mathematics and Astronomy, California Institute of Technology, Pasadena, CA 91125, USA

Mark Friedl

Department of Geography and Environment, Center for Remote Sensing, Boston University, Boston, MA 02215, USA

Hiroyuki Fujisada

Sensor Information Laboratory Corp., Hosoda Bldg 2F-D, 3-14-17 Azuma, Tsukuba, 305-0031, Japan

Roberto Furfaro

Department of Aerospace & Mechanical Engineering, University of Arizona, Tucson, AZ 85721, USA

Feng Gao

Earth Resources Technology Inc., 8106 Stayton Dr., Jessup, MD 20794, USA

Louis Giglio

Science Systems and Applications Inc., 10210 Greenbelt Road, Suite 600, Lanham, MD 20706, USA

Alan Gillespie

Department of Earth and Space Sciences, University of Washington, Seattle, WA 98195, USA

Ed Glenn

Environmental Research Laboratory, University of Arizona, Tucson, AZ 85721, USA

Samuel Goward

Department of Geography University of Maryland College Park, MD 20742, USA

Bruce Guenther

GEST-University of Baltimore-Maryland County, and NASA/Goddard Space Flight Center, Greenbelt, MD 20771, USA

Dorothy K. Hall

Cryospheric Sciences Branch, NASA Goddard Space Flight Center, Greenbelt, MD 20771, USA

Matt Hansen

Geographic Information Science Center of Excellence, South Dakota State University, Wecota Hall, Brookings, SD 57007, USA

Faith Ann Heinsch

Numerical Terradynamic Simulation Group, University of Montana, Missoula, MT 59812, USA

Robert Hewson

CSIRO Exploration and Mining, Australian Resources Research Centre (ARRC),
26 Dick Perry Avenue, Kensington, WA 6151, Australia

Alfredo Huete

Department Soil, Water & Environmental Science,
University of Arizona, Tucson, AZ 85721, USA

Christian Huggel

Department of Geography, University of Zurich, CH-8057, Zurich, Switzerland

James Irons

NASA Goddard Space Flight Center, Greenbelt, MD 20771, USA

Akira Iwasaki

University of Tokyo, 7-3-1 Hongo, Bunkyo-ku, Tokyo, 113-8656, Japan

Anthony Janetos

Joint Global Change Research Institute, 5825 University Research Court,
College Park, MD 20740, USA

Calli Jenkerson

NASA LP DAAC, USGS Center for Earth Resources Observation and Science,
Sioux Falls, SD 57198, USA

Christopher O. Justice

Department of Geography, University of Maryland, College Park,
MD 20742, USA

Andreas Kääb

Department of Geosciences, University of Oslo, Postbox 1047,
Blindern, 0316, Oslo, Norway

Anne Kahle

NASA Jet Propulsion Laboratory (retired), California Institute
of Technology, Pasadena, CA 91109, USA

Marilyn Kaminski

National Snow and Ice Data Center DAAC, Boulder, CO 80309, USA

Yoshiaki Kannari

Earth Remote Sensing Data Analysis Center, Forefront Tower,
3-12-1 Kachidoki, Chuo-ku, Tokyo, 104-0054, Japan

Jeffrey Kargel

Department of Hydrology & Water Resources, University of Arizona,
Tucson, AZ 85721, USA

Georg Kaser

Tropical Glaciology Group, Institut für Geographie,
Innrain 52, A – 6020, Innsbruck, Austria

Soushi Kato

Graduate School of Environmental Studies, Nagoya University, Japan
Current address: Department of Earth Sciences and Earth Dynamic System
Research Center, National Cheng Kung University, Tainan, Taiwan

Siri Jodha Singh Khalsa

National Snow and Ice Data Center, University of Colorado,
Boulder, CO 80309, USA

Larry Klein

Wyle Information Systems, Lanham, MD, USA

Yuri Knyazikhin

Department of Geography and Environment, Boston University,
Boston, MA 02215, USA

Stefania Korontzi

Department of Geography, University of Maryland,
College Park, MD 20742, USA

Svetlana Kotchenova

Department of Geography, University of Maryland, College Park,
MD 20742, USA

Fred Kruse

Department of Geological Sciences & Engineering,
Arthur Brant Laboratory for Exploration Geophysics,
University of Nevada, Reno, NV 89557, USA

John Latham

Food and Agriculture Organisation of the United Nations (FAO),
Environment and Natural Resources Service (SDRN),
Viale delle Terme di Caracalla, 00153, Rome, Italy

Willem van Leeuwen

Department of Geography and Regional Development & Office
of Arid Lands Studies, University of Arizona, Tucson, AZ 85721, USA

Gregory J. Leonard

Department of Hydrology & Water Resources, University of Arizona,
Tucson, AZ 85721, USA

Zhao-Liang Li

TRIO/LSIIT/ENSPS, Parc d'Innovation, Bd. Sebastien Brant,
BP10413, 67412, Illkirch, France;
Institute of Geographic Sciences and Natural Resources Research,
Beijing 100101, China

Jichung Liu

Department of Geography and Environment, Boston University,
Boston, MA 02215, USA

Jiyuan Liu

Institute of Geographical Sciences and Natural Resources Research,
Chinese Academy of Sciences, 11A, Datun Road, Beijing, 100101, China

Martha Maiden

Earth Science Data Systems, Science Mission Directorate, NASA Headquarters,
300 E St. SW, Washington, DC 20546, USA

Edward Masuoka

Terrestrial Information Systems Branch, NASA Goddard Space Flight Center,
Greenbelt, MD 20771, USA

Matthew McCabe

Department of Civil and Environmental Engineering, University of New South
Wales, Sydney, NSW 2052, Australia

Akira Miura

Earth Remote Sensing Data Analysis Center, Forefront Tower,
3-12-1 Kachidoki, Chuo-ku, Tokyo, 104-0054, Japan

Tomoaki Miura

Department of Natural Resources and Environmental Management,
University of Hawaii, Honolulu, HI 96822, USA

Matthias S. Möller

Austrian Academy of Sciences–GIScience, Schillerstraße 30,
5020 Salzburg, Austria

Jeffrey Morisette

Fort Collins Science Center, 2150 Centre Ave, Fort Collins, CO 80525, USA

Amit Mushkin

Geological Survey of Israel, 30 Malkhe Israel St, Jerusalem, 95501, Israel

Ranga Myneni

Department of Geography and Environment, Boston University,
Boston, MA 02215, USA

Evelyn Nakamura

Raytheon Information Solutions, 5700 Rivertech Court,
Riverdale, MD 20737, USA

Tomoko Nakano

Department of Economy, Chuo University, Japan

Ramakrishna R. Nemani

NASA Ames Research Center, Moffett Field, CA 94035, USA

Maik Netzband

Helmholtz Centre for Environmental Research-UFZ, Leipzig, Germany

Jaime Nickeson

Terrestrial Information Systems Branch, NASA Goddard Space Flight Center,
Greenbelt, MD 20771, USA

Dennis Ojima

The H. John Heinz III Center for Science, Economics and the Environment,
900 17th Street, NW, Washington, DC 20006, USA

Kelley O'Neal

Department of Geography, University of Maryland, College Park,
MD 20742, USA

Sandra Perry

Perry Remote Sensing LLC, 22 Sedgwick Drive, Englewood,
CO 80110, USA

Robin Pfister

NASA Goddard Space Flight Center, Greenbelt, MD 20771, USA

David Pieri

NASA Jet Propulsion Laboratory, California Institute of Technology,
Pasadena, CA 91109, USA

Dan Plafcan

Department of Science, Technology, and Society, School of Engineering
and Applied Science, 351 McCormick Road, A237 Thornton Hall,
University of Virginia, Charlottesville, VA 22904, USA

Cid Praderas

Science Systems and Applications, Lanham, MD 20706, USA

Jeff Privette

Remote Sensing and Applications Division, NOAA National Climatic
Data Center, Asheville, NC 28801, USA

Bhaskar Ramachandran

NASA LP DAAC, USGS Center for Earth Resources Observation and Science,
Sioux Falls, SD 57198, USA

H.K. Ramapriyan

NASA Goddard Space Flight Center, Greenbelt, MD 20771, USA

Bruce H. Raup

National Snow & Ice Data Center, University of Colorado,
Boulder, CO, USA

John M. Reynolds

Reynolds International Ltd, Mold, Flintshire CH7 1XP, UK

George A. Riggs

Science Systems and Applications Inc., Lanham, MD 20706, USA

Tamara Rockvam

NASA LP DAAC, USGS Center for Earth Resources Observation and Science,
Sioux Falls, SD 57198, USA

David Roy

Geographic Information Science Center of Excellence, South Dakota State
University, 1021 Medary Ave, Wecota Hall, Brookings SD 57007, USA

Steven W. Running

Numerical Terradynamic Simulation Group, University of Montana,
Missoula, MT 59812, USA

Nazmi Saleous

Department of Geography, United Arab Emirates University,
P.O. Box 15551, Al-Ain, United Arab Emirates

Vincent Salomonson

NASA Goddard Space Flight Center (Emeritus), University of Utah, Greenbelt,
MD 20771, USA

Andrey Savtchenko

Wyle Information Systems, Lanham, MD, USA

Crystal Barker Schaaf

Department of Geography and Environment, Boston University, Boston,
MA 02215, USA

Nikolay Shabanov

Department of Geography and Environment, Boston University,
Boston, MA 02215, USA

Christiane Schmullius

Friedrich-Schiller University, Geoinformatik und Fernerkundung, Institut für
Geographie, Abteilung Fernerkundung, Lobdergraben 32, 07743, Jena, Germany

Elisabeth Schöpfer

Zentrum für GeoInformatik (Z_GIS), Hellbrunnerstraße 34,
A-5020 Salzburg, University of Salzburg, Austria

W. Schroeder

Department of Geography, University of Maryland,
College Park, MD 20742, USA

Alain Sei

Algorithms, Models and Simulation Department, Northrop Grumman
Space Technology, Redondo Beach, CA 90278, USA

Ashbindu Singh

Division of Early Warning & Assessment-North America,
United Nations Environment Programme (UNEP), 1707 H Street,
N. W., Washington, DC 20006, USA

Scott Sinno

Terrestrial Information Systems Branch, NASA Goddard Space Flight Center, Greenbelt, MD 20771, USA

Robert Sohlberg

Department of Geography, University of Maryland, College Park, MD 20742, USA

Karla Sprenger

NASA LP DAAC, USGS Center for Earth Resources Observation and Science, Sioux Falls, SD 57198, USA

Alan H. Strahler

Department of Geography and Environment, Boston University, Boston, MA 02215, USA

Hongbo Su

Center for Research on Environment and Water, 4041 Powder Mill Road, Calverton, MD 20705, USA

Z. Su

International Institute for Geo-Information Science and Earth Observation (ITC), Hengelosestraat 99, 7514 AE Enschede, Netherlands

Abe Taaheri

Raytheon Information Systems, Riverdale, MD, USA

Wataru Takeuchi

Institute of Industrial science, University of Tokyo, 7-3-1 Hongo, Bunkyo-ku, Tokyo 113-8656, Japan

Thierry Toutin

Natural Resources Canada, Canada Centre for Remote Sensing, 580 Booth, Ottawa, ON, K1A 0E4, Canada

John Townshend

Department of Geography, University of Maryland, College Park, MD 20742, USA

Jeff Tschirley

Food and Agriculture Organisation of the United Nations, Environment and Natural Resources Service (SDRN), Viale delle Terme di Caracalla, 00153, Rome, Italy

Michael Teague

Terrestrial Information Systems Branch, NASA Goddard Space Flight Center, Greenbelt, MD 20771, USA

Kurt Thome

Optical Sciences, University of Arizona, Meinel Building, 1630 East University Boulevard, Tucson, AZ 85721, USA

Hideyuki Tonooka

Department of Computer & Information Sciences, Ibaraki University,
4-12-1, Nakanarusawa-cho, Hitachi 316-8511, Japan

Minoru Urai

Geological Survey of Japan, AIST, Tsukuba, Ibaraki, Japan

Eric Vermote

Department of Geography, University of Maryland,
College Park, MD 20742, USA

Raghuveer Vinukollu

Department of Civil and Environmental Engineering,
Princeton University, Princeton, NJ 08544, USA

Zhengming Wan

ICESS, University of California, Santa Barbara, CA 93106, USA

Hiroshi Watanabe

National Institute for Environmental Studies, 16-2 Onogawa,
Tsukuba-shi, Ibaraki, 305-8506, Japan

Beth Weinstein

NASA Goddard Space Flight Center, Greenbelt, MD 20771, USA

Darrel Williams,

NASA Goddard Space Flight Center, Greenbelt, MD 20771, USA

David F. G. Wolfe

Department of Environmental Science, Alaska Pacific University,
Anchorage, AK 99508, USA

Robert Wolfe

Earth Sciences Directorate, NASA Goddard Space Flight Center,
Greenbelt, MD 20771, USA

Eric Wood

Department of Civil and Environmental Engineering,
Princeton University, Princeton, NJ 08544, USA

Karl Wurster

Department of Geography, University of Maryland, College Park,
MD 20742, USA

Xiaoxiong Xiong

Earth Sciences Directorate, NASA Goddard Space Flight Center,
Greenbelt, MD 20771, USA

Yasushi Yamaguchi

Nagoya University, Graduate School of Environmental Studies,
D2-1(510), Furo-cho, Chikusa-ku, Nagoya City, 464-8601, Japan

Yoshifumi Yasuoka

National Institute for Environmental Studies, 16-2 Onogawa,
Tsukuba-shi, Ibaraki, 305-8506, Japan

Marco Zapata

Unidad de Glaciología y Recursos Hídricos, Instituto Nacional de Recursos
Naturales (INRENA), Av. Confraternidad Internacional Oeste 167, Huarás,
Ancash, Peru

Xiaoyang Zhang

Department of Geography and Environment, Center for Remote Sensing,
Boston University, Boston, MA 02215, USA

Maosheng Zhao

Numerical Terradynamic Simulation Group, University of Montana,
Missoula, MT 59812, USA

The Earth Observing System and the Evolution of ASTER and MODIS

Global environmental change is a constant theme that resonates in practically all physico-ecological and socio-economic systems worldwide. NASA's early endeavors in space-based Earth observations include the Earth Resources Technology Satellites (later dubbed Landsat), Seasat, and the Nimbus series. NASA initiated the Mission to Planet Earth in the early 1990s, which later became the Earth Science Enterprise (ESE) primarily to study and understand all interacting components of the Earth as a dynamic system. The Earth Observing System (EOS) mission consists of a space-based Earth observing system, a data and information system (EOSDIS), and a scientific research program. Three successful, EOS satellite platforms were launched between December 1999 and July 2004, and remain operational to date. Each carries a specialized payload of remote sensing instruments, which provide the first coordinated and simultaneous measurements of the interactions of the oceans, atmosphere, solid Earth, and hydrological and biogeochemical cycles.

Land science studies mainly benefit from the first two EOS satellite platforms, Terra (launched in December 1999) and Aqua (launched in May 2002). Terra contains the Moderate resolution Imaging Spectroradiometer (MODIS) and Advanced Spaceborne Thermal Emission and Reflection Radiometer (ASTER) among its five instruments, while Aqua contains a MODIS instrument as one of six others. The opening chapter traces the history and evolution behind the development and implementation of these two instruments, which constitutes the central focus of enquiry in this compendium (Salomonson et al. – *in this volume*). MODIS and ASTER are unique instruments with different footprints, observation duty cycles, and dedicated application communities. Notwithstanding their spatial, spectral, and temporal resolutions and specifications, they continue to facilitate distinct, and on occasion, synergistic science applications. Sections 4 and 5 in this volume provide representative examples of those applications.

NASA's EOSDIS is the fundamental infrastructure to support the EOS science mission. It provides the vital ground-based data and information management system, which facilitates both the EOS and pre-EOS missions as well as other data sources (Pathfinder, NASA-funded field campaigns, and human dimensions-derived data). EOSDIS caters to a wide variety of services from data capture,

telemetry processing, and spacecraft command and control to data production, archive, management, and distribution. It includes a number of widely distributed components ranging from the eleven data centers, science investigator-led processing systems, EOS data operations system, EOSDIS core system, EOS Clearinghouse, Flight Operations Segment, EOS networks, and polar ground stations.

The EOSDIS data centers process, archive, and distribute over 2400 Earth science data products from current and past satellite-derived and field programs. Currently, EOSDIS supports daily production volumes of over 3 terabytes of Earth science data collectively from all these sources. The eleven data centers archive over 4 petabytes of data and products. The design and architecture of such a complex system makes EOSDIS challenging indeed. The second chapter provides a narrative on the philosophy and architecture of the EOSDIS (Maiden – *in this volume*). EOSDIS, from its original conception to its present incarnation reinforces the fundamental importance of satellite-derived data and information, and how an efficient, operational data management infrastructure is imperative to scientific investigations of global environmental change at regional and global scales. EOSDIS also provides the framework for future international cooperative efforts like the Global Earth Observing System of Systems (GEOSS), where providing reliable access to data and information will largely determine the success of Earth science applications globally.

The EOSDIS core system (ECS) is a key component of the EOS science mission. Some of the ECS requirements were descoped during Terra's pre-launch phase, but it provides a set of core capabilities, which contribute to the systems engineering of the data and information management systems at the Distributed Active Archive Centers (DAAC). They include the following functions and capabilities: software engineering, Science Data Processing toolkit development and maintenance, ECS metadata and Earth Science Data Types (ESDT) development, and hardware specifications and support. ECS was primarily developed to support very large volumes of data at each data center, and provide all complementary functions related to ingest, processing, archival, distribution, science data product releases and decommissioning, science quality and metadata management, and data management. The ultimate purpose of such a massive, distributed system is to cater to the science data search, discovery, and distribution needs of large, disparate, and diverse national and international user communities. The science products distributed include a vast array of multispectral and multitemporal data products, whose science applications contribute to further our understanding of global environmental change.

The challenges to manage enormous data volumes within a dynamic ingest, production and distribution framework, and a multi-petabyte archive only grow with time. ECS continues to evolve and grow in concert with the constant advances in information technology, and software and hardware engineering. ECS' growth over the years since the 1993 System Requirements Review has produced valuable lessons learned from the engineering experience (Nakamura – *in this volume*). Engineering lessons learned also include how mode management can provide cost-effective virtual implementations of multiple baselines, and how DAAC-

specific system customization proves cost-effective. Overall, all lessons learned indicate how far the ECS has evolved to the point of facilitating universal access to all the land data products via a spinning disk-based online archive.

ASTER and MODIS: Instrument Design, Radiometry, and Geometry

The Earth Observing System (EOS) mission offers remote sensing data and derived products acquired from observations collected from different multispectral and sounding instruments. Two of them, ASTER and MODIS, are the focus of this volume. The ASTER instrument aboard the Terra platform generates data at high to medium spatial resolutions, whose derived products cater to a number of geological, geophysical, and biophysical applications. The twin MODIS instruments aboard the Terra and Aqua platforms offer data at moderate spatial resolutions designed to furnish inputs for the terrestrial, oceanic, and atmospheric science models and applications. Both remote sensing instruments owe their pedigree to previous sensors. Overall, ASTER advanced the direction charted by Landsat Thematic Mapper and Satellite Pour l'Observation de la Terre (SPOT) with certain enhancements. The ASTER Visible and Near Infrared (VNIR) sensor is based on the technology used in the Multi-spectrum Electronic Scanning Radiometer (MESSR) optical sensor carried by the Japanese Marine Observation Satellites (MOS-1 and MOS-1B), and the Optical Sensor (OPS) aboard the Japanese Earth Resources Satellite-1 (JERS-1). ASTER's Shortwave Infrared (SWIR) sensor follows the design of the SWIR radiometer aboard JERS-1. ASTER's Thermal Infrared (TIR) sensor was a completely new development, with fabrication knowledge drawn from MOS-1. The MODIS instrument's land imaging component builds upon second and third generation sensor systems, which include the Advanced Very High Resolution Radiometer (AVHRR), and the Landsat Thematic Mapper instruments. It further includes additional spectral bands in the middle- and longwave infrared wavelengths. The two practically identical MODIS instruments (aboard Terra and Aqua) cross the equator at different times, and their continuous four acquisitions per day ensures a multi-temporal, global data record, which is a critical requirement for monitoring global changes in the Earth's lands, oceans, and atmosphere.

The ASTER instrument emerged from early blueprints and designs, and later collaborations, which include the Thermal Infrared Multispectral Scanner (TIMS) and Thermal Infrared Ground Emission Radiometer (TIGER) on the U.S. side, and the Intermediate Thermal Infrared Radiometer (ITIR) on the Japanese side. Japan was responsible for the complex task of building and assembling the three different instrument systems, cryocoolers, and master power supply. The instrument design incorporates a stereoscopic assembly as part of the VNIR sensor, enhanced spatial and spectral resolutions, and instrument pointing capabilities (Fujisada – *in this volume*). The wisdom in implementing independent design and functionality in each of the three sensor subsystems was well justified by later problems experienced

with the SWIR sensor. ASTER's geometric accuracy specifications including both inter- and intra-telescope registration, and pixel geolocation knowledge, have remained exceedingly better than the original goals. ASTER digital elevation data provide the basis for a vital 30-meter spatial resolution global DEM product, which was released to the public in 2009 summer.

The sensor electronics in any electro-optical remote sensing system are expected to experience a change in their response over time. The radiometric quality requires consistent monitoring to understand and characterize the system response behavior as a precursor to calibration. ASTER's radiometric calibration and atmospheric correction processes help create accurate geophysical data products. The ASTER VNIR and SWIR sensors incorporate redundant on-board calibration hardware. They include on-board calibrators, and also accommodate independent vicarious calibration approaches. ASTER's radiometric calibration and atmospheric correction processes address two distinct spectral regions, the solar reflective (VNIR and SWIR), where reflected sunlight is the principal source, and the TIR, where emitted terrestrial radiation is the main source. These processes facilitate conversion of the solar reflective digital numbers to at-sensor reflectance and spectral radiance (Arai et al. – *in this volume*). Another issue also addressed is the SWIR crosstalk problem, which was identified and analyzed early in the post-launch mission. The TIR sensor has a fixed telescope with mechanical scanning and pointing functions performed by a scanning mirror. For calibration purposes, the scanning mirror rotates 180° from nadir to view an internal blackbody with a greater than 0.99 emissivity. This particular dual scanning/pointing mirror design does not allow observations of the deep space, and permits only a single temperature measurement for each Earth observation. ASTER TIR calibration uses both onboard and vicarious calibration approaches. The ASTER level-1B TIR scaled at-sensor radiance data are atmospherically corrected using a radiative transfer model (Tonooka – *in this volume*).

MODIS is a unique example of a multispectral, cross-track scanning radiometer that acquires continuous, multi-temporal, global data at moderate resolutions from both its Terra and Aqua incarnations. This allows the MODIS science mission to generate a wealth of moderate resolution data products at sufficient spectral and temporal granularity to monitor global environmental processes. Santa Barbara Remote Sensing built both MODIS instruments per NASA's specifications. The major component systems include the mainframe, imaging radiometer, optical system, scan mirror assembly, radiative cooler, door assemblies, electronics systems, and on-board calibration systems. Its optical systems include a set of linear arrays with spectral interference filters located in four focal plane assemblies. They include the visible, near infrared, shortwave and midwave infrared, and longwave infrared, the latter two of which require cryogenic cooling of their detector arrays (Xiong et al. – *in this volume*).

A number of system design trade-offs enable a single MODIS instrument to meet the diverse data acquisition needs of the terrestrial, oceanic, and atmospheric elements. The MODIS instrument design incorporates spectral channels specifically to help characterize atmospheric effects as well as clouds, which information is also used to atmospherically correct the land surface observations besides

providing crucial atmospheric measurements as well. Another major MODIS advance since the AVHRR era is its incorporation of a sophisticated array of on-board calibration hardware used in recent remote sensing history. They include a solar diffuser, solar diffuser stability monitor, spectroradiometric calibration assembly, and full aperture blackbody. They facilitate radiometric calibration of the solar reflective and thermal emissive bands, whose calibration uncertainty at typical scene radiances are maintained within specifications.

The MODIS instrument's scanning method is more advanced in its style of Earth observation. In contrast to single-line-per-scan sensors like AVHRR and SeaWiFs, MODIS observes 40 lines of 250 m resolution and 20 lines of 500 m resolution within a single ten-line (1 km resolution) scan. Therefore, the MODIS pixel size increases with scan angle, which overlaps along the scan borders every 10 lines. These unique characteristics produce the panoramic "bow-tie effect" at the scan edges. Given such a wide field-of-view, the MODIS instrument contends with unique sensing geometries and the Earth's curvature to produce a swath width that is roughly 2340 km. The along-track and along-scan geolocation accuracies between the Terra and Aqua MODIS instruments vary slightly, but in general are much better than the specifications. Specific correction approaches are implemented to ensure that the geolocation of individual MODIS observations conform to sub-pixel accuracies, which facilitate terrestrial global change science applications.

ASTER and MODIS: Data Systems

Global change research and applications strongly depend on a continuous, reliable, and assured data and information stream to produce meaningful long-term results. Each EOSDIS data center contains the organizational structures to perform data management, which literally provides the foundation for a large science and research enterprise. The EOSDIS experience with its distributed data centers across the country provides ample evidence of the engineering complexity and challenges involved in operating such an enterprise. The first section of this volume looks at EOS evolution, and establishes the framework for the EOSDIS infrastructure, and also outlines engineering lessons learned from nearly a decade of operations. EOSDIS is constantly evolving and responding to the advances in information technology, and software and hardware engineering. Nevertheless, it is indisputable that in accordance with Moore's law, advances in hardware outpace those in the software field, a well-known experience across EOSDIS and its data centers. This section provides insights into how EOS land data are managed at two different data centers, how those data are distributed to the users, and the role of the Hierarchical Data Format (HDF) in rendering a common data exchange foundation across the EOS mission.

The ongoing history and evolution of the Landsat program was largely responsible for the creation of the U.S. Geological Survey's Earth Resources Observation

and Science (EROS) Center outside Sioux Falls, South Dakota. Given its proficiency in managing the world's largest collection of remotely sensed land data, it was the logical choice to archive and manage EOS land collections from the MODIS and ASTER missions. The Land Processes Distributed Active Archive Center (LP DAAC) was established in 1990 to manage MODIS and ASTER land data products. ASTER level-1 products are transmitted from the Ground Data System (GDS) facility in Tokyo to LP DAAC, where higher-level ASTER data products are generated (Watanabe et al. – *in this volume*). As part of a pre-launch descope of EOSDIS, the MODIS data production component was moved under Science Team management to the MODIS Adaptive Data Processing System (MODAPS) at the NASA Goddard Space Flight Center (GSFC) (Masuoka et al. – *in this volume*). MODAPS produces and transmits MODIS land products to the LP DAAC and the National Snow and Ice Data Center (NSIDC) DAAC for distribution. To date, the LP DAAC remains one of the largest data centers with over 1 petabyte archived data volume, and serves a vast national and international user community. The MODIS snow and sea ice products were logically destined for the NSIDC at the University of Colorado's Cooperative Institute for Research in Environmental Sciences in Boulder, Colorado. The NSIDC DAAC was established in 1993, and hosts and distributes cryospheric products from other EOS and heritage sensors as well. The variety of data products at NSIDC includes brightness temperature data, polar atmospheric data, remote sensing-derived satellite images, sea ice, snow cover, and ice sheet data. Consistent with EOSDIS' evolution, both data centers continue to maintain sustaining engineering activities, and after a decade of data stewardship, both centers have transitioned from serving data stored on a near-line archive to a direct, instantaneous online access capability (Daucsavage et al. – *in the volume*).

Both DAACs rely on EOSDIS-provided generic search, discovery, order and distribution tools to serve MODIS and ASTER data users (Ramapriyan et al. – *in this volume*). These tools have evolved in the last two decades, and include the Version-0 Information Management Subsystem (V0-IMS), EOS Data Gateway (EDG), Warehouse Inventory Search Tool (WIST), EOS Clearinghouse (ECHO), and EOS Data Pools. Both DAACs also provide data discovery tools, some of which also accommodate certain data services. Service-oriented architecture is defining the future of our data discovery and distribution systems. A good example in the EOSDIS context is ECHO, which is a metadata brokerage system to facilitate a wider use of NASA's EOS data products. It provides registries for both EOS metadata and data services through which, clients and users may search, browse, order and access online data from multiple EOS data providers. All ECHO services are offered to the public through Internet-accessible Application Programming Interfaces. The continuing focus on technology infusion, Web services architecture, Open GIS, and Open Geospatial Consortium standards are likely to define the future trends in how Earth science data are distributed to applied researchers and scientists.

NASA anticipated global change research to involve very large volumes of data stemming from multiple instruments and sensors. These data comprise diverse

product suites with varying complexity in size, dimensions, and metadata. A critical requirement was data storage, retrieval and access from multiple data repositories by a globally distributed user community. The requirements for a portable, multi-object, and platform-independent format led NASA to pick HDF in 1993. HDF was originally developed in 1988 by the National Center for Supercomputing Applications to store, organize, and represent large mathematical arrays in heterogeneous computing network environments. HDF supports a number of different data models including multidimensional arrays, raster images and tables.

HDF-EOS is a specific implementation of HDF to handle EOS data products. EOS-specific data models were developed to handle grid, swath, and point structures, which facilitates geospatial queries based on Earth coordinates and time (Klein et al. – in this volume). Notwithstanding its elegant data structure, HDF presented some teething troubles, which both the commercial and non-commercial software development and user communities have helped overcome.

ASTER Science and Applications

The ASTER mission completes a decade of successful operations in December 2009. Given the historical evolution of the EOS program, as exemplified by the opening chapter in this volume (Salomonson et al.), the success of the ASTER mission owes a large part to the bilateral cooperation between the U.S. and Japan. This section provides an eclectic selection of ASTER science applications, which cover a variety of geosciences indicative of the ASTER instrument's multispectral and spatial versatility. The ASTER Data System (Watanabe et al. – *in this volume*) describes how U.S. and Japan's cooperation resulted in an infrastructure to command and control the complex data acquisitions on a daily basis. This includes both complementary and duplicative processing systems to acquire raw ASTER data, convert them to geophysical data products, and archive and disseminate them to users via an online ordering interface.

The ASTER instrument's unique capabilities with multispectral thermal infrared and short wavelength infrared channels are extremely well suited to study and monitor volcanoes. ASTER is also capable of measuring changes in thermal phenomena, such as lava domes, fumaroles, and crater lakes. In addition, the thermal bands allow measurement of sulfur dioxide gas emissions, a potential precursor for volcanic eruptions (Urai and Pieri – *in this volume*). Geologic mapping highlights one of the real strengths of the ASTER instrument: the presence of multispectral capability in the short wavelength infrared part of the spectrum. Many rock-forming minerals, in this part of the spectrum, evince diagnostic spectral absorption features, which help researchers to either separate and/or identify them. This facilitates mineral resource exploration enormously, as evidenced in the Mt. Fitton, South Australia case study (Hewson and Cudahy – *in this volume*). This subject extends into mining applications, which focuses on mineral exploration capabilities exemplified by copper mining in Iran, Chile, and Mongolia (Perry and Kruse – *in*

this volume). It provides a demonstration on how to use ASTER data for reconnaissance mineral prospecting with insights on scaling up from the regional to the district levels before committing geologists on the ground.

Glaciology is another Earth science discipline, which benefits from the ASTER instrument. The Global Land Ice Measurements from Space (GLIMS) project, headed by the U.S. Geological Survey, relies on satellite-derived data, primarily ASTER, to study and monitor thousands of glaciers in every continent. Satellite-derived data helps glaciologists highlight the role of glaciers as indicators of climate change, and as potential contributors to global sea-level change. They also help monitor the direct dangers posed by glacial hazards to people and infrastructure. Examples of glacial hazard impacts include those from South America and Central Asia, where lives were lost, and threats due to changes in glacial behavior continue (Kargel et al. – *in this volume*).

Urban ecology presents interesting challenges to try and resolve with remotely sensed data. The ASTER instrument affords a good spatial and spectral complement to study urban ecology. Two examples in this volume attest this capability. An urban heat balance analysis evaluates ASTER data applications in urban studies. The urban heat island effect results in increased local atmospheric and surface temperatures in urban areas compared to their surroundings. This results from the conversion of natural surfaces to artificial ones like asphalt streets, tarred roofs, and concrete roadways. ASTER thermal infrared images, particularly nighttime acquisitions, offer the data necessary to measure the temperature differences, and provide inputs for local weather perturbation, energy loading, and water runoff models (Kato and Yamaguchi – *in this volume*). ASTER data constitute an important part in the Urban Environmental Monitoring (UEM) project at Arizona State University. A major UEM project goal is to monitor 100 cities worldwide, and characterize their urbanization profiles, heat island effects, effects on peri-urban environment, and growth. ASTER data use is complemented by other, higher-resolution satellite data, which can resolve individual urban objects (Netzband et al. – *in this volume*).

ASTER and MODIS data are jointly used to estimate methane emission in the West Siberian Lowland, the world's largest high-latitude wetland ecosystem (Takeuchi et al. – *in this volume*). ASTER data are initially used to map land cover types in six wetland ecosystems, and supplemented by field observations followed by a spectral mixture analysis between Terra MODIS and ASTER data of same timeframes. Field measurements of methane production for each land cover type are scaled up for both ASTER and MODIS data, and their coverage fraction at the sub-pixel level is derived via a spectral mixture analysis. The average emission rates and the fractional coverage in each MODIS pixel help derive the methane emission estimates for the whole area.

A unique design feature of the ASTER instrument is its ability to generate stereoscopic data with which to build digital elevation models (DEM). ASTER acquires along-track stereo images, which eliminates the problem of dynamic viewing conditions that plague instruments that acquire cross-track image pairs from different orbits. Two chapters deliberate on stereoscopic views with very different

goals. The first deals exclusively with ASTER-derived DEMs (Toutin – *in this volume*). It provides detailed accounts of both ASTER and DEM stereoscopy, and the U.S. and Japanese DEM production systems. Since this chapter was written, the ASTER mission has released a Global Digital Elevation Model (GDEM), covering the entire global land surface from 83 degrees north and south, at 30 m postings. GDEM, to date, is the most complete, and highest-resolution DEM available outside the classified, military world. ASTER’s stereoscopic skills are used in a novel approach to determine the roughness of the Earth’s surface (Mushkin and Gillespie – *in this volume*). It determines the amount of shadow (and hence, roughness) by comparing the amount of shadow within a pixel viewed from two different view-directions. Surface roughness is a key parameter in many geological, hydrological, and planetary studies. It further provides an essential variable in remote sensing applications, and a critical input to atmosphere-surface boundary layer energy-exchange models.

All the preceding selections demonstrate how the ASTER instrument contributes to specific scientific applications and enquiries. They all depend on the physics of remote sensing along with engineering design, which provides the basis to facilitate the three sensor systems specializing in different parts of the electromagnetic spectrum. The final selection on “Technoscientific Diplomacy” (Plafcan – *in this volume*) delineates the international politics of technical decision-making and scientific judgment, which successfully led to the development of the ASTER remote sensing system. Bilateral cooperation and collaboration between Japan and U.S. is ultimately credited with the success of the ASTER mission. Several scientists, engineers, and government officials from both countries were responsible in articulating the political calculus, which catalyzed collective judgment, and a shared interest to advance and achieve common international scientific goals.

The Landsat satellite program remains a pioneer in land remote sensing for nearly four decades. Set against the origin and evolution of that program, Goward et al. (*in this volume*) deliberate upon the future of Landsat-class remote sensing. They assess the current status of Landsat-class observatories, the immediate future plans, the next phase in this class of observations, and possible future mission goals. Given the developments in the U.S. National Land Imaging Program, and the international convergence on a Global Earth Observing System of Systems, the Landsat-class of observations are poised to continue their contributions to long-term global monitoring well into the future.

MODIS Science and Applications

The requirements for the MODIS instrument were developed in the late 1980s, when the imaging requirements for the NASA Earth Observing System (EOS) were being developed (Justice et al. – *Chapter 34 in this volume*). At that time, the community was benefiting from the optimized design of Landsat 5 Thematic Mapper and the daily temporal frequency of the NOAA AVHRR for vegetation monitoring.

The next logical step for the land community was to develop a sensor with the daily, temporal frequency of the AVHRR and the spectral band selection of the Thematic Mapper. This basic requirement was enhanced to provide global coverage at increased spatial resolution over the AVHRR, with additional capability for thermal remote sensing (including fire), and bands placed to facilitate cloud detection and atmospheric correction. The strength of this combination has now been well demonstrated by MODIS research and applications. MODIS proved superior to the AVHRR in band-placement, spatial resolution, calibration and geolocation, and has become the instrument of choice for coarse resolution land monitoring. Since MODIS was launched, other international instruments have adopted similar capabilities, including the French SPOT Vegetation instrument and the Japanese Global Land Imager (GLI), which included multiple 250m channels.

The EOS data system proved a challenge in the early days of the program, particularly with respect to large volumes and loads associated with MODIS data. Innovative solutions were developed and implemented after the MODIS Science team inherited the responsibility of the MODIS processing system (Masuoka et al. – *in this volume*). Currently, several ways to access MODIS data exist. Tools exist to help users analyze the data and value-added data products and services developed by the Science Team and various data brokers. For example, the MODIS Rapid Response System provides quick access to data, and the Fire Information for Resource Management System (FIRMS) provides Web-GIS capabilities for MODIS fire data. The NASA Distributed Active Archive Center at the USGS EROS Center is the primary source for MODIS land products, which currently distributes over 30 Terabytes of data per month. The number of direct readout stations receiving MODIS data has also significantly grown. The development of shareware-code to generate similar land products has allowed ground stations to generate some new products with the cooperation of an international group formed to share their experience and code.

Dr. Vince Salomonson, who was formerly the Project Scientist for Landsat 5, formed and led the NASA MODIS Science Team. The team's success is partly attributed to Dr. Salomonson's two decades of leadership and personal commitment to the MODIS instrument design, its calibration and characterization, the data processing systems, and the Science Team. Under his guidance, the MODIS Science Team worked closely with the instrument developers and the EOS Data and Information System to overcome the initial obstacles encountered, and to identify their solutions. The science discipline sub-teams worked to develop the algorithms and products and provide outreach to the science and applications communities. The discipline sub-team developed to provide the land products (MODLAND) has made a number of important contributions to the field. In addition to growing the number of standard land products available to the science and applications communities, it developed an overarching approach to coarse resolution land product quality assessment and validation (Masuoka et al. – *in this volume*). All the MODIS land products are currently at Stage 2 or 3 validation. MODIS product validation and multi-scale research has greatly benefited from the collocation of the ASTER instrument on the Terra platform. The international community now recognizes the

need for land product validation, and the Land Product Validation (LPV) Working Group of the Committee on Earth Observation Satellites (CEOS) was established to support this requirement (Townshend et al. – *in this volume*).

The chapters in this section represent the status of all the MODIS land products at the time of writing (close to the completion of Collection 5), which was the fourth major reprocessing (Masuoka et al. – *in this volume*). The MODIS Surface Reflectance product provides state-of-the-art atmospheric correction and takes advantage of the MODIS bands selected for atmospheric characterization and provides a foundation for the higher-order vegetation products (Vermote et al. – *in this volume*). The MODIS Albedo and Reflectance Anisotropy product, championed by Dr. Alan Strahler in the early years of the MODIS program, provides an important product to study the surface energy budget (Schaaf et al. – *in this volume*). Relying on multiple observations to characterize the BRDF, this latter product benefits from having two MODIS instruments in orbit. Similarly, the MODIS Land Surface Temperature and Emissivity product intended for energy balance studies takes advantage of the two instruments (Wan and Li – *in this volume*). The Vegetation Index product builds and expands on the AVHRR NDVI legacy (Huete et al. – *in this volume*). The LAI product is designed for the study of fluxes of energy, mass, and momentum between the land source and the atmosphere (Myneni et al. – *in this volume*). The MODIS-derived Primary Production products under the direction of Dr. Steve Running were developed for use in both scientific and applied global vegetation studies (Zhao et al. – *in this volume*). The MODIS Fire products, developed in partnership with Dr. Yoram Kaufman from the MODIS Atmospheres Team, are used widely by the fire science and management communities around the world (Justice et al. – *Chapter 29 in this volume*). The MODIS Snow and Ice products were developed for a number of cryospheric and climate science purposes (Riggs and Hall – *in this volume*). The MODIS Land Cover products build on the legacy of the AVHRR 1km land cover product providing enhancements in a number of areas associated with the algorithm, the implementation and additional new information on vegetation dynamics (Friedl et al. – *in this volume*). The Vegetation Continuous Fields product pioneered by Drs. John Townshend and Matt Hansen, moves the community beyond land cover classification to direct parameterization of vegetation cover (Carroll et al. – *in this volume*). With the free and open access to MODIS data, a number of new and experimental products are being developed within the research community, and are in various stages of maturity. McCabe et al. (*in this volume*) provide an example for evapotranspiration developed within the Science Team. Since these chapters were submitted, the Collection 5 reprocessing for the MODIS land products was completed. Collection 6 reprocessing is currently in planning; this reprocessing will include additional improvements to some of the products and is scheduled for completion in 2011. At that time, the MODIS Collection will consist of 11 years of Terra data and 8 years of Aqua data. This consistent global data record will help detect trends in land surface characteristics, and provide the basis for science quality climate data records. Several geophysical products being derived from MODIS are identified as Essential Climate Variables (ECV) that are required to support the U.N. Framework Convention on Climate Change.

The MODIS instruments were launched in December 1999 and May 2002, and were designed for a 5-year on-orbit life. Both instruments continue to operate and perform satisfactorily. Aqua MODIS has performed somewhat better than Terra MODIS. Calibration monitoring of both instruments continues while the anticipated large-optics degradation is being quantified. Both instruments are subject to a NASA Senior Review every two years to determine their continued service. The data record from MODIS extends the AVHRR record, which started in the early 1980s. Developing the long-term record requires an understanding of the relationship between the instruments and benefits from an overlapping operation. The VIIRS instrument on the NPOESS Preparatory Project (NPP), currently expected to launch in October 2011, will continue the legacy of the MODIS land remote sensing in the operational domain (Justice et al. – *Chapter 34 in this volume*). Overlapping operation of NPP VIIRS with the Aqua MODIS will prove essential to help establish data continuity and the relationship between the land products from the two systems. We hope that the experience gained from MODIS in terms of the instrument characterization, data system, and land products can help the VIIRS mission continue a high quality, long-term data record of moderate resolution data and products for land science and applications.

Future Systems

While continuing to operate ASTER, Terra and Aqua MODIS, and Landsat-7, NASA is working on three future instruments that will continue systematic acquisition of coarse and mid-resolution data described in this volume. The Landsat Data Continuity Mission (LDCM), which is being developed in cooperation with the USGS, is the eighth in the Landsat series of polar orbiting scanners, and will extend the long history and unparalleled data record of the Landsat series, and more recently, ASTER data record. It will add two new bands to the Landsat-7 configuration: one for detecting cirrus clouds, and another for coastal zone observations. A standalone thermal sensor compatible with the Landsat system has been proposed and NASA is currently evaluating options to include this instrument on the LDCM, or flying it separately. LDCM is under construction, and is scheduled for launch in December 2012. The Hyperspectral Infrared Imager (HyspIRI) is a 2-instrument package (VSWIR hyperspectral scanner, and multispectral TIR scanner) recommended by the recent National Research Council's Decadal Survey. The mission is at the study stage, and decisions about its funding and schedule will occur in late 2009. The Visible Infrared Imaging Radiometer Suite (VIIRS) is being developed in partnership with DOD and NOAA as part of the NPOESS Preparatory Project expected to launch in October 2011. With successful deployment of these instruments, the science and applications communities can look forward to several years of continued systematic observations. The challenge facing the nation is how to transition the proven research satellite systems into the operational domain, and secure the long-term data record, which is imperative to study global climate and environmental change.

Part I

The Earth Observing System and the Evolution of ASTER and MODIS

Global environmental change is a constant theme that resonates in practically all physico-ecological and socio-economic systems worldwide. NASA's early endeavors in space-based Earth observations include the Earth Resources Technology Satellites (later dubbed Landsat), Seasat, and the Nimbus series. NASA initiated the Mission to Planet Earth in the early 1990s, which later became the Earth Science Enterprise (ESE) primarily to study and understand all interacting components of the Earth as a dynamic system. The Earth Observing System (EOS) mission consists of a space-based Earth observing system, a data and information system (EOSDIS), and a scientific research program. Three successful, EOS satellite platforms were launched between December 1999 and July 2004, and remain operational to date. Each carries a specialized payload of remote sensing instruments, which provide the first coordinated and simultaneous measurements of the interactions of the oceans, atmosphere, solid Earth, and hydrological and biogeochemical cycles.

Land science studies mainly benefit from the first two EOS satellite platforms, Terra (launched in December 1999) and Aqua (launched in May 2002). Terra contains the Moderate resolution Imaging Spectroradiometer (MODIS) and Advanced Spaceborne Thermal Emission and Reflection Radiometer (ASTER) among its five instruments, while Aqua contains a MODIS instrument as one of six others. The opening chapter traces the history and evolution behind the development and implementation of these two instruments, which constitutes the central focus of enquiry in this compendium (Salomonson et al. this volume). MODIS and ASTER are unique instruments with different footprints, observation duty cycles, and dedicated application communities. Notwithstanding their spatial, spectral, and temporal resolutions and specifications, they continue to facilitate distinct, and on occasion, synergistic science applications. Parts IV and V in this volume provide representative examples of those applications.

NASA's EOSDIS is the fundamental infrastructure to support the EOS science mission. It provides the vital ground-based data and information management system, which facilitates both the EOS and pre-EOS missions as well as other data sources (Pathfinder, NASA-funded field campaigns, and human dimensions-derived data). EOSDIS caters to a wide variety of services from data capture, telemetry processing, and spacecraft command and control to data production, archive, management, and distribution. It includes a number of widely distributed components ranging from

the 11 data centers, science investigator-led processing systems, EOS data operations system, EOSDIS core system, EOS Clearinghouse, Flight Operations Segment, EOS networks, and polar ground stations.

The EOSDIS data centers process, archive, and distribute over 2,400 earth science data products from current and past satellite-derived and field programs. Currently, EOSDIS supports daily production volumes of over 3 terabytes of earth science data collectively from all these sources. The 11 data centers archive over 4 petabytes of data and products. The design and architecture of such a complex system makes EOSDIS challenging indeed. The second chapter provides a narrative on the philosophy and architecture of the EOSDIS (Maiden this volume). EOSDIS, from its original conception to its present incarnation reinforces the fundamental importance of satellite-derived data and information, and how an efficient, operational data management infrastructure is imperative to scientific investigations of global environmental change at regional and global scales. EOSDIS also provides the framework for future international cooperative efforts like the Global Earth Observing System of Systems (GEOSS), where providing reliable access to data and information will largely determine the success of Earth science applications globally.

The EOSDIS core system (ECS) is a key component of the EOS science mission. Some of the ECS requirements were descoped during Terra's prelaunch phase, but it provides a set of core capabilities, which contribute to the systems engineering of the data and information management systems at the Distributed Active Archive Centers (DAAC). They include the following functions and capabilities: software engineering, Science Data Processing toolkit development and maintenance, ECS metadata and Earth Science Data Types (ESDT) development, and hardware specifications and support. ECS was primarily developed to support very large volumes of data at each data center, and provide all complementary functions related to ingest, processing, archival, distribution, science data product releases and decommissioning, science quality and metadata management, and data management. The ultimate purpose of such a massive, distributed system is to cater to the science data search, discovery, and distribution needs of large, disparate, and diverse national and international user communities. The science products distributed include a vast array of multispectral and multitemporal data products, whose science applications contribute to further our understanding of global environmental change.

The challenges to manage enormous data volumes within a dynamic ingest, production and distribution framework, and a multi-petabyte archive only grow with time. ECS continues to evolve and grow in concert with the constant advances in information technology, and software and hardware engineering. ECS' growth over the years since the 1993 System Requirements Review has produced valuable lessons learned from the engineering experience (Nakamura this volume). Engineering lessons learned also include how mode management can provide cost-effective virtual implementations of multiple baselines and how DAAC-specific system customization proves cost-effective. Overall, all lessons learned indicate how far the ECS has evolved to the point of facilitating universal access to all the land data products via a spinning disk-based online archive.

Chapter 1

Evolution of NASA's Earth Observing System and Development of the Moderate-Resolution Imaging Spectroradiometer and the Advanced Spaceborne Thermal Emission and Reflection Radiometer Instruments

Vincent Salomonson, Michael J. Abrams, Anne Kahle, William Barnes, Xiaoxiong Xiong, and Yasushi Yamaguchi

1.1 Introduction

This chapter provides insight into the development and implementation of two key instruments for NASA's Earth Observing System (EOS): the Moderate Resolution Imaging Spectroradiometer (MODIS) and the Advanced Spaceborne Thermal Emission and Reflection Radiometer (ASTER). A summary of the basis and evolution of the EOS sets the background and historical context for the development of these two instruments. MODIS and ASTER continue to provide data that improve understanding of the Earth-atmosphere processes and trends in various associated parameters. Additionally, they improve capabilities to monitor the Earth's natural resources.

1.2 Evolution of NASA's Earth Observing System

The use of spaceborne observations has grown exponentially since their inception nearly 60 years ago. The beginning of Earth-system science is traceable to the early V-2 rocket launches. (Herring and King 2001). Following World War II, the Naval Research Laboratory experimented with V-2 rockets and smaller vehicles called "sounding rockets." The first space-based picture (Fig. 1.1) was taken on March 7, 1947 from a V-2 ~100 miles above New Mexico. Subsequent pictures acquired by a scientist named Otto Berg showed a large tropical storm over Brownsville, Texas.

V. Salomonson (✉)

NASA Goddard Space Flight Center (Emeritus), University of Utah,
Greenbelt, MD 20771, USA

e-mail: vincent.v.salomonson@nasa.gov



Fig. 1.1 Picture taken from a V-2 rocket over New Mexico in 1947 (Herring and King 2001)

These images demonstrated the potential for spaceborne cameras to help understand the dynamic processes taking place in the Earth-atmosphere system.

The launch of Explorer-7 in 1959 provided an early attempt to study the Earth's radiation balance using a simple bolometer-based sensor. Verner Suomi, a Medal of Science winner from the University of Wisconsin, Madison, was the study's principal investigator.

America's experience with sustained satellite-based Earth observations began with the launch of Television InfraRed Observation Satellite (TIROS) from Cape Canaveral, Florida, in 1960 (Fig. 1.2a). In Fig. 1.2b, the satellite's vidicon camera points west towards Nova Scotia and the St. Lawrence River to photograph both clouds and sea/ice cover.

The two decades (1960–1980) following the launch of the TIROS-1 satellite saw an armada of satellites and accompanying sensors launched into low Earth orbit by the United States and other countries to understand Earth-atmosphere processes and trends better. Over time, the sensors became more capable, and the lifetime of the spacecraft and sensors increased. By the late 1970s and early 1980s, missions and accompanying sensors often operated for several years. Key missions launched and operated by the United States that demonstrated these points are Nimbus-7, TIROS-N, National Oceanic and Atmospheric Administration/NOAA-6, and the Landsat series. Nimbus-7, in particular, carried the Coastal Zone Color Scanner (CZCS), the Total Ozone Mapping Spectrometer (TOMS), and the Scanning Multichannel Microwave Radiometer (SMMR). The CZCS demonstrated how we could monitor biological activity in the surface waters of oceans from space. TOMS observations documented the existence and extent of the “ozone hole” over Antarctica, leading to efforts to limit injection of chlorofluorocarbons into the

atmosphere; and SMMR extended microwave observations that began with Nimbus-5 to document global and hemispheric trends in sea ice and snow cover extent for over 35 years. NOAA-6 carried the first of a series of Advanced Very High Resolution Radiometers (AVHRR) that have provided global observations of vegetation dynamics and processes spanning almost three decades; and the TIROS Operational Vertical Sounder (TOVS) package containing the High Resolution Infrared Sounder (HIRS), the Stratospheric Sounding Unit (SSU), and the

a

New York Times. CITY EDITION
 U. S. Weather Bureau Report (Page 28) - Forecast: Chance of rain today. Windy. 20-30, chance of showers tomorrow. Temp. today: 56-45; yesterday: 63.6-45.5.

NEW YORK, SATURDAY, APRIL 2, 1960. 12 cents beyond 10-mile zone from New York City. Extra 10¢ for Long Island. Higher in NY delivery zone. M FIVE CENTS

U.S. ORBITS WEATHER SATELLITE; IT TELEVISES EARTH AND CLOUDS; NEW ERA IN METEOROLOGY SEEN

2 CAMERAS USED
270-Pound Vehicle to Transmit Pictures for 3 Months

By RICHARD WITKIN
Special to The New York Times.
CAPE CANAVERAL, Fla., April 1—The first artificial satellite able to provide detailed photographs of the earth's weather was fired into orbit here today by the United States.

Two television cameras looking down from an altitude of about 450 miles made initial pictures of the earth's cloud patterns during the satellite's second orbital trip.

Four pictures, taken by the wider-viewing camera and therefore less-precise camera of the two, were proudly distributed this evening by the National Aeronautics and Space Administration. The space agency has over-all responsibility for the project.

The pictures showed the cloud cover that lay over the Gulf of the St. Lawrence River. The curvature of the earth was clearly recognizable.

President Sees Photos
 Before being made public, the pictures had been taken to the White House by Dr. T. Keith Glennan, the head of the agency.

SENT BY SATELLITE: One of TV pictures from Tiros 1 **CLOUDS: White mass is cloud cover on U. S. and Canada.**

1,014 BILLS LEFT FOR ROCKEFELLER
 Albany Weighs Effects of Legislative Session on Prestige of Leaders
 Summary of the 1960 session is printed on Page 10.
 By WARREN WEAVER Jr.
Special to The New York Times.
ALBANY, April 1—The adjournment of the Legislature early today left conflicting and confused opinions as to who had

SENATE REJECTS A REFEREE CURB
 Quarreling Marks Debate as Kefauver Plan Fails—Courts to Set Hearings
 By RUSSELL BAKER
Special to The New York Times.
WASHINGTON, April 1—In an afternoon of angry personal quarreling, the Senate killed the Kefauver amendment to the civil-rights bill today. The vote was 69 to 22.
 The amendment, sponsored by Senator Walter Kefauver

AREA: Same places as in TV photos, depicted on a globe

Fig. 1.2 Announcement of the TIROS-1 satellite launch on 1 April, 1960. (a) Front page of the New York Times, April 2, 1960. (b) The first television picture from space taken by the TIROS vidicon on April 1, 1960 (<http://www.nasa.gov/topics/earth/features/tiros1-50th.html>)

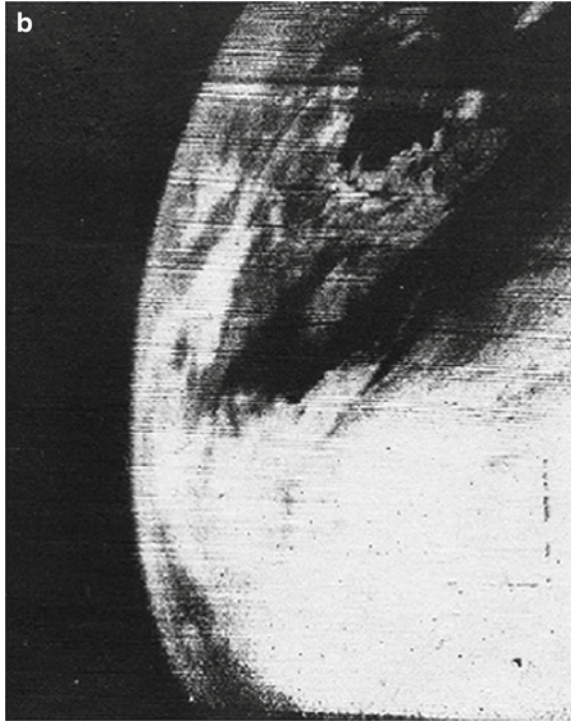


Fig. 1.2 (continued)

Microwave Sounding Unit (MSU) has provided vertical profiles of atmospheric temperature and water vapor for more than two decades. The Landsat missions made high-resolution detailed observations of the Earth's land features and their changes, beginning in 1972 and continuing to the present.

The above-mentioned satellites together with those developed and operated by other countries including notably Russia, Japan, India, Canada, Brazil, and the European Space Agency/ESA and associated countries such as France and England have shown that spaceborne observations can provide a long time-series of data which, especially in combination with in situ observations, have advanced our understanding of the Earth-atmosphere processes and trends. Assimilation of these observations into numerical models (e.g. General Circulation Models, or GCMs) remains especially powerful, leading to improved descriptive and predictive capabilities. These capabilities are increasingly needed to examine such questions as the relative roles of natural and anthropogenic causes to environmental change.

The 1970s and 1980s ushered in an era of growing concern that humans were more than just passive observers and passengers on what was called "Spaceship Earth." Evidence grew that humankind's ever-increasing demands on Earth's limited resources were degrading the land, ocean, and atmosphere systems that comprise our environment. Legislation calling for a National Climate Program was introduced

in 1975, and was eventually established by public law in 1978 (Pielke 2000). This law delegated responsibilities and roles for executing a climate program to various agencies, including NASA.

In the 1970s, NASA proposed a mission to Mars that would rely heavily on the space shuttle and a still undeveloped space station. This proposal eventually led to substantial support in the U.S. Congress for a broad-based solar-system exploration program that would bring NASA activities back to a level similar to that of the Apollo era, when NASA reached the Moon. Earth science had made substantial progress with unmanned spaceborne observations to monitor Earth-atmosphere processes, but NASA placed strong emphasis to human spaceflight efforts. For NASA, the question was how to merge programs based on unmanned platforms with human spaceflight.

In the early 1980s, NASA blended the Earth science efforts with the human spaceflight program by defining observational missions that would take advantage of the shuttle's cargo launch capabilities. This merger materialized despite the controversy and programmatic turbulence within and between federal agencies responsible for conducting climate and global-change studies. These efforts were initially designated "System Z." Its philosophy was to obtain funding support for spaceborne remote-sensing efforts from the human spaceflight budget [Taubes (1993) and Pielke (2000) provide a detailed description of the circumstances leading to System Z]. As explained by Pielke (2000), System Z became the EOS in 1983, and part of NASA's "Mission to Planet Earth" was established in 1987.

In the beginning, the System Z Earth-observation system was to consist of two, large (15-ton) platforms called EOS-A and EOS-B. Each would include a payload of approximately 15 instruments. This set of instruments would allow comprehensive observational efforts ranging from collecting data on the electric and magnetic fields of the Earth to improved instruments for acquiring observations of terrestrial processes and trends. These planned observations were based on instruments flown on the Nimbus series (Nimbus-7 being a prime example) that would extend previously acquired databases. In addition, newly planned future instruments included a Synthetic Aperture Radar (SAR), and a high spectral resolution, hyperspectral instrument (later called High Resolution Imaging Spectroradiometer, or HIRIS). Launching such large payloads was deemed possible using either the space shuttle or a Titan-4 rocket.

EOS-A was planned for launch in 1996 and EOS-B in 1998. The initial concept also indicated that a 15-year dataset was required for climate studies. This would require a repeat launch of each EOS satellite, since the projected lifetime of each satellite was five years. Cost estimates were ~\$30 billion at the outset, but soon were reduced to ~\$17 billion due to spending constraints mandated by the U.S. Congress. By 1991 (Taubes 1993) the U.S. Congress budget allocation was down to \$11 billion through the year 2000. Further review, debate, and discussion resulted in further downsizing, so that by 1993 the budget was only ~\$8 billion. The program was considerably downsized ("descoped" in NASA terminology). EOS-A and EOS-B were smaller than planned, and planned launches were delayed two years, until 1998 and 2000, respectively. The planned follow-on satellites were replaced by smaller ones, another cost-saving measure. In addition, all the electric and

magnetic field instruments were dropped, along with HIRIS, the SAR, and a tilting MODIS called MODIS-T, a companion instrument to the nadir MODIS-N (providing wide swath scanning, but did not tilt fore and aft along the satellite track), that was to fly on both EOS-A and EOS-B (NASA 1985b). MODIS-N and MODIS-T characteristics are provided in the next section of this chapter. Following the elimination of MODIS-T, MODIS-N was just called MODIS.

The results of all the planning efforts, discussions, and studies alluded to above are summarized in Fig. 1.3. The original sun-synchronous EOS-A mission was renamed “EOS-AM-1” because of its descending (north to south) polar orbit with an equator-crossing time of ~10:30 A.M. The name changed again to “EOS-Terra,” indicating the mission’s principal emphasis on land processes. Similarly, EOS-B, with its ascending (south to north) polar orbit and an equator-crossing time of ~1:30 P.M., was renamed “EOS-PM-1,” later changed to “EOS-Aqua” to highlight the mission’s principal emphasis on the hydrological cycle, the water budget, and the dynamics of the Earth-atmosphere system. Terra was launched in December 1999, and Aqua in May 2002. Both satellite platforms carry a MODIS instrument, but only the Terra platform carries the ASTER instrument.

The missions depicted in Fig. 1.3 span the time from 1997 to 2003. Together with the EOS Aura mission launched in 2004 and the Cloudsat and Calipso missions launched in 2006, this collection of missions represent a new level of

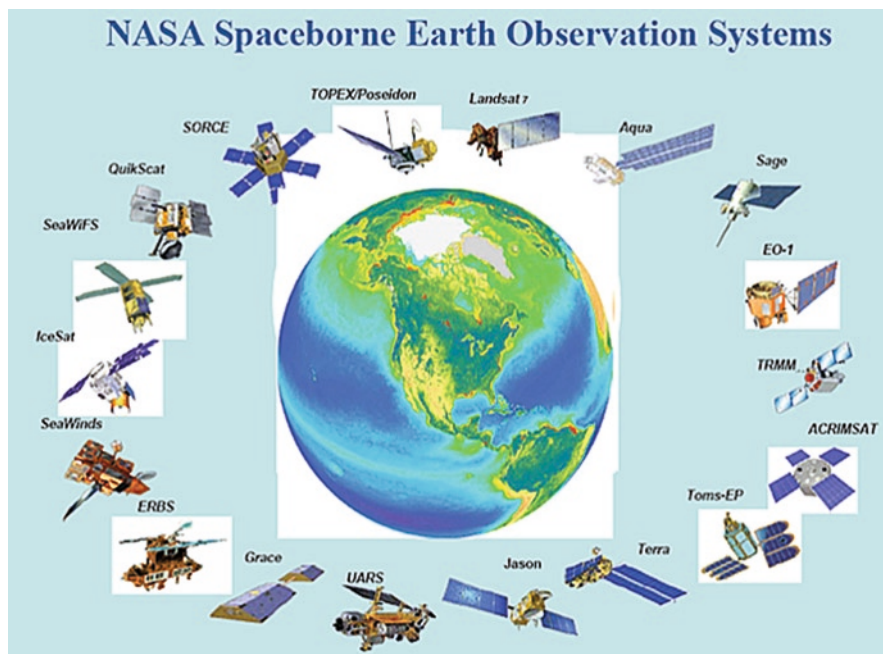


Fig. 1.3 NASA EOS missions flown from 1997 through 2003. The EOS Aura mission launched in 2004 extends studies of atmospheric chemistry beyond the scope of the Upper Atmosphere Research mission (UARS)

accomplishment for NASA in implementing spaceborne observations for Earth studies. A current list of the EOS satellites is available from http://eospsso.gsfc.nasa.gov/eos_homepage/mission_profiles/index.php.

The two instruments discussed in this chapter relate to the Terra and Aqua missions, whose payloads are as follows:

Terra (five instruments):

Advanced Spaceborne Thermal Emission and Reflection Radiometer (ASTER)
Multi-angle Imaging SpectroRadiometer (MISR)
Moderate Resolution Imaging Spectroradiometer (MODIS)
Measurement of Pollution In The Troposphere (MOPITT)
Clouds and Earth's Radiant Energy System (CERES)

Descriptions of each instrument are available at the following URL: <http://terra.nasa.gov/About/>.

Aqua (six instruments):

Advanced Microwave Scanning Radiometer (AMSR-E)
Atmospheric Infrared Sounder (AIRS)
Advanced Microwave Sounding Unit (AMSU)
Clouds and the Earth's Radiant Energy System (CERES)
Humidity Sounder for Brazil (HSB)
Moderate Resolution Imaging Spectroradiometer (MODIS)

Descriptions of each instrument are available at the following URL: <http://aqua.nasa.gov/about/instruments.php>.

The following sections are devoted to more detailed descriptions of the development of MODIS and ASTER.

1.3 Development, Characterization, and Performance of the Earth Observing System Moderate Resolution Imaging Spectroradiometer Sensors

This section examines the conceptual development, implementation, characterization, and calibration of MODIS, and concludes with a short overview of its present status and future.

1.3.1 Background

In the spring of 1983, NASA formed the EOS Science and Mission Requirements Working Group (EOSMRWG) to outline requirements for observing the Earth as a system from low Earth orbit. This group's report (NASA 1984) discussed the need for several new sensors, prominent among which was MODIS because of its capability

Table 1.1 MODIS instrument panel

| | Name | Affiliation |
|-----|-----------------------------------------|-------------------------------------------------|
| 1. | Wayne Esaias (Chairman) ^a | NASA Headquarters (HQ) |
| 2. | William Barnes (Secretary) ^a | NASA Goddard Spaceflight Center (GSFC) |
| 3. | Mark Abbott ^a | Scripps/Jet Propulsion Lab. (JPL) |
| 4. | Steve Cox | Colorado State University |
| 5. | Robert Evans ^a | University of Miami |
| 6. | Robert Fraser | NASA/GSFC |
| 7. | Alexander Goetz | NASA/JPL |
| 8. | Howard Gordon ^a (Ex-officio) | University of Miami |
| 9. | Christopher Justice ^a | University of Maryland |
| 10. | E. Paul McClain | National Oceanic and Atmospheric Administration |
| 11. | Marvin Maxwell | NASA/GSFC |
| 12. | Robert Murphy | NASA HQ |
| 13. | John Prospero | University of Miami |
| 14. | Barrett Rock | NASA/JPL |
| 15. | Steven Running ^a | University of Montana |
| 16. | Raymond Smith | University of California, Santa Barbara |
| 17. | Jerry Solomon | NASA/JPL |
| 18. | Michael Spanner (Ex-officio) | NASA/Ames Research Center (ARC) |
| 19. | Joel Susskind | NASA/GSFC |

^aMODIS Science Team Member (1989 – Present)

for frequent global surveys at ≤ 1 km spatial resolution. Then, in early 1984, NASA created six instrument panels to study requirements for the sensors identified by the EOSMRWG. One of these was the MODIS Instrument Panel consisting of 18 scientists and engineers under the direction of Dr. Wayne Esaias from NASA Headquarters (Table 1.1 – listing members and their affiliations at the time).

As discussed above, the MODIS Instrument Panel (Esaias 1986; Barnes 1985) divided the MODIS requirements between two sensors: MODIS-N (nadir) and MODIS-T (tilt). MODIS-N was similar to the Advanced Very High Resolution Radiometer (AVHRR), and MODIS-T was conceived as a fore-aft pointing imaging spectrometer similar to the Coastal Zone Color Scanner (CZCS). MODIS-T was expected to help in two areas: to minimize sun-glint “contamination” of images when measuring ocean color and to measure bi-directional reflectance over land. It was to have 64 (10-nm wide) VIS/NIR spectral bands (visible and near-infrared spectral wavelengths dominated, 0.4–1.2 μm), and 1-km nadir resolution. The MODIS-N design included 25 VIS/NIR bands (12 with 0.5-km nadir resolution and 13 with 1-km resolution), and ten SWIR/MWIR/LWIR bands (shortwave reflected infrared, midwave emitted infrared, and longwave emitted infrared spectral wavelengths, 1.2–2.7, 3–5, and 6–25 μm , respectively), all at 1-km resolution. Assuming a 100% duty cycle and 17 spectrally aggregated MODIS-T bands, the 52 bands transmitted from the two sensors were to have an average data rate of 5.0 Mbit/s.

NASA management decided to develop the MODIS-T in-house at the Goddard Space Flight Center (GSFC), and the MODIS-N via a contract with a competitively selected aerospace firm. Prior to starting the detailed design studies for the two

sensors in mid-1985, six-month feasibility (phase A) studies (NASA 1985a, b; Barnes et al. 1986) were conducted to aid in developing preliminary specifications for the phase B studies. Two firms were then selected for the year-long (June 1988–August 1989) MODIS-N phase B studies (NASA 1989). In the meantime, the MODIS-T team was assembled at GSFC. A phase B in-house study was completed for MODIS-T in 1989, followed by a CDR in 1990. Science input during this period was supplied by an ad hoc science team that included a number of participants from the instrument panel. By 1989, the MODIS-N concept had evolved to a 40-band instrument with 25 bands in the 0.4–2.2 μm region and 15 bands in the 3.7–14.2 μm region, while MODIS-T retained the 64-band concept mentioned above (Salomonson et al. 1989).

Towards the end of 1989, NASA announced the 24 members of the competitively selected MODIS Science Team (Table 1.2). The team was selected to provide

Table 1.2 MODIS Science Team during the period 1989–2004

| | Atmospheres group | Affiliation |
|-----|---------------------------------------|-----------------------------------------|
| 1. | Michael King (Group Leader) | NASA GSFC |
| 2. | Bo-Cai Gao | NASA GSFC |
| 3. | Yoram Kaufman | NASA GSFC |
| 4. | Paul Menzel | NOAA/University of Wisconsin |
| 5. | Didier Tanré | University of Lille, France |
| | <i>Land group</i> | |
| 1. | Christopher Justice (Group Leader) | NASA Headquarters (HQ) |
| 2. | Alfredo Huete | University of Arizona, Tucson |
| 3. | Jan-Peter Muller | University College London, UK |
| 4. | Ranga Myneni | Boston University |
| 5. | V. Salomonson (Team Leader) | NASA GSFC |
| 6. | Steven Running | University of Montana, Missoula |
| 7. | Alan Strahler | Boston University |
| 8. | John Townshend | University of Maryland |
| 9. | Eric Vermote | NASA GSFC |
| 10. | Zhengmin Wan | University of California, Santa Barbara |
| | <i>Oceans group</i> | |
| 1. | Wayne Esaias (Group Leader) | NASA GSFC |
| 2. | Mark Abbott | Oregon State University |
| 3. | Ian Barton | CSIRO, Australia |
| 4. | Otis Brown | University of Maimi |
| 5. | Janet Campbell | University of New Hampshire |
| 6. | Kendall Carder | University of South Florida |
| 7. | Dennis Clark | NOAA NESDIS |
| 8. | Robert Evans | University of Miami |
| 9. | Howard Gordon | University of Miami |
| 10. | Frank Hoge | NASA GSFC |
| 11. | John Parslow | CSIRO, Australia |
| | <i>Calibration group</i> | |
| 1. | Phil Slater (Group Leader) | University of Arizona |
| 2. | Kurt Thome (Group Leader 1999 – date) | University of Arizona |
| 3. | William Barnes | NASA GSFC |

scientific guidance during the MODIS development (C/D) phase and to supply algorithms for the envisioned MODIS science products. In 1997, the results of a second call for participation in the science team were announced, and four more members were added (Table 1.2). More recently, additional members were added to the MODIS Science Team via a NASA “recompetition.” This was done primarily to engage more of the science community in MODIS data analyses. In 2006, the MODIS Science Team was composed of over 90 members from the United States and beyond. A complete list of MODIS Science Team members is available at the following URL: http://modis.gsfc.nasa.gov/sci_team/.

Prior to the start of the MODIS-N and MODIS-T C/D phase, the decision was made to combine the requirements for the two sensors into a single, 36-band, nadir-pointing system, including identical versions on both the EOS-AM and EOS-PM satellites. At that time, three AM and three PM satellites were envisaged in order to develop a 15-year climate dataset. The phase B results were used by the two contractors to develop proposals for six flight units.

Eventually, in 1991, the MODIS C/D contract was awarded to Hughes/Santa Barbara Research Center (SBRC: later changed to Santa Barbara Remote Sensing, a separate enterprise of Raytheon Corporation). A Critical Design Review (CDR) was conducted in 1993, and the first flight (Proto-flight) unit was shipped to the EOS-AM integrator contractor in 1997. During the MODIS development period, the EOS program was restructured as described in the EOS section of this chapter. The decision was made to include only two identical versions of the MODIS instrument, one each onboard Terra and Aqua. Terra was launched on December 18, 1999, and Aqua on May 4, 2002. Earth observations from the Terra MODIS began on February 24, 2000, and continue as of January 2010. The first Earth observations from the Aqua MODIS began on June 24, 2002, and they continue as well.

1.3.2 Sensor Concepts

During the first few years of its development, MODIS evolved from the two-sensor concept of the Instrument Panel Report into the final 36-band system (Barnes and Salomonson 1992, 1994) developed by SBRC. Early conceptual (phase A) designs of MODIS-T and MODIS-N are depicted in Figs. 1.4 and 1.5. The MODIS-T design was based around a 64 x 64 element silicon (Si) detector array, and a sensor that tilted both fore and aft, and scanned $\pm 45^\circ$ by rotating the entire sensor (Magner and Salomonson 1991). An integrating sphere for periodic radiometric calibration is also included. The design evolved into a larger system mounted on a 1-m² base plate before its ultimate “de-selection.” The original MODIS-N design (Fig. 1.5) included a mechanical cooler for the thermal emissive bands and a single-sided double-gimbaled scan mirror that reversed directions at the end of each scan. The slow-scan second axis was corrected for spacecraft velocity, thereby generating scan lines orthogonal to the ground track with a scan efficiency of 80%. The final design developed by SBRC used a passive radiative cooler and a double-sided, continuously rotating scan mirror.

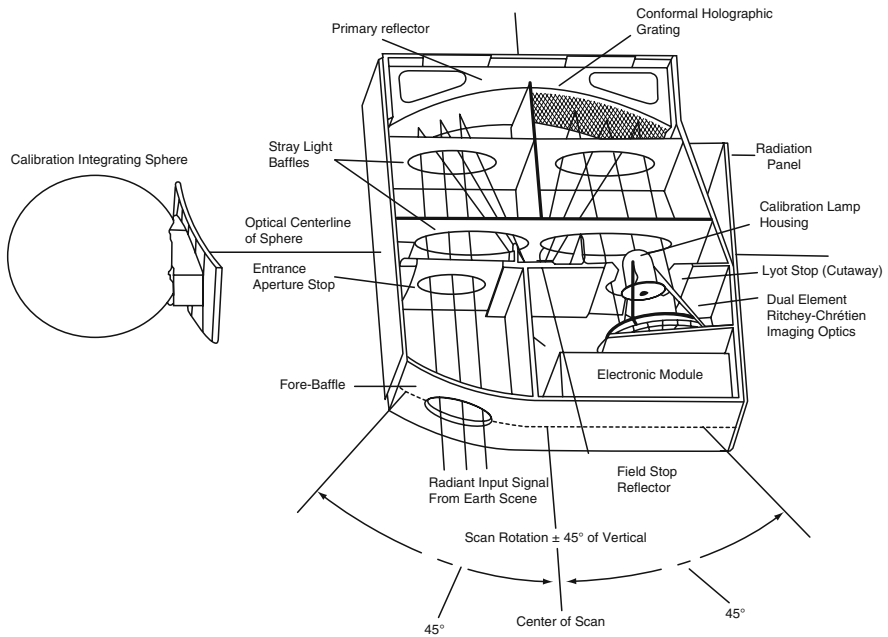


Fig. 1.4 MODIS-T phase A concept

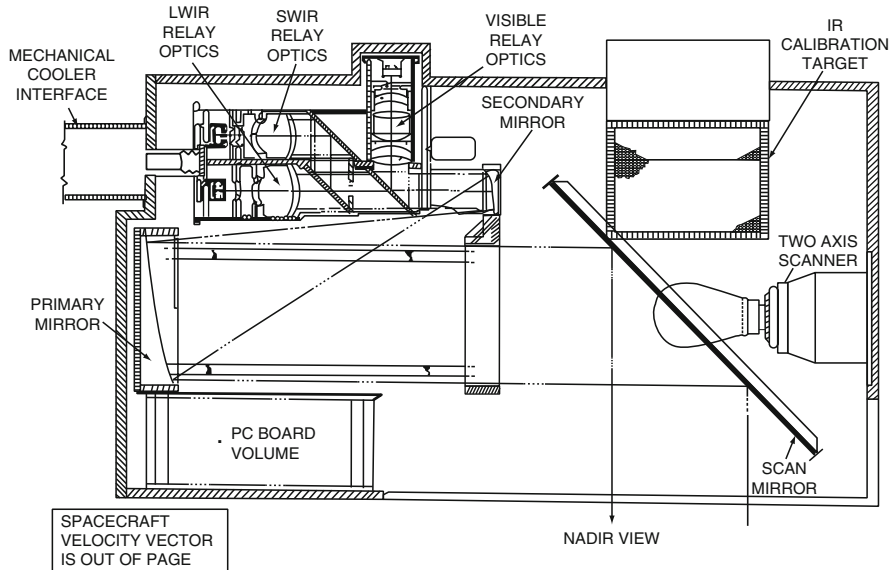


Fig. 1.5 MODIS-N phase A concept

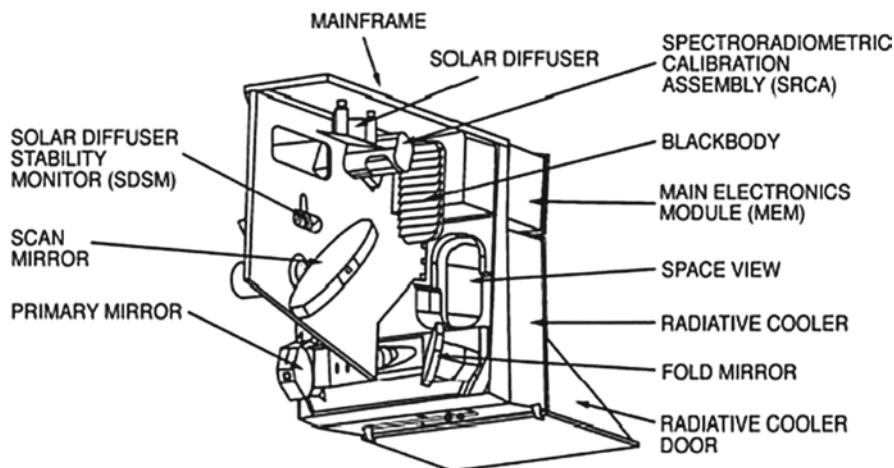


Fig. 1.6 Final MODIS design

The final MODIS design, as illustrated in Fig. 1.6, is similar to the phase A concept in certain respects (cooler and scan mirror design), but differs in other ways. Several calibration subsystems were added and the volume (and to some extent the subsequent weight) increased by greater than a factor of four. The large, 60-cm scan mirror was the primary driver of the volume (2.07 m^3 vs. 0.45 m^3 for MODIS-N). The MODIS optics concept remained fairly stable, including an off-axis telescope and refractive aft optics. The number of focal plane assemblies (FPA) was increased from three to four when the VIS and NIR bands were placed on separate FPAs. In addition, the number of bands was reduced from 40 to 36. This resulted in eliminating three polarization bands. The two bands, both at $0.555 \mu\text{m}$ but with 250- and 500-m spatial resolution, and two other bands at $0.880 \mu\text{m}$ with 250- and 500-m spatial resolution were reduced to two bands with 250-m resolution (Bands 1 and 2 in Table 1.3). Also, oxygen A bands at 0.765 and $0.865 \mu\text{m}$ were eliminated for a total reduction of seven bands. However, based on results by Kaufman and Gao (1992) obtained from the Airborne Visible/Infrared Imaging Spectrometer (AVIRIS), bands near $0.9 \mu\text{m}$ were added for atmospheric-correction purposes (bands 17–19 in Table 1.3). Lastly, also based on results from Gao and Kaufman (1995), a $1.36\text{-}\mu\text{m}$ band (band 26 in Table 1.3) was added to detect sub-visible cirrus clouds, and a band at $4.565 \mu\text{m}$ was deleted.

1.3.3 Performance

The Terra MODIS was the proto-flight model (PFM), and the later Aqua MODIS was the first flight model (FM1). These versions of MODIS were nearly identical although some improvements, as is normally done, occur in the FM-1 vs. the

Table 1.3 Final MODIS parameters

| Orbit: | 705 km, 10:30 a.m. descending node or 1:30 p.m. ascending node, sun-synchronous, near-polar, circular | | | | | | | | |
|-----------------------|-------------------------------------------------------------------------------------------------------|------------------------|--------------------------------|---------------------------|---------------------------|------|------------------------|--------------------------------|-------------------------------|
| Scan rate: | 20.3 rpm, cross track | | | | | | | | |
| Swath dimension: | 2,330 km (across track) by 10 km (along track at nadir) | | | | | | | | |
| Telescope: | 17.78 cm diam. off-axis, afocal (collimated), with intermediate field stop | | | | | | | | |
| Size: | 1.0 × 1.6 × 1.0 m | | | | | | | | |
| Weight: | 250 kg | | | | | | | | |
| Power: | 225 W (orbital average) | | | | | | | | |
| Data rate: | 11 Mbps (peak daytime) | | | | | | | | |
| Quantization: | 12 bits | | | | | | | | |
| Spatial resolution: | 250 m (bands 1–2) | | | | | | | | |
| (at nadir): | 500 m (bands 3–7), 1,000 m (bands 8–36) | | | | | | | | |
| Design life: | 5 Years | | | | | | | | |
| Primary use | Band | Bandwidth ^a | Spectral radiance ^b | Required SNR ^c | Primary use | Band | Bandwidth ^a | Spectral radiance ^b | Required NEΔT(K) ^e |
| Land/cloud boundaries | 1 | 620–670 | 21.8 | 128 | Surface/cloud temperature | 20 | 3,660–3,840 | 0.45 | 0.05 |
| Land/cloud properties | 2 | 841–876 | 24.7 | 201 | Atmospheric temperature | 21 | 3,929–3,989 | 2.38 | 2.00 |
| | 3 | 459–479 | 35.3 | 243 | | 22 | 3,929–3,989 | 0.67 | 0.07 |
| | 4 | 545–565 | 29.0 | 228 | | 23 | 4,020–4,080 | 0.79 | 0.07 |
| | 5 | 1,230–1,250 | 5.4 | 74 | | 24 | 4,433–4,498 | 0.17 | 0.25 |
| | 6 | 1,628–1,652 | 7.3 | 275 | | 25 | 4,482–4,549 | 0.59 | 0.25 |
| | 7 | 2,105–2,155 | 1.0 | 110 | | 26 | 1,360–1,390 | 6.00 | 150 ^d |

(continued)

Table 1.3 (continued)

| Primary use | Band | Bandwidth ^a | Spectral radiance ^b | Required SNR ^c | Primary use | Band | Bandwidth ^a | Spectral radiance ^b | Required NE Δ (K) ^c |
|---------------------------------------------------|------|------------------------|--------------------------------|---------------------------|---------------------------------------|------|------------------------|--------------------------------|---------------------------------------|
| Ocean color/ phytoplankton/ biogeochemistry | 8 | 405–420 | 44.9 | 880 | Water vapor | 27 | 6.535–6.895 | 1.16 | 0.25 |
| | 9 | 438–448 | 41.9 | 838 | | 28 | 7.175–7.475 | 2.18 | 0.25 |
| | 10 | 483–493 | 32.1 | 802 | Ozone Surface/cloud temperature | 29 | 8.400–8.700 | 9.58 | 0.05 |
| | 11 | 526–536 | 27.9 | 754 | | 30 | 9.580–9.880 | 3.69 | 0.25 |
| | 12 | 546–556 | 21.0 | 750 | | 31 | 10.780–11.280 | 9.55 | 0.05 |
| | 13 | 662–672 | 9.5 | 910 | | 32 | 11.770–12.270 | 8.94 | 0.05 |
| Atmospheric water vapor | 14 | 673–683 | 8.7 | 1,087 | Cloud top altitude | 33 | 13.185–13.485 | 4.52 | 0.25 |
| | 15 | 743–753 | 10.2 | 586 | | 34 | 13.485–13.785 | 3.76 | 0.25 |
| | 16 | 862–877 | 6.2 | 516 | | 35 | 13.785–14.085 | 3.11 | 0.25 |
| | 17 | 890–920 | 10.0 | 167 | | 36 | 14.085–14.385 | 2.08 | 0.35 |
| | | 18 | 931–941 | 3.6 | 57 | | | | |
| | | 19 | 915–965 | 15.0 | 250 | | | | |

^aBands 1–19 nm; bands 20–36 μm ^b(W/m² μm sr)^cSNR signal-to-noise ratio;NE Δ noise-equivalent temperature difference } Performance goal is 30% – 40%

better than required

^dSNR

protoflight model. Prelaunch characterization data from the PFM (Barnes et al. 1998) and FM1 (Xiong et al. 2002a) have proven very useful for on-orbit characterization and calibration. Both systems are performing at or above the majority of their specifications. The PFM has had a power supply and a formatter failure, but both subsystems were redundant, and there was no perceptible impact on performance (Xiong et al. 2003a, b; Barnes et al. 2003). The extensive onboard calibration subsystems including the blackbody, solar diffuser, solar-diffuser stability monitor, and spectral radiometric calibration assembly together with lunar views and spacecraft roll, pitch, and yaw maneuvers have enabled an unprecedented level of on-orbit calibration and characterization (Xiong et al. 2002b, c, d, e, f; Barnes and Xiong 2002). As of early 2008, with over eight years of on-orbit performance on the Terra mission, and nearly six years on the Aqua, the MODIS system is working as planned. Several measures of that performance are shown in Figs. 1.7–1.9. The methods by which these performance metrics were obtained are described in another chapter.

Experience has shown that spectral band passes and centers wavelengths (CW) may shift slightly after launch. Figure 1.7 shows the MODIS spectral band locations relative to their prelaunch values over the life of the Terra and Aqua satellites. For the Terra MODIS, the CW shifts have been <0.5 nm for most of the VNIR/SWIR bands, and <0.2 nm for all other bands. For the Aqua MODIS, CW shifts have been <0.5 nm for nearly all of the VNIR/SWIR bands (the exception is a 1-nm shift for band 2) and <0.2 nm for all other bands.

Figure 1.8 shows the band-to-band registration for the two MODIS instruments, normalized to band 1. The performance specification for band-to-band registration was 0.2 of a 1-km pixel (200 m) with a goal of 0.1 pixel (100 m). Terra MODIS clearly has met this specification and, in most cases, has met or exceeded the goal. However, for Aqua MODIS the registration of the SWIR/MWIR and LWIR bands (bands 5–7 and 20–36) on the cooled focal planes did not meet the specification of <0.2 pixel. There are 300-m along-scan misregistrations and 350-m along-track misregistrations for the cooled focal planes. This problem was known before launch but resource constraints prevented any attempt to correct it. This performance has caused some problems with algorithms and data products that require bands from both the cooled and un-cooled focal planes, but the problems have been circumvented for most of the MODIS products albeit as algorithms are refined, the effects are still being examined.

The radiometric calibration requirements for the MODIS VNIR/SWIR bands are $\pm 2\%$ in reflectance and $\pm 5\%$ in radiance at designated typical radiance viewing angles within $\pm 45^\circ$ of nadir. Most bands met these specifications with the exception of the Terra MODIS SWIR bands and the Aqua MODIS Band 6 ($1.65 \mu\text{m}$). The requirement for most of the LWIR bands is $\pm 1\%$ at typical radiances within $\pm 45^\circ$ of nadir and $\pm 0.5\%$ for bands 31 and 32, which are used to estimate sea-surface temperature. Overall, the thermal bands have met the calibration requirements except for the LWIR bands 33–36 on the Terra MODIS, and several Terra MODIS bands with somewhat “noisy” detectors (Fig. 1.10).

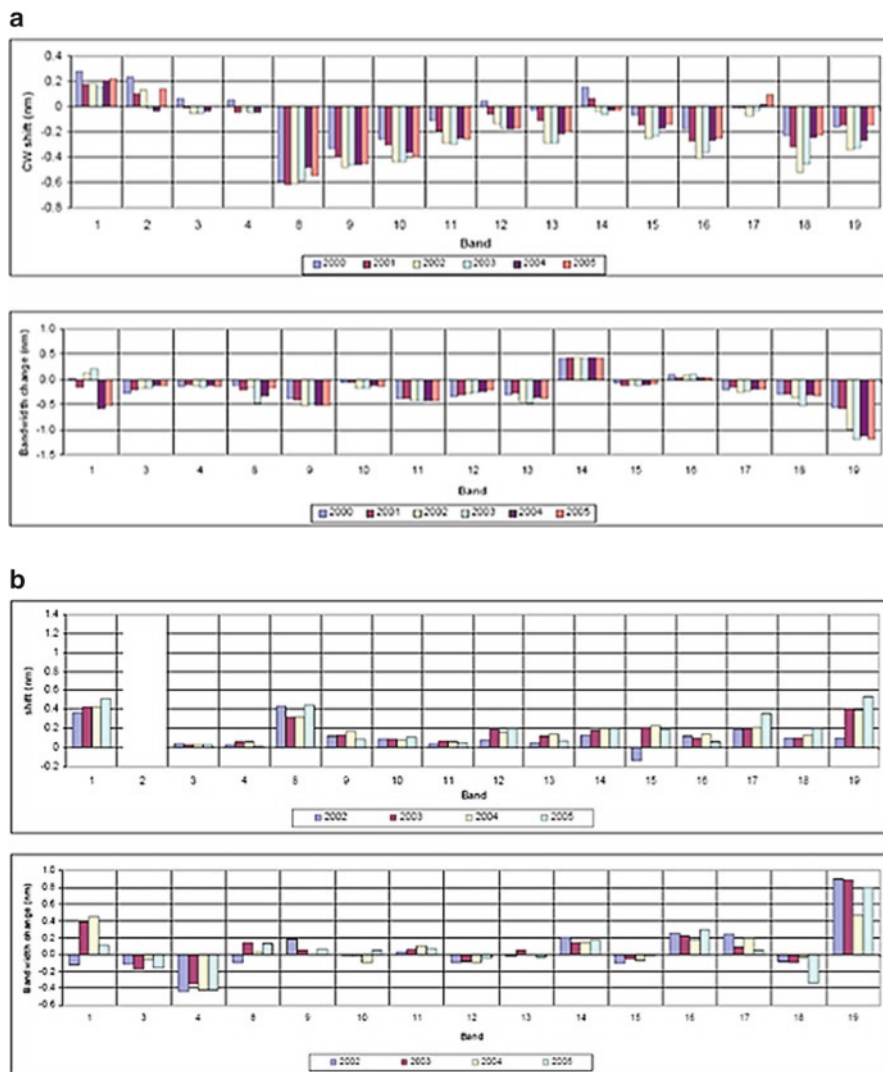


Fig. 1.7 MODIS spectral band location relative to design: (a) Terra, (b) Aqua

Another measure of MODIS performance is the signal-to-noise ratios (SNR) of the VNIR/SWIR bands. Figure 1.9 shows SNRs for both Terra and Aqua. In this figure, the red line for each band is the specification, and the data points represent on-orbit performance of each detector. The specifications were mostly met or exceeded, with a slightly more uniform performance by Aqua MODIS relative to the Terra MODIS.

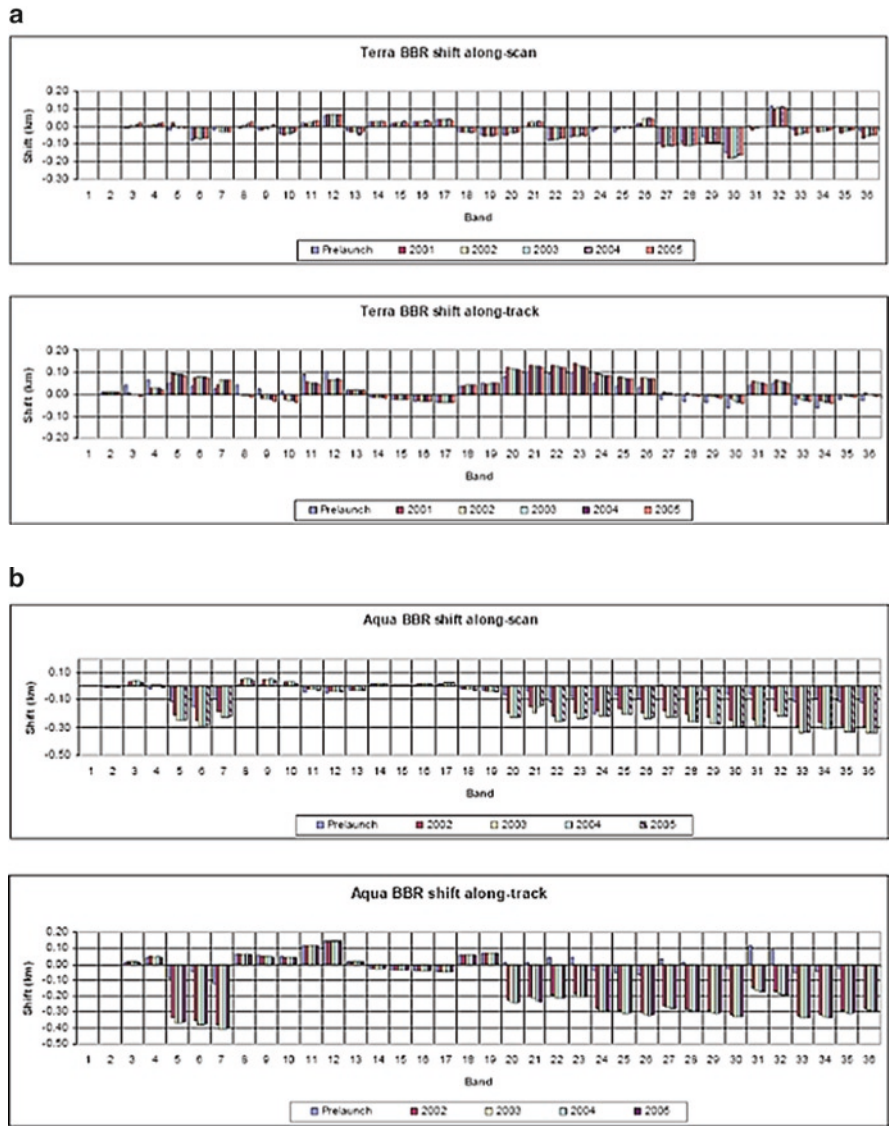


Fig. 1.8 MODIS band-to-band registration (BBR): (a) Terra, (b) Aqua

For the MWIR/LWIR bands the metric equivalent to SNR is $NE\Delta T$, the Noise Equivalent Delta Temperature. The MODIS designers wanted to have a lower $NE\Delta T$ than the design specified. The prelaunch measurements of $NE\Delta T$ and on-orbit performance for both MODIS instruments are shown in Fig. 1.10. In general, the instruments meet their specifications with the exception of Terra MODIS Band 36. As a consequence, it is necessary to use pixel averaging or the Terra

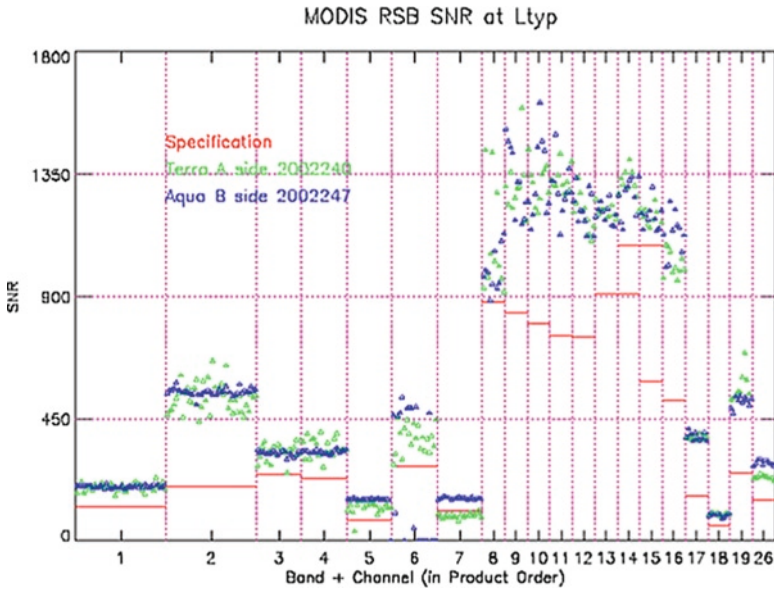


Fig. 1.9 Terra and Aqua MODIS SNR performance for the VNIR/SWIR reflected solar bands (RSB). L_{typ} is meant to indicate the typical radiance observed in these bands, i.e., not the maximum radiance. The wavelengths corresponding to each band are given in Table 1.3. The *dots* in each band column reflect the SNR for each detector

MODIS cloud-height product, which depends on that band. In 2005, after six years of operation, noise levels began increasing for certain Terra MODIS detectors and bands. Fortunately, bands 20, 22, 23 and 31 and 32, used to determine sea-surface temperature, have remained unaffected. Overall, the later-built Aqua MODIS is performing somewhat better than the earlier Terra version.

1.3.4 The Post-MODIS Future

Due to the success of the MODIS instruments in acquiring valuable land, ocean, and atmosphere observations over several years, a similar capability is being planned for the National Polar Orbiting Environmental Satellite Series (NPOESS) – the follow-on to the present NOAA Polar Orbiting Environmental Satellites (POES). This will help achieve the original EOS goal of collecting a 15-year global dataset to address questions on climate change. Subsequent to this decision, the design specifications for an instrument called the Visible and Infrared Imaging Radiometer Suite (VIIRS), slated to fly on the NPOESS, were adjusted to match new NOAA-developed climate requirements. These, together with the original VIIRS requirements, called for a sensor with many of the attributes of MODIS. After a competitive selection process, the NPOESS Integrated Program Office

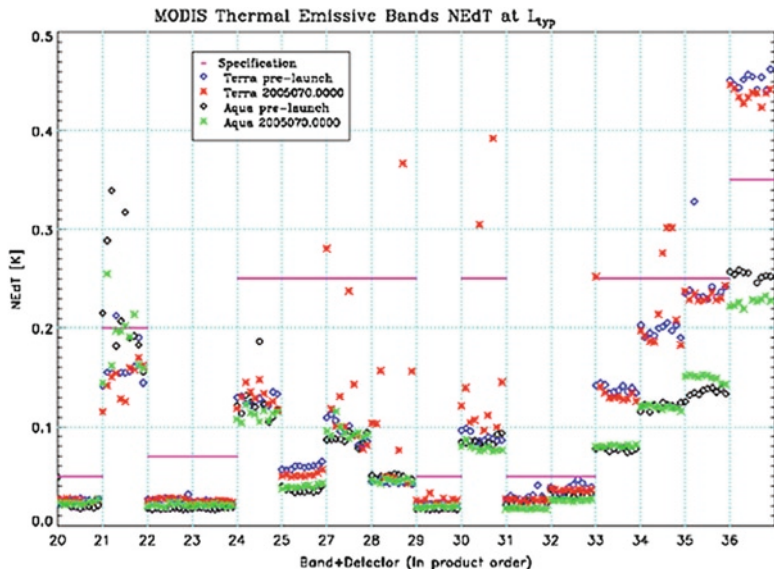


Fig. 1.10 Terra and Aqua MODIS Noise Equivalent Delta Temperature (NE Δ T) for the MWIR/LWIR thermal emission bands. L_{typ} is meant to indicate the typical radiance observed in these bands, i.e., not the maximum radiance. The wavelengths corresponding to each band are given in Table 1.3. The *dots* in each band column reflect the SNR for each detector

(IPO) chose Raytheon/SBRS (the original MODIS instrument builder) to develop the VIIRS. In addition, the IPO together with NASA's Earth Science Enterprise developed a risk-reduction mission that will also fill any data gap between EOS/MODIS and the first NPOESS/VIIRS. This mission is the NPOESS Preparatory Project (NPP) expected to launch in October 2011.

The VIIRS (Fig. 1.11a) is, in many ways, a smaller version of the MODIS (Fig. 1.11b). VIIRS has 21 spectral bands, but the use of dual gains in several bands allows it to reproduce the clear majority of attributes for MODIS bands. The other major difference between MODIS and VIIRS is the replacement of the MODIS double-sided scan mirror with a rotating telescope (Fig. 1.12). This approach will result in a major reduction in far-field scattered light.

In summary, the MODIS instrument has met its specifications. Approximately, 40 MODIS data products are being routinely produced. They continue to significantly contribute towards scientific efforts to better understand Earth-atmosphere processes and associated parameter trends globally. MODIS observations are additionally being used in applications related to monitoring pollution, assessing and managing resources, and assessing the extent of disasters or problems due to forest fires, drought, and floods. These applications are facilitated by the fact that MODIS data are obtained directly from the Terra and Aqua satellites by the direct broadcast (DB) capability that now is implemented at over 100 DB ground-receiving stations worldwide.

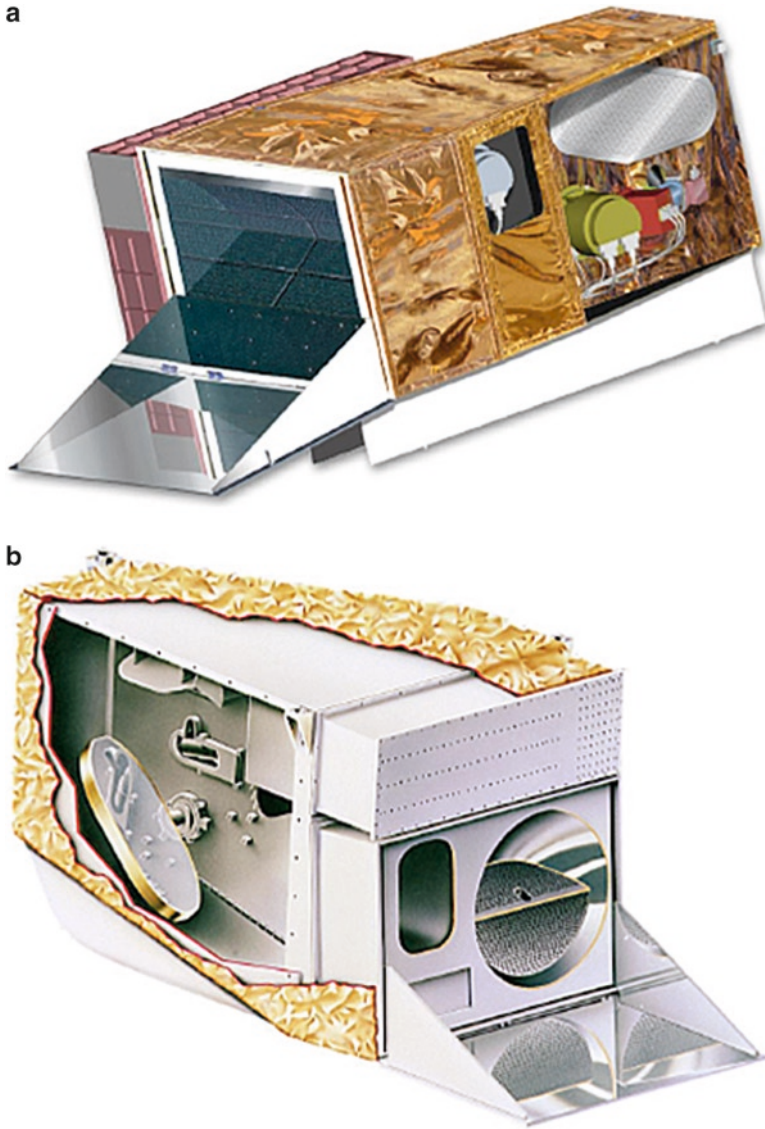


Fig. 1.11 VIIRS and MODIS: (a) The VIIRS design calls for a volume of 1.2 m^3 , a mass of 250 kg, and uses 200 W of power, (b) MODIS has a volume of 2.0 m^3 , a mass of 230 kg, and uses 147 W of power

1.4 History of the Advanced Spaceborne Thermal Emission and Reflection Radiometer

The ASTER has its roots in various instruments. The long history of the Landsat instruments (Multispectral Scanner, or MSS, and Thematic Mapper, or TM) in the VNIR and SWIR wavelengths has fostered a large user community accustomed to

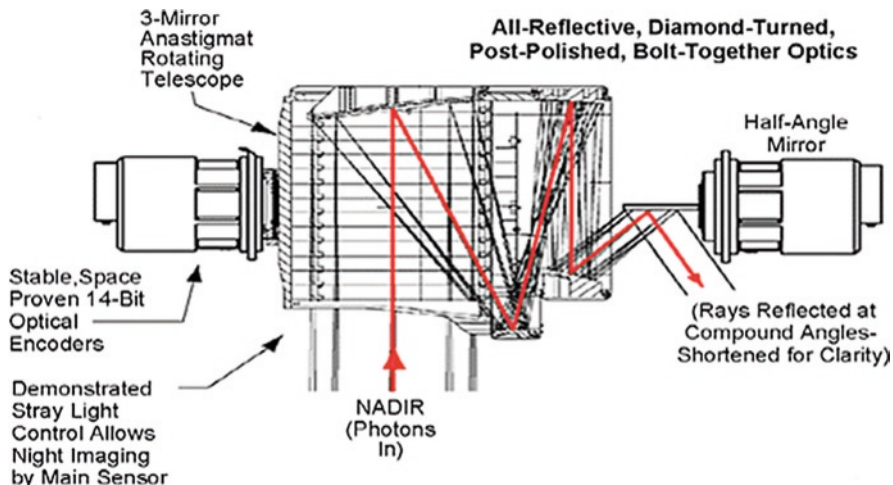


Fig. 1.12 VIIRS rotating telescope assembly including the telescope and half-angle mirror motors

working with moderate-resolution multispectral data. The TM provides users with four bands in the VNIR, two in the SWIR, and a single thermal band. The first six bands have 30-m resolution, and the TIR (LWIR thermal infrared) band has 60–120 m resolution. TM scanners have operated continuously from 1982 until the present day. Perhaps the second most-used dataset of this type is provided by the French SPOT (Satellite Pour l’Observation de la Terre) series of instruments. First launched in 1986, SPOT provided users with 10–20 m data in the VNIR, and a cross-track stereo capability to generate digital elevation models (DEM).

The Japanese JERS-1 (Japanese Earth Resource Satellite) Optical Sensor (OPS) instrument was launched in 1992, and acquired data in three VNIR bands, four SWIR bands, and along-track stereo. During its six years of operations, images were acquired over most of the Earth’s land surface. JERS-1 proved the value of multi-spectral SWIR data for mineralogical mapping, and demonstrated the improvement of along-track stereo compared to between-orbit stereo (such as SPOT).

Early work in the multispectral thermal infrared (TIR) used one- and two-band imaging devices to construct thermal inertia images based on differences in thermal properties expressed at night and during the day (Sabins 1969; Watson 1975; Kahle et al. 1976; Gillespie and Kahle 1977). This provided only limited capability to separate mineralogical groups due to the paucity of bands, and to low radiometric sensitivity.

In order to measure the spectral emissivity contrast of materials on the Earth’s surface, a more sensitive scanner with more bands was required. In 1980, Kahle and Rowan (1980) were successful in obtaining data in six thermal bands (8–13 μm) with an aircraft scanner over the East Tintic Mountains, Utah, USA. Although results were promising, the scanner was nevertheless dismantled. A short time later, NASA purchased the Thermal Infrared Multispectral Scanner (TIMS), a six-channel

TIR airborne instrument with an improved sensitivity of 0.1–0.3 K $NE\Delta T$. Almost 20 years of operation, starting with Kahle and Goetz's (1983) first report, demonstrated the utility and value remote sensing in the 8–13 μm TIR region for discriminating and identifying surface materials. Processing algorithms for separating temperature and emissivity in multispectral TIR data were developed over a period of time using both empirical and rigorous modeling techniques (Gillespie 1985; Realmuto 1990; Hook et al. 1992).

The EOS ASTER program began as two separate instruments proposed from two different countries: the United States and Japan. In mid-1988, Anne Kahle (JPL) submitted a proposal to the EOS Announcement of Opportunity for a "Thermal Infrared Ground Emission Radiometer (TIGER) for Polar Orbiting Platforms." It consisted of two components: a multispectral imager, or Thermal Infrared Mapping Spectrometer (TIMS) with 14 bands (four in the 3–5 μm MWIR region and ten in the 8–13 μm LWIR region) and a nonimaging Thermal Infrared Profiling Spectrometer (TIPS) with three profilers of 0.1- μm resolution. TIGER would have 90-m spatial resolution over a 30-km swath, with $\pm 24^\circ$ cross-track pointability. At the same time, Japan's Ministry of International Trade and Industry (MITI) through the Japan Resources Observation System Organization (JAROS) was planning the Intermediate Thermal Infrared Radiometer (ITIR) (Yamaguchi et al. 1992). ITIR was offered as a Japanese facility instrument to EOS. In 1987, its characteristics were different from TIGER's: one band in the NIR with stereo capability, five SWIR bands, one band in the 3–5 μm region, and four TIR bands. MITI viewed ITIR as the follow-on to JERS-1 that successfully orbited the Earth and acquired multispectral VNIR/SWIR images.

On February 7, 1989, NASA's Leonard Fisk sent an EOS acceptance letter to Kahle (Fisk 1989), which stated:

I am pleased to offer you partial selection for definition of your proposal.... Specifically NASA is offering selection of the TIMS but is declining the non-imaging TIPS. Furthermore, NASA is asking you to try to implement the design advances in your TIMS concept by influencing the Japanese design for ITIR.... the TIMS is being considered in the context of flight on NASA Polar Orbiting Platform 1 (NPOP-1) as an integral technology improvement for ITIR. NPOP-1 is planned for launch during the fourth quarter of 1996.

NASA sought the efforts of Kahle's team as a means to further international cooperation for EOS (Plafcan 2007). In a 1989 email message, the NASA EOS chief project scientist, Dixon Butler, stated that MITI's ITIR was "the essence of cooperation between Japan and NASA" [Butler 1989 cited in Plafcan (2007)].

U.S. and foreign scientists were also given the opportunity to propose to EOS to participate as members of instrument science teams, perform calibration/validation experiments, and form interdisciplinary science teams. From this solicitation, the first U.S. Science Team was selected by NASA and assigned to Dr. Kahle for oversight and direction (Table 1.4). About 12 scientists were selected and funded. In addition, Kahle proposed to employ a number of people at JPL as the US ASTER project (mission operations, scheduling, project manager, calibration/validation, etc.). This proposal was approved and budgeted by NASA.

Table 1.4 Original U.S. ASTER science team

| |
|---------------------------------------------------|
| Dr. Anne Kahle, Jet Propulsion Laboratory |
| Dr. Francois Becker, University of Strasbourg |
| Mr. Stillman Chase, Hughes Santa Barbara Research |
| Dr. Phil Christensen, Arizona State University |
| Dr. Alan Gillespie, University of Washington |
| Dr. Hugh Kieffer, U.S. Geological Survey |
| Mr. Frank Palluconi, Jet Propulsion Laboratory |
| Dr. David Pieri, Jet Propulsion Laboratory |
| Dr. Larry Rowan, U.S. Geological Survey |
| Dr. Jack Salisbury, Johns Hopkins University |
| Dr. Tom Schmugge, U.S. Department of Agriculture |
| Dr. Phil Slater, University of Arizona |
| Dr. Ron Welch, North Dakota State University |

Shelby Tilford, Director of the NASA Office of Space Science and Applications, sent a letter to S. Hashimoto, Executive Managing Director of JAROS, and to T. Tanaka, at the Japanese National Space Development Agency (NASDA) outlining NASA's interest in cooperating with the Japanese ITIR effort (Plafcan 2007). In March, 1989, Kahle, Frank Palluconi (JPL), and Still Chase (Hughes) traveled to Tokyo to discuss TIGER and ITIR with their Japanese colleagues. Following this meeting, discussions took place at the National Research Laboratory of Metrology in Tsukuba with A. Ono and others in the Thermal Measurement Section. They include H. Fujisada (Electro-Technical Laboratory), H. Tsu, Y. Yamaguchi (Geological Survey of Japan), and representatives from MITI. The ITIR had evolved since 1987, and was now described as a three-band TIR instrument, without any bands in the 3–5 μm range; six bands in the SWIR, and three VNIR bands with full color stereo. Spatial resolution was reduced from 60 to 90 m. The SWIR spatial resolution was reduced from 15 to 30 m. Four reasons were given for the reduced capability: funding, resources, user demand, and instrument technology (Plafcan 2007). In a later meeting with Professor Y. Ishii, at the University of Tokyo, Kahle explained the U.S. users' requirements for greater capability in the TIR (more bands and better spatial resolution). This first meeting ended with both sides agreeing to consult their respective working groups/teams, and continue discussions in the future.

In the ensuing months, Kahle and her team continued to negotiate the thermal sensor's specifications with MITI's Space Industry Division, JAROS management, and the engineers who advised JAROS. Eventually, Kahle and her team convinced MITI and JAROS that five bands in the TIR would not only help the TIGER team realize its science goals, but also help MITI, JAROS, and their user community achieve their natural resource and instrument development goals (Plafcan 2007). As to the reduced spatial resolution in the SWIR and TIR, the proposed parameters from the Japanese contractors were accepted due to the constraints mentioned earlier.

In November 1989, the next ITIR/TIGER meeting was held in Tokyo and attended by Kahle and nine members of her TIGER team. Japanese participants included engineers from the instrument contractors, principal science advisors to MITI (Tsu, Ono, and Fujisada), and other university and industry participants. At this time, a Japanese Science Team had not been selected. This reflects the difference in the early phases of mission design and formulation. In Japan, the sponsoring organization asks industry to provide prephase A studies, and individuals in various organizations (government and university) are assigned as representatives to advise. In the United States, a science team is involved with the very first steps of instrument formulation and definition, and is part and parcel of the entire process. Discussions focused mostly on geologic applications of ITIR, due to the makeup of Japan's participants.

One year later, in November 1990, the first joint U.S./Japan ASTER Science Team (AST) meeting was held at JPL in Pasadena. It was attended by nine Japanese and 19 U.S. participants. By this time, an official Japanese Science Team was formed and funded by MITI to support the EOS mission, and to work together with the U.S. Science Team. Hiroji Tsu of the Geologic Survey of Japan was selected as the Japanese AST Leader; Anne Kahle was his U.S. counterpart. Tsu announced that the name of the project and instrument was changed from ITIR to ASTER to more appropriately reflect the broader spectral window of the planned instrument (visible through thermal infrared) (Kahle et al. 1991). Tsu and Kahle defined the structure of the joint science team working groups, and recommended individuals to act as co-chairs for each working group. Table 1.5 shows the co-chairs of these committees in 1998. The subjects emphasized that (1) ASTER started out as a resource exploration sensor for the petroleum and mining industries in Japan; (2) ASTER data would benefit many scientific disciplines, hence the creation of an Ecosystems Working Group and inclusion of scientists like Dr. Yasuoka of the National Institute of Environmental Studies. Both sides agreed to convene joint science team meetings every six months, with alternating venues between Japan and the United States.

By this time, the instrument's specifications were fairly well solidified. Most importantly, the number of TIR bands was increased to five, and the stereo band

Table 1.5 Japanese and U.S. ASTER working groups and their co-chairs

| Working group | Japanese members | U.S. members |
|-----------------------------------------|--------------------|-------------------|
| Level-1 Data and Geometry | Hiroyuki Fujisada | Hugh Kieffer |
| Calibration | Yasushi Yamaguchi | Phil Slater |
| Atmospheric Correction | Tsutomu Takashima | Anne Kahle |
| Digital Elevation Models | Yoshinori Miyazaki | Harold Lang |
| Temperature-Emissivity Separation | Shuichi Rokugawa | Phil Christensen |
| Operations/Mission Planning | Yasushi Yamaguchi | Anne Kahle |
| Higher-Level Data Products | Isao Sato | Anne Kahle |
| Airborne Sensors | Shuichi Rokugawa | Simon Hook |
| Geology | Minoru Urai | Lawrence Rowan |
| Spectral Library | Yoshiki Ninomiya | Simon Hook |
| Oceanography and Limnology | Motoaki Kishino | Michael J. Abrams |
| Ecosystems and Land Surface Climatology | Hajime Kayanne | Tom Schmugge |

MITI awarded contracts for the instrument construction to three different companies: Nippon Electric Company (NEC) for the VNIR; Mitsubishi Electric Company (MELCO) for the SWIR, and Fujitsu for the TIR. The reason was that MITI wanted to expand the aerospace industry in Japan. By awarding three such separate contracts, several industrial companies were expected to gain valuable experience in designing and building spaceborne sensors. Equally important was a strong technical reason to divide the ASTER instrument into three subsystems. From an engineering standpoint, it was deemed extremely difficult to build a single instrument that used a single focal plane to cover from the VNIR to SWIR to TIR with high radiometric performance, and more spectral bands than TM. This decision made it possible to use cryocoolers for the SWIR and TIR, and different optimized scanning mechanisms: pushbroom for the VNIR and SWIR, and mechanical whiskbroom scanning for the TIR. This configuration (Fig. 1.14) led to some additional operational complexities on the platform to ensure that all three instruments pointed to the same area on the ground. And, in addition, the Ground Data System (GDS) required development of automated software to co-register bands from all three telescopes.

Meanwhile, EOS was moving along with plans for data products, and instrument teams were instructed to develop a list of products they would create for users. An overriding philosophy was that for the first time, a large suite of higher-level geophysical data products was planned for production obviating the need for individual scientists to reinvent these products to carry out their research. The U.S. AST proposed 26 data products, ranging from thermal inertia to eruption cloud properties, to sea-ice parameters. These were envisaged for routine production for all acquired data or produced on-demand by the EOSDIS facilities at the EROS Land Processes DAAC.

As noted in the EOS section of this chapter, budget restrictions and fiscal realities set in for EOS and the project was scaled back. The Polar Orbital Platform, serviceable by the Space Shuttle was the originally conceived vehicle for these instruments. It was envisioned that new instruments in the future would replace existing ones in a continuous refurbishment of the platform. This plan was abandoned as too costly. Ensuing discussions focused on “deselecting” instruments; much of these discussions took place at the Interdisciplinary Science Working Group (IWG) meetings, at which time, a defense was presented regarding why ASTER was a necessary upgrade to Landsat, and complementary to MODIS.

In early 1992, Kahle received another letter from NASA’s Fisk (1992), stating:

NASA has recently completed restructuring EOS to fly the instruments on a series of intermediate and small spacecraft.... The ASTER instrument is assigned the first flight on the morning (AM) series of spacecraft.

A similar letter was sent to Japan’s MITI and NASDA:

Consistent with the results of the restructuring process, you will note that there are two “anchor” missions – EOS-AM and EOS-PM. ASTER is proposed for flight on the first EOS-AM spacecraft scheduled for launch in June 1998...NASA values the international cooperation that has taken place in planning EOS... We appreciate MITI and NASDA’s willingness to accommodate NASA-sponsored scientists participating in the ASTER science team, which is an important aspect of our joint endeavor.

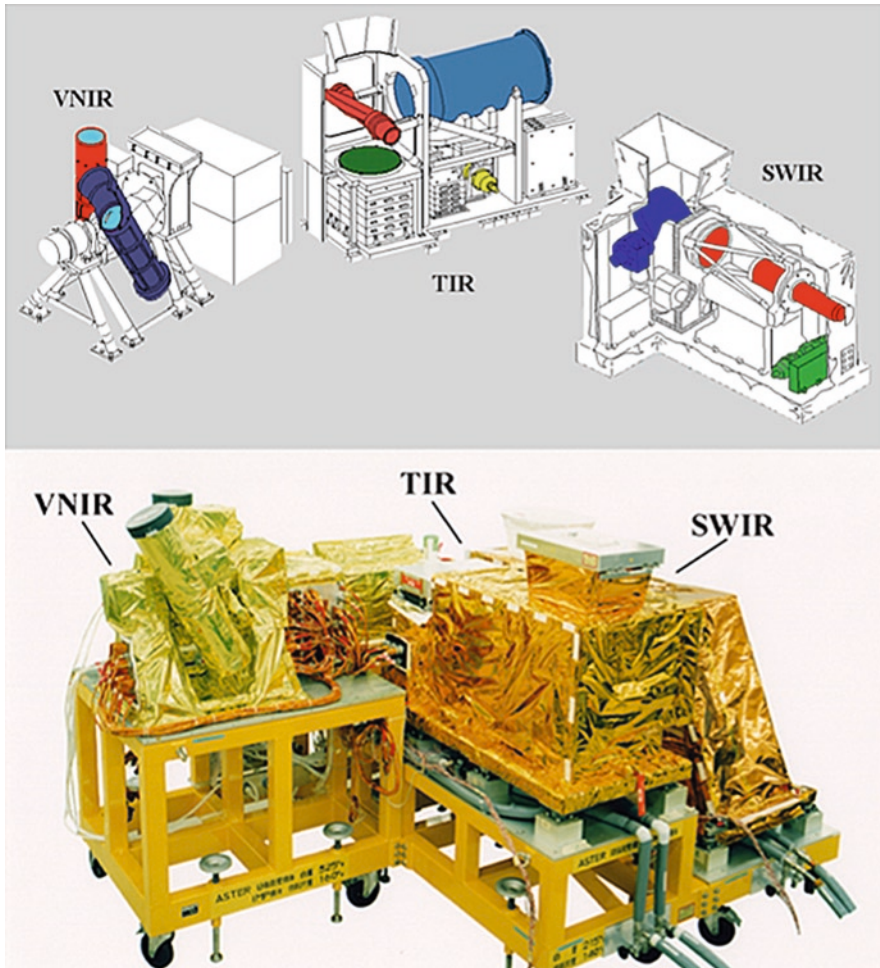


Fig. 1.14 Diagrams and photograph of the three ASTER subsystems. Each operates in a different spectral region with its own telescope(s) and pointing capabilities. The ASTER subsystems are physically located at separate locations on the Terra platform. Telescopes are shown in *blue*, focal planes in *green*, and mirrors in *red*. Photo courtesy of JAROS

The EOS-AM platform resource constraints were now defined by NASA and provided to ASTER to help guide instrument design and mission operations. One factor, over the life of the mission, has dominated and limited the ASTER data acquisition potential: duty cycle. The AM platform uses solid-state recorders (SSR) to record data from the five instruments, prior to transmission to ground stations. The capacity of the SSR, and ASTER's allocation of this resource, limits ASTER to an average duty cycle of 8% per orbit (about 8 min of data, or 700 scenes/day). So ASTER operations require scheduling for every orbit of every day to instruct the instrument regarding what data to acquire and record on the SSR. It was immediately

realized that such a complex scheduling was not possible on a manual basis. An automatic scheduler software was deemed necessary to command and control the daily ASTER operations. The AST formulated mission goals and defined categories of data acquisition; one goal was to obtain cloud-free images over the entire land area of the Earth, under optimal illumination conditions and during favorable seasons. This was called the Global Map, and simulations indicated it would require about five years to achieve 85% success due to cloud cover. A second category of observations was regional data acquisitions for various science disciplines. Team members solicited ideas and suggestions from the broad research community. Examples of these large, focused acquisitions are (1) the world's temperate glaciers, as defined by the GLIMS project (Global Land Ice Measurements from Space), that number several thousand; (2) the world's active volcanoes, imaged several times per year; (3) coral reefs; and (4) the Amazon Basin. The third category of observation is local requests to support individual researchers who need limited amounts of data (ten scenes or less) over a particular area at specific times. These would, for instance, support field campaigns or multitemporal land-use change studies.

To accommodate the various kinds of requests, a scheduling algorithm was developed jointly by the U.S. and Japan Science Teams to schedule ASTER data acquisitions considering observation priority and instrument constraints within the guidelines provided by the AST. The scheduler assigned weighting values to about 15 parameters and provided an overall priority rating. All the competing requests for any given day (about 2,000) were evaluated using a priority evaluation function to arrive at a daily schedule. This was modified using a cloud-forecasting algorithm for the next day to refine the schedule and maximize the probability of acquiring acceptable data based on cloud cover percentage. A one-day schedule is developed and uploaded to the instrument for execution. This part of the operation is mostly automatic. Significant human intervention is required in the individual data request approval process as well as assistance with entering routine instrument data acquisition request schedules. Similar schedules are input for expedited emergency data acquisitions for natural disasters such as volcanic eruptions.

The Japan GDS, as part of ERSDAC, was originally in charge of processing ASTER data from level 0 (raw instrument data) to level 1A (band-separated data, with geometric and radiometric correction coefficients calculated but not applied) and then to level 1B (band-separated data, with geometric and radiometric correction coefficients applied). Currently, about 600 scenes/day are acquired, and processed to level 1A. Of these about 150 are further processed to level 1B, the staple form used by most end users, and input to produce higher-level derived data products. The primary factor used to determine which scenes are processed to level 1B is cloud cover percent. Currently, GDS uses a modified version of the Landsat cloud cover assessment algorithm.

The originally planned 26 ASTER science algorithms were seen by NASA as too many and too costly, so the instrument science teams were told to reduce their number of higher-level products drastically. This resulted in a new list of only eight ASTER products. For each product, a peer-review process was devised, and the science team member responsible for a particular product (and algorithm) was

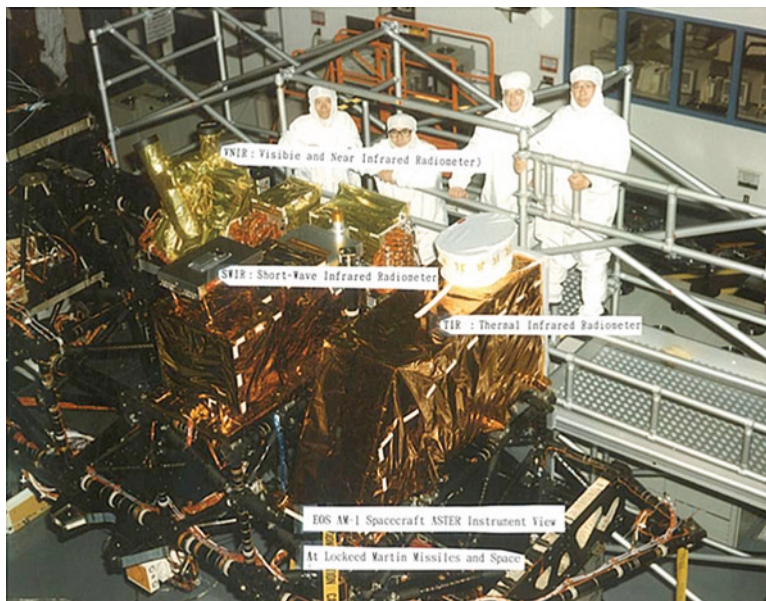


Fig. 1.15 The ASTER instrument integrated onto the Terra platform. Photo courtesy of JAROS

required to produce an Algorithm Theoretical Basis Document (ATBD). These were eventually released publicly (Lang and Welch 1999). These documents describe the scientific basis for a product, what algorithm was selected and why, and detailed discussions of error budgets, accuracy, and validation plans.

Finally, in December 1999, EOS-AM1 was launched and renamed “Terra,” after a 19-month delay from the June 1998 date mentioned in the 1992 letter to MITI. ASTER was happily aboard (Fig. 1.15), reflecting the overall success of U.S.-Japan cooperation. In February 2000, ASTER returned its first image of the Earth, and the AST verified that the instrument performed as expected. Then began the nearly instantaneous transition from planning and designing to operations, data processing, and distribution. The AST activities shifted to characterizing the instruments’ on-orbit behavior through calibration/validation experiments; validation of algorithms for data products; promoting the use of ASTER data within the science community and the general users; and performing their individual science research projects.

Calibration/validation of ASTER involves members of the combined AST as well as engineers from the Japanese contractors responsible for building the ASTER instrument. A two-pronged approach is used for calibration and validation. One method relies on on-board calibration lamps and a blackbody to provide a known signal to the instruments that is measured and the instrument performance evaluated (Sakuma et al. 2005). A second, complementary, method uses vicarious calibration through field excursions to (relatively) homogeneous targets (such as lakes) to measure reflectance or temperature parameters simultaneously with ASTER overpasses. Then, by also characterizing the intervening atmosphere, the instrument response is

compared to the ground measurements and the instrument performance evaluated (Tonooka et al. 2005). Vicarious calibration is carried out separately in Japan and the United States, and also jointly by scientists from both countries in cooperative field campaigns. The results verify that the instrument performance is meeting or exceeding prelaunch requirements, and the collaboration has strengthened our collective understanding of the behavior of all three ASTER sensor systems.

Validation of the product generation algorithms is similar to calibration and validation to assess instrument characteristics. For example, validating the algorithm that provides calibrated kinetic temperature requires simultaneous ground measurement of large targets, characterization of the intervening atmosphere, and comparison of the two temperature measurements. Often, this also leads to uncovering bugs in the software codes and regular updating of the algorithms.

The Terra mission has now exceeded its original planned operational lifetime, and therefore, several re-competitions in the United States both for the AST and for the instrument team at JPL have taken place. The AST was “recompeted” in 2004, and new members selected by NASA. The AST expanded to 20 members, with the return of some original participants and the addition of about ten new scientists. The result was an infusion of fresh ideas, and an expansion of science activities, alongside with calibration and validation, and algorithm maintenance. In 2004, NASA science reorganized by combining the Earth Science and Space Science Divisions into a single Science Division. As a result, Earth Science missions were required to undergo a senior review requiring an extensive proposal to justify continued funding. The ASTER project contributed to a combined proposal from the Terra platform, requesting an extended mission. It was successful, and was awarded extended mission support until September 2009. In Japan, the ASTER management structure changed in April 2005, and as a result the National Institute of Advanced Industrial Science and Technology (AIST) now oversees ASTER. If the platform and instruments continue until September 2009 (and there is no a priori reason to think otherwise), ASTER would have functioned for almost ten years since its launch in December 1999.

Acknowledgments Hundreds, perhaps thousands, of people worked diligently to ensure the success of EOS, MODIS, and ASTER. Although, it is not possible here to acknowledge the contributions of all the individuals involved, the scientific community (especially the MODIS and ASTER) acknowledge and salute all those who contributed to the success achieved. Work done by Abrams was performed at the Jet Propulsion Laboratory, California Institute of Technology, under contract to the National Aeronautics and Space Administration.

References

- Barnes WL (1985) Science requirements for a Moderate Resolution Imaging Spectrometer (MODIS) for EOS. Proc. AIAA/NASA Earth Observing System (EOS) Conference, AIAA-85-2085, Virginia Beach, VA, 8–10 Oct.
- Barnes WL, Salomonson VV (1992) MODIS: a global imaging spectroradiometer for the Earth Observing System. Proc. Critical Review of Optical Technologies for Aerospace Sensing, CR47, pp 1–23, OE/Technology '92, Boston, MA, 15–20 Nov.

- Barnes WL, Salomonson VV (1994) Design and projected performance of MODIS – a moderate resolution imaging spectroradiometer for the Earth Observing System (EOS). Proceedings of International Conference on Applications of Photonic Technology, Toronto, Canada, pp 171–178, 21–23 June.
- Barnes WL, Xiong X (2002) Early on-orbit calibration results from Aqua MODIS. Fujisada H (ed) Proceedings of SPIE – Sensors, Systems, and Next Generation Satellites VIII, p 4881.
- Barnes WL, Ostrow H, Salomonson VV (1986) Preliminary system concept for MODIS: moderate resolution imaging spectrometer for EOS. Proc. SPIE Tech. Symp. Southeast on Optics and Optoelectronic Systems, Orlando, FL, Mar 31–Apr 4.
- Barnes WL, Pagano T, Salomonson VV (1998) Pre-launch characteristics of the Moderate Resolution Imaging Spectroradiometer (MODIS) on EOS AM-1. IEEE Trans Geosci Remote Sens 36(4):1088–1100.
- Barnes WL, Xiong X, Salomonson VV (2003) Status of Terra MODIS and Aqua MODIS. Adv Space Res 32(11):2099–2106.
- Butler D (1989) NASA Mail message from the NASA EOS Project Scientist to L. Lincoln, Re: Message from Benn Martin, msg NJIJ-2847–2908, 12 Nov.
- Esaias WE (1986) Moderate Resolution Imaging Spectrometer (MODIS); MODIS instrument panel report. Earth Observing System Rep Vol. IIb.
- Fisk L (1989) Letter from NASA Associate Administrator to Anne Kahle, 7 Feb.
- Fisk L (1992) Letter from NASA Associate Administrator to Anne Kahle, 5 Feb.
- Gao B-C, Kaufman YJ (1995) Selection of the 1.375 μm MODIS channel for remote sensing of cirrus clouds and stratospheric aerosols from space. J Atmospheric Sci 52(23):4231–4237.
- Gillespie A (1985) Lithologic mapping of silicate rocks using TIMS. TIMS Data Users Workshop, JPL Publ. 86–38, 29–44.
- Gillespie AR, Kahle AB (1977) The construction and interpretation of a digital thermal inertia image. Photogramm Eng Remote Sensing 43:983–1000.
- Herring D, King M (2001) The encyclopedia of astronomy and astrophysics, IOP Publishing, Macmillan, London.
- Hook S, Gabel A, Green A, Kealy P (1992) A comparison of techniques for extracting emissivity information from thermal infrared data for geologic studies. Remote Sensing Environ 42:123–135.
- Kääb A, Huggel C, Paul F, Wessels R, Raup B, Kieffer H, Kargel J (2003) Glacier Monitoring from ASTER Imagery: accuracy and applications. Proceedings of EARSeL-LISSIG-Workshop Observing our Cryosphere from Space, Bern, 2002. EARSeL e Proc 2:43–53.
- Kahle A, Goetz A (1983) Mineralogical information from a new airborne thermal infrared multi-spectral scanner, Science 222:24–27.
- Kahle A, Rowan L (1980) Evaluation of multispectral middle infrared aircraft images for lithologic mapping in the east Tintic mountains, Utah. Geology 8:234–244.
- Kahle A, Gillespie A, Goetz A (1976) Thermal inertia imaging: a new geologic mapping tool. Geophys Res Lett 3:26–28.
- Kahle A, Palluconi F, Hook S, Realmuto V, Bothwell G (1991) The Advanced Spaceborne Thermal Emission and Reflection Radiometer (ASTER). Int J Imaging Syst Technol 3:144–156.
- Kaufman YJ, Gao B-C (1992) Remote-sensing of water vapor in the near-IR from EOS/MODIS. IEEE Trans Geosci Remote Sens 30(5):871–884.
- Lang H, Welch R (1999) ATBD-AST-08 Algorithm Theoretical Basis Document for ASTER Digital Elevation Models (Standard Product AST14). http://eosps0.gsfc.nasa.gov/eos_homepage/for_scientists/atbd/docs/ASTER/atbd-ast-14.pdf
- Magner TJ, Salomonson VV (1991) Moderate Resolution Imaging Spectrometer-Tilt (MODIS-T). Int J Imaging Syst Technol 3:121–130.
- NASA (1984) Earth Observing System, Science and Mission Working Group Report. Volume 1 (Parts 1 and 2). NASA Technical Memorandum No. 86129, Goddard Space Flight Center, Greenbelt.
- NASA (1985a) Phase-A study for a Moderate Resolution Imaging Spectrometer-Nadir (MODIS-N). Final Report NASS-27145.

- NASA (1985b) Phase-A study for a Moderate Resolution Imaging Spectrometer-Tilttable (MODIS-T). Final Report NAS5-27147.
- NASA (1989) Moderate Resolution Imaging Spectrometer-Nadir (MODIS-N), Phase-B final report. NAS5-30149.
- Pielke RA (2000) Policy history of the U.S. Global Change Research Program: part I. Administrative development, *Global Environmental Change*, 19, 9.
- Plafcan D (2007) "Trying to Share Separately," Chapter four in *Between State and Transnational Community: U.S.-Japan Technoscientific Diplomacy in Earth Observation*. Ph.D. Dissertation, Department of Science and Technology Studies, Cornell University, Ithaca.
- Realmuto V (1990) Separating the effects of emissivity and temperature: emissivity spectrum normalization, in *Proc. 2nd TIMS Workshop*, JPL Publ. 90-55.
- Sabins F (1969) Thermal infrared imagery and its application to structural mapping in southern California. *Geol Soc Am Bull* 80:397-404.
- Sakuma F, Ono A, Tsuchida S, Ohgi N, Inada H, Akagi S, Ono H (2005) Onboard calibration of the ASTER instrument. *IEEE Trans Geosci Remote Sens* 43:2715-2724.
- Salomonson VV, Barnes WL, Maymon PW, Montgomery HE, Ostrow H (1989) MODIS: advanced facility instrument for studies of the Earth as a system. *IEEE Trans Geosci Remote Sens* 27(2).
- Taubes G (1993) Earth scientists look NASA's gift horse in the mouth. *Science* 259:912-914.
- Tonooka H, Palluconi F, Hook S, Matsunaga T (2005) Vicarious calibration of ASTER thermal infrared bands. *IEEE Trans Geosci Remote Sens* 43:2733-2746.
- Watson K (1975) Geologic applications of thermal infrared images. *Proc IEEE* 63:128-137.
- Xiong X, Chiang K, Chen N, Barnes WL (2002a) Aqua MODIS thermal emissive bands pre-launch calibration results and applications. In: Barnes WL (ed) *Proceedings Earth Observing Systems VII*, SPIE, p 4814.
- Xiong X, Che N, Adimi F, Barnes WL (2002b) On-orbit spatial characterizations for Terra MODIS. In: Barnes WL (ed) *Proceedings Earth Observing Systems VII*, SPIE, p 4814.
- Xiong X, Wu A, Esposito J, Sun J, Che N, Guenther B, Barnes WL (2002c) Trending results of Terra MODIS optics on-orbit degradation. In: Barnes WL (ed) *Proceedings Earth Observing Systems VII*, SPIE, p 4814.
- Xiong X, Sun J, Barnes WL (2002d) MODIS on-orbit characterization using the Moon. In: Fujisada H (ed) *Proceedings of SPIE - Sensors, Systems, and Next Generation Satellites VIII*, p 4881.
- Xiong X, Sun J, Esposito J, Guenther B, Barnes WL (2002e) MODIS reflective solar bands calibration algorithm and on-orbit performance. *Proceedings Asia-Pacific Symposium on Remote Sensing of the Atmosphere and Clouds III*, 4891.
- Xiong X, Chiang K, Guenther B, Barnes WL (2002f) MODIS thermal emissive bands calibration algorithm and on-orbit performance. *Proceedings Asia-Pacific Symposium on Remote Sensing of the Atmosphere and Clouds III*, 4891.
- Xiong X, Chiang K, Esposito J, Guenther B, Barnes WL (2003a) MODIS on-orbit calibration and characterization. *Metrologia* 40:89-92.
- Xiong X, Barnes WL, Guenther B, Murphy RE (2003b) Lessons learned from MODIS. *Adv Space Res* 32(11):2107-2112.
- Yamaguchi Y, Sato I, Tsu H (1992) ITIR design concept and science missions. In: Gille JC, Visconti G (eds) *The Use of EOS for Studies of Atmospheric Physics*, 229-310, North-Holland Elsevier Science Publications, Amsterdam.

Chapter 2

Philosophy and Architecture of the EOS Data and Information System

Martha Maiden

2.1 Introduction

In 2009, NASA's EOS Data and Information System (EOSDIS) is the world's largest distributed data and information system infrastructure principally supporting science, a coupled, complex network of production capabilities and data systems. Data and information are easily available through the World Wide Web from searchable, on-line data stores with sophisticated metadata schema, data dictionaries, and comprehensive scientific and technical documentation of its holdings. NASA is moving towards adoption of a service-oriented approach deploying Web services, which enable users to make connections between distributed and heterogeneous elements of environmental data and services internal to and external from EOSDIS as needed. Pertinent Web services are accessible via EOSDIS. Examples of data services include subsetting, data reformatting, and search services such as a thesaurus. The principal subject matter of this book, the MODIS and ASTER instruments, and their derived data, products and applications owe their existence and success to EOSDIS.

2.2 Inception and Early History

The Data and Information System designed to serve the Earth Observing System (EOS), a major endeavor shaped by years of community planning by the many disciplines of Earth science, was conceived starting in 1982 as a multidisciplinary and interdisciplinary effort to provide the scientific basis for understanding global change of the Earth system. The EOS Science Steering Committee's recommendations for Earth science in the 1990s include the following:

M. Maiden (✉)

Earth Science Data Systems, Science Mission Directorate, NASA Headquarters,
300 E St. SW, Washington, DC 20546, USA
e-mail: martha.e.maiden@nasa.gov

1. A program must be initiated to ensure that present time-series of Earth science data are maintained and continued. Collection of new datasets should be initiated.
2. A data system that provides easy, integrated, and complete access to past, present, and future data must be developed as soon as possible.
3. A long-term research effort must be sustained to study and understand these time-series of Earth observations.
4. The Earth Observing System should be established as an information system to carry out those aspects of the above recommendations, which go beyond existing and currently planned activities.
5. The scientific direction of the Earth Observing System should be established and continued through an international scientific steering committee (NASA 1987).

From the outset there were five precepts guiding the development of EOS. The scientists who formulated the mission provided these precepts, summarized as follows:

1. Take today's data today, take it well. Later, one cannot reconstruct the state of the Earth today as well as one can measure it.
2. Provide a data system to put the data easily in the hands of those who can use it. Researchers should work to understand the data rather than struggle to obtain a copy of it.
3. Sustain a community of scientists to do the work of understanding the Earth so that they can devote themselves to research.
4. Implement an Earth Observing System as an information system. Recognize that the satellites, their instruments, the ground system are all means to the end, which is information, and focus EOS on the delivery of the information.
5. EOS must be established to serve the international research community. Global change research cannot succeed as a national enterprise (NASA 1987).

Although only two of these recommendations dealt with the data system per se, a successful EOSDIS is imperative to adequately implementing any of the above. It was recognized that a successful EOSDIS must preserve past, present, and future datasets, which are combined from a variety of sources.

EOSDIS was conceived as an end-to-end ground system, including the mission and instrument operations, communications, computational facilities at investigator sites, generation of standard and special data products, archiving of data, products, and research results, data and information cataloging, searching, browsing and ordering, effective distribution of all information holdings, and user support (Fig. 2.1). The philosophy of EOSDIS has always been to deploy a distributed, open system architecture. And the need for "EOSDIS Evolution," as new information technologies emerge, and science understanding advances, and user needs commensurately change, was articulated from the beginning.

This sophisticated articulation of such a robust philosophy and architecture for EOSDIS was enabled by a lengthy and intimate community involvement in shaping functional requirements for the system. A central tenet of EOS was the availability

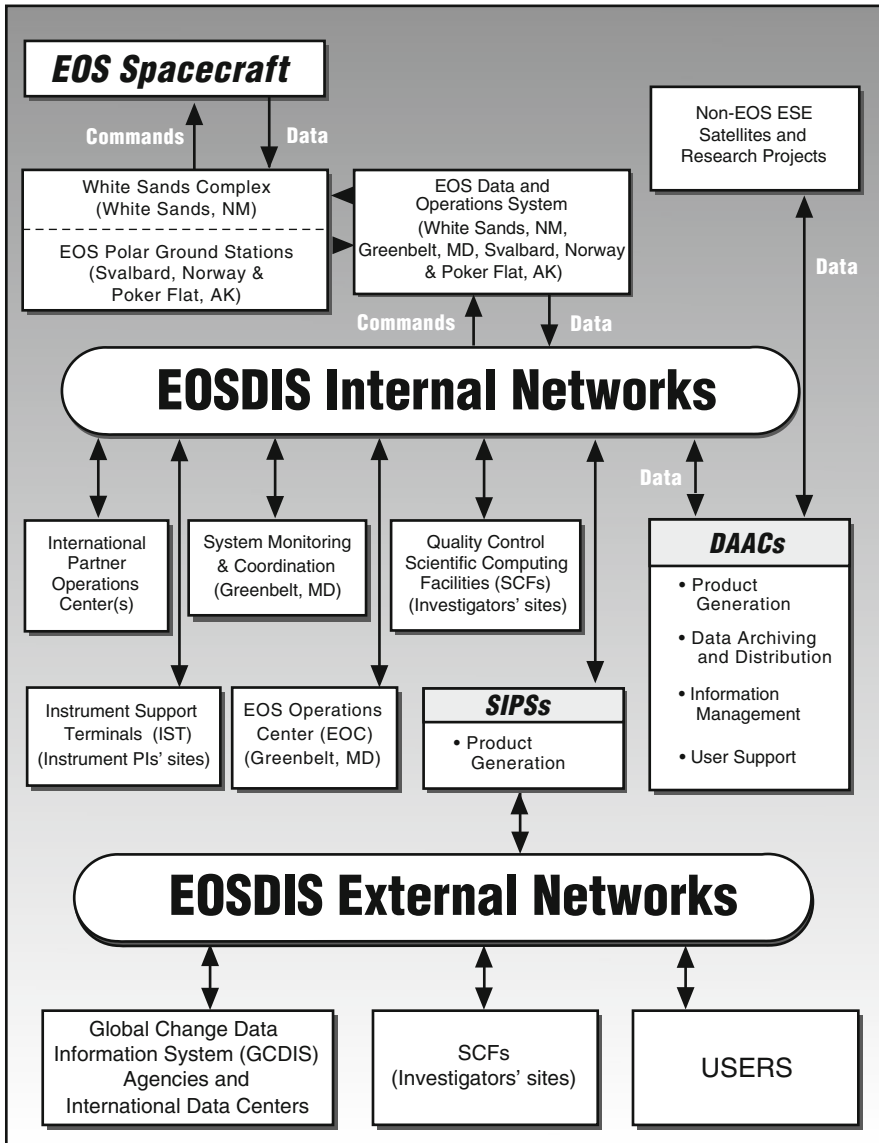


Fig. 2.1 EOSDIS Architecture depicted in 1999, after an adaptive approach was taken to data processing, initiating SIPS

of very diverse and lengthy data records from multiple sources for long-term understanding of the Earth, to empower the Earth science community to make maximum use and reuse of these measurements. EOSDIS was recognized as central to the ultimate success of the EOS Program, with its series of missions to observe or infer many key variables and processes, to meet the needs of the Earth science community.

EOSDIS was conceived to appear as a single logical entity to the user, notwithstanding its distributed architecture, both logically and geographically. Central to EOSDIS' requirements from the beginning was its vital link to the user communities it was to serve, and that service entailed users ability to easily discover, access, and use data from multiple sources. The NASA-embraced data policy was key to this requirement. Just as the system evolved from its early articulation in 1991, NASA took the bold step to offer all its data free of charge and openly available to any requestor. This Earth science data policy has driven the scale of the EOSDIS, and challenged its managers to stay ahead of the technology curve to keep up with the volume of data orders from its huge and ever-growing global customer base.

As early as 1990, it appeared that EOSDIS was quite likely the largest scientific data system ever implemented. The current system's size and functionality, its number of users, and the number of products and volume of data distributed would astound even those whose bold vision started NASA down the path to EOSDIS. The successes and failures along the way have led to valuable "lessons learned," and to a seemingly resilient management philosophy summed up in "best practices."

2.3 Early Architecture

EOSDIS was built upon the existing data system activities of the day, and on going efforts at several future EOSDIS archives sites. They include the NASA Climate Data System at Goddard Space Flight Center, NASA's first attempt to provide a data system in support of the Earth science research community independent of a specific satellite mission. The Pilot Land Data System, also originated at the Goddard Space Flight Center, and evolved into a distributed system with three working nodes. A working group of researchers appointed for consultation helped make this evolution successful. The NASA Ocean Data System, located at the Jet Propulsion Laboratory, was devoted to satellite ocean measurements related to altimetry, scatterometry, and microwave radiometry. The snow and ice segment of the Earth science community was supported by a NOAA facility, the National Snow and Ice Data Center at University of Colorado. A system developed at JPL was transferred to the NSIDC. NASA also established the Alaska SAR Facility at the University of Alaska at Fairbanks. The USGS EROS Data Center was tapped to create a NASA archive for land processes, building upon the expertise of the land group, which specialized in Landsat data at EROS in South Dakota (Fig. 2.2).

Version 0 EOSDIS emerged in August of 1994, a system of systems that had a functional information management system spanning seven data and archive distribution centers' functioning elements connected through an internal network, and providing a significant level of interoperability among these system elements. The Version 0 was termed a "working prototype," and one of its purposes was to approximate EOSDIS' architecture sufficiently to permit an extensive test of its viability.

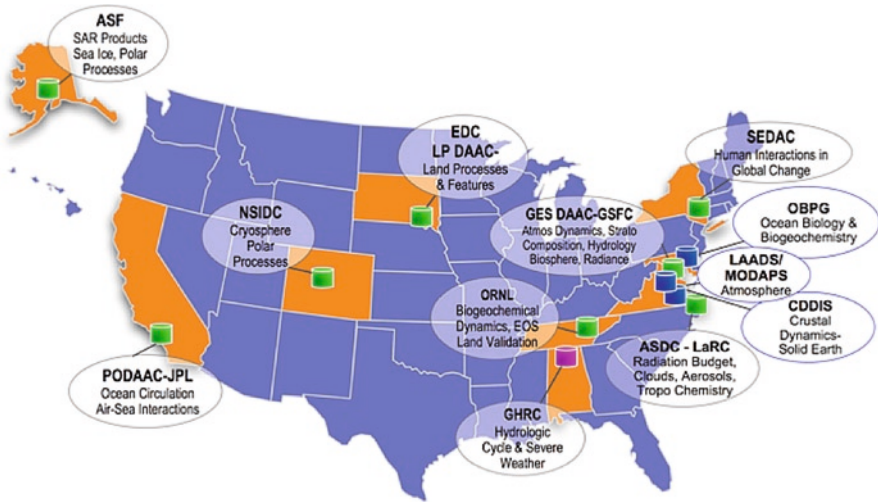


Fig. 2.2 EOSDIS – supported data distribution systems

Version 0 was a marked success. The EOSDIS data centers became known as Distributed Active Archive Centers (DAACs), which became the implementers and conveyors of key practices and responsibilities at this time to ensure that data products were well documented, maintained in easily available form, and supplied to those who requested them. EOSDIS’ vision soon started developing into reality.

2.4 An EOSDIS to Support the EOS Missions

Subsequent Versions of EOSDIS were entrusted to a single contract managed by the NASA Project at Goddard Space Flight Center. Version 1, originally scheduled for the mid-1990s, was to involve a continuing effort to prototype improved capabilities in handling data and additional functionality, including command and control functions. Version 1 would also include the advent of using the National Research and Education Network (NREN), which was emerging as an entity to provide broad linkages to the science community, including ties to EOSDIS.

Version 2 would have full capacity for Terra, and fully capable command and control functions for the mission. Successive versions, slated for delivery at roughly 30-month intervals would support the increased capacity requirements from the launch of the EOS satellites and instruments, and the growth in data rate in the subsequent payloads of the EOS series.

Specific individuals and groups within the scientific community were responsible to develop the algorithms (and encoded in scientific software) with which to generate standard data products. Those researchers were to deliver fully tested,

ready-to-run computer code implementations to the DAACs. The DAACs, through the core system, were to provide the environments in which those codes would routinely run to produce the standard products. Standard data products were defined as products selected as needed by the research community that are spatially and/or temporally extensive and always available when the antecedent data for their production are available. EOSDIS was committed to reprocessing all previous data using the new algorithm when it was adopted as the standard so that a consistent long-term dataset was made available. The plans included documenting the algorithms as part of the overall dataset.

Problems in achieving these ambitious goals were likely inevitable. In hindsight, one could see that problems would ensue from the software development methodology deployed, the “waterfall methodology,” which sought to manage risk by segmenting development into a hierarchy of stages, activities, tasks and steps. This methodology was used primarily for major defense systems development, and the EOSDIS model as “the wisdom of the time.” Fatally, this methodology presumed that the system requirements were already defined and scrubbed exhaustively. In addition, the sheer size of the development strained possibility. During the key development period of 1994–2000, information technology generation cycles shortened, dramatic revolutionary changes occurred, including the inception of the Internet and the World Wide Web, and the information technology bubble meant that turnover in key jobs both in the government and in EOSDIS contracts topped at over 40% per year. Complex development of EOSDIS Core System with “strongly coupled” components proved difficult.

Software version releases were behind, and the functionality thinned and pushed out. The evolution of Version 1 was cancelled. The command and control functionality, being procured through a subcontract, did not function. The subcontract was cancelled and a commercial package was built upon. Cost estimates to complete the EOSDIS Core System soared.

The launch date for the first of the EOS satellite platforms, later dubbed *Terra*, was nearing, and EOSDIS’ implementation was a firm requirement. NASA and the contractor searched for a way forward. NASA lessened its dependence on a single contractor, reducing the content of the contract to a tractable scope, and turned to internal NASA experts and those in the community. NASA allocated most of the processing to new Science Investigator-led Processing Systems (SIPS). NASA was eventually successful in completing this system of systems, which was somewhat more distributed and heterogeneous than initially conceived.

The integrated core infrastructure now had loosely coupled components, including this mix of EOSDIS Core System, and SIPS to process many of the standard data products outside of the DAACs, Data Center-developed capabilities, and community capabilities. EOSDIS still had a common data model, with automated metadata creation and ingest, without need for cross-site metadata translation as in Version 0, and compliance to the new Federal Geographic Data Committee standards. EOSDIS provided an expanded set of software tools and services. The system management became more flexible, and entertained options to support or interoperate with external data sources.

2.5 Science Investigator-Led Processing Systems

The original EOSDIS concept included processing and reprocessing capacity for all instrument-derived data and products located at the DAACs. Instrument teams were contracted to develop scientific software using peer-reviewed and well-documented algorithms at their Science Computing Facilities. When the EOSDIS Core System was descoped in the late 1990s, NASA invited proposals from all the Instrument Team leaders (termed Team Leaders if leading NASA facility instruments, and Principal Investigators for an instrument that was proposed to NASA from the community) to develop processing systems to perform these functions. Proposals were reviewed for technical capability and cost efficiencies. At this time, processing for eight of 12 instruments flown on the Terra, Aqua, ICESat, and Aura were moved out of the DAACs and slated for processing by the science teams with very light touch requirements (Fig. 2.3).

Most of the EOS standard products are produced at facilities under the direct control of the instrument Principal Investigators/Team Leaders or their designees. These facilities are referred to as SIPS. The SIPS are geographically distributed across the United States, and are generally, but not necessarily, collocated with the scientific computing facilities of an instrument Team Leader or Principal Investigator. SIPS-produced products use investigator-provided systems and software, and are sent to appropriate DAACs for archive and distribution. Level-0 Data Products and Ancillary Data that begin the processing sequence are stored at the data centers and retrieved by the SIPS. Agreed-upon interfaces allow machine-to-machine data flows.

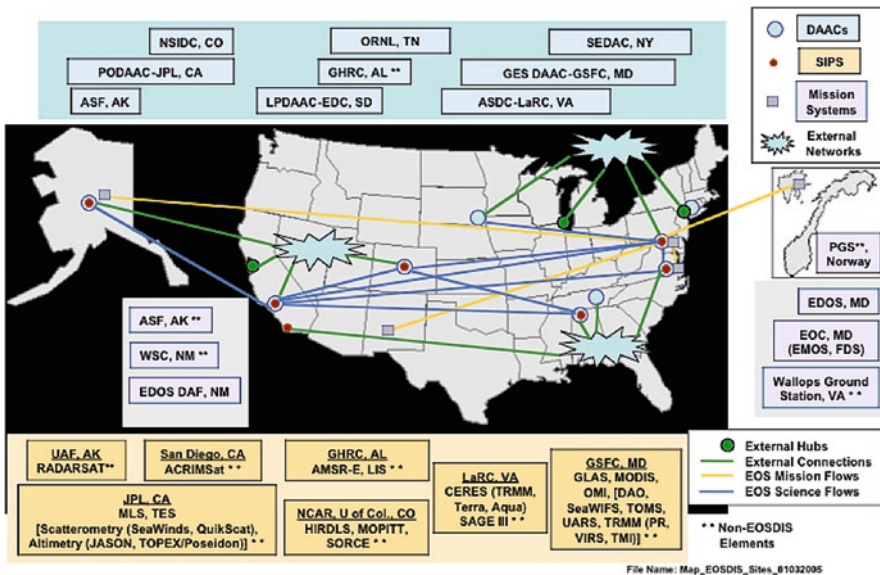


Fig. 2.3 Geographic distribution of DAACs, SIPS, and interfacing Earth science elements

Without configuration control and risk-aversion engineering practiced by the EOSDIS to ensure data management and stewardship, these SIPS approached their systems as community tools. Some deployed cutting-edge technologies and the latest information technology, taking advantage of Moore's law to achieve great gains in processing capability while shedding system maintenance contracts on older hardware. The original requirement for EOSDIS across the board for all instrument data production was for 4× processing (i.e., the ability to process four days of data in one day). These targets were cut back to initially support Terra at 1/2×, and funds were provided to gradually increase the SIPS to 4×. The SIPS' managers used these funds to greatly surpass 4×.

2.6 Data Policy

EOS data policy was designed to further the EOS objectives of acquiring a comprehensive, global 15-year dataset maximizing data utility for scientific purposes; and simplifying long-term access to and analysis of EOS data. To that end, an 11-point policy setting forth the policy attributes and requirements was created for formal subscription by all EOS researchers. The guiding principle required the universal availability of all EOS data and products to all users without any exclusive access periods.

This was revolutionary within NASA. NASA had granted science team members of earlier satellites two years of exclusive use, both as incentives to science discovery and because it was felt that these data were too complicated for general use.

NASA EOS was promoting the full and open sharing of all data with the research and applications communities, private industry, academia, and the general public. The greater the availability of the data, the more quickly and effectively the user communities could use the information to address basic Earth system science questions and provide the basis to develop innovative and practical applications to benefit the general public.

A common set of carefully crafted data exchange and access principles were created by the Japanese, European, and U.S. International Earth Observing System (IEOS) partners during the 1990s as well.

While initially adhering to U.S. Government policy to charge the nominal, incremental cost to reproduce and deliver the data requested to research users, the IEOS agreement opened the data access for EOS-participating countries' research users. Operational agency users (e.g., NOAA, EUMETSAT) were to obtain real-time access to data from instruments of interest through their own direct readout facilities and/or via data relay satellites. NOAA was to acquire near-real-time data feeds for distribution to its user community, using its own data processing by NASA at the incremental cost of reproduction and delivery. Consistent with the Land Remote Sensing Commercialization Act, other primarily commercial users were served on a non-discriminatory basis.

Before the 1994 commencement of operations of EOSDIS Version 0, NASA made a crucial decision to make data available free of charge. There was an incentive

to fully exercise this working prototype, and a decision on whether to charge for the more voluminous EOS data in the future was held in reserve.

Scientists were pleased by this decision. The argument that the NASA-collected data represented a significant public investment in research, which NASA held in a public trust, consequently continued to influence NASA to provide the data free of charge when possible. While public law states that the government should charge the cost of dissemination, it excepted cases where such dissemination cost would unduly inhibit use. NASA's Earth science goals are consistent with promoting comprehensive, long-term Earth system science research. To ensure that data are fully understood and well-utilized, NASA defined the term *data* to include observation data, metadata, products, information, algorithms, including scientific source code, documentation, models, images, and research results.

NASA restricts access, and/or charges the marginal cost, only to the extent required by appropriate memoranda of understanding (MOU) agreed for data products supplied from an international partner or other agency. Arrangements with international partners are made to meet the data needs of the U.S. in this endeavor to understand and characterize the Earth system, which requires working in concert with its international partners.

Today, the decision not to charge the marginal cost of data distribution undoubtedly has driven the scale of EOSDIS, and dramatically increased the use and understanding of data and information derived from satellite instrument measurements by the broad research and applied science communities.

2.7 EOSDIS and Participating Communities

The struggles of an operational EOSDIS in the early years are best exemplified by last-minute implementation changes to ensure readiness to support the Terra mission launched in December 1999. This involved organized debugging of the system during the first several years of Terra support operations, which culminated in assembling many working groups and advisory councils.

The common tenets of the advice from these groups harkened back to early EOS formulation – to place the system close to the science user communities, which it serves.

Initially, NASA's response to this advice was to refrain from creating yet another point or reference architecture as more ideal. Instead, NASA efforts culminated in parallel program investments in community infrastructure. They included supporting competitively selected information partners who would work on advanced information product creation and access, prototyping an Earth Science Federation for data and information exchange, and instituting NASA Earth Science Data System Working Groups as Plural of forum fora for research and development in areas of Standards Processes, Technology Infusion, Reuse, and Metrics Planning and Reporting. These efforts have matured during this decade, providing a marketplace to promote best practices and advance innovative technologies in NASA's core infrastructure.

With this decade's advance, the EOSDIS infrastructure increasingly turned from development to maintenance and operations for the multiple EOS missions currently deployed, including the heritage NASA Earth science data streams vital for long-term global change research. Some NASA managers clearly realized that the EOSDIS was seriously aging, and could dangerously fall behind multiple information technology generations in the years ahead. This was disconcerting when viewed against the fact that NASA is the premier space agency, which leads the study of planet Earth from its key vantage point in space. NASA had stretched the limits of advancing information technology to create EOSDIS. Its community researchers should continue to have access to all EOS data through services at least as rich as any contemporary science information system.

In early 2005, NASA embarked on an EOSDIS Evolution Study. A vision for the 2015 timeframe was developed by a selected EOSDIS Elements Evolution Study Team to guide the conduct of study (Table 2.1).

A concerted EOSDIS Evolution plan was created by the GSFC Project team, which addressed multi-faceted goals including managing archive volume growth, improving response and data access, reducing recurring costs of operations and

Table 2.1 2015 Vision goals

| Vision tenet | Vision 2015 goals |
|-----------------------------------|---------------------------------------------------------------------------------------------------------------------------------------------------------------------------------------------------------------------------------------------------------------------------------------------------------------------------------------------------------------------------------------------------------------------------------------------------|
| Archive management | <ul style="list-style-type: none"> ✓ NASA will ensure safe stewardship of the data through its lifetime ▪ The EOS archive holdings are regularly peer reviewed for scientific merit |
| EOS data interoperability | <ul style="list-style-type: none"> ▪ Multiple data and metadata streams can be seamlessly combined ▪ Research and value added communities use EOS data interoperably with other relevant data and systems ▪ Processing and data are mobile |
| Future data access and processing | <ul style="list-style-type: none"> ✓ Data access latency is no longer an impediment ✓ Physical location of data storage is irrelevant ✓ Finding data is based on common search engines ✓ Services invoked by machine-machine interfaces ✓ Custom processing provides only the data needed, the way needed ✓ Open interfaces and best practice standard protocols universally employed |
| Data pedigree | <ul style="list-style-type: none"> ▪ Mechanisms to collect and preserve the pedigree of derived data products are readily available |
| Cost control | <ul style="list-style-type: none"> ✓ Data systems evolve into components that allow a fine-grained control over cost drivers |
| User community support | <ul style="list-style-type: none"> ✓ Expert knowledge is readily accessible to enable researchers to understand and use the data ✓ Community feedback directly to those responsible for a given system element |
| IT currency | <ul style="list-style-type: none"> ✓ Access to all EOS data through services at least as rich as any contemporary science information system |

sustaining engineering, updating aging systems and components, and moving towards an even more distributed environment. NASA now viewed our EOSDIS system of systems as being a part of a larger, indeed international, Earth science system of systems.

This concerted EOSDIS Evolution was implemented beginning in 2006; the final stages approach completion in the fall of 2008. Its key features include taking data off from tapes and loading them on spinning disks, which are immediately accessible to users.

2.8 Metrics

The scale of the EOSDIS is difficult to convey. The persistent EOSDIS mission science objective is to provide measurements and information from a large number of operating environmental missions to several broad and diverse research communities. This also entails providing multi-mission science operations. The key science functions are production of standard science data products, active archival of Earth science data, ordering and distribution, and user services. System components comprise 11 DAACs and Data Centers, nine SIPS, the EOSDIS Core System's Science Data Processing System, the system elements to ingest, process, archive and distribute data, and the networks needed to transport elements. EOSDIS maintains continuous operations, while evolving to respond to changing requirements. EOSDIS products continue to grow in record length and improve in quality. During the U.S. Government fiscal year October 2007–September 2008, over 150 million science data products were delivered to EOSDIS users. Approximately 525,000 distinct users (counted monthly) of Earth science data and services, with more than ten million unique accesses, have visited EOSDIS (Fig. 2.4).

2.9 Lessons Learned and Best Practices Today

A single statement best exemplifies the EOSDIS lessons learned: *One size does not fit all*. Scientific disciplines have different ways of looking at the data and different vocabularies. Large system developers and managers need to understand that flexibility is a key to success. Of course, some consistency is needed to facilitate search and access across datasets. Community evolution of standards works better than a top-down approach. The emerging capabilities in Service-Oriented Architecture and Web Services appear to offer great promise to provide interoperability to users who traverse EOSDIS' heterogeneous and distributed systems.

NASA had the foresight to adopt and maintain an open data policy over the years. This was done for the most idealistic reasons, and arguably, is a unique strength of how the U.S. Government operates and drives our leadership in science technology innovation. NASA provides open access to data with no period of

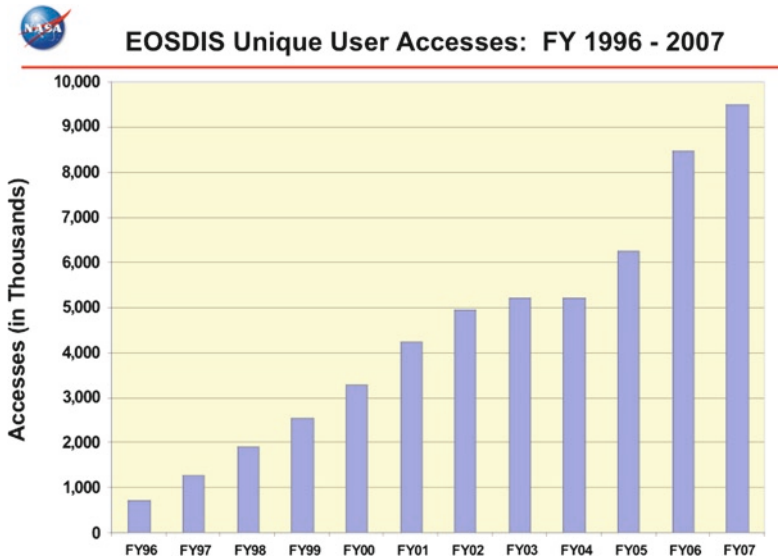


Fig. 2.4 EOSDIS unique user accesses: FY 1996–2008

exclusive access. Most of the data are provided at no charge to any requesting user, with the exception of restricted access to the extent required by agreements with data supplied from an international partner or another agency.

Both “core” and “community” capabilities are essential to meet NASA’s Earth Science Data System program objectives. Core capabilities are needed for long-term stability and dependable capture, processing, and archiving of data and distribution of data to broad and diverse communities of users. Community capabilities provide innovative, new scientific products as well as a path to technology infusion.

Earth Science Working Groups provide community-vetted recommendations to NASA to consider for implementation. These recommendations, as well as those from EOSDIS Data Centers, annual user feedback through surveys and at community conferences, and interagency and international discussions influence NASA’s programmatic direction. NASA recognizes the need to strengthen its effort to facilitate technology infusion from community to core systems.

Loosely coupled, heterogeneous systems can work together. EOSDIS Version 0 involved making heterogeneous systems successfully interoperate in the “pre-WWW” era, using well-defined interfaces and a “thin” translation layer to spread queries to multiple databases and gather responses to present to users. The complex development of EOSDIS Core System with “strongly coupled” components proved difficult, and was hence, descoped. Managing standards and interfaces was key to success.

Data systems must evolve over time. Otherwise, systems become so outdated that starting over is the only way to proceed. This is quite risky, and often does not preserve the intricate connections among the systems and supporting communities,

which were incrementally built over time. Managing transitions of an operational system that serves large numbers of users is critical.

2.10 Next Generation Challenges

Information technology is moving at a record pace. Advanced information systems technology investments in Earth science systems research has motivated many Earth sciences to become interested in facilitating easy access and use of our data and information.

Over time, the EOSDIS systems managers have adopted an evidently successful process to provide services at least as rich as any contemporary science information system. This requires staying at the crest of the technology infusion curve following their proven capabilities and economic affordability.

EOSDIS was built during a revolutionary time. These evolutionary principles might not always carry our systems smoothly forward. How will Earth science data systems best make use of tools like Google? And what will emerge in the next ten years?

To best take advantage of the new Service-Oriented Architecture, to lessen data latency for societal benefit needs, and to enable machine-to-machine transactions, more infrastructure work on the availability of the data description is crucial. Collection, preservation, availability and use of the derived data product's lineage are very essential to the larger Earth science community. Readily accessible and open communication of data quality and fitness for use are very essential towards realizing the full potential of the Earth science data products.

EOSDIS embodies our progress with science and systems in the last two decades. It reveals the size, scale, and scope of an enormous infrastructure engineered through the integration of several components to ultimately benefit the global Earth science community. It further highlights how it helps the globalization of science as NASA satellite data and products interoperate with other relevant data and systems through an international Earth science system of systems.

Reference

NASA (1987) From pattern to process: the strategy of the Earth Observing System (EOS Science Steering Committee report, vol II). NASA Publication

Chapter 3

Lessons Learned from the EOSDIS Engineering Experience

Evelyn Nakamura

3.1 EOSDIS Core System Background

The EOSDIS Core System (ECS) began as NASA's vision for a geographically distributed system to support the operation and management of satellite-derived earth observations, and facilitate interdisciplinary scientific research of the Earth System and the interaction among its components (Settle 1995). The ECS serves as a major component in support of the EOS mission to process, archive, and distribute data.

During the design, development, maintenance, and operation of the ECS, we have learned many valuable lessons, which we apply to meet the challenges of an evolving system (Fox 2002a, b). They include the following:

3.1.1 Incremental Method of Requirements Elaboration Proved Effective

One of the earliest lessons we learned was that the traditional waterfall methodology for software development was not deemed a good fit for the ECS. Requirements that were developed and presented at the System Requirements Review (SRR) in September 1993 proved that the project needed to revamp its approach to meet the expectations of the NASA-sponsored EOSDIS Science Panel. The SRR panel findings were as follows:

- The ECS requirements development lacked sufficient science community involvement.
- The requirements need to expand the incorporation of evolutionary concepts.
- We need to include external prototyping and/or alternative approaches.
- The requirements conveyed a preconceived design.
- The design was too centralized.

E. Nakamura (✉)

Raytheon Information Solutions, 5700 Rivertech Court, Riverdale, MD 20737, USA
e-mail: Evelyn_N_Nakamura@raytheon.com

The Science Panel then challenged the ECS team to provide a plan to address their concerns, and deferred the System Design Review originally scheduled for December 1993 until the following spring. A Progress Review was scheduled, where NASA evaluated the progress of the SRR closure items.

The ECS Progress Review was held in December 1993, and the ECS team presented a number of concepts, which directly addressed the issues from the SRR.

- More innovative architectural concepts that present a multi-tiered approach as opposed to a centralized approach to the system;
- Results of architectural trades including their evaluation criteria, with an increased emphasis on system evolution, which addressed the notion that the design was preconceived, and was static;
- A “closed loop” working-level process with joint visits and coordination meetings with key GSFC personnel and organizations, to more fully engage the science community;
- A multi-track development process that would accommodate the inclusion of prototypes as well as formally developed components.

The trades and concepts developed during and as a result of the Progress Review were documented in a series of white papers, before they were incorporated into the systems requirements and system design.

The ECS team went on to adapt the white paper approach to requirements development into an incremental model of requirements development. Instead of developing requirements in terms of subsystems or software configuration items, we developed operations concepts, which grouped system functions into threads or capabilities. The operations concepts were elaborated upon to produce requirements and testing criteria, and were encapsulated into “tickets.” The tickets served as the baseline description for all perspectives associated with the capability – operations, engineering, development, and testing – and were reviewed by all stakeholders prior to the inception of design. The main benefit over the waterfall model was the early definition and review of testing acceptance criteria by all stakeholders versus a single independent test organization. Tickets were then subsequently grouped into system releases to define major upgrades to functionality. The ticket approach was a very effective mechanism to communicate system features and evoke participation by stakeholders during the requirements reviews, and ensure that system verification tests addressed the most relevant and realistic scenarios.

3.1.2 Heavy Dependence on COTS Technology Increases the System’s Complexity in the Long Run

One of the outcomes from the Progress Review concluded that ECS should exist as an “open system,” which applied industry standards for technology versus proprietary ones for it to evolve and remain responsive to technology innovations. This was envisioned as a way to maximize the availability of commercial off-the-shelf (COTS) technology, and enabled the ECS to leverage off of the competition inherent in the COTS marketplace to acquire solutions with the best value. While this principle

of maximization of COTS has allowed the ECS to deploy several major technology upgrade releases, it has presented the program with unique and unanticipated challenges as well. At one point, the ECS integrated over 50 software products and was hosted on UNIX platforms from IBM, HP, SUN, and SGI. The ECS team analyzed approximately 400 candidate vendor patches each year, which were required for bug fixes, security patches, and routine product upgrades. In a given year, around 40 of these candidate patches were eventually deployed. The ECS team learned valuable lessons in how to manage COTS integration, which include the following:

- COTS requires an adaptive COTS upgrade process: The release of COTS patches and upgrades followed the same deployment approach as that for ECS custom software releases, with respect to release documentation, test reports, and installation instructions. As far as possible, the ECS releases upgrades and patches that are both backward- and forward-compatible with future custom code releases to avoid disruptive transitions in the field. COTS patches were also delivered out-of-cycle from custom software releases, to afford the maximum flexibility for the operations staff at the sites, and to keep the patch installation time within a preventative maintenance window.
- COTS requires management involvement: The ECS team frequently found itself pushing the envelope with its vendors, in terms of performance specifications, timeliness of upgrades, and responsiveness to product bug reports. By fostering a management relationship with its key vendors, the ECS team was able to ensure that schedules are met. Senior management and NASA customer participation in face-to-face meetings with the vendors went a long way to gain leverage with vendor schedules and priorities. Future program plans and vendor status on new products helped to forge long-term commitments on the most critical COTS, such as the archive management COTS.
- COTS requires significant effort and expertise: The ECS sustained a dedicated team and test bed laboratory to test candidate patches. COTS experts were identified on the ECS team and were tasked to remain abreast of vendor product innovations as well as upgrade notices. The ECS team developed and documented escalation processes with each vendor, which kept the COTS experts as well as management in the loop. And finally, the ECS team placed a heavy dependence on vendor-provided training for both its COTS experts and operations staff from the field.

In a nutshell, the COTS-specific ECS experience has taught us that reliance on COTS represents a significant commitment of resources and expertise to achieve maximum benefits.

3.1.3 Incremental Releases Are a Much Better Way to Deploy Capability than Big-Bang Releases

Traditionally, ECS-size systems are compelled to add new features by deploying well-spaced, infrequent system releases. System releases typically involve major transition activities, which interrupt operations for extended periods of time, because

they almost always involve simultaneous changes in many custom and COTS software components. Furthermore, risk is increased when a system release represents the accumulation of many new components that will replace those currently in operation. Through the management of multiple development and sustaining engineering environments and baselines, we were able to support the release of new functionality every 9–12 months. Eventually, the ECS Configuration Management team learned to consolidate multiple DAAC-unique baselines into a generic baseline, which represented that site so as to cover all significant risk areas. The frequency of the installation impact to operations was often compensated by the reduced footprint size of the smaller incremental releases. This also enabled the sites to install the releases during routine PM outages, thereby eliminating the need to schedule additional outages for system upgrades. Many system upgrades required companion upgrades to COTS products. To reduce the impact of these types of releases, COTS products were deployed as backward compatible upgrades ahead of the associated custom code release. In addition, high priority fixes, which were critical to operation, were delivered as emergency fixes that were surgically applied to the system, also during normal PM hours. The incremental approach to deployment enabled us (and the sites) to manage system upgrades, while minimizing the impact to operations.

3.1.4 Mode Management Approach to Software Development and Testing

The anticipated longevity of the ECS program compelled the development and test teams to manage multiple system baselines within the budget and resource limitations. The cost of maintaining separate hardware strings for each unique system baseline would have been prohibitive; at any one time, ECS would need to have a baseline for operations, performance testing, development, development testing, sustaining engineering, as well a test string for the insertion of new technology, and testing of release transitions. Mode management provided the cost-effective virtualization of multiple system baselines while minimizing the number of unique hardware strings needed. Custom code and databases were designed as mode-configurable based on the operator's parameter settings in the code or database name. This helped to isolate software baselines from each other while enabling their coexistence on the same hardware. This approach was extended to the DAACs, where separate operations and test baselines were maintained on a single hardware string. The modes at the DAACs eventually became important enablers to help phase-in mission changes.

3.1.5 Development of DAAC-Unique Extensions

As each ECS DAAC pursued its related albeit independent science objectives, it was necessary for ECS to provide an extensible architecture, which enabled customizing the system to meet each site's unique requirements. Common systems

requirements for ingesting, archiving, and distributing data, as well as services that support system administration, security, backup, and failure recovery, were naturally provided with each ECS release. However, certain aspects of each DAAC's mission were best left up to them to develop. The ECS facilitated the application of DAAC-Unique Extensions (DUE) through the publication of database design and schema documents, and application programming interfaces (API) to ECS services for data search and distribution. Each DAAC maintained its own DUE that were enabled by a peer review of anticipated changes to the ECS database schema or APIs in advance of their release, which provided them an opportunity to assess the impacts of change. An example of the DUE process facilitated by ECS is the metrics reporting systems. The DAACs initially developed their own reporting systems, but this eventually led to the establishment of generic reporting requirements and tools, which currently serves the entire EOS enterprise. Facilitating DUE development is a cost-effective approach to satisfy site-unique requirements.

3.1.6 Data Migration in Multi-petabyte ECS Archives Is a Continuous Operational Function

The ECS has undergone two major data migrations. Approximately 350 TB were migrated from STK D3 to STK 9940A technology in a little over a year. The STK 9940A archives were then migrated to 9940B technology in about a 4-year period, by which time the archives had grown to around 2.5 PB (Behnke et al. 2005). The ECS architecture was designed with data migration in mind, and was built to support multiple generations of storage technology. We sought and gained commitment for the automated support of data migration from vendors to expedite the transition and reduce risk. We also sized the system to support concurrent operations and migration workloads, and further enabled throttling the data migration to handle peak operational workloads in parallel. In short, systems with the longevity and petabyte-scale ECS archives must embrace data migration as a continuous operations function.

3.1.7 Silent Data Corruption Will Occur if Data Volumes Are Large Enough

Silent data corruption occurs when hardware or software fails in a way that leads to corrupted data, with no associated error indicated during its transfer, storage, or retrieval. Several instances of silent data corruption occurred, which are attributable to the following causes – failed storage processor, broken pin on an I/O controller card, COTS software error, and a failed network router. Some of these instances went undetected until the data were received by the end-user. As mitigation against future silent data corruption occurrences, we resolved to add an end-to-end checksum

verification capability to key system data flows. Data providers were encouraged to compute checksums when generating data objects and supplying them to the ECS upon ingest. ECS ingest protocols were updated to support the inclusion of a data provider checksum, which ECS would store and re-verify prior to distribution. Finally, ECS includes checksums with metadata, so end-users have the option of re-verifying checksums after receipt of their data.

3.1.8 Providing Access to Online Data

At the onset of the ECS contract, the Internet had not yet reached its current state of ubiquity. Users now increasingly demand more data availability via the Web as against compact digital media or tape. As disk storage costs have decreased and network bandwidths have increased, it is more feasible to make available large portions of ECS data holdings online. In 2001, ECS deployed its Data Pool capability, which provided an online cache of popular data products via FTP or the Web. The Data Pool data are catalogued in a warehouse database that provides a subset of the metadata available in the inventory. A simple Web user interface allows users to search and view metadata, and browse granules from any Web browser. Downloads are accessible via this interface or directly via FTP. ECS further enhanced its download capability with services for re-projection and reformatting from HDF-EOS to GeoTIF format. In 2008, NASA authorized the ECS to begin the transition to an on-line archive, in which, the primary storage for all data are on disk, and tapes provide only a backup recovery source. This offers a more efficient method to stage data for distribution, and also provide them to users for direct download or Web access. The transition from 9940 tape libraries to the LTO-4 technology will drastically reduce the archiving footprint for the ECS data centers, and also provide a just-in-time technology insertion for the 9940 libraries, which are nearing their end-of-service life.

In conclusion, the ECS owes its longevity and success to the continuous application of lessons learned during its 10-year lifespan, many of which are unique to petabyte-scale systems, and also to any system whose mission includes the archival and distribution of large volumes of science data.

References

- Behnke J, Watts TH, Kobler B, Lowe D, Fox S, Meyer R (2005) EOSDIS petabyte archives: tenth anniversary. 22nd IEEE 13th NASA Goddard Conference on Mass Storage Systems and Technologies.
- Fox S (2002a) Summary of the EOSDIS Core System (ECS) Science Data Processing Segment (SDPS). Presentation to NASA headquarters.
- Fox S (2002b) EOSDIS (ECS) Science Data Processing System (SDPS) Lessons Learned in System Development. Presentation to NASA Headquarters.
- Settle M (1995) Project Development History for the ECS Project. Document Number 218-CD-001-001, CDRL Item 038.

Part II

ASTER and MODIS: Instrument Design, Radiometry, and Geometry

The Earth Observing System (EOS) mission offers remote sensing data and derived products acquired from observations collected from different multispectral and sounding instruments. Two of them, ASTER and MODIS, are the focus of this volume. The ASTER instrument aboard the Terra platform generates data at high-to-medium spatial resolutions, whose derived products cater to a number of geological, geophysical, and biophysical applications. The twin MODIS instruments aboard the Terra and Aqua platforms offer data at moderate spatial resolutions designed to furnish inputs for the terrestrial, oceanic, and atmospheric science models and applications. Both remote sensing instruments owe their pedigree to previous sensors. Overall, ASTER advanced the direction charted by Landsat Thematic Mapper and Satellite Pour l'Observation de la Terre (SPOT) with certain enhancements. The ASTER Visible and Near Infrared (VNIR) sensor is based on the technology used in the Multi-spectrum Electronic Scanning Radiometer (MESSR) optical sensor carried by the Japanese Marine Observation Satellites (MOS-1 and MOS-1B), and the Optical Sensor (OPS) aboard the Japanese Earth Resources Satellite-1 (JERS-1). ASTER's Shortwave Infrared (SWIR) sensor follows the design of the SWIR radiometer aboard JERS-1. ASTER's Thermal Infrared (TIR) sensor was a completely new development, with fabrication knowledge drawn from MOS-1. The MODIS instrument's land imaging component builds upon second and third generation sensor systems, which include the Advanced Very High Resolution Radiometer (AVHRR), and the Landsat Thematic Mapper instruments. It further includes additional spectral bands in the middle- and longwave infrared wavelengths. The two practically identical MODIS instruments (aboard Terra and Aqua) cross the Equator at different times, and their continuous four acquisitions per day ensures a multi-temporal, global data record, which is a critical requirement for monitoring global changes in the Earth's lands, oceans, and atmosphere.

The ASTER instrument emerged from early blueprints and designs, and later collaborations, which include the Thermal Infrared Multispectral Scanner (TIMS) and Thermal Infrared Ground Emission Radiometer (TIGER) on the USA side, and the Intermediate Thermal Infrared Radiometer (ITIR) on the Japanese side. Japan was responsible for the complex task of building and assembling the three different instrument systems, cryocoolers, and master power supply. The instrument design incorporates a stereoscopic assembly as part of the VNIR sensor, enhanced spatial

and spectral resolutions, and instrument pointing capabilities (Fujisada – *in this volume*). The wisdom in implementing independent design and functionality in each of the three sensor subsystems was well justified by later problems experienced with the SWIR sensor. ASTER's geometric accuracy specifications including both inter- and intra-telescope registration and pixel geolocation knowledge, have remained exceedingly better than the original goals. ASTER digital elevation data provide the basis for a vital 30-m spatial resolution global DEM product, which was released to the public in 2009 Summer.

The sensor electronics in any electro-optical remote sensing system are expected to experience a change in their response over time. The radiometric quality requires consistent monitoring to understand and characterize the system response behavior as a precursor to calibration. ASTER's radiometric calibration and atmospheric correction processes help create accurate geophysical data products. The ASTER VNIR and SWIR sensors incorporate redundant on-board calibration hardware. They include on-board calibrators, and also accommodate independent vicarious calibration approaches. ASTER's radiometric calibration and atmospheric correction processes address two distinct spectral regions, the solar reflective (VNIR and SWIR), where reflected sunlight is the principal source, and the TIR, where emitted terrestrial radiation is the main source. These processes facilitate conversion of the solar reflective digital numbers to at-sensor reflectance and spectral radiance (Arai et al. *this volume*). Another issue also addressed is the SWIR crosstalk problem, which was identified and analyzed early in the postlaunch mission. The TIR sensor has a fixed telescope with mechanical scanning and pointing functions performed by a scanning mirror. For calibration purposes, the scanning mirror rotates 180° from nadir to view an internal blackbody with a greater than 0.99 emissivity. This particular dual scanning/pointing mirror design does not allow observations of the deep space, and permits only a single temperature measurement for each Earth observation. ASTER TIR calibration uses both on-board and vicarious calibration approaches. The ASTER level-1B TIR scaled at-sensor radiance data are atmospherically corrected using a radiative transfer model (Tonooka *this volume*).

MODIS is a unique example of a multispectral, cross-track scanning radiometer that acquires continuous, multitemporal, global data at moderate resolutions from both its Terra and Aqua incarnations. This allows the MODIS science mission to generate a wealth of moderate resolution data products at sufficient spectral and temporal granularity to monitor global environmental processes. Santa Barbara Remote Sensing built both MODIS instruments per NASA's specifications. The major component systems include the mainframe, imaging radiometer, optical system, scan mirror assembly, radiative cooler, door assemblies, electronics systems, and on-board calibration systems. Its optical systems include a set of linear arrays with spectral interference filters located in four focal plane assemblies. They include the visible, near infrared, shortwave and midwave infrared, and longwave infrared, the latter two of which require cryogenic cooling of their detector arrays (Xiong et al. *this volume*).

A number of system design trade-offs enable a single MODIS instrument to meet the diverse data acquisition needs of the terrestrial, oceanic, and atmospheric elements. The MODIS instrument design incorporates spectral channels specifically

to help characterize atmospheric effects as well as clouds, which information is also used to atmospherically correct the land surface observations besides providing crucial atmospheric measurements as well. Another major MODIS advance since the AVHRR era is its incorporation of a sophisticated array of on-board calibration hardware used in recent remote sensing history. They include a solar diffuser, solar diffuser stability monitor, spectroradiometric calibration assembly, and full aperture blackbody. They facilitate radiometric calibration of the solar reflective and thermal emissive bands, whose calibration uncertainty at typical scene radiances are maintained within specifications.

The MODIS instrument's scanning method is more advanced in its style of Earth observation. In contrast to single-line-per-scan sensors like AVHRR and SeaWiFs, MODIS observes 40 lines of 250 m resolution and 20 lines of 500 m resolution within a single ten-line (1 km resolution) scan. Therefore, the MODIS pixel size increases with scan angle, which overlaps along the scan borders every 10 lines. These unique characteristics produce the panoramic "bow-tie effect" at the scan edges. Given such a wide field-of-view, the MODIS instrument contends with unique sensing geometries and the Earth's curvature to produce a swath width that is roughly 2,340 km. The along-track and along-scan geolocation accuracies between the Terra and Aqua MODIS instruments vary slightly, but in general are much better than the specifications. Specific correction approaches are implemented to ensure that the geolocation of individual MODIS observations conform to sub-pixel accuracies, which facilitate terrestrial global change science applications.

Chapter 4

Terra ASTER Instrument Design and Geometry

Hiroyuki Fujisada

4.1 Overview

The ASTER instrument is used to study the interactions between the Earth's geosphere, hydrosphere, cryosphere, and atmosphere. ASTER's specific areas of science investigations include the following: (a) geology and soils, (b) volcanology, (c) carbon cycling and the marine ecosystem, (d) aerosols and cloud studies, (e) evapotranspiration, (f) hydrology, (g) vegetation and ecosystem dynamics, and (h) land surface climatology.

The ASTER instrument was designed to acquire quantitative spectral radiance data from the earth's surface in the 0.5–2.5 and 8–12 μ m atmospheric windows at spatial and spectral resolutions appropriate for various science objectives. ASTER's key features compared to those of other optical imagers are (a) spectral data acquisition with a high spatial resolution of 15m in visible and near infrared (VNIR) regions, (b) stereoscopic capability in the along-track direction, (c) high spectral resolution in the short wave infrared (SWIR) region, and (d) high spectral and spatial resolutions in the thermal infrared (TIR) region (Yamaguchi et al. 1993).

4.2 Baseline Performance

The ASTER instrument design meets certain baseline performance requirements as delineated in Table 4.1, which were defined in accordance with the scientific objectives of the mission. Several improvements were incorporated to better ASTER's performance relative to the existing optical sensors such as Landsat TM, SPOT HRV, and JERS OPS. They include the following: (a) an increase in the base-to-height ratio (B/H) of stereo imaging from 0.3 to 0.6 for improved surface elevation;

H. Fujisada (✉)

Sensor Information Laboratory Corp., Hosoda Bldg 2F-D, 3-14-17 Azuma,
Tsukuba 305-0031, Japan
e-mail: fujisada@silc.co.jp

Table 4.1 ASTER baseline performance requirements

| Subsystem | Band no. | Spectral range (μm) | Radiometric resolution | Absolute accuracy (σ) | Spatial resolution | Signal quantization levels |
|-----------------------------------------------------|----------|----------------------------------|--------------------------------------------|--------------------------------|--------------------|----------------------------|
| VNIR | 1 | 0.52–0.60 | | | | |
| | 2 | 0.63–0.69 | $\text{NE}\Delta\rho \leq 0.5\%$ | $\leq \pm 4\%$ | 15 m | 8 bits |
| | 3N | 0.78–0.86 | | | | |
| | 3B | 0.78–0.86 | | | | |
| SWIR | 4 | 1.600–1.700 | $\text{NE}\Delta\rho \leq 0.5\%$ | | | |
| | 5 | 2.145–2.185 | $\text{NE}\Delta\rho \leq 1.3\%$ | | | |
| | 6 | 2.185–2.225 | $\text{NE}\Delta\rho \leq 1.3\%$ | | | |
| | 7 | 2.235–2.285 | $\text{NE}\Delta\rho \leq 1.3\%$ | $\leq \pm 4\%$ | 30 m | 8 bits |
| | 8 | 2.295–2.365 | $\text{NE}\Delta\rho \leq 1.0\%$ | | | |
| | 9 | 2.360–2.430 | $\text{NE}\Delta\rho \leq 1.3\%$ | | | |
| | 10 | 8.125–8.475 | | | | |
| TIR | 11 | 8.475–8.825 | | $\leq 3\text{K}$ (200–240K) | | |
| | 12 | 8.925–9.275 | $\text{NE}\Delta\text{T} \leq 0.3\text{K}$ | $\leq 2\text{K}$ (240–270K) | 90 m | 12 bits |
| | 13 | 10.25–10.95 | | $\leq 1\text{K}$ (270–340K) | | |
| | 14 | 10.95–11.65 | | $\leq 2\text{K}$ (340–370K) | | |
| | | | | | | |
| Stereo base-to-height ratio | | | | | | |
| Swath width | | | | | | |
| Total coverage in cross-track direction by pointing | | | | | | |
| Mission life | | | | | | |
| MTF at Nyquist frequency | | | | | | |
| Band-to-band registration | | | | | | |
| Peak data rate | | | | | | |
| Mass | | | | | | |
| Peak power | | | | | | |

(b) an increase in the number of SWIR bands from four to six to enhance the surface lithological mapping capability; (c) the addition of five TIR spectral bands to derive accurate surface temperatures and emissivities; and (d) improved radiometric resolutions and accuracies (Fujisada 1998; Iwasaki and Fujisada 2005).

4.3 System Layout

The ASTER instrument's wide spectral range requires three separate sensor subsystems. They include the VNIR, the SWIR, and the TIR subsystems. The VNIR subsystem has two telescopes, a nadir-viewing telescope and a backward-viewing telescope. Both telescopes enable a stereoscopic view, and a large 0.6-in. base-to-height ratio in the along-track direction with a minimum mass resource. The JERS/OPS sensor contained only one telescope, which limited its base-to-height ratio. A three-telescope design concept is ideal for a large base-to-height ratio but it requires both extra mass and data transmission rates. A combination of the nadir- and backward-viewing telescopes is the consequence of a trade-off between performance and resources (Fujisada et al. 1999).

The pointing function is provided for global coverage in the cross-track direction by changing the center of the swath. ASTER's swath width is 60 km, and the distance between neighboring orbits is 172 km. The optical axes of the VNIR and SWIR telescopes are tiltable in the cross-track direction to cover a wide range in that direction. The TIR telescope contains a scanning mirror, which provides both the scanning and pointing functions. The tilt range is specified so as to cover 272 km from a 705-km spacecraft altitude. The total coverage of 272 km is obtained by adding a spacecraft recurrent inaccuracy of ± 20 km to the user's requirement (232 km). An extra range is provided for the VNIR channels to observe special targets of opportunities quickly. All components are integrated on the spacecraft (Fig. 4.1).

Figure 4.2 shows the stereo configuration of the backward-viewing telescope. The relationship between B/H ratio and α is $B/H = \tan\alpha$, where α is the angle between the nadir and the backward directions at an observation point on the earth's surface. The angle α which corresponds to B/H ratio of 0.6 is 30.96° . By considering the curvature of the earth surface, the setting angle between the nadir-viewing and the backward-viewing telescopes is calculated at 27.60° (Fujisada et al. 2005).

4.4 System Components

Table 4.2 summarizes the primary ASTER functions and components. A different type of telescope is employed for each optical sensor subsystem to meet its wavelength region and size of focal plane requirements. Band pass filters carry out exact spectral separation of all bands. Both VNIR and SWIR images are obtained by pushbroom scanning with Si-CCD and PtSi-CCD linear array detectors, respectively.

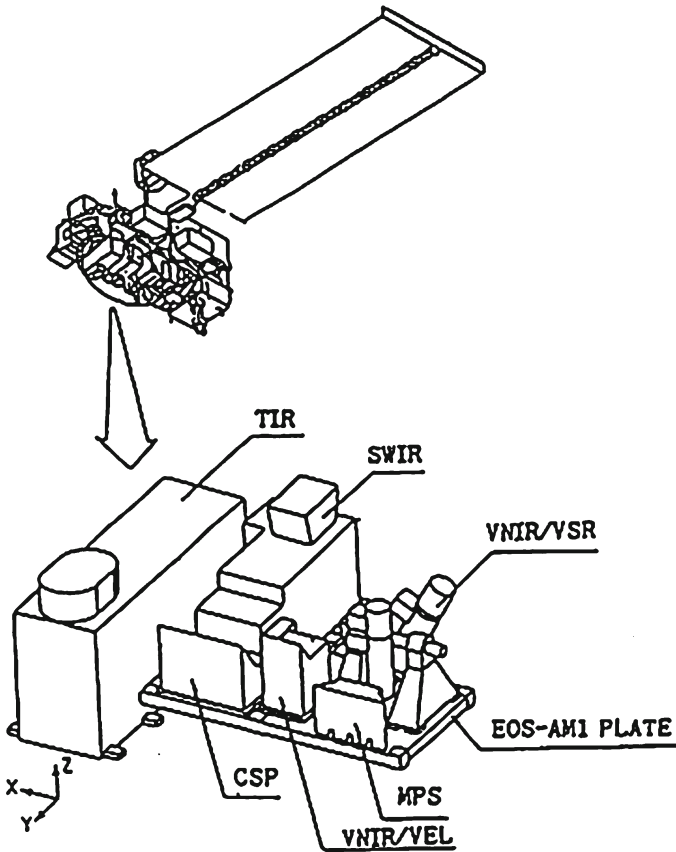


Fig. 4.1 EOS-AMI on-orbit configuration with ASTER

The TIR images are obtained by mechanical scanning with ten HgCdTe PC type detectors per spectral band, with a total of 50 detectors. ASTER has four uncooled and two cooled focal planes. The SWIR and TIR subsystem band pass filters are integrated together with detectors on the cooled focal planes to suppress thermal radiation from the filters. The SWIR and the TIR focal planes are cooled by separate mechanical Stirling cycle cryocoolers.

4.5 Spectral Performance

The central wavelength is defined by the center of the bandwidth, and the bandwidth is defined at a half value of the peak responsivity. Spectral separation capability is one of the most important features of the ASTER instrument. The central wavelength and width of each band were carefully selected to meet the

Fig. 4.2 Stereo configuration

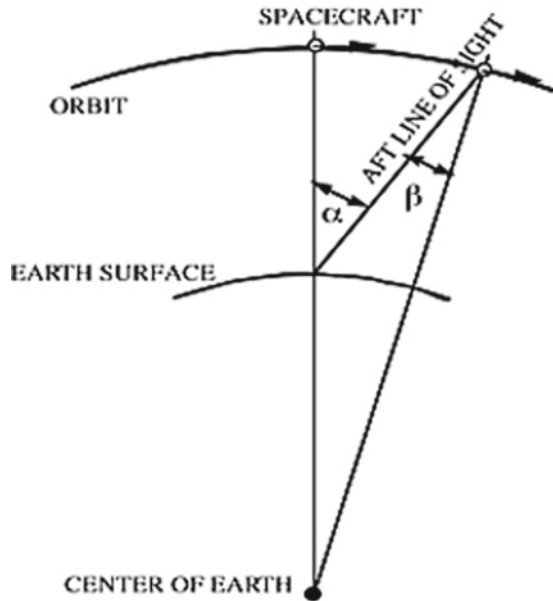


Table 4.2 Significant ASTER functions and components

| Item | VNIR | SWIR | TIR |
|--------------------------|-----------------------------------------------------------------------------|----------------------------------------------|------------------------------------------|
| Scan | Pushbroom | Pushbroom | Whiskbroom |
| Telescope optics | Reflective (Schmidt) $D = 82.25$ mm (Nadir) $D = 94.28$ mm (Backward) | Refractive $D = 190$ mm | Reflective (Newtonian) $D = 240$ mm |
| Spectrum separation | Dichroic and band pass filter | Band pass filter | Band pass filter |
| Focal plane (Detector) | Si-CCD $5,000 \times 4$ | PtSi-CCD $2,048 \times 6$ | HgCdTe (PC) 10×5 |
| Cryocooler (temperature) | Not cooled | Stirling cycle, 77 K | Stirling cycle, 80 K |
| Cross-track pointing | Telescope rotation $\pm 24^\circ$ | Pointing mirror rotation $\pm 8.55^\circ$ | Scan mirror rotation $\pm 8.55^\circ$ |
| Thermal control | Radiator | Cold plate and radiator | Cold plate and radiator |
| Calibration method | Two sets of Halogen lamps and monitor diodes | Two sets of halogen lamps and monitor diodes | Blackbody 270–340 K |

scientific requirements, especially for SWIR and TIR bands. Table 4.3 shows the measured values of the central wavelength, the momentum center, and the bandwidth together with the specification. It bears pointing out that the difference between the central wavelength and the momentum center is very small.

Table 4.3 Spectral performance

| Bands | Central wavelength (μm) | | Momentum center (μm) | Band width (μm) | |
|-------|--------------------------------------|----------------|-----------------------------------|------------------------------|----------------|
| | Specified value | Measured value | Measured value | Specified value | Measured value |
| 1 | 0.56 ± 0.01 | 0.556 | 0.556 | 0.08 ± 0.02 | 0.09 |
| 2 | 0.66 ± 0.01 | 0.659 | 0.661 | 0.06 ± 0.02 | 0.06 |
| 3N | 0.81 ± 0.01 | 0.807 | 0.807 | 0.10 ± 0.02 | 0.10 |
| 3B | 0.81 ± 0.01 | 0.804 | 0.804 | 0.10 ± 0.02 | 0.11 |
| 4 | 1.650 ± 0.010 | 1.657 | 1.656 | 0.10 ± 0.020 | 0.092 |
| 5 | 2.165 ± 0.007 | 2.169 | 2.167 | 0.04 ± 0.010 | 0.035 |
| 6 | 2.205 ± 0.007 | 2.209 | 2.208 | 0.04 ± 0.010 | 0.040 |
| 7 | 2.260 ± 0.007 | 2.263 | 2.266 | 0.05 ± 0.010 | 0.047 |
| 8 | 2.330 ± 0.010 | 2.334 | 2.336 | 0.07 ± 0.015 | 0.070 |
| 9 | 2.395 ± 0.010 | 2.400 | 2.400 | 0.07 ± 0.015 | 0.068 |
| 10 | 8.30 ± 0.08 | 8.274 | 8.291 | 0.35 ± 0.08 | 0.344 |
| 11 | 8.65 ± 0.08 | 8.626 | 8.634 | 0.35 ± 0.08 | 0.347 |
| 12 | 9.10 ± 0.08 | 9.072 | 9.075 | 0.35 ± 0.08 | 0.361 |
| 13 | 10.60 ± 0.10 | 10.654 | 10.657 | 0.70 ± 0.12 | 0.667 |
| 14 | 11.30 ± 0.10 | 11.303 | 11.318 | 0.70 ± 0.12 | 0.593 |

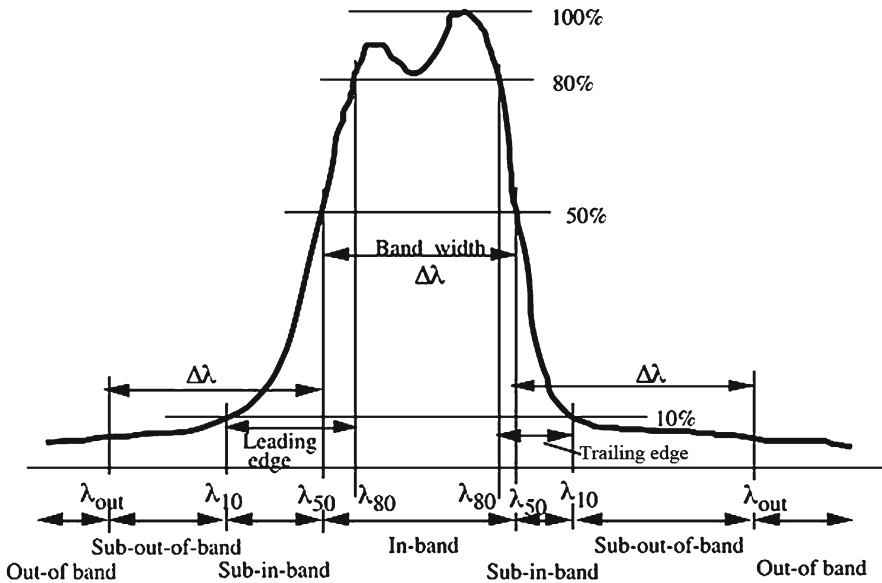


Fig. 4.3 Definition of spectral characteristics

Figure 4.3 shows the spectral response profiles of all bands as a function of the wavelength. A sharp band edge response is also required to satisfy the high spectral resolution. Figure 4.4 shows the spectral response profiles of all bands as a function of the wavelength.

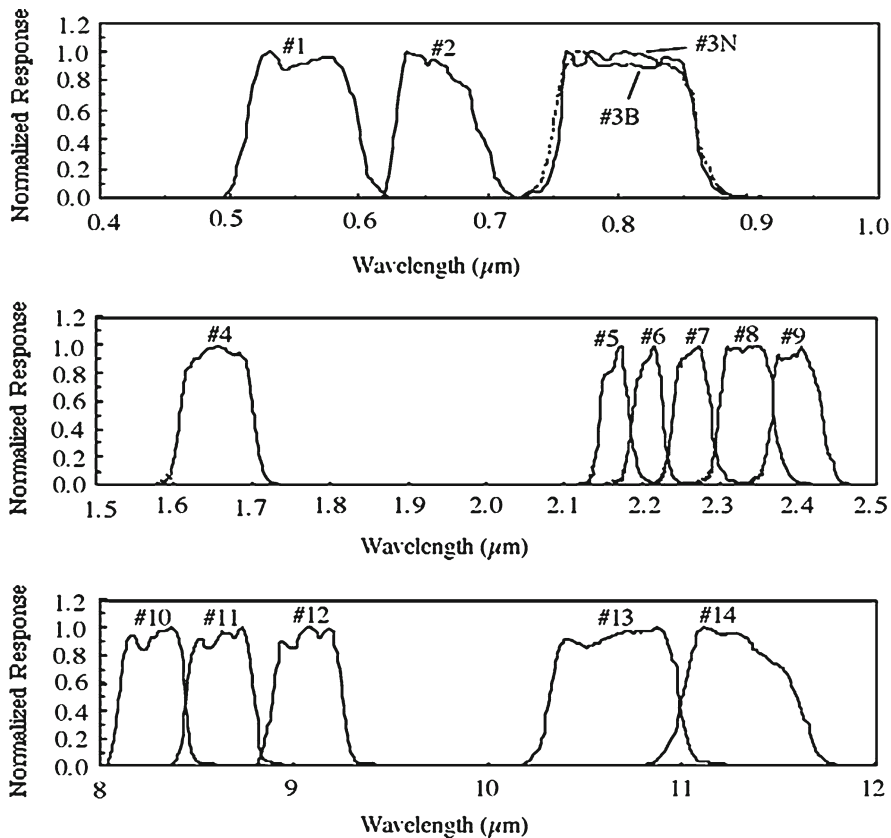


Fig. 4.4 Spectral response

4.6 Radiometric Performance

Figure 4.5 shows the radiometric signal flow of the ASTER instrument. Reflected or emitted radiation from the earth surface reaches the detectors through the optics and is converted into an electrical signal. Incident radiation may include stray light from the large Earth disk, which is one of the radiometric error sources. The electric current in case of the VNIR and SWIR is integrated in the detector during a sampling period to convert to the electric charge. The electric current or the electric charge is then converted into voltage, followed by amplification with variable gain and digitization by the AD converters. The TIR detectors receive radiation not only from the target but also from the optics and the TIR structure itself. The initial stage of the TIR electronic circuit is in AC operation to avoid the effects of a large offset. A DC signal is restored prior to the main part of the electronic processing.

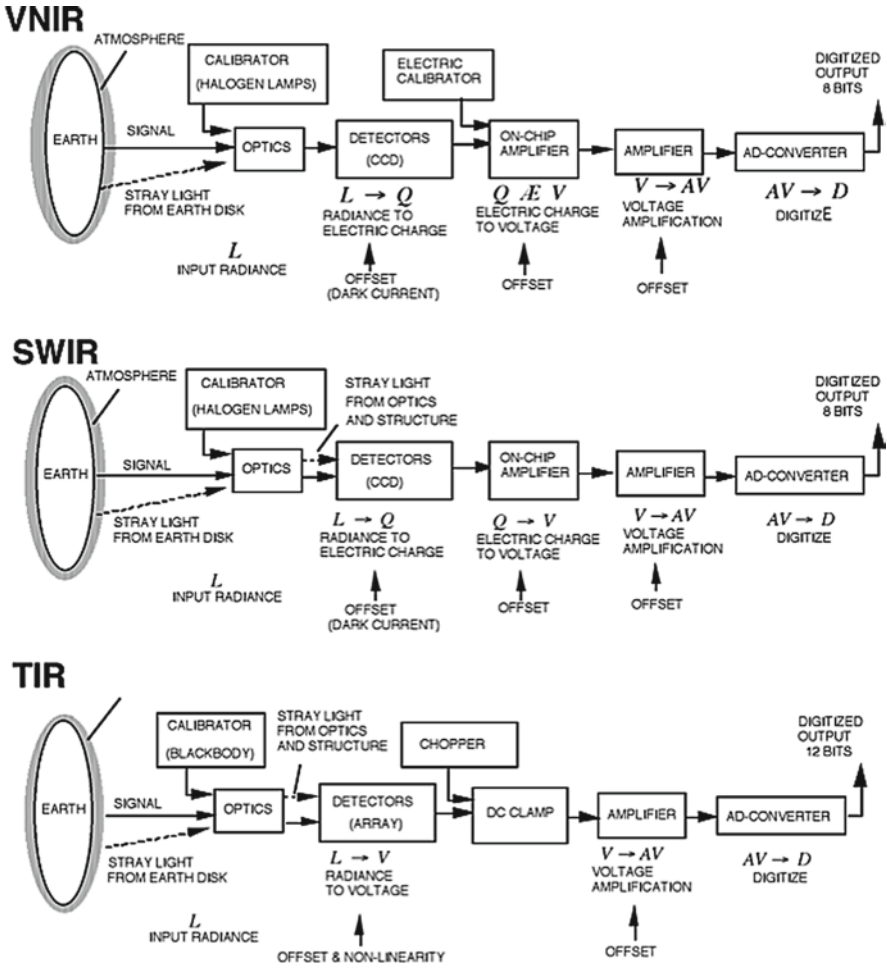


Fig. 4.5 Radiometric signal flow

The input radiance is one of the most important parameters for the instrument design. Properly constrained values are essential for the effective use of the Digital Number (DN) values, and to avoid radiometric signal saturation over bright targets. The input radiance was carefully calculated with the method outlined below by the ASTER science team, and used by the instrument design and fabrication teams.

Table 4.4 shows the maximum, high-, and low-level radiances defined by the target radiance in front of each radiometer. The radiometric accuracy specification is applied to the high-level radiance. In the case of the VNIR and SWIR wavelengths, the radiances above the atmosphere were estimated with two kinds of calculation codes: LOWTRAN-7 and Meteorological Research Institute (MRI) code. Calculation conditions, which are used to determine the input radiance, are

Table 4.4 Input radiance ($\text{W/m}^2/\text{sr}/\mu\text{m}$)

| Band no. | Maximum input radiance | High-level input radiance | Low-level input radiance |
|----------|-----------------------------|-----------------------------|-----------------------------|
| 1 | 427 | 356 | 71.2 |
| 2 | 358 | 298 | 59.6 |
| 3N | 218 | 182 | 36.4 |
| 3B | 218 | 182 | 36.4 |
| 4 | 55.0 | 45.8 | 9.16 |
| 5 | 17.6 | 14.7 | 2.94 |
| 6 | 15.8 | 13.2 | 2.64 |
| 7 | 15.1 | 12.6 | 2.52 |
| 8 | 10.55 | 8.79 | 1.76 |
| 9 | 8.04 | 6.70 | 1.34 |
| 10–14 | Radiance of 370 K blackbody | Radiance of 300 K blackbody | Radiance of 200 K blackbody |

shown below. The condition that produces the largest radiance was used for each code. The assumed spacecraft orbit parameters include a 10:30 a.m. local equatorial crossing time, a sun-synchronous descending node, and a 98.2° orbit inclination.

The MRI code (for VNIR bands 1–3) incorporates the following:

- (1) The atmosphere is divided into five layers: (0–2, 2–5, 5–13, 13–25, and 25–100 km).
- (2) No aerosol correction is employed.
- (3) Rayleigh scattering is calculated using LOWTRAN-6 for mid latitude in summer.
- (4) A complete diffuse target with a 70% reflectance.
- (5) A solar zenith angle of 24.5° corresponds to the 45° N latitude at the summer solstice.

LOWTRAN-7 (for SWIR bands 4–9) incorporates the following:

- (1) The 1976 US standard atmosphere model.
- (2) An aerosol model for the desert.
- (3) A complete diffuse target with a 70% reflectance.
- (4) A solar zenith angle of 20.7° corresponds to the equator at the vernal equinox.

For VNIR bands 1–3, the MRI code produces a larger radiance than LOWTRAN-7. The difference was attributed to multi-scattering between the atmosphere and the Earth's surface, which is not included in the calculation by LOWTRAN-7. Therefore, the radiance calculated by the MRI code under the above conditions is used as the high-level input radiance of VNIR bands.

For SWIR bands 4–9, LOWTRAN-7 gives a slightly larger radiance than the MRI code. The small difference was attributed to atmospheric scattering. The radiance calculated by LOWTRAN-7 under the above conditions is used as the high-level input radiance of SWIR bands.

A concept of the maximum input radiance, specified as 20% larger than the high-level input radiance, is used not only to avoid saturation for targets with very high reflectance, such as clouds, but also to compensate any ambiguity of the calculation model. A low-level input radiance was also defined at 20% of the high-level input radiance. The low-level input radiance is necessary to specify the radiometric performance for targets with low reflectance and for a large solar zenith angle.

A blackbody temperature specifies the input radiance for the TIR bands (10–14 μm). This proves not only simple but is also convenient for the instrument performance test, which uses the blackbody as a radiation source.

The VNIR and SWIR subsystems have independent gain switching functions. The specified gain setting accuracy is $\pm 1\%$ or less. The electronics of each subsystem, including its detector elements, are not expected to saturate if the input radiance is lower than the maximum radiance divided by the multiplication factor.

The high gain setting is necessary to allocate a large DN output for a low reflectance target input. The low gain-1 setting provides a redundancy for unexpected high reflectance targets, although most target observations will employ a normal gain setting.

Certain SWIR observations are specially equipped with a “low gain-2” setting to facilitate high temperature targets, such as volcanic lava. The highest observable target temperature is about 650 K, corresponding to a saturation input radiance of 130 $\text{W}/(\text{m}^2/\text{sr}/\mu\text{m})$ of the CCD linear array.

Table 4.5 shows the measured values of the VNIR and SWIR spectral band gains. The gains for some bands have slightly different values for odd and even pixels, since different electronic circuits process this output. The TIR subsystem does not have a gain setting function because its 12-bit quantization is precise enough to meet user requirements.

The instrument parameter for the radiometric resolution is signal-to-noise ratio (S/N) rather than $\text{NE}\Delta\rho$ described in Table 4.1. Therefore, $\text{NE}\Delta\rho$ is translated into S/N by using the relation $\text{S/N} = (\text{target reflectance})/\text{NE}\Delta\rho$. That is, S/N for a given $\text{NE}\Delta\rho$ changes with the target reflectance. The high-level input radiance is generally applied to evaluate a user’s requirement. Therefore, 70% target reflectance, which is used to estimate the high-level input radiance, is used to convert between $\text{NE}\Delta\rho$ and S/N. For TIR bands, the radiometric resolution is specified directly by the user-required parameter noise equivalent temperature difference ($\text{NE}\Delta T$), which is convenient for the instrument performance test.

The radiometric resolution for the low-level input radiance is specified, though not included in the user requirements. A decrease in photon noise for the low-level input radiance is taken into account. The total noise is expected to decrease to 70% for VNIR bands and 80% for SWIR bands compared to the high input radiance noise in this specification. $\text{NE}\Delta T$ for the low input radiance TIR bands is specified at 2.5 K or 1.5 K depending on the bands in view of the fact that the required accuracy is 3 K, and the input radiance for bands 10–12 is very low at a 200-K blackbody target specification.

Table 4.6 shows the measured radiometric sensitivities with the specified values for the high- and low-level input radiances defined by the S/N for VNIR and

Table 4.5 Gain setting

| Subsystem | Band no. | Height/normal | | | | Low-1/normal | | | | Low-2/normal | | | |
|-----------|----------|---------------|----------------|-------|-----------|----------------|-------|-----------|----------------|--------------|-----------|----------------|------|
| | | Specified | Measured value | | Specified | Measured value | | Specified | Measured value | | Specified | Measured value | |
| | | | Odd | Even | | Odd | Even | | Odd | Even | | Odd | Even |
| VNIR | 1 | 2.5 | 2.475 | 2.469 | 0.75 | 0.749 | 0.752 | N/A | | | | | |
| | 2 | 2.0 | 1.989 | 1.998 | 0.75 | 0.758 | 0.752 | | | | | | |
| | 3N | 2.0 | 2.055 | 2.028 | 0.75 | 0.759 | 0.754 | | | | | | |
| SWIR | 3B | 2.0 | 1.987 | 2.012 | 0.75 | 0.758 | 0.760 | | | | | | |
| | 4 | 2.0 | 1.993 | 1.993 | 0.75 | 0.751 | 0.751 | 0.75 | 0.751 | 0.75 | 0.751 | 0.751 | |
| | 5 | 2.0 | 1.988 | 1.988 | 0.75 | 0.748 | 0.748 | 0.17 | 0.167 | 0.17 | 0.167 | 0.167 | |
| | 6 | 2.0 | 1.988 | 1.988 | 0.75 | 0.748 | 0.748 | 0.16 | 0.157 | 0.16 | 0.157 | 0.157 | |
| | 7 | 2.0 | 1.989 | 1.989 | 0.75 | 0.748 | 0.748 | 0.18 | 0.171 | 0.18 | 0.171 | 0.171 | |
| | 8 | 2.0 | 1.988 | 1.988 | 0.75 | 0.748 | 0.748 | 0.17 | 0.162 | 0.17 | 0.162 | 0.162 | |
| | 9 | 2.0 | 1.989 | 1.989 | 0.75 | 0.748 | 0.748 | 0.12 | 0.116 | 0.12 | 0.116 | 0.116 | |

Table 4.6 Radiometric sensitivity

| Subsystem | Band no. | S/N or NEAT for high level radiance | | S/N or NEAT for low level radiance | |
|-----------|----------|-------------------------------------|----------------|------------------------------------|----------------|
| | | Specified value | Measured value | Specified value | Measured value |
| VNIR | 1 | ≥140 | 370–278 | ≥40 | 170–78 |
| | 2 | ≥140 | 306–256 | ≥40 | 122–74 |
| | 3N | ≥140 | 202–173 | ≥40 | 70–58 |
| | 3B | ≥140 | 183–150 | ≥40 | 72–56 |
| SWIR | 4 | ≥140 | 466–292 | ≥35 | 368–63 |
| | 5 | ≥54 | 254–163 | ≥13.5 | 77–45 |
| | 6 | ≥54 | 229–150 | ≥13.5 | 73–36 |
| | 7 | ≥54 | 234–151 | ≥13.5 | 72–35 |
| | 8 | ≥70 | 258–165 | ≥17.5 | 81–34 |
| TIR | 9 | ≥54 | 231–156 | ≥13.5 | 73–44 |
| | 10 | ≤0.3 K | 0.17–0.07 K | ≤2.5 K | 1.34–0.68 K |
| | 11 | ≤0.3 K | 0.14–0.09 K | ≤2.5 K | 1.27–0.63 K |
| | 12 | ≤0.3 K | 0.13–0.07 K | ≤2.5 K | 1.05–0.42 K |
| | 13 | ≤0.3 K | 0.09–0.05 K | ≤1.5 K | 0.49–0.26 K |
| | 14 | ≤0.3 K | 0.13–0.09 K | ≤1.5 K | 0.65–0.33 K |

SWIR subsystems, and NEAT for TIR subsystem. ASTER’s excellent radiometric performance is expected based on the preflight evaluation of PFM on the ground.

Large integration spheres illuminated at the high-level input radiance for each band were used to perform the absolute radiometric calibration of the PFM VNIR and SWIR radiometers.

The integration spheres were calibrated against fixed-point blackbodies of copper (1084.62°C), zinc (419.527°C), and tin (231.928°C) through variable temperature blackbodies. The calibration uncertainty was evaluated at better than 3% for VNIR, and 6% for SWIR, considering the cross-calibration results among NASA GSFC, NIST, University of Arizona, and NRLM in 1995 and 1996. The nonlinearity of both radiometers was measured, and was less than 1% of the high-level input radiance.

The two on-board calibration lamps for VNIR and SWIR were calibrated through the radiometer itself against the integration sphere. Following ASTER’s launch, the on-board calibration is conducted once every 17 days to correct the radiometer responses.

In-flight calibration is planned and implemented to ensure and correct, when necessary, the performance of the on-board calibrators.

PFM TIR is calibrated against a standard blackbody in a thermal vacuum chamber. The standard blackbody’s temperature was varied at ten different points from 200 to 370 K in both the hot and cold cases, which correspond to 25 and 20°C cold plate temperatures, respectively. Three calibration coefficients were determined from these cases, viz. constant, linear, and second-order. Following launch, TIR views the on-board blackbody at 270 K before each observation. The constant term is corrected by this blackbody observation (also termed short-term calibration). The on-board blackbody’s temperature is changed from 270 to 340 K once every 17 days for long-term calibration, and the linear term is corrected.

4.7 Geometric Performance

Figure 4.6 shows the ASTER instrument's focal plane configuration. The detector layout is expressed by the footprint on the ground in relation to the spacecraft's flight direction and the boresight of each telescope. The focal plane sizes are shown

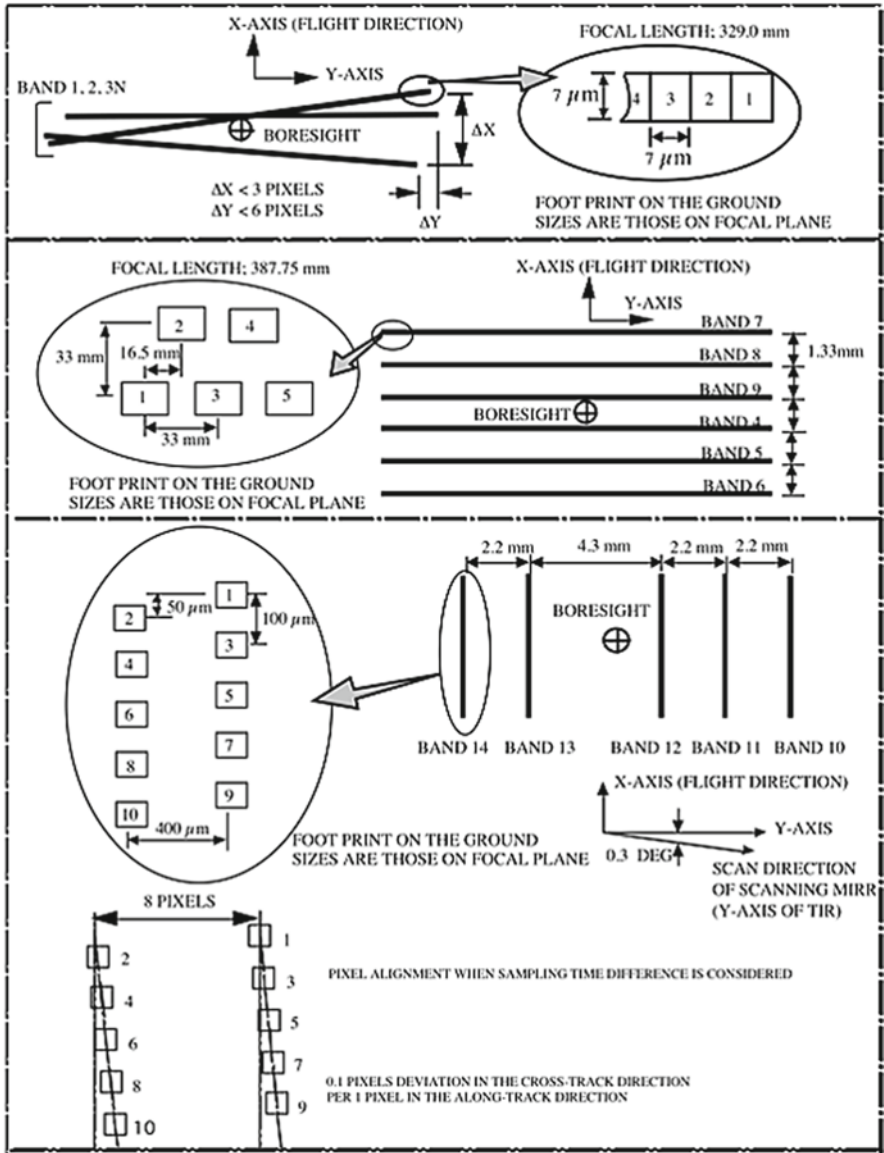


Fig. 4.6 Focal plane configuration

with the configuration, because the sizes on the ground depend on the spacecraft altitude. These sizes are designed to meet the baseline requirement for the spatial resolution within the fabrication accuracy of the focal length at a 705-km spacecraft altitude.

The SWIR and TIR subsystems use a staggered detector alignment in the cross-track and along-track directions, respectively, to enhance the radiometric sensitivity. Such a staggered alignment permits a larger detector size than the pixel-to-pixel spacing (center-to-center dimension), which defines the Nyquist spatial resolution. However, the larger detector size sacrifices the MTF. The SWIR detector sizes are 20 μm in the cross-track direction and 17 μm in the along-track direction, while the pixel-to-pixel spacing is 16.5 μm in the cross-track direction and 33 μm in the along-track direction. The TIR detector size is 50 $\mu\text{m} \times 50 \mu\text{m}$, which equals the pixel-to-pixel spacing in the along-track direction.

A single line of image data for all the VNIR and SWIR bands in the cross-track direction is acquired simultaneously because of the CCD detector arrays' data sampling function. For the TIR subsystem, they are acquired time-sequentially in accordance with the scanning speed of the mirror because of the whiskbroom scanning method. A 0.3° tilt angle is set for the earth rotation's compensation during the scan period to align the swath line at a right angle to the spacecraft's flight direction. All scan directions in the cross-track direction are designed to align at a right angle to the spacecraft's flight direction.

The focal plane configuration was carefully designed to meet the accuracy and stability specifications, which were necessary to meet the geometric performance requirements such as the band-to-band registration.

The spatial resolution or the pixel size is defined on the basis of the Nyquist sampling theorem. Therefore, the pixel size implies the spacing between the nearest data sampled for both the cross-track and the along-track directions.

The VNIR and SWIR subsystem's spatial resolution parameter in the cross-track direction is the linear array detector's pixel spacing (center-to-center dimension). The similar parameter in the TIR subsystem is the data sampling distance described by the angle as shown in Table 4.7. Therefore, the spatial resolution on the ground depends not only on the spacecraft's altitude but also on the pointing angle. The spatial resolution angles are designed to meet a ground spatial resolution at nadir direction from a nominal 705km spacecraft altitude.

The scan period delineated by the data sampling interval for every swath line is shown in Table 4.7, and defines the instrument's spatial resolution in the

Table 4.7 Geometric parameters

| Subsystem | | IFOV angle in cross-track (μ rad) | Scan period in along-track (ms) |
|-----------|----------|----------------------------------------|---------------------------------|
| VNIR | Nadir | 21.3 \pm 0.4 | 2.199 \pm 0.02 |
| | Backward | 18.6 \pm 0.3 | 2.199 \pm 0.02 |
| SWIR | | 42.6 \pm 0.8 | 4.398 \pm 0.044 |
| TIR | | 127.5 \pm 2.5 | 131.94 \pm 0.13 |

along-track direction. Therefore, the ground spatial resolution directly depends on the spacecraft’s velocity, which itself depends on the altitude and the latitude of the nadir direction. The scan periods are designed to meet the spacecraft’s equatorial crossing at a 705-km altitude.

Table 4.8 shows the pixel geolocation knowledge, which is predicted from the spacecraft’s position and pointing knowledge, and the ASTER pointing knowledge. Only the dynamic error is important for the geolocation accuracy, because the static error is removable using ground control points (GCP) data during the initial checkout period. A geolocation accuracy of about 50 m was anticipated for targets without terrain error (targets in the nadir direction).

The pointing range in the cross-track direction is defined as the angle from the nadir direction of the spacecraft. Other pointing parameters are defined for each subsystem’s installed plane, and applied only for the pointing range of $\pm 8.55^\circ$. These pointing functions are specified in Table 4.9. The specifications are applied for a $\pm 8.55^\circ$ range except for the VNIR subsystem.

The pointing function provides global coverage in the cross-track direction by changing the center of the swath. The range is specified to cover 272 km from a 705-km platform altitude. The total coverage of 272 km is obtained by adding a platform recurrent inaccuracy of ± 20 km to the user’s requirement (232 km). In VNIR’s case, the extra range is provided to observe a special target with a shorter period.

The pointing repeatability and accuracy are important parameters for band-to-band registration among different telescopes. The accuracy and the repeatability

Table 4.8 Pixel geolocation knowledge (Prediction)

| | | Specification | Dynamic error (3σ) | Static error (3σ) |
|-----------------|------------|---------------|-----------------------------|----------------------------|
| Along-track (m) | Spacecraft | ± 342 | ± 28 | ± 111 |
| | ASTER/VNIR | ± 205 | ± 38 | ± 99 |
| | Total | ± 431 | ± 47 | ± 149 |
| Cross-track (m) | Spacecraft | ± 342 | ± 25 | ± 148 |
| | ASTER/VNIR | ± 205 | ± 48 | ± 103 |
| | Total | ± 437 | ± 54 | ± 180 |

Table 4.9 Pointing functions (requirement)

| Items | VNIR | SWIR | TIR |
|----------------------------------|-----------------------------------|-----------------------|-------------------|
| Range | $\geq \pm 24^\circ$ | | $\geq 8.55^\circ$ |
| Accuracy of pointing axis | $\leq \pm 360$ arcsec from X axis | | |
| Setting resolution | | $\leq \pm 45$ arcsec | |
| Repeatability (3σ) | | $\leq \pm 180$ arcsec | |
| Detecting resolution | | $\leq \pm 20$ arcsec | |
| Detection accuracy (3σ) | | $\leq \pm 27$ arcsec | |
| Variable frequency | $\geq 20,000$ | | $\geq 200,000$ |
| Pointing time | | 60s | |

specified correspond to 41 and 6.1 pixels of a VNIR resolution of 15 m, respectively. Therefore, new parameters for band-to-band registration among different telescopes are derived through ground processing methods like correlation when the pointing mode is changed.

4.8 Modulation Transfer Function

Table 4.10 shows the measured values of the modulation transfer function (MTF) at the Nyquist and the 1/2 Nyquist spatial frequencies for the along-track and the cross-track directions with the specified values. The square wave response is used to specify the MTF. The pushbroom scanning-based VNIR and SWIR subsystems incorporate the signal integration effect in the along-track direction. A moving target is used to measure the MTF to determine the integration effect for VNIR. The SWIR’s integration effect is evaluated by calculation to correct the measured values using a fixed target. This situation is not applied to the TIR subsystem, which uses a whiskbroom scanning method.

The VNIR subsystem’s lower MTF in the along-track direction is a consequence of the deterioration due to the signal integration effect. The SWIR subsystem’s MTF in the cross-track direction has nearly the same values as those in the along-track direction. This stems from the fact that the SWIR’s detector size is larger than its pixel spacing, which is designed to enhance the radiometric sensitivity.

Table 4.10 MTF (measured values, square wave response)

| Subsystem | Band no. | Along-track | | Cross-track | |
|---------------|----------|-------------|-------------|-------------|-------------|
| | | Nyquist | 1/2 Nyquist | Nyquist | 1/2 Nyquist |
| VNIR | 1 | 0.23–0.28 | 0.72–0.77 | 0.40–0.51 | 0.82–0.84 |
| | 2 | 0.22–0.28 | 0.71–0.75 | 0.48–0.58 | 0.84–0.87 |
| | 3N | 0.26–0.29 | 0.74–0.75 | 0.50–0.55 | 0.81–0.84 |
| | 3B | 0.26–0.30 | 0.78–0.81 | 0.30–0.64 | 0.78–0.89 |
| SWIR | 4 | 0.34–0.36 | 0.79–0.83 | 0.40–0.43 | 0.79–0.92 |
| | 5 | 0.32–0.36 | 0.80–0.85 | 0.39–0.44 | 0.73–0.86 |
| | 6 | 0.34–0.36 | 0.79–0.84 | 0.37–0.45 | 0.74–0.84 |
| | 7 | 0.31–0.34 | 0.75–0.84 | 0.35–0.40 | 0.74–0.85 |
| | 8 | 0.33–0.36 | 0.81–0.84 | 0.32–0.44 | 0.71–0.86 |
| | 9 | 0.35–0.39 | 0.83–0.89 | 0.33–0.43 | 0.70–0.85 |
| | 10 | 0.36–0.41 | 0.79–0.83 | 0.34–0.38 | 0.79–0.83 |
| TIR | 11 | 0.37–0.42 | 0.78–0.81 | 0.34–0.36 | 0.77–0.81 |
| | 12 | 0.37–0.39 | 0.78–0.81 | 0.34–0.37 | 0.79–0.82 |
| | 13 | 0.34–0.37 | 0.74–0.78 | 0.35–0.37 | 0.79–0.83 |
| | 14 | 0.31–0.37 | 0.69–0.76 | 0.34–0.39 | 0.78–0.83 |
| Specification | | ≥0.20 | ≥0.50 | ≥0.25 | ≥0.50 |

4.9 Level-1A Data Product

Figure 4.7 shows an outline of level-1A data product. Level-1A data are formally defined as reconstructed, unprocessed instrument data at full resolution. According to this definition, the ASTER level-1A data consist of the image data, the radiometric

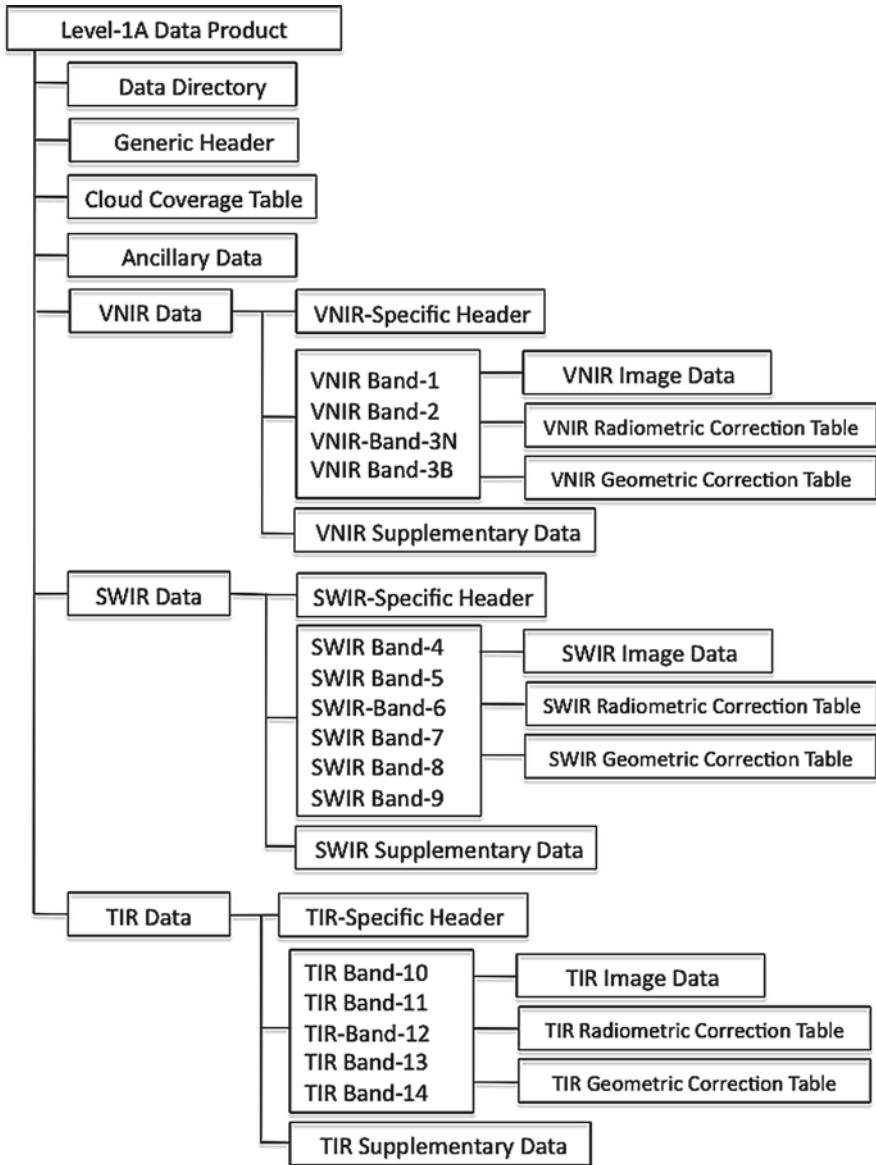


Fig. 4.7 Level-1A data product structure

calibration coefficients, the geometric correction coefficients, and other auxiliary data, without applying the coefficients to the image data, thus maintaining the original data values (Fujisada 1998).

Scene cutting is applied to level-0B data according to the predetermined World Reference System (WRS). Each data group is divided into scenes every 60 km in the along-track direction. Each scene size is 63 km to include a 5% overlap with neighboring scenes except for band 3B. A band 3B scene size is 81 km, which includes a 6 km additional overlap to compensate for the terrain error and scene rotation for a large cross-track pointing.

The level-1A data product is an HDF file, which contains a complete set of image data for one scene, radiometric and geometric correction coefficients, and other auxiliary tables, as shown in Figure 4.7.

Figures 4.8 and 4.9 show the image data structure and a set of more detailed stereo image structures, respectively. (Note: a total of 5,400 lines for band 3B is valid based on version 2.0 geometric database.) Data processed with earlier than version 2.0 geometric database contain 4,600 lines for band 3B. The pixel sizes (ground sampling distance) are 15, 30, and 90m for VNIR, SWIR, and TIR, respectively.

The DN values are converted into radiance as follows:

$$L = A V/G + D \text{ (VNIR and SWIR bands)}$$

$$L = AV + CV^2 + D \text{ (TIR bands)}$$

Here, L : radiance ($W/m^2/sr/\mu m$), A : linear coefficient, C : nonlinear coefficient, D : offset, V : DN value, G : gain.

The radiometric correction table is extractable from the HDF file.

The geometric correction table contains the latitude and the longitude values at lattice points and is also extractable from the HDF file. The lattice point tables are

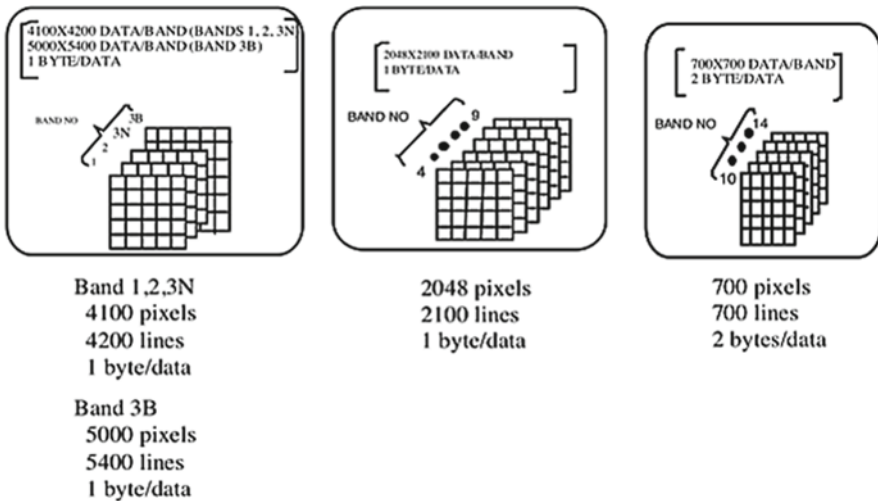


Fig. 4.8 Image data structure

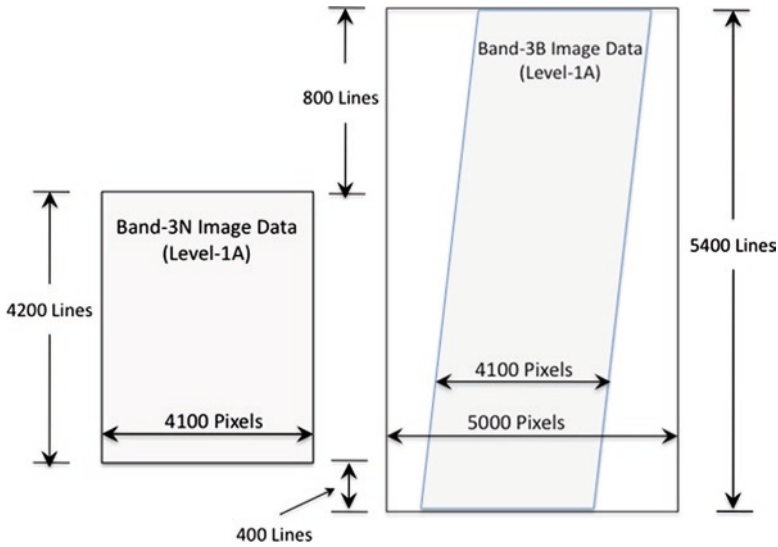


Fig. 4.9 Relationship between level-1A product’s band-3N and band-3b at zero elevation. (Note: 5,400 lines for band-3b is valid since geometric database version 2.0 was implemented)

also part of the HDF file. One could calculate the latitude and the longitude values at other pixel positions by linear interpolation from the values at the lattice points except for the TIR bands. For TIR bands, in addition to the linear interpolation, a correction is required to calculate the latitude and the longitude values precisely. See the TIR focal plane configuration in the User’s Guide Part I for more details.

The latitude values are expressed in geocentric coordinates. Note that the geometric correction values (the latitude and longitude values) are defined as being at the center of each pixel. The Earth ellipsoid is limited to WGS-84. (Please note that the observation point expressed as latitude and longitude is the intersection of the WGS-84 ellipsoid and an extension of the line-of-sight vector.) The terrain error caused by the difference between WGS-84 ellipsoid and the actual Earth’s surface is included in the latitude and longitude values. The geocentric latitude ψ is easily converted into the geodetic latitude ϕ as follows:

$$\tan \phi = C \tan \psi$$

$$C = 1.0067395$$

4.10 Level-1B Data Product

Figure 4.10 shows the level-1B data outline. The level-1B data product is generated by applying the level-1A radiometric calibration and geometric resampling coefficients.

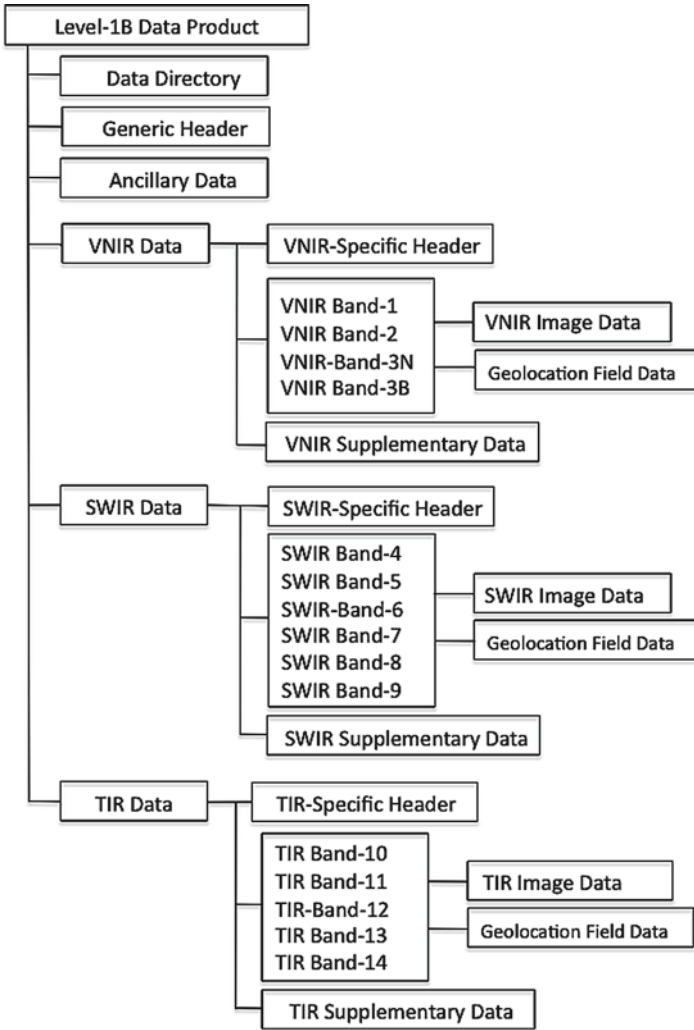


Fig. 4.10 Level-1B data product structure

Figures 4.11 and 4.12 show the image data structure and a set of more detailed stereo image structures, respectively.

Figure 4.13 shows the direction of both the daytime and nighttime path-oriented level-1B image. (Note that the spacecraft’s flight direction for the nighttime image is opposite that for the daytime direction.)

Unit conversion coefficients, which are defined as radiance per 1 DN, are used to convert DN values to radiance. Radiance (spectral radiance) is expressed in unit of $W/(m^2/sr/\mu m)$. The relationship between DN values and radiances is shown below and illustrated in Figure 4.14.

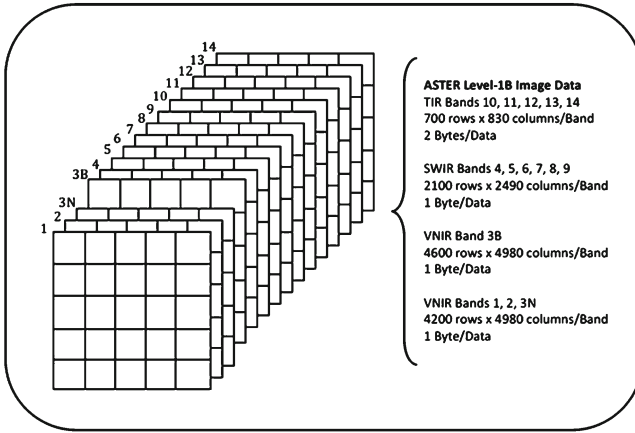


Fig. 4.11 Image data structure

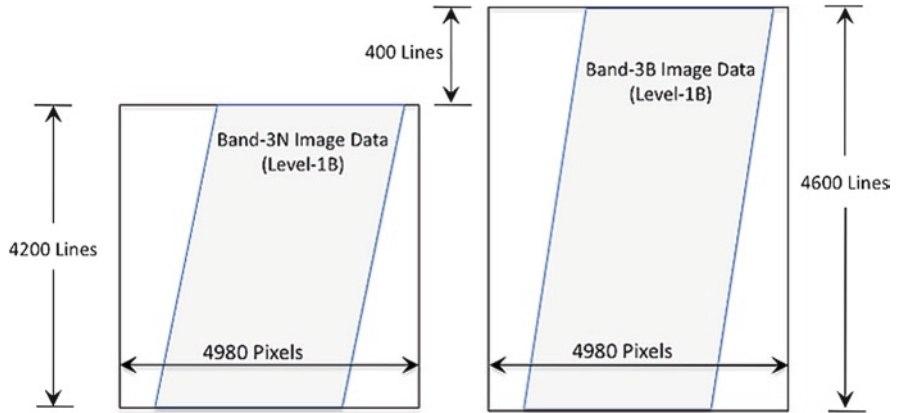


Fig. 4.12 Relationship between level-1B product's band-3N and band-3b at zero elevation

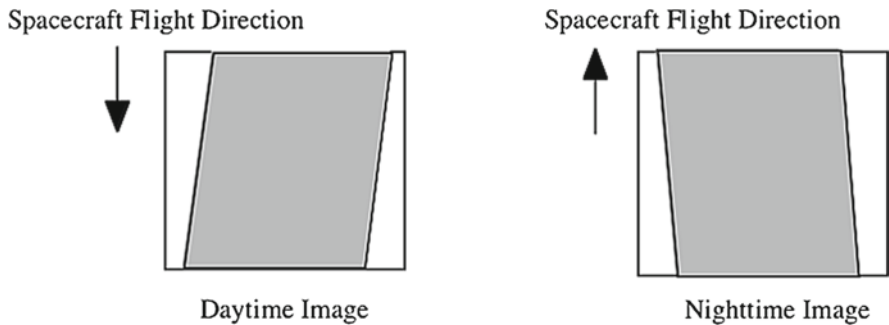


Fig. 4.13 Spacecraft's orbital flight direction for daytime and nighttime level-1B images

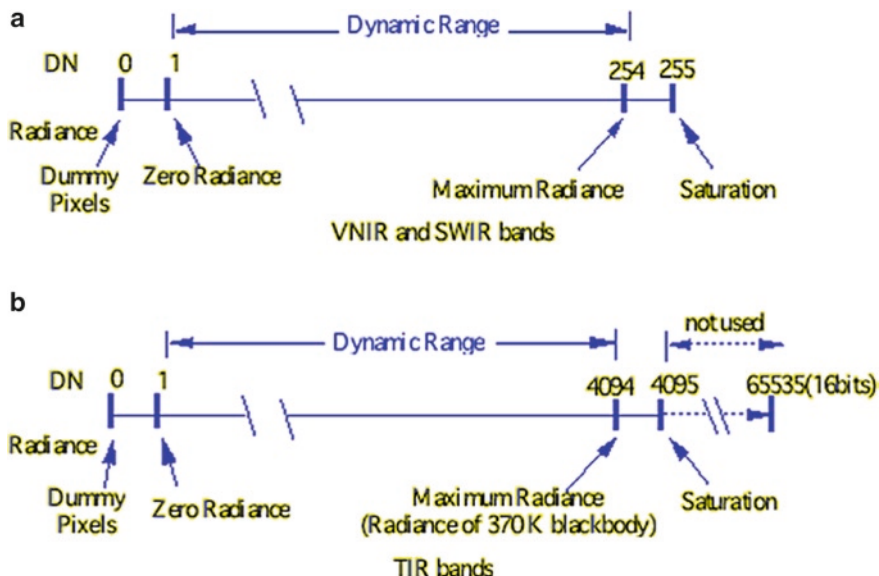


Fig. 4.14 Relationship between DN values and radiances

- (1) A DN value of zero is allocated to dummy pixels.
- (2) A DN value of 1 is allocated to zero radiance.
- (3) A DN value of 254 is allocated to the maximum radiance in the VNIR and SWIR bands.
- (4) A DN value of 4,094 is allocated to the maximum radiance in the TIR bands.
- (5) A DN value of 255 is allocated to saturated pixels in the VNIR and SWIR bands.
- (6) A DN value of 4,095 is allocated to saturated pixels in the TIR bands.

Table 4.11 shows the unit conversion coefficients for each band. The radiance values are obtained from DN values as follows:

Radiance = (DN value - 1) × Unit conversion coefficient

$$L_{\lambda} = \left(\frac{LMAX_{\lambda} - LMIN_{\lambda}}{Q_{cal\ max} - Q_{cal\ min}} \right) (Q_{cal} - Q_{cal\ min}) + LMIN_{\lambda}$$

$$Q_{cal\ max} = 255$$

$$Q_{cal\ min} = 1$$

$$LMIN_{\lambda} = 0$$

$$L_{\lambda} = G_{rescale} (Q_{cal} - 1)$$

$$G_{rescale} = \frac{LMAX_{\lambda}}{Q_{cal\ max} - Q_{cal\ min}}$$

Table 4.11 Unit conversion coefficients

| Band no. | Coefficient (W/(m ² /sr/μm)/DN) | | | |
|----------|--------------------------------------------|------------------------|------------|------------|
| | High gain | Normal gain | Low gain-1 | Low gain-2 |
| 1 | 0.676 | 1.688 | 2.25 | N/A |
| 2 | 0.708 | 1.415 | 1.89 | |
| 3N | 0.423 | 0.862 | 1.15 | |
| 3B | 0.423 | 0.862 | 1.15 | |
| 4 | 0.1087 | 0.2174 | 0.290 | 0.290 |
| 5 | 0.0348 | 0.0696 | 0.0925 | 0.409 |
| 6 | 0.0313 | 0.0625 | 0.0830 | 0.390 |
| 7 | 0.0299 | 0.0597 | 0.0795 | 0.332 |
| 8 | 0.0209 | 0.0417 | 0.0556 | 0.245 |
| 9 | 0.0159 | 0.0318 | 0.0424 | 0.265 |
| 10 | N/A | 6.882×10^{-3} | N/A | N/A |
| 11 | | 6.780×10^{-3} | | |
| 12 | | 6.590×10^{-3} | | |
| 13 | | 5.693×10^{-3} | | |
| 14 | | 5.225×10^{-3} | | |

Parameters related to geometric properties are map projection, ellipsoid, pixel size, and resampling method. Key features of these parameters are as follows:

(1) Map projection

- (i) Map projections are limited to Universal Transverse Mercator (UTM), Lambert Conformal Conic (LCC), Polar Stereographic (PS), Space Oblique Mercator (SOM), and uniform Lat/Long.
- (ii) Map direction is limited to path-oriented.
- (iii) UTM: two-standard longitude line method is adopted with a reduction rate of 0.9996 to define the cylinder.
- (iv) LCC: two standard latitude lines of 53° and 67° are adopted to define the cone position and angle.
- (v) PS: a standard 70° latitude line is adopted to define the plane position.
- (vi) SOM: the nominal orbit path line is used as the position for contacting the projected plane.
- (vii) The default map projection is UTM, regardless of latitude.

(2) Ellipsoid

The Earth ellipsoid is limited to WGS-84. Therefore, the observation point expressed as latitude and longitude is the intersection of WGS-84 ellipsoid and an extension of the line-of-sight vector. The terrain error caused by a difference between the WGS-84 ellipsoid and the actual Earth's surface is included in the latitude and longitude values as shown in Figure 4.15.

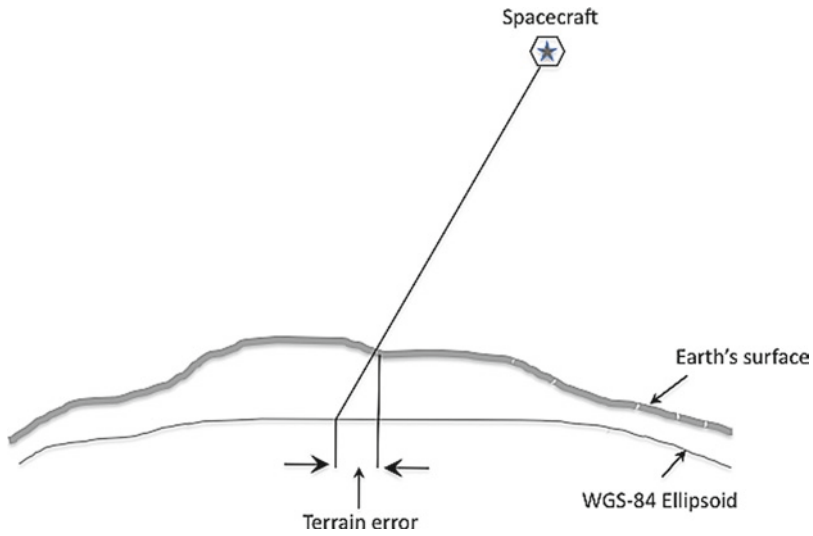


Fig. 4.15 Terrain error

References

- Fujisada H (1998) ASTER Level-1 data processing algorithm, *IEEE Trans Geosci Remote Sens* 36(4):1101–1112
- Fujisada H, Sakuma F, Ono A, Kudo M (1999) Design and preflight performance of ASTER instrument protoflight model, *IEEE Trans Geosci Remote Sens* 36(4):1152–1160
- Fujisada H, Bailey GB, Kelly GG, Hara S, Abrams MJ (2005) ASTER DEM performance, *IEEE Trans Geosci Remote Sens* 43(12):2707–2714
- Iwasaki A, Fujisada H (2005) ASTER geometric performance, *IEEE Trans Geosci Remote Sens* 43(12):2700–2706
- Yamaguchi Y, Tsu H, Fujisada H (1993) Scientific basis of ASTER instrument design, *Proc. SPIE* 1939:150–160

Chapter 5

ASTER VNIR and SWIR Radiometric Calibration and Atmospheric Correction

Kohei Arai, Kurtis Thome, Akira Iwasaki, and Stuart Biggar

5.1 Introduction

As described in the previous chapter, ASTER relies on three separate subsystems to cover the full spectral range from the visible and near infrared (VNIR), short-wave infrared (SWIR), to the thermal infrared (TIR). Establishing the accuracy of data from all three subsystems requires both sensor-related calibration and atmospheric correction. The dominance of reflected solar energy in the VNIR and SWIR, and emitted terrestrial radiation in the TIR allows separate treatment of the two spectral regions. TIR calibration and correction are covered in a separate chapter. This chapter has two main goals: (1) to allow the user to understand ASTER's radiometric calibration and atmospheric correction processes that enable conversion of VNIR and SWIR digital numbers (DN) to at-sensor reflectance and spectral radiance, and (2) to provide a succinct analysis of the SWIR crosstalk problem and its solutions.

Radiometric calibration and atmospheric correction first require the conversion of the ASTER DN to at-sensor spectral radiance. This conversion involves a set of VNIR and SWIR radiometric calibration coefficients (RCC) derived from the pre-flight, onboard, and vicarious calibration (VC) sources, and also from knowledge of the data artifacts. The first step in the process of converting to surface reflectance involves radiometric calibration to convert at-sensor DN to at-sensor spectral radiance. The specific methods for converting raw ASTER data to at-sensor spectral radiance are described in Sect. 5.2. The approaches used to determine ASTER's

K. Arai (✉)
Saga University, Honjo 1, Saga-shi 840-8502, Japan
e-mail: arai@is.saga-u.ac.jp

radiometric calibration are described in Sect. 5.3.1, including a brief description of the preflight calibration process.

Any electro-optical sensor is expected to degrade once in orbit, and therefore requires a mechanism to monitor the data's radiometric quality over time. Many sensors, including ASTER, employ onboard calibration devices to evaluate temporal changes in the sensor responses. Onboard calibrators (OBC), in general, provide excellent temporal sampling of the sensor's radiometric behavior over time. In addition, the repeatability and precision of the onboard systems allow the use of these data to characterize the sensor's response trends. Typical approaches for onboard calibration include lamp-based, diffuser-based, and detector-based methods. ASTER's VNIR and SWIR use lamp-based OBC. The specific design of the ASTER OBC is described in Sect. 5.3.2.

One issue with OBC is that their absolute in-flight calibration accuracy is worse than that of the preflight calibration because the preflight calibration source is used to calibrate the OBC. Another problem is that the OBCs themselves can degrade over time. Both issues justify the inclusion of calibration approaches that are independent of the preflight calibration. They include VC approaches. High-resolution sensors, including ASTER, have extensively used vicarious approaches over time. They are covered in Sect. 5.3.3.

Known data artifacts that affect the radiometric and spatial quality are described in Sect. 5.4, including a description of the SWIR optical crosstalk. The final portion of the chapter discusses the atmospheric correction of ASTER's reflective bands used to convert the at-sensor radiance to surface reflectance.

5.2 Conversion to At-Sensor, Spectral Radiance

Similar to the other sensors on the Terra platform, ASTER follows a hierarchy of data levels from level-0, level-1, and higher. The level-0 data correspond to raw ASTER instrument data. Level-1A and -1B products are generated from the level-0 data. The level-1A image data are, in fact, identical to the level-0, except that they contain geometric and radiometric correction coefficients that are attached in the header. The level-1B product is the result of applying these appended coefficients to produce a radiometrically calibrated, and geometrically corrected data set.

5.2.1 Unit Conversion Coefficients

The level-1B processing produces scaled radiance values quantized in 8-bits. Users convert these scaled radiances to at-sensor radiances using the unit conversion coefficients (UCC) supplied in the metadata. A DN value of 0 is allocated to dummy or non-data pixels, while a DN value of 1 is allocated to zero radiance.

Table 5.1 Maximum radiance (in $W/m^2/str/\mu m$) and unit conversion coefficient (UCC) for ASTER VNIR (bands 1, 2, and 3N (Nadir) and 3B (Backward telescope) and SWIR (bands 4–9))

| Band | High gain | | Normal gain | | Low gain 1 | | Low gain 2 | |
|-----------|-----------|--------|-------------|--------|------------|--------|------------|-------|
| | Max Rad. | UCC | Max Rad. | UCC | Max Rad. | UCC | Max Rad. | UCC |
| 1 | 170.8 | 0.676 | 427 | 1.688 | 569 | 1.688 | N/A | N/A |
| 2 | 179.0 | 0.708 | 358 | 1.415 | 477 | 1.415 | N/A | N/A |
| 3N and 3B | 106.8 | 0.423 | 218 | 0.862 | 290 | 0.862 | N/A | N/A |
| 4 | 27.5 | 0.1087 | 55.0 | 0.2174 | 73.3 | 0.2174 | 73.3 | 0.29 |
| 5 | 8.8 | 0.0348 | 17.6 | 0.0696 | 23.4 | 0.0696 | 103.5 | 0.409 |
| 6 | 7.9 | 0.0313 | 15.8 | 0.0625 | 21.0 | 0.0625 | 98.7 | 0.39 |
| 7 | 7.55 | 0.0299 | 15.1 | 0.0597 | 20.1 | 0.0597 | 83.8 | 0.332 |
| 8 | 5.27 | 0.0209 | 10.55 | 0.0417 | 14.06 | 0.0417 | 62.0 | 0.245 |
| 9 | 4.02 | 0.0159 | 8.04 | 0.0318 | 10.72 | 0.0318 | 67.0 | 0.265 |

A DN value of 254 is allocated to the maximum VNIR and SWIR radiances, while a DN value of 255 is allocated to saturated pixels. Table 5.1 shows the maximum radiances for VNIR and SWIR bands along with the UCC.

The conversion from scaled radiance to spectral radiance is accomplished via the following equation:

$$L_{\lambda} = (DN - 1)UCC \quad (5.1)$$

where UCC denotes the unit conversion coefficient as shown in Table 5.1, and DN is the scaled radiance. This implies that the level-1B product offset is 1 DN. This offset, however, is not the same as the instrument offset as measured with a zero-radiance source, but is a result of the scaling approach described above.

As is clear from Table 5.1, the UCC values depend upon the instrument gain setting. VNIR bands have three possible settings: high, normal, and low-1, while the SWIR bands have an additional low-2 gain setting. The gain setting and the actual UCC needed for a given data set are included in the header metadata. The values for UCC given in Table 5.1 are constant with time thus simplifying the conversion from scaled to unscaled radiance. The constancy of the UCC is accomplished by varying the scaled radiance values to account for changes in the sensor's RCC.

5.3 Determination of Radiometric Calibration Coefficients

As discussed previously, at-sensor radiance is estimated from the scaled radiance that is calculated with the DN and the UCC besides accounting for the RCC. The UCC are constants, while the RCC are variable for the time being. In this section, preflight RCC are described followed by the post-launch RCC trends.

5.3.1 Preflight Determination of Radiometric Calibration Coefficients

ASTER's VNIR and SWIR channels use lamp-based OBC for monitoring temporal changes in the sensor responses. Space restrictions aboard the Terra platform disallow a solar-based calibration, and therefore, onboard calibration is lamp-based. The VNIR and SWIR have two onboard calibration lamps, lamp-A and -B. Both are used periodically, and as a backup system. The VNIR calibration lamp output is monitored by a silicon photo monitor, and is guided to the calibration optics. The calibration optics output is itself monitored by a similar photo monitor that illuminates a portion of the VNIR aperture's observation optics. Meanwhile, the SWIR calibration assembly does not have a second silicon photo monitor. In the preflight phase, the OBC were well characterized with integration spheres calibrated with fixed freezing point blackbodies of Zn (419.5 K), Pb (327.5 K) and Sn (231.9 K). This was accomplished by comparing the VNIR and SWIR output derived from the integration sphere's illumination of the two sensors. The same comparison was made by the calibration lamp's (A and B) illumination of the two sensors. Next, the preflight gain and offset data (no illumination) were determined. In addition, modulation transfer function (MTF) was measured with slit light from a collimator while stray light effect was measured with the integration sphere illumination, which is blocked at the full aperture of the VNIR and SWIR observation optics entrance. The preflight calibration data also includes (1) the spectral response, (2) out-of-band response, and (3) signal-to-noise ratio measured with a double grating monochromator (Thome et al. 1998).

OBC cannot provide results of a higher accuracy than the preflight laboratory calibration. This means that the accuracy of the inflight (absolute) calibration is inferior to the preflight results because the preflight calibration source is used to calibrate the OBC. In addition, the uncertainty of the OBC typically increases with time. Hence, it makes good sense to include additional calibration approaches that are independent of the preflight calibration. Besides the normal and expected degradation of the OBC, they also run the risk of failing or operating improperly. Therefore, vicarious approaches are employed to provide further checks on the sensor's radiometric behavior.

5.3.2 Onboard Calibration

Given the understanding that the orbiting sensor's response will change over time, the ASTER science team developed a methodology, based on OBC results, to update preflight RCC that are input to generate the level-1B product. The OBC results are also combined with vicarious calibration to produce the most accurate knowledge of ASTER's radiometric calibration. This section describes the in-flight determination of the RCC based on the OBC and VC results.

The VNIR has two onboard calibration halogen lamps (A and B). The light from these lamps is led to the VNIR optics via a set of calibration optics. Filters and photomonitors are located fore and aft of the calibration optics to monitor the output of the lamps as well as any possible degradation in the calibration optics. Lamp output and photo monitor data are collected every 33 days (primarily it was 16 days of the Terra orbital revisit cycle plus 1 day = 17 days), and RCC are calculated from the VNIR output taking into account the photomonitor output. The RCC values are normalized by the preflight data to determine their final estimate. This procedure is the same for the SWIR RCC calculation except that the SWIR OBC does not include a photo monitor system at the lamp. Thus, only data from a photo monitor that is aft of the calibration optics are taken into account. The sources of VNIR and SWIR radiometric calibration uncertainties are shown in Table 5.2.

The uncertainty in the band-to-band response ratio is 2.3% with the root sum square among 2.0% of the in-orbit lamp's spectral radiance changes. It registers 0.4% of the radiometer output measurements, and 1.0% of the others. Uncertainty in the detector-to-detector response ratio is 0.8% with the root sum square among 0.6% of the integration sphere, 0.4% of the radiometer output measurements, and 0.4% of the others. The most significant uncertainty is contamination and lamp radiance changes due to a gravity shift followed by photomonitor sensitivity variations due to temperature changes and degradation.

The largest uncertainty is the radiometer output measurement followed by the photo monitor degradation, and lamp radiance dynamics due to temperature changes. Due to filter and detector sensitivity changes in the SWIR region, the uncertainty of the radiometer's output measurements are not so good, and vary by band. SWIR's absence of an aft photo monitor disallows monitoring the lamp output degradation, and hence, uncertainty in that regard is greater than that of VNIR. For the same reason, the uncertainty of the lamp radiance dynamics due to temperature changes is added to the VNIR uncertainty source. The influence due to non-uniform contamination of SWIR is smaller than that of VNIR because the SWIR wavelength coverage is longer than that of VNIR (similar particle size for the same contamination material is assumed).

Table 5.2 Uncertainty in the absolute responsivity for normal gain mode of VNIR and SWIR at post-launch phase. Uncertainty depends on the band (RSS of each band is 2.8, 3.9, 3.4, 5.2, 4.4, 3.9 for bands 4–9, respectively)

| Source of uncertainty | VNIR uncertainty (%) | SWIR uncertainty (%) |
|------------------------------------------------------------|-------------------------|-------------------------|
| Photomonitors sensitivity change due to temperature change | 1.5 | 0.7 |
| Degradation of photomonitors | 1.0 | 2.0 |
| Photomonitor output measurements | 0.4 | 0.5 |
| Lamp radiance change due to gravity shift | 2.0 | 0.5–0.6 |
| Radiometer output measurements | 0.4 | 1.4–4.5 |
| Lamp radiance change due to temperature change | N/A | 1.0–1.2 |
| Others (non-uniform contamination) | 2.0 | 0.2 |
| Root sum square (RSS) | 3.4 | 2.8–5.2 |

From these proto-flight model test data, and analyses derived with the previous mission instrument data, VNIR OBC is reliable at the 2% (1 sigma value) level while SWIR is at a 4% level. Thus the following RCC determination method is adopted. The ASTER RCC are generated via the OBC data. The first 3 months of ASTER operation corresponded to the sensor activation and evaluation (A&E) phase during which the OBC results alone were used to determine the RCC. The OBC data have since been further evaluated by a panel of radiometric scientists relative to the VC results. The panel determined a set of trend equations used until a subsequent calibration panel review. The panel also determined the weightings used in the merging of the OBC and VC results. The best estimates of the ASTER RCC are publicized quarterly through newsletters, an Internet server, and other means. The user may then modify results obtained using the level-1B product according to how large the difference is between the OBC results and the OBC-merged-with-VC results. The first panel meeting was held late during the A&E period to determine the weights for OBC and VC as well as version 1.0 RCC.

ASTER's current approach to determine the RCC for level-1 processing is as follows:

1. Check for consistency between the halogen lamp system A and B (system A and B are turned on every 17 days).
2. Check for inter-channel dependency to find out if all bands within a telescope display similar tendencies.
3. Calculate RCC if both (1) and (2) are satisfied.
4. Calculate calibration coefficients based on cross-calibration results if (1) and (2) are not satisfied.
5. Calculate calibration coefficients based on other vicarious calibration data sets if (1) and (2) are not satisfied, and no cross-calibration coefficients exist.

Basically, RCC for level-1 processing are determined with the current RCC, if the deviation of the current RCC is within a range of the uncertainty, 2% for VNIR and 4% for SWIR in comparison to the previous RCC. If the RCC trend shows inconsistent behavior, then cross calibration and vicarious calibration are taken into account.

5.3.3 Vicarious Calibration

Earth observation satellites have a long history of being characterized by vicarious methods. They include the Marine Observation Satellite-1 (Arai 1988), Landsat-7 Enhanced Thematic Mapper Plus (Barker et al. 1999), SeaWiFS (Barnes et al. 1999), SPOT-1 and 2 (Gellman et al. 1993), Hyperion (Folkman et al. 1997), and POLDER (Hagolle et al. 1999). Vicarious approaches also provide a cross-comparison between sensors to characterize mission instruments onboard the same satellite (Arai 1997) via the use of well-understood ground areas such as desert sites (Cosnefroy et al. 1996). Vicarious methods are not limited to the determination of

the RCC (gain) but are useful for other radiometric performance parameters such as noise equivalent reflectance, bias (or offset), and MTF. These methods are discussed in Sect. 5.4.

5.3.3.1 Reflectance-Based Approach

Three separate groups have collected VNIR and SWIR data as part of the ASTER Science Team's work to understand ASTER's radiometric calibration. All three groups have used the same reflectance-based method, with slight differences in implementation. The University of Arizona Remote Sensing Group's (RSG) work is described first followed by descriptions of Japan's Saga University's and the Advanced Institute of Science and Technology's (AIST) approaches. A discussion of the calibration test sites is also included.

The basic philosophy of the reflectance-based approach relies on ground-based surface reflectance measurements of a selected site. These test sites are described in the following section. The results of the ground-based measurements are input into a radiative transfer code. Inherent to the radiative transfer codes are solar irradiance models that allow for the conversion of relative radiance (also regarded as reflectance) to absolute radiance. The solar model for the current work is based on the World Radiation Center (WRC) model. The ASTER Science Team selected this solar model since the ESE adopted it as the standard for Terra sensors. The choice of the solar model is important because results can differ significantly based on the chosen model. This is reiterated in Sect. 5.5, which discusses the conversion of surface radiance to surface reflectance.

Once the at-sensor, hyperspectral, absolute radiances are determined, they are band-averaged across the sensor's spectral response to give a predicted, at-sensor, spectral radiance for a specific band of interest. This absolute radiative transfer code output is compared to output from the sensor to derive the calibration, or to validate the reported at-sensor radiance. ASTER's reflectance-based method is compared to the level-1B radiance and the level-1A DN.

The joint field campaigns for ASTER took place at Ivanpah Playa, California, and Railroad Valley Playa in Nevada. These test sites are described in detail elsewhere. Both sites are clay-dominated dry lakes, and are used for other sensors since the mid-1990s. The Ivanpah Playa is a hard surface, located south of Las Vegas, Nevada on the California-Nevada border. Figure 5.1a shows a full-scene ASTER image for band 2, and the test site is at the bottom-center of the image with the city of Las Vegas visible on the upper right. Figure 5.1b shows a 6-km by 6-km portion of the full scene showing the area of the playa used for the work described here. The dark point within the dashed circle in the figure indicates the specific location of the test site used by all groups. This dark point in the image indicates the blue tarpaulin target placed on the northeast corner of the test site.

Figure 5.2 shows the ASTER level-1B data of the Railroad Valley Playa test site. Figure 5.2a shows the full-scene ASTER image for band 2 with the Railroad Valley Playa being the dominant feature in the scene. Figure 5.2b shows a 6-km by 6-km

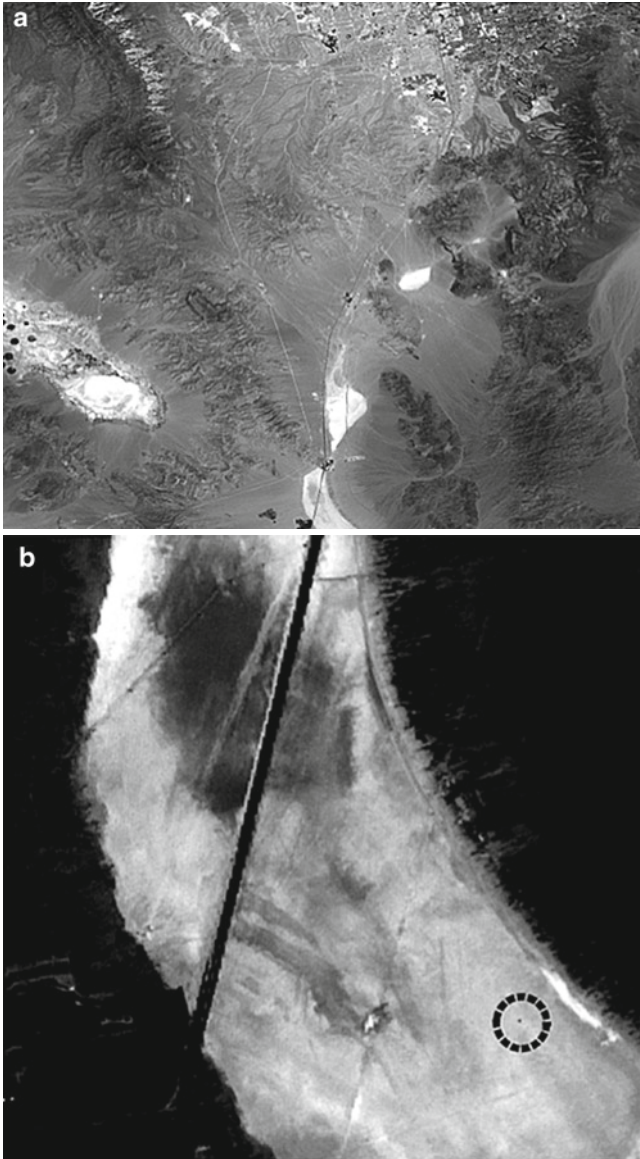


Fig. 5.1 ASTER band 2 image of Ivanpah playa test site at the state border between California and Nevada. *Panel (a)* shows the full scene of the image, while *panel (b)* shows a portion of the image. The *dotted circle* center indicates the test site

area (dashed box in Fig. 5.2a shows approximate location) to indicate details of the area surrounding the test site. The dashed circle denotes the test site, and the dark point within the circle indicates the tarpaulin target placed on the southwest corner

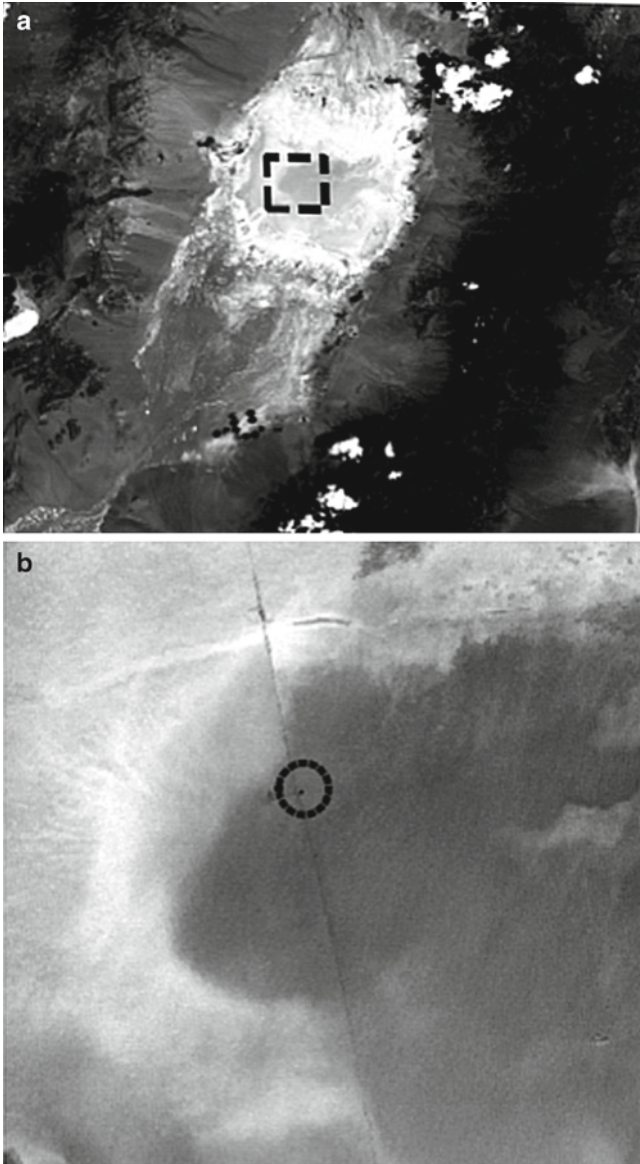


Fig. 5.2 ASTER band 2 image of Railroad Playa test site in Nevada. *Panel (a)* shows the full scene of the image, while *panel (b)* shows the portion of the image. The *dotted circle center* indicates the test site

of this test site. The linear feature to the left of the site is a gravel access road used to reach the test site. This road is necessary because the surface material at Railroad Valley is much softer than at Ivanpah, and vehicles are not readily able to drive across the rough surface.

As described above, the reflectance-based approach relies on surface reflectance measurements, and atmospheric properties at the time of the sensor overpass. The reflectance of the test site is measured using a spectral radiometer across a predetermined area. The primary instruments for measuring surface reflectance are commercially available spectrometers. The instrument is carried across the site using a handheld boom arm, or as part of a backpack device. These extend the instrument's fore optic away from the body of the user, and the fore optic is held between 1 and 2 m height above the ground. The site reflectance is determined by ratioing the site measurements to those of a reference panel for which the bidirectional reflectance factor was determined in the laboratory.

The second piece of information needed in the reflectance-based method is a characterization of the atmosphere. Both custom-made and commercially available solar radiometers are used. The solar radiometers are relatively calibrated immediately prior to, during, or after each field campaign via the Langley method, and this allows for the determination of spectral atmospheric optical depths. The optical depth results are used as a part of an inversion scheme to determine ozone optical depth and an aerosol size distribution. The aerosols are assumed to follow a power law distribution, also referred to as a Junge distribution. Columnar water vapor is derived from the solar extinction data using a modified Langley approach.

The atmospheric and surface data are used in a radiative transfer code. There are a variety of codes available that satisfy all the requirements of predicting the at-sensor radiance to the required accuracy. The original work is based on a Gauss–Seidel iteration approach developed at the University of Arizona in the 1960s. Past work has shown that similar conclusions are drawn for other code types such as doubling-adding, and the methods used in the 6S code. Besides these, another method takes into account polarizations in the calculation of down-welling and up-welling radiation. It uses ground-based solar direct, diffuse and aureole radiance measurements as well as polarized radiance with several polarization angles (Arai and Liang 2005; Liang and Arai 2005). This study is based on a Lambertian view of the surface. The near-nadir view for the majority of the ASTER overpasses reduces the uncertainty of this assumption since the dominant direct-reflected solar irradiance is correctly taken into account. Thome and Nandy (2000) show that the non-Lambertian effect on the diffuse component is negligible for the near-nadir view at both Ivanpah and Railroad Valley playas.

Strong gaseous absorption effects due to water vapor are determined using MODTRAN to compute transmittance for the sun-to-surface-to-satellite path for 1-nm intervals from 350 to 2,500 nm. This sun-to-ground-to-sensor transmittance is multiplied by the at-sensor radiance output from the radiative transfer code to correct the radiances for this strong absorption. While this approach is an approximation that excludes interactions between diffusely scattered radiances and absorption, it does not cause large uncertainties for ASTER applications because of the small absorption effect within most of the bands, and the typically high surface reflectance of the test sites used in this work.

Arai and Thome (2000) published an error budget analysis of solar reflectance-based vicarious calibration. The most dominant factor for vicarious calibration is

surface reflectance measurement, followed by optical depth measurement, estimation of refractive index, aerosol size distribution, and identification error in test site pixels. Typical vicarious calibration accuracy is around 4%. The reflectance-based measurement results (in relation to those of OBC and preflight) are provided in Sect. 5.3.5.1.

5.3.4 Cross Calibration

An additional vicarious calibration approach used by ASTER is cross-calibration or cross-comparison. The goal of a cross-calibration approach is to transfer the calibration of another known sensor to ASTER. Typically, there are two methods: (1) a direct comparison of near-coincident data sets between the sensors and (2) a comparison of the radiometric calibration results for the two sensors based on a common method of absolute radiometric calibration, such as the reflectance-based approach. ASTER's advantage is that it is co-located on the same platform as two other instruments, Moderate-Resolution Imaging Spectroradiometer (MODIS) and Multi-Angle Imaging Spectroradiometer (MISR), and orbits approximately 30 min behind ETM+. All three instruments are used in ASTER's vicarious calibration.

5.3.5 OBC RCC Trends and Comparison to the Vicarious Calibration

5.3.5.1 RCC Trends

Figures 5.3 and 5.4 show the RCC trends for VNIR and SWIR, respectively. The RCC were changed relatively rapidly in the early stage of the launch, and is changed gradually for the time being. These are approximated with an exponential function with a bias and a negative coefficient. If the trend is approximated with the function of $RCC = B \exp(-At) + C$, then A, B, and C equal the following values:

VNIR Band 1: A = 0.00190, B = 0.360, C = 0.735

Band 2: A = 0.00168, B = 0.282, C = 0.807

Band 3: A = 0.00150, B = 0.216, C = 0.860

During 2,500 days after the launch, VNIR OBC RCC were degraded about 10% for Band 3, 16% for Band 2 and 23% for Band 1, respectively while SWIR OBC RCC were degraded approximately 2.0–3.5% depending on bands. These trends are very similar to the vicarious calibration-derived RCC, and also look similar to the OBC RCC trend of the Optical Sensor onboard the JERS-1 satellite, a legacy precursor to the ASTER instrument.

The results shown in Figs. 5.3 and 5.4 are verified to a large extent using the reflectance-based measurements. The data are collected approximately twice per

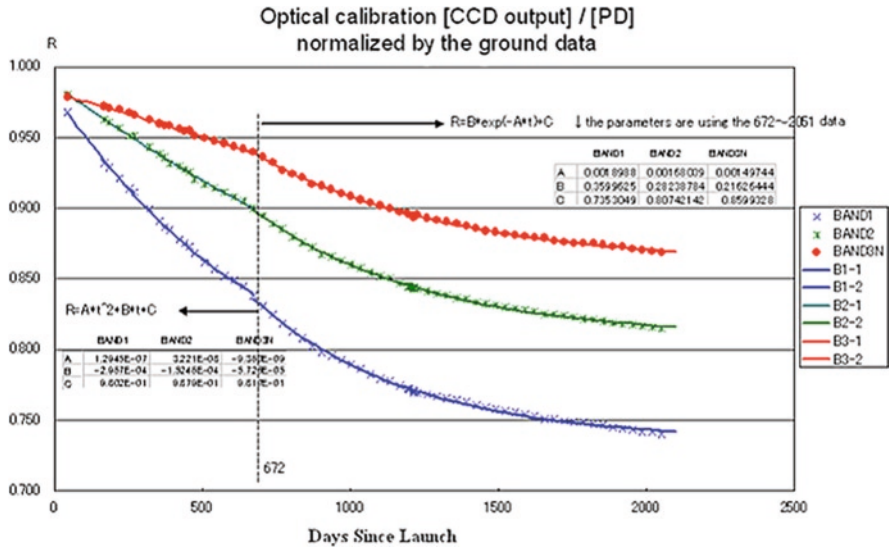


Fig. 5.3 Radiometric calibration coefficients (RCC) for VNIR derived from the optical calibration data taking into account the photomonitor data, and after normalization using the preflight ground data. Note that the RCC trend appears to change on day-672 following launch. The period from launch to day-672 is approximated with a linear function, while the RCC after day-672 are approximated through an exponential function

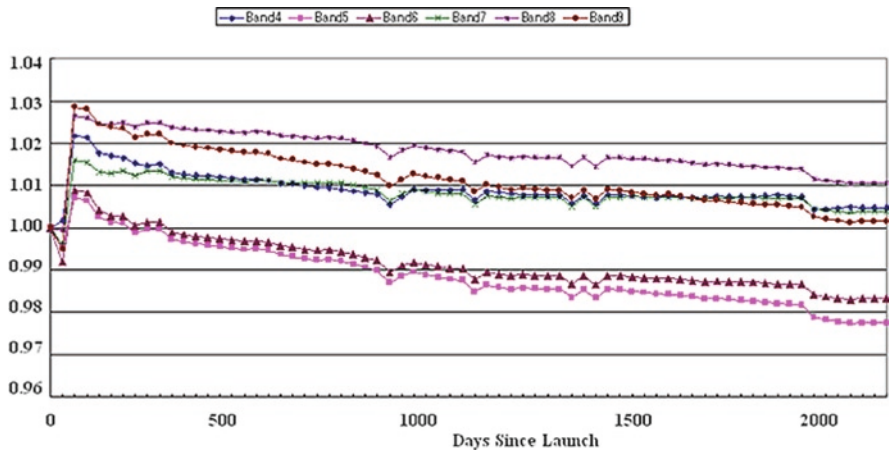


Fig. 5.4 RCC for SWIR subsystem derived from the optical calibration data with Lamp B system taking into account the photomonitor data normalized using the preflight ground data. The RCC shown indicate a small decrease of a few percent over the more than 5 years of data shown

year and Fig. 5.5 shows results for the VNIR bands for a total of 15 dates between April 2000 and July 2003. At least two of the groups were present during these dates, and ASTER viewed the test site at near-nadir views. During this period, there are a total of eight dates for which all three groups successfully collected ground data, the weather conditions remained clear, and ASTER successfully acquired the test site data as well. These data are scaled calibration coefficients in counts per unit

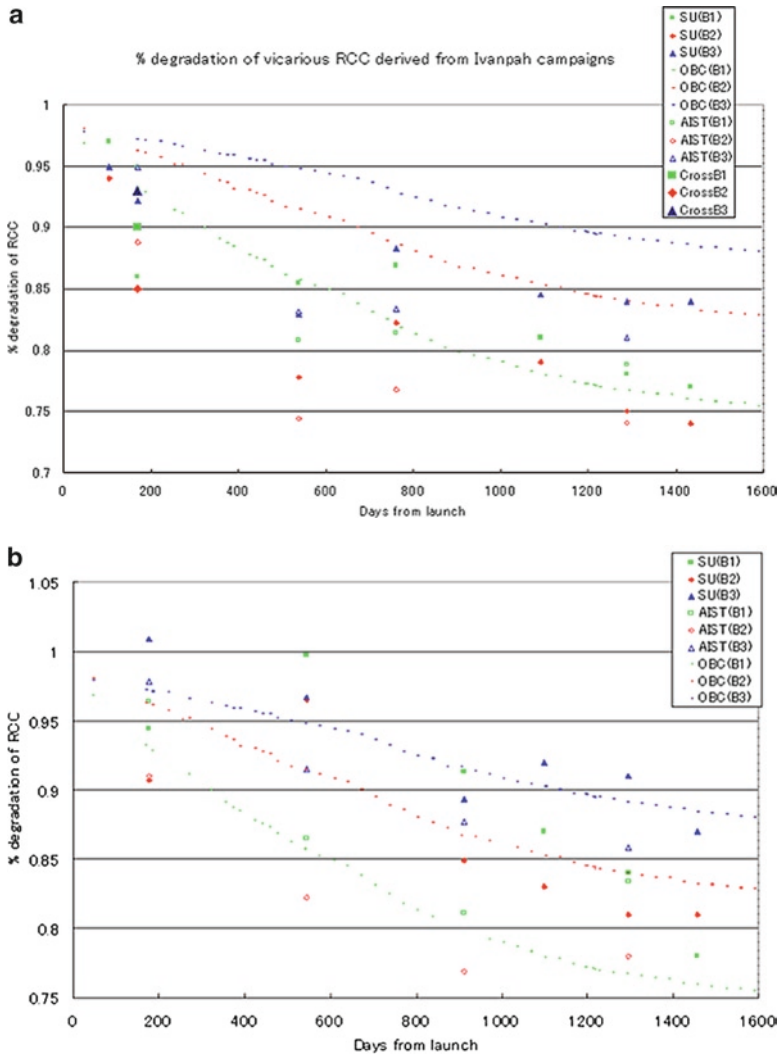


Fig. 5.5 A comparison between OBC data-derived RCC and vicarious calibration data-derived RCC for VNIR; (a) RCC derived from Ivanpah test site vicarious calibration data; (b) RCC derived from Railroad test site vicarious calibration data

radiance scaled to give a value of unity on day-168 since launch. Each of the VNIR bands is shown, as are the OBC results for these bands in a fashion similar to that shown in Fig. 5.3.

5.3.5.2 Comparison to the Vicarious Calibration

The vicarious results for Ivanpah Playa shown in Fig. 5.5a indicate degradation in all three bands since launch. The OBC data also show degradation. In addition, the superior precision of the OBC is clearly evident in the data. The vicarious results from each group agree well with each other but differ from the OBC results. This is discussed further in Sect. 5.3.5.3. Similar results are seen for Railroad Valley in Fig. 5.5b. The VC results for the ASTER SWIR bands are shown in similar fashion for the two sites in Fig. 5.6. The results in this figure indicate a scatter that is larger than the degradation shown by the OBCs in Fig. 5.4. Differences exist between the VC and OBC results in an absolute sense.

Figure 5.7 describes the average percent differences between the VC and OBC results between the SU and AIST groups relative to the RSG results. This provides an indication of the level of agreement between the groups. In addition, the standard deviation of the average is also given to indicate how repeatable the results are between the groups. Thus, the best average agreement between the groups is for bands 5, 6, and 7 with <1% difference between groups. This indicates very little bias between the groups for these bands. The standard deviation of the average in these bands is 3–4%, and although this indicates there is no bias for these bands, there still are day-to-day differences between the groups. Note that band 8 shows very little bias between the groups but a larger standard deviation. This is most likely due to differences in retrieved column water vapor between the groups.

Figure 5.8 shows the average percent difference between the RSG results and the level-1B data based on the RCC derived from the OBC data. Two sets of ASTER results based on VC data collected before and after the changes in RCC values are described in the next section. Clear biases exist in bands 1–4 and 9. The bias in band 9, as well as the very large standard deviation is attributed to water vapor effects. The center band and bandwidth of band 9 make it susceptible to water vapor absorption. In addition, absorption in this part of the spectrum also causes larger uncertainties in the retrieved surface reflectance due to reduced signal-to-noise ratio in the field measurements. RSG's measurements especially confirm this because it uses a longer than typical fiber optic in its field spectrometer leading to larger attenuation in the fiber due to water absorption. Further work is currently underway to improve the understanding of the results in band 9, but since there is also a strong optical crosstalk as discussed in Sect. 5.4, work related to water vapor effects has not attracted enough attention.

The biases in the other bands are not as clearly understood at this time. The bias seen in band 2 is most likely caused by differences in retrieved ozone amounts between the groups but the small standard deviation indicates a bias in retrieved ozone or the treatment of ozone absorption within the radiative transfer codes.

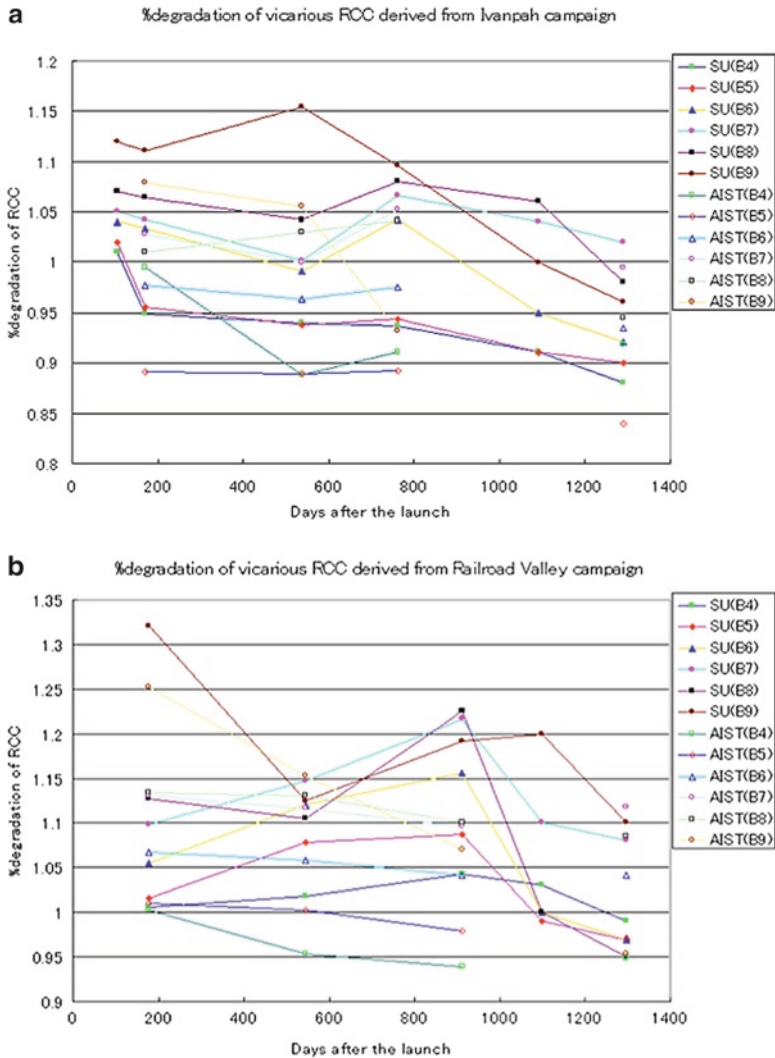


Fig. 5.6 A comparison between OBC data-derived RCC and vicarious calibration data-derived RCC for SWIR; (a) RCC derived from Ivanpah test site vicarious calibration data; (b) RCC derived from Railroad test site vicarious calibration data

While the biases in bands 1, 3, and 4 are significant, they still are reasonably small. The most curious issue at this stage is the large standard deviation in band 4.

Overall, the above results show that the VC results for all three groups agree with each other to within 3–5% for all bands except band 9. In addition, bands 1–3 have shown levels of degradation in both the OBC data and vicarious results, but the results shown here indicate a possible discrepancy between the sensor behavior

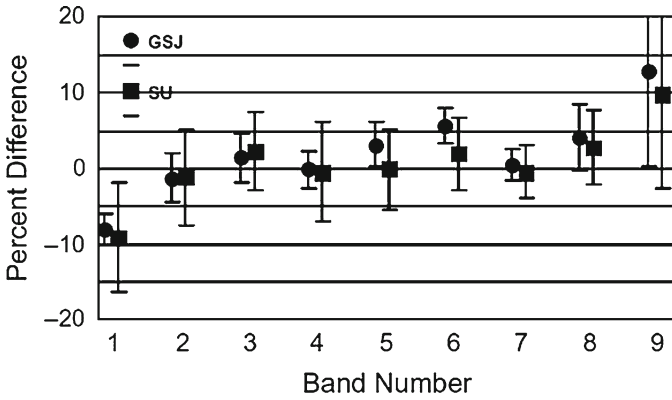


Fig. 5.7 Average percent difference between Saga University and Advanced Institute for Science and Technology results relative to the University of Arizona Remote Sensing Group's results

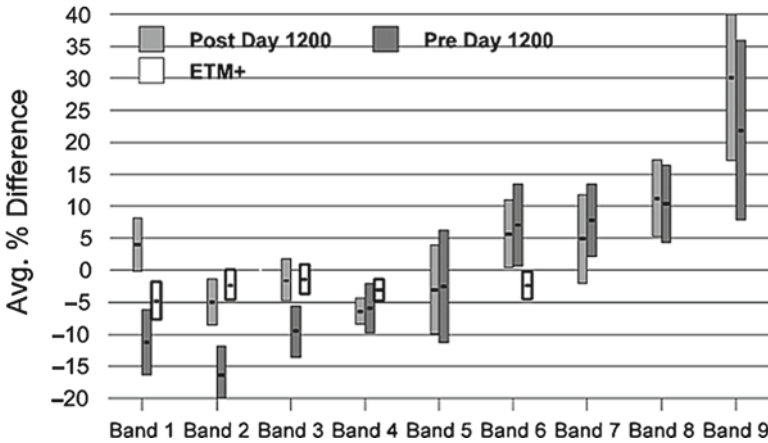


Fig. 5.8 Percent difference between ASTER VNIR, SWIR data, and the closest Landsat ETM+ data bands

derived from the OBC and the VC. The SWIR bands do not show a significant level of degradation. These results depend more on the precision of the vicarious approach.

The second set of results in Fig. 5.9 examines the average percent difference between the ASTER vicarious results compared to those of the Landsat-7 Enhanced Thematic Mapper Plus (ETM+) sensor. ETM+ has similar spatial resolution and spectral bands as well as an orbit that places it approximately 30–45 min ahead of ASTER. Thus, ETM+ provides a check on ASTER's vicarious results. The first notable feature in the figure is ASTER SWIR's very large standard deviation compared to similar ETM+ bands. The optical crosstalk described in Sect. 5.4

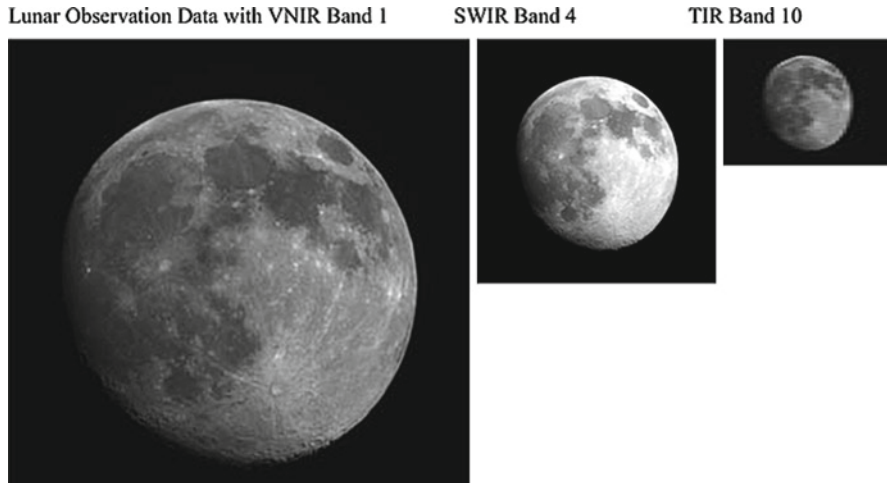


Fig. 5.9 ASTER VNIR, SWIR, and TIR image data observed during Deep Space and Lunar Calibration maneuvers during from March 26, and April 15, 2003 (about 3.5 years after the launch)

explains this behavior. The second notable feature in Fig. 5.8 is the band 1 results. The shift in calibration is clearly evident between the pre- and post-day-1200 results. Also noticeable is ASTER's larger standard deviation relative to the ETM+ results, and the large difference between ETM+ radiance and ASTER radiance for the comparable bands at 550 nm. A disagreement exists between ETM+ and ASTER of approximately 7% before day-1200 and 9% after day-1200, which is larger than the expected combined uncertainties of the method in both cases.

Similarly large differences are seen in bands 2 and 3 in the data prior to day-1200. This difference decreases after day-1200 such that ETM+ and ASTER are in excellent agreement. ASTER Band 4 does not suffer strongly from the optical crosstalk effect. This band shows reasonably good agreement with ETM+ and shows little change in the average in the post- and pre-day-1200 phases. What is of interest is that the standard deviation of the band 4 results decreases after day-1200, even with the smaller sample size.

5.3.5.3 Radiometric Calibration Coefficients for VNIR and SWIR

Table 5.3 lists the RCC for the VNIR/SWIR bands based on the results shown above and the coefficient generation approach described above. These RCC are adjusted in accordance with the version number listed when any RCC changes by more than 2% as indicated by the OBC. The RCC for the SWIR bands have not been updated as of December 2005 due to use of the photo monitors, and dual lamps show consistency of the OBC over time.

Table 5.3 Radiometric calibration coefficients as a function of the version number

| Version no. | Band 1 | Band 2 | Band 3 | Since when |
|-------------|--------|--------|--------|------------|
| 1.00–2.00 | 1 | 1 | 1 | 1996/11/9 |
| 2.01 | 0.972 | 0.982 | 0.978 | 2000/2/2 |
| 2.02–2.03 | 0.948 | 0.972 | 0.982 | 2000/6/4 |
| 2.04 | 0.931 | 0.966 | 0.985 | 2000/11/4 |
| 2.05–2.06 | 0.921 | 0.959 | 0.982 | 2001/2/14 |
| 2.07–2.08 | 0.892 | 0.950 | 0.983 | 2001/12/26 |
| 2.09–2.11 | 0.802 | 0.872 | 0.917 | 2002/5/8 |
| 2.12–2.15 | 0.779 | 0.852 | 0.902 | 2002/12/23 |
| 2.16–2.17 | 0.760 | 0.833 | 0.886 | 2003/11/11 |
| 2.18 | 0.758 | 0.831 | 0.883 | 2004/1/05 |

5.4 Other Radiometric Performance Issues

The RCC are not the only parameters determined for ASTER. This section describes the evaluation of other radiometric performance parameters such as noise equivalent reflectance, bias (or offset), and MTF. All these parameters are typically determined during the preflight characterization. The preflight characterization often does not point out likely problems in the on-orbit phase. Thus, vicarious methods are also used in this characterization. This includes the Terra roll maneuvers to obtain deep space calibration (DSC) data, and lunar calibration (LC) data. In addition, the radiometric scientists and ASTER engineers have also obtained nighttime observation (NTO) data. These data are often collected for science evaluation of the TIR subsystem but the VNIR/SWIR subsystems are not activated unless part of a specific request.

The work presented here includes the work of engineers at ERSDAC, GDS, and SISS in Japan as well as the ASTER calibration scientists in both Japan and the U.S. Homogeneous area images of the earth collected during the initial checkout period confirmed the knowledge of the detector-to-detector striping. Stray light and other MTF characteristics were examined through scenes containing sharp water boundaries as well as lunar calibration. The lunar source and associated DSC are excellent methods for determining noise, gain and offset (Kieffer et al. 1996). Noise equivalent reflectance and sensor noise are characterized by computing the standard deviation of the ASTER instrument data over homogeneous sites. The accuracy of noise characterization depends on homogeneity of the target over the scenes, and therefore, NTO data and/or deep space data are typically used. Meanwhile MTF in both along-track (AT) and cross-track (CT) directions are characterized by using images, which includes knife-edges of spatial features in both AT and CT directions. The lunar calibration data are used to characterize the MTF accuracy, which depends on the sharpness of the knife-edge. To avoid the influence stemming from differences between in-phase and out-of-phase MTF characterization, slant edges were used in the characterization.

The following sections provide the results of the VC determination of the above characteristics. Discussion of how these results compare to the preflight characterization is given when appropriate. In addition, the SWIR optical crosstalk characterization and correction are described below.

5.4.1 Offset

On March 26 and April 15 in 2003 (JST), a DSC maneuver and a lunar calibration (LC) maneuver were conducted, respectively. The DSC data are used to determine the offsets of the VNIR and SWIR by taking the average 512 by 512 VNIR pixels and 256 by 256 SWIR pixels of the level-1A product. Table 5.4 shows the results of this work together with the preflight offset measured for the lamp system-A. The table also includes an estimate for the rate of change per year together with noise (STD) changes. The results show an almost three-time increase in the VNIR bands 1 and -2 offsets while band 3 is stable at around half percent annually. Meanwhile the SWIR offsets have increased by 5–8% a year displaying a stabler response relative to VNIR.

NTO data are useful in evaluating solar reflection offsets for different channels. The nighttime data from April 1, 2003 is used to evaluate VNIR and SWIR. Two arrays of 512 by 512 VNIR pixels and 256 by 256 SWIR pixels were extracted from the level-1B product for offset evaluation. The results of this evaluation are presented in Table 5.5. The VNIR bands 1 and 2 offsets along with their standard deviation are relatively high compared to the other bands. The level-1B product is defined as radiometrically corrected data where offset, gain as well as detector-to-detector sensitivity differences are removed. Offset correction is made by subtracting measured offset as preflight data, thus these band offsets equal a value of one. The remaining offsets for bands 1 and 2 are 2.1 and 1.6, respectively. These values are not so small, and are becoming bigger with the passage of time.

Table 5.4 Preflight offset ($M(La)$: mean of Lunar calibration output) for the lamp system A, in-flight offset calculated with deep space calibration data and the change rate a year together with noise (STD : standard deviation) changes

| Band no. | $M(La)$ | $M(DS)$ | Change rate | $STD(DS)$ | $STD(La)$ | Change rate |
|----------|---------|---------|-------------|-----------|-----------|-------------|
| 1 | 1.00063 | 3.51178 | 0.71702 | 0.2781 | 0.0006 | 102.778 |
| 2 | 1.00654 | 2.85358 | 0.524297 | 0.1250 | 0.9874 | -0.043 |
| 3 | 4.93656 | 5.03125 | 0.00548 | 10.2756 | 14.4159 | -0.064 |
| 4 | 1.96722 | 2.49365 | 0.076457 | 0.2534 | 0.4038 | -0.082 |
| 5 | 8.9892 | 10.96 | 0.06264 | 1.1445 | 0.9320 | 0.051 |
| 6 | 9.05017 | 10.5942 | 0.048745 | 0.5382 | 0.7515 | -0.063 |
| 7 | 9.23627 | 11.2623 | 0.062673 | 1.6354 | 1.4711 | 0.025 |
| 8 | 7.97601 | 9.49884 | 0.05455 | 0.2661 | 0.3625 | -0.059 |
| 9 | 8.60181 | 10.5697 | 0.065365 | 0.6035 | 0.4602 | 0.069 |

Table 5.5 Offset evaluated with the nighttime observation data of April 1, 2003

| Band no. | Mean (offset) | Standard deviation |
|----------|---------------|--------------------|
| 1 | 2.1324 | 0.4485 |
| 2 | 1.6148 | 0.6239 |
| 3 | 1.0791 | 0.2699 |
| 4 | 1.0001 | 0.0117 |
| 5 | 1.1015 | 0.3021 |
| 6 | 1.0932 | 0.2913 |
| 7 | 1.1031 | 0.3046 |
| 8 | 1.0940 | 0.2923 |
| 9 | 1.0438 | 0.2048 |

Table 5.6 Specified and measured S/N: signal-to-noise ratio and noise equivalent DN: digital number (*DSC*: deep space calibration, *NTO*: nighttime observation)

| Band no. | Specified | | Measured | | |
|----------|-----------|----------|------------------|-----------------|-----------------|
| | S/N | Noise DN | At preflight S/N | At DSC noise DN | At NTO noise DN |
| 1 | 40 | 1.275 | 170–78 | 0.2781 | 0.4485 |
| 2 | 40 | 1.275 | 122–74 | 0.1250 | 0.6234 |
| 3 | 40 | 1.275 | 70–58 | 10.2756 | 0.2699 |
| 4 | 35 | 1.457 | 368–63 | 0.2534 | 0.0117 |
| 5 | 13.5 | 3.778 | 77–45 | 1.1449 | 0.3021 |
| 6 | 13.5 | 3.778 | 73–36 | 0.5382 | 0.29135 |
| 7 | 13.5 | 3.778 | 72–35 | 1.6354 | 0.3046 |
| 8 | 13.5 | 3.778 | 81–34 | 0.2661 | 0.2923 |
| 9 | 13.5 | 3.778 | 73–44 | 0.6035 | 0.2048 |

5.4.2 Noise Equivalent Reflectance and Temperature

As shown in Table 5.4, noise (Standard Deviation) is <1 DN except for bands 3, 5, and 7. In particular, noise for band 3 is significantly large compared to the other bands. The specified and measured S/N at preflight phase for low input radiance (which corresponds to DN of 51) are shown in Table 5.6 together with the DN that corresponds to S/N measured at preflight phase, DSC, and NTO. The measured noise equivalent DN registers better compared to its specified component except for band 3 measured as part of the DSC.

5.4.3 Modulation Transfer Function

The LC images are depicted in Fig. 5.9. MTF was evaluated in both AT and CT directions using the knife-edge spatial features in the LC data. Since the LC data were not acquired during a full moon, the bottom and left-edges are not useful as illustrated in Fig. 5.10. A nearly identical MTF estimation method for TIR is

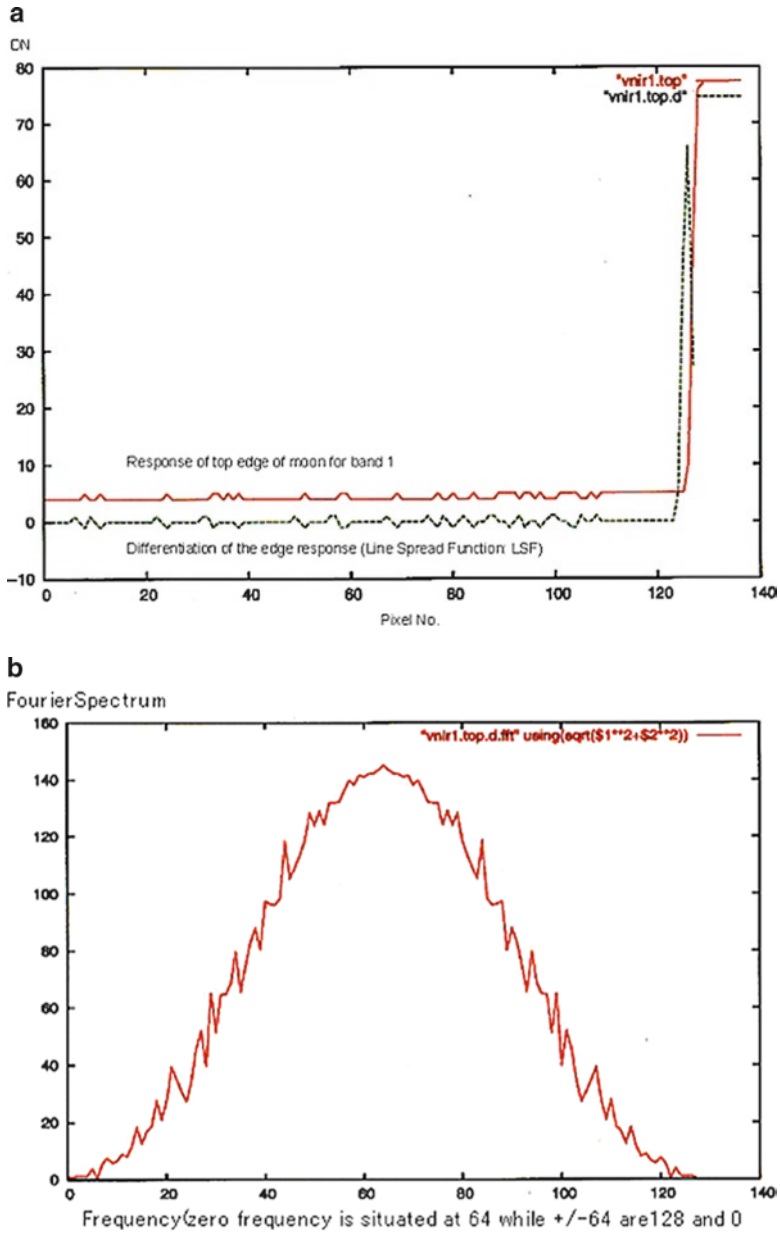


Fig. 5.10 (a) An example of the edge response, and its differentiation (Line Spread Function: *LSF*).
 (b) The Fourier spectrum of the LSF (MTF) at the top of the moon for band 1

applied to the VNIR and SWIR components of the LC data. The edge response example, differentiation of the edge response (Line Spread Function (LSF)) and the Fourier spectrum of the LSF (MTF) at the top of the moon for band 1 are shown in Fig. 5.6. Through a third-order polynomial curve fitting, MTF at the Nyquist and 1/2 Nyquist frequencies are estimated. The estimated MTF for VNIR and SWIR in both AT and CT directions are shown in Table 5.7.

The estimated MTF with LC data are greater than the MTF of preflight data at Nyquist and 1/2 Nyquist frequencies for VNIR bands 1–3, and SWIR bands 4–9.

5.4.4 SWIR Crosstalk

The existence and effects of stray light on the ASTER SWIR radiometer was discovered following Terra's launch (Iwasaki and Tonooka 2005; Iwasaki et al. 2002). Figure 5.11 shows examples of SWIR images (bands 4, 5, and 9 of a Nagoya image, acquired on July 10, 2000) enhanced by decorrelation stretch. We find that the peninsula and seashore images are overlaid multiple times in the along-track direction, and appear as ghostly patterns on the sea. Even though use of multispectral SWIR images is effective in applications, such as mineral mapping, the crosstalk effects generate anomalous artifacts with potential to introduce uncertainties.

Figure 5.12 shows the configuration of the SWIR focal plane. Six spectral bands in the 1.6–2.43 μm wavelength region with a ground sampling distance of 30 m are available using parallel arrays of Pt–Si Schottky barrier CCD detectors arranged on the focal plane. Neighboring bands observe the same ground target with a time difference of 360 ms; this corresponds to 81 lines in the acquired image. Pixel data are quantized in 8 bits, and the radiometric accuracy is better than 4%.

We find that the greater the distance from band 4, (1) the crosstalk image appears more distant, (2) the crosstalk component is as much weaker, and (3) the crosstalk influence area is more diffused. The presence and effects of a stray light component from band 4 (1.6–1.7 μm) on the other bands explain this crosstalk phenomenon. We can explain this thus: band 4's spectral bandwidth is larger than those of the others, and its typical input radiance is about five times larger as well. We define this stray light problem as the crosstalk phenomenon. Although crosstalk probably exists between any pair of bands, it is sufficient to only consider the optical crosstalk effects from band 4 on the other bands since the other contributions are small.

Figure 5.13 shows the most likely mechanism for stray light generation, and how it is transported to the other bands. The Pt–Si detectors are built on the bottom surface of a silicon substrate. The top surface is covered with an anti-reflection (AR) coating. Since the optical absorption of a Pt–Si Schottky detector is small, an aluminum reflection film is attached on the backside of the detectors to double the sensitivity. Since the silicon substrate has a refractive index about 2.5 times higher than that of the coating, light is confined in the silicon substrate when the incident angle is greater than the critical angle of about 25°. Thus the incident light to band 4 is transferred to the other bands by multiple reflection mechanisms. The light

Table 5.7 Preflight and the estimated MTF at Nyquist and 1/2 Nyquist frequency for VNIR bands 1–3 and SWIR bands 4–9 (AT: along track, CT: cross track)

| | Band 1 | Band 2 | Band 3 | Band 4 | Band 5 | Band 6 | Band 7 | Band 8 | Band 9 |
|-------------|-----------|-----------|-----------|-----------|-----------|-----------|-----------|-----------|-----------|
| 1/2 Nyquist | 0.72–0.77 | 0.71–0.75 | 0.74–0.75 | 0.79–0.83 | 0.80–0.85 | 0.79–0.84 | 0.75–0.84 | 0.81–0.84 | 0.83–0.89 |
| Nyquist | 0.23–0.28 | 0.22–0.28 | 0.26–0.29 | 0.34–0.36 | 0.32–0.36 | 0.34–0.36 | 0.31–0.34 | 0.33–0.36 | 0.35–0.39 |
| 1/2 Nyquist | 0.82–0.84 | 0.84–0.87 | 0.81–0.84 | 0.79–0.92 | 0.73–0.86 | 0.74–0.84 | 0.74–0.85 | 0.71–0.86 | 0.70–0.85 |
| Nyquist | 0.40–0.51 | 0.48–0.58 | 0.50–0.55 | 0.40–0.43 | 0.39–0.44 | 0.37–0.45 | 0.35–0.40 | 0.32–0.44 | 0.33–0.43 |
| 1/2 Nyquist | 0.79 | 0.816 | 0.83 | 0.902 | 0.833 | 0.775 | 0.72 | 0.735 | 0.864 |
| Nyquist | 0.357 | 0.392 | 0.432 | 0.706 | 0.5 | 0.352 | 0.264 | 0.324 | 0.644 |
| 1/2 Nyquist | 0.932 | 0.797 | 0.864 | 0.872 | 0.815 | 0.8 | 0.794 | 0.75 | 0.706 |
| Nyquist | 0.693 | 0.568 | 0.682 | 0.651 | 0.463 | 0.393 | 0.515 | 0.419 | 0.412 |

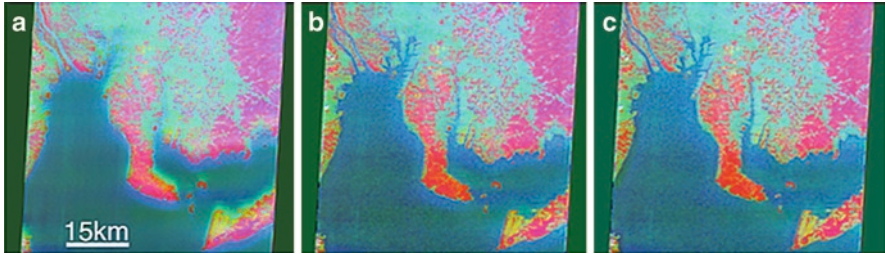


Fig. 5.11 ASTER SWIR image of Nagoya, Japan, acquired on July 10, 2000. The crosstalk effects are enhanced by applying a decorrelation stretch to bands 4 (red), 5 (green), and 9 (blue); (a) before correction, (b) default, and (c) optimized correction

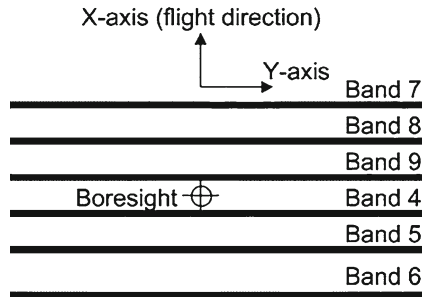


Fig. 5.12 Detector array alignment of the SWIR sensor

reflected at a small reflection angle passes through the AR coating and reaches the bottom surfaces of the interference filters, and then returns to the silicon substrate. In these cases, the crosstalk pattern appears at the location in multiples of 81 lines in the along-track direction. Another stray light component is caused by scattering or refraction at the filter boundaries although the interference filter of each band is completely glued side-by-side. In this case, the crosstalk pattern appears at the location in multiples of 41 lines in the along-track direction.

Due to propagation of the stray light from band 4, the image pattern becomes diffused. The crosstalk component is approximated by the convolution of the band 4 image with a blurring function.

$$\tilde{f}^{(k)}(x, y) = f^{(4)}(x - x_{(k)}, y - y_{(k)}) * h^{(k)}(x, y), (k = 5, 6, 7, 8, 9) \tag{5.2}$$

Here, $\tilde{f}^{(k)}(x, y)$ and $f^{(k)}(x, y)$ denote the crosstalk component and band k 's original image, respectively. Assuming that the stray light transport mechanism is multi-reflective with the cosine law, the Gaussian approximation of the stray light pattern is used.

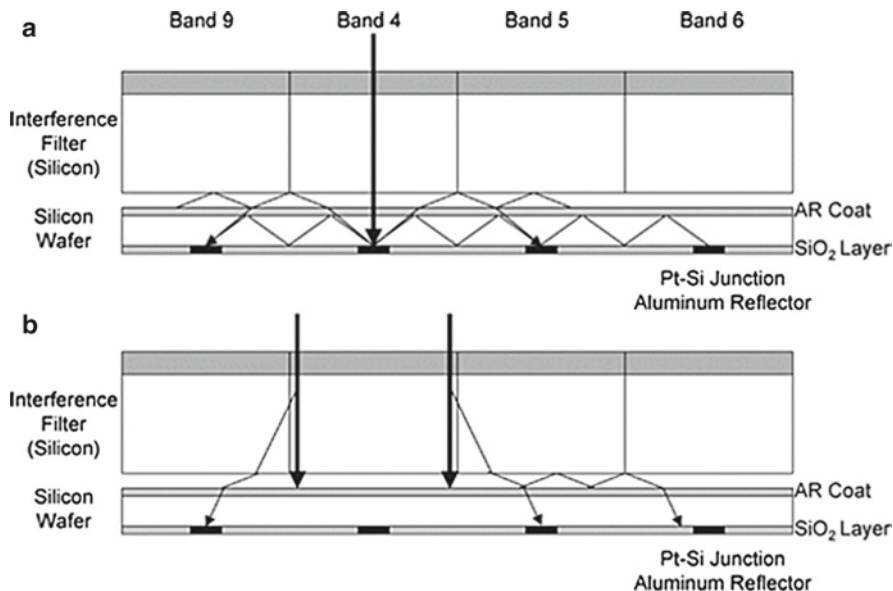


Fig. 5.13 Illustrative view of the crosstalk effects from band 4 to the other neighboring bands. (a) Reflected light at the SiO₂ cover of the silicon wafer is irradiated within the wafer and within the anti-reflection (AR) coating and the interference filter. (b) Irradiation that occurs within the interference filter

$$h^{(k)}(x, y) = \frac{a^{(k)}}{2\pi\sigma_x^{(k)}\sigma_y^{(k)}} \exp\left\{-\frac{1}{2}\left[\frac{x^2}{\sigma_x^{(k)2}} + \frac{y^2}{\sigma_y^{(k)2}}\right]\right\} \quad (5.3)$$

Here, the parameters, $a^{(k)}$, $\sigma_x^{(k)}$, $\sigma_y^{(k)}$, $x_{(k)}$, and $y_{(k)}$ are the amplitude, widths of the stray light in the cross-track and along-track directions, and displacement of the ghostly image in the cross-track and along-track directions, respectively.

The incorporation of the crosstalk component and their effects render the radiometric coefficients for all the detectors (determined in the preflight test with an integration sphere) wrong. Therefore, following correction of the crosstalk components, the detectors' sensitivity input contributions require changes. We next derive the sensitivity factor applied to the input radiance in the sensor. Using the values of $b^{(k)}$ and $c^{(k)}$, which were measured during the preflight test (Table 5.8), the crosstalk correction is written thus:

$$f_{corrected}^{(k)}(x, y) = \frac{f^{(k)}(x, y) - h^{(k)}(x, y) * f^{(4)}(x - x_{(k)}, y - y_{(k)})}{1 - b^{(k)}a^{(k)}c^{(k)}} \quad (5.4)$$

The crosstalk parameters were first estimated to fit the cross-sectional profile. Next, the crosstalk correction was carried out using the parameters adjusted to

Table 5.8 Crosstalk parameters for Level-1A

| Band no. | Offset | | Correction | | | Default | | Optimized | | |
|----------|----------------------|----------------------|------------|-----------|-----------|-----------------------------|-----------------------------|-----------|-----------------------------|-----------------------------|
| | $x_{(k)}$ (pixel) | $y_{(k)}$ (pixel) | $b^{(k)}$ | $c^{(k)}$ | $a^{(k)}$ | $\sigma_x^{(k)}$ (pixel) | $\sigma_y^{(k)}$ (pixel) | $a^{(k)}$ | $\sigma_x^{(k)}$ (pixel) | $\sigma_y^{(k)}$ (pixel) |
| 4 | — | — | 1.000 | 1.000 | — | — | — | — | — | — |
| 5 | 0 | 65 | 3.282 | 0.316 | 0.09 | 28 | 20 | 0.13 | 38 | 32 |
| 6 | 0 | 146 | 3.329 | 0.287 | 0.03 | 30 | 26 | 0.05 | 38 | 35 |
| 7 | 0 | -227 | 3.635 | 0.285 | 0.02 | 34 | 30 | 0.02 | 44 | 36 |
| 8 | 0 | -146 | 5.224 | 0.198 | 0.03 | 30 | 26 | 0.03 | 38 | 35 |
| 9 | 0 | -65 | 6.072 | 0.146 | 0.09 | 28 | 20 | 8 | 38 | 32 |
| | | | | | | | | 0.14 | | |

 $y_{(k)} = \pm(65 + 81d), (d = 0, 1, 2)$

eliminate ghostly patterns. Table 5.8 shows the parameters for the crosstalk model determined during the initial checkout period, called the default parameters. We find that larger the distance from band 4 detectors, the amplitude is smaller with a wider crosstalk influence area.

The displacement of band 5 in the along-track direction ($y_{(k)}$) is smaller than the value calculated from the time difference between neighboring bands (81 lines). Both the detector line and the filter boundaries are considered as the source of the crosstalk component.

Figure 5.11b shows the image following the crosstalk correction with the default parameters, and further enhanced by decorrelation stretch. We find that this process mainly corrects the seashore artifacts. This crosstalk correction method works well because the coastline is clearer in the corrected images quite similar to the opposite seashore, which is free from crosstalk effects. Moreover, the difference here in reflectance between the sea (about 2%) and the peninsula (about 25% for band 4, and about 10% for bands 5–9) is very large.

However, we find a faint stray light pattern remains in the enhanced image because the sea turbidity and the atmospheric effects influence the stray light estimation. To minimize the influence of aerosol scattering, a crosstalk optimization was carried out for Pozuelos Lake in Argentina (Path 231, Row 210; acquired on August 27, 2001). Its 3,000 m elevation minimizes the atmospheric influences. Furthermore, the lakeshore is rich in high reflectance minerals that enable the precise determination of the crosstalk parameters. The crosstalk parameters are adjusted by minimizing the standard deviation of the lake radiance, listed in Table 5.8. Figure 5.11c shows the image processed using the optimized parameters. All traces of the ghostly patterns are significantly reduced, indicating that the optimized parameters are more suitable than the default values. Presently, ERSDAC and NASA LP DAAC process the higher-level data products, such as the atmospherically corrected surface radiance and reflectance, with the default crosstalk correction parameters. Since over-correction is undesirable, the correction based on default parameters is deemed sufficient for geological applications. However, users may tune the crosstalk correction parameters using the correction software supplied by ERSDAC.

The SWIR sensor was mainly developed for geological applications and research. SWIR's high spectral resolution allows the precise discrimination of a number of minerals. Carbonates, hydrates, and hydroxide spectra display their molecular absorption features. Rowan and Mars (2003) evaluated SWIR data in Mountain Pass, California, and reported that the magnitude of any anomalous reflectance appears small compared to the spectral reflectance differences among the lithologic categories. Hewson et al. (2005) report on the influence of the crosstalk correction on the Broken Hill – Curnamona province of Australia. They find that the correction works well qualitatively, and mapping the Al-OH composition is possible using ((band 5 + band 7)/band 6) data. However, crosstalk correction limitations exist especially in the boundary region between high and low albedo, such as land-sea boundary and cloud edges. The residual crosstalk components prove problematic to map ferrous iron components using (band 5/band 4).

The influence of water vapor on band 9 during the atmospheric correction further complicates quantitative analysis.

Certain complicated components of the crosstalk phenomenon were revealed through validation studies using small islands and the moon. The principal component appears at positions shifted by multiples of 81 lines in the along-track direction. We find that band 4 spreads in the cross-track directions, indicating that the ghostly source image is also influenced by stray light (Iwasaki and Oyama 2005). The other components appear at positions shifted by ± 41 lines from their true positions. For bands 5 and 9, these components are notable on the band 4 side because of strong incident radiation in band 4. As for bands 6 and 7, these components also appear on the side with no adjacent band. Since there is no special structure at the middle of the linear detector arrays, such as a reflector or an electrode, the filter boundary is the cause for these error components. These results show that the crosstalk phenomenon in the present model is separated into at least two components: one stems from the band 4 detectors, and the other from the band 4 filter boundaries. Furthermore, there do exist other, yet unmodeled crosstalk components with smaller amplitudes.

5.5 Atmospheric Correction

One of the objectives of the ASTER is to provide estimates of the surface-leaving radiance by applying an atmospheric correction to the data. Atmospheric correction provides estimates of the radiation reflected at the surface, and is necessary for observing parameters that are intrinsic to the surface. Accurate atmospheric correction removes the effects of changes in satellite-sun geometry and atmospheric conditions due to aerosol scattering (Teillet 1992). Atmospherically corrected surface reflectance images improve the accuracy of surface-type classification (Fraser et al. 1977; Kaufman 1985), and are a basis for estimating the radiation budget of the Earth (Kimes and Sellers 1985). Full use of satellite data for agricultural resource management also requires atmospheric correction (Moran et al. 1990).

5.5.1 Method Description

The atmospheric correction for the VNIR and SWIR is based on a look-up-table (LUT) approach assuming that atmospheric scattering optical depths and aerosol parameters are known from outside sources as described below. A set of piecewise-linear fits is determined from the LUT using the input parameters (Slater and Jackson 1982). The satellite radiance derived from the image DN is matched to the pair of values from the LUT, and the corresponding reflectance factor is obtained by linear interpolation. LUT approaches were used successfully over water (Fraser et al. 1997; Stowe et al. 1997) and land (Fraser et al. 1992) and the approach

reduces computational requirements while avoiding the complexity of maintaining radiative transfer codes in an operational environment (Teillet 1992).

The atmospheric correction starts by computing the atmospheric transmittance using MODTRAN based on columnar amounts of absorbing gases, and the satellite radiances are divided by these transmittances. While this is a crude approach, it is sufficient for typical surface targets, and the low absorption in the ASTER bands. This gives an at-sensor radiance corrected for absorption effects, and this radiance is used along with the input parameters to determine which portion of the LUT to use.

In most cases, the values of the input parameters will not match those of the LUT. The resolution of the LUT is chosen to ensure that there is less than a 1% effect caused by the use of the table. This includes developing set cases that are sufficient in number to allow the correction to use the nearest LUT case. The molecular scattering optical depth and view angle are treated in this fashion. Unfortunately, it is computationally expensive to generate the large number of runs needed to keep differences to <1% for all parameters, and this requires a linear interpolation of the LUT cases. The solar zenith and aerosol scattering optical depth are also treated in this manner. The radiative transfer code used to calculate the LUT radiances is a Gauss–Seidel iteration code that assumes the earth is flat with a homogeneous, Lambertian surface, and a plane-parallel, homogeneous atmosphere divided into optically thin layers (Herman and Browning 1965). The input parameters for the radiative transfer code include solar zenith angle, surface reflectance, and desired view angle. Other inputs include molecular and aerosol scattering optical depths, aerosol index of refraction, and aerosol size distribution.

5.5.2 LUT Resolution

The goal of selecting parameters to generate the LUT is to develop the smallest possible table while producing accurate results. The access time for the LUT does not strongly depend on the size of the table because the results are stored in a relational database, but a smaller table requires less time to generate. We studied the sensitivity of the Top-of-the-Atmosphere (TOA) radiances to LUT parameters to determine the resolution of input parameters. They were required to generate a table where changes in the input parameters cause a <1% change in at-sensor radiance.

The study showed that only two wavelengths are required to generate the LUT, one for the VNIR (band 2) and one for the SWIR (band 5). One wavelength-related effect is the scattering phase function and the other is related to aerosol absorption (single scatter albedo). The error in phase function caused by assuming a constant wavelength is small when compared to uncertainties in the phase function. These are caused by uncertainties in the size distribution and index of refraction, and using the appropriate single scatter albedo negates the need for using the correct wavelength.

Figure 5.14 illustrates the percent difference in scattering phase function. Similar studies of other parameters lead to the intervals of the LUT that are selected.

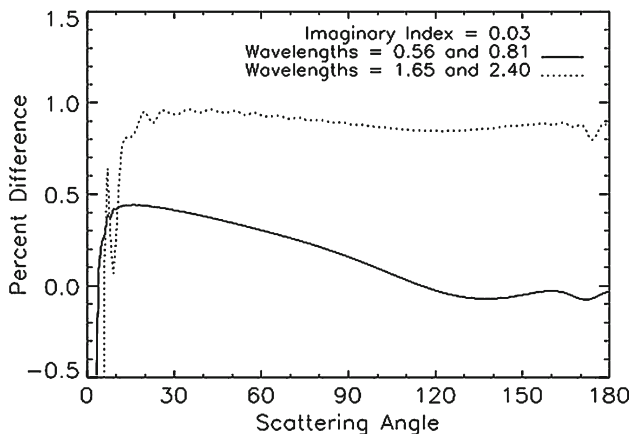


Fig. 5.14 Percent difference in scattering phase function at 0.56 μm and 1.65 μm wavelengths, which correspond to Bands 1 and 4, respectively

The interval for the view nadir angle is selected at 1° intervals from 0 to 9° for the SWIR band, and 0 to 24° at 1° intervals for the VNIR band. The view azimuth is selected relative to the solar azimuth between values of 0 and 180° at 15° intervals for reflectances larger than 0.1 and an interval of 7.5° was selected for reflectances of 0.0 and 0.1 . The solar zenith must vary <0.01 in the cosine of the solar zenith to ensure that the percent change in at-sensor radiance is $<1\%$ for a nearest-case method, so the current approach in the LUT uses interpolation techniques to account for changes in solar zenith based on 15 values for solar zenith angles ranging from 0 to 72.5° at 0.05 intervals in cosine. Aerosol optical depth results are highly dependent on the surface reflectance, where an interval of 0.15 in optical depth with interpolation produces differences of $<0.3\%$. The maximum value for the aerosol optical depth is 0.9 because the use of an operational code for such high turbidity cases is not recommended. The 0.15 optical depth interval covers the entire range of expected molecular optical depths for ASTER, thus a nearest-case approach is adopted using 13 values of molecular optical depth from 0.01 to 0.13 at 0.01 intervals for the VNIR, and 1 value of 0.002 for the SWIR bands. The final parameter is surface reflectance, and values of 0.0 , 0.1 , 0.2 , 0.3 , 0.5 , 0.7 , and 1.0 are adequate with interpolation causing $<0.2\%$ differences.

The key to this LUT approach is that it requires knowledge of the atmospheric parameters to access the appropriate part of the LUT. The fact that the ASTER instrument was not originally designed to retrieve atmospheric information complicates this requirement. Therefore, the ASTER Science Team relies on outside sources for atmospheric parameters including results from other Terra platform sensors, such as the MISR, and MODIS or other sensors such as TOMS (Total Ozone Mapping Spectrometer). The correction relies on climatological values or data derived from numerical weather prediction models when daily values from

satellite-based measurements are unavailable. The atmospheric information needed for the calculation of the atmospheric correction is at lower resolutions to that of ASTER. The same holds true for surface topographic data, where the only global digital elevation model (DEM) available for ASTER is ETOPO5 that has elevations posted approximately every 10 km (Gesch 1994). Interpolation across the ASTER scene is not done at this time until a better understanding of the spatial variability of input parameters is known.

5.5.3 Uncertainty Estimates

Table 5.9 lists the uncertainty sources for atmospheric correction. The table shows results for a low reflectance case (reflectance <0.1) and a high reflectance case (>0.1). The reason for dividing the table is that many of the uncertainties strongly depend on reflectance. These values are consistent with what is expected for such work. The total error column reports at-sensor radiance error in percentage. The overall total is the root sum of squares of all the error sources. The choice of the root sum of squares is not necessarily valid, as the sources are not independent in some cases. These tables are intended to indicate which parameters might cause problems when the atmospheric correction is implemented.

The first source of uncertainty is the sensor calibration related to the error in converting the satellite digital numbers to radiance. The absolute specification for ASTER is 4%. The LUT shows the largest expected uncertainty in computing the radiance. Also shown is the uncertainty in the scattering optical depth, which is $<1\%$ at surface reflectance >0.1 , and optical depth uncertainties of 0.05. This increases to an 8% error when the surface reflectance is <0.1 . Large uncertainties due to the aerosol size distribution are not preferred because errors from retrieving the aerosol types should cancel to some extent when applied to ASTER. The idea is that, the aerosol type selected by the MISR and MODIS algorithms best match the measured radiance distribution at the top of the atmosphere. If these aerosol

Table 5.9 List of the uncertainty sources for the atmospheric correction

| Source | Low reflectance | High reflectance |
|-----------------------------------|-----------------|------------------|
| | Error (%) | Error (%) |
| Sensor radiometric calibration | 4 | 4 |
| Scattering optical depth | 8 | 1 |
| Aerosol type | 10 | 5 |
| Surface height | 4 | 1 |
| LUT | 3 | 3 |
| Surface BRDF | 1 | 1 |
| Inherent code accuracy | 1 | 1 |
| Total error (root sum of squares) | 14 | 7 |

types are used with ASTER data, they should accurately portray the atmospheric effects allowing for good reflectance retrieval. Surface elevation is used to adjust the scattering optical depths. A 100 m uncertainty due to the surface height derived from the input DEM is assumed to produce a 4% uncertainty for low reflectance, and <0.5% for high reflectance.

Uncertainty due to surface slope is not included because it is not possible to assess this with the current RTC.

The LUT assumes a Lambertian surface because including bidirectional reflectance function (BRF) effects in the LUT make the table prohibitively large, and there is no BRF information available at the 30-m ASTER scale. The effects of this assumption were investigated with the radiative transfer code for three surface BRFs: (1) a BRF for angles within 30° of the horizon that is ten times that of the nadir value; (2) a simulated hotspot effect that is a factor of 2 greater than that for nadir; and (3) the same as for case 2 except with a smaller solar zenith angle allowing the ASTER to view the hot spot. The percent difference for all three cases is <1%, except when the sensor directly views the hotspot. One BRF effect not examined is that due to specular reflection. While the current radiative transfer code can use a non-Lambertian surface, it does not treat specular reflection correctly. The effect of specular reflection is not important for most ASTER applications.

The total uncertainty from all these factors, assuming the component uncertainties in the table, is 14% for the low reflectance case, and 7% for the high reflectance case. The corresponding error in the retrieved surface reflectance for a moderately turbid atmosphere is 30–70% at a reflectance of 0.05 (or 0.02–0.04 units in reflectance). A 7% uncertainty leads to a 7–9% uncertainty in surface reflectance at a reflectance of 0.5 (or 0.04 units in surface reflectance). These values correspond well to those found using a similar atmospheric correction applied to TM (Holm et al. 1989) and HRV (12) at a low turbidity agricultural site, and other sensors (Moran et al. 1992).

Acknowledgement The authors would like to express special thanks to Dr. Fujisada (SILC), Dr. Ono (AIT), Dr. Sakuma (AIST), Dr. Tsuchida (AIST), Dr. Iwasaki (University of Tokyo), Dr. Slater (formally worked for University of Arizona), Dr. Biggar (University of Arizona), and Dr. Keiffer (USGS) for all their help and discussions.

References

- Arai K (1988) Preliminary assessment of radiometric accuracy for MOS-1 sensors. *Int J Remote Sens* 9(1):5–12
- Arai K (1997) In-flight test site cross calibration between mission instruments onboard same platform. *Adv Space Res* 19(9):1317–1328
- Arai K, Liang X (2005) Method for the top of the atmosphere radiance estimation taking into account the polarization in down and up welling radiance calculations. *J Jap Soc Photogramm Remote Sens* 44(3):4–12
- Arai K, Thome K (2000) Error budget analysis of the reflectance based vicarious calibration for satellite-based visible to near infrared radiometers. *J Jap Soc Photogramm Remote Sens* 39(1):99–105

- Arai K, et al. (1994a) Requirements on preflight geometric calibration for ASTER
- Arai K, Fujisada H, et al. (1994b) End-to-End Data System Concept. JPL D-11199
- Barker JL, Dolan SK, Sabelhaus PA, Williams DL, Irons JR, Markham BL, Bolek JT, Scott SS, Thompson RJ, Rapp JJ, Arvidson TJ (1999) Landsat-7 mission and early results. *SPIE* 3870:299–311
- Barnes RA, Eplee RE, Patt FS, McClain CR (1999) Changes in the radiometric sensitivity of SeaWiFS determined from lunar and solar-based measurements. *Appl Opt* 38:4649–4664
- Cosnefroy H, Leroy M, Briottet X (1996) Selection and characterization of Saharan and Arabian desert sites for the calibration of optical satellite sensors. *Remote Sens Environ* 58:110–114
- Folkman MA, Sandor-Leahy SR, Thordarson S, Hedman TR, Gleichauf DA, Casement S, Quon BH, Jarecke PJ (1997) Updated results from performance characterization and calibration of the TRWIS III Hyperspectral Imager. *Proc SPIE* 3118-17:142
- Fraser RS, Bahethi OP, Al-Abbas AH (1977) The effect of the atmosphere on the classification of satellite observations to identify surface features. *Remote Sens Environ* 6:229–249
- Fraser RS, Ferrare RA, Kaufman YJ, Markham BL, Mattoo S (1992) Algorithm for atmospheric correction of aircraft and satellite imagery. *Int J Remote Sens* 13:541–557
- Fraser RS, Mattoo S, Yeh EN, McClain CR (1997) Algorithm for atmospheric and glint corrections of satellite measurements of ocean pigment. *J Geophys Res* 102:17 107–17 118
- Gellman DI, Bigyggar SF, Dinguirard MC, Henry PJ, Moran SM (1993) Review of SPOT-1 and 2 calibrations at White Sands from launch to the present. In: *Proceedings SPIE, conf. no. 1938*, pp 118–125
- Gesch DB (1994) Topographic data requirements for EOS global change research. U.S. Geological Survey
- Hagolle O, Goloub P, Deschamps P-Y, Cosnefroy H, Briottet X, Bailleul T, Nicolas J-M, Parol F, Lafrance B, Herman M (1999) Results of POLDER in-flight calibration. *IEEE Trans Geosci Remote Sens* 37:1550–1566
- Herman BM, Browning SR (1965) A numerical solution to the equation of radiative transfer. *J Atmospheric Sci* 22:559–566
- Hewson RD, Cudahy TJ, Mizuhiko S, Ueda K, Mauger AJ (2005) Seamless geological map generation using ASTER in the Broken Hill-Curnamona province of Australia. *Remote Sens Environ* 99:159–172
- Holm RG, Jackson RD, Yuan B, Moran MS, Slater PN, Biggar SF (1989) Surface reflectance factor retrieval from Thematic Mapper data. *Remote Sens Environ* 27:47–57
- Iwasaki A, Oyama E (2005) Correction of stray light and filter scratch blurring for ASTER imagery. *IEEE Trans Geosci Remote Sens* 43(12):2763–2768
- Iwasaki A, Tonooka H (2005) Validation of crosstalk correction algorithm for ASTER/SWIR. *IEEE Trans Geosci Remote Sens* 43(12):2747–2751
- Iwasaki A, Fujisada H, Akao H, Shindou O, Akagi S (2002) Enhancement of spectral separation performance for ASTER/SWIR. *Proc SPIE* 4486:42–50
- Kaufman YJ (1985) The atmospheric effect on the separability of field classes measured from satellites. *Remote Sens Environ* 18:21–34
- Kieffer HH, Widely RL (1996) Establishing the moon as a spectral radiance standard. *J Atmos Ocean Technol* 13:360–375
- Kimes DS, Sellers PJ (1985) Inferring hemispherical reflectance of the Earth's surface for global energy budgets from remotely sensed nadir or directional radiance values. *Remote Sens Environ* 18:205–223
- Liang X, Arai K (2005) Method for aerosol refractive index and size distribution with the solar direct, diffuse, aureole and polarization radiance. *J Remote Sens Soc Japan* 25(4):357–366
- Moran MS, Jackson RD, Hart GF, Slater PN, Bartell RJ, Biggar SF, Gellman DI, Santer RP (1990) Obtaining surface reflectance factors from atmospheric and view angle corrected SPOT-1 HRV data. *Remote Sens Environ* 32:203–214
- Moran MS, Jackson RD, Slater PN, Teillet PM (1992) Evaluation of simplified procedures for retrieval of land surface reflectance factors from satellite sensor output. *Remote Sens Environ* 41:169–184

- Rowan LC, Mars JC (2003) Lithologic mapping in the Mountain Pass, California area using Advanced Spaceborne Thermal Emission and Reflection Radiometer (ASTER) data. *Remote Sens Environ* 84:350–366
- Slater PN, Jackson RD (1982) Atmospheric effects on radiation reflected from soil and vegetation as measured by orbital sensors using various scanning directions. *Appl Opt* 21:3923–3931
- Stowe LL, Ignatov AM, Singh RR (1997) Development, validation, and potential enhancements to the second-generation operational aerosol product at the National Environmental Satellite, Data, and Information Service of the National Oceanic and Atmospheric Administration. *J Geophys Res* 102:16 923–16 934
- Teillet PM (1992) An algorithm for the radiometric and atmospheric correction of AVHRR data in the solar reflective. *Remote Sens Environ* 41:185–195
- Thome KJ, Nandy P (2000) Accuracy of ground-reference calibration of imaging spectroradiometers at large sensor view angles. *J Remote Sens Soc Japan* 20:112–124
- Thome K, Arai K, Hook S, Kieffer H, Lang H, Matsunaga T, Ono A, Palluconi F, Sakuma F, Slater P, Takashima T, Tonooka H, Tsuchida S, Welch R, Zalewski E (1998) ASTER preflight and in-flight calibration and validation of level 2 products. *IEEE Trans Geosci Remote Sens* 36:4

Chapter 6

ASTER TIR Radiometric Calibration and Atmospheric Correction

Hideyuki Tonooka

6.1 ASTER TIR Radiometry

6.1.1 Onboard Calibration

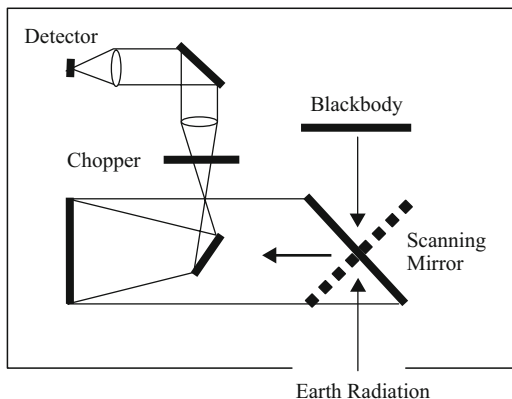
The ASTER/TIR subsystem obtains images by mechanical scanning with ten mercury–cadmium–telluride (MCT) photoconductive detectors, which are aligned along the track for each band (50 detectors in total) and cooled to 80 K using a mechanical split Stirling-cycle cooler (Fujisada et al. 1998). The TIR subsystem’s fixed gain covers the input radiance up to 370 K. Uncalibrated digital numbers (DN) observed by each detector are converted to calibrated radiance (I) using a quadratic formula:

$$I = C_0 + C_1 \times DN + C_2 \times DN^2 \quad (6.1)$$

Here, C_0 , C_1 , and C_2 are radiometric calibration coefficients (RCC). Since RCC are affected by sensor conditions (detector, optics, and electronics), they are best determined on a detector-by-detector basis in orbit. For this purpose, the TIR subsystem has a heatable honeycombed blackbody with an emissivity greater than 0.99 (Ono et al. 1996), and measures the blackbody by rotating a scanning mirror (Fig. 6.1). A blackbody measurement before each Earth observation is made at only one temperature point so that only one of the C_0 , C_1 , and C_2 calibration coefficients is determined. Such a single point measurement is made because the blackbody cannot change its temperature in a short term, and also the ASTER/TIR subsystem cannot view deep space. In reality, the C_0 coefficient of each detector is adjusted in this calibration under a blackbody temperature of 270 K called the short-term calibration (STC). On the other hand, all VNIR, SWIR, and TIR subsystems are periodically and

H. Tonooka (✉)
Department of Computer & Information Sciences, Ibaraki University,
4-12-1 Nakanarusawa-cho, Hitachi 316-8511, Japan
e-mail: tonooka@mx.ibaraki.ac.jp

Fig. 6.1 Optics of the ASTER TIR subsystem



simultaneously calibrated by the long-term calibration (LTC). As for TIR, the C_1 coefficient of each detector is obtained by each LTC in which the blackbody is measured at four temperature points of 270, 300, 320, and 340 K. In the early mission period, LTC was executed every 17 days, but the interval was changed to every 33 days in April 2001 because the sensor's degradation rate became stable.

The C_2 coefficients are fixed to preflight values, which were obtained from a ground test using a thermal-vacuum chamber, because they are sensitive to blackbody measurements at 340 K, which are less accurate in orbit than measurements at 270, 300, and 320 K.

6.1.2 Responsivity Trend

The sensor response to input radiance will usually degrade with time due to usage in space. All the ASTER TIR bands are reportedly degrading since the instrument's launch, and the ten detectors in each band show a common trend (Sakuma et al. 2002, 2005; Tonooka et al. 2003, 2005). Figure 6.2 shows the average of gain coefficients C_1 over ten detectors for each band as a function of the number of days since launch (December 18, 1999). The figure indicates how the degradation rate is band-dependent – largest in band 12 and smallest in band 10, and discontinuously changes at times (see around day-300).

Table 6.1 shows the odd-detector average, the even-detector average, and the total average of sensor response reduction between the first LTC day (March 12, 2000) and November 7, 2005, where the sensor response is defined as the reciprocal of C_1 . As shown, the degradation rate is dependent on an odd/even difference of the detector number (Tonooka et al. 2003). The sensor response reduction reaches 28% in band 12 as of November 7, 2005, while it is about 10% in band 10, and further, it is 1–2% larger in even detectors (Nos. 2, 4, 6, 8, 10) than in odd detectors (Nos. 1, 3, 5, 7, 9). We cannot explain such differences between odd and even detectors, but the observed trend is explainable by some combination of a decrease in lens transmission, mirror reflection, or detector performance (Tonooka et al. 2005).

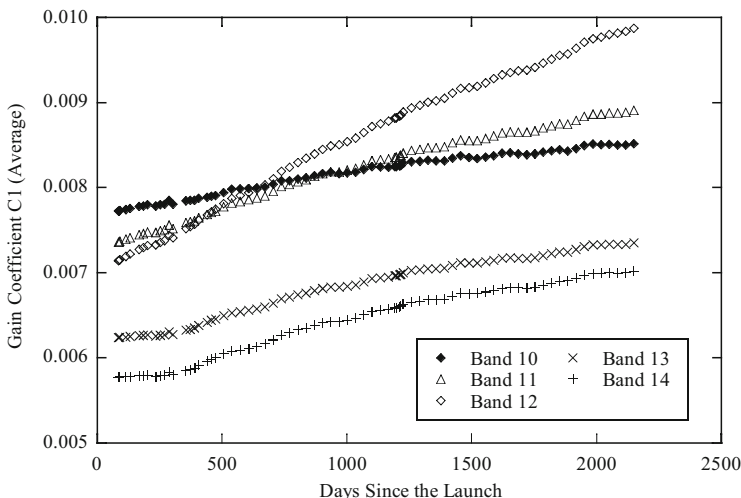


Fig. 6.2 Trend of the average of gain coefficients C_1 over ten detectors for each band

Table 6.1 Sensor response reduction (%) as of November 7, 2005

| Average | Band 10 | Band 11 | Band 12 | Band 13 | Band 14 |
|----------------|---------|---------|---------|---------|---------|
| Odd detectors | -8.3 | -16.6 | -27.1 | -14.4 | -16.8 |
| Even detectors | -10.3 | -18.1 | -28.3 | -15.8 | -18.8 |
| Total | -9.3 | -17.4 | -27.7 | -15.1 | -17.8 |

6.1.3 Radiometric Calibration for Products

Each LTC provides blackbody measurements for the four temperature points. The blackbody measurements are used to calculate the optimum C_1 coefficients by a least-squares method. However, not all LTC results are used for product generation. The RCCs used for level-1 processing are obtained from the RCC online database, which is only updated if a calibration error caused by using old RCCs exceeds 0.5 K at 300 or 320 K, or 1 K at 340 K. Thus, the C_1 coefficients used for level-1 processing are stepwise functions of time, while the C_0 coefficients for level-1 processing are adjusted before every Earth observation. Figure 6.3 displays the C_1 coefficients of band 12 obtained from LTC (ten dots on each LTC day indicate band 12's ten detectors), and also band 12's maximum and minimum C_1 coefficients included in the RCC online database (stepwise functions with RCC database versions), as a function of the day number, i.e., the days since launch (December 18, 1999). Table 6.2 gives the LTC date and its day number since launch for each of RCC version 2.x. As shown, the database was not always updated in a timely manner because of the delays in the analysis and validation of the coefficients derived from the LTC, which often causes calibration errors (Tonooka et al. 2003). In particular, the RCCs for database versions 2.05 and 2.06, applied to products observed from

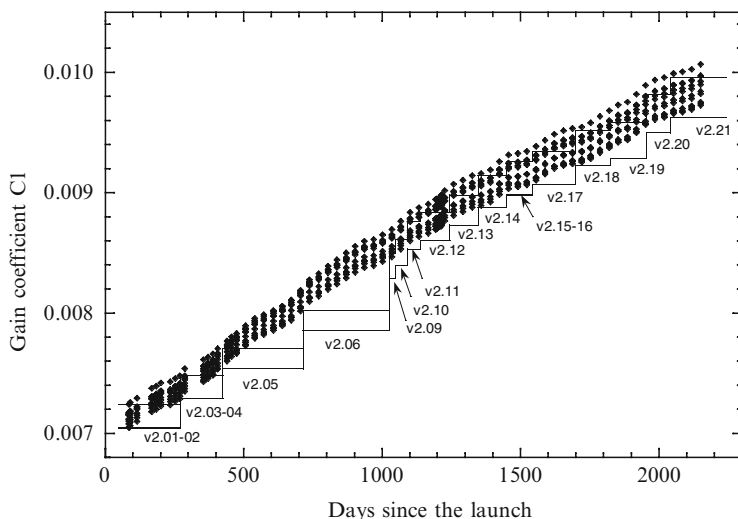


Fig. 6.3 Gain coefficients C_1 of ten detectors in band 12, which were obtained from LTC (shown by *dots*), and the maximum and minimum C_1 coefficients included in the RCC database (shown by *solid lines*). RCC database versions are also shown

Table 6.2 LTC date and its day number since the launch for each of RCC version 2.x

| RCC version | LTC date | Day number |
|-------------|------------|------------|
| 2.01–2.02 | 2000/3/12 | 85 |
| 2.03–2.04 | 2000/9/13 | 270 |
| 2.05 | 2001/1/27 | 406 |
| 2.06 | 2001/8/16 | 607 |
| 2.09 | 2002/5/7 | 871 |
| 2.1 | 2002/8/13 | 969 |
| 2.11 | 2002/11/20 | 1068 |
| 2.12 | 2002/12/23 | 1101 |
| 2.13 | 2003/4/17 | 1216 |
| 2.14 | 2003/8/4 | 1325 |
| 2.15–2.16 | 2003/11/11 | 1424 |
| 2.17 | 2004/2/18 | 1523 |
| 2.18 | 2004/6/29 | 1655 |
| 2.19 | 2004/10/6 | 1754 |
| 2.2 | 2005/3/20 | 1919 |
| 2.21 | 2005/6/27 | 2019 |

Note: Versions 2.07 and 2.08 are not used for level-1 processing

February 2001 to October 2002 (see Table 6.2), were not updated in time, which resulted in an error in the reported radiances (for example, a reported error at 320 K in band 12 reached 3 K around the end of v2.06), although these errors have been reduced for database versions 2.09 or later. To correct these errors, a

user-based recalibration method for level-1 products was developed (Tonooka et al. 2003). This method is expressed thus:

$$I_{\text{re-cal}} = (I_{\text{org}} - I_{270\text{K}}) \frac{F(D_{\text{scene}})}{F(D_{\text{LTC}})} + I_{270\text{K}} = a(D_{\text{scene}}, D_{\text{LTC}}) \times I_{\text{org}} + b(D_{\text{scene}}, D_{\text{LTC}}) \quad (6.2)$$

Here, $I_{\text{re-cal}}$ is the recalibrated radiance, I_{org} is the original radiance, $I_{270\text{K}}$ is the radiance at 270 K, D_{scene} is the day number when the scene was observed, D_{LTC} is the day number of LTC, which provides RCCs applied to the scene, and F is a fitting function of C_1 for each band, and the unit of radiance is in $\text{W}/\text{m}^2/\text{sr}/\mu\text{m}$. The coefficients a and b are recalibration coefficients, which are applied to the correction for a given scene. Figure 6.4 shows the predicted calibration error of the original radiance and the recalibrated radiance for band 12 at 320 K, as a function of the day number. The expected recalibrated radiance error is around ± 0.3 K in this case.

The C_1 coefficients for database versions 3.x applied to product generation after February 2006 were determined by regression equations for each image acquisition date (Sakuma et al. 2005). The regression equations are expressed thus:

$$C_1 = p + q \times D_{\text{scene}} \quad (\text{for } D_{\text{scene}} \leq 304)$$

$$C_1 = \frac{1}{r \times \exp(-s \times D_{\text{scene}}) + t} \quad (\text{for } D_{\text{scene}} > 304) \quad (6.3)$$

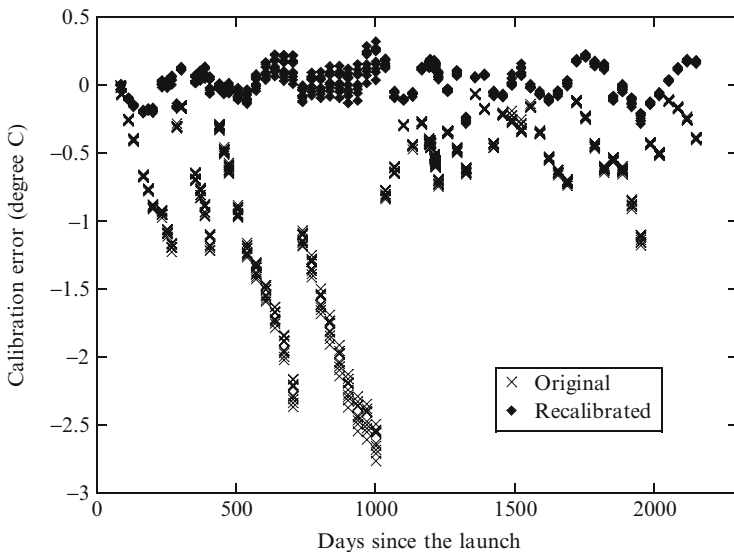


Fig. 6.4 Comparison of the predicted calibration error between the original radiance and the recalibrated radiance for band 12 at 320 K

Here p , q , r , s , and t are regression coefficients given for each detector. After April 2006, these equations were implemented for all products delivered to users, including scenes observed in the past. The RCC database versions 3.x are accurate enough (a typical error is within approximately 0.3 K), but still include some observation date-dependent errors because regressively “predicted” coefficients are applied to newly acquired data. Especially, data acquired in late June and early July 2006 contain appreciable error (0.4–0.6 K at 300–320 K temperature range for the most degrading band 12). Thus, recalibration coefficients a and b for all RCC versions (including versions 3.x) are provided by the ASTER Science Project. They are calculated on a day-by-day basis by a linear interpolation method improved from (6.2), and the recalibrated radiances are always consistent with LTC.

6.1.4 Vicarious Calibration

Vicarious calibration (VC) is an in-flight or on-orbit technique in which calibrated ground-based or airborne radiometers deployed on or above a spectrally and spatially homogeneous target take simultaneous measurements during periods of aircraft or satellite instrument overpasses (Slater et al. 1996). Instead of using VC as an alternative to the onboard calibration (OBC) in level-1 processing, the ASTER Project has used VC to validate the OBC. For the ASTER/TIR instrument, ground-based VC experiments were organized at “water sites” such as Lake Tahoe (CA/NV, USA), Salton Sea (CA, USA), and Lake Kasumigaura (Japan), and also at land sites such as Railroad Valley Playa, Lunar Lake, and Alkali Lake (NV, USA) (Tonooka et al. 2005).

Ground-based VC is performed in the TIR spectral region using either a temperature-based method or a radiance-based method (Tonooka et al. 2005). In the temperature-based method, at-sensor radiance is estimated with a radiative transfer model based on a surface kinetic temperature measured on site, surface emissivity measured on site or in a laboratory or derived from a spectral library, and atmospheric profiles measured on site or derived from other sources such as a numerical forecast system. The radiance-based method is a similar approach, but the at-sensor radiance is estimated using the surface radiance measured on site instead of surface kinetic temperature and emissivity.

Both methods are used in the VC of the TIR bands using test sites like Salton Sea, Lake Tahoe, Railroad Valley Playa, Lunar Lake (NV), Alkali Lake (NV), Cold Springs Reservoir (NV), Coyote Lake (CA), and Lake Kasumigaura. Figure 6.5 displays photos from these VC experiments. Tonooka et al. (2005) report the results from 79 experiments conducted under clear sky conditions. The results indicate the average difference between the predicted and the ASTER-measured radiances were not more than 0.5% or 0.4 K in any TIR band, demonstrating that the TIR bands have exceeded the preflight design accuracy of 1 K for an at-sensor brightness temperature range of 270–340 K. The results also indicate a responsivity decline over the first 1,400 days of the Terra mission (roughly a 20% decline in band 12 which is the most degrading band).



Fig. 6.5 Photos from VC experiments. *Upper:* multi- and single-band radiometer measurements at Salton Sea, CA (*left*), and Alkali Lake, NV (*right*). *Lower:* thermistor measurement (*left*) and radiosonde measurement (*right*) at Lake Kasumigaura, Japan

6.1.5 Stray Light

Stray light is unwanted light entering a sensor by ghosting or scattering. Tonooka (2005a) presents an inflight stray light analysis for ASTER TIR. The paper first introduces three VC experiments conducted at the smallest Cold Springs Reservoir (CSR) VC site, NV, which is a small artificial reservoir about 1.6 km long, 400–800 m wide, and 0.5–5 m deep. These experiments were conducted in the same way as those at other sites, but indicated a large discrepancy (1.5–2 K in temperature) between the ASTER image radiance and the VC predicted radiance unlike the other experiments. Stray light was determined to cause this discrepancy by analyzing the ASTER/TIR images acquired during the Terra deep-space calibration maneuver on April 14, 2003, which reveals significant ghosting around the lunar disk (Fig. 6.6). Using the lunar images, a stray-light correction algorithm based on deconvolution was established, and then applied to the ASTER images at CSR, which showed that the discrepancy between the ASTER and the VC radiance was greatly reduced. Stray-light analysis with artificially created targets indicates that a radiance change caused by stray light will reach 6–8% of a radiance contrast if the target is a square smaller than 10×10 pixels or a line narrower

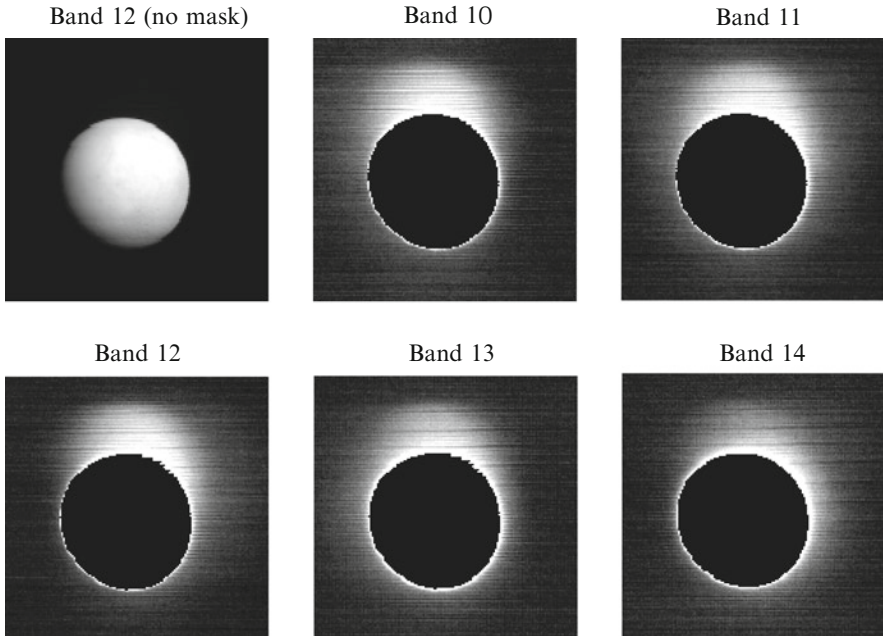


Fig. 6.6 Lunar disk images acquired in the Terra deep-space calibration maneuver on 14 April 2003. Original image of band 12 and masked images of bands 10–14

than 5 pixels, and that stray-light effects will reach about 20 pixels away from the step edge. Stray light in ASTER TIR images are probably not very large for most targets, but may introduce errors in targets with high radiance contrasts. They include, for example, small or narrow water bodies (ponds, reservoirs, lakes, rivers, etc.), water boundary areas (riverside, lakeside, seaside, etc.), and hot-spot targets (volcanoes, power plants, etc.).

6.1.6 Other Radiometric Performances

The specification of the noise-equivalent delta temperature ($NE\Delta T$) is 0.3 K at 300 K (Fujisada et al. 1998). The in-flight validation results using homogeneous targets like a lake and the sea indicate a $NE\Delta T$ predicted range from 0.1 to 0.2 K in both along-track and cross-track directions (Arai and Tonooka 2005).

The noise frequency in TIR was analyzed with images obtained from the Terra deep-space calibration maneuver on April 14, 2003 (Arai and Tonooka 2005). An area away from the lunar disk was evaluated for each detector of each band using a two-dimensional fast Fourier transform. The results demonstrated that the along-track direction does not have strong frequency components, but the cross-track

direction possesses some strong components, particularly around 85.1 kHz, probably caused by circuits on the TIR motherboard.

The specification for modulation transfer function (MTF) is 0.2 (along-track direction) and 0.25 (cross-track direction) at Nyquist frequency (NF), and 0.50 in both directions at 1/2 NF. The MTF values measured in the ground test were 0.31–0.42 at NF and 0.69–0.83 at 1/2 NF in both directions, which were better than the designed values. The MTF was also evaluated on-orbit using nine scenes, which included high-contrast natural features similar to knife edges in both directions (Arai and Tonooka 2005). The estimated MTF values were 0.22–0.27 at NF and 0.69–0.72 at 1/2 NF in both directions, which indicates that TIR meets the specification.

6.2 ASTER TIR Atmospheric Correction

6.2.1 Theoretical Basis

In the TIR region (8–14 μm in wavelength), reflected solar radiation is a much smaller component of the observed signal compared to Earth's emitted radiation (about 0.1% or less in a typical case). In addition, the atmospheric downward radiance at ground level is smaller than the surface-emitted radiance, and the surface reflectance in this spectral region is generally small. Thus, the assumption that the surface is Lambertian will not produce a large error in the TIR spectral region, and is reasonable, particularly for ASTER/TIR, which has a 60 km swath width and a maximum $\pm 8.55^\circ$ pointing angle. Hence, the at-sensor radiance under a clear sky condition is expressed thus:

$$I_\lambda(\theta) = \tau_\lambda(\theta)(\varepsilon_\lambda B_\lambda(T_s) + (1 - \varepsilon_\lambda)F_\lambda^\downarrow / \pi) + I_\lambda^\uparrow(\theta) \quad (6.4)$$

Here, λ is the wavelength, θ the view angle, ε_λ the surface emissivity, T_s the surface kinetic temperature, $B_\lambda(T_s)$ the Planck function in spectral radiance, $\tau_\lambda(\theta)$ the atmospheric spectral transmittance, $I_\lambda^\uparrow(\theta)$ the path spectral radiance, and F_λ^\downarrow the downward atmospheric spectral irradiance at ground level. Here, $\tau_\lambda(\theta)$, $I_\lambda^\uparrow(\theta)$, and F_λ^\downarrow are called atmospheric effect parameters. In practical cases, (6.4) is approximately rewritten as:

$$I_i(\theta) = \tau_i(\theta)(\varepsilon_i B_i(T_s) + (1 - \varepsilon_i)F_i^\downarrow / \pi) + I_i^\uparrow(\theta) \quad (6.5)$$

Here, each variable x_i with the subscript i is the weighted mean over λ with the normalized response function Φ_i , λ of band i :

$$x_i = \int_0^\infty \phi_{i,\lambda} x_\lambda d\lambda \quad (6.6)$$

6.2.2 Standard Atmospheric Correction for ASTER/TIR

6.2.2.1 Algorithm Overview

An atmospheric correction is essential to retrieve surface parameters because the radiance reaching the sensor is modified by atmospheric emission, attenuation, and scattering. ASTER/TIR level-1B images (registered scaled radiance at the sensor) (Fujisada 1998) are atmospherically corrected by a standard atmospheric correction algorithm (Palluconi et al. 1999) and provided as an on-demand product via the ERSDAC and LP DAAC web sites. This algorithm follows a traditional approach based on radiative transfer calculations. The atmospheric effect parameters ($tl(q)$, $\Pi\uparrow(q)$, and $Fl\downarrow$) are calculated by a radiative transfer code such as MODTRAN (Kneizys et al. 1996), combined with atmospheric profiles and elevation data, and subsequently, the at-surface radiance $I_{S,i}$ is derived from the at-sensor radiance thus:

$$I_{S,i} = (I_i(\theta) - I_i^\uparrow(\theta)) / \tau_i(\theta) \quad (6.7)$$

where $I_{S,i}$ is expressed by

$$I_{S,i} = \varepsilon_i B_i(T_S) + (1 - \varepsilon_i) F_i^\downarrow / \pi \quad (6.8)$$

ASTER TIR did not adopt the proven split-window or multichannel algorithms (McMillin 1975; Deschamps and Phulpin 1980) used to retrieve sea surface temperatures. This was largely because these algorithms need emissivity as a key input parameter for land observations. But the ASTER Project planned to produce emissivity as a standard product, and all the TIR bands are located in the clearest part of the atmospheric window in the TIR spectral region (Palluconi et al. 1999).

6.2.2.2 Implementation

The standard atmospheric correction is applied on a pixel-by-pixel basis, but a radiative transfer calculation using MODTRAN is not executed for all pixels from the point of view of processing time (Palluconi et al. 1999). First, the input data to MODTRAN are interpolated to a uniform grid across an ASTER image ($60 \times 60 \text{ km}^2$). Next, the atmospheric effect parameters for each grid point are calculated for several elevations representative of the surrounding terrain, and then those for each pixel are determined by spatial interpolation from the surrounding grid points as a function of latitude, longitude, and elevation. This procedure will not produce any significant additional error, because all the primary input data to MODTRAN, including surface elevation, are available only at a lower resolution than ASTER/TIR's 90 m pixel (the typical horizontal resolution is 1° in atmospheric profiles, and 1 km in elevation, as mentioned below) (Palluconi et al. 1999).

6.2.2.3 Input Parameters to MODTRAN

1. *Atmospheric profile:*

The atmospheric profile data input to the code should match each image in space and time. In particular, the humidity and air-temperature profiles match is important for better accuracy. The primary atmospheric sources used in ASTER/TIR atmospheric correction are described below.

The Global Data Assimilation System (GDAS) (Kalnay et al. 1990) operated by the National Centers for Environmental Prediction (NCEP) is a typical 4-D real-time analysis system, which provides a first guess to other numerical forecast systems. The GDAS assimilates various meteorological data measured by balloons, ships, planes, satellites, ground stations, etc., and predicts the subsequent atmospheric situation globally. The system produces various atmospheric parameters, such as temperature, humidity, geopotential height, and wind speed for each 3-D grid-point at 6 h intervals. In the standard atmospheric correction, air temperature, humidity, and geopotential height are extracted from GDAS products, which have 1-degree horizontal spacing and 28 vertical layers up to 2.7 hPa, and spatially/temporally interpolated profiles are then input to MODTRAN. On the other hand, the Naval Research Laboratory (NRL) climatology (Summers and Sawchuck 1993) is a model generated from observational datasets and 1-D and 2-D chemical–dynamical model results. The model includes zonally averaged atmospheric profiles for altitudes up to 120 km for 27 species (pressure, temperature, total density, H₂O mixing ratio, etc.) for each month at 10° latitudinal spacing. In the standard atmospheric correction, pressure, air temperature, and H₂O mixing ratio at each height in the observation month for each ASTER image are interpolated in latitude, and input to MODTRAN. This profile set, which is based on climatology, is used only when no other profile information is available, and an atmospherically corrected ASTER product is still needed. This method does not specifically relate to the spatio-temporal location of ASTER images, and therefore, is deemed the least accurate to atmospherically correct ASTER TIR data.

In the original plan (Palluconi et al. 1999), the MODIS atmospheric profile product (MOD07) (Menzel and Gumley 1998) was the prime option and GDAS was a backup option, but GDAS and NRL have been used as a prime and a backup options, respectively, until now, because validation of the MOD07 product has taken some time. The MOD07 remains a viable option in the future.

The other atmospheric profiles not described above are basically derived from the US standard 1976 model included in MODTRAN except for O₃, CH₄, CO, and N₂O. Although these four species are not significant for ASTER/TIR bands, the O₃ profile is modified with the total-ozone product from the Total Ozone Mapping Spectrometer (TOMS) (McPeters et al. 1998) and the profiles of CH₄, CO, and N₂O are extracted from the NRL model. Since aerosols are often not significant, the “Rural-Visibility=23 km” model with seasonal modification, included in MODTRAN, is used for all ASTER images.

2. *Elevation:*

The surface elevation for each pixel is interpolated from Global 30 Arc-Second Elevation Dataset (GTOPO30) (USGS 2004) as a function of latitude and longitude.

Since GTOPO30 is based on data derived from eight sources of elevation information, the absolute vertical accuracy of GTOPO30 varies by location according to the source data (USGS 2004). The maximum atmospheric correction error caused by an elevation error is about 0.003 K m^{-1} (Palluconi et al. 1999).

6.2.2.4 Validation

Several validation studies for the standard algorithm were made using actual ASTER data or alternative airborne sensor data. Tonooka and Palluconi (2005) have presented validation results for the standard atmospheric correction algorithm using water surfaces. In this paper, in situ lake surface temperatures measured in 13 VC experiments were first compared with surface temperatures retrieved from ASTER data. Among the results, the mean bias was 0.8 and 1.8 K for GDAS and NRL, respectively. The NRL model performed worse than GDAS for four experiments at Salton Sea (CA, USA) probably because the model was not suitable for this site, which has typically higher surface temperature and humidity than other VC sites. Next, the algorithm was validated based on the max–min difference (MMD) of water surface emissivity retrieved from each of 163 scenes acquired globally. The MMD retrieved will equal the MMD of water emissivity derived from a spectral library ($\gg 0.0076$) if the atmospheric correction has no error. Actually, MMD increased quadratically with the precipitable water vapor (PWV) content of the atmosphere as follows:

$$\text{MMD} = \begin{cases} 00164 + 000331W + 0.00247W^2 \text{ (GDAS)} \\ 00303 - 001063W + 0.00761W^2 \text{ (NRL)} \end{cases} \quad (6.9)$$

where W is PWV in centimeters. For example, the MMD retrieved was 0.049 and 0.067 for GDAS and NRL, respectively, with a PWV of 3 cm, where 0.05 on MMD roughly corresponds to -0.8 or $+2.3$ K on the retrieved surface temperature error. The algorithm performance degraded markedly when the surface temperature exceeded about 25°C , particularly for NRL. Thus, this study concludes that GDAS performs better than NRL as expected, while both will perform less well for humid conditions.

6.2.3 *Alternative Atmospheric Correction: Water Vapor Scaling Method*

6.2.3.1 Algorithm Overview

The water vapor scaling (WVS) method (Tonooka 2001, 2005b) is based on the standard atmospheric correction algorithm for ASTER/TIR, but atmospheric profiles input to MODTRAN will improve on a pixel-by-pixel basis by the

Extended Multi-Channel/Water Vapor-Dependent (EMC/WVD) algorithm (Tonooka 2000). The EMC/WVD algorithm is an improved split-window algorithm expressed thus:

$$\begin{cases} T_{g,i} = \alpha_{i0} + \sum_{k=1}^n \alpha_{ik} T_k \\ \alpha_{ik} = p_{ik} + q_{ik} W + r_{ik} W^2 (k = 0, 1, \dots, n) \end{cases} \quad (6.10)$$

Here, i is the band number, n is the number of bands, W is the rough estimate of the total water-vapor amount (g/cm^2), p , q , r are the regression coefficients for each band, T_k is the brightness temperature (K) measured by band k , and $T_{g,i}$ is the at-surface brightness temperature for band i , defined by

$$T_{g,i} = B_i^{-1}(I_{S,i}) \quad (6.11)$$

where $B_i^{-1}(\ast)$ is the inverse Planck function. In the WVS method, various errors in atmospheric profiles are aggregated as a water vapor profile error, and reduced using the water-vapor scaling factor γ , which is estimated by the EMC/WVD algorithm. The EMC/WVD algorithm is a type of split-window algorithm, and is therefore, affected by uncertainty in surface emissivity. This algorithm is hence, only applied to spectrally “gray” pixels, which are covered by materials with nearly constant emissivity close to unity, such as water, vegetation, and some soils. Thus, the WVS method involves the following tasks: (1) select gray pixels from an image; (2) estimate the γ values of gray pixels by the EMC/WVD algorithm; (3) estimate the γ values of non-gray pixels by horizontal interpolation; and (4) improve the water vapor profiles for all pixels with the γ values.

One can select gray pixels by the multiple-source approach using VNIR/SWIR images, a land cover database, and thermal log residuals (Tonooka 2005a). Once a gray pixel map is obtained, the γ value for each gray pixel is calculated thus:

$$\gamma^{\alpha_i} = \frac{\ln \left(\frac{\tau_i(\theta, \gamma_2)^{\gamma_1^{\alpha_i}} \left[\frac{B_i(T_{g,i}) - I_i^\uparrow(\theta, \gamma_1) / (1 - \tau_i(\theta, \gamma_1))}{I_i - I_i^\uparrow(\theta, \gamma_1) / (1 - \tau_i(\theta, \gamma_1))} \right]^{\gamma_1^{\alpha_i} - \gamma_2^{\alpha_i}}}{\tau_i(\theta, \gamma_1)^{\gamma_2^{\alpha_i}}} \right)}{\ln(\tau_i(\theta, \gamma_2) / \tau_i(\theta, \gamma_1))} \quad (6.12)$$

Here, θ is the view angle, γ_1 and γ_2 are the appropriate different γ values (e.g., $\gamma_1 = 1$, $\gamma_2 = 0.7$), α_i is the band model parameter (1.2790, 1.4344, 1.6544, 1.8994, and 1.8988 for bands 10–14). Once γ values for all gray pixels are obtained, they are horizontally interpolated and smoothed, so that γ values for all pixels are obtained. Thus, improved atmospheric effect parameters are calculated accordingly:

$$\tau_i(\theta, \gamma) = \tau_i(\theta, \gamma_1)^{\frac{\gamma^{\alpha_i} - \gamma_2^{\alpha_i}}{\gamma_1^{\alpha_i} - \gamma_2^{\alpha_i}}} \cdot \tau_i(\theta, \gamma_2)^{\frac{\gamma_1^{\alpha_i} - \gamma^{\alpha_i}}{\gamma_1^{\alpha_i} - \gamma_2^{\alpha_i}}} \quad (6.13)$$

$$I_i^\uparrow(\theta, \gamma) = I_i^\uparrow(\theta, \gamma_1) \cdot \frac{1 - \tau_i(\theta, \gamma)}{1 - \tau_i(\theta, \gamma_1)} \quad (6.14)$$

$$I_i^\downarrow(\gamma) = a_i + b_i I_i^\uparrow(0, \gamma) + c_i I_i^\uparrow(0, \gamma)^2 \quad (6.15)$$

Here a_i , b_i , c_i are regression coefficients, and $I_i^\uparrow(0, \gamma)$ is derived by

$$I_i^\uparrow(0, \gamma) = I_i^\uparrow(\theta, \gamma) \cdot \frac{1 - \tau_i(\theta, \gamma)^{\cos \theta}}{1 - \tau_i(\theta, \gamma)} \quad (6.16)$$

Since a water-vapor profile is band-independent, it is theoretically expected that (6.12) always produces an identical band-independent value, but the γ value is determined in each band to reduce an error induced by some factors such as incorrect atmospheric profiles (Tonooka 2005a). In actual implementation, processing time is an important factor. In the WVS method, it is reduced by an interpolation approach used in the standard atmospheric correction algorithm.

6.2.3.2 Validation

The EMC/WVD equations determined using a global simulation model (416,448 cases) and VC data (13 experiments) demonstrate a root mean square error (RMSE) from 0.61 to 0.67 K for “gray” materials like water, ice, vegetation, and some soils (Tonooka 2005a).

Tonooka (2005a) used 183 ASTER scenes observed over water bodies in various locations distributed globally, 13 VC scenes, and 3 day/night scenes from two test sites (Hawaii Island and Tokyo Bay) to validate the WVS method. The results indicate that the WVS method will allow the retrieval of more accurate surface temperature and emissivity in most conditions, while the standard algorithm will perform well in dry conditions but less well in humid conditions. In an extreme case, the lake surface temperature retrieved by the WVS method from a test scene over Lake Volta was consistent with the MODIS SST and a climate report, but the standard algorithm retrieved 8 K higher temperature. Although the standard algorithm will degrade markedly when the surface temperature exceeds about 25°C (Tonooka and Palluconi 2005), such problems are not expected in the WVS method. Accuracy in the gray pixel selection and cloud detection processes is very important, because the WVS method is degraded by errors in these processes.

References

- Arai K, Tonooka H (2005) Radiometric performance evaluation of ASTER/VNIR, SWIR and TIR. *IEEE Trans Geosci Remote Sens* 43:2725–2732

- Deschamps PY, Phulpin T (1980) Atmospheric correction of infrared measurements of sea surface temperature using channels at 3.7, 11 and 12 Mm. *Bound Layer Meteorol* 18:131–143
- ERSDAC, ASTER Ground Data System. Earth Remote Sensing Data Analysis Center. Tokyo. <http://imsweb.aster.ersdac.or.jp/>
- ERSDAC, ASTER Science Project. Earth Remote Sensing Data Analysis Center (ERSDAC). Tokyo. <http://www.science.aster.ersdac.or.jp/en/index.html>
- Fujisada H (1998) ASTER level-1 data processing algorithm. *IEEE Trans Geosci Remote Sens* 36(4):1101–1112
- Fujisada H, Sakuma F, Ono A, Kudoh M (1998) Design and preflight performance of ASTER instrument protoflight model. *IEEE Trans Geosci Remote Sens* 36:1152–1160
- Kalnay E, Kanamitsu M, Baker WE (1990) Global numerical weather prediction at the national meteorological center. *Bull Am Meteorol Soc* 71(10):1410–1428
- Kneizys FX, Abreu LW, Anderson GP, Chetwynd JH, Shettle EP, Berk A, Bernstein LS, Robertson DC, Acharya P, Rothman LS, Selby JEA, Gallery WO, Clough SA (1996) The MODTRAN 2/3 Report and LOWTRAN 7 Model. Phillips Lab., Hanscom AFB, MA, F19628-91-C-0132.
- LP DAAC, Earth Observing System Data Gateway. Land Processes Distributed Active Archive Center, Sioux Falls, SD. U.S. Geological Survey, <http://edcimswww.cr.usgs.gov/pub/ims/welcome/>
- McMillin LM (1975) Estimation of sea surface temperatures from two infrared window measurements with different absorption. *J Geophys Res* 80(36):5113–5117
- McPeters RD, Bhartia PK, Krueger AJ, Jaross JR, Torres O, Moy L, Labow G, Byerly W, Taylor SL, Swisler T, Cebula RP (1998) Earth probe Total Ozone Mapping Spectrometer (TOMS) data products user's guide. NASA, Greenbelt, MD, NASA Tech. Pub. 1998-206895.
- Menzel WP, Gumley LE (1998) MODIS atmospheric profile retrieval. Algorithm Theoretical Basis Document, Version 4, University of Wisconsin, Madison, WI
- Ono A, Sakuma F, Arai K, Yamaguchi Y, Fujisada H, Slater P, Thome K, Palluconi F, Kieffer H (1996) Preflight and in-flight calibration plan for ASTER. *J Atmos Ocean Technol* 13:321–335
- Palluconi F, Hoover G, Alley R, Nilsen MJ, Thompson T (1999) An atmospheric correction method for ASTER thermal radiometry over land. Algorithm Theoretical Basis Document, Revision 3, Jet Propulsion Laboratory, Pasadena, CA
- Sakuma F, Ono A, Kudoh M, Inada H, Akagi S, Ohmae H (2002) ASTER on-board calibration status. *Proc SPIE* 4881:407–418
- Sakuma F, Tonooka H, Ohgi N, Ono H (2005) Prediction of the radiometric calibration coefficients of ASTER/TIR. *Proc SPIE* 5978:277–284
- Slater P, Biggar SF, Thome K, Gellman DI, Spyak PR (1996) Vicarious radiometric calibrations of EOS sensors. *J Atmos Ocean Technol* 13:349–359
- Summers ME, Sawchuck W (1993) Zonally averaged trace constituent climatology. Naval Research Laboratory, Washington, DC, NRL Tech. Pub. RL/MR/7641-93-7416.
- Tonooka H (2000) Introduction of water vapor dependent coefficients to multispectral algorithms. (In Japanese). *J Remote Sens Soc Japan* 20(2):27–38
- Tonooka H (2001) An atmospheric correction algorithm for thermal infrared multispectral data over land – A water vapor scaling method. *IEEE Trans Geosci Remote Sens* 39(3):682–692
- Tonooka H (2005a) Inflight stray light analysis for ASTER thermal infrared bands. *IEEE Trans Geosci Remote Sens* 43(12):2752–2762
- Tonooka H (2005b) Accurate atmospheric correction of ASTER thermal infrared imagery using the WVS method. *IEEE Trans Geosci Remote Sens* 43(12):2778–2792
- Tonooka H, Palluconi F (2005) Validation of ASTER/TIR standard atmospheric correction using water surfaces. *IEEE Trans Geosci Remote Sens* 43(12):2769–2777
- Tonooka H, Sakuma F, Kudoh M, Iwafune K (2003) ASTER/TIR onboard calibration status and user-based recalibration. *Proc SPIE* 5234:191–201

- Tonooka H, Palluconi F, Hook S, Matsunaga T (2005) Vicarious calibration of ASTER thermal infrared bands. *IEEE Trans Geosci Remote Sens* 43:2733–2746
- USGS (2004) GTOPO30 – Global Topographic Data. U.S. Geological Survey, Sioux Falls, SD.
http://eros.usgs.gov/#/Find_Data/Products_and_Data_Available/gtopo30_info

Chapter 7

Terra and Aqua MODIS Design, Radiometry, and Geometry in Support of Land Remote Sensing

Xiaoxiong Xiong, Robert Wolfe, William Barnes, Bruce Guenther, Eric Vermote, Nazmi Saleous, and Vincent Salomonson

7.1 Introduction

The NASA Earth Observing System (EOS) mission includes the construction and launch of two nearly identical Moderate Resolution Imaging Spectroradiometer (MODIS) instruments. The MODIS proto-flight model (PFM) is onboard the EOS Terra satellite (formerly EOS AM-1) launched on December 18, 1999 and hereafter referred to as Terra MODIS. Flight model-1 (FM1) is onboard the EOS Aqua satellite (formerly EOS PM-1) launched on May 04, 2002 and referred to as Aqua MODIS. MODIS was developed based on the science community's desire to collect multiyear continuous datasets for monitoring changes in the Earth's land, oceans and atmosphere, and the human contributions to these changes. It was designed to measure discrete spectral bands, which includes many used by a number of heritage sensors, and thus extends the heritage datasets to better understand both long- and short-term changes in the global environment (Barnes and Salomonson 1993; Salomonson et al. 2002; Barnes et al. 2002). The MODIS development, launch, and operation were managed by NASA/Goddard Space Flight Center (GSFC), Greenbelt, Maryland. The sensors were designed, built, and tested by Raytheon/Santa Barbara Remote Sensing (SBRS), Goleta, California. Each MODIS instrument offers 36 spectral bands, which span the spectral region from the visible (0.41 μm) to long-wave infrared (14.4 μm). MODIS collects data at three different nadir spatial resolutions: 0.25, 0.5, and 1 km. Key design specifications, such as spectral bandwidths, typical scene radiances, required signal-to-noise ratios (SNR) or noise-equivalent temperature differences (NE Δ T), and primary applications of each MODIS spectral band are summarized in Table 7.1. These parameters were the

X. Xiong (✉)
Earth Sciences Directorate, NASA Goddard Space Flight Center,
Greenbelt, MD 20771, USA
e-mail: xiaoxiong.xiong-1@nasa.gov

Table 7.1 MODIS design specifications

| Orbit | 705 km, 10:30 AM descending node or 1:30 PM ascending node, sun-synchronous, near-polar, circular | | | |
|-------------------------------------------|---------------------------------------------------------------------------------------------------|------------------------|--------------------------------|---------------------------|
| Scan rate | 20.3 rpm, cross track | | | |
| Swath dimension | 2,330 km (cross track) by 10 km (along track at nadir) | | | |
| Telescope | 17.78 cm diameter off-axis, a focal (collimated), with intermediate held stop | | | |
| Size | 1.0 × 1.6 × 1.0 m | | | |
| Weight | 250 kg | | | |
| Power | 225 W (orbital average) | | | |
| Data rate | 11 Mbps (peak daytime) | | | |
| Quantization | 12 bits | | | |
| Spatial resolution (at nadir) | 250 m (bands 1–2) | | | |
| | 500 m (bands 3–7), 1,000 m (bands 8–36) | | | |
| Design life | 5 years | | | |
| Primary use | Band | Bandwidth ^a | Spectral radiance ^b | Required SNR ^c |
| Land/cloud/aerosols boundaries | 1 | 620–670 | 21.8 | 128 |
| | 2 | 841–876 | 24.7 | 201 |
| | 3 | 459–479 | 35.3 | 243 |
| Land/cloud/aerosols properties | 4 | 545–565 | 29 | 228 |
| | 5 | 1,230–1,250 | 5.4 | 74 |
| | 6 | 1,628–1,652 | 7.3 | 275 |
| | 7 | 2,105–2,155 | 1 | 110 |
| Ocean color/phytoplankton/biogeochemistry | 8 | 405–420 | 44.9 | 880 |
| | 9 | 438–448 | 41.9 | 838 |
| | 10 | 483–493 | 32.1 | 802 |
| | 11 | 526–536 | 27.9 | 754 |
| | 12 | 546–556 | 21 | 750 |
| | 13 | 662–672 | 9.5 | 910 |
| | 14 | 673–683 | 8.7 | 1,087 |
| | 15 | 743–753 | 10.2 | 586 |
| | 16 | 862–877 | 6.2 | 516 |

| Primary use | Band | Bandwidth ^a | Spectral radiance ^b | Required NE Δ T(K) ^d |
|---------------------------|------|------------------------|--------------------------------|----------------------------------------|
| Atmospheric water vapor | 17 | 890–920 | 10 | 167 |
| | 18 | 931–941 | 3.6 | 57 |
| | 19 | 915–965 | 15 | 250 |
| Surface/cloud temperature | 20 | 3.660–3.840 | 0.45 | 0.05 |
| | 21 | 3.929–3.989 | 2.38 | 0.2 |
| | 22 | 3.929–3.989 | 0.79 | 0.07 |
| | 23 | 4.020–4.080 | 0.17 | 0.07 |
| Atmospheric temperature | 24 | 4.433–4.498 | 0.59 | 0.25 |
| | 25 | 4.482–4.549 | 0.59 | 0.25 |
| Cirrus clouds/water vapor | 26 | 1.360–1.390 | 6 | 150 (SNR) ^e |
| | 27 | 6.535–6.895 | 1.16 | 0.25 |
| | 28 | 7.175–7.475 | 2.18 | 0.25 |
| Cloud properties | 29 | 8.400–8.700 | 9.58 | 0.05 |
| Ozone | 30 | 9.580–9.880 | 3.69 | 0.25 |
| Surface/cloud temperature | 31 | 10.780–11.280 | 9.55 | 0.05 |
| | 32 | 11.770–12.270 | 8.94 | 0.05 |
| Cloud top altitude | 33 | 13.185–13.485 | 4.52 | 0.25 |
| | 34 | 13.485–13.785 | 3.76 | 0.25 |
| | 35 | 13.785–14.085 | 3.11 | 0.25 |
| | 36 | 14.085–14.385 | 2.08 | 0.35 |

^aBands 1–19 (nm); bands 20–36 (μm)

^bW/m² sr μm

^cSNR signal-to-noise ratio

^dNE Δ T noise-equivalent temperature difference

Performance goal is 30–40% better than required

basis for the MODIS design. More details on the evolution of the NASA EOS and development of the MODIS instruments are provided in Chap. 1.

This chapter focuses on the MODIS sensor design, radiometry, and geometry as they apply to land remote sensing. With near-daily coverage of the Earth's surface, MODIS provides comprehensive measurements that enable scientists and policy makers to better understand and effectively manage the natural resources on both regional and global scales. Terra, the first large multisensor EOS satellite, is operated in a 10:30 AM (local equatorial crossing time, descending southwards) polar orbit. Aqua, the second multisensor EOS satellite is operated in a 1:30 PM (local equatorial crossing time, ascending northwards) polar orbit. With complementing morning and afternoon observations, the Terra and Aqua MODIS, together with other sensors housed on both satellites, have greatly improved our understanding of the dynamics of the global environmental system.

Following a brief description of the MODIS (Terra and Aqua) sensor design, this chapter discusses the radiometric calibration methodologies used for the Level-1B (L1B) scene radiance and reflectance retrievals, and on-orbit calibration and characterization activities involving the onboard calibrators (OBCs). Also presented is the MODIS pixel geometry, calibration approach, and pointing knowledge (Sect. 7.4). Finally, an example of vicarious calibration and sensor on-orbit performance validation with a target on the Earth's surface is also presented (Sect. 7.5). Additional information on sensor design, radiometric and geometric calibration, and validation using ground targets are available in Barnes et al. (2003), Guenther et al. (1998), Xiong et al. (2002a, b, 2003a, b, 2005a), Nishihama et al. (1997), Wolfe et al. (1998), Hook et al. (2006), Thome et al. (2003), Wan et al. (2004), Minnett et al. (2004), and Franz et al. (2005).

7.2 MODIS Sensor Design

7.2.1 MODIS Optics

MODIS is a whiskbroom scanning radiometer using a double-sided paddle wheel scan mirror that rotates at 20.3 rpm. Figure 7.1 depicts the MODIS scan cavity with its key components and subsystems including the OBCs. The scan mirror consists of a polished, nickel-plated beryllium substrate, coated with high purity silver, which is over-coated with a proprietary silicon monoxide/silicon dioxide mixture. In each scan (1.478 s), mirror side 1 or mirror side 2 collects Earth view (EV) data over a $\pm 55^\circ$ field-of-view (FOV) centered on instrument nadir, which produces a 10 km wide swath (at nadir) in the along-track direction by 2,330 km long in the cross-track direction. As shown in Fig. 7.1, the EV radiant flux is reflected from the scan mirror to a fold mirror and then through an off-axis telescope consisting of a primary and secondary mirror. The aft optics includes a dichroic beam splitter assembly that has three beam splitters, four objective assemblies, fold mirrors, and blocking and spectral band-pass filters. The combined effect of the optical components, from

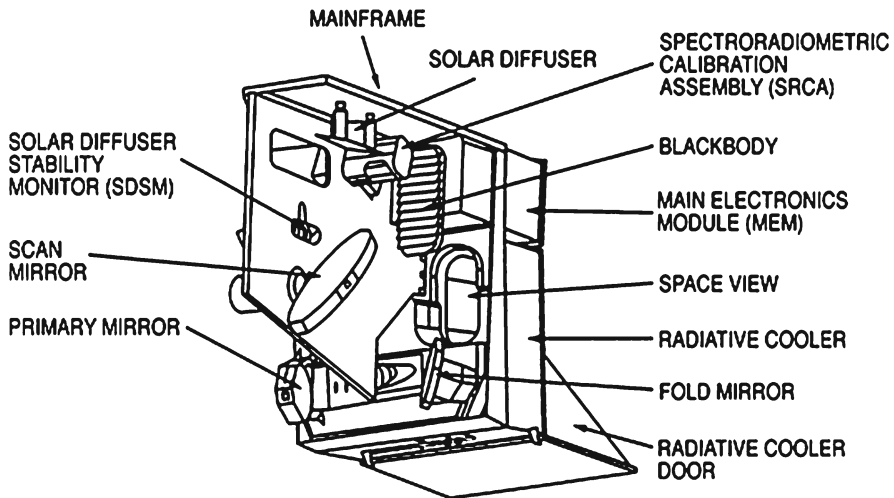


Fig. 7.1 MODIS scan cavity and onboard calibrators

scan mirror through detectors, on the sensor's spectral response was characterized at prelaunch by measuring the system-level relative spectral responses (RSRs). Other MODIS optical subsystems include the OBCs (Sect. 7.2.3).

7.2.2 Focal Plane Assemblies

The 36 spectral bands, with a total of 490 detectors, are located on four focal plane assemblies (FPAs) as shown in Fig. 7.2. The spectral bands are distributed on the visible (VIS), near infrared (NIR), short- and mid-wave infrared (SMIR), and long-wave infrared (LWIR) FPAs. Bands with smaller instantaneous fields of view (IFOV) are located near the FPA centers. The SMIR and LWIR FPAs are temperature-controlled by a radiative cooler to 83 K (both sensors). The VIS and NIR FPAs are at-sensor ambient. Bands 1–2 are the 0.25 km resolution bands with 40 detectors each. Bands 3–7 are the 0.50 km resolution bands with 20 detectors each. The remaining bands (8–36), with ten detectors each, collect data at 1 km spatial resolution. Detectors in each spectral band are aligned in the along-track direction. Bands 13 and 14 each use a pair of detector arrays to observe at high and low gains via time-delay and integration (TDI). For each 1 km resolution data sample in bands 8–36, detectors in the 0.50 km resolution bands (3–7) and in the 0.25 km resolution bands (1–2) collect two and four subsamples, respectively. MODIS bands 1–19 and 26, with wavelengths from 0.41 to 2.2 μm , are reflective solar bands (RSBs). They are located on the un-cooled FPAs, except for the SWIR bands (5–7 and 26) that are co-located with the MWIR bands (20–25) on the SMIR FPA.

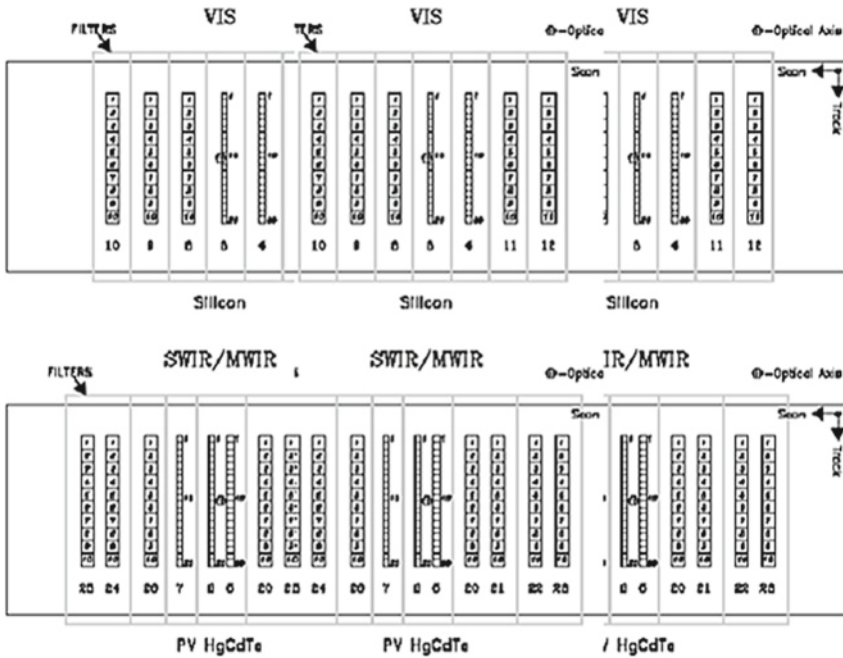


Fig. 7.2 MODIS focal plane assemblies (FPAs)

MODIS bands 20–25 and 27–36, with wavelengths from 3.5 to 14.4 μm , are thermal emissive bands (TEBs) and are located on the cold FPAs.

7.2.3 Onboard Calibrators

MODIS has one of the most comprehensive sets of OBCs ever flown on a remote sensing instrument. As shown in Fig. 7.3, the MODIS OBCs include a solar diffuser (SD), a solar diffuser stability monitor (SDSM), a blackbody (BB), and a spectroradiometric calibration assembly (SRCA). In addition, the sensor’s deep space view (SV) through the instrument’s SV port provides a zero signal reference. The MODIS OBCs are operated either continuously or periodically as required for the sensors’ on-orbit calibration and characterization. The SD/SDSM system is used to calibrate the RSBs and the BB is used to calibrate the TEBs. The SRCA normally tracks the sensor’s spatial and spectral stability (Barnes et al. 2005; Xiong et al. 2005b).

The MODIS SD panel, comprised of space-grade spectralon, is a near-Lambertian diffuser. Its bidirectional reflectance factor (BRF) was characterized at prelaunch by the sensor vendor with reference diffuser samples traceable to the National Institute of Standards and Technology (NIST) reflectance standards. A retractable

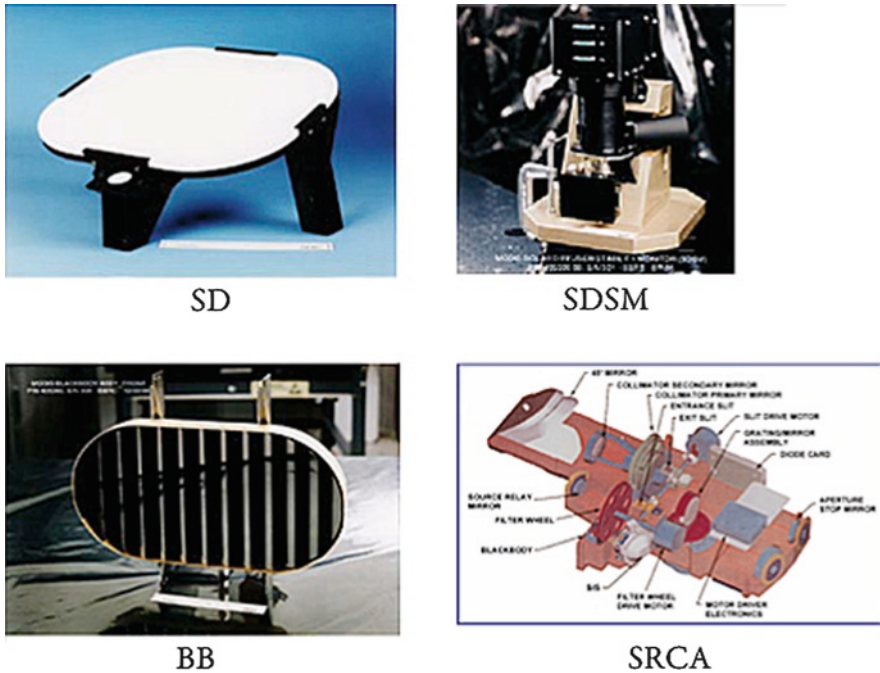


Fig. 7.3 Pictures of MODIS onboard calibrators: solar diffuser (SD), solar diffuser stability monitor (SDSM), blackbody (BB), and spectroradiometric calibration assembly (SRCA)

transmissive solar diffuser screen (SDS) is also part of the SD calibration subsystem and is used to calibrate the MODIS high-gain RSBs, whose responses saturate when exposed to direct solar illumination. Typically, a full RSB calibration consists of two sets of SD observations: one with the SDS and another without. To prevent excessive direct solar exposure of the SD panel, the solar diffuser aperture door is closed between calibration events.

The SDSM is normally scheduled to operate during SD observations. It functions as a passive ratioing radiometer. It has nine filtered detectors embedded in a mini solar integrating sphere that cover wavelengths from 0.41 to 0.94 μm . The SDSM is designed to track the SD BRF on-orbit degradation with alternate observations of direct sunlight and sunlight diffusely reflected from the SD panel. To match the SDSM Sun view and SD view-responses, a fixed attenuation screen with a nominal 1.44% transmission is mounted at the SDSM Sun view port. This approach eliminates any potential impact on SD degradation monitoring due to SDSM detector's nonlinearity. A rotating prism inside the SDSM assembly is controlled via a stepping motor to direct the Sun view, SD view, and a dark background view into the SDSM solar integrating sphere. The time-series of the ratios of SD view to Sun view, both with background subtracted, determines SD degradation. It bears pointing out that the SDSM views only part of the SD surface. The footprints

on the SD from different detectors of each spectral band (aligned along-track) do not completely overlap. But the same detectors from different spectral bands can have the same footprint on the SD surface. The SD surface uniformity was characterized at prelaunch and validated on-orbit, meeting calibration requirements. Its on-orbit degradation is measured by the SDSM and removed from the SD calibration.

The MODIS onboard calibrator blackbody (OBC BB) serves as a known source for the TEBs, which is a v-grooved panel with a near 1.0 emissivity when viewed via the MODIS scan mirror. The OBC BB was characterized at prelaunch against a high-quality laboratory blackbody calibration source (BCS). The blackbody temperature is measured by a set of 12 thermistors embedded in the substrate of the BB panel. The temperature conversion coefficients of these thermistors were characterized at prelaunch with traceability to a NIST temperature scale. On-orbit, the BB is operable from an instrument ambient of about 270–315 K via a heater attached to its back. The accuracy of the thermistors is better than 0.05 K. Since launch, the nominal temperature settings of the OBC BB have been 290 K for Terra MODIS and 285 K for Aqua MODIS. These settings were used extensively during the sensors' pre-launch calibration and characterization. The space view (SV) is a hole in the MODIS scan cavity wall through one of the electronics modules. The OBC BB and SV comprise an in-flight two-point calibration system for the MODIS TEB. On a regular basis, the OBC BB is cycled between instrument ambient and 315 K, providing datasets useful to determine the sensor's TEB nonlinear calibration coefficients.

The MODIS SRCA is a complex and unique optical instrument. It includes its own sources, a grating monochromator/optical relay system, and a collimator. The SRCA is configured and operated in three modes: radiometric, spatial, and spectral. To the best of our knowledge, SRCA remains one of the first such devices used in a global Earth-observing sensor.

The MODIS SRCA optical sources include a spherical integration source (SIS) with four 10 W lamps and two 1 W lamps, and a thermal IR source. The grating monochromator is used in the SRCA's spectral, which is configured as an optical relay system by replacing the grating with a plain mirror when the SRCA is operated in spatial mode. A didymium filter, with stable and well-calibrated spectral peaks (thus wavelength references), and a pair of silicon photodiodes (SiPD), one for calibration and one for reference, are used for SRCA spectral characterization. This wavelength self-calibration capability has made the MODIS SRCA extremely useful in tracking the sensors' on-orbit spectral stability. For SRCA spatial characterization, two reticles with different shapes are used: one for along-scan and the other for along-track. The collimator and MODIS optics image the reticles onto the FPAs for band-to-band registration measurements. The SRCA's radiometric, spatial, and spectral parameters were characterized at pre-launch by operating the SRCA in concert with ground-based calibration and characterization systems with higher accuracy and resolution. The spatial characterization applies to all 36 bands, while spectral characterization only applies to the VIS and NIR bands due to the SRCA calibration source and monochromator grating order limitations.

7.3 Radiometric Calibration

A multitude of science data products are generated using MODIS observations. The quality of these products strongly depends on the sensors' radiometric calibration accuracy and stability. The specified calibration uncertainty at typical scene radiances for the solar reflective bands is $\pm 2\%$ in reflectance and $\pm 5\%$ in radiance. The specified calibration uncertainty at typical scene radiances for most of the TEBs is $\pm 1\%$. Exceptions are the requirements of $\pm 0.5\%$ uncertainty for the two sea-surface temperature (SST) bands at 11 and 12 μm and $\pm 10\%$ for the low gain fire detection band at 4.0 μm . The uncertainty requirements specified above are also limited to scene-viewing angles within a $\pm 45^\circ$ range (relative to instrument nadir). For non-typical radiance levels or at viewing angles outside the $\pm 45^\circ$ range, an additional 1% is added to the calibration uncertainty requirements (GSFC 1993).

Given the stringent requirements on calibration uncertainty and data product quality, both Terra and Aqua MODIS went through extensive prelaunch calibration and characterization activities including radiometric, spatial, and spectral measurements of all bands at the sensor system level. After launch, each instrument was calibrated frequently using its OBCs. At each scan, the sensor views the OBCs and the Earth view (EV) consecutively, collecting 50 (SD), 10 (SRCA), 50 (BB), 50 (SV), and 1,354 (EV) data samples from each 1 km resolution detector. Data samples from 0.5 and 0.25 km resolution detectors are doubled and quadrupled, respectively. Calibration coefficients derived from the OBCs are used in the MODIS level-1B (L1B) algorithms to convert the sensors' digital responses to EV top-of-the-atmosphere (TOA) reflectance factors for the RSB and in-band spectral radiances for both the RSB and TEB. MODIS L1B algorithms are developed and maintained by the MODIS Characterization Support Team (MCST) with inputs from the MODIS Science Team (MST), the sensor vendor (SBRS), and NASA calibration scientists (Isaacman et al. 2003).

7.3.1 Reflective Solar Band Calibration

The MODIS RSBs are calibrated on-orbit by the SD and SDSM system using a simple linear algorithm. For a given detector sample, the EV TOA reflectance factor is determined from its response to the EV scene and the calibration coefficient derived from its response to the SD (Xiong et al. 2002a, 2003a). Thus, the reflectance factor is given by:

$$\rho_{EV} \cos(\theta_{EV}) = m_1 \cdot dn_{EV}^* \cdot d_{ES_EV}^2 \quad (7.1)$$

where $\rho_{EV} \cos(\theta_{EV})$ is the EV reflectance factor at a solar zenith angle of θ_{EV} , m_1 is the SD calibration coefficient, and dn_{EV}^* is the detector's digital response to the EV scene with dark background (deep space view) subtracted, and system-level

response versus scan angle (RVS) and temperature dependency corrected. The d_{ES_EV} term (in AU) is the Earth–Sun distance at the time of the EV observation. Applying (7.1) to the SD observations (replacing the EV subscript with SD), the calibration coefficient m_1 is determined from the same detector’s response to solar illumination reflected from the SD panel (Xiong et al. 2002a, 2003a):

$$m_1 = \frac{\rho_{SD} \cos(\theta_{SD})}{dn_{SD}^* \cdot d_{ES_SD}^2} \Gamma_{SDS} \cdot \Delta_{SD} \quad (7.2)$$

where ρ_{SD} is the SD BRF characterized prelaunch. Two additional factors in (7.2) are the SD on-orbit degradation factor, Δ_{SD} , and the SDS vignetting (or transmission) function, Γ_{SDS} . The SD degradation is determined using SDSM data collected during each SD calibration. $\Gamma_{SDS} = 1$ when no SDS is used in the SD calibration. As described previously, the SDS is used to attenuate direct sunlight impinging onto the SD panel when calibrating the high gain bands (8–16). In addition to the SD calibration coefficient, m_1 , and SD degradation factor, Δ_{SD} , many other parameters are used in the L1B RSB calibration algorithm. They are either derived from prelaunch calibration datasets or from on-orbit characterization.

The primary RSB calibration source used in prelaunch calibration and characterization was the SIS-100, a 100-cm diameter spherical integrating source with traceability to NIST irradiance standards. Key radiometric calibration activities were performed at the system-level in a thermal vacuum chamber. Each detector’s response and nonlinearity were characterized using the SIS-100 at different radiance levels (i.e., lamp configurations). Instrument temperature dependency was characterized by measuring each detector’s response at three temperature plateaus (cold, nominal, and hot) in the thermal vacuum chamber. The RSB response versus scan angle was characterized using the sensor’s response to the SIS-100 at different angles of incidence. This was achieved by placing MODIS on a rotary table such that its nadir direction was in the horizontal plane. At each angle the SIS-100 was cycled through a few radiance levels selected to optimize the responses for most of the spectral bands. The MODIS RSB prelaunch calibration and characterization activities also included characterization of detector noise, polarization sensitivity, and RSR. As mentioned earlier, the SD was characterized at prelaunch (in a comparison mode) using reference diffusers traceable to NIST reflectance standards. The MODIS SDS vignetting function, Γ_{SDS} , was not characterized at prelaunch, but was derived on-orbit from SD observations (with and without the SDS in place) during spacecraft maneuvers using bands that do not saturate when the SDS is not used. To reduce measurement uncertainty, observations from different bands are used to derive the SDS vignetting function, which, in principle, is spectrally uniform.

For the SWIR bands 5–7, and 26, a thermal leak correction is applied in the L1B code for both Terra and Aqua MODIS (Xiong et al. 2004a). The correction coefficients are derived from SWIR band responses to nighttime scenes. The RSB calibration coefficients, such as m_1 and RVS, are regularly (varying from bi-weekly to monthly) updated via Look-up Tables (LUTs) that are input to the L1B code.

7.3.2 Thermal Emissive Band Calibration

The MODIS TEBs are calibrated via the L1B code using coefficients derived from the onboard blackbody (BB). MODIS TEB on-orbit calibration is performed on a scan-by-scan basis using a quadratic algorithm. This algorithm was selected based on prelaunch radiometric calibration data analyses, including linearity measurements. For a given detector, the EV TOA radiance, L_{EV} , is computed from its digital response to the EV scene, dn_{EV} (with instrument background subtracted), and the calibration coefficients derived from its response to the blackbody (Xiong et al. 2002b, 2003a). Thus the TEB spectral radiance L_{EV} is given by:

$$RVS_{EV} \cdot L_{EV} + (RVS_{SV} - RVS_{EV}) \cdot L_{SM} = a_0 + b_1 \cdot dn_{EV} + a_2 \cdot dn_{EV}^2 \quad (7.3)$$

where RVS_{EV} and RVS_{SV} are the detector's RVS at the EV and SV angle of incidence (AOI) to the scan mirror, L_{SM} is the scan mirror emitted radiance, which is difficult to completely eliminate by subtracting the background since RVS_{EV} in general, is not equal to RVS_{SV} . In this quadratic algorithm, b_1 , the dominant linear coefficient (units of radiance per digital count), is computed at each scan at a fixed BB temperature. The offset term (a_0) and nonlinear term (a_2) are updated periodically using the detector's response over a range of BB temperatures, namely the datasets from BB warm-up and cool-down cycles. The scan mirror temperature, measured via instrument telemetry data, is used to compute its thermal emission. All the spectral radiance terms used in the L1B algorithms are calculated using Planck's equation weighted over the detectors' in-band RSR.

Applying (7.3) to BB observations (by replacing the EV subscripts with BB) the TEB linear coefficient b_1 is computed at each scan by the following equation (Xiong et al. 2002b, 2003a):

$$\begin{aligned} &RVS_{BB} \cdot \epsilon_{BB} \cdot L_{BB} + (RVS_{SV} - RVS_{BB}) \cdot L_{SM} + RVS_{BB} \cdot (1 - \epsilon_{BB}) \cdot \epsilon_{CAV} \cdot L_{CAV} \\ &= a_0 + b_1 \cdot dn_{BB} + a_2 \cdot dn_{BB}^2 \end{aligned} \quad (7.4)$$

The extra term L_{CAV} in (7.4) is related to the scan cavity thermal emission reflected from the BB panel. ϵ_{BB} is the BB emissivity and ϵ_{CAV} the scan cavity emissivity. Both were determined during prelaunch characterization. Details of the MODIS TEB calibration algorithms are reported in Xiong et al. (2002b). During on-orbit operation, the BB temperature is typically set at 290 K for Terra MODIS and 285 K for Aqua MODIS. While in orbit, the scan mirror and scan cavity temperatures are approximately 268 ± 2 K for Terra MODIS and 266 ± 2 K for Aqua MODIS. Compared to the BB radiance, the contributions from the scan mirror and the scan cavity (LHS of (7.4)) are typically very small.

A laboratory BCS was used for MODIS TEB prelaunch calibration and characterization. The BCS is a large-aperture blackbody source using a buried-first bounce design with a better than 0.9999 emissivity. The OBC BB emissivity was

determined by comparing the TEB responses to the BCS and OBC BB at fixed temperatures. The BCS was operated in a thermal vacuum chamber at temperatures between 170 and 340 K during TEB radiometric calibration. The BCS temperatures were measured by thermistors that were traceable to NIST temperature scales. Another blackbody, designed to operate at extremely low temperatures, was used to provide a simulated deep space view. This BB source is called the space view source (SVS). Both the BCS and SVS were inside the thermal vacuum chamber during the sensor's system-level radiometric calibration. Operating the BCS at different temperatures provides different spectral radiance levels for all TEBs. The SVS provides the instrument's thermal background measurements. Like the RSB calibration, the TEB calibration was also performed at three instrument temperature plateaus (cold, nominal, and hot) and, additionally, at three cold focal plane assembly (CFPA) temperatures (83, 85, and 88 K). The same algorithm as expressed in (7.3), with EV subscripts replaced by BCS, was applied during TEB prelaunch calibration and characterization.

Other MODIS prelaunch calibration and characterization activities for the TEB included measurements of RVS and RSR. The setup used for TEB RVS characterization was nearly identical to that used for the RSB with the MODIS on a rotary table. The SIS used for RSB RVS measurements was replaced by the BCS for the TEB RVS measurements. Because this characterization was performed at laboratory ambient, a bench-test cooler was used to cool the SMIR and LWIR FPAs. Furthermore, a charge-subtraction technique was used to prevent the TEB detectors from saturation. Due to test difficulties, datasets collected from Terra MODIS TEB RVS measurements were not adequate for reliable RVS characterization. With improvements based on the lessons learned from Terra MODIS RVS measurements, Aqua MODIS RVS characterization was performed successfully. The National Physical Laboratory (NPL) verified the prelaunch RVS in comparison with high accuracy spectral reflectance measurements of a scan mirror witness sample. Therefore, the Terra MODIS TEB RVS at launch was constructed using parameters derived from Aqua RVS and reflectance measurements of Terra MODIS scan mirror witness samples. On-orbit, the relative RVS (mirror side 1 relative to mirror side 2) was measured with data from scanning the closed instrument nadir aperture door for both Terra and Aqua MODIS. The absolute RVS was successfully measured on-orbit for Terra MODIS with data collected during spacecraft deep space maneuvers (DSM).

Although both Terra and Aqua MODIS were built using the same design parameters, opto-mechanical components, and subsystems, there are still several noticeable differences between the two, which include the following:

1. Optical leak in Terra MODIS from 11 μm (band 31) to those bands with wavelengths greater than 11 μm (bands 32–36). This leak often referred to as the PC optical leak since the detectors used in bands 31–36 are photoconductive. The Aqua MODIS improvements were based on Terra MODIS' prelaunch characterization, which included the PC optical leak elimination. A PC optical leak correction algorithm is applied in the Terra MODIS L1B code. On-orbit

lunar observations are used to derive the correction coefficients and track their stability (Li et al. 2005).

2. The Aqua MODIS 11 and 12 μm bands (31–32) saturation temperatures were adjusted from 400 K used in Terra to 340 K. These two bands are typically used for SST and land surface temperature (LST). The reduction of the dynamic range significantly increased measurement resolution.
3. Since there was no valid prelaunch RVS characterization data for the Terra MODIS TEB, on-orbit datasets collected during Terra spacecraft DSM were used for its RVS characterization (Xiong et al. 2005d). The new TEB RVS data derived from the DSM observations are used to generate the latest Terra MODIS L1B data. The Aqua MODIS TEB RVS data used in the L1B are the prelaunch measurements.
4. Both the Terra and Aqua MODIS SWIR bands have an out-of-band (OOB) thermal leak problem coupled with electronic crosstalk. These effects are complicated and extremely difficult to eliminate, and, therefore, increase calibration uncertainty. They cause concerns not only for calibration quality but also for calibration consistency when the sensor is operated in different configurations. Given the lessons from Terra MODIS prelaunch calibration and characterization, Aqua MODIS was designed with less OOB thermal leak and electronic crosstalk in the SWIR bands, thereby improving its overall performance (Xiong et al. 2004a).

7.3.3 On-Orbit Performance

As noted previously, MODIS has 36 spectral bands, with a total of 490 detectors. The sensor's on-orbit performance, to a large extent, depends on the detectors' functionality and noise characterization. The specified requirements are evaluated in terms of SNR for the RSBs and NE Δ T for the TEBs. The higher the SNR or the lower the NE Δ T, the better the sensor performs. These two parameters are also key contributors to calibration uncertainty. Table 7.2 summarizes the MODIS (Terra and Aqua, TEB, and RSB) detectors' noise performance. It includes the specified requirements, prelaunch characterization results, and current on-orbit performance. The prelaunch noise characterization was performed using the SIS-100 for the RSBs and the BCS for the TEBs. On-orbit noise characterization was performed using the SD (with and without the SDS) and SV for the RSB, and the OBC BB and SV for the TEB. All the values are interpolated to the spectral bands' typical radiance levels in order to compare them with their specifications. Instead of showing each and every detector's performance, the results in Table 7.2 are averaged over all functional detectors within a spectral band. There are 330 RSB detectors and 160 TEB detectors. Table 7.3 summarizes the numbers of inoperable and noisy detectors identified at prelaunch and on-orbit (February 2006) for both Terra and Aqua MODIS.

Currently, there are no inoperable detectors in Terra MODIS. Prelaunch, 30 noisy detectors were identified in bands 7 (all 20 detectors) and 36 (all 10 detectors).

Table 7.2 Status of MODIS noisy detectors (RSB = SNR; TEB = NEAT)

| RSB band | Specification | Terra MODIS | | Aqua MODIS | |
|----------|---------------|-------------|------------------|------------|------------------|
| | | Prelaunch | On-orbit 2005329 | Prelaunch | On-orbit 2005066 |
| 1 | 128 | 171 | 197 | 182 | 201 |
| 2 | 201 | 418 | 486 | 447 | 507 |
| 3 | 243 | 309 | 295 | 315 | 304 |
| 4 | 228 | 309 | 309 | 309 | 313 |
| 5 | 74 | 114 | 86 | 158 | 132 |
| 6 | 275 | 386 | 321 | 386 | 246 |
| 7 | 110 | 69 | 102 | 141 | 156 |
| 8 | 880 | 902 | 770 | 977 | 912 |
| 9 | 838 | 1,147 | 1,076 | 1,389 | 1,078 |
| 10 | 802 | 1,100 | 1,032 | 1,311 | 1,038 |
| 11 | 754 | 1,152 | 1,052 | 1,282 | 990 |
| 12 | 750 | 983 | 995 | 1,183 | 995 |
| 13 | 910 | 680 | 1,009 | 1,208 | 937 |
| 14 | 1,087 | 711 | 1,046 | 1,209 | 995 |
| 15 | 586 | 754 | 918 | 1,076 | 871 |
| 16 | 516 | 713 | 832 | 945 | 828 |
| 17 | 167 | 360 | 355 | 251 | 376 |
| 18 | 57 | 92 | 94 | 88 | 92 |
| 19 | 250 | 464 | 506 | 381 | 502 |
| 26 | 150 | 212 | 255 | 224 | 294 |
| TEB band | Specification | Prelaunch | On-orbit 2006055 | Prelaunch | On-orbit 2006055 |
| 20 | 0.05 | 0.03 | 0.03 | 0.02 | 0.02 |
| 21 | 0.20 | 0.16 | 0.16 | 0.23 | 0.18 |
| 22 | 0.07 | 0.03 | 0.03 | 0.02 | 0.02 |
| 23 | 0.07 | 0.02 | 0.02 | 0.02 | 0.02 |
| 24 | 0.25 | 0.13 | 0.13 | 0.13 | 0.11 |
| 25 | 0.25 | 0.06 | 0.05 | 0.04 | 0.04 |
| 27 | 0.25 | 0.10 | 0.11 | 0.09 | 0.09 |
| 28 | 0.25 | 0.04 | 0.08 | 0.05 | 0.04 |
| 29 | 0.05 | 0.02 | 0.02 | 0.02 | 0.02 |
| 30 | 0.25 | 0.09 | 0.11 | 0.09 | 0.08 |
| 31 | 0.05 | 0.03 | 0.03 | 0.02 | 0.02 |
| 32 | 0.05 | 0.04 | 0.04 | 0.03 | 0.03 |
| 33 | 0.25 | 0.14 | 0.13 | 0.08 | 0.08 |
| 34 | 0.25 | 0.20 | 0.20 | 0.12 | 0.12 |
| 35 | 0.25 | 0.24 | 0.23 | 0.13 | 0.15 |
| 36 | 0.35 | 0.45 | 0.44 | 0.25 | 0.23 |

Some noisy detectors in Terra MODIS were only observed recently since this instrument has operated continuously for more than 6 years. Nearly all the inoperable detectors in Aqua MODIS are from band 6. This was a known problem pre-launch (the decision was made to fly “as is”). Except for band 6, there are significant

Table 7.3 MODIS inoperable and noisy detectors (as of February 24, 2006)

| Inoperable detectors | | | | |
|----------------------|-------------|----------|------------|----------|
| | Terra MODIS | | Aqua MODIS | |
| | Prelaunch | On-orbit | Prelaunch | On-orbit |
| RSB | 0 | 0 | 13 | 15 |
| TEB | 0 | 0 | 0 | 0 |
| Total | 0 | 0 | 13 | 15 |
| Noisy detectors | | | | |
| | Terra MODIS | | Aqua MODIS | |
| | Prelaunch | On-orbit | Prelaunch | On-orbit |
| RSB | 20 | 21 | 3 | 3 |
| TEB | 10 | 25 | 3 | 5 |
| Total | 30 | 46 | 6 | 8 |

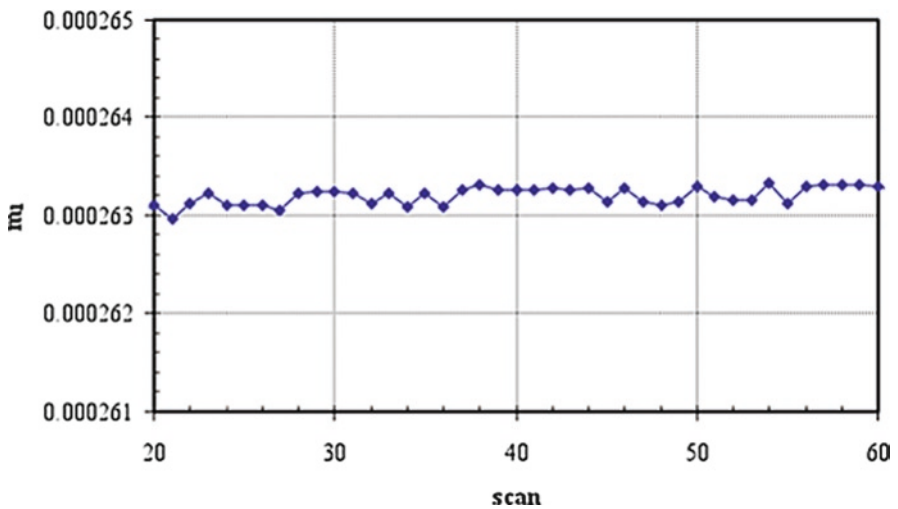


Fig. 7.4 Example of MODIS reflective solar bands scan-by-scan calibration coefficients (Aqua MODIS, band 3, middle detector, mirror side 1, subsample 1)

improvements in Aqua that have led to better overall performance than the Terra MODIS.

The MODIS RSBs are calibrated by solar illumination reflected from its onboard solar diffuser (SD). The calibration coefficients are derived using SD calibration data collected during the time when the SD is fully illuminated. A set of scan-by-scan determined calibration coefficients (m_1) using data from the SD calibration “sweet spot” is shown in Fig. 7.4 for Aqua MODIS band 3 (middle detector, subsample 1, and mirror side 1). Each point in the plot is an average over 50 frames.

The average value over all scans is used as a detector's calibration coefficient for a given calibration event. The MODIS RSB calibration is band-, detector-, subsample- (for sub-kilometer resolution bands), and mirror side-dependent. Due to the inherent stability of the RSB detectors, calibration events were scheduled weekly during the first year of operation and bi-weekly since. MODIS TEB calibration is performed continuously on a scan-by-scan basis using the OBC BB. Figure 7.5 shows an example of TEB response (b_1) short-term stability (band 31, middle detector and mirror side 1) using data from a 5-min granule. The SRCA is primarily used for sensors' on-orbit spectral and spatial characterization. Its performance in tracking RSB calibration stability remains satisfactory, providing useful information on mirror side differences and RVS angle changes.

Figures 7.6–7.9 present examples of Aqua MODIS long-term response trends using bands 8 and 3 on the VIS FPA, bands 15 and 16 on the NIR FPA, bands 22 and 25 on the SMIR FPA, and bands 31 and 34 (on the LWIR FPA). Since its launch in May 2002, Aqua MODIS uses the same electronic configuration. The response trend, normalized to the beginning of the time-series, is presented as an average over all functional detectors within each spectral band. The response trend is expressed in terms of $1/m_1$ for the reflected solar bands and $1/b_1$ for the TEBs. Noticeable response changes at the beginning of the mission are due to spacecraft safe-hold events. After 3.5 years of on-orbit operation, the largest decreases in responsivity appear in the VIS spectral region: 10.5% for band 8 at 0.41 μm , 8% for band 9 at 0.44 μm , 6% for band 3 at 0.47 μm , and less than 5% for other VIS bands (10–12). At the beginning of the Aqua mission, there were three spacecraft safe-hold events that caused MODIS to restart (reset). Ignoring the changes due to these resets, the response changes are less than 3% for all the NIR bands and less

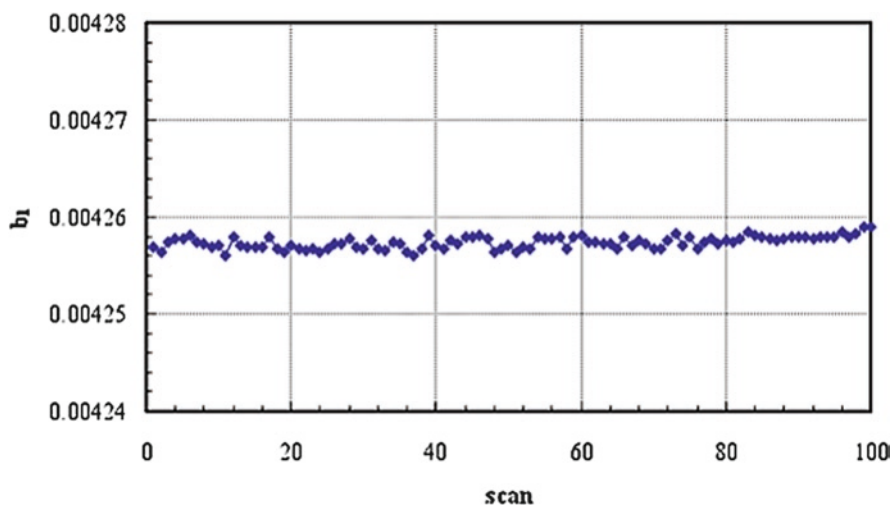


Fig. 7.5 Example of MODIS thermal emissive bands scan-by-scan calibration coefficients (Aqua MODIS, band 31, middle detector, mirror side 1)

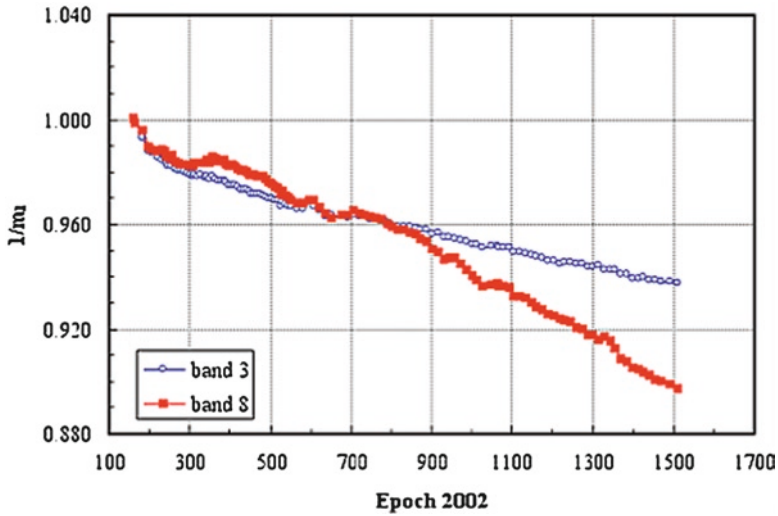


Fig. 7.6 Aqua MODIS long-term response trending for VIS spectral bands 8 and 3

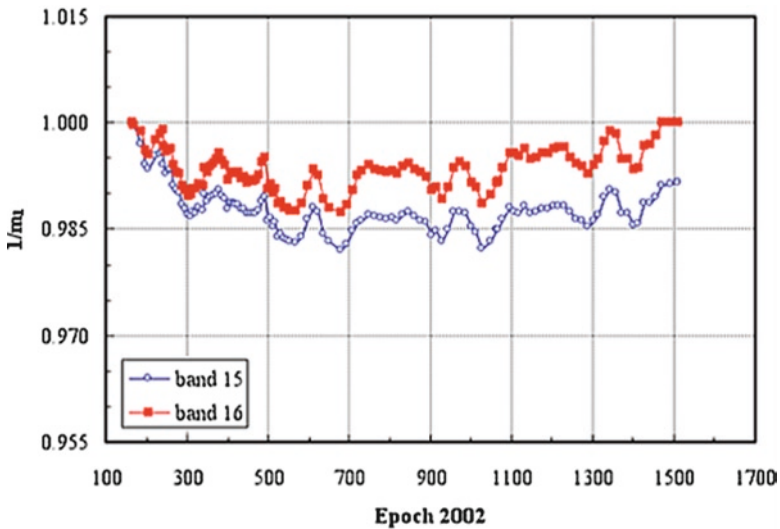


Fig. 7.7 Aqua MODIS long-term response trending for NIR spectral bands 15 and 16

than 1% for all the bands on SMIR and LWIR FPAs. The response changes include degradation in optical, detector, and electronic response. Our analysis indicates that the largest changes in the VIS spectral region are primarily due to optical degradation of the scan mirror. The scan mirror degradation has led to noticeable changes in the

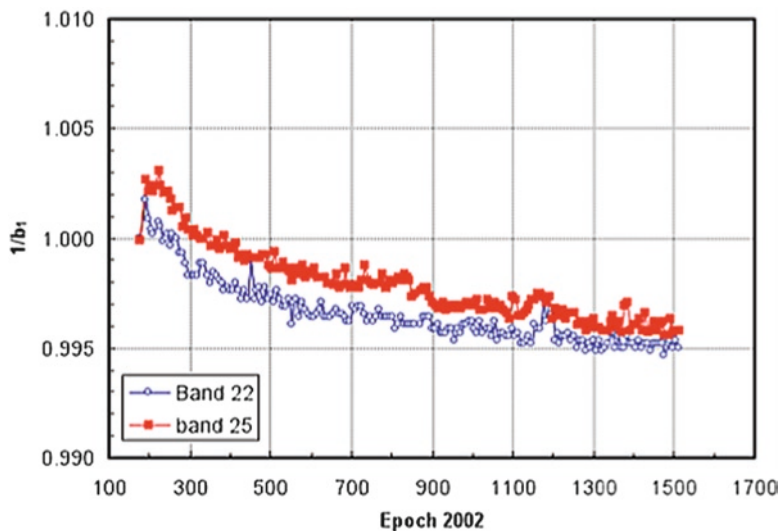


Fig. 7.8 Aqua MODIS long-term response trending for MWIR spectral bands 22 and 25

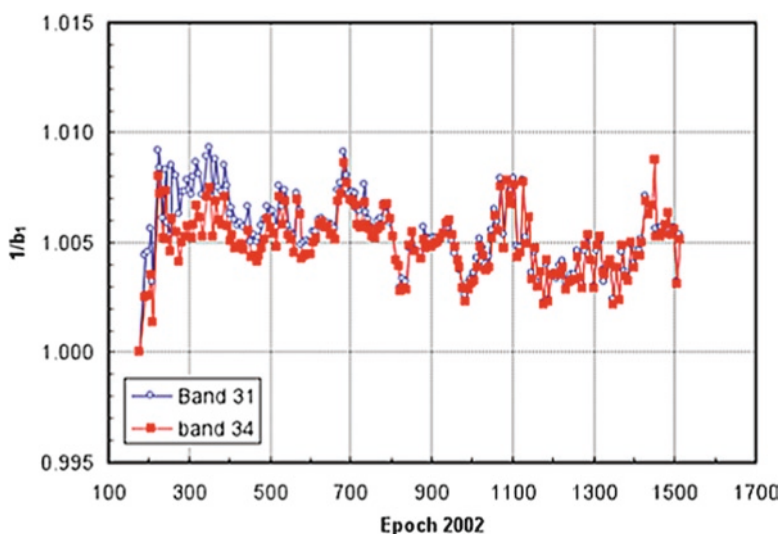


Fig. 7.9 Aqua MODIS long-term response trending for LWIR spectral bands 31 and 34

shape of the RVS for the VIS spectral bands. The RVS changes are monitored on-orbit using detector responses at different AOI (Barnes et al. 2005).

Terra MODIS remains in operation for more than 6 years. Like Aqua MODIS, the largest decreases in responsivity are also in the VIS spectral region: 28% for

band 8 at 0.41 μm , 15% for band 9 at 0.44 μm , 13% for band 3 at 0.47 μm , and less than 10% for the other VIS bands (10–12). Ignoring the differences expected due to different operational configurations, the response changes are less than 5% for all the bands on the NIR FPA and less than 2.5% for all bands on the SMIR and LWIR FPAs. For Aqua MODIS, the response differences between mirror sides 1 and 2 are less than 1% for all spectral bands. On the other hand, Terra MODIS mirror side 2 has shown much faster degradation than mirror side 1, primarily in the VIS spectral region. As of February 24, 2006, the response differences between Terra MODIS mirror sides 1 and 2 are approximately 10% for band 8 at 0.41 μm , 6% for band 9 at 0.44 μm , 4% for band 3 at 0.47 μm , and less than 2% for all other bands. Terra MODIS operation has exceeded its original design life of 5 years. Following a recent NASA Headquarters Senior Review, the Terra mission was extended for three more years with a 1-year option.

Most of the spectral bands (detectors), excluding a few inoperable and noisy detectors, in both Terra and Aqua MODIS meet their calibration uncertainty requirements. However, there are a few bands that do not meet some of the requirements. Included in this group are the Terra MODIS SWIR bands (5–7, and 26) due to large OOB thermal leaks and electronic crosstalk. Two Terra MODIS PC bands (35 and 36) have optical leaks and Aqua MODIS band 6 has lost more than half of its detectors. These bands were deemed deficient at prelaunch time. Detailed uncertainty analyses for both Terra and Aqua MODIS TEB and RSB are available in Esposito et al. (2004), Chiang et al. (2004), and Xiong et al. (2005c). In addition to the problems that existed at prelaunch, changes in some of the on-orbit measured calibration parameters have major impacts on calibration uncertainty. These include SD BRf, scan mirror reflectance, and RVS angle (Xiong et al. 2001, 2004b). These parameters are functions of time- and wavelength-dependent optics degradation, and in general, have the most impact on the RSB VIS bands. Therefore, there are a few VIS bands that met their calibration uncertainty requirements during initial on-orbit operation but slowly, as system optics changed, started to perform with uncertainties that do not meet the design requirements. Since the impacts due to optics degradation were effectively tracked and thus, corrected in the L1B, most of these bands still meet their calibration requirements. To reduce the sensor degradation effects, MODIS MCST at NASA/GSFC performs constant calibration and monitoring. Details on MODIS sensor and calibration issues, L1B algorithms, and L1B LUT updates are available on the MCST webpage: <http://www.mcst.ssai.biz/mcstweb/index.html>.

Other sensor performance issues, such as spectral and spatial characterization monitored on-orbit using the SRCA, are not discussed in this chapter. The experiences and lessons learned from MODIS instrument design, prelaunch, and especially on-orbit calibration and characterization activities (Xiong et al. 2003b) are extremely valuable. They are applied to the design, development, and testing of future remote sensing sensors, such as the Visible Infrared Imaging Radiometer Suite (VIIRS) scheduled for launch on the National Polar-orbiting Operational Environmental Satellite System (NPOESS) and the NPOESS Preparatory Project (NPP) missions.

7.4 MODIS Geometry

As noted in Sect. 7.1, but repeated here for discussion of the MODIS geometric performance, the two MODIS instruments orbit the Earth at an altitude of 705 km in near polar orbits with an inclination of 98.2° and a mean period of 98.9 min (Salomonson et al. 1989). The orbits are sun-synchronous with a 16-day repeat cycle, i.e., the orbit ground track repeats every 16 days. The daytime equatorial local crossing time is 10:30 AM (descending) for Terra and 1:30 PM (ascending) for Aqua. Periodic drag makeup and inclination adjustment maneuvers maintain the ground track and solar geometry throughout the mission's lifetime. MODIS has a 110° across-track field-of-view and senses the entire equator every 2 days with full daily global coverage above 30° latitude approximately. MODIS is a whiskbroom scanning radiometer that uses the forward motion of the satellite to provide the along-track dimension as shown in Fig. 7.10. A single scan line includes 1,354 (1 km), 2,708 (500 m), or 5,416 (250 m) observations. This section contains a summary of the MODIS instrument geometry (Nishihama et al. 1997).

MODIS detectors from different spectral bands are laid out on the focal planes in the along-scan (cross-track) direction, which allows the sampling of the same Earth location at different times by different bands (Fig. 7.10). Each 1, 0.5, and 0.25 km detector is sampled every 333.333, 166.667, and 83.333 μs , respectively. To allow for detector readout, the detector integration time is 10 μs less than the data-sampling rate at each of the three MODIS resolutions. To the first order, the MODIS point-spread function is triangular in the scan direction (Fig. 7.11). The centers of the integration areas of the first observation in each scan are aligned in a "peak-to-peak" alignment. In the track direction, the point-spread function is rectangular and the observations at the different resolutions are nested, allowing four rows of 250 m observations and two rows of 500 m observations to cover the same area as one row of 1 km observations.

Each scan of the Earth's surface is elongated because of the MODIS instrument's sensing geometry and the Earth's curvature such that the swath width is approximately 2,340 km. The mirror angular velocity (2.127 rad/s) and the forward velocity of the satellite (7.5 km/s) are configured such that at nadir, in the track direction, the leading edge of one scan abuts the trailing edge of the next scan. Adjacent scans begin to overlap away from nadir with a 10% overlap occurring at 24° scan angles from nadir. This overlap increases to almost 50% at the scan edge (Fig. 7.12). The same point on the Earth's surface is observable by up to three consecutive scans at the scan edge. This phenomenon is called the "bow-tie" effect and is seen in other whiskbroom wide-field-of-view sensors such as the Advanced Very High Resolution Radiometer (AVHRR), though this effect is less evident for scanners with only one detector per band. At the scan edge, the projection of a MODIS detector's IFOV onto the surface (also the ground sample distance and pixel size) is approximately 2.0 and 4.8 times larger than at nadir in the track and scan directions, respectively (Fig. 7.13). A small time delay occurs between the readout of the leading and trailing bands on the focal planes, which means the spacecraft moves forward by a small

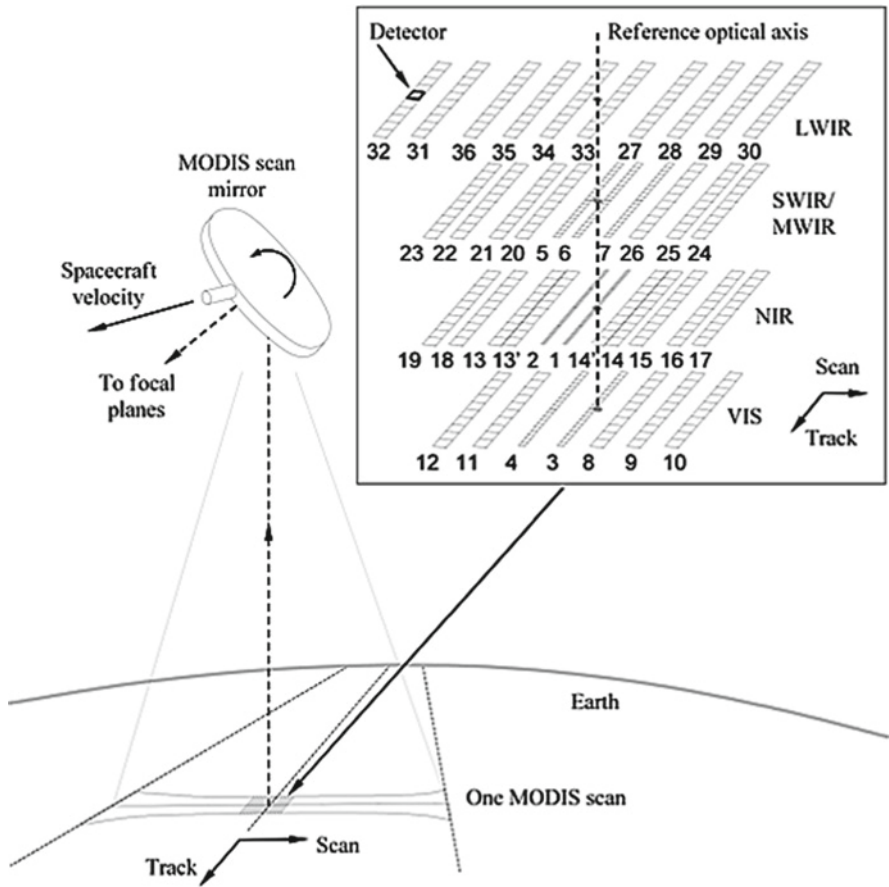


Fig. 7.10 Overview of MODIS sensing geometry. One MODIS data scan is performed over a half revolution of the MODIS double-sided scan mirror, and is focused onto four focal planes containing the 1, 0.5, and 0.25 μm bands (36 bands total). The instantaneous sensing of the four co-registered focal planes is shown, illustrating the MODIS “paddle broom” sensing geometry

amount in the time the two bands are sampled. A small constant focal plane rotation was built into the instrument to compensate for that along-track motion and minimize along-track band-to-band misregistration.

All MODIS products are generated in a hierarchy of levels: sensor data (Level-1) retrieved geophysical parameters at the same Earth location as the MODIS instrument data (Level-2), Earth-gridded geophysical parameters (Levels-2G and -3), and Earth-gridded model output (Level-4). The smallest amount of MODIS land data processed at any one time is defined at Levels-1 and -2 as a granule and corresponds to approximately 5 min of MODIS sensing and consists of 203 scans approximately. A granule covers an area approximately 2,340 km across-track by 2,030 km

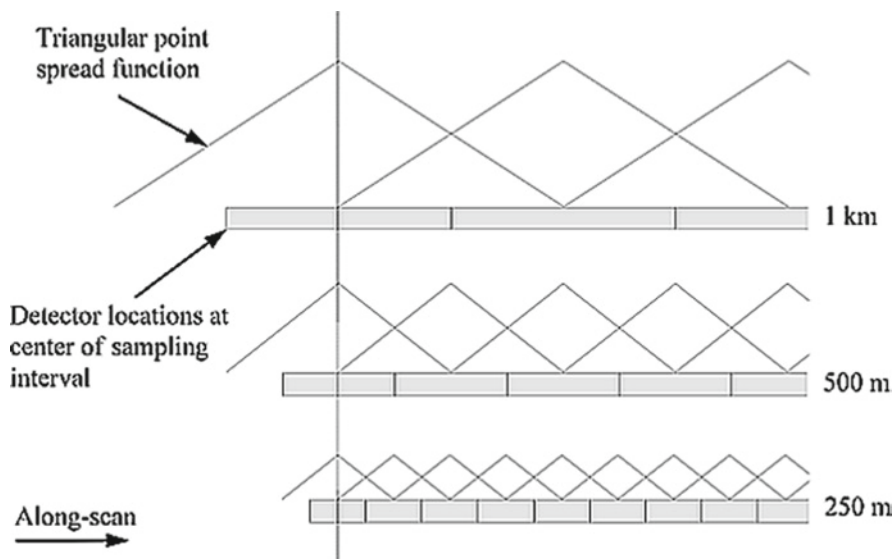


Fig. 7.11 Detector along-scan triangular point spread function and the peak-to-peak alignment of the three MODIS spatial resolutions

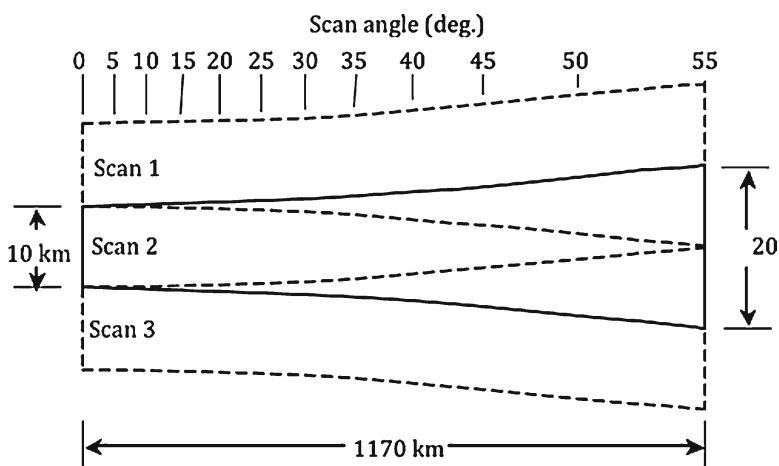


Fig. 7.12 Ground projection of the right half of three consecutive scans showing the scan geometry and the “bow-tie” effect (along-track dimension exaggerated). A solid line bounds the area sensed by Scan 2, and shows the overlap between it and two adjacent scans (dashed lines)

along-track. The MODIS geolocation product is a level-1 product and defines the geodetic latitude and longitude, terrain height, sensor zenith angle, sensor azimuth, slant range to the sensor, solar zenith angle, and solar azimuth for each 1 km

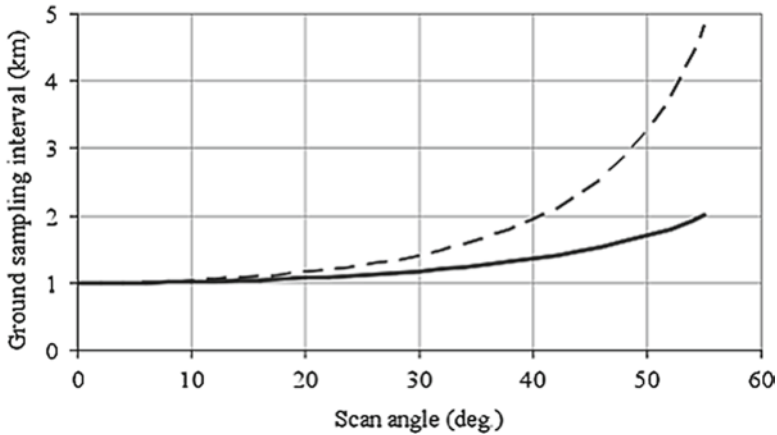


Fig. 7.13 Ground sampling interval (pixel size) in the scan (*dashed line*) and track (*solid line*) directions plotted as a function of scan angle (nadir is 0°)

MODIS observation (Nishihama et al. 1997). These geolocation data are stored in the MODIS L1B calibrated radiance products, in several MODIS level-2 products and in the MODIS land L2G products (Wolfe et al. 1998).

MODIS sensor data contain geometric distortions introduced by the instrument's sensing geometry, perturbations in the motion of the sensor relative to the Earth's surface, the curvature of the surface, and surface relief. The Terra and Aqua satellites have orientation (position and attitude) measurement systems designed to enable unaided navigation of MODIS data to within approximately 150 m (1σ) at nadir (Fleig et al. 1993). To precisely determine the intersection of each 1 km observation's line of sight with the Earth's surface, the MODIS geolocation software uses a geometric model of the instrument, the satellite motion and orientation relative to the Earth, and an Earth model that includes a digital terrain model. Prelaunch tests measured various geometric parameters of each MODIS instrument.

Analysis of MODIS/Terra geolocation was performed after launch using a global network of higher-resolution ground control points and a digital elevation model (Wolfe et al. 2002). This analysis revealed instrument-to-spacecraft alignment biases. Corrections were made to wedge angles between the two sides of the scan mirror and to the tilt of the scan mirror axis of rotation. A detailed on-orbit error analysis enabled reduction of the initially large on-orbit geolocation errors to within the science community's accuracy goals. Results from the long-term trend analysis were then used to quantify and reduce errors caused by yearly cycles and long-term trends in the MODIS data to maintain the accuracy within the goals. The long-term trend for Terra MODIS, shown in Fig. 7.14, is fitted with a combination of three models: a low-order temporal polynomial fit, a periodic (yearly) sinusoidal term, and a solar angle-dependent within-orbit term. The same approach is used for the Aqua MODIS long-term trend, although the solar angle-dependent within-orbit trend is not currently being used.

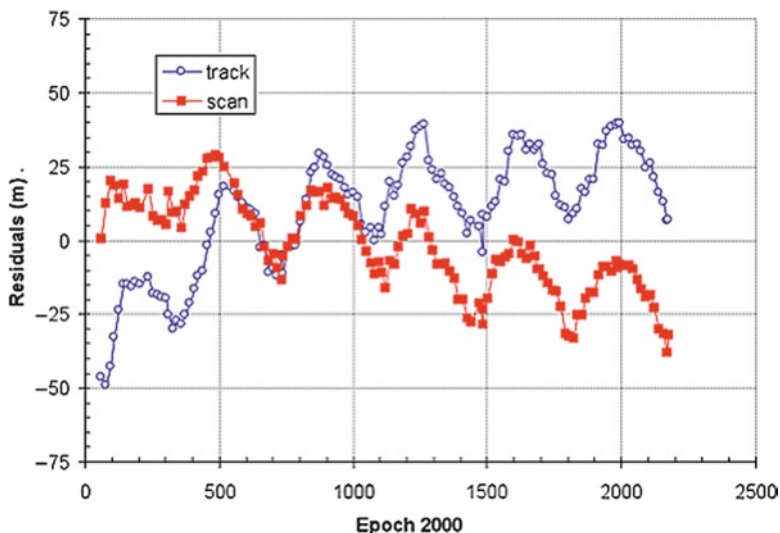


Fig. 7.14 Terra MODIS geolocation control point residuals in the track (along-track) and scan (cross-track) directions

After removing both the static errors and the dynamic long-term trend, the geolocation accuracy improved to better than 45 m for Terra MODIS and to better than 55 m for Aqua MODIS. This approach allows an operational characterization of the MODIS geolocation errors and enables geolocation of individual MODIS observations to the subpixel accuracies required for terrestrial global change applications (Townshend et al. 1992; Justice et al. 1998).

7.5 Cross-Calibration of Terra and Aqua MODIS

This section presents an approach to cross-calibrate the MODIS instruments on Terra and Aqua using a stable desert site in the visible to short-wave infrared spectral domain. The agreement is better than 1% for bands 1 (0.67 μm), 2 (0.87 μm), and 7 (2.13 μm). The selected site is a bright area of the Sahara desert, centered at 21.5° latitude and 14.4° longitude measuring roughly 20 km by 20 km.

We used approximately 2 years of Terra MODIS data from a period when the instrument configuration was stable (Julian day 307 of 2000 to Julian day 250 of 2002) and applied a rigorous cloud screening to the data based primarily on standard deviations observed in MODIS band 7. We excluded observations within 15° of the backscattering conditions to avoid the hot spot that is not taken into account in the MODIS kernel bidirectional reflectance distribution function (BRDF) models (Vermote and Roy 2002; Schaaf et al. 2002). We also excluded views with zenith angles

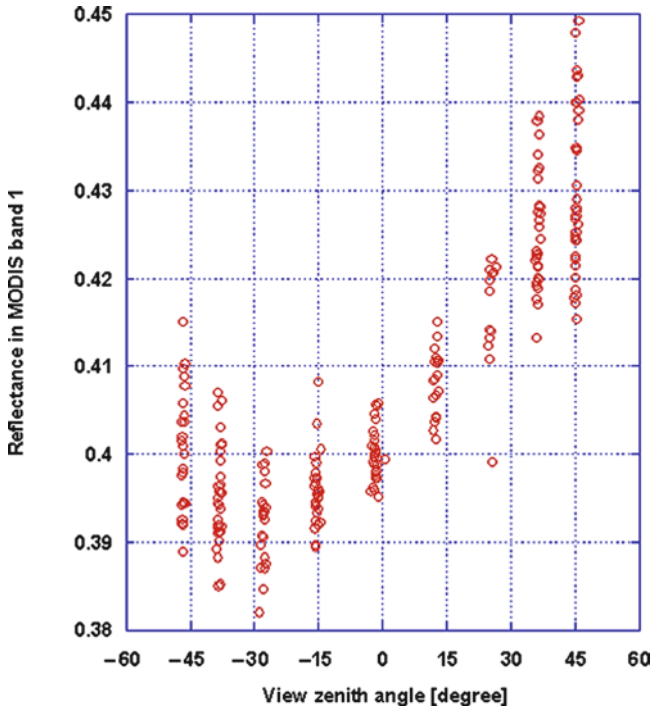


Fig. 7.15 Variation of the reflectance in Terra MODIS band 1 as a function of view-zenith angle during the 2-year period used to characterize the desert site

greater than 50° since it is difficult to extract the same area at high view-zenith angles due to variations in pixel geometry. Figure 7.15 shows the variations in reflectance from MODIS band 1 ($0.645 \mu\text{m}$) during this period as a function of view-zenith angle. We have arbitrarily chosen the sign of the view-zenith angles. If the relative azimuth is between 0° and 90° we consider the view-zenith angle as negative, and if the relative azimuth is between 90° and 180° we consider the view-zenith as positive. As evident in Fig. 7.15, the reflectance, although varying with relative azimuth and solar zenith angle for each class of view-zenith angle, shows systematic variations that are due to directional effects. These directional effects are relatively small ($\sim 20\%$) because they involve a desert surface type, especially when compared to observations over vegetation targets. But these results are important and useful for vicarious calibration.

Figure 7.16 shows the comparison between the modeled and observed reflectances using the MODIS BRDF kernel models (Schaaf et al. 2002). The generic kernels used (Isotropic, Rosstthick LiSpare-R) explain the majority of the variability in the dataset. The standard deviation between observed and modeled reflectance is 4.2×10^{-3} in reflectance units, which roughly corresponds to 1% of the observed values.

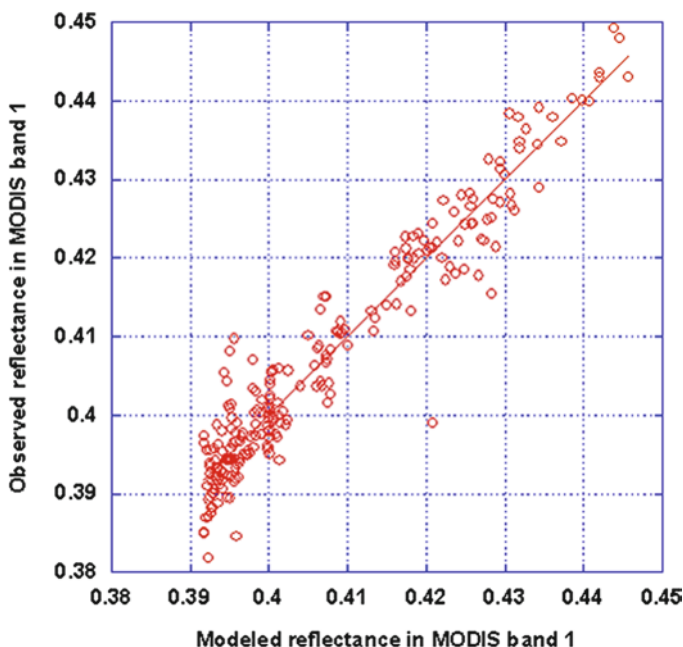


Fig. 7.16 Comparison of the modeled and the observed reflectances in band 1 using the linear kernel MODIS BRDF models

The ratio between the observed and modeled reflectances for Terra MODIS bands 1, 2, and 6 as a function of time (for the period: day 307 of 2000 to day 250 of 2002) was plotted to verify the suitability of the site for cross-calibration (Fig. 7.17a–c). The majority of the points are within $\pm 2\%$ of 1.0 (98.5% for band 1, 94.2% for band 2 and 96.9% for band 6).

Predictions were made of observable Aqua MODIS reflectances for bands 1, 2, and 7 using the Terra MODIS-derived site characterization data for the first 7 months of operation. (Too many nonfunctioning detectors in Aqua band 6 render it less useful.)

Figure 7.18a–c presents the ratios between the observed and predicted reflectances using the Terra MODIS model plotted as a function of days since January 1, 2002. It also shows the preflight to in-flight calibration ratio determined by the MCST on day 198 of 2002. For the first few days since the nadir aperture door opening (on day 180 of 2002), the ratio of predicted to observed reflectance is several percent greater than 1.0. The in-flight calibration ratio derived by MCST compares very well with the estimate of the calibration during this period (the ratios are within 1%). After day 220, the in-flight calibration derived MCST on day 198 was used to normalize the data. The ratio of (normalized) observed to predicted reflectances after day 220 is then within 1% of 1.0 for bands 1, 2, and 7 with some occasional outliers within 2%.

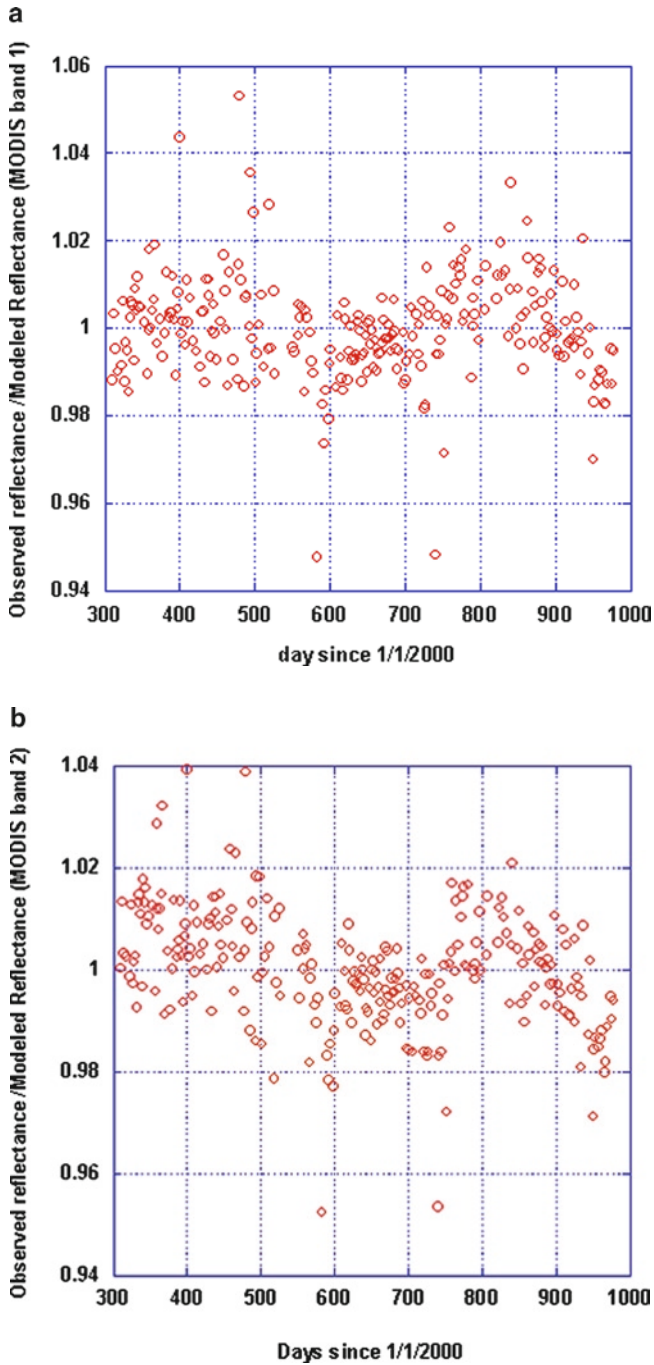


Fig. 7.17 Ratio between the observed and modeled reflectances in (a) band 1, (b) band 2, and (c) band 6 during the site characterization period (day 307 of year 2000 to day 250 of year 2002)

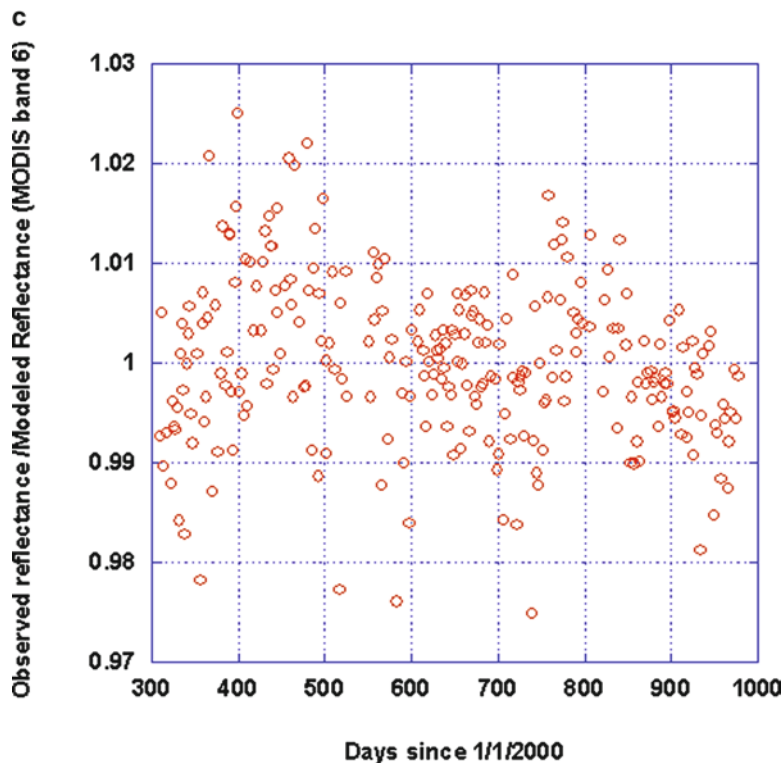


Fig. 7.17 (continued)

Therefore, the data collected over this site are definitely useful to cross-calibrate both Terra and Aqua MODIS VIS/NIR/SWIR bands. These results show that Terra and Aqua MODIS bands 1, 2, and 7 are consistently calibrated to within 1%.

7.6 Summary

This chapter provides a description of the MODIS sensor design, characterization, and applications of its OBCs. A SD and a SDSM are used for radiometric calibration of the RSBs and a blackbody (BB) for the TEBs. The MODIS L1B algorithms for RSB reflectance calibration and TEB radiance retrieval are presented. Examples derived from on-orbit observations are provided to illustrate sensor performance, including response, noise characterization, and short- and long-term stability. A global network of ground control points and a digital elevation model are used to maintain and improve geolocation accuracy for both Terra and Aqua MODIS. In addition to the OBCs, an approach using observed and modeled reflectances from stable ground targets to cross-calibrate the Terra and Aqua MODIS

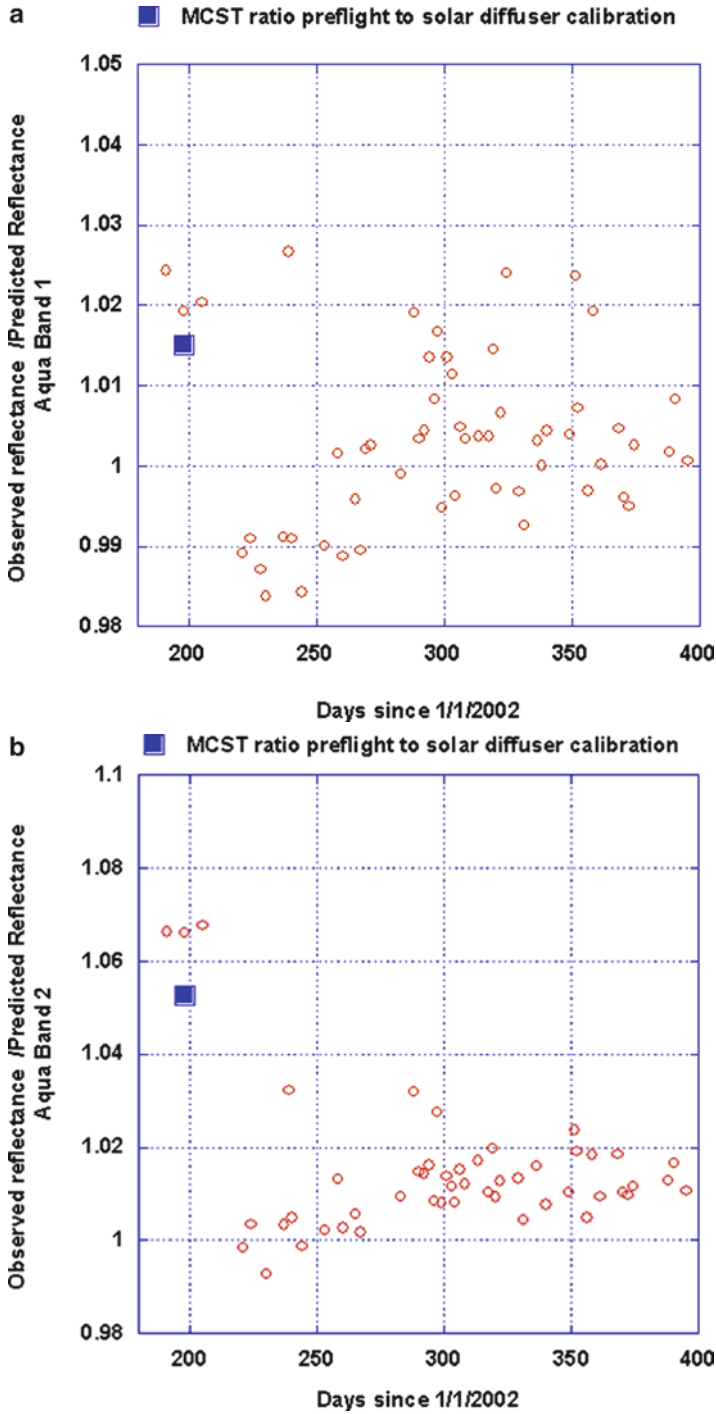


Fig. 7.18 Ratio of observed Aqua MODIS reflectances in (a) band 1, (b) band 2, and (c) band 7 to predicted reflectances (using Terra MODIS characterization of the desert site) for the first 7 months of operation

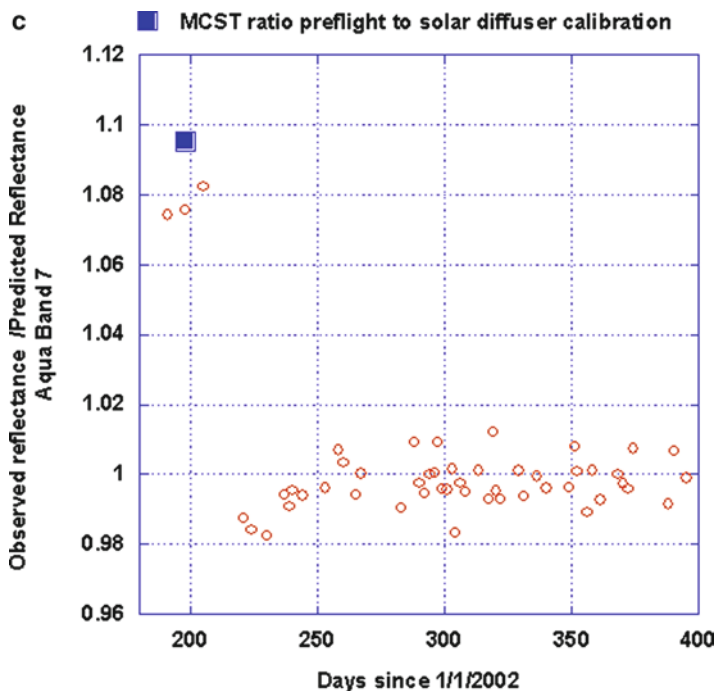


Fig. 7.18 (continued)

RSBs is presented. Comprehensive calibration efforts in both radiometry and geometry using onboard systems and ground validation targets have enabled Terra and Aqua MODIS to continuously produce high quality data products for use in land remote sensing.

References

- Barnes WL, Salomonson VV (1993) MODIS: a global image spectroradiometer for the Earth Observing System. *Crit Rev Opt Sci Technol* CR47:285–307
- Barnes WL, Xiong X, Salomonson VV (2002) Status of Terra MODIS and Aqua MODIS. In: *Proceedings of IGARSS 2002*
- Barnes WL, Salomonson VV, Guenther B, Xiong X (2003) Development, characterization, and performance of the EOS MODIS sensors. *Proc SPIE Earth Observing Systems VIII* 5151: 337–345
- Barnes WL, Xiong X, Salerno T, Breen B, Salo C (2005) Operational activities and on-orbit performance of MODIS on-board calibrators. *Proc SPIE Earth Observing Systems X* 5882:1–12. doi:10.1117/12.615384, 58820Q
- Chiang K, Xiong X, Wu A, Barnes WL (2004) MODIS thermal emissive bands calibration uncertainty analysis. *Proc SPIE Earth Observing Systems IX* 5542:437–447

- Esposito J, Xiong X, Wu A, Sun J, Barnes WL (2004) MODIS reflective solar bands uncertainty analysis. *Proc SPIE Earth Observing Systems IX* 5542:448–458
- Fleig AJ, Hubanks PA, Storey, JC, Carpenter, L (1993) An analysis of MODIS Earth location error, Version 2.0. NASA GSFC, Greenbelt, MD
- Franz BA, Werdell PJ, Meister G, Bailey SW, Eplee RE Jr, Feldman GC, Kwiatkowska E, McClain CR, Patt FS, Thomas D (2005) The continuity of ocean color measurements from SeaWiFS to MODIS. In: *Proceedings of SPIE, Earth Observing Systems X*, San Diego, July 31–August 2
- GSFC (1993) Specifications for the moderate resolution imaging spectroradiometer. Goddard Space Flight Center, GSFC 422-20-02, Rev. A, March 24
- Guenther B, Godden, G, Xiong X, Knight E, Montgomery H, Khayat, M, Hao Z (1998) Pre-launch algorithm and data format for the Level 1 calibration products for the EOS AM-1 moderate Resolution Imaging Spectroradiometer (MODIS). *IEEE Trans Geosci Remote Sens* 36(4):1142–1151
- Hook SJ, Greg Vaughan R, Tonooka H, Schladow SG (2006) Absolute radiometric in-flight validation of mid and thermal infrared data from ASTER and MODIS using the Lake Tahoe CA/NV, USA automated validation site. *IEEE Trans Geosci Remote Sens* 45(6):1798–1807
- Isaacman A, Toller G, Guenther B, Barnes WL, Xiong X (2003) MODIS Level-1B calibration and data products. *Proc SPIE Earth Observing Systems VIII* 5151:552–562
- Justice CO, Vermote E, Townshend JRG, Defries R, Roy DP, Hall DK, Salomonson VV, Privette JL, Riggs G, Strahler A, Lucht W, Myneni RB, Wolfe R, Knyazikhin Y, Running SW, Nemani RR, Wan Z, Huete AR, van Leeuwen W, Giglio RE, Muller J-P, Lewis P, Barnsley MJ (1998) The Moderate Resolution Imaging Spectroradiometer (MODIS): land remote sensing for global change research. *IEEE Trans Geosci Remote Sens* 36(4):1228–1249
- Li W, Xiong X, Chiang K, Toller G (2005) Evaluation of Terra MODIS PC Bands optical leak correction algorithm. *Proc SPIE Earth Observing Systems X* 5882:1–9. doi:10.1117/12.614509, 588219
- Minnett PJ, Brown OB, Evans RH, Key EL, Kearns EJ, Kilpatrick K, Kumar A, Maillet KA, Szczodrak M (2004) Sea-surface temperature measurements from the Moderate-Resolution Imaging Spectroradiometer (MODIS) on Aqua and Terra. In: *Proceeding of IGARSS 2004*
- Nishihama M, Wolfe RE, Solomon D, Patt FS, Blanchette J, Fleig AJ, Masuoka E (1997) MODIS Level 1A Earth location Algorithm Theoretical Basis Document Version 3.0, SDST-092. Lab Terrestrial Physics. NASA GSFC, Greenbelt, MD
- Salomonson VV, Barnes WL, Maymon PW, Montgomery HE, Ostrow H (1989) MODIS: advanced facility instrument for studies of the Earth as a system. *IEEE Trans Geosci Remote Sens* 27:145–153
- Salomonson VV, Barnes WL, Xiong X, Kempler S, Masuoka E (2002) An overview of the earth observing system MODIS instrument and associated data systems performance. In: *Proceedings of IGARSS 2002*
- Schaaf CB, Gao F, Strahler AH, Lucht W, Li X, Tsang T, Strugnell NC, Zhang X, Jin Y, Muller J-P, Lewis P, Barnsley M, Hobson P, Disney M, Roberts G, Dunderdale M, Doll C, d'Entremont RP, Hu B, Liang S, Privette JL, Roy D (2002) First operational BRDF, albedo nadir reflectance products from MODIS. *Remote Sens Environ* 83(1):135–148
- Thome K, Czapla-Myers J, Biggar S (2003) Vicarious calibration of Aqua and Terra MODIS. *Proc SPIE Earth Observing Systems VIII* 5151:395–405
- Townshend JRG, Justice CO, Gurney C, McManus J (1992) The impact of mis-registration on change detection. *IEEE Trans Geosci Remote Sens* 30:1054–1060
- Vermote EF, Roy DP (2002) Land surface hot-spot observed by MODIS over central Africa. *Int J Remote Sens (Cover Letter)* 11:2141–2143
- Wan Z, Zhang Y, Zhang Q, Li ZL (2004) Quality assessment and validation of the MODIS global land surface temperature. *Int J Remote Sens* 25(1):261–274
- Wolfe RE, Roy DP, Vermote E (1998) MODIS land data storage, gridding and compositing methodology: Level 2 Grid. *IEEE Trans Geosci Remote Sens* 36(4):1324–1338

- Wolfe RE, Nishihama M, Fleig AJ, Kuyper JA, Roy DP, Storey JC, Patt FS (2002) Achieving sub-pixel geolocation accuracy in support of MODIS land science. *Remote Sens Environ* 83(1–2):31–49
- Xiong X, Esposito J, Sun J, Pan C, Guenther B, Barnes WL (2001) Degradation of MODIS optics and its reflective solar bands calibration. *Proc SPIE Sensors Systems Next Generation Satellite V* 4540:62–70
- Xiong X, Sun J, Esposito J, Guenther B, Barnes WL (2002a) MODIS reflective solar bands calibration algorithm and on-orbit performance. *Proc SPIE Passive Optical Remote Sensing Atmosphere Clouds III* 4891:95–104
- Xiong X, Chiang K, Guenther B, Barnes WL (2002b) MODIS thermal emissive bands calibration algorithm and on-orbit performance. *Proc SPIE Passive Optical Remote Sensing Atmosphere Clouds III* 4891:392–401
- Xiong X, Chiang K, Esposito J, Guenther B, Barnes WL (2003a) MODIS on-orbit calibration and characterization. *Metrologia* 40:89–92
- Xiong X, Barnes WL, Guenther B, Murphy RE (2003b) Lessons learned from MODIS calibration and characterization. *J Adv Space Res* 32(11):2017–2122
- Xiong X, Chiang K, Li W, Adimi F, Yatagai H, Barnes WL (2004a) The MODIS correction algorithm for out-of-band response in the short-wave IR bands. *Proc SPIE Sensors Systems Next Generation Satellites VII* 5234:605–613
- Xiong X, Chiang K, Sun J, Che N, Barnes WL (2004b) MODIS on-orbit calibration: key issues and approaches. *Proc SPIE Earth Observing Systems IX* 5542:24–34
- Xiong X, Che N, Barnes WL (2005a) Terra MODIS on-orbit spatial characterization and performance. *IEEE Trans Geosci Remote Sens* 43(2):355–365
- Xiong X, Barnes WL, Xie X, Salomonson VV (2005b) On-orbit performance of the Aqua MODIS onboard calibrators. *Proc SPIE Sensors Systems Next Generation Satellites IX* 5978:1–9. doi:10.1117/12.627619, 59780U
- Xiong X, Sun J, Wu A, Chiang K, Esposito J, Barnes WL (2005c) Terra and Aqua MODIS calibration algorithms and uncertainty analysis. *Proc SPIE Sensors Systems Next Generation Satellites IX* 5978:1–10. doi:10.1117/12.627631, 59780V
- Xiong X, Salomonson VV, Chiang K, Wu, A, Guenther B, Barnes WL (2005d) On-orbit characterization of RVS for MODIS thermal emissive bands. *Proc SPIE Passive Optical Remote Sensing Atmosphere Clouds IV* 5652:210–218

Part III

ASTER and MODIS: Data Systems

Global change research and applications strongly depend on a continuous, reliable, and assured data and information stream to produce meaningful long-term results. Each EOSDIS data center contains the organizational structures to perform data management, which literally provides the foundation for a large science and research enterprise. The EOSDIS experience with its distributed data centers across the country provides ample evidence of the engineering complexity and challenges involved in operating such an enterprise. The first part of this volume looks at EOS evolution, establishes the framework for the EOSDIS infrastructure, and also outlines engineering lessons learned from nearly a decade of operations. EOSDIS is constantly evolving and responding to the advances in information technology, and software and hardware engineering. Nevertheless, it is indisputable that in accordance with Moore's law, advances in hardware outpace those in the software field, a well-known experience across EOSDIS and its data centers. This part provides insights into how EOS land data are managed at two different data centers, how those data are distributed to the users, and the role of the Hierarchical Data Format (HDF) in rendering a common data exchange foundation across the EOS mission.

The ongoing history and evolution of the Landsat program was largely responsible for the creation of the US Geological Survey's Earth Resources Observation and Science (EROS) Center outside Sioux Falls, SD. Given its proficiency in managing the world's largest collection of remotely sensed land data, it was the logical choice to archive and manage EOS land collections from the MODIS and ASTER missions. The Land Processes Distributed Active Archive Center (LP DAAC) was established in 1990 to manage MODIS and ASTER land data products. ASTER level-1 products are transmitted from the Ground Data System (GDS) facility in Tokyo to LP DAAC, where higher-level ASTER data products are generated (Watanabe et al. this volume). As part of a prelaunch descope of EOSDIS, the MODIS data production component was moved under Science Team management to the MODIS Adaptive Data Processing System (MODAPS) at the NASA Goddard Space Flight Center (GSFC) (Masuoka et al. – *in this volume*). MODAPS produces and transmits MODIS land products to the LP DAAC and the National Snow and Ice Data Center (NSIDC) DAAC for distribution. To date, the LP DAAC remains one of the largest data centers with over 1 petabyte archived data volume, and serves a vast national and international user community. The MODIS snow and sea ice products were

logically destined for the NSIDC at the University of Colorado's Cooperative Institute for Research in Environmental Sciences in Boulder, CO. The NSIDC DAAC was established in 1993 and it hosts and distributes cryospheric products from other EOS and heritage sensors as well. The variety of data products at NSIDC includes brightness temperature data, polar atmospheric data, remote sensing-derived satellite images, sea ice, snow cover, and ice sheet data. Consistent with EOSDIS' evolution, both data centers continue to maintain sustaining engineering activities, and after a decade of data stewardship, both centers have transitioned from serving data stored on a near-line archive to a direct, instantaneous online access capability (Daucsavage et al. the volume).

Both DAACs rely on EOSDIS-provided generic search, discovery, order and distribution tools to serve MODIS and ASTER data users (Ramapriyan et al. this volume). These tools have evolved in the last two decades, and include the Version-0 Information Management Subsystem (V0-IMS), EOS Data Gateway (EDG), Warehouse Inventory Search Tool (WIST), EOS Clearinghouse (ECHO), and EOS Data Pools. Both DAACs also provide data discovery tools, some of which also accommodate certain data services. Service-oriented architecture is defining the future of our data discovery and distribution systems. A good example in the EOSDIS context is ECHO, which is a metadata brokerage system to facilitate a wider use of NASA's EOS data products. It provides registries for both EOS metadata and data services through which, clients and users may search, browse, order, and access online data from multiple EOS data providers. All ECHO services are offered to the public through Internet-accessible Application Programming Interfaces. The continuing focus on technology infusion, Web services architecture, Open GIS, and Open Geospatial Consortium standards are likely to define the future trends in how Earth science data are distributed to applied researchers and scientists.

NASA anticipated global change research to involve very large volumes of data stemming from multiple instruments and sensors. These data comprise diverse product suites with varying complexity in size, dimensions, and metadata. A critical requirement was data storage, retrieval and access from multiple data repositories by a globally distributed user community. The requirements for a portable, multi-object, and platform-independent format led NASA to pick HDF in 1993. HDF was originally developed in 1988 by the National Center for Supercomputing Applications to store, organize, and represent large mathematical arrays in heterogeneous computing network environments. HDF supports a number of different data models including multidimensional arrays, raster images, and tables.

HDF-EOS is a specific implementation of HDF to handle EOS data products. EOS-specific data models were developed to handle grid, swath, and point structures, which facilitates geospatial queries based on Earth coordinates and time (Klein et al. this volume). Notwithstanding its elegant data structure, HDF presented some teething troubles, which both the commercial and non-commercial software development and user communities have helped overcome.

Chapter 8

ASTER and MODIS Land Data Management at the Land Processes, and National Snow and Ice Data Centers

John Daucsavage, Marilyn Kaminski, Bhaskar Ramachandran,
Calli Jenkerson, Karla Sprenger, Ron Faust, and Tamara Rockvam

8.1 Introduction

Chapters 4 and 5 provide a variety of examples of how ASTER and MODIS land science applications are predicated on the availability of consistent and quality data. This chapter portrays a narrative of how those data come to exist at two different data centers, which manage them.

The term *data management* conjures up different perceptions for those who produce and/or use data. The Data Management Association (DAMA) defines data management in fairly broad terms, thus: “Data Resource Management is the development and execution of architectures, policies, practices, and procedures that properly manage the full data lifecycle needs of an enterprise” (DAMA 2008).

Data management in the context of the distributed active archive centers (DAACs) has several dimensions and interpretations. Once processed data are transmitted to the DAACs, several functions define how scientific data management ensures data integrity, quality, and stewardship. Broadly, these functions include data ingest, production, archival, and distribution. A major difference between ASTER and MODIS data management at both the Land Processes (LP) and National Snow and Ice Data Center (NSIDC) DAACs is the absence of the production element with the latter (National Research Council 1998).

This chapter describes the history, evolution, contemporary practice, and future of the ASTER and MODIS data management activities at the NASA LP DAAC hosted by the US Geological Survey and the NASA NSIDC DAAC hosted by the University of Colorado. It attempts to portray the constant and adaptive engineering processes, which serve the needs of the dynamic science data producers and user communities. The data management efforts at these two DAACs are a manifestation

J. Daucsavage (✉)
SGT Inc., USGS Center for Earth Resources Observation and Science,
Sioux Falls, SD 57198, USA
e-mail: jdaucs@usgs.gov

of the philosophy and architecture of the larger EOS Data and Information System (EOSDIS), which is described in Chap. 2.

The Earth Resources Observation and Science (EROS) Center is a USGS data management and distribution, and research facility for remotely sensed data as well as other forms of geographic information. The EROS Program was established in 1966. In 1972, Landsat-1 was launched just as EROS moved to its current location outside Sioux Falls, South Dakota. From 1973 through 1999, Landsat-2, -3, -4, -5, and -7 were successfully launched. EROS holds the world's largest collection of civilian remotely sensed data covering the Earth's land surface. Its archive contains over 2 Petabytes of digital data. This archive serves to develop and promote remote sensing data-based science applications to identify, monitor, and understand varying spatial dimensions of change in the Earth's terrestrial landscape.

The LP DAAC was established at EROS in 1990 as part of NASA's EOSDIS initiative to process, archive, and distribute land-related data collected by the EOS MODIS and ASTER instruments. These activities continue to help promote the interdisciplinary study and understanding of the integrated Earth system. LP DAAC's role includes ingest, archival, and higher-level processing and distribution of ASTER data products, and ingest, archival, and distribution of MODIS land products derived from both the Terra and Aqua platforms.

NSIDC is part of the University of Colorado's Cooperative Institute for Research in Environmental Sciences in Boulder, Colorado. Chartered in 1982 to serve as an information center to support cryospheric research and science, NSIDC also has a long history in scientific data management. NSIDC's roots go back to 1957 when the World Data Center (WDC) for Glaciology was established at the American Geographical Society in New York. The WDC relocated to the University of Colorado in 1976, and NSIDC was created in 1982. It supports vast arrays of both field-collected as well as satellite-derived polar and cryospheric science data, which enable important scientific research on the global geography of our cryosphere.

In 1993, NASA established the NSIDC DAAC to serve as its repository for cryospheric data products within the EOSDIS. With Terra's launch in December 1999, NSIDC began archiving and distributing MODIS snow and sea ice products. With Aqua's launch in 2002, a parallel data stream was created. Cryospheric products from other EOS sensors (such as AMSR-E on Aqua and GLAS on ICESat), heritage sensor products (such as AVHRR), and in situ data products complement the MODIS cryospheric product suite.

Scientific data management is fundamental to both the terrestrial and cryospheric science applications supported by LP and NSIDC DAACs, respectively. Quality and consistent long-term data enhance scientific understanding of the terrestrial and cryospheric processes and their impacts on global climate. Both DAACs follow a systematic approach to data management, which ensures quality and consistency.

8.2 ASTER Data Management at LP DAAC

8.2.1 History of ASTER Data Management

The ASTER mission is a joint collaboration between USA and Japan. Japan was responsible for design and construction of the triple-sensor ASTER instrument and processing the Level-1 data, while USA was responsible for launching the instrument aboard the Terra platform, maintaining all requisite flight operations, and command and control functions. Japan also maintains and updates the ASTER level-1 algorithm, which is also made available to LP DAAC to cater to their level-1B and higher-level processing requests. Further details on the Japan-US level-1 data flows, and each country's responsibilities are available in Chap. 11.

The EOSDIS Core System (ECS) provided the initial capabilities to manage the ASTER mission at the LP DAAC. ECS provided all the data ingest, archive, production, and distribution functions described in the following sections.

Data Ingest. From late-2000, the ASTER Level-1 data were processed by the Ground Data System (GDS) facility at the Earth Remote Sensing Data Analysis Center (ERSDAC) in Tokyo. GDS received the ASTER level-0 data from the EOS Data Operations System (EDOS) on StorageTek D3 tapes, processed them to ASTER level-1A and level-1B, and transferred those datasets via courier-transported D3 tapes to LP DAAC. The ECS ingest subsystem would read the tape, store the data into the silo, and record the metadata in the database. This rather circuitous route meant that the time from data acquisition to user accessibility was typically 3 weeks; longer still when tape anomalies delayed data ingest into the archive. To reduce the high error rates with the D3 tapes, EDOS, GDS, and the LP DAAC transitioned to Sony DTF2 media in 2002. This improved the overall process but the tapes themselves, which differed in packaging from the D3 media, did not handle the repeated intercontinental transit well, and were increasingly problematic after as few as three write cycles. The ECS ingest process also included some ASTER-unique features such as the day/night acquisition flag calculation, and association of the full-resolution images with browse images.

Data Archive. The ECS archive consisted of a database to store relevant metadata identifiers for each ASTER image and a near-line tape storage silo to store the image data files. The near-line tape storage silo included a large cabinet with several thousand tapes, drives to read and write tapes, and a robotic arm to load tapes into drives. Two commercial software systems, Advanced Digital Information Corporation's Archival Management and Storage System (AMASS) and Automated Cartridge System Library Software (ACSL), were used to coordinate the read/write functions and keep track of each file's location. Given the ASTER instrument's limited duty cycle and its discontinuous acquisition schedule, its volume-related impacts on the archive are negligible.

Data Production. The LP DAAC is responsible for the production of level-2 and level-3 products. This was accomplished by integrating ECS components with the JPL-provided software. The ECS system managed the production process through its Planning and Data Processing Subsystems (PDPS), which took care of staging level-1B images, executing the JPL software, and transferring the resulting higher-level products back into the ECS archive. PDPS provided the tools to define and execute production jobs, and monitor their progress.

PDPS performed level-2 production in two different ways. The first was routine production, whereby every level-1B received from GDS was used to create a set of level-2 products, which were stored in the ECS archive, and ready for customers to order through the EOS Data Gateway (EDG). The second method was on-demand production, wherein users could order any level-2 product from a specific level-1B input image. The ECS system offered a web interface called the “ASTER On-Demand Form” that allowed users to provide the level-1B image identifier and specify instructions to generate desired level-2 products. PDPS would process and store the resulting level-2 product in the ECS archive, and trigger distribution to the user in a manner similar to a level-1 product. Following a period of time, the level-2 product was deleted from the ECS archive.

LP DAAC also produced a level-3 ASTER Digital Elevation Model (DEM) product. A DEM operator, using commercial geomatics software, manually produced two to three DEM products per day. Customers placed orders through the EDG, which were recorded in PDPS, which itself did not manage the DEM product generation. Instead, the DEM operator would manually generate a DEM, and notify PDPS to pick up and deliver the product to the customer similar to other on-demand products. All ASTER level-2 and level-3 products were available at no charge (until August 2002); however, system restrictions precluded customers from ordering a large number of images.

In addition to the level-1A and level-1B images produced in Japan, the LP DAAC is also responsible for archiving expedited ASTER Level-0 data. Expedited data are collected in response to urgent requests for certain time-sensitive acquisitions, and were downlinked directly to EDOS/GSFC. They were electronically transferred to the GSFC DAAC and subsequently to the LP DAAC, thus eliminating tape shipment delays following the route from Japan. PDPS processed the expedited level-0 data to level-1A and level-1B using the GDS-provided level-1 software, stored them in the ECS archive, and provided them to users via EDG as well (Fig. 8.1).

Data Distribution. Users could order level-1A or level-1B images through the EDG. In response to a user’s order, the ECS system would retrieve the image file from the archive, create a metadata file, and place the files on the user’s requested media – either on an FTP site for electronic download, or on a CD, DVD, or tape. Users also could order ASTER data through the USGS GloVis interface. Both EDG and GloVis systems were tied to the USGS accounting system, since ASTER data are provided for a monetary charge. All ASTER data products were available without a charge to the user community from March 2000 until August 2002. Since that time, ASTER data were provided for a monetary charge, and both EDG and GloVis systems were tied to the USGS accounting system.

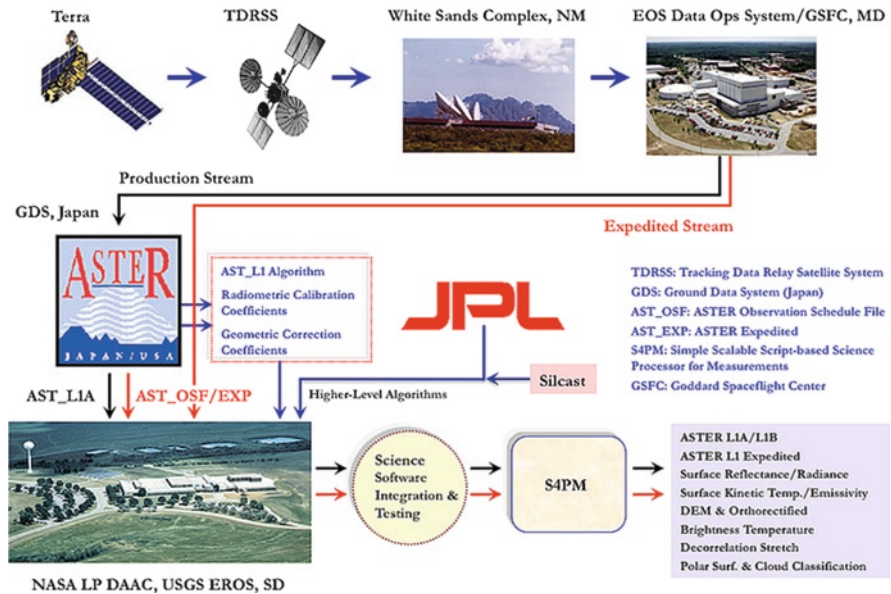


Fig. 8.1 ASTER data flow dynamics at the LP DAAC

8.2.2 ASTER Data Archival, Production, and Distribution Statistics

From 2000 to 2008, 183 terabytes (TB) of ASTER data comprising over 2 million granules were archived at LP DAAC. Distributed ASTER products include 544 TB in volume, which is comprised of over 10 million files based on 0.5 million orders received.

8.2.3 Contemporary ASTER Data Management

Over time, nearly every aspect of ASTER data management has undergone a significant change, as exemplified by the following.

Electronic Data Transfer. In 2005, lower network costs, greater bandwidth, and a desire to reduce the data acquisition-to-access lag time led to another transition in the ingest process. This involved replacing the tape transfer mechanism with electronic transfer of level-1A and level-1B data from GDS to the LP DAAC. In early 2005, the Asia Pacific Area Network (APAN) began transmitting the ASTER level-1A and level-1B datasets to LP DAAC. To accomplish this, the existing GDS and ECS systems at either end were not changed, but special software was developed to interface between the two entities, retrieving the data electronically from the GDS

server via FTP and staging them on a LP DAAC server, wherefrom the ECS system could ingest the data into its archive. This change, completed in early 2005, rendered ASTER images from GDS available to US customers within 1 week of acquisition, rather than 3–4 weeks when transferring data by tape.

Data Pool. In 2001, the ECS system implemented a large online distribution mechanism called the Data Pool. The Data Pool contains selected products online for immediate, free download, and also provides the FTP staging space for customers' ASTER orders. The Data Pool includes ASTER level-1B datasets over the USA and its territories, which are populated on a 2-year rolling archive basis.

S4PM and Linux Platform Transition. In 2006, both GDS and JPL announced their intention to port their level-1 and level-2 software, respectively, from a Silicon Graphics platform to a Linux platform. Since the PDPS portion of ECS that interfaced with their software was only available on Silicon Graphics, the LP DAAC opted to replace PDPS with another image-processing framework. The Simple, Scalable, Script-based Science Processor for Missions (S4PM) was an open-source system developed by the GSFC DAAC, and already operational on a Linux platform. S4PM supported both the "routine" and "on-demand" processing scenarios that were available with PDPS. Since S4PM was developed primarily for MODIS processing, it was modified to support the unique ASTER requirements at the LP DAAC. With S4PM and new versions of GDS and JPL software, the ASTER production capability was transitioned to a Linux platform in 2005. With this change, the ASTER On-Demand Form was retired, and all ASTER products were made available through the EDG.

On-Demand Paradigm. In 2006, GDS, through mutual agreement, stopped sending level-1B data to the LP DAAC, which then assumed the responsibility to produce them for its customers. Level-1B images over the conterminous USA were routinely created as a standard product and staged on the Data Pool for immediate download. All other level-1B images were produced for customers on an on-demand basis. This allowed customers to order level-1B from any level-1A image in the archive, where previously only a subset of the archived images was available in level-1B form. The existing on-demand ordering interfaces and S4PM system were used to produce these level-1B images. Also at this time, a level-1A correction algorithm was applied, which enabled LP DAAC to produce an updated ASTER level-1 dataset incorporating certain adjustments and algorithm changes to ASTER's geometry and radiometry implemented by GDS in Japan.

Silcast-Based DEMs. Also in 2006, new DEM production software from Silcast Inc. was integrated into the S4PM system. This enabled automating the DEM production process and eliminated the manual operator-driven limited production. At transition time, there was a backlog of over 3,000 DEM orders, which were worked off within weeks. Thus by 2006, all levels of ASTER data (level-1, -2, and -3) were produced on-demand, and for a fee. The lone exception to this policy was the set of standard level-1B scenes over USA and its territories available for immediate download via the Data Pool.

New Media. Through 2006, all ASTER on-demand products were only available to customers through an FTP download mechanism. In 2007, the LP DAAC implemented the capability to write on-demand products to DVD, providing users a choice of media options. Also in 2007, the full range of level-2 and level-3 on-demand products and media types were also made available through the GloVis ordering interface.

Expedited Data Handling. The ASTER expedited data handling also changed as the GSFC DAAC retired its ECS system. While previously, expedited level-0 data were routed from EDOS through the GSFC DAAC, and then to LP DAAC, the GSFC DAAC functions were transitioned to LP DAAC. The level-0 data are transmitted directly from EDOS to LP DAAC, which then forwards them to GDS, and also processes them to level-1A and level-1B expedited products.

8.3 MODIS Land Data Management at LP DAAC

The LP DAAC was originally geared to handle all Science Software Algorithm Integration and Testing activities as part of a MODIS data production system. However, the original EOSDIS plans to process all instrument-derived data and products at the DAACs were descope in the late 1990s, which led to the creation of the Science Investigator-led Processing Systems (SIPS) (Chap. 2). The MODIS SIPS is located at the MODIS Adaptive Processing System (MODAPS) facility at GSFC.

MODIS data from the Terra and Aqua satellite platforms follow the same path today as they did at launch. Raw instrument data are downlinked to the White Sands ground segment of the Tracking Data Relay Satellite System (TDRSS), transferred through high-speed networks to the EDOS at the GSFC for level-0 processing, and then transmitted to MODAPS/GSFC, where the higher-level land data products are produced and made available to the LP DAAC. Standard communication protocols are employed to ensure that the data are successfully transferred from MODAPS to the LP DAAC archive. The following sections deliberate upon the ingest, archive, and distribution functions.

Data Ingest. The LP DAAC receives higher-level Standard Data Products directly from the MODAPS through a SIPS interface. The SIPS interface is designed within ECS to accommodate electronic transfer of an unprecedented daily volume of data. LP DAAC was originally scoped to receive 6,196 MODIS granules with a total volume of 303.3 GB per day, but has achieved a peak 2.1 TB daily insert rate, which involved over 100,000 granules. The magnitude of the MODIS land product collections requires a robust data transfer interface that permits both efficient insert to the archive and accurate accounting of data reception.

Successfully building the MODIS land product archive is based on three elements: an Earth Science Data Type (ESDT), a Product Delivery Record (PDR), and a Product Acceptance Notice (PAN). The ESDT is a fundamental key, which facilitates data into and out of the archive. An ESDT is an abstract data type or

template that defines the parameters characterizing both the science and system requirements for any archived product. It serves as a validation tool to guarantee proper insertion into the archive, and also determines the search criteria used to access and find the products. ESDTs are installed in the ECS at the LP DAAC, and form the basis for the product metadata generated at MODAPS.

The PDR and PAN are used to control interaction between MODAPS as a data provider and the DAAC as a data storage facility. They initiate and terminate the ingest process, respectively, by providing the information needed to track whether all products exported to the DAAC are successfully ingested and archived. PDRs and PANs provide the primary validation and communication mechanisms driving the SIPS-based ingest process.

The SIPS is a polling-based interface, which facilitates the DAAC to archive products within minutes of completing production. As a product is generated, its science, browse, and metadata files (collectively called a granule) are exported to a high-capacity staging server. The granule specifications, such as directory location, volume, checksum value, and file names, are extracted and written to a PDR. The PDR is pushed into a polling directory on a staging server (PDRServer), which is constantly monitored (polled) by the DAAC. When a new PDR arrives in the polling directory, file transfer protocol (FTP) is initiated to pull it into a verification area at the DAAC. The available granule specifications listed in the PDR are provided to file retrieval software, which picks up the data files and delivers them to the DAAC's preprocessing staging server via FTP.

The science and browse files in a granule are temporarily stored, while the metadata file is parsed and validated against ESDT-controlled information hard-coded into the DAAC inventory database. If all expected fields are present and acceptable, the transfer of the science and browse files to the archive cache is authorized and the metadata are written to the database. At this point, the DAAC composes a PAN describing the status of the granule insert and sends it back to a PAN directory on the MODAPS PDRServer. A PAN serves as a reconciliation tool, which the data provider may use to track the success of the data exported for insert to archive. Upon a failure, the PAN will contain high-level information on the problem, which the data provider may use to rectify the error before attempting to re-export the affected granules.

Four potential reasons may account for a failure: export software bugs, network connectivity, DAAC system issues, and invalid metadata. The most common manifestation of the first is an inconsistently formatted PDR. If any part of the PDR delineating the granule specifications exported for insert disagrees with the regulated format, the DAAC will return a Product Delivery Record Discrepancy (PDRD) to the PDRServer immediately, and not follow through with the data transfer. DAAC preprocessing software will identify network glitches by tracking checksum and file size values before and after every data transfer, including that from the PDRServer as well as the internal transfers from temporary cache to the physical archive. Discrepancies are spelled out in the associated PAN to alert the data provider of the need to retry export. If at any time DAAC insert processes fail due to internal system issues, the aborted activity will result in a PAN statement to that effect and initiate a resend. Metadata failures surface when fields in the exported

metadata files are not populated according to the ESDT definitions in the inventory database. If an incorrect field is defined as mandatory for insert, the granule will fail the insert and archive processes. The PAN statement will provide a general indication of the nature of the failure. In some cases, metadata fields are desirable but not necessary. If such invalid metadata are presented for insert, the granule may successfully archive, but the associated metadata are not recorded in the science inventory database tables.

Data Archive. When the first MODIS data arrived at LP DAAC, the current storage technology was a tape-based library stored in a silo and outfitted with robotics to load tapes into drives for writing files to the archive. This model is excellent for long-term storage of infrequently accessed data, but creates some service limitations at the DAACs. The phenomenally high ingest rates (tape writes) and distribution frequencies (tape reads) associated with MODIS land products accelerates the degradation of physical media storage. Online storage has gained momentum as a preferred archive model, so the DAACs each support an array of disks intended to house copies of the most-frequently accessed data products. These online electronic disk caches called Data Pools are expanding to satisfy user requirements for extensive time-series data products. Data ingest still populates a tape archive, but in parallel transfers a copy of each granule to the direct online-access Data Pool.

Data Distribution. The distribution of MODIS land products from LP DAAC is similar to other DAACs. LP DAAC products are available through the following mechanisms:

- ECHO-WIST (<https://wist.echo.nasa.gov/~wist/api/imswelcome/>)
- Data Pool (<http://lpdaac.usgs.gov/datapool/datapool.asp>)
- Via subscriptions (contact LP DAAC User Services at lpdaac@eos.nasa.gov)
- Machine-to-Machine Gateway (contact LP DAAC User Services lpdaac@eos.nasa.gov)

These common mechanisms are derived from the perspective of universal support for all EOS products, and each provides advantages and disadvantages related to a data product or research application. While maintaining full access through standard EOS interfaces, LP DAAC has also developed site-specific methods to serve its land remote sensing community.

USGS GloVis (<http://glovis.usgs.gov/>).

The US Geological Survey (USGS) Global Visualization (GloVis) tool supports remotely sensed earth science data at EROS. It provides a simple browse image-based product selection process, which accounts for its popularity in the user community. The GloVis inventory includes MODIS land products and provides an alternative search and order method.

MRTWeb (<http://lpdaac.usgs.gov/datapool/datapool.asp>).

The MRTWeb interface combines browse-based data discovery with the processing options offered in the MODIS Reprojection Tool (MRT). Using the GloVis model,

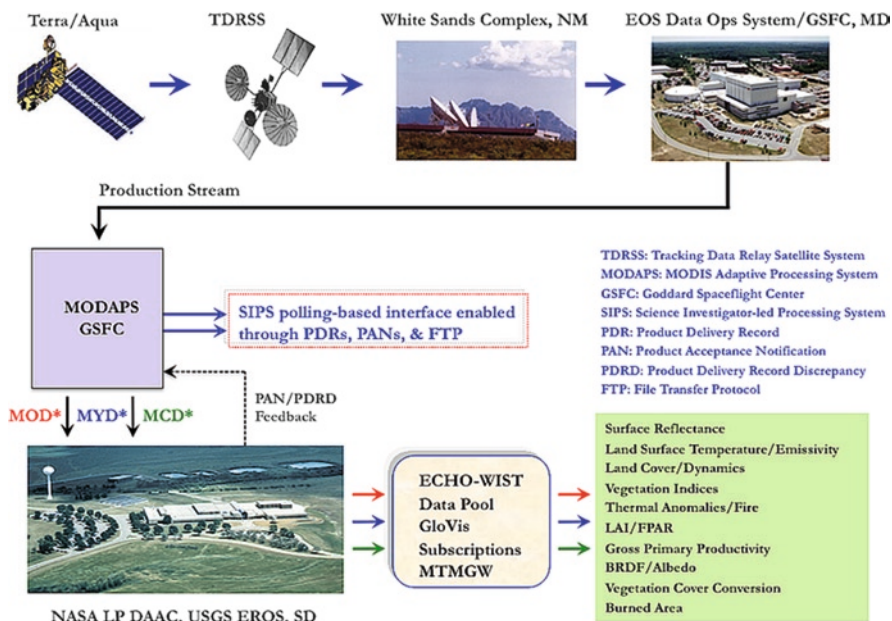


Fig. 8.2 MODAPS to LP DAAC MODIS data flow dynamics

users may select tiles of interest from a composite image of relevant browse files and also request additional processing, which include spatial and spectral subsetting, mosaicking, reprojecting, and reformatting. All MODIS land products populated in the LP DAAC Data Pool are available through this interface (Fig. 8.2).

8.3.1 MODIS Land Data Archival and Distribution Statistics

From 2000 to 2008, 1,613 TB of MODIS (Terra and Aqua) data were archived at LP DAAC, which consists of 31 million data granules. Distributed MODIS products include 1,685 TB in volume, which is comprised of 61 million files based on 1.1 million orders.

8.4 MODIS Snow and Sea Ice Data Management at NSIDC DAAC

The NSIDC DAAC archives and distributes a variety of cryospheric data products derived from a range of operational instruments as well as historical sources. Examples of their data include satellite images, polar atmosphere data, sea ice data, snow cover data, and ice sheet data. In the MODIS realm, the NSIDC DAAC specializes in snow

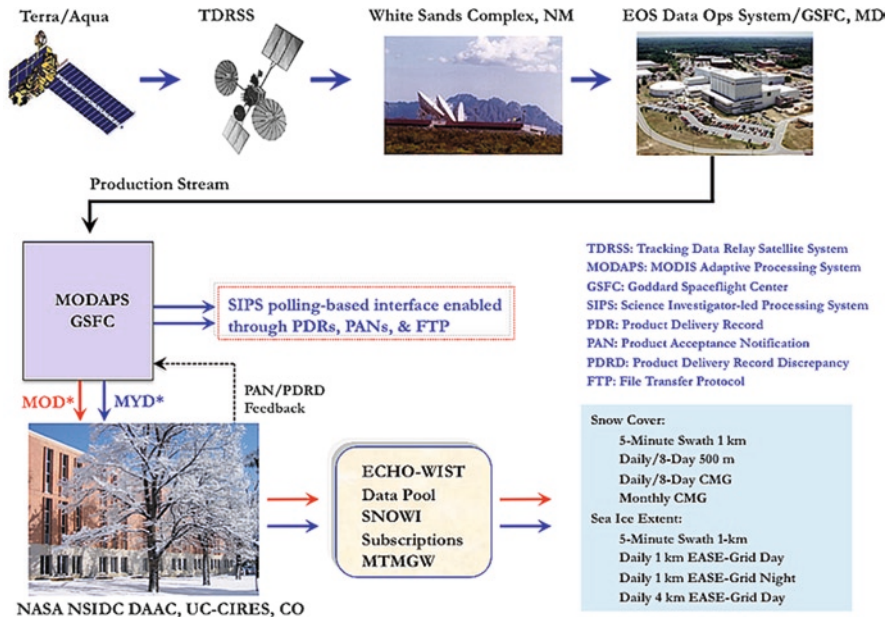


Fig. 8.3 MODAPS to NSIDC DAAC MODIS data flow dynamics

and sea ice product suites derived from both the Terra and Aqua incarnations. The data ingest, archive, and distribution mechanisms, described below, are quite similar to those followed by LP DAAC (Fig. 8.3).

Data Ingest. The MODIS snow and sea ice products are based on the Snow and Sea Ice Global Mapping Project algorithms (Chap. 30). NSIDC plays an active role in the algorithm development process through its product evaluation and testing processes. Approved algorithms are integrated into the MODAPS production stream (Chap. 22). Final MODAPS-generated snow and sea-ice products are packaged with a Product Delivery Record (PDR), and placed on a dedicated PDR server along with a metadata file. Browse image files are either included with a granule or sent separately and linked to the granule at ingest time. NSIDC software periodically polls the PDR server for available data and transfers them via FTP to an ingest server, which processes the PDR, inserts the accompanying metadata into the database, and stages the data to the archive. The same data are also inserted into the Data Pool as they are staged to the archive. For the most part, this automated process is trouble-free. The few anomalies that do occur are automatically corrected through the reconciliation process with minimal impact to operations staff.

Data Archive. The data archive system is undergoing an evolutionary change. Currently, EOS data at NSIDC are archived on a StorageTek Powderhorn tape library, which holds up to 5,000 StorageTek 9940 tapes, each of which has a storage capacity of roughly 120 GB. ADIC/AMASS software maintains a database of all the files and their addresses. The Powderhorn reads from or writes to any tape in its

inventory by moving the tape from its home slot into one of several tape drives via a robotic arm. Each tape has a unique bar code that the robotic arm optically senses to learn details of the tape being handled. Communication between AMASS and the Powderhorn is handled via StorageTek's ACSLS.

As data products are staged to the archive, they are also written to the Data Pool for near-term access. The Data Pool is an array of disks, originally 5 TB in capacity with a subsequent growth potential of 74 TB. As originally conceived, it was intended as a repository of frequently accessed and presumably the most recently ingested data. At NSIDC, users' data retrieval patterns do not match that presumption – data access is most typically accomplished through requests for a large number of historical data granules. Given NSIDC's small-sized Data Pool, it was infeasible to store all its MODIS data permanently, which only allowed the handling of a few user requests through the Data Pool. This necessitated a disproportionately large percentage of tape requests (compared to the other ECS DAACs) to fulfill user distribution orders.

When the ECS requirements were written, a tape-based archive was the only practical option to handle the anticipated amounts of data. Even as it provided a good storage medium, accessing it in a dual ingest and distribution system has not proved very efficient. As disk systems grow more compact and affordable, they prove financially feasible to store more data online. NSIDC is deploying new hardware and software in early 2009 to move all its ECS data to an online archive, with a tape-based offline backup system. Besides decreased access times for MODIS products, this facilitates the potential for more interactive online services.

Data Distribution. NSIDC distributes data to users through a variety of methods, ranging from very simple interfaces appropriate for users who only request data occasionally and have simple search requirements, to automated systems that regularly download data directly to users without intervention. Data distribution is an area that has witnessed the most change and improvement since ECS' inception. NSIDC DAAC products are available through the following mechanisms, which are described in detail:

- ECHO-WIST (<https://wist.echo.nasa.gov/~wist/api/imswelcome/>)
- Data Pool (http://nsidc.org/data/data_pool/index.html)
- Search 'N Order Web Interface (SNOWI) (<http://nsidc.org/data/snowi/>)
- Via subscriptions (contact NSIDC User Services: nsidc@nsidc.org)
- Machine-to-Machine Gateway (contact NSIDC User Services: nsidc@nsidc.org)

NSIDC Data Pool. The Data Pool is an online data cache, which offers quicker retrieval than through the permanent tape-based archive. At NSIDC, the Data Pool is populated with MODIS data granules during the ingest process (as well as AMSR-E, GLAS, and NISE products, which are outside the scope of this discussion). We may also populate the Data Pool with historical data upon user request, although no such request has so far been made. Using a simple hierarchical web interface, users can search for granules, display browse images, and order granules. The web interface employs a "drill-down" strategy that quickly narrows the search space based on user input. Search options include data group, dataset, date/time, spatial coverage, and dataset parameters such as cloud cover, science quality, and day/night flag. Users may request data con-

version options through the HDF-EOS to GIS tool (HEG). HEG options include file format conversion, reprojection, and subsetting. Once orders are placed, the transformed data are delivered either via FTP or on media (CD or DVD).

Users who access the Data Pool may frequently streamline the order process by directly accessing the FTP site and download the desired granules; they may bypass the hierarchical interface altogether. Users may also write scripts to automatically download granules of interest to an FTP site, mimicking the functionality of a user subscription.

Search ‘N Order Web Interface. Notwithstanding the versatility of the erstwhile EDG and the current WIST, users often have simple data requests. SNOWI was developed at NSIDC in response to early user feedback for a simple, basic tool. SNOWI offers a basic search and order interface that allows the user to select data using only the dataset name (either the long or short name), temporal range, and geographic bounding box or range of tile numbers. To reduce search times, the user may either specify the maximum number of granules they wished returned, or specify a search time limit. Browse images are available to preview data before ordering. Similar to WIST, these images allow users to determine a priori whether the full-resolution granule is suitable for their use. Given the frequent cloud coverage in MODIS data in the polar and snow-covered regions, NSIDC users particularly value the browse feature. Keeping it simple for the casual user, the SNOWI interface limits order options to FTP-Push and FTP-Pull only.

Subscriptions. Subscriptions are an excellent option for users who wish to regularly receive the latest data as they are ingested into the archive. Users establish the subscription by submitting a simple form to NSIDC User Services, following which the data are automatically staged for them on a routine basis without further intervention. Several data selection and distribution options are available for subscriptions, including granule restriction by spatial coordinates or product-specific parameters, delivery via FTP-Push or FTP-Pull, and bundling options to moderate the number of individual data deliveries and their frequency. This renders subscriptions more manageable, especially for frequently produced swath and gridded products. Hence, subscriptions are the most effective means for users who require current data delivered quickly. Both users and NSIDC personnel need to interact minimally with the ECS system. Any granules reprocessed by the science team (to correct a quality problem) are also automatically redelivered via the subscription, which ensures the user always receives the most scientifically accurate data.

Machine-to-Machine Gateway (MTMGW). The MTMGW was devised as an efficient way for MODAPS and other science computing facilities to quickly obtain large quantities of data necessary to support reprocessing. Its ability to allow external users to directly access NSIDC machines renders it a trusted interface easily implemented through a mutually approved user agreement.

Data Delivery Options. Data are delivered to users via FTP, CD, DVD, or DLT. Orders for data on hard media are created using software, which interfaces between ECS and various CD-ROM and DVD burners and DLT drives. After NSIDC operations staff successfully generates an order using such software, the media and

printouts are then provided to User Services for shipping. At current capacities, a CD holds up to 640 MB, a DVD holds 4.7 GB, and a DLT tape holds up to 40 GB of uncompressed data.

Due to the resource-intensive nature of media preparation, some DAACs have already removed media from their delivery options, and now offer only FTP-Push and FTP-Pull. NSIDC is considering that possibility, while continuing to evaluate ways to efficiently service our users while offering them the options they require.

The various user interfaces have diverged in terms of the tools that are accessible through them. New users may find it difficult to know ahead of time, which tools they wish to use, and inadvertently experience some inefficiency by choosing what later becomes a poor option. NSIDC is developing a more integrated system architecture to address these issues and provide more cohesive tools to support user needs.

8.4.1 MODIS Snow and Sea Ice Data Archival and Distribution Statistics

From 2000 through 2008, a total of 73 TB of MODIS (Terra and Aqua) data were archived at NSIDC, which consists of 12 million data granules. Distributed MODIS products include 40 TB in volume, which is comprised of 9.2 million files based on over 281,000 orders.

8.4.2 MODIS Metadata Management and Quality Assurance Updates at Both Data Centers

The following description is common to both the LP and Snow and Ice Data Centers. The MODIS Science Team and the Land Data Operational Production Evaluation (LDOPE) facility strive to directly assess the science quality of approximately 10% of the average daily production volume (Lutz et al. 2000; Roy et al. 2002), and infer the quality of related data from that assessment. Quality determinations are documented on the MODIS Land QA web pages, from which the DAAC Data Manager retrieves the information necessary to run a tool that updates the metadata in the primary catalog. Any catalog changes, including inserts, deletions, and updates are transferred to the replicated Data Pool and ECHO catalogs via a metadata extraction tool called the Bulk Metadata Generator Tool (BMGT) at least once a day. Once the transactions are committed in the replicated catalog, the changes are available to the user community, which can determine the science quality status through the requisite flags.

The intent to update the science QA flags of millions of postarchived granule metadata files for dozens of Terra- and Aqua-derived MODIS land collections has certainly posed challenges to tool development, implementation, timeliness, and execution, all of which are creatively addressed both by ECS and the two Data Centers.

8.4.3 ECS Evolution-Related Changes at Both Data Centers

EOSDIS, which remains one of the world's largest science data processing, archiving, and distribution systems, has continued to operate since 1994. The diversity and volume of data have grown enormously in parallel with advances and improvements in software and hardware engineering, and information technology. With a rich variety of lessons learned and experience gained, NASA convened an EOSDIS Elements Evolution Study Team and a Technical Team to garner guidance with which to develop and implement the 2015 Vision goals (see Chap. 2). Relevant 2015 Vision objectives included the following: Increasing end-to-end data system efficiency and autonomy while decreasing operations costs; Increasing data interoperability and usability by the science research, application, and modeling communities; Improving data access and processing; and Ensuring continued safe stewardship (Esfandiari et al. 2006).

The LP and NSIDC DAACs are two components of the larger EOSDIS where ECS is integral. ECS provides the core software along with numerous COTS packages. Beginning in 2006, the ECS system evolution involved porting to Linux platforms, retirement of some functions, upgrades to several ECS-used commercial software components, and transition to a new archive management system. The ingest process was modified to receive and stage the data on the Data Pool rather than on a separate disk. The ECS archive itself switched from the AMASS/ACSLs software to a StorNext storage system, which manages the tape library and makes archive files available on a storage area network. Beginning in 2008, further work was initiated that defines the evolution of the online and offline archives. The online archive is a complement of spinning-disk hardware, which is universally accessible by all data users. The offline archives are a collection of Linear Tape-Open (LTO) magnetic storage tapes that provide the data backup.

ECS evolution also effected changes in the data ordering interfaces. ECS no longer provides a searchable catalog of images; instead, metadata are exported to the EOS Clearing House (ECHO) system. ECHO is a metadata brokerage system, which allows users to develop discipline-specific clients through published Application Program Interfaces (APIs) to facilitate data discovery (see Chap. 9). A new Web interface, the Warehouse Inventory Search Tool (WIST), replaces the EDG. WIST is the primary interface to search and order through the ECHO inventory.

ECS evolution, therefore, is an overall endeavor in slimming its software architecture and moving its hardware component toward commodity-based computing systems. All activities are driven by the 2015 Vision objectives toward developing a cost-effective EOSDIS with a smaller footprint.

8.5 Closing Thoughts

The experiences of the LP and NSIDC DAACs attest to the fact that data management to serve the needs of a large scientific research and applications enterprise is by no means a trivial task. Both DAACs are only a subset of the larger EOSDIS, but a number of factors contribute to the challenges of efficient data management and

stewardship at both locations. Nakamura delineates the larger lessons learned from the EOS engineering experience in Chap. 3, all of which have a bearing on both DAACs. The development and growth of ECS is predicated on evolving trends and decisions made regarding the software and hardware environments, and trends in information technology, which will continue to evolve.

The tape-based archive technology has engendered its share of data access and retrieval problems. No current archival technology is inherently robust enough to trust for long-term data stewardship. This implies that we must physically exercise and handle the data at regular intervals to ensure that they remain intact and acceptable to migrate to the next incremental technology improvement. The economics of disk-based storage was not conducive a decade earlier, which today provides an ideal option for large data centers. Therefore, disk-based data access and retrieval are becoming more common. This along with on-demand processing systems may further reduce the need to store certain archived higher-level data products.

MODIS produces continuous, global, multitemporal collections, which are reprocessed with improved algorithms every 18–24 months. This especially makes version management a critical data management practice to ensure how multiple data versions are expeditiously managed and served in parallel before decisions to decommission earlier versions are implemented. The physical estrangement of the data producer and data archive also requires constant vigilance to ensure archived data remain reconciled to the best possible levels.

The continuing ECS evolution is largely driven by evolving trends in technology and economics. Technology will likely continue to prove more beneficial to Earth science data management in the future. A number of computing and Internet-related technologies hold much promise and prospect. They include service-oriented architecture in concert with Web service technologies, which facilitate interoperability and machine-to-machine interactions over the network. Other areas to watch for include Cloud computing (Nebula 2009), which can potentially expedite on-demand processing, and Semantic Web frameworks to improve the data discovery and use processes.

References

- Data Management Association (2008) <http://www.dama.org/i4a/pages/index.cfm?pageid=1>
Accessed 4 July 2009
- Esfandiari M, Ramapriyan H, Behnke J, Sofinowski E (2006) Evolution of the earth observing system (EOS) data and information system (EOSDIS). IEEE Int Geosci Remote Sensing Symp 309–312
- Lutz R, Roy DP, Leff C, Lewicki S, Geier E, Ziskin D, Kilpatrick K, Chu A (2000) A review of EOS terra quality assessment. IEEE Int Geosci Remote Sensing Symp 5:2092–2095
- National Research Council (1998) Review of NASA's distributed active archive centers. National Academy, Washington, DC, p 233
- Nebula (2009) <http://nebula.nasa.gov/> Accessed 4 July 2009
- Roy DP, Borak JS, Devadiga S, Wolfe RE, Zhang M, Desclotres J (2002) The MODIS land product quality assessment approach. Remote Sensing Environ 83:62–76

Chapter 9

An Overview of the EOS Data Distribution Systems

H.K. Ramapriyan, Robin Pfister, and Beth Weinstein

9.1 Introduction

The Earth Observing System Data and Information System (EOSDIS) is the primary data system serving the broad scope of NASA's Earth Observing System (EOS) program and a significant portion of the "heritage" Earth science data. EOSDIS was designed to support the Earth sciences within NASA's Science Mission Directorate (previously the Earth Science Enterprise (ESE) and Mission to Planet Earth). The EOS Program was NASA's contribution to the United States Global Change Research Program (USGCRP) enacted by Congress in 1990 as part of the Global Change Act. ESE's objective was to launch a series of missions to help answer fundamental global change questions such as "How is Earth changing?" and "What are the consequences for life on Earth?" As part of supporting that objective, EOSDIS distributes a wide variety of data to a diverse user community (Fig. 9.1).

The EOSDIS data are held in 11 geographically distributed Data Centers. These centers are responsible for archiving and distributing data to users. Most of the EOS standard data products are produced at the Science Investigator-led Processing Systems (SIPS) and sent to the Data Centers for archiving. The Data Centers interoperate with each other and also with several international archives. Figure 9.2 is a context diagram showing Data Centers, SIPS, and other components of EOSDIS and external interfacing entities. This figure provides an end-to-end view of the EOSDIS context that runs from data collection on the left, to data distribution on the right. Data are collected from the satellite and sent to a facility for backup and initial processing. Raw data are distributed to the Data Centers and SIPS (collocated with science teams), where they are processed to higher-level products. The products are archived at the Data Centers (Fig. 9.3)

H.K. Ramapriyan (✉)
NASA Goddard Space Flight Center, Greenbelt, MD 20771, USA
e-mail: hampapuram.k.ramapriyan@nasa.gov

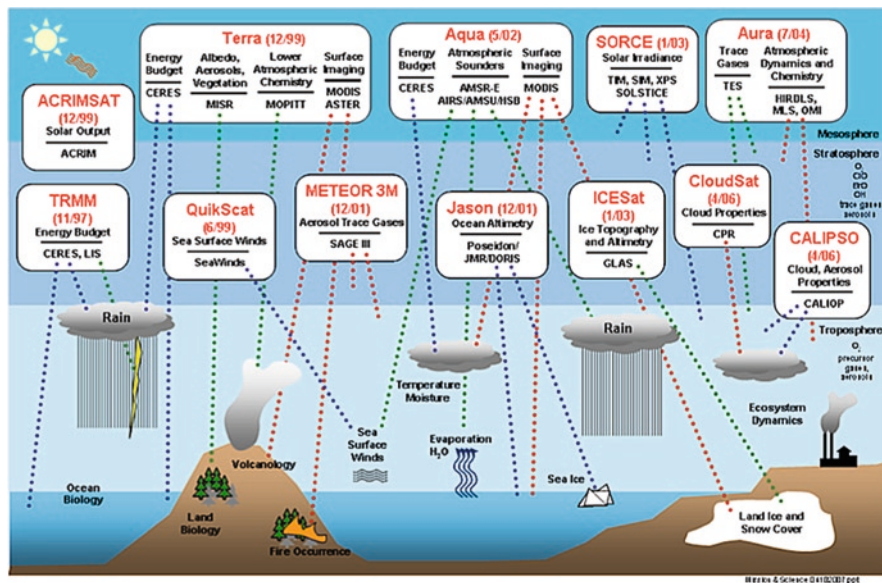


Fig. 9.1 Earth Observing System missions, instruments, and platforms

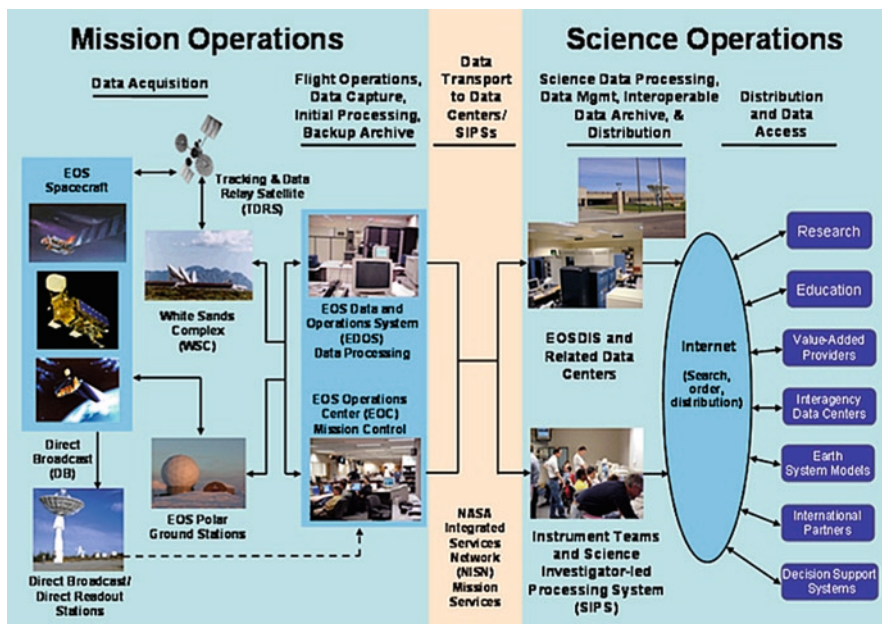


Fig. 9.2 EOS Data and Information System context

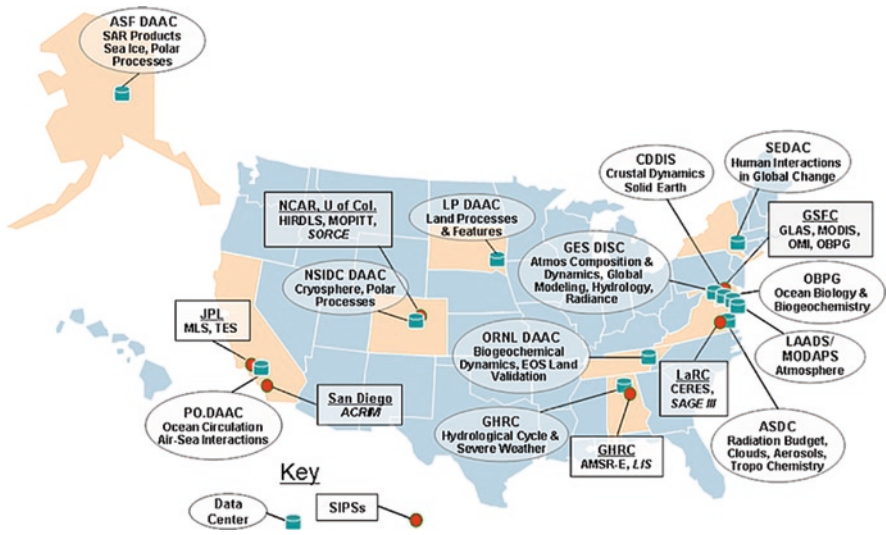


Fig. 9.3 Geographic distribution of the EOS Data and Information System Data Centers and Science Investigator-led Processing System

and distributed to users automatically via subscriptions or via various search and order interfaces.

EOSDIS provides general-purpose tools that enable location of and access to all data held in the EOSDIS system, and to related Earth science data held by NASA’s international partners. Such tools include the EOS Data Gateway (EDG), which is evolving into the Warehouse Inventory Search Tool (WIST), EOS Data Pools, and the EOS Clearinghouse (ECHO). EDG and WIST provide general search and access capabilities to the EOSDIS repository. Data Pools support direct, on-line access to high-priority data in individual EOSDIS archives and are accessible either directly from the Data Pool’s interface at each of the Data Centers, from EDG or WIST, or via a third-party user interface built on ECHO. ECHO is a data and service middle-ware tool that provides application program interfaces (APIs) upon which users can build their own machine-to-machine or human-to-machine search clients. In combination, EDG, WIST, Data Pools, and ECHO enable flexible and efficient access to data held in the EOSDIS archives. In addition to these general interfaces, EOSDIS also supports discipline-specific access mechanisms through its Data Centers. Information on and access to the EOSDIS data access tools are found at <http://nasadaacs.eos.nasa.gov/>.

As of September 2007, EOSDIS had over 4.9 petabytes of data in its archives. Data generation and storage continue at an average rate of 3.2 terabytes/day. During fiscal year 2007 (year ending September 30, 2007), EOSDIS distributed over 100 million products to end-users at a rate of about 4.2 terabytes/day.

9.2 History and Evolution

Information technology has undergone revolutionary changes since the original formulation of EOSDIS in the late 1980s and its initial design in the early-to-mid-1990s. This has led to significant changes in the user community’s needs and expectations. Consequently, EOSDIS continues to advance in response to these changes, which drive the evolution of the data distribution components’ basic architecture and design. Also, NASA is complementing its core infrastructure consisting of EOSDIS and mission data systems with community components selected through peer-reviewed competitions. Such components include Research, Education and Applications Solution Network (REASoN) and Advancing Collaborative Connections for Earth–Sun System Science (ACCESS) projects. Thus, NASA’s Earth science data systems are evolving toward a more distributed, heterogeneous, and easily accessible on-line environment. Figure 9.4 shows the evolution of EOSDIS over its first decade of operations.

9.2.1 Version-0 Information Management Subsystem

EOSDIS started with eight heritage archives that each held data for a specific Earth science discipline and housed the science expertise to ensure proper stewardship

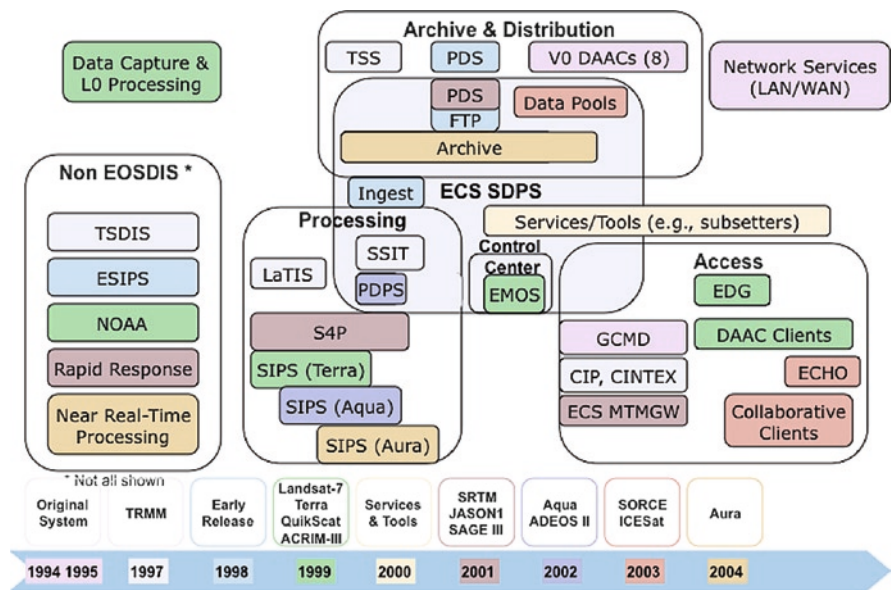


Fig. 9.4 Historical evolution of EOS Data and Information System (acronyms are given in Appendix)

and data use. The design concept was based on the philosophy that each of these heritage archives embodied specific expertise, which did not warrant their relocation to a centralized archive. The development was focused on an “inventory level” interoperability system to support a single-point search and access interface. This mechanism would allocate searches to the distributed archives, and receive and organize result sets (of specific files or “granules” that meet use-specified criteria), which end-users could evaluate before placing orders. The Version-0 (V0) Information Management Subsystem (IMS) was a proof-of-concept “working prototype” for interoperability among distributed archives (Ramapriyan and McConaughy 1991). The 4-year V0 development effort (1990–1994) was coincident with a major information technology revolution that directly impacted the technology on which this system was based. The challenges in balancing user requirements for system functionality, user expectations (driven by newly available desktop technologies), and technology maturity issues made for quite an exciting and challenging development environment. As technology evolved, the user community expected the user interface configured with the latest technology on their desktop. In the beginning of V0 IMS development, character-based user interfaces that ran on VT100 terminals were the standard. After a year into prototyping, X-Windows-based graphical user interfaces (GUI) took over the market. At the operational release of the X-Windows-based V0 IMS GUI, HTML interfaces emerged and reigned supreme. The users were barely getting used to HTML’s click-and-wait interactive method that Java emerged as a better interactive option. The V0 IMS development team could barely develop basic functionality before it needed to incorporate a new user interface technology.

The V0 infrastructure was designed to provide basic data search, browse (viewing a sample image), and order functions to users ranging from Earth scientists to the general public. This functionality was achieved by using metadata that was commonly used across all the archives. By limiting the set to only common attributes with consistent definitions, search criteria were limited to those that describe whole datasets rather than individual data granules (smallest inventoried unit of data in the system). However, end-users required a system able to return individual granules. So the V0 IMS system architecture was designed to distribute search messages to the individual Data Centers. The archives would execute the searches, each using their own, autonomous mechanisms, and then pass the results back to the V0 IMS client. The V0 IMS client would assemble the result sets and display them for end-users in a Web-based GUI. Artifacts of this distributed query architecture drove a degree of complexity that sometimes resulted in confusion or frustration to the end-user. This lesson learned was incorporated in developing the ECHO approach described later.

Despite the project’s challenges, major successes came from the V0 IMS development effort. V0 IMS was one of the first of its kind to provide single-point search and access to distributed holdings. In addition, as a result of this effort, the V0 IMS Protocol was developed. This protocol formed the basis for future protocols used by the CEOS (Committee on Earth Observing Satellites) Interoperability Experiment (CINTEX) that connected international archives with those from EOSDIS.

This international protocol became known as the CEOS Interoperability Protocol (CIP). The V0 IMS and CIP Protocols, and related message passing dictionaries were fundamental inputs in the creation and evolution of current interagency and international standards and protocols.

9.2.2 Overview of EDG and WIST

In 1998, the Earth Science Data and Information System (ESDIS) Project, which is responsible for the development and operation of EOSDIS, decided to use the V0 IMS as the basis for the search and order interface to EOSDIS data to support the first major milestone, the launch of Landsat-7 in April 1999. To meet the Landsat-7 launch milestone and support granule level metadata searches for Landsat-7 and the subsequent EOS missions, an extension of the V0 IMS, renamed EDG, was used. The initial EDG provided basic end-to-end data search and order capabilities. Over time, to meet specific needs of EOS instrument teams and discipline-specific science communities, new capabilities were added including some data-related services such as subsetting.

During this time, ESDIS realized that EOSDIS' long-term needs were to support a broader set of interoperability requirements. These requirements included the ability to support search and access by alternative clients, and the flexibility to support data-related services. As a result, the ECHO was initiated as an enhancement to EOSDIS. Thus the two efforts, EDG operations and ECHO development, were carried out in parallel.

As ECHO development continued, ESDIS decided that ECHO would replace the middleware portion of EDG, and that the WIST, a user interface similar to EDG that interacts with the ECHO middleware, would replace the EDG user interface. The resulting end-user experience is similar in EDG and WIST. Therefore, they are described together below.

9.3 Key User Interfaces for EOS MODIS and ASTER Data Products

9.3.1 EDG and the WIST

Until recently, the EDG search-and-order tool (Moses 2003) was the primary access point to 2,100 EOSDIS and other Earth science datasets archived at the EOSDIS data centers and several international data centers. During 2007, a total of 73,383 orders were placed and 7.47 million products were ordered via EDG. As of this writing, all EDG users are being transitioned to WIST, as EDG is retired. WIST is accessible from <https://wist.echo.nasa.gov>. At the top of the WIST homepage, the

user is presented options to login or create an account. Registered users may acquire access to data that are restricted to the public/guest users. Registered user may also update their profile along with their contact, shipping, and billing address to later recall and to complete a data order.

WIST's main search interface behaves very similar to the EDG, which reflects architecture driven by technologies available in the early-to-mid-1990s, and the requirement to meet many different users' needs. The EDG and WIST user interfaces are complex, yet users find that they provide the most efficient way to search and access data, and related information from EOSDIS. ECHO's introduction is expected to propel the user communities to create their own views into ECHO, which are tailored and appropriate to their discipline-specific user community. ECHO and WIST provide user tutorials, and also, access to User Services, which responds to user questions and receives system- or data-related feedback.

9.3.1.1 Searching for Data

The WIST Primary Data Search is the default search setting and is divided into four major search criteria areas: data keywords, spatial criteria, temporal criteria, and specialized search constraints (e.g., only granules with browse, day/night flag). It also allows a registered user to save a search to restore in a later session. Alternative search options are available for users with knowledge of Data Center-specific data identifiers (referred to as Data Granule ID and/or Local Granule ID) and simply need to order them from the archives. Users may choose between these search types using the toggle options in the middle of the search screen in the "Choose a Data Search Type" section. All these types are fully described in the "help for this page" link that is available at the top of every page. Also, the title at the top of the search screen indicates which search type is active at a given time.

The first section of the Primary Data Search option is the data keyword selection. The default keyword selection allows users to select keyword criteria "By Discipline." However, important alternatives to select by discipline exist, which are briefly described below.

The first special search feature is the ability to enter criteria into the "Text Search," if the user knows exactly what is needed. For example, if the user knows a dataset's short-name, or a geophysical parameter name, the user needs only to enter that term into the text box at the top right of the search page and select the "go" button to the right of the search box. The search will return a list of datasets that satisfy the term entered into the text search box. The user can then scroll the list of resulting datasets and select the preferred products.

The second special search feature is the content list-driven search defined by various data characteristics (attributes). This mode has two benefits. First, it helps users who are unfamiliar with specific dataset names in EOSDIS, but do know how to characterize data of interest (e.g., Land Cover over Eastern US for January 2007). Second, it helps dataset experts who need to query by detailed dataset and

product-specific characteristics. This option is initiated by scrolling past the list of discipline toggles in the “Choose Dataset” section and selecting the “By Category/Attribute” toggle. This feature was initially developed to assist users unfamiliar with EOSDIS data terminology to navigate the criteria so that informative selections are possible. The extension of this capability to include very specific dataset granule- and product-specific terminology might make this difficult for novices to use. Although dataset experts gain the most benefit here, a novice can still benefit by confining the use of this feature to search by dataset-level attributes (i.e., characteristics that describe whole datasets). Dataset-level attributes include Campaign, DataSet, Parameter, Processing Level, Instrument (sensor), and Source (platform). The novice user can select a category (e.g., Instrument), then select the specific instruments of interest (e.g., MODIS, ASTER). On the basis of these selections, the system will only display applicable (valid) categories and characteristics in subsequent dataset category lists. User caution is prudent when exploring more detailed or product-specific categories. Dataset descriptions are not equally populated. For example, ASTER products do not have a “CLOUD PERCENT” in their descriptions. If a user selects the MODIS and ASTER instruments from the Instrument category, then selects to search by a “CLOUD PERCENT” range in the “Cloud Amount” keyword section, the user will not see ASTER data returned in the results sets. Similarly, if the user selects to search by Day/Night Flag from the “Choose Additional Options” section, the user will not see ASTER data returned in the results sets because the system will not find a match for “Day/Night Flag” for ASTER data. On the other hand, if a user selects a single instrument, or a single dataset, the user can navigate other categories and content listings to view valid information, and thereby use this feature as a tool to become more knowledgeable about EOS data product metadata.

Searching by spatial, temporal, and other optional criteria is described in the on-line tutorial. Once the search is constructed and initiated, WIST searches ECHO to find the data holdings that match the search parameters. Although the EDG search takes place at each archive site using the database search mechanism specific to that archive, and may return results with different terminology standards, WIST sends its searches to the ECHO search engine, where more standards are enforced. The results are therefore presented more consistently.

9.3.1.2 Navigating Search Results

The on-line tutorial describes a straightforward navigation through the results sets. Some unique features of navigation are described below. The first is the capability to customize the results table. With this capability, the user may configure how many result items to display on a page, change the displayed metadata columns, change the displayed order columns, and choose different columns on which to sort at up to three levels. The second feature is the ability to save a text-only version of the results table. This allows the user to save the results set into a table for printing or importing into a spreadsheet for more flexible analysis.

Using “My Folder” is important when performing multiple searches to collect the results set and save those results from one session to the next. Otherwise, starting a new search clears the prior result sets, which are lost.

You can select and display 20 data granules for inter-comparison of geographic footprint coverage using the “Show Map Coverage” button. This display also shows a box that represents the geographic search area specified in the search criteria. Similarly, you can compare temporal coverage using the “Show Time Coverage” button.

9.3.1.3 Browse Images

Users may tap into sample images or other forms of summarized content prior to ordering them. In most cases browse images provide a visual display of subsampled data. Particular products may also offer sample two-dimensional plots or tables. The “Image Quicklook” feature offers users a subsampled JPEG version of the image within the WIST session. Users may also download the original browse image to visualize it with non-WIST tools, although not all products provide easily viewable browse files.

9.3.1.4 Data Access

Several datasets are available on-line on the Data Pools and other on-line archives as discussed in more detail below. The WIST results page indicates the availability of such datasets under its “On-line Access” column. Users may directly download such datasets by accessing the appropriate links in the results page.

9.3.1.5 Ordering

Data not available via on-line access are orderable through a standard process. Users move them to a shopping cart and select ordering options (FTP-Pull, FTP-Push, or media) to place an order. The data granules are acquired from the data center archive and staged for delivery by the user-selected mechanism. The user is informed via e-mail about the order status. An interesting trend in recent years is the decreasing demand for data distribution via media in favor of electronic transfer.

9.3.1.6 Subsetting

WIST allows users to find granules of their choice. However, a granule may contain significantly more data than desired by the user. It may intersect with the user-identified spatial region, but may contain data not in the specific area of interest.

The granule may contain many parameters, although the user is only interested in a few. Reducing the data granule to the interest subset is advantageous both to the user and the data provider. This capability is not uniformly available for all the EOSDIS datasets, and is handled according to the dataset. Presently, some Data Centers offer options through the order mechanism, but the actual subsetting is invoked independently of WIST for the datasets, which offer this capability. Product-specific subsetting capabilities are available in respective Data Center Web sites. Future plans include the ability to invoke subsetting, and other services like reformatting and reprojection through ECHO's middleware.

9.3.2 Data Pools

As Earth science applications become more interactive and/or automated, the community's need for high-performance, direct-access systems increases. The EOS Data Pool's approach to offer current data products via direct on-line access is a high priority (Moore and Lowe 2002). Several Data Centers are now taking advantage of this concept. In particular, the three EOSDIS Data Centers where the EOSDIS Core System (ECS) is currently operating use Data Pools that are built into the ECS. These Data Centers include: the Atmospheric Science Data Center (ASDC), Distributed Active Archive Center (DAAC) at NASA Langley Research Center (LaRC), the Land Processes (LP) DAAC, and the National Snow and Ice Data Center (NSIDC) DAAC. While they share common software, these Data Pools are operated independently. Each Data Center determines how and which high-demand products to offer on-line to meet its user community's needs. Users may request a Data Center's User Services to stage specific products in the Data Pool following their archival, hence tailoring the content to specific user community needs. Products staged in the Data Pool are available to all users. Generally the data flow into and out of the "pool" on a first-in, first-out basis. The product lifetime in the Data Pool depends on the size of the pool itself. As of this writing, the total capacity of the Data Pools at the three DAACs (indicated above) is about 320 terabytes. The on-line storage capacity at all the Data Centers (including ECS and non-ECS components) is about 2 petabytes. Decreasing disk storage costs will enable more data availability on-line. As indicated above, the EDG and WIST interfaces facilitate on-line data access via the Data Pool and also off-line access.

Data Pools' data access interfaces provide a simple browse and click navigation, which allows users to drill down to select specific products. With each selection, the user potentially reduces the number of granule results returned. Once the results are narrowed down to specific granules, the user may directly access the data via FTP. The user may also view the metadata and browse for the granules. The user can "drill-down" using the following search parameters: Data Group, Dataset, Spatial, Date, Time, Cloud Cover, Day/Night Flag, and Science Quality

Flag. The Data Group parameter is the grouping of the data based on the instrument, mission, and major discipline. The Dataset parameter is the primary identifier for the ECS data collection. The Data Group and Dataset parameters are the only required fields. The Spatial parameter is the geographic coverage, represented by latitude/longitude points, wherein, the granules of interest should overlap. The spatial region is selected by drawing a rectangle or a polygon on the map applet, or by specifying the latitude and longitude coordinates for a bounding rectangle in text fields. The Date parameter is the acquisition date range of the granule, which is selected by specifying a month, week, or day on a calendar, or by selecting a beginning date and ending time. The Time parameter is the acquisition time of day for the days within the selected data range. The time of day is selected by specifying a particular time increment in the table, or by selecting a beginning and ending time. The Cloud Cover parameter indicates what percentage of a granule is cloud-covered. The Day/Night Flag parameter indicates whether the granule was collected during the day, night, or both. The Science Quality Flag parameter indicates the science quality (e.g., Passed, Failed, Not Investigated) of a granule's measured parameter.

The granules that match the selected search parameters are displayed as individual rows in the results table. For each granule, the results table displays the granule identifier, granule size, beginning and ending date and time, and day/night flag value. Each row also has linked icons that allow the user to download the data with or without compression, access the full granule metadata record, access the browse image, and add the granule to a shopping cart. The user should add granules to the shopping cart only if they would like to subject them to additional processing (e.g., reformatting, reprojection, subsetting) through the HDF-EOS to GIS (HEG) conversion tool before delivery.

9.3.2.1 LP DAAC's Data Pool

The LP DAAC's Data Pool provides selected data products free of charge at <http://lpdaac.usgs.gov/datapool/datapool.asp>. The available geographic coverage varies by product. Geographic coverage for ASTER data products includes the United States and Territories. ASTER data have no scheduled removal from the Data Pools. Global coverage is available for MODIS land products. Daily MODIS products are in the pool for at least 10 days after acquisition. A minimum of 12 months of acquisitions is available for other MODIS products.

9.3.2.2 NSIDC DAAC's Data Pool

The NSIDC DAAC's Data Pool provides selected data products free of charge at http://nsidc.org/data/data_pool/index.html. Global coverage is available for most MODIS Snow and Ice products. MODIS products are retained in the pool for about 30 days after acquisition.

9.3.3 *EOS Clearinghouse*

ECHO was initiated to expand the search and access options for users trying to access EOSDIS data, allowing users to develop their own tailored user interfaces and applications in contrast to a “one-size-fits-all” solution, EDG. ECHO is middleware that facilitates the sharing of data products and data services in the Earth science community (Burnett and Wichmann 2005; Wichmann and Pfister 2002). ECHO provides a metadata registry and a data services registry comprised of EOSDIS data, and contributions from the wider science community. Via these registries, ECHO enables clients and users to search, browse, place orders, and directly access on-line data across multiple resource providers. ECHO partners with data providers to ingest their metadata and provides application programming interfaces (APIs) for data providers to restrict their metadata using access control lists. ECHO offers open interfaces for clients (machine-to-machine or human-to-machine) to find and use these products and services. ECHO’s capabilities are available to the community via a set of Internet-accessible APIs. ECHO provides client APIs for user registration, searching, and ordering. The Catalog Service API allows users to search for datasets and granules using Spatial (e.g., point, line, polygon, multipolygon, circle), Temporal (e.g., date range, day/night/both), Keyword (e.g., dataset id, sensor name), Numeric (e.g., cloud cover percentage), and Boolean (e.g., only products with browse data, only on-line products) search parameters. Once the data of interest are found, the user can directly access the data if they are on-line, or can place an order, which ECHO will broker to the appropriate data provider. ECHO also allows users to establish data subscriptions. With these APIs, clients are free to provide community-specific views, or to implement new technologies for interacting with users. Clients exist in the form of a GUI that provides a discipline- or application-focused search and access service for a particular community, or in the form of a set of machine scripts, which drive application, modeling, or decision support system functions. In either case, the ECHO middleware is hidden from the end user.

The ECHO Web site (<http://eos.nasa.gov/echo>) provides information needed for data and service providers and client developers to become partners in ECHO. It provides operational system status, information for and about data, client and service partners, ECHO development status and future plans, a mechanism to submit comments and feedback, latest ECHO news and announcements, and references including presentations from ECHO partner training sessions.

9.3.4 *Global Change Master Directory*

The Global Change Master Directory (GCMD; Olsen 2000; <http://gcmd.nasa.gov>) holds more than 25,000 Earth science dataset and service descriptions relevant to the Earth science community. Specific dataset and service descriptions are found by using the “drill-down” interface made up of discipline-specific keywords. Each description includes information, such as a text summary, geographic and temporal

coverage, data archive center information, and location of the data or service, which can help determine whether the data or service meets the users' needs. Users may utilize the GCMD to search for information about Earth science data and services. The users are then directed to the EDG, WIST, or Data Center-specific systems to order or access EOSDIS data.

9.3.5 Interfaces Specializing in Land Processes Data

In addition to the general EOSDIS user interfaces (e.g., EDG, WIST) to search and order or access data, there are several discipline-focused user interfaces offered by the Data Centers and their host organizations. This section presents three examples that are tailored to search and obtain land processes data. Other examples are discussed in Chap. 8.

9.3.5.1 United States Geological Survey: Global Visualization Viewer

The Global Visualization Viewer (GloVis) developed and operated by the USGS is an on-line, browse-based search and order tool. This tool offers access to all available browse images from EO-1, Landsat (1–5 and 7) and MRLC from the USGS inventory, and ASTER and MODIS from the LP DAAC inventory. GloVis users start with a graphic map display of the world, and may select any area of interest. GloVis displays a browse image of the selected area and the adjacent scene locations immediately. The user can pan and select any of the scenes around the area of interest. The user can also select the observation dates for the specific regions of interest. The selected images are added to a list of items to order. GloVis provides additional features such as cloud cover information, date limits, user-selected map layers (e.g., political boundaries, roads, railroads), and access to metadata. Users, through GloVis' ordering interface, may specify images to order, their preferred format and type of media or electronic delivery. The ordering interface also provides pricing information (if relevant) and a mechanism to collect user payments.

9.3.5.2 Oak Ridge National Laboratory's Mercury System

The Mercury system, developed by the Department of Energy's Oak Ridge National Laboratory, allows users to search the ORNL DAAC and other providers' data. The Mercury system harvests metadata on a regular basis to facilitate searches, and directs users to other providers' sites for access to data. The providers (e.g., Land Validation team, Safari 2000 campaign, Long Term Ecological Research Network) may select which of their metadata and data are made visible via Mercury by maintaining text files of URL lists. Mercury uses these lists to harvest the metadata on a daily basis. To search and order data, a user can specify a set of keywords, spatial

and temporal bounds, and/or a set of sources (databases). The user is then provided with a display of the database names and the number of entries found in each of the databases matching the user's specifications. The user selects a database name to display a summary of the metadata. The metadata summary includes links to the datasets, which are downloadable either immediately or later. A shopping cart facilitates accumulating datasets that are identified and downloaded together as a group.

9.3.5.3 MODIS Search 'N Order Web Interface

The MODIS Search 'N Order Web Interface (SNOWI) is a quick and simple way to search and order MODIS gridded Snow and Ice products from the NSIDC DAAC. The user specifies a few search parameters, such as dataset name, temporal date range, and latitude/longitude coordinate range.

9.4 Future

As discussed above, EOSDIS continues to serve a broad user community by disseminating large amounts of data on a regular basis for the past several years. EOSDIS has undergone several technological and requirements changes since it was conceptualized in the late 1980s. Several incremental improvements in processing and performance have materialized, while new functionality continues to improve user access, distribution, and archive management. The underlying design, however, remained essentially the same until recently. A recent examination of EOSDIS' operations and lessons learned has generated a desire to achieve significant improvements in a variety of areas. To accomplish this, in 2004, NASA established an EOSDIS Elements Evolution Study Team (EEEST) and an EOSDIS Elements Evolution Technical Team (EEETT; Esfandiari et al. 2006). The EEEST's role was to provide an external viewpoint and guidance. The EEEST developed a data systems' vision for the year 2015. The EEETT was also responsible to develop an approach and an implementation plan to fulfill the objectives set forth in the vision. The results of these efforts are published at <http://eosdis-evolution.gsfc.nasa.gov>. The goals established in the Vision 2015 parsed into IT systems management tenets are shown in Table 9.1.

Although these goals are important to achieve the Vision, from the point of view of data distribution systems, those relating to the tenets titled "EOS Data Interoperability" and "Future Data Access and Processing" are particularly significant. Currently, a first step in the evolution of EOSDIS elements was defined, and is being implemented. This step is expected to move the system in the direction articulated in the Vision. Some of the characteristics of this current work are shown in Table 9.2.

The future steps in evolution specific to EOSDIS elements will depend on the outcome of the initial step indicated above. However, based on the Vision, we

Table 9.1 EOS Data and Information System evolution vision tenets and goals

| Vision Tenet | Vision 2015 Goals |
|-----------------------------------|---------------------------------------------------------------------------------------------------------------------------------------------------------------------------------------------------------------------------------------------------------------------------------------------------------------------------------------------------------------------------------------------------------------------------------------------|
| Archive Management | <ul style="list-style-type: none"> NASA will ensure safe stewardship of the data through its lifetime. The EOS archive holdings are regularly peer reviewed for scientific merit. |
| EOS Data Interoperability | <ul style="list-style-type: none"> Multiple data and metadata streams can be seamlessly combined. Research and value-added communities use EOS data interoperably with other relevant data and systems. Processing and data are mobile. |
| Future Data Access and Processing | <ul style="list-style-type: none"> Data access latency is no longer an impediment. Physical location of data storage is irrelevant. Finding data is based on common search engines. Services invoked by machine-machine interfaces. Custom processing provides only the data needed, the way needed. Open interfaces and best practice standard protocols universally employed. |
| Data Pedigree | <ul style="list-style-type: none"> Mechanisms to collect and preserve the pedigree of derived data products are readily available. |
| Cost Control | <ul style="list-style-type: none"> Data systems evolve into components that allow a fine-grained control over cost drivers. |
| User Community Support | <ul style="list-style-type: none"> Expert knowledge is readily accessible to enable researchers to understand and use the data. Community feedback provided directly to those responsible for a given system element. |
| IT Currency | <ul style="list-style-type: none"> Access to all EOS data through services at least as rich as any contemporary science information systems. |

Table 9.2 Characteristics of first step in EOS Data and Information System evolution

| Action | Expected result |
|--------------------------------------------------------------------------------------------------------------------------------------------------------------|--------------------------------------------------------------------------------------------------------|
| Produce some of the high-volume data products on-demand | Reduction in archive size |
| Increase on-line archive capacities | Improved access to frequently used and key data products |
| Rearchitect elements of existing systems: transition to commodity-based hardware; automate more functions; streamline functions to reduce custom code | Reduced maintenance and operations costs; improved scalability |
| Provide more postprocessing (e.g., subsetting and reprojection) of granules on-demand than currently available | Better tailored products; increased flexibility for users; reduction in network bandwidth requirements |
| Consolidate operations at any given Data Center to a single system | Reduced maintenance and operations costs |
| Transition some of the data system functions to science team organizations | Improved alignment with day-to-day science activities |
| Improve middleware services including performance and easier access; provide improved methodologies to facilitate users to become value-added data providers | Increased support for distributed, heterogeneous provider environment |

can speculate here about the future in the broader community context from the perspective of data distribution. To help in this discussion, we first define four levels of interoperability: Directory Level, Inventory Level, Data Object Level, and Service Level:

- Directory-level interoperability implies that a user is able to find, through a directory, the location of the data or service. The directory facilitates the process by providing a link (URL) to the data/service provider (DSP). The user then obtains the data or service from the DSP. GCMD offers this type of interoperability.
- Inventory-level interoperability implies that a user is able to locate from a single location, the data granules that a set of DSPs can provide. One or more data granules are obtained (ordered or accessed) from the DSPs. WIST supports this type of interoperability. The ECHO middleware helps provide this type of interoperability by being a metadata clearinghouse and supports development of additional specialized clients with at least the same level of interoperability.
- Data object-level interoperability implies that a user is able to locate and access data (e.g., records) within granules located at a set of DSPs and manipulate from within his/her software. Enabling this level of interoperability involves, for example, conversions of native formats into those acceptable to the software that manipulates the data. OPeNDAP is an example of a protocol that provides this type of interoperability.
- Service-level interoperability implies that a user is able to access individual data objects within granules located at a set of DSPs, link them with appropriate services, chain the services to perform a sequence of meaningful operations, execute the software in a fully distributed environment, and obtain the required results.

The present state of technology offers directory level interoperability among a large community of DSPs, granule level interoperability within smaller subsets of DSPs (e.g., Data Centers) with a mutually agreed upon set of interface protocols, and data object level interoperability within subsets of DSPs that have (as in the case of granule level interoperability) agreed upon interface protocols. Service level interoperability is not common among DSPs in the remote sensing community. The Vision calls for the interoperability that is significantly more widespread than is currently being achieved wherein a highly distributed and heterogeneous set of DSPs interoperate at the service level. The following are the main challenges to achieve this aspect of the Vision:

- On-line availability and access of all user-sought data are important to remove data latency concerns. The EOSDIS has made initial strides to make more data available on-line. As the storage and computing costs decrease, facilitating on-line availability or quickly processing the desired data becomes more feasible.
- Data needs to flow where the services are and vice versa. In the former case, bandwidth becomes a limiting factor as data providers need to send large datasets to the service provider's site. The cost of network bandwidth is quite rapidly declining. Therefore, this limitation should gradually disappear. In the latter case,

software compatibility and data system security are of concern, since it involves execution of externally developed software on a given DSP's system.

- Agreements are needed among participating DSPs regarding data formats, naming conventions, and gridding schemes. Data format compatibility, naming conventions, and gridding schemes are all critical if data from multiple sources are to provide inputs to feed models, applications, and decision support systems. This requires community consensus, and open sharing of interfaces and protocols.

The science and information technology communities are making progress to address these challenges. For example, The Earth Science Information Partners (ESIP) Federation (with its Foundation for Earth Science – <http://www.esipfed.org/foundation/index.html>) is developing a portal to consolidate the information resources from the participating organizations, and to provide basic visualization tools. The ESIP Federation consists of over 110 member organizations, which include the NASA-funded Data Centers and REASoN Projects, as well as NOAA data centers, universities, non-profit organizations, non-governmental organizations, and commercial entities. The Earth Information Exchange portal is being architected as a gateway for viewing and accessing Earth science data, applications and supporting documentation. The Global Grid Forum (<http://www.gridforum.org/>), an international community representing over 400 organizations, is leading global standardization for grid computing in various scientific and technical areas. The Global Alliance (<http://www.globus.org/>) is actively developing technologies needed for “grid” that enables sharing of computational capacity, databases and other on-line tools securely among multiple organizations while preserving local autonomy. The Federal Geographic Data Committee's (FGDC) Geospatial Applications and Interoperability Working Group is promoting the use of geo-referenced information from multiple sources over the Internet. The geospatial interoperability is based on voluntary consensus standards governing geospatial concepts and their inclusion in communication protocols, software interfaces, and data formats (<http://gai.fgdc.gov/girm/v1.1>). In addition, NASA has established a set of four Earth Science Data System Working Groups addressing technology infusion, software reuse, standards processes, and metrics. These working groups are active since 2004, and are an important mechanism to provide community-best practices and guidance to NASA.

In 2005, 16 proposals were selected for NASA's ACCESS (Advancing Collaborative Connections for Earth System Science) Program. These awards focus on improving NASA's Earth science data systems and also help NASA evolve EOSDIS. The overall goals of these first ACCESS projects are “...to enhance existing or create new tools and services that support NASA's evolution to Earth-Sun System Division science measurement processing systems and support NASA's Science Focus Area (SFA) community data system needs.” Abstracts for all these 2005 ACCESS awards are available at http://nspires.nasaprs.com/external/viewrepositorydocument/29166/NNH05ZDA001_ACCESS_SUMMARIES.pdf. Many of these projects apply Web services architecture and open Geographical Information System (GIS) standards, specifically those from the Open Geospatial

Consortium (OGC). The use of existing information technology capabilities, standards, and protocols is essential for these projects to rapidly enable more robust tools and services in support of NASA's science user communities. ACCESS projects of interest to the land remote sensing community are described below:

- *R. Barry (University of Colorado) – Discovery, Access, and Delivery of Data for the International Polar Year (IPY).* Adopt principles of Web Services architecture to develop and implement a portal for cryospheric data and related information
- *A. Bingham (Jet Propulsion Laboratory) – Earth Science Datacasting – Informed Data Pull and Visualization.* On the basis of the popular concept of podcasting, which gives listeners the capability to download only those MP3 files that match their preference, develop “earth science datacasting” to give users control to download only the Earth science data files that are required for a particular application
- *Y. Bock (Scripps Institution of Oceanography, UCSD) – Modeling and On-the-fly Solutions in Solid Earth Science.* Develop a unified, on-the-fly, Web Services-based observation/analysis/modeling environment for geophysical modeling and natural hazards research, a plug-in service for early warning systems and transfer of rapid information to civilian decision makers and the media, and an educational tool
- *J. Masek (Goddard Space Flight Center) – Building a Community Land Cover Change Processing System.* Create infrastructure for a distributed Land Cover Change Community-based Processing and Analysis System (LC-ComPS). The LC-ComPS environment is envisioned as a distributed network of processing centers, linked with data archives via Data Grid technology, to allow regional- and continental-scale land cover analysis at high resolution
- *K. McDonald (Goddard Space Flight Center) – The Development and Deployment of a Coordinated Enhanced Observing Period (CEOP) Satellite Data Server.* Interconnect two existing technologies, the OGC Web Coverage Server and the OPeNDAP. Utilize geospatial processing capabilities of the OGC Web Coverage Server and provide transparent data access to OPeNDAP-enabled science data applications and analysis for clients used by most of CEOP scientists
- *J. Morisette (Goddard Space Flight Center) – Improving Access to Land and Atmosphere science products from Earth Observing Satellites – Helping NACP Investigators Better Utilize MODIS Data Products.* Streamline access to MODIS data products, reduce data volume by providing only those data required by the user, and improve the utility of data products. Provide North American Carbon Program (NACP) investigators with custom preprocessing of MODIS data that will allow for direct ingest into an investigators modeling framework

These projects are good examples of progress being made both by NASA and its affiliated user communities that are expected to have a guiding influence on the future of Earth science data distribution systems. As attested by the history of information technology over the past decade, accurately predicting how data systems

will evolve over the next 10 years is difficult if not impossible. However, Vision 2015, discussed above, provides the community's expectations, and NASA's initial steps and external developments support progress toward that vision.

9.5 Appendix: Acronyms

| | |
|---------|--------------------------------------------------------|
| API | Application Programming Interface |
| CEOS | Committee on Earth Observing Satellites |
| CINTEX | CEOS Interoperability Experiment |
| CIP | CEOS Interoperability Protocol |
| DAACs | Distributed Active Archive Systems |
| ECHO | EOS Clearinghouse |
| ECS | EOSDIS Core System |
| EDG | EOS Data Gateway |
| EDGRS | Earth Data Gathering and Reporting System |
| EMSn | EOS Mission Support Network |
| EO-1 | Earth Observing-1 |
| EOS | Earth Observing System |
| EOSDIS | EOS Data and Information System |
| ESDIS | Earth Science Data and Information System |
| ESSn | EOS Science Support Network |
| GCMD | Global Change Master Directory |
| GSFC | Goddard Space Flight Center |
| LaTIS | LaRC TRMM Information System |
| LTA | Long Term Archive |
| MBS | Measurement-based Systems |
| MODAPS | MODIS Adaptive Processing System |
| MRLC | Multiresolution Land Characteristics |
| NOAA | National Oceanic and Atmospheric Administration |
| OCDPS | Ocean Color Data Processing System |
| OPeNDAP | Open-source Project for a Network Data Access Protocol |
| SDPS | Science Data Processing Segment |
| SIPS | Science Investigator-led Processing System |
| SPSO | Science Processing Support Office |
| TSS | TRMM Support System |
| USGS | United States Geological Survey |

Acknowledgments Figure 9.1 is adapted from the EOS Reference Handbook, NASA, 1993, page 18, modified and updated. Figure 9.2 has evolved over time from several presentations by managers at the ESDIS Project, NASA GSFC. Figure 9.4 is adapted from a presentation titled "EOSDIS Elements Evolution Tiger Team Progress Report," January 20, 2004, by Glenn Iona, NASA GSFC. The authors appreciate the detailed review and comments by Frances Lindsay and Martha Maiden (NASA Headquarters) on a draft version of this chapter. They also appreciate the encouragement and support of Mary Ann Esfandiari (NASA Goddard Space Flight Center).

References

- Burnett M, Wichmann K (2005) ECHO – leveraging web service technologies to support a net-centric science enterprise. In: IGARSS 2005, Seoul, South Korea, July 25–29, 2005
- Esfandiari MA, Ramapriyan HK, Behnke J, Sofinowski E (2006) Evolution of the Earth Observing System (EOS) Data and Information System (EOSDIS). In: IGARSS 2006, Denver, CO, July 31–August 4, 2006
- Moore JM, Lowe D (2002) Providing rapid access to EOS data via data pools. In: SPIE Annual Meeting, Earth Observing Systems VII, Seattle, WA, July 7–10, 2002
- Moses JF (2003) EOS data gateway: the latest in data and data access. In: American Society for Photogrammetry and Remote Sensing (ASPRS) 2003 Annual Conference, Anchorage, AK, May 5–9, 2003
- Olsen LM (2000) Discovering and using global databases. In: Tateishi R, Hastings D (eds) Global environmental databases: present situation; future directions. International Society for Photogrammetry and Remote Sensing (ISPRS), Amsterdam
- Ramapriyan HK, McConaughy GR (1991) Version 0 EOSDIS – an overview. In: Technical Papers, ACSM-ASPRS Annual Convention, vol. 3, pp 352–362, March 1991
- Wichmann K, Pfister R (2002) ECHO – a message-based framework for metadata and service management. In: Earth Science Technology Conference, Pasadena, CA, June 11–13, 2002

Chapter 10

The Language of EOS Data: Hierarchical Data Format

Larry Klein, Andrey Savtchenko, Abe Taaheri, Cid Praderas,
and Siri Jodha Singh Khalsa

Abstract This chapter describes the data storage format used by NASA's Earth Observing System (EOS), which was chosen to package the heterogeneous data products produced by the ASTER and MODIS instruments. HDF was chosen as the most efficient, general-purpose format at the time to store and distribute Earth science data. We discuss extensions to HDF created to store measurements acquired by the EOS instruments, and also discuss particular adaptations by the MODIS and ASTER teams. We also discuss several applications, which are capable of accessing data in HDF directly.

10.1 Introduction

As part of the NASA Earth Observing System (EOS) requirements definition process, several driving forces for data storage and distribution emerged. The sheer volume and number of files of anticipated data were considered, as was the number of scientific disciplines represented. Data storage and retrieval from multiple archive centers, and the need to intercompare data from different instruments was essential. Data complexity, granule size, complex metadata, rapid access, software development on diverse platforms, and computer languages also loomed large. System designers were driven to consider standard data models and generalized data formats as solutions to the storage and access problem. The desire to move away from paper documentation required self-describing formats. Production and distribution requirements favored disk-based over sequential storage formats. This chapter describes the history and development of the data standard for the project. We also survey how the MODIS and ASTER science and instrument teams, and data users use HDF.

L. Klein (✉)
Wyle Information Systems, Lanham, MD, USA
e-mail: lklein@sesda2.com

10.2 Brief History and Evolution of HDF

10.2.1 Early History of Scientific Data Formats

Science data formats have evolved dramatically over the decades since computers were first employed in scientific work. Early storage mechanisms for science data were machine and computer language-dependent. They were built for sequential or tape storage, were not self-describing, and were transferable between different computer architectures only with great difficulty. The development of general purpose data storage formats was driven by several factors, including the complexity of modern science data, which can have heterogeneous parts and multiple interdependent files; accessibility to grid or parallel computing systems; and accessibility by many common computer languages on diverse computing platforms. Another driving factor was a format, which was distributed, accessible to several users, science disciplines, and varied software applications. Some of the more popular scientific application data formats to have emerged are as follows:

- *ASCII (American Standard Code for Information Interchange)*: forerunner of encoding text for computers
- *FITS (Flexible Image Transport System)*: used by the astronomical community to store image and numerical data
- *BUFR (Binary Universal Form Representation of meteorological data)*: used by the weather community to store numerical data in an internal format. BUFR access software contains translators to convert data to native machine formats
- *GRIB (Gridded Binary)*: used by the meteorological community to store variable length arrays of science data

The above formats are not general purpose ones, and were designed for sequential access, and to store specific types of data. Note that BUFR and GRIB are operational formats, used by the meteorological community.

The following formats are disk-based and randomly accessible. CDF, netCDF, and HDF, in particular, were designed as general-purpose formats capable of handling a variety of data models:

- *TIFF (Tagged Image File Format)*: developed primarily to store raster images
- *GeoTIFF*: an extension of TIFF, which includes geolocation information associated with the image data
- *CDF (Common Data Format)*: designed by NASA as a general purpose standard for science data. The format is disk-based or random access and uses External Data Representation (XDR) format to represent data in a machine-independent manner. CDF is accessible in several common languages, including C and FORTRAN
- *netCDF*: developed by the National Center for Atmospheric Research extended CDF to include information on dimension, variables and attributes. The netCDF format is accessed through a user interface, rich in functionality
- *HDF (Hierarchical Data Format)*: developed by the National Center for Supercomputing Applications (NCSA), University of Illinois, supports a variety

of data models commonly used by scientists and engineers; HDF is described in more detail in Sect. 10.2.2

- *XFDU (XML (eXtensible Markup Language) Formatted Data Unit)*: a standard recommended by the Consultative Committee on Space Data Systems (CCSDS)

10.2.2 *Origins of HDF*

HDF was developed to aid scientists and programmers to store, transfer, and distribute data and products created on various machines and with different software. HDF was selected by the NASA Earth Science Data and Information Systems (ESDIS) Project as the format for production, distribution, and storage of science and engineering products produced by the EOS series of spacecraft. HDF files are accessed through an Applications Programming Interface (API) and functionality provided by a subroutine library. The API provides access in FORTRAN, C, and C++. The HDF library is discussed in detail in Sect. 10.3.

10.2.2.1 **Features of HDF**

HDF is a multiobject file format to share and store scientific data. Some of the most important features of HDF include the following:

- *Self-describing*. For each data object in an HDF file, information (or metadata) about the data type, size, dimensions, and location are stored within the file itself.
- *Extensible*. HDF is designed to accommodate new data types and data models as they emerge.
- *Versatile*. HDF supports six different data types and provides software and applications to read and write these data types in HDF.
- *Flexible*. HDF allows grouping and storing different data types either in the same file, or in more than one file; an HDF file's various datasets are stored in external files, which potentially allow separating large data files into smaller files.
- *Portable*. HDF software is platform-independent, and shared across most common computer platforms.
- *Standardization*. HDF standardizes the formats and descriptions for several commonly used data types (i.e., arrays, images, etc.).
- *Accessibility*. HDF is freeware and is available in the public domain. See <http://www.hdfgroup.org> and references therein.

10.2.2.2 **The HDF Data Model**

HDF was designed to support data structures most commonly used by scientists and engineers. For example, the library supports raster images, color or gray scale palettes, multidimensional arrays, text strings, and statistical data (in the form of tables). The library enables users to build, populate, and access the following data types:

- *Scientific Datasets (SDS)* – multidimensional integer or floating point arrays
- *Tables (Vdata or Vertex Data)* – multivariant data stored as records in a table
- Raster images (8-bit and 24-bit) and accompanying palettes
- *Annotations* – text strings to describe files and parts of files (global and attribute metadata)

See Sect. 10.3.1 for details on the HDF Data Model.

10.2.3 Why NASA Chose HDF for EOS; What Other SDFs Were Considered?

In the early 1990s, NASA undertook a study of available formats in which to store and distribute the volumes of data expected from its EOS program. At least three space platforms, which carried a number of imagers, profilers and sounders, were slated to produce many Petabytes (10^{18} bytes) of useful science data. A flexible format extensible enough to support heterogeneous data on varied operating systems was required.

For reference, we include the initial NASA direction concerning EOS and standard formats for EOS standard products:

The Earth Science Data and Information System Project has undertaken an analysis of available data format standards over the last four years. This analysis received input from Distributed Active Archive Centers (DAACs), EOS Instrument Investigators, related earth science projects, international investigators, computer scientists, and other members of the EOS community. As a result of this study, the ESDIS Project selected the National Center for Supercomputing Applications' Hierarchical Data Format (HDF) as the Standard Data Format (SDF) for Version 0 System distribution of science data. Based on successful experience in Version 0, including use by EOSDIS Core System (ECS) DAACs, the Pathfinder project, and associated earth science projects, the ESDIS Project plans to adopt HDF as the baseline EOSDIS Standard Data Format for science and science-related data. In 1994, HDF was adopted as a baseline standard for EOSDIS Core System development of standard data product generation, archival, ingest, and distribution capabilities. The ESDIS Project will support the evolution of the EOSDIS SDF as needed to meet the requirements of science data users and producers.

This statement (ESDIS Internal Document, 1996) provided the beginnings of HDF and HDF-EOS development for the ESDIS Project. ESDIS is the ground system supporting the EOS mission.

Other general purpose formats available at the time of this study were CDF and netCDF. CDF had a more limited data model than HDF and also limited access to the disk format. netCDF is an extension of CDF that has a user interface rich in functionality, but like CDF, does not expose the underlying disk format. Knowledge of the disk format was considered important for the development of the mission ground system, since that knowledge provided flexibility to build the most efficient data storage and access functionality. The other formats identified in Sect. 10.2.1 were considered too machine-specific or function-specific for the heterogeneous requirements of the EOS.

10.2.4 *Pros and Cons of HDF (With Respect to Earth Science Data)*

As noted above, HDF met criteria for flexible storage format, portability, extensibility, and accessibility. There were several disadvantages, however. A primary problem was that the format lacked necessary features for Earth science data. For example, there were no standards to store geolocation data. The user interface was very complex; more so than the specialized interfaces to which prospective users are accustomed. Scientists and engineers used to simple C and FORTRAN I/O ran the risk of being confronted by a steep HDF learning curve. In addition, it is easy for data producers to create complex data structures for processing convenience. These complex data structures may prove problematic while accessing the data, and may create inefficiencies for applications using the data. Tasks such as postprocessing could become very inefficient.

10.3 Overview of the HDF Data Model

10.3.1 *HDF4*

HDF supports several different data models, methods by which users may store and access most scientific data types. The components of the model include the following:

- *SDSs* are used to store n -dimensional gridded data. Any of the “standard” numeric data types are supported: 8-, 16-, and 32-bit signed and unsigned integers, and 32-bit and 64-bit floating point values. In addition, the Science Data (SD) interface allows creation of datasets with variable bit lengths (1–32 bits). Metadata such as dimension scales and attributes are stored in an SDS. With the SD interface, user-defined as well as predefined attributes are available.
- *Raster Data*. HDF supports the storing of general, 8-bit, and 24-bit raster images. The General Raster Image interface is designed to provide a means to store raster image data in 8-bit and 24-bit formats, similar to the SDS dataset model. The raster palette and dimension information storage is included. Similar to other HDF data models, the raster model supports all standard HDF compression methods (e.g., RLE, JPEG, GZIP, SZIP, and adaptive Huffman).
- *Text Data*. Any object in an HDF file can have associated annotations. A number of annotation types exist: labels are short strings with the “name” of a data object; descriptions are longer text segments, which are useful to provide more in-depth information about a data object; and file annotations apply to all the objects in a single file.
- *Table*. The Vdata model provides an interface to two basic HDF building blocks, Vgroups and Vdatas. Vgroups are generic grouping elements, which

allow a user to associate related objects within an HDF file. As Vgroups can contain other Vgroups, it is possible to build a hierarchical file. *Vdatas* are generic list objects (tables). Data are organized into “fields” within each Vdata. Each field is identified by a unique “field name.” Each field type may represent any of the basic HDF-supported number types. Fields of different types may exist within the same Vdata. By combining Vdatas in Vgroups, it is possible to represent higher-level data constructs such as mesh data, multi-variant datasets, sparse matrices, finite-element data, spreadsheets, splines, non-Cartesian coordinate data, etc. User-defined attributes are available with both Vdatas and Vgroups.

10.3.2 HDF5

In 2001, a new version of the HDF format and API were introduced. HDF5 provides many upgrades over its predecessor, including a more generalized data model, updated user interface, and ability to perform parallel I/O. It also provides a completely different user interface from HDF4. The EOS Aura mission employs the HDF5 and EOS extensions, while the HDF4 format is used by EOS Terra and Aqua missions. The latter includes MODIS and ASTER. As of this writing, both teams are investigating conversion of HDF4- to HDF5-based format, but have not yet done so. For this reason, we will not elaborate on HDF5 or its EOS extensions in this chapter. For further information, please refer the following URL: <http://www.hdfgroup.org>

We note that HDF5 has been proposed as a NASA Earth Sciences Enterprise (ESE) Community Standard. The reader is referred to HDF5 Data Model, File Format and Library HDF5.1.6 ESE RFC, 2005, for details of the proposal. This effort was undertaken to promote HDF5 as a standard for science data packaging beyond the EOS program. No similar proposed standard for HDF4-based format exists.

10.3.3 HDF-EOS

HDF data models map well to data types required by the earth sciences community. Examples include raster images, multidimensional arrays, and text blocks. Other EOS data types exist, which do not map directly to HDF data models, especially geolocated data types. Examples include projected grids, satellite swaths, and field campaign or point data. Therefore, some additions to conventional HDF data models were required to fully support these data types.

To bridge the gap between the needs of EOS data products and HDF’s capabilities, new EOS-specific data models – *Point*, *Swath*, and *Grid* – were defined within the HDF framework. Each of these new data models was constructed using conventions for combining standard HDF data models, and is

supported by an API, which aids the data product user or producer in the application of the conventions. The APIs enable creation and manipulation of data products specific to each data type without the users' need to manipulate the underlying HDF objects. The sum of these new APIs comprises the HDF-EOS library. The *Point* interface is designed to support data with associated geolocation information, but is not organized or well-defined spatially or temporally. The *Swath* interface is tailored to support time-ordered data such as satellite swaths (which consist of a time-ordered series of scan lines) or profilers (which consist of a time-ordered series of profiles). Profile data are swath-like data without georeferencing information attached. The *Grid* interface is designed to support data stored in a rectilinear array based on a well-defined and explicitly supported projection.

HDF-EOS files have four distinguishing components: (1) a data model that describes Grid, Point, and Swath; (2) a file format (HDF); (3) an API, which implements the data model and enforces the standard; and (4) EOSDIS Core System (ECS) standard metadata written as global attributes. The *data model* provides the format to allow creation, storage, and access to Grid, Point, and Swath structures. It specifies the packaging of geolocation data, science data, and metadata. The *file format* describes how the HDF-EOS data structures are represented in basic HDF4 objects. These objects in turn specify how the structures are stored in memory, or on disk or other media. HDF-EOS is self-describing in that the internal structure of the files is described within the file. The *I/O library* implements the data model in a number of programming languages, including FORTRAN, C, and C++.

The HDF4 data model and user interface are very different from that of the newer HDF5 model and interface. The corresponding HDF-EOS data models are the same, and the user interface is very similar. See details in the [HDF-EOS Library Users Guide](#), Volumes 1 and 2, and the [HDF-EOS Interface based on HDF5 Volumes 1 and 2](#) (consult the URLs provided in the References). HDF-EOS was developed in consultation with the [HDF Group](#) at NCSA (now known as *The HDF Group*, www.hdfgroup.org).

10.3.3.1 Swath Data Model

The Swath concept for HDF-EOS is based on a typical satellite swath, where an instrument acquires a series of scans across the ground track of the satellite as it moves along that ground track. Figure 10.1 shows this traditional view of a swath.

A standard Swath is comprised of four primary parts: data fields, geolocation fields, dimensions, and dimension maps. An optional fifth part called an index may additionally support certain kinds of access to Swath data. Each of the parts of a Swath is described below:

- *Data Fields* are the main part of a Swath from a science perspective. Data fields usually contain the raw data (often as *counts*) acquired by the sensor or

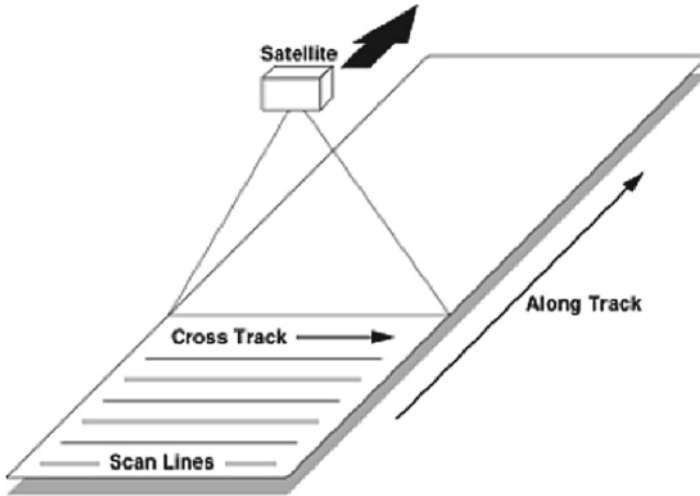


Fig. 10.1 A typical satellite instrument swath

parameters derived from that data on a value-for-value basis. All other parts of the Swath exist to provide information about the data fields or to support particular types of access to them. Data fields typically are two-dimensional arrays, but may have as few as one dimension or as many as eight, in the current library implementation. They can have any valid C data type.

- *Geolocation Fields* enable accurately linking the Swath to particular points on the Earth's surface. To do this, the Swath interface requires the presence of at least a time field ("Time") or a latitude/longitude field pair. Geolocation fields are by necessity either one- or two-dimensional, and either float or double data type. The "Time" field is always in International Atomic Time (TAI) format.

Figure 10.2 shows a "data view" of a swath structure. Here, time may represent the track parameter.

- *Dimensions* define the data axes and geolocation fields by giving them names and sizes. The library use requires defining the dimensions before using them to describe data or geolocation fields. Every axis of every data or geolocation field must have a dimension associated with it. However, there is no requirement regarding their uniqueness. In other words, different data and geolocation fields may share the same named dimension. Sharing dimension names allows the Swath interface to make some assumptions about the data and geolocation fields involved, which may reduce the complexity of the file and simplify the program creating or reading the file.
- *Dimension Maps* are the glue that holds the Swath together. They characterize the relationship between data fields and geolocation fields by defining, one-by-one,

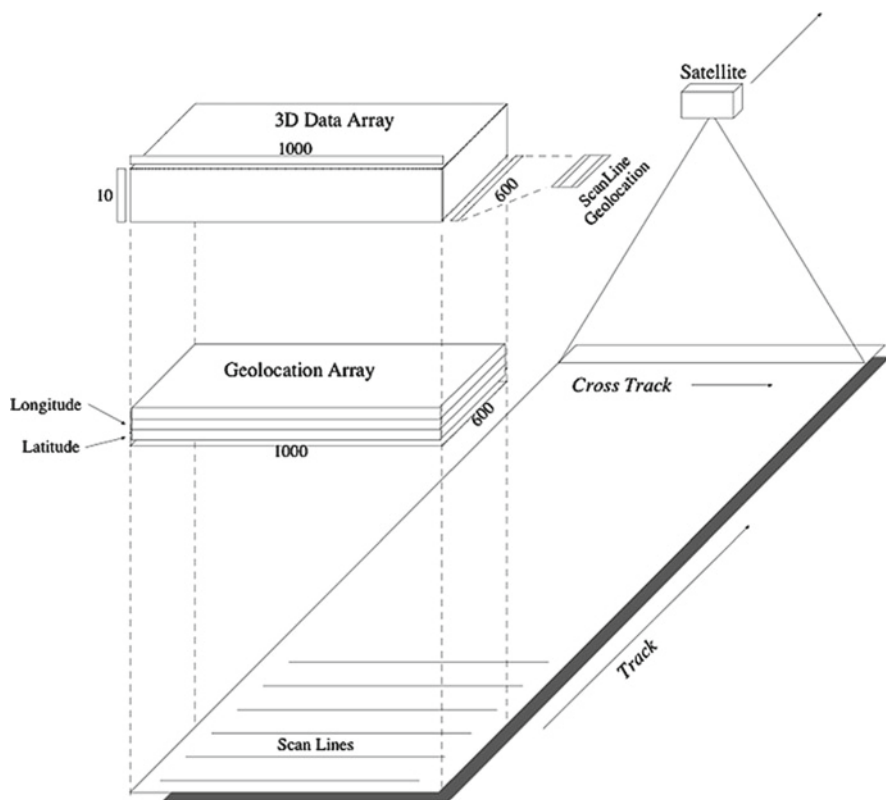


Fig. 10.2 Conceptual view of a swath example, with 3D array, time/geolocation array, and geolocation table

the relationship of each dimension of each geolocation field with the corresponding dimension in each data field. In cases where a data field and a geolocation field share a named dimension, no explicit dimension map is needed. In cases where a data field has more dimensions than the geolocation fields, the “extra” dimensions are left unmapped.

10.3.3.2 GRID Data Model

As described in Sect. 10.3.3.1, Swaths carry geolocation information as a series of individually located points (tie points or ground control points). Grids, though, carry their geolocation in a much more compact form. A grid merely contains a set of projection equations (or references to them) along with relevant projection parameters. Together, these relatively few pieces of information define the location of all points in the grid. The equations and parameters are then used to compute the latitude and longitude for any point in the grid.

Each data field constitutes a map in a given standard projection. Although several independent Grids may exist in a single HDF-EOS file, within each Grid, only one projection is chosen, which applies to all data fields. Figure 10.3 shows how a single data field may look in a Grid using the Mercator projection.

Three important features of a Grid dataset include the data fields, the dimensions, and the projection. Each of these is discussed in detail below:

1. *Data Fields* are the most important part of the Grid. Data fields in a Grid dataset are rectilinear arrays of two or more dimensions. Most commonly, they are simply two-dimensional rectangular arrays. Generally, each field contains data of similar scientific nature, which must share the same data type. The data fields are related to each other by common geolocation. That is, a single set of geolocation information is used for all data fields within one Grid dataset.
2. *Dimensions* are used to relate data fields to each other and to the geolocation information. Correct interpretation requires that each data field use the two predefined dimensions: “XDim” and “YDim.” These two dimensions are defined when the grid is created, and are used to refer to the *X* and *Y* dimensions of the chosen projection. A Grid dataset’s data field may contain eight dimensions, but it is unlikely that many fields may need more than three predefined dimensions, XDim, YDim, and a third one for height or depth.
3. *Projections* are the heart of the Grid. Using a projection in a Grid creates a substantial difference from a Swath. The projection provides a convenient way to encode geolocation information as a set of mathematical equations, which are capable of transforming Earth coordinates (latitude and longitude) to *X–Y* coordinates on a map. The choice of a projection to use in a Grid is a critical decision for a data product designer. Cartographic history has witnessed several projections in use. Many projections are supported by the HDF-EOS API, including

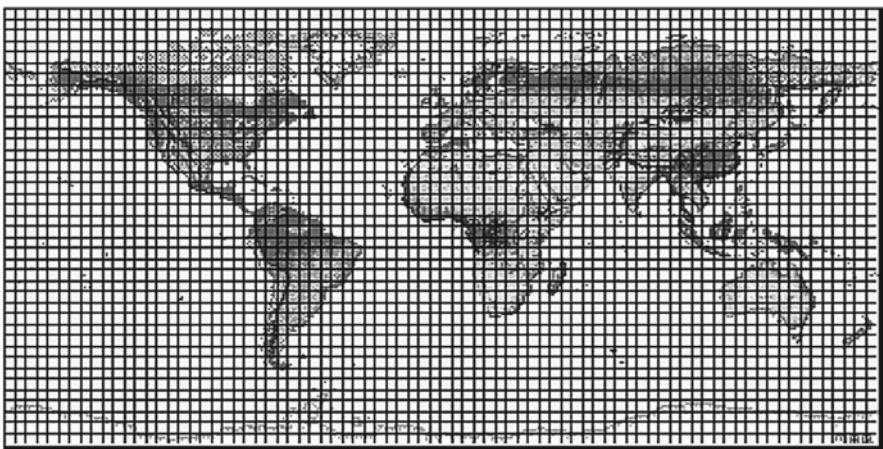


Fig. 10.3 A data field in a Mercator-projected grid

Geographic, Universal Transverse Mercator (UTM), Albers Conical Equal Area, Lambert Conformal, Mercator, Polar Stereographic, Polyconic, Transverse Mercator, Lambert Azimuthal Equal Area, Hotin Oblique Mercator, Space Oblique, Interrupted Goode's Homolosine, Integerized Sinusoidal, and Cylindrical Equal area. In addition, HDF-EOS supports user-defined projections and associated information.

10.3.4 The EOS Metadata Standard

10.3.4.1 Metadata Data Model

During the development of the ECS ground system, the diversity of science disciplines involved, and the volume of anticipated data distributed across many archive centers were recognized as challenges to the efficient data archival and distribution to users. An extensive data model was developed consisting of data attributes, implemented through a standardized software interface. Several requirements were taken into account in developing the model:

- Archival and retrieval requirements
- Search, acquisition, distribution, and other service requirements
- Federal mandates, e.g., Federal Geographic Data Committee (FGDC)
- Documentation requirements

The developers recognized that data access both through collections of similar data granules and by individual ones were likely. A model was developed that included several metadata attribute modules:

- Collection
- Granule
- Spatial (collection and granule)
- Temporal (collection and granule)
- Contact (role, name, address, phone, etc.)
- Data Originator (instrument/sensor/model)
- Delivered Algorithm Package (one collection for all)

These modules contain more than 250 individual attributes grouped in 120 different classes. Attributes can apply at the Collection level, the Granule level, or both. Data providers select subsets of these classes to describe their data. A few attributes are mandatory. They include time stamps, geolocation information, and data originator. Other attributes are chosen by the producer and contain information the producer wants passed to archive centers and users. These latter metadata are denoted as product-specific, and are not part of the searchable database. Consult the [Science Data Processing Toolkit](http://newsroom.gsfc.nasa.gov/sdptoolkit/TKDownload.html) for the EMD Project, V5.2.16 for details through the following URL: <http://newsroom.gsfc.nasa.gov/sdptoolkit/TKDownload.html>.

10.3.4.2 Attribute Storage in HDF-EOS Files

ECS metadata are implemented and accessed via a standard interface called the ECS Toolkit ([Science Data Processing Toolkit](#) for the ECS Project). The interface provides functions to create, store and access metadata within HDF-EOS files. The following three types of HDF text attributes are created:

1. *Core Metadata* represent information to which system-wide services, such as searching, are applied. These metadata, which are defined in DID 311, are contained in the “CoreMetadata.X” family of global attributes within an HDF-EOS file. The syntax of these metadata is compliant with the Object Description Language (ODL).
2. *Archive Metadata* represent information which, by definition, are not searchable. They contain any information the file creator considers as necessary, but to which, system-wide services are not applied. These metadata are also accessed via Science Data Processing (SDP) Toolkit calls, and are written in ODL syntax into the “ArchiveMetadata.X” family of global attributes.
3. *Structural Metadata* describe the contents and structure of an HDF-EOS file. These metadata are present in the file only if the HDF-EOS library was invoked to create a Grid, Point, or Swath structure. These metadata are stored in the “StructMetadata.X” family of global attributes, and are created and maintained by the HDF-EOS library. These metadata are not intended for direct access by data producers or users. Therefore, these metadata are only accessed via appropriate function calls in the HDF-EOS library. These metadata are the Dimensions, Dimension Maps, and Projections described in Sect. 10.3.3.

HDF-EOS data files contain metadata, and a subset of that metadata is distributed to users as an additional file along with the shipped data. Originally, the metadata files were in ODL format only. With the introduction of the new ECS distribution system in 2005, data centers started distributing metadata in XML format, which is how a majority of them are distributed currently.

The external metadata file contains, in addition to the core metadata, collection-level metadata from the Earth Science Data Type (ESDT). In the ODL (.met) version, all core attributes were included. In the xml version, the only collection-level metadata included are ShortName and VersionID.

In contrast, the metadata inside the HDF-EOS data files are still in ODL format. Those metadata are written as one or more global string attributes, using relevant libraries from the SDP Toolkit, during the Product Generation Executable (PGE) execution. They form a global HDF attribute called “CoreMetadata,” and if needed, further split into several global attributes if the string is longer than 65,536 characters.

The metadata file accompanying each shipped data file is a copy of the core metadata. It does not contain product-specific metadata. This file is a global HDF attribute that is a string (or several of them). Users may retrieve and parse the string at the command-line level using “ncdump,” “hdp,” or “awk.” However, other sophisticated users have started exploiting the unquestionable benefits of the metadata files in XML format, and retain the metadata files to build their own databases, queries, and searches.

10.4 How MODIS Uses HDF

10.4.1 MODIS

The MODIS instrument was planned to fly on both the EOS Terra and Aqua missions. The MODIS Science Team comprises of more than 30 Principal Investigator teams, representing atmospheric, land, and oceanic science disciplines. Visible and infrared images in 250-m, 500-m, and 1-km pixels are available. Notwithstanding HDF's selection for the EOS mission, there was a probability that PIs would develop their own substandards, which would lead to millions of lines of redundant applications software. MODIS requirements largely drove the development of the HDF-EOS swath structure. Storage requirements for ASTER image data, AIRS, and other profiling instrument data were also considered in the design.

10.4.2 MODIS LIB as an Example of Hybrid HDF and HDF-EOS

MODIS was designed to provide measurements to investigate science problems of unprecedented breadth for a single instrument. The mission was organized into several disciplines: Calibrated Radiances, Atmospheres, Oceans, and Land – including Snow and Ice. The HDF-EOS format was widely employed, which is exemplified as we introduce relevant elements of HDF and HDF-EOS structures.

The calibrated radiances, designated as “level-1B,” serve as input to produce subsequent products, thus ensuring an identical starting point for all science products. The MODIS level-1B is a “swath,” which fully exploits the advantages of the HDF and HDF-EOS structures. Users new to the EOS mission frequently ask natural questions like “What exactly are the benefits of having HDF-EOS?” or “Why not just have HDF-EOS instead of HDF and HDF-EOS?” or “Why not upgrade the standard HDF libraries so that I don't have to worry about all libraries?” The MODIS level-1B data address these questions, and also highlight on the benefits of the HDF and HDF-EOS structures.

The MODIS level-1B comes in three pixel resolutions, as three distinct data types (files), for every 5 min of satellite observation. Given the sheer volume, none of them have a one-to-one mapping of science data to geolocation data. (All geolocation data for a 5-min swath granule are stored in a separate level-1A Earth Location granule; MOD03.) Each of the three data types has a different mapping (offset and stride) between data and geolocation pixels. In the 1-km product, the first geolocation pixel corresponds to the third column and third row of radiance data (offset = 3), and then geolocation pixels are only provided for every fifth data pixel (stride = 5). In the 500-m product, the offset = 0 and the stride = 2, and finally in the 250-m product, the offset = 0 and the stride = 4. These details are impossible

to obtain from the HDF-EOS file with native HDF functions. However, the HDF-EOS makes these details transparent to the user by using the HDF-EOS API. HDF-EOS data are self-describing. The library functionality provides access to geolocation data without a need to understand storage details. The same functionality is reusable for a different instrument or data that uses HDF-EOS.

The HDF-EOS format allows numerous geolocation mappings within a single file, between geolocation arrays of different sizes (resolutions) on one hand, and science data on the other. This approach was applied in the MODIS Atmospheres joint product that contains two swath structures. The joint product contains the most popular atmospheric parameters, some of which are at 10-km, while others are at 5-km pixel resolution. The 1-km geolocation is vitally required to interpolate the center of the 10-km geolocation tile, but the center of the 5-km tile is simply subset from the 1-km geolocation. Hence, there always exists a noninteger offset of 2.5 relative to some of the data, regardless of which geolocation resolution is chosen, and noninteger offsets are not allowed in HDF-EOS. The solution was to have one swath structure for the 5-km data, and another one for the 10-km data. Even though this solution creates some additional processing overhead (each swath structure has its own geolocation arrays), the benefits include accuracy and transparency to the user.

In summary, an important part of the MODIS level-1B product is the calibrated radiance data that are tightly coupled with geolocation data, and these couplings are available through the HDF-EOS swath API. The radiance and geolocation arrays are stored within HDF-EOS swaths as SDS, and are readable with the “native” HDF functions as data arrays. However, no easy access to the important relations between geolocation and data is available using the native HDF functions. The user would have to read through documentation or parse the swath structure metadata string, which contains the offset and stride mappings and is readable as a simple HDF global attribute. However, to code a universal swath structure parser is an immense waste of time and effort, when relevant HDF-EOS functions are available.

10.4.3 HDF Objects

The next important piece, in particular for large-sized MODIS products, is called Local Attributes. The local attributes are attached to a vanilla HDF SDS structure, thus “local.” They include string and numerical types, scalars or vectors. The numerical local attributes, as scaling factors, are provided when data are stored as integers (to save file space) and require conversion to physical units for science use. Such is the case with all SDS contained in MODIS level-1B, Atmosphere and Ocean products.

The local attributes are likely very long strings, and thus may provide valuable descriptions to the SDSs to which they are attached. For instance, MODIS Atmosphere level-2 products have local attributes that represent entire tables of bit masks descriptions. When the HDF “ncdump” command is used on these products,

the ASCII output shows attributes in an orderly and organized fashion, readily prompting on data content. Frequently, the local attributes prompt on fill values that are assigned to pixels where retrievals fail. Users should check if such attributes exist, eventually retrieve their values, and use them to exclude bad pixels from their computations.

A vanilla HDF object, a “Vdata” or table data, is sometimes found in MODIS files. For instance, MODIS level-1B files contain a “lone” Vdata table, where every record describes every scan of the MODIS mirror in terms of several fields: beginning scan time, mirror side, scan type (day or night), nadir frame, solar azimuth of nadir frame, etc. The advantage of Vdata is that every record can contain fields of different type (e.g., one byte, float, string, etc.). This aids in storing self-descriptive mnemonics, like “D” and “N” for day- and night-type scan line, correspondingly, while storing the start time of the scan line as long-word integer in the same record. Such mixing of data types, of course, cannot possibly materialize within one SDS. Users should note, however, that scanning HDF files for Vdatas may prove confusing, because all local and global attributes are stored using the Vdata hierarchy. In other words, even if the data provider uses functions relevant to strictly local and global attributes to write them to the HDF file, these attributes are populated in the Vdata structures automatically. Thus, it may look like the data provider has written dozens of Vdatas to the file, whereas they are just local attributes attached to their “parent” SDS, or global attributes relevant to the particular file.

An important feature to note is that non-ECS local attributes, global attributes, and Vdatas contained in MODIS granules are not readable using HDF-EOS functions. Rather, they are accessible with native HDF functions only. Users should understand though, that as with any other file, they open an interface to the HDF file when they work with it. Opening two interfaces, one native HDF and the second HDF-EOS, to the same file is perfectly legal. This enables acquiring all objects inside the file, regardless of their status as HDF or HDF-EOS objects.

10.4.4 Higher-Level Products

Similar to most NASA Earth Science missions, MODIS level-3 data represent science retrievals aggregated to a global grid. The HDF-EOS Grid type was created to handle exactly such global maps. For the most part, everything already discussed about SDSs, attributes, Vdatas, etc. in the high-resolution level-1 and level-2 swath data (local scenes), also applies to level-3 data. The major difference is that, in contrast to the swath, the Grid data are mapped to a certain map projection, which is described within the Grid structure in the HDF-EOS file. The projection and projection information are provided, as well as the pixel resolution and the map corner coordinates. Thus, Grid files do not contain geolocation values for each grid cell. Nevertheless, data subsetting is accomplished using HDF-EOS functions by

providing the coordinates of the subset box. One could copy an SDS on a map, which is predefined with information in the Grid structure. In other words, there is no need to calculate positions of data pixels on the map, if the map projection used is the same as the projection in the Grid structure. One caveat regarding MODIS data is worth noting. Certain products contain arrays, which span multiple words. MOD35, for example, has a 48-bit flag array spanning 10 bytes, which renders it difficult to work with most application packages.

Another interesting note is that the MODIS Ocean Discipline was recomputed and awarded to the SeaWiFS project. SeaWiFS chose not to use the HDF-EOS format, and instead have used native HDF. These SeaWiFS products began production in the native HDF format in 2005, therefore making it difficult to align with older MODIS Ocean products or other MODIS products in general.

In summary, if the product designers include sufficient information inside the HDF file, users should not need any extra documentation to use that product. Functions are available, which allow users to query files down to the smallest HDF and HDF-EOS details and return a variety of information including: the number of SDS; their names, sizes, and number of local attributes; names and values of the local attributes; number of global attributes and their names and values; number of swaths or grids and their names and attributes; dimension mappings; number of Vdata tables and their names, etc. Every object or field is retrievable by its name – a vast alleviation to the everlasting hurdles in calculating offsets to objects in the multiobject binary files, and keeping records of what is actually inside the binary file. The GRIB binary format, used for certain ancillary datasets proved so burdensome that it was more cost-effective to develop and run converters to the HDF format. Data storage in HDF allowed for greater flexibility in platform use during science tests and operational production.

10.4.5 MODIS Metadata

As stated earlier, external MODIS and ASTER product metadata are now distributed in XML format. In contrast, the metadata inside the HDF-EOS data files are still in ODL format. That metadata are written as one or more global string attributes, using relevant libraries from the SDP Toolkit, during the PGE execution. We next concentrate on specific metadata groups, which are relatively more important.

10.4.5.1 Collection Description

This group contains the short name of the particular data collection, also called an ESĐT, and its collection version. The short name and the version are common for all granules within the collection, thus the name “CollectionDescriptionClass” for this group. The version is very important, as it indicates the data maturity. The higher the number, the more mature the data. The short name, on the other hand, is

of primary importance during data searches. Users first select data by ESDT and the search query is then limited to this collection only, thereby speeding up the query. The short name is also frequently used by HDF tools to determine the type of MODIS data being processed.

10.4.5.2 Spatial Domain Container

The ECS data model allows for two types of content in this group. One gives the coordinates for all four corners of the data granule, while the other provides just the box that encloses the granule. The former is known as “GPolygon” and the latter as “Bounding box” (see Fig. 10.4a). The GPolygon is used in general for swath data, and is a more accurate description of the granule location. GPolygon is primarily used in MODIS level-1B collections. The Bounding box contains four values only: the north and south latitudes, and the east and west longitudes of the box bounding the image file. For grid data (global maps) the bounding box is sufficiently accurate. However, for swath data, which is “raw” satellite raster not aligned with the latitudinal circles (parallels), the Bounding box is as inaccurate as the granule is closer to the planetary poles (see Fig. 10.4b). Searches on MODIS level-2 Atmosphere swath products use Bounding Box. One impact of this is that high-latitude searches of granules return more level-2 granules than level-1B. This potentially causes confusion because users expect to see identical numbers returned from the search since each level-2 granule is produced from the corresponding level-1B. Examples of differences in search results are demonstrated using Fig. 10.4c, d. Users who want to build fast and accurate algorithms that check if a ground point is within a level-2 data granule must use the GPolygon from the corresponding level-1B data granule or level-1A geolocation granule.

10.4.5.3 Range Date Time

This group contains the data collection’s beginning and ending date and time in UTC, which includes the leap second adjustment. MODIS file names conveniently contain the year, Julian day, and the acquisition range beginning time. For level-1 and level-2 products, the beginning time of granules is at 5-min intervals, reflecting the fact that 5 min of satellite overpass is contained in one granule. MODIS Atmospheres global grid data (Level-3) contain three types – daily, 8-day, and monthly. Correspondingly, the time in the file name shows the beginning of the period – every Julian day, every 8th Julian day starting January 1, and the Julian day of the 1st day of every month. For search purposes, the time range in this group and the time reflected in the filename are all sufficiently accurate. Users of global L3 products, who pursue accurate intercomparisons of MODIS with other instruments, such as Atmospheric Infrared Sounder (AIRS) and Ozone Monitoring Instrument (OMI), need know that the MODIS data day value is not necessarily identical with these instruments. In the latter case, the aforementioned temporal

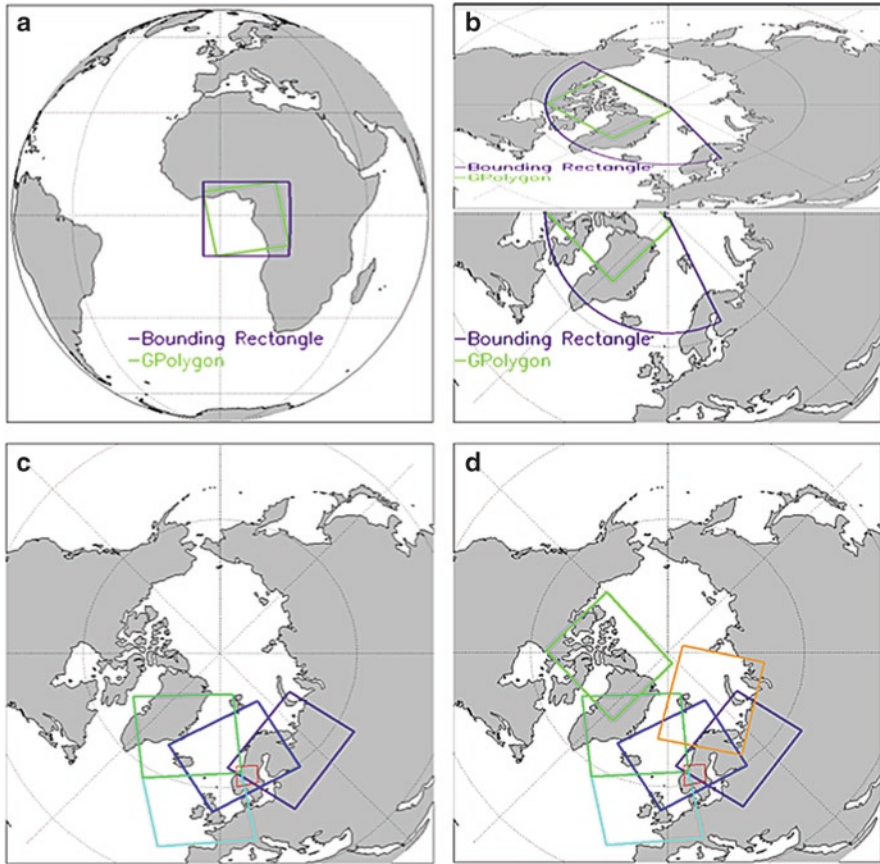


Fig. 10.4 Spatial domain container types and usage. (a) A granule’s region represented as GPolygon versus Bounding Rectangle. The GPolygon accurately reflects the data coverage, whereas the Bounding Rectangle covers a larger area. The difference between the two for tropical granules is small, resulting from orbital inclination. (b) A polar granule’s region represented as GPolygon versus Bounding Rectangle. GPolygon still corresponds closely to actual data coverage, but Bounding Rectangle does not. The North and South bounding latitudes project into arcs. (c) Spatial search results using “GPolygon” (e.g., MODIS Level 1B). The red box indicates the spatial search parameter. (d) Spatial search results using “Bounding Rectangle” (e.g., MODIS Atmospheres Level 2)

metadata objects, even though sufficiently accurate for search purposes, is probably about 12 h off of the actual time of the first swath (Level-2) granule that participated in the daily grid aggregation. Thus, these users should pay close attention to another (quite long) object named “InputPointer.” It should accurately list all participating *level-2* granules, which is a good source for more accurate beginning and ending times.

10.4.5.4 Orbital Spatial Domain Container

This group is supplied for swath (Level-1 and Level-2) data granules, and it associates the particular granule with the corresponding orbit. Users may find the orbit number, equatorial crossing longitude, date and time useful for various reasons. Very likely, this group will gain popularity as more and more interdisciplinary studies are conducted, where data from certain instruments are organized in orbital portions. Examples include the Microwave Limb Sounder (MLS), OMI, and CloudSat from the A-train mission.

10.4.5.5 Additional Attributes

This group contains the Product Specific Attributes (PSA), which are important parameters at granule level; they allow categorizing of granules, which enables searches using their parameter values. MODIS level-1B PSA, for instance, includes important calibration parameters describing the temperature of the mirror and all focal planes. The level-2 Atmospheres cloud product, on the other hand, offers different PSAs that describe various detected fractions for the particular granule: thick clouds, thin cirrus, ice and water and mixed clouds, low and high clouds, etc.

10.5 How ASTER Uses HDF-EOS

10.5.1 ASTER

ASTER level-1A, level-1B, and higher-level products follow HDF-EOS swath conventions closely with only subtle variations in their metadata based on where the data are produced. The HDF version of ASTER level-1 data and metadata are produced by the Ground Data System (GDS) in Japan and transmitted to the Land Processes Distributed Active Archive Center (LP DAAC) in the US. ASTER level-2 and level-3 products are generated at LP DAAC. (GDS Japan similarly produces several higher-level products as well; Refer to the ASTER Data System chapter in this volume for details.) The need to contend with ASTER level-1A (reconstructed unprocessed instrument data) and level-1B (registered radiance at the sensor) data often emphasized the need to correctly understand and interpret the metadata attributes. Early in the mission, this proved challenging with the commercial vendors, who gradually began developing HDF-EOS handling capabilities in their image processing software. LP DAAC's early experience in this area was formalized in an online document on "Georeferencing ASTER Level-1B Data."

10.5.1.1 ASTER Level-1A Data

The ASTER instrument provides a triple-sensor system, which include Visible Near-Infrared (VNIR), Shortwave Infrared (SWIR), and Thermal Infrared (TIR), each of which provides data acquired in unique bandwidths of the electromagnetic spectrum. The level-1A dataset caters to a variety of instrument-specific parameters and their metadata values for each band. They include satellite position and velocity, attitude angle and rate, observation time, geographic coordinates, line-of-sight vectors, parallax and intertelescope offsets, radiometric correction tables, etc. The ASTER level-1A data include dedicated Vgroups for each subsystem, and for each band's image data, geolocation fields, and instrument parameters within that subsystem. (Fig. 4.7 in Chap. 4 outlines an ASTER level-1A's HDF-EOS data structure.)

10.5.1.2 ASTER Level-1B Data

ASTER level-1B data include dedicated Vgroups for each subsystem. The difference with the level-1A data structure is that each of those Vgroups provides subgroups for the entire subsystem's image data and geolocation fields. (Fig. 4.10 in Chap. 4 outlines an ASTER level-1B's HDF-EOS data structure.) The HDF data structure helps contrast the instrument data versus the calibrated radiance data, which users need to understand and appreciate. The level-1A data provide digital numbers in raw geographic coordinates, while the level-1B data provide calibrated at-sensor radiance values in $\text{w/m}^2/\text{sr}/\mu$, and the data are gridded in the UTM projection. The data are path-oriented along the spacecraft's ground track (path-orientation is not the same as being map-oriented, or North-up). The MAPORIENTATIONANGLE metadata value in the HDF global attribute "productmetadata.0" provides the angle of rotation from the North. A major difference between the level-1B data and the higher-level products is that the Level-1B data are in geocentric coordinates (referenced to a spherical globe), while all the higher-level products are in geodetic coordinates (referenced to a digital elevation model).

10.5.1.3 ASTER Level-2 and Level-3 Products

The ASTER higher-level products are generated at the LP DAAC based on user-initiated requests. All the higher-level products (except the ASTER Digital Elevation Model (DEM) and Orthoimage products) are based on algorithms developed and approved by the ASTER Science Team. JPL, which houses the ASTER Science Project, is responsible for developing and packaging the production software and data product algorithms, which are ultimately run in LP DAAC's operations. The HDF-EOS structure of the higher-level products is simple with a single Vgroup, which provides the image data field (Band(s), QA Data Planes), and geolocation field (Geodetic latitude and longitude).

10.5.2 *ASTER Metadata*

LP DAAC-provided ASTER level-1 data contain two sources of metadata: the embedded HDF metadata and the external ECS metadata. A number of similarities and differences exist between them. The values delineated in the embedded HDF metadata are recommended for georeferencing purposes. Other product-specific and core metadata are good to refer from either source.

The HDF metadata file contains information that are embedded within a level-1 file header. They are written in ODL, an ASCII-based “parameter = value” format, and contain a number of attributes relating to the level-1 dataset. The level-1 HDF metadata file broadly contains eight attribute groups with a number of specific attributes in each of them. The ASTER User Handbook (http://asterweb.jpl.nasa.gov/content/03_data/04_Documents/aster_user_guide_v2.pdf) provides details of the individual attributes contained in each of these attribute groups.

Certain valuable metadata attributes are only available from the embedded HDF ASTER level-1A metadata. They include instrument-specific parameters identified in Sect. 10.5.1.1. Both ASTER L1A and L1B HDF embedded metadata includes following attributes deemed essential for georeferencing and analytical purposes:

- SCENEFOURCORNERS, SCENECENTER, FLYINGDIRECTION, SOLARDIRECTION, POINTINGANGLES, MAPORIENTATIONANGLE, RADIOMETRICDATABASEVERSION, GEOMETRICDATABASEVERSION, ACQUISITIONDATEANDTIME, and PRODUCTIONDATEANDTIME. Further details on each of these attributes are available from the LP DAAC ASTER level-1B product notes: https://lpdaac.usgs.gov/lpdaac/products/aster_product_table/on_demand/registered_radiance_at_the_sensor/v1/ast_11b (under the Layers tab).
- The ECS metadata file is the external.met file written in xml, which is delivered to the user along with the level-1 dataset. It contains a number of level-1 dataset attributes, which essentially provide a subset of the HDF metadata. It contains three broad groups of information: INVENTORYMETADATA, COLLECTIONMETADATA, and ARCHIVEMETADATA.
- The ASTER higher-level products are also packaged similarly with embedded HDF metadata, and external ECS metadata. The only difference is that their external.met file is in ODL format. The JPL-developed code-based products also extract and populate a user-friendly subset of key HDF-EOS metadata attributes (called product summary) for all higher-level products except the DEM and Orthoimage products.

10.6 Software Support for HDF and HDF-EOS

Users have several options to access, analyze, and visualize the science data stored in ASTER, MODIS, and other EOS data. Tables 10.1 and 10.2 provide an overview of some of the more popular tools available in the public and commercial software domains.

Table 10.1 Free software

| Tool | Features and URL | Pluses | Minuses |
|-------------------------------|--------------------------------------------------------------------------------------------------------------------------------------------------------------------------------------------------------------------------------------------------------------------------------------------------------------------------------------------------------------------------------------------|--------------------------------------------------------------------------------------------------------------|--------------------------------------------------------------------------------------------------------|
| HEG (HDF-EOS to GeoTIFF) | <p>Reprojection; spatial and spectral subsetting; subsampling; supports MODIS, ASTER, AIRS, AMSR-E, MISR; output formats to GeoTIFF, HDF-EOS, binary; mosaicing; JAVA GUI and command line interfaces; http://newsroom.gsfc.nasa.gov/sdptoolkit/HEG/HEGHome.html</p> | <p>Supports all HDF-EOS datasets – Grid and swath; wide variety of features; supports multiple platforms</p> | <p>Needs GIS software to visualize output GeoTIFFs</p> |
| HDFView | <p>View all HDF-EOS data internals, including metadata; examine data in spreadsheet and graphics modes; statistics, histograms, contour plots; control visual image through range stretching; convert to jpeg; http://newsroom.gsfc.nasa.gov/sdptoolkit/HDFView_PluginV2.2_Announcement.htm</p> | <p>Excellent for detailed examination of data internals</p> | <p>No reprojection capabilities or output to GeoTIFF</p> |
| MODIS Reprojection Tool | <p>Reprojection; spatial and spectral subsetting; supports level-3 MODIS HDF-EOS GRID data; output formats to GeoTIFF, HDF-EOS, binary; mosaicing; JAVA GUI and command line interfaces; supports multiple platforms; http://edcdaac.usgs.gov/landdaac/tools/modis/index.asp</p> | <p>Supports MODIS HDF-EOS swath data</p> | <p>Does not support full range of HDF-EOS product; needs GIS software to visualize output GeoTIFFs</p> |
| MODIS swath Reprojection Tool | <p>Reprojection; spatial and spectral subsetting; supports MODIS level-1B and level-2; output formats to GeoTIFF, HDF-EOS, binary; command line interface; http://lpdaac.usgs.gov/landdaac/tools/mrts swath/index.asp</p> | <p>Supports MODIS HDF-EOS swath data</p> | <p>Does not support full range of HDF-EOS projects; no GUI, only command line processing</p> |

| | | | |
|------------------------------------------------------|---------------------------------------------------------------------------------------------------------------------------------------------------------------------------------------------------------------------------------------------------------------------------------------------------------------------------------------------------------------------------------------------------------------------------------------------------------------------------------------------------------------------------------------------------|-----------------------------------------------------------------------------------------|----------------------------------------------------------------------------------------------|
| MS2GT (MODIS swath-to-grid toolbox) | <p>Reprojection; spatial and spectral subsetting; mosaicing; output to binary; http://nsidc.org/data/modis/ms2gt/#overview</p> <p>Supports MODIS, ASTER, AIRS HDF-EOS data; multifunctional data processing and visualization tool; GUI and command line driven; reprojections, spatial subsetting, etc.; output to GeoTIFF; supported on many platforms; http://www-loa.univ-lille1.fr/Hdflook/hdflook_gb.html</p> | Support MODIS HDF-EOS swath data | Does not support full range of HDF-EOS products; IDL is required |
| HDFLOOK | <p>Supports MODIS, ASTER, AIRS HDF-EOS data; multifunctional data processing and visualization tool; GUI and command line driven; reprojections, spatial subsetting, etc.; output to GeoTIFF; supported on many platforms; http://www-loa.univ-lille1.fr/Hdflook/hdflook_gb.html</p> | Supports wide range of HDF-EOS datasets; wide functionality | Output to HDF-EOS not available |
| HEW (HDF-EOS Web-based Subsetter) | <p>Supports all HDF-EOS data; supports spatial, band, and temporal subsetting; subsampling; http://subset.org/</p> | Supports all HDF-EOS data; supports spatial, band, and temporal subsetting; subsampling | Programming skills are required to install |
| McIDAS-Lite | <p>Data visualization; supports MODIS HDF-EOS; map overlays; performs basic quantitative analysis; save image in jpeg, gif, ASCII/binary formats; supported on many platforms; http://www.ssec.wisc.edu/mcidas/software/mclite/</p> | Supports wide range of HDF-EOS datasets; wide functionality | No output to GeoTIFF |
| GRASS (Geographic Resources Analysis Support System) | <p>All conventional GIS features are supported; http://grass.itc.it/</p> | Supports HDF-EOS data | Tool is a little complicated to use; usually requires basic knowledge of GIS and cartography |

Table 10.2 Tools requiring a license

| Tool | Features and URL | Pluses | Minuses |
|---------------|----------------------------------------------------------------------------------------------------------------------------------------------------------------------------------------------------------------------------------------------------------------------|---------------------------------------------------------------------------------|-------------------------------|
| IDL | Supports all HDF-EOS data; ability to create visual plots; direct processing of data through the IDL programming language; wrappers to entire HDF library; http://www.itvis.com/ProductServices/IDL.aspx | Can do just about anything one desires by using the IDL programming language | Programming skills are needed |
| MATLAB | Supports all HDF-EOS data; ability to create visual plots; direct processing of data through MATLAB programming language; wrappers to entire HDF library; http://www.mathworks.com/ | Can do just about anything one desires by using the MATLAB programming language | Programming skills are needed |
| PCI Geomatica | Reads generic HDF and utilizes geometric and radiometric calibration data for ASTER data; http://www.pcigeomatrics.com/ | Fully featured; no programming required; DEM extractions | |
| ERDAS Imagine | Fully featured GIS package; had import functions for all HDF and some HDF-EOS products; http://www.erdas.com/Products/tabid/56/Default.aspx | Fully featured; no programming required; DEM extractions | |
| ENVI | All conventional GIS features are supported; able to utilize HDF-EOS geolocation information for ASTER and some MODIS products; http://www.itvis.com/ProductServices/ENVI.aspx | Supports HDF-EOS data | |

Tools specific to MODIS and ASTER data:

- *LP DAAC TOOLS (for MODIS and ASTER data)*: <http://lpdaac.usgs.gov/datatools.asp>
- *MODIS DATA TOOLS and SERVICES*: <http://daac.gsfc.nasa.gov/MODIS/software.shtml>
- *HDF/HDF-EOS tools*: <http://www.hdfgroup.org/tools/> and <http://www.hdfeos.org/software.php>

Acknowledgments The authors wish to thank Calli Jenkerson and Bhaskar Ramachandran of the USGS EROS Data Center, Sioux Falls, SD, for providing content to this chapter.

References

HDF-EOS and related Software Documentation and User Guides: <http://newsroom.gsfc.nasa.gov/sdptoolkit/TKDocuments.html>

HDF4-related Documentation: <http://www.hdfgroup.org/doc.html>

HDF5-related Documentation: <http://www.hdfgroup.org/HDF5/doc/index.html> (Release 1.8.3) and <http://www.hdfgroup.org/HDF5/doc1.6/index.html> (Release 1.6.9)

Science Data Processing Toolkit Site: <http://newsroom.gsfc.nasa.gov/sdptoolkit/TKDownload.html>

The HDF Group: <http://www.hdfgroup.org/>

Part IV

ASTER Science and Applications

The ASTER instrument's unique capabilities with multispectral thermal infrared and short wavelength infrared channels are extremely well suited to study and monitor volcanoes. ASTER is also capable of measuring changes in thermal phenomena, such as lava domes, fumaroles, and crater lakes. In addition, the thermal bands allow measurement of sulfur dioxide gas emissions, a potential precursor for volcanic eruptions (Urai and Pieri, this volume). Geologic mapping highlights one of the real strengths of the ASTER instrument: the presence of multispectral capability in the short wavelength infrared part of the spectrum. Many rock-forming minerals, in this part of the spectrum, evince diagnostic spectral absorption features, which help researchers to either separate and/or identify them. This facilitates mineral resource exploration enormously, as evidenced in the Mt. Fitton, South Australia case study (Hewson and Cudahy, this volume). This subject extends into mining applications, which focuses on mineral exploration capabilities exemplified by copper mining in Iran, Chile, and Mongolia (Perry and Kruse, this volume). It provides a demonstration on how to use ASTER data for reconnaissance mineral prospecting with insights on scaling up from the regional to the district levels before committing geologists on the ground.

Glaciology is another earth science discipline, which benefits from the ASTER instrument. The Global Land Ice Measurements from Space (GLIMS) project, headed by the US Geological Survey, relies on satellite-derived data, primarily ASTER, to study and monitor thousands of glaciers in every continent. Satellite-derived data helps glaciologists highlight the role of glaciers as indicators of climate change and as potential contributors to global sea-level change. They also help monitor the direct dangers posed by glacial hazards to people and infrastructure. Examples of glacial hazard impacts include those from South America and Central Asia, where lives were lost, and threats due to changes in glacial behavior continue (Kargel et al., this volume).

Urban ecology presents interesting challenges to try and resolve with remotely sensed data. The ASTER instrument affords a good spatial and spectral complement to study urban ecology. Two examples in this volume attest this capability. An urban heat balance analysis evaluates ASTER data applications in urban studies. The urban heat island effect results in increased local atmospheric and surface temperatures in urban areas compared to their surroundings. This results from the

conversion of natural surfaces to artificial ones like asphalt streets, tarred roofs, and concrete roadways. ASTER thermal infrared images, particularly nighttime acquisitions, offer the data necessary to measure the temperature differences, and provide inputs for local weather perturbation, energy loading, and water runoff models (Kato and Yamaguchi, this volume). ASTER data constitute an important part in the Urban Environmental Monitoring (UEM) project at Arizona State University. A major UEM project goal is to monitor 100 cities worldwide, and characterize their urbanization profiles, heat island effects, effects on peri-urban environment, and growth. ASTER data use is complemented by other higher-resolution satellite data, which can resolve individual urban objects (Netzband et al., this volume).

ASTER and MODIS data are jointly used to estimate methane emission in the West Siberian Lowland, the world's largest high-latitude wetland ecosystem (Takeuchi et al., this volume). ASTER data are initially used to map land cover types in six wetland ecosystems, and supplemented by field observations followed by a spectral mixture analysis between Terra MODIS and ASTER data of same timeframes. Field measurements of methane production for each land cover type are scaled up for both ASTER and MODIS data, and their coverage fraction at the sub-pixel level is derived via a spectral mixture analysis. The average emission rates and the fractional coverage in each MODIS pixel help derive the methane emission estimates for the whole area.

A unique design feature of the ASTER instrument is its ability to generate stereoscopic data with which to build digital elevation models (DEM). ASTER acquires along-track stereo images, which eliminates the problem of dynamic viewing conditions that plague instruments that acquire cross-track image pairs from different orbits. Two chapters deliberate on stereoscopic views with very different goals. The first deals exclusively with ASTER-derived DEMs (Toutin, this volume). It provides detailed accounts of both ASTER and DEM stereoscopy, and the US and Japanese DEM production systems. Since this chapter was written, the ASTER mission has released a Global Digital Elevation Model (GDEM), covering the entire global land surface from 83° degrees north and south, at 30 m postings. GDEM, to date, is the most complete, and highest-resolution DEM available outside the classified, military world. ASTER's stereoscopic skills are used in a novel approach to determine the roughness of the Earth's surface (Mushkin and Gillespie, this volume). It determines the amount of shadow (and hence, roughness) by comparing the amount of shadow within a pixel viewed from two different view-directions. Surface roughness is a key parameter in many geological, hydrological, and planetary studies. It further provides an essential variable in remote sensing applications, and a critical input to atmosphere-surface boundary layer energy-exchange models.

All the preceding selections demonstrate how the ASTER instrument contributes to specific scientific applications and enquiries. They all depend on the physics of remote sensing along with engineering design, which provides the basis to facilitate the three sensor systems specializing in different parts of the electromagnetic spectrum. The final selection on "Technoscientific Diplomacy" (Plafcan, this volume) delineates the international politics of technical decision-making and scientific judgment, which successfully led to the development of the ASTER remote sensing system.

Bilateral cooperation and collaboration between Japan and the USA is ultimately credited with the success of the ASTER mission. Several scientists, engineers, and government officials from both countries were responsible in articulating the political calculus, which catalyzed collective judgment, and a shared interest to advance and achieve common international scientific goals.

The Landsat satellite program remains a pioneer in land remote sensing for nearly four decades. Set against the origin and evolution of that program, Goward et al. (this volume) deliberate upon the future of Landsat-class remote sensing. They assess the current status of Landsat-class observatories, the immediate future plans, the next phase in this class of observations, and possible future mission goals. Given the developments in the US National Land Imaging Program, and the international convergence on a Global Earth Observing System of Systems, the Landsat-class of observations are poised to continue their contributions to long-term global monitoring well into the future.

Chapter 11

The ASTER Data System: An Overview of the Data Products in Japan and in the United States

Hiroshi Watanabe, Bryan Bailey, Kenneth Duda, Yoshiaki Kannari, Akira Miura, and Bhaskar Ramachandran

Abstract The Advanced Spaceborne Thermal Emission and Reflection Radiometer (ASTER) data system is a cooperative system, which is operated jointly by Japan's Ministry of Economy, Trade, and Industry (METI) through its Earth Remote Sensing Data Analysis Center (ERSDAC), and by the National Aeronautics and Space Administration (NASA) primarily through its Goddard Space Flight Center (GSFC) and Land Processes (LP) Distributed Active Archive Center (DAAC). ASTER is a moderate-resolution land remote sensing system onboard the Earth Observing System (EOS) Terra spacecraft. ASTER-acquired data are received at the White Sands, New Mexico, ground receiving station, and then transmitted via land network to the EOS Data and Operations System (EDOS) within the Goddard DAAC, located at the GSFC. EDOS pre-processes raw ASTER data to Level-0 (L0) data, and sends them via the high-speed Asia-Pacific Advanced Network (APAN) to the ASTER Ground Data System (GDS) in Japan. ASTER GDS processes the L0 data to level-1 (L1) datasets; they distribute these data to users, and also use them to generate higher-level products for their user community. ASTER GDS sends a copy of all L1A data they produce to NASA's LP DAAC, located at the U.S. Geological Survey's Center for Earth Resources Observation and Science (EROS) near Sioux Falls, South Dakota. All L1 data received from Japan are ingested, archived, and available for users at LP DAAC. The LP DAAC also generates and distributes higher-level products from L1 data based on requests from users. To meet time-critical needs related to sensor health and performance, natural disasters, national emergencies, and certain field campaigns, the ASTER Expedited Data System (EDS) was developed, and is operated jointly by U.S. and Japanese partners.

H. Watanabe (✉)
National Institute for Environmental Studies, 16-2 Onogawa,
Tsukuba-shi, Ibaraki, 305-8506, Japan
e-mail: watanabe.hiroshi@nies.go.jp

11.1 Introduction

This chapter describes the Advanced Spaceborne Thermal Emission and Reflection Radiometer (ASTER) end-to-end data system, and the ASTER data products that are routinely available to users around the world. The chapter traces the ASTER data flow from acquisition onboard Terra to the generation and distribution of higher-level ASTER data products, and it examines key data management activities along the way.

ASTER is an advanced multispectral imager developed by Japan's Ministry of Economy, Trade, and Industry (METI) and launched onboard the Terra spacecraft in December 1999. Terra is the flagship of the National Aeronautics and Space Administration (NASA) Earth Observing System (EOS) program, and carries four other remote sensing instruments, including the Moderate Resolution Imaging Spectroradiometer (MODIS). The Terra spacecraft flies in a circular, near-polar orbit at an altitude of 705 km at the equator. The orbit is sun-synchronous with a 10:30 A.M. local equatorial crossing time in the descending node. In this orbit, the 60-km-wide ASTER nadir track has a 16-day repeat period after 233 revolutions. ASTER uses off-nadir pointing to acquire a 180-km-wide coverage, but such coverage requires a minimum of three 16-day cycles. ASTER was not designed to provide frequent or routine global coverage. Rather, ASTER is operated at an 8% duty cycle, with most observations scheduled to fulfill long-term global mapping mission requirements and to meet the specific needs of scientific investigators, including members of the joint Japan/U.S. ASTER Science Team. ASTER records reflected and emitted electromagnetic radiation in 14 wavelength bands derived from three separate telescopes and sensor systems. These bands include three visible and near-infrared (VNIR) bands at 15 m spatial resolution, six shortwave infrared (SWIR) bands at 30 m spatial resolution, and five thermal infrared (TIR) bands at 90 m spatial resolution. The VNIR Band-3 is capable of acquiring a stereo pair with its two (nadir- and backward-viewing) independent telescope assemblies, which provide along-track stereo coverage. The ASTER sensor's general characteristics are summarized in Table 11.1 (Fujisada et al. 1998; Yamaguchi et al. 1994).

Table 11.1 General characteristics of the ASTER sensor

| | Number of bands | Wavelength (μm) | Spatial resolution (m) | Maximum pointing angle ($^\circ$) | Swath (km) |
|-------------------|---------------------------|------------------------------|------------------------|-------------------------------------|------------|
| VNIR | 3 + Backward ^a | 0.52–0.86 | 15 | ± 24 | 60 |
| SWIR ^b | 6 | 1.60–2.43 | 30 | ± 8.55 | 60 |
| TIR | 5 | 8.125–11.65 | 90 | ± 8.55 | 60 |

^aBand-3B points 27.6° aft of nadir

^bThe ASTER SWIR sub-system failed in April 2008, and no useful SWIR data were acquired thereafter

ASTER is an excellent example of successful international collaboration in land remote sensing. NASA and METI have concluded numerous formal agreements (including ones related to the ASTER data system) to establish and conduct several cooperative activities, which ensure ASTER’s continuing success.

11.2 ASTER Data Flow Overview

Figure 11.1 is a general illustration of the end-to-end ASTER data flow. It highlights the key functions of the primary data systems (Watanabe 1995), which include the following:

- Data capture by the ASTER instrument onboard the Terra satellite;
- Relay through the Tracking and Data Relay Satellite System (TDRSS);
- Ground data reception;
- Data transmission for initial processing;
- Data transfer to Japan for level-1 (L1) processing, product generation, and data distribution by the Earth Remote Sensing Data Analysis Center (ERSDAC);

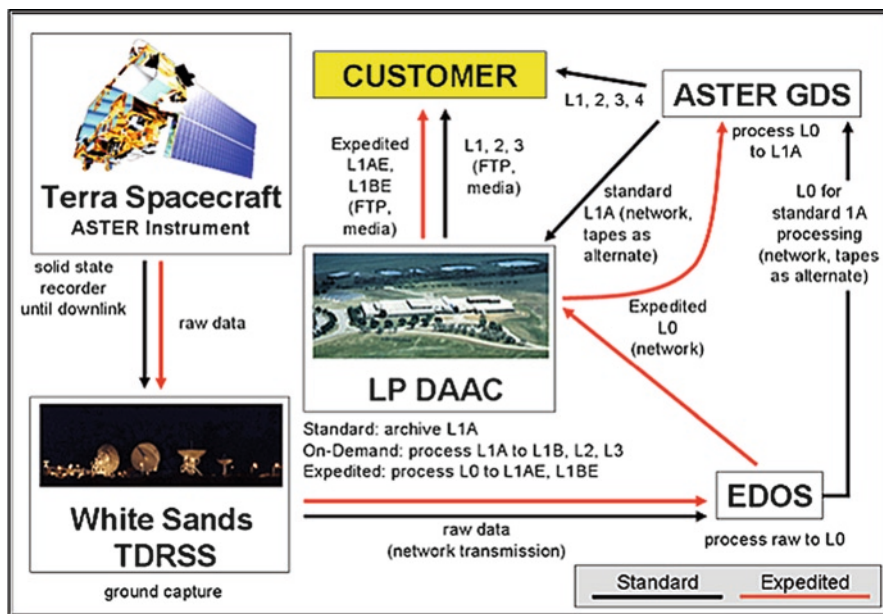


Fig. 11.1 ASTER data flow

- Transfer of L1A data to the Land Processes (LP) Distributed Active Archive Center (DAAC);
- Product generation and data/product distribution by the LP DAAC.

Prior to April 2005, level-0 (L0) data transfer from EOS Data and Operations System (EDOS) at Goddard Space Flight Center (GSFC) to the Ground Data System (GDS) in Japan was through tapes shipped via air courier, and L1A and L1B data produced by GDS were transferred to the LP DAAC via the same mechanism. As a result, it often took 3 weeks or more from the time of acquisition until L1 data products were available for distribution from the LP DAAC. Since April 2005, transfer of L0 data to GDS is accomplished via the Asia-Pacific Advanced Network (APAN), and since May 2005, the APAN is used by GDS to deliver L1A data to the LP DAAC. In general, these changes to network transfer of ASTER data and products reduced the turnaround time for data availability at GDS from 1 week or more to about 2 days, and from 3 weeks to about 4 days at the LP DAAC.

ASTER data required for emergency use, and to meet quality assurance requirements, are available in less than 24 h since shortly after launch using the ASTER Expedited Data System (EDS). The EDS relies on network transfer of data and products, but has a throughput limitation of ten scenes per day. Adaptation of APAN did not change the functionality or use of the ASTER EDS.

11.3 The Role of ASTER GDS

11.3.1 Mission Operations

A part of ASTER mission operations is conducted by the GDS ASTER Operations Segment (AOS) with the help of the Science Scheduling Support Group (SSSG) from ERSDAC and the Jet Propulsion Laboratory (JPL). Every day, a One-Day Schedule (ODS) is generated by the AOS using a scheduling system that accounts for a variety of factors: ASTER's 8% duty cycle, pending data acquisition requests, spacecraft information, weather forecasts for the target areas, the cumulative number of required pointings, and other additional factors. The scheduler's output plays a very important role, which includes defining the switch on/off time, and pointing angles to maximize the priority functions established by the ASTER Science Team. The generated ODS is sent to the EOS Mission Operations Center (MOC) at NASA's GSFC, where each day it is uploaded to the Terra spacecraft for execution (Yamaguchi et al. 1995).

Figure 11.2 presents the ASTER data acquisition history from shortly after launch through November 2008, and verifies that ASTER data acquisition has remained quite stable. Under normal operations, approximately 600 scenes per day are acquired, but starting in mid-2003, that number decreased to closer to 500 scenes per day; in part, this was due to problems with the onboard solid state recorder (SSR),

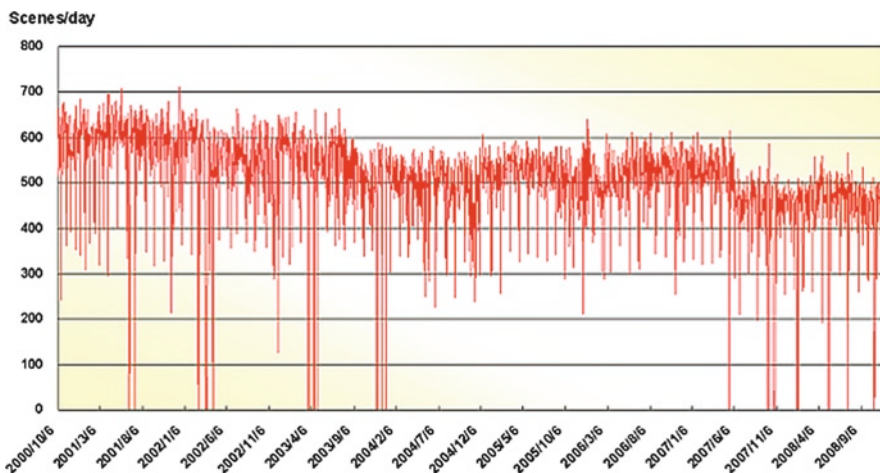


Fig. 11.2 Daily acquisition of ASTER data

and partly because target areas have become more scattered, resulting in some inefficiency in data acquisition. To date, the ASTER instrument has acquired more than 1.6 million ASTER scenes worldwide.

11.3.2 Data Processing

ASTER GDS is responsible for processing L0 data received from EDOS to L1A data products using the ASTER L1 processing system specially developed for this purpose (Fujisada 1998). L0 data delivered from EDOS are ingested by the L1 processing system, which generates depacketized, demultiplexed, and realigned instrument image data from the telemetry streams of the three ASTER telescopes. Geometric correction coefficients (Iwasaki and Fujisada 2005) and radiometric calibration coefficients (Arai and Tonooka 2005) are calculated as part of L1 processing, and these coefficients are appended (but not applied) to the L1A data. Appended coefficients are based on current calibration data, which are acquired every 33 days. Information to help correct the SWIR parallax, and intra- and inter-telescope misregistration are also included. Radiometric unit conversion coefficients in $W/m^2/sr/\mu m$ are available online: http://www.science.aster.ersdac.or.jp/en/documnts/users_guide/part2/05_03.html.

ASTER GDS routinely produced a significant amount of L1B registered radiance at the sensor data, until May 2006, by applying the previously calculated radiometric calibration and geometric correction coefficients to the L1A data. GDS distributed these L1B data, and also used them to generate higher-level products. In addition, they were sent to the LP DAAC for similar distribution, and higher-level data production. Both GDS and LP DAAC have offered L1B data as

an on-demand product only since May 2006. L1B data are corrected for SWIR parallax, and both intra-telescope and inter-telescope registration corrections for all of the bands are accomplished relative to the reference band for each subsystem. The L1B radiance product includes the same number of bands at the same resolution as the L1A product.

Figure 11.3 summarizes the ASTER L1A and L1B data production history at GDS, which shows the stable production of L1A data since operational data production began. In principle, all acquired scenes are processed to L1A. However, media errors and various processing errors prevent that from happening. Even prior to onset of L1B on-demand processing, not all L1A data were processed to L1B. Rather, L1B data (with default parameters applied) were produced automatically for data acquired under the “Global Mapping” category, and for data with cloud cover less than a fixed value (normally 20%), as determined by an automatic cloud estimation program. Upon request, ASTER GDS also generated L1B data with user-defined parameters.

Following GDS’ implementation of on-demand L1B processing, users may order L1B data from any scene in the archive. The L1B data product is produced using radiometric correction coefficients appropriate for the date of acquisition and current geometric correction coefficients. Consequently, the L1B data provided are as accurate as current knowledge of the system allows. Likewise, users who order L1A data receive a product with the most current and accurate correction coefficients appended.

L1B data provide the input to generate most higher-level ASTER data products. Most GDS-produced higher-level products are *standard data products*, which means they are products approved by an Algorithm Theoretical Basis Document (ATBD) review, and are produced both by ASTER GDS in Japan and by the LP DAAC in the United States. Standard data products are described in Sect. 11.5.

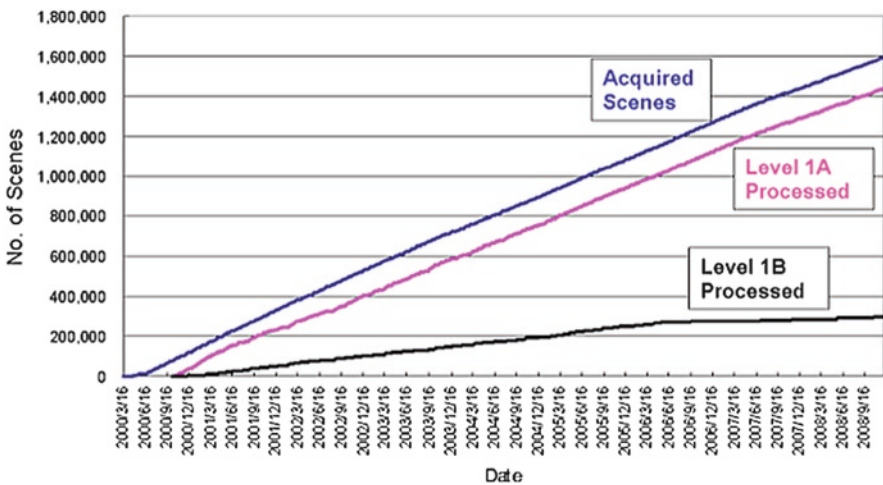


Fig. 11.3 ASTER data acquisition and Level-1 data production at ASTER GDS

ASTER GDS produces two products that are termed “semi-standard” products. One is the Orthorectified Image, which is associated with the ASTER Digital Elevation Model (DEM) and is available as a VNIR, SWIR, and TIR product with 15-, 30-, and 90-m spatial resolutions, respectively. The other semi-standard product is the ASTER DEM, which is produced from L1A data with 30-m postings as the default. The ASTER DEM is produced without use of ground control points (GCP), but its accuracy is still high because of the inherent geometric accuracy of ASTER data. The GDS-generated ASTER DEM is referenced to the Earth ellipsoid (WGS84), not the geoid or mean sea level (Watanabe 2005).

11.4 The Role of the Land Processes DAAC

In the late 1980s, NASA selected the U.S. Geological Survey’s Center for Earth Resources Observation and Science (formerly EROS Data Center) as the site for its EOS DAAC to house land processes data. The LP DAAC has worked with NASA since the early 1990s to develop, implement, and now operate the systems that process, archive, and distribute land-related EOS data and products, specifically those from ASTER and MODIS. To fulfill its role with ASTER data, the LP DAAC has relied on close cooperation with various partners, including ASTER GDS in Japan. The LP DAAC’s role with ASTER data includes data ingest and archive, product generation and distribution, and user support. In many respects, the LP DAAC provides similar functions in the United States that ASTER GDS provides in Japan.

The LP DAAC receives ASTER L1A data from ASTER GDS via the APAN network from Japan. Those data are ingested and archived by the DAAC, and made available to users via the ESDIS Warehouse Inventory Search Tool (WIST). L1B data are produced on-demand from any L1A scene archived at the DAAC. Appropriate radiometric and current geometric correction coefficients are applied so that users receive L1B data that are as accurate as current knowledge of the system allows. Likewise, users who order L1A data receive a product with the most current and accurate correction coefficients appended.

In addition to ASTER L1A and L1B data, users may order various level-2 (L2) and level-3 (L3) on-demand, standard data products from the LP DAAC. These higher-level, standard products are produced on-demand using algorithms developed by the ASTER Science Team. The correspondence of these algorithms (between LP DAAC and GDS) ranges from very similar to identical (see Sect. 11.5).

Similar to ASTER GDS, the LP DAAC also produces DEMs from ASTER L1A data. The LP DAAC implemented a new DEM generation system in May 2006. This system produces relative DEMs at 30-m postings that are generated without use of ground control points. LP DAAC-produced DEMs provide elevations in meters with corresponding x - y coordinates reported in latitude and longitude, as well as in Universal Transverse Mercator (UTM) coordinates, and they are referenced to the geoid. Similar to GDS-produced DEMs, the LP

DAAC-produced DEMs have high accuracies, often better than 25 m root mean square error (RMSE)_{xyz}. These DEMs were subject to an ATBD review, and are considered standard data products by the U.S. partners. In Summer 2006, the LP DAAC began offering orthorectified image products, produced during the DEM generation process, as a separate data product available to users. Orthoimages are produced (and orderable) for each spectral band, bundled by telescope: VNIR, SWIR, and TIR.

The LP DAAC produces two higher-level products not produced by ASTER GDS in Japan. They also are considered standard data products by the U.S. side, because they are subject to an ATBD review. One is the Brightness Temperature at the Sensor, and the other on-demand product unique to the U.S. partners is the Polar Surface and Cloud Classification.

11.5 ASTER Standard Data Products

Most ASTER higher-level, standard data products are produced by and are available from both ASTER GDS and the LP DAAC. Corresponding products from each side present nearly identical geophysical values from any given ASTER dataset, because they are produced by algorithms that are based on the same ATBD. With the exception of the Decorrelation Stretch products, the following higher-level products are available from both ASTER GDS and the LP DAAC as on-demand, standard data products. ASTER GDS stopped producing Decorrelation Stretch products in mid-2005.

Decorrelation Stretch – VNIR. This product is a color-enhanced image of the VNIR radiance produced from ASTER level-1B data. Decorrelation stretch is a process used to enhance the color differences in an image by removing the inter-band correlation in the radiance values of the input VNIR pixels, providing a general overview emphasizing reflectance variations.

Decorrelation Stretch – SWIR. This product is procedurally similar to the VNIR Decorrelation Stretch product, but uses three SWIR bands from an ASTER level-1B dataset as input.

Decorrelation Stretch – TIR. This product is similar to the VNIR and SWIR Decorrelation Stretch products, except that it uses three TIR bands and emphasizes emissivity variations.

Surface Radiance. Three surface radiance products are available, one for each of the three sensors: VNIR, SWIR, and TIR. All three products are atmospherically corrected datasets whose values are in units of $W/m^2/sr/\mu m$. All three products have unique band scale conversion factors for each of their respective bands that are available from the embedded hierarchical data format (HDF) metadata. The TIR surface radiance product further provides down-welling sky irradiance values in units of $W/m^2/\mu m$. The TIR surface radiance data also provide the

input to produce the surface spectral emissivity and surface kinetic temperature higher-level products.

Surface Reflectance. Two surface reflectance products are available, one each for VNIR and SWIR. Both products are atmospherically and topographically (slope and aspect) corrected datasets whose values represent unitless reflectance. Percent reflectance is derived from the product by multiplying each value by 0.001. Atmospheric correction is based on available climatological data or on data collected by other Terra sensors. Topographic correction is based on global digital elevation datasets.

Surface Emissivity. This product is generated using the five atmospherically corrected TIR bands, acquired either during the daytime or nighttime. It reports surface emissivity over the land at 90-m spatial resolution as derived from a temperature/emissivity separation algorithm. The possible range of emissivity values between 0 and 1 are encoded as values between 0 and 1,000 in the product.

Surface Kinetic Temperature. This product provides the surface kinetic temperature as calculated from the emissivity values derived from the five atmospherically corrected TIR bands using a temperature/emissivity separation algorithm. Temperatures in degrees Kelvin are obtained by multiplying product values by 0.1.

Products unique to the LPDAAC include the following:

Brightness Temperature at the Sensor. This product is derived from the five TIR bands in the L1B dataset. Brightness temperature is the apparent temperature of the imaged surface assuming a surface emissivity of 1. Brightness temperature is defined as the temperature required for a blackbody to produce the radiance measured by the sensor. As the name implies, the Brightness Temperature at Sensor product ignores atmospheric effects. The output product is a 5-band dataset in units of degrees centigrade, scaled by a factor of 100.

Polar Surface and Cloud Classification. This product provides a classification map discriminating between different surface and cloud features over polar areas. The primary aim of this product is to classify the cloud and snow-ice spectral signatures in both the visible and infrared wavelengths.

Table 11.2 lists the ASTER standard data products, including the L1 products, produced by and/or available from ASTER GDS and/or the LP DAAC. It also lists the products uniquely generated by each side.

11.6 Access to ASTER Data and Products

The ASTER data and products listed in Table 11.2 are available from both ASTER GDS and the LP DAAC via different data search and order systems. In addition, the data pricing policies of the two partners vary somewhat, as do the support services offered to users.

Table 11.2 ASTER data products available from ASTER GDS and the LP DAAC (V = VNIR, S = SWIR, T = TIR)

| ASTER Data Product Name | | | | |
|---------------------------------------|-----------------------------|----------------------------------------------------|-----------------------------------|----------|
| ASTER GDS | | LP DAAC | | |
| | | | Spatial Resolution | |
| Standard | Level-1A | Level 1 data | AST_L1A | V (15 m) |
| | | | AST_L1AE | S (30 m) |
| | Level-1B | | AST_L1B | T (90 m) |
| | | | AST_L1BE | V (15 m) |
| | None | | AST_L1BE | S (30 m) |
| | | | AST_L1BE | T (90 m) |
| | None | | AST_06TD | 90 m |
| | None | | L2 decorrelation stretch TIR | |
| | | | AST_06VD | 15 m |
| | None | | L2 decorrelation stretch VNIR | |
| | | | AST_06SD | 30 m |
| | On-demand products | | L2 decorrelation stretch SWIR | |
| | | | AST_09VD L2 surface radiance VNIR | 15 m |
| | | | AST_09SD L2 surface radiance SWIR | 30 m |
| AST_09T L2 surface radiance TIR | | 90 m | | |
| AST_07VD | | 15 m | | |
| L2 surface reflectance VNIR | | | | |
| AST_07SD | | 30 m | | |
| L2 surface reflectance SWIR | | | | |
| AST_08 L2 surface kinetic temperature | | 90 m | | |
| AST_05 L2 surface emissivity | | 90 m | | |
| Semi-standard | Orthorectified image (3A01) | AST140TH L3 orthorectified image | V (15 m) | |
| | Relative DEM Z (4A01Z) | | S (30 m) T (90 m) | |
| Standard | | | 30 m | |
| | | AST14DEM L3 digital elevation model (DEM) | 30 m | |
| | | AST_04 L2 brightness temperature at the sensor | 90 m | |
| | | AST13POL L2 polar surface and cloud classification | 30 m | |

11.6.1 ASTER GDS

Users may acquire ASTER data and products from Japan via the ERSDAC ASTER GDS Information Management System (IMS), which is accessible via the Internet (http://www.gds.aster.ersdac.or.jp/gds_www2002/index_e.html). The ASTER GDS IMS allows both directory and inventory searches. That is, users may search by dataset (directory) or by individual data granules (inventory). For L1B data and higher-level products produced from L1B data, path-oriented UTM

and cubic convolution are the default map projection and resampling options, respectively. However, users may specify alternative map projections and resampling methods for all products, and they may specify a different (than WGS 84) reference ellipsoid for the DEM product. ASTER data and products are available on CD-ROM and DVD or via network transfer from ERSDAC. Shipment of media products typically occurs within 1 day for L1 data and within 3 days for higher-level products.

ASTER GDS provides ASTER data and products on a non-discriminatory basis to anyone who agrees to certain use restrictions. ERSDAC provides ASTER data and products free to authorized ASTER Science Team members, EOS Instrument Team members, EOS Interdisciplinary Science investigators, and certain educational users, as well as to the GDS Project for system monitoring and other operational requirements. ASTER data and products are available to other users from ASTER GDS for a nominal charge.

In 2004, ASTER GDS began accepting general programming requests (GPR), which allow the general user to request specific observations by the ASTER sensors. Submission of GPRs carries an obligation to purchase L1A, L1B, and level-3A (L3A) products once the data are successfully acquired. In the case of nighttime data acquisition, the obligation is to buy L1A, L1B, and level-2B03T products.

11.6.2 LP DAAC

The WIST is the primary search and order system used by the LP DAAC to provide users with access to ASTER L1A data archived by the DAAC. The WIST is accessible via the Internet at <http://wist.echo.nasa.gov>. The WIST also provides users access to ASTER L1B data and L2 products, as well as to the L3 DEM and orthoimage products. The WIST allows users to designate their preferred processing options for those products where options are offered. Users are notified via email when their products are ready for File Transfer Protocol (FTP) pickup, and they are provided instructions for initiating the FTP pull to retrieve their product(s). ASTER data and products are available from the LP DAAC via FTP pull, and on DVD. ASTER data and products are available from the LP DAAC for a nominal fee, which is approximately comparable to that charged by ASTER GDS. The Global Visualization (GloVis) Tool (<http://glovis.usgs.gov/>) and the Data Pool (http://lpdaac.usgs.gov/lpdaac/get_data/data_pool) are alternative search and order methods for some ASTER data and products available from the LP DAAC.

In response to national emergencies, such as natural disasters, and to meet very high priority science requirements, the ASTER EDS is capable of delivering ASTER L1A and L1B data within 6 h following acquisition. The system relies on a combination of short-notice acquisition scheduling, priority processing to L0 by EDOS, FTP transfer of level-0 data from EDOS to the LP DAAC, priority activation of a standby L1 processing capability at the ASTER GDS and LP DAAC, and

non-routine FTP staging of the L1A and/or L1B data for customer retrieval. The system has very limited throughput capabilities and is tasked sparingly only in response to requirements such as those noted above.

11.7 Conclusions

The ASTER Data System is an example of a highly successful and unique international collaboration in land remote sensing. Together, the United States and Japan have developed a system that efficiently provides users around the world with inexpensive access to high-quality ASTER data and products, which continue to contribute to a wide range of earth and environmental science investigations. The ASTER Data System, indeed the entire ASTER Project, exemplifies what is accomplishable through close cooperation between nations, and serves as an outstanding model for future missions based on international collaboration.

References

- Arai K, Tonooka H (2005) Radiometric performance evaluation of ASTER VNIR, SWIR and TIR. *IEEE Trans Geosci Remote Sens* 43:2725–2732.
- Fujisada H (1998) ASTER Level-1 data processing algorithm. *IEEE Trans Geosci Remote Sens* 36(4):1101–1112.
- Fujisada H, Sakuma F, Ono A, Kudo M (1998) Design and preflight performance of ASTER instrument protoflight model. *IEEE Trans Geosci Remote Sens* 36(4):1152–1160.
- Iwasaki A, Fujisada H (2005) ASTER geometric performance. *IEEE Trans Geosci Remote Sens* 43:2700–2706.
- Watanabe H (1995) Development of ASTER ground data system. *J Remote Sens Soc Japan* 15(2):24.
- Watanabe H (2005) Accuracy of geolocation and DEM for ASTER. *Proc SPIE* 5978:21–30.
- Yamaguchi Y, Tsu H, Kahle AB, Nichols DA (1994) ASTER instrument design and science objectives. American Institute of Aeronautics and Astronautics, Reston, VA, Paper No. 94-0597.
- Yamaguchi Y, Tsu H, Kawakami T, Watanabe H, Kahle AB, Nichols DA, Morrison AD (1995) ASTER data acquisition scenario. *Proc SPIE* 2583:41–50.

Chapter 12

ASTER Applications in Volcanology

Minoru Urai and David Pieri

12.1 Introduction

Satellite remote sensing is a powerful tool for volcano monitoring. The Advanced Spaceborne Thermal Emission and Reflection radiometer (ASTER), which was launched on the Terra platform in 1999, is a high spatial resolution imaging spectroradiometer in the visible to near infrared, shortwave infrared (SWIR), and thermal infrared regions (Yamaguchi et al. 1998). ASTER data are useful to study volcanoes through the following activities: (1) topographic and geologic analysis, (2) mapping volcanic products, (3) eruption plume analysis, (4) discolored seawater and crater lake monitoring, (5) generating digital elevation models, (6) surface temperature mapping, and (7) sulfur dioxide emission analysis (Pieri et al. 1995). The unique features of the ASTER instrument such as along-track stereo imaging and multispectral thermal infrared radiometry allow deriving additional information about volcanoes. In this chapter, we discuss some of the capabilities of ASTER for volcanological observations and analyses, and summarize some case studies.

12.2 Surface Temperature Mapping

The Thermal Infrared Radiometer (TIR) instrument is designed for surface temperature and emissivity mapping. The TIR instrument can observe surface temperatures up to 300 K. Radiance from active lava flows, lava lakes, and pyroclastic flows saturates the TIR detectors. The SWIR bands, equipped with a special gain mode (Low Gain-2), can observe these high temperature targets. Table 12.1 shows the temperature ranges covered by the ASTER instrument, from the prevailing temperature to 460°C and from 670 to 999°C.

M. Urai (✉)
Geological Survey of Japan, AIST, Tsukuba, Ibaraki, Japan
e-mail: urai-minoru@aist.go.jp

Table 12.1 ASTER measurable temperature ranges (Urai et al. 1999)

| Subsystem | Band no | Gain mode | Gain factor | Maximum input radiance (W cm ⁻² μm ⁻¹ sr ⁻¹) | Brightness temperature range ^a (°C) |
|-----------|---------|-----------|-------------|--------------------------------------------------------------------------------|------------------------------------------------|
| VNIR | 1 | L1 | 0.75 | 56.9 | N/A |
| | | N | 1 | 42.7 | |
| | | H | 2.5 | 17.1 | |
| | 2 | L1 | 0.75 | 47.7 | N/A |
| | | N | 1 | 35.8 | |
| | | H | 2 | 17.9 | |
| | 3N, 3B | L1 | 0.75 | 29.1 | 999–721 |
| | | N | 1 | 21.8 | 973–705 |
| | | H | 2 | 10.9 | 915–669 |
| SWIR | 4 | L2 | 0.75 | 7.33 | 467–283 |
| | | L1 | 0.75 | 7.33 | 467–283 |
| | | N | 1 | 5.50 | 449–273 |
| | 5 | H | 2 | 2.75 | 410–250 |
| | | L2 | 0.167 | 10.54 | 387–203 |
| | | L1 | 0.75 | 2.35 | 301–156 |
| | 6 | N | 1 | 1.76 | 288–149 |
| | | H | 2 | 0.88 | 257–131 |
| | | L2 | 0.157 | 10.06 | 378–195 |
| | 7 | L1 | 0.75 | 2.11 | 290–148 |
| | | N | 1 | 1.58 | 277–140 |
| | | H | 2 | 0.79 | 246–123 |
| | 8 | L2 | 0.171 | 8.83 | 362–184 |
| | | L1 | 0.75 | 2.01 | 280–140 |
| | | N | 1 | 1.51 | 267–132 |
| | 9 | H | 2 | 0.755 | 237–115 |
| | | L2 | 0.162 | 6.51 | 333–165 |
| | | L1 | 0.75 | 1.407 | 254–122 |
| | 10 | N | 1 | 1.055 | 242–115 |
| | | H | 2 | 0.528 | 213–99 |
| | | L2 | 0.116 | 6.93 | 329–160 |
| 11 | L1 | 0.75 | 1.072 | 234–108 | |
| | N | 1 | 0.804 | 222–101 | |
| | H | 2 | 0.402 | 195–86 | |
| TIR | 12 | N | 1 | Radiance of 370 K blackbody | –73 to 97 |
| | 12 | | | | |
| | 12 | | | | |
| | 14 | | | | |

^aLower limits of the temperature range are calculated from 2% of maximum input radiance

12.3 Volcano Observations with ASTER

12.3.1 Sulfur Dioxide Flux Estimation at Miyakejima Volcano, Japan

12.3.1.1 Introduction

Satellite-based remote sensing for sulfur dioxide (SO₂) observation has at least two major advantages. One is the ability to collect repetitive measurements in a safe and cost-effective manner even in remote areas, or for active volcanoes, where manually collecting such measurements would sometimes present unacceptable risks. Such capability is especially important for monitoring volcanoes in developing countries, where extensive in situ or airborne chemical sensing resources are not always readily available. Another advantage is the ability to measure the two-dimensional spatial and temporal distribution of SO₂ over a broad region of a volcanogenic plume or cloud.

12.3.1.2 The SO₂ Flux Estimation Using a Thermal Infrared Multispectral Scanner

We assume that SO₂ concentrates in a specific layer and radiance sensed at the satellite level is a summation of the Earth's surface emission, SO₂ and atmospheric scattering/emission in the thermal infrared region as follows (Urai 2004):

$$R_{\lambda} = \tau_{\text{so}_2} \tau_{\lambda} R_g(\lambda, T) + \tau_1(1 - \tau_{\text{so}_2})R_{\text{so}_2}(\lambda, T_{\text{so}_2}) + R_{u,\lambda} \quad (12.1)$$

Here, R_{λ} is the spectral radiance sensed at the satellite [$\text{W m}^{-2} \text{m}^{-1} \text{sr}^{-1}$], τ_{so_2} the spectral transmittance of the SO₂ layer, t_l the spectral transmittance of atmosphere except for SO₂, $R_g(\lambda, T)$ the upward spectral radiance from ground at the ground level [$\text{W m}^{-2} \text{m}^{-1} \text{sr}^{-1}$], λ the wavelength [m], T the Surface temperature [K], τ_1 the spectral transmittance of atmosphere above the SO₂ layer, $R_{\text{so}_2}(\lambda, T_{\text{so}_2})$ the upward spectral radiance from the SO₂ at the top of the SO₂ layer [$\text{W m}^{-2} \text{m}^{-1} \text{sr}^{-1}$], T_{so_2} the atmospheric temperature at the SO₂ layer [K], $R_{u,\lambda}$ the upward spectral radiance of atmosphere except for SO₂ [$\text{W m}^{-2} \text{m}^{-1} \text{sr}^{-1}$].

SO₂ has an absorption feature at 8–9.5 μm . The first term of the right part of (12.1) is reduced due to the presence of SO₂. On the other hand, the second term of the right part of (12.1) is increased. Generally, the atmospheric temperature at the SO₂ layer is lower than the surface temperature, and total radiance at the satellite sensor is decreased. Thus, the radiance decrease at the sensor is large when the temperature contrast between SO₂ layer and the surface is large. Outside the SO₂ absorption bands (for example, band 13), SO₂ does not affect the radiance at sensor because τ_{so_2} is almost 1.

We calculate the two-dimensional SO_2 distribution based on the sea surface temperature derived from band 13 radiance, combined with band 11 observations and with the calculated MODTRAN model radiance predicted for SO_2 in band 11, as shown in Fig. 12.1. The SO_2 discharged from Miyakejima volcano flows and diffuses eastward from the vent. Water clouds are potentially mistaken as SO_2 ; however, they are identifiable and eliminated from the analysis because of their high reflectance in the visible region. Water clouds in the northern part of the scene and on the vent were masked using visible and near infrared (VNIR) data, and appear black in Fig. 12.1. The detectable lower limit of emitted volcanogenic SO_2 concentration for Miyakejima is $1\text{--}2 \text{ g m}^{-2}$ based on radiance values of band 11, where there is no discernable SO_2 spectral signature. The lower limit varies with the plume height and atmospheric conditions. At Mt. Etna, however, mean plume SO_2 volume concentrations have been measured at values as low as 0.5 g m^{-2} using ASTER (Pugnaghi et al. 2006).

By contrasting the plume position as seen in ASTER visible band 3 nadir and backward views, wind speed and direction are measured. This velocity estimate, when combined with concentration data from ASTER TIR bands, allows us to estimate volcanic SO_2 flux using ASTER data alone. For the November 2000 eruption of Miyakejima Volcano, Japan, the SO_2 flux derived from ASTER is around $5 \times 10^4 \text{ ton/day}$ (580 kg s^{-1}) (Urai 2004).

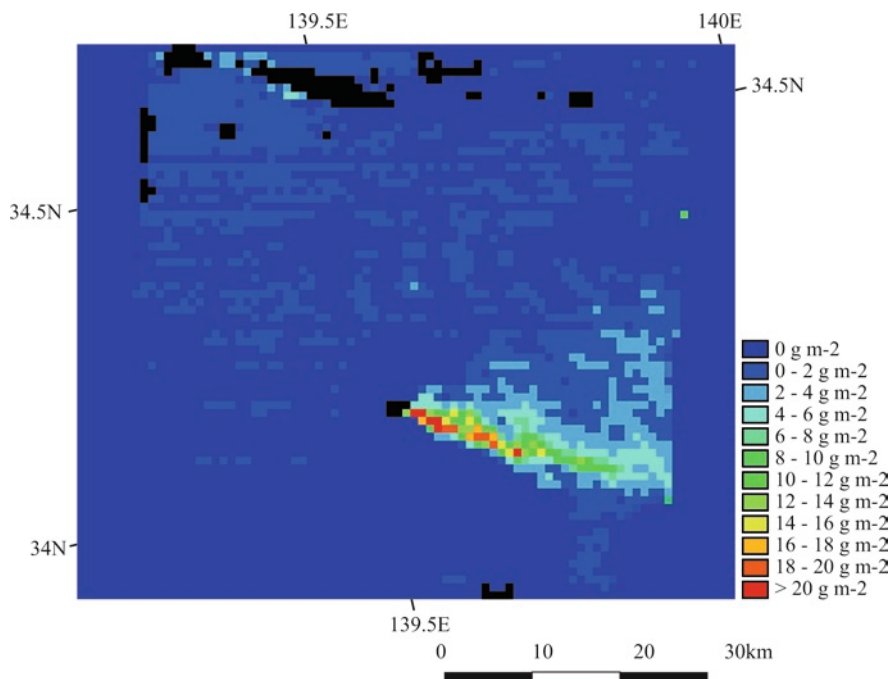


Fig. 12.1 Column SO_2 derived from ASTER TIR on November 8, 2000 (Urai 2004)

12.3.2 Thermal Monitoring of the 2006 Merapi Volcano Eruption, Indonesia

12.3.2.1 Introduction

Merapi volcano, one of the Earth's most active volcanoes, is located in central Java, Indonesia (Fig. 12.2). Thermal anomalies due to volcanic activity have been frequently observed by low spatial resolution satellite remote sensing (Carn and Oppenheimer 2000). Detailed monitoring and thermal mapping of Merapi, however, have rarely been possible due to frequent cloud cover (~10% of Merapi ASTER images appear cloud-free). Over the life of the mission, the Joint ASTER Science Team has implemented a Global Volcano Monitoring Plan (Urai et al. 1999). Over 900 volcanoes are monitored periodically according to their historic level of volcanic activity. For instance, under this plan, Merapi volcano is monitored as a "Class A" volcano that is observed every 48 days and every 32 nights. In addition to the normal observation schedule, the ASTER Science Scheduling Support Group (SSSG) conducted additional emergency observations for Merapi volcano from April 26 to July 8, 2006. During this period, 19 images were acquired within 43 days.

12.3.2.2 Volcanic Activity of Merapi Volcano

Merapi Volcano is a stratovolcano with an andesite lava dome at its summit, which frequently collapses to form pyroclastic flows on its southwestern slopes. The 2006 eruption began with intensive seismic activities in March 2006. On April 28, a lava



Fig. 12.2 Index map of Java Island, Indonesia

flow traveled 1.5 km in a southwest direction from the summit to the Lamat River. On and after May 14, frequent pyroclastic flows traveled to the west, southwest, and southeast from the summit area (<http://www.volcano.si.edu>).

12.3.2.3 Analysis of Daytime ASTER Images of the Merapi 2006 Eruption

ASTER, in the last nine years of its mission, has observed Merapi Volcano more than 100 times both in daytime and nighttime, but cloud-free images have been rare. In one such cloud-free sequence during the 2006 eruption, however, a part of the lava dome and fumaroles are visible at the summit of Merapi Volcano in the daytime ASTER VNIR view (Fig. 12.3a). In SWIR data, a bright spot is observed at the summit (Fig. 12.3b) due to thermal radiance from the active lava dome, and the strong thermal anomaly signatures of both the dome and an associated pyroclastic flow are prominent in a simultaneously acquired ASTER TIR image (Fig. 12.3c). ASTER TIR also detects thermal anomalies due to solar heating not related to volcanic activity.

12.3.2.4 Analysis of Nighttime ASTER Images of the Merapi 2006 Eruption

In the absence of the solar reflected radiance in nighttime observation, ASTER SWIR detects only thermal radiance from hot targets as seen in Fig. 12.4a. The nighttime observation was conducted at 22:16 local time. The solar heat contribution to the surface temperature detected by ASTER TIR (Fig. 12.4b) is small compared with the daytime observation (Fig. 12.3c). Figure 12.5 shows a time-series of surface temperatures at Merapi volcano, as detected by ASTER TIR from October 2001 to July 2006. On April 28, 2006, ASTER TIR data analysis revealed thermally elevated pixels clustered near the summit with a smaller anomaly approximately 650 m to the southwest, downslope from the summit (Ramsey 2006).

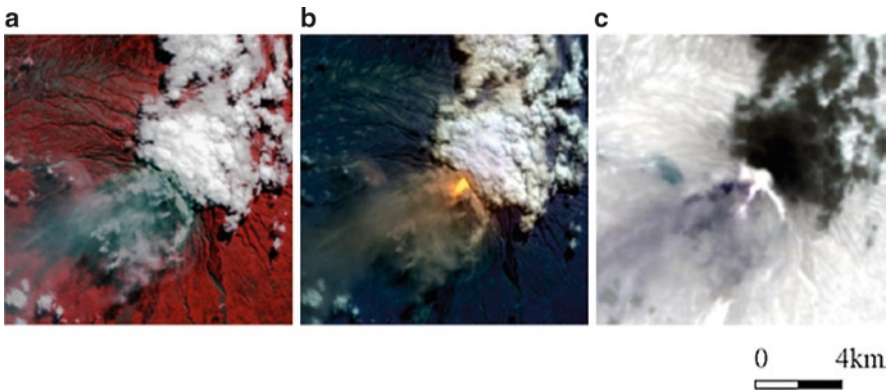


Fig. 12.3 ASTER daytime image acquired at Merapi volcano on June 6, 2006. (a) VNIR, RGB bands 3, 2, 1; (b) SWIR, RGB bands 9, 7, 4; (c) TIR RGB bands 14, 13, 11

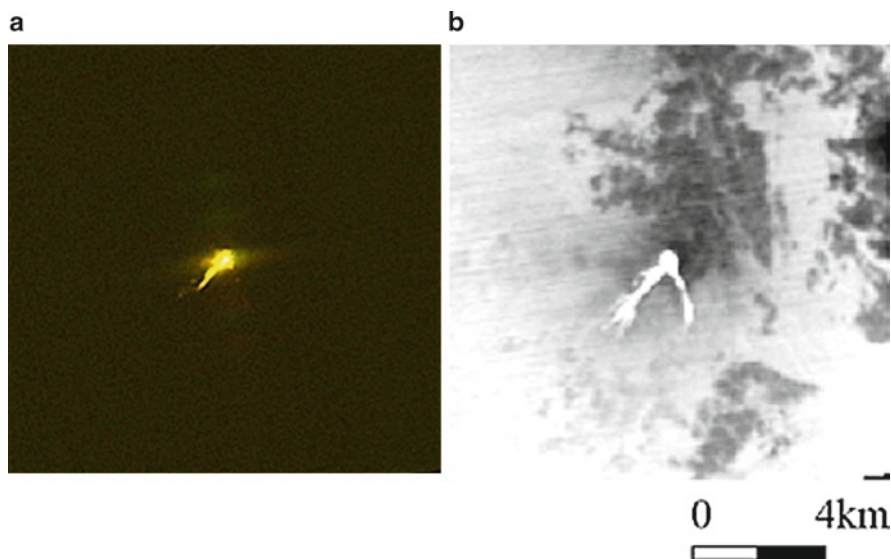


Fig. 12.4 ASTER nighttime image at Merapi volcano acquired on June 6, 2006. (a) SWIR, RGB bands 9, 7, 4; (b) TIR RGB bands 14, 13, 11

Our determination of surface temperature generally depends on the level of volcanic activity and elevation if the surface is cloud-free. Cloud cover (e.g., high cirrus or low-level volcanic fume) may present some confusion whenever the ASTER TIR-detected surface temperature is lower than expected, or when temperature gradients due to elevation change are not detected.

The Merapi volcanic activities, over ASTER's observations from 2001 to present, are divided into three periods based on ASTER TIR-detected (band 13) maximum temperatures (Fig. 12.6). The first period, which lasted from October 2001 to August 2002, was relatively active. The second period, from October 2002 to October 2005, was relatively calm. In the last period, which began in April 2006, the maximum temperature sharply increased to 29°C on May 5, 2006, ten days before the pyroclastic flow activity on May 14. A maximum temperature of 94°C was observed on June 6, and traces of active lava flows and pyroclastic flows were clearly seen in the ASTER thermal image on and after May 14 (Fig. 12.5).

12.3.3 *The 2005 Sierra Negra Eruption, Galapagos Islands*

12.3.3.1 Introduction

Sierra Negra is a large shield volcano with a large oval-shaped caldera that measures 11 km long by 6 km wide, located at the southern end of Isabela Island, the largest

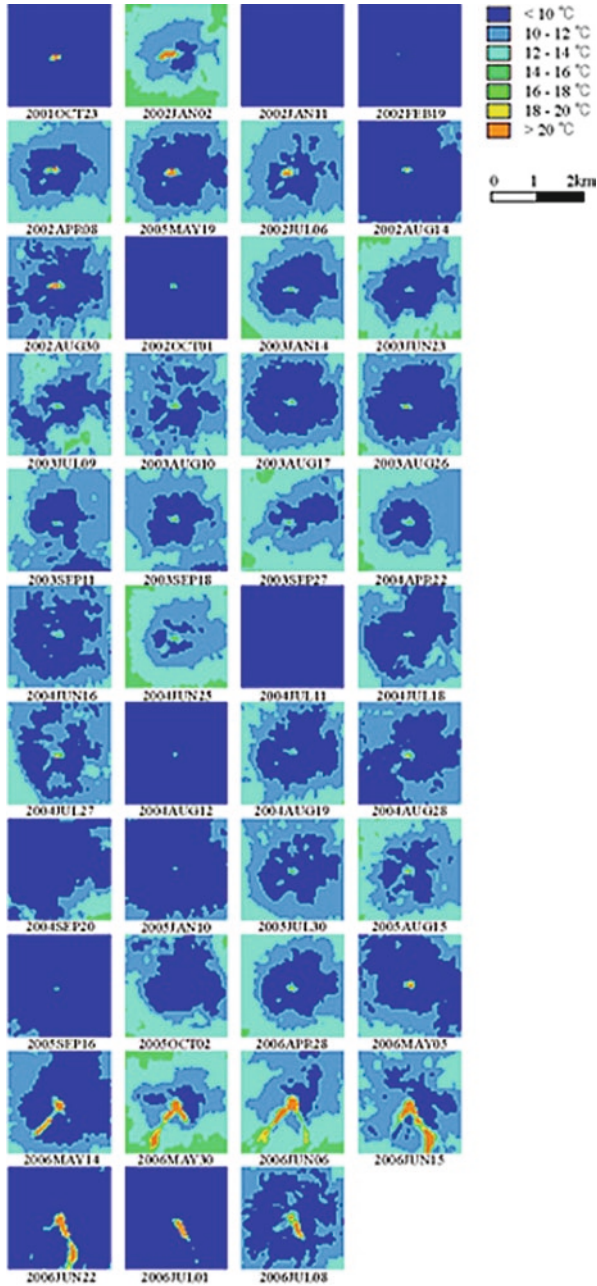


Fig. 12.5 Time-series of surface temperature at Merapi volcano detected by ASTER TIR band 13

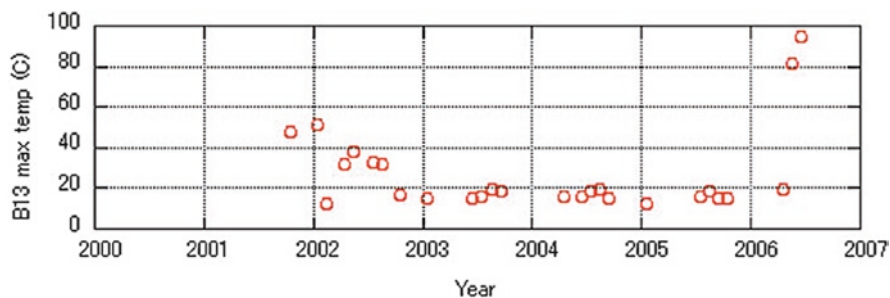


Fig. 12.6 Maximum temperatures at Merapi volcano detected by ASTER TIR band 13

of the Galapagos Islands. A 2.4-m uplift was observed at the Sierra Negra caldera floor between 1992 and 1998 (Amelung et al. 2000).

The 2005 eruption began at the northeastern edge of the caldera on October 22, 2005, and the associated eruption column reached an estimated altitude of 20 km. Most lava flows were contained within the caldera; however, several lava flows moved outside the caldera to the north. The eruption appeared to end on October 30, with new lava flows covering about 14 km² of the caldera floor, with an erupted volume of about 0.05 km³ (<http://www.volcano.si.edu/world/>).

12.3.3.2 ASTER Image Analyses

The ASTER SSSG conducted two emergency observations for Sierra Negra volcano. The first one was conducted in daytime with VNIR-only mode because of a large pointing angle of 14° required by orbital geometry on October 30. However, we could not detect any volcanic phenomena in the VNIR image. The second emergency observation was conducted at night on November 2 in TIR + SWIR Mode. We found thermal anomalies both on TIR and SWIR corresponding to the new lava flows (Fig. 12.7). The hot area inside the caldera was estimated at 14.2 km², which agreed with the field survey.

The location of the lava vents was estimated as within the red ellipse in Fig. 12.8 on the basis of ASTER-derived thermal anomalies and SRTM DEM topography, which confirmed that the vent was at the highest elevation within the thermal anomaly areas.

12.3.4 *Discolored Seawater Observation at Satsuma-Iwojima, Japan*

12.3.4.1 Introduction

Discolored seawater is one of the indicators of volcanic activity at submarine volcanoes or around volcanic islands (Nogami et al. 1993; Ossaka et al. 2000).

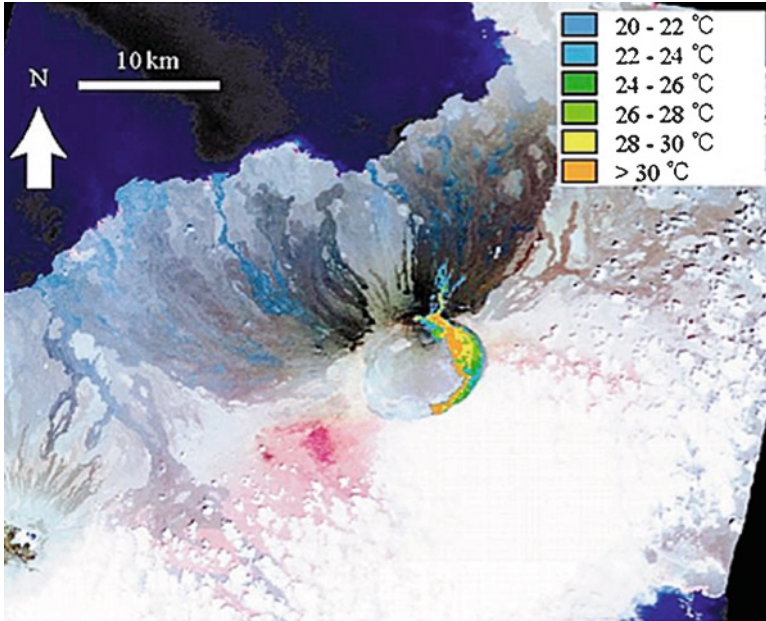


Fig. 12.7 ASTER VNIR image of Sierra Negra volcano observed on October 30 overlaid by color-coded surface temperature distribution derived from ASTER TIR band 13 observed at night on November 2

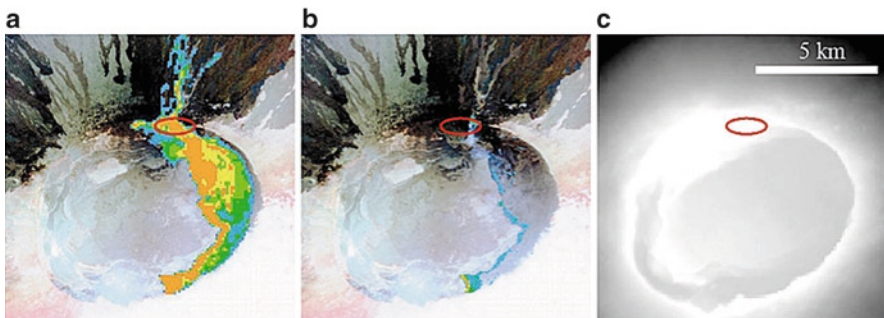


Fig. 12.8 Thermal anomaly and topography of the Sierra Negra volcano. (a) Enlarged image of Fig. 12.7, (b) VNIR image overlaid by color-coded surface temperature distribution derived from ASTER SWIR band 7, with temperatures more than 100 °C observed on November 2 indicated in blue, (c) SRTM DEM with the red ellipse indicating the estimated location of the lava vents

Discolored seawater is caused by very fine $\text{SiO}_2\text{-Al}_2\text{O}_3\text{-Fe}_2\text{O}_3\text{-H}_2\text{O}$ particles that are precipitated from the mixture of hot-spring water and seawater as seen in observations of the Nishinoshima submarine volcano, Japan (Ossaka 1975). Observed colors that change from milky white to reddish-brown correspond to the Fe_2O_3 content of the seawater (Ossaka 1975). In a subsequent study of the Fukutoku-Okanoba

Submarine Volcano, the seawater color changed from milky white to yellow, yellow-brown, or yellow-green depending on the Fe and Al contents that increased with amplified volcanic activity (Ossaka et al. 1996). The sensitivity of remotely sensed images to color changes renders them useful to evaluate the nature and intensity of volcanic activity. Indeed, discolored seawater was found at Fukutoku-Okanoba and Hukuzin Kaizan seamount in Landsat MSS images (Tsuchide and Ohtani 1983).

Satsuma-Iwojima is a volcanic island located 90 km south of Kagoshima city, Kyushu, Japan. This island is a good target for discolored seawater monitoring using satellite remote sensing because two different shades of discolored seawater have been observed continuously around the island. ASTER reflectance products were used to detect discolored seawater at Satsuma-Iwojima, Japan (Urai and Machida 2005), and we summarize those results in the following paragraphs.

12.3.4.2 Geologic Setting of Satsuma-Iwojima

Satsuma-Iwojima is located on the northwest rim of the Kikai Caldera, which extends about 20 km east–west and 17 km north–south (Fig. 12.9). Most of the Kikai Caldera is covered by the sea (Ono et al. 1982). Two different discrete hues of discolored seawater related to volcanic activity have been observed continuously

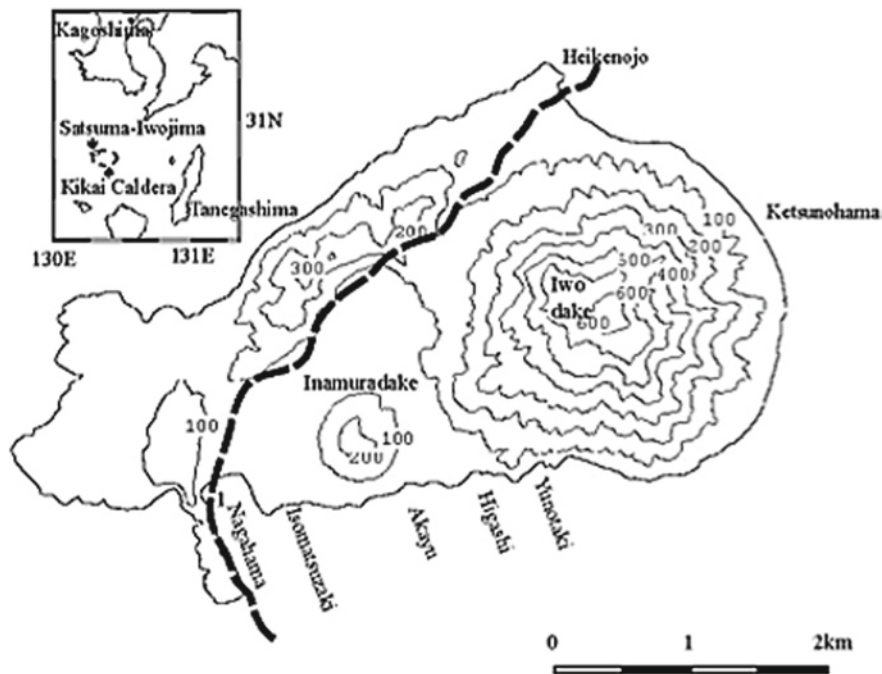


Fig. 12.9 Topographic map of Satsuma-Iwojima (elevation in meters). The *thick broken lines* indicate the rim of the Kikai Caldera

around the island. One is reddish-brown and is due to the outflow of neutral-pH, iron-bicarbonate water (Kamada 1964; Hedenquist et al. 1994) around the seacoast of Inamuradake. The other is white to green and is due to hydrous oxides formed when the Al- and Fe-rich acidic waters mix with seawater (Nogami et al. 1993) around the seacoast of Iwodake. Estimates of the amount of acidic hot water discharged from Satsuma-Iwojima (Kamada 1964) yearly range from $1,020 \times 10^6$ ton.

12.3.4.3 Satellite Image Analyses

Figure 12.10 shows the ASTER surface reflectance images (L2B05V) of Satsuma-Iwojima displayed in false color with bands 1, 2, and 3 represented by blue, green, and red, respectively. Discolored seawater is seen at the southern and eastern coastlines from Nagahama to Heikenjojo; however, no discolored seawater is found at the northwestern coastline, which is outside of the Kikai Caldera rim. The discolored seawaters are divided into two different colors. One appears as a “greenish area” in ASTER images of Nagahama, Isomatsuzaki, and Akayu. In the field, this seawater is reddish-brown and was attributed to the outflow of neutral-pH, iron-bicarbonate water by Kamada (1964). [Note that since ASTER does not have a band corresponding to the blue spectral range (0.45–0.52 μm), the colors represented in an ASTER image are different from colors detected by the naked eye.] The other is a “bluish area” at Higashi, Yunotaki, Ketsunohama, and Heikenjojo, which appear white-to-green in the field, and is attributed to hydrous oxides formed when the Al- and Fe-rich acidic waters mix with seawater (Kamada 1964; Nogami et al. 1993). The discolored seawater drifts with tides and ocean currents, generally within 3 km of the seacoast.

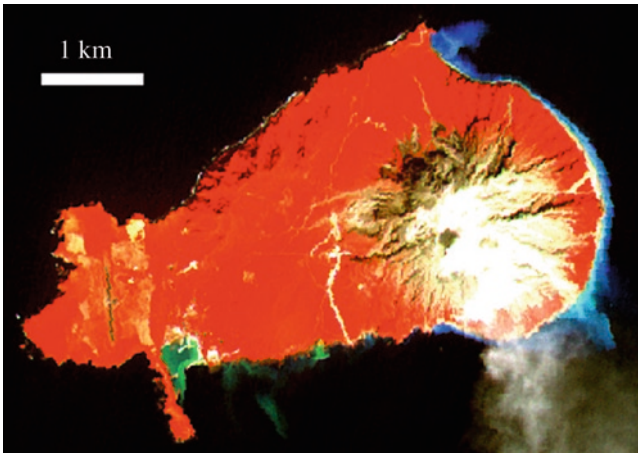


Fig. 12.10 ASTER reflectance image (2B05V) around Satsuma-Iwojima, observed on March 19, 2001. ASTER bands 1, 2, and 3 are assigned to *blue*, *green*, and *red*, respectively

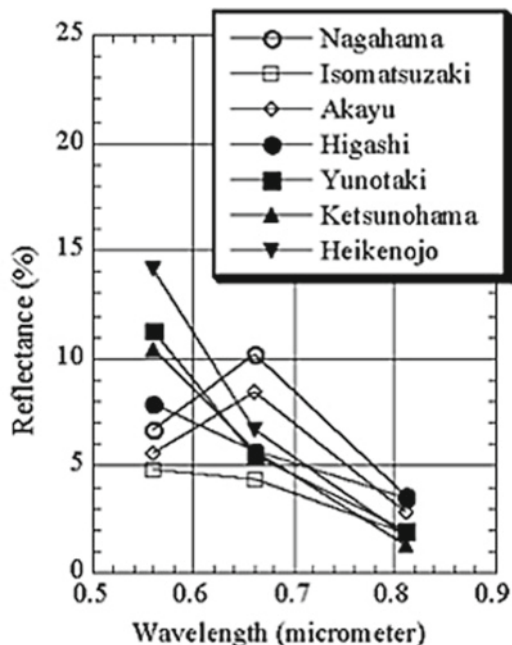


Fig. 12.11 Corrected reflectance of discolored seawater derived from ASTER VNIR image data

To obtain corrected and normalized reflectance (Fig. 12.11), we subtract the “normal” clear sea reflectance from discolored seawater reflectance of the same observation date. Heikenojo and Yunotaki’s corrected reflectances are distinguished from other seawaters due to their high band-1 reflectance with a 0.56 μm central wavelength (cw), medium band-2 reflectance (0.66 μm cw), and low band-3 reflectance (0.81 μm cw).

12.3.5 The 2005 Fukutoku-Okanoba Submarine Volcano Eruption, Japan

12.3.5.1 Introduction

Fukutoku-Okanoba is one of the world’s most active submarine volcanoes, located about 1,300 km south of Tokyo, Japan. New islands were formed by submarine eruptions in 1904, 1914, and 1986; however, they disappeared rapidly due to wave erosion (<http://www.volcano.si.edu/world/>). Trachyte pumice was found at Fukutoku-Okanoba in 1986 (Kato 1988), and discolored seawater is frequently observed from aircraft surveys and by satellite remote sensing instruments.

A submarine eruption was reported at Fukutoku-Okanoba by the Japanese Self Defense Forces while in Iwojima on July 2, 2005. A large amount of steam rose about a kilometer above the sea at Fukutoku-Okanoba. The Japanese Coast Guard conducted an airborne survey, which found steaming lava blocks, discolored seawater, and floating pumices on the sea surface.

12.3.5.2 Discolored Seawater and Floating Objects Analysis with ASTER VNIR

The ASTER SSSG conducted an emergency observation for Fukutoku-Okanoba submarine volcano on July 5, three days after the eruption. Discolored seawater is seen in blue (false color) in the ASTER VNIR image (Fig. 12.12) because of its high reflectance in band 1 ($0.56 \mu\text{m}$) as much as 3.5%. In contrast, the reflectance of weakly discolored seawater is less than 1%, a level that is difficult to detect with the ASTER VNIR instrument.

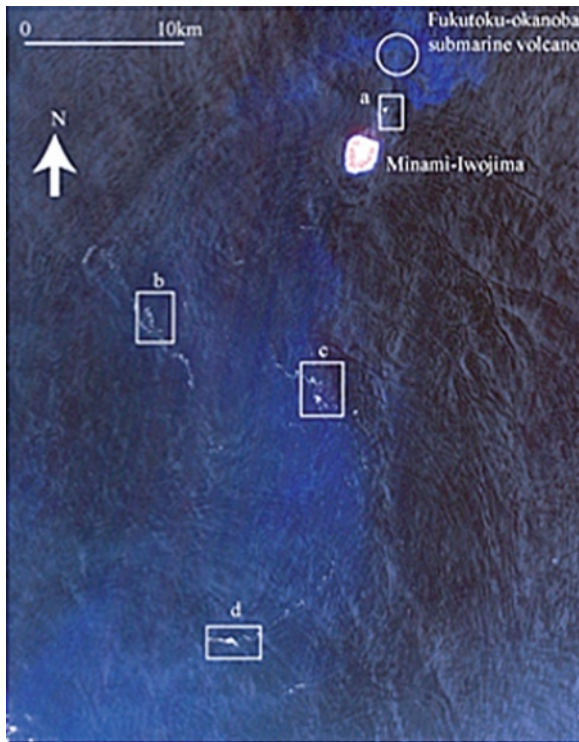


Fig. 12.12 ASTER VNIR image of Fukutoku-Okanoba submarine volcano and surrounding area on July 5, 2005. The *open circle* indicates the location of the submarine volcano summit

ASTER VNIR-derived reflectance spectra of submarine volcano-discharged floating objects appear similar to clouds. However, stereo images facilitate separating such floating debris masses from clouds. Floating materials exhibit unique shapes (Fig. 12.13), and ASTER stereo images can help determine their height, movement, direction, and pace. Colored objects in Fig. 12.13a are clouds that exhibit large apparent displacements between nadir and backward views. Objects in Fig. 12.13b–d are floating pumices erupted from the submarine volcano as distinguished by their unique shapes, which appear similar to small pieces of thread, and lack any appreciable displacement between their nadir and backward images. The pumice masses' horizontal movement velocities (Fig. 12.13b–d) are 1.4 km h^{-1} toward the northeast, 1.4 km h^{-1} toward the northwest, and 0, respectively. The area

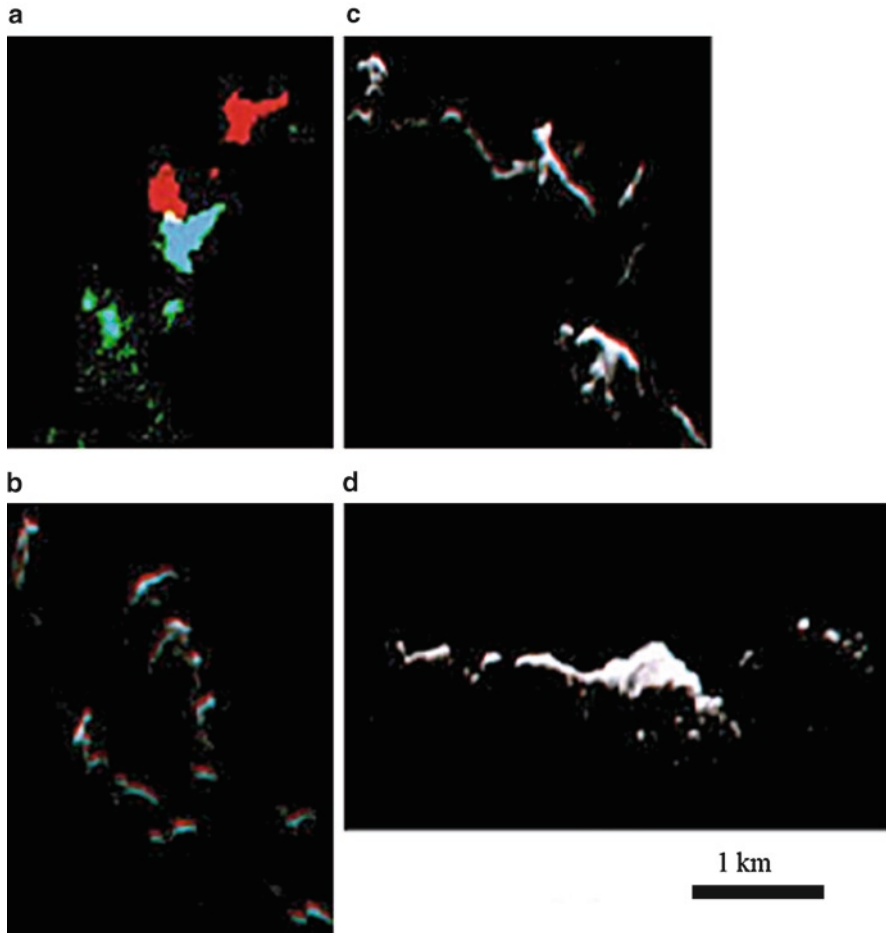


Fig. 12.13 ASTER stereo image of floating pumice rafts and clouds. The nadir views are assigned to *red* and *green*, and the backward image is assigned to *blue*. Panels **a–d** are enlargements of images **a–d** from Fig. 12.12

extent of discolored seawater and floating pumice masses detected by ASTER is 6.34 and 1.14 km², respectively.

12.3.6 *The 2006 Home Reef Submarine Volcano Eruption in Tonga*

12.3.6.1 Introduction

The Home Reef submarine volcano is located midway between Metis Shoal and Late Island in the central Tonga islands. A 1984 eruption produced a 12-km high eruption plume, copious amounts of floating pumice, and a 500 m by 1,500 m wide ephemeral island (<http://www.volcano.si.edu/world/volcano.cfm?vnum=0403-08>).

The ASTER instrument observed submarine eruptions at Home reef on August 2006, and large-scale pumice rafts were found from Tonga to Fiji. A new island was formed during the eruption (Vaughan et al. 2007).

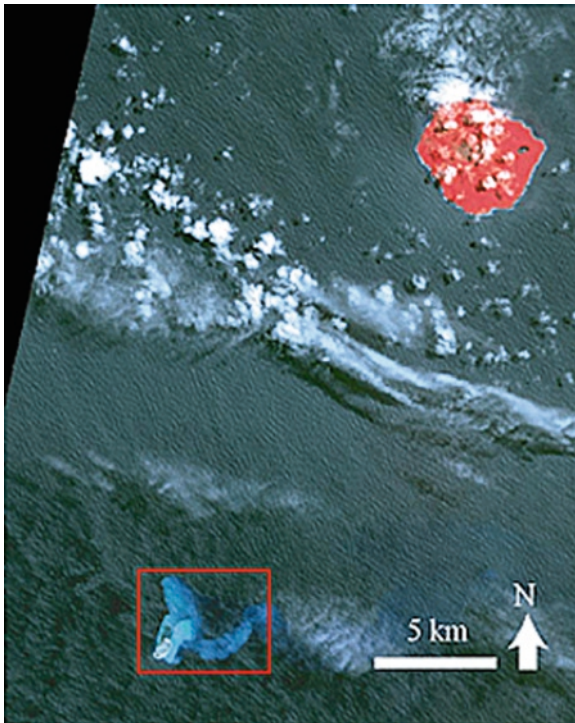


Fig. 12.14 ASTER VNIR image of Home reef submarine volcano and the surrounding sea area observed on October 4, 2006. The new island at Home reef is shown in the *red rectangle*. Late Island is shown at the *upper right corner* of the image

12.3.6.2 ASTER Images of Home Reef

The new volcanogenic island was discovered at Home reef through an ASTER observation on October 4, 2006 (Fig. 12.14). The ellipsoidal island is located $18^{\circ}59' 27''\text{S}$, $174^{\circ}46' 03''\text{W}$, with its semimajor axis oriented NE–SW. The length of the semimajor and semiminor axes and the area are approximately 900 m, 600 m, and 0.2 km², respectively, as of October 4, 2006. A large crater exists at the center of the island, and discolored seawater was clearly identified surrounding the new island. Discolored seawater is seen in blue-green color in ASTER VNIR images (Fig. 12.14) because of high reflectance in band 2 (0.66 μm), medium reflectance in band 1 (0.56 μm), and low reflectance in band 3 (0.81 μm), as depicted in Fig. 12.15. This discolored seawater is probably of the iron-bicarbonate type, as described in the Satsuma-Iwojima discolored seawater image (Fig. 12.11). The discolored water annulus' temperature around Home Reef is 4°C higher at maximum than the more distal surrounding seawater.

In the ASTER image acquired on November 12, 2006, the island's area was about two-thirds (Fig. 12.16b) the area observed previously (Fig. 12.16a). The areal extent of discolored seawater was also reduced. These facts indicate that the volcanic activity was waning when ASTER acquired the data.

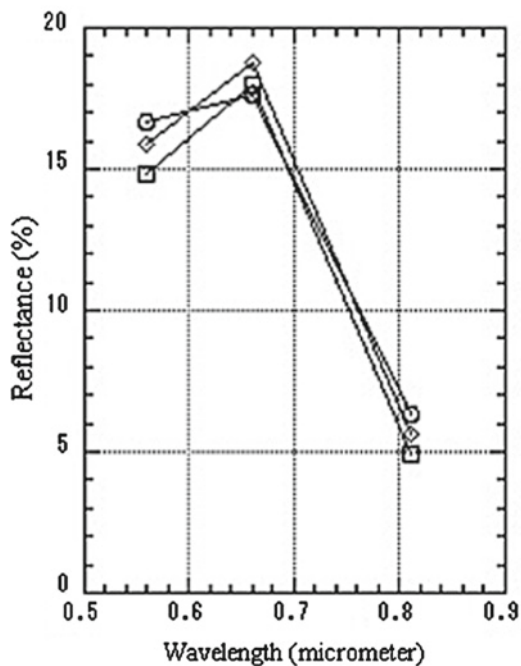


Fig. 12.15 Corrected reflectance of discolored seawater at Home reef submarine volcano derived from ASTER VNIR data, as observed on October 4, 2006

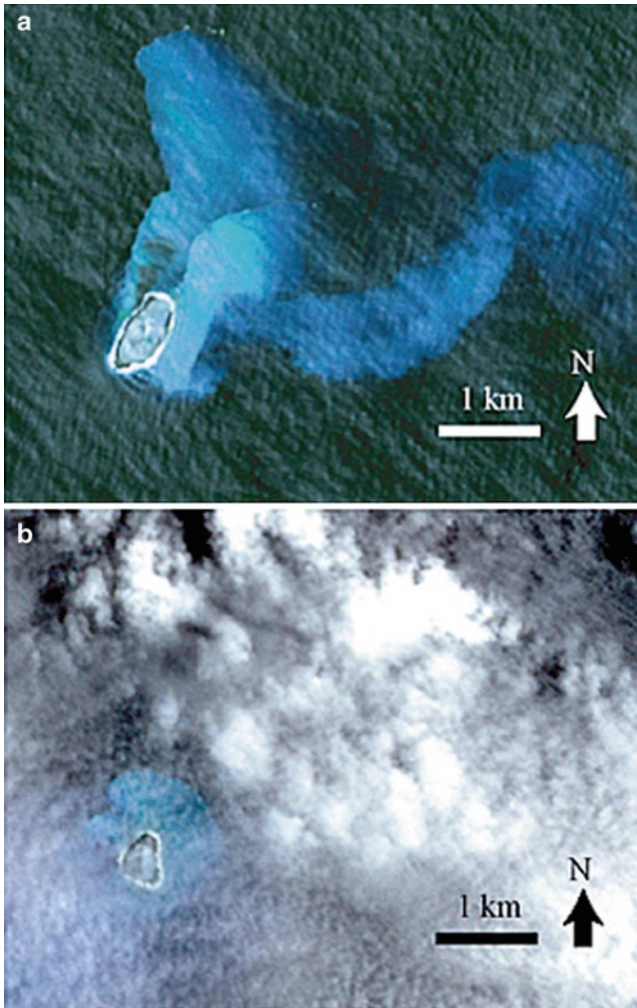


Fig. 12.16 Enlarged ASTER VNIR image of the new island. (a) Observed on October 4, 2006; (b) Observed on November 12, 2006

12.3.7 Detection of Flank and Summit Thermal Anomalies in Advance of the Chikurachki Volcano's 2003 Eruption

12.3.7.1 Introduction

Chikurachki (50°20'N, 155°27'E; elevation 1,816 m, stratovolcano) is the highest volcano on Paramushir Island in the northern Kurile Island chain. Chikurachki is among the youngest of the Kurile Volcanoes, with its oldest volcanogenic deposits

dating as recently as 20–23,000 BP (Braitseva et al. 1995), is also the most active volcano on Paramushir Island, having erupted in 1690, 1853, 1933, 1957, 1958, 1961, 1964, 1967, 1973, 1986, 2002, and 2003 (McClelland et al. 1989; Siebert and Simkin 2002; Dvigalo et al. 1988), and remains in a constant state of unrest for the last several years. Its most recent eruption began in April 2003, and was preceded by an eruption between January and May 2002. Though the volcano is remote (about 60 km from the small village of Severo-Kurilsk with a few thousand people), it nevertheless remains a potent hazard for the local population and air traffic; thus ongoing orbital remote sensing of gas, ash, and thermal emissions from this volcano are important (Girina and Neal 2002).

The most recent eruption began on April 18, 2003, and generated gas and steam plumes from almost continuous explosions at the volcano summit. Explosively erupting ash clouds rose up to 4,000 m above the summit crater, and a dilute ash plume often stretched up to 400 km E and ESE from the summit (Girina and Neal 2002; Schneider et al. 2003). ASTER cloud-free data over Chikurachki summit, during this period, are available for January 29, 2003, and February 14, 2003. By July 3, the Kamchatka Volcanic Eruption Response Team (KVERT) reported that the eruption probably finished, and satellite data apparently showed no activity of the volcano between June 25 and July 11 (Girina and Neal 2002). Knowing that Chikurachki Volcano began erupting in April 2003, we wished to look at earlier imaging data to ascertain the location of any thermal precursors, especially in the summit area. A January 29 ASTER (nighttime) TIR image showed little to no indication of thermal activity, and the volcano summit area appeared heavily snow-covered. A February 14, 2003 (nighttime) image, however, appears to reveal two areas of enhanced thermal emissions (Figs. 12.17 and 12.18) approximately 2 months before the onset of eruptive activity.

12.3.7.2 Analysis

The following analysis of Chikurachki thermal features is adapted from Pieri and Abrams (2005). To better illustrate the structure of the thermal anomalies within the summit crater, Fig. 12.18 shows ASTER TIR pixel values in false color. The color scale ranges from black (coldest) through purple, blue, green, yellow, orange, and red (warmest). On the left, the summit image is “draped” over an ASTER-derived digital elevation model from an image taken the previous summer in a perspective projection visualized in a west-southwestern view with Fuss Peak rising in the background. Two areas of enhanced TIR response are visible – one within the summit crater and another on the south flank of the volcano. Both are 100–200 m in characteristic dimension. At right is the indicated enlargement of the summit area. Here, however, altitude is replaced with radiance value number for the vertical axis for emphasis.

Figures 12.19a, b show two histograms of the 10.5 μm estimated pixel-averaged surface temperature (atmospherically corrected – ASTER On-Demand L2 Surface Kinetic Temperature (KT)), for Chikurachki volcano recovered from ASTER TIR

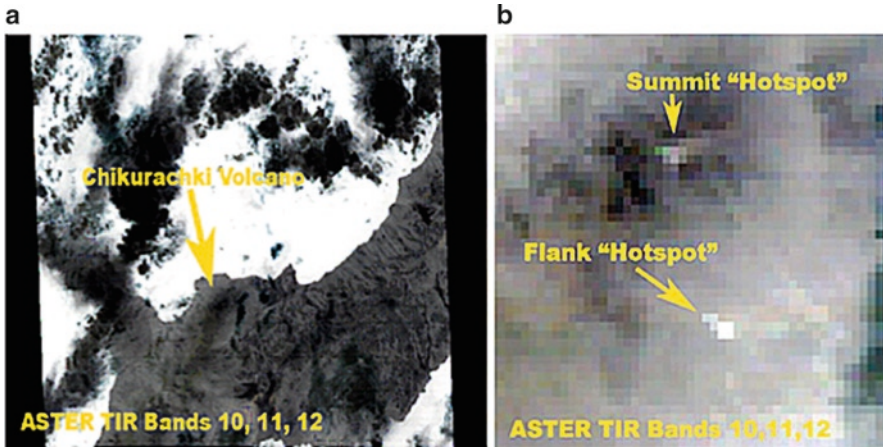


Fig. 12.17 A February 14, 2003, ASTER nighttime TIR image (a) of Paramushir Island. Note that water appears white (warm) and clouds appear black (cold). Land is generally intermediate (gray) while snow appears black. The image is 60 km across (full ASTER frame width). The figure on the right (b) shows an enlargement of the summit of Chikurachki Volcano. These images preceded the eruption by approximately 2 months

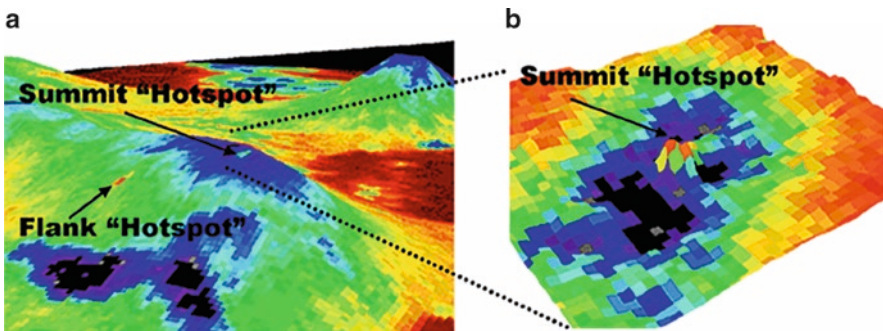


Fig. 12.18 (a) False color image draped over an ASTER-derived digital elevation; (b) enlargement of the summit area with temperature portrayed as topography (100×)

image data on February 14, 2003. Temperatures for the warmest pixels and their adjacent “background” pixels are displayed. On the right is the histogram for recovered KT’s observed within the summit crater. The pixel-averaged KT’s range between -22 and -23°C . For the warmest parts of the summit crater, the pixel-averaged KT ranges between -19 and -16°C . For the thermal anomaly on the Chikurachki flank, we observed a background KT range of -17 and -14°C , and a range of -14 and -7°C for the “hotspot.”

To resolve the temperatures and fractional radiant areas of thermal sources that are smaller than the pixels in which they are resident, we used the standard technique (Matson and Dozier 1981; Rothery et al. 1988; Glaze et al. 1989; Pieri et al.

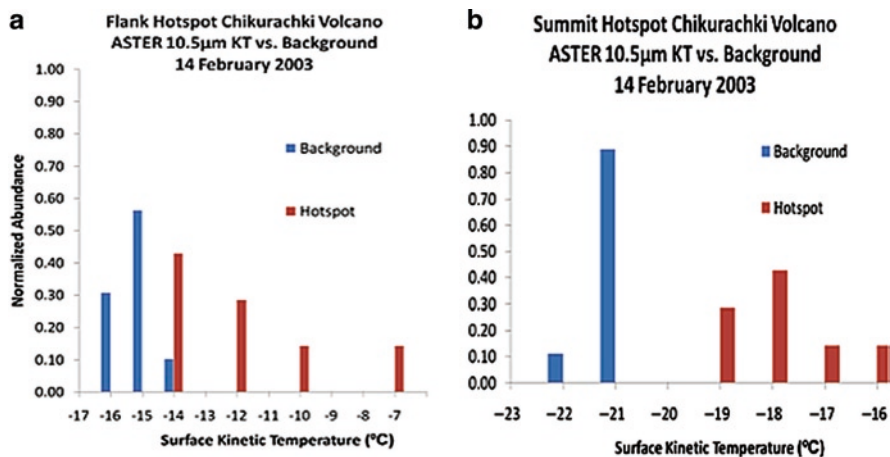


Fig. 12.19 Chikurachki Volcano (ASTER TIR; February 14, 2003); (a) ASTER 10.5 μm (Band 13) Flank Hotspot histogram and surrounding estimated surface kinetic temperatures; (b) ASTER 10.5 μm (Band 13) Summit Hotspot histogram and surrounding estimated surface kinetic temperatures

1990; Realmuto 1995) to solve the Planck equation for two measured radiance channels at different wavelengths simultaneously, in the TIR channel pairs where the curve fits were most consistent. Following Pieri et al. (1990), if we measure T_{en} and T_{bn} , for $n = i, j$, we arrive at two equations in two unknowns (T and f), namely,

$$T_{\text{ei}}^4 = fT^4 + (1-f)T_{\text{bi}}^4 \quad (12.2)$$

$$T_{\text{ej}}^4 = fT^4 + (1-f)T_{\text{bj}}^4 \quad (12.3)$$

where f is the warm fraction of the pixel. Solving (12.2) and (12.3) for the warmest pixels within the summit crater in the ASTER scenes, and measuring the pixel integrated kinetic temperatures in ASTER channel 10 (8.125–8.475 μm) ($T_{\text{e}10}$) and channel 11 (8.475–8.825 μm) ($T_{\text{e}11}$), where we achieved our most consistent fits, we calculate a summit “hotspot” size of roughly 1,300 m^2 (i.e., $f \sim 0.16$) at a temperature of $\sim 3^\circ\text{C}$ for a measured adjacent-pixel background temperature -22 to -21°C . Similarly, for several “hot” pixels on the flank of Chikurachki, we calculate somewhat higher sub-pixel temperatures of $\sim 14^\circ\text{C}$ corresponding to a sub-pixel area of roughly 2,800 m^2 (ASTER TIR channels 11 and 12 – most consistent fits) and a sub-pixel temperature of ~ -19 and 23°C corresponding to a sub-pixel area of about 2,000 m^2 (ASTER TIR channels 12 and 14 – most consistent fits). Background temperature for the flank anomaly was measured at -15.5°C .

ASTER TIR images of Chikurachki Volcano indicate that thermal anomalies existed within the summit crater and on one flank of the volcano at least 2 months

before the major explosive eruption in April 2003. If volcanogenic heat flow were uniformly diffused across the ASTER pixels, a warmer sub-freezing zone – comparable to the size of ASTER TIR pixels (i.e., $\sim 90 \times 90 \text{ m}^2$), or larger – could have existed at the summit and on the flanks of Chikurachki Volcano at that time. The area of enhanced heat flow on the flank appears somewhat warmer and larger than the “hotspot” within the summit crater. Notwithstanding an absence of direct evidence of any parasitic vents or active fumaroles on the volcano’s flanks, reason dictates that they may have existed.

Alternatively, we speculate that increased heat flow associated with the ascent of magma toward the surface sustained melt water – a few to tens of °C above freezing – in quantities significant enough to detect at sub-pixel spatial scales by the ASTER TIR sensor, with the surrounding terrain having temperatures well below the freezing point of water. The presence of a well-saturated overburden before the eruption is consistent with observations and reports of summit steam explosions implying a strong phreato-magmatic component to the April–July 2003 eruption (Girina and Neal 2002).

The availability of ASTER TIR imaging data at relatively high spatial resolution (90 m/pixel) and low $NE\Delta T$ (0.1–0.3 K) permitted the detection of low contrast thermal anomalies under certain conditions. In the case studied here, low surrounding background temperatures, fortuitous cloud-free conditions, and nighttime observations combined to permit the thermal “less cold” anomalies to stand out. Such observations could become crucial in assessing the occasional extreme hazards that snow-capped volcanoes present from even relatively minor melt-off thermal events summit (Voight and Cornelius 1991; Francis 1993).

12.4 Global Volcano Observation Plan, the ASTER Image Database for Volcanoes, and the ASTER Volcano Archive

12.4.1 Introduction

Compiled to achieve the ASTER science objective of volcano monitoring (Yamaguchi et al. 1998), the ASTER target list of over 1,500 volcanoes has yielded a (still growing) inventory of over 140,000 volcano views from over 75,000 individual ASTER day and night images, acquired as part of the Global Volcano Observation Plan of the ASTER Science Team (Urai et al. 1999) and under the ASTER Global Mapping program. A significant emerging challenge for ASTER is how to access effectively this burgeoning data archive in a way that allows the survey, extraction, and distribution of important information in a timely way. This issue is particularly acute in general for ASTER, which has produced a multispectral, high spatial resolution, feature-specific targeted global database of over one million image data granules worldwide.

While remote sensing data have obvious utility for volcano monitoring, many volcanologists have difficulty using them because prompt access is often problematic due to unfamiliarity with catalog, search and order generation protocols. In an effort to make ASTER data more accessible to both the general public and the scientific community, the ASTER Science Team has recently developed two Web-based data access tools, namely (a) the ASTER Image Database for Volcanoes in Japan and (b) the ASTER Volcano Archive in the United States.

12.4.2 *The Global Volcano Observation Plan with ASTER*

At the beginning of the ASTER mission, Urai et al. (1999) proposed a global volcano monitoring plan using ASTER data. Over 1,500 volcanoes in the Japan Meteorological Agency volcano catalog (Japan Meteorological Agency 1991) and the Smithsonian Holocene volcano catalog (Simkin and Siebert 1994) were monitored periodically over the life of the ASTER mission. Observing strategies for individual volcanoes varied according to the historical frequency of their eruption activity. The volcanoes monitored were selected from the aforementioned two catalogs, and divided into three classes, A, B, and C. Class A volcanoes have several recorded eruptions in the last ten years, and are observed every 48 days during daytime, and every 32 days at nighttime. Class B volcanoes have several recorded eruptions in the last 100 years, and are observed every 3 months during daytime and nighttime. Other volcanoes classified as Class C are observed every 6 months during daytime and nighttime. Figure 12.20 shows the locations of ASTER-monitored volcanoes.



Fig. 12.20 Volcano locations monitored by ASTER

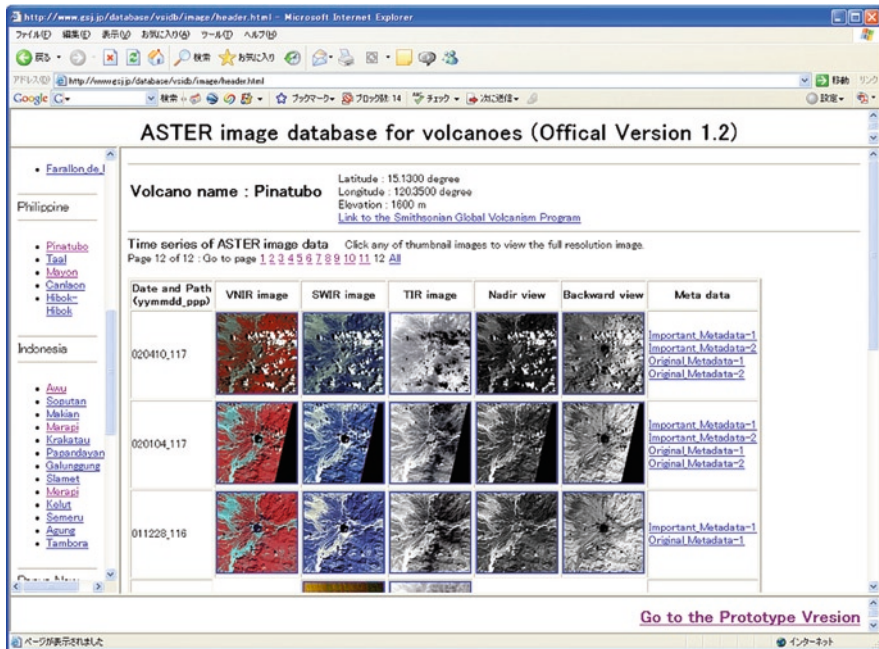


Fig. 12.21 Volcano selection menu of the ASTER Image Database for Volcanoes

12.4.3 ASTER Image Database for Volcanoes

The image database is designed to respond to requests from volcanologists for ASTER data. Acquired ASTER volcano images are stored within the database and are displayed as time-series data, useful to monitor activity at a particular volcano, as well as potentially useful in the mitigation and response to volcanic disasters. A 20 km by 20 km sub-image, centered on the volcano's geographic location appears in the archive. A mosaic is constructed automatically if the volcano is at a scene boundary.

Figure 12.21 shows the database's volcano selection menu. The user may choose a volcano from the menu displayed on the left-hand side, accessing ASTER images that are sorted by each data acquisition date, including VNIR, SWIR, TIR nadir and backward images. Small thumbnail links (Fig. 12.22) provide access to the full resolution browse images. The database is updated once every two days, and contains 964 global volcanoes, and its images are available to the public on the Internet through the following URL: <http://www.gsj.jp/database/vsldb/image/index-E.html>.

12.4.4 The ASTER Volcano Archive

The U.S. counterpart is a specialty domain called the JPL ASTER Volcano Archive (AVA: <http://ava.jpl.nasa.gov>), created to efficiently access and manage voluminous

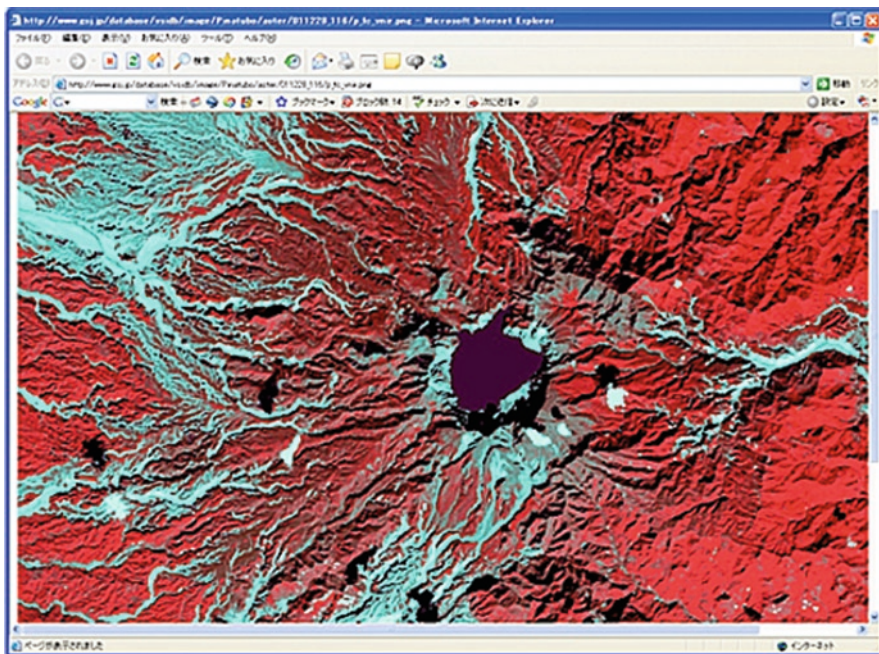


Fig. 12.22 Full-resolution image display of the ASTER Image Database for Volcanoes

volcano data within a large ASTER image library. It also houses other ancillary correlative volcanological data from MISR, MODIS, EO-1, SRTM, and related in situ data (Pieri et al. 2007).

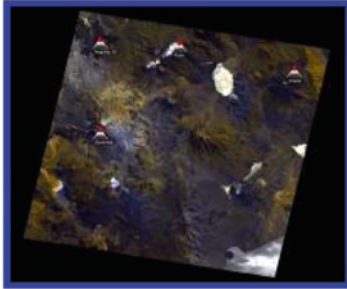
The AVA currently provides public access to $4,200 \times 4,200$ pixel “JPEG world files” of ASTER daytime data, with cloud-cover $<20\%$ by area, worldwide for all volcanoes listed in the current ASTER volcano “Science Team Acquisition Request (STAR).” In general, the ASTER STAR allows the ASTER GDS to request systematic acquisitions of ASTER data that are geographically, topically, or temporally related. The more specific Volcano STAR is used to implement the Global Volcano Observation Plan, as described in the previous section.

The AVA graphical user interface allows selection of volcanoes by geographic location or by name, after which an interactive array of browse frames appears. The user may display and/or download full-resolution JPEG worldfile images, and has hyperlink access to the volcano-specific web page within the Smithsonian Global Volcanism Project, and to the Google Earth tool. Figure 12.23 is an example of a typical AVA graphical user interface.

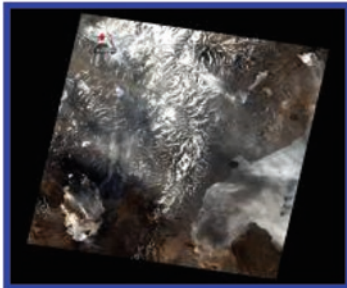
By the end of calendar year 2009, AVA expects to expand to its full capacity, including approximately 85,000 individual ASTER volcano frames (or granules), producing over 175,000 separate volcano observations (multiple volcanic centers are often contained within a single ASTER granule). The full library will include all ASTER granules containing volcanic centers, including day/night VNIR, SWIR, and TIR data, besides at least, one DEM for each volcano.

Socompa

Smithsonian Description



| | |
|--------------------------------------------------------------------------------------------------------------------------------------------------|--------------------------------------------------------------|
| Resolutions: | 1200x1200 Full Resolution |
| Data Acquired: (yyyy/mm/dd) | 2000/04/09 |
| Granule ID: | SC:AST_L1A.003:2006268377 |
| Load into Google Earth XML Metadata Full Resolution .jpgw Corner Points | |



| | |
|--------------------------------------------------------------------------------------------------------------------------------------------------|--------------------------------------------------------------|
| Resolutions: | 1200x1200 Full Resolution |
| Data Acquired: (yyyy/mm/dd) | 2000/05/18 |
| Granule ID: | SC:AST_L1A.003:2006547758 |
| Load into Google Earth XML Metadata Full Resolution .jpgw Corner Points | |

Fig. 12.23 A typical AVA graphical user interface depicts the entry for Socompa Volcano. All links in *blue* are active HTML hyperlinks. Reduced resolution and full resolution options are shown besides the internal granule ID, which references the image within the master data repository at the USGS Land Processes DAAC. These images are also directly displayable within Google Earth. All GIS metadata are provided, including image corner coordinates. Selecting the “Smithsonian description” link displays the related Web page within the Smithsonian Global Volcanism Program Web site

12.5 Conclusions

Launched in December 1999, the ASTER instrument has observed several volcanic eruptions. These data acquisitions help validate ASTER’s ability to monitor various volcanic activities, such as volcanic plumes, thermal anomalies, and volcanogenic seawater discoloration. The twin efforts fostered by Japan and the United States in developing an image database/archive help advance ASTER data use among volcanologists.

References

- Amelung F, Jónsson S, Zebker H, Segall P (2000) Widespread uplift and 'trapdoor' faulting on Galápagos volcanoes observed with radar interferometry. *Nature* 407:993–996.
- Braitseva OA, Melekestsev IV, Ponomareva VV, Sulerzhitsky LD (1995) Ages of calderas, large explosive craters and active volcanoes in the Kuril-Kamchatka region, Russia. *Bull Volcanol* 57(6):383–402.
- Carn SA, Oppenheimer C (2000) Remote monitoring of Indonesian volcanoes using satellite data from the Internet. *Int J Remote Sens* 21:873–910.
- Dvigalo VN, Andreev VI, Gavrilenko GM, Ovsyannikov AA, Razina AA, Chirkov AM (1988) Activity of the southeast Kamchatka and north Kuriles volcanoes in 1985–1986. *Volcanol Seismol* (3):13–20 (English translation 1990, 10:347–359).
- Francis PW (1993) *Volcanoes: a planetary perspective*. Oxford: Oxford University Press, pp. 283–289.
- Japan Meteorological Agency (1991) *National catalogue of the active volcanoes in Japan*, 2nd edn. Tokyo: Japan Meteorological Agency.
- Girina O, Neal T (2002) Kamchatkan Volcanic Eruption Response Team Reports, 30 January–05 March 2002 and 13 March–19 March 2002; available at http://www.avo.alaska.edu/avo4/updates/kvert_020102.htm.
- Glaze LS, Francis PW, Self S, Rothery DA (1989) The 16 September 1986 of Lascar volcano, north Chile: satellite investigations. *Bull Volcanol* 51:149–160.
- Hedenquist JW, Aoki M, Shinohara H (1994) Flux of volatiles and ore-forming metals from the magmatic-hydrothermal system of Satsuma Iwojima volcano. *Geology* 22:585–588.
- Kamada M (1964) Volcanoes and geothermy of Satsuma-Iwojima, Kagoshima prefecture. *J Jpn Geothermal Energy Assoc* 3:1–23 (in Japanese).
- Kato Y (1988) Gray pumices drifted from Fukutoku-oka-no-ba to the Ryukyu Islands. *Bull Volcanol Soc Jpn Ser 2* 33(1):21–30 (in Japanese with English abstract).
- Matson M, Dozier J (1981) Identification of subresolution high-temperature sources using a thermal IR sensor. *Photogramm Eng Remote Sens* 47(9):1311–1318.
- McClelland L, Simkin T, Summers M, Nielsen E, Stein TC (1989) *Global volcanism 1975–1985*. Washington, DC: American Geophysical Union.
- Nogami K, Yoshida M, Ossaka J (1993) Chemical composition of discolored seawater around Satsuma-Iwojima, Kagoshima, Japan. *Bull Volcanol Soc Jpn Ser 2* 38(3):71–77.
- Ono K, Soya T, Hosono T (1982) *Geology of the Satsuma-Io-Jima District*. Quad-range Series: Scale 1:50,000. Tsukuba: Geological Survey of Japan.
- Ossaka J (1975) The eruption of Nishinoshima submarine volcano and geochemical study of the composition of the ejecta and the volcanic activity. *Chemistry Today (Gendai Kagaku)* 55:12–20 (in Japanese).
- Ossaka J, Hirabayashi J, Nogami K, Tsuchide M, Adachi N (1996) Chemical composition of discolored seawater corresponding to activity of Fukutoku-Oka-no-Ba Submarine Volcano as an index of submarine volcanism. *Bull Volcanol Soc Jpn Ser 2* 41:107–113 (in Japanese with English abstract).
- Ossaka J, Adachi N, Tsuchide M, Nogami K (2000) Chemical compositions of discolored sea water around Izu-Oshima at the 1986 eruption. *Bull Volcanol Soc Jpn Ser 2* 45:271–280 (in Japanese with English abstract).
- Pieri D, Abrams M (2005) ASTER observations of thermal anomalies preceding the April 2003 eruption of Chikurachki volcano, Kurile Islands, Russia. *Remote Sens Environ* 99(1/2):84–94.
- Pieri DC, Glaze LS, Abrams MJ (1990) Thermal radiance observations of an active lava flow during the 1984 eruption of Mount Etna. *Geology* 18:1023–1027.
- Pieri DC, Crisp J, Kahle AB (1995) Observing volcanism and other transient phenomena with ASTER. *J Remote Sens Soc Jpn* 15(2):148–153.

- Pieri D, Abrams M, Tan H (2007) Eruptions on a virtual globe: The ASTER Volcano Archive, abst., San Francisco, CA: American Geophysical Union Fall Meeting.
- Pugnaghi S, Gangale G, Corradini S, Buongiorno MF (2006) Mt. Etna sulfur dioxide flux monitoring using ASTER-TIR data and atmospheric observations. *J Volcanol Geothermal Res* 152(1–2):74–90.
- Ramsey MS (2006) The critical need for moderate to high resolution thermal infrared data for volcanic hazard mitigation and process monitoring from the micron to the kilometer scale. American Geophysical Union, Fall Meeting 2006, abstract# H32D-06.
- Realmutu VJ (1995) Thermal Anomaly – High Spatial Resolution (Ver. 3), EOS IDS Volcanology Team Data Product Document # 3291, available at <http://eos.higp.hawaii.edu/docs/3291v3.pdf>
- Rothery DA, Francis PW, Wood CA (1988) Volcano monitoring using short wavelength infrared data from satellites. *J Geophys Res* 93:7993–8008.
- Schneider DJ, Girina OA, Neal CA, Kotenko L, Terentiev NS, Izbekov P, Belousov I, Senyukov S, Ovsyannikov AA (2003) Eruption of Chikurachki Volcano, Paramushir Island, Northern Kuriles, Russia, *Eos Trans. AGU*, 84(46), Fall Meeting Supplement, Abstract V42B-0348.
- Siebert L, Simkin T (2002) Volcanoes of the world: an illustrated catalog of holocene volcanoes and their eruptions. Smithsonian Institution, Global Volcanism Program Digital Information Series, GVP-3, (<http://www.volcano.si.edu/world/>).
- Simkin T, Siebert L (1994) Smithsonian Institution Volcanoes of the world, 2nd edn. Tucson: Geoscience Press.
- Tsuchide M, Ohtani Y (1983) Surveillance of submarine volcanoes – the possibility of Manmade Satellites and Hydrophones. *Bull Volcanol Soc Jpn Ser 2* 28:375–394.
- Urai M (2004) Sulfur dioxide flux estimation from volcanoes using Advanced Spaceborne Thermal Emission and Reflection Radiometer – a case study of Miyakejima volcano, Japan. *J Volcanol Geothermal Res* 134(1–2):1–13.
- Urai M, Machida S (2005) Discolored seawater detection using ASTER Reflectance Products: a case study of Satsuma-Iwojima, Japan. *Remote Sens Environ* 99:95–104.
- Urai M, Fukui K, Yamaguchi Y, Pieri DC (1999) Volcano observation potential and global volcano monitoring plan with ASTER (in Japanese with English abstract). *Bull Volcanological Soc Jpn* 44(3):131–141.
- Vaughan RG, Abrams MJ, Hook SJ, Pieri DC (2007) Satellite observations of New Volcanic Island in Tonga. *Eos Trans AGU* 88(4):37.
- Voight B, Cornelius RR (1991) Prospects for eruption prediction in near real-time, *Nature* 350:695–698.
- Yamaguchi Y, Kahle AB, Tsu H, Kawakami T, Pniel M (1998) Overview of advanced spaceborne thermal emission and reflection radiometer (ASTER). *IEEE Trans Geosci Remote Sens* 36(4):1062–1071.

Chapter 13

Issues Affecting Geological Mapping with ASTER Data: A Case Study of the Mt Fitton Area, South Australia

Robert Hewson and Thomas Cudahy

13.1 Introduction

The minerals industry uses multispectral Advanced Spaceborne Thermal Emission Reflectance Radiometer (ASTER) data for geological mapping with enthusiasm around the world. ASTER represents an advance beyond the capabilities of the 7-band Landsat Thematic Mapper, measuring radiant energy from 14 bands, within the visible-near infrared (VNIR), the shortwave infrared (SWIR), and thermal infrared (TIR) wavelength regions, at spatial resolutions ranging from 15 to 90 m (Yamaguchi et al. 1998). Geologists used ASTER data for its multispectral coverage in the mineralogically significant SWIR wavelength region (Yamaguchi et al. 1998), where OH-bearing and carbonate minerals have diagnostic spectral features (Clark et al. 1990; Grove et al. 1992). ASTER also provides multispectral coverage within TIR wavelengths (Yamaguchi et al. 1998), where many other silicates (and carbonates) have diagnostic features (Salisbury and D’Aria 1992).

13.1.1 Sensor Resolution Issues

Reliable geological mapping with remote sensing data requires both the correct identification of minerals, based on compositionally diagnostic spectral signatures, as well as its accurate spatial representation as map products. The issue of spectral resolution of the sensor is an important factor determining the reliability

R. Hewson (✉)
CSIRO Exploration and Mining, Australian Resources Research Centre (ARRC),
26 Dick Perry Avenue, Kensington, WA 6151, Australia
e-mail: Rob.Hewson@csiro.au

of any derived geological products based on diagnostic spectral features. Remote sensing products that discriminate, rather than help identify the mineralogy, require extensive interpretation and field validation to associate the various anomalies highlighted within the processed images. Less effort is necessary to generate geological maps from remote sensing data if sensors of higher spectral resolution (e.g., narrower bands) and more bands are available within compositionally important wavelength regions. A sensor's spatial pixel dimensions and spatial geo-location performance are additional issues, which potentially affect the reliability of derived geological products. High topographic relief may generate terrain errors within the images, although this generally is not a problem in Australia.

Airborne hyperspectral systems such as HyMap (Cocks et al. 1998), comprising over 100 spectral bands, can detect diagnostic information from narrow and subtle spectral features. Atmospheric effects within hyperspectral data, once corrected, may help generate surface reflectance with water vapor estimates derived from their in-scene water-sensitive bands. The resulting processed images from HyMap are shown to correctly identify minerals (e.g., chlorite and talc) as well as mineral chemistry (e.g., white mica) from extensive field sampling and laboratory spectral measurements and mineral analysis (X-ray diffraction) (Cudahy et al. 2005). The United States Geological Survey (USGS) VNIR-SWIR laboratory-measured spectral signatures for several minerals, relevant to this study, are shown in Fig. 13.1a (Clark et al. 1990). The equivalent, calculated spectral signatures, assuming HyMap resolution, indicate the major diagnostic absorption features are still resolved within the 2.1–2.4 μm wavelength range (Fig. 13.1b). The absolute geo-location performance of the HyMap images is generally high (5–10 pixels, e.g., ≤ 50 m), being related to the pixel resolution, usually 5 m, and its registration using digital elevation models and on-board inertial navigation systems (Cocks et al. 1998). These high-resolution attributes of hyperspectral sensors enable the generation of reliable mineralogical maps, comparable to detailed published geological maps (e.g., 1:100,000) (Cudahy et al. 2005).

By comparison, ASTER's modest spectral resolution with its 14 bands (9 within the VNIR-SWIR) generally provides spectral signatures of mineral groups, rather than specific minerals (Hewson et al. 2005) (Fig. 13.1c). For example, carbonate minerals calcite and dolomite are not clearly discriminated using ASTER, although the presence of the ferrous iron spectral ramp between 0.8 and 1.6 μm helps to distinguish MgOH minerals chlorite and talc (Fig. 13.1c). ASTER's spatial resolution is also coarser than typical airborne HyMap survey data, varying from 15 m for the three VNIR bands to 30 m for the six SWIR bands. Iwasaki and Fujisada (2005) ascertained ASTER data's absolute geolocation accuracy at 50 m in areas not significantly affected by terrain. This study examines these resolution issues by comparing an Australian example of geological mapping generated from satellite-borne ASTER data and those from higher-resolution airborne hyperspectral images. Laboratory measurements of field samples are also used to examine the spectral signatures of the major units.

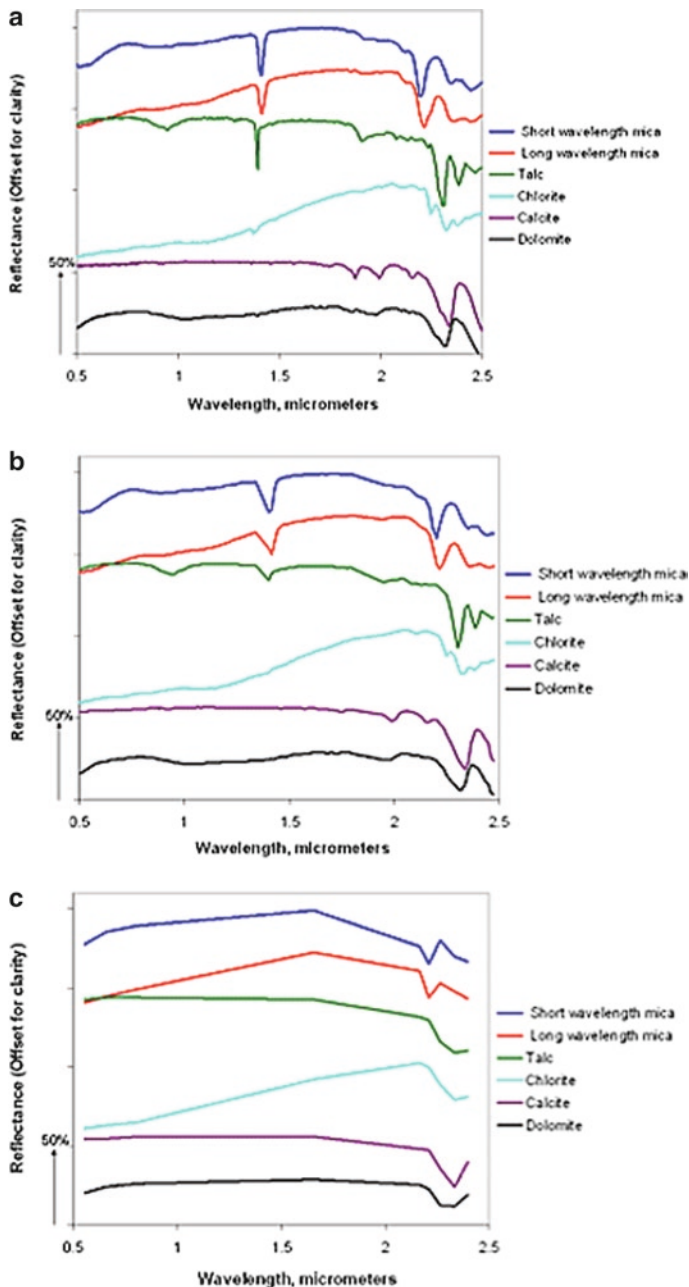


Fig. 13.1 (a) USGS spectral library examples of short and long wavelength mica, talc, chlorite, calcite, and dolomite (Clark et al. 1993), at laboratory measurement resolution; (b) at HyMap's spectral resolution; (c) at ASTER's spectral resolution

13.1.2 Atmospheric Effects and SWIR Crosstalk Issues

Atmospheric scattering, absorption, and emission effects within remote sensing images potentially affect the discrimination of these diagnostic mineral (group) spectral features, previously described. In particular, uncorrected atmospheric effects may potentially produce artifacts within the reflected spectral signature, including those bands closest to water vapor absorption (e.g., 2.7 μm). Therefore, uncorrected and varying atmospheric conditions may affect the repeatability of derived mineral (group) products from different acquisitions. Correction of atmospheric water ideally requires in-scene estimates of water vapor derived from that acquisition. However, in-scene atmospheric water vapor information, coincident at ASTER's pixel-scale, does not exist for hyperspectral VNIR-SWIR data from specific water-sensitive bands. ASTER's surface reflectance product is generated from atmospheric models using NOAA-NCEP (National Oceanic and Atmospheric Administration – National Centers for Environmental Prediction) and MODIS (Moderate Resolution Imaging Spectroradiometer) (Thome et al. 1998) profile information.

The “SWIR Crosstalk Effect” (Iwasaki et al. 2001) is another important issue to address when using ASTER for geological mapping. The SWIR crosstalk issue involves the leakage of photons across the SWIR detector array that affects the spatial distribution of image features and spectral signatures (Iwasaki and Tonooka 2005). In particular, the crosstalk effect results in offset or additive errors in radiance, particularly for bands 5 and 9 but also present in all other SWIR bands (Iwasaki et al. 2001). The relative size of the crosstalk error is related to illumination conditions or albedo. For example, within very dark pixels adjacent to bright pixels, the crosstalk effect will approach 100% of the input radiance signal (Hewson et al. 2005).

An understanding of these atmospheric and crosstalk issues is required before tiled mosaics of individual ASTER scenes and their derived products are generated using multi-temporal images from multiple date acquisitions (Hewson et al. 2005). The resulting product aims to generate “seamless geological maps” over large areas such as geological provinces (Curnamona Province; Hewson et al. 2005).

This study uses mosaics of multi-temporal ASTER images, collected from the well-exposed Mt Fitton area in South Australia (Fig. 13.2), to examine these



Fig. 13.2 Location of Mt Fitton test site, South Australia

atmospheric and crosstalk issues. In particular, this study investigates the ability to generate repeatable geological products from variable atmospheric and illumination conditions, with and without applying crosstalk corrections. This work follows several previous case studies detailing the generation of geological maps in Australia, using single acquisition ASTER data (Rowan et al. 2005; Hewson et al. 2001), and from multi-temporal ASTER datasets (Hewson et al. 2005).

13.2 Mt Fitton Test Site, South Australia

The Mount Fitton area in the northern Flinders Ranges, 600 km north–northeast of Adelaide (139°25'E, 29°55'S), (Fig. 13.2) has a semi-arid climate, which receives less than 250 mm rainfall per year. Generally, the vegetation is sparse, ranging between 5 and 15% total cover (Fig. 13.3). Regional topography provides a relief of up to 1,000 m, but Mt Fitton's localized relief is generally only 100 m. Flash flooding has stripped unconsolidated regolith material, leaving abundant fresh exposures of bedrock.

Mt Fitton contains a variety of intrusive and sedimentary units, with some greenschist metamorphic and localized hydrothermal alteration. Geological mapping by Coats et al. (1969) and Coats and Blissett (1971), summarized in Fig. 13.4, found Precambrian granites, amphibolite dykes, and tightly folded and faulted tillites, siltstones, and carbonates. Precambrian (Carpenterian) granitic basement rocks of the Mount Babbage Block (Terrapinna Granite) are exposed in the northeast part of the study area. This area is overlain by Adelaidean sediments of the Umberatana Group, which includes the Mount Curtis Tillite and Bolla Bollana Formation. The published maps do not identify zones of alteration and mineralization, such as the greenschist-facies, dolomite, and magnesite development (replacement of Ca by Mg)



Fig. 13.3 Typical view of weathered outcrop and vegetation at Mt Fitton

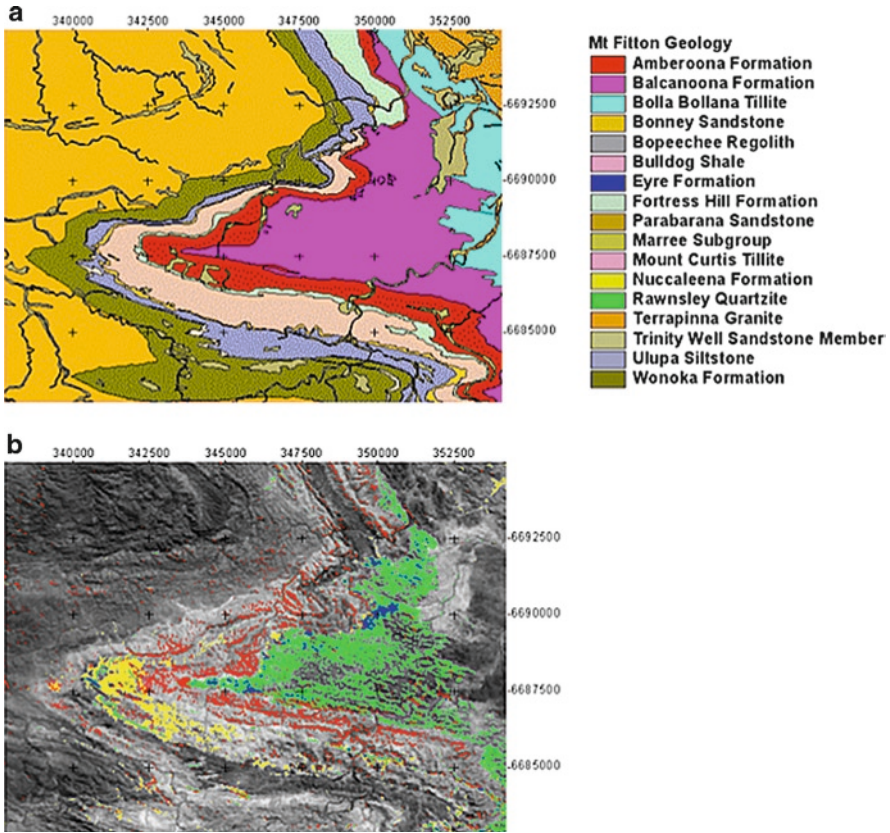


Fig. 13.4 (a) Published geology of the Mt Fitton Test Site (Coats et al. 1969); (b) unmixed mineral-rich endmembers extracted from ASTER, highlighting areas of carbonate-rich Balcanoona Formation (*green*); talc-rich deposits (*blue*); chlorite-rich alteration (*red*); and mica-rich units (*yellow*) overlain over ASTER band 4 albedo image

within the Balcanoona Formation. Localized hydrothermal alteration has resulted in the formation of talc, tremolite, chlorite, scapolite, muscovite, and/or quartz in the carbonate sequences. Talc has been mined from the area for over 30 years.

13.3 Previous Remote Sensing Studies at Mt Fitton

The exposure of a wide variety of rocks and minerals renders Mt Fitton an excellent validation site for remote sensing instruments. They include airborne sensors, like HyMap, (Denniss et al. 1999), TIMS (Hook et al. 1998), MIRACO2LAS (Cudahy et al. 1999) as well as the satellite-borne Hyperion (Cudahy et al. 2001a, b) and ASTER sensors (Hewson et al. 2001).

Previous analysis of ASTER data acquired over the Mt Fitton test site in April 2000 showed the power of multi-spectral VNIR-SWIR-TIR images for geological mapping (Hewson et al. 2001). The ASTER-based maps were validated by comparison to maps derived from data acquired with the airborne hyperspectral HyMap (Cocks et al. 1998) and TIMS (Thermal Infrared Multispectral Scanner) (Palluconi and Meeks 1985) sensors. In our previous study, we applied log residual processing (Green and Craig 1985) to radiance data for the six ASTER SWIR bands to remove systematic atmospheric multiplicative effects, and generate pixel-specific mineralogical signatures. We then applied match filter techniques (Kruse et al. 1993) to separate the contributions of specific minerals to the derived log residual spectra. Match filtering aims to separate or “unmix” the spectral components of each image pixel signature into estimated proportions of minerals or “endmembers.” The end result is to generate maps, which represent the abundance proportions of these endmember minerals. We found that similarities in the exposed material’s spectra and uncertainty of their nature required *a priori* field-mapping knowledge to help identify these materials discriminated by the ASTER data. Calibrating the log residual signatures with laboratory measurements of Mt Fitton Talc Mine improved the ability to interpret the spectral absorption features. This calibration involved the application of a simple multiplicative gain factor derived from the comparison of the average log residual signature for the exposed Mt Fitton Talc Mine with laboratory spectral measurements of collected talc samples, resampled to ASTER’s band resolution.

The current study, which yields similar results to the earlier one (Hewson et al. 2001) for the Mt Fitton test site, used the ASTER level-2 Surface Reflectance product, unavailable at the time of the original study (Fig. 13.4). The level-2 ASTER product is produced from level-1B radiance-at-sensor data, corrected for atmospheric effects (Thome et al. 1998), and produced by both Earth Remote Sensing Data Applications Center (ERSDAC) and the USGS EROS Center. The derived mineral maps, shown in Fig. 13.4b, allow us to discriminate areas of talc-rich alteration (blue), within the carbonate units (green) of the Balcanoona Formation. We also mapped greenschist chlorite alteration within the Amberoona Formation at the nose of the Mt Fitton anti-form (red, Fig. 13.4b). Mica-rich areas within the Mount Curtis Tillite and Ulupa Siltstone, particularly in the vicinity of the Mt Fitton anti-form, were also highlighted (yellow, Fig. 13.4b).

The reflectance spectra of a large number of field samples from the Mt Fitton test site were measured using a variety of instruments including a dual-beam GER Mk IV IRIS spectrometer, which measures bi-directional reflectance from 0.4 to 2.5 μm . These high-resolution spectra were convolved with the ASTER response functions to yield the equivalent six ASTER SWIR spectral bands (Fig. 13.5a). Figure 13.1a–c depicts mineral library spectra from three sources: the USGS, HyMap, and ASTER. The spectral absorption features, which distinguish talc, chlorite, and dolomite within the 2.1–2.4 μm , are considerably reduced at ASTER’s resolution.

The differences between the resampled field sample spectra (Fig. 13.5a) and ASTER-based signatures associated with each derived endmember (Fig. 13.5b) were reduced when the ASTER endmember signatures were calibrated (Fig. 13.5c),

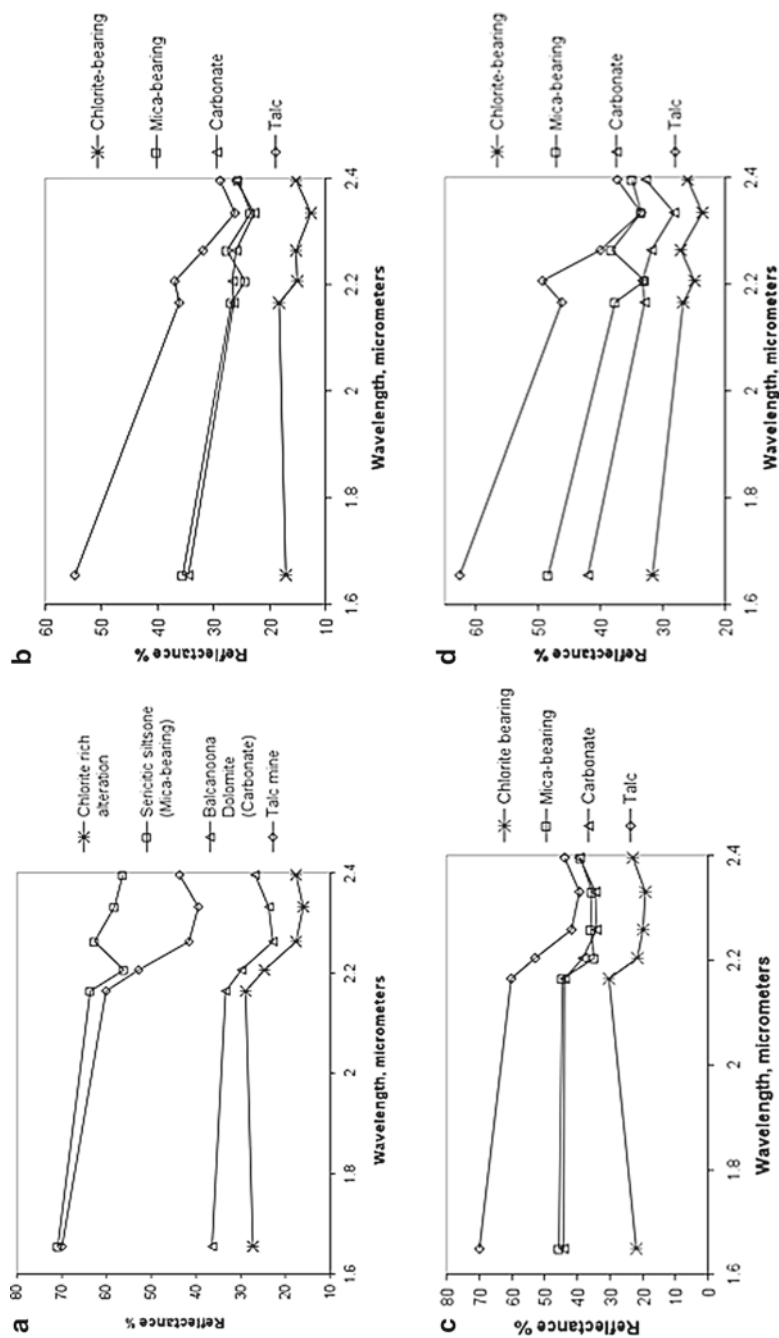


Fig. 13.5 (a) Laboratory spectral measurements of Mt. Fitton field samples (GER IRIS spectrometer); (b) ASTER surface reflectance (24th Apr 2000) endmember signatures used to match filtering/unmixing results; (c) unmixed endmember signatures derived from ASTER surface reflectance data calibrated using Mt. Fitton Talc Mine reference spectra; (d) spectral signatures for endmember sites determined from unmixing of 24th Apr 2000 ASTER acquisition using crosstalk-corrected surface reflectance data acquired 4th Dec 2000

shown in earlier studies (Hewson et al. 2001). For example, the absorption feature between 2.3 and 2.35 μm , associated with talc, chlorite, and/or carbonate, is apparent in both the resampled field (Fig. 13.5a) and calibrated ASTER (Fig. 13.5c) spectra. The 2.2- μm absorption feature, indicative of AlOH minerals (produced by the alteration of the Ulupa Siltstone), was more apparent within this calibrated ASTER signature (Fig. 13.5c). ASTER's bands 4 (1.6 μm) and 5 (2.15 μm) assisted in the discrimination between talc, chlorite, and carbonate in the images. Reduced reflectance at shorter SWIR wavelengths (e.g., 1.6 μm) relative to longer SWIR wavelength (e.g., 2.15 μm) reflectance is attributable to the ferrous (Fe^{2+}) iron content of several minerals (Clark et al. 1990). In particular, the presence of an upward ramp in spectral reflectance from band 4 to band 5 suggests the presence of ferrous iron (e.g., chlorite), but the ramp is absent in the talc and siltstone spectra (Fig. 13.5a, c).

Another set of Mt Fitton unmixed spectral signatures were generated using the crosstalk-corrected ASTER level-2 surface reflectance product (acquired on 4th Dec 2000) (Fig. 13.5d). ERSDAC produced this newer crosstalk-corrected ASTER level-2 surface reflectance product (Iwasaki et al. 2001) from corrected level-1B ASTER radiance data.

The endmember signatures shown are from the same areas identified by the results derived from log residuals and crosstalk-uncorrected surface reflectance (Fig. 13.5b, c). These crosstalk-corrected ASTER SWIR spectral signatures were still different from those measured by the GER-IRIS of representative field samples, although the comparison with carbonate-, talc-, and mica-bearing sample signatures showed some improvements (Fig. 13.5d). In summary, the most favorable comparison with field sample spectra occurs for those endmember signatures obtained from ASTER surface reflectance products calibrated with reference spectral measurements (Fig. 13.5c).

13.4 ASTER Pre-processing and Mineral Map Generation

13.4.1 ASTER Data Levels and Products

Reliable geological mapping with ASTER radiance at-sensor data requires the removal or minimizing of atmospheric effects. This involves either an attempt to normalize (e.g. band ratios) variable atmospheric effects or correct the surface reflectance data. LP DAAC and ERSDAC generate ASTER level-2 surface reflectance and emissivity products from level-1B radiance at-sensor data using atmospheric corrections designed from seasonal default atmospheric models (Thome et al. 1998). The surface emissivity uses atmospherically corrected TIR radiance data, followed by the separation of surface emissivity from temperature (Gillespie et al. 1998). A material's surface emissivity is essentially a dimensionless measure of its ability to absorb and emit radiation at different wavelengths. The maximum

possible emissivity is 1.0, and approached by water and moist ground or vegetation. The surface reflectance and emissivity products, generated by ERSDAC and LP DAAC, are supplied in hierarchical data format (HDF) and include 1,000 as a gain factor. Level-1B ASTER data are also supplied in HDF files, which include a set of unit conversion coefficients, to calculate calibrated radiance at-sensor values in $W/m^2/sr/\mu m$ units. Radiance values are calculated with the formula: $(DN - 1) \times G$, where DN is the supplied digital number from the ASTER sensors, and G , the unit conversion coefficient for each band (Abrams et al. 2002).

Both ASTER level-1B radiance at-sensor and level-2 surface reflectance and emissivity data products were used to generate geological products at Mt Fitton. This study examines the consistency of the geological mapping derived from the ASTER level-1B and level-2 products. The input scenes were acquired on eight different dates, which span different seasons, atmospheric conditions, and sun angles (Table 13.1). The solar illumination and sensor pointing angles for the eight ASTER acquisitions are summarized in Table 13.1. The effect of the ASTER pointing angle on spectral radiance is negligible relative to the effect of solar incidence angles. The radiance at-sensor is a function of the cosine of the solar incidence angle. For example, the sensor at-radiance on 4th Dec 2000 (cosine = 0.93) was roughly twice that of the radiance on 29th May 2001 (cosine = 0.55). The maximum overlap area between these eight multi-temporal ASTER acquisitions defined the Mt Fitton study area (Fig. 13.6a). This study included most of the Mt Fitton test site, described previously (Fig. 13.4a), but encompassed a larger range of topographic relief and geology. The larger area also included some hyperspectral HyMap images, acquired on 19th Sept 2000 at 4.4-m-pixel resolution (Fig. 13.6a).

Table 13.1 Solar and ASTER sensor pointing angles for the eight acquisitions within the Mt Fitton study area, and their effect on illumination conditions assuming a horizontal Lambertian ground surface

| ASTER acquisition date | Solar elevation (θ degrees) | Solar azimuth (degrees from S) | Pointing angle (δ degrees) | Solar elevation effect ($\cos \theta$) | Combined solar and pointing effects ($\cos \theta \times \cos \delta$) |
|------------------------|-------------------------------------|-----------------------------------|------------------------------------|------------------------------------------|--------------------------------------------------------------------------|
| 12-Jan-2001 | 65.56 | 103.71 | 2.821 | 0.91 | 0.91 |
| 11-Apr-2001 | 44.43 | 142.82 | -8.558 | 0.70 | 0.69 |
| 24-Apr-2000 | 41.52 | 148.58 | -5.73 | 0.66 | 0.66 |
| 29-May-2001 | 33.08 | 151.86 | -8.591 | 0.55 | 0.54 |
| 29-Jul-2000 | 35.22 | 149.23 | -8.503 | 0.58 | 0.57 |
| 1-Oct-2000 | 56.16 | 137.82 | -8.58 | 0.83 | 0.82 |
| 28-Nov-2001 | 67.98 | 107.79 | 5.727 | 0.93 | 0.92 |
| 4-Dec-2000 | 68.34 | 105.37 | -8.58 | 0.93 | 0.92 |

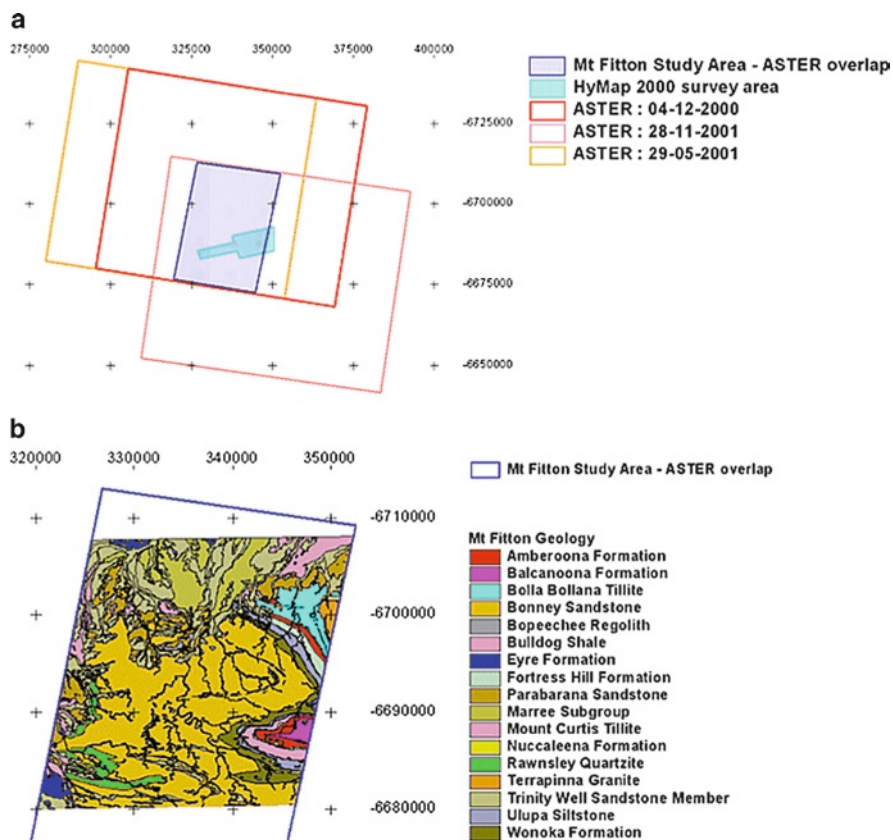


Fig. 13.6 (a) Mt Fitton Study Area in relation to summer-winter ASTER scenes, and airborne HyMap survey area; (b) published geology of Mt Fitton (Coats et al. 1969) within Mt Fitton Study Area

Mineral maps generated from this HyMap data were used as a reference to compare with the ASTER-derived map products.

The stereo-image pairs, acquired with ASTER’s band-3, are used to generate Digital Elevation Model (DEM) products, which are useful to relate the geology to geomorphology. LP DAAC and ERSDAC both produce relative ASTER DEM products.

In the ancient and weathered Australian terrain, discriminating transported and regolith material from in situ elevated outcrops has proved useful to improve the geological interpretation (Hewson et al. 2006). In this study, relative ASTER DEMs are integrated with ASTER geological products to ascertain the effects of topography on illumination conditions over different seasons. In particular, the ASTER DEMs were used to display shaded relief based on the solar elevation and aspect at image acquisition time.

13.4.2 ASTER SWIR Crosstalk Correction

A spatially dependent software correction for crosstalk was developed by Iwasaki et al. (2001), and is incorporated by the Japanese ASTER Ground Data System (GDS) as a part of its level-1B pre-processing. GDS publicly provides this software to users to correct crosstalk effects in their ASTER level-1B data. Hewson et al. (2005) evaluated the ASTER SWIR crosstalk effects in their geological mapping study of the Curnamona-Broken Hill Province, Australia. In particular, areas of low input signal (e.g., low albedo, cloud shadows, and shadowed topographic relief) exhibit anomalous geological results associated with this SWIR crosstalk issue. This source of error on geological mapping is further examined in this study at Mt Fitton by comparing geological mapping derived from ASTER radiance data before and after a crosstalk correction, with ERSDAC-provided software (Iwasaki et al. 2001; Iwasaki and Tonooka 2005). This software correction was applied to level-1B radiance at-sensor data with the default input parameters (Iwasaki et al. 2001). In addition, this study also incorporates products derived from ASTER-level 2 surface reflectance data, based on ERSDAC crosstalk-corrected level-1B radiance at-sensor data supplied by GDS.

13.4.3 Geological and Mineral Information Extraction Techniques for Multitemporal Mapping

Relative Band Depth (RBD) procedures (Crowley et al. 1989) are an alternative to spectral unmixing (Kruse et al. 1993). RBDs have been used to generate map products from ASTER data and initialize spectral unmixing analyses (Rowan and Mars 2003). Simple band ratio techniques and RBDs are also useful to normalize the atmospheric and seasonal illumination differences between scenes in a multi-temporal mosaic (Ninomiya et al. 2005, Hewson et al. 2005). The RBD technique is defined by three sensor bands:

$$[R(\lambda_1) + R(\lambda_2)] / R(\lambda_3), \quad \lambda_1 < \lambda_3 < \lambda_2$$

Here, $R(\lambda_1)$ and $R(\lambda_2)$ are typically reflectance values processed from radiance at-sensor data, at the shoulders of the targeted spectral absorption feature at band wavelengths, λ_1 and λ_2 , and $R(\lambda_3)$ is the band value located in closest proximity to the absorption feature. At ASTER's spectral resolution, the targeted absorption features are characteristic of mineral groups rather than individual minerals. These groups include the AlOH and MgOH/carbonate mineral groups, with diagnostic absorption features within the 2.1–2.2 μm and 2.3–2.35 μm wavelength regions, respectively. Higher values for an RBD result are indicative of deeper spectral absorption features, where $R(\lambda_3)$ is lower than either, relative to $R(\lambda_1)$ and/or $R(\lambda_2)$. We assume that the RBDs are directly related to the

Table 13.2 ASTER RBD and band ratio parameters used in the study

| Mineral (group) products | ASTER band parameters |
|--------------------------|-----------------------|
| MgOH–carbonate abundance | (b6+b9)/b8 |
| Carbonate abundance | b13/b14 |
| AlOH abundance | (b5+b7)/b6 |
| AlOH composition | b5/b6, b7/b6, b7/b5 |
| Ferrous iron content | b5/b4 |
| Quartz abundance | b13/b10 |

abundance of the targeted mineral, although grain size and desert varnish effects may make this a semi-quantitative measure at best (Crowley 1986; Rivard et al. 1992). Table 13.2 shows the list of the ASTER RBDs and band ratios designed to estimate AlOH, MgOH, carbonate, ferrous iron, and quartz contents. We also attempted to map muscovite, including Al-substitution, using a red green blue (RGB) color ratio composite (b5/b6, b7/b6; b7/b5). This ratio combination was designed to detect shifts in the wavelength of the 2.2- μm mica absorption feature (Duke 1994).

The airborne HyMap hyperspectral data were also processed into carbonate abundance and AlOH compositional image products, with band parameters targeting SWIR absorption features, (Cudahy et al. 2005) to validate the generated ASTER products. However, the increased spectral resolution of the HyMap sensor (average SWIR bandwidth: 19 nm) allowed us to design reliable maps, which target the particular mineral spectral feature. Applying binary masking techniques helped reduce confusion with other similar mineral spectral features (Cudahy et al. 2005). In particular, we designed HyMap's carbonate band ratio product to target the 2.33- μm absorption feature, and applied a series of masks, which excluded pixels, spectrally characteristic of talc or chlorite. We attempted to map AlOH composition by fitting a fourth order polynomial to any 2.2- μm absorption feature and save the minima wavelength. Masking techniques were also applied to include only AlOH wavelength pixel values in the presence of significant AlOH abundance and in the absence of kaolinite. The hyperspectral HyMap reflectance data were resampled to ASTER's spectral resolution to simulate equivalent RBD and ASTER product's band ratio as a check of its spectral integrity. ASTER's five TIR bands within the 8–12 μm wavelength region also offered new opportunities to map silicates (Abrams and Hook 1998). Rowan et al. (2005) demonstrated the mapping and discrimination of felsic and ultramafic units, together with quartz-rich sandstones and alluvium/colluvium using RBD, band ratio, and spectral matching techniques. The generation of quartz content map was accomplished using a mosaic of ASTER TIR images acquired under variable atmospheric and ground temperature conditions (Hewson et al. 2005). In particular, a band ratio product designed to map quartz content (e.g., b13/b10) was applied to 35 separate ASTER's level-2 surface emissivity products acquired on 14 different dates (Hewson et al. 2005). These products were combined into a

“seamless” mosaic without obvious boundary issues or artifacts. The issue of combining multiple radiance and emissivity data products into mosaics was further examined in this study.

13.5 Results

13.5.1 *AlOH, MgOH/Carbonate, and Ferrous Iron Mapping Using ASTER SWIR Radiance-at-Sensor Data*

Examples of RBD and band ratio processing for AlOH, MgOH/carbonate and ferrous iron content (Fig. 13.7a–c), within the Mt Fitton study area (Fig. 13.6a, b), were generated with ASTER level-1B data, acquired during summer (4th Dec 2000). Increased AlOH abundance and ferrous iron content, associated with chlorite, is apparent from these products at the nose of the Mt Fitton anti-form, as identified by previous studies (Hewson et al. 2001) (Fig. 13.7a, c). The ASTER MgOH/carbonate RBD product (Fig. 13.7b) maps both the Balcanoona Formation’s carbonate (dolomite) and the MgOH minerals, talc, and chlorite, associated with alteration (Hewson et al. 2001). Previous studies have noted that at ASTER’s spectral resolution, the primary spectral absorption diagnostic feature of MgOH and carbonate group minerals, within the SWIR wavelength region, are not distinguishable (Rowan et al. 2005; Hewson et al. 2005). The discrimination between the carbonate and MgOH minerals in this Mt Fitton ASTER product requires the use of the ferrous iron images and *a priori* mapping information. However, overall these examples indicate that ASTER level-1B radiance at-sensor data can successfully generate image map products related to either geological units or overprinted alteration mineralogy.

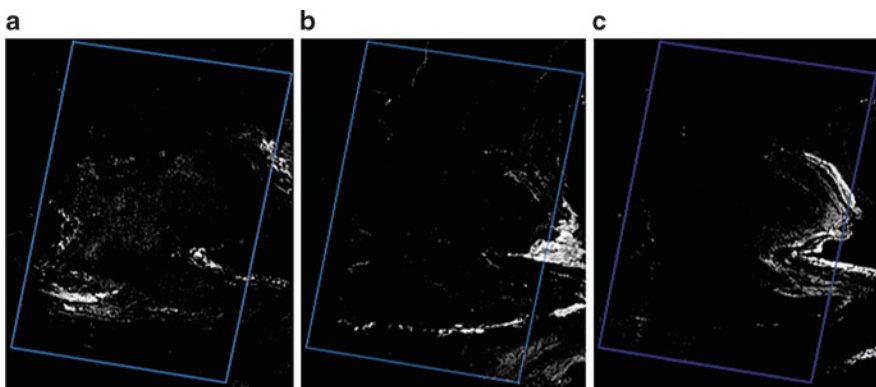


Fig. 13.7 (a) Crosstalk-corrected summer-time at-sensor ASTER radiance (4th Dec 2000) processed into AlOH abundance; (b) MgOH/Carbonate abundance; and (c) ferrous iron abundance. High abundance is represented by bright areas. Mt Fitton study area boundary is shown in blue

13.5.2 Seasonal and Pre-processing Effects on ASTER SWIR Mapping Results

To test the repeatability to generate geological maps from multiple date ASTER data, a series of RBD map products were produced (Table 13.1), with different ASTER products and pre-processing strategies. For example, MgOH/carbonate RBD products were generated from eight acquisitions using the level-2 surface reflectance (Fig. 13.8), crosstalk-corrected level-1B (Fig. 13.10), and non-cross talk-corrected level-1B (Fig. 13.11) radiance at-sensor products. The same linear thresholds were applied in each case. The MgOH/carbonate RBD product using level-2 surface reflectance data showed some variation in the overall albedo and noise levels (Fig. 13.8). The carbonate (and talc) within the Balcanoona Formation was mapped by each acquisition; however, it was apparent that the applied atmospheric correction was variable in its success and possibly introduced offsets, which the RBD processing could not normalize. For example the MgOH/carbonate RBD product derived from the 12th Jan 2001 ASTER acquisition is considerably noisier and elevated in response than results from the other seven acquisitions, including that from 4th Dec 2000, 6 weeks earlier (Fig. 13.8). The calculated mean ASTER SWIR spectral signatures within the study area for 12 Jan 2001 and 4 Dec 2000 acquisitions show that the band-9 response is considerably higher within the 12th Jan 2001 ASTER images (Fig. 13.9). ASTER's band-9, centered at 2.4 μm , occurs at the edge of the SWIR atmospheric window, and is highly sensitive to atmospheric water vapor. This high band-9 reflectance suggests that the elevated MgOH/carbonate RBD product (e.g., $[b6+b9]/b8$), derived for the 12th Jan 2001 ASTER, is possibly related to uncorrected atmospheric water vapor.

MgOH-Carb. ($b6+b9$)/ $b8$: Crosstalk-uncorrected surface reflectance

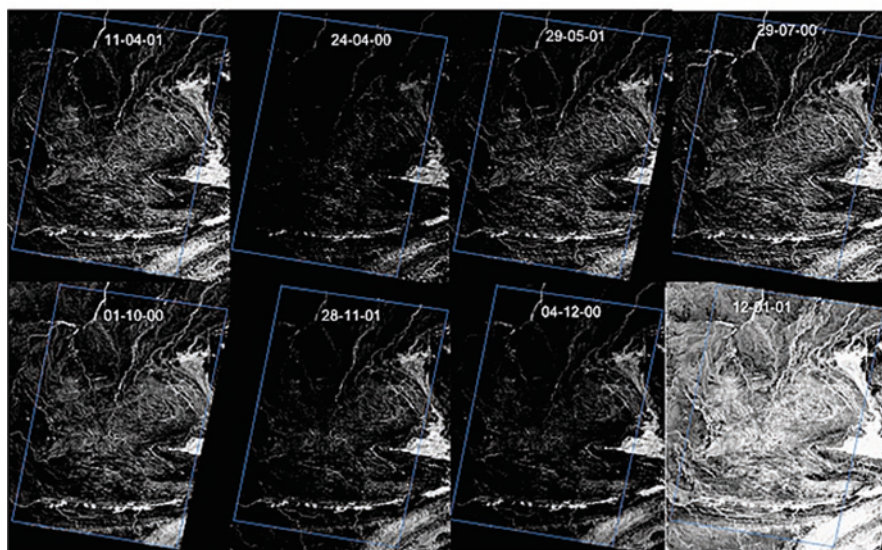


Fig. 13.8 MgOH/carbonate RBD product generated from multi-seasonal ASTER level-2 Surface Reflectance data. Mt Fitton study area boundary is shown in blue

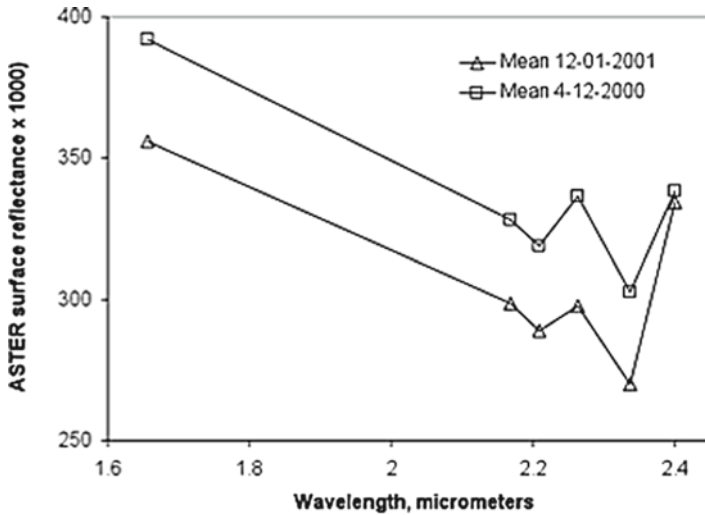


Fig. 13.9 Mean SWIR signatures derived from crosstalk-uncorrected ASTER level-2 Surface Reflectance data for 4th Dec 2000 and 12th Dec 2001 acquisitions, within the study area

Little difference was observed between the MgOH/carbonate RBD products compared to corresponding ASTER level-1B products, either crosstalk-corrected (Fig. 13.10) or uncorrected (Fig. 13.11). The most significant result was the noticeable consistent increase in apparent noise and anomalous MgOH/carbonate occurrences within the winter and near-winter acquisitions (e.g., 29th Jul 2000 and 29th May 2001). Although level-1B data are influenced by the atmospheric water vapor, its effect is mainly multiplicative and is normalized and reduced by the RBD technique. Mt Fitton is located within a semi-arid climate, with erratic non-seasonal rainfall; these factors are unlikely to explain these trends. A closer examination of the MgOH/carbonate RBD products, generated from crosstalk-uncorrected ASTER level-1B data and acquired during different seasons, reveals the extent of the noisy and anomalous nature of the winter acquisitions compared to the summer ones. In particular, MgOH/carbonate maps generated from summer (4th Dec 2000) and winter (29th May 2001) acquisitions are shown in Fig. 13.12a and b, respectively. The summer acquisition-derived MgOH/carbonate RBD products compare favorably with the HyMap reflectance data-derived carbonate map (Fig. 13.12c). The high spatial and spectral resolutions of the HyMap images were previously shown to produce reliable mineral maps, including carbonate (Cudahy et al. 2001a, b). Chlorite and talc were masked to exclude possible ambiguities with carbonate-rich areas. Masking also helped refine the HyMap carbonate map (Fig. 13.12c). The noisy anomalies present in the winter ASTER product appear to mimic the topography (Fig. 13.12b).

The noisy nature of these geological maps derived from winter-acquired ASTER data was further investigated by comparing the summer and winter ASTER level-1B (with and without crosstalk correction) data-derived AIOH compositional image products (Fig. 13.13a–g). The same linear thresholds were applied to all the

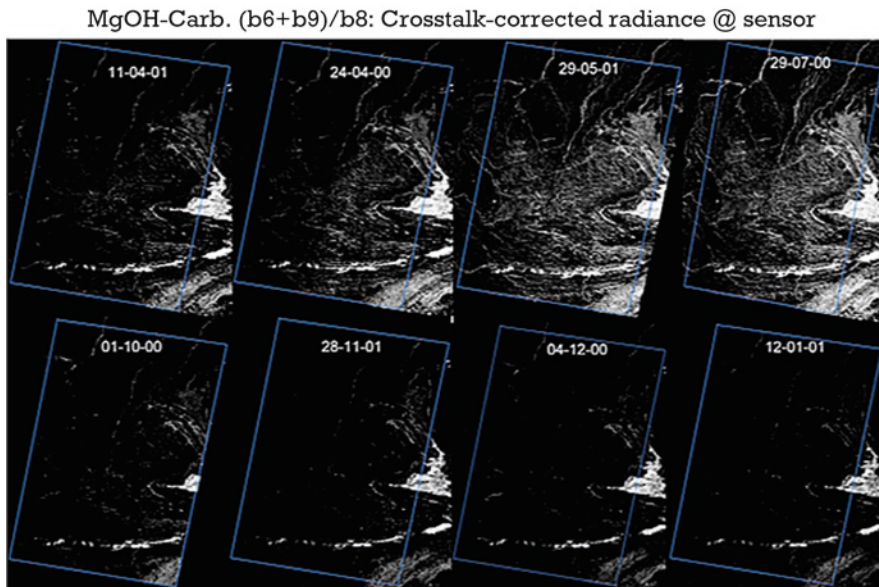


Fig. 13.10 MgOH/carbonate RBD product generated from multi-seasonal crosstalk-corrected ASTER level-1B at-sensor radiance data. Mt Fitton study area boundary is shown in blue

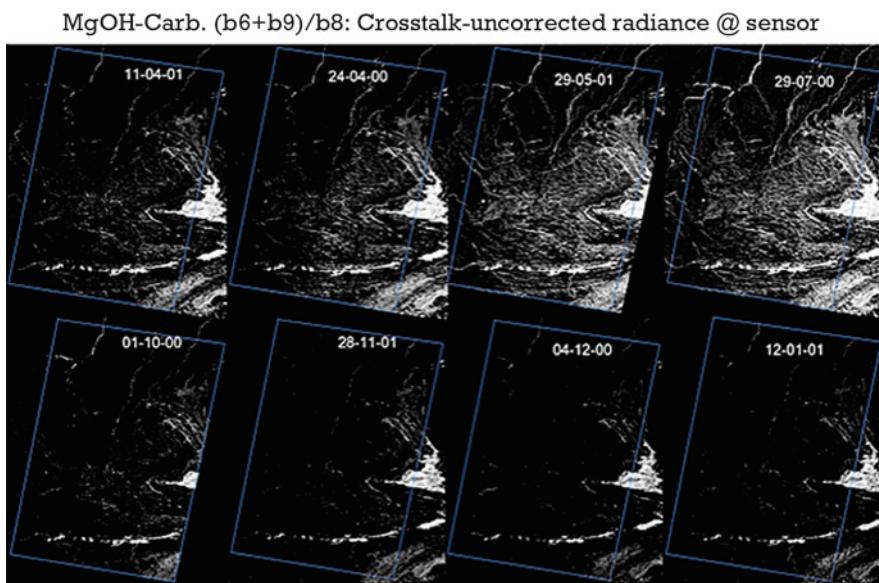


Fig. 13.11 MgOH/carbonate RBD product generated from multi-seasonal crosstalk-uncorrected ASTER level-1B at-sensor radiance data. Mt Fitton study area boundary is shown in blue

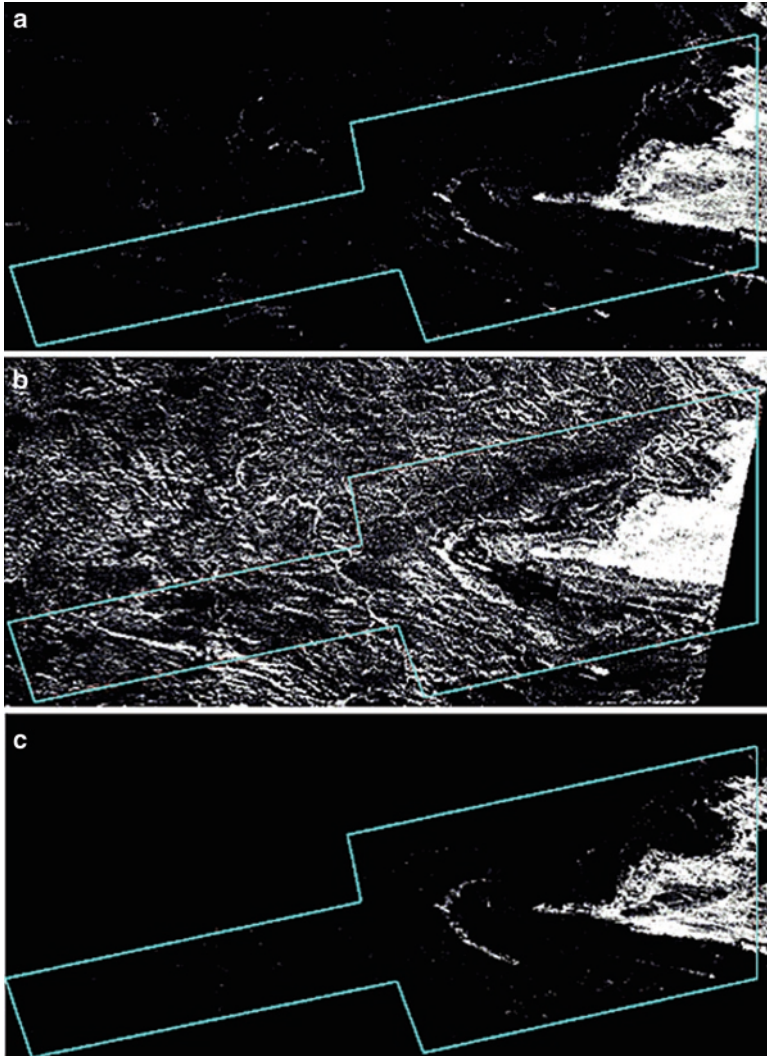


Fig. 13.12 (a) MgOH/carbonate RBD product for Mt Fitton, derived from summer-time ASTER level-1B acquisition (4th Dec 2000); (b) MgOH/carbonate RBD product for Mt Fitton, derived from winter-time ASTER level-1B acquisition (29th May 2001); (c) carbonate abundance generated from airborne hyperspectral HyMap reflectance data. High abundance is represented by bright areas. HyMap survey area boundary is shown in cyan, and located in Fig. 13.6a

Fig. 13.13 (continued) summer-time ASTER at-sensor radiance; (c) ASTER band 4 albedo; (d) AIOH compositional map derived from crosstalk-uncorrected summer-time ASTER at-sensor radiance image; (e) derived from crosstalk-corrected summer-time ASTER at-sensor radiance image; (f) derived from crosstalk-uncorrected winter-time ASTER at-sensor radiance image; and (g) derived from crosstalk-corrected winter-time ASTER at-sensor radiance image. Interpreted Al-poor AIOH composition: *red*; Al-rich AIOH: *green*; kaolinitic: *blue*

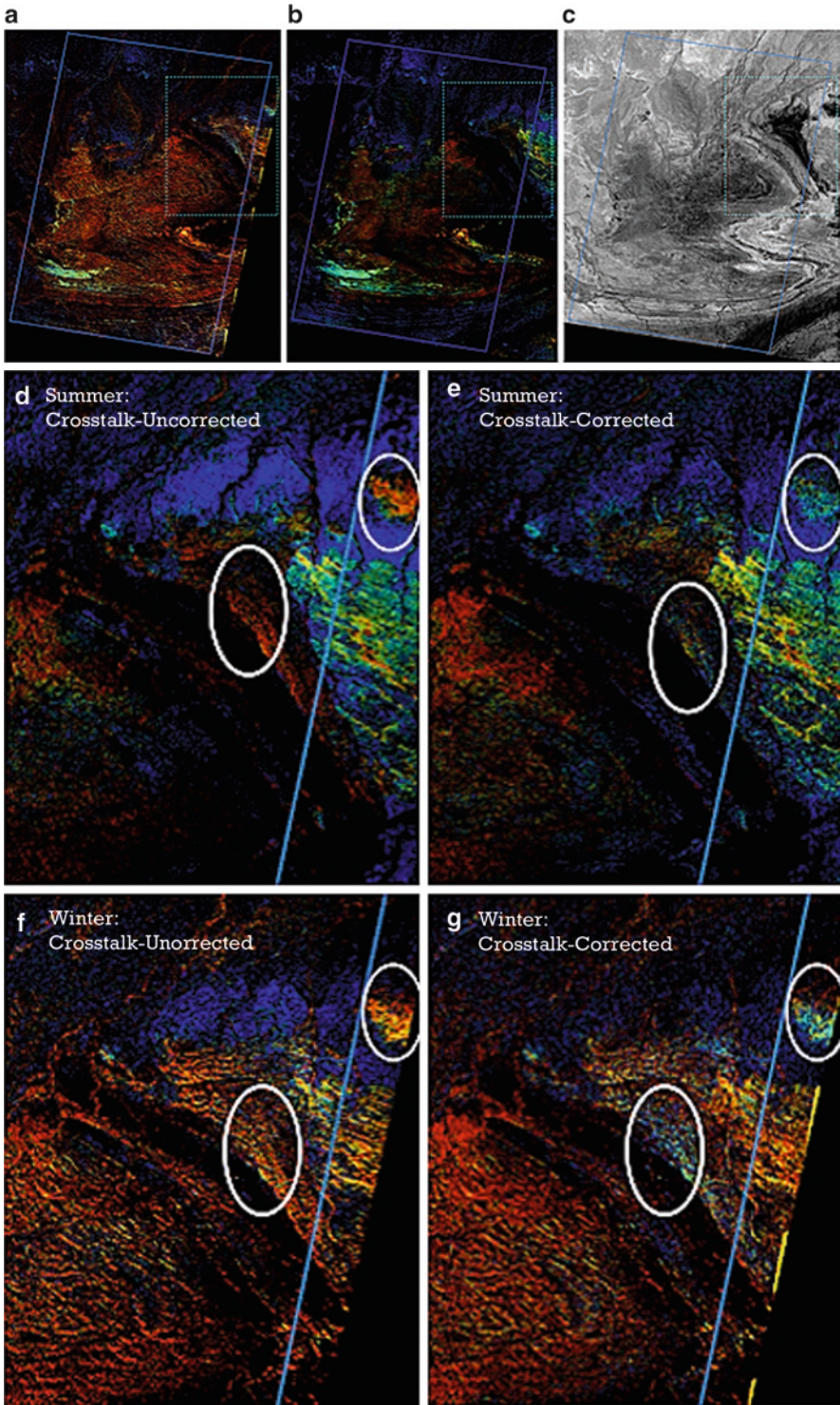


Fig. 13.13 (a) AIOH compositional map interpreted from crosstalk-corrected winter-time ASTER at-sensor radiance data; (b) AIOH compositional map interpreted from crosstalk-corrected

RGB composite images. The winter acquisition-derived AIOH compositional product (Fig. 13.13a) generally shows a higher red component in the display of colors compared to the summer acquisition-derived results (Fig. 13.13b). An increase in red, or the b5/b6 ratio, represents a shift in the absorption feature to longer wavelengths, indicative of Al-poor mica composition (Duke 1994). We also see distinctly different AIOH anomalies in the north-eastern corner of the Mt Fitton study area, as indicated by the ASTER albedo image (Fig. 13.13c). A close up of this area is shown in Fig. 13.13d–g, which compares the winter and summer results together with the effects of applying crosstalk correction to the ASTER level-1B data. The winter scene-derived AIOH compositional image, with and without crosstalk correction (Fig. 13.13f, g), yet again appears to reveal topography-related anomalous noise. However, the crosstalk-corrected results have a lower b5/b6 response, particularly for the summer acquisition (Fig. 13.13d, e). Comparison with the ASTER band-4 albedo (Fig. 13.13c) suggests that the greatest apparent changes in AIOH composition are in areas of low albedo, which is consistent with previous studies, and is associated with crosstalk issues (Hewson et al. 2005).

We further checked the reliability of the ASTER summer acquisition-derived AIOH compositional images (Fig. 13.14a) by comparing the equivalent HyMap reflectance data-derived band ratio product resampled to ASTER's spectral resolution (Fig. 13.14b). The equivalent HyMap product showed a favorable comparison with the summer-acquired ASTER AIOH composition product, and qualitatively demonstrated the potential to extract AIOH information with ASTER SWIR radiance at-sensor data. The AIOH composition information interpreted at ASTER's spectral resolution (Fig. 13.14a, b) was also compared with shifts in the wavelength of the 2.2- μm AIOH spectral absorption feature mapped by HyMap (Fig. 13.14c). The variation of the HyMap spectral data-derived AIOH composition (e.g., Al-poor to Al-rich mica) was limited, as inferred by the small shift in wavelength from 2.197 μm (blue) to 2.210 μm (red) for the major anomalies shown in Fig. 13.14c. However, favorable comparisons between the ASTER AIOH compositional ratio and the HyMap-derived AIOH wavelength products were apparent in the vicinity of the Mt Fitton anti-form nose and toward the south-east (Fig. 13.14a, c).

13.5.3 The Significance of Topographic Illumination Effects on ASTER SWIR Results

The ASTER DEM product provides a useful means to understand the relationship between various ASTER products and topography at the same spatial resolution. Shaded relief versions of the Mt Fitton topography were generated to simulate the solar illumination at the time of the summer (4th Dec 2000) and winter (29th May, 2001)

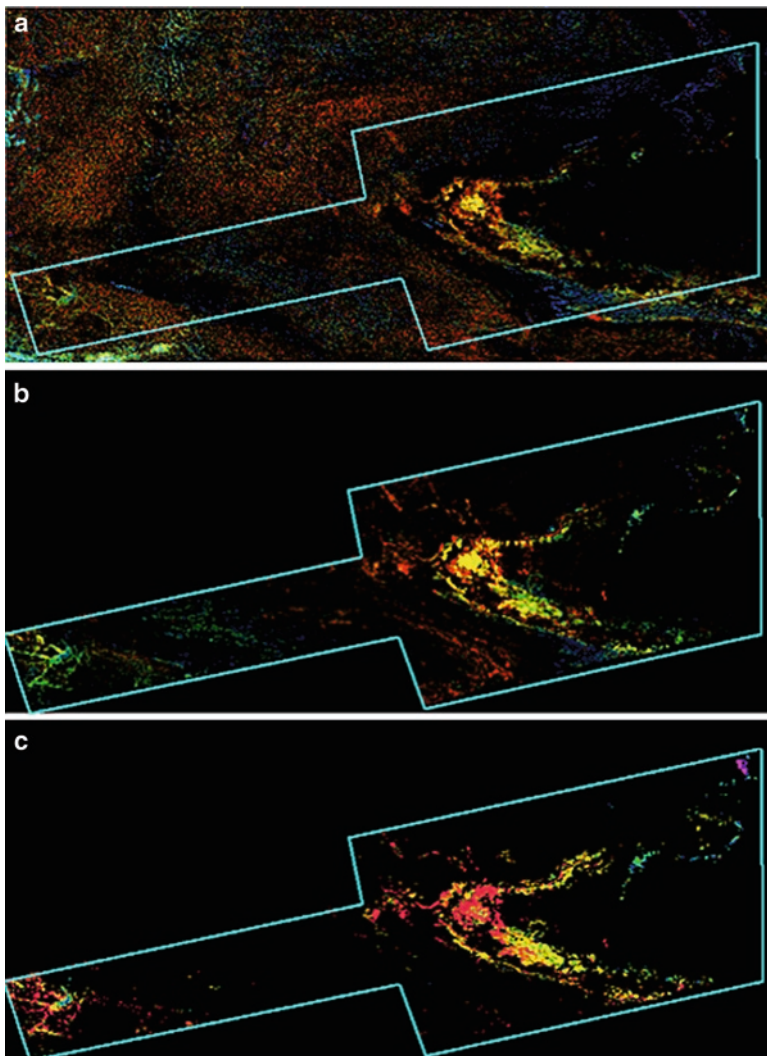


Fig. 13.14 Close-up comparison between (a) interpreted AIOH composition derived from crosstalk-corrected ASTER at-sensor radiance interpreted Al-poor AIOH composition: *red*; Al-rich AIOH: *green*; more kaolinitic: *blue*; (b) equivalent image composite product derived from ASTER resampled HyMap data; and (c) AIOH composition determined from HyMap’s wavelength index Al-rich AIOH, 2.187 μm : *blue*; Al-poor AIOH, 2.248 μm : *red*. The *blue* boundary indicates the outline of the HyMap survey area shown in Fig. 13.6a

acquisitions. Figure 13.15 shows our comparisons between the shaded relief and respective ASTER AIOH-abundance products. The decrease in solar elevation from 68 to 33° (Table 13.1) produces a marked reduction in irradiance (Fig. 13.15a versus b). This reduction in irradiance appears associated with “false” AIOH anomalies as

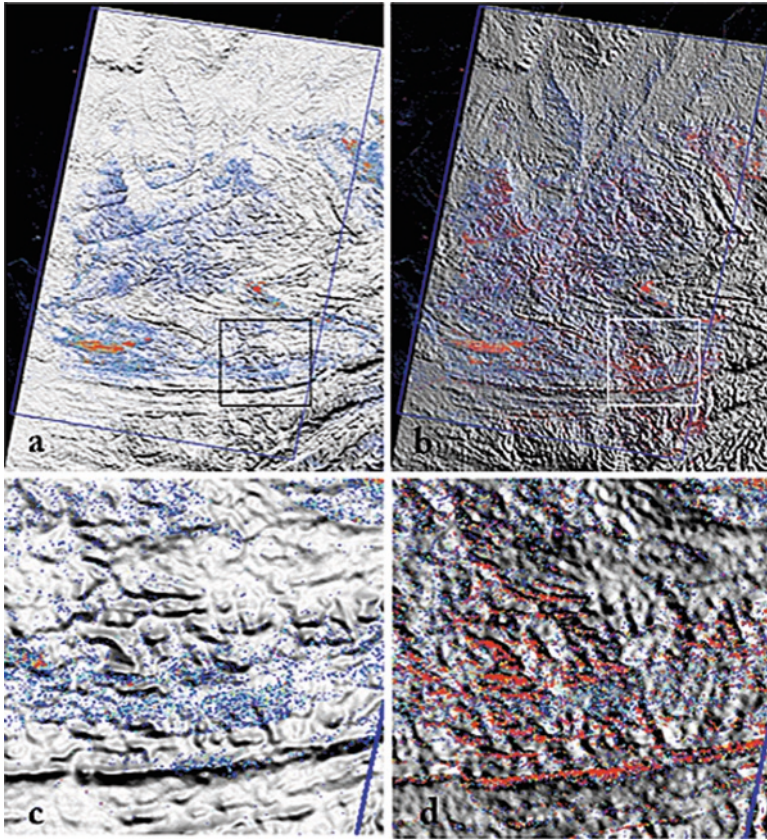


Fig. 13.15 (a) AIOH abundance derived from crosstalk-uncorrected summer-time ASTER at-sensor radiance data draped over artificial sun-illuminated ASTER DEM (Elevation 68°, Azimuth 105°); (b) AIOH abundance derived from crosstalk-uncorrected winter-time ASTER at-sensor radiance data draped over artificial sun-illuminated ASTER DEM (Elevation 33°, Azimuth 152°); (c) close-up of (a) (*black box*); and (d) close-up of (b) (*white box*)

highlighted in close up images (Fig. 13.15c versus d). This correlation suggests that the low irradiance introduces a bias, or additive offset to the ratio products. Hewson et al. (2005) reported similar crosstalk effects when studying ASTER data acquired over the nearby Broken Hill mining district, which is located at similar latitudes.

13.5.4 Estimation and Correction of ASTER SWIR Radiance Offsets

A scene-based correction technique to determine SWIR offsets, attributable at least in part to crosstalk, was devised using scatter plot-type analysis of the ASTER

radiance at-sensor level-1B data. Scatter plots for each SWIR band against band-4 of the winter level-1B ASTER data were generated. Figure 13.16 shows the example of the scatter plot for ASTER band-5 versus band-4 radiance values. Net SWIR offset values for each band were estimated by extrapolating trends from the radiance values for a variety of different geological units in areas of topographic relief and minimal vegetation cover. The intersection of the outer envelopes of the scatter between each SWIR band was interpreted to represent the true “origin” of the scatter plot, minus the effect of the additive ASTER crosstalk contribution. The band offsets estimated from the “origin” coordinate were then subtracted from each SWIR band to provide an approximate, empirically derived correction for the level-1B radiance data. For example, a value of 3.0 was estimated and subtracted as the band-5 ASTER offset (Fig. 13.16). Further work, using multiple scatter plots of ASTER radiance data at different radiance levels, is expected to improve the accuracy of this scene-based offset determination as a means for SWIR crosstalk correction. However, the results of this simple technique show a significant improvement for the AIOH and MgOH–carbonate RBD image products generated from the winter ASTER acquisition (29th May, 2001) displayed earlier (Fig. 13.17a, c). A favorable comparison between the offset-corrected winter and summer acquisition RBD products is shown, with less noise associated with the topographic relief (e.g., Fig. 13.17a versus b; Fig. 13.17c versus d).

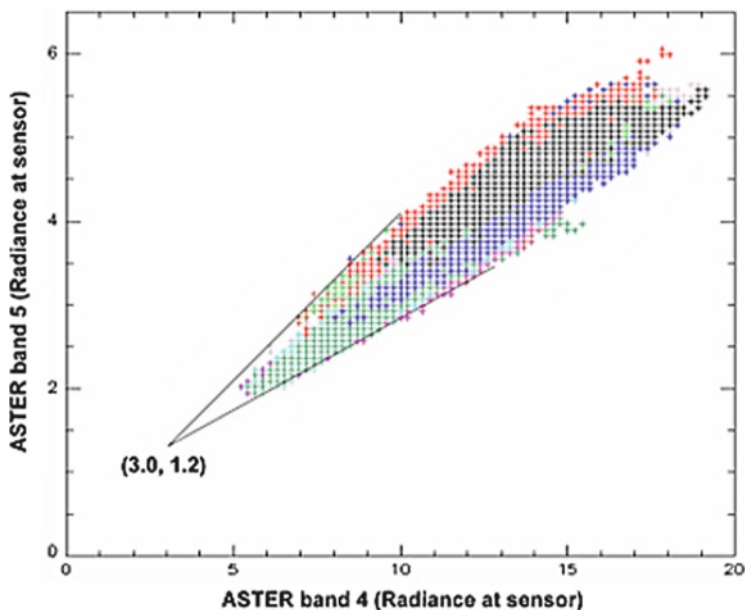


Fig. 13.16 ASTER band 4 versus 5 radiance scatterplot from different geological units shown in different colors within the Mt Fitton ASTER study area. Total radiance data offset including crosstalk for bands 4 and 5 estimated from extrapolation and intersection (3.0, 1.2) of outer envelope of the scatter shown

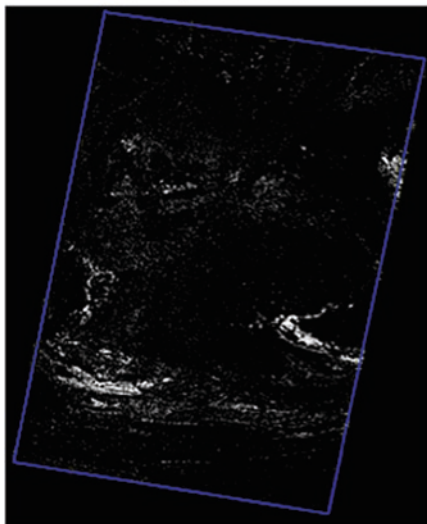
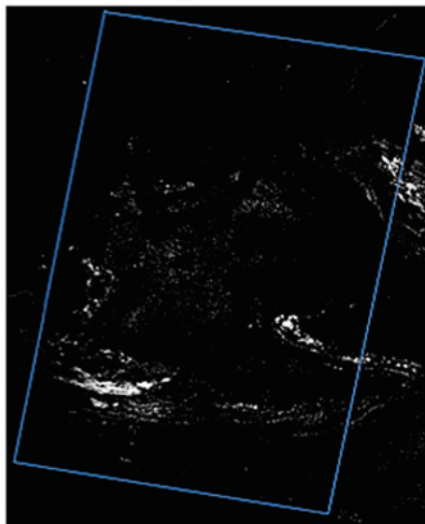
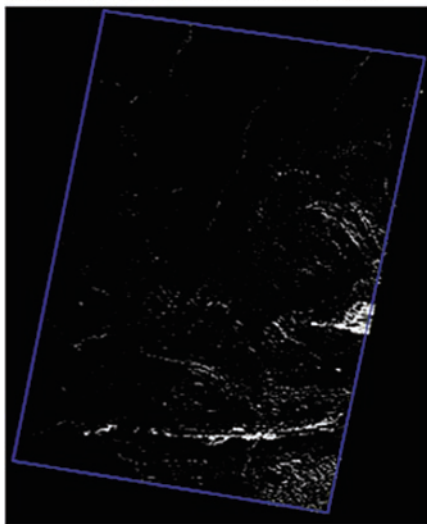
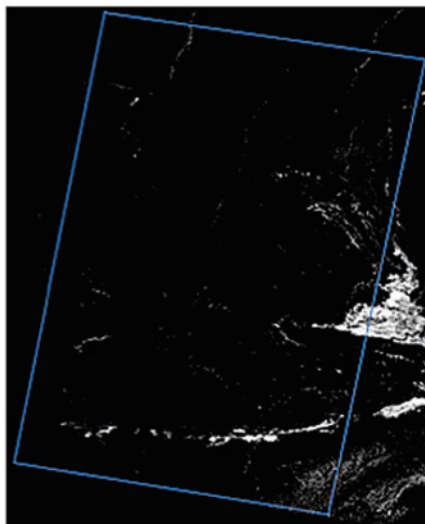
a Crosstalk scatter-plot correction: Winter**b** Crosstalk scatter-plot correction: Summer**c** Crosstalk scatter-plot correction: Winter**d** Crosstalk scatter-plot correction: Summer

Fig. 13.17 (a) AIOH abundance derived from winter-time (29th May) offset-corrected ASTER level-1B data; (b) AIOH abundance derived from summer-time (4th Dec) ASTER level-1B data; (c) MgOH-carbonate abundance derived from winter-time (29th May) offset-corrected ASTER level-1B data; (d) MgOH/carbonate abundance derived from summer-time (4th Dec) ASTER level-1B data. Boundary of the Mt Fitton study area is shown in *blue*

13.5.5 Geological Mapping Results with ASTER Thermal Infrared Data

ASTER TIR products over Mt Fitton were also examined to characterize the influence of changes in the atmospheric and surface conditions. ASTER level-2 surface emissivity product mosaics derived from winter and summer data acquisitions (Fig. 13.18) reveal the degree of repeatability of ASTER's surface emissivity product and derived mineral maps. Figure 13.18a, b shows mosaics of band-10 and band-14 emissivities, respectively. Despite the changes in atmospheric and ground conditions, the atmospheric correction applied to the ASTER's TIR radiance at-sensor level-1B data (Thome et al. 1998), and its subsequent temperature-emissivity separation (TES) (Gillespie et al. 1998), produced seamless images (Fig. 13.18a, b). We could potentially combine the quartz-abundance maps derived from the emissivity ratio (b_{13}/b_{10}) into seamless mosaics over the greater Mt Fitton area (Fig. 13.18c). Higher quartz content is observed in this image product within the Bolla Bollana Tillite and in the adjacent Quaternary alluvium of the floodplains

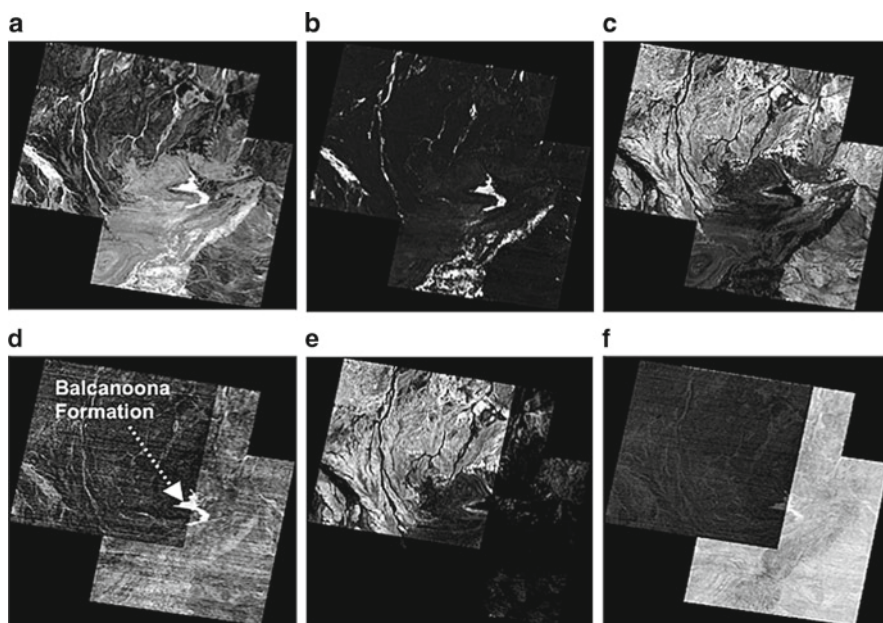


Fig. 13.18 (a) Mosaicked ASTER band 10 level-2 surface emissivity product from winter (29th May 2001) and summer-time (4th Dec 2000, 28th Nov 2001) acquisitions; (b) band 14 surface emissivity; (c) interpreted quartz abundance from surface emissivity data (b_{13}/b_{10}); (d) interpreted carbonate abundance from surface emissivity data (b_{13}/b_{14}); (e) interpreted quartz abundance from ASTER at-sensor radiance data (b_{13}/b_{10}); (f) interpreted carbonate abundance from ASTER at-sensor radiance data (b_{13}/b_{14}). *White*: interpreted high abundance. *Grey*: interpreted low abundance. Outline and location of ASTER TIR images indicated in Fig. 13.6a

to north and the north-west (Fig. 13.18c). An attempt to map carbonate abundance, based on the thermal band emissivity ratio, b_{13}/b_{14} , is shown in Fig. 13.18d. This carbonate abundance product does highlight the Balcanoonna Formation, despite significant cross-track noise, and was not seamless between the winter and summer acquisitions. The use of both bands 13 and 14 within this product rendered it more vulnerable to low radiance signal, or, imperfect atmospheric or TES corrections, occurring on the edge of the TIR atmospheric window (e.g., for wavelengths approaching 12 μm). The corresponding band ratios for quartz and carbonate abundances were also attempted using the level-1B ASTER data (Fig. 13.18e, f), and showed significant differences between the summer and winter acquisitions. The combined nonlinear effects of variable atmospheric and temperature conditions on TIR radiance explain this result.

13.6 Conclusions

Previous and more recent studies of Mt Fitton demonstrated that spectral unmixing of single-scene ASTER SWIR data could successfully generate map products, which discriminated either geological units or overprinted alteration mineralogy, including talc, mica, chlorite, and carbonate. However, *a priori* information and image calibration improves the identification of the dominant mineral (group) of each endmember and their spectral signatures. The presence of ferrous iron (Fe^{2+}), and its effects on the SWIR signature, also contributed to ASTER's ability to discriminate mineralogy at Mt Fitton.

Band ratio and RBD processing of both ASTER radiance at-sensor and reflectance data from Mt Fitton successfully generated abundance image products for mineral groups including AIOH, MgOH/carbonate, and those bearing ferrous iron (e.g., chlorite). AIOH compositional and MgOH/carbonate-abundance image products derived from summer ASTER data compared favorably with results generated from high signal-to-noise airborne hyperspectral data. However, significant detrimental effects were observed for those geological image products processed from areas of low albedo (e.g., winter ASTER data). False anomalous areas, in both abundance and compositional image products, were found to correlate with low albedo from shadowed topographic relief associated with winter acquisitions. Such an increase in anomalous areas within RBD-normalized products under low illumination points to the additive bias of ASTER's SWIR crosstalk effects.

A technique to calculate an estimate of the additive crosstalk offset was devised using scatterplot analysis for each band of ASTER SWIR radiance data from areas of different geological units, variable topographical relief and low vegetation. RBD geological map products derived from winter ASTER data corrected for these SWIR offsets compared well with equivalent summer ASTER products.

The Mt Fitton ASTER surface emissivity and derived geological products indicated that atmospheric corrections and temperature-emissivity processing were generally seamless with different acquisitions with the exception of the carbonate

product. Seamless geological mapping of quartz using ASTER's TIR surface emissivity product with different ASTER acquisitions was also successful.

Acknowledgments ASTER data products for this case study were gratefully supplied by Japan's ERSDAC and NASA's LP DAAC. ERSDAC also provided crosstalk-correction software used for pre-processing level-1B data. Software license support from ERMapper is also gratefully acknowledged for this study. Mike Caccetta of CSIRO provided software and advice for the scatter plot and ASTER data's SWIR offset analysis. Mt Fitton HyMap data, used as a control for comparative studies, were supplied by the HyVista Corporation. Geological GIS vector information for the Mt Fitton area was obtained from the Geological Survey of South Australia.

References

- Abrams M, Hook SJ (1998) Simulated ASTER Data for geologic studies, *IEEE Trans Geosci Remote Sens* 33(3):692–699.
- Abrams M, Hook S, Ramachandran B (2002) *ASTER User Handbook*. Version 2, Pasadena, JPL Publication, p. 25.
- Clark RN, King TVV, Klejwa M, Swayze G, Vergo N (1990) High spectral resolution reflectance spectroscopy of minerals. *J Geophys Res* 95:12653–12680.
- Clark RN, Swayze GA, Gallagher A, King TVV, Calvin WM (1993) The USGS Digital Spectral Library: Version 1: 0.2 to 3.0 microns, U.S. Geol. Surv. Open File Rep., 93–592, pp 1340.
- Coats RP, Blissett AH (1971) Regional and economic geology of the Mount Painter Province. *South Aust Geol Surv Bull* 43.
- Coats RP, Horwitz RC, Crawford AR, Campana B, Thatcher D (1969) 1:125,000 scale geological map of the Mount Painter Province, Geological Atlas Species Series, Adelaide, Geological Survey of South Australia.
- Cocks T, Jenssen R, Stewart WI, Shields T (1998) The HyMap airborne hyperspectral sensor: The system, calibration, and performance. In *Proc. of 1st EARSEL Workshop on Imaging Spectroscopy*, Zurich, p. 7.
- Crowley JK (1986) Visible and near-infrared spectra of carbonate rocks: reflectance variations related to petrographic texture and impurities. *J Geophys Res* 91(B5):5001–5012.
- Crowley JK, Brickey DW, Rowan LC (1989) Airborne imaging spectrometer data of the Ruby Mountains, Montana: Mineral discrimination using relative absorption band-depth images. *Remote Sens Environ* 29:121–134.
- Cudahy TJ, Caccetta M, Cornelius A, Hewson RD, Wells M, Skwarnecki M, Halley S, Hausknecht P, Mason P, Quigley M (2005) Regolith geology and alteration mineral maps from new generation airborne and satellite remote sensing technologies; and Explanatory Notes for the Kalgoorlie-Kanowna 1:100,000 scale map sheet, remote sensing mineral maps. Perth, MERIWA Report No. 252, p. 114.
- Cudahy TJ, Hewson RD, Huntington JF, Quigley MA, Barry PS (2001a) The performance of the satellite-borne Hyperion Hyperspectral VNIR-SWIR imaging system for mineral mapping at Mount Fitton, South Australia. In *Proc. IEEE 2001 International Geoscience and Remote Sensing Symposium (IGARSS)*, Sydney 9–13 July, p. 4.
- Cudahy T, Wilson J, Hewson R, Linton P, Harris P, Sears M, Okada K, Hackwell J (2001b) Mapping Porphyry-Skarn Alteration at Yerington, Nevada, Using Airborne Hyperspectral VNIR-SWIR-TIR Imaging Data. *IEEE 2001 Int Geosci Remote Sens Symp (IGARSS)*, 9–13 July, p. 3.
- Cudahy TJ, Whitbourn LB, Connor P, Mason P, Phillips RN (1999) Mapping surface mineralogy and scattering behaviour using backscattered reflectance from a hyperspectral mid infrared airborne CO₂ laser system (MIRACO2LAS). *IEEE Trans Geosci Remote Sens* 37(4): 2019–2034.

- Denniss A, Huntington J, Hore S (1999) Mount Fitton hyperspectral mineral mapping collaborative project. *MESA J* 15:12–14.
- Duke EF (1994) Near infrared spectra of muscovite. Tschermak substitution and metamorphic reaction process: implications for remote sensing. *Geology* 22:621–624.
- Gillespie AR, Matsunga T, Rokugawa S, Hook SJ (1998) Temperature and emissivity from advanced spaceborne thermal emission and reflection radiometer. *IEEE Trans Geosci Remote Sens* 36(4):1113–1126.
- Green AA, Craig MD (1985) Analysis of aircraft spectrometer data with logarithmic residuals. *JPL Publication* 85–41:111–119.
- Grove CI, Hook SJ, Paylor ED II (1992) Laboratory reflectance spectra of 160 minerals, 0.4 to 2.5 micrometers. *JPL Publication* 92–2.
- Hewson RD, Cudahy TJ, Drake-Brockman J, Meyers J, Hashemi A (2006) Mapping geology associated with manganese mineralisation using spectral sensing techniques at Woodie Woodie, East Pilbara. *Explor Geophys* 37:389–400.
- Hewson RD, Cudahy TJ, Huntington JF (2001) Geologic and alteration mapping at Mt Fitton, South Australia, using ASTER satellite-borne data. In *IEEE 2001 International Geoscience and Remote Sensing Symposium (IGARSS)*, 9–13 July, p. 3.
- Hewson RD, Cudahy T, Mizuhiko S, Ueda K, Mauger AJ (2005) Seamless geological map generation using ASTER in the Broken Hill-Curnamona Province of Australia. *Remote Sens Environ* 99:159–172.
- Hook SJ, Cudahy TJ, Kahle AB, Whitbourn LB (1998) Synergy of active and passive airborne thermal infrared systems for surface compositional mapping. *J Geophys Res* 103(B8):18, 269–276.
- Iwasaki A, Fujisada H (2005) ASTER geometric performance. *IEEE Trans Geosci Remote Sens* 43(12):2700–2706.
- Iwasaki A, Fujisada H, Akao H, Shindou O, Akagi S (2001) Enhancement of spectral separation performance for ASTER/SWIR. In *Proc. of SPIE – The International Society for Optical Engineering*, vol. 4486, pp. 42–50.
- Iwasaki A, Tonooka H (2005) Validation of a crosstalk correction algorithm for ASTER/SWIR. *IEEE Trans Geosci Remote Sens* 43(12):2747–2751.
- Kruse FA, Lefkoff AB, Boardman JB, Heidebreicht KB, Shapiro AT, Barloon PJ (1993) The Spectral Image Processing System SIPS -interactive visualization and analysis of imaging spectrometer data. *Remote Sens Environ* 44:145–163.
- Ninomiya Y, Fu B, Cudahy TJ (2005) Detecting lithology with advanced spaceborne thermal emission and reflection radiometer (ASTER) multispectral thermal infrared “radiance-at-sensor” data. *Remote Sens Environ* 99:127–139.
- Palluconi FD, Meeks GR (1985) Thermal infrared multispectral scanner TIMS: an investigators guide to TIMS data. *JPL Publication* 85–32.
- Rivard B, Arvidson RE, Duncan IJ, Sultan M, El Kailouby B (1992) Varnish, sediment, and rock controls on spectral reflectance of outcrops in arid regions. *Geology* 20:295–298.
- Rowan LC, Mars JC (2003) Lithologic mapping in the Mountain Pass, California area using advanced spaceborne thermal emission and reflection radiometer ASTER data. *Remote Sens Environ* 84:350–366.
- Rowan LC, Mars JC, Simpson CJ (2005) Lithologic mapping of the Mondor, NT, Australia ultramafic complex by using the ASTER spaceborne thermal emission and reflection radiometer ASTER. *Remote Sens Environ* 99:105–126.
- Salisbury JW, D’Aria DM (1992) Emissivity of terrestrial materials in the 8–14 μm atmospheric window. *Remote Sens Environ* 42:83–106.
- Thome K, Palluconi F, Takashima T, Masuda K (1998) Atmospheric correction of ASTER. *IEEE Trans Geosci Remote Sens* 36(4):1199–1211.
- Yamaguchi Y, Kahle AB, Tsu H, Kawakami T, Pniel M (1998) Overview of advanced spaceborne thermal emission and reflection radiometer (ASTER). *IEEE Trans Geosci Remote Sens* 36(4):1062–1071.

Chapter 14

ASTER Data Use in Mining Applications

Sandra Perry and Fred Kruse

14.1 Introduction

The mining industry, faced with international mining operations and worldwide exploration, has increasingly turned to remote sensing for solutions. Over the past decade, mining companies have found themselves in countries with few or no geologic or topographic maps. Satellite multispectral systems offer consistent image data sets that provide a wealth of geological and logistical information, especially for poorly mapped and remote locations.

Generally, remote sensing applications for mining include three broad categories:

1. *Structural/geomorphic interpretation*: Estimating strike/dip, mapping key contacts, drainage analysis, identifying folds and faults, interpreting linear/circular features, predicting geologic hazards
2. *Compositional mapping*: Rock/soil type prediction, alteration mineral modeling, vegetation/vegetation-stress mapping, environmental monitoring
3. *Logistical information*: Accurate map preparation, integration with global positioning systems (GPS) and geographic information systems (GIS), real-time mapping with palm-PC computers, and generation of digital elevation models (DEM).

The Advanced Spaceborne Thermal Emission and Reflection Radiometer (ASTER) is a NASA facility instrument on the Earth Observing System (EOS) Terra platform that provides visible/near-infrared/shortwave-infrared/long-wave-infrared (VNIR/SWIR/LWIR) Earth observations in 14 spectral bands (plus one backward-looking band) (Kahle et al. 1991; Fujisada 1995; Yamaguchi et al. 1998; ERSDAC 2001) (Table 14.1). ASTER and/or simulated ASTER data (MODIS/

S. Perry (✉)
Perry Remote Sensing LLC, 22 Sedgwick Drive, Englewood, CO 80110, USA
e-mail: sandyp@rm.incc.net

Table 14.1 ASTER characteristics (<http://asterweb.jpl.nasa.gov/characteristics.asp>)

| Characteristic | VNIR | SWIR | LWIR |
|-------------------|-----------------------------------------------------|------------------------------------------------------------------------|------------------------------------|
| Spectral range | Band 1: 0.52–0.60 μm Nadir looking | Band 4: 1.600–1.700 μm | Band 10: 8.125–8.475 μm |
| | Band 2: 0.63–0.69 μm Nadir looking | Band 5: 2.145–2.185 μm | Band 11: 8.475–8.825 μm |
| | Band 3: 0.76–0.86 μm Nadir looking | Band 6: 2.185–2.225 μm | Band 12: 8.925–9.275 μm |
| | Band 3: 0.76–0.86 μm Backward looking | Band 7: 2.235–2.285 μm | Band 13: 10.25–10.95 μm |
| | | Band 8: 2.295–2.365 μm Band 9: 2.360–2.430 μm | Band 14: 10.95–11.65 μm |
| Ground resolution | 15 m | 30 m | 90 m |
| Swath width | 60 km | 60 km | 60 km |

ASTER Airborne Simulator or “MASTER”, Hook et al. 2001) have been successfully used for geologic applications, providing basic mapping capabilities using both the VNIR/SWIR and LWIR spectral ranges (Hook 1990; Kruse 2000, 2002; Rowan and Mars 2003). The four VNIR bands provide information about iron mineralogy and some rare earth minerals (Rowan and Mars 2003). The six SWIR bands allow mapping of molecular vibration absorption features commonly seen in minerals such as carbonates and clays (Hook 1990; Kruse 2002; Rowan and Mars 2003). The five LWIR bands are principally useful to map silica content in surface exposures (Kahle et al. 1991; Kruse 2002; Rowan and Mars 2003).

From a mining perspective, ASTER satellite images provide a three-fold improvement compared to Landsat Thematic Mapper (TM) and Enhanced Thematic Mapper (ETM) data: (1) ASTER VNIR bands offer a true 15-m pixel size, sharp and clear down to 1:50,000 map scale; (2) ASTER SWIR and thermal infrared (TIR) bands are better suited to map alteration minerals associated with precious and base metal deposits; and (3) an aft-looking telescope on board ASTER enables stereoscopic images, DEM development, and orthorectification, which yield improved positional accuracy of resulting image data sets. With nearly 95% coverage of Earth’s landmass, ASTER images are a readily available data set that can provide timely and accurately positioned spatial information to facilitate fast-paced mining activities around the world.

Specifically, ASTER images are useful for exploration and development on three different levels:

1. *Regional reconnaissance at 1:250,000 or 1:200,000 international map scales* – useful in assessing countries or large geologic/political provinces for mineral deposit styles and potential, often the first look at a region.
2. *District-scale mapping, geologic data integration, and interpretation at 1:100,000 map scale* – 1:100,000-metric scale is an international standard for topographic and geologic mapping; images are useful to augment and extend geologic maps or provide first-hand interpreted information.

3. *Localized fieldwork and logistics at 1:50,000 map scale* – used to undertake and plan field operations, exploration surveys, and mobilization of personnel and equipment. This map scale is imperative for detailed mapping and field observations and measurements.

These applications are illustrated by case histories in the following sections.

14.2 Regional Reconnaissance and Mineral Assessment

14.2.1 High Zagros and Jebal Barez Mountains, Zagros Magmatic Arc, Iran

A recent assessment of copper porphyry deposits in Iran by the USGS utilized 62 ASTER scenes to regionally evaluate approximately 150,000 km² of the Zagros magmatic arc of southeastern Iran (Mars and Rowan 2006; Fig. 14.1). Logical operator algorithms applied to ASTER data offered an automated approach to map phyllic and argillic altered rocks, characteristic of copper porphyry systems. The idealized copper porphyry deposit is comprised of a core of quartz and

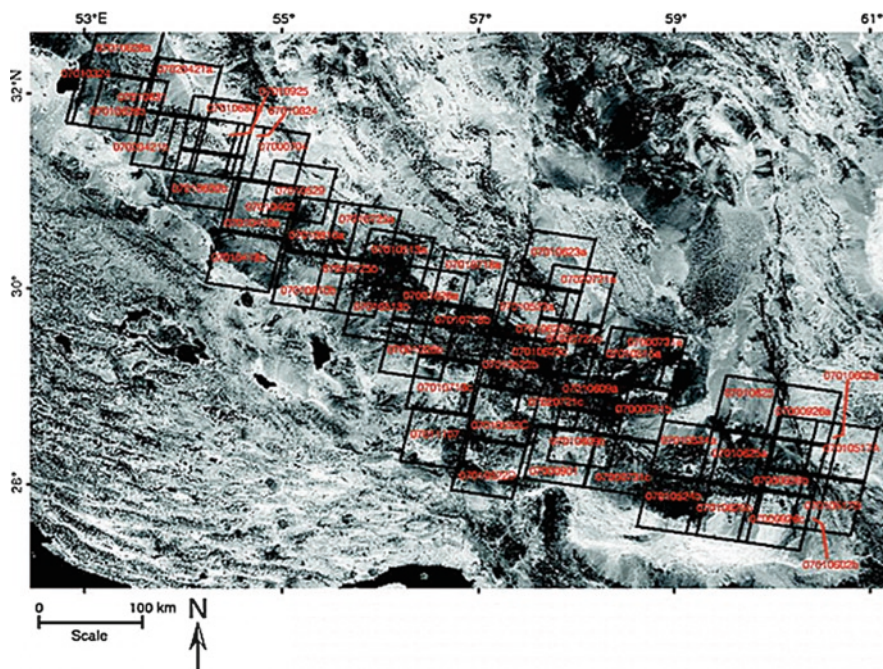


Fig. 14.1 Index map shows ASTER scenes used in the Iran mineral assessment area. Red numbers represent each ASTER scene product obtained from the USGS EROS Center with the last six numbers indicating the year, month, and day of acquisition. Labels with letters at the end reflect scenes acquired on the same day (from Mars and Rowan, 2006)

potassium-bearing minerals surrounded by distinctive zones of alteration minerals (Lowell and Guilbert 1970; Fig. 14.2). These outer zones, particularly the “phyllitic” and “argillic” zones, consist of minerals that are spectrally characterized by diagnostic absorption features (Fig. 14.3).

The USGS evaluation sought to map phyllic and argillic alteration zones using spectral characteristics of respective minerals in each zone. Phyllic alteration is dominated by illite/muscovite, exhibiting a strong Al-OH absorption feature at 2.20 μm (ASTER band 6) and a less intense absorption feature at 2.38 μm (ASTER band-8) (Fig. 14.4). Argillically altered rocks are characterized by alunite and kaolinite, which also display an Al-OH absorption feature at 2.20 μm, but both minerals have different spectral shapes compared to muscovite and illite. Finally, propylitic alteration minerals are characterized by Fe, Mg-OH absorption features along with CO₃ spectral features dominated by chlorite, epidote, and carbonates, situated in the 2.35 μm region (ASTER band-8). In summary, mineral-assemblage spectral reflectance features contrast strongly between phyllic, argillic, and propylitic alteration forming the basis to distinguish and map altered rocks associated with copper porphyry deposits.

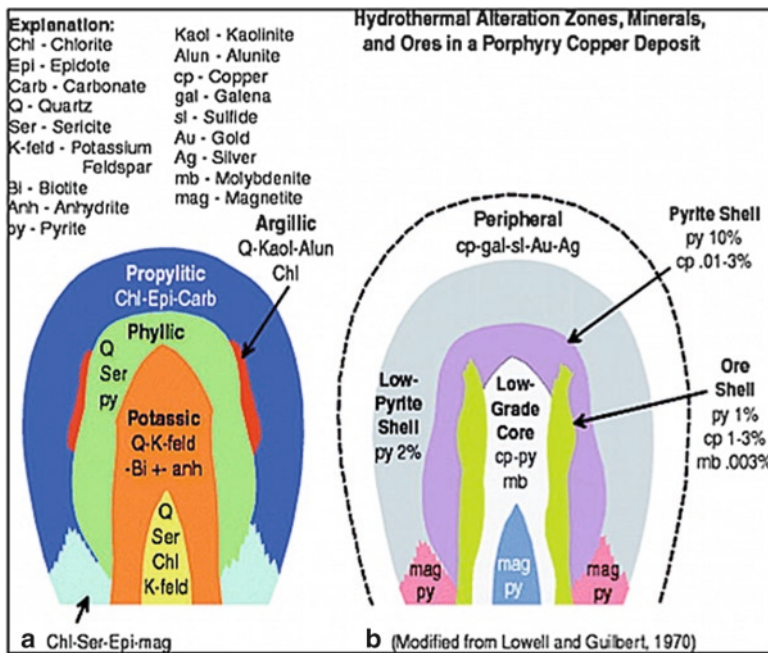


Fig. 14.2 Illustrated deposit model of a generalized, porphyry copper deposit (modified from Lowell and Guilbert 1970). (a) Schematic cross section of hydrothermal alteration minerals and types, which include propylitic, phyllic, argillic, and potassic alteration. Typically, the broad phyllic zone is characterized by illite/muscovite (also referred to as sericite), whereas the narrower argillic zone yields kaolinite and alunite. The outer “propylitic” zone is more variable in composition but generally includes chlorite, epidote, and carbonates. (b) Schematic cross section of ores associated with each alteration type (Mars and Rowan 2006)

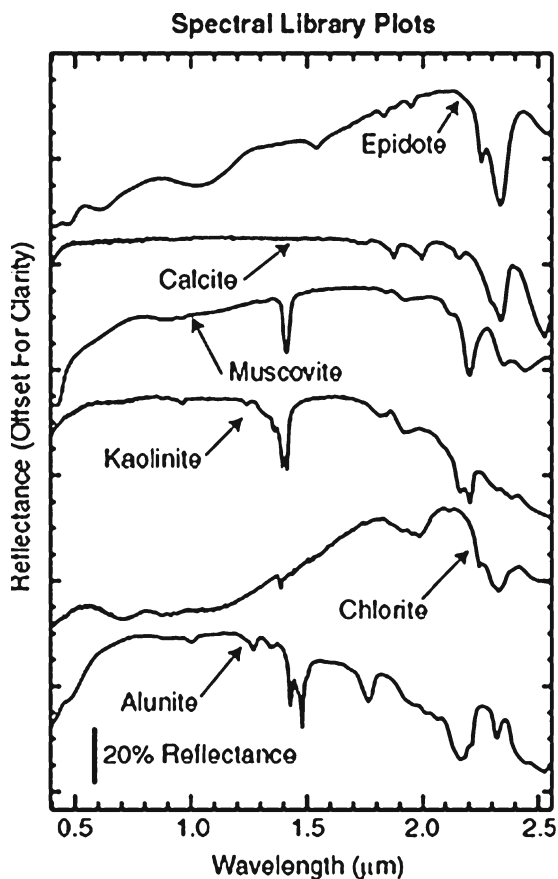


Fig. 14.3 Lab spectra of epidote, calcite, muscovite, kaolinite, chlorite, and alunite, all common hydrothermal alteration minerals (Clark et al. 1993a, b). Alunite and kaolinite have Al–O–H absorption features at 2.17 and 2.20 μm . Muscovite has a prominent Al–O–H 2.20- μm absorption feature and a secondary 2.35 μm absorption feature. Chlorite and epidote have a Fe–Mg–O–H 2.32 μm absorption feature and a broad Fe²⁺ feature from 0.6 to 1.65 μm . Calcite has a conspicuous 2.33 μm CO₃ absorption feature (from Mars and Rowan 2006)

The USGS approach sought to streamline ASTER mineral mapping as much as possible to evaluate a large regional area. First processing steps sought to geometrically correct ASTER scenes to a common base, which in this case included the orthorectified Landsat database in UTM projection and WGS-84 datum. Afterward, ASTER VNIR and SWIR reflectance bands were atmospherically corrected consistently with an indirect method, which uses a matching technique to corresponding (resampled) Hyperion hyperspectral bands that were corrected with ACORN atmospheric correction software. After geometric and atmospheric corrections, ASTER bands were fed into a logical operator algorithm performing a series of band ratios. Each logical operator then assigns a “true” or “false” value for each ratio by comparison with predetermined threshold values. All ratios in the algorithm are required to hold true for an assignment of 1 as a pixel value; otherwise 0 is assigned.

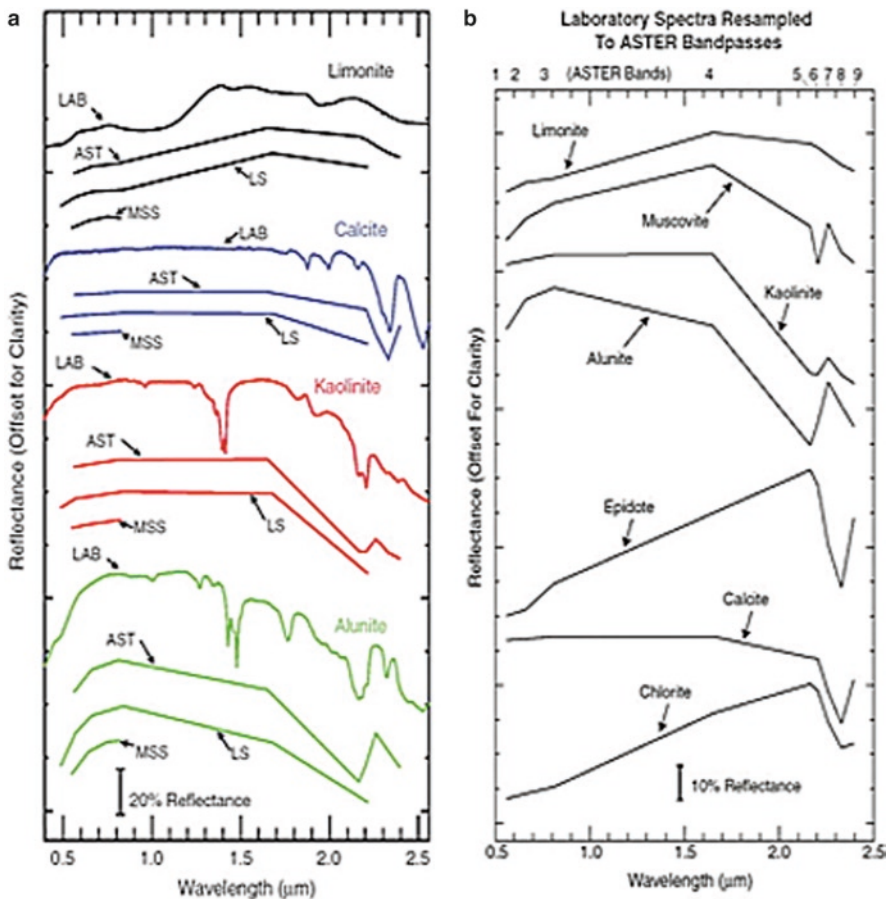


Fig. 14.4 (a) Lab spectra of limonite, calcite, kaolinite, and alunite, resampled to Landsat Multispectral Scanner (MSS), Thematic Mapper (TM), and ASTER band-passes (from Mars and Rowan 2006). (b) Lab spectra of limonite, muscovite, kaolinite, alunite, epidote, calcite, and chlorite, resampled to ASTER band-passes. Spectra include limonite with a broad 0.66–1.165 μm absorption feature; muscovite (typical to phyllic alteration) with a 2.20 μm absorption feature; kaolinite and alunite (common to argillic alteration) have 2.165 and 2.20 μm absorption features; and epidote, calcite, and chlorite (typical in propylitic alteration sequences) display 2.32, 2.33, and 2.32 μm absorption features, respectively. Epidote and chlorite have a broad Fe²⁺ absorption feature that affects ASTER bands 2, 3, and 4 (0.66–1.65 μm). Numbers at the top of each graph indicate ASTER band centers (from Clark et al. 1993a, b)

Logical operators were developed for argillic and phyllic alteration, complete with built-in masks for vegetation and dark pixels. Ratio sequences used for mapping phyllically-altered rocks include band 4/band 6, band 5/band 6, and band 7/band 6, all helping to define the 2.20 μm absorption feature. For argillic alteration, ratios used include band 4/band 5, band 5/band 6, and band 7/band 6, accentuating the 2.17 μm absorption feature. Pixels with green vegetation and low reflectance

(dark pixels) are masked (or turned off) by the band ratio band 3/band 2 and a band 4 threshold, respectively. This technique was extensively tested and validated at the Cuprite, Nevada test site, where discussion of pitfalls sited several issues of mineral mixing and unmixing with ASTER 30-m SWIR bands. Overall, test site results showed a high correlation between ASTER results and existing phyllic and argillic maps, although, in both cases, the ASTER logical operator approach tended to map more alteration than was mapped by other means. However, the ratio technique proved effective to differentiate argillic and phyllic alteration assemblages in an automated fashion, and was readied for mapping the Zagros regional terrain.

The new mapping method was applied to regional mineral assessment and structural/tectonic identification for the Zagros Magmatic Arc in Iran. This area is known for extensive hydrothermally altered exposures and major copper porphyry deposits (Fig. 14.5). Regional mapping using the logical operator method and

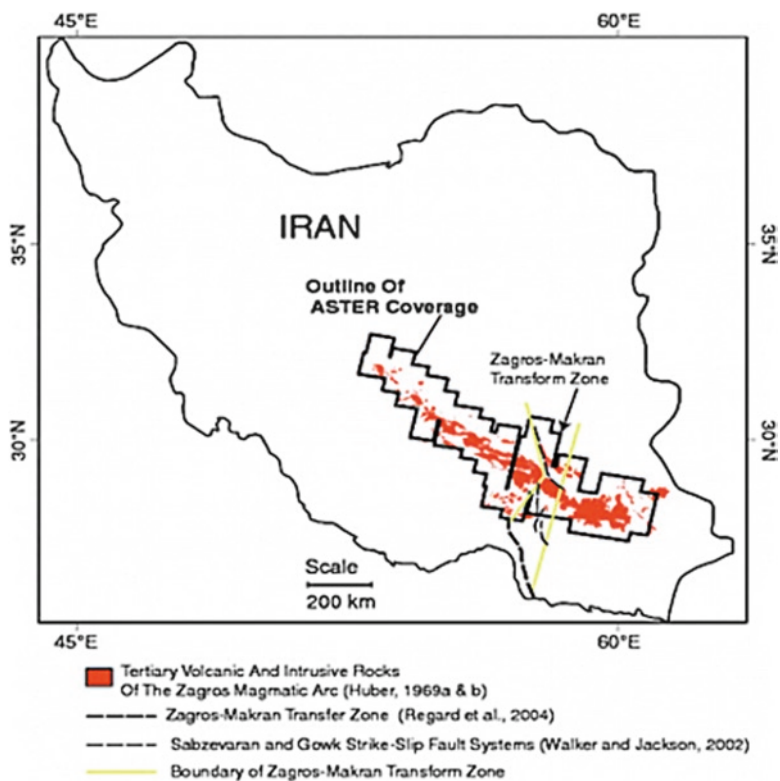


Fig. 14.5 Location map of Tertiary volcanic and igneous intrusive rocks of the Zagros magmatic arc and outline of ASTER scenes used to map hydrothermally altered rocks (from Mars and Rowan 2006). The Sabzevaran and Gowk strike-slip fault systems and the Makran transfer zone are defined as the Zagros-Makran transform zone (*yellow dashed lines*), dividing the active part of the arc (to the southeast) from the more dormant northwest portion (Regard et al. 2004; Walker and Jackson 2002)

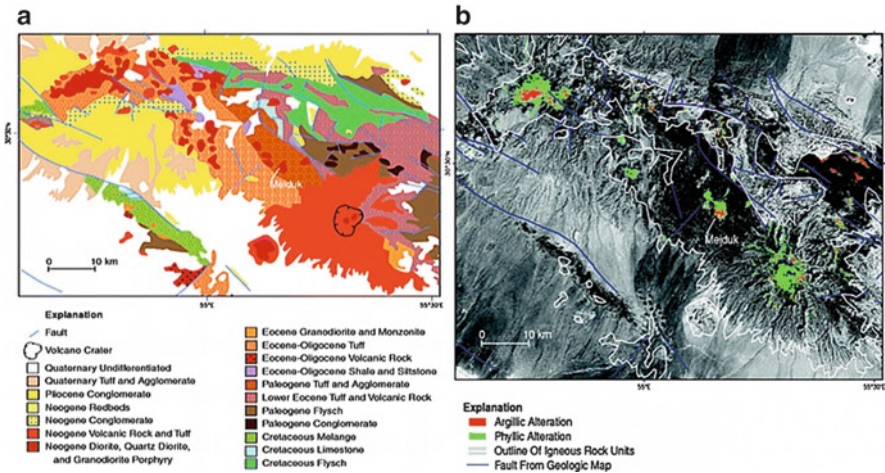


Fig. 14.6 (a) Geologic map (modified from Huber, 1969) and (b) Landsat TM band-7 with ASTER-derived argillic and phyllic alteration of the area around Meiduk copper mine, located in the central part of the Iran study area (from Mars and Rowan 2006)

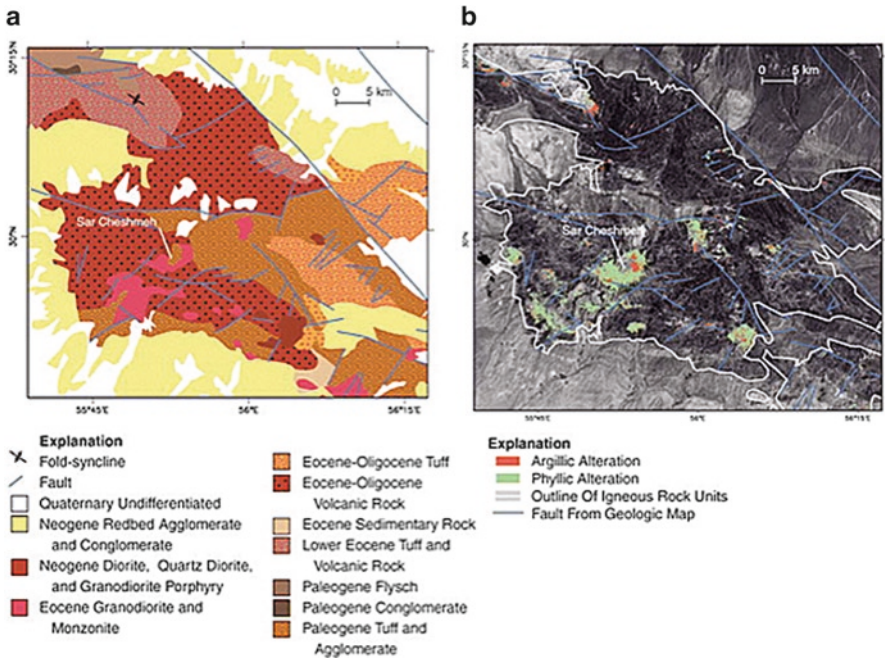


Fig. 14.7 (a) Geologic map (modified from Huber, 1969) and (b) Landsat TM band-7 with ASTER-derived argillic and phyllic alteration of the area around Sar Cheshmeh copper mine, located in the central part of the Iran study area (from Mars and Rowan 2006)

ASTER VNIR and SWIR bands recognized distinctive patterns of argillic and phyllic alteration associated with regional structures, which together aided regional mineral assessment of this remote location. Large curvilinear and pervasive linear patterns coincident with mapped phyllic and argillic rocks reflect potential locations for copper porphyry systems, as seen at known copper deposits, such as Meiduk and Sar Cheshmeh (Figs. 14.6 and 14.7). Large semicircular patterns of mapped alteration may represent igneous intrusions, which often host copper porphyry systems; extensive linear patterns of mapped alteration may relate to fault and fracture zones associated with epithermal and polymetallic vein deposits. On the basis of argillic and phyllic patterns and observation, a total of 61 potential porphyry copper deposits were mapped and identified throughout the magmatic arc. This approach illustrates the effectiveness of automated alteration mapping with ASTER reflectance bands, and is a systematic approach for mineral assessment of regional and remote locations.

14.3 District-Scale Alteration Mapping

14.3.1 *Chimborazo-Zaldivar Mining District, Northern Chile*

During the late 1990s, the Escondido copper district was the largest copper producer in the world (Richards et al. 2001). High-grade ore occurs as enriched copper sulfide and oxide blankets associated with multiple intrusive events. The northern part of the district is comprised of two primary deposits, Chimborazo and Zaldivar, situated in the copper metallogenic belt of northern Chile (Fig. 14.8). Chimborazo hosts copper mineralization in silicified, brecciated volcanics, in contrast to Zaldivar, which is largely hosted by rhyolitic intrusions (Richards et al. 2001). The district has experienced several pulses of Tertiary-age intrusive and extrusive events, overprinting Paleozoic and Mesozoic volcanics, sediments, and intrusions (Fig. 14.9). Complicating the geology further, multiple phases of hydrothermal alteration are recognized, characterized by potassic, propylitic, argillic, and advanced argillic mineral assemblages. Since the district has been extensively altered universally, it becomes important to identify alteration associated with known copper deposits and predict these alteration minerals and patterns elsewhere. In addition to copper potential, the region also hosts epithermal high- and low-sulfidation gold systems. Mapping alteration in this setting is paramount to discovering and developing copper and gold deposits elsewhere in the district.

In the example described here, Perry Remote Sensing used ASTER images to provide alteration mineral mapping for the district and adjacent areas at 1:100,000 map scale. Since most of district around Chimborazo and Zaldivar was geologically mapped, locations of known alteration would serve as “ground truth” to calibrate ASTER mineral models, used to characterize the deposits and map unknown areas to the north. Situated in the Atacama Desert, the arid setting and good exposure provide

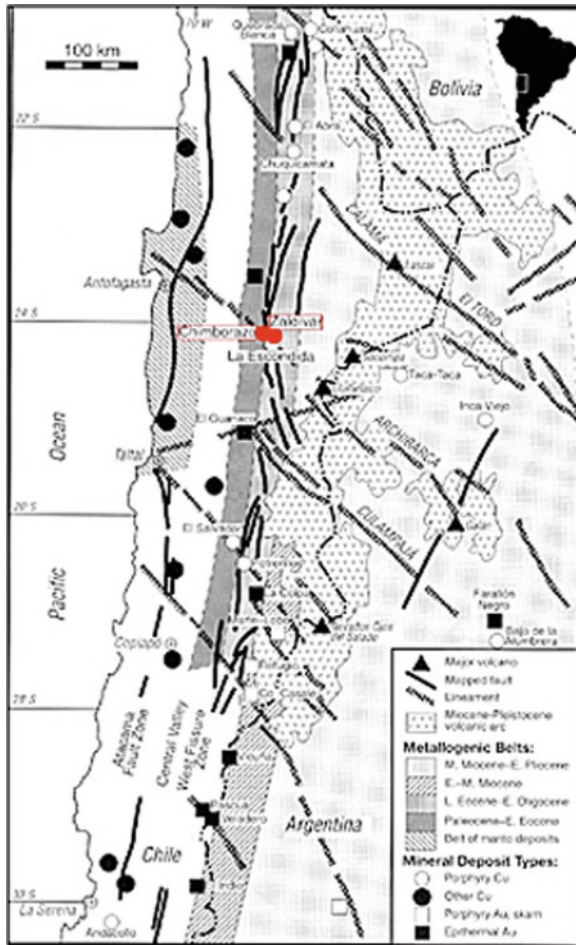


Fig. 14.8 Regional geologic map of northern Chile, which show locations of Chimborazo and Zaldivar copper porphyry deposits along with other significant deposits (from Richards et al. 2001)

excellent conditions for remote sensing analysis. Two ASTER scenes cover the mining district plus unmapped areas to the north, totaling approximately 7,800 km².

As discussed in the previous Zagros case history, many alteration minerals have distinct spectral signatures that are useful to identify mineral distribution and concentration from ASTER data (Mars and Rowan 2006). In the present example, the goal of ASTER processing was to identify specific minerals and mineral mixtures, not just map broad categories of phyllic or argillic alteration. Since alteration is widespread in this environment, it is important to observe key mineral associations and mixtures that attempt to identify metal-bearing systems (Table 14.2).

Silicified and brecciated rocks at Chimborazo reflect advanced argillic alteration associated with silica, pyrophyllite, alunite, and kaolinite arranged in a concentric,

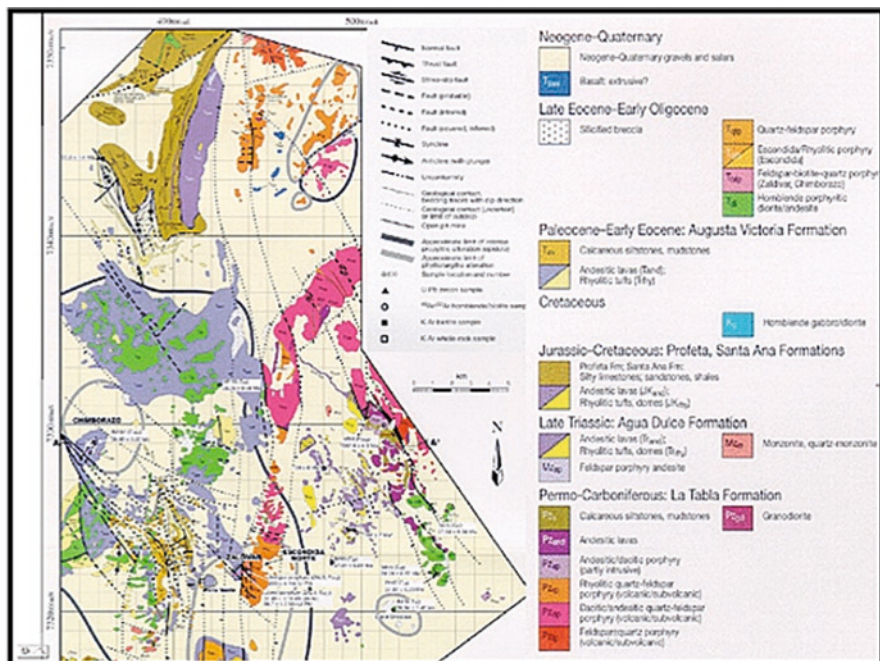


Fig. 14.9 Geologic map of the northern Escondida mine district, including Chimborazo and Zaldivar deposits. Majority of outcrop is volcanic and intrusive rocks. The extent of intense propylitic and argillic/phyllitic hydrothermal alteration is delineated (modified from Richards et al. 2001)

Table 14.2 Key minerals categorized by alteration system and environment

| | | |
|--------------------------------------------------------------------------------------------------------------------|-------------------|-------------------------------------------|
| Chlorite*, actinolite*, feldspar, silica, biotite, magnetite | Potassic | Increasing temperature high pH |
| Chlorite*, calcite*, dolomite*, smectite*, illite*, zeolites*, epidote*, adularia, albite | Propylitic | Intermediate temperature high pH |
| Pyrophyllite*, dickite*, sericite/muscovite*, silica, carbonates*, mica, feldspar, chlorite*, andalusite, corundum | Phyllic | Increasing temperature high pH |
| Kaolinite*, halloysite*, dickite*, illite*, smectite*, siderite, carbonates*, diaspore | Argillic | Decreasing temperature intermediate pH |
| Pyrophyllite*, alunite*, kaolinite*, dickite*, diaspore, mica, zunyite, andalusite, corundum | Advanced argillic | All temperatures low pH |

*Minerals with an asterisk signify those that are spectrally characterizable using SWIR wavelengths at laboratory spectral resolution (modified from Corbett and Leach 1998)

zoned pattern (Petersen et al. 1996). In contrast, alteration at Zaldivar is expressed as phyllic to argillic style, represented mostly by kaolinite, sericite/muscovite, illite, and carbonates (personal communication, Keith Blair 2004). Altered zones at Zaldivar are typically broad and elongate, reflecting fault control on the porphyry intrusion. Therefore, mapping and observing alteration mineral distribution and

patterns should prove useful to predict similar mineral systems in unmapped areas of the district. ASTER mineral-model results could later guide field investigations, helping geologists accomplish in one field season what might otherwise take three or four field seasons to identify and map.

Two ASTER scenes (radiance at sensor data acquired on the same date) were mosaicked, and contiguous SWIR bands 5–9 were atmospherically corrected using an empirical-line technique (ENVI software, Research Systems 2006), emphasizing rock and soil exposures, which resulted in a floating-point data set with values between 0 and 1. SWIR bands are emphasized in this effort since ASTER bands 5–9 are nearly continuous in wavelength and are well suited to differentiate minerals of interest. Public-domain spectral libraries (SLI) from USGS and Johns Hopkins University were resampled to fit ASTER SWIR bands 5–9 for selected alteration minerals (Fig. 14.10). Atmospherically corrected ASTER SWIR bands and resampled public-domain SLI were input to image classification utilizing the spectral-angle mapper (SAM) algorithm (ENVI software; Research Systems 2006).

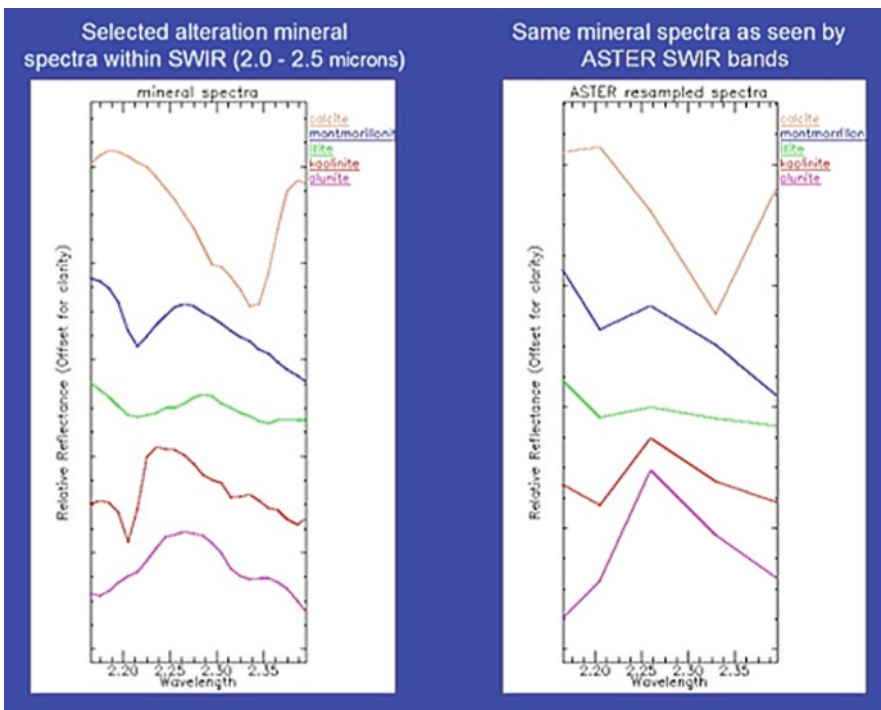


Fig. 14.10 Lab spectra from selected alteration minerals (*left*) compared to the same spectra, resampled to fit ASTER shortwave infrared (SWIR) wavelength intervals (*right*). Using image classification algorithms focusing on spectral-feature fitting (SFF) and spectral angle mapping (SAM), ASTER SWIR bands have the potential to map specific minerals. Lab spectra courtesy USGS Mineral Spectral Library

“Ground truth” locations of known alteration helped select and refine class thresholds for each mineral with results saved to an image format. In addition, classified pixels were randomly tested per mineral class with Spectral Analyst, tabulating scores from combined SAM and spectral-feature fitting (SFF) algorithms against resampled SLI (ENVI software, Research Systems 2006). This process aided in further refining rule class thresholds.

A similar approach was used to model silica from ASTER TIR radiance at sensor data. More care is necessary in applying atmospheric corrections to TIR bands (compared to the SWIR bands) because of undefined temperature extremes in this desert environment. TIR modeling ideally requires that we exclude calibration sites from the coldest and warmest exposures, which relate to super-heated black volcanics, exceptionally warm sunlit slopes, bright saline playas, cool shadow areas, and other extreme temperature features. Terrain within the interest area exhibits moderate shadowing but has intense differences in albedo (or reflectivity), affecting thermal surface or temperature readings. The best attempts were made to model silica from ASTER TIR bands, acknowledging the lack of independent field-measured temperature control. Known silica-rich locations helped select thresholds to refine silica classes resulting from SAM classification.

Once mineral classes were finalized, ASTER VNIR, SWIR, and TIR bands were georectified to Landsat ETM orthorectified mosaics in UTM/WGS-84 map base, preserving native pixel sizes of 15, 30, and 90 m, respectively. Mineral classifications were also georectified using SWIR and TIR ground control points (GCPs). Preparing for field location and mobilization demanded positionally accurate image maps conforming to Chilean topographic maps (± 50 m). Therefore, georectified VNIR bands and mineral classifications were converted to the Chilean map base (UTM/PSAD'56). Applying georectification after mineral classification preserves pixel values and reduces artifacts caused by multiple resampling iterations. It was necessary to generate bright and dark pixel masks for finalized mineral classification due to false-positives, which arise from extreme pixel values in this terrain (i.e., bright playas, dark shadows, black volcanic rocks). ASTER band 3 (near infrared) helped generate bright-target and dark-pixel masks for the two-scene ASTER area. No vegetation masks were necessary given the desert terrain location.

Mineral classes were color-coded and presented on edge-enhanced ASTER band 3 at 15-m pixel size. The ASTER alteration minerals and the geologic map were directly compared within the same map base and at the same pixel size (Fig. 14.11). Viewing the Chimborazo area, ASTER mineral classification identified advanced argillic minerals located at this site (Fig. 14.11). In addition, alunite and kaolinite/alunite classes are observed in a somewhat concentric fashion, coincident with three other mapped silicified breccias (A, B, and C on Fig. 14.11). Good correlation was also observed for the Zaldivar site, where ASTER characterized argillic alteration minerals in outcrop. Fieldwork sampled 30 sites within the geologically mapped area and verified 80% of ASTER classes, not including extensive alteration mapped on alluvial slopes. Poorest results were observed for silica (~30% field confirmed), probably relating to atmospheric correction issues previously discussed.

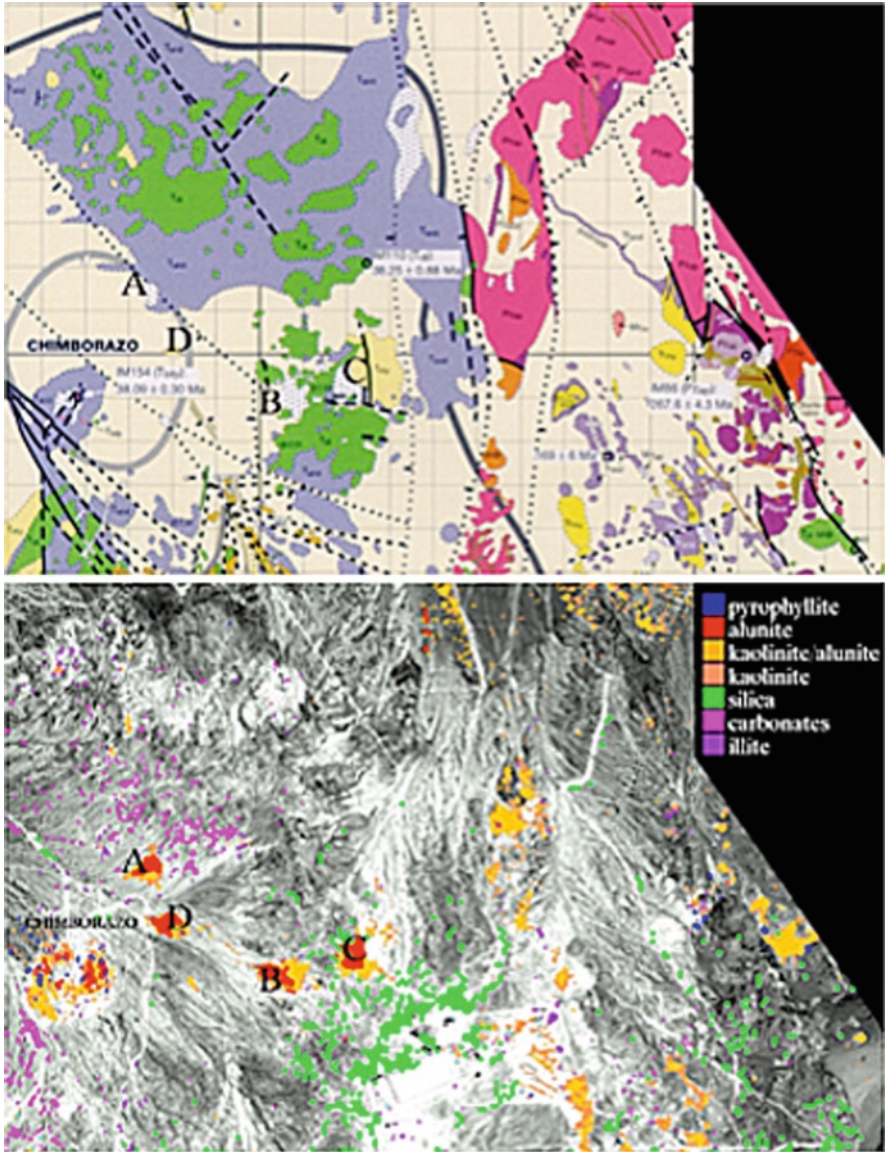


Fig. 14.11 Close-up of Chimborazo area showing mapped geology (*top*, modified from Richards et al. 2001) and corresponding ASTER alteration mineral mapping (*below*). Locations A, B, C, and D represent field locations verifying the presence of alunite and kaolinite. Both images measure approximately 20 kilometers in width. For geologic map explanation, see Fig. 14.9

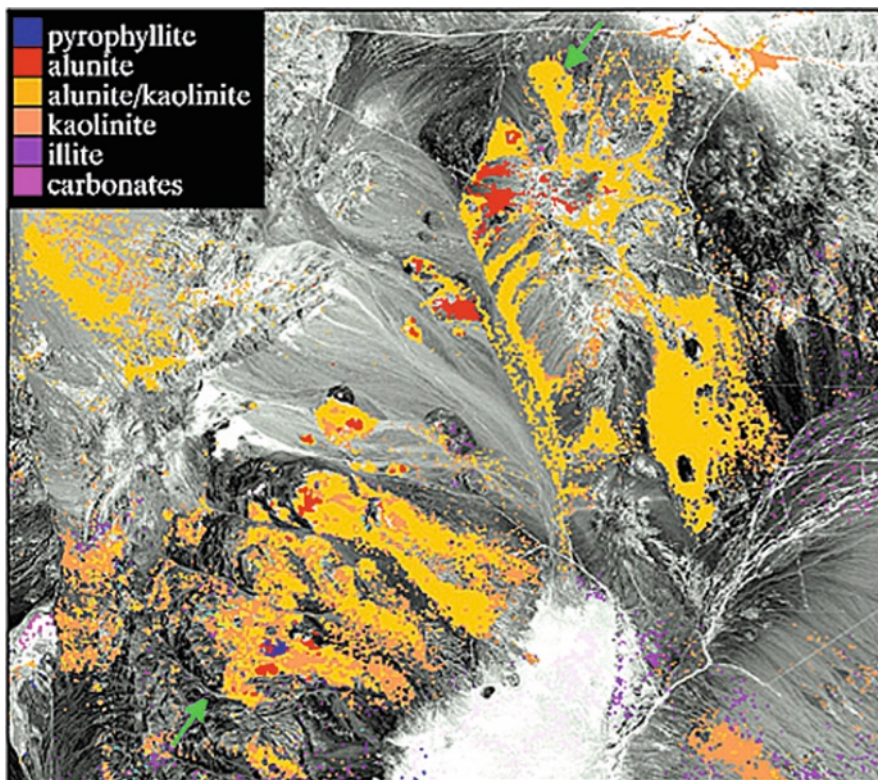


Fig. 14.12 Selected area for field investigation showing a northeast alignment of argillically altered exposures (highlighted by *green arrows*). Much of the alteration response is from weathered pediment surfaces, leading to upslope outcropping sources. Image width measures 23 km

Pyrophyllite classification encountered spurious results, but proved likely correct when found clustered together near alunite classes.

Moving north, several locations were selected for fieldwork based upon ASTER alteration mineral mapping and predicted mineral coincidence. Figure 14.12 shows a location with a northeast-trending alignment of multiple alunite/kaolinite pods. While much of the alteration mineral response appears to come from detritus and pediment aprons, isolated outcrops of alunite encircled by kaolinite trend northeast-southwest, suggesting mineral zonation and fault control. These areas look similar to Chimborazo, although no pyrophyllite was predicted. Fieldwork sampled three of these features and confirmed the presence of alunite and kaolinite using a field spectrometer. Pyrophyllite was also identified in the field but not mapped by ASTER. From field mapping, the alteration pods were identified as silicified breccias, positioned along a northeast-trending fault zone, although no fault escarpment was found in the field.

Overall, ASTER alteration mineral modeling evaluated over 5,000 km² of unmapped terrain and helped field geologists target locations for exploration and mapping. This task was accomplished in one field season, drastically reducing the amount of field time and expense necessary to identify quality field targets. As a result of the mapping program, sampling and drilling surveys were initiated along with several new claims.

14.4 Localized Fieldwork and Logistics

14.4.1 *Oyu Tolgoi Mining District, Mongolia*

The Oyu Tolgoi mining district of the southern Gobi Desert was discovered in the late 1990s, and is a world-class copper, gold, and molybdenum porphyry system (Perello et al. 2001). After the discovery, many companies were attracted to Mongolia in search of similar giant deposits. A virtual land rush tied up all exploration blocks in the Oyu Tolgoi trend, and many junior exploration companies were faced with evaluating blocks sight unseen. Many groups experienced the frustration of conducting business in a country covering five time zones with only one primary railway, leading to massive downtime, budget overruns, and field mobilization nightmares.

The project area is situated in southern Mongolia, and covers 215 km², adjacent to the Oyu Tolgoi block within a Silurian–Carboniferous volcanic arc known as the Barga terrane (Fig. 14.13). This tectonic province hosts another significant porphyry system called Tsagaan Suvarga as well as several other notable copper and gold prospects (Perello et al. 2001). As with most of the country, the site is extremely remote with few roads and intermittent villages. Topographic map availability for this region ranges from difficult to impossible, and no geological maps are available. As a result, field mobilization is costly and time consuming. Geologists and other field personnel are faced with formidable communication, logistics, and survey planning challenges.

Porphyry targets in this region are intruded along an island-arc sequence of rocks, consisting of pillow basalts and andesites interbedded with fine grained sedimentary layers and covered by Carboniferous terrigenous sequences (Badarch and Orolmaa 1998). Intrusions range from syenite to alkaline granite with ancillary dikes and stocks of monzonitic and dioritic composition (Carboniferous to Permian age). Typically, intrusions display multiple-phase hydrothermal alteration, fracturing, and brecciation. Gold mineralization is associated with pyrophyllite, alunite, silica, dickite, sericite, and zunyite, often found along fault and fracture zones and breccia surfaces. Copper deposits generally exist as enrichment blankets flanking intrusions comprised of sulfide suites and related to advanced argillic alteration.

The project area is in an arid setting with seasonal rainy periods. Poorly consolidated Cretaceous sediments, yielding widespread alluvial fans on pediment surfaces,

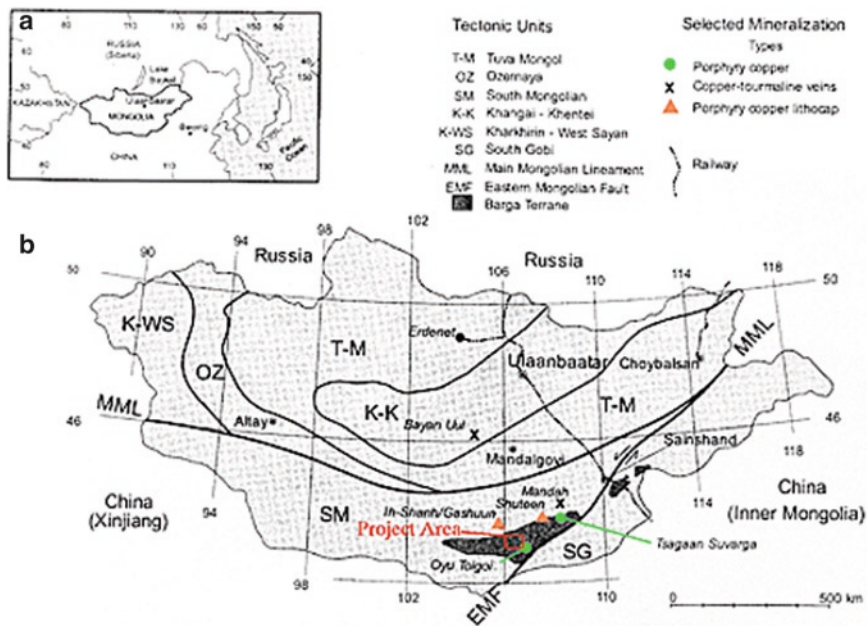


Fig. 14.13 (a) Location map of Mongolia. (b) Simplified tectonic map of Mongolia showing project area situated with Silurian–Carboniferous volcanic arc, known as the Barga Terrane (modified from Perello et al. 2001)

cover much of the area. Outcrop patterns reveal inundated and highly weathered exposures. The outcrop for Oyu Tolgoi discovery was an altered, isolated knob sticking up through pediment gravels. Therefore, identifying even small, altered exposures is significant while exploring this terrain. Propylitic, phyllic, argillic, and advanced argillic alteration-mineral assemblages typify gold and copper mineralization and are important to distinguish. Alteration mineral maps become critical elements to guide field investigation and sampling, which in this remote terrain can take years to accomplish.

The goals of the ASTER image analysis conducted by Perry Remote Sensing for this project were threefold: (1) predict and map alteration minerals likely associated with copper/gold porphyry deposit models (see Fig. 14.2); (2) prepare orthorectified image maps at 1:50,000 map scale for field navigation and integration with GPS; and (3) generate ASTER 30-m DEM for use with topographic contouring and generating perspective views. All aspects of the ASTER work were prepared in raster and vector file formats such that field geologists could review them with GIS software on field-portable computers. Final image products were orthorectified to UTM projection, WGS-84 datum to conform to the map base being used by GPS in the field. The ability to identify specific map coordinates for altered locations and previewing field conditions was essential to plan field traverses and anticipate necessary equipment.

The project area is covered by adjacent north-south images, and therefore required an image mosaic, later trimmed to maximize the exploration block (Fig. 14.14). As described in the previous case history, many alteration minerals of interest are characterized using SWIR and TIR wavelengths. Therefore, contiguous ASTER SWIR radiance at sensor bands 5–9 and TIR bands 10–14 were atmospherically corrected using an empirical-line technique, emphasizing rock, and soil exposures, which resulted in a floating-point data set with values between 0 and 1. Corrected SWIR and TIR bands were kept in native pixel sizes of 30 and 90 m, respectively. VNIR bands did not require atmospheric correction, since they were not used for mineral modeling. Public-domain SLI from USGS and Johns Hopkins University were resampled to fit SWIR and TIR bands for selected alteration minerals. Atmospherically corrected ASTER bands and resampled public-domain SLI were input to SAM image classification algorithm (ENVI software,



Fig. 14.14 View of southern Gobi project area using an ASTER color-infrared composite (Bands 3, 2, and 1 in RGB). Red reflects vegetation, *yellow/green* represent red-colored rocks and soils, *black* is dark-colored exposures, and *white* indicates evaporitic salts or bright sediments in drainage. The image is orthorectified to UTM/WGS-84 map base and measures approximately 54 km in width

Research Systems, Inc 2006). Each alteration mineral class was interactively scrutinized, randomly tested using SLIs and the ENVI Spectral Analyst, tabulating scores from combined SAM and SFF algorithms. Refined thresholds were selected to generate final classification files. Next, mineral classification results were orthorectified to UTM/WGS-84 and converted to vector polygons for easy import into GIS software.

With no topographic maps for this region, field crews relied on ASTER images to provide necessary detail for navigation throughout the exploration block. Orthorectified ASTER 15-m pixels generate sharp images at 1:50,000 map scale with an estimated positional accuracy of ± 30 m. The color-infrared (CIR) composite of the area provided an excellent image backdrop for GIS layers, plus were useful to interpret structures, outline intrusions, estimate strike/dip, plus digitize trails, roads, and drainage. One important aspect of ASTER data is the ability to generate DEM data from which topographic contours are extractable (Fig. 14.15). In this example, 30-m DEM data were prepared using 20-m contour intervals (CI), which are converted to vector format as polylines. The ASTER CIR was used to digitize drainage, artesian springs (oases), unknown tracks/trails, and other features valuable for field logistics. All features were saved in vector polyline format for direct import into GIS

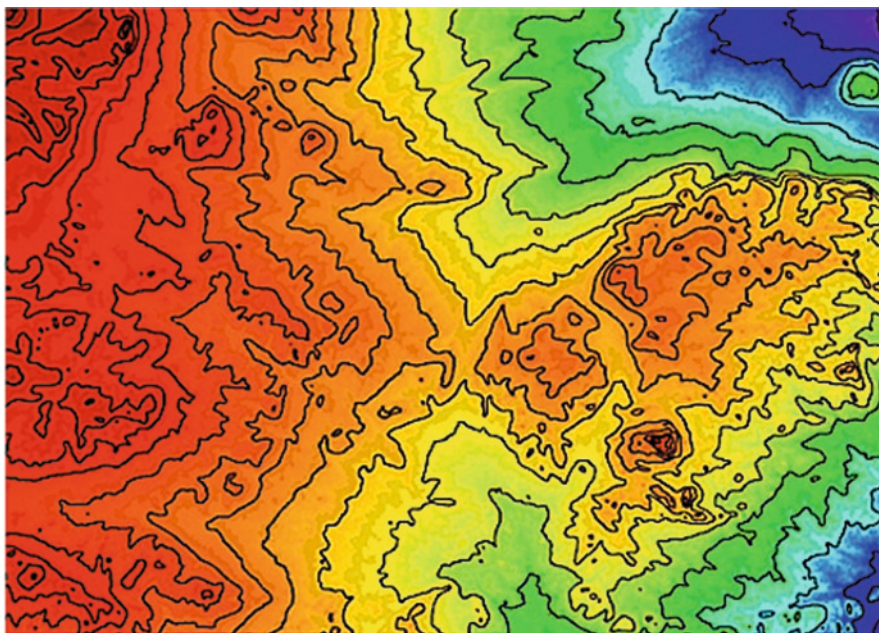


Fig. 14.15 Close-up of ASTER-derived digital elevation model (DEM) with applied color table reflecting low (*blue*) to high (*red*) elevation. Topographic contours are generated from DEM data. In this case, 20-meter contour intervals (CI) were prepared (*black lines*). Image width measures approximately 30 km

software. Images were also interpreted for faults and potential intrusions, both important to explore porphyry copper and gold in this region. ASTER data-derived image components and layers were set up to produce maps for fieldwork with GIS software (Fig. 14.16).

ASTER images proved invaluable to explore this area within a 1-year time period. ASTER processing, digital products, and maps were generated during winter months. Roads and trails were digitized, and exploration targets that appeared accessible were prioritized. ASTER data-derived drainage maps helped field geologists identify locations for stream-sediment geochemical sampling, especially those drainage systems positioned down-slope from predicted alteration. Several

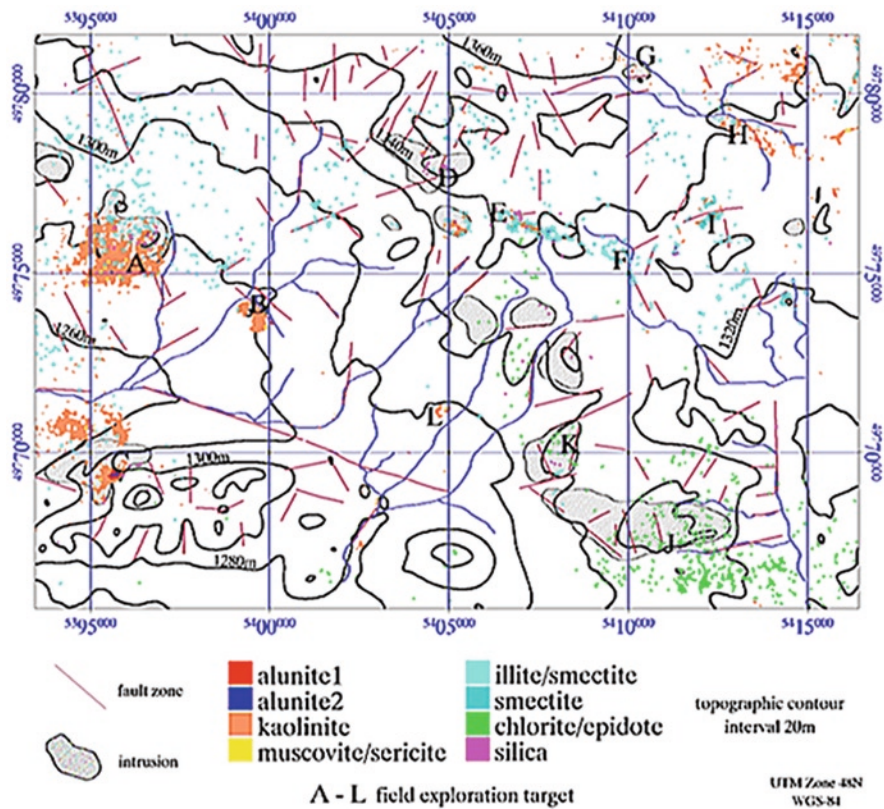


Fig. 14.16 Example field map showing components derived from ASTER images: (1) alteration mineral mapping; (2) topographic contours (generated from ASTER DEM data); (3) drainage; (4) interpreted fault zones; and (5) proposed intrusions. Original ASTER data were orthorectified to the designated map base with field maps prepared at 1:50,000 scale. Field exploration targets were identified where significant alteration coincided with interpreted structure and/or intrusions. Expected positional accuracy when used with GPS in the field approaches ± 30 m

sites near artesian springs (highlighted by vegetation) documented potential areas for human camp set up, especially those located away from large wadis, where dangerous flash floods could occur during isolated summer storms. In addition, the ASTER images and DEM data helped find suitable locations for fuel storage, which was compulsorily air-transported to chosen sites.

The field team departed during late spring to set up an operational camp with the first order of business to determine passable roads and trails. ASTER images were used to navigate these roads and field personnel documented jeep traverses with GPS continuous readings. Field parties worked throughout the summer visiting and sampling all exploration target areas. While no spectrometer was available for field use, all ASTER mineral models were verified by field geologists in varying amounts with the exception of silica, more widespread in field observation as compared to ASTER classification. Overall, ASTER catapulted the exploration program for this block and helped identify sites for year-two geochemical and geophysical surveying plus drilling.

14.5 Summary and Conclusions

The examples/case histories described here demonstrate ASTER data use for regional reconnaissance and mineral assessment, district-scale mapping, and support of localized fieldwork and logistics. ASTER data were used to identify and map distributions of alteration minerals associated with alteration zones using specific band ratios. In addition, mineral modeling with ASTER band-passes also resulted in discrimination of areas revealing key alteration minerals, including pyrophyllite, alunite, kaolinite, silica, carbonates, and illite/muscovite.

Work by the USGS in Iran applied standardized ASTER mineral mapping on a regional scale, outlining a large number of potential porphyry copper deposits. Their systematic approach, with over 60 ASTER scenes covering approximately 150,000 km² illustrated the effectiveness of automated alteration mapping with ASTER in exploring remote locations and over large areas. District-scale alteration mapping by Perry Remote Sensing at the Chimborazo-Zaldivar Mining District, Northern Chile helped field geologists target locations to explore and map by evaluating over 5,000 km² of unmapped terrain. This work dramatically reduced the effort and expense required to identify quality field targets. Many new prospects were identified and sampling and drilling surveys were initiated as a result of the ASTER mapping program. At the finest scale, localized fieldwork and logistics in southern Mongolia were greatly simplified by ASTER data use. Perry Remote Sensing used ASTER to predict and map alteration minerals likely associated with copper/gold porphyry systems. Orthorectified image maps were produced at 1:50,000 scale, which along with ASTER-generated DEMs provided the detail required by field crews to conduct field evaluation and exploration. The ASTER work in Mongolia leads to additional geochemical and geophysical surveying plus drilling.

Remote sensing analysis with ASTER data has evolved as a major source of information for the mining industry and mining applications. ASTER data offer consistent image data sets that provide a wealth of geological and logistical information in key areas of structural/geomorphic interpretation, compositional mapping, and logistics planning.

References

- Badarch G, Orolmaa D (1998) Overview of the geology and tectonic evolution of southern Mongolia. *Mong Geoscientist* 10:10–16 (Special Issue)
- Clark RN, Swayze GA, Gallagher AL (1993a) Mapping minerals with imaging spectroscopy. *U.S. Geol Surv Bull* 2039B:141–150
- Clark RN, Swayze GA, Gallagher A, King TVV, Calvin WM (1993b) The U.S. Geological Survey, Digital Spectral Library: Version 1: 0.2 to 3.0 microns. U.S. Geological Survey Open File Report 93–592, p 1340 <http://speclab.cr.usgs.gov> (Accessed August 1999)
- Corbett GJ, Leach TM (1998) Southwest Pacific Rim gold-copper systems: structure, alteration, and mineralization. *Soc Econ Geol* 6:100–140 (Special Publication)
- Crosta AP, Souza Filho CR (2005) Remote sensing in mineral exploration: South American examples of benefits gained from recent advances in sensor and processing technologies. In Rhoden HN, Steininger RC, Vikre PG (eds) *Proceedings of the geological society of Nevada symposium*, pp 999–1006, Window to the World, Reno, Nevada
- ERSDAC (2001) ASTER User's Guide, Part I, General (ver. 3.1), 101 p. ERSDAC, Tokyo
- Fujisada H (1995) Design and performance of ASTER instrument. In: Fujisada H, Sweeting MN (eds) *Advanced and next-generation satellites*, vol. 2583, pp 16–25. International Society Optical Engineering
- Hook SJ, Myers JJ, Thome KJ, Fitzgerald M, Kahle AB (2001) The MODIS/ASTER airborne simulator (MASTER) – a new instrument for earth science studies. *Remote Sens Environ* 76:93–102
- Hook SJ (1990) The combined use of multispectral remotely sensed data from the short wave infrared (SWIR) and thermal infrared (TIR) for lithological mapping and mineral exploration. In: *Proceedings of the fifth Australasian remote sensing conference*, Perth, Western Australia, vol. 1, pp 371–380
- Huber H (1969) Geological map of Iran sheet no. 5, south central Iran. Tehran, National Iranian Oil Company, scale 1:1,000,000
- Kahle AB, Palluconi FD, Hook SJ, Realmuto VJ, Bothwell G (1991) The Advanced Spaceborne Thermal Emission and Reflectance Radiometer (ASTER). *Int J Imaging Syst Technol* 3:144–156
- Kruse FA (2000) Mapping active and fossil hot springs systems using AVIRIS, HYMAP, TIMS and MASTER (Abst). In: *Proceedings of the 14th thematic conference, applied geologic remote sensing*, Las Vegas, NV, p 122. Environmental Research Institute of Michigan (ERIM), Ann Arbor, MI, 6–8 Nov 2000
- Kruse FA (2002) Combined SWIR and LWIR Mineral Mapping Using MASTER/ASTER. In: *Proceedings of IGARSS 2002*, Toronto, Canada, 24–28 June 2002 (Published on CD ROM – Paper Int1_B15_04, ISBN: 0–7803–7537–8. Also in hardcopy, vol. IV, pp 2267–2269, IEEE Operations Center, Piscataway, NJ)
- Lowell JD, Guilbert JM (1970) Lateral and vertical alteration-mineralization zoning in porphyry ore deposits. *Econ Geol Bull Soc Econ Geol* 65(4):373–408
- Mars JC, Rowan LC (2006) Regional mapping of phyllic- and argillic-altered rocks in the Zagros magmatic arc, Iran, using Advanced Spaceborne Thermal Emission and Reflection Radiometers (ASTER) data and logical operator algorithms. *Geosphere* 2(3):161–186. doi: 10.1130/GES00044.1

- Perello J, Cox D, Garamjav D, Sanjdorj S, Diakov S, Schissel D, Munkhbat TO, Oyun G (2001) Oyu Tolgoi, Mongolia: Siluro-Devonian porphyry Cu-Au/(Mo) and high-sulfidation Cu mineralization with a Cretaceous chalcocite blanket. *Econ Geol Bull Soc Econ Geol* 96(6):1407–1428
- Petersen CR, Rivera SL, Peri MA (1996) Chimborazo copper deposit, II Region, Chile: exploration and geology. *Soc Econ Geol* 5:71–80 (Special Publication)
- Regard V, Bellier O, Thomas JC, Abbassi MR, Mercier J, Shabanian E, Feghhi K, Soleymani S (2004) Accommodation of Arabia-Eurasia convergence in the Zagros-Makran transfer zone, SE Iran: a transition between collision and subduction through a young deforming system. *Tectonics* 23(4):24
- Research Systems Inc. (RSI) (2006) ENVI User's Guide, Research Systems Inc, Version 4.3
- Richards JP, Boyce AJ, Pringle MS (2001) Geologic evolution of the Escondida Area, northern Chile: a model for spatial and temporal localization of porphyry Cu mineralization. *Econ Geol Bull Soc Econ Geol* 96(2):271–305
- Rowan LC, Mars JC (2003) Lithologic mapping in the Mountain Pass, California area using Advanced Spaceborne Thermal Emission and Reflection Spectrometer (ASTER) data. *Remote Sens Environ* 84:350–366
- Walker R, Jackson J (2002) Offset and evolution of the Gowk fault, S.E. Iran: a major intra-continental strike-slip system. *J Struct Geol* 24:1677–1698. doi: 10.1016/S0191–8141(01)00170–5
- Yamaguchi Y, Kahle AB, Tsu H, Kawakami T, Pniel M (1998) Overview of advanced spaceborne thermal emission reflectance radiometer. *IEEE Trans Geosci Remote Sens* 36:1062–1071

Chapter 15

ASTER Imaging and Analysis of Glacier Hazards

**Jeffrey Kargel, Roberto Furfaro, Georg Kaser, Gregory Leonard,
Wolfgang Fink, Christian Huggel, Andreas Käab, Bruce Raup,
John Reynolds, David Wolfe, and Marco Zapata**

15.1 Introduction

Most scientific attention to glaciers, including ASTER and other satellite-derived applications in glacier science, pertains to their roles in the following seven functions: (1) as signposts of climate change (Kaser et al. 1990; Williams and Ferrigno 1999, 2002; Williams et al. 2008; Kargel et al. 2005; Oerlemans 2005), (2) as natural reservoirs of fresh water (Yamada and Motoyama 1988; Yang and Hu 1992; Shiyin et al. 2003; Juen et al. 2007), (3) as contributors to sea-level change (Arendt et al. 2002), (4) as sources of hydropower (Reynolds 1993); much work also relates to the basic science of glaciology, especially (5) the physical phenomenology of glacier flow processes and glacier change (DeAngelis and Skvarca 2003; Berthier et al. 2007; Rivera et al. 2007), (6) glacial geomorphology (Bishop et al. 1999, 2003), and (7) the technology required to acquire and analyze satellite images of glaciers (Bishop et al. 1999, 2000, 2003, 2004; Quincey et al. 2005, 2007; Raup et al. 2000, 2006a, b; Khalsa et al. 2004; Paul et al. 2004a, b). These seven functions define the important areas of glaciological science and technology, yet a more pressing issue in parts of the world is the direct danger to people and infrastructure posed by some glaciers (Trask 2005; Morales 1969; Liboutry et al. 1977; Evans and Clague 1988; Xu and Feng 1989; Reynolds 1993, 1998, 1999; Yamada and Sharma 1993; Hastenrath and Ames 1995; Mool 1995; Ames 1998; Chikita et al. 1999; Williams and Ferrigno 1999; Richardson and Reynolds 2000a, b; Zapata 2002; Huggel et al. 2002, 2004; Xiangsong 1992; Käab et al. 2003, 2005, 2005c; Salzmann et al. 2004; Noetzli et al. 2006).

J. Kargel (✉)

Department of Hydrology & Water Resources, University of Arizona,
Tucson, AZ 85721, USA
e-mail: kargel@hwr.arizona.edu

Global death tallies from natural disasters are imprecise and incomplete. Sources (e.g., <http://www.intute.ac.uk/sciences/hazards/timeline.html>; Richardson and Reynolds 2000b) indicate that since 1940, glaciers and their lakes and moraines have killed nearly one-tenth as many people as hurricanes and 4% as many as earthquakes. Glaciers are on a par with volcanoes as natural killers; commonly, the two phenomena together kill even more than either alone would. Like volcanoes, but unlike hurricanes and earthquakes, which distribute their threats against about two billion people, glaciers focus their threats on a few million. However, where glacier-related dangers exist, such concerns override all others related to natural hazards.

Nepal, Bhutan, India, China/Tibet, and other Asian countries have long histories of glacier disasters (Xu and Feng 1989; Xiangsong 1992; Yamada and Sharma 1993; Mool 1995; Richardson and Reynolds 2000b; Kattelmann 2003) (Table 15.1). Andean glaciers in Perú are the deadliest, where over 22 disastrous glacier-related floods and mass movements have occurred since 1702; most occurred from within the Cordillera Blanca region, where six events killed over 1,000 people each (Liboutry et al. 1977; Williams and Ferrigno 1999; Richardson and Reynolds 2000b; Carey 2005). Richardson and Reynolds (2000b) tally about 32,000 killed by glaciers in Perú, mainly from the Cordillera Blanca, which historically has been most prone to glacier disasters (Zapata 2002). Carey (2005) counts 6,000 killed in the Cordillera Blanca by lake outbursts in the past 150 years and 22,000 killed by

Table 15.1 Glaciological hazards: types of process, affected locations, and significant events

| | | Location | | | | | |
|---------------------------|--------------------------------------------------------------------------|-------------------------|----------------|---------------------------------|-------------------------------|---------------------------------|--------------------------------------|
| | | Cordillera Blanca, Peru | Nepal Himalaya | Hindu Kush/ Himalaya in Kashmir | Caucasus (Mt. Kazbek, Elbrus) | Copper River Basin, Alaska, USA | Caseasus, e.g., Mt. Rainier, WA, USA |
| Glaciological hazard type | Ice avalanche | X | X | X | X | X | |
| | Moraine avalanche | X | X | X | X | X | |
| | Volcanic lahar | | | | X | X | X |
| | Lake outburst | X | X | | | X | |
| | Glacier surge | | | X | X | X | |
| | Flood due to blocked drainage due to surge, ice/rock avalanche, or lahar | | X | X | X | X | X |
| | Thermokarstic collapse of buried glacier ice | | | | | X | |

glacier avalanches in the past 100 years. Other alpine regions (e.g., in Alaska and Switzerland), exhibit similar glacier dynamics, but fewer fatalities result from lower population densities or more hazard-wary development patterns.

Satellite-based remote sensing is used to detect, monitor, and assess glacier hazards, and enables rapid follow-up in the aftermath of disasters (Kääb et al. 2003). Remote sensing has its limits, but it enables repeated surveys of whole mountain ranges and detailed assessments of individual glaciers, glacier lakes, and moraines. Here we examine the general types of glacier hazards globally, and then focus on the glacier hazard regime in the Cordillera Blanca, Perú, to highlight some capabilities and limitations of satellite remote sensing of hazardous glaciers. We highlight the evolution and history of glacier lake outbursts of Palcacocha,¹ Perú, as an example of satellite remote sensing of hazardous glaciers, adding to what others have presented about that case (Lliboutry et al. 1977; Kaser et al. 1990; Mark 2002; Zapata 2002; Racoviteanu and Arnaud 2005; Carey 2005). We argue for a new approach to increased automation of data analysis related to glacier hazards. We exclude the special danger posed by glaciers to trekkers, river runners, fishers, alpinists, glaciologists, and glacier flight seers and pilots, and focus instead on hazards to cities and major infrastructure. We also offer ideas to improve communication about glacier hazards, building on lessons learned from the 2003 “Palcacocha crisis” (Kaser and Georges 2003).

15.2 Why Are Glaciers Dangerous, and How Can Satellite Imaging Assist?

Unstable or unconsolidated parts of the solid surface of Earth are potentially hazardous if critical infrastructure or people reside there. Coastal dunes, barrier islands, river flood plains, marine deltas, active and dormant volcanic slopes, and active faults are examples. In most such places in industrially advanced nations, land-use zoning restricts habitation and guides development. Glaciers and ice sheets are among the largest unstable parts of the solid Earth. Glaciers are so devoid of resources (other than water), so uncomfortable and dangerous, and so unstable that no infrastructure is normally built directly on glacial surfaces. In some rare cases where lucrative extraction of mineral or petroleum deposits is possible, major infrastructure is built on glaciers either in ignorance of the risk, or with some calculation showing an advantageous benefit to risk ratio. Examples include (1) major mine transport infrastructure built a century ago through the Copper River corridor, including a crossing of several glacier lake outburst flood (GLOF) impacted drainages and the stagnant, ice-cored

¹“Cocha” is Quechua for “lake,” and “palca” means “valley” or “divided in two,” and is the specific lake, probably named for the nearby peak, Ranrapalca.

terminal lobe of Allen Glacier (Alaska)², and (2) the Trans-Alaska oil pipeline built on or adjacent to surge deposits and ice-cored moraines of three Alaskan glaciers, and also crossing multiple GLOF impacted drainages, so far with minimal ill effect. A major copper mine in Chile has been developed by excavating through a series of glaciers to gain access to the ore beneath.

Areas down valley from large alpine glaciers also commonly are unstable due to landslide potential of moraines, debris flows, snow avalanches, outburst floods from glacier lakes, and other dynamic alpine processes; yet there exists much development and human occupation of some disaster-prone areas. Some fundamental instabilities operate cyclically or episodically. In seeming disregard to danger, or with an accepted risk, construction within and inhabitation of danger zones are probably due to the perceived stability (or metastability) of glacier systems for decades or centuries; thus, ski resorts and skiers, mountain getaways and tourists, hikers, hunters, fishers, miners, loggers, and other users and inhabitants are lured to these alpine splendors and riches. Some cities grew before a science- and engineering-based understanding of these hazardous settings developed (Tacoma, Washington, population 200,000; Huaraz, Perú, population 80,000).

Many glaciers are so dynamic, especially as climate shifts, and development is so rapid that the array of threats is evolving (Kaser et al. 1990; Evans and Clague 1994; Portocarrero 1995; Morales Arnao 1998; Georges 2004, 2005; Wolfe 2009). This evolution is where satellite imaging can provide cost-effective and critical time-dependent information. In some cases (e.g., at the glacier-capped Popocatepetl volcano looming over Mexico City) recent reductions in glacier mass are alleviating a threat to large numbers of people (Huggel and Delgado 2000). Elsewhere, warming exacerbates the threat as thawing destabilizes permafrost, ice-cored moraines, and glacier beds; as glacier tributaries detach and promote formation of ice-marginal lakes; as stagnating glacier tongues are replaced by coalescing supraglacial lakes and moraine-dammed lakes; and as glacier recession and downwasting removes mechanical support from hanging glaciers.

Glaciers and their outbursts move by gravity, so the physical pathway and causes/sources of initiation of potential disasters are sometimes known precisely (Huggel et al. 2003; Noetzli et al. 2006). Glacier-related hazards thus sometimes encompass a degree of predictability and enable far-advance warnings or mitigation

²The Million Dollar Bridge, 128 other bridges, a highway, the Copper River and Northwestern Railway, and a telegraph line were built by the Kennecott Copper Corporation to move copper ore from the Kennecott mines to the Alaskan port of Cordova. Completed in 1911, the railway included 8 km built on a stagnant, forested, debris-covered surge lobe of Allen Glacier. The Million Dollar Bridge across the Copper River, damaged during construction in 1909 by a deadly winter GLOF, narrowly escaped destruction by a surge of Childs Glacier in 1911; from 1911 to 1938 it was used to move 600,000 metric tons of copper (10-year value of \$200 million; at July 2008 prices, \$5 billion). The \$20-million project paid for itself and the purchase of Alaska from Russia seven times over, despite risks from glacier surges and floods, thaw of buried ground ice, and seismicity. The Million Dollar Bridge partly collapsed during the 1964 earthquake; it was repaired in 2005. The story highlights both hazards and lucrative possibilities even in precarious situations.

not so readily possible when planning for most types of natural disasters. Many volcanic eruptions, for example, threaten broad radial zones around the volcano, hurricanes threaten entire coastal plains, and earthquakes threaten broad expanses around fault zones, whereas glacier hazards are more commonly focused on specific, predictable curvilinear destruction pathways. Consequently, investments of a few million dollars can offer cost-effective mitigation of glacier hazards facing hundreds of thousands of people (Morales 1969; Lliboutry et al. 1977; Mool 1995; Rana et al. 2000; Richardson and Reynolds 2000a). However, other types of glacier hazards are controllable only by relocation of people and critical infrastructure.

ASTER and other satellite images can help monitor the sizes and outlines of glaciers, and their lakes, activity such as iceberg calving and debris accumulation, and changing thicknesses and flow speeds of glaciers (Bishop et al. 2004; Paul et al. 2004a, b; Kääb 2005; Kargel et al. 2005; Raup et al. 2006b; Rivera et al. 2007). Satellite imaging also enables preliminary identification of specific hazardous spots, and allows preliminary assessment of possible modes of future disaster occurrence. In the aftermath of disasters, ASTER and other images can quickly identify the likely causes of trouble, and possible further instabilities (Kääb et al. 2003).

15.3 Types and Case Examples of Glacier Hazards and Disasters

Below we list some glacier hazards according to type, trigger mechanism, and potential loss type (Tables 15.1–15.3). Superscripted numeric notes identify some potential hazards for a selection of heavily populated areas or valuable infrastructure near glaciers in the Cordillera Blanca (Perú); the Himalaya of Nepal; the Hindu-Kush/Himalaya of Kashmir and northern Pakistan; the Caucasus; the Copper River Basin (Alaska); and the Cascades, especially Mount Rainier (Washington). Hazards occur in a heterogeneous geographic mosaic. Illustrative examples of historic disasters include the 2002 Kolka–Karmadon event; twentieth-century events in the Nepal Himalaya; twentieth-century events in the Cordillera Blanca; surges of the Bering Glacier and other Alaskan glaciers, which override critical habitat; and the 1980 eruption and lahars of Mount Saint Helens (Washington). Some events involve multiple glaciological processes and at times nonglacial triggers (Kääb et al. 2003; Huggel et al. 2004).

In other cases, otherwise minor glaciological events could potentially trigger other destructive forces. For example, in January 2007 a relatively minor GLOF discharge occurred from the Harding Icefield and Skilak Lake (Alaska); the minor event fractured normal seasonal river ice, which then produced a large and destructive ice jam and flood, causing \$3.7M in damages, along the Kenai River (State of Alaska 2007).

A transient glacier dynamic event in an unpopulated area without valuable infrastructure or critical habitat is not a disaster, and threat of such an event is not a hazard. At the lower magnitude of possible consequences, there are grounds to

Table 15.2 Glaciological hazards: trigger mechanisms and causal events

| | Location | | | | | |
|---------------------------------------------------------------------------------------------------------------------------------------|-------------------------|----------------|---------------------------------|----------------------------------------|---------------------------------|--------------------------------------------------|
| | Cordillera Blanca, Peru | Nepal Himalaya | Hindu Kush, Himalaya in Kashmir | Caucasus (e.g., Mt Kazbek, Mt. Elbrus) | Copper River Basin, Alaska, USA | Cascades (e.g., Mt. St. Helens, Mt. Rainier, WA) |
| Seismic activity (rock, ice, or avalanche, landslide) | X | X | X | X | X | X |
| Volcanic activity | | | | X | X | X |
| Surface loading of glacier (anomalous snowfall or large rock landslide) | X | X | X | X | X | X |
| Unseasonably warm summer/hot season weather | X | X | X | X | X | X |
| Long-term climate warming (global warming or decadal oscillation) | X | X | X | X | X | X |
| Bed thaw or thaw of ice-cemented moraine | | | | X | X | X |
| Geothermal anomaly (e.g., subglacial volcanic episode) | | | | X | X | X |
| Debuttressing (removal of supporting ice, bedrock, or debris mass) | X | X | X | X | X | X |
| Melting of glacier ice dam of a lake or melting of ice-cemented moraine dam | X | X | | | X | |
| Erosion by overtopping moraine or ice dam (triggered by increased meltwater, plugging of lake drainage conduit, avalanche surge wave) | X | X | | | X | X |

Glaciological hazard trigger mechanisms

| Rise of hydraulic head, reduction in shear stress of glaciers or water-saturated moraines | | | | | | | |
|---------------------------------------------------------------------------------------------------------------------|---|---|---|--|--|--|---|
| Lake level rise due to increased melt rate or increased retention of water | X | X | X | | | | X |
| Flotation of glacier dam in a lake | X | X | X | | | | X |
| Thaw or seismicity induced collapse of moraine into lake and displacement wave | X | X | X | | | | X |
| Drainage of seasonal meltwater or rain runoff to the bed of the glacier | X | X | X | | | | X |
| Ice flow or debris plugging of crevasses and moulins (drainages), then sudden unplugging and change in glacier flow | X | X | X | | | | X |
| Saturation of unstable moraines by melting snow/ice or sustained rains | X | X | X | | | | X |
| Poorly executed hazard mitigation or poor luck during emergency mitigation | X | X | | | | | X |

Table 15.3 Glaciological hazards: potential future losses per disaster event (F) and documented cumulative historic losses (H) 1800–2008

| | | Location | | | | | |
|-----------------------------------------------------------------------|--|-------------------------|-------------------------------------------------------|---------------------------------------------------|-----------------------------------------|----------------------------------|-------------------------------------------------------|
| Region | | Cordillera Blanca, Peru | Nepal Himalaya | Hindu Kush/Himalaya in Kashmir | Caucasus (e.g., Mt. Elbrus, Mt. Kazbek) | Copper River Basin, Alaska, USA | Cascades (e.g., Mt. Rainier and Mt. Saint Helens, WA) |
| Some key population vulnerabilities | | Huaraz (pop. 100,000) | Small villages | Small villages | Small villages | Small villages | Tacoma (pop. 200,000), Puyallup (pop. 33,000) |
| Some key economic vulnerabilities | | Tourism | Small hydroelectric and major trade corridors/bridges | Tourism, binational tensions over water resources | Tourism, multinational tensions | Alyeska oil pipeline and tourism | Tourism |
| Loss of human life, deaths: | | | | | | | |
| XX = tens | | | | | | | |
| XXX = hundreds | | | | | | | |
| XXXX = thousands | | XXXX (F) | XXX (F) | XXX (F) | XXX (F) | XXX (F) | XXXXX (F) |
| XXXXX = tens of thousands | | XXXXX (H) | XXX (H) | XXX (H) | ? | Few if any | XX (H) |
| Loss of infrastructure or habitable or productive land and resources: | | | | | | | |
| \$ = millions of \$, | | | | | | | |
| \$\$ = tens of millions of \$, | | | | | | | |
| \$\$\$ = hundreds of millions of \$, | | | | | | | |
| \$\$\$\$ = billions of \$, | | | | | | | |
| \$\$\$\$\$ = tens of billions of \$, | | \$\$\$\$ (F) | \$\$ (F) | \$\$\$ (F) | \$\$\$ (F) | \$\$\$\$\$ (F) | \$\$\$\$\$ (F) |
| of \$, \$\$\$\$\$\$ = hundreds of billions of \$ | | \$\$\$ (H) | \$ (H) | \$ (H) | \$\$ (H) | \$ (H) | \$\$ (H) |

Glaciological hazard-related type of loss

consider hazards of transient glacier dynamics even in the remotest areas, as very few of these events are likely inconsequential at the ecological level, or for trekkers, hunters, trappers, and other occasional occupants of the land. Thus, almost any large transient glacier dynamic event is potentially hazardous, but we need to concentrate our main focus on areas where the consequences are potentially calamitous. A deleterious change in glacier regime over the lifetime of valuable infrastructure represents a serious hazard to it. A major hazard to human life generally occurs when many people reside or work within the area potentially affected by a likely transient change in glacier regime that could occur faster than the people could walk away.

Glaciers and permafrost are important natural elements in many alpine regions' hydrology, physical geography, and ecology. Glacier dynamics both create and destroy habitat in a continuing cycle, and cause ecological catastrophes as well create diverse habitats. No region better illustrates the ecological significance of glaciers than the Copper River Basin in Alaska, where valuable protected coastal and deltaic plains and marshland, lowland permafrost, temperate rainforest, and alpine tundra ecosystems are integrated in one region, and all are influenced by glaciers (<http://www.inforain.org/copperriver/content/pages/background/ecology.htm>). Whether fluctuating glaciers are ecologically hazardous and cause ecological disasters depends on a point of view, but glacier changes certainly have profound local and even global impacts on ecosystems. These processes are best viewed as the cryospheric ecological equivalent of fire, both as destroyer and the creator of habitats, and an integral part of the ecological mosaic. However, in terms of transient high-magnitude impacts, glacier dynamics are viewable in a similar context and with similar methodologies as glaciological hazards and disasters affecting people.

Most glacier hazards and disasters involve composite dynamic events, e.g., the Kolka–Karmadon disaster in the Russian Caucasus in 2002, which claimed >120 lives (Kääb et al. 2003). That event probably involved an initial small ice avalanche from a hanging glacier; subsequently a growing debris avalanche and debris flow developed as water, ice from two more glaciers, and more debris was ingested; the debris flow was dammed by a ridge, where it buried a small village; then the deposit issued a mud flow. In all, the mass movements traversed 33 km, killing life along the way. Disaster recovery was complicated by lake formation caused by a blocked drainage (Kääb et al. 2003). That case highlights the potential for relatively small initiating events to amplify and propagate as gravitational potential energies of additional unstable masses are released.

In a further illustration of the complexity and poor predictability of such dangerous dynamical events, in April 2002 a large landslide/rockfall collapsed onto the glacier that drains into Laguna Safuna Alta in the Cordillera Blanca. The debris, and the speed with which it moved into the lake, displaced about half the water volume and formed an initial displacement wave that ran up and overtopped the terminal moraine in a wave up to 110 m high (Hubbard et al. 2005). The wave retreated back into the lake basin and effectively washed back and forth up to ten times, each successive wave decreasing in amplitude as its energy dissipated. The terminal moraine, although badly damaged, survived. However, a similar volume of

rock material is liable to collapse, and a similar event could happen as those that wrecked Karmadon and Huaraz. Given such conditions, the moraine dam is likely to fail with a flood or debris flow ensuing downstream. Regionally, the specific types and magnitude of glacier hazards can vary from valley to valley, or with differences of just a few hundred meters in location. Hazard mitigation in Perú and Nepal especially remains effective in reducing some hazards (Morales 1969; Lliboutry et al. 1977; Rana et al. 2000; Reynolds 1998, 1999; Reynolds et al. 1998; Richardson and Reynolds 2000a, b).

There always remains a risk that a glacier hazard mitigation attempt could go awry. Indeed, Lliboutry et al. (1977) describe one such occurrence at Laguna Jancarush in Peru on October 20, 1950. An open channel was being excavated as part of mitigation works to reduce the lake level. What was not appreciated was that the glacier tongue had been partially afloat; by lowering the lake level, that support was removed and the glacier tongue collapsed into the lake, which produced a large displacement wave that washed through the unfinished channel and into the construction camp. Official reports said 200 people were killed, although unofficially the figure was 500.

The remediation of Raphstreng Tsho in Bhutan in 1999 potentially made a bad situation worse. Lowering the water level in that lake through an engineered channel increased the piezometric gradient in the already unstable moraine separating it from an adjacent higher glacier and its rapidly developing lake at Thorthormi Glacier (cf. Richardson and Reynolds 2000a, Fig. 12). This could lead to a failure in due course. Of course in many cases, when dangerous conditions motivate our efforts to thwart disaster, inaction, sometimes, either draws disaster closer or delays it. We do not weigh the engineering details or cost benefits of particular decisions to act or not, but we offer this example as one where the wisest course is not always clear, and our sense of what is best may change as we learn more.

Obviously, natural hazards afflict the local peoples of an affected area; satellite remote sensing specialists are distant observers through their eyes in the sky and are limited in how they identify or clarify a hazardous situation (or help understand and/or assist in the recovery from a disaster). However, even given the limitations and feasibilities of satellite image analysis, much realistic work to aid the hazards community (scientists, engineers, and civil authorities), the local communities in areas affected, the decision support personnel in governments, and relief workers in aid agencies is possible. Regular rules of science conduct and reporting do not pertain to issues of extreme natural hazards. In this spirit we present some general concepts regarding satellite monitoring or assessment of glacier hazards, and we illustrate these concepts with analysis related to the hazard-prone Cordillera Blanca, near Huaraz, Perú.

Huaraz experienced glacier-related disasters claiming over a thousand lives each in 1702, 1725, and 1941 (Carey 2005). Nearby Yungay experienced such disasters in 1917, 1962, and 1970, and many other catastrophic or potentially deadly glacier-related mass flows have affected other areas near the Cordillera Blanca. We chose this area because it is demonstrably, by its history, hazard-prone; because much is published already in the technical literature and mass media about its glacier

hazards; and because in 2003, an error in scientific approach caused a public and scientific uproar, and this deficiency requires further appreciation, analysis, and understanding.

15.4 Satellite Vision: Capabilities and Limitations

We consider the capabilities of civilian multispectral remote sensing systems, emphasizing ASTER, with its least expensive (for the user), and most widely used of current satellite-derived data. We do not discuss other types of satellite remote sensing data, especially RADAR and microwave methods, which add greatly to capabilities discussed here. ASTER has 14 wavelength bands ranging from the visible and near infrared (three bands, 15 m resolution, one band in stereo) to the short-wave infrared (six bands, 30 m resolution) to the thermal infrared (five bands, 90 m resolution). Other satellite multispectral systems have more or less advantageous resolution, different numbers or spectral placement of bands, with or without stereo imaging capability or thermal infrared resources, differing data downlink rates, differing data pricing, and other tradeoffs. The specific capabilities of each satellite remote sensing system depend on the engineering attributes of the system, the ground-based data (support) systems, and imaging repeat rates. The overall attributes of ASTER combined with the intense imaging of glaciers for GLIMS (Global Land Ice Measurements from Space; www.glims.org) have made it popular.

15.4.1 *Palcacocha: What Is Visible from the Ground and Space?*

Huaraz, Perú, lies in a high intermontane valley between the Cordillera Blanca and Cordillera Negra of the Andean Cordillera. The population currently is around 100,000. On December 13, 1941, then home to ~60,000 people, Huaraz suffered ~10% population loss in just minutes due to an aluvi³ from the lake, Palcacocha. The lake, at an elevation of 4,566 m, 23 km upstream from Huaraz (elevation

³*Terminology:* Spanish *aluvión* (pl., *aluviones*), used in Andean geomorphology, refers to a flood or fast-moving debris flow – typically a flood moving abundant boulders and cobbles or low-viscosity mud with suspended gravel, boulders, and ice, descending rapidly through a glacial valley. *Aluvión* derives from the Latin *alluvi* and *alluvin-*, from *alluere*, meaning *to wash against*, and is related to the Latin *alluvies*, *alluviei*, *alluvio*, and *alluvionis*: sediment or flood plain deposited by a river; or lapping of waves, inundation, or flood. Variations on use of *aluvión* refer either to (1) any debris flow, hyperconcentrated flow, or flood emanating from mountains, or (2) mass flows and floods triggered by or involving glaciers (this is our use). In the Himalaya, a subset of *aluviones* is termed Glacial Lake Outburst Floods (GLOFs). Icelandic *jökulhlaup* refers to outburst floods or debris floods from glacier-stored waters, with or without involvement of volcanic activity (Thorarinnsson 1939). A *lahar* (Javanese) is any aqueous mass flow from a volcano; many, but not all lahars involve volcanic interactions with glaciers.

3,091 m), is immediately below the glaciated peaks Palcaraju (6,274 m), and Puncatanca (6,156 m).

The 1941 disaster apparently initiated when part of a glacier collapsed into the moraine-dammed lake. Presumably, a surge wave mobilized and burst through the high unstable moraine, releasing 95% of the contained lake volume plus moraine debris which moved down the Cojup canyon, ingested additional sedimentary debris down valley, and consumed another small lake. The aluvi3n, >15 million m³ of water and debris, coursed 23 km down the narrow Cojup canyon at an estimated average velocity of 25 m/s. At the canyon's mouth, the flow dispersed and sediment was deposited on a densely populated part of Huaraz (Fig. 15.1). This was the third comparably deadly glacier-induced disaster in the city's history. Another even more devastating mega-landslide wiped out tens of thousands of lives in nearby Yungay almost 30 years later. These and other disasters resulted in an aggressive study and engineering program, which continues to mitigate the hazards due to aluviones and other related mass movements throughout and beyond the Cordillera Blanca.

At Palcacocha, two chief engineering works have reduced the chances and magnitude of most types of potential future disasters. Although some of the mitigation projects at 35 controlled glacier lakes in Per3 (Carey 2005), including two projects at Palcacocha, are humble in relation to the unstable masses and potential consequences of a further disaster, one of the two projects at Palcacocha has thus far succeeded in maintaining a lower lake level, and a much lower lake volume. This reduces (1) the size of any surge wave, (2) the chances of an outburst flood, and (3) the volume and fluidity of any aluvi3n. The other chief engineering work at Palcacocha has produced a secondary emergency overflow route that would function if the first work failed to regulate water level. Even so, a small flood issued from the lake in March 2003 when an unstable moraine mass collapsed.

Huaraz city residents, its managers, and national glacier experts consider the continuing hazards seriously, but they correctly point to several decades when Palcacocha and other glacier lakes in Per3 have not issued a single deadly aluvi3n. The experts and authorities also point to high, unstable moraines, the risk of a large mountain collapse (like the 1970 collapse of part of Huascar3n that buried Yungay) that nobody can either forecast or ward off, and the many other unstable glaciers, glacier lakes, and moraines in the region. Some fundamentals of the system are not easily alterable. The relief of the moraines containing Palcacocha is just one of several unstable elements. The lake itself is situated near 4,600 m altitude, compared to the adjacent glaciated summits Palcaraju (6,274 m) and Pucaranca (6,156 m), and Huaraz near 3,091 m. With 1,700 m of local relief at the top end of the canyon and much unstable ice mass, and with steep rock slopes that can collapse in the style of Huascar3n Norte, there are numerous points of instability, especially as climate warms and thawing propagates to the highest elevations.

The capacity of this region's debris flows to travel such large distances at high speeds involves (1) highly unstable masses of ice that can initiate movement of (2) additional larger unstable masses of moraine debris and lake water, combined with (3) the high gravitational potential energy of the contributing masses, (4) a ratio of rock and water sufficient to maintain fluidity, and finally (5) topographic constriction

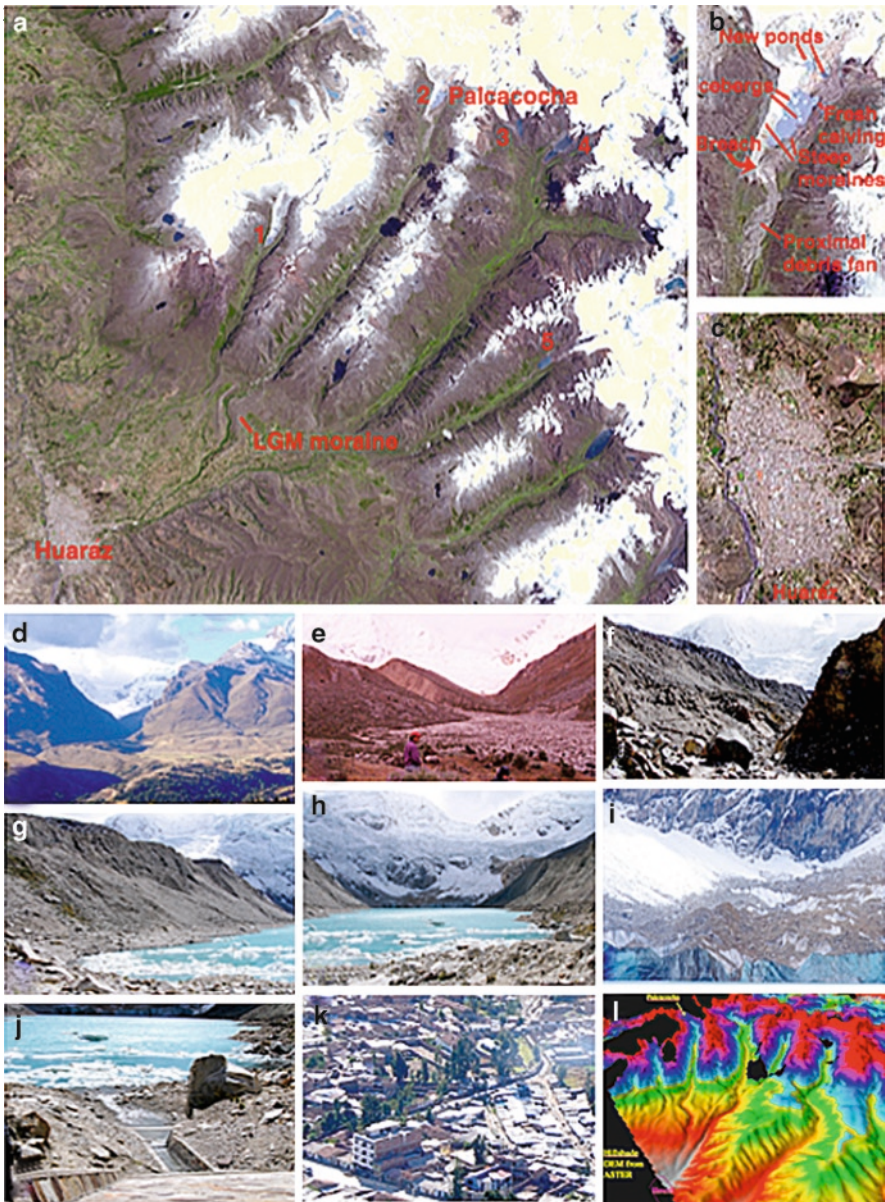


Fig. 15.1 Palcacocha and the Cojup Valley. (a) ASTER image acquired November 5, 2001 spanning the 27 km between the cirque headwall to the city of Huaraz. (b) Enlargement of area of Palcacocha showing some plainly visible features. (c) Enlargement showing Huaraz. (d–j) Features observed from the ground in 2004 by Kargel, including the late glacial moraine at the mouth of Cojup Valley (d), the breached moraine and proximal boulder facies of the 1941 outburst (e); within the breached moraine (f); Palcacocha and the unstable lateral moraine (g); Palcacocha and the cirque glacier (h); debris-covered, calving terminus of the glacier (i); and hazard mitigation works built to lower and regulate lake level (j). (k) A vulnerable part of the city center. (l) ASTER DEM showing funnel-like topography that has repeatedly acted to channel debris flows and floods onto Huaraz; black areas are null spots

of the Cojup canyon along the debris flow route. Multiple mass killings by aluviones in Huaraz also are due to Huaraz' placement at the divergence of and deposition from the constricted flow, thus enabling the debris flows to bury large areas of the city. This "perfect storm" has been repeated again and again—not just in the Cojup Valley, but also in several other nearby glaciated valleys. The fact that so many historic debris flows have reached as far as the main axial drainages of the intermontane valleys on both sides of Cordillera Blanca indicates that the tendency of the system is to shed excess rock and ice mass this way to achieve greater stability, even as tectonics and snowfall drives instability. It forms a deadly, geophysically idealized balance of processes where many people reside at the destructive confluence of topographic building-up and leveling-out forces.

The 1941 aluvión included an estimated $9.5 \pm 1.0 \times 10^6$ m³ of lake water (Ojeda 1974; Zapata et al. 2004) plus several million cubic meters of suspended sediment and bed load derived from the breached moraine. After the initial mobilization of this large mass, viscous dissipation of the debris flow was balanced by the conversion of potential energy into kinetic energy as the mass moved down valley. The commonality of such an event in the Cordillera Blanca points to a natural regulation of the system, and natural selection of events such that the valley gradients and the volumes of unstable material released at each event are just right, and combine to efficiently transport material out of the mountains. Smaller events no doubt happen but simply move material down valley some small distance; that mass is then picked up by later debris flows that can finally move all the mass out of the Cordillera Blanca into lower valleys.

Effective mitigation requires intercession in such manner that smaller masses are released at each event and/or that the fluidity of the masses is artificially reduced; both goals have been achieved by reduction in lake level and lake volume at Palcacocha and in several other dangerous lakes. Palcacocha's reduced lake size occurred partially by nature (the 1941 breach of the dam reduced lake volume by 95%; Carey 2005) and partially by engineering (which has limited the regrowth of the lake to about half the volume of its pre-1941 disaster size). The fact that a small flood was released during the 2003 event perhaps indicates a success of this strategy, but any floods, however inconsequential, point out the continuing instabilities in this and nearby glacial/lake/moraine systems; so far, the continuing events remain acceptable.

In August 1988, at Hualcán in the Cordillera Blanca, an ice-cored terminal moraine with a measured subsidence of 11 cm/month, and a freeboard of less than 1 m dammed an unnamed lake (Laguna "513"). It had already subsided by over 4 m. It was thought that if nothing were done to mitigate the situation, the moraine would fail within 2 months, probably destroying Carhuaz with the loss of many thousands of lives (Reynolds et al. 1998). In an emergency response, siphons were installed, and were used successfully to reduce the lake level by 5 m by June 1989. However, a significant ice avalanche occurred in 1991 that destroyed the terminal moraine and produced a flood downstream. As siphoning reduced the lake volume, the damage was contained locally, and no lives were lost. In 1993, to lower the lake another 20 m a 2-m diameter tunnel 155-m long through a bedrock was constructed (Reynolds 1998).

Reliance on flood control, or reductions in mass and fluidity of debris are not factors that would remain effective over geologic time scales; as mentioned, eventually, the mass must move out of the Cordillera Blanca, and large debris flows will facilitate that movement. However, mitigation may prove effective for periods of possibly several centuries, far exceeding the time in which global warming will have eliminated the glaciers. New regulating processes, presumably also involving massive debris flows, will subsequently take over because eroded mass ultimately await delivery to the intermontane valleys. Arguably, larger postglacial debris flows are eventually required to enable acoustic fluidization to compensate for reduced aqueous fluidity once the lakes disappear. However, the lower erosion rate of non-glacial fluvial systems is indicative of a reduced long-term recurrence frequency of major aluviones. As the general layout of the valley networks (Fig. 15.1) indicates, there are already many valleys that have entered this postglacial geomorphological regime, which encompasses other hazard processes. The most acute danger, although partly alleviated by recent engineering, remains the glacier-lake-moraine systems, but intense rain runoff and other processes also pose problems.

Human interest in mitigating glacier hazards perhaps spans a hundred years, which also defines the deglaciation time scale for remaining glacier masses (Silverio and Jaquet 2005). During this period, lakes may shrink in size artificially, but as additional unstable moraine mass is debuttressed, and high slopes and peaks begin to thaw, the variety of hazard mechanisms will shift. As Carey (2005) reviews, the number of glacier lakes in the Cordillera Blanca increased dramatically between two surveys in 1953 and 1997. Mitigation must adapt and keep pace with these changes, observed in recent decades by satellite, and generate future assessment scenarios through modeling with satellite observations of past behavior. Satellite imaging facilitates frequent reassessments of the complete mountain/glacier/lake system at Palcacocha and elsewhere in the Cordillera Blanca; ASTER data contribute to an improved understanding of each of the five above-listed elements of the “perfect storm” and are especially well suited to track the dynamic evolution of the potential initiating masses (hanging glaciers, unstable moraines, and lakes) where ASTER has a special niche.

The instability of the moraine and glacier containing Palcacocha is evident upon inspection of ASTER images, particularly along most of the moraine-impounded border of the lake and along the entire length of the meandering breach through the moraine that resulted from the 1941 event (Fig. 15.1e–h). The moraine’s instability was highlighted in a 2003 collapse and a small ensuing flood; yet on the other hand, such small collapses decrease the gravitational potential energy of unstable masses and reduce surface slopes to less than the angle of repose, thereby diminishing the overall hazard situation. The risk, of course, is that a future collapse may prove instantly catastrophic, or that a small collapse could occur along the lake outlet, and/or produce debris-laden icebergs that may congregate at the lake outlet. This may potentially jam or bury the artificial drainage outlet, raising the lake level over time, and again elevating the hazard level toward the pre-1941 event threat potential. Beyond these obvious possibilities, nobody can protect against some types of instantaneous high-magnitude events, caused for instance, by a large local

earthquake, which by itself would probably prove deadly. However, the most likely remaining threat of glaciological disaster at Palcacocha involves the lake's volume and area, and the threat posed by mixture of the lake water with moraine debris. The good news is that even if the outlet were blocked, it would take about a year for the lake volume to reach critical levels, such that any increasing hazard situation and disaster threat are likely to give a reliable advance warning and a renewed chance at mitigation.

A benefit of major aluviones, such as the 1941 Palcacocha event (though itself a first-order disaster) is that they reduce the lake level and the unstable mass; hence, there is a reduction of the hazard potential from possible subsequent events, barring of course, glacial readvance and reformation of the moraine. Despite rapid regrowth in Palcacocha's area as documented by satellite evidence (Figs. 15.2 and 15.3), the engineering mitigations have been effective in further limiting the lake level at Palcacocha (Klimes et al. 2005); similar works control many other lakes in the area. The retreat of the glacier discharging into Palcacocha has helped reduce the ice mass available for mass movements, but the recent intense calving and attendant increase in meltwater entering the lake has also caused elongation of the lake and an increase in its area, which tends to heighten the hazard related to lake volume; increased length of unstable moraines adjoining the lake also increases the chances of a large collapse of unstable, debuttressed moraines. Though the glacier volume has decreased, some debuttressing of the glacier also has occurred.

A major remaining problem relates to the effects from a possible large earthquake, which could cause a larger moraine mass to collapse than in 1941, and an aluvión potentially could make up in larger mass what it lacks in fluidity. Furthermore, increased temperatures associated with global warming might induce bed thaw and increased water flow at the bed, allowing glacier masses or ice-cemented moraines or previously unthawed massif material to collapse, which could initiate a self-amplifying event reminiscent of the 2002 Kolka/Karmadon event. However, instead of a small village at risk as was the case with the Kolka/Karmadon disaster, Huaraz is a small city with three orders of magnitude more lives at risk.

The evolution of Palcacocha was recorded on camera by trekkers and glaciologists (Fig. 15.4). Figure 15.4 includes a three time-series (1939, 2002, and July 3, 2004), with the photos taken from similar but not identical vantage points, and registered by distorting the earlier photos to match the newest. The lowering of the lake level caused by the 1941 event is evident, as is the recession of the calving front of the glacier at the far (north) end of the lake. Small icebergs are evident in the 2004 photo, as is a fresh calving face. The 2002 photo and some satellite photos show a moraine or debris-covered ice mass collapsed into the lake, but this material had melted away or further collapsed and submerged into the lake in 2004; evidently this mass was largely ice-based, which highlights the danger posed by remaining parts of the moraine and debris-covered glacier, as both can potentially increase the fluid mass of the lake and cause displacement waves within the lake. Substantial downwasting and backwasting of the glacier is evident, as some cliffs that were covered by glacier seracs in 1939 had become exposed by 2002 and further exposed by 2004. Some other parts of the glacier, especially at the highest

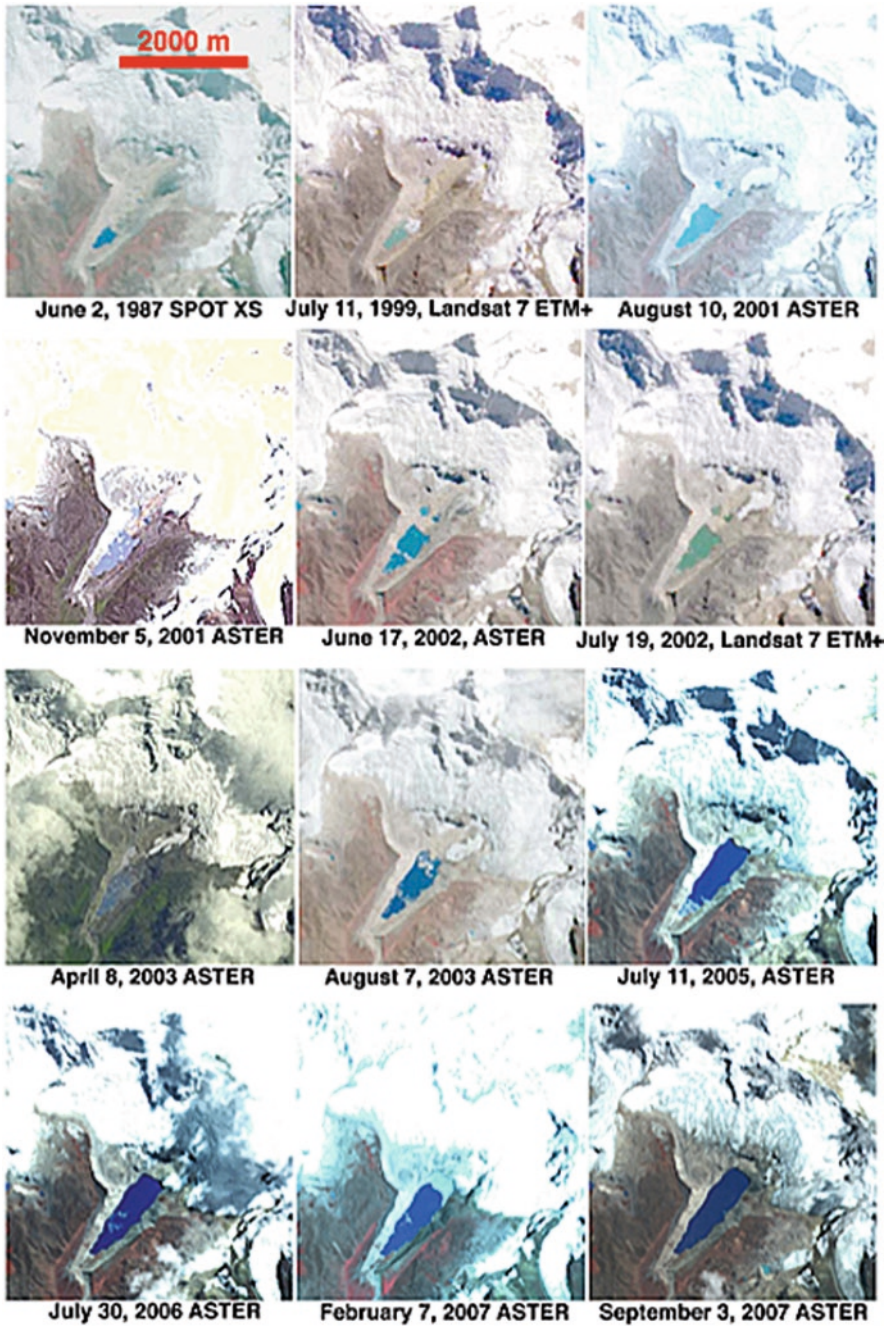


Fig. 15.2 ASTER, SPOT, and Landsat time-series covering Palcacocha and its glacier

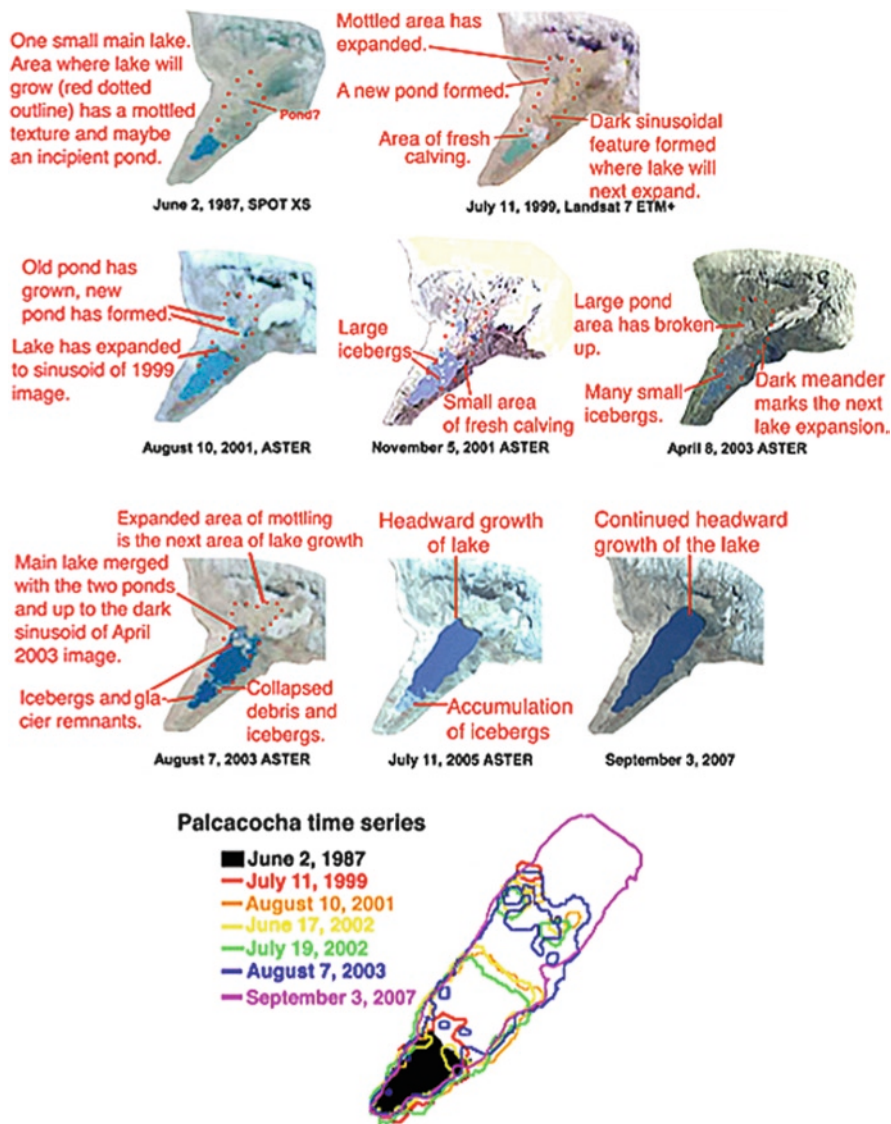


Fig. 15.3 Extracted portion of the images showing temporal evolution of Palcacocha, including a registered composite of the lake outlines in the last panel

elevations, appear almost unchanged from 1939 to 2002–2004, aside from differences in light snow cover.

The 1941 rupture is evident from the ground all along the Cojup valley, especially near the breach of the moraine (Fig. 15.1f), which deposited a proximal boulder facies (Fig. 15.1e) deposited by the outburst. Huaráz exists at the outlet of a geomorphological constriction, shaped like the nozzle of a funnel that is formed

Fig. 15.4 Time-series of ground photos showing changes in Palcacocha and its glacier; 1939 photo from Kinzl (1941) and 2002 photo from Kaser and Georges (2003) have been registered to a 2004 photo by Kargel



1939 (Kinzl 1941)



2002 (Georges and Kaser)



July 3, 2004 (Kargel)

by moraines deposited during the latest glacial maximum. The buried part of the city was rebuilt on top of the debris flow, as there exists a strong cultural motive for descendants (survivors) to inhabit exactly the same real estate as their ancestors, regardless of the evident danger to the descendants' lives.

The satellite image sequence in Figs. 15.2 and 15.3 documents recent past behavior, but it also allows projections into the future. In the most recent image in Fig. 15.3, the lake has grown almost up to a bedrock cliff, so Palcacocha is expected to stabilize after just a little more growth. Calving will slow down, as there is almost nothing left of the glacier below the cliff to calve into the lake. With the injection of heat from the lake into the calving margin, which soon will become longer possible, the glacier should reach a metastable point above the cliff, though it may exhibit some stick-slip behavior with oscillating thickening and sliding, thinning, and avalanching into the lake.

The southward-tapering shape of the lake causes some concern about hazards, as a surge wave produced by collapse of the last calving remnants of ice, or produced by a collapsing segment of the moraine is likely transmitted southward, where the narrowing and shoaling lake could cause wave focusing and a rise in the amplitude. The lake shore on the east and west sides have a series of prominences from small rock avalanches, which may cause wave refraction and complex destructive and constructive wave interferences. These influences of lake basin shape potentially can make any waves more destructive as they interact further with the moraine and drainage outlet channel. Continued control of the lake level, including monitoring of iceberg and sediment buildup at the south end of the lake, remains crucial to stabilize or reduce the overall glacier hazard. Iceberg buildups are evident in some of the images. As the glacier calves back toward the bedrock cliff, a series of icefalls that hitherto have discharged ice onto the lower part of the glacier will now experience direct discharge into the lake; this will produce a slightly different dynamic condition than heretofore has existed, and hence, difficult to say how that process will unfold. With less overall calving into the lake, the energy balance will shift, and this too will affect the dynamics. The last glacier remnants in the higher elevations remain a factor, as debuitressing and increased melting at the glacier bed and cirque backwall could make for an unstable hanging-glacier type of mechanics. In most respects, the diminished glacier, along with controlled water depth in the lake, make for a less dangerous system.

In sum, while some aspects of the hazard potential posed to Huaraz have worsened or simply changed, most are improved due to artificially reduced water volume in Palcacocha and other lakes, accomplished by a succession of agencies since the 1950s (Carey 2005). The hazards are not eliminated or marginalized; although we conclude, as Peru's scientific authorities have, that the overall hazards are greatly reduced.

The capacity of ASTER to map and monitor glacier lakes across large areas is represented by the image time-series and the classified image shown in Fig. 15.5. In the latter image, a simple supervised classification using data clusters isolated manually in ASTER band-1 intensity versus band 3/4 ratio was used to extract glacier lakes, ice/snow, vegetation, and bedrock/moraine units. The classification output appears fairly accurate based on comparison with field observations, such as in Fig. 15.1. For example, ice cliffs that are common at the calving edges of debris-covered glacier termini are evident in the mapped distribution of exposed ice. In other regions, notably at Alaska's sediment-laden glacier lakes, such simple classifiers fail and require

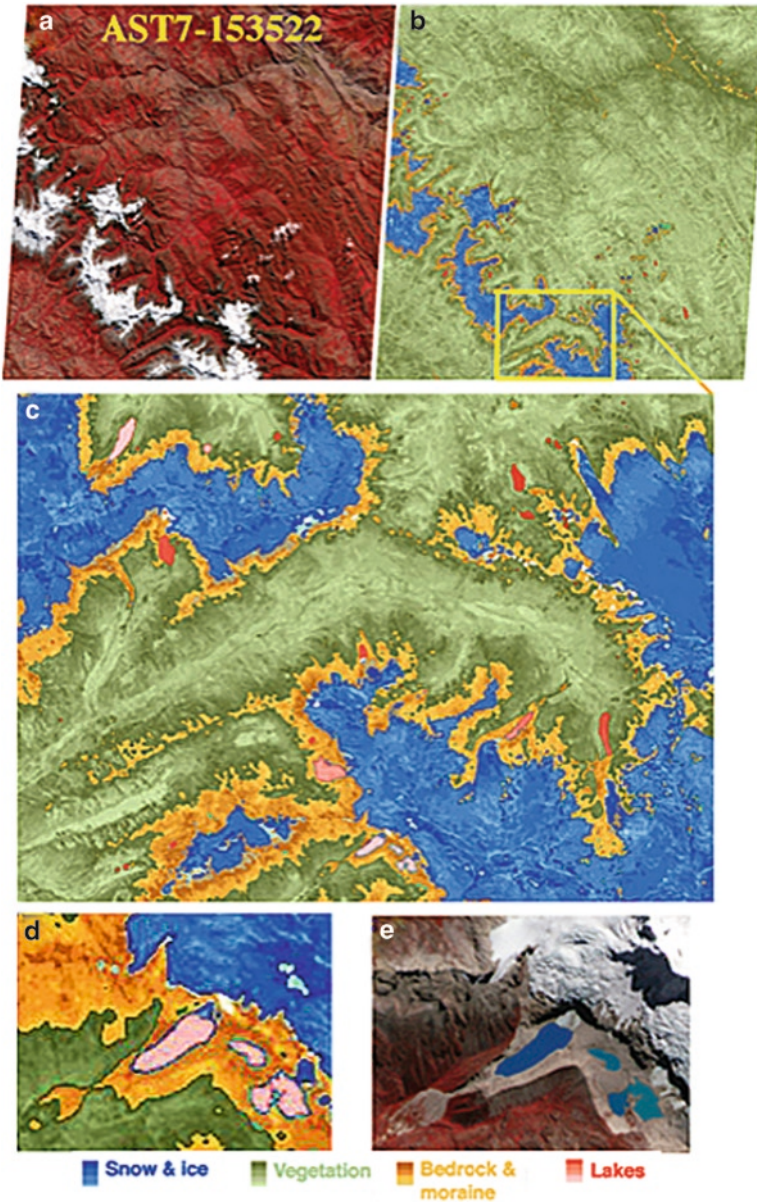


Fig. 15.5 Results of a simple supervised classification of ASTER image AST7-153522, acquired with calibrated ratio of band 3/band 1 radiance and band 3 intensity. (a) RGB band 3–2–1 false-color composite image, ~60 km across, used for the analysis. (b) Classified version of part (19 km across) of AST7-153522. (c, d) Enlarged portions of the classified image. (e) Enlarged portion of the RGB composite corresponding to area in (d), ~2,500 m across. Figure modified after Kargel et al. 2005

more sophisticated approaches. One successful approach tested at the University of Arizona is fuzzy C-means clustering of multispectral data assessed through neural networks.

15.4.2 *The 2003 Palcacocha Crisis*

The history of disasters in the Cordillera Blanca, the rapid evolution of glaciers and their lakes, and the intense media coverage of the hazard situation understandably put the entire vulnerable population on edge. It was in this historical context, with the March 2003 moraine collapse and small flood to underscore, that prompted NASA to issue a series of press releases in April 2003 (based on ASTER imaging November 5, 2001 and April 8, 2003). NASA pointed to a perceived anomalous crack in the glacier feeding into Palcacocha. That set of press releases (Steitz and Buis 2003) spurred intense media and public interest. Major news outlets, such as BBC and others, carried the story, including this slight rephrasing of NASA's news release in *New Scientist* (Bhattacharya 2003):

A glacial flood is threatening to sweep away a Peruvian city, satellite imagery has revealed. An ominous crack has been spotted in a large glacier high in the Peruvian Andes. The glacier feeds into Lake Palcacocha, which is at the head of a valley leading down to the city of Huaraz. NASA scientists are warning that if a large glacier chunk breaks off and falls into the lake, it will flood the Rio Santa Valley and devastate Huaraz in less than 15 minutes.

Scientists recognized immediately that NASA's interpretation of ASTER images was faulty⁴, that any major new dynamics in the system (if present) were incorrectly interpreted by NASA, and that there was no immediate new threat to Huaraz (Kaser and Georges 2003; Carey 2005). A limitation of the ASTER images that was not acknowledged in the press release was the inclusion of a heavily saturated image used in the time comparison and image interpretation. The image in question contains some shadows and rock outcrops that appear like cracks relative to the saturated snow and ice. Typically, the use of heavily saturated images diminishes or prohibits the accurate interpretation of the earth scenes in question. The concerned public did not recognize the technical deficiencies of the interpretation; rather they were cognizant of the city's history and the very real continuing dangers, and they,

⁴GLIMS was not consulted before NASA issued the press releases, and had no role in making or disseminating the interpretation that spurred the Palcacocha Crisis public relations disaster. Several GLIMS researchers (including some authors) played a back-scene role in quickly identifying weaknesses of NASA's interpretation. The first author also helped to calm the public, to deflect some further inaccurate media reporting, and to defuse the explosive mix of anxiety, anger, and mistrust that developed among Huaraz residents; he also helped potential litigants to see the likely unintended destructive effect of a class action on NASA's Earth Observing System (which was under severe budgetary and political stress) and on the interests of all the nations utilizing Earth remote sensing data.

like others around the world, held NASA in high esteem in any matters involving satellite/spacecraft observations. Now they were being told that an imminent catastrophe loomed. Much of Huaraz panicked. The public relations fiasco was exacerbated after the initial press release, when NASA issued two more releases, but further statements simply fanned the flames as the media repeated NASA's words and added to them.

This case prompts deeper questions: What can ASTER or other remote sensing systems see of a glacier's state and dynamics? What features are not detectable or reliably interpreted from space?

We have addressed the first question above, but the second question remains crucial. Figure 15.6 highlights some elements in a glacial valley near Palcacocha that heighten concerns about satellite-based assessments of possible hazards. Hazard mitigation works are plainly evident on the ground (e.g., the tunnel in Fig. 15.6e – invisible in the satellite image); an artificially lowered lake level is evident from the ground (Fig. 15.6f) and discerned by satellite (Fig. 15.6a), but the satellite image gives no indication of the cause of the lowering. This is similar to the situation at Palcacocha. The existence of hanging glaciers (Fig. 15.6b, c) is a legitimate concern, but hanging glaciers are not visible in the satellite images due to the nadir view and deep shadow. However, lake cover is readily evident and quantifiable from satellite images. Lake volume is not so readily assessed. Like satellite-derived images, ground-based vantages are not always optimal either. For example, from the ground, the incipient lake indicated by arrow G in Fig. 15.6a is barely visible without having a proper vantage (Fig. 15.6g). Thus, a combination of monitoring that includes frequent repeat satellite coverage, ground and aerial surveys, and ground-based instrumentation would seem best. This still would require people to do the field work and data analysis; this requires funding. Clearly, if the satellite exists already, comprehensive satellite-based surveys of whole mountain ranges are most cost effective, keeping the limitations strictly in mind.

15.5 Alpine Glacier Hazards Evolution in this Century of Global Warming

Each region's glaciers, being dynamic, produce a changing mosaic of hazards. As listed below, a glacier deemed nonhazardous for its entire observed history may become hazardous, a hazardous glacier may become relatively safe, or the type of hazards may change. In Alaska, for example, Wolfe (2009) documented (1) a 40% turnover of glaciers that dam ice-marginal lakes in a 30-year time period and (2) a general increase in elevation of new lakes over the same period. Glaciers can undergo long-term retreat or growth, or other conditions can change, and thus affect the spectrum and intensity threat of possible hazards. Many hazards-related features are observable with ASTER multispectral, stereo, and thermal imaging.



Fig. 15.6 Another area of glacier-related hazards in the Cordillera Blanca. (a) Portion of ASTER image 00307132003153923 acquired July 13, 2003. Photos obtained by Kargel in 2004. (b, c) Hanging glacier. (d) Glacier-fed lake (but no ice contact) with breached end moraine. (e) Hydropower and lake/flood control works. (f) Lake with artificially much-reduced lake level, and old breach of a tributary glacier valley/moraine at F*. (g) End moraine of a wasting glacier

For alpine/glacier/human systems in a regional steady state, the total regional hazards remain in a long-term steady state, as they are the sum of the individual hazards, which may oscillate individually but collectively have an average state. For conditions of long-term trending of alpine/glacier/human systems (including either the natural part of the system or that caused by civilization), hazards will have a trending due to climatically induced changes of glacier sizes, dynamical states, and configurations as well as trends in urbanization and land use.

15.5.1 List of Causes of Evolution of Glacier Hazards

Glaciers can undergo oscillatory growth and retreat due to decadal climate oscillations:

- Change of annual or peak temperatures (change in melting and balance of snow/rain)
- Change of annual and seasonal precipitation, precipitation type, clouds, or winds

Glaciers can oscillate due to intrinsic dynamics without climatic forcing:

- Surge/waste cycle
- Tidewater glacier or lake calving glacier advance/breakup cycle
- Hanging glacier growth and collapse cycle
- Seismic activity, rock avalanching/landsliding, and shear stress loading of glaciers
- Thermal insulation, stabilization, and lengthening of glaciers due to debris cover

Glaciers can evolve into a more or less hazardous regime, or the hazard type may evolve:

- Size and configurations of glaciers, moraines, and lakes may change
- Retreat of tributaries of valley glaciers can create ice-dammed lakes
- Accumulation of thin debris can increase melting; thick debris can decrease melting
- Surface debris accumulation can plug drainage conduits and cause lake formation
- Large rock avalanches/landslides can produce unstable moraines or may dam lakes
- Glacier retreat can remove support from moraines and glaciers (debuitressing)
- Frozen glacier beds can thaw as climate change elapses
- Ice-cement of moraines can melt and weaken the moraine
- Normal erosion of moraine crests can produce incisions that lower lake level
- Glacier oscillation or advance can rebuild moraines and initiate new lakes
- Surge-type glaciers may stop surging, or nonsurging glaciers may begin surging
- Changes in geothermal/volcanic environment can affect basal melting
- Glaciers and their hazards can disappear; moraines can vegetate and stabilize

Dangerous events can instantly reduce future hazards of moraines and moraine-dammed lakes:

- Outburst flood can breach the dam and reduce lake level or drain the lake entirely
- Collapse of moraine can render it into a more stable configuration

Adequate hazard assessment and reliable warning systems can reduce the overall loss potential:

- Development of cost-effective and timely mitigation strategies is possible
- Evacuations during crises can prevent fatalities while enabling long-term productivity
- Reliable information flow can reduce panic and permit economic productivity

Artificial stabilization of moraine-dammed lakes, moraines, and hanging glaciers can reduce hazards:

- Siphoning of water or construction of drainage conduits can reduce lake levels
- Careful dynamiting of hanging glaciers or unstable moraines can reduce hazards
- Debris flow/flood diversion corridors or retention basins may offer protection

Changes in land use can reduce or increase glacier hazards:

- Expansion of settlements and infrastructure into hazard pathways
- Resettlement of populations, redesign or relocation of infrastructure
- Redevelopment of hazard-prone urban areas as parks, urban open space, or agriculture
- Establishment of secure emergency shelters can reduce the impact of disasters

A fundamental problem in alpine systems is active tectonism combined with glaciation; both act together to render an unstable and sometimes dangerous landscape. For example, the average uplift and denudation rates in Cordillera Blanca, Perú have been several millimeters per year for several million years while deglaciating areas of Alaska show uplift of 30 mm/year. More recently, the rate for Cordillera Blanca, Perú may have slowed toward 1 mm/year (Montario 2001; Garver et al. 2003; Farber and Hancock 2005), but even this rate produces huge amounts of rock debris. As indicated by the geomorphology of the higher parts of the Cordillera Blanca (e.g., U-shaped valleys), glaciation in recent millennia has remained the most effective process driving erosion across an area $>20 \text{ km} \times 90 \text{ km}$, or $>1,800 \text{ km}^2$, although this period shows signs of ending across most of the mountain range due to recent glacial retreat.

A system approaching steady state on the century to millennial time scale (typical periods of interest to human history) with an average 1 mm/year denudation rate corresponds to $1.8 \times 10^6 \text{ m}^3/\text{year}$ of erosional material, of which a large fraction consists of coarse clastics deposited primarily in moraines. A typical aluvión capable of reaching as far as Huaraz and Yungay occurs about five times per century (though not necessarily overriding a city) and typically carries $10\text{--}30 \times 10^6 \text{ m}^3$ of debris, plus comparable amounts of water. These numbers suggest that a large fraction, perhaps most, of the erosional debris produced in Cordillera Blanca is deposited near the glaciers, and then is regularly removed by aluviones into the intermontane basins and lower valleys. Most of the local people live in these areas.

No academic understanding of aluviones or hazard mitigation, short of total relocation of the populations (not a cultural possibility), could drastically reduce the long-term hazard due to some types of aluviones. Glacier recession in the Cordillera Blanca has reduced glacier area by about 5–10% per decade in the latter third of the twentieth century (Georges 2005; Racoviteanu and Arnaud 2005; Silverio and Jaquet 2005); presumably the continued recession of glaciers is causing some alleviation of risk due to certain types of aluviones. Understanding of aluviones and adequate hazard assessment and advance warning can contribute to a reduction, but not an elimination of risks. This limitation is understood by the public and the authorities, who also weigh other issues alongside the glacier hazards problem, such as hydroelectric power generation, economic productivity of the people within the hazard-prone regions, cultural behaviors, and so on.

While these remain important issues, we do not address them in further depth here; rather, we show an example of how satellite studies can aid in the detection and assessment of glacier hazards in Perú and elsewhere. Current satellite remote sensing is able to detect, quantify, and monitor hazardous systems and human land use in hazard zones. However, how to deal with the huge amounts and diverse types of data in any robust and integrated space- and field-based approach to hazards monitoring and assessment remains a challenge. Acknowledging that effective monitoring of glacier hazards will require even more data than is now available, the challenge is only resolved by increasing the efficiency and reliability of data analysis. We do not make this step here, but we do chart a possible future course toward this goal. Automation of data analysis, however, will not reduce the need for experienced people to make difficult decisions; it is to the contrary. The improved availability and analysis of data will enhance the accuracy and timeliness of decision support, which will provide people with the increased capacity to make effective choices.

15.6 A Future Technological Approach to Hazards Detection and Predictive Modeling

Satellite-based remote sensing can contribute to the monitoring of large areas containing hazardous glaciers and glacier lakes (Georges 2004, 2005; Kargel et al. 2005; Quincey et al. 2005; Racoviteanu and Arnaud 2005; Silverio and Jaquet 2005; Wolfe 2009). Repeat surveys using satellite-based terrain classification and elevation mapping are useful to detect and monitor some likely hazard situations, and to develop input for models of likely sources, volumes, gravitational potential energy, and routes of outburst floods and debris flows. The economic impacts and their probabilities are assessable through a collective analysis with Geographic Information Systems (GIS), infrastructure locations, land use, and population distribution. Furthermore, complementing these techniques and tools with data on seismicity, volcanic hazards, and historic locations of past glacier dynamical events creates another potential. We could develop advanced methodologies to detect and

periodically reassess glacier hazards with merged satellite and ground-based data, which provide the inputs to generate mitigation strategies and hazard/disaster warning systems. Finally, these tools combined with models of global warming and regional climate change, glacier numerical modeling, and urban/land use change are potentially useful to forecast future glacier hazards, and thus provide input to land use planning and zoning in hazard-prone areas.

To support glacier hazard analysts, new satellite remote sensing systems are needed in addition to more complete information from the ground. An idealized, technically-feasible advanced satellite remote sensing system would combine attributes of ASTER, MODIS (MODerate resolution Imaging Spectroradiometer), and GLAS (Geoscience Laser Altimeter System). In addition, we could extend on-demand multispectral coverage with higher-resolution (perhaps 5 m) and higher temporal frequency acquisitions to obtain denser grids of laser altimetry tied directly to the multispectral imaging (thus aiding geospatial registration). Onboard autonomous systems for cloud detection/screening, and observation scheduling would immensely help as well. A finer resolution than ASTER's 15 m would help resolve additional trackable features; this would facilitate deriving improved glacier flow-fields, and determining more precise glacier outline changes through multitemporal image analysis. A higher resolution is not always important; however, a system that could make autonomous or user-assisted decisions regarding requisite resolution requirements is an improvement. The typical annual ASTER image acquisition frequency is sufficient for most circumstances, but an autonomously commanded or user-assisted option to acquire images at higher temporal frequency (daily or weekly) would facilitate studying various transient phenomena. For instance, it would help monitor the progression of glacier surges, lake outburst floods, and ice shelf breakups, and better enable prompt follow-up after disasters. The ground-based part of the system would include a new software-driven approach to assess hazards and predict future trends in glacier hazards. Autonomous cloud detection, scene cropping, ordering of images, and resolution selection could ensure that we obtain much higher quality data, and analyze them promptly without increasing the total data load on the overall system. The specification of enhanced observation capabilities is a tradeoff between the technical features we desire and the cost of developing that remote sensing capability (Table 15.4), but relative to the orbital hardware costs, the needed software improvements are deemed inexpensive.

The combination of instrument capabilities suggested above, on the same platform, is not currently supported by the most recent NASA Decadal Study; unless a new decadal study is authorized, the best we can hope for is active collaboration among disparate instrument and spacecraft teams, and furthermore, hope that the spacecraft carrying the complementary instruments can overlap in their operational lifetimes. However, there are no plans for a sustained multispectral Earth monitoring program. That may fall within the interest of rising global powers, such as China, to implement. A near-term partial solution may rely on the planned series of missions recently announced by NASA to satisfy part of the goals of the Decadal Study,

Table 15.4 Range of satellite imaging resolutions needed for each feature type

| Observable | Region (mm) | Resolution (m) | Other capability/requirements |
|----------------------------------|----------------|----------------|----------------------------------|
| Surface temperature | 4–5 | 30–100 | Active cooling needed |
| <i>Water ice absorptions</i> | | | |
| Visible continuum slope | 0.4–0.7 | | No cooling system needed |
| NIR, multiband | 0.7–1.1 | | No cooling system needed |
| SWIR, multiband | 1.1–2.5 | | Active cooling if 1 > 1.5 mm |
| Transient snow line | 0.4–1.1 | 15–30 | A few broad bands needed |
| Mixed ice, debris, vegetation | 0.4–1.1 or 2.5 | 1–30 | More narrower bands better |
| Texture-based classifiers | 0.4–0.7 | 0.5–30 | High dynamic range needed |
| DEM-based classifiers | 0.4–0.7 | 5–15 | Stereo imaging |
| Reflectance-based classifiers | 0.4–1.1 or 2.5 | 5–15 | 4 bands OK; more are better |
| Elevation change | 0.4–0.7 | 5–15 | Stereo imaging, 10 m vertical |
| Improved geodetic control | 0.4–0.7 | 50–100 | In-image LASER altimetry |
| <i>Trackable features</i> | | | |
| Moraines and landslides | 0.4–0.7 | 5–30 | Panchromatic or broad bands |
| Ogives | 0.4–0.7 | 5–30 | |
| Seracs, large crevasses | 0.4–0.7 | 5–15 | |
| Small crevasses | 0.4–0.7 | 1–5 | |
| Large moulins | 0.4–0.7 | 1–5 | |
| Large boulders | 0.4–0.7 | 1–2 | |
| Perennial ponds | 0.4–0.7 | 5–30 | |
| Exposed ice cliffs | 0.4–0.7 | 5–15 | |

supplemented with additional NASA Small Explorer Earth missions to provide further capabilities and aid continuity (Baker and Worden 2008).

Table 15.4 gives a range of imaging resolutions needed for each feature type. Most observing needs require multiband data in the VNIR out as far as ASTER SWIR band 4. Shortwave infrared covered by ASTER SWIR bands 5–9 are desired but not needed for many glacier classification and tracking purposes. The more numerous and narrower the bands, the better the overall deemed capability, but as few as four broad bands (e.g., ASTER's 1–4) could satisfy most objectives, without requiring a cooling system. An ASTER VNIR-like image resolution of 15 m can accomplish much of what is needed, but for smaller glaciers and more precise work on larger ones, an optional resolution ≤ 5 m is ideal. Additionally stereo imaging with ASTER and SPOT (Satellite Pour l'Observation de la Terre) has proven its worth; and ideally, LASER altimetry and thermal imaging warrants integration with advanced multispectral imaging.

To help assess glacier hazards in an automated fashion, we envisage a set of fuzzy logic-based modules, i.e., “fuzzy expert systems” which also includes human input. The continued improvements in Earth observation instruments and increased remote sensing data volumes call for a higher level of on-board automation to optimally monitor glaciers’ states and dynamics. Ultimately, we need a system to autonomously assess the potential exhibited by glaciers to cause disasters, and which can evaluate the effectiveness of different strategies as mitigating factors. Such systems should (1) include software packages that enable fully automated and comprehensive identification, characterization, and quantification of feature information within an operational region (e.g., GIS or Automated Global Feature Analyzer – AGFA; Fink et al. 2005, 2008) and (2) integrate existing information with in-transit-acquired spatial and temporal sensor data to automatically perform intelligent assessment of glaciers hazards including identification of glaciers with the highest potential to generate adverse social and economic impacts. Humans should remain a part of this “fuzzy system,” but rapid, automated data analysis will provide the first and fastest information needed by people on the ground, and even before that, by automated observation sequencers on the spacecraft.

The fuzzy logic framework are considered ideal to implement such systems because fuzzy experts store knowledge in a linguistic form easily understood by computing machines and humans alike, thus providing a common ground for artificial intelligence programmers and glaciologists to work together for effective implementation. Fuzzy experts have been recently proposed as intelligent systems for autonomous, science-driven planetary reconnaissance (Furfaro et al. 2006, 2008a), including systems specifically designed for autonomous assessment of the potential habitability on Mars (Furfaro et al. 2008a) and Titan (Furfaro et al. 2008b), and for geologic terrain assessments.

For distant locations as Titan, the demand for such systems is caused by light travel time exceeding the time available for instrument retargeting during fast-paced observing sequences. In the case of Earth hazards detection/monitoring, the need for autonomy and rapidity is dictated by the fast pace of dangerous dynamic phenomena compared to the interval between satellite passes and the time needed by humans to make observations and decisions on terabytes of data. For example, in an Internet posting January 11, 2008, describing a recent glacier outburst flood in Pakistan, an eyewitness, Noor Muhammad’s first clue of something amiss was a sudden change in color of a glacier’s outlet stream: “The Shimshal River had suddenly changed its winter color. It was greenish-blue the day before but we saw it acquiring dark muddy colors and, of course, we all were afraid. Then we heard that a glacier in Passu had burst and flooded the village.” The discoloration was later established to result from sediment-laden water discharged by the glacier (<http://pamirtimes.wordpress.com/2008/01/11/preparedness-beyond-prayers/>). It is unclear whether the color change was a leading indicator presaging imminent flooding, or if flooding had already occurred. In any case, relationships of the suspended sediment concentration of glacier meltwater with discharge rates, nonsteady glacier motions, and water color are well established (e.g., Willis et al. 1996; Haritashya et al. 2006); water color comprises a key, easily quantified, remotely sensed observation closely related to glacier dynamics.

Ideally, when a satellite detects a marked anomaly unrelated to expected seasonal variation, for instance a change in lake color out of bounds of normal seasonal changes, or a change in lake size, then we could downlink acquired and stored data at lower compression than otherwise might occur for standard operations; we could also modify observing sequences within seconds, thus allowing a satellite instrument to order and reprioritize further observations during the same orbital pass (or as soon as possible). Such a capability requires effective autonomous anomaly detection and interpretation, and ranking of the anomaly threat significance, besides incorporating a sophisticated scheduler. For hazards assessment, even more than event anomaly characterization, we call to extend the proposed methodology to autonomous and intelligent assessment of conditions resulting in glacier hazards in sufficient time to weigh and issue a warning, if necessary.

15.6.1 Fuzzy Logic for the Autonomous Assessment of Glacier Hazards

The design of expert systems for autonomous assessment of potential glacier hazards is a knowledge engineering problem, formulated as follows: given the domain-containing input data, find a suitable solution among all possible candidates occurring in the solution space. Adapting the general knowledge of the engineering problem to a glacier observation scenario, “input data” refers to information collected via Earth observing sensors, and via ground-based observations, as well as existing information (e.g., historic observations and dynamic trends of glaciers). An interpreted solution is required to allow an actionable assessment of a glacier’s hazard regime. The automatic and remote bases of glacier hazards assessment necessitates that the knowledge provided by glaciologists are recorded and used on a computer. From an operational perspective, we define knowledge as condensed information consisting of rules or methods, which enable us to perform plausible reasoning to obtain new facts and hypotheses. To autonomously evaluate and infer new facts from data, knowledge is necessarily coupled with inference schemes (i.e., the process of matching data and knowledge to infer something not previously known). Knowledge is usually acquired and integrated also via inference.

The effective implementation of autonomous systems for glacier-induced hazards assessment is possible by selecting appropriate Artificial Intelligence (AI) algorithms to perform reasoning with data. The overall architecture relies on the ability of the system to fulfill the following: (1) ingest observations about the current state of the glacier, its geomorphology and observed regional processes, including human settlement and vulnerable infrastructure; (2) identify relevant changes in the above; and (3) provide an intelligent assessment of the hazard caused by the observed glacier and its environment by autonomously reasoning over the appropriate acquired knowledge. Whatever AI scheme is chosen, a crucial issue is how to adequately represent knowledge and inference. Key design factors to analyze involve knowledge representation, inference, learning, generalization, explanation,

and adaptation capabilities. Various frameworks are available to design and implement an intelligent system for hazard assessment. Three classical examples include the following: (a) symbolic AI, (b) fuzzy logic, and (c) artificial neural network schemes. While the method of choice depends on the designer and the problem at hand, a specific architecture is preferable. Understanding and contrasting such algorithms may help to make a case for the selected architecture.

Neural Networks (NNs) are connectionist systems (i.e., knowledge is distributed among various nodes). NNs learn by example (training), by doing or by analogy providing a framework where the knowledge is unstructured. They can provide good generalization and they easily adapt to new input data. They are so named because of a parallelism between computer NNs and biological NNs (e.g., human brains). Symbolic AI and fuzzy experts have been conceived to represent and implement structured knowledge (i.e., knowledge is explicitly represented and organized by human experts). The inference process also depends on the selected architecture. Fuzzy experts and NNs implement approximate reasoning, while Symbolic AI systems perform exact inference. The latter algorithms do not deal well with missing, corrupted, or inexact data.

A critical aspect to address when selecting the appropriate framework for autonomous assessment of glacier-induced hazards is the representation of uncertain knowledge and uncertain data. Fuzzy methods are inherently capable of dealing with uncertainties and are perhaps the premier choice. Probabilistic methods are a good choice where the input probabilities are either expressed quantitatively or qualitatively. Such techniques rely on the axioms of probability, and are based on estimating the posterior probability of accepting any inferred conclusion as true or false. Generally, probabilistic methods do not do well in scenarios where ambiguity and contradictory or partial information is available. The latter is due to Bayes' theorem failure in situations where multiple rules reach different conclusions. On the contrary, fuzzy systems are designed to work with multiple ambiguous or contradictory rules; the fuzzy architecture naturally performs a tradeoff at the inference level (i.e., multiple rules are activated simultaneously and make decisions in tandem). As such, these systems can mimic human thinking and decision-making, or even group reasoning.

Fuzzy-based expert systems currently may represent the best next step in the development of autonomous, real-time, on-board assessment of glacier-induced hazards. Embedded in their system architecture, structured knowledge is directly implemented by intuitive, easy-to-devise, fuzzy rules, which comprise the knowledge base as defined by glaciologists, promoting interaction between Earth scientists and AI experts. Importantly, the basis for fuzzy logic is also a basis of human communication. While observing a glacier's current state, fuzzy expert systems have the ability to make autonomous decisions, and provide solid explanations allowing scientists to evaluate whether the system is reasoning correctly. Glaciologists and other Earth scientists are required to provide their knowledge to implement in the fuzzy architecture. They are expected to contribute to the expert design and testing phase while working to find common ground with computer and AI engineers. Humans also are potentially integrated into the framework of the

fuzzy architecture as one of the expert systems (the others being silicon-based). Whereas there are no fundamental limits to the complexity and novelty of such automated systems, early-phase concept designs are intended to achieve fairly simple types of feature recognition with interpretive characterization and process assessment followed by decision-making regarding observation prioritization and ordering; a heavy computational requirement arises from the need to process large volumes of diverse data.

15.6.2 Fuzzy Expert Systems for Glacier-Induced Hazards Assessment

The design and implementation of fuzzy expert systems capable of assessing the potential for glacier hazards is nontrivial. Even the automated answering of a question such as, “Is the probability of a moraine landslide into a lake increasing or decreasing?” is complex. However, our conceptual design is intended to consider how multiple, potential hazard processes may interact; for example, a wasting glacier may reduce the chance of ice calving into a lake but increase the chance that a debuttressed moraine falls into the lake, and changing downstream development may affect the hazard due to each of those processes and many others. Development of such a fuzzy system requires a team with multidisciplinary skills ranging from Earth science to civil engineering to artificial intelligence. Within the proposed fuzzy framework, a variety of design options are available; the expert architectures require selection depending on the observational data acquired by the orbiting platforms (and the ground observational data). Ideally, one would like to have a single expert system capable of ingesting all possible available data, and perform reasoning with the largest available amount of information. Such a system does not currently exist, but the technology to develop it is available. At the time of this writing, our team has begun to look at how to design knowledge bases that demonstrate the proof-of-concept establishing fuzzy expert systems for autonomous reasoning with satellite data.

Figure 15.7a shows the general architecture of an intelligent fuzzy-based expert system embedded into the orbiting platform software system, for real-time, autonomous assessment of glacier-induced hazard potential. The system is conceived as follows: the orbiting satellite acquires data from satellite-borne sensors. The acquired data are preprocessed and categorized using image processing algorithms and GIS-like software to extract geophysical indicators that (1) indicate evidence of glacier dynamics and (2) are directly related to the potential of the glacier to generate hazards. Other GIS data, such as prior locations of lakes, glaciers, and moraines are preloaded. Indicators of changing conditions are then fed to the fuzzy expert system that processes the available information and assesses the potential for glacier-induced hazards or changes in hazards. The fuzzy expert then interacts with a lower-level control system that reprioritizes and reschedules observations (if required), or

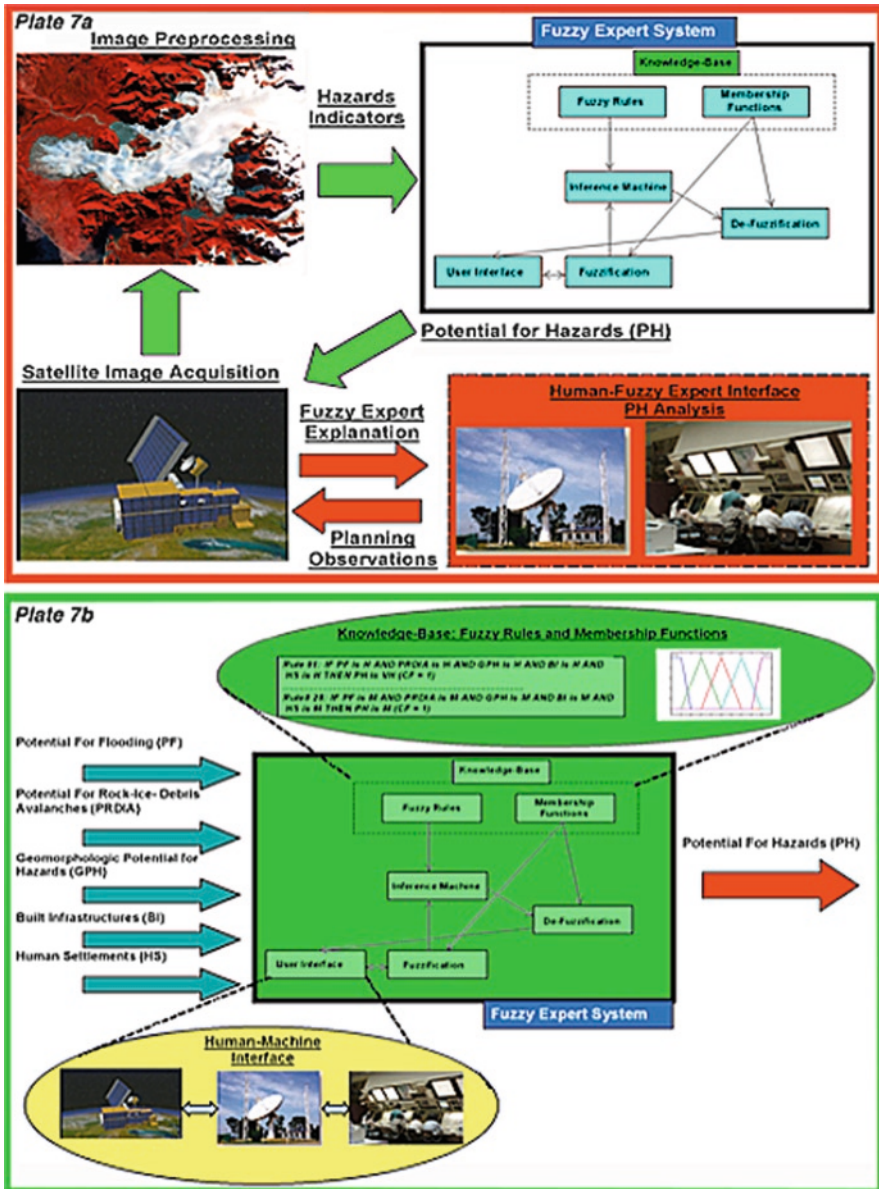


Fig. 15.7 Top: conceptual design of an integrated human/artificial intelligence fuzzy expert system for assessing satellite imagery for the potential for glacier hazards and for further data acquisitions, partially by autonomous artificial decision-making. Bottom: additional design elements of the human/artificial assessment of glacier hazards, including potentials from three hazardous classes of processes and inputs from the distribution of vulnerable populations and infrastructure

provides an alarm to the ground if the hazard potential is high. The observation scheduler potentially could enable new observation acquisitions, or downlink previous full-resolution observations.

Figure 15.7a shows the elements forming the backbone of the fuzzy expert system. The core of the fuzzy system (i.e., the knowledge base) is comprised of fuzzy rules and membership functions. Such rules are defined as linguistic statements, which embed the human expertise, methods, and skills derived from theoretical and field studies. For our design and simulation, we employ Mamdani-type IF-THEN rules (Mamdani 1977). The fuzzy inference engine defines the process of formulating the mapping of the given data. Such an inference engine uses predefined rules, (fuzzy) data, and observations to infer new facts. Finally, a user interface (explanation module) is required to explain why and how the solution was reached. Humans use this module to monitor system operations.

In providing a first level of interpretation, the expert fuzzy system goes far beyond simple feature detection and change detection. It could, for instance, automatically attribute one particular observed change to a seasonal change in snow cover, which the system considers inconsequential, whereas another change is possibly interpreted as growth of a new lake significantly affecting the overall hazard environment. At an appropriate level of concern, the system might issue a warning, or order new observation acquisitions quickly.

Scientists on the ground are required to assess the information and interpretations provided by the expert system, and may provide further explanation or intercede in some way with the data scheduler. If the system provides an explanation consistent with the scientists' conclusions, and if deemed urgent, an immediate warning message is issued to other scientists involved at another level of the global system; alerts are also passed to other satellite systems, which may potentially assist. If the situation so merits, public officials are then notified. No public alert is yet made until the scientists and public officials have agreed on an appropriate course of action. Even though fuzzy expert systems are designed and tested to reason as humans, false conclusions are always possible; humans must vet automated warnings at each level. Success of such a system will require not only a competent and tested fuzzy expert system, but also a well-integrated system of human experts.

As an example of the design of fuzzy expert systems to assess glacier hazards, we focus on a simple, proof-of-concept system that operates with higher-level, data-derived input parameters. Figure 15.7b shows the architecture of a fuzzy expert system that operates with five inputs and one output. Table 15.5 shows the parameters under consideration. The system ingests five parameters described qualitatively by three fuzzy attributes (i.e., Low, L; Medium, M; and High, H) (see Fig. 15.8a, top panel). The input parameters are high-level indicators connected to the potential exhibited by the observed region as a glacier-induced dynamic site, which is probably hazardous to humans and their infrastructure. For example, Potential for Flooding (PF) and Potential for Rock-Debris-Ice Avalanches (PRDIA) indicate the assessed potential of the region to experience flooding and rock/ice and debris avalanches, respectively. Clearly, those are high-level parameters derivable from observational data.

Table 15.5 Fuzzy input–output parameters

| Fuzzy input–output parameters | Qualitative attribute | Range |
|---------------------------------------------------------|----------------------------------------|-------|
| Potential for flooding (PF, input) | High, Medium, Low | [0,1] |
| Potential for rock-ice-debris avalanches (PRDIA, input) | High, Medium, Low | [0,1] |
| Geomorphological potential for hazards (GPH, input) | High, Medium, Low | [0,1] |
| Built infrastructures (BI, input) | High, Medium, Low | [0,1] |
| Human settlements (HS, input) | High, Medium, Low | [0,1] |
| Potential for hazards (PH, output) | Very Low, Low, Medium, High, Very High | [0,1] |

Satellite images may reveal evidence of an increase in a glacial lake’s water level, which may increase flooding probability. The PF may increase if time sequence observations show that the observed glacier is retreating, causing an increase of available meltwater, or if the waterline is rising/expanding. The presence of hanging glaciers might cause ice avalanches, which in turn generate water waves, so the presence of hanging glaciers affects the hazard significance attributed to a growing lake. Glacier retreat may cause debuttressing, which increases the probability of the observed region to experience rock/ice avalanches, such that a lake growing at the same time glaciers are retreating, while hanging glaciers persist, would create increasingly hazardous conditions. In this example, we assume that PF and PRDIA are indicators one can derive by considering remote sensing-based geophysical data.

Geomorphological Potential for Hazards (GPH) is another parameter potentially observable by satellite images. GPH is connected to the geomorphology and topography of the terrain below a glacier lake. Human Settlements (HS) is a parameter that indicates the presence of humans (cities, villages, etc.) below the glaciers. Built Infrastructures (BI) indicates the presence of economically valuable human-built structures below the observed glacier (highways, railways, bridges, pipelines, etc.). The output parameter is generically indicated as Potential for Hazards (PH), and is inferred by the fuzzy expert while reasoning over the input data. Five attributes qualitatively describe PH (i.e., Very Low, VL; Low, L; Medium, M; High, H; and Very High, VH) (Fig. 15.8a, bottom panel).

PH is inferred by the fuzzy expert system using an appropriate knowledge base properly defined to implement human knowledge and expertise within the fuzzy framework. As previously mentioned, we describe the knowledge base as a set of IF–THEN rules (Mamdani-type). Each rule has the following structure:

$$\text{IF } X_1 \text{ is } A_1 \text{ AND } X_2 \text{ is } A_2 \text{ AND } \dots X_j \text{ is } A_j \text{ THEN } Y \text{ is } B \quad (0 \leq \text{CF} \leq 1)$$

Here, X_1, \dots, X_j represent the input parameters ($j = 1, 2, 3, 4, 5$) and Y is the output parameter (i.e., PH). A_1, \dots, A_j are qualitative attributes of the input parameters (L, M, H) while B is the qualitative attribute of the output (VL, L, M, H, VH). CF is

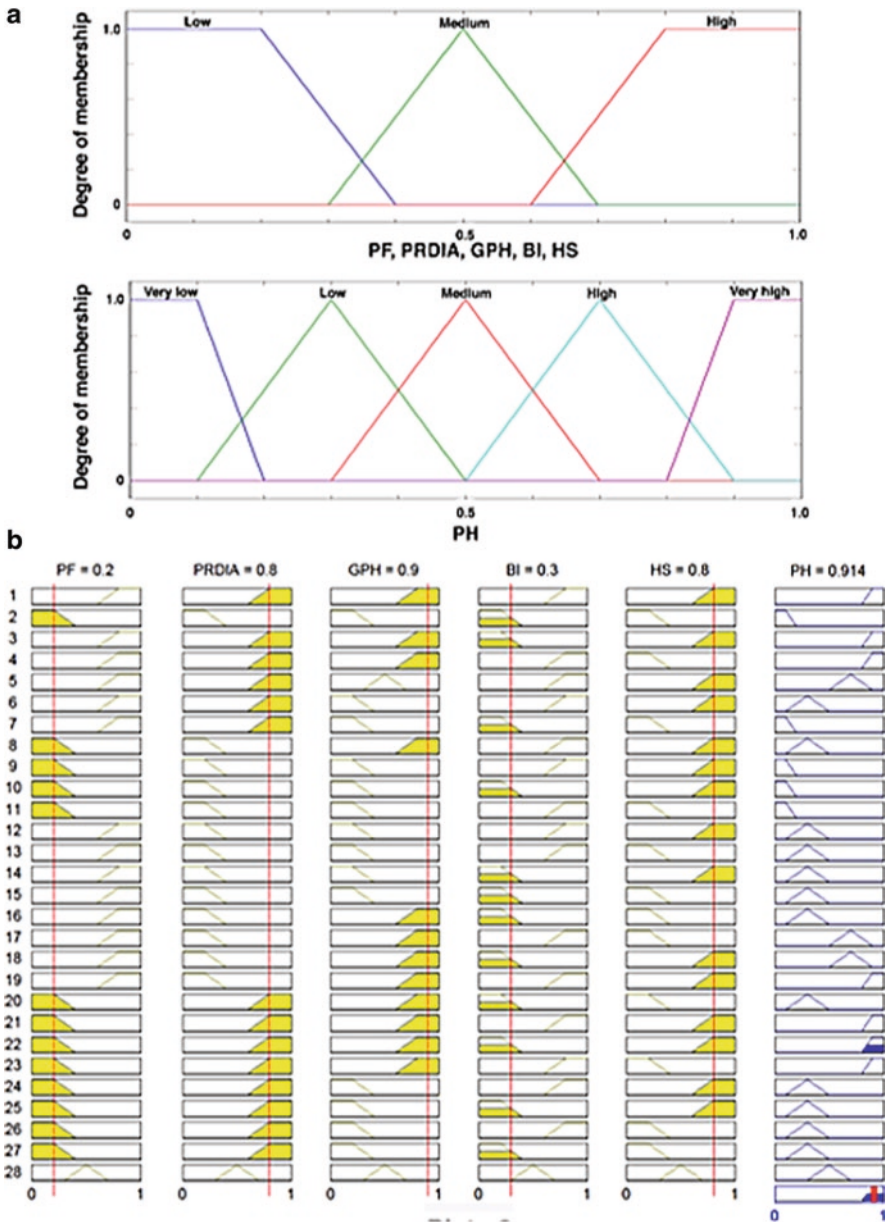


Fig. 15.8 (a) Membership functions for the input-out parameters. (b) Inference process performed by the designed fuzzy system

the confidence factor of the considered rule (i.e., a parameter ranging between 0 and 1, which indicates the importance of the rule relative to the knowledge base: 1 = highest importance, 0 = lowest importance). For our case, the knowledge base is

Table 15.6 Rules that define the knowledge base

| Rule | PF | PRDIA | GPH | BI | HS | PH | Conn | CF |
|------|----|-------|-----|----|----|----|------|-----|
| 1 | H | H | H | H | H | VH | AND | 1 |
| 2 | L | L | L | L | L | VL | AND | 1 |
| 3 | H | H | H | L | H | VH | AND | 1 |
| 4 | H | H | H | H | L | VH | AND | 0.8 |
| 5 | H | H | M | H | H | H | AND | 1 |
| 6 | H | H | L | H | H | L | AND | 1 |
| 7 | H | H | L | L | L | VL | AND | 1 |
| 8 | L | L | H | H | H | L | AND | 1 |
| 9 | L | L | L | H | H | VL | AND | 1 |
| 10 | L | L | L | L | H | VL | AND | 1 |
| 11 | L | L | L | H | L | VL | AND | 0.8 |
| 12 | H | L | L | H | H | L | AND | 0.8 |
| 13 | H | L | L | H | L | L | AND | 0.8 |
| 14 | H | L | L | L | H | L | AND | 1 |
| 15 | H | L | L | L | L | L | AND | 0.8 |
| 16 | H | L | H | L | L | L | AND | 0.8 |
| 17 | H | L | H | H | L | H | AND | 0.7 |
| 18 | H | L | H | L | H | H | AND | 0.8 |
| 19 | H | L | H | H | H | VH | AND | 0.8 |
| 20 | L | H | H | L | L | L | AND | 1 |
| 21 | L | H | H | H | H | VH | AND | 1 |
| 22 | L | H | H | L | H | VH | AND | 1 |
| 23 | L | H | H | H | L | VH | AND | 0.8 |
| 24 | L | H | L | H | H | L | AND | 1 |
| 25 | L | H | L | L | H | L | AND | 1 |
| 26 | L | H | L | H | L | L | AND | 0.8 |
| 27 | L | H | L | L | L | L | AND | 1 |
| 28 | M | M | M | M | M | M | AND | 1 |

comprised of 28 rules as illustrated in Table 15.6. The table is an attempt to concisely report the knowledge structure. For example rule 1 is read as follows:

IF PF is H AND PRDIA is H AND GPH is H AND BI is H AND
HS is H THEN PH is VH (confidence factor = 1)

The rule states that if all input parameters are high, then the potential for hazards is very high (with the highest importance). The knowledge base is built using our expertise and intuition in relation to hazards induced by glacier dynamics. Rules 1 and 2 are fairly obvious. Rule 6 indicates that even if the potential for flooding and avalanches is high, and valuable infrastructures and settlements are present, the geomorphology of the region is such that neither infrastructure nor humans are threatened. Confidence factors are set lower for rules containing high PF and BI, and low PRDIA and HS because infrastructure flooding has less impact than rock avalanches and presence of human settlements. For vital infrastructure, such as the

Trans-Alaska Pipeline, a different choice is possible. Importantly, the rules are not exhaustive or rigid and are refinable for a more complex and comprehensive knowledge base. The knowledge base in this example is designed for the reader to understand how the rules are implemented.

The fuzzy expert system was implemented using the MATLAB Fuzzy Logic Toolbox (Mathwork, Inc.) for rapid prototyping and simulation. The fuzzy expert acquires the input parameters, fuzzifies them (i.e., makes them readable by fuzzy expert systems) according to the membership functions defined in Fig. 15.8a (top), and processes them according to the IF–THEN rules comprised in the knowledge base. The 28 rules are fired concurrently to infer the potential for hazards. For any available rule, if the antecedent is composed of several parts connected by logical operators (e.g., AND), the fuzzy logical operator is applied to combine the antecedent and provide the support for the rule. Conventional MIN and MAX constructs (Ross 2004) are used for AND/OR operators, respectively. The MIN implication method (Ross 2004) is employed to shape the output membership function. All rules are finally aggregated via summation. The output is defuzzified by computing the centroid of the area under the output membership function.

Three scenarios are considered in the following to simulate the designed fuzzy expert. The goal is to show consistency with our reasoning (i.e., the fuzzy expert reaches the same conclusion as human experts do). Table 15.7 shows the quantitative inputs to the fuzzy expert for PH assessment, as well as the results of the simulation (PH fuzzy expert assessed value, bottom line of Table 15.4). Region 1 represents low potential for flooding, a high potential for rock-ice-debris avalanches, contains a geomorphological feature, which is highly prone to hazards, and has a low level of infrastructure and high level of human settlements. The region is clearly expected to have a very high potential for glacier-induced hazards, since avalanches may reach the human settlements. Figure 15.8b shows the inference process performed by the fuzzy system. The system outputs a PH value of 0.91, which indicates a very high potential for hazards. Region 2 indicates a high potential for flooding, low potential for rock-ice-debris avalanches, a geomorphological configuration that does not threaten possible settlements and/or major infrastructure, a very high level of economically valuable infrastructures, and very low human settlements. The fuzzy system outputs a PH value equal to 0.3, which

Table 15.7 Quantitative inputs to the fuzzy expert for PH assessment, and simulation results

| | Region 1 | Region 2 | Region 3 |
|--------------------------------------|----------|----------|----------|
| <i>Fuzzy expert input parameters</i> | | | |
| PF | 0.2 | 0.8 | 0.1 |
| PRDIA | 0.8 | 0.2 | 0.1 |
| GPH | 0.9 | 0.3 | 0.7 |
| BI | 0.3 | 0.9 | 0.8 |
| HS | 0.8 | 0.1 | 0.9 |
| <i>Fuzzy expert output parameter</i> | | | |
| PH | 0.91 | 0.3 | 0.2 |

indicates a low potential for hazards. Indeed, despite the high potential for flooding, an immediate threat to the infrastructure is not expected because the terrain is not conducive to either the flood's reach or damage. Region 3 displays a very low potential for flooding, very low potential for rock-ice-debris avalanches, a geomorphological configuration that poses high possible threats to settlements and/or built infrastructure, a high level of economically valuable infrastructure, and very high level for human settlements. The fuzzy expert outputs a PH value of 0.2, which indicates a low potential for hazards. Indeed, despite the numerous human settlements and economically valuable infrastructures, and despite a region shaped to transport water and debris down to such settlements/infrastructures, the very low potential for flooding or avalanches causes the system to conclude that no immediate threat is posed. This is consistent with human expertise and reasoning.

15.7 Toward a System and Protocol for Glacier Hazards Research and Communications

Figure 15.9 highlights the advanced stage of deglaciation in the area near Palcacocha with many moraine-dammed lakes, most of which show a characteristic downslope breach with an adjacent coarse debris fan. This indicates that the lake has already breached its dam, and dispensed a flood or debris flow at least once in the past. The cirque and small remnant glacier near Palcacocha and in adjoining valleys, shown in Fig. 15.6a, b, shows abundant evidence of snow avalanches but very little evidence of crevasse formation and glacial flow; yet the three ground-based photos in Fig. 15.4 show clear evidence of glacial deformation. The small hanging glacier visible in Fig. 15.9c in the background, and also in Fig. 15.6c, presumably has a cycle of building up and shedding ice at some interval of time.

Note that the hanging glacier is readily discerned as a possible hazard in the ground-based field photos (Figs. 15.6c and 15.9c), but it is not evident in the nadir satellite view of Fig. 15.6a. Also note that some aspects of glacier dynamics are evident at 15 m resolution of ASTER data, but others are not, and require 5 m/pixel or better to ensure resolution. And since some of the most dangerous ice masses occur on the steepest slopes, which commonly are shadowed or saturated white in ASTER images, imaging systems with the dynamic range and ability to distinguish shadows and sun-illuminated mountain faces is imperative.

In sum, the perspectives gained by nadir-viewing satellites (best for measuring many features and to discern lakes), oblique-viewing satellites and low-altitude oblique airphotos, and ground-based perspectives are all complementary. Improvements in satellite image resolution, multispectral characteristics, stereoscopic characteristics, dynamic range, and frequency of imaging, as well as efficiency of image analysis and image rendering onto relief models are all needed. Advantages of a multiperspective system may allow terrain and geomorphometric analyses far beyond what traditional stereo-viewing systems or current Google Earth-type products offer. Perspective is as important as image resolution, image multispectral capability, and

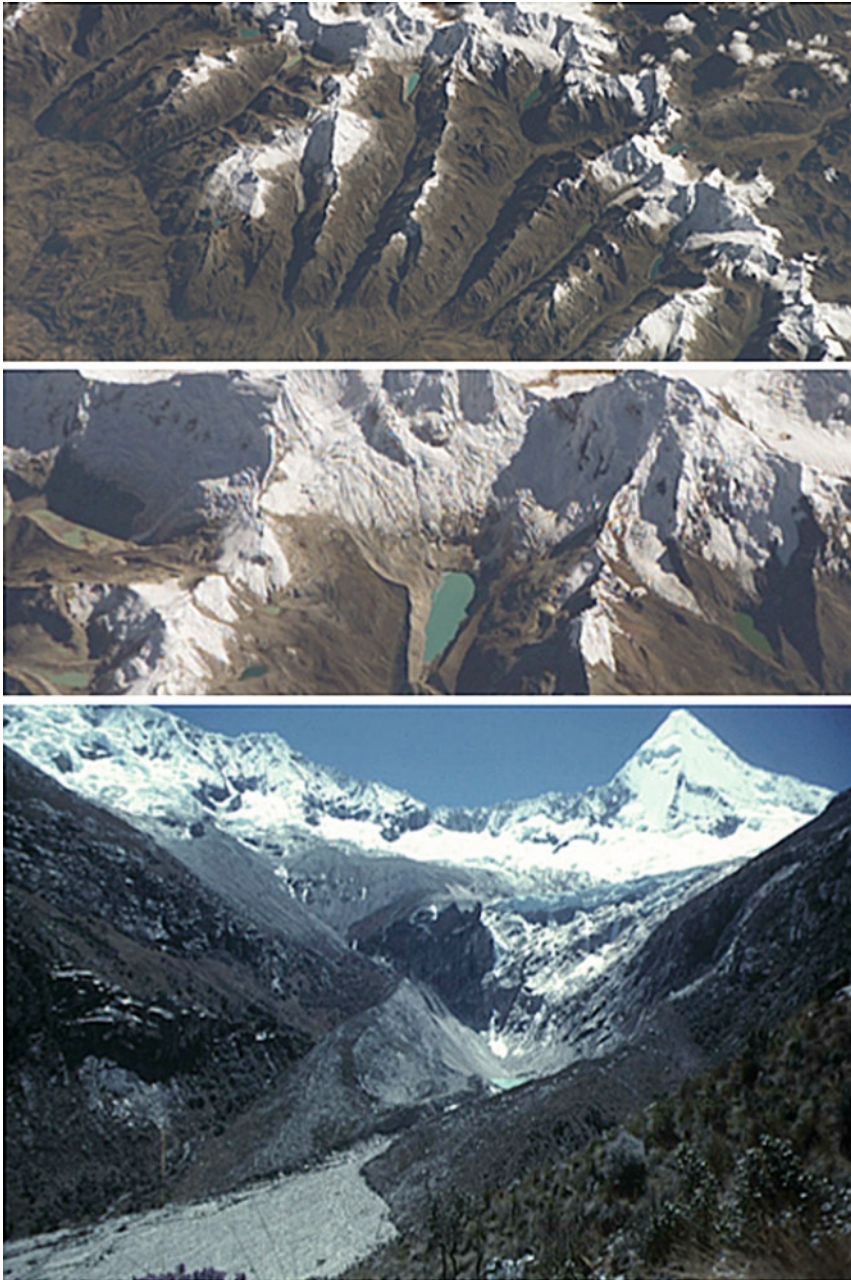


Fig. 15.9 High-resolution oblique photography can catch details and dynamics that nadir low-resolution data cannot. (a, b) Oblique astronaut photography from the International Space Station (image ISS014_ISS014-E-5469, taken with $3,060 \times 2,036$ pixel CCD array, RGBG, October 11, 2006) of Cordillera Blanca, featuring Palcacocha (above center, panel a, and enlarged

so on. Each observing system (including eyes and hand-held cameras mounted on boots on the ground) has its merits, but the real advantages are realized when these data are merged. An ideal future hazards assessment system would integrate various satellite, air, and ground views and other measurements taken from various perspectives. They should include ASTER- and SPOT-like satellite systems, and permanent field-mounted imaging systems and in situ data acquisition systems (such as flood gauges and weather monitors) in known dangerous situations. The components of such systems currently exist and are used, but exploitation of the full benefits will come with an electronically linked multitier system and some degree of autonomous assessment of data and autonomous early warning. Data cannot flood experts so that they are unable to assess the data soon enough to avert floods of water. The system must include image projection onto relief models and nadir map-projection views. It should also incorporate autonomous terrain and surface material characterization, so that if icebergs fill a lake, or sediment-rich water displaces clear water, or a moraine collapses, these events are instantly known, assessed autonomously for their hazard likelihood, and any needed warnings are issued to experts qualified and ready to assess the data.

Humans, obviously, must remain integral components of the system, who use autonomous data analysis and automated warnings as a tool, not as an end product. Ultimately, humans and our infrastructures are at risk, and humans must make the intelligent assessments of what to do in particular circumstances. Technology provides tools, not decisions, even if autonomous systems go far beyond anomaly detection and begin to venture into robust terrain and dynamics characterization. We need this artificial intelligence to help us manage the great volumes of data that are needed for a fully adequate hazards assessment, monitoring, and warning system. The human element, of course, is the most difficult to deal with because of the many complex impacts of any decision to act or not in a given situation.

Government funding agencies and those operating Earth remote sensing satellites are responsible to find the political and moral strength, the right approach, and financial resources to deal with glacier hazards. People who observe and understand hazardous conditions should not remain silent given perceived and imminent threats to lives or critical infrastructure; neither is it acceptable to raise undue anxiety in local populations. The issues and special responsibilities are similar to those experienced in the volcanological hazards community.

As people's lives and livelihoods are at risk, we need a prudent balance between professional, scientific, ethical, and communication skills. There often exist intercultural and language differences between those potentially in danger on the

Fig. 15.9 (continued) in panel **b**). (c) John Reynolds captured this photograph of Artesancocha (slightly below and right of center), its breached moraine dam, and the proximal boulder facies due to outburst floods, in Cordillera Blanca in 1988. This is the small breached moraine-dammed lake shown in Fig. 15.6, panel **(d)** and located in panel **(a)**. Artesancocha produced two aluviones in 1951 into the next lake in the chain, Laguna Parón. The small hanging glacier that was visible in 2004 on a summit (Fig. 15.6c) is also visible in this photo in the background

ground, scientists in the country of concern, government officials and civic authorities, and foreign scientists. In some hazardous glacierized areas, there exist special economic pressures, where economically helpful changes (such as permits to build a resort or permits to raise lake levels and hydroelectric generating potential) are possibly in opposition to public safety. Add to that the interests of funding agencies, research grant recipients, hazard mitigation engineering contractors, the public media, and the research and reporting protocols established within the international science community, and we encounter a multiplicity of potentially explosive set of motivations, cultural ethos, professional ethics, and linguistic barriers, not usually dealt with concurrently in basic or applied science. People experiencing conflicts and their narratives juxtaposed with fears of an error, economic impacts and their very lives, and desperation over nowhere to go may lead to premature pronouncements, refusals to get involved, outright obfuscation, or panicked responses to new information. The combination may prove deadly, costly, or both. It also may prove toxic for scientific relations with the public, and the public's trust in their civic officials. Our obligation requires that we do our best, discuss mistakes when they happen, and adjust our approach as needed.

Due in part to the controversy and impacts surrounding the Palcacocha science/media debacle, a working group on "Glacier and Permafrost Hazards in Mountains" (GAPHAZ, <http://www.geo.uio.no/remotesensing/gaphaz/about.html>) was established and endorsed by the Commission on Cryospheric Sciences (CCS) and the International Permafrost Association (IPA) (Kääb et al. 2005, 2006). Among other goals, GAPHAZ aims to compile general recommendations to the glaciology community to deal with scientific assessments, public communications, and programmatic guidance pertaining to glacier- and permafrost-related hazards in mountains. Until GAPHAZ was established, there was no formal collaborative scientific initiative under the auspices of a leading international scientific body focusing on such hazards. Its preliminary recommendations are as follows:

- (1) Climate change induces disturbances in glacier and permafrost equilibria, and is shifting hazard zones and changing the specific types of hazards in each area beyond historical knowledge. In many regions, human settlements, activities, and major infrastructure (e.g., pipelines and highways) are encroaching on hazardous zones, thus increasing overall risk. As a result, historical data alone are insufficient for hazard assessments, and require blending with new observation and modeling approaches, which must find support from government agencies and major industries concerned with glacier hazards.
- (2) Glacier- and permafrost-related disasters often include a combination of processes and chain reactions. Hazard assessments, therefore, require an integrative approach, which considers such variety and interaction of processes and indirect results.
- (3) Due to the accelerated change in high-mountain environments, routine and regular hazard assessments combined with appropriate monitoring are a must.
- (4) Performing an integrative risk assessment through the interdisciplinary cooperation of experts, and the application of modern observation and modeling techniques designed for such an integrative approach is essential. Risk evaluation requires hazard and vulnerability assessment.

- (5) Modern space technologies enable a near universal estimation of hazards potential independent of political and geographical restrictions. This fundamental “democratization” process related to high-mountain (and other) hazards involves a number of new opportunities, dangers and responsibilities for the public, for the authorities in charge, and for the scientific and engineering experts. The risk to vulnerable populations stems not only from the glaciers and permafrost but also from unsound risk pronouncements. Therefore, to reduce unintended consequences and possible legal liabilities related to potential missteps, scientifically initiated public discussion of cryospheric hazards generally should follow discussions among experts (especially local ones) and vetted with public officials responsible for public safety.
- (6) Researchers should remain responsive to the public’s legitimate need for information. Attempts to secure adequate vetting of and agreement on observations, models, and assessments should not lead to a perception that the research community is in some way “holding back” important information. Ultimately, however, governments and local research authorities are responsible to disseminate critical/urgent information to the public; the local authorities should remain the first conduit linking the hazard experts and the public, and following their communications, the experts should engage the public media as warranted. The experts have a special responsibility to weigh in clearly and accurately, and not exaggerate the concerns, or succumb to undue political pressure one way or another.
- (7) The general mass media is a vital part of the communications link between the experts and other authorities and the general public. The media has special responsibilities, but the experts and other authorities must proactively ensure that any hazards-related stories are told truthfully and objectively. The media should remain fully accountable for important disparities between what they tell the public and what the experts/authorities tell the media.
- (8) The transfer and dissemination of expert hazard assessments to the authorities and to the public, and thus the efficiency of assessments, is to a large degree dependent on the socioeconomic and cultural context and the hazard perception of the endangered population. Communication of results from glacier and permafrost hazard assessments should consider each set of unique circumstances. No single, rigid protocol alone is sufficient. An evaluation of the real natural risk and likely responses of the local populations should weigh strongly on each decision to make public disclosures of risk or warnings of impending disaster.

References

- Ames A (1998) A documentation of glacier tongue variations and lake development in the Cordillera Blanca, Perú. *Z Gletsch Glazialgeol* 34:1–36
- Arendt AA, Echelmeyer KA, Harrison WD, Lingle CS, Valentine VB (2002) Rapid wastage of Alaska glaciers and their contribution to rising sea level. *Science* 297:382–385
- Baker DN, Worden SP (2008) The large benefits of small-satellite missions. *EOS Trans Am Geophys Union* 89(33):301–302

- Berthier E, Arnaud Y, Kumar R, Ahmad S, Wagnon, P, Chevallier P (2007) Remote sensing estimates of glacier mass balances in the Himachal Pradesh (Western Himalaya, India). *Remote Sens Environ* 108:327–338
- Bhattacharya S (2003) Glacier crack places Peruvian city in peril. *New Sci.* <http://www.newscientist.com/news/news.jsp?id=ns99993634>
- Bishop MP, Shroder JF Jr, Hickman BL (1999) SPOT panchromatic imagery and neural networks for information extraction in a complex mountain environment. *Geocarto Int* 14(2):19–28
- Bishop MP, Kargel J, Kieffer H, MacKinnon DJ, Raup BH, Shroder JF (2000) Remote sensing science and technology for studying glacier processes in high Asia. *Ann Glaciol* 31:164–170
- Bishop MP, Shroder JF Jr, Colby JD (2003) Remote sensing and geomorphometry for studying relief production in high mountains. *Geomorphology* 55:345–361
- Bishop MP, Barry RG, Bush ABG, Copeland L, Dwyer JL, Fountain AG, Haeberli W, Hall DK, Kääh A, Kargel JS, Molnia BF, Olsenholler JA, Paul F, Raup BH, Shroder JF, Trabant DC, Wessels R (2004) Global Land Ice Measurements from Space (GLIMS): remote sensing and GIS investigations of the Earth's cryosphere. *Geocarto Int* 19(2):57–85
- Carey M (2005) Living and dying with glaciers: peoples' historical vulnerability to avalanches and outburst floods in Peru. *Global Planet Change* 47:122–134
- Chikita K, Jha J, Yamada T (1999) Hydrodynamics of a supraglacial lake and its effect on the basin expansion: Tsho Rolpa, Rolwaling Valley, Nepal Himalaya. *Arctic Antarctic Alpine Res* 31:58–70
- DeAngelis H, Skvarca P (2003) Glacier surge after ice shelf collapse. *Science* 299:1560–1562
- Evans SG, Clague JJ (1988) Catastrophic rock avalanches in glacial environments. In: Bonnard C (ed) *Landslides – Proceedings of the 5th International Symposium on Landslides, Lausanne, Switzerland*, pp 1153–1158
- Evans SG, Clague JJ (1994) Recent climatic change and catastrophic geomorphic processes in mountain environments. *Geomorphology* 10(1–4):107–128
- Farber DL, Hancock G (2005) Uplift and topography formation in the Cordillera Blanca, Central Peruvian Andes. *Eur Geosci Union Geophys Res Abstr* 7:10374
- Fink W, Datta A, Baker V (2005) AGFA: (Airborne) automated geologic field analyzer. *Geochim Cosmochim Acta* 69(10S):A535
- Fink W, Datta A, Dohm JM, Tarbell MA, Jobling FM, Furfaro R, Kargel JS, Schulze-Makuch D, Baker V (2008) Automated global feature analyzer (AGFA) – a driver for tier-scalable reconnaissance. In: *IEEE Aerospace Conference Proceedings*, paper no. 1273, Big Sky, Montana
- Furfaro R, Dohm JM, Fink W (2006) Fuzzy logic expert system for tier-scalable planetary reconnaissance. In: *Ninth International Conference on Space Operations, AIAA, Rome, Italy, June 19–23, 2006*
- Furfaro R, Dohm JM, Fink W, Kargel JS, Schulze-Makuch D, Fairén AG, Ferré PT, Palmero-Rodriguez A, Baker VR, Hare TM, Tarbell M, Miyamoto HH, Komatsu G (2008a) The search for life beyond earth through fuzzy expert systems. *Planet Space Sci* 56:448–472
- Furfaro R, Lunine J, Kargel JS, Fink W (2008b) Intelligent systems for the autonomous exploration of titan and enceladus. In: *Space Exploration Technology Conference, Proceedings of the SPIE, Orlando, FL, March 2008*
- Garver JI, Schiffman CR, Perry SE (2003) Rapid tectonic exhumation of the Cordillera Blanca. In: *Annual Meeting, Geological Society of America, Seattle, November 2–5, 2003, Abstract no. 169-9*
- Georges C (2004) 20th-century glacier fluctuations in the Tropical Cordillera Blanca, Peru. *Arctic Antarctic Alpine Res* 36(1):100–107
- Georges C (2005) Recent glacier fluctuations in the tropical Cordillera Blanca and aspects of the climate forcing. Ph.D. Dissertation, Leopold-Franzens-Universität
- Haritashya UK, Singh P, Kumar N, Gupta RP (2006) Suspended sediment from the Gangotri Glacier: Quantification, variability and associations with discharge and air temperature. *J Hydrol* 321:116–130
- Hastenrath S, Ames A (1995) Recession of Yanamarey Glacier in Cordillera Blanca, Perú, during the 20th century. *J Glaciol* 41:191–196

- Hubbard B., Heald A, Reynolds JM, Quincey D, Richardson SD, Zapata M, Santillan N, Hambrey MJ (2005) Impact of a rock avalanche on a moraine-dammed proglacial lake: Laguna Safuna Alta, Cordillera Blanca, Peru. *Earth Surf Process Landf* 30:1251–1264
- Huggel C, Delgado H (2000) Glacier monitoring at Popocatepétl volcano, México: glacier shrinkage and possible causes. In: Hegg C, Vonder Muhl D (eds) *Beiträge zur Geomorphologie. Proceedings der Fachtagung der Schweizerischen Geomorphologischen Gesellschaft, Bramois, WSL Birmensdorf*, pp 97–106
- Huggel C, Kääb A, Haerberli W, Teysseire P, Paul F (2002) Satellite and aerial imagery for analysing high mountain lake hazards. *Can Geotech J* 39(2):316–330
- Huggel C, Kääb A, Haerberli W (2003) Regional-scale models of debris flows triggered by lake outbursts: the June 25, 2001 debris flow at Täsch (Switzerland) as a test study. In: Rickenmann D, Chen C (eds) *Debris-flow hazards mitigation: mechanics, prediction, and assessment*. Millpress, Rotterdam, pp 1151–1162
- Huggel C, Kääb A, Salzmann N (2004) GIS-based modeling of glacial hazards and their interactions using Landsat TM and Ikonos imagery. *Norwegian J Geogr* 58:61–73
- Juen I, Kaser G, Georges C (2007) Modelling observed and future runoff from a glacierized tropical catchment (Cordillera Blanca, Perú). *Global Planet Change* 59:37–48
- Kääb A (2005) Combination of SRTM3 and repeat ASTER data for deriving alpine glacier flow velocities in the Bhutan Himalaya. *Remote Sens Environ* 94:463–474
- Kääb A, The GAPHAZ Working Group (2006) Towards a set of general recommendations for assessing glacier and permafrost hazards in mountains. *Geophys Res Abstr* 8:04608, SRef-ID: 1607-7962/gra/EGU06-A-04608
- Kääb A, Wessels R, Haerberli W, Huggel C, Kargel J, Khalsa SJS (2003) Rapid ASTER imaging facilitates timely assessment of glacier hazards and disasters. *EOS Trans Am Geophys Union* 84(13):117–121
- Kääb A, Reynolds JM, Haerberli W (2005) Glacier and permafrost hazards in high mountains. In: Huber UM, Bugmann HKM, Reasoner MA (eds) *Global change and mountain regions (a state of knowledge overview)*. *Advances in Global Change Research*. Springer, Dordrecht, pp 225–234
- Kargel JS, Abrams MJ, Bishop MP, Bush A, Hamilton G, Jiskoot H, Kääb A, Kieffer HH, Lee EM, Paul F, Rau F, Raup B, Shroder JF, Soltesz DL, Stearns L, Wessels R (2005) Multispectral imaging contributions to Global Land Ice Measurements from Space. *Remote Sens Environ* 99:187–219
- Kaser G, Georges C (2003) A potential disaster in the Icy Andes: a regrettable blunder. University of Innsbruck, Austria. Available online: <http://www.uibk.ac.at/geographie/forschung/klima-eis/tropic/huaraz/huaraz.pdf>
- Kaser G, Ames A, Zamora M (1990) Glacier fluctuations and climate in the Cordillera Blanca, Peru. *Ann Glaciol* 14:136–140
- Kattelmann R (2003) Glacial lake outburst floods in the Nepal Himalaya: a manageable hazard? *Nat Hazards* 28:145–154
- Khalsa SJS, Dyrgerov MB, Khromova T, Raup BH, Barry RG (2004) Space-based mapping of glacier changes using ASTER and GIS tools. *IEEE Trans Geosci Remote Sens* 42:2177–2183
- Kinzel H (1941) *Die Andenkundfahrt des Deutschen Alpenvereins nach Peru im Jahr 1939*. *Zeitschrift des Deutschen Alpenvereins*. München
- Klimes J, Vilímek V, Zapata M, Santillán N (2005) Influence of rapid glacial tongue retreat on a surface area of the glacial lakes in the Cordillera Blanca, Peru. *Geophys Res Abstr* 7:06767, SRef-ID: 1607-7962/gra/EGU05-A-06767
- Liboutry LA, Morales Armao B, Pautre A, Schneider B (1977) Glaciological problems set by the control of dangerous lakes in Cordillera Blanca, Perú, I: Historical failures of morainic dams, their causes and prevention. *J Glaciol* 18(79):239–254
- Mamdani EH (1977) Applications of fuzzy logic to approximate reasoning using linguistic synthesis. *IEEE Trans Comp* 26(12):1182–1191
- Mark BG (2002) Observations of modern deglaciation and hydrology in the Cordillera Blanca. *Acta Montana A Geodynamica* 19(123):23–36
- Montario MJ (2001) Exhumation of the Cordillera Blanca, Northern Peru, based on apatite fission track analysis. Unpublished Thesis, Department of Geology, Union College

- Mool PK (1995) Glacier lake outburst floods in Nepal. *J Nepal Geol Soc* 11:273–280
- Morales B (1969) Las lagunas y glaciares de la Cordillera Blanca y su control. *Revista Peruana de Andinismo y Glaciologica* 8:76–79
- Morales Arnao B (1998) Desglaciación y disminución de recursos hídricos. *Bol Soc Geogr Lima* 111:7–20
- Noetzi J, Huggel C, Hoelzle M, Haerberli W (2006) GIS-based modelling of rock-ice avalanches from Alpine permafrost areas. *Comput Geosci* 10:161–178. DOI 10.1007/s10596-005-9017z
- Oerlemans J (2005) Extracting a climate signal from 169 glacier records. *Science* 308:675–677
- Ojeda N (1974) Consolidación laguna Palcacocha. *Electroperu*, Huarás 42 pp
- Paul F, Huggel C, Kääb A (2004a) Mapping of debris-covered glaciers using multispectral and DEM classification techniques. *Remote Sens Environ* 89(4):510–518
- Paul F, Kääb A, Maisch M, Kellenberger T, Haerberli W (2004b) Rapid disintegration of Alpine glaciers observed with satellite data. *Geophys Res Lett* 31:L21402. DOI 10.1029/2004GL020816
- Portocarrero C (1995) Retroceso de glaciares en el Perú: consecuencias sobre los recursos hídricos y los riesgos geodinámicos. *Bull Inst Fr Etudes Andines* 24(3):697–706
- Quincey DJ, Lucas RM, Richardson SD, Glasser NF, Hambrey MJ, Reynolds JM (2005) Optical remote sensing techniques in high-mountain environments: application to glacial hazards. *Progr Phys Geogr* 29(4):475–505
- Quincey DJ, Richardson SD, Luckman A, Lucas RM, Reynolds JM, Hambrey MJ, Glasser NF (2007) Early recognition of glacial lake hazards in the Himalaya using remote sensing datasets. *Global Planet Change* 56:137–152
- Racoviteanu A, Arnaud Y (2005) The 2003 SPOT5-derived glacier inventory for Cordillera Blanca, Peru: A contribution to the GLIMS Geospatial Glacier Database. Abstract for the New Zealand GLIMS Workshop
- Rana B, Shrestha AB, Reynolds JM, Aryal R, Pokhrel AP, Budhathoki KP (2000) Hazard assessment of the Tsho Rolpa Glacier Lake and ongoing remediation measures. *J Nepal Geol Soc* 22:563–570
- Raup B, Kieffer H, Hare T, Kargel J (2000) Generation of data acquisition requests for the ASTER satellite instrument for monitoring a globally distributed target. *IEEE Trans Geosci Remote Sens* 38:1105–1112
- Raup B, Kääb A, Kargel JS, Bishop MP, Hamilton G, Lee E, Paul F, Rau F, Soltész D, Khalsa SJS, Beedle M, Helm C (2006a) Remote sensing and GIS technology in the Global Land Ice Measurements from Space (GLIMS) Project. *Comput Geosci*. DOI 10.1016/j.cageo.2006.05.015
- Raup B, Racoviteanu A, Khalsa SJS, Helm C, Armstrong R and Arnaud Y (2006b) The GLIMS Geospatial Glacier Database: a new tool for studying glacier change. *Global Planet Change* 56(1–2):101–110
- Reynolds JM (1993) The development of a combined regional strategy for power generation and natural hazard risk assessment in a high-altitude glacial environment: an example from the Cordillera Blanca, Peru. In: Merriman PA, Browitt CWA (eds) *Natural disasters: protecting vulnerable communities*. Thomas Telford, London, pp 38–50
- Reynolds JM (1998) Managing the risks of glacial flooding at hydro plants. *Hydro Rev Worldwide* 6 (2):18–22
- Reynolds JM (1999) Photographic feature: Glacial hazard assessment at Tsho Rolpa, Rolwaling, Central Nepal. *Q J Eng Geol* 32(3):209–214
- Reynolds JM, Dolecki A, Portocarrero C (1998) The construction of a drainage tunnel as part of glacial lake hazard mitigation at Hualcán, Cordillera Blanca, Peru. In: Maund J, Eddleston M (eds) *Geohazards in engineering geology*, vol. 15. Geological Society Engineering Group Special Publication, London, pp 41–48
- Richardson SD, Reynolds JM (2000a) Degradation of ice-cored moraine dams: Implications for hazard development. In: Nakawo M, Raymond CF, Fountain A (eds) *Debris-covered glaciers*, vol. 264. International Association of Hydrological Sciences Publication, Seattle, WA, pp 187–197
- Richardson SD, Reynolds JM (2000b) An overview of glacial hazards in the Himalayas. *Q Int* 65–66:31–47

- Rivera A, Benham T, Casassa G, Bamber J, Dowdeswell JA (2007) Ice elevation and areal changes of glaciers from the Northern Patagonia Icefield, Chile. *Global Planet Change* 59:126–137
- Ross TJ (2004) Fuzzy logic with engineering applications, 2nd edn. Wiley, Hoboken, NJ
- Salzmann N, Kääh A, Huggel C, Allgöwer B (2004) Assessment of the hazard potential of ice avalanches using remote sensing and GIS-modelling. *Norwegian J Geogr* 58:74–84
- Shiyin L, Wenxin S, Yongping S, Gang L (2003) Glacier changes since the Little Ice Age maximum in the western Qilian Shan, northwest China, and consequences of glacier runoff for water supply. *J Glaciol* 49:117–124
- Silverio W, Jaquet J-M (2005) Glacial cover mapping (1987–1996) of the Cordillera Blanca (Peru) using satellite imagery. *Remote Sens Environ* 95:342–350
- State of Alaska (2007) All-hazard risk mitigation plan, p. 91, October 2007. http://www.ak-prepared.com/plans/pdf_docs/StateHazardMitigationPlan07/5-2%20Floods.pdf
- Steitz DE and Buis A (2003) Peril in Peru? NASA takes a look at menacing glacier. NASA Press Release 03-138, April 11, 2003. http://www.nasa.gov/home/hqnews/2003/apr/HP_News_03138.html. See also <http://photojournal.jpl.nasa.gov/catalog/PIA03899> and <http://photojournal.jpl.nasa.gov/catalog/PIA03899,OrigCaption>
- Thorarinsson S (1939) The ice-dammed lakes of Iceland, with particular reference to their value as indicators of glacier oscillations. *Geogr Ann* 21:216–242
- Trask PD (1953) El problema de los aluviones de la Cordillera Blanca. *Bol Soc Geogr Lima* 70:1–75
- Wessels R, Kargel JS, Kieffer HH (2002) ASTER measurement of supraglacial lakes in the Mount Everest region of the Himalaya. *Ann Glaciol* 34:399–408
- Williams RS, Ferrigno JG (1999) Glacier Hazards. In: *Glaciers of South America*, vol. I. <http://pubs.usgs.gov/prof/p1386i/peru/hazards.html>
- Williams RS, Ferrigno JG (eds) (2002) *Glaciers of North America (vol. J) and other volumes in the series Satellite Image Atlas of the Glaciers of the World, U.S. Geological Survey Prof. Paper 1386-J*, p. 405, and other volumes in Prof. Paper 1386. U.S. Government Printing Office, Washington, DC
- Williams RS, Ferrigno JG (eds), Contributing Authors (2008, estimated publication) Introduction (volume A) to series, *Satellite Image Atlas of the Glaciers of the World, U.S. Geological Survey Professional Paper 1386-A (State of the Earth's Cryosphere at the Beginning of the 21st Century): Glaciers, Snow Cover, Floating Ice, and Permafrost*
- Willis IC, Richards KS, Sharp MJ (1996) Links between proglacial stream-suspended sediment dynamics, glacier hydrology and glacier motion at Midtdalsbreen, Norway. *Hydrological Processes* 10:629–648
- Wolfe DFG (2009) Glacier dammed lakes impacting different Alaskan drainages after 30 years. In: *American Water Resources Association Spring Specialty Conference, Extended Abstracts, Anchorage*
- Xiangsong Z (1992) Investigation of glacier bursts of the Yarkant River in Xinjiang, China. *Ann Glaciol* 16:135–139
- Xu D, Feng Q (1989) Characteristics of dangerous glacier lakes and their outburst, Tibet, Himalaya Mountain. *Acta Geogr Sinica* 44 (4):343–345
- Yamada T, Motoyama H (1988) Contribution of glacier meltwater to runoff in glacierized watersheds in the Langtang Valley, Nepal Himalayas. *Bull Glacier Res* 6:65–74
- Yamada T, Sharma CK (1993) Glacier lakes and outburst floods in the Nepal Himalaya. *Int Assoc Hydrol Sci Publ* 218:319–330
- Yang Z, Hu X (1992) Study of glacier meltwater resources in China. In: Hooke RL (ed) *Symposium on mountain glaciology Lanzhou, Gansu Province, China, 26–30 August 1991*. *Proc Ann Glaciol* 16:141–145
- Zapata ML (2002) La dinamica glaciär en lagunas de la Cordillera Blanca. *Acta Montana A Geodynamica* 19(123):23–36
- Zapata ML, Gómez RJL, Rapre AC, Santillán NP, Montalvo CA, Lizarme GG (2004) Memoria Annual 2003. INRENA, Huarás, 170 pp

Chapter 16

ASTER Application in Urban Heat Balance Analysis: A Case Study of Nagoya

Soushi Kato and Yasushi Yamaguchi

16.1 Introduction

The urban heat-island effect results in increased local atmospheric and surface temperatures in urban areas compared to the surrounding rural areas. This effect is due primarily to the concentration of human activities and artificial land surface changes. Anthropogenic heat discharges due to energy consumption, and an expanding land surface covered by artificial materials with high heat capacities and conductivities amplify surface and atmospheric temperatures. This is exacerbated by the associated reduction in vegetation and water-pervious surfaces, which help reduce surface temperatures through evapotranspiration. The individual contributions to the resultant temperature rise require clarification to mitigate the urban heat island effect. A simple comparison of the temperatures between an urban and its surrounding rural areas cannot distinguish the complicated interaction in the abovementioned factors. Rather, the heat balance for both urban and rural surfaces require analysis to quantitatively investigate the individual contributions to this temperature increase.

For decades, surface heat-flux analyses were conducted over wide vegetation areas with remote sensing data to quantify transpiration (e.g., Bastiaanssen et al. 1998; Schmugge et al. 1998) in agriculture and forestry. These analysis methods were also applied to urban areas (Zhang et al. 1998; Chrysoulakis 2003). In these methods, heat fluxes are inferred with not only remote sensing data but also locally observed meteorological data or an atmospheric model, particularly for atmospheric temperature and wind velocity. The authors proposed a new technique to estimate artificial increase in sensible heat to assess the effect of anthropogenic heat discharge on the heat-island phenomenon (Kato and Yamaguchi 2005). This study investigates heat fluxes in an urban area with estimates based on the

S. Kato(✉)

Graduate School of Environmental Studies, Nagoya University, Japan,
and

Department of Earth Sciences and Earth Dynamic System Research Center,
National Cheng Kung University, Tainan, Taiwan

e-mail: kato.soushi@nies.go.jp

Advanced Spaceborne Thermal Emission and Reflection Radiometer (ASTER) and the Landsat Enhanced Thematic Mapper Plus (ETM+) data-derived heat-balance models. The anthropogenic heat discharge is then inferred to determine the heat-island effect.

ASTER has three spectral bands in the visible and near-infrared (VNIR), six bands in the shortwave-infrared (SWIR), and five bands in the thermal infrared (TIR) regions, with 15-, 30-, and 90-m spatial resolutions, respectively. The ASTER data possess wide spectral coverage with relatively high spatial resolution, which allows us to discriminate various surface materials.

The ASTER thermal band's spatial resolution is coarser than that of Landsat ETM+ (60 m). However, for the first time, ASTER provides high-spatial resolution multispectral thermal infrared data, which allows us to more accurately determine the variable spectral emissivity of the land surface and, hence, the land surface temperature. Moreover, altitudinal information is obtainable from an ASTER along-track stereo data-derived Digital Elevation Model (DEM) for the same area. ASTER DEM data are used in this study to altitudinally correct ground-based meteorological data. ASTER data are particularly suited to estimate the local heat-flux, and is therefore used throughout. Landsat ETM+ data are used when appropriate ASTER data were unavailable.

16.2 Study Area and Data Used

16.2.1 Description of the Study Area

The study area is approximately 1,700 km² that includes Nagoya city, Japan, a major metropolitan area, which significantly exhibits the heat island effect. Nagoya's commercial, industrial, agricultural, and natural areas are distributed within a relatively small range covered by one ASTER scene. Therefore, Nagoya is an ideal site to study the heat balance in various different land cover types with ASTER data. Its topography is hilly in the eastern part while the central part contains a plateau. The other parts contain an alluvial plain. Figure 16.1 depicts the ASTER DEM of the study area. The commercial, business, and governmental districts are concentrated in the city's central area, which is characterized by high-rise buildings arranged along a north-south and east-west grid of roads. Expanding suburban residential areas surround the urban areas. Nagoya contains limited vegetation cover. Hence, the surrounding rural areas are included in the study area to facilitate comparison between the heat balance characteristics of impervious and pervious surfaces. Figure 16.2 shows the study area, which contains Nagoya's central commercial, and business districts in the center of the image, a coastal industrial region at bottom center, and the surrounding residential, agricultural, and forest areas.

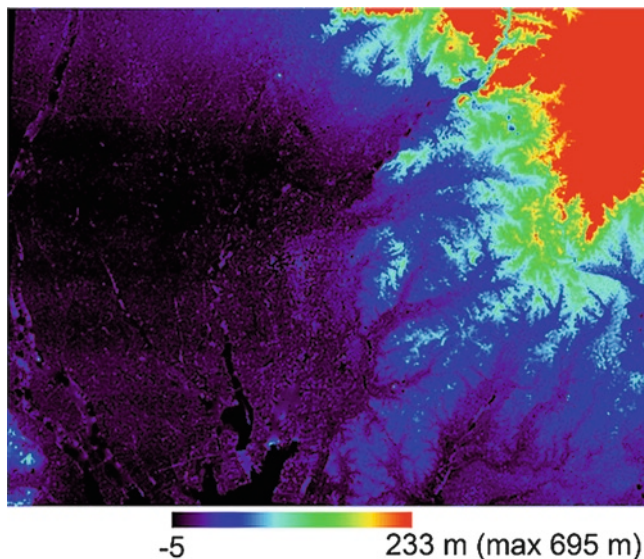


Fig. 16.1 Shaded relief map of the study area derived from ASTER DEM data of July 10, 2000

16.2.2 *Satellite Data and Preprocessing*

This study is based on ASTER and Landsat ETM+ data. The Earth Remote Sensing Data Analysis Center (ERSDAC) provided the ASTER data, and the Remote Sensing Technology Center (RESTEC) provided the Landsat ETM+ data. The following data were used to compare seasonal and temporal differences in heat balance: ASTER data observed at 10:55 JST on July 10, 2000 (summer) and at 22:15 JST on September 17, 2000 (autumn), and ETM+ data observed at 10:18 JST on December 8, 2000 (winter) and 10:17 JST on April 2, 2002 (spring). We used the following atmospherically corrected ASTER data products: surface spectral reflectance (level 2B05V for VNIR and 2B05S for SWIR), spectral emissivity (2B04) and surface temperature (2B03). Detailed algorithm-related information on these products is provided in Thome et al. (1999) and Gillespie et al. (1998). The ETM+ input includes level-1G radiometrically and geometrically corrected data.

These data were converted to surface albedo, broadband emissivity, and the Normalized Difference Vegetation Index (NDVI). The ASTER VNIR data and NDVI were used to classify the land cover type through a combination of minimum distance, maximum-likelihood, and decision-tree classification methods. Eventually, the land surface was classified into nine types of land cover: water, bare soil, field, grassland or rice field, lawn, forest, suburban, urban, and industrial at 15- and 30-m spatial resolutions for ASTER and ETM+, respectively. The July 10, 2000 surface coverage data were used instead of the September 17, 2000 nighttime data based on

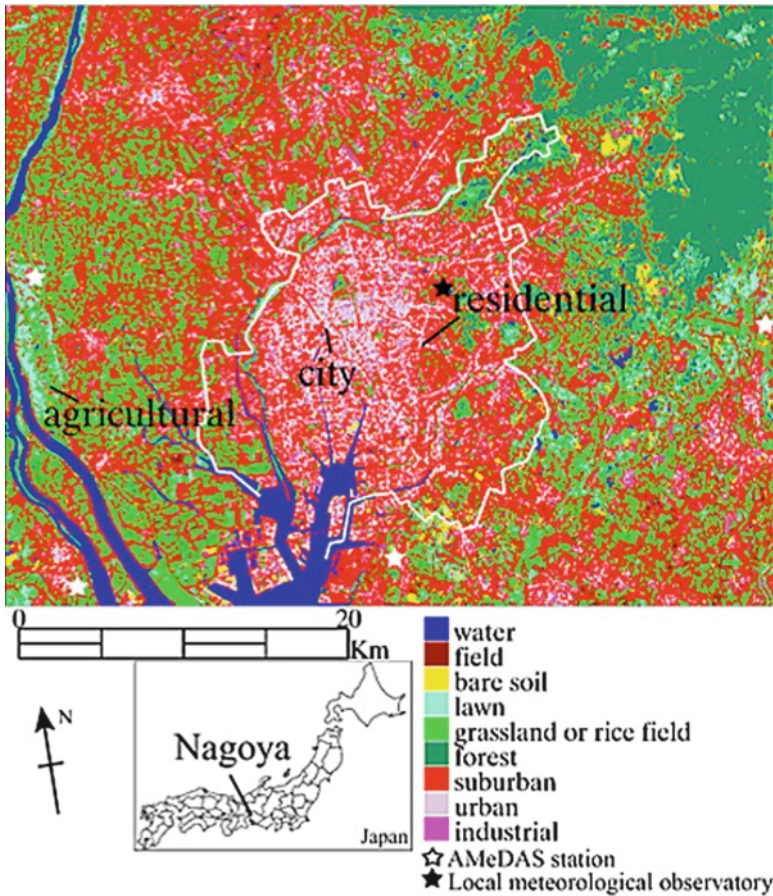


Fig. 16.2 Land surface classification map for Nagoya, Japan and the surrounding area derived from July 10, 2000 ASTER data. The *white line* indicates the boundary of Nagoya city. The analyses described in Sects. 16.4.3 and 16.4.4 are based on the central part of the city, and its residential and agricultural areas

the assumption that the land use change related to urbanization did not occur significantly over approximately 2 months. Figure 16.2 shows the July 10, 2000 surface coverage classification map.

ETM+ based spectral reflectance was calculated from the VNIR (bands 1, 2, 3, and 4) and SWIR (bands 5 and 7) from level-1G data based on Chavez's method (1996). The Chavez method cannot correctly convert the ETM+ band-4 DN to surface reflectance if the water vapor content is high and the NIR radiance is absorbed by atmospheric moisture (Hadjimitsis and Clayton 2004). The water vapor content was 0.85 and 0.80 g/cm² for December 8, 2000 and April 2, 2002, respectively, as calculated based on the vertical air temperature and relative humidity profile data observed at 09:00 JST by the Hamamatsu Rawinsonde Observatory

located approximately 100 km southeast of the study area. Since these values are interpreted as relatively low, we decided to neglect ETM+ band-4's absorption by water vapor in this particular case. The surface temperature was also converted from the TIR radiance (band-6) according to Jiménez-Muñoz and Sobrino (2003) using the above-mentioned water vapor content for atmospheric correction, and the surface emissivity observed via ASTER on July 10, 2000.

Both ASTER and ETM+ spectral reflectance data were converted to albedo according to Liang (2000). ASTER spectral emissivities were converted to broadband emissivity according to Ogawa's equation (2003).

In addition, the ASTER relative DEM data product (level 4A01) acquired on July 10, 2000 was used to determine land-surface altitude. Absolute surface altitude was inferred by comparison with a topographical map provided by the Geographical Survey Institute of Japan. The same ASTER DEM was used for the entire analyses because of the paucity of the land cover changes in the 2000–2002 period. The Sect. 16.3 procedure uses the surface albedo, broadband emissivity, and surface temperature data at 90-m resolution. The NDVI and surface coverage are based on the 15-m ASTER and 30-m ETM+ visible bands.

16.2.3 Meteorological Data and Preprocessing

The meteorological data used in this study were obtained from observations at local meteorological observatories, and from the Automated Meteorological Data Acquisition System (AMeDAS) managed by the Japan Meteorological Agency. Solar radiation, relative humidity, and air-pressure data acquired hourly at the local meteorological observatory, and atmospheric temperature and wind speed data acquired every 10 min by AMeDAS were used in the following preprocessing steps. Data from ten local meteorological observatories and 45 AMeDAS stations, which are installed at approximately 21-km intervals, in and around the study area were used to infer the horizontal distribution of climatic factors.

The meteorological data measured at the time closest to each satellite overpass were interpolated to grid data of the entire study area. Wind speed and solar radiation were assumed constant throughout the study area, so that the wind speed was averaged over the observed data at all AMeDAS stations in the study area. Solar radiation flux (W/m^2) was calculated from the hourly integrated data (MJ/m^2) obtained from the Nagoya Local Meteorological Observatory located in the study area. Atmospheric temperature was horizontally interpolated and corrected with respect to altitude to obtain the atmospheric temperature distribution at 1.5 m above surface, where AMeDAS thermometers were mounted according to the following procedures. First, the virtual atmospheric temperature at 0 m above sea level was inferred from the original AMeDAS data, assuming 6.5 K/km as the environmental lapse rate, which is the international standard value set by the International Civil Aviation Organization (ICAO). Using these values as inputs, the horizontal temperature distribution at 0 m above sea level for the entire study

area was interpolated using a Triangular Irregular Network (TIN) interpolation method with a fifth-order polynomial. Finally, the atmospheric temperature distribution at land surface was calculated from the temperature distribution at 0 m above sea level and the ASTER DEM data, assuming 6.5 K/km as the environmental lapse rate, conversely to infer the temperature at sea level. Relative humidity was simply interpolated to grid data from the original observed data using a TIN interpolation method without altitudinal correction, because of the weak localized distribution and the small number of observatories. Air-pressure p was inferred from the hydrostatic equation:

$$p = p_s \left(\frac{T_a}{T_0} \right)^{g/R_d \Gamma}, \quad (16.1)$$

where p_s is the air-pressure at 0 m above sea level in hPa, T_a is the atmospheric temperature in K, T_0 is the atmospheric temperature at 0 m above sea level in K, g is the gravitational acceleration ($=9.8 \text{ m/s}^2$), R_d is the specific gas constant for dry air ($=287.0 \text{ J/kg K}$), and Γ is the environmental lapse rate in K/m. Here, p_s was approximated from the linear regression with altitude, in which both the slope and the intercept were calculated from air-pressure data for each day and the observatory heights to obtain p_s on the observation dates. Vapor pressure was calculated from relative humidity and saturation water vapor pressure, which is obtainable from the atmospheric temperature (Brutsaert 1982):

$$e^* = 1,01325 \exp(133185t_R - 19760t_R^2 - 06445t_R^3 - 01299t_R^4), \quad (16.2)$$

$$t_R = 1.0 - \frac{373.15}{T}, \quad (16.3)$$

where e^* is the saturation water vapor pressure in hPa and T is the temperature in K. Table 16.1 lists the meteorological data used herein. No precipitation was observed 48 h prior to each satellite overpass, and the impervious land surface was therefore assumed dry.

Table 16.1 Meteorological data used to estimate heat fluxes

| Variable | July 10, 2000 10:55 JST | December 8, 2000 10:18 JST | April 2, 2002 10:17 JST | September 17, 2000 22:15 JST |
|---------------------------------------------|----------------------------|-------------------------------|----------------------------|---------------------------------|
| Short-wave radiation (W/m ²) | 922 | 487 | 766 | – |
| Wind speed (m/s) | 1.5 | 1.7 | 2.7 | 2.2 |
| Atmospheric temperature (K) | 303.9 | 281.2 | 293.1 | 295.6 |
| Air pressure (hPa) | 1,007.1 | 1,017.9 | 1,006.5 | 999.1 |
| Relative humidity (%) | 40 | 44 | 34 | 62 |

Atmospheric temperature, air pressure, and relative humidity were obtained from Nagoya local meteorological observatory, since these variables varied with location

16.3 Methodology of Heat Flux Calculation

For natural land surface, absorbed net radiation (R_n) should balance outgoing fluxes of ground heat (G), sensible heat (H), and latent heat (LE):

$$R_n = G + LE + H \quad (16.4)$$

The heat storage at the surface layer is negligible if the land surface is considered as a thin layer. Net radiation is the sum of incoming solar and long-wave radiation emitted from the atmosphere to land surface, and from the land surface to the atmosphere. During the day, ground heat is conducted into the ground. Heat stored in the ground during the daytime is conducted to the atmosphere at night. Latent heat and sensible heat are transferred to the atmosphere as turbulent flow. Latent heat is produced by transpiration of vegetation and evaporation of land surface water. The sensible heat increases the atmospheric temperature.

However, in urban areas, in addition to the net radiation, the anthropogenic heat discharge, generated from the energy consumption due to human activities in buildings, factories and residences and transportation, also cause heat fluxes. Consequently, heat balance in urban areas is described as follows:

$$R_n + A = G + LE + H, \quad (16.5)$$

where A is the total anthropogenic heat discharge. In this case, energy is transformed into latent heat through phase changes of water due to power generation machinery and the generation and supply of hot water. Anthropogenic sensible heat is mainly transferred from inside urban areas to the atmosphere as heated gas exhausted through chimneys and outdoor air conditioning units, for example. Anthropogenic sensible heat heats the atmosphere directly, but also contributes to increased surface temperature. Since surface temperature measurement by remote sensing is influenced by this anthropogenic heating, heat fluxes that are estimated from these surface temperature data are inevitably affected by anthropogenic heat discharge. Anthropogenic heating influences the surface temperature measurement through remote sensing, and consequently the estimated heat fluxes as well. Based on the concept of surface heat balance, the effect of anthropogenic heat discharge on sensible heat flux is calculated by the following procedures. First, each surface heat flux is estimated individually.

Net radiation R_n is calculated as

$$R_n = (1 - \alpha)R_s + \varepsilon R_{L\downarrow} - R_{L\uparrow}, \quad (16.6)$$

where R_s is the short-wave radiation in W/m^2 , $R_{L\downarrow}$ and $R_{L\uparrow}$ are the downward and upward long-wave radiation in W/m^2 , respectively, α is the surface albedo, and ε is the surface emissivity and absorptance of the downward long-wave radiation. Long-wave radiation is calculated using Stefan–Boltzmann’s law.

Here, the atmospheric emissivity ϵ_a for $R_{L\downarrow}$ is calculated based on the following empirical equation (Brutsaert 1982):

$$\epsilon_a = 1.24 \left(\frac{e_a}{T_a} \right)^{1/7}, \quad (16.7)$$

where e_a is the atmospheric water vapor pressure in hPa and T_a is the atmospheric temperature in K.

Accurate estimation of ground heat flux G requires knowledge of the heat conductivity of the land surface material and the vertical temperature profile, and its temporal change under the ground for soil, and inside walls, roofs, and floors for buildings. Obtaining such data throughout the study area is difficult; therefore, G is roughly estimated from the net radiation:

$$G = c_g R_n. \quad (16.8)$$

The coefficient c_g is fixed according to surface type and season by referring to actual measurements (Brutsaert 1982; Anandakumar 1999; Silberstein et al. 2001). The value of c_g depends on the heat capacity and heat conductivity of surface materials. A high heat capacity results in a low c_g , and a high heat conductivity results in a high c_g . The opposite relationships are also true. The surface materials of developed areas (e.g., concrete and asphalt pavement) generally have both higher heat capacities and higher heat conductivities than soil or vegetation. Based on the assumption of heat balance on the thin layer of the surface, the effect of heat capacity on G is negligible. In the present study, the c_g values of developed areas are fixed based on the findings of Anandakumar (1999), who measured ground heat flux in asphalt pavement. The c_g values used are listed in Table 16.2. If the surface type is grassland or rice field, the c_g is modified in proportion with NDVI, and the c_g thresholds coincide with the values for bare soil and forests. The c_g values for each pixel are obtained by simply averaging the decided values for corresponding surface coverage types, which have higher spatial resolutions than resultant heat fluxes.

Table 16.2 Coefficient c_g used to calculate ground heat flux G_n for different surface coverage types and seasons

| Land cover | Season | | |
|-------------------------|---------|---------|---------|
| | Spring | Summer | Winter |
| Bare soil | 0.3 | 0.3 | 0.3 |
| Field | 0.3 | 0.3 | 0.3 |
| Grassland or rice field | 0.1–0.3 | 0.1–0.3 | 0.1–0.3 |
| Lawn | 0.3 | 0.3 | 0.3 |
| Forest | 0.1 | 0.15 | 0.13 |
| Suburban | 0.7 | 0.4 | 1.0 |
| Urban | 0.7 | 0.4 | 1.0 |
| Industrial | 0.6 | 0.4 | 0.8 |

Each value was inferred from the measurement results for the heat fluxes (Brutsaert 1982; Anandakumar 1999; Silberstein et al. 2001)

If the surface type is water, then G is calculated as the remainder of the radiant heat balance using (16.4). Because G is derived from the c_g values of a small number of measurements in other areas, we should consider the obtained G as a potential value for the condition without anthropogenic heat discharge.

Sensible and latent heat fluxes are obtained using the bulk resistance approach. Sensible heat flux H is given by

$$H = \rho C_p \frac{T_s - T_a}{r_a}, \quad (16.9)$$

where ρ is the air density in kg/m^3 , C_p is the specific heat of air at constant pressure in J/kg K , T_s is the surface temperature in K , and r_a is the aerodynamic resistance in s/m . C_p is corrected based on air pressure and vapor pressure to adjust for atmospheric humidity. r_a is calculated with the following equation (Brutsaert 1982):

$$r_a = \frac{\left[\ln \left(\frac{z_u - d_0}{z_{0M}} \right) - \Psi_M \right] \left[\ln \left(\frac{z_t - d_0}{z_{0H}} \right) - \Psi_H \right]}{k^2 u}, \quad (16.10)$$

where z_u and z_t are the respective heights where the wind speed u (in m/s) and atmospheric temperature are measured, d_0 is the displacement height, and z_{0M} and z_{0H} are the roughness lengths for momentum and heat transport, respectively. All measurements are in meters. In addition, Ψ_M and Ψ_H are stability correction functions for momentum and heat, which depend on the Monin–Obukhov length (Brutsaert 1982), and k is von Karman's constant ($=0.4$). Typical values of roughness lengths, z_{0M} and z_{0H} , for selected surface types are used in this study (Brutsaert 1982; Yasuda 1995; Kondo 1994, 2000; Hansen 1993). The roughness length in each resultant pixel was adjusted by a logarithmic averaging procedure (Noilhan and Lacarrere 1995) as follows:

$$z_0 = \exp \left\{ \frac{1}{n} \left(\sum_{i=1}^n \ln z_{0,i} \right) \right\}, \quad (16.11)$$

where $z_{0,i}$ is the roughness length for the corresponding surface coverage type (spatial resolution is 15 m for ASTER and 30 m for ETM+) and n is the number of relevant pixels (i.e., 36 for ASTER and 9 for ETM+). Therefore, the roughness length does not necessarily correspond to the actual local surface form, but rather varies with location. The roughness lengths used are listed in Table 16.3. Here, z_u , z_t , and d_0 on complex terrain areas are inferred using local dispersion of the DEM data, the spatial resolution of which is narrower than that of the results of the present analysis. The sum of the height of the AMeDAS instruments and the difference between local maximum height and local average height are used as z_u and z_t . The value of d_0 is calculated using the method proposed by Macdonald et al. (1998):

$$d_0 = z_h \{1.0 + a^{-\lambda P} (\lambda P - 1.0)\}, \quad (16.12)$$

where z_h is the height of the obstacles, a is a constant ($=4.43$ for staggered arrays), and λP is the plan area density of obstacles, i.e., the ratio of the built-up area to the

Table 16.3 Roughness length for different surface coverage types

| Land cover | z_{0M} (m) | z_{0M}/z_{0H} |
|-------------------------|----------------------|-----------------|
| Water | 0.3×10^{-4} | 0.34 |
| Bare soil | 0.001 | 50 |
| Field | 0.004 | 50 |
| Grassland or rice field | 0.1 | 100 |
| Lawn | 0.01 | 50 |
| Forest | 0.5–1.0 | 1,000 |
| Suburban | 0.5 | 1,000 |
| Urban | 1.5 | 1,000 |
| Industrial | 0.9 | 1,000 |

total area. To apply this equation to the ASTER DEM data, z_h is approximated by the difference between local maximum and local minimum heights. Moreover, the ratio of the number of pixels with an altitude higher than the local average height to the number of total pixels (i.e., $x/9$) is used in place of λP .

Latent heat flux LE is expressed as

$$LE = \frac{\rho C_p}{\gamma} \frac{e_s^* - e_a}{r_a + r_s}, \quad (16.13)$$

where γ is the psychrometric constant in hPa/K, e_s^* is the saturation vapor pressure in hPa at the surface temperature calculated using (16.2), and r_s is the stomatal resistance in s/m. Accurate estimation of stomatal resistance is difficult, because its value depends on vegetation species, meteorological and atmospheric conditions. The main goal of this study is not to monitor latent heat flux, but rather urban heat balance; therefore, stomatal resistance is simply calculated by recursion of (16.13) to converge the results of LE and r_s . The latent heat flux is not calculated when the surface type is urban, suburban, or industrial based on the assumption that artificial land surfaces are dry.

The influence of anthropogenic heat on heat balance is estimated from the abovementioned heat fluxes. Equation (16.9) indicates a composite of results from radiant heat balance, and the effect of anthropogenic heat discharge, because in this equation, the sensible heat flux is calculated based on observed surface and atmospheric temperatures. On the other hand, (16.13) shows the latent heat due to evapotranspiration, but the anthropogenic factor is not included. Although the net radiation depends on surface and atmospheric temperatures in the form of long-wave radiation, the net radiation is affected little by temperature changes because the amount of incoming short-wave radiation is much greater than the outgoing net long-wave radiation at the time of satellite overpass under clear skies. Because (16.8) is used to calculate the ground heat flux that arises from the net radiation and is assumed as a potential quantity, the effect of temperature change on G is considered small.

Based on these considerations, the influence of temperature rise on heat flux is considered negligible, with the exception of sensible heat, and the surplus in the radiant heat balance is due to the anthropogenic effect on the urban surface materials.

The sensible heat flux due to radiant heat balance, and expressed as H_n in the following, is calculated as the residue of the heat balance equation:

$$H_n = R_n - G - LE. \quad (16.14)$$

Finally, the sensible heat flux due to the artificial effects is calculated as the difference between the total sensible heat flux and H_n as

$$H_{as} = H - H_n, \quad (16.15)$$

where H_{as} is the net increase in sensible heat flux given by surface heat balance and is not equivalent to A in (16.5), because, as mentioned above, A includes other forms of heat flux. When the total H calculated by (16.9) is smaller than H_n calculated by (16.14), H is substituted for H_n , considering that $H_{as} = 0 \text{ W/m}^2$.

16.4 Results and Discussion

The artificial increases in sensible heat flux H_{as} on July 10, 2000, December 8, 2000, and April 2, 2002, obtained using (16.15), are shown in Figs. 16.3–16.5, respectively. Because H_{as} is basically inferred as a difference from the radiant heat balance (16.4), H_{as} can contain errors for each flux calculated by (16.6), (16.8), (16.9), and (16.13). For instance, some vegetation or bare soil areas have either positive or negative H_{as} values, ranging from -170 to 160 W/m^2 , although theoretically,

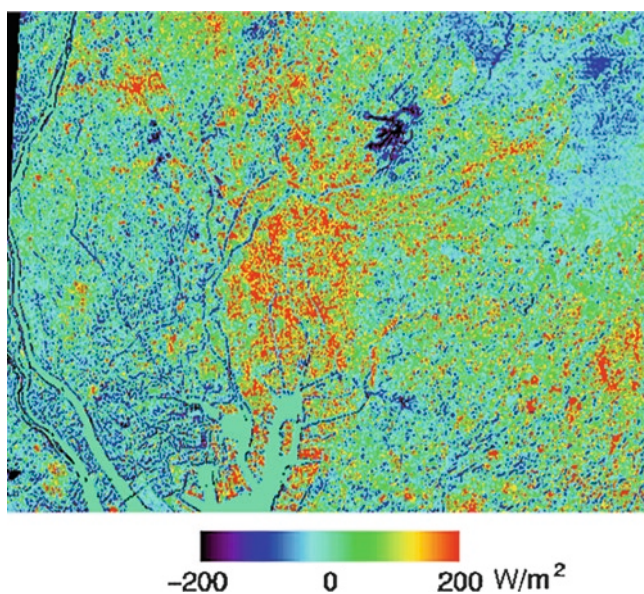


Fig. 16.3 Artificial increase in sensible heat flux on July 10, 2000

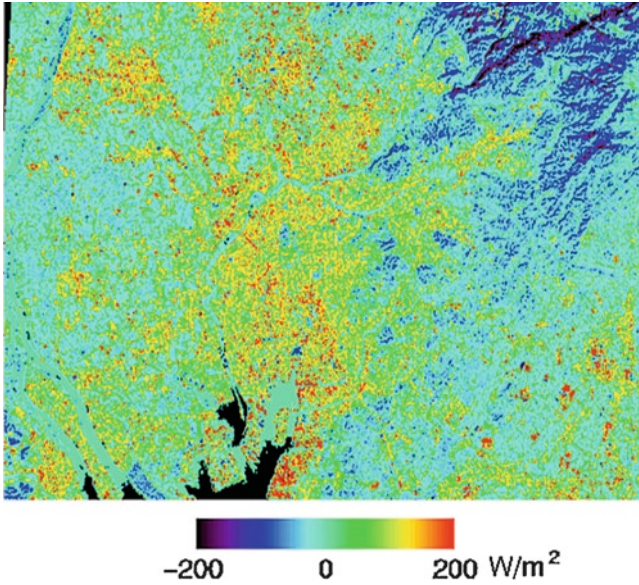


Fig. 16.4 Artificial increase in sensible heat flux on December 8, 2000

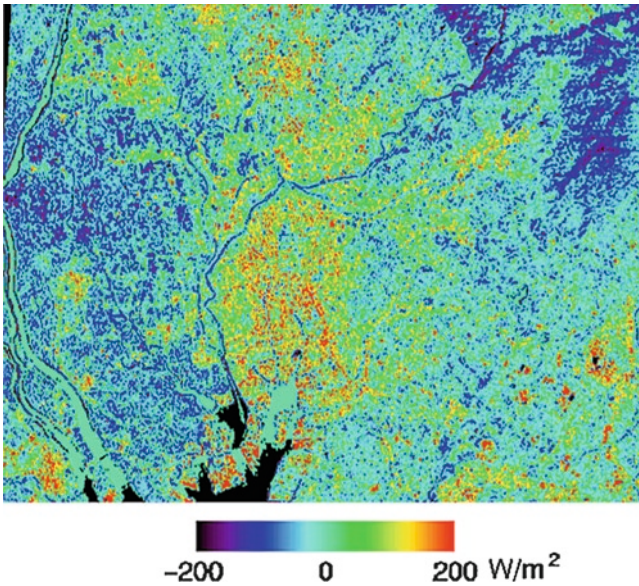


Fig. 16.5 Artificial increase in sensible heat flux on April 2, 2002

H_{as} should remain 0 W/m^2 . These values are deemed errors in the estimation. This error should include the errors due to the misclassification of land cover, errors in the calculation equations, errors in the empirical parameters used, errors

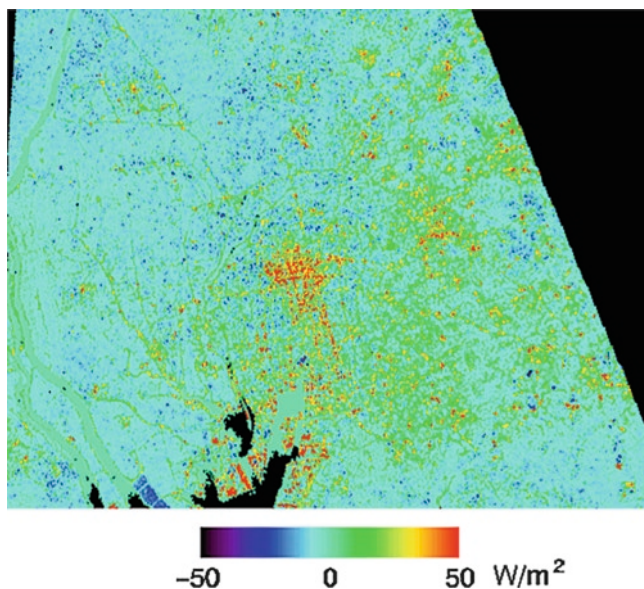


Fig. 16.6 Sensible heat flux at night on September 17, 2000

in the spatial resolution difference of multispectral data and errors originating from the data products.

For the night of September 17, 2000, the results shown in Fig. 16.6 are not H_{as} , but rather H , because to calculate H_{as} to sufficient accuracy using (16.15) is difficult due to the absence of solar radiation, which causes the effects of surface and atmospheric temperatures on heat fluxes, R_n , H_n , and G , relatively significant. However, in (16.9) results, no sensible heat flux was discharged from most of the land surface, except for the urban and industrial areas and water that have high heat capacity. Therefore, we concluded that H is usable in place of H_{as} for the night of September 17, 2000.

16.4.1 *Spatial Pattern and Temporal Variation of Artificial Increase in Sensible Heat Flux*

For all daytime results in developed areas, H_{as} was high, and in areas with natural surfaces, H_{as} was low, despite seasonal differences. This tendency implies that our analysis results correspond reasonably to the actual spatial pattern. In Nagoya, the central commercial, governmental, and business areas ($\sim 0.8 \text{ km}^2$) had lower H_{as} than the surrounding urban areas for the three daytime results. One of the reasons for this phenomenon is that the uneven landscape presented by systematically arranged high-rise buildings causes shadows to block the solar radiation on the northwestern side of obstacles in the central part of the city. As a result, the surface temperature

of the shaded roads and building roofs is low, and the satellite sensor observes them as thermal infrared radiation almost directly above the land surface. Another reason is the thermal inertia of tall building areas, which have a large volume of concrete surface with high heat capacities. This also affects the surface temperature change. Consequentially, the surface temperature of the central area, for the 10:17–10:55 AM satellite overpasses, did not increase compared to the surrounding areas.

The industrial area, situated in the southern part of the study area, for instance, had high H_{as} values that were similar for all four results, regardless of seasonal or temporal differences, which implies that the influence of anthropogenic heat discharge is detectable with H_{as} .

At night, surface temperatures of urban areas are generally higher than those of natural surfaces, because artificial surface materials store heat during the day and discharge heat at night. Sensible heat, H , was discharged only from the central part of the urban area (center of the study area) and the industrial areas (bottom center) on September 17, 2000 night. On the other hand, relatively low, or even negative, H was observed in the residential areas. The surface temperature in the residential areas cooled relatively quickly after dusk because many Japanese houses have wooden walls and thin tile roofs (~10- to 20-mm thick), which have smaller heat capacities than concrete. Based on these results, we concluded that, at night, H is due primarily to anthropogenic heat discharge in industrial areas. On the other hand, the abovementioned occurrence of low H_{as} in the daytime and high H at night in the central urban area implies that these results are largely affected by the heat capacity of the urban surface.

16.4.2 Assessment of the Accuracy of H_{as} Estimation

H_{as} averages and standard deviations for each surface coverage are listed in Table 16.4 to compare the quantitative values for the four cases, and to check whether H_{as} in the urban areas is reasonable compared to its rural counterpart. Given that natural surface's H_{as} should remain 0 W/m², H_{as} averages and standard deviations for bare soil and the vegetation areas are an indication of the accuracy of the heat flux calculations.

The fact that the H_{as} average was the highest in the urban areas for all cases implies that the calculated H_{as} is adequate. The average H_{as} of 197 W/m² in urban areas on July 10, 2000 was much higher than in other seasons, and was noticeable even with respect to the artificial increase in sensible heat when considering the standard deviation of 143 W/m². The average H_{as} of 117 W/m² on December 8, 2000 and the average H_{as} of 141 W/m² on April 2, 2002 were slightly higher than the standard deviations of 76 and 112 W/m², respectively. On the other hand, H was not distinguishable at night on September 17, 2000 due to large standard deviations. This is because the pixels classified as “urban” do not include only the central urban area of Nagoya. Although a great deal of energy is consumed for heating in urban areas in winter as well, the H_{as} average on December 8, 2000 was much lower than that on

Table 16.4 Averages and standard deviations of H_{as} for different surface coverage types on four different dates

| Surface coverage | July 10, 2000 | | December 8, 2000 | | April 2, 2002 | | September 17, 2000 | |
|-------------------------|-----------------------------|----------------------------------------|-----------------------------|----------------------------------------|-----------------------------|----------------------------------------|-----------------------------|----------------------------------------|
| | Average (W/m ²) | Standard deviation (W/m ²) | Average (W/m ²) | Standard deviation (W/m ²) | Average (W/m ²) | Standard deviation (W/m ²) | Average (W/m ²) | Standard deviation (W/m ²) |
| Water | -2 | 20 | 0 | 18 | -1 | 10 | 17 | 5 |
| Bare soil | 10 | 73 | -32 | 30 | -50 | 29 | -1 | 4 |
| Field | 26 | 49 | -28 | 15 | -62 | 44 | -3 | 3 |
| Grassland or rice field | 16 | 70 | -6 | 25 | -9 | 39 | -3 | 6 |
| Lawn | -1 | 53 | 20 | 26 | -30 | 33 | -3 | 4 |
| Forest | -55 | 60 | -57 | 54 | -64 | 49 | 5 | 19 |
| Suburban | 16 | 92 | 74 | 41 | 36 | 65 | -1 | 14 |
| Urban | 197 | 143 | 117 | 76 | 141 | 112 | 17 | 28 |
| Industrial | 36 | 129 | 77 | 64 | 42 | 116 | -2 | 16 |

July 10, 2000. This difference was primarily due to the surface temperature rise caused by incoming solar radiation and immense energy consumption during the summer.

Because the average H_{as} on natural surfaces was negative on December 8, 2000 and April 2, 2002, we assume that seasonal constant parameters in flux calculation or atmospheric correction for reflectance and surface temperature cause errors in these cases. One of the reasons for this is that the latent heat flux probably includes errors, because the stomatal resistance is inferred at low accuracy. Moreover, ground heat flux is possibly underestimated for forest areas, because the H_{as} average on July 10, 2000 is also negative (-55 W/m²). The stomatal resistance and ground heat flux require careful estimation to adjust to the actual surface conditions.

16.4.3 Comparison of Seasonal and Temporal Variations in H_{as} at Specific Sites

To compare seasonal and temporal changes of H_{as} , three typical land use areas were examined: the central part of the city (surface is less than 1% vegetation and over 99% impervious), residential areas (15% vegetation), and agricultural areas (70% vegetation) (Fig. 16.2 and Table 16.5). Each H_{as} is the average over an area of approximately 3 km². Comparing daytime H_{as} in the central part of the city, the H_{as} of 99 W/m² on July 10, 2000 was higher than those on December 8, 2000 (82 W/m²) and April 2, 2002 (79 W/m²). This trend, in which H_{as} was the highest in summer, is consistent with the quantity of energy consumption and incoming solar radiation. In the residential areas, H_{as} was 41 W/m² on July 10, 2000, 35 W/m² on December 8, 2000, and 0 W/m² on April 2, 2002, and was lower than half of that in the city for all seasons. Vegetation transpiration in this area was possibly responsible for low surface temperatures. In the agricultural area, H_{as} was negative for all daytime

Table 16.5 Calculated H_{as} and H_n for three typical land use areas

| Date | July 10, 2000 | | December 8, 2000 | | April 2, 2002 | | September 17, 2000 |
|--------------------------------|---------------|-------|------------------|-------|---------------|-------|--------------------|
| Sensible heat flux (W/m^2) | H_{as} | H_n | H_{as} | H_n | H_{as} | H_n | H |
| Location | | | | | | | |
| City | 99 | 320 | 82 | 9 | 79 | 161 | 27 |
| Residential | 41 | 258 | 35 | 22 | 0 | 141 | 4 |
| Agricultural | -11 | 97 | -13 | 45 | -44 | 89 | -4 |

The locations are shown in Fig. 16.2

cases, and was particularly low on April 2, 2002 ($-44 W/m^2$). More significant errors exist in the results for vegetation areas on April 2, 2002 than for the other cases. The H of $27 W/m^2$ in the city at night on September 17, 2000 was much higher than that in the residential area ($4 W/m^2$). These results are possibly attributed to daytime heat storage in concrete buildings and energy consumption in the city, as mentioned in Sect. 16.4.1.

16.4.4 Contributions of H_{as} and H_n as Causes of the Heat-Island Effect

The heat-island effect is caused by increased sensible heat flux, i.e., increases in both H_{as} and H_n . To examine the individual contributions of H_{as} and H_n to the heat-island effect, the calculated fluxes were compared for the three locations described in Sect. 16.4.3. (Table 16.5). On July 10, 2000, H_n of $320 W/m^2$ was much higher than the H_{as} of $99 W/m^2$ in the city, and H_n in the city was much larger than that in the agricultural area ($97 W/m^2$). Transpiration of vegetation stomata keeps H_n low in the agricultural area. These results imply that the decrease in latent heat flux due to a decrease in vegetation has a more significant impact on temperature rise than the artificial increase in sensible heat flux in the summer. On December 8, 2000, H_{as} of $82 W/m^2$ was much larger than the H_n of $9 W/m^2$ in the city, because G in the urban areas is assumed large (i.e., $G = R_n$) in winter. On April 2, 2002, H_{as} was less than 50% of H_n in the city and $0 W/m^2$ in residential areas. Since energy usage for human activities in spring is less than in other seasons, this result is reasonable.

16.4.5 Sensitivity Study of H_{as} Calculation

Calculated H_{as} can contain errors, because H_{as} is derived as a difference in radiant heat balance among other heat fluxes (cf. (16.14) and (16.15)). The influence of each heat flux on H_{as} is discussed below. Latent heat flux does not have a great effect on H_{as} in urban areas because of the reduced moisture and vegetation amount. As the net radiation is calculated using observed data, its error is usually small. On

Table 16.6 Averages and standard deviations of H_{as} in urban areas having low c_g and z_{OM} values

| July 10, 2000 | | December 8, 2000 | | April 2, 2002 | |
|---------------------|--------------------------------|---------------------|--------------------------------|---------------------|--------------------------------|
| Average (W/m^2) | Standard deviation (W/m^2) | Average (W/m^2) | Standard deviation (W/m^2) | Average (W/m^2) | Standard deviation (W/m^2) |
| 80 | 117 | 22 | 57 | -2 | 91 |

the other hand, sensible heat and ground heat fluxes are calculated using parameters that correspond to surface coverage classified from remote sensing data. They are not necessarily adjusted to the actual circumstances, and inevitably include classification inaccuracies, and hence, we cannot ignore the errors in these two fluxes. To analyze the effect of these errors, H_{as} was calculated with considerably small G and H for the three daytime analyses. G was taken as 70% of the usual calculated value to adjust the c_g during the summer to that of the soil surface. In addition, H was calculated by changing the roughness length for momentum z_{OM} for an urban area from 1.5 to 1.0 m, since the typical z_{OM} for a large city is in the range of approximately 1.0–3.0 m (Kondo 2000). The resulting averages and standard deviations of H_{as} in urban areas (Fig. 16.2, city) are listed in Table 16.6. The average H_{as} of 80 W/m^2 in urban areas is only narrowly positive on July 10, 2000. However, the standard deviation of H_{as} on July 10, 2000 (117 W/m^2) is larger than the average. Therefore, it is difficult to distinguish H_{as} from the error. H_{as} shows almost the same tendencies as those for other types of surfaces on April 2, 2002 (Table 16.4). If z_{OM} is changed from 1.5 to 1.0 m without changing any of the other parameters, H decreases to approximately 83% of the original value based on (16.9) and (16.10). The error of ground heat flux G has the most significant effect on the calculation of H_{as} for low-temperature seasons in the present procedure.

16.4.6 Comparison of Heat Flux Ratio with in Situ Observations

Ground measurements corresponding to H_{as} are not available. Therefore, the total sensible heat flux H is compared to in situ measurements reported by Oke et al. (1999) and Spronken-Smith (2002). In both studies, net radiation was observed with a radiometer and sensible and latent heat fluxes were observed via an eddy correlation method using a one-dimensional sonic anemometer, a fine-wire thermocouple system, and a krypton hygrometer, which were mounted approximately 20–30 m above the ground. Oke et al. (1999) observed heat fluxes in urban areas, which contain approximately 1% vegetation and water during the winter, and Spronken-Smith (2002) observed heat fluxes in residential areas, which are composed of approximately 60% pervious surfaces in both winter and summer. Since these sites are comparable to the urban and the suburban areas of the present study, the average values in urban areas on December 8, 2000 and in suburban areas on July 10, 2000 and December 8, 2000 are compared. Table 16.7 shows the ratios

Table 16.7 Ratios of heat flux to the net radiation of the present daytime analysis and to the net radiation previously measured in urban areas

| Original reference | Site | Height of measurement (m) | Observation period | H/R_n | LE/R_n | G/R_n |
|--------------------------|---------------------------------------------------------------------------|---------------------------|---------------------------------------|---------|----------|---------|
| Present study | Urban (average) | – | December 8, 2000 (winter) | 0.46 | 0.02 | 0.96 |
| | Suburban (average) | | July 10, 2000 (summer) | 0.56 | 0.10 | 0.39 |
| Oke et al. (1999) | Mexico City, Mexico (urban: 99% impervious) | 28 | December 8, 2000 (winter) | 0.35 | 0.02 | 0.93 |
| | | | December 1–7, 1993 (winter) | 0.38 | 0.04 | 0.58 |
| Spronken-Smith (2002) | St. Albans, Christchurch, New Zealand (residential: 44% impervious) | 20 | January 29–February 18, 1996 (summer) | 0.46 | 0.22 | 0.32 |
| | | | July 16–August 9, 1997 (winter) | 0.16 | 0.10 | 0.74 |
| | Beckenham, Christchurch, New Zealand (residential: 36% impervious) | 18 | August 11–24, 1995 (winter) | 0.38 | 0.23 | 0.39 |

Measured fluxes are daytime ($R_n > 0$) averages

of heat flux to the net radiation for these measurement cases, since the comparison of fluxes is meaningless due to site and methodological differences. In the Oke and Spronken-Smith studies, the sensible heat flux is 46% of the net radiation for summer and 16–38% for winter. The H/R_n ratio of the present study is comparable to these values. However, LE and G are under- and overestimated, respectively, in winter for both urban and suburban areas. We attribute this to differences in methodology. The ground heat flux (from in situ measurements) is calculated by the energy balance residual. In the present study, the latent heat flux in developed areas was neglected, resulting in the underestimation of LE. Despite the site and methodological differences, the comparison generally indicates that the results are reasonable, especially with respect to sensible heat.

16.5 Summary

Based on the energy balance model for the land surface, the increase in sensible heat flux, H_{as} , due to anthropogenic heat discharge was calculated. H_{as} is estimated with remote sensing data, and is useful as an index to assess the urban heat-island effect. To compare seasonal and day–night differences in H_{as} or H , this method was applied to four cases, namely, daytime in summer, winter and spring, and nighttime in autumn, between 2000 and 2002, based on the available remote sensing data around Nagoya city, Japan.

The spatial distribution and seasonal trends of H_{as} during the daytime corresponded adequately with the actual land cover or use. Namely, H_{as} was high in developed areas and low in rural areas. H_{as} in the central part of Nagoya was highest in July, followed by that in December, and was lowest in April. The industrial areas, where huge amounts of energy are consumed, had extremely high H_{as} in all seasons. During the night in autumn (September), the spatial distribution of H implied that H is due primarily to anthropogenic heat discharge in industrial areas and heat storage in buildings during the daytime in the central urban area. In the urban areas in July, H_{as} was much lower than H_n . Therefore, the decrease in vegetation is regarded as the most significant contributor to the heat-island effect on summer days.

The present results agree well with previous in situ sensible heat flux measurements for suburban areas during the summer, but shows poor agreement with respect to latent heat flux during the winter. This disagreement is due to differences in the measurement and inference methods. In particular, the inference procedures for latent and ground heat flux presented herein require improvement to estimate H_{as} accurately. It would help to understand the thermal environment in particular areas to separate heat fluxes according to their sources.

Another new method to evaluate the storage heat flux in urban surfaces was developed by the authors based upon the heat balance equation (Kato and Yamaguchi 2007). The storage heat flux in the central urban area was higher than those of the surrounding residential areas. Moreover, the negative storage heat flux in the central urban area was greater at night. This tendency implies that the urban

surface stores heat during the daytime and discharges it at night. The difference in the storage heat flux between the central urban and residential areas is magnified by the large heat capacity of the high-rise buildings in the central urban area. Conversely, extremely large negative storage heat fluxes occurred primarily in the industrial areas for both daytime and nighttime as a result of the enormous energy consumption by factories. These results suggest that anthropogenic heat is large in industrial areas, and is responsible for the actual energy consumption. These differences in the heat balance patterns between the urban and industrial areas were due to the existence of buildings in the urban areas and the amount of energy consumption in the industrial areas.

We used ASTER and Landsat ETM+ data both to derive physical quantities (such as surface temperature and reflectance), and as supplementary data for corrections. ASTER has a relatively higher spatial resolution, a wider spectral range and a higher spectral resolution than Landsat ETM+. The five TIR bands are especially useful to determine surface emissivity and temperature with high accuracy and spatial resolution. ASTER data are suitable to obtain detailed information on a local scale. These advantages help estimate heat flux in urban areas, where surface temperature and surface materials form complex patterns, and present interesting challenges.

References

- Anandakumar K (1999) A study on the partition of net radiation into heat fluxes on a dry asphalt surface. *Atmos Environ* 33(24–25):3911–3918
- Bastiaanssen WGM, Menenti M, Feddes RA, Holtslag AAM (1998) A remote sensing surface energy balance algorithm for land (SEBAL) 1. Formulation. *J Hydrol* 212–213:198–212
- Brutsaert W (1982) *Evaporation into the atmosphere: theory, history, and applications*. D. Reidel, London, p 299
- Chavez PS Jr (1996) Image-based atmospheric corrections – revisited and improved. *Photogramm Eng Remote Sens* 62(9):1025–1036
- Chrysoulakis N (2003) Estimation of the all-wave urban surface radiation balance by use of ASTER multispectral imagery and in situ spatial data. *J Geophys Res* 108(D18):4582. DOI 10.1029/2003JD003396
- Gillespie AR, Matsunaga T, Rokugawa S, Hook SJ (1998) Temperature and emissivity separation from advanced spaceborne thermal emission and reflection radiometer (ASTER) images. *IEEE Trans Geosci Remote Sens* 36(4):1113–1126
- Hadjimitsis DG, Clayton CRI (2004) An assessment of the effectiveness of atmospheric correction algorithms through the remote sensing of some reservoirs. *Int J Remote Sens* 25(18):3651–3674
- Hansen SV (1993) *Surface roughness lengths*. ARL Technical Report, U.S. Army, White Sands Missile Range, NM 88002-5501
- Jiménez-Muñoz JC, Sobrino JA (2003) A generalized single-channel method for retrieving land surface temperature from remote sensing data. *J Geophys Res* 108(D22):4688. DOI 10.1029/2003JD003480
- Kato S, Yamaguchi Y (2005) Analysis of urban heat-island effect using ASTER and ETM+ Data: Separation of anthropogenic heat discharge and natural heat radiation from sensible heat flux. *Remote Sens Environ* 99(1–2):44–54
- Kato S, Yamaguchi Y (2007) Estimation of storage heat flux in an urban area using ASTER data. *Remote Sens Environ* 110(1):1–17

- Kondo J (1994) Meteorology of the water environment – water and heat balance of the land surface. Asakura, Tokyo, Japan, p 350 (in Japanese)
- Kondo J (2000) Atmospheric science near the ground surface. University of Tokyo Press, Tokyo, Japan, p 324 (in Japanese)
- Liang S (2000) Narrowband to broadband conversions of land surface albedo I Algorithms. *Remote Sens Environ* 76(2):213–238
- Macdonald RW, Griffiths RF, Hall DJ (1998) An improved method for the estimation of surface roughness of obstacle arrays. *Atmos Environ* 32(11):1857–1864
- Noilhan J, Lacarrere P (1995) GCM grid-scale evaporation from mesoscale modeling. *J Clim* 8(2):206–223
- Ogawa K, Schmugge T, Jacob F, French A (2003) Estimation of land surface window (8–12 mm) emissivity from multispectral thermal infrared remote sensing – a case study in a part of Sahara Desert. *Geophys Res Lett* 30(2). DOI 10.1029/2002GL016354
- Oke TR, Spronken-Smith RA, Jáuregui E, Grimmond CSB (1999) The energy balance of central Mexico City during the dry season. *Atmos Environ* 33(24–25):3919–3930
- Schmugge TJ, Kustas WP, Humes KS (1998) Monitoring land surface fluxes using ASTER observations. *IEEE Trans Geosci Remote Sens* 36(5):1421–1430
- Silberstein R, Held A, Hatton T, Viney N, Sivapalan M (2001) Energy balance of a natural jarrah (*Eucalyptus marginata*) forest in Western Australia: measurements during the spring and summer. *Agric Forest Meteorol* 109(2):79–104
- Spronken-Smith RA (2002) Comparison of summer- and winter-time suburban energy fluxes in Christchurch, New Zealand. *Int J Climatol* 22(8):979–992
- Thome K, Biggar S, Takashima T (1999) Algorithm theoretical basis document for ASTER level 2B1 – surface radiance and ASTER level 2B5 – surface reflectance, p 45. http://eosps0.gsfc.nasa.gov/eos_homepage/for_scientists/atbd/docs/ASTER/atbd-ast-07-09.pdf. Last Accessed 28 March 2007
- Yasuda N (1995) Fundamental atmospheric science. Asakura, Tokyo, Japan, p 204 (in Japanese)
- Zhang X, Aono Y, Monji N (1998) Spatial variability of urban surface heat fluxes estimated from Landsat TM data under summer and winter conditions. *J Agric Meteorol* 54(1):1–11

Chapter 17

Monitoring Urban Change with ASTER Data

Maik Netzband, Elisabeth Schöpfer, and Matthias S. Möller

17.1 Introduction

The appearance of urban areas manifested by human congregation and concentration is a phenomenon characteristic of the development of modern humankind. Historically, every ancient high culture was based on large agglomerations of people (e.g., Angkor Wat, Machu Picchu, Alexandria). Human concentration in urban areas offer a lot of advantages to those in areas with less benefits, especially rural areas. Urban areas provide economic welfare, efficient communication and transportation paths, a dense social and healthcare network, and numerous entertainment opportunities compared to remote and sparsely settled areas. Urban areas today provide home to more than 50% of the people worldwide. Urban areas display strong growth trends, especially in less-developed countries, where a rapid growth of unplanned informal settlements are evident.

The use of remotely sensed images has increasingly proved successful to analyze urban structure, and the appearance and phenology of urban areas. Such images provide a synoptic overview of a large area. The images are explicitly interpretable without any a priori knowledge. The public availability of Google Earth (<http://earth.google.com/>) has heightened the attractiveness of satellite images as a source of information about remote places all over the globe. Even urban areas are re-established in 3D objects, which provide an increasingly realistic representation of the Earth.

M. Netzband (✉)

Helmholtz Centre for Environmental Research-UFZ, Leipzig, Germany
e-mail: maik.netzband@ufz.de

17.1.1 *Scale and Resolution*

Urban remote sensing can involve scaling multiple datasets with multiple temporal, spatial, and spectral resolutions. In a remote sensing application, the derived data's scale depends on the image's spatial resolution. An application scale larger than 1:50,000 is highly recommended to analyze urban areas. Table 17.1 provides an overview of different satellite sensor systems, their spatial resolution and individual monitoring purposes.

A fairly large collection of remotely sensed images exists to analyze and monitor urban changes. However, with the passage of time, older image data with coarser resolutions render the application scale smaller. Urban change detection over the past three decades has benefited from MSS- and TM-derived data. In combination with more recent image data acquired by sensors such as ASTER or SPOT, a high frequency multitemporal monitoring of urban growth is possible, and leads to meaningful results (Möller 2004).

A new generation of "very high resolution" satellite data are acquired by 1-m spaceborne sensors originally developed for spying and reconnaissance purposes, but now are operated by commercial enterprises. Such data show great potential for mapping and surveying purposes, especially in urban areas, because they facilitate the recognition of most urban objects, and thus provide a realistic view of the Earth's surface. Urban areas represent various different objects that constitute the urban landscape. Buildings, single trees, backyard pools and even cars are clearly identifiable in this very high-resolution image (Fig. 17.1, left image). However, such an image cannot directly compete with an ASTER image. ASTER data with its 15 m (VNIR) and 30 m (SWIR) multispectral bands, in most cases, do not represent individual urban objects like buildings in a single pixel (exception: large buildings mainly located in the central business district of metropolitan areas). Instead, a mixed pixel contains the spectral average of several building's objects. Objects with a larger extent and more homogeneous shape such as meadows, lawns or water bodies appear more coherent in an ASTER image. In an automated image analysis, using the spectral properties to differentiate object classes produces an averaging effect, viewed sometimes as an advantage. Figure 17.1 provides NIR images from Quickbird, ASTER and ETM+ to visually appreciate differences in spatial resolution and direct object recognition.

In practice, urban remote sensing is often combined with ancillary GIS data in an interdisciplinary study. These data may include socioeconomic, sociopolitical, environmental, or other variables common in urban studies. These data have their own spatial and temporal resolutions, which may prove to be the limiting factor in an urban remote sensing study. For example, high-resolution images from Quickbird are potentially able to highlight vegetation changes from backyard to backyard, but if the unit being studied is at a neighborhood scale or higher, the Quickbird data requires "scaling up" (Quattrochi and Goodchild 1997).

Phenomena such as the urban heat island effect can benefit from being studied at multiple spatial scales to both better resolve the connections between urban microclimates and the overall heat island (Gluch et al. 2006; Hartz et al. 2006;

Table 17.1 Spatial resolution and application scale of optical remote sensing image products (modified after Neer 1999)

| Spatial resolution (m) | Definition | Remote sensing sensor | Application scale | Urban monitoring purposes |
|------------------------|---------------------------|----------------------------------------------------|---------------------|---------------------------------------------------------------|
| 0.1–0.5 | Extremely high resolution | Aircraft: ADS40, DMC, HRSC-AX, Ultracam | 1:500–1:5,000 | Cadastral mapping and surveying (e.g., streets and buildings) |
| >0.5–1.0 | Very high resolution | Satellite: Ikonos, Orbview, Quickbird (pan) | 1:5,000–1:10,000 | Vegetation, single tree mapping, traffic monitoring |
| >1.0–4.0 | High resolution | Satellite: Ikonos, Orbview, Quickbird (ms) | 1:10,000–1:15,000 | Vegetation health analysis |
| >4.0–15 | Medium resolution | Satellite: SPOT (ms), ASTER, IRS (pan), ETM+ (pan) | 1:15,000–1:25,000 | Identification of urban blocks |
| >15–50 | Low resolution | Satellite: ASTER, IRS, Landsat ETM (ms) | 1:25,000–1:100,000 | Urban structure mapping |
| >50–250 | Very low resolution | Satellite: Landsat MSS, MODIS | 1:100,000–1:500,000 | Definition of urban areas |
| >250 | Extremely low resolution | Satellite: NOAA, Meteosat | >1:500,000 | Identification of populated areas |

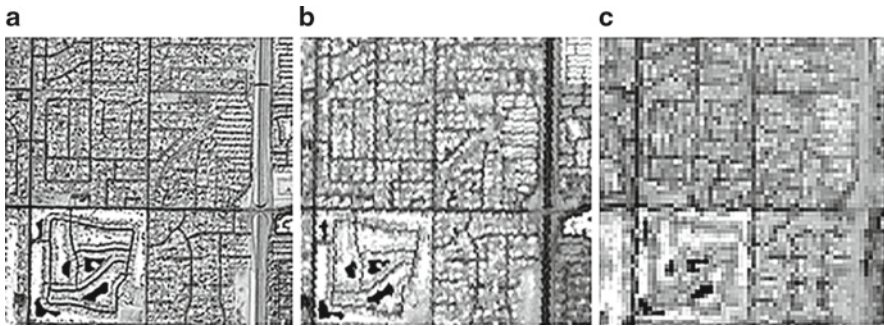


Fig. 17.1 (a) Quickbird (March 2, 2002, pixel size: 2.39 m), (b) ASTER (February 24, 2005, pixel size: 15 m), and (c) enhanced thematic mapper (April 19, 2000, pixel size: 30 m) images of Scottsdale, AZ, USA (spatial extent: 2,000 × 2,000 m)

Dousset and Gourmelon 2003; Oke 1973) Working with images at multiple spatial scales can also resolve linkages between remotely sensed phenomena, like the urban heat island effect, and socioeconomic variables at varying scales, such as between a small neighborhood and a census tract (Harlan et al. 2006; Jenerette et al. 2007)

Temporal resolution is sometimes overlooked, but it has particular importance in urban remote sensing. Temporal resolution is also referred to as “repeat time” and refers to the period of time it takes a sensor to return to a location for reimaging. Urban remote sensing is frequently used in studies that assess change in urban form over time. While a very high-resolution aerial image may yield a desired spatial resolution and/or spectral resolution, a lack of the desired repeat coverage may not serve the study’s needs (Quattrochi and Goodchild 1997; Möller 2005).

17.1.2 Spectral and Radiometric Properties for Urban Monitoring

Urban areas represent various objects. Most of them are human engineered features and artificial objects built from various different materials. These surface materials often vary only in slight ranges. For example, a new terra cotta roof appears brighter when compared to a roof made of the same material under daily weather influence for a 10-year time period. As a consequence, urban objects usually appear with a large number of individual spectral signatures in a remote sensing image (Lacherade et al. 2005), depending on the surface materials and the their condition (e.g., concrete, clay and tar, or metal).

Spectral libraries form the basis for a comprehensive investigation of materials such as minerals, rocks, vegetation, and man-made materials. Price (1995) developed the first urban spectral library for urban areas. Ben-Dor (2001) used Price’s library

to investigate the urban surface materials in Tel-Aviv, Israel. Herold et al. (2004) and Small (2003) studied urban areas in North America. Hook (1998) developed the ASTER spectral library, which is a compilation of natural and man-made materials, and includes data from three sources: the Johns Hopkins University (JHU) spectral library, the Jet Propulsion Laboratory (JPL) spectral library, and the United States Geological Survey (USGS) spectral library. The existing urban libraries always collect spectral reflectance measurements in their specific region of interest. Thus, a new spectral library was developed to assess spectral characteristics of urban surface materials used in German cities by Heiden et al. (2007).

Small and Lu (2006) examine some characteristics of vegetation distributions for several contrasting urban settings. Spectral mixture analyses are used to estimate areal fractions of vegetation, substrate, and nonreflective surfaces from high spatial resolution Quickbird multispectral images.

The ASTER spectral library (<http://speclib.jpl.nasa.gov/>) lists a number of specific reflectance curves for different construction materials. Almost 1,800 different reflectance curves for specific surface materials are listed in this library, of which, at least 56 individual reflectance curves relate to different human-made materials. A selection of these curves for typical urban material is depicted in Fig. 17.2. A sensor with a wide spectral range and resolution (e.g., number of bands) is highly recommended for use in an urban monitoring or change detection analysis. The ASTER sensor offers such spectral resolution. The VNIR and SWIR bands are excellent image data sources to differentiate urban surface materials.

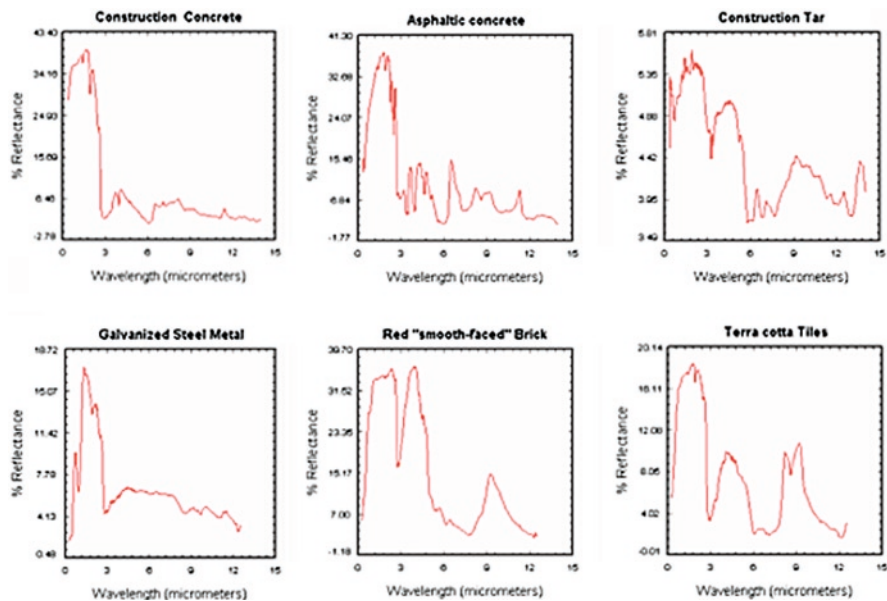


Fig. 17.2 Reflectance curves for typical urban surfaces. *Source:* ASTER spectral library source: <http://speclib.jpl.nasa.gov/>

A comparison of the spectral curves in Fig. 17.2 with ASTER's spectral ranges in Fig. 17.3 clearly shows how artificial surface materials are differentiated. Vegetation is another important urban material to detect and differentiate several tasks. ASTER bands 2 and 3 sense the red and near infrared portions of the reflected electromagnetic spectrum, and provide reliable sources to calculate vegetation indices like normalized difference vegetation index (NDVI) or SARVI (Huete et al. 1994).

ASTER bands are also designed for an optimum atmospheric transmission. Figure 17.4 shows a comparison of the ASTER band layout with those of Landsat ETM+. The Landsat series has become the main workhorse for land use/land cover (LULC) analysis and mapping over the past three decades. This band layout has therefore become a standard for other optical sensor systems such as Ikonos, Quickbird, and Orbview. As a consequence, present and future remote sensing systems are recommended to consider this highly approved layout. This guarantees a LULC change detection analysis even over long time periods. Not only ASTER, but also the series of high spatial resolution satellite sensors such as Ikonos, Orbview, and Quickbird follow the spectral band ranges introduced originally by the Landsat sensor series. This enables a multisensor long term monitoring of urban changes on different scales.

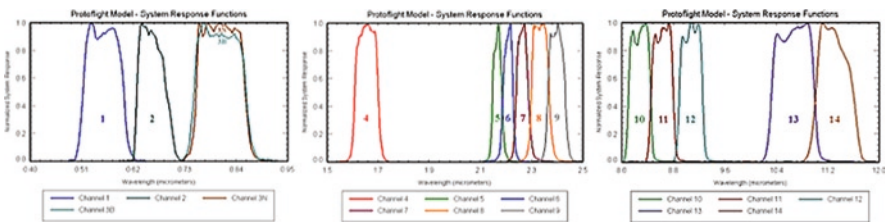


Fig. 17.3 ASTER spectral band properties. Source: <http://asterweb.jpl.nasa.gov/characteristics.asp>

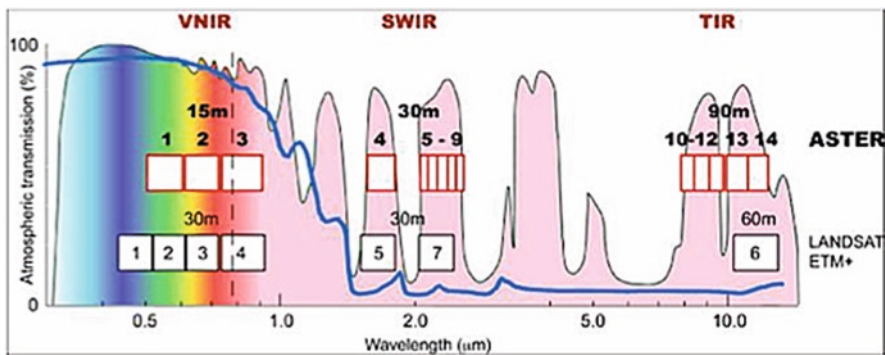


Fig. 17.4 ASTER and ETM band ranges and atmospheric transmission. Source: <http://asterweb.jpl.nasa.gov/images/spectrum.jpg>

17.1.3 Height Extraction

Compared to undisturbed natural land, most urban areas vary in different object heights, leading to a very inhomogeneous surface with a high frequency. This specific urban texture is extractable from high-resolution digital surface model (DSM) data using edge-sharpening filters, proven as a reliable method to delineate urban areas. Texture information is an input source for urban climate models, because wind patterns are influenced by the height of buildings. Summer surface ozone, for example, cannot lead out of the inner city if the wind field is weak. A redirected wind stream might disturb the entire urban heat flux. To avoid these phenomena, detailed information about urban building height in combination with textural analysis of the urban upper surface may prove beneficial.

ASTER records spectral information in the visible, near and short-wave infrared wavelengths with two identical sensors pointing in two directions: nadir (band 3N) and backward in flight direction (band 3B), each with 15-m spatial resolution. The data with two different viewing angles are combined in a stereoscopic model to compute a Digital Elevation Model (DEM). An ASTER relative DEM is one of the several standard products available from the Land Processes DAAC in the US, and ERSDAC in Japan.

17.1.4 ASTER Science Team Acquisition Request (City STAR) for Urban Areas and Urban Environmental Monitoring Project at Arizona State University

Regional monitoring datasets and the Global Map are acquired by ASTER, in response to acquisition requests submitted by the ASTER Science Team acting on behalf of the science community. The ASTER Science Team submits a Science Team Acquisition Request (STAR) for regional monitoring following the submission and acceptance of a relevant proposal. The purpose of the urban STAR is to provide a dedicated observation strategy for urban environmental monitoring around the world. The Urban Environmental Monitoring (UEM) project, recently renamed the “100 Cities Project” (<http://100cities.asu.edu>), at Arizona State University as part of the ASTER Science team, is the major user of the urban STARs and serves as multiplier for urban applications around the globe. The project studies approximately 100 of the largest urban centers with an emphasis on those in arid and semiarid environments (~75% of STAR requests). The chosen cities represent areas experiencing rapid growth and/or currently have populations of approximately 1 million people (Fig. 17.5). Today, the project sees its role as a platform to bring policymakers and researchers together to address cities and their problems with urban remote sensing.

ASTER data are being integrated within the project with a wide range of other remotely sensed data (MODIS, Landsat, and astronaut photography). The project focuses on nine cities. They include Chiang Mai/Thailand, Berlin/Germany,

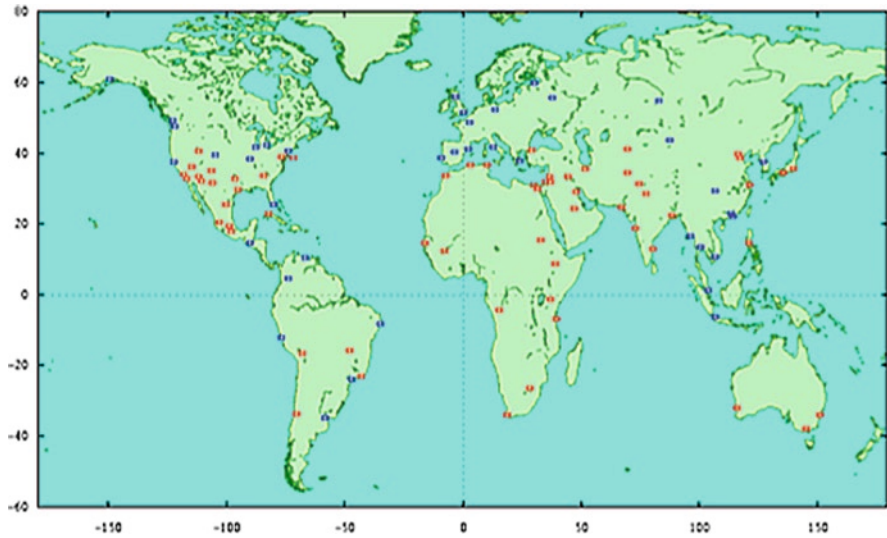


Fig. 17.5 Location map of city targets

Cairo/Egypt, Canberra/Australia, Delhi/India, Lima/Peru, Manila/Philippines, Mexico City/Mexico, and Phoenix/Arizona, USA. They were selected because they represent varying stages of urban development, and their location within a wide range of geographic, geologic, climatic, social, and historical contexts. The UEM project has extensively used ASTER data for urban analysis (Netzband and Stefanov 2003, 2004; Ramsey 2003; Stefanov and Netzband 2005, 2010; Stefanov et al. 2001). Recently, Wentz et al. (2008) report about efforts to duplicate the expert system model developed for Phoenix, Arizona (Stefanov et al. 2001; Stefanov and Netzband 2005) as a generalized approach for urban land use classification, exemplified for Delhi, India. Results suggest that reusing some parts of the methodology is viable, but certain local factors (e.g., data availability and specific land features) necessitate modifying the approach.

The main objectives of the Urban Environmental Monitoring (UEM) research are as follows:

- (1) Timely and continuous monitoring of rapidly urbanizing regions using EOS (and other) remotely sensed datasets to characterize rates of urban change and provide policy makers with information about their urban development trajectories.
- (2) Mapping and modeling of urban/peri-urban, biogeophysical and climatic properties (both current and historic) complementary to field-based studies.
- (3) Advance the understanding of urban development trajectories and urban futures using these mapping and modeling results.
- (4) Develop an international network of urban data providers, researchers and end-users to rapidly disseminate and archive data, analytical approaches and results.

17.2 Technical Specification and Applications for Urban Analysis

17.2.1 *Urban Vegetation and Open Space Detection Versus Developed and Impervious Surfaces*

Monitoring urban vegetation, their extent and biophysical characteristics are very important for urban planning, environmental protection and policymaking. Precise, reliable, and meaningful measurement of urban vegetation cover helps planners, decision-makers and urban researchers in their daily work. The NDVI, which is representative of vegetation's photosynthetic efficiency, is widely used to present vegetation cover from different data sources (see an overview in Zhu et al. 2003) and for various applications. In arid regions, the soil adjusted vegetation index (SAVI) is often used since it takes into account the high soil reflectance values in arid landscapes and other environments (Rondeaux et al. 1996; Huete 1988). ASTER's broad SWIR wavelength coverage allows for the measurement of important biogeophysical variables in urban/peri-urban regions such as vegetation density. Vegetation density is also important for modeling of urban climate, urban ecology, hydrology, and water use (Jenerette et al. 2007; Grove et al. 2006; Hope et al. 2003; Avissar 1996; Quattrochi and Ridd 1998).

Figure 17.6 is a Visible and Near Infrared (VNIR) false color composite of parts of the Greater Phoenix area, USA; regions with reddish tones having high density of actively photosynthesizing vegetation, and bluish/greenish regions having little to no vegetation. These are primarily exposed bedrock and soils. Urban built materials show as other blue-green, reddish-purple, and white colors.

Braun and Herold (2003) explore ASTER data and common techniques of linear spectral unmixing and NDVI to map and visualize the degree of imperviousness in the urban areas of Cologne-Bonn (Germany). The results indicate that spectral unmixing is disturbed if rural agricultural areas with significant amount of bare soil (spectrally highly variable) are included in the analysis. The remote sensing-derived vegetation parameters (NDVI, vegetation fraction) were found most suitable to estimate the impervious surface composition. A regression between them and the measured degree of imperviousness did indicate a good negative correlation. The mapping from the built-up fraction cover is less successful because of their high spectral variability, all of which is not accounted by the linear spectral unmixing technique. The resulting maps of impervious cover show a good representation of the impervious surface pattern in the urban areas and emphasize the urban morphology. In rural areas, however, this approach is less successful and the estimated degrees of imperviousness require a cautious treatment.

Zhu et al. (2003) propose a new method based on advanced segmentation techniques and classification for urban vegetation extraction to overcome the so-called modifiable areal unit problem (MAUP) caused by per-pixel vegetation distribution of traditional NDVI-based methods. This method uses ASTER data to build a hierarchical multiresolution structure, so as to reflect the inherent relationship between

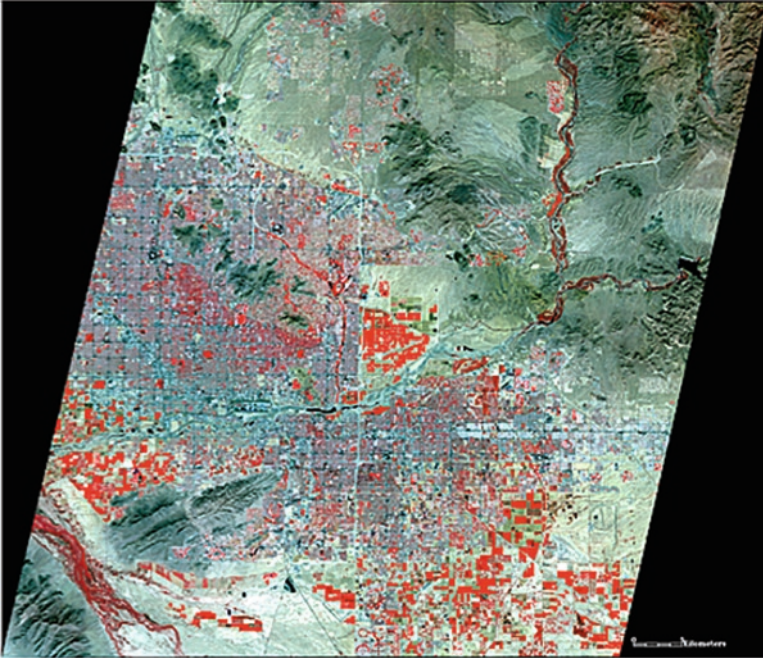


Fig. 17.6 ASTER VNIR image of the Phoenix/USA metropolitan region

ground features under various scale levels. By analyzing the hierarchical structure, a flexible measurement of urban vegetation cover index (VCI) is issued based on remotely sensed images.

17.2.2 Urban Landscape Structure

Continuing development inevitably changes and constrains the structure and area of natural green spaces in conurbations. Pervious natural surfaces are frequently rendered impervious by the emplacement of built materials. Also, partly new open spaces result from conversion of former industrial sites to commercial and residential uses. In addition, within the suburban area, new potential for open space and increased ecosystem services may result from revaluation and transformation to park, woodland and forest surfaces. Such a situation also calls for observation and evaluation instruments to plan for the future regional development across the entire city region.

Landscape metrics deliver a starting point to compare urban areas not dependant on their physical and cultural setting by providing measures of the distribution and shape of ecological patches on the landscape (McGarigal and Marks 1994;

Zipperer et al. 2000). Those metrics have been applied to remotely sensed data at different mapping scales to emphasize the spatial content and patch distribution of classified data (Turner et al. 1989; Wu et al. 2000). Several recent studies (Alberti and Waddell 2000; Barnsley and Barr 2000; Herold et al. 2002; Rainis 2003; Whitford et al. 2001) demonstrate the usefulness of landscape metrics to assess and evaluate urban structure and ecology. Patch sizes for urban ecological studies have been delineated through the use of multiple scales of remote sensing images and use of both object- and pixel-based classification (Grimm et al. 2008; Cadenasso et al. 2007; Keitt et al. 1997).

Stefanov and Netzband (2005) investigate the usefulness of MODIS NDVI data at scales of 1 km/pixel, 500 m/pixel, and 250 m/pixel to characterize, monitor, and model biophysical change related to arid urban landscape structure (as defined by a suite of landscape metrics). For this task, a six-class ASTER land cover classification for the Phoenix area (Asphalt, Soil and Bedrock, Agriculture, Undifferentiated Vegetation, Built and Water) was used to compare with the MODIS data. Those classes were found to retain the physical variability of the major land cover classes in the Phoenix study area at the 15 m/pixel scale while also reducing the number of segments for landscape metric calculation. Three grids (250 × 250 m, 500 × 500 m, and 1 × 1 km) were created from the reprojected MODIS data pixels to directly compare with the landscape metric results. The metric results were averaged over each grid element to compare with the MODIS NDVI data using Pearson correlation coefficients at the three grid scales.

A large number of metrics are available for urban analysis; some examples include class area, mean patch size (a measure of the clump size of similarly classified pixels), edge density (a measure of patch or class neighborhood shape complexity) and interspersion/juxtaposition index (how dispersed or clumped together a class is on the landscape). This suite of metrics was selected as best capturing the key spatial aspects of urban landscape structure to compare with the different scales of MODIS NDVI data. Figure 17.7 depicts the interspersion/juxtaposition index (IJI) for the Built land cover classes in the Phoenix urban core area, and illustrates the relatively high degree of mixing with other land cover classes in the region.

A correlation analysis between the landscape metric results and MODIS NDVI data reveals that even at the 250-m pixel scale, there is no clear control of the vegetation pattern by the landscape structure. This warrants consideration particularly for comparative studies of numerous urban agglomerations. While the MODIS data demonstrate their usefulness for regional assessments of vegetation pattern and time-series analysis, the results suggest a need for data with both higher spatial and temporal resolution (or application of data fusion/sharpening techniques) to address the urban and peri-urban landscape change research needs of urban environmental studies.

In general, while using spatial metrics on classified mid- to high-resolution remote sensing data, considering the spatial resolution, the study area extent, and the classification level of detail are important. Changes can significantly alter the metric results and limit the value of inter-urban comparisons. Given a uniform grid scheme, this method provides a practical solution.

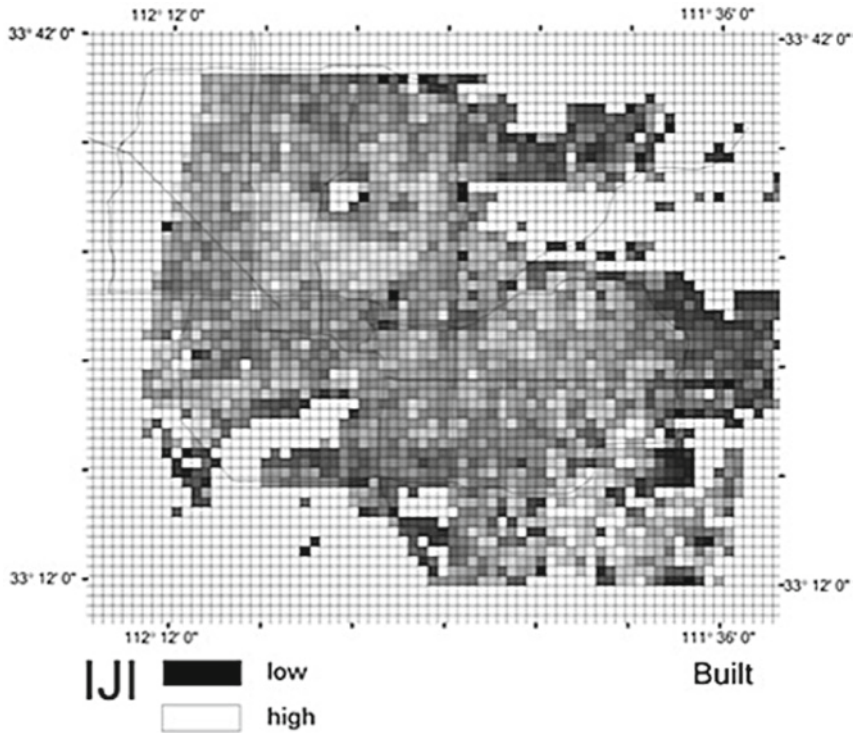


Fig. 17.7 Interspersion/juxtaposition index calculated from Phoenix land cover data

17.2.3 Thermal Analysis and Pattern

The ASTER instrument's forte is its ability to collect multispectral thermal infrared data. In particular, nighttime data over urban regions can deliver urban/peri-urban surface temperature gradients to evaluate urban heat islands. The distribution of built materials in an urban landscape is an important consideration while constructing thermal budgets. However, how the surrounding natural materials potentially contribute to the regional thermal budget is equally important. Satellite-derived data provide a dense grid of near-instantaneous temperature measurements over a city, which facilitates visualizing spatial relationships between temperature patterns and urban land use. For example, the Phoenix, AZ metropolitan region is bounded by mountain ranges with little vegetation cover; these ranges act as large thermal emitters during night and have surface temperatures equivalent to urban core asphalt and concrete (Fig. 17.8). This surface temperature information is valuable to investigate urban climatic patterns and initialize climate models.

This validated version of the TIR surface leaving radiance product (asterweb.jpl.nasa.gov/content/03_data/01_Data_Products/SurfaceRadiance-TIR.pdf) provides



Fig. 17.8 Surface temperature map of the Phoenix metropolitan area

an estimate of the total radiance leaving the surface including any reflected sky component and an estimate of the sky irradiance for each of the five ASTER TIR bands. Since the surface leaving radiance is closely associated with the thermal properties of the surface itself, the surface kinetic temperature is directly obtainable, given the information provided with this product, provided that the spectral emissivity of the surface is known. Spectral emissivity is useful to estimate surface land cover composition, a major component in urban ecological planning. Remote sensing-derived thermal images provide great potential to improve our understanding of the urban surface energy budgets, and observing the urban heat island (UHI) effect. Remotely sensed thermal images can provide a time-synchronized dense grid of temperature data over a whole city and distinctive temperatures for individual buildings. A number of studies based on ASTER thermal infrared data exist, as described by the following examples.

Fukui et al. (2002) present an ASTER and LIDAR data study based on the surface temperature distribution and the urban structure in Tokyo. Two different ASTER scenes were used to calculate the surface temperature. The correlation of

the surface temperature and the urban structure demonstrates the impact of green areas on the urban heat environment and the falling of surface temperature in tall buildings during daytime and increasing surface temperature during nighttime.

According to Yamaguchi et al. (2004), a new method was developed that separately evaluates the contributions of anthropogenically discharged heat and natural heat radiation to heat flux, based on a heat balance model using satellite remote sensing and ground meteorological data. This method was applied to the ASTER and ETM+ data of Nagoya, Japan. The authors found that the increased sensible heat flux due to anthropogenic activities in the central part of the city was approximately twice than that in the surrounding residential areas during summer. MODIS data were also used to estimate temporal variations in surface heat fluxes in urban areas. In daytime, the sensible heat flux was high in urban areas, and was nearly zero in all areas at nighttime. The authors contend that a combination of ASTER/ETM+ and MODIS data is a powerful tool to analyze the spatial and temporal variations of surface heat fluxes in urban areas.

Nichol et al. (2003) performed an urban climate study comparing daytime and nighttime thermal images of Hong Kong. This microclimate monitoring study evaluates thermal infrared data in two densely built high-rise towns in Hong Kong's New Territories. The ASTER surface kinetic temperature data derived from ASTER thermal bands corrected for emissivity and atmospheric effects were used.

Buyantuyev et al. (2006) implement the method proposed by Schmugge et al. (1998) and Kato and Yamaguchi (2005) to estimate heat fluxes and separate the anthropogenic discharged heat and natural heat radiation from the sensible heat flux in urban areas by combining remote sensing and meteorological data. They used cloud-free and atmospherically corrected ASTER level-1B data and level-2 surface spectral reflectance, spectral emissivity, and surface temperature products. The nominal ground spatial resolution is as follows: 15 m for VNIR, 30 m for SWIR, and 90 m for the TIR channels. Narrow band spectral emissivities were converted to broadband emissivity using the linear equation proposed by Ogawa et al. (2003).

In a study conducted by Nakamura et al. (2002), ASTER/TIR is considered appropriate to make a surface temperature map, because it has multiple thermal infrared bands, so surface temperature and emissivity are resolved independently. It was confirmed that medium-resolution ASTER data and ground truth data could facilitate producing distribution maps of surface and air temperature with similar high resolution. After adjusting these two maps, the convective heat transfer rate value is multiplied.

To better understand the relationship between urban biophysical and thermal conditions, Lu and Weng (2006) explored thermal features and their relationship with biophysical descriptors by analyzing multitemporal ASTER images in an urban environment. Linear spectral mixture analysis was used to unmix the five TIR bands into hot-object and cold-object fraction images, and to unmix the nine VNIR, and SWIR bands into impervious surface, green vegetation, and soil fractions. Land surface temperatures (LSTs) were computed from ASTER band 13 (10.25–10.95 μm). LST and the five derived fraction variables (ranging across 15–90 m spatial resolution) were correlated to examine their relationship. Multiple regression models were further developed to reveal how LSTs were related to urban

biophysical descriptors (i.e., impervious surface, green vegetation, and soil) and to the thermal feature fractions (i.e., hot-object and cold-object). Results indicate that impervious surfaces were positively correlated, while vegetation was negatively correlated with LST. Hot objects displayed a more significant role in influencing LST patterns than cold objects.

Roy et al. (2007) describe an approach to assess atmospheric pollutants in the troposphere and their spectral characteristic signatures by using high-spectral and spatial resolution ASTER data and its analysis of variance with in situ data obtained with ground-based sensors. This investigation aims to analyze air pollutants in urban and industrial areas with satellite images, and create a model to observe air pollution transport from its source. They use ASTER's high spectral and spatial resolution SWIR and TIR bands and EPA-derived pollutant concentration data, and emission data. Data fusion techniques are used to increase the satellite-derived data's spatial resolution while preserving ASTER data's spectral characteristics. Principal component analysis technique is applied to transform the number of correlated bands into a smaller number of uncorrelated bands. "Density slicing" and "band ratioing" techniques are also applied to extract atmospheric pollutants from the datasets. Traversing techniques across several band sets helped to compare the pollution's spectral signatures. Despite ASTER's broader bandwidth compared to hyperspectral data, a strong correlation between the spectral signatures and the appearance of air pollutants was achieved in the entire study area.

Chrysoulakis (2002) studied multispectral remote sensing's potential to support urban planning by estimating the spatial distribution and intensity of physical parameters in relation to the urban radiation budget. Sustainable urban planning demands the study of urban climatic environments, and the application of this knowledge to improve the inhabitant's quality of life. ASTER multispectral images enable a better understanding of energy aspects, and their causes and effects provide an important addition to conventional methods of monitoring the urban environment. The optical characteristics of materials used in urban environments, and especially, the albedo to solar radiation, and emissivity to long wave radiation relationships have significant impacts on the urban energy balance. The study finds ASTER visible and TIR images provide substantial information to examine the microclimatic conditions of the Athens area, while VNIR data facilitate defining land cover composition by urban, industrial, and vegetated areas.

17.3 Monitoring Urban Areas: Latest Urban Environmental Monitoring Project Research Endeavors

This chapter's larger aim focuses attention on two studies recently performed in the UEM program, which use an object-based image analysis. This approach provides new classification opportunities that are beyond conventional pixel-based methods, since spectral information, texture, form and location (neighborhood) are all taken

into account (Blaschke and Strobl 2001; Burnett and Blaschke 2003; Benz et al. 2004). In an object-based image analysis, two procedures are distinguished (1) one-level representation (OLR) (Lang and Langanke 2006) and (2) multiscale segmentation/object-relationship modeling (MSS/ORM) (Burnett and Blaschke 2003). Both studies use the latter procedure.

17.3.1 Object-Oriented Land Use/Land Cover Classification: Phoenix Versus Las Vegas

Heavy construction activity is observed especially in areas with ample surrounding space and inexpensive land. Both Las Vegas, NV and Phoenix, AZ belong to these typical boom areas in the Southwest U.S., and are included in the UEM's recently renamed the 100 Cities Project. The study's overall objective is to develop a robust and transferable algorithm to automatically detect and analyze urban features, which is valid for these two natural regions (Schöpfer and Moeller 2006). Existing methods to detect and map LULC for urban areas are mainly based on pixel-based classification approaches, whereas this study uses an object-based image analysis approach.

Both studies use ASTER images acquired April 1, 2005 for Phoenix, and May 1, 2005 for Las Vegas. The Phoenix site covers an area of approximately $48 \times 60 \text{ km}^2$, whereas the Las Vegas ASTER mosaic contains two images clipped to a $60 \times 60 \text{ km}^2$ area. The desert-inspired very low absolute humidity and lack of meteorological influences like fog render atmospheric correction inessential.

The first step involved establishing a sophisticated cognition network based on UEM project definitions for the Phoenix metropolitan area (Stefanov et al. 2001) to generate the class hierarchy. The Phoenix image was used to develop a rule-based classification system with specific descriptive features and fuzzy membership functions. The object-based approach increases the set of features to use in the class modeling process. Besides spectral information, additional parameters are available to distinguish target classes and calculate custom features. The NDVI was calculated to identify vegetated areas. Mean values from the SWIR bands 4 and 5 were computed to increase the separability between clouds and shadows. Table 17.2 provides the class definitions.

Finally, the developed classification scheme was transferred to the Las Vegas image. The values of the class membership functions defined were not adjusted to test the ability for an automated transferability of the class hierarchy. The classifications on such a medium scale resulted in an overall accuracy rate of 84.24% ($K^{\wedge} = 0.8268$) for Phoenix, and 83.33% ($K^{\wedge} = 0.8148$) for Las Vegas using 195 randomly distributed points. Figure 17.9 shows both ASTER data and classification results for Phoenix and Las Vegas.

The most challenging task of this study was to develop a class hierarchy, applicable with little or no adaptations, from one particular metropolitan urban area to another in a similar natural environment. This mainly depends on the features used to describe classes. The study reveals that object form and shape properties

Table 17.2 Rule-based class definition for object-based classification; the fuzzy membership functions describe feature intervals wherein the objects do belong to a certain class or not by a certain degree

| Class name | Features/rules | Membership function |
|-----------------------|-------------------------------------------|---------------------|
| Disturbed | Stddev VNIR 1 | |
| Asphalt | NDVI | |
| | Length/width | |
| Commercial/industrial | NDVI | |
| Mesic residential | NDVI | |
| Xeric residential | NDVI | |
| Soil | Stddev VNIR 1/ Stddev VNIR 2 | |
| Compacted soil | Similarity to classes not Canals | |
| Canals | Rel. border to WATER neighbor objects | |
| | Distance to WATER neighbor objects (m) | |
| Undisturbed | Stddev VNIR 1 | |
| Vegetation | NDVI | |
| Cultivated land | Area (km ²) | |
| | Rectangular fit | |
| Cultivated grass | NDVI | |
| Cultivated vegetation | NDVI | |
| Vegetation | Similarity to classes not cultivated land | |
| Water | Mean VNIR 3 | |
| Clouds | (Mean TIR 4) – (Mean TIR 5) | |
| | Area (m ²) | |
| Shadow | (Mean TIR 4) – (Mean TIR 5) | |
| | Area (m ²) | |

appear relatively stable for class definitions, whereas spectral properties appear slightly variable. The usability and reusability of rule sets are feasible for ASTER images from one specific natural environment.

Notwithstanding the fact that an object-oriented classification may lead to more defined boundaries, users should carefully note if their classification leads to errors of commission or omission.

17.3.2 Urban Land Cover Mapping Using ASTER: A Concept for Designing Practical Classification Schemes for “100 Cities”

The 100 Cities Project considers performing urban land cover mapping for 100 global cities. A study was conducted with the goal to develop a classification method, which provides >80% accuracy with ASTER data alone. The overall target

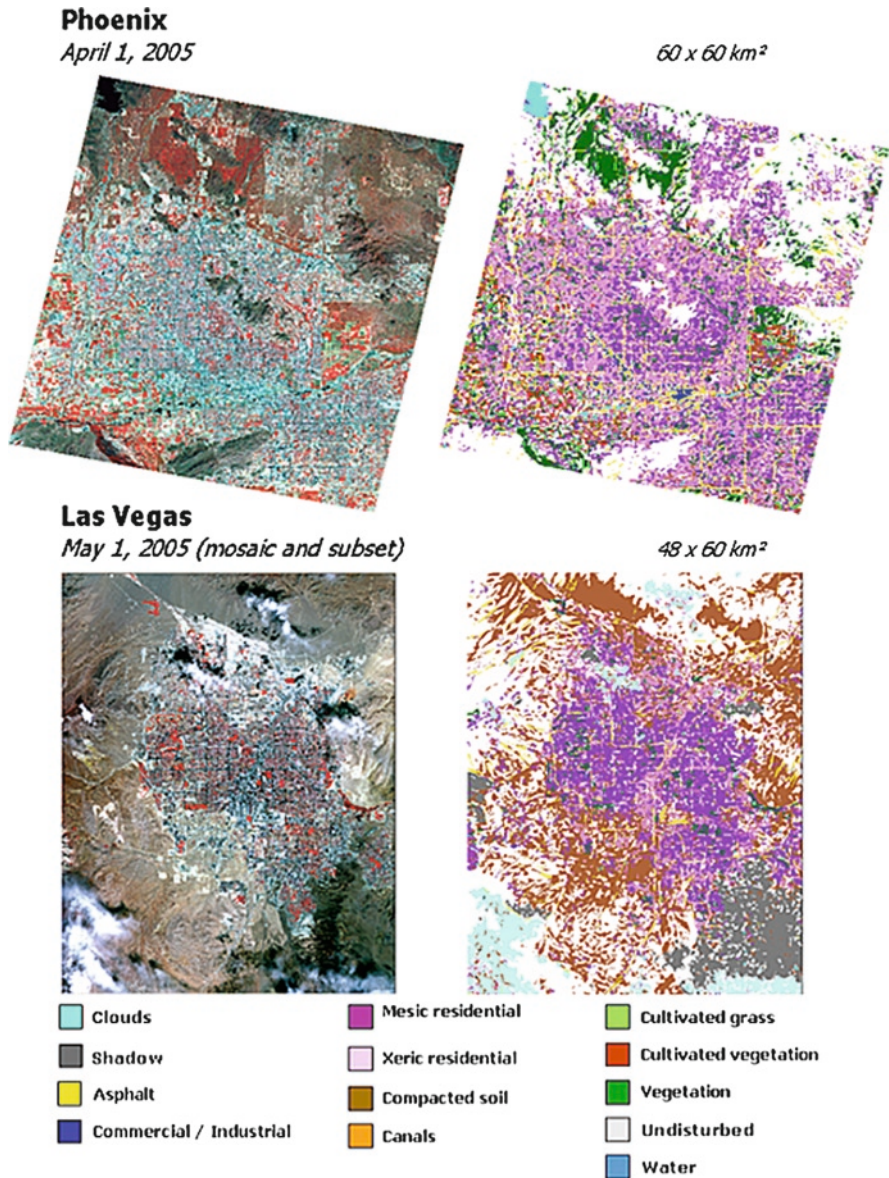


Fig. 17.9 ASTER images and classification results for Phoenix (April 1, 2005) and Las Vegas (May 1, 2005)

is to design a more universal and transferable urban classification scheme with five basic classes using an object-based approach.

For the study, eight so-called “intensive study” cities from the 100 Cities project were selected, and ASTER data acquired (see Table 17.3).

Table 17.3 ASTER satellite data for the eight intensive study cities

| City | Acquisition date |
|-----------------------|-------------------|
| Phoenix (USA) | April 1, 2005 |
| Mexico City (Mexico) | April 4, 2005 |
| Delhi (India) | February 4, 2001 |
| Chiang Mai (Thailand) | February 20, 2001 |
| Berlin (Germany) | May 9, 2002 |
| Canberra (Australia) | February 12, 2001 |
| Lima (Peru) | March 19, 2001 |
| Manila (Philippines) | March 18, 2002 |

Table 17.4 Classification scheme (modified after NLCD)

| Class | Properties |
|------------------------|------------------------------------------------------------------------------------------------------------------------------------------------------------------|
| High density developed | Constructed materials account for 80–100% of the cover; vegetation accounts for less than 20% of the cover |
| Low density developed | Constructed materials account for 30–80% of the cover; vegetation may account for 20–70% of the cover |
| Water | All areas of open water or permanent ice/snow cover |
| Barren | Areas characterized by bare rock, gravel, silt, clay or other earthen material, with little or no “green” vegetation. Most pronounced in arid urban environments |
| Vegetation | Areas characterized by vegetation (tree canopy, shrub land, herbaceous upland, planted/cultivated vegetation or other “green” vegetation) |

In the beginning, target classes were defined based on the NLCD classification system (see Table 17.4). In addition, *shadow* and *clouds* classes were introduced and classified to create a mask for the respective scenes.

In the first step, the *clouds* and *shadows* classes were classified. Hence, a new feature introduced by Schöpfer and Moeller (2006) using the SWIR band’s (4 and 5) mean value was calculated. Additionally, the green band’s mean value, and the ratio between the green band and the overall brightness were used. The *developed areas* are classified on a very fine sublevel using the green band’s standard deviation. Subsequently, a threshold is defined to distinguish between *high* and *low density developed* on a coarser segmentation scale. Therefore, a relationship between the subobjects is defined accordingly. The barren class is separated using the green band’s standard deviation. The mean values of the NIR band 3 and SWIR band 4 are used to classify water. Finally, the NDVI is calculated and also used to detect vegetated areas.

17.4 Conclusions and Outlook

This ASTER urban application demonstrates significant potential to further urban landscape analysis and measures of ecosystem function, and may benefit urban ecologists, climatologists, and planners. Remote sensing provides useful monitoring

tools to analyze regional habitats and climatic alteration associated with urbanization. Remote sensing affords a uniform spatial reference system, which enables a quantitative evaluation of existing developed and open spaces. The current use of remote sensing in urban studies on various temporal, spectral, and spatial scales facilitate scientists to investigate ecological, climatic and socioeconomic effects of increasing global urbanization. The current UEM/100 cities project integrates a wider range of remotely sensed data (ASTER, MODIS, Landsat, and astronaut photography) to characterize and model urban-development trajectories and resilience to environmental stressors for eight intensively studied cities: Chang Mai, Thailand; Berlin, Germany; Canberra, Australia; Delhi, India; Lima, Peru; Manila, Philippines; Mexico City, Mexico, and Phoenix, USA. The primary goal is to develop an international network of urban data providers, researchers and end-users by making urban remote sensing products and processes useful and available to cities for planning and policymaking. With a growing team of researchers and practitioners at Arizona State University, and at other institutions around the world that share datasets and collaborate on publications and research, the project further intends to make a significant contribution to urban remote sensing applications.

Acknowledgments Funding was provided by a NASA EOS/ASTER Team Member Investigation grant to P.R. Christensen. Additional funding was provided by a National Science Foundation Long Term Ecological Research grant to N.B. Grimm and C.L. Redman.

References

- Alberti M, Waddell P (2000) An integrated urban development and ecological simulation model. *Integr Assess* 1:215–227
- Avisar R (1996) Potential effects of vegetation on the urban thermal environment. *Atmos Environ* 30(3):437–448; Conference on the Urban Thermal Environment Studies in Tohwa, Japan, pp 437–448
- Barnsley MJ, Barr SL (2000) Monitoring urban land use by Earth observation. *Surv Geophys* 21:269–289
- Ben-Dor E (2001) Imaging spectrometry for urban applications. In: Van der Meer FD, De Jong SM (eds) *Imaging spectrometry: basic principles and prospective applications*. Kluwer, Dordrecht
- Benz U, Hofmann P, Willhauck G, Lingenfelder I, Heynen M (2004) Multi-resolution, object-oriented fuzzy analysis of remote sensing data for GIS-ready information. *ISPRS J Photogramm Remote Sens* 58:239–258
- Blaschke T, Strobl J (2001) What's wrong with pixels? Some recent developments interfacing remote sensing and GIS. In: *Proceedings of GIS – Zeitschrift für Geoinformationsysteme*, vol. 6, pp 12–17
- Braun M, Herold M (2003) Mapping imperviousness using NDVI and linear spectral unmixing of ASTER data in the Cologne-Bonn Region (Germany). In: *Proceedings of the SPIE 10th International Symposium on Remote Sensing*, Barcelona, Spain, 8–12 September 2003
- Burnett C, Blaschke T (2003) A multi-scale segmentation/object relationship modelling methodology for landscape analysis. *Ecol Model* 168(3):233–249
- Buyantuyev A, Brazel A, Eisinger C (2006) Estimating heat fluxes and the Urban Heat Island (UHI) of Phoenix with remote sensing and meteorological data. In: Poster presented at the 8th Annual Central Arizona – Phoenix Long-Term Ecological Research Poster Symposium

- Cadenasso ML, Pickett STA, Schwarz K (2007) Spatial heterogeneity in urban ecosystems: reconceptualizing land cover and a framework for classification. *Front Ecol Environ* 5(2):80–88
- Chrysoulakis N (2002) Energy in the urban environment: use of Terra/ASTER imagery as a tool in urban planning. *J Indian Soc Remote Sens* 30:245–254
- Doussot B, Gourmelon F (2003) Satellite multi-sensor data analysis of urban surface temperatures and landcover. *ISPRS J Photogramm Remote Sens* 58(1–2):43–54; Algorithms and Techniques for Multi-Source Data Fusion in Urban Areas
- Fukui Y, Hirose Y, Mushiaki N (2002) A study on the surface temperature distribution and the urban structure in Tokyo with ASTER and LIDAR data. In: Proceedings of Geoscience and Remote Sensing Symposium (IGARSS'02), vol. 4, pp 24–28
- Gluch R, Quattrochi DA, Luvall JC (2006) A multi-scale approach to urban thermal analysis. *Remote Sens Environ* 104(2):123–132
- Grimm NB, Grove JM, Pickett STA, Redman CL (2008) Integrated approaches to long-term studies of urban ecological systems. In: Marzluff JM, Shulenberger E, Endlicher W, Alberti M, Bradley G, Ryan C, Simon U, ZumBrunnen C (eds) *Urban ecology*. Springer, New York, pp 123–141
- Grove JM, Cadenasso ML, Burch WR Jr, Pickett ST, Schwarz K, O'Neil-Dunne J, Wilson M, Troy A, Boone C (2006) Data and methods comparing social structure and vegetation structure of urban neighborhoods in Baltimore, Maryland. *Soc Nat Resour* 19:117–136
- Harlan SL, Brazel AJ, Prashad L, Stefanov WL, Larsen L (2006) Neighborhood microclimates and vulnerability to heat stress. *Soc Sci Med* 63(11):2847–2863
- Hartz DA, Prashad L, Hedquist BC, Golden J, Brazel AJ (2006) Linking satellite images and hand-held infrared thermography to observed neighborhood climate conditions. *Remote Sens Environ* 104(2):190–200
- Heiden U, Segl K, Roessner S, Kaufmann H (2007) Determination of robust spectral features for identification of urban surface materials in hyperspectral remote sensing data. *Remote Sens Environ* 111(4):537–552
- Herold M, Scepan J, Clarke KC (2002) The use of remote sensing and landscape metrics to describe structures and changes in urban land uses. *Environ Plann A* 34(8):1443–1458
- Herold M, Roberts DA, Gardner ME, Dennison PE (2004) Spectrometry for urban area remote sensing – development and analysis of a spectral library from 350 to 2400 nm. *Remote Sens Environ* 91:304–319
- Hook SJ (1998) ASTER Spectral Library. Available online: <http://speclib.jpl.nasa.gov>
- Hope D, Gries C, Zhu W, Fagan WF, Redman CL, Grimm NB, Nelson AL, Martin C, Kinzig A (2003) Socioeconomics drive urban plant diversity. *Proc Natl Acad Sci USA* 100(15):8788–8792
- Huete AR (1988) A soil-adjusted vegetation index (SAVI). *Remote Sens Environ* 25:295–309
- Huete A, Justice C, Liu H (1994) Development of vegetation and soil indices for MODIS-EOS. *Remote Sens Environ* 49(3):224–234
- Jenerette GD, Harlan SL, Brazel A, Jones N, Larsen L, Stefanov WL (2007) Regional relationships between surface temperature, vegetation, and human settlement in a rapidly urbanizing ecosystem. *Landsc Ecol* 22:353–365
- Kato S, Yamaguchi Y (2005) Analysis of urban heat-island effect using ASTER and ETM+ Data: Separation of anthropogenic heat discharge and natural heat radiation from sensible heat flux. *Remote Sens Environ* 99(1–2):44–54
- Keitt TH, Urban DL, Milne BT (1997) Detecting critical scales in fragmented landscapes. *Conserv Ecol* 1:4
- Lacherade S, Miesch C, Lemaitre F, Briottet X, Le Men H, Boldo D, Valorge C (2005) Analysis of the spectral variability of urban materials for classification. A case study over Toulouse (France). In: Proceedings of URBAN 2005 and URS 2005, International Archives of Photogrammetry, Remote Sensing and Spatial Information Sciences, vol. 36, Part 8/W27, ISSN 1682-1777 (on CD)
- Lang S, Langanke T (2006) Object-based mapping and object-relationship modeling for land use classes and habitats. *Photogramm Fernerkund Geoinf* 1–2006:5–18

- Lu D, Weng Q (2006) Spectral mixture analysis of ASTER images for examining the relationship between urban thermal features and biophysical descriptors in Indianapolis, Indiana, USA. *Remote Sens Environ* 104(2):157–167
- McGarigal K, Marks BJ (1994) FRAGSTATS: spatial pattern analysis program for quantifying landscape structure. Oregon State University, Corvallis
- Möller M (2004) Monitoring long term transition processes of a metropolitan area with remote sensing. In: Proceedings of the IEEE International Geoscience and Remote Sensing Symposium (IGARSS), Anchorage, AK
- Möller M (2005) Remote sensing for the monitoring of urban growth patterns. In: Proceedings of the International Society for Photogrammetry and Remote Sensing, Joint Conference
- Nakamura M, Hirano Y, Ochi S, Yasuoka Y (2002) Characterization of urban heat radiation flux using remote sensing imagery. <http://www.gisdevelopment.net/aars/acrs/2002/urb/216.pdf>
- Neer JT (1999) High resolution imaging from space – a commercial perspective on a changing landscape. *Int Arch Photogramm Remote Sens* 32(7C2):132–143
- Netzband M, Stefanov WL (2003) Assessment of urban spatial variation using ASTER data. *Int Arch Photogramm Remote Sens Spatial Inf Sci* 34(7/W9):138–143
- Netzband M, Stefanov WL (2004) Urban land cover and spatial variation observations using ASTER and MODIS satellite image data. *Int Arch Photogramm Remote Sens Spatial Inf Sci* 35(B7):1348–1353
- Nichol J, Hang LK, Wai-Shun AY (2003) A comparison of daytime and night-time thermal satellite images of Hong Kong for urban climate studies. In: Proceedings Map Asia 2003. <http://www.gisdevelopment.net/application/environment/climate/envwm001.htm>
- Ogawa K, Schmutge T, Jacob F, French A (2003) Estimation of land surface window (8–12 mm) emissivity from multispectral thermal infrared remote sensing – a case study in a part of Sahara Desert. *Geophys Res Lett* 30(2)
- Oke TR (1973) City size and the urban heat island. *Atmos Environ* 7(8):769–779
- Price JC (1995) Examples of high resolution visible to near-infrared reflectance and a standardized collection for remote sensing studies. *Int J Remote Sens* 16:993–1000
- Quattrochi DA, Goodchild MF (1997) Scale in remote sensing and GIS. CRC, Boca Raton, FL, p 406
- Quattrochi DA, Ridd MK (1998) Analysis of vegetation within a semi-arid urban environment using high spatial resolution airborne thermal infrared remote sensing data. *Atmos Environ* 32(1):19–33; Conference on the Benefits of the Urban Forest
- Rainis R (2003) Application of GIS and landscape metrics in monitoring urban land use change. In: Hashim NM, Rainis R (eds) *Urban ecosystem studies in Malaysia – a study of change*. Universal Publishers, Parkland, pp 267–278
- Ramsey MS (2003) Mapping the city landscape from space: the advanced spaceborne thermal emission and reflectance radiometer (ASTER) urban environmental monitoring program. In: Heiken G, Fakundiny R, Sutter J (eds) *Earth science in the city: a reader*. American Geophysical Union, Washington, DC, pp 337–361
- Rondeaux G, Steven M, Baret F (1996) Optimization of soil-adjusted vegetation indices. *Remote Sens Environ* 55(2):95–107
- Roy P, Brumfield JO, Vaseashta A (2007) Smog analysis in urban areas using ASTER data and its analysis of variance with in-situ sensors data. In: Technical Proceedings of the 2007 Nanotechnology Conference and Trade Show, vol. 2
- Schmutge TJ, Kustas WP, Humes KS (1998) Monitoring land surface fluxes using ASTER observations. *IEEE Trans Geosci Remote Sens* 36(5):1421–1430
- Schöpfer E, Moeller MS (2006) Comparing metropolitan areas – a transferable object-based image analysis approach. *Photogramm Fernerkund Geoinf* 1/2006:277–286
- Small C (2003) High spatial resolution spectral mixture analysis of urban reflectance. *Remote Sens Environ* 88:170–186
- Small C, Lu J (2006) Estimation and vicarious validation of urban vegetation abundance by spectral mixture analysis. *Remote Sens Environ* 100:441–456

- Stefanov WL, Netzband M (2005) Assessment of ASTER land cover and MODIS NDVI data at multiple scales for ecological characterization of an arid urban center. *Remote Sens Environ* 99(1–2):31–43
- Stefanov WL, Netzband M (2010) Characterization and monitoring of urban/peri-urban ecological function and landscape structure using satellite data. In: Rashed T, Jürgens C (eds) *Remote sensing of urban and suburban areas*. Springer, New York
- Stefanov WL, Ramsey MS, Christensen PR (2001) Monitoring the urban environment: an expert system approach to land cover classification of semiarid to arid urban centers. *Remote Sens Environ* 77(2):173–185
- Turner MG, O'Neill R, Gardner RH, Milne BT (1989) Effects of changing spatial scale on the analysis of landscape pattern. *Landsc Ecol* 3:153–162
- Wentz E, Nelson D, Rahman A, Stefanov WL, Roy SS (2008) Expert system classification of urban land use/cover for Delhi, India. *Int J Remote Sens* 29(15):4405–4427
- Whitford V, Ennos AR, Handley JF (2001) City form and natural process – indicators for the ecological performance of urban areas and their application to Merseyside, UK. *Landsc Urban Plann* 57:91–103
- Wu J, Jelinski DE, Luck M, Tueller PT (2000) Multiscale analysis of landscape heterogeneity: scale variance and pattern metrics. *Geogr Inf Sci* 6:6–19
- Yamaguchi Y, Kato S, Okamoto K (2004) Surface heat flux analysis in urban areas using ASTER and MODIS data. In: *International Symposium on Geoinformatics for Spatial Infrastructure Development in Earth and Allied Sciences*
- Zhu G, Bian F, Zhang M (2003) A flexible method for urban vegetation cover measurement based on remote sensing images. In: *Proceedings Joint ISPRS/EARSel Workshop: High Resolution Mapping from Space 2003*, October 6–8
- Zipperer WC, Wu J, Pouyat RV, Pickett STA (2000) The application of ecological principles to urban and urbanizing landscapes. *Ecol Appl* 10(3):685–688

Chapter 18

Estimation of Methane Emission from West Siberian Lowland with Subpixel Land Cover Characterization Between MODIS and ASTER

Wataru Takeuchi, Tomoko Nakano, and Yoshifumi Yasuoka

Abstract Wetlands are one of the most important ecosystems in the world. The West Siberian Lowland (WSL) is the world's largest high-latitude wetland covering nearly two-thirds of western Siberia; thus, remote sensing techniques play an important role in monitoring them. At least half of this area consists of peatlands, which sequester atmospheric carbon in the form of slightly decomposed plant matter. WSL is considered a net source of methane gas, which is one of the most important greenhouse gases.

High spatial resolution satellite data are effective for monitoring land cover type changes, but cannot cover a wide area because of a narrow swath width. On the other hand, global scale data are indispensable in covering large areas, but are too coarse to acquire detailed information because of their low spatial resolution. We need to devise a method for data fusion with different spatial resolutions for monitoring such scale-variant phenomena.

In this chapter, a Terra ASTER image near Noyabrsk mire is used to map six wetland ecosystems (bare soil, birch forest, conifer forest, open bog, open water, and palsa) supplemented by field observation. Spectral mixture analysis is then performed between Terra MODIS and ASTER data acquired on the same day.

Field observations of CH_4 flux are subsequently scaled up with these different spatial resolution satellite data. Each of the wetland ecosystem coverage fraction at the subpixel level is provided by spectral mixture analysis. Field observation shows that the mean rate of CH_4 emission from open bog and open water averaged 123.1 and 24.6 mg $\text{C}/\text{m}^2/\text{day}$, respectively. The methane emission from the area is estimated by multiplying these average methane emission rates and the fraction coverage in each MODIS pixel.

W. Takeuchi (✉)

Institute of Industrial Science, University of Tokyo, 7-3-1 Hongo, Bunkyo-ku,
Tokyo 113-8656, Japan
e-mail: wataru@iis.u-tokyo.ac.jp

Finally, the total methane emission over MODIS coverage is estimated at 1.86×10^9 g CH₄/day and the mean methane emission over MODIS coverage was calculated as 43.1 mg C/m²/day. We conclude that this mean value is within the probabilistic variability when compared with the other research results.

18.1 Introduction

CH₄ or methane is a particularly effective greenhouse gas whose atmospheric concentration is increasing at a rate of approximately 1% per year, yet its source strengths are still poorly quantified. The most comprehensive assessment of global sources of atmospheric CH₄ and their future dynamics was conducted by the United Nation's Intergovernmental Panel on Climate Change (IPCC). The IPCC data suggest that natural wetlands are now responsible for approximately 21% of global CH₄ emissions (Houghton et al. 1998). In situ measurements suggest that northern high-latitude wetlands are probably a major source of CH₄ gas because of anaerobic bacterial decomposition in waterlogged peat lands. The WSL is the world's largest high-latitude wetland covering nearly two-thirds of western Siberia. Since its global warming potential is very high, estimation of CH₄ from different sources is now one of the urgent tasks in tackling global warming. However, huge spatial and seasonal variation in CH₄ emission from natural wetlands is often observed and regional differences are significant even when the sites are similar in climate, vegetation, and topography (Ding et al. 2004). This may affect the accuracy of the estimated amount of CH₄ emission from wetlands. However, given the extensive spatial coverage of wetlands, it is not easy to investigate their distribution with ground observations alone. Remote sensing of wetlands from satellite plays an important role in monitoring their condition, and in extracting them from other land cover types (Yasuoka et al. 1995).

Several remote sensing tools are available to produce land cover maps of individual wetlands using data with high spatial resolution such as Landsat ETM, SPOT HRV, or Terra ASTER. High spatial resolution data are effective in monitoring wetland environments at local or regional scale; however, their narrow swath widths may disallow large coverage areas. Another obstacle to mapping the world with high-resolution data is the cost and logistics of handling the data volume. Extending the area would require use of wide coverage data such as NOAA AVHRR, SPOT VEGETATION or Aqua/Terra MODIS. On the other hand, MODIS data may not detect fine spatial structures in mixtures of vegetation, soil, and water because of their coarse spatial resolution. Therefore, we need to devise a data fusion method, which integrates data with different spatial resolutions (Takeuchi et al. 2003).

In this chapter, an ASTER image near Noyabrsk mire was used to map six wetland ecosystems (bare soil, birch forest, conifer forest, open bog, open water, and palsa) supplemented by field observation. Subsequently, spectral linear mixture analysis was performed between MODIS and ASTER data acquired on the same date. Field observations of CH₄ flux were then scaled up with the different spatial resolution satellite datasets. Each wetland ecosystem's coverage ratio at the

subpixel level was provided by the spectral mixture analysis. The CH_4 emission from the area was estimated by multiplying these average CH_4 emission fluxes and the area percentage of open bog and open water.

18.2 Methodology

18.2.1 Outline of this Research

Figure 18.1 provides an outline of this research. Composed of three main parts, it includes satellite data processing, CH_4 emission measurement and CH_4 emission estimation. First, a Terra ASTER image near Noyabrsk mire was used to map six wetland ecosystems supplemented by field observation. Next, a spectral mixture analysis was performed between Terra MODIS and Terra ASTER data acquired on the same date. Second, field observations were scaled up with the different spatial resolution satellite datasets. Each of the wetland ecosystem's coverage fraction at the subpixel level was provided by the spectral mixture analysis. Finally, the CH_4 flux from the area was estimated by multiplying average CH_4 flux and the fractional coverage, and the total CH_4 emission over the MODIS coverage was estimated.

18.2.2 Study Area

The WSL was selected as a study area since it comprises one of the largest wetlands in the world, recognized as a high potential area for CH_4 emission due to global warming. This area is mainly covered by forests and wetlands. The wetlands belong

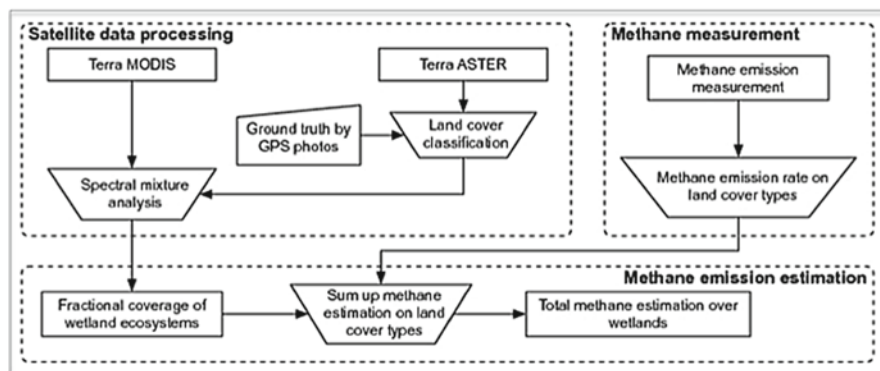


Fig. 18.1 Research flowchart

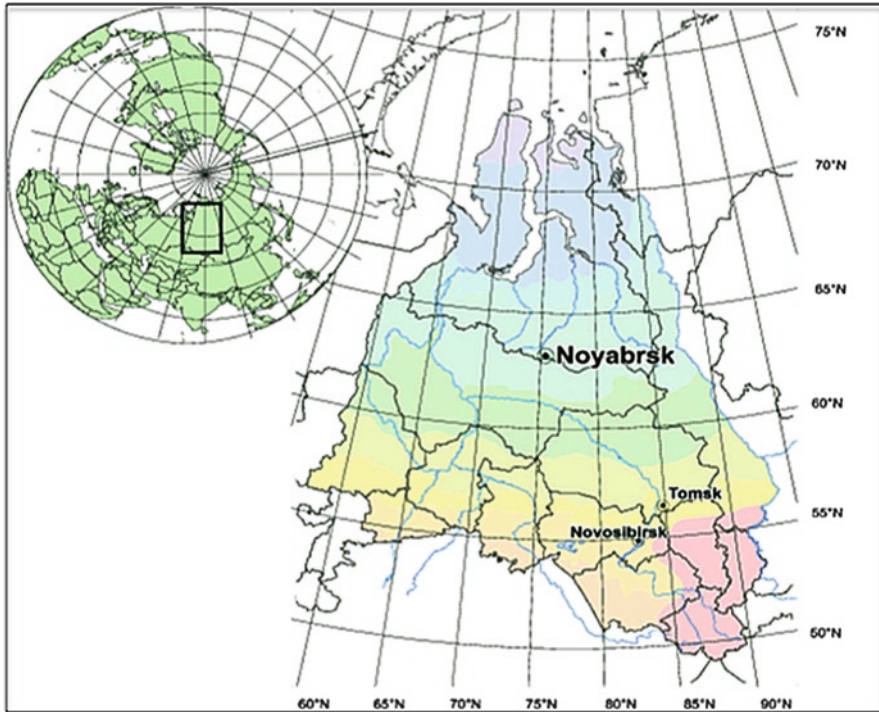


Fig. 18.2 Noyabrsk mire in the West Siberian Lowland

to a belt of ombrotrophic *Sphagnum* bogs of western Siberia. Bogs are peat-producing wetlands in moist climates, where organic material has accumulated over long periods. Their characteristic feature is that water and nutrient inputs into the system are entirely through precipitation. They are extremely acidic and nutrient-deficient (Crill et al. 1988). In this study, one type of bog is subjectively defined based on their CH_4 emission estimates. Open bog is mainly composed of lichens, where the water position is relatively higher. Birch forests are dominant in forested areas, and coniferous forests are found along rivers.

The research mire is located in the north taiga zone in a transitional strip between palsa bog and raised bog zones shown in Fig. 18.2. Palsas are peat mounds with permafrost cores that occur in regions of discontinuous permafrost, and their vegetation composition is wild rosemary (*Ledum palustre*). The taiga zone consists of birch (*Betula platyphylla*) and conifer forests (*Pinus sylvestris*). The bog vegetation (hummocks) is represented mainly by *Sphagnum fuscum* (Fig. 18.3). During the summer of 2001, we conducted a major field survey and remote sensing study in collaboration with Russian scientists. Central to that study was the measurement of CH_4 and CO_2 emissions from wetlands and forests near Noyabrsk mire in a discontinuous permafrost area. It also involved investigations of soil temperature and water acidity (pH). This ground survey along with photographs and GPS measurements provided the bulk of the validation data for image classification.



Fig. 18.3 Wetland ecosystems of the Northern Taiga subzone of the West Siberian Lowland near Noyabrsk: (a) big lake in an oligotrophic bog; (b) oligotrophic string bog complex with primary lakes and palsa; (c) palsa (primary) up to 1–2 m high, peat mounds with permafrost cores that occur in discontinuous permafrost regions; and (d) primary (up to 15 m high) mixed pinus species and birch forests on 10-cm thick peat layer

18.2.3 CH_4 Flux Measurement

The net CH_4 and CO_2 fluxes were determined by a static chamber technique (Nakano et al. 2006). Figure 18.4 shows a schematic diagram of a static chamber measurement system. Open-bottomed 0.4-m-tall transparent acrylic plastic chambers were placed on stainless-steel collars installed at the measurement sites for the entire study period. Each collar enclosed an area of 0.16 m^2 and was inserted into the ground to a depth of about 10 cm. Each chamber fit into a water-filled notch

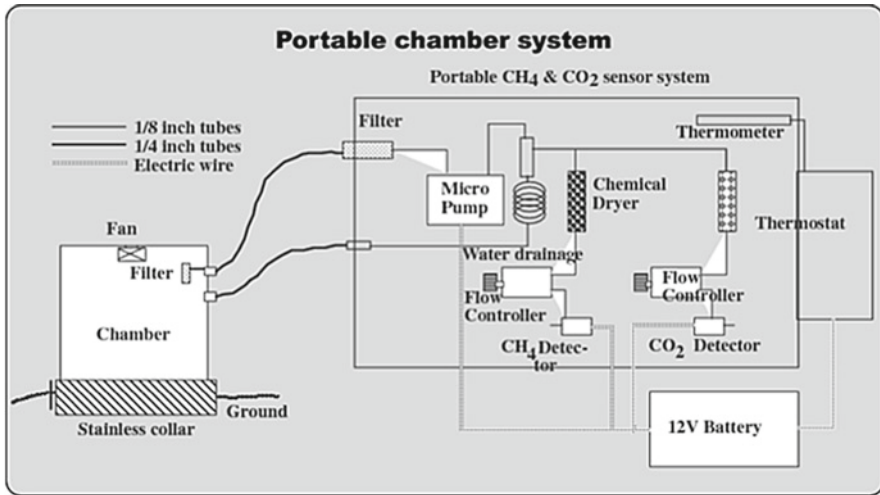


Fig. 18.4 Static chamber measurement system of CH₄ and CO₂

in the collar and was well sealed. A portable CH₄/CO₂ analyzer was equipped with a semiconductor CH₄ detector, a 12-V lead-acid battery, sampling ports, a Tedlar bag to equalize pressure, a thermometer, and a battery-operated fan.

The observations were conducted from 10:30 to 15:30 (local time) during August 15–16, 2001. The chamber was closed for 10 min by fitting a water-filled groove into the collar for the measurements, and the CH₄ concentration in the chamber was recorded at 5-s intervals with a data logger. The detection limit was approximately ± 0.03 mg C/m²/day. A positive CH₄ flux represents a transfer from the soil surface to the atmosphere and a negative flux indicates CH uptake by the soil.

Environmental data were collected concurrently with flux measurements. Ground temperatures at 5- and 10-cm depth were measured with a thermocouple. The soil moisture (volumetric water content) was measured by time domain reflectometry (TDR) from the surface to depths of 10 and 20 cm after each flux measurement.

To estimate the CH₄ emission from the MODIS area, we used the CH₄ flux data measured on the ground. The four measurement sites for open bogs are indicated by circle symbols in Fig. 18.5. The measurements for the other open bog and forested bogs were made outside the ASTER image area.

18.2.4 ASTER and MODIS Data Sets Used in the Study

Terra ASTER's green, red, and near-infrared channels at 15-m spatial resolution were used to classify the wetland ecosystems. Figure 18.6 shows two ASTER scenes in natural color composite acquired on July 19, 2001. They were geometrically corrected to Plate Carrée projection (latitude–longitude system) and were

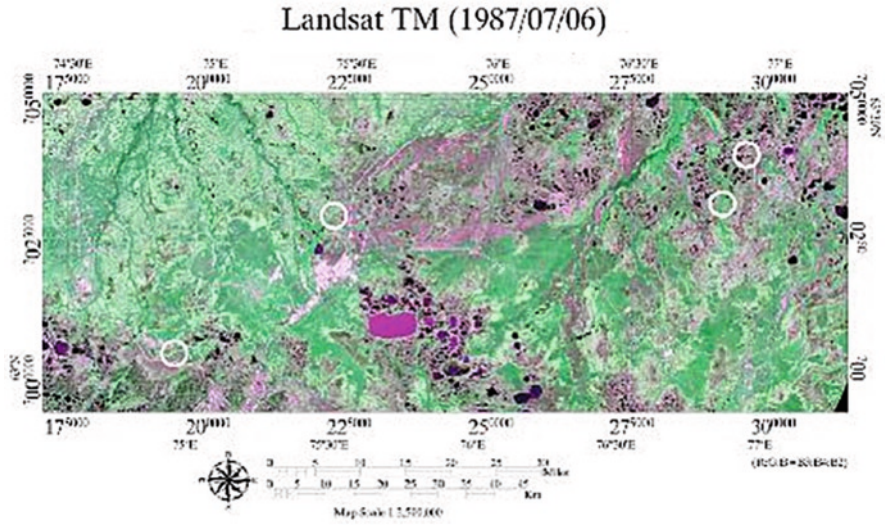


Fig. 18.5 Location of four measurement sites on open bogs indicated by circle symbols

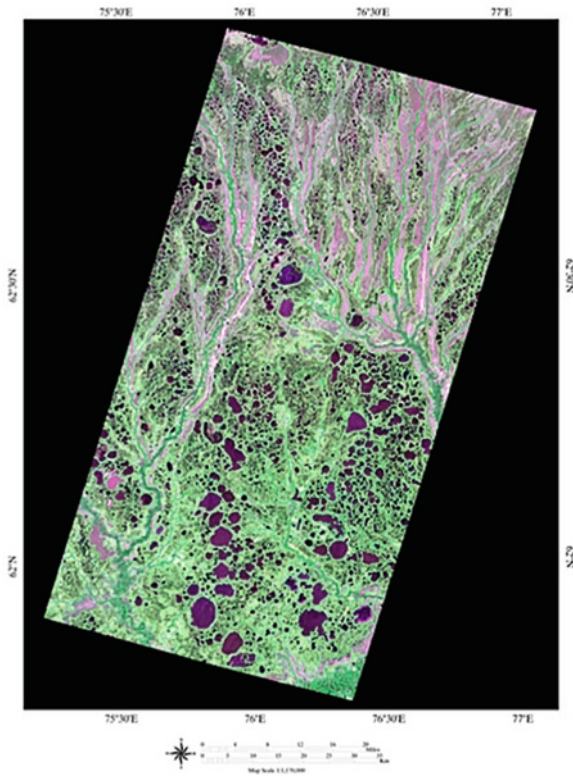


Fig. 18.6 ASTER image (acquired on July 19, 2001)

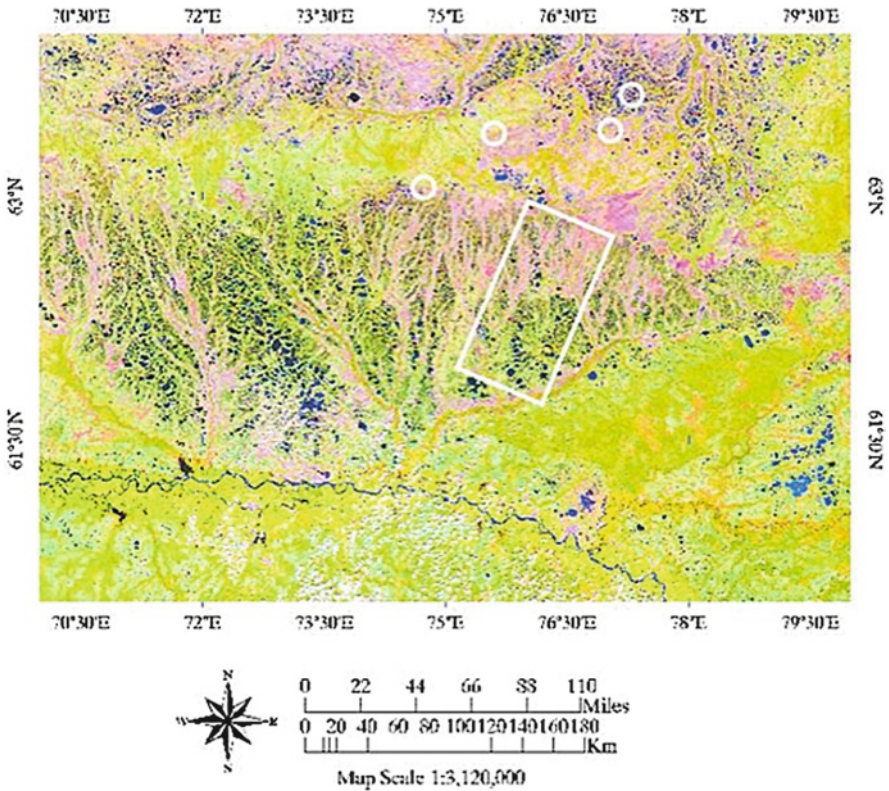


Fig. 18.7 Terra MODIS image (acquired on July 19, 2001)

calibrated to the top of the atmosphere reflectance. The 500-m Terra MODIS image acquired on July 19, 2001 was downloaded from NASA/DAAC (<http://daac.gsfc.nasa.gov/>). It was geometrically corrected to overlay on the same map projection with the ASTER image. Channels 1–7 were calibrated to the top of the atmosphere reflectance, and pixels with a sensor scan angle over 45° were considered unacceptable. A cloud-free area was carefully selected by visual interpretation, and area of interest in this study is defined by a rectangular area from 62.0° to 63.5° north latitude, and from 72.5° to 76.5° east longitude, covering $43,200 \text{ km}^2$ (Fig. 18.7). Atmospheric and bidirectional reflectance distribution (BRDF) corrections were not performed.

ASTER and MODIS images were geometrically overlaid so that one MODIS pixel (500 m) covers a set of ASTER pixels in a rectangular block of 33×33 . Root-mean-square errors of image-to-image registration between ASTER and MODIS were evaluated using an image matching technique on NDVI images. We found a geometric correction error between these two images was tolerably high; 5 pixels for ASTER and 0.15 pixels in the case of MODIS.

18.2.5 Spectral Mixture Analysis

Terra MODIS is one of the few space-borne sensors currently capable of acquiring radiometric data over a range of view angles. However, its relatively coarse spatial resolution (250 m–1 km) often results in measurements of mixed land covers, and thus pixel unmixing becomes indispensable (Bateson et al. 2000). It involves a scaling model, which is focused on unmixing the MODIS pixels using high-resolution data. Each category's area ratio in a single MODIS pixel becomes fundamentally important data (Shimabukuro and Smith 1991; Price 1999).

If we assume a remotely sensed dataset has n channels, and the coverage is composed of k types of categories ($\omega_1, \dots, \omega_k$). The spectral characteristics of the category ω_i are expressed by the n -dimensional spectral vector m_i ($i = 1, \dots, k$). If the pixel p_{lm} is composed of one category ω_i (pure pixel), then $p_{lm} = m_i$. A linear spectral mixture analysis models the reflectance spectrum of each pixel in a MODIS image in terms of endmember reflectance according to the equations and constraints below:

$$p_{lm} = \sum_{i=1}^k a_{lm}^i m_i, \quad (18.1a)$$

$$a_{lm}^i \geq 0 \quad (i = 1, \dots, k), \quad (18.1b)$$

$$\sum_{i=1}^k a_{lm}^i = 1, \quad (18.1c)$$

where a_{lm}^i is the fractional coverage of the category ω_i in the pixel. Equation (18.1a) is called the category combination, which is the combination of the spectral characteristics of multiple categories by the space average. In this case, the pixel data p_{lm} is expressed by the linear combination of the area ratio a_{lm}^i . Equation (18.1b) expresses the positivity constraint of each category and (18.1c), the constraint equation of each category ratio, respectively. If the number k of end members equals the number of bands plus one, then in (18.1a) and (18.1c) above, there are k equations in k unknown, which are uniquely inverted to solve for the a_{lm}^i in (18.1a).

All the fractions should sum to unity, therefore, a constraint equation is incorporated into the problem, besides positivity constraints on the fraction estimates. Apart from indirect applications, there are several classes of problems that are naturally expressed in quadratic terms. Examples of such problems are found in planning, scheduling, game theory, and many problems in economics (Floudas et al. 1995). The general quadratic programming method provides an answer a_{lm}^i with the nonnegative condition. Objective function $Q(a_{lm})$ is defined as follows:

$$Q(a_{lm}) = \frac{1}{2} a_{lm}^t D a_{lm} + C^t a_{lm}, \quad Q(a_{lm}) = \frac{1}{2} a_{lm} D a_{lm} + C^t a_{lm}, \quad (18.2a)$$

where

$$D = [D_{ij}] = [2(m_i, m_j)], \quad (18.2b)$$

$$C^t = -2[(p_{lm}, m_1), \dots, (p_{lm}, m_k)], \quad (18.2c)$$

with the condition

$$a_{lm}^i \geq 0 \quad (i = 1, \dots, k), \quad (18.3a)$$

$$\sum_{i=1}^k a_{lm}^i \leq 1, \quad (18.3b)$$

$$\sum_{i=1}^k a_{lm}^i \geq 1. \quad (18.3c)$$

If D is a positive-definite matrix, (18.2a) becomes a convex programming problem. Since any local optimum is equivalent to the global optimum in convex problems, there are many algorithms for convex quadratic programming. In this study, a gradient ascent algorithm (Uzawa algorithm) was applied to the dual functional with an augmented Lagrangian method (Elman and Golub 1994).

18.3 Results and Discussions

18.3.1 Spectral Mixture Analysis

For ecosystem characterization, six categories were selected including bare soil, birch forest, conifer forest, open bog, open water, and palsa. First, around 30 training areas were selected for each class on the basis of the GPS locations. All field data points were used to train the classifier. Subsequently, the entire ASTER image was classified into the above-mentioned six categories using a maximum likelihood supervised classification. Figure 18.8 shows the classification result.

The ordinary least squares method was applied to solve for a mean MODIS reflectance representative of the entire scene using (18.1a). The coefficients represent the derived reflectances (end members f) in (18.4a–e):

$$\text{MOD}_1 = 16.2\text{BS} + 4.65\text{BF} + 4.24\text{CF} + 5.30\text{OB} + 3.40\text{OW} + 6.34\text{PL}, \quad R = 0.81, \quad (18.4a)$$

$$\text{MOD}_2 = 21.1\text{BS} + 19.9\text{BF} + 16.7\text{CF} + 13.5\text{OB} + 5.85\text{OW} + 26.2\text{PL}, \quad R = 0.84, \quad (18.4b)$$

$$\text{MOD}_4 = 14.7\text{BS} + 5.76\text{BF} + 5.82\text{CF} + 6.16\text{OB} + 4.53\text{OW} + 7.71\text{PL}, \quad R = 0.76, \quad (18.4c)$$

$$\text{MOD}_5 = 25.4\text{BS} + 18.6\text{BF} + 18.0\text{CF} + 16.7\text{OB} + 5.49\text{OW} + 24.8\text{PL}, \quad R = 0.79, \quad (18.4d)$$

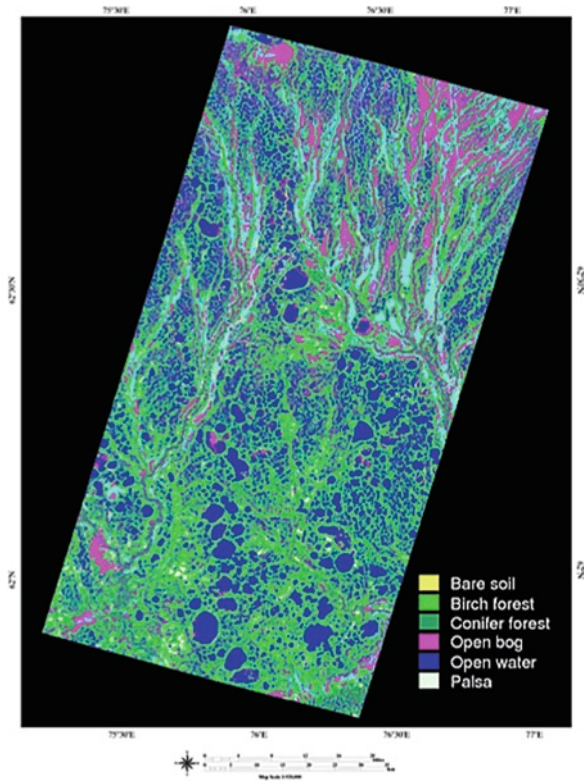


Fig. 18.8 Classified ASTER image (acquired on July 19, 2001)

$$MOD_6 = 28.5BS + 10.1BF + 11.0CF + 13.2OB + 3.04OW + 14.6PL, \quad R = 0.84, \quad (18.4e)$$

where MOD_1 , MOD_2 , MOD_4 , MOD_5 , MOD_6 , and MOD_7 are reflectance values of MODIS channels 1, 2, 4, 5, and 6, respectively, which are calibrated at the top of the atmosphere. BS, BF, CF, OB, OW, and PL are the fractional coverages of bare soil, birch forest, conifer forest, open bog, open water, and palsa, respectively. R is the correlation coefficient.

The derived spectral mixture model was applied to the entire MODIS data to generate maps showing the distribution of spectrally distinct chaparral birch forest, conifer forest, forested bog, and open bog. By solving (18.4a–e) and (18.1c), which shows the fractions sum to unity simultaneously, fractional coverage for each of the classes was calculated. Figure 18.9 presents the result of spectral mixture analysis of wetland ecosystems near Noyabrsk. Bright values indicate areas of high fractional abundance of that endmember. Figure 18.10 shows classification accuracy of mixture classes for each category for ASTER and MODIS.

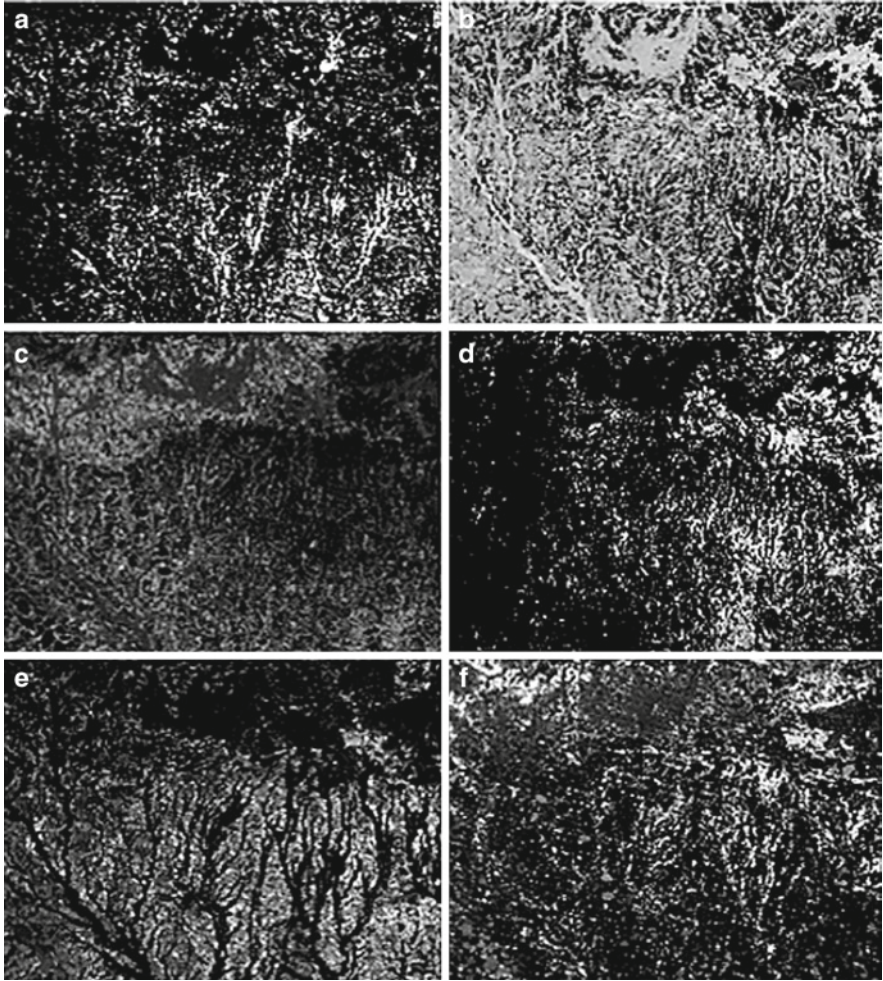


Fig. 18.9 Results of spectral mixture analysis of wetland ecosystems near Noyabrsk. *Bright values* indicate areas of high fractional abundance of that endmember: (a) bare soil, (b) birch forest, (c) conifer forest, (d) open bog, (e) open water, and (f) palsa

18.3.2 Accuracy Assessment

The performance of the spectral mixture analysis model was evaluated in terms of the root mean squared (RMS) error. For the given six classes (bare soil, birch forest, conifer forest, open bog, open water, and palsa), the RMS error with respect to that class is as follows:

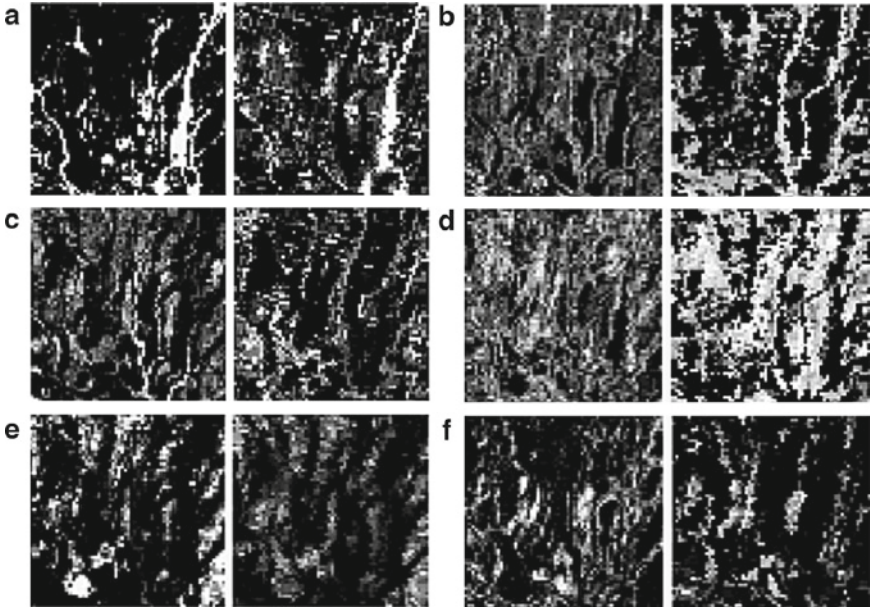


Fig. 18.10 Classification accuracy of mixture fractions for each category. *Bright values* indicate areas of high fractional abundance of that endmember (*Left*: ASTER-derived aggregated classification image; *Right*: estimated MODIS-derived fraction image): (a) bare soil, (b) birch forest, (c) conifer forest, (d) open bog, (e) open water, and (f) palsa

$$E_k = \sqrt{\frac{1}{N_p} \sum_{n=1}^{N_p} (B_{k,n} - B_{k,n}^*)^2}, \quad (18.5a)$$

$$E_t = \frac{1}{N_p} \sum_{n=1}^{N_p} \sqrt{\frac{1}{N_k} \sum_{k=1}^{N_k} (B_{k,n} - B_{k,n}^*)^2}, \quad (18.5b)$$

where $B_{k,n}$ is the original fraction value of category k of pixel n , $B_{k,n}^*$ is the estimated fraction value, N_p is the number of pixels, and N_k is the number of categories.

The results of the classification accuracy are presented in Table 18.1. Overall, the accuracies were tolerably high and consistent across the individual classes. Individual class accuracies reveal that bare soil is the most accurately identified ecosystem category followed by open water, open bog, birch forest, conifer forest, and palsa. The validation described above is obviously incomplete in that it relies entirely on the ASTER data-based classification results, and the assumption that all the ASTER pixels are pure. The inability of the validation method to quantify the uncertainty of other neglected categories is a significant issue to resolve in future studies. In spite of the acknowledged inability of the validation method to constrain the number of categories, this may cause a real limitation imposed by the satellite-derived data.

Table 18.1 Classification accuracy evaluation by a simple percent agreement value

| Land cover | RMSE (%) |
|----------------|----------|
| Bare soil | 14.6 |
| Conifer forest | 24.7 |
| Birch forest | 23.9 |
| Open bog | 21.7 |
| Open water | 17.8 |
| Palsa | 27.2 |

18.3.3 Estimation of CH₄ Emission

Summary statistics of the CH₄ flux and environmental variables for the entire study period are presented in Table 18.2. Soil atmosphere exchanges of CH₄ were always zero at bare soil, birch and conifer forest, and palsa indicating that the dry soil on the forest floor was a net consumer of CH₄. In contrast, CH₄ flux was always positive (net emission) in bog and open water. The flux varied widely with bog, ranging from 4.209 to 6.284 (mg C/m²/day), whereas it was close to 0 in open water, ranging from 0.492 to 1.670. CH₄ flux for birch and conifer forests were zero because they were less than the detection limit (± 0.03 mg C/m²/day). It gives a consistent result because in many cases, forests consume atmospheric CH₄ at very low rates (Bartlett and Harriss 1993). Soil temperatures at a depth of 10 cm showed slight variations (approximately 10–15° C) at all sites. The Volumetric Water Content (VWC) of the soils differed markedly among the land covers: at bog and open water, the values were saturated over 100% and at bare soil, the land surface was very dry and the values were zero, whereas birch and conifer forests or palsa experienced drought conditions (VWC < 20%) for the entire period. Mean temperatures for palsa were recorded and its variations were very low.

Field measurements show that the mean rate of CH₄ emission from open bog and open water averaged 5.246 and 1.081 (mg C/m²/h), respectively. The results obtained in spectral mixture analysis enable us to scale up field measurements of CH₄ emission to areas covered by MODIS. The total CH₄ flux F_{total} and the mean CH₄ flux F_{mean} over the MODIS coverage are calculated as follows:

$$F_{\text{total}} = \sum_{i=1}^n A_i f_i, \quad (18.6a)$$

$$F_{\text{mean}} = \frac{F_{\text{total}}}{\sum_{i=1}^n A_i}, \quad (18.6b)$$

where n is the number of categories, A_i is the total area of each category, and f_i is the CH₄ emission rate of each category. Table 18.3 presents results of these calculations for the roughly 43,200 km² MODIS-covered study area. The total CH₄ flux

Table 18.2 Summary statistics of CH₄ flux and environmental variables in wetland ecosystems

| Land cover | T_s at 10 cm | VWC (%) | CH ₄ flux (mg C/m ² /h) |
|----------------|----------------|------------|-----------------------------------------------|
| Bare soil | – | – | – |
| Birch forest | 8.6 ± 0.7 | 17.2 ± 4.1 | – |
| Conifer forest | 8.6 ± 0.7 | 17.2 ± 4.1 | – |
| Open bog | 10.0 ± 0.1 | – | 5.246 ± 1.038 |
| Open water | 10.0 ± 0.1 | – | 1.083 ± 0.589 |
| Palsa | 8.4 ± 0.8 | 29.1 ± 5.0 | – |

Table 18.3 CH₄ emission estimates from extensive wetlands covered by MODIS (62.0–63.5N, 72.5–76.5E, 43,200 km²)

| Land cover | Area (10 ³ km ²) | CH ₄ flux (mg C/m ² /day) | Total CH ₄ flux (10 ⁹ g/day) |
|----------------|-----------------------------------------|-------------------------------------------------|----------------------------------------------------|
| Bare soil | 4.66 | – | – |
| Birch forest | 7.00 | – | – |
| Conifer forest | 5.59 | – | – |
| Open bog | 14.68 | 123.1 ± 24.9 | 1.807 ± 0.366 |
| Open water | 2.31 | 24.6 ± 13.5 | 0.057 ± 0.032 |
| Palsa | 8.96 | – | – |
| Total | 43.20 | – | 1.864 ± 0.398 |

over the MODIS coverage was calculated at 1.864 (10⁹ g C/day) and the mean CH₄ flux over MODIS coverage was calculated at 43.1 (mg C/m²/day).

18.4 Discussions

Following is a discussion of the CH₄ emission variability. Table 18.3 shows that the CH₄ emission in open bog was statistically calculated as 123.1 ± 24.9 (mg C/m²/day) and that of open water at 24.6 ± 13.5 (mg C/m²/day). Net flux of CH₄ from boreal and subarctic peat lands to the atmosphere is difficult to estimate, and thus there are uncertainties in determining how many different types of measurements are needed to characterize the source (Morrissey and Livingston 1992). As with temperate and subtropical wetlands, CH₄ emission fluxes from northern wetlands are extremely variable. CH₄ estimates are affected strongly by pH, temperature and the water table's depth (Macdonald et al. 1998); however, the correlation between CH₄ emission and such environmental factors was very low (determination coefficient less than 0.11) (Panikov 1994; Panikov et al. 1997). Thus, the only valuable predictor among available soil-ecological indicators is vegetation cover.

Tohjima et al. (1994) estimated the CH₄ fluxes from wetlands over the southern part of the WSLs from vertical profile measurements. The accumulation period and estimated regional CH₄ fluxes spanned three measurement days. They indicate large variations from 34 to 126 (mg C/m²/day). Such a large variation points to

spatial and temporal variability of CH₄ concentration. The average CH₄ flux for three days of observations was 83 (mg C/m²/day), which is roughly twice our estimate of 43.1 (mg C/m²/day), calculated from the combination of remote sensing analysis and ground measurements. This discrepancy may result in part because we neglected the contributions from water. However, if we note that both estimates are based on measurement results with large variations, we could conclude that our result is well within a range of probabilistic variability.

18.5 Concluding Remarks

This research investigated the use of spectral mixture analysis to map the wetland ecosystem in the WSL using single-date ASTER and MODIS images. Field observations were scaled up with satellite data and the CH₄ emission from the area covered by MODIS was estimated.

This study demonstrated that scaling techniques provide a tool to extrapolate the local information from high spatial resolution data to larger scale by using lower spatial resolution data. First, spectral mixture analysis was conducted between Terra MODIS and Terra ASTER, and the distribution of six wetland ecosystems (bare soil, birch forest, conifer forest, grassland, open bog, open water, and palsa) was estimated at the subpixel level. Subsequently, the total CH₄ flux over the MODIS coverage was estimated with the combination of remote sensing classification and the ground CH₄ measurement results. Finally, the mean CH₄ flux over the MODIS area was calculated at 43.1 (mg C/m²/day), which is within the range of probabilistic variability when compared with airborne measurement results (Tohjima et al. 1994).

As most of the global issues including deforestation or desertification originate from local events, monitoring Earth surface changes require that the observation of land cover examine the terrain from local to global scales. Linking the local with global is one of the key aspects in tackling global environmental issues, and the method proposed here is expected to play an important role in bridging the local and the global components in future remote sensing studies.

References

- Bartlett KB, Harriss RC (1993) Review and assessment of methane emissions from wetlands. *Chemosphere* 26:261–320
- Bateson CA, Asner GP, Wessman CA (2000) Endmember bundles: a new approach to incorporating endmember variability into spectral mixture analysis. *IEEE Trans Geosci Remote Sens* 38:1083–1094
- Crill PM, Bartlett KB, Harriss RC, Gorham E, Verry ES, Sebacher DI, Mazdar L, Sanner W (1988) Methane flux from Minnesota peatlands. *Global Biogeochem Cycles* 2:317–384
- Ding W, Cai Z, Wang D (2004) Preliminary budget of methane emissions from natural wetlands in China. *Atmos Environ* 38:751–759

- Elman HC, Golub GH (1994) Inexact and preconditioned Uzawa algorithms for saddle point problems. *SIAM J Numer Anal* 31:1645–1661
- Floudas CA, Visweswaran V (eds) (1995) Quadratic optimization. In: Horst R, Pardalos PM (eds) *Handbook of global optimization*. Kluwer, Dordrecht, pp 217–269
- Houghton JT, Meira Filho LG, Callander BA, Harris N, Kattenberg A, Maskell K, (eds) (1998) *Climate change 1995: the science of climate change*. Cambridge University Press, New York
- Macdonald JA, Fowler D, Hargreaves KJ, Skiba U, Leith ID, Murray MB (1998) Methane emission rates from a northern wetland; Response to temperature, water table and transport. *Atmos Environ* 32:3219–3227
- Morrissey LA, Livingston GP (1992) Methane emissions from Alaska Arctic tundra: an assessment of local spatial variability. *J Geophys Res* 97:16661–16670
- Nakano T, Takeuchi W, Inoue G, Fukuda M, Yasuoka Y (2006) Temporal variations in soil–atmosphere methane exchange after fire in a peat swamp forest in West Siberia. *Soil Sci Plant Nutr* 52:29–40
- Panikov NS (1994) CH₄ and CO₂ emission from northern wetlands of Russia. In: *Proceedings of the International Symposium on Global Cycles of Atmospheric Greenhouse Gases*, pp 100–112
- Panikov NS, Glagolev MV, Kravchenko IK, Mastepanov MA, Kosykh NP, Mironycheva-Tokareva NP, Naumov AV, Inoue G, Maxutov S (1997) Variability of methane emission from West-Siberian wetlands as related to vegetation type. *Ecol Chem* 6:59–67
- Price JC (1999) Combining multi-spectral data of differing spatial resolution. *IEEE Trans Geosci Remote Sens* 37:1199–1203
- Shimabukuro YE, Smith JA (1991) The least-squares mixing models to generate fraction images derived from remote sensing multispectral data. *IEEE Trans Geosci Remote Sens* 29:16–20
- Takeuchi W, Tamura M, Yasuoka Y (2003) Estimation of the methane emission from West Siberian wetland by scaling between NOAA/AVHRR and SPOT/HRV data. *Remote Sens Environ* 85(4):21–29
- Tohjima Y, Maksyutov S, Machida T, Inoue G (1994) Airborne measurement of atmospheric CH₄ over the West Siberian Lowland during the 1994 Siberian Terrestrial Ecosystem–Atmosphere–Cryosphere Experiment (STEACE). In: *Proceedings of the 3rd Symposium on the Joint Siberian Permafrost Studies between Japan and Russia*, pp 50–57
- Yasuoka Y, Sugita M, Yamagata Y, Tamura M, Suhama T (1995) Scaling between NOAA AVHRR and Landsat TM data for monitoring and mapping of wetland. In: *Proceedings of the International Symposium on Vegetation Monitoring*, pp 95–98

Chapter 19

ASTER Stereoscopic Data and Digital Elevation Models*

Thierry Toutin

19.1 Introduction

Digital elevation models (DEMs) provide a digital representation of the Earth's relief, and are used in a variety of applications in geo-spatial analysis. Elevation data as DEMs are required to produce geocoded, orthorectified raster images, which often are incorporated in a geographic information system. The atmospheric, geometric, and radiometric correction of satellite data from optical and microwave instruments also require topographic information. Satellite data-derived DEMs form a vibrant research and development (R&D) topic for the last 30 years since the launch of the first civilian remote sensing satellite (Toutin 2000). Various methods exist to extract DEMs from both active and passive sensor-based satellite data-derived images (clinometry, stereoscopy, interferometry, polarimetry, and altimetry).

Stereoscopy, as it applies to the Advanced Spaceborne Thermal Emission and Reflection Radiometer (ASTER) data, is the most common method used by the mapping, photogrammetry, and remote sensing communities to model elevation, mainly with visible and infra-red (VIR) data. In modern photogrammetry, "stereoscopy is the science and art that deals with the use of images to produce a 3D visual model with characteristics analogous to that of actual features viewed using true binocular vision" (La Prade et al. 1966). The binocular disparity (or parallax) is the disparity or the "difference" between the images of an object projected on to each retina. The degree of disparity between the two projected images depends on the convergence angle. The binocular disparity is used in stereo photogrammetry for quantitative elevation extraction, and consequently to generate DEMs.

Global DEMs with sufficient detail and accuracy are not always available. The Shuttle Radar Topography Mission (SRTM) has helped fill that gap. The

* Earth Sciences Sector Contribution number: 20090185

T. Toutin (✉)

Natural Resources Canada, Canada Centre for Remote Sensing,
580 Booth, Ottawa, ON K1A 0E4, Canada
e-mail: Thierry.Toutin@NRCan-RNCan.gc.ca

ASTER data complement this lack with a new source of topographic information for the Earth's land surface (Yamaguchi et al. 1998; Welch et al. 1998). The ASTER was launched aboard the Terra platform on December 18, 1999 as part of NASA's Earth Observing System (EOS) mission. ASTER is the only high spatial resolution instrument on the Terra platform. Built in Japan, it is supported by the Ministry of Economy Trade and Industry. A Joint U.S./Japan Science Team is responsible for the instrument design, calibration, and validation. The ASTER mission's main objectives are to obtain high spatial resolution global, regional, and local images of the Earth in 14 spectral bands. To foster ASTER's DEM production capability, a key objective is to acquire cloud-free stereo data, which covers 80% of the Earth's land surface between 82°N and 82°S.

This chapter provides an overview of the ASTER stereo processing to generate DEMs (Sect. 19.1), reviews the methods and algorithms applied to generate DEMs at NASA LP DAAC (Sect. 19.2), at ERSDAC (Sect. 19.3), and concluding remarks (Sect. 19.4).

19.2 ASTER, Stereoscapy, and DEMs

Other chapters in this volume offer additional details germane to this one, and hence, do not warrant repetition. Chapter 5 deals with the radiometric calibration and atmospheric correction of visible and near infrared (VNIR) and the shortwave infrared (SWIR), while Chap. 4 provides details regarding ASTER's geometric design. Chapter 11 provides details regarding the ASTER data system, and its product suites. A few key attributes of the ASTER instrument are important to bear in mind. Although the line-of-sight vectors and the pointing axes were determined prelaunch through ground-based measurements (Fujisada et al. 1998), they were not precise enough, and hence postlaunch inflight calibration and validation results were used to estimate the ASTER instrument's geometric performance (Iwasaki and Fujisada 2005). Intra-telescope (VNIR band-to-band registration) and inter-telescope (VNIR/SWIR/TIR band-to-band registration) geolocation error were performed with about 30 scenes acquired globally, each using 10–20 accurate Ground Control Points (GCP) (around 2–3 m in the three axes) to evaluate the geolocation accuracy. The final registration performance results were as follows: less than 0.1 and 0.2 pixels for the intra- and inter-telescope registrations, respectively, and less than 50 m for the geolocation accuracy (3-s) (Iwasaki and Fujisada 2005).

19.2.1 *Basic Aspects of ASTER Stereoscopic Data*

The ASTER stereo subsystem follows the implementation of the Stereosat–Mapsat concept to acquire global stereo data coverage of the land areas with an along-track digital sensor (Colvocoresses 1982). These data are used to produce DEMs based on photogrammetric principles. Earlier sensors including the JERS-1 OPS and the German Modular Opto-Electronic Multi-Spectral Stereo Scanner (MOMS) were

Table 19.1 General characteristics of the three ASTER subsystems (<http://asterweb.jpl.nasa.gov/>)

| Characteristics | VNIR | SWIR | TIR |
|-------------------------------------|----------------------------------------------------------------------------------------|-------------------------------------|--------------------------------------|
| Spectral range | Band 1 0.52–0.60 μm Nadir looking | Band 4 1.600–1.700 μm | Band 10 8.125–8.475 μm |
| | Band 2 0.63–0.69 μm Nadir looking | Band 5 2.145–2.185 μm | Band 11 8.475–8.825 μm |
| | Band 3N 0.76–0.86 μm Nadir looking | Band 6 2.185–2.225 μm | Band 12 8.925–9.275 μm |
| | Band 3B 0.76–0.86 μm Backward looking | Band 7 2.235–2.285 μm | Band 13 10.25–10.95 μm |
| | | Band 8 2.295–2.365 μm | Band 14 10.95–11.65 μm |
| | | Band 9 2.360–2.430 μm | |
| Ground Resolution (m) | 15 | 30 | 90 |
| Data Rate (mbits/s) | 62 | 23 | 4.2 |
| Across-track pointing (deg.) | ± 24 | ± 8.55 | ± 8.55 |
| Across-track pointing (km) | ± 318 | ± 116 | ± 116 |
| Swath width (km) | 60 | 60 | 60 |
| Quantization (bits) | 8 | 8 | 12 |

able to provide along-track stereo images. However, they were not designed to provide a global coverage, and besides the JERS-OPS single telescope design only afforded a small base-to-height (B/H) ratio, which impacted the DEM's quality.

Benefitting from past experience, ASTER was designed with three different subsystems: VNIR, SWIR, and the thermal infrared (TIR). Table 19.1 shows the basic characteristics of these subsystems. Characteristics of interest to stereo processing are provided in bold. Additional information on ASTER is available in other chapters of this volume.

The VNIR subsystem alone provides stereo capability. It consists of two independent telescope assemblies to minimize image distortion in its backward- and nadir-looking telescopes (Yamaguchi et al. 1998). The focal plane of the nadir telescope contains three silicon charge-coupled detector line arrays (bands 1, 2, and 3N in Table 19.1), while the focal plane of the backward telescope has only one (3B). The nadir- and backward-looking telescope pair is thus used for same-orbit stereo imaging (along-track stereo). The two near-infrared spectral bands, 3N and 3B, generate an along-track stereo image pair with a base-to-height (B/H) ratio of about 0.6 and an intersection angle of about 27.7° (Fig. 19.1). Only 9 s are required to acquire a 60-km by 60-km image, and 64 s for a stereo pair. The two VNIR telescopes are rotatable $\pm 24^\circ$ to provide extensive across-track pointing capability and a 5-day revisit capability at the equator. Therefore, across-track multirate

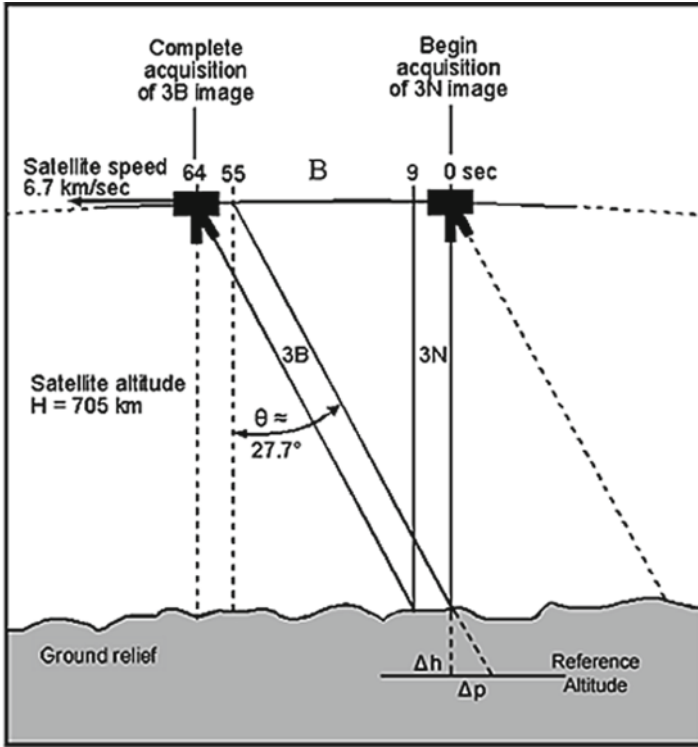


Fig. 19.1 Along-track stereo geometry of the ASTER VNIR backward and nadir subsystem (Modified from: http://lpdaac.usgs.gov/aster/ast14dem_AlongTrackGeometry.pdf)

stereo imaging with better stereo geometry and B/H ratio are rendered possible. However, the same-date along-track solution, even with an inferior stereo geometry, is preferred to the multidate across-track solution with a better stereo geometry for scientific and operational reasons discussed below.

The Terra platform is on a sun-synchronous, near-polar, quasi-circular orbit. The equator-crossing time is $10:30 \pm 15$ min local time, which depends on both latitude and off-nadir viewing angle. Near-polar implies that all orbits approximately intersect over the poles. With a quasi-circular orbit, the altitude is relatively constant to generate similar pixel spacing. The mean altitude is around 705 km and the orbital inclination $98.2^\circ \pm 0.15$ at the equator. The orbit period is 98.9 min with a repeat cycle of 16 days, resulting in 233 revolutions in 16 days with a distance of 172 km between adjacent orbits at equator. Even if the ASTER swath is 60 km, narrower than the orbital spacing (172 km), it can observe the entire globe with its across-track pointing capability. Although Terra's repeat cycle is 16 days, ASTER's global observation cycle is 48 days due to its swath. ASTER can, however, perform an emergency observation within 5 days (worst case) using its VNIR sensor's cross-track pointing capability.

With its 8-min/orbit duty cycle, ASTER can acquire a maximum of around 770 stereo pairs per day. During the six-year mission, ASTER is potentially capable of acquiring 45,000 cloud-free, digital stereo pairs required to cover the land surface

of the Earth between 82°N and 82°S. The Terra platform's 98.2° orbital inclination without across-track pointing explains this capability, which restricts the latitudinal coverage. These conclusions are based on nine mission simulation results, five of which were conducted prior to 1994, during early mission planning. All five studies incorporate Willard's (1992) cloud climatology. Each simulation used a different value for acceptable cloud cover, and window size to estimate cloud cover; these values ranged from 0 to 20% and 30–90 km, respectively. These simulations also incorporated seasonal and latitudinal restrictions to assure optimal illumination. The four other simulations, conducted in late 1998 and early 1999, resulted in the lowest acquisition rate, because they incorporated an additional requirement. The ASTER instrument was required to observe all-known EOS study targets multitemporally, and under extremely conservative mission operation scenarios. They further assumed a less efficient cloud prediction algorithm, which is in the ASTER scheduler (Lang and Welch 1999). Consequently, this assured an acquisition of one cloud-free, stereo data collection, which covered 80% of the Earth's land surface by the end of the 6-year mission.

19.2.2 Basic Aspects of DEM Stereoscopy¹

To obtain stereoscopic images from satellite-based VNIR sensors, two solutions are possible:

1. Along-track stereoscopy from the same orbit using fore and aft images.
2. Across-track stereoscopy from two different orbits.

Three examples of the latter solution used since the 1980s include the following: use of Landsat data from two different orbits (Welch and Lo 1977); SPOT-1 data used with across-track steering capabilities (CNES 1987), and finally, IRS-1C/D data used by rolling the satellite (Gopala Krishna et al. 1996). This solution was also applied to mixed sensors (Welch et al. 1990). Since 1990, the first solution was popularly received with the medium-resolution sensors, e.g., JERS-1 OPS (Maruyama et al. 1994), the German MOMS scanner (Raggam et al. 1997), ASTER-VNIR (Toutin 2002; Toutin and Cheng 2002; Käab 2002, 2005; Hirano et al. 2003), and SPOT5-HRS (Bouillon et al. 2006; Toutin 2006). In the last few years, most of the new high-resolution sensors (Formosat-2, Cartosat-1, ALOS-PRISM, CBERS-2B, etc.) and the agile very high-resolution satellites (Ikonos, QuickBird, Orbview, EROS, WorldView-1, etc.) (Toutin 2004) have also adopted this along-track solution. Table 19.2 summarizes nonexhaustive general results for DEM extraction from different stereo satellite sensors.

The tendency to compute elevation parallaxes is to apply an image-matching process using (a) the image gray levels with a least-squares approach (Förstner 1982), (b) the image features, or (c) a hybrid approach with additional geometry/

¹By default, the accuracy metric is 1- σ unless otherwise stated.

Table 19.2 Summary of the accuracy results (1-s) (in meters) of the elevation extraction with VIR scanners using the stereoscopic method (last three columns)

| Stereo pairs | Resolution (m) | <i>B/H</i> | Adjacent track (m) | Across track (m) | Along track (m) |
|------------------|----------------|------------|--------------------|------------------|-----------------|
| Landsat MSS | 80 | 0.1–0.2 | 100–300 | | |
| Landsat TM | 30 | 0.1–0.2 | 45–70 | | |
| IRS 1A | 72 | 0.1 | 35 | | |
| SPOT1–4 HRV | 10 | 0.6–1.0 | | 5–15 | |
| IRS 1C/D | 6 | 0.8–1.0 | | 10–30 | |
| MOMS-2 | 13.5 | 0.8 | | | 5–15 |
| MOMS-2P | 18 | 0.8–1.0 | | | 10–30 |
| JERS OPS | 20 | 0.3 | | | 20–40 |
| EROS | 2.8 | 1.0 | | | 10 |
| Ikonos/QuickBird | 1 | 1.0 | | | 2–5 |
| SPOT5 HRG | 2.5, 5 | 0.6–1.0 | | 2–5 | |
| SPOT5 HRS | 5 × 10 | 0.8 | | | 3–5 |
| Formosat-2 | 2 | 1.0 | | | 2–3 |
| Cartosat-1 | 2.5 | 0.58 | | | 3–7 |
| ALOS PRISM | 2.5 | 1.0 | | | 5–7 |

The variations in the results for each stereo configuration are due to the different research studies over different types of relief and different 3D mathematical models and algorithms (Toutin 2000)

surface constraints. More details on DEM and image matching are available in the following papers (Ackermann 1994; Grün 1997; Toutin 2000).

The main drawback of applying image matching to across-track stereoscopy is the use of multirate stereo data with radiometric variations stemming from different dates, seasons, or environmental conditions. These radiometric variations mainly reduce the match-success rate and increase mismatched areas, which could result in prolonged semiautomatic postprocessing. The ASTER instrument's simultaneous along-track stereo-data acquisition offers a strong advantage in terms of radiometric variations versus the multirate across-track stereo data acquisition. The images are acquired in a few seconds instead of days or months, which result in quasi-similar images that are better suited for any image matching process (Colvocoresses 1982; Fujisada 1994; Toutin 2000). This was confirmed by a very high correlation success rate (82.6%) obtained with JERS-OPS stereo images (Raggam et al. 1997) and more than 90% with ASTER stereo data (Toutin 2002; Toutin and Cheng 2002; Hirano et al. 2003).

Notwithstanding the wide range of sensors in Table 19.2, elevation accuracy as ordered by the system instantaneous field of view (or approximately the pixel spacing) was derived by also considering the *B/H* ratio. In most cases, the accuracy obtained with real data was better than those predicted by prelaunch information alone. This was also confirmed with simulated stereo ASTER data from SPOT stereo data resampled at 15 m. The simulated ASTER DEM posting was set to 30 m to match the USGS 7½-min DEM. Based on 63 spot elevation points, an accuracy of 13 m was obtained, which corresponds to a 0.5-pixel matching accuracy (Welch et al. 1998).

However, this accuracy evaluation based on a reduced number of spot elevations is a little biased and optimistic because DEM points are rarely easily identifiable unlike spot elevations. On the other hand, an accuracy of around 20 m was obtained in independent studies over a mountainous Japanese site or a French site (Dowman and Neto 1994), which provides a more conservative potential accuracy for ASTER DEMs. The theoretical accuracy of an ASTER DEM is governed by the accuracy of the control data, the B/H ratio, and the matching. Only a relative DEM is derivable in the absence of control data, and its accuracy will depend on the other two parameters only. A simplified 1D model to compute the elevation from the measured parallax is used as follows (19.1):

$$\Delta h(x, y) \approx \Delta p(x, y)/\tan\theta \approx \Delta p(x, y)H/B \quad (19.1)$$

where Δh and Δp are the relative height and parallax at each image point (x, y) , respectively, and θ is the stereo-intersection angle. This equation is only useful in a practical sense to determine elevation as a first approximation. Better 3D photogrammetric models, as mentioned earlier, are better suited to accurately determine 3D positioning.

Since an error of ± 0.5 –1 pixel or better (half pixel or better in areas when well-defined features are present, and one pixel in more homogeneous areas) for the parallax measurements in the automated matching process is achieved with different datasets from other sensors (along-track and across-track), the potential relative accuracy for the along-track stereo-derived DEM from ASTER ($B/H = 0.6$; pixel spacing of 15 m) is possibly around 12–25 m or better (Welch et al. 1998). Simulated ASTER stereo pairs were generated from along-track JERS-1 OPS stereo data and processed to generate a DEM. The errors were computed by comparison with a DEM generated from a 1:25,000 topographic map of the Geographical Survey of Japan. It produced a root mean square (RMS) error of 12 m with less than 1-m bias and 200-m maximum error (Tokunaga et al. 1996). The accuracy of the relative DEM depends on the geometric calibration as well as the accuracy of the ephemeris and attitude data. Recent studies with commercial off-the-shelf (COTS) photogrammetric software produced less than 10-m accuracy results for relative DEMs (Toutin 2008). These results are better compared to expected outcomes from using only the new calibrated geometric parameters (line-of-sight and pointing axis vectors and across-track pointing axis). These parameters were precisely adjusted (50-m 3-s geolocation accuracy and 15-m 3-s internal accuracy) with several accurate GCPs in the geometric validation phase of the initial checkout period (Iwasaki and Fujisada 2005). The accuracy of the absolute DEM mainly depends on the control data used (accuracy, number, and distribution) to compute the mathematical geometric modeling (image-to-map relationship), or to transform the relative DEM into an absolute map-oriented DEM. At least twice more precise (compared to the expected final DEM) control data help avoid errors in the absolute DEM. For example, with the 12–25-m accuracy previously discussed, control data derived from 1:50,000 topographic maps and smaller, with 10 m accuracies (A1 or A2 according to NATO standard) are deemed adequate. Absolute ASTER DEMs were validated in both Japan and the United States to verify their accuracies (Fujisada et al. 2005). Further results on the relative and absolute DEM's accuracies are discussed in the following sections.

19.3 ASTER DEM Production at the LP DAAC

The LP DAAC began to produce its first ASTER DEMs for public end users in July 2000. They initially selected a low production rate for programmatic reasons consistent with different capability and cost scenarios (Lang and Welch 1999). This section is based on the *Algorithm Theoretical Basis Document for ASTER Digital Elevation Models (ATBD-AST-08), Version 3.0* (Lang and Welch 1999).

From 2000 to 2006, two types of standard ASTER DEM products (relative and absolute) were produced at LP DAAC and their main specifications are given in Table 19.3 based on prelaunch simulations by the U.S./Japan Science Team DEM Working Group (Fig.19.4). Relative DEMs with 10–30 m accuracy were produced without GCPs, and were referenced to the lowest elevation in the scene with only satellite ephemeris data. Inadequate pointing and ephemeris information (~300 m in *X* and *Y*) require referencing absolute DEMs to a map coordinate system using GCPs (O’Neill and Dowman 1993). The design specifications of the absolute DEMs were thus defined at 7–50 m accuracy depending of the number of GCPs. Absolute ASTER DEMs are thus more accurate than the Digital Terrain Elevation Data-1 (DTED-1), even though they do not provide complete coverage of the land surface. As pointed out by Ackermann (1994), the elevation accuracy is, however, not a sufficient measure by itself for defining the DEM quality. The posting (DEM grid), the *Z*-increment, the slope measurement accuracy, and the equivalent mapping scales are four other parameters to consider. A 30-m selection posting was based on expected accuracy and practical considerations. Performing successful image matching is possible at each 15-m pixel in good imaging situations. Therefore, generating a 30-m posting DEM only requires 25% success rate, which is accomplishable in all terrain and imaging situations. Based on 10–50 m *Z*-accuracy, a 5° slope accuracy is attainable over a 100–500 m measurements distance or more. These specifications render ASTER DEM’s usefulness at 1:100,000 to 1:250,000 mapping scales. In some cases, a 1:50,000 mapping scale is achievable.

The LP DAAC started producing a single standard relative DEM since the summer of 2006. Table 19.3 provides its specifications. A major change includes providing the DEM in GeoTIFF.

Table 19.3 Definitions and specifications for the standard ASTER DEM products [adapted from Lang and Welch (1999)]

| | | | |
|------------------|----------------------------------------------------------------------------------------------------------------------------------------|-----------------------------------|------------------------------|
| Unit of coverage | 60 km by 60 km ASTER scene; 2,500 rows and 2,500 columns | | |
| Format | Data consist of a regular array of elevation (in meters) referenced to a specific elevation and projected in the UTM coordinate system | | |
| Resolution | <i>XY</i> : 30-m posting | <i>Z</i> : 1-m smallest increment | |
| Format/Size | HDF-EOS; 32-bit signed integer and ~ 25 MB file size | | |
| Product name | Minimum Nb. of GCPs | GCP RMS error (<i>XYZ</i>) | DEM RMS error (<i>XYZ</i>) |
| Relative DEM | 0 | – | 10–30 m ^a |
| Absolute DEM | 1 | 15–30 m | 15–50 m ^b |
| Absolute DEM | 4 | 5–15 m | 7–30 m ^b |

^a*Z* values referred to local vertical datum

^b*Z* values referred to absolute vertical datum (mean sea level)

19.3.1 DEM Generation Algorithms

From 2000 to 2006, the LP DAAC used PCI's *OrthoEngine*^{SE} photogrammetric software to produce standard ASTER DEM products. This software's capabilities to process ASTER stereo data were developed in 1999 under USGS contract with the collaboration of Canada Centre for Remote Sensing, Natural Resources Canada for the mathematical and 3D modeling aspects (Toutin 1995, 2002). This commercial system was acquired and operated at the LP DAAC to produce ASTER DEMs at a rate of one per day, but production rates were somewhat larger (Hirano et al. 2003). Absolute DEMs require a theoretical minimum of six accurate user-supplied GCPs to produce the DEM product. However, the number of GCPs mainly depends on their source and accuracy. When GCPs are not accurate enough (less than 5–10 m), a larger number of them is necessary to reduce GCP error propagation in the iterative least-squares stereo-bundle adjustment. As described by Clavet et al. (1993), the main sources for GCPs used in satellite photogrammetry include the following: (a) topographic maps, (b) photogrammetric triangulation from aerial surveys, and (c) global positioning system (GPS) data. On the other hand, notwithstanding differential GPS' high accuracy, it is deemed too expensive for the expected accuracy. Topographic maps are the most available control data for most of the land areas of the world, but their utility depends on scale, source, and format (paper, raster scanned, digital vector). Topographic maps at 1:25,000 scale, as well as inexpensive handheld GPS receivers provide 5–10 m accurate GCPs; 6–8 GCPs are usually a sufficient amount to process a DEM. At 1:50,000 scale, GCPs are 10–15 m accurate; 10–12 GCPs are enough. Finally, 1:100,000 scale maps yield 15–30 m accurate GCPs; 15–20 such GCPs are deemed adequate.

The general flowchart and algorithms to produce Standard DEM products at the LP DAAC are described in Fig. 19.2. Prior to May 2006, users placed orders for either an absolute (with user-provided GCPs) or a relative DEM (which relied on instrument-derived ephemeris data). Two main tasks constitute the DEM output creation: (1) the first task includes three processes (enter GCPs or extract corner/center points, select TPs, and compute 3D physical model), that address the image-to-ground relationship computation; (2) the second task includes the last three processes identified in Fig. 19.2 (resampling $3N$ and $3B$ in quasi-epipolar geometry, image matching, and DEM editing), which address the DEM generation. The image-to-ground relationship was based on a 3D multisensor physical modeling approach, developed at CCRS, to address the geometry of push-broom scanners like SPOT-HRV (Toutin 1983) or ASTER (Toutin 2002; Toutin and Cheng 2002). This approach was subsequently adapted as an integrated and unified model to geometrically process a variety of multisensor data (Toutin 1995, 2004).

Following the first two processes, the full coordinates of the mono and stereo GCPs or the corner/center points and the image coordinates of the automatically collected tie-points (TP) between the $3N$ and $3B$ images are used with the metadata (ephemeris, pointing angles, etc.) to compute the 3D physical model. The model is first initialized with approximate values computed from the metadata, and then refined by an iterative least-squares stereo-bundle adjustment with the GCPs/TPs

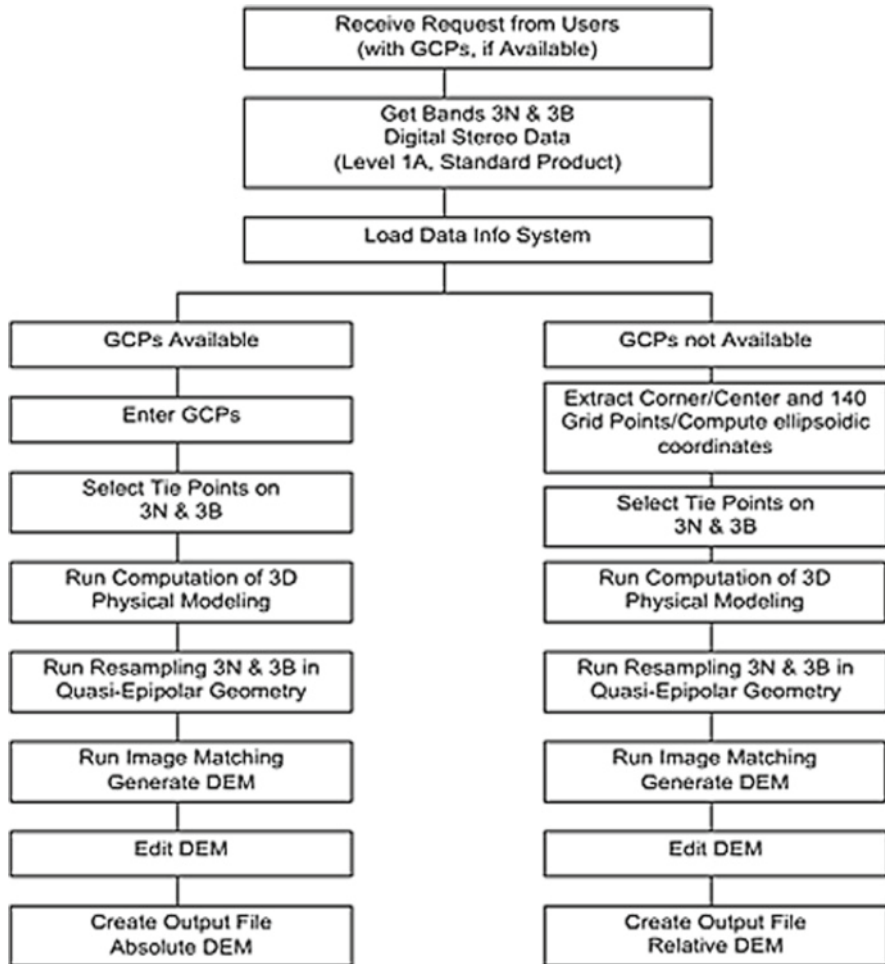


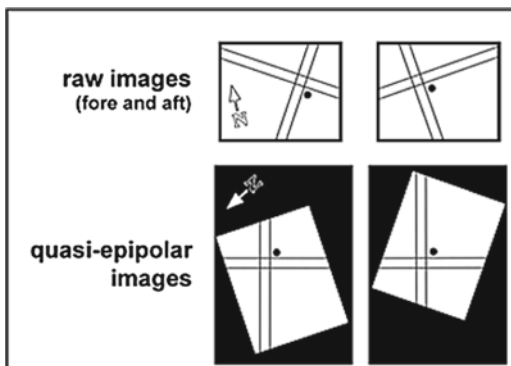
Fig. 19.2 Flowchart for producing standard DEM products at LP DAAC

and orbital constraints. Stereo GCPs and TPs are used to create a mathematical link in the error equations between the stereo images (coplanarity condition) to increase the relative accuracy between the stereo images.

The second main task relates to DEM generation performed with an image-matching algorithm. The resampling of stereo images (3N and 3B) in quasi-epipolar geometry (where the only remaining distortion is related to the elevation parallax in the longitudinal direction) was first performed (Fig. 19.3). The quasi-epipolar images are stereo pairs with the same pixel spacing that are reprojected so that the two images have a common orientation and matching features between the images along a common *x*-axis (Baker and Binford 1981).

Using quasi-epipolar images simplify the matching algorithm, increase the computation speed, and reduce the possibility of incorrect matches. The image-matching

Fig. 19.3 Geometric relationship between the stereo raw images (fore and aft) and the stereo quasi-epipolar images



process helps extract elevation parallaxes by finding corresponding pixels between the quasi-epipolar stereo images (Fig. 19.3). The process uses a three-step multiscale mean-normalized cross-correlation method, which computes the maximum correlation coefficient at the subpixel level. This method produced good results, and was commonly used with satellite images (Gülch 1991). The difference in location between the quasi-epipolar images yields the parallax for each pair of matched points. The result was a regular grid-spaced DEM in the quasi-epipolar geometry with occasional small pits and hills as artifacts, particularly in flat areas, and with mismatched values over failed correlations with clouds, water, or featureless terrain (dry lakes, snow, etc.). Therefore, the DEM editing required a series of automatic and interactive routines (filtering, smoothing, interpolating) to correct spikes, noise, and mismatched areas. The quasi-epipolar images and DEM are in the same geometry; therefore, interactive routines with the images are possible either viewed in 2D or 3D anaglyph, or polarized glasses. The edited epipolar DEM was finally reprojected as a regularly spaced grid into the user-map projection with absolute elevations above the mean sea level, while the map coordinates were computed with 3D space intersections using the previously computed 3D physical model. ASTER relative elevations may have a systematic bias compared to reference elevation data, while planimetric position errors (X - Y) showed a systematic offset as high as 700 m. When these two offsets were removed with at least one control point, the values typically are within 10–25 m of a reference position, which was within specifications.

The LP DAAC implemented a new production software, called Silcast,TM in summer of 2006, to efficiently produce quality DEMs. Based on an automated stereo-correlation method, the new software generates a relative DEM without GCPs. It uses the ephemeris and attitude data derived from both the ASTER instrument and the Terra spacecraft platform. An ASTER level-1A dataset is used for both digital elevation extraction and orthorectification. Larger water bodies are automatically detected and typically have a single value, but they no longer are manually edited. Any failed areas remain as they occur. Cloudy areas typically appear as bright regions, rather than as manually edited dark areas. Users may need

to postprocess some of these areas. A water detection option was also implemented. The default option is “water = on,” but users may select “water = off.” The default option generally produces satisfactory results. However, certain scene-specific conditions may warrant turning off the water detection.

19.3.2 DEM Products and Validation

The previous relative and absolute DEMs were stored in an HDF-EOS output file with relevant quality control and related metadata information provided in the header (Table 19.4). In the early years, the DEM’s geocoding information was handled by the PCI™ image-processing package. In most cases, users manually georeferenced the DEM with coordinates from the metadata file. Since May 2006, however, the ASTER DEM product is provided in GeoTIFF.

The PCI™-produced first DEMs were validated over 11 global sites, designated by the U.S./Japan ASTER DEM Working Group, which also possessed accurate DEMs based on other data sources (Table 19.5).

Three validation methods were performed over each site after the launch (Thome et al. 1998):

1. The elevation accuracy was evaluated by subtracting the DEM’s height from the ASTER stereo-derived DEMs covering the same area on a per-pixel basis. Reported results include an elevation difference histogram, mean, standard deviation (one sigma), minimum and maximum.
2. The planimetric accuracy was evaluated by computing the horizontal displacements of the same distinct topographic features on elevation profiles between the reference and stereo-derived DEMs.
3. The planimetric and elevation accuracies were evaluated by comparing the 3D coordinates of GCPs with those extracted from the stereo-derived DEM.

In addition to the postlaunch validation, yearly validations with the above-described methods were performed for DEMs over each validation site. It was performed at least once per year to monitor and validate system stability over the first 6-year mission. The DEM validation was performed by the USGS, Jet Propulsion Laboratory, and the University of Georgia. The production of absolute DEMs appears satisfactory because differences of the means between reference DEMs and ASTER DEMs range from +4 to +27 m, for the validation datasets evaluated thus far. Other validation experiments on both absolute and relative DEM accuracies were performed over two U.S. study sites (Fujisada et al. 2005):

1. The Drum Mountains, Utah exhibit mountainous terrain typical of the Basin and Range province of the western United States.
2. Okoboji, Iowa exhibits low, gently rolling terrain typical of the Midwest regions of the United States.

The results indicate that the absolute DEM accuracies (RMS errors of 9–14 m) meet or exceed prelaunch specifications. Elevation differences were, however, more

Table 19.4 Relevant quality assurance and related metadata reported in an ASTER DEM header (after Lang and Welch 1999)

Carry through for the two level-1 input scenes (3N and 3B)

Scene date
 Scene-unique ID number
 Cloud assessment – percent
 Bad/suspect pixel QA image data plane

GCP input data

Number
 Location – line and sample
 Location – X, Y, Z and horizontal and vertical datum
 Provider(s) – name and address
 Source: GPS instrument type, surveying, map, photogrammetry
 Type of feature: road intersection, stream intersection

Product specification

Cell spacing
 Relative or absolute
 Percent of successful correlations
 Correlation method and matrix/window size used
 Lowest and highest elevation values
 Filtered or not – type of filter used
 Edited: yes or no
 Overall quality assessment per operator and criteria
 Correlation coefficient QA image data plane

Table 19.5 Test sites used to validate the general procedure to generate stereo-extracted ASTER DEMs (after Lang and Welch 1999)

| Validation site | Approximate geographic coordinates |
|------------------------------|------------------------------------|
| Mount Kiso-Komagatake, Japan | 36°N/138°E |
| Huntsville, AL, USA | 35°N/85°W |
| Mount Fuji, Japan | 33°N/130°E |
| Taxco/Iguala, Mexico | 18°N/99°W |
| Mount Tsukuba, Japan | 36°N/140°E |
| Drum Mountains, Utah, USA | 40°N/113°W |
| Mount Aso, Japan | 33°N/132°E |
| Mount Etna, Italy | 38°N/15°W |
| Mount Utzen, Japan | 33°N/130°E |
| Saga Plain, Japan | 33°N/130°E |
| Lake Okoboji, Iowa, USA | 43°N/96°W |

pronounced in the high-relief areas of the Drum Mountains site while a “noisier” DEM was noticed in lower relief areas of Okoboji site where sometimes image correlation was more difficult to accomplish. On the other hand, relative DEMs were not declared validated until a problem in the LP DAAC’s original version, possibly related to certain positional inaccuracies in the ASTER metadata caused by

incomplete correction of the nutation, was fixed (Fujisada et al. 2005). The horizontal geolocation accuracy was also calculated by determining the differences in UTM coordinates for the same identifiable point (generally road intersection) in the ASTER orthoimage and a USGS digital orthophoto quad. This geolocation accuracy appears limited by the satellite's positional accuracy (around 50 m, 3-s).

In 2005–2006, the USGS completed a thorough validation of the new ASTER DEM product, which indicates much improvement. The new DEM's accuracy meets or exceeds accuracy specifications set for the ASTER relative DEMs by the ATBD. Validation testing has further shown that DEMs are frequently more accurate than 25 m (RMSE_{xyz}), thus approaching the accuracy specified for absolute DEMs.

Besides this unpublished USGS validation study, few other scientific experiments were published to evaluate the capability of the Silcast software, except by Cuartero et al. (2005). Even if DEMs are generated without GCPs, a RMS error of ± 6.1 m was achieved when compared to 40 independent check points (ICPs). While these results are limited, it gives a good indication of the excellent performance of Silcast. Unfortunately, no information on the software and its algorithms can explain why these final results (± 6.1 m) are more accurate than the ± 15 m geolocation accuracy obtained for DEMs generated using only the metadata (Iwasaki and Fujisada 2005; Fujisada et al. 2005), because no GCPs were used to refine their geolocation accuracy.

19.4 ASTER DEM Production at ERSDAC, Japan

One of the Japanese objectives of the ASTER along-track stereo experiment was to produce DEM products at the Earth Remote Sensing Data Analysis Center (ERSDAC) (Tokunaga et al. 1996). The ASTER DEM products are divided into relative and absolute DEMs. Relative DEMs are generated on an operational basis as a semistandard product, while absolute DEMs requiring GCPs are generated as a special product based on users' request. These products have a compatible format to the LP DAAC's standard products. Some of their DEM generation policies are, however, somewhat different from those of the LP DAAC (Tokunaga et al. 1996):

1. DEM are operationally generated with 30-m grid spacing.
2. GCPs are not used on an operational basis.
3. Coarse DEMs (1-km GLOBE or DCW products) are used on an operational basis.
4. DEM generation over Southeast Asia is the highest priority.

In addition, potential errors or abnormal elevations traced to specific data (clouds, water bodies) and to the DEM generation algorithm (mismatched areas) are automatically detected and marked in the final products to insure quality control and validation. The algorithm and process used to operationally generate DEM products at ERSDAC are reported in the *ASTER User's Guide, Part III, Standard and Semistandard Data Products (DEM) (L4A01) Version 1.1* (ERSDAC 2005). This section is based on that *User's Guide*, as well as on published scientific papers (Tokunaga et al. 1996; Fujisada et al. 2001, 2005; Iwasaki et al. 2001; Iwasaki and Fujisada 2005).

19.4.1 DEM Generation Algorithms

Figure 19.5 describes the DEM generation flowchart, and Fig. 19.6 provides further details on the algorithm. ERSDAC performs certain tasks in parallel alongside the DEM generation (Fig. 19.6). They include the extraction and marking of clouds and

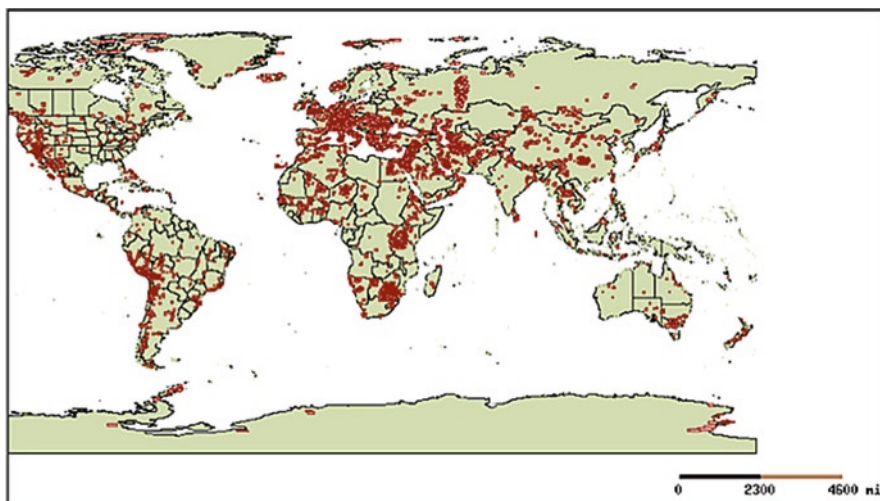


Fig. 19.4 Reference map of the world showing the areas where standard DEM products from ASTER stereo data were generated at LP DAAC

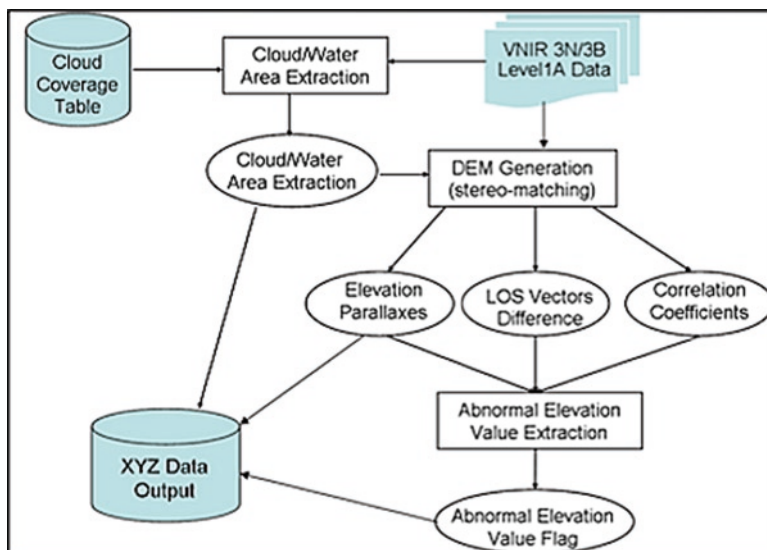


Fig. 19.5 General flowchart at ERSDAC for DEM XYZ data output [adapted from Tokunaga et al. (1996)]

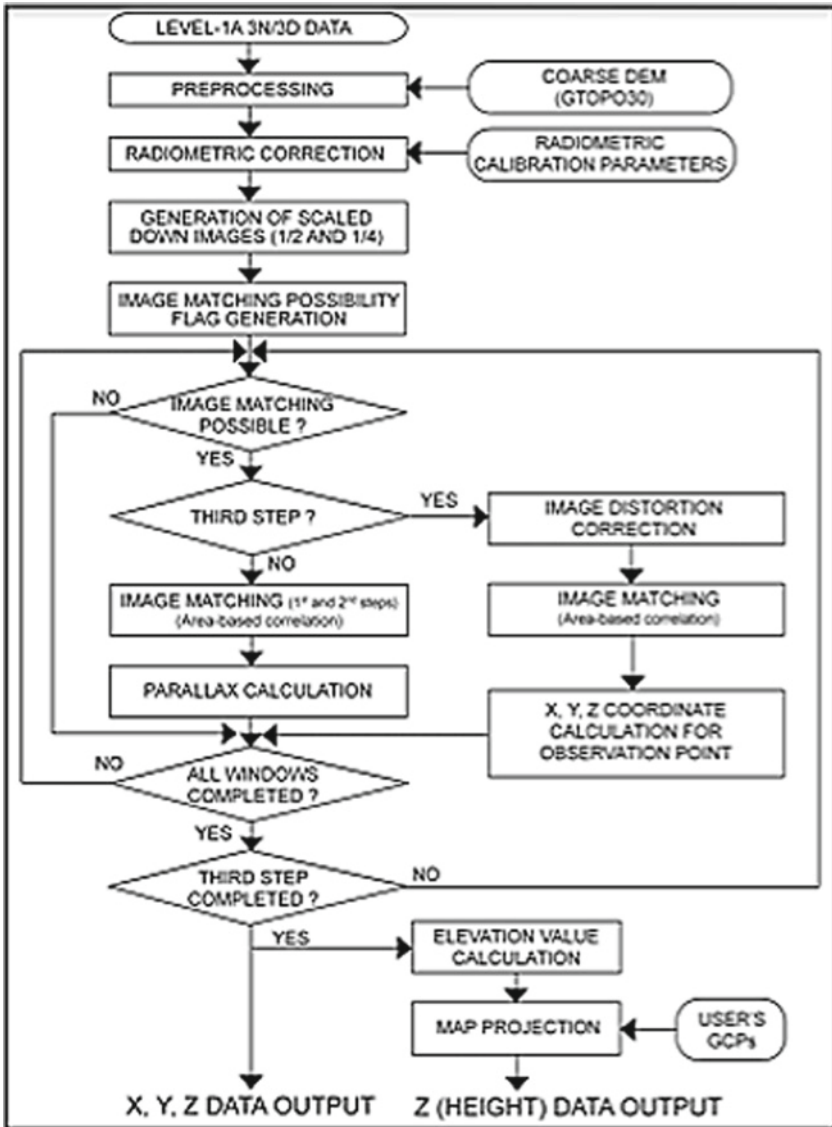


Fig. 19.6 Algorithm flowchart developed at ERSDAC with the various tasks for DEM generation [adapted from Fujisada et al. 2001; ERSDAC, 2005]

water areas with external data besides abnormal elevation values with output data from the stereo-matching task. ERSDAC's DEM generation shares similarities with LP DAAC, which include the following: (a) radiometric aspect is used to extract the elevation parallaxes with multiscale image-matching methods, and (b) the

geometry is used to compute the elevation with only the instrument and spacecraft ephemeris and attitude parameters. The main differences include the following: (a) the match is performed in the original image geometry, not in a quasi-epipolar geometry (elevation parallaxes only in the transverse direction, Fig. 19.3), and (b) no GCPs are used operationally. Figure 19.6 describes the different tasks of the ERSDAC DEM generation process.

19.4.2 Products Description and Validation

Single scene-based DEM H products are orderable by the public (Fig. 19.7), and a large area mosaicked DEM is provided as well (Fig. 19.8). The product processing and distribution service helps users with their data orders and deliveries (http://www.gds.aster.ersdac.or.jp/gds_www2002/service_e/g.t.u.p_e/g.t.u.p7_e.html).

These products (in HDF format) contain three kinds of data: (1) metadata, (2) DEM H grid, and (3) DEM supplemental data, which are separated in the following structure (ERSDAC 2002, 2005):

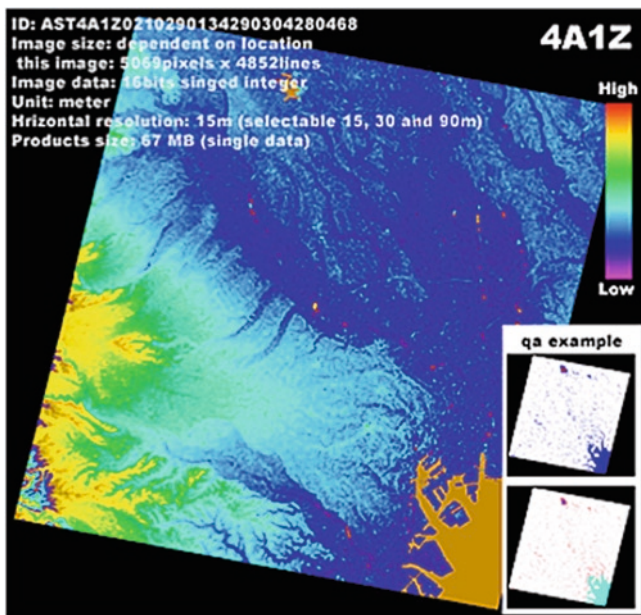


Fig. 19.7 Example of a relative DEM H data product (4A01) with QA planes offered per scene http://www.gds.aster.ersdac.or.jp/gds_www2002/exhibition_e/a_products_e/a_product2_e.html (© ERSDAC)

Fig. 19.8 Example of relative DEM H data product offered over large areas by mosaicking four individual DEMs per scene. (© ERSDAC)



1. Metadata

- Inventory metadata
- ASTER generic metadata
- Ground Data System generic metadata
- DEM specific metadata

2. DEM H grid

- DEM H data
- First quality assurance (QA) data plane
- Second QA data plane
- Correlation coefficient
- Local maximum slope data

3. DEM supplemental data

Further details on the product specifications are available from ERSDAC (2002).

The DEM performance was evaluated in terms of accuracy of both the horizontal (geolocation) and vertical values (elevation). The DEMs were generated from 14 stereo pairs over five validation sites in Japan (Tsukuba, Mount Yatsugatake, Mount Fuji, Unzen, Saga); Yatsugatake and Mount Fuji have a mountainous alpine relief with 3,000-m elevation variation. Two different methods and reference datasets were applied to verify DEM accuracies (Fujisada et al. 2001, 2005):

1. Evaluation of horizontal and vertical accuracies against 5–20 accurate ICPs. The ICPs were measured using differential GPS with ± 3.5 -m horizontal accuracy and ± 1 -m vertical accuracy.
2. Evaluation of only vertical accuracy against accurate DEM database derived from 1:25,000 topographic maps.

The horizontal geolocation accuracy for the 14 DEMs computed with differential GPS ICPs is generally better than ± 50 m (3-s) in both axes with less than 5-m bias, which is consistent with the 50-m (3-s) spacecraft position accuracy obtained using the calibrated instrument parameters (Iwasaki and Fujisada 2005; Fujisada et al. 2005). This geolocation accuracy thus appears limited by the spacecraft's position accuracy. The vertical accuracy is ± 10 m (1-s) with almost no bias, which is also consistent with the ± 10 m (1-s) vertical accuracy of the calibrated instrument system parameters (Fujisada et al. 2005). These evaluations are, however, a little biased due to the reduced number of ICPs, which are in addition, well-defined features on the stereo images, where the image matching performed well.

The second method gives more confident results because the vertical accuracy was computed over millions of checked points of topographic DEMs. Figure 19.9 shows results for Mount Yatsugatake site with the stereo-extracted DEM with elevation and elevation error profiles. While the elevation error histograms were also provided for this DEM and some other DEMs over Tsukuba and Saga sites (Fujisada et al. 2005), the standard deviations were not given. Nevertheless, the histograms show biases of around -12 and 0 m, as well as the minimum/maximum errors of ± 50 and ± 30 m for Yatsugatake and Tsukuba DEMs, respectively. The elevation errors are consistent with the previous method and calibrated system parameters accuracy, except for the sharp error peaks in the mountainous areas, which tend to show that elevation errors are correlated with the terrain relief.

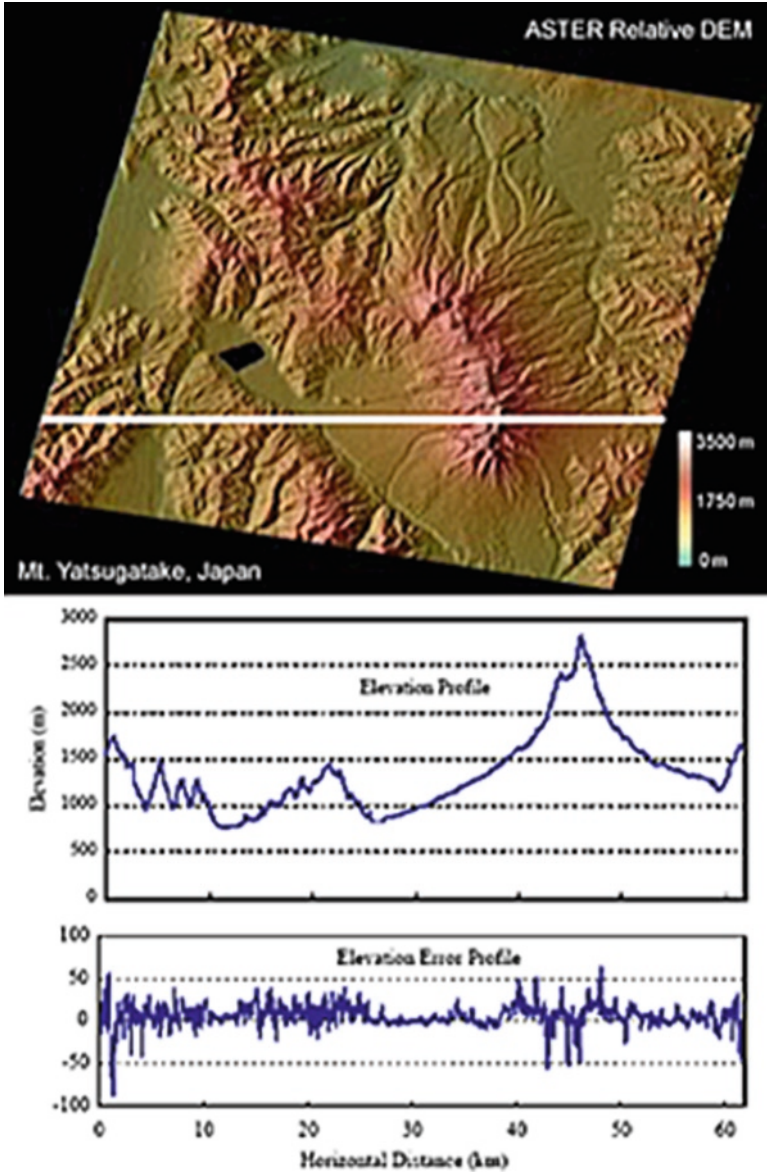


Fig. 19.9 ASTER relative DEM over Mount Yatsugatake with an elevation profile and the elevation error profile (Fujisada et al. 2005). The profiles are elevation data along the horizontal white line in ASTER DEM image (Fujisada et al. 2005). (© ERSDAC)

19.5 Concluding Remarks

The ASTER instrument on the Terra platform was designed and launched to acquire multispectral data from which to generate detailed maps of land surface temperature, radiance, reflectance, and elevation. It also provides a new source of topographic data to study the Earth's land surface (Yamaguchi et al. 1998; Welch et al. 1998). The expected geometric and stereoscopic performances of the standard DEM products were $\pm 10\text{--}30$ m (1-s) for the geopositioning and elevation accuracy depending upon the number and quality of GCPs used. A Joint U.S./Japan Science Team was responsible for instrument design, calibration, and validation. Both countries fulfill these general objectives with slightly different policies. Methods, algorithms, and software were specifically defined and developed to take into account the characteristics of the system and instrument. Relative DEMs are accurately derivable due to the quality spacecraft ephemeris and the instrument parameters. The geolocation accuracy (better than 50 m, 3-s) for relative DEMs appears, however, limited by the spacecraft's position accuracy. On the other hand, the elevation accuracy is around 10 m with larger errors in mountainous areas. The precise in-flight calibration of the instrument parameters during the initial checkout period was one of the main reasons for the high-quality relative DEMs. User-supplied GCPs only slightly improved absolute DEMs, especially their elevation accuracy. In all comparisons of ASTER relative/absolute DEMs generated before 2006 and validated at USGS and ERSDAC, the geopositioning and elevation accuracy meets or exceeds prelaunch specifications (Fujisada et al. 2005).

Apart from the operational production on a regular basis in the United States and Japan, numerous research scientists, in government, university and private organizations look at the quality and the performance of ASTER DEMs for cartographic/topographic and geoscientific applications (Toutin 2008). In general, all studies using COTS or proprietary software achieved good results (10–20 m accuracy depending on terrain relief) consistent with prelaunch specifications and USGS/ERSDAC products. These DEMs were very useful in many geoscientific applications in remote areas, where accurate DEMs are nonexistent. The Global Land Ice Measurements from Space (GLIMS: <http://www.glims.org>) project aims to compile a global glacier inventory, and acquire an annual image of the world's leading glaciers. The GLIMS project characterizes a leading application example of how ASTER-derived products contribute to understanding global glaciers and climate change (Kääb 2005).

References

- Ackermann F (1994) Digital elevation models-techniques and applications, quality standard. *International Archives of Photogrammetry and Remote Sensing* 30(4): 421–432
- Baker HH, Binford TO (1981) Depth from edge and intensity-based stereo. *Proceedings of the Seventh International Joint Conference on Artificial Intelligence*, Martin Kaufman Publishers, Vancouver, BC, Canada, (San Diego, USA), 631–636

- Bouillon A, Bernard M, Gigord P, Orsoni A, Rudowski V, Beaudoin A (2006) SPOT-5 HRS geometric performances: Using block adjustment as a key issue to improve quality of DEM generation. *ISPRS J Photogramm Remote Sensing* 60(3):170–181
- Clavet D, Lasserre M, Pouliot J (1993) GPS control for 1:50,000-scale topographic mapping from satellite images. *Photogramm Eng Remote Sensing* 59 (1):107–171
- CNES, Centre National d'Etudes Spatiales (1987) SPOT-1: Utilisation des images, bilan, résultats. SPOT-1 Symposium, France, Paris, pp 1163–1392
- Colvocoresses AP (1982) An automated mapping satellite system (Mapsat). *Photogramm Eng Remote Sensing* 48(10):1585–1591
- Cuartero A, Quirós E, Felicísimo AM (2005) A study of ASTER DEM accuracies and its dependence of software processing. Proceedings of 6th International Conference on Geomorphology, Zaragoza, Spain, Abstracts Vol. 382, 7–11. Available online at http://www.unex.es/eweb/kraken/pdf/6Geom_05.pdf (accessed March 15, 2009)
- Dowman I, Neto F (1994) The accuracy of along-track stereoscopic data for mapping: Results from simulations and JERS OPS. *Int Arch Photogramm Remote Sensing* 30(4):216–221
- ERSDAC (2002) ASTER Level 4A01 Data Products Specifications (GDS Version), Version 1.1, p 65 http://www.gds.aster.ersdac.or.jp/gds_www2002/libraly_e/4adoc/AG-E-E-2211-R031.doc (last accessed March 15, 2009)
- ERSDAC (2005) ASTER User's Guide, Part III, Standard and Semi-standard data products (DEM) (L4A01) Version 1.1, p 21 http://www.science.aster.ersdac.or.jp/en/documents/users_guide/part1/pdf/Part3D_1.1E.pdf (last accessed March 15, 2009)
- Förstner W (1982) On the geometric precision of digital correlation. *International Archives of Photogrammetry Helsingfors, Finland, (Helsinki, Finland: ISPRS)*, 24:(B3), pp. 176–189
- Fujisada H (1994) Overview of ASTER instrument on EOS-AM1 platform. Proceedings of SPIEvol. 2268:International Society of Optical Engineering, pp 14–36
- Fujisada H, Sakuma F, Ono A, Kudo M (1998) ASTER DEM performance. *IEEE Trans Geosci Remote Sensing* 36(4):1152–1160
- Fujisada H, Iwasaki A, Hara S (2001) ASTER stereo system performance. Proceedings SPIE: Sensor, System, and next-Generation Satellites V vol. 4540, pp 39–49
- Fujisada H, Bailey GB, Kelly GG, Hara S, Abrams MJ (2005) ASTER DEM Performance. *IEEE Trans Geosci Remote Sensing* 43(12):2707–2713
- Gopala Krishna B, Kartikeyan B, Iyer KV, Mitra R, Srivastava PK (1996) Digital photogrammetric workstation for topographic map updating using IRS-1C stereo imagery. *Int Arch Photogramm Remote Sensing* 31(B4):481–485
- Grün A (1997) Digital photogrammetric stations: A short list of unmatched expectations. *Geo Info Magazine* 11(1):20–23
- Gülch E (1991) Results of test on image matching of ISPRS WG III/4. *ISPRS J Photogramm Remote Sensing* 46(1):1–8
- Hirano A, Welch R, Lang H (2003) Mapping from ASTER stereo image data: DEM validation and accuracy assessment. *ISPRS J Photogramm Remote Sensing* 57(5–6):356–370. http://www.crms.uga.edu/pubs/isprs_aster_2003.pdf (last accessed March 15, 2009)
- Iwasaki A, Fujisada H, Tsujimoto S (2001) ASTER geometric performance. Proceedings SPIE: Sensor, System, and next-Generation Satellites V vol. 4540, pp 27–38, 17–20
- Iwasaki A, Fujisada H (2005) ASTER geometric performance. *IEEE Trans Geosci Remote Sensing* 43(12):2700–2706
- Kääb A (2002) Monitoring high-mountains terrain deformation from air- and spaceborne optical data. *ISPRS J Photogramm Remote Sensing* 57(1–2):39–52
- Kääb A (2005) Combination of SRTM3 and repeat ASTER data for deriving alpine glacier flow velocities in the Bhutan Himalaya. *Remote Sensing of Environment* 94:463–474
- Lang HR, Welch R (1999) Algorithm Theoretical Basis Document for ASTER Digital Elevation Models (ATBD-AST-08), Version 3.0. Jet Propulsion Laboratory, Pasadena, CA, 63
- La Prade G, Briggs SJ, Farrell RJ, Leonardo ES (1966) Stereoscopia. *Manual of Photogrammetry* (Chapter X), Third Edition, Bethesda, USA, ASPRS, pp 519–544

- Maruyama H, Kojiroi R, Ohtsuka T, Shimoyama Y, Hara S, Masaharu H (1994) Three-dimensional measurement by JERS-1 OPS stereo data. *Int Arch Photogramm Remote Sensing* 30(B4): 210–215
- O'Neill MA, Dowman IJ (1993) A simulation study of the ASTER sensor using a versatile general purpose rigid sensor modelling system. *Int J Remote Sensing* 14(3):565–585
- Raggam J, Gutjahr K, Almer A (1997) MOMS-2P und RADARSAT: Neue Sensoren zur stereometrischen Geländemodellerstellung. *Vermessung Geoinformatics*, Heft 4/97:267–280
- Thome K, Arai K, Hook S, Kieffer H, Lang H, Matsunaga T, Ono A, Palluconi F, Sakuma H, Slater P, Takashima T, Tonooka H, Tsuchida S, Welch RM, Zalewski E (1998) ASTER pre-flight and inflight calibration and the validation of Level 2 products. *IEEE Trans Geosci Remote Sens* 36(4):1161–1172
- Tokunaga M, Hara S, Miyazaki Y, Kaku M (1996) Overview of DEM product generated by using ASTER data. *Int Arch Photogramm Remote Sensing* 31(B4):874–878
- Toutin T (1983) Analyse mathématique des capacités stéréoscopiques du satellite SPOT. *Mémoire de DEA, Ecole Nationale des Sciences Géodésiques*, France, 74
- Toutin T (1995) Multi-source data fusion with an integrated and unified geometric modelling. *EARSeL Adv Remote Sensing* 4(2):118–129
- Toutin T (2000) Elevation modeling from satellite data. In: *Encyclopaedia of analytical chemistry*, Meyers R (ed) Wiley, Chichester, UK, vol. 10, pp 8543–8572
- Toutin T (2002) 3D topographic mapping with ASTER stereo data in rugged topography. *IEEE Trans Geosci Remote Sensing* 40(10):2241–2247
- Toutin T (2004) Comparison of stereo-extracted DTM from different high-resolution sensors: SPOT-5, EROS-A, IKONOS-II, and QuickBird. *IEEE Trans Geosci Remote Sensing* 42(10): 2121–2129
- Toutin T (2006) Generation of DSM from SPOT-5 in-track HRS and across-track HRG stereo data using spatiotriangulation and autocalibration. *ISPRS J Photogramm Remote Sensing* 60(3):170–181
- Toutin T (2008) ASTER DEM for geomatic and geoscientific applications: a review. *Int J Remote Sensing* 29(7):1855–1875, DOI: 10.1080/01431160701408477
- Toutin T, Cheng P (2002) Comparison of automated digital elevation model extraction results using along-track ASTER and across-track SPOT stereo images. *Opt Eng* 41(9):2102–2106
- Welch R, Jordan RT, Luvall JC (1990) Geocoding and stereo display of tropical forest multi-sensor datasets. *Photogramm Eng Remote Sensing* 56(10):1389–1392
- Welch R, Lo CP (1977) Height measurements from satellite images. *Photogramm Eng Remote Sensing* 43(10):1233–1241
- Welch R, Jordan T, Lang H, Murakami H (1998) ASTER as a source for topographic data in the late 1990s. *IEEE Trans Geosci and Remote Sensing* 36(4):1282–1289
- Willard JH (1992) Database blending for the climatology of cloud statistics program. Phillips Laboratory, Hanscom Air Force Base, Massachusetts, Publication PL-TR-92-2344, p 57
- Yamaguchi Y, Kahle A, Tsu H, Kawakami T, Pniel M (1998) Overview of Advanced Spaceborne Thermal Emission and Reflection Radiometer (ASTER). *IEEE Trans Geosci Remote Sensing* 36(4):1062–1071

Chapter 20

Using ASTER Stereo Images to Quantify Surface Roughness

Amit Mushkin and Alan Gillespie

Abstract The unresolved topographic expression of surfaces, surface roughness (SR), is a fundamental surface property that conveys useful information for a wide range of Earth and planetary sciences. Yet, this information is difficult to measure remotely because most spaceborne imagers have resolutions on the order of meters to hundreds of meters and SR can vary significantly below these scales. One way to measure SR is to exploit differential shadowing in stereo images, and in particular, Advanced Spaceborne Thermal Emission and Reflection Radiometer (ASTER), with its nadir (3N) and backward-looking (3B) near-infrared channels. We have proposed a simple ratio of land-leaving radiance in those two channels as a measure of relative SR at scales <15 m/pixel. This “two-look” relative SR measure is simple, robust, and insensitive to atmospheric conditions, and thus ASTER 3B/3N ratio images are suggested as a useful and readily accessible tool for photo-interpretation. Moreover, one could calibrate the ratio data to physical parameters, such as RMS height, and translate to SR maps at 15 m/pixel resolution. Two calibration schemes enable this translation: empirical calibration against independent in situ roughness measurements and model-based calibration against forward simulations of two-look ratios from very high-resolution (<5 mm) digital elevation models of natural surfaces, measured with a ground-based light detection and ranging system. Here, we focus on the latter scheme that enables construction of calibration curves for any given viewing and illumination geometries encountered by ASTER. ASTER now provides a global archive of images, and the two-look approach with ASTER stereo data enables a unique quantitative mapping capability of SR at 15 m/pixel spatial resolution for almost anywhere on Earth.

A. Mushkin (✉)

Geological Survey of Israel, 30 Malkhe Israel St., Jerusalem 95501, Israel
e-mail: mushkin@gsi.gov.il

20.1 Introduction

Surface roughness (SR) describes the unresolved topographic expression of the surface below the spatial resolution of available digital elevation models (DEM). The SR is a scale-dependent, fundamental surface property and a key parameter in many geological, hydrological, and planetary studies, as well as an essential variable in remote sensing applications and atmosphere – surface boundary layer energy-exchange models. Ground-based measurements of SR are unrealistic for large-scale investigations; therefore, SR characterization from remotely sensed data was the focus of many previous studies. In this regard, successful efforts for terrestrial environments included the use of radar backscatter (Zebker and Goldstein 1986; Evans et al. 1992; Weeks et al. 1997), multichannel visible to near-infrared (VNIR) (0.4–1.1 μm) reflectance data (Li et al. 1998), a combination of both radar and VNIR reflectance data (Evans and Smith 1991; Weeks et al. 1996), as well as multispectral thermal infrared (TIR) images (Ramsey and Fink 1999). In planetary studies, SR was also remotely mapped from thermal inertia measurements (Jakosky 1979; Palluconi and Kieffer 1981; Christensen 1986) and “Hapke” parameter (Hapke 1993) estimation derived from multidirectional data (Pinet et al. 2005). A common difficulty in all these approaches remains the complexity of natural surfaces commonly exceeding the dimensionality of available data, thus typically rendering remote roughness inversions as underdetermined problems with nonunique solutions (Weeks et al. 1997).

The specific problem of distinguishing between the subpixel effects of SR and surface composition (i.e., surface dielectric, reflectivity and emissivity for radar, VNIR and TIR data, respectively) remains a major obstacle in the way of stable SR inversions from remotely sensed data. Mushkin and Gillespie (2005) suggested the use of Advanced Spaceborne Thermal Emission and Reflection Radiometer (ASTER) stereo images to obtain relative estimates of SR that are independent of surface composition and largely insensitive to atmospheric effects. This two-look approach is based on the measurable deviation of natural rough surfaces from Lambertian reflection at the pixel scale of orbiting imagers, due to unresolved shadows. The approach is characterized by fairly stable SR inversions, though its main disadvantage is that it yields relative, nonphysical SR estimates that are difficult to use quantitatively. In this chapter, we discuss a general calibration scheme to translate relative two-look SR estimates into physically meaningful quantitative roughness parameters using high-resolution DEMs (HR-DEMs) acquired at <5 mm/pixel using a ground-based laser scanner.

Recent advances in airborne “Light Detection and Ranging” (LiDAR) systems enable explicit characterization of the topographic expression of surfaces at unprecedented ~ 1 m/pixel spatial resolutions, and thus offer us a powerful new tool to study Earth’s surface (Wallace et al. 2006). Due to the large data-processing efforts required to produce LiDAR topography maps and the relatively high cost of data acquisition campaigns, LiDAR surveys of Earth’s surface remain, at present, limited to local scales. The two-look approach discussed here complements LiDAR topography mapping in that its SR measurements integrate SR over all

subpixel scales down to the wavelength of light, and are also fairly simple to derive. ASTER stereo data enable nearly global coverage for two-look SR measurements, and thus we anticipate that cross-calibration with LiDAR measurements may offer a method to extrapolate LiDAR measurements beyond their local scales.

20.2 Approach

20.2.1 Relative SR Estimates

At-sensor radiance (L_{sensor}) in the VNIR wavelengths is approximated by

$$L_{\text{(sensor)}} = \frac{1}{\pi} (I \tau_{\text{(sun)}} + S_{\downarrow}) \rho \tau_{\text{(sensor)}} (1 - f_{\text{sh}}) + \frac{1}{\pi} S_{\downarrow} \rho \tau_{\text{(sensor)}} f_{\text{sh}} + S^{\uparrow} \quad (20.1)$$

where I is solar irradiation at top of atmosphere, $\tau_{\text{(sun)}}$ and $\tau_{\text{(sensor)}}$ are atmospheric transmissivities in the sun- and sensor-surface paths, respectively, ρ is reflectivity for a smooth Lambertian surface, S_{\downarrow} is downwelling sky irradiance (skylight), and S^{\uparrow} is upwelling path radiance. Parameter f_{sh} is defined here as the effective fraction of the pixel area under shadow, which for a given pixel varies with solar incidence angle (i) and sensor view angle (θ) (Fig. 20.1), and accounts for the deviation of rough surfaces from Lambertian reflection at the pixel scale of orbital data. Atmospheric S^{\uparrow} is removable effectively from (20.1) using standard dark-object

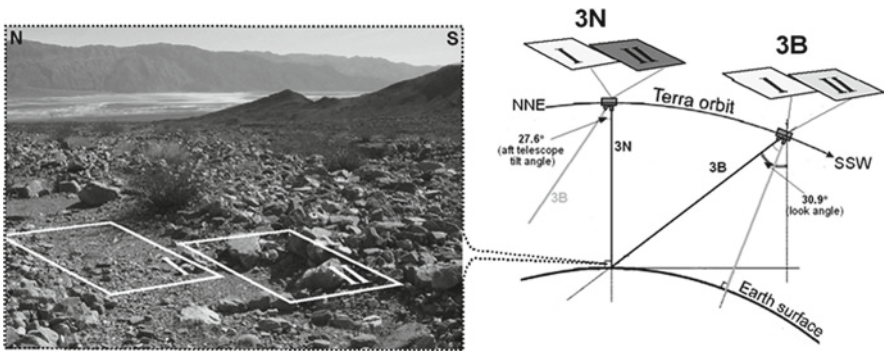


Fig. 20.1 Subpixel shadowing effects and illustration of the two-look approach to estimate subpixel surface roughness (SR) using ASTER. ASTER stereo images are acquired at nadir (3N) and at 30.9° (3B) 55 s later along the SSW orbit of Terra using the aft-looking telescope. A pixel in the rough section of the surface viewed from nadir (3N-II) will have a lower DN value than the same pixel viewed down-sun (3B-II), because shadows become hidden behind sunlit surface elements. A pixel in the smoother part of the surface will have a smaller difference in DN values between 3N-I and 3B-I because fewer shadows become hidden. The DN values for pixels for a perfectly smooth Lambertian surface will not change with view angle because there are no shadows. Accordingly, the ratio between DN values of corresponding pixels in stereo images is usable as a proxy for relative variations in subpixel SR

subtraction, and thus this single-scatter description of L_{sensor} is re-arranged and reduced thus:

$$L_{(\text{sensor})} = \frac{1}{\pi} I \tau_{(\text{sun})} \tau_{(\text{sensor})} \rho (1 - f_{\text{sh}}) + \frac{1}{\pi} S_{\downarrow} \rho \tau_{(\text{sensor})} \quad (20.2)$$

so that the last term in (20.2) is independent of f_{sh} and in effect describes reflected skylight from both the sunlit and shadowed parts of the surface. Following (20.2), the ratio between $L_{(\text{sensor})}$ for co-registered pixels within an overlapping image pair is expressed as follows:

$$\frac{L_{(\text{sensor})1}}{L_{(\text{sensor})2}} = \frac{\frac{1}{\pi} I_1 \tau_{(\text{sun})1} \tau_{(\text{sensor})1} \rho_1 (1 - f_{\text{sh}1}) + \frac{1}{\pi} S_{\downarrow 1} \rho_1 \tau_{(\text{sensor})1}}{\frac{1}{\pi} I_2 \tau_{(\text{sun})2} \tau_{(\text{sensor})2} \rho_2 (1 - f_{\text{sh}2}) + \frac{1}{\pi} S_{\downarrow 2} \rho_2 \tau_{(\text{sensor})2}} \quad (20.3)$$

Although this system is inherently underdetermined, as it comprises two measurements and ten unknowns, if a pair of stereo images acquired at approximately the same time (i.e., similar solar illumination) are considered, then for similarly sloping pixels at similar elevations I_1 , $\tau_{(\text{sun})1}$, ρ_1 , and $S_{\downarrow 1}$ are equal to I_2 , $\tau_{(\text{sun})2}$, ρ_2 , and $S_{\downarrow 2}$ respectively, and (20.3) is rewritten as follows:

$$\frac{L_{(\text{sensor})1}}{L_{(\text{sensor})2}} = k_{\tau} \frac{k_I (1 - f_{\text{sh}1}) + S_{\downarrow}}{k_I (1 - f_{\text{sh}2}) + S_{\downarrow}} \quad (20.4)$$

where $k_{\tau} = \tau_{(\text{sensor})1} / I_2 \tau_{(\text{sensor})2}$, $k_I = I_1 \tau_{(\text{sun})1} = I_2 \tau_{(\text{sun})2}$, and $S_{\downarrow} = S_{\downarrow 1} = S_{\downarrow 2}$. Under these conditions, although k_{τ} , k_I , and S are unknown, they are constants in the $L_{(\text{sensor})1} / L_{(\text{sensor})2}$ ratio image, which is therefore proportional, but not equal to the $(1 - f_{\text{sh}1}) / (1 - f_{\text{sh}2})$ ratio image (Conel and Alley 1984). The latter is directly related to SR because perfectly smooth surfaces display unity $(1 - f_{\text{sh}1}) / (1 - f_{\text{sh}2})$ values ($f_{\text{sh}} = 0$ at both view angles) and increasingly rough, disordered surfaces yield diverging $(1 - f_{\text{sh}1}) / (1 - f_{\text{sh}2})$ ratios (Fig. 20.1) as the difference between $f_{\text{sh}1}$ and $f_{\text{sh}2}$, for constant $\theta_{1,2}$, increases with SR (Mushkin and Gillespie 2005). $L_{(\text{sensor})1} / L_{(\text{sensor})2}$ ratios are therefore used as a proxy to map subpixel SR variations without the need to determine ρ or the constants in (20.4) explicitly.

An important limitation of the two-look approach is that SR estimates derived from it remain valid only for similarly sloping pixels. Because f_{sh} itself is a nonlinear function of SR, I and θ (Fig. 20.2), differences in f_{sh} between two measurements are usable as proxies for differences in SR only in cases where i and θ remain nearly constant within each of the stereo images used, i.e., for similarly sloping pixels in the scene. The term ‘‘similarly sloping’’ is used because numerical simulations indicate the effect of pixel slope on $L_{(\text{sensor})1} / L_{(\text{sensor})2}$ values for rough surfaces is typically $<9\%$ for slope differences of up to $\pm 5^\circ$ from horizontal (Fig. 20.3). Sensitivity to pixel slope increases significantly for steep gradients where the 9% criterion described above implies a smaller range of valid slopes. High solar elevations and signal-to-noise ratio (SNR) may also affect SR detectability and warrants consideration on a sensor-specific basis.

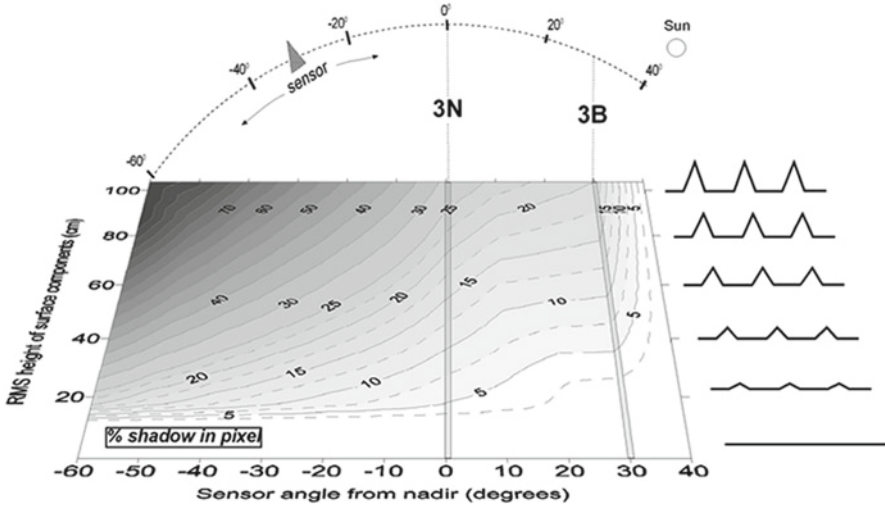


Fig. 20.2 Numerical simulations showing the dependence of the amount of shadows on rough surfaces and sensor view angle. *Contours* represent the % area of the pixel that is in shadow (f_{sh}), and form a concave surface that dips diagonally to the *upper left* (i.e., towards low view angles facing the sun and the roughest surface). The *shaded lines* at 0 and 30° represent ASTER stereo view angles. The ratio between f_{sh} at 3B and 3N is proportional to SR. Sun was fixed at 40° from nadir and sensor view angle varied along the principal plane

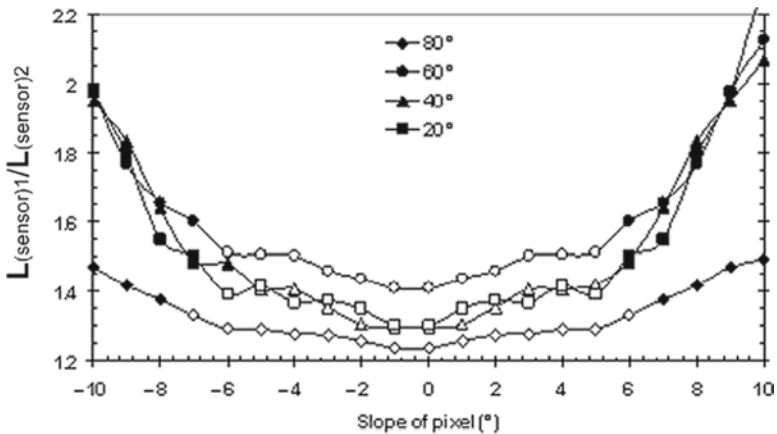


Fig. 20.3 Numerical simulations showing the effect of pixel-scale slope on the ratio between measured radiances from the same rough surface at two stereo view angles. *Symbols* represent different solar elevations. A 0° slope implies a horizontal rough surface. *Open symbols* represent ratio values that are within 9% from their value at horizontal. Sensitivity to slope varies with solar elevation and increases significantly for slopes of more than $\pm 5^\circ$

20.2.2 Calibration

Relative SR estimates obtained with the two-look approach described above require additional calibration for retrieval of “absolute” quantitative roughness parameters. Such calibration are potentially achieved through (a) empirical calibration in cases

where independent in situ roughness measurements are available for a given study site (Mushkin and Gillespie 2006), or (b) more general model-based calibrations, as presented in this study. For the latter calibration scheme, we use a single-scatter reflection model to simulate $L_{(\text{sensor})1}/L_{(\text{sensor})2}$ values for high-resolution surface DEMs. Sensor view angles and illumination geometry are adjustable in the reflection model to match the stereo data used, and the simulated ratios are then used to construct a calibration curve to translate atmospherically corrected $L_{(\text{sensor})1}/L_{(\text{sensor})2}$ values into quantitative “absolute” roughness parameters derived from the DEMs. In this respect, high-resolution self-affine synthetic models have been previously used to describe the subpixel roughness of natural surfaces, and for calibration of remote roughness measurements from radar and VNIR data (Kierein 1997). Yet, it appears that because of the complexity of natural surfaces and the multiple physical processes, rather than a single one, that determine their topographic expression at subpixel scales, a fractal description for SR of natural surfaces is probably not sufficient (Weeks et al. 1996). In this study, we measured the 3D topographic expression of selected natural surfaces with a ground-based laser scanner, and used these HR-DEMs (~5 mm) to calibrate two-look SR estimates, as described above.

20.2.3 ASTER Stereo Data

The U.S.-Japanese ASTER sensor (Yamaguchi et al. 1998) onboard NASA’s “Terra” platform is especially suited for application of the two-look approach in terrestrial environments because of its stereoscopic imaging capability, which is made possible by an additional channel of data (3B) routinely acquired using an aft-looking telescope tilted 27.6° backwards from nadir. Channel 3B data are acquired at the same wavelengths and spatial resolution (i.e., 15 m/pixel) as the nadir channel at ~0.81 μm (3N), but 55 s later along the S-SW near-polar orbit of Terra, accounting for an effective 30.9° stereo phase angle between 3N and 3B image data (Fig. 20.1). Thus, for scenes with southern illumination (northern hemisphere) ASTER 3B/3N ratio will remain proportional to SR, and for scenes with northern illumination (southern hemisphere) ASTER 3B/3N will remain inversely proportional to SR (Fig. 20.1). Both stereo channels display a comparable SNR <1%, and thus uncertainties in 3B/3N ratios due to measurement error are estimated as lower than ~1.5%.

The number of separable roughness levels that are derivable using the two-look approach depends on sensor SNR, the magnitude of the differences in f_{sh} between the two view angles (Δf_{sh}), and the additive atmospheric-scattering terms (20.4) (i.e., upwelling and downwelling “skylight”). For a given SR, differences in f_{sh} are proportional to the stereo angle of the images used, and the solar incidence angle. Larger stereo angles imply that more “shadow hiding” can occur between the two view angles and lower sun elevations imply longer shadows and thus a larger Δf_{sh} . The angle α between the orbit track and the solar principal plane is also an important factor because Δf_{sh} is potentially maximized when the satellite orbit is

along the principal solar plane (Fig. 20.1) and reduced to $\Delta f_{sh} = 0$ when the satellite track is orthogonal to it and no “shadow hiding” occurs between the two view angles (i.e., $f_{sh1} = f_{sh2}$). In the case of ASTER stereo image data, the stereo angle is fixed at 30.9° , and Terra’s sun-synchronous orbit implies that α and solar elevation at time of data acquisition, for a given location, are highly correlated.

20.3 Methods

20.3.1 Field Work

The fieldwork portion of this study focused on acquiring HR-DEMs (<5 mm/pixel) of natural bare surfaces displaying a range of different roughnesses. Two field sites with low (<10%) vegetation cover were selected: (1) a bedrock outcrop of Tertiary granite in the Alabama Hills, California, USA, and (2) a sequence of Late Pleistocene–Holocene alluvial terraces in Death Valley, California, USA. We used a Trimble GS200 3D scanner mounted on a surveying tripod (Fig. 20.4) to measure the microtopographic expression of representative surfaces at these sites.



Fig. 20.4 Ground-based 3D laser scanner (Trimble GS200) used in this study. To achieve the high-resolution mapping required for this study (i.e., <5 mm postings), each surface required multiple (~3–5) measurements of the scene from different view angles, to overcome the problem of areas hidden behind roughness elements at the grazing view angles of a ground-based system

20.3.2 Reflection Model

To simulate ASTER $3B/3N$ ratio for the HR-DEMs of the real surfaces, we use a single-scatter reflection model that assumes Lambertian reflection from the individual, mm-scale surface elements. The model simulates land-leaving radiances for ASTER $3B$ and $3N$ view angles, and accounts for the effects of shading and shadowing at specified illumination geometry. Key illumination geometry variables considered in the model are terrain slope, solar elevation, and angle between the solar principal plane and the satellite orbit track. The ASTER standard product DEM helps to determine terrain slope, which is used to help compensate for slope effects on two-look roughness estimates. The remaining illumination variables are determined from the metadata files associated with ASTER level-1B images.

20.3.3 Atmospheric Corrections

Calibration of level-1B $3B/3N$ ratios against the simulated land-leaving radiance values obtained from the reflectance model described above requires compensation for atmospheric effects. As the ASTER level-2 surface radiance product (Thome et al. 1998) does not include $3B$ data, ASTER level-1B radiance-at-sensor data are used. We use dark-object subtraction to remove the additive atmospheric path radiance term and the MODTRAN radiative transfer code (Ontar 2001) to determine the downwelling sky irradiance and the atmospheric transmissivities for both ASTER look angles.

Typically, model-based atmospheric corrections introduce errors into the data. However, because ASTER stereo images are acquired only 55 s apart through different but well-known path lengths in the same atmosphere, the errors in MODTRAN approximations of $3B$ and $3N$ transmissivities and S_{\downarrow} are highly correlated, and therefore their effects are significantly reduced in the $3B/3N$ ratio. Sensitivity analyses indicate that for typical illumination conditions in the mid-latitudes, the maximum error introduced to the $3B/3N$ ratio from the MODTRAN corrections is $\pm <1.1\%$ (i.e., using the driest atmosphere coefficients to correct the wettest model atmosphere). The use of ancillary information such as atmospheric profiles from MODIS (King et al. 2003) or other climatological measurements (e.g., <http://www.cdc.noaa.gov/cdc/reanalysis/reanalysis.shtml>) can help reduce this error further.

20.4 Results

The effects of illumination geometry on relative two-look SR estimates were evaluated using 12 ASTER datasets acquired over the Trail Canyon field site and adjacent playa deposits during different seasons of the year (i.e., at different solar elevations and azimuths ranging from 35° to 74° above the horizon and 131° – 167° east of north, respectively). Level-1B radiance-at-sensor $3B/3N$ ratios (no atmospheric

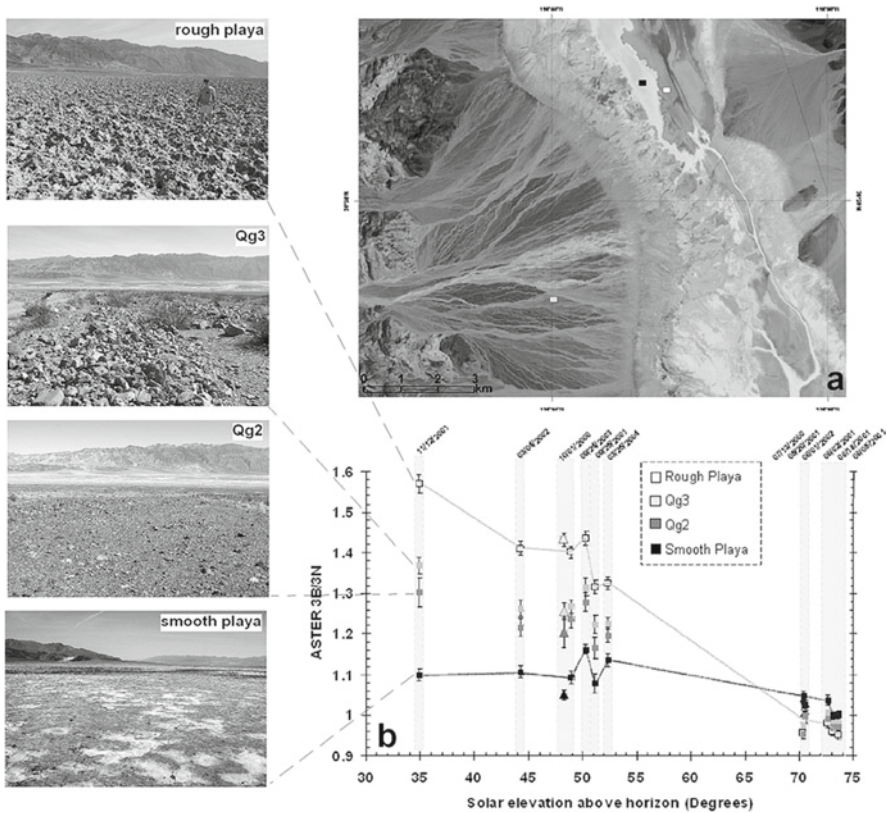


Fig. 20.5 Sensitivity of ASTER relative roughness estimates to solar elevation. (a) ASTER image of Trail Canyon fan and adjacent playa deposits in Death Valley, California, USA. (b) Each column of data represents ASTER $3B/3N$ ratios extracted from a single dataset over four different surfaces (locations shown in a), with solar elevation at time of data acquisition plotted on the x -axis. Data were compiled from 12 ASTER datasets and dates of acquisition are displayed at the top of each column. Surfaces are listed in order of decreasing roughness with Qg3 and Qg2 representing Early Holocene and Late-Pleistocene alluvial surfaces, respectively. *Square symbols* represent ratios derived without applying atmospheric compensation and *error bars* represent 1-sigma standard deviations ($n > 20$). *Triangles* represent a single case for which atmospheric corrections were applied, and have been slightly offset to the left for comparison with ratios derived from the same dataset prior to atmospheric corrections. The *wedge-shaped envelope* demonstrates that relative roughness resolution with this approach is inversely proportional to solar elevation, and that data acquired at solar elevations exceeding $\sim 60^\circ$ are best avoided

corrections applied) from four selected locations representing horizontal surfaces with different SR were extracted from the 12 datasets and plotted as a function of solar elevation in Fig. 20.5. Results of this analysis show that atmospheric effects did not change the positive correlation between $3B/3N$ values and SR, but do appear to decrease the contrast between the ratios. This analysis also demonstrates that separability of ASTER $3B/3N$ ratio values for a given set of roughnesses is inversely proportional to solar elevation at the time of data acquisition, and that sensor noise dominates ASTER $3B/3N$ ratio values at high ($>70^\circ$) solar elevations.

Two calibration schemes are available to translate relative two-look roughness estimates into physically meaningful, quantitative roughness parameters. The main advantage of the empirical calibration scheme, which relies on comparing radiance-at-sensor ratio values to independent in situ measurements of a roughness parameter, is that it does not require atmospheric corrections. In the example shown here for Gusev crater on Mars (Mushkin and Gillespie 2006), where atmospheric effects are generally poorly constrained, at-sensor radiance ratios derived from co-registered nearly simultaneous orbital ~ 30 m/pixel stereo images acquired by the High Resolution Stereo Camera (HRSC; Neukum et al. 2004) onboard the Mars Express (MEx) platform, were calibrated to ground-based % clast-coverage counts (Golombek et al. 2005) obtained from “point” measurements along the Mars Exploration Rover traverse through Gusev crater. This calibration of two-look SR estimates did not require compensation for the largely unconstrained effects of the Martian atmosphere and enabled unprecedented quantitative mapping of % clast coverage for the floor of Gusev crater (Fig. 20.6). Nonetheless, a fundamental disadvantage of the in-scene calibration scheme is that it is only applicable to the specific atmospheric conditions, and viewing and illumination geometries in which it was determined.

The second model-based calibration scheme discussed here relies on comparing radiance-at-sensor ratios to simulated ratios from a reflection model for HR-DEMs of natural surfaces. For this calibration scheme, the microtopographic expression of selected surfaces was measured at 2–5 mm resolution using a GS200 3D laser scanner mounted on a surveying tripod. Figure 20.7 displays examples for such surfaces; a granite outcrop in the Alabama Hills, California, and an alluvial surface near the Kit Fox Hills in Death Valley, California. The shaded-relief images produced from these data illustrate the fine details resolvable at such resolution (e.g., the coarse-grained texture of the granite surface, the “grusy” soil next to it, and the cm-scale cracks in the outcrop). The HR-DEMs of alluvial surfaces from Death Valley (Fig. 20.7b) document the topographic expression of the multiple geomorphic processes that shape the surfaces of the fans (e.g., bar-and-swale topography resulting from fluvial erosion and deposition, in situ clast fragmentation and in-filling by aeolian processes). The SR is parameterized here as RMS height of the surface elements and ranges from <2 to 13 cm for the surfaces measured in the Death Valley sites.

Examples for calibration curves are presented in Fig. 20.8. Upwelling path radiance was removed using dark-object subtraction from each image separately, and atmospheric downwelling irradiance and transmissivities were determined using MODTRAN. The different calibration curves represent different illumination geometries (i.e., a different solar azimuth and elevation in each case). All surfaces were assumed as horizontal and sensor view angles were fixed at nadir and 30.9° looking backwards

Fig. 20.6 (continued) depicted. **(b)** Calibrated % rock abundance map. Roughness estimates were obtained from HRSC stereo data, orbit 24 at ~ 30 m/pixel resolution. *Dotted line* represents Spirit’s approximate traverse and lettering is the same as in **(a)**. **(c)** Radiance ratios were calibrated using % rock abundance as estimated by Golombek et al. (2005) at three locations along Spirit’s traverse. An additional point from the relatively rock-free (assumed 1% rock abundance), sandy floor of BC was added to the calibration curve. *Dashed lines* represent the $1\text{-}\sigma$ error bounds associated with this regression

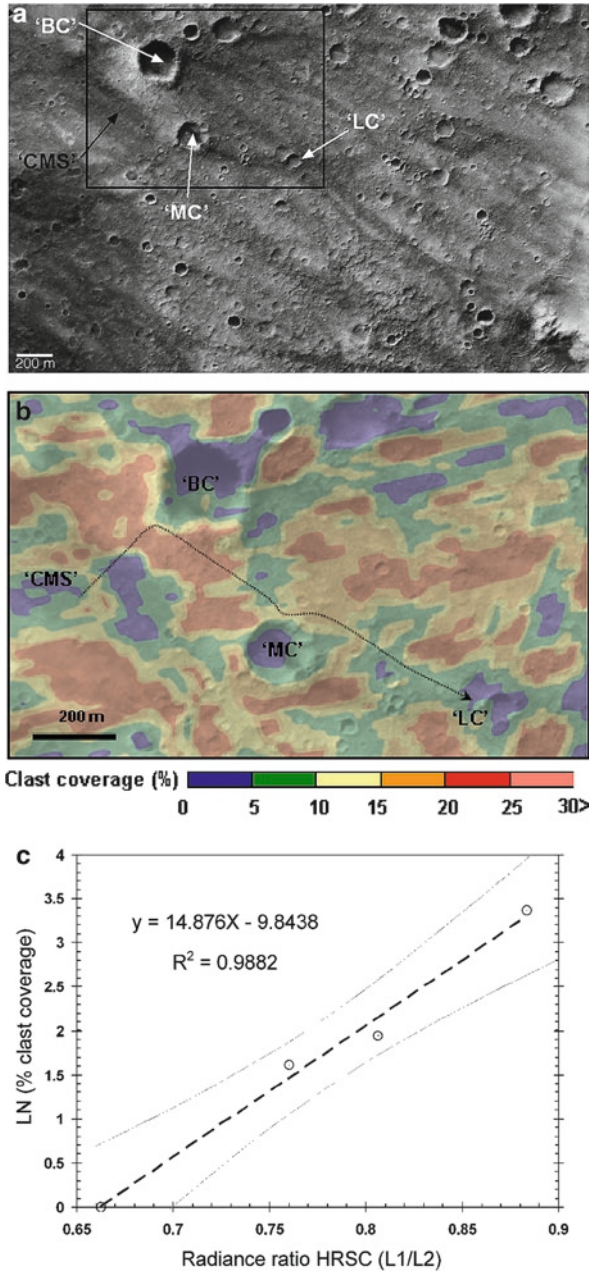


Fig. 20.6 Empirical calibration of the two-look approach on Mars (Mushkin and Gillespie 2006). (a) A high-resolution (~1.5 m/pixel) image (http://www.msss.com/mars_images/moc/2005/01/03) of Spirit's (Mars Rover) landing site at Gusev crater. The Spirit's traverse from its landing location at the Columbia Memorial Station (CMS) through Bonneville Crater (BC), Missoula Crater (MC), Lahontan Crater (LC), and towards the Columbia Hills (not shown) are

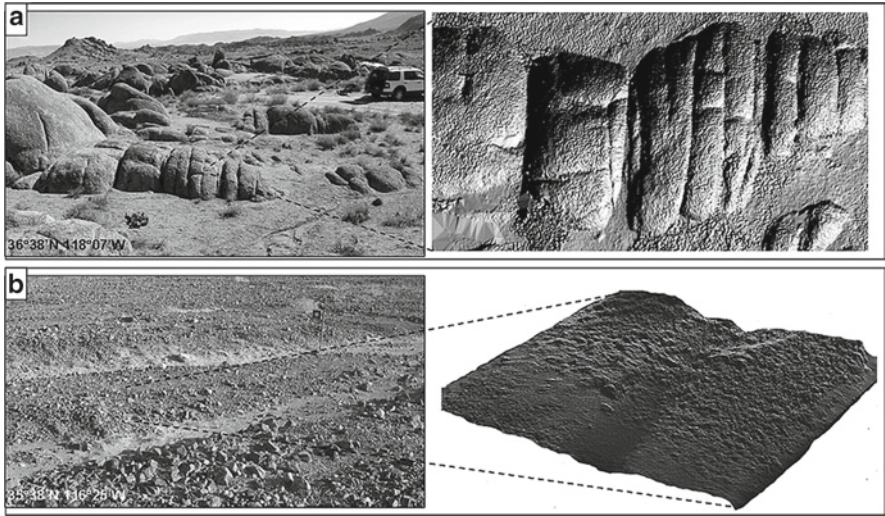


Fig. 20.7 HR-DEMs. (a) A view south onto the $1 \times 3 \text{ m}^2$ granite outcrop that was scanned with the Trimble GS200 (Fig. 20.4), and a corresponding shaded relief image viewed from directly overhead with illumination from the *bottom right*. This 2 mm/pixel scan comprises $\sim 6.5 \times 10^5$ data points (image displayed was under-sampled for clarity). (b) A view south onto the Kit Fox alluvial fan surface that was scanned, and a corresponding shaded relief image (oblique view from north; illumination from *upper right*) produced from the 5 mm/pixel scan

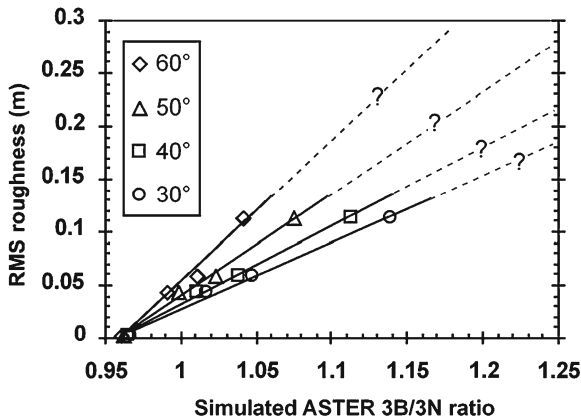


Fig. 20.8 Calibration curves of relative ASTER stereo roughness estimates to surface RMS using the reflection model. *Curves* represent four different cases of solar elevations above the horizon, and demonstrate the improved roughness resolution at lower solar elevations. *Dashed gray lines* represent unconstrained extrapolation of the linear regressions, and thus RMS values above 0.14 m are regarded as uncertain

along a S-SW (i.e., 200° east of north) orbit. The results suggest that a linear regression between surface RMS and ASTER $3B/3N$ ratio is adequate for the range of measured RMS roughnesses, i.e., $< \sim 0.13$ m. The slope of the regression is proportional to solar elevation implying, as expected, decreased separability between roughness levels as solar elevation increases. The 50° solar elevation regression curve in Fig. 20.8 was used to translate an ASTER $3B/3N$ ratio image from October 1, 2000 into a quantitative surface RMS image (Fig. 20.9) of Trail Canyon fan in Death Valley. Errors for the

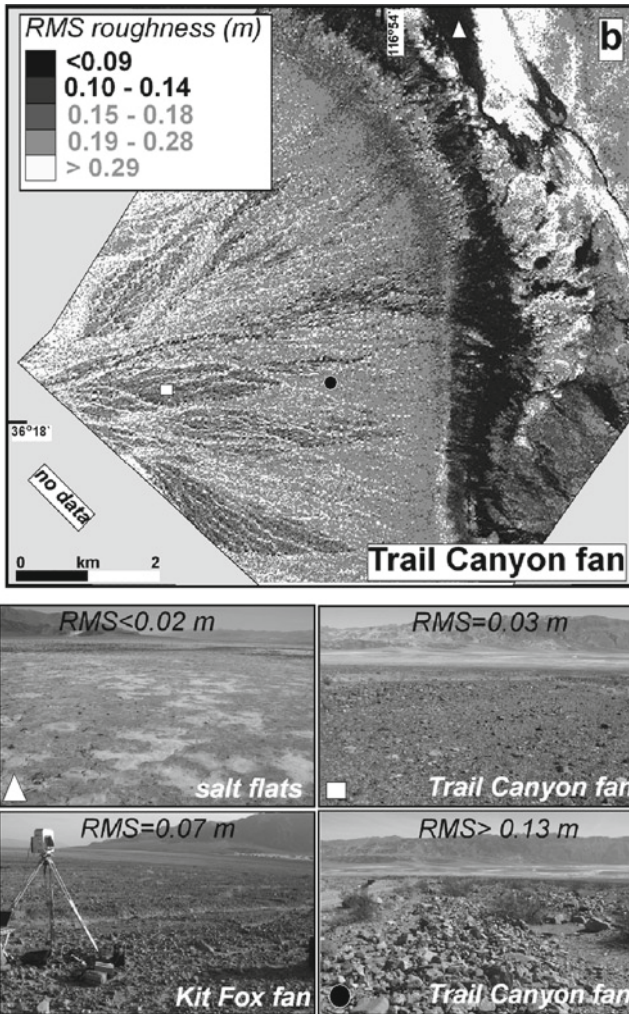


Fig. 20.9 Calibrated surface RMS height map of Trail Canyon fan and adjacent playa deposits. ASTER $3B/3N$ ratio image from October 1, 2000 was calibrated to RMS roughness using the 50° calibration curve in Fig. 20.8. RMS values in *gray* are regarded as uncertain because they are from the extrapolated part of the calibration curve (Fig. 20.8). Representative pictures of selected surfaces are shown below and marked on the roughness map

ASTER $3B/3N$ ratio are estimated as $<1.5\%$ and errors in the HR-DEM measurements are ignored. Compensation for atmospheric transmissivities and downwelling sky irradiance was calculated using the “1976 Standard Atmosphere” model in MODTRAN. Estimated RMS roughness values were binned into five classes, accounting for up to 5% uncertainty associated with system noise, image-to-image registration, atmospheric corrections, and local variations in surface slope.

20.5 Discussion

The sensitivity of ASTER-derived two-look roughness estimates to solar elevation was analyzed using the set of 12 ASTER level-1B datasets acquired over Trail Canyon fan, Death Valley, at different seasons of the year (i.e., at different solar elevations; Fig. 20.5). At-sensor radiance ratio values, not corrected for atmospheric effects, remained correlated with SR at solar elevations $<52^\circ$ and became dominated by measurement noise at solar elevations $>70^\circ$. No ASTER data were available at this location for the range of solar elevations between 52° and 70° , yet interpolation between these values suggest that ASTER two-look roughness estimates from level-1B ratios remain valid up to solar elevations of $\sim 60^\circ$ in the mid-latitudes of the northern hemisphere. Figure 20.5 also demonstrates that as expected, the contrast between the stereo ratios for the same SR range, and thus the number of separable roughness levels derivable, decreases with increasing solar elevations. Removal of atmospheric scattered upwelling path radiance from each of the stereo channels independently (e.g., dark-object subtraction) can significantly improve the contrast in the radiance ratios, and thus the number of roughness levels derivable from the data.

The ASTER stereo roughness images require additional calibration for retrieval of “absolute” quantitative roughness parameters. Such calibrations are achieved through empirical calibration in cases where independent in situ roughness measurements are available for a given study site (Fig. 20.6) or more general calibrations based on a reflection model for HR-DEMs of natural surfaces (Fig. 20.8). The main advantages of the empirical calibration scheme are that it does not require radiometric calibration or atmospheric corrections, which are both accounted for through the calibration. It also allows us to avoid the uncertainties in modeling the interaction of light with complex vegetated surfaces on Earth or with poorly known planetary surfaces, such as those on Mars. The main disadvantages of the empirical calibration are that independent in situ measurements, which are not always available, are required, and that calibration is site-specific, and not quantitatively extrapolated to other locations with different illumination conditions.

The HR-DEMs enable more general calibration of relative stereo roughness estimation to “absolute” roughness parameters, e.g., surface RMS (Fig. 20.9). Because illumination and viewing geometries are adjustable in the reflection model, calibrations curves specific to the image data used are constructible as long as the sun position and sensor characteristics are well known. Moreover, this calibration scheme enables corrections for general terrain slopes (i.e., slopes at the

scales of “conventional” DEMs) by mathematically adjusting the HR-DEMs in the reflection model. This calibration scheme also requires radiometric calibration and atmospheric corrections. In the case of ASTER stereo data, error analysis suggests that for typical conditions on Earth, MODTRAN atmospheric corrections are expected to leave <1.1% error into the ratio image.

The HR-DEM calibration is terrain-specific and requires careful application. For example, a calibration curve calculated for alluvial surfaces is probably not appropriate for bedrock surfaces because these two surface types have a distinctly different organization, and regression coefficients relating the $3B/3N$ ratio and SR are possibly different. Establishing a HR-DEM library for a wide variety of terrain types (e.g., alluvial surfaces, playa deposits, bedrock surfaces, planetary analogs) is now in progress. Additional aspects of this approach that require further study are the effect of sparse vegetation on roughness estimates and improving the characterization of the rougher surfaces (RMS > ~0.13 m), for which the present HR-DEMs are not adequate.

Stereo images acquired simultaneously yield the most robust two-look SR estimates. However, the two-look approach is also applicable using repeat overlapping images acquired at similar viewing angles, but at different illumination geometries (Mushkin and Gillespie 2006). The change in solar incidence angle between two repeat images has a similar effect as the change in view angle between stereo images, in that the difference in the amount of shadows seen by the sensor increases together with SR in both cases. The main advantages of repeat images are wider availability of such data (e.g., Landsat or MODIS, and relatively simple co-registration between repeat images acquired at nadir-viewing, as the geometric distortions associated with off-nadir-viewing are avoided). The main disadvantages of repeat images are the different atmospheric conditions during the two data acquisitions, and more importantly, the possibility of surface reflectivity change between the two measurements. A fundamental assumption of the two-look approach is that surface reflectivity may vary across the scene, but does not change between the two measurements. In case such a change does occur (e.g., moisture, vegetation, or dust deposition), the critical transition between (20.3) and (20.4) becomes erroneous, and thus the radiance ratio may also reflect changes in surface albedo between the two measurements in addition to SR variation across the scene. A test case comparing SR estimates derived from stereo and repeat images on Mars (Mushkin and Gillespie 2006) demonstrated that dust deposition on the surface between the two repeat images did in fact mimic SR variations in the scene, and that stereo SR estimates for the same location were not affected by this complication. An additional parameter to consider is the pixel size of the data used, which is important because the two-look approach responds to the integrated effect of all subpixel roughness elements. For example, SR estimates obtained from MASTER (MODIS/ASTER Airborne Simulator; Hook et al. 2001) 50 m/pixel stereo images over Trail Canyon fan in Death Valley were not comparable to those obtained from ASTER 15 m/pixel stereo images (Pinet et al. 2005).

Quantitative ASTER stereo SR estimates described in this chapter are applicable to a wide range of Earth science disciplines. They have been used to compensate for subpixel roughness effects on remote TIR measurements (Mushkin et al. 2006) and for geomorphic mapping in the context of recent tectonic activity in the Gobi-Altay

strike-slip fault system in southwestern Mongolia (Mushkin 2007). ASTER stereo SR estimates are also used to predict off-road vehicle trafficability in desert terrain as well as to facilitate more robust soil-moisture measurements from radar data, which helps separate between the effects of soil roughness and soil moisture on radar returns (Rahman et al. 2008).

The ASTER stereo SR estimates also complement spectral mixture analysis (SMA; Adams and Gillespie 2006), which offers one of the most powerful and widely used quantitative tools to analyze the surface from remotely sensed data. The SMA utilizes a linear unmixing model to estimate the effective contribution of each spectral endmember to the measured spectral signal from the pixel. For cases in which the spectral endmembers used represent the primary physical constituents of the surface, SMA is useful to estimate surface composition. In SMA, a “shade” endmember is typically involved to account for the darkening of the surface due to unresolved shadows and shading at the pixel scale of remotely sensed data, and was previously used to infer SR (Combe et al. 2006). It appears that in some desert environments, however, darkening of surfaces is attributable to absorption by ubiquitous rock varnish rather than to unresolved shadows (Sultan et al. 1986), accounting for the darker appearance of older and smoother alluvial surfaces with respect to younger and rougher surfaces with the same parent material. A combination of ASTER spectral and stereo data enables a simple test of this hypothesis (Fig. 20.10). The SMA using the ASTER VNIR-SWIR nine spectral channels was carried out for Trail Canyon fan, and compared with the surface RMS map (Fig. 20.9) derived from $3B/3N$ ratios from the same ASTER dataset (10/1/2000). Spectral endmembers in the unmixing model were chosen to represent the main bedrock units from which those fans were derived, vegetation and “shade.” Trail Canyon Late-Pleistocene surfaces Qg2 and Qg3 appear darker than the recent Holocene Qg4 surfaces, but surface albedo are not usable to distinguish between Qg3 and the Qg2 surfaces in all cases, because both are heavily varnished.

The SMA “shade” endmember image (Fig. 20.10c) does not display consistent “shade” values for Qg2 nor for Qg3, most likely because of the competing effects of decreasing SR and increasing the effective thickness of the varnish over time. However, the ASTER-derived surface RMS map (Fig. 20.10d) enables a clear distinction between Qg2 and Qg3 surfaces: it responds only to SR and thus useful to assess surface age better than the “shade” fraction image alone. In areas such as Death Valley, where varnish is common, the RMS image is usable in conjunction with the “shade” fraction image to estimate effective varnish thickness and even surface composition, provided, a relationship between lithology and weathering exists.

20.6 Summary and Conclusion

The ASTER two-look approach described in this chapter enables remote subpixel SR estimations that complement other techniques in that it does not require determination of surface composition, and is largely insensitive to atmospheric effects. A simple ratio image between co-registered ASTER $3B$ and $3N$ level-1B data are useful as a proxy for roughness variation within the scene at ~ 15 m/pixel spatial

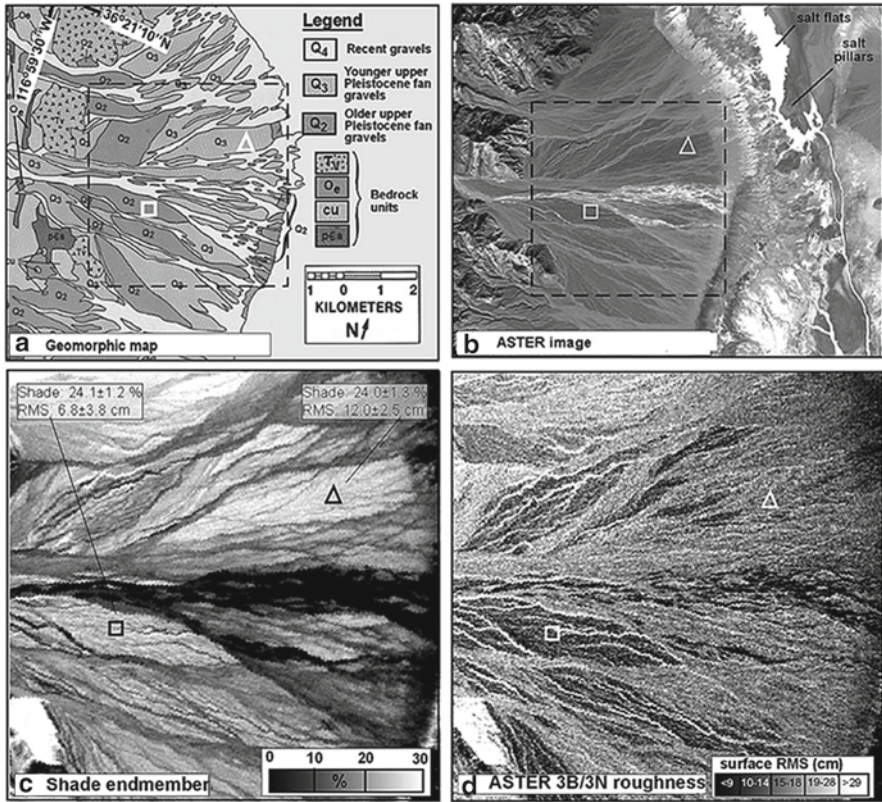


Fig. 20.10 Comparison between the “shade” endmember extracted from a spectral mixture analysis (SMA) and ASTER-derived surface RMS roughness for Trail Canyon fan, California USA. (a) Geomorphic map taken from Gillespie et al. (1984). These alluvial surfaces become smooth over time as a desert pavement progressively develops on them. (b) ASTER channel 3N (~0.810 μm) image showing that in most cases, the older Qg2 surfaces are darker than the younger Qg3 surfaces. (c) Shade-fraction image from the SMA showing that Qg2 and Qg3 do not display consistent “shade” values. (d) Surface RMS derived from ASTER 3B/3N ratios. Roughness is not correlated with albedo and appears consistent with the geomorphic map. Qg2 surfaces are mapped as smoother than Qg3 surfaces. Squares and triangles mark the same Qg2 and Qg3 surfaces, respectively. Vegetation effects dominate both analyses in the active channel in (c) and (d) centers

resolution, and is offered as a robust qualitative tool for photo-interpretative purposes. The number of SR levels resolvable decreases as solar elevation at time of data acquisition increases, with measurement noise dominating the ASTER 3B/3N ratio image at solar elevations >60°. Removal of upwelling atmospheric scattered light (e.g., via dark-object subtraction, from each data channel separately) can increase the number of roughness levels resolved in the ratio image.

Calibration of ASTER 3B/3N relative SR estimates into physically meaningful and quantitative SR parameters is achievable through two calibration schemes: (1) calibration to independent in situ roughness measurements and (2) calibration to model-based simulation of ground-leaving radiance from HR-DEMs (<5 mm) of

natural surfaces. The latter scheme enables construction of calibration curves for any given viewing and illumination geometries encountered by ASTER. Moreover, as ASTER now provides an archive of nearly global land coverage, the two-look approach with ASTER stereo data enables a unique quantitative mapping capability of SR at 15 m/pixel spatial resolution for nearly any location on Earth.

Acknowledgments We thank M. O’Neal and L. Pietro for their help in producing the HR-DEMs, and I. Danilina, E. Abbot and J. Macey for their assistance in the field. We also thank L. Gilson for her help in the spectral mixture analysis, and G. Yamada for her help in processing the ASTER 3B and 3N data. Reviews by A. French and D. Gesch helped improve the clarity of the manuscript. Funding for this project was NASA contract NNG04HZ55C (ASTER), the U.S. Department of Energy, Office of Nonproliferation Technology Development contract W-7405-ENG-36 and contract DE-AC52-06NA25396 to Los Alamos National Laboratory subcontract to the University of Washington, and a University of Washington, Department of Earth and Space Sciences scholarship to AM.

References

- Adams JB and Gillespie AR (2006) *Spectral Remote Sensing of Landscapes*. Cambridge University Press, Cambridge
- Christensen PR (1986) The spatial distribution of rocks on Mars. *Icarus* 68:217–238
- Combe JP, Adams JB, McCord TB (2006) Mapping geological units on Mars by analyzing the spectral properties of the surface from the Mars-express high resolution stereo camera (HRSC). *EOS, Transactions, American Geophysical Union*, vol. Fall Meeting Supplement
- Conel JE, Alley RE (1984) Lisbon Valley, Utah, Uranium Test Site Report. In: *The Joint NASA/Geosat Test Case Project*, Paley H (ed) AAPG, Tulsa, OK
- Evans DL, Smith MO (1991) Separation of vegetation and rock signatures in thematic mapper and polarimetric SAR images. *Remote Sens Environ* 37:63–75
- Evans DL, Farr TG, van Zyl JJ (1992) Estimates of surface roughness derived from synthetic aperture radar (SAR) data. *IEEE Trans Geosci Remote Sens* 30(2):382–389
- Gillespie AR, Kahle AB, Palluconi FD (1984) Mapping alluvial fans in Death Valley, California, using multispectral thermal infrared images. *Geophys Res Lett* 11:1153–11556
- Golombek MP, Arvidson RE, Bell JF, Christensen PR, Crisp JA, Crumpler LS, Ehlmann BL, Fergason RL, Grant JA, Greeley R, Haldemann AFC, Kass DM, Parker TJ, Schofield JT, Squyres SW, Zurek RW (2005) Assessment of Mars Exploration Rover landing site predictions. *Nature* 436:44–48
- Hapke B (1993) *Theory of reflectance and emittance spectroscopy*. Cambridge University Press, Cambridge
- Hook S, Myers J, Thome K, Fitzgerald M, Kahle AB (2001) The MODIS/ASTER Airborne Simulator (MASTER) – a new instrument for earth science studies. *Remote Sens Environ* 76:93–102
- Jakosky BM (1979) Effects of nonideal surfaces on the derived thermal properties of Mars. *J Geophys Res* 84:8252–8262
- Kierein KS (1997) The integration of optical and radar data to characterize mineralogy and morphology of surfaces in Death Valley, California, U.S.A. *Int J Remote Sensing* 18(7):1517–1541
- King MD, Menzel WP, Kaufman YJ, Tanre D, Gao BC, Platnick S, Ackerman SA, Remer LA, Pincus R, Hubanks PA (2003) Cloud and aerosol properties, precipitable water, and profiles of temperature and water vapor from MODIS. *IEEE Trans Geosci Remote Sens* 41:442–458
- Li W-H, Weeks RJ, Gillespie AR (1998) Multiple scattering in the remote sensing of natural surfaces. *Int J Remote Sens* 19:1725–1740

- Mushkin A, Gillespie AR (2005) Estimating sub-pixel surface roughness using remotely sensed stereoscopic data. *Remote Sens Environ* 99:75–83
- Mushkin A, Gillespie AR (2006) Mapping sub-pixel surface roughness on Mars using high-resolution satellite image data. *Geophys Res Lett* 33, L18204
- Mushkin A, Gillespie AR, O’Neal M, Danilina I, Abbot EA, Balick LK (2006) Using sub-pixel roughness estimates from ASTER stereo images to compensate for roughness effects in the thermal infrared. In: *Recent Advances in Quantitative Remote Sensing II*. Sobrino JA (ed), Servicio de Publicaciones. Universitat de Valencia. Valencia, Spain, pp 255–260
- Mushkin A (2007) Quaternary deformation in the central segment of the Gobi-Altay Fault System, Southwestern Mongolia. In: *Earth & Space Sciences*, University of Washington, Seattle
- Neukum G, Jaumann R, Hoffmann H, Hauber E, Head JW, Basilevsky AT, Ivanov BA, Werner SC, van Gasselt S, Murray JB, McCord T (2004) Recent and episodic volcanic and glacial activity on Mars revealed by the high resolution stereo camera. *Nature* 432:971–979
- Ontar (2001) “PcModWin v 4.0.” North Andover, MA 01845, USA
- Palluconi FD, Kieffer HH (1981) Thermal inertia mapping of Mars from 60-Degrees-S to 60-Degrees-N. *Icarus* 45:415–426
- Pinet PC, Cord A, Jehl A, Daydou Y, Chevrel S, Baratoux D, Greeley R, Williams DA, Neukum G (2005) Mars Express Imaging Photometry and surface geologic processes at Mars: what can be monitored within Gusev Crater? *Lunar and Planetary Science XXXVI*, #1721
- Rahman MM, Moran MS, Thoma DP, Bryant R, Holifield Collins CD, Jackson T, Orr BJ, Tischler M (2008) Mapping surface roughness and soil moisture using multi-angle radar imagery without ancillary data. *Remote Sens Environ* 112:391–402
- Ramsey MS, Fink JH (1999) Estimating silicic lava vesicularity with thermal remote sensing: a new technique for volcanic mapping and monitoring. *Bull Volcanol* 61:32–39
- Sultan M, Arvidson RE, Sturchio NC (1986) Mapping of Serpentinites in the eastern desert of Egypt by using Landsat Thematic Mapper Data. *Geology* 14:995–999
- Thome K, Arai K, Hook S, Kieffer H, Lang H, Matsunaga T, Ono A, Palluconi F, Sakuma H, Slater P, Takashima T, Tonooka H, Tsuchida S, Welch RM, Zalewski E (1998) ASTER preflight and inflight calibration and the validation of level 2 products. *IEEE Trans Geosci Remote Sens* 36:1161–1172
- Wallace J, Morris B, Howarth P (2006) Identifying structural trend with fractal dimension and topography. *Geology* 34:901–904
- Weeks RJ, Smith MO, Pak K, Li W-H, Gillespie AR, Gustafson W (1996) Surface roughness, radar backscatter, and visible and near-infrared reflectance in Death Valley, California. *J Geophys Res* 101(E10):23077–23090
- Weeks RJ, Smith MO, Pak K, Gillespie AR (1997) Inversions of SIR-C and AIRSAR data for the roughness of geological surfaces. *Remote Sens Environ* 59:383–396
- Yamaguchi Y, Kahle AB, Tsu H, Kawakami H, Pniel M (1998) Overview of advanced spaceborne thermal emission and reflection radiometer (ASTER). *IEEE Trans Geosci Remote Sens* 36(4):1062–1071
- Zebker HA, Goldstein RM (1986) Topographic mapping from interferometric synthetic aperture radar observations. *J Geophys Res* 91(B5):4993–4999

Chapter 21

Technoscientific Diplomacy: The Practice of International Politics in the ASTER Collaboration

Dan Plafcan

ASTER is not only an instrument of geophysics but also an instrument of geopolitics.

– Dr. Ishii Yoshinori, speaking in 2003 (original in Japanese). Dr. Ishii was an advisor to Japan’s Ministry of International Trade and Industry and a member of the board of directors of the Japan Resources Observation System organization, an industry consortium. He was also President of the Society of Exploration Geophysics of Japan, President of the Remote Sensing Society of Japan, and Director General of Japan’s National Institute for Environmental Studies.

I was a geopolitician and a geophysicist.

– Dr. Anne Kahle, speaking in 2003. Dr. Kahle was the U.S. ASTER Team Leader from 1990 until 2003, when she retired from the U.S. National Aeronautics and Space Administration’s Jet Propulsion Laboratory. At the Jet Propulsion Laboratory, she was a senior research scientist and the leader of the geologic remote sensing group.

21.1 Introduction

Most chapters in this volume focus on the scientific and technical aspects of the design, performance, operations, and applications of the MODIS and Advanced Spaceborne Thermal Emission and Reflection Radiometer (ASTER) instruments. In contrast, this final chapter focuses on politics – specifically, the politics of technical decision making and scientific judgment. When scientific objectives, engineering design decisions, and familiar forms of scientific and technical authority

D. Plafcan (✉)

Department of Science, Technology, and Society, School of Engineering and Applied Science,
351 McCormick Road, A237 Thornton Hall, University of Virginia, Charlottesville,
VA 22904, USA
e-mail: dan.plafcan@virginia.edu

are uncertain or otherwise unsettled, how do they become certain and settled? What facilitates collective judgment and the exercise of power in efforts to advance and achieve common scientific goals, especially in the international arena?

This chapter helps to understand these political questions by examining the development of the ASTER remote sensing system. The ASTER system and its operations were a product of collaboration between the United States' National Aeronautics and Space Administration (NASA) and Japan's Ministry of International Trade and Industry (MITI) (MITI is now METI – the Ministry of Economy, Trade, and Industry). While MITI was, in general terms, primarily responsible for providing and maintaining the ASTER instrument, and NASA the launch vehicle and satellite platform, this collaborative arrangement's seemingly "clean" hardware and managerial interfaces were necessarily complicated through the formation and work of a Japan–U.S. joint science team that was collectively responsible for ensuring that the ASTER instrument and its data and information system produced useful and credible knowledge about the earth's land surface (NASA and MITI 1996; Goddard Space Flight Center 1995; and especially Goddard Space Flight Center 1997). This chapter illustrates how members of that joint team, as well as other scientists and engineers who were involved in the ASTER collaboration, concurrently negotiated in their technical decision making and collective exercise of scientific judgment not only for the production of scientific knowledge but also Japan–U.S. relations.

A growing literature in the humanities and social sciences empirically explores the politics of technical decision making and scientific judgment. [Shapin and Schaffer (1985) is a seminal work; Collins (2004) and Jasanoff (2005) are two recent, prominent studies; and chapters in Hackett et al. (2008) review the field]. The politics of technical decision making and scientific judgment have been portrayed as, for example: the mustering and questioning of credentials, technical standards, and literature citations (e.g., Latour 1987; Hilgartner 2000); the nurturing and undermining of professional reputations, relationships, and communities (e.g., Abbott 1988; MacKenzie 1990; Shapin 1994; Epstein 1996); and the stabilization and destabilization of technical practices, ways of knowing, and associated expertise with the cultures, organizations, and national institutions in which they are embedded (e.g., Hughes 1983; Jasanoff 1990; Vaughan 1996; Hecht 1998; Eden 2004). In general, however, this literature has not ventured into the international arena, where crucial assumptions regarding shared culture, institutions, scientific and political authority, and language are especially problematic [Krige and Barth (2006) is a recent exception to this generalization about the literature].

Elsewhere I have contributed to this literature by analyzing significant aspects of the development and operations of the ASTER remote sensing system in terms of international politics as these politics are articulated and projected in the regular work of the ASTER collaboration (see Plafcan 2007). These analyses showed the projection of Japan and U.S. state power and the enactment of relations between the states of Japan and United States as integral to the building and operation of the ASTER remote sensing system. Algorithms, instruments, methods, and procedures were engineered and performed to take into account, and shape fields of meaning that included political meaning as well as scientific and technical meaning. In no way should this intermingling of the political with the technical misconstrued as

suggesting a failure in work practices. Rather, this intermingling is arguably part and parcel to the work of scientific and technological collaboration between states.

This chapter draws from those more thorough analyses mentioned above to illustrate the practice of international politics in the ASTER collaboration with two episodes of what I have called “technoscientific diplomacy” (Plafcan 2007).¹ The concept of “technoscientific diplomacy” highlights three fundamental qualities of the negotiating practices of the members of the Japan–U.S. ASTER team: (1) team members’ positioning of themselves as independent scientists who nevertheless worked on behalf of their respective states; (2) the projection and enactment of Japan, the United States, and Japan–U.S. relations; and (3) the synthesis of state power and scientific knowledge. This chapter’s first episode of technoscientific diplomacy comprises negotiations among Japan and U.S. scientists, engineers, and government officials over the specifications of the thermal infrared radiometer (TIR) that would eventually become the TIR for the ASTER instrument. This first episode illustrates especially qualities #1 and #3 of technoscientific diplomacy. The second episode is a negotiation over instrument operations – more specifically, a negotiation over how to regulate the large-angle pointing capability of the visible near-infrared radiometer (VNIR). This episode illustrates quality #2 and, to a lesser extent, qualities #1 and #3. Taken together, these two episodes of technoscientific diplomacy provide a glimpse into the concurrent negotiation of Japan–U.S. relations and the production of scientific knowledge in the development of the ASTER remote sensing system.

21.2 Trying to Share Separately

In response to a proposal submitted to NASA’s (1988) Earth Observing System (EOS) Announcement of Opportunity, NASA Headquarters wrote to Dr. Kahle at the Jet Propulsion Laboratory (JPL) an acceptance letter that Dr. Kahle and her deputy team leader later described as the “strangest one [they] had ever seen” (Palluconi 2001; Kahle 2003).² NASA explained in the letter that NASA had selected Kahle’s proposed team as an EOS science team, but that NASA had *not* selected the thermal instrument that Kahle’s team had proposed to develop for the purpose of carrying out their proposed science. The instrument that Kahle’s team had proposed was called TIGER, for Thermal Infrared Ground Emission Radiometer, and Kahle’s team was called the TIGER team (Kahle and Palluconi 1988). Instead of NASA sponsoring TIGER, NASA Headquarters asked Kahle and her TIGER team to somehow realize the design of their proposed TIGER instrument and their proposed science “by influencing the Japanese design” of an instrument that had been proposed – and

¹This chapter is primarily composed of edited and revised excerpts from Plafcan (2007), which is a book-length study.

²The exact quote is from an interview with Frank Palluconi, but Kahle voiced the same opinion in her interview and explicitly agreed with Palluconi’s characterization of the letter, when asked.

would be paid for – by Japan’s MITI (Fisk 1989:1). This MITI facility instrument for EOS was called ITIR, for Intermediate Thermal Infrared Radiometer (NASA 1988:180–187; MITI 1990).

What was implicitly suggested by NASA’s “partial selection” letter, and what was later confirmed explicitly, was that NASA wanted Kahle’s TIGER team to serve – from the perspective of NASA Headquarters – as a means to NASA’s end of international cooperation by helping to ensure that cooperation was scientifically and technically justified as a legitimate and important element of EOS (Kahle 2003; Butler 2005). In the contemporary words of NASA headquarters’ chief project scientist for EOS, MITI’s ITIR instrument was “the essence of cooperation between Japan and NASA” (Butler 1989). The stakes of demonstrating scientifically credible international cooperation with Japan in the EOS became even more important for NASA Headquarters as there was less international cooperation elsewhere, such as with the European Space Agency (Butler 2005).³

The instrument that Kahle’s team and MITI’s scientists and engineers ultimately developed and operated was the ASTER. The “U.S. science team” and the “Japan science team,” as the two groups of scientists and engineers later were called,⁴ set out in the initial years of their collaboration to achieve the goals of their states by adopting the strategy of trying to build ASTER as an instrument that would accomplish both teams’ goals without either team having to embrace the other’s goals. For Dr. Kahle and her colleagues, thermal remote sensing was integral to their scientific practice and professional goals, especially for those colleagues at the JPL. On the other hand, MITI’s scientists and engineers from the Geological Survey of Japan – which was under the jurisdiction of MITI – and those from MITI’s industry consortia for remote sensing and natural resources – specifically, the Japan Resources Observation System (JAROS) organization and the Earth Resources Satellite Data Analysis Center (ERSDAC) – were all predominantly interested in shortwave infrared remote sensing. Furthermore, the two teams differed at the time in their technical practices. For instance, Kahle and her team were accustomed to opening up, examining, and modifying the proverbial “black boxes” of instrumentation as part of NASA’s “principal investigator” system for advancing the field of remote sensing. The scientists and engineers who advised and worked for MITI and its consortia were organized much differently; their

³The history of another EOS instrument, the Advanced Microwave Scanning Radiometer, is especially relevant here. Around this time, the contributor of the instrument shifted from Japan’s National Space Development Agency to Italy and the European Space Agency (Butler 2005). It eventually was allocated back to Japan’s National Space Development Agency. Another work of the author describes in detail both the scientific and political importance of international cooperation in EOS for NASA’s goals (Plafcan 2007:112–132).

⁴The formation, organization, and sociopolitical dynamics of the “U.S. team” and the “Japan team” were more complex than what was explainable here. For example, in the late 1980s, Anne Kahle, Frank Palluconi, and Alan Gillespie had also proposed to become members of the ITIR team in addition to being members of Kahle’s TIGER team. To avoid losing sight of the forest among the trees, the above narrative slightly anticipates the ASTER instrument and the U.S. and Japan science teams [for a more detailed analysis, see Plafcan (2007:154–165, 207–230)].

scientific investigations in the late 1980s largely accommodated natural resource exploration and technology development as driving motivations (Plafcan 2007:89–110).

The question of how many thermal infrared bands the instrument, later called ASTER, would have was discussed in the first meeting of the first trip that the TIGER team leadership took to Japan, in early March 1989. During this trip, the TIGER team delegation first explored with their future Japanese colleagues how they could “influence the Japanese design” of what was then called the ITIR instrument. In their original TIGER proposal to NASA, Dr. Kahle and her TIGER team had proposed to push their field of geologic remote sensing by building a space-based instrument that would make thermal measurements to distinguish, and in some cases, identify, “geologically important materials” and to facilitate “global studies of volcanic provinces, sedimentary basins, and weathering history of soils and rocks related to paleoclimate” (Kahle and Palluconi 1988:iii). The proposed design of their TIGER instrument incorporated an imaging subinstrument that promised a potential to map electromagnetic radiation in 14 different spectral bands, including ten bands in the thermal region (i.e., in the 8–13 μm region).⁵ In addition to this imaging mapper, their proposal included another subinstrument – a profiler – which pinpointed particular spots (rather than mapping an area), and which measured the thermal electromagnetic emission over a wide spectrum of thermal wavelengths (rather than focusing on just several wavelength bands in that spectrum, as an imaging mapper would).⁶ “The synergism between an imager and a profiling spectrometer,” Kahle’s team had argued in their TIGER proposal, “is exceedingly powerful, greatly enhancing the value of either data set taken separately” (Kahle and Palluconi 1988:iii).

In their TIGER proposal, Kahle’s team had also stated that they “recognized that the TIGER appears to be in competition” with MITI’s proposed ITIR instrument (Kahle and Palluconi 1988:iii). Kahle’s TIGER team had argued that while both instruments took on the “thermal” label, underneath the hood were vastly different instruments, capabilities, and potential benefits for EOS science. Although the exact number of thermal bands that MITI’s instrument would propose to offer was still unclear (NASA 1988:180–187), it was clear that MITI would propose fewer bands in the thermal region than the ten bands that Kahle’s team had proposed for TIGER’s imaging mapper. ITIR’s shortwave infrared radiometer – which arguably was the focus of ITIR in terms of performance – had proposed five bands. It was unlikely that ITIR would offer many more bands than that for its TIR, and it was much more likely that they would offer fewer. TIGER was anticipated to offer more bands in the same thermal spectral region than ITIR, and hence, its spectral resolution was perceived as greater. Furthermore, the thermal noise in the TIGER instrument’s imaging mapper was proposed at one-third of that proposed for ITIR. TIGER, having no bands in the shortwave infrared

⁵This TIGER subinstrument was called the Thermal Infrared Mapping Spectrometer (TIMS).

⁶The profiler’s name was the Thermal Infrared Profiling Spectrometer (TIPS).

region, was a better complement to another proposed facility instrument for the EOS platform, the HIRIS instrument. ITIR's shortwave infrared radiometer overlapped with the shortwave infrared capability that HIRIS was proposing, and therefore was argued as redundant. In summary, the team had argued, "only TIGER has been specifically designed to exploit...the [scientific] potential of the thermal infrared wavelength regions" (Kahle and Palluconi 1988:iii).

In light of the apparent competition between ITIR and TIGER, and knowing that NASA would need to pay for TIGER's development whereas the Government of Japan would fund the development of ITIR, the TIGER team appealed to EOS science objectives and suggested that:

Both ITIR and TIGER proceed through the definition phase, during which time the Japanese be requested to consider upgrading the proposed ITIR to increase significantly the signal-to-noise and to include additional spectral bands. If these modifications prove feasible, JPL could then build only the profiling spectrometer part of TIGER as a significant and complementary adjunct to ITIR. If, however, the Japanese do not desire or are unable to achieve the signal-to-noise requirements, JPL could proceed to build the entire TIGER as proposed in order to reach the EOS science objectives (Kahle and Palluconi 1988:iii).

By suggesting to NASA that it select both instruments to better ensure the fulfillment of EOS science goals, Kahle and her colleagues had arguably opened the door for a response from NASA that they had not anticipated: the selection of Kahle's TIGER team and MITI's ITIR instrument for the first EOS satellite platform, but not Kahle's TIGER instrument.

In the letter of introduction that NASA Headquarters had written to Kahle's team (i.e., Tilford 1989), which was NASA's only advance work for the first meeting in Japan, and which was sent just days before Kahle and two of her colleagues from the TIGER team showed up for talks at the door of MITI's JAROS consortium to try to "influence" the design of ITIR, NASA Headquarters explained that "NASA remains firmly committed" to the flight of MITI's instrument "even if technology improvements such as those proposed by Ms. Kahle cannot be achieved" (Tilford 1989:2). Dr. Kahle and her colleagues were in no position to make demands backed up by even subtle coercion, perhaps of the kind insinuating that NASA might not select MITI's instrument for flight on EOS if MITI and JAROS did not acquiesce to her team's design preferences.

NASA Headquarters' letter of introduction did suggest to its readers in Japan three deductions about the relationship between Kahle's team and NASA, which likely influenced the weight that MITI and its consortia would give to Kahle's team and to the team's recommendations (Plafcan 2007:165–174).⁷ First, NASA

⁷The key readers of the letter with whom the leadership of the TIGER team interacted during this first trip to Japan were the Executive Managing Director of JAROS (the formal recipient of the letter of introduction), the Director and Deputy Director of the MITI Space Industry Division, Dr. Ono Akira of the National Research Laboratory of Metrology, and Dr. Ishii Yoshinori, then a Professor at the University of Tokyo and chair of JAROS's users' committee. Also in attendance were Dr. Fujisada Hiroyuki from MITI's Electro-technical Laboratory, and Dr. Tsu Hiroji, Dr. Satō Isao, and Dr. Yamaguchi Yasushi from the Geological Survey of Japan (Chase 1989a; Kahle and Palluconi 1989).

Headquarters supported the goals of the TIGER team. Second, NASA's launching of ITIR was conditioned on MITI's, and its consortia's, cooperation with the TIGER team in some significant but vague way, at least in the short term. Third, NASA was willing to go out of its way to help Kahle's TIGER team achieve its goals. Even if MITI ultimately did not need to implement the TIGER team's recommendations concerning "technology improvements" for the ITIR instrument (whatever those recommendations may have been), the letter of introduction was a first step in convincing MITI and its consortia that NASA Headquarters needed the involvement of Kahle's TIGER team to ensure that NASA's cooperation with MITI was conducted in a scientifically justifiable manner. Given that need, there was no reason for anyone to think that NASA Headquarters would not agree with changes to the ITIR remote sensing system which stemmed from the recommendations of the TIGER team, even those in the realm of "technology" which may come at some inconvenience or cost to NASA. While NASA Headquarters conceded that it was their expectation that Kahle's TIGER team may have less sway over "technology," NASA still wanted "technology" on the negotiating table. NASA's Director of Earth Science and Application explained in the letter of introduction that, "in light of [NASA's] current desire to see the best possible ITIR developed under Japanese leadership, NASA is willing to reconsider [NASA's earlier stance concerning] the question of export licenses" and would also "consider a limited hardware contribution...to enable increases in ITIR performance" (Tilford 1989:1-2).

For matters other than technology, NASA had cast Kahle's team with much more authority. Although the NASA Director had written only a paragraph earlier that NASA was "firmly committed" to the flight of ITIR, he took two paragraphs to emphasize that ITIR was still in a definition phase, that ITIR had not yet been selected for flight, and that "all instrument investigations will require confirmation for execution phase." The confirmation decision, the author wrote, "will depend on many factors including successful progress between Ms. Kahle and you on the ITIR effort." What constituted "successful progress" from the perspective of NASA Headquarters, however, went unspecified. Using language grafted from NASA's earlier partial acceptance letter to Kahle's TIGER team, the NASA Director noted that:

The key product of a combined definition phase study would be a cohesive and technically sound plan demonstrating the feasibility of improved ITIR capabilities and an approach to ITIR whereby the Japanese agree to implement this improved approach to ITIR with Ms. Kahle's advice.... Among the results of this definition phase effort will be improved science, management, data, calibration, and cost plans for the portion of the combined investigation (Tilford 1989:3).⁸

In summary, NASA's awkward stance seemed to suggest to its readers in Japan that NASA was not going to insist that MITI implement the TIGER team's hardware recommendations to ensure ITIR's incorporation into EOS. It further suggested that NASA did have some ill-defined yet substantive expectation – an expectation that

⁸NASA Headquarters' and Dr. Tilford's consistent reference to Anne Kahle as "Ms. Kahle" rather than as "Dr. Kahle" raises questions about the politics of gender, which are beyond the scope this chapter but which nevertheless are worth noting.

was probably assumed to verge on a non-negotiable requirement – that MITI and its consortia allow Kahle’s TIGER team to help “the Japanese” implement an “improved approach to ITIR.” This was the negotiating position in which NASA placed Kahle’s TIGER team. In no way did NASA’s letter of introduction anywhere label Kahle’s team as a “U.S. team.” Kahle’s team eventually acquired that label themselves, formalizing the bilateral practices of their negotiations with Japan (Plafcan 2007:207–214).

According to trip reports written by the TIGER team delegation, the “key message” in their first meeting with their future Japanese colleagues was that MITI’s instrument “did not satisfy the requirements” of Kahle’s TIGER team “because there were too few spectral bands in the thermal IR [infrared]” (Chase 1989a:2). The delegation was under the impression that just five thermal bands were planned for MITI’s instrument, and that was simply not enough for the research that the TIGER team wanted to conduct and promote. In response, the representative at the meeting from MITI pointed out that MITI was “responsible for promoting the industrial use of space and, while the thermal infrared was of interest to Japanese geology users and scientists, ITIR placed major emphasis in the visible and near infrared and short wavelength infrared.” (Kahle and Palluconi 1988:1).⁹ Given the technology that was available to MITI’s preferred contractors, it was simply too expensive to do everything, the MITI representative explained, and difficult choices were required. In this conversation, Kahle conceded that the instrument’s thermal bands were “sufficient for operational assessment,” but she still impressed upon the MITI and JAROS management at the meeting that the proposed thermal bands of the MITI instrument were not sufficient for the “scientific purposes” that Kahle had proposed for her instrument, scientific purposes that Kahle and much of her team had been refining for years at JPL (Chase 1989a:2). Kahle asserted, and MITI and JAROS management seemed to have agreed, that there were two different sets of goals proposed for the instrument – operational goals for natural resource exploration and scientific goals of Kahle’s TIGER team. These two sets of goals were each side’s particular articulation of broader state goals that were pushed by their respective bureaucracies, such as MITI’s interest in space industry development and energy security, and NASA’s interest in demonstrating U.S. leadership in global change research (Plafcan 2007:111–145). But how these technopolitical goals would come together in what would become the design concept for the ASTER instrument was still far from apparent.

In subsequent meetings over the next 2 days, Kahle and her colleagues met with key scientists who advised MITI and JAROS on the design of MITI’s ITIR instrument, and explored how much leeway there was to implement design changes. Dr. Ono, who was head of the thermal measurement section of Japan’s and MITI’s National Research Laboratory of Metrology, explained that the users’ committee had settled on two options, and a request for proposals had already gone out to contractors

⁹Without a doubt, despite the polite words of the MITI official, for the key Japanese geologists and scientists who were consulted about the design of MITI’s instrument, the shortwave infrared region was of much more interest than the thermal infrared region (see Plafcan 2007:89–110; 133–145).

based upon those two options. The details of those two options were not shared with Kahle and her colleagues. In her meeting with Ono, Kahle inquired that “if it would be possible, in light of the additional goals of EOS and the international community represented by the TIGER team, to convince [Japan’s] user groups to add capability to ITIR in the thermal infrared and get that capability implemented” (Kahle and Palluconi 1989:3). With this rhetorical move, the goals of Kahle’s team were being asserted not only as the goals of her team, but also as the goals of EOS (and thus, by implication, the goals of NASA), and then, on top of that, as the goals of an international community. This was foreign pressure in the making – what politicians, diplomats, and political commentators in Japan commonly call *gaiatsu* (literally, outside pressure). While there was no appeal here to some shared notion of a Japan–U.S. relationship that needed nurturing or protection, assertions of representing an “international community” could be argued as presumptuous. According to Kahle’s trip report, Ono replied that “it was late, and strong user support would be needed” (Kahle and Palluconi 1989:3). With that response, Kahle and her two colleagues set up an appointment for the next day with Dr. Ishii Yoshinori, then a Professor of Geophysics at the University of Tokyo in the College of Engineering and the chair of JAROS’s users’ committee.

Dr. Kahle and her colleagues debated with Ishii the pros and cons of what Kahle’s team considered the small number of thermal bands in the MITI instrument.¹⁰ According to the trip report of one of Kahle’s colleagues, Kahle “advanced several arguments for having at least five and preferably six bands while Prof. Ishii argued for four bands max. Dr. Kahle did admit that [MITI’s] ITIR probably would satisfy the needs of the operational community but not the international science community represented by her team” (Chase 1989a:4). Onlookers could interpret this discussion as haggling tactics over the number of bands, where one side starts from a “low price” and the other from a “high price” in their attempts to arrive at a “middle price” closer to their preconceived preferences. Kahle had said on the first day of their trip that five bands would not satisfy her team’s requirements. Now in day 3, the leadership of her team was in the position of having to argue for, at a minimum, the restoration of five bands.

Yet, importantly, this discussion was more than just an exchange of preferences about how many bands were desired. After all, the relevant parties already knew the basics of each other’s preferences by the first day. Ishii and Kahle were ascribing political meaning and stakes to their preferences (e.g., “operational” goals vis-à-vis “science” goals). Kahle asserted that her team’s goals were not just science goals, or even just the goals of her team, but the science goals of an “international community”

¹⁰Hiroji Tsu, the Chief of the Applied Geophysics Section of the Geological Survey of Japan, also attended this meeting, but judging from Kahle’s and Palluconi’s trip report (i.e., Kahle and Palluconi 1989) and from Chase’s trip report (i.e., Chase 1989a), Tsu did not assume much of a role in the meeting. Tsu had been and was still then a student of Ishii’s. Tsu and his colleagues at the Geological Survey of Japan were among those who had advised MITI on the conceptual design of the MITI’s proposed instrument. Tsu would later become the chair of ERSDAC’s advisory committee on the EOS science mission, and with that position, he would serve as Japan’s science team leader for the ASTER instrument.

that her team represented. Ishii was advising an organization and users who needed to justify the instrument in terms of what it could do for Japan's pursuit of energy and mineral resources. Each of the two sides of these negotiations was politically explaining themselves and characterizing the other. Again, any appeal to a Japan–U.S. relationship was neither noted in trip reports nor remembered by participants.

While reports of these particular discussions did not indicate in what way Kahle's team was said to have represented an international community, such representation was likely largely asserted by virtue of the international ambitions of EOS. Kahle's claim of representation is not easily justified with reference to the national composition of the TIGER team. When Kahle had proposed her TIGER team, 12 of the 14 investigators were of U.S. nationality. Before this meeting, one of the two who were not of U.S. nationality – an Australian national – had withdrawn from the TIGER team (Green 1988). Was the anticipated participation of a single Frenchman among a dozen Americans enough for Kahle to say that the TIGER team represented an “international community?” Since Ishii, as well as MITI's other advisors, was perhaps already aware of the composition of Kahle's TIGER team – or at the very least was expected to soon become aware of its composition as consultations proceeded – Kahle's rhetorical framing of Japan's operational interests versus the interests of the international science community did not likely rest upon a mere willingness to strategically deploy the word “international” on the basis of one non-American among a dozen team members. Such a literal interpretation of “international” too narrowly captures this rhetoric. Amid the contemporary EOS rhetoric of “global” studies of the earth (e.g., NASA, Earth Observing System Science Steering Committee 1987), and considering the explicitly “global” ambitions of the TIGER team's proposal (Kahle and Palluconi 1988), it is just as conceivable, if not more so, that Kahle and the TIGER team leadership saw themselves as spokespersons for the international science community, especially in this situation of contrasting their “science” interests against the “operational” interests of their Japanese counterparts.

I suggest that to understand this rhetoric and its utility, an inclusive interpretation is required. In the United States, “real” geologic remote sensing science and especially “global” EOS science were considered as endeavors of international scale, and if the TIGER team considered themselves practicing real geologic remote sensing science as part of the EOS enterprise, which they certainly did, then their science was by association international, even if the science in particular was only sponsored by the U.S. government. The TIGER team leadership was funded by NASA, and they could claim to work on behalf of NASA, but they were not unambiguous agents for the U.S. state. They carried with them ideals of scientific autonomy and universalism to recall and deploy when useful. Such an interpretation is only justifiable with the benefit of additional illustrations [see Plafcan (2007)]. Nevertheless, I suggest that the TIGER team's identification of their science with the international was not merely a strategic enactment. It was an assumption potentially strategic in its articulation. To say that the rhetoric was deployed strategically is not to also say that the sensibility was disingenuous.

When these Americans claiming to represent international science pressed Dr. Ishii to justify scientifically, the rationale for ITIR's thermal bands, he supported

his position by moving outside the rhetorical realm of his domestic “operational” concerns, and into the rhetorical realm of “international science.” He cited a study that was also “international,” in that the authors were not Japanese. The study, in fact, was of American origin. Ishii explained that the design of ITIR “was taken directly and exactly” from a public–private study paper on space-based thermal instrumentation, which was jointly produced by NASA and the EOSAT company (EOSAT was a company of the late 1980s, which developed and managed the United States’s Landsat series of satellites in an ultimately failed attempt to privatize Landsat’s development and operations). This study, Kahle learned from Ishii, “was treated as something of a ‘bible’ in Japan” (Kahle and Palluconi 1989:4; the study paper is Putnam 1986).

Dr. Kahle herself had actually chaired the Geology Working Group of that NASA–EOSAT joint study. If it was “treated as something of a ‘bible’ in Japan,” Kahle could provide an authoritative exegesis. In response to Ishii’s referencing of that study, Kahle explained that “the Eosat [i.e., EOSAT] report was strongly conditioned and constrained to fit within the modest modifications permitted by working within an existing design for the Thematic Mapper” [a satellite in the Landsat series] (Kahle and Palluconi 1989:4). Kahle added that a Landsat with more extensive thermal capabilities “was viewed by at least some of the EOSAT Working Group members as a preliminary step to a more capable instrument we hoped would be a part of Eos” (Kahle and Palluconi 1989:4). According to Kahle’s and Palluconi’s trip report, in this discussion Ishii eventually conceded that “three bands in the thermal infrared represented a step back from current capability...and [Ishii] did not consider that three bands...could adequately represent the spectral information content in this region” (Kahle and Palluconi 1989:4). Dr. Ishii asked the TIGER team leadership for copies of the TIGER proposal and a white paper that would justify additional bands in the thermal infrared region. He said he would discuss the TIGER team’s arguments with the ITIR users’ committee. In this meeting, while common understandings of the capabilities of various designs were worked out, Dr. Ishii made no commitments or promises about changing ITIR’s design.

Kahle and Palluconi took away from their exploratory trip to Japan that what the TIGER team wanted out of the ITIR instrument (and presumably what they hoped NASA wanted out of the instrument) and what MITI and JAROS wanted out of the ITIR instrument were three very different things – different capabilities, different operations, different measurements. In their trip report, which was distributed to the other TIGER team members as well as to NASA, Kahle and Palluconi wrote that:

From the Japanese point of view, ITIR, as currently specified, strongly supports commercial exploration applications by incorporation [*sic*] and, in some areas, extending the most attractive exploration features of SPOT (high resolution stereo, 15 meter resolution, same orbit stereo not available with SPOT), Landsat (VNIR and SWIR bands) and TIMS (three TIR bands). From out [*sic*] point of view, ITIR, as currently [*sic*] specified, duplicates the VNIR and SWIR spectral coverage of the Eos HIRIS instrument, is a step back in terms of spectral coverage and sensitivity from the aircraft TIMS, and does not have the spectral bands, spectral coverage, and sensitivity in the TIR to fully satisfy exploration requirements, let alone research requirements (Kahle and Palluconi 1989:4).

Kahle and Palluconi did not seek to transform this technopolitical fact by trying to mandate changes that directly competed with MITI's objectives for ITIR or by trying to convince the JAROS users' committee to adopt as their interests those of the TIGER team or those of NASA. Rather, they conveyed to NASA Headquarters a strategy of sharing separately – the possibility of working with their Japanese counterparts to modify ITIR so that the instrument was better able to accomplish the TIGER team's goals without trying to challenge or dominate those of MITI and JAROS:

On the positive side, we found the Japanese to be very open, direct, communicative and quite willing to listen and consider what we had to say. There is a possibility (whose probability cannot be estimated) that the TIGER Science Team can influence the design and performance specification of ITIR; but the potential is likely limited to the addition of one or two bands, extending the wavelength limit and improving the signal to noise ratio. It does not appear possible to incorporate the major design innovations of TIGER in ITIR nor to capture the full research potential of TIGER in some modification of ITIR. ITIR funding and motivation is provided by a Japanese user community, lacking first hand experience with multispectral thermal data, interested in a practical, bread and butter instrument that exploits existing remote sensing knowledge (Kahle and Palluconi 1989:5).¹¹

Kahle's and Palluconi's assessment of the situation was not optimistic for fulfilling their research goals. The path they outlined for possibly influencing the instrument in order to achieve their goals (goals that might or might not have been NASA's goals) was not overly ambitious. They largely accepted at face value what they were told about the realities of the situation by the Deputy Director of the MITI Space Industry Division, by Dr. Ono, and by Dr. Ishii. Even if they were able to modestly improve the instrument for their research goals – restoring the number of TIR bands back to five from three, increasing the instrument's sensitivity, etc. – the ITIR instrument would still remain unsatisfactory for the research that the TIGER team members had hoped to conduct with the TIGER instrument.¹²

Yet, a cooperative arrangement with MITI on the ITIR instrument was probably the best the ITIR team could do in terms of a thermal instrument. They proceeded

¹¹This Kahle and Palluconi trip report should not be interpreted naively. They were, after all, writing to NASA Headquarters, which was still considering how the TIGER team would or would not incorporate into the ITIR enterprise and into EOS. For instance, Kahle and Palluconi might have shared with NASA Headquarters their counterargument to Ishii's marshalling of the EOSAT study for the purpose of clarifying the value-added of the TIGER instrument to NASA Headquarters. For the arguments that I am advancing, however, the question of how Kahle and Palluconi crafted their report for the NASA Headquarters audience does not require an answer, especially if another trip report, written for a completely different audience, is available for comparison and cross-referencing, in this case Chase (1989a). Kahle also distributed the Kahle–Palluconi trip report to her team members for their reference, so the trip report's audience cannot be said to have consisted of only NASA Headquarters. Along with the Kahle–Palluconi trip report, Kahle sent a letter to the TIGER team (which was not copied to NASA Headquarters) which supports my interpretation of sharing separately (Kahle 1989).

¹²In addition to the fact that ITIR would have fewer thermal bands than required by the TIGER team's scientific goals, Kahle "steadfastly maintained" (Chase 1989b:1) that to do their thermal remote sensing science, ITIR would need to be at least three times more sensitive than it was being designed to be (Kahle 1989).

to make the most of the situation by trying to share separately. After their trip, Kahle wrote to her team members (a letter not copied to NASA Headquarters) that “we need to consider what we should do if we fail with the Japanese. Quit?, [*sic*] Try to convince NASA to fly TIGER? Help the Japanese anyway? other options?” (Kahle 1989b:1). Answers to these questions were months away. The TIGER team first had to find out what, if any, instrument modifications MITI and JAROS would accommodate, and what NASA Headquarters’ bottom-line requirements for ITIR were (see, e.g., Butler 1989). Not knowing the answer to the second question, however, did not impede them from speaking for EOS’s goals in order to accomplish the first.

Of especial assistance to Dr. Kahle in making the case to Dr. Ishii for an increase in thermal bands was a white paper in which Kahle asserted that five TIR bands were not just important for the goals of the TIGER team or the “international community” in general, but that five bands were “important to achieving the goals of EOS” (Kahle 1989a). This assertion about EOS’s goals implicitly brought NASA to the negotiating table behind Kahle, even if NASA seemed to have not specifically stated, given currently available records, that five bands in the thermal region were “important to achieving the goals of EOS” (Butler 1989, 2005; Plafcan 2007:193). Although the TIGER team was not NASA, they were in a position to use their scientific judgment to translate and legitimately assert what EOS’s high-level goals meant for ITIR.

The TIGER team leadership continued to negotiate the thermal radiometer’s specifications with MITI’s Space Industry Division, JAROS management, and the scientists and engineers who advised JAROS. Eventually, Kahle and her team were able to convince MITI and JAROS that five bands in the thermal region would not only help Kahle’s team realize their science goals, but also help MITI, JAROS, and their user community achieve their natural resource and instrument development goals. The TIGER team was not able to negotiate, however, more ambitious specifications in other areas, such as signal to noise and spatial resolution – certainly not what the TIGER team originally desired (which was, namely, 0.1 K and 60 m, respectively) [see Chase (1989b) and Plafcan (2007:197)]. All along, however, Kahle’s strategy was one of sharing separately: you have your “operational” goals; I have my “science” goals; and let’s make this instrument work for the both of us, so we can each do our own thing our own way. Beyond the instrument itself, little, if any, commonality of interest or shared understanding of a Japan–U.S. relationship was expected or articulated during this time period in the (pre)history of the ASTER collaboration. Perhaps, because MITI and JAROS went along with this strategy of trying to share separately, any explicit use of a shared understanding of a Japan–U.S. relationship was simply unnecessary.

This strategy of sharing separately was not sustained throughout the ASTER collaboration. On March 15, 1990, Dr. Kahle submitted a proposal to NASA Headquarters in which she posited that her appointment as the “U.S. ITIR Team Leader” would keep “science high in the Japanese priorities as they proceed with the ITIR development” (Kahle 1990:1–2). This proposal’s “overall objective,” wrote Kahle and her colleagues, was “to maximize the capability and utility of ITIR

for meeting the science goals of the EOS mission” (Kahle 1990:3). When ITIR was in competition with TIGER, Kahle and her colleagues had argued in their 1988 proposal that the two instruments were in fact dramatically different, and so were their specific scientific objectives (Kahle and Palluconi 1988:iii). In the ITIR U.S. Team Leader proposal to NASA, Kahle now wrote that while her team members “proposed approaches to using the modified ITIR instrument may be somewhat different from the original TIGER concept, the science objectives are basically the same” (Kahle 1990:2). With that U.S. Team Leader proposal, the former TIGER team committed themselves to MITI’s ITIR instrument as well as to NASA’s EOS goals. That dual commitment proved to require more than merely sharing separately an instrument with MITI’s scientists and engineers. In the fall of 1990, while ITIR was renamed ASTER to indicate that the instrument had bands in the visible and shortwave infrared regions besides the thermal, the renaming also suggested that both MITI’s and the TIGER team’s remote sensing goals were revisable for something that was a product of Japan–U.S. collaboration.

21.3 Enacting Japan–U.S. Partnership

In addition to working out the design specifications for the capabilities of the ASTER instrument, the Japan and U.S. teams also had to negotiate operational issues concerning who could use ASTER’s various capabilities, and how much of its scarce capabilities these users could consume. The ASTER instrument’s capability to point its three telescopes a limited number of times over its expected life was just such an issue. The two teams needed to decide how the consumption of ASTER’s scarce pointing maneuvers was regulated. Their technoscientific diplomacy over this issue deployed technical reasoning and asserted and ascribed state power, and the closure of two teams’ discussions concerning this issue was facilitated by the enactment of Japan–U.S. partnership.

Questions about how to regulate ASTER’s pointing capabilities came to a head in March of 1997, a couple of years before ASTER’s launch, when the team was evaluating the (simulated) performance of their routines for scheduling ASTER’s observations. At a joint Operations and Mission Planning Working Group meeting, a mission analyst working at and for ERSDAC as a contractor explained that the scheduling algorithm that his firm was developing for the system was expectedly too slow. Because the U.S. and Japan teams had not finished collecting what they considered “realistic” data requests to run scheduling simulations, no one knew how slow the scheduling software was, or even if it was actually slow (ASTER Operations and Mission Planning Working Group 1996:1, 1997a:4–6; Ohno 1997). But the two teams suspected that the scheduler was indeed slow, particularly because they were experiencing other problems with the scheduler that ERSDAC’s diligent but “overcommitted” contractor was developing [Cohen 1996; the quote is from ASTER Operations and Mission Planning Working Group (1996:2)].

One way by which processing was sped up was by strict scheduling of observations requiring the visible telescope to point at large angles (Pniel 1997:4; Yamaguchi 1997:1). Eliminating large angles removed many potential observations that required

consideration in the scheduler's search to compile an optimal 1-day schedule. The two teams had already agreed that large-angle pointing observations were appropriate only in emergencies, such as to monitor an erupting volcano or a forest fire. But now, they had to specify and implement this general guideline. They left the meeting with this issue unresolved, and the Operations and Mission Planning Working Group posted it as their 116th action item (ASTER Operations and Mission Planning Working Group 1997a:8). This action item was an important one for the working group, but it was only one in a long list that was opened and closed over their years of collaboration.

A couple of months later before the next joint team meeting, the Japan co-chair of the joint working group, Dr. Yamaguchi Yasushi, e-mailed the U.S. co-chair of the working group, Moshe Pniel. To resolve the question about how to restrict the use of large-angle pointing, Dr. Yamaguchi had proposed that only U.S. and Japan team members hold authority to submit large-angle pointing requests, which were only done for specific observation requests. His proposal seemed to draw a sharp distinction between who could and could not use the visible telescope's capability to point sideways at large angles (Pniel 1997:2–4).

The co-chair of the Operations and Mission Planning Working Group, Pniel, in an e-mail response to Yamaguchi, stated that it was Pniel's and Kahle's recommendation that they discuss this issue with the two teams as a whole during the plenary session of the upcoming meeting (Pniel 1997:3). Everyone involved with the development of the ASTER remote sensing system – the U.S. and Japan teams, ERSDAC and JAROS managers, even sometimes representatives from NASA Headquarters – typically attended the plenary session of team meetings. Kahle and Pniel desired to retain the flexibility of the large-angle viewing for users other than the two teams, and they suspected that the U.S. and Japan teams as a whole would agree with them. They also thought that the two teams as a group should determine a method by which the data and information system could calculate when to limit the use of the large-angle pointing. Kahle and Pniel wanted the above-mentioned scheduling program of the data and information system, which the ERSDAC contractor was developing, to integrate this calculation into its scheduling routines. This proposal for a technological fix was e-mailed to Yamaguchi (Pniel 1997:4–6).

Yamaguchi e-mailed a response to Kahle and Pniel, reiterating his position on the matter, arguing that they should not ask the two teams about this question at the upcoming Japan–U.S. joint team meeting before the joint working group had come to a position among themselves. He had reasoned that it was a “very political matter” and that it was best for the working group to present a single rationale to the two teams together as a group (Pniel 1997:5). Dr. Yamaguchi's hesitancy to broach the question of how to regulate the consumption of ASTER's pointing capabilities during a plenary session stemmed from a number of general concerns: (1) JAROS engineers had already requested that the ASTER instrument, for whose technical health they were directly responsible, was not needlessly taxed with pointing maneuvers; opening up pointing capabilities to general users was a risk in that regard; (2) industry users associated with ERSDAC were concerned that emergency pointing maneuvers would detract from their more regular and less-time dependent observation goals; and (3) as was mentioned above, ERSDAC's contractor for the scheduling program

for ASTER was already overcommitted and was having some problems developing the complex scheduler. Because Dr. Yamaguchi did not list in his e-mail these general concerns, concerns, which were explicitly voiced in other forums in which Yamaguchi was involved, the salience of these concerns is a matter of interpretive judgment. Without doubt, these concerns would have complicated any discussion of the issue during a plenary session. For different reasons, many parties had a stake in this issue. Wide-ranging discussions at the relatively large plenary session risked a contentious scene pitting Japan's two consortia against scientists from both the Japan and U.S. teams.

In his e-mail to Kahle and Pniel, Yamaguchi suggested that he feared that any discussion at the plenary would highlight ERSDAC's and its contractor's inability to develop, given their tight budget allocations, a scheduler that could fulfill a likely request from both teams to manage large pointing angles (Pniel 1997). Yamaguchi's alternative proposal, to decide at the working group level to restrict pointing maneuvers for everyone but team members, had the merit to ensure that the general consumption of ASTER's limited pointing maneuvers are strictly limited without burdening the scheduling software. He also proposed that exceptions to this rule are allowed on a case-by-case basis determined by a joint committee. Barring a consensus on such a procedure to regulate pointing maneuvers, Yamaguchi wanted to learn in advance of the plenary session, other deliberations on the procedure (Pniel 1997:7).

Dr. Yamaguchi's response pushed Kahle, Pniel, and others at JPL who were discussing the issue to name their specific objections to Yamaguchi's proposal. They disagreed with Yamaguchi's proposal on the grounds that it would appear to favor the two teams – in their words, “the insiders” – over the general users. And on that basis, they would expect to receive complaints. EOS teams were, in general, under consistent pressure by NASA Headquarters to level user hierarchies and avoid insider advantages. In addition to exacerbating possible outsider complaints about a system allegedly rigged for the insiders, the U.S. team argued that Yamaguchi's proposal would require a joint team working group to evaluate every urgent request, instead of leaving it to the computer processing system to calculate whether or not an urgent request would fit into the schedule (Pniel 1997:6). The U.S. members of this scheduling committee did not want to have any direct agency in this scheduling calculation. Instead, they preferred to leave it to computer algorithms to sort out – algorithms, which of course required consensus and designing in advance.

Yamaguchi persisted with his position, pointing out that other insider/outsider discrepancies were already embedded into the Japan–U.S. team's user classification scheme (Pniel 1997:7–8). He closed by writing “if you [Pniel and others] still want to nominate this issue [for the plenary], we agree, but please understand our feeling which were mentioned in this and previous mail” (Pniel 1997:7). Notes on the U.S. team's discussion show that the plea to “understand our feeling” solidified the issue as not just a request from Yamaguchi but as a request from Yamaguchi speaking for “Japan” (Pniel 1997:9). Dr. Yamaguchi, whose English was excellent, often served as a spokesperson for the Japan team in negotiations with the U.S. team. Pniel reported to the U.S. team that it was “Japan's STRONG feelings that this was a closed issue”

(emphasis in original) (U.S. ASTER Science Team Meeting 1997:3). Yamaguchi's rhetoric had ascribed primacy to a Japan–U.S. partnership, arguing that that partnership should trump any domestic insider/outsider concerns that the U.S. team had. Yamaguchi's invocation of this partnership did not allow the U.S. team to easily insist that ERSDAC fund the integration of a new calculating routine into a complex scheduling program that ERSDAC's contractor was already having problems developing. Would the U.S. team deny the importance of that Japan–U.S. partnership that buttressed their international authority over the ASTER remote sensing system?

Ultimately, after the U.S. team members discussed the matter, Kahle and Pniel decided that they would “concede” to what by now had moved from being just Yamaguchi's request to the “Japan team's position.” The U.S. team wanted to avoid any further escalation of the issue. Nevertheless, they thought it amounted to what they characterized as a “loss of science.” They strategized, however, that that concession would leave enough goodwill for them to “go for” another issue of importance to the U.S. team leader regarding ASTER operations and data acquisition (U.S. ASTER Science Team 1997:3; ASTER Operations and Mission Planning Working Group 1997b). Dr. Yamaguchi's proposal became policy, and rather than going for a technological fix, the two teams further enacted partnership in the Japan–U.S. relationship and enhanced the ASTER team's international authority in the particular sociopolitical practices of the two teams: on a case-by-case basis, a joint ASTER team working group would evaluate requests for observations that required using the visible and near infrared telescope at large angles, and through that practice, the ASTER team would engineer yet another element of the ASTER remote sensing system not as a MITI system or a NASA system, but as a Japan–U.S. system.

21.4 Conclusion

In 2004, NASA's Earth Science Enterprise and Office of External Relations published a thick glossy book called *Global Reach: A View of International Cooperation in NASA's Earth Science Enterprise* (NASA 2004). The book's preface celebrates the Earth Observation Summit held in Washington, DC in the summer of 2003 as “one of the most significant recent events in Earth science” (NASA 2004:1). The preface elaborates further that:

The Summit was an unprecedented gathering of senior representatives from 34 countries and 21 international organizations. The Summit promoted a political commitment to the development of comprehensive, coordinated, and sustained Earth observation systems among governments and the international community in order to understand and address global environmental and economic challenges of the 21st century. Following the Summit, an ad hoc Group on Earth Observations was established to begin the process to develop a 10-year implementation plan for building these comprehensive, coordinated, and sustained Earth observation systems (NASA 2004).

Beyond the preface, the book's 100 pages are filled with single-page profiles of earth observing instruments and other projects that involved collaboration in some

way with a government other than that of the United States. Each profile, indexed first by the name of the international partner, and then by the name of the instrument or project, is written in English on the front side of the page, and then in the language of the international partner on the back side. The profiles are generously illustrated with images and pictures of instruments. A reader is perhaps forgiven for being left with the impression that international collaboration is effected by governments, national space agencies, their budgets, and international organizations, and that, furthermore, the products of their collaboration are only instruments and images that inherently transcend cultures, organizations, institutions, and nations without any difficult social and political work.

What this chapter – and indeed this volume – conveys is that behind governments, instruments, and images are people who make it all happen, especially with respect to international collaboration. More often than not, these people are scientists and engineers who are too frequently relegated in high-level planning documents to being merely “implementers.” Yet, it is these scientists and engineers who often do the work of politics, including the diplomatic work of articulating state goals and of translating scientific practices, technologies, and policies across cultures, organizations, and nations, in search of advantageous collaboration and international partnership.

This chapter has illustrated in particular how scientists and engineers involved in the ASTER collaboration negotiated Japan–U.S. relations in their work as well as technical specifications, algorithms, and scientific procedures. I have shown that these two negotiations are often intertwined and carried out in the same discussion, in a practice of international politics that I call “technoscientific diplomacy.” In this chapter’s first episode of technoscientific diplomacy – when Dr. Ishii and Dr. Kahle were negotiating the number of bands for ITIR/ASTER’s TIR – Kahle positioned herself as an independent scientist representing the “international community.” Yet, when Dr. Kahle spoke for the national goals of EOS in asserting the importance of five bands in the thermal, she projected U.S. state power. In the second episode of technoscientific diplomacy, the ends and means of the regulation of the VNIR telescopes’ large-angle pointing maneuvers were decided in part as a result of Dr. Yamaguchi’s implicit invocation of a Japan–U.S. partnership, the U.S. team’s respect for that partnership, and the possible consequences of dismissing it. Moreover, by placing a joint ASTER working group in charge of evaluating requests for using the VNIR telescopes’ large-angle pointing, the decided means of regulation further enacted Japan–U.S. partnership in the two teams’ sociopolitical practices.

International collaboration was no easy feat for the Japan–U.S. ASTER team. Certainly, for the first several years of the collaboration, and then for the first few years after ASTER’s launch in December 1999, I would argue that – judging from historical documents, interviews, and first-person observations of meetings – it was a struggle for both teams (see Plafcan 2007). Nevertheless, believing that in the long term they had little choice but to collaborate if ASTER was to succeed, each team practiced technoscientific diplomacy in order to make the most of their circumstances and bring states as well as people together around common goals. Space agencies with grand, high-level plans for international cooperation are well

advised to keep in mind the sociopolitical demands of technoscientific diplomacy within international collaborations when they select teams and manage projects. Notwithstanding the importance of memoranda of understanding, shared project documents, “clean” interfaces in technologies, and other ways of facilitating collaboration, the practice of technoscientific diplomacy was central to Japan’s and the United States’ joint development of the ASTER remote sensing system.

References

- Abbott A (1988) *The System of Professions*. University of Chicago Press, Chicago
- ASTER Operations and Mission Planning Working Group (1996) *Very Brief OMPWG Meeting Narrative Notes*. Yokohama, Japan. December 5
- ASTER Operations and Mission Planning Working Group. (1997a) *OMPWG Splinter Meeting Minutes*. Tokyo, Japan. March 5–7
- ASTER Operations and Mission Planning Working Group. (1997b) *Operations and Mission Planning Working Group Narrative Minutes*. Sioux Falls, SD. May 22
- Butler DM (1989) NASA Mail message from the NASA EOS Project Scientist to L. Lincoln, Re: Message from Benn Martin, msg NJIJ-2847–2908, November 12
- Butler DM (2005) Personal correspondence with author, June 18
- Chase S (1989a) Santa Barbara Research Center Internal Memorandum, Subject: report of trip to Japan to discuss the ITIR, March 7, 8, and 9, 1989, March 10
- Chase S (1989b) Santa Barbara Research Center Internal Memorandum, Subject: Trip to Japan: ITIR/TIGER Science Team Meeting; 11/25/89 to 11/30/89, December 5
- Cohen R (1996) Use of Cloud Simulation by Scheduler. In *Very Brief OMPWG Meeting Narrative Notes*, held at Yokohama, Japan, December 5
- Collins H (2004) *Gravity’s shadow: the search for gravitational waves*. The University of Chicago Press, Chicago
- Eden L (2004) *Whole world on fire*. Art RJ, Jervis R, Walt SM (ed) Cornell studies in security affairs. Cornell University Press, Ithaca
- Epstein S (1996) *Impure science: AIDS, activism, and the politics of knowledge*. University of California Press, Berkeley
- Fisk LA (1989) EOS selection letter from the NASA associate administrator to Anne B. Kahle, February 7
- Goddard Space Flight Center (1995) [signed in 1996]. *Project Implementation Plan, Volume I: Advanced Spaceborne Thermal Emission and Reflection Radiometer and EOS-AM Projects*. GSFC 421–12–01–01. Greenbelt, MD, January
- Goddard Space Flight Center (1997) [signed in 1997]. *Project Implementation Plan, Volume II - Ground Data System: Advanced Spaceborne Thermal Emission and Reflection Radiometer (ASTER) and ESDIS and EOS-AM Projects*. CCR 505–10–11–002-A. Greenbelt, MD. September
- Green A (1988) Letter to Anne B. Kahle, August 17
- Hackett EJ, Amsterdamska O, Lynch M, Wajcman J (eds) (2008) *The handbook of science and technology studies*, 3rd ed. MIT, Cambridge
- Hecht G (1998) *The radiance of France: nuclear power and national identity after World War II*. Bijker WE, Bernard Carlson W, Pinch T (eds) *Inside technology*. MIT, Cambridge
- Hilgartner S (2000) *Science on stage: expert advice as public drama*. Lenoir T, Gumbrecht HU (ed) *Writing science*. Stanford University Press, Stanford
- Hughes TP (1983) *Networks of power: electrification in Western Society, 1880–1930*. Johns Hopkins University Press, Baltimore

- Jasanoff S (1990) *The fifth branch: science advisors as policymakers*. Harvard University Press, Cambridge
- Jasanoff S (2005) *Designs on nature: science and democracy in Europe and the United States*. Princeton University Press, Princeton
- Kahle AB (1989a) Letter to Ishii Yoshinori, Re: Rationale for Additions to the Proposed ITIR Instrument, April 4
- Kahle AB (1989b) Letter to TIGER team members, March 17
- Kahle AB (1990) U.S. Team Leader: Intermediate Thermal Infrared Radiometer (ITIR) for EOS Polar Orbiting Platform, A Proposal to the National Aeronautics and Space Administration Office of Space Science and Applications, Vol 1. Jet Propulsion Laboratory. March 15
- Kahle AB (2003) Interview by author, Pasadena, CA, August 4
- Kahle AB (2005) Interview by author, Phone call to Castle Rock, WA, August 26
- Kahle AB, Palluconi FD (1988) Thermal Infrared Ground Emission Radiometer (TIGER): A Proposal to the National Aeronautics and Space Administration Office of Space Science and Applications. Jet Propulsion Laboratory. July 5
- Kahle AB, Palluconi FD (1989) Trip Report to Shelby G. Tilford and Dixon M. Butler, March 17
- Krige J, Barth K-H (eds) (2006) *Global power knowledge: science and technology in international affairs*. Edited by Olesko KM Vol. 21. Osiris. University of Chicago Press, Chicago
- Latour B (1987) *Science in action: how to follow scientists and engineers through society*. Harvard University Press, Cambridge
- MacKenzie D (1990) *Inventing accuracy: a historical sociology of nuclear missile guidance*. Bijker WE, Bernard Carlson W, Pinch T (eds) *Inside technology*. MIT, Cambridge
- Ministry of International Trade and Industry (1990) A Phase C/D Proposal in Response to the Earth Observing System, Intermediate and Thermal Infrared Radiometer (ITIR) for Eos-A Polar Orbiting Platform: Investigation and Technical Plan, Data Plan, and Management Plan – Volume 1. 90JS-POP-TS009. Tokyo, Japan. May 30
- National Aeronautics and Space Administration (1988) Earth Observing System (Eos) Background Information Package (BIP) Announcement of Opportunity, Part Five: Research Facility and Operational Facility Instrument Descriptions. OSSA-1–88. National Aeronautics and Space Administration. January 19
- National Aeronautics and Space Administration, and Ministry of International Trade and Industry (1996) Implementing Arrangement between the National Aeronautics and Space Administration of the United States of America and the Ministry of International Trade and Industry of Japan concerning Cooperation on the Advanced Spaceborne Thermal Emission and Reflection Radiometer (ASTER) Program. November 7
- National Aeronautics and Space Administration, Earth Observing System Science Steering Committee (1987) *From Pattern to Process: The Strategy of the Earth Observing System, Eos Science Steering Committee Report*. Butler DM (ed) 11h vols. Vol. II. Earth observing system reports. National Aeronautics and Space Administration, Washington, DC
- National Aeronautics and Space Administration, Earth Science Enterprise and Office of External Relations (2004) *Global reach: a view of international cooperation in NASA's earth science enterprise*. National Aeronautics and Space Administration, Washington, DC
- Taijiri O (1997) Schedule on performance-check-simulation. In *OMPWG Splinter Meeting*, held at Tokyo, Japan, March 5–7
- Palluconi FD (2001) Interview by author, Pasadena, CA, May 30
- Plafcan DJ (2007) *Between State and Transnational Community: U.S.-Japan Technoscientific Diplomacy in Earth Observation*, Doctoral Dissertation, Department of Science and Technology Studies, Cornell University, Ithaca, New York, January
- Pniel M (1997) Large Angle Pointing > 8.55 degrees. In *US ASTER Science Team Meeting Minutes*, held at Sioux Fall, SD, May 19
- Putnam ES (1986) Commercial applications and scientific research requirements for thermal-infrared observations of terrestrial surfaces: a report of the Joint EOSAT/NASA Thermal Infrared Working Group. National Aeronautics and Space Administration, Earth Observation Satellite, Co, Lanham, MD

- Shapin S (1994) *A social history of truth: gentility, credibility, and scientific knowledge in seventeenth-century England*. University of Chicago Press, Chicago
- Shapin S, Schaffer S (1985) *Leviathan and the Air-Pump: Hobbes, Boyle, and the Experimental Life*. Princeton University Press, Princeton
- Tilford SG (1989) Letter from NASA Earth Science and Applications Division Director Shelby G. Tilford to JAROS Executive Managing Director Hashimoto Shoichi and to T. Tanaka of NASDA, March
- U.S. ASTER Science Team (1997) *US ASTER Science Team Meeting Narrative Minutes*. Sioux Falls, SD. May 19
- Vaughan D (1996) *The Challenger Launch Decision: Risky Technology, Culture, and Deviance at NASA*. University of Chicago Press, Chicago
- Yasushi Y (1997) Policy for VNIR > 8.55 pointing angles. In *Operations and Mission Planning Working Group Minutes*, held at Sioux Falls, SD, May 22
- Yoshinori I (2003) Keynote Address. Presented at *Earth Remote Sensing Data Analysis Center Annual Business Meeting*, June 3, held at Tokyo (Aoyama), Japan

Part V

MODIS Science and Applications

The requirements for the MODIS instrument were developed in the late 1980s, when the imaging requirements for the NASA Earth Observing System (EOS) were being developed (Justice et al., this volume). At that time, the community was benefiting from the optimized design of Landsat 5 Thematic Mapper and the daily temporal frequency of the NOAA AVHRR for vegetation monitoring. The next logical step for the land community was to develop a sensor with the daily, temporal frequency of the AVHRR and the spectral band selection of the Thematic Mapper. This basic requirement was enhanced to provide global coverage at increased spatial resolution over the AVHRR, with additional capability for thermal remote sensing (including fire), and bands placed to facilitate cloud detection and atmospheric correction. The strength of this combination has now been well demonstrated by MODIS research and applications. MODIS proved superior to the AVHRR in band-placement, spatial resolution, calibration, and geolocation and has become the instrument of choice for coarse resolution land monitoring. Since MODIS was launched, other international instruments have adopted similar capabilities, including the French SPOT Vegetation instrument and the Japanese Global Land Imager (GLI), which included multiple 250-m channels.

The EOS data system proved a challenge in the early days of the program, particularly with respect to the large volumes and loads associated with MODIS data. Innovative solutions were developed and implemented after the MODIS Science team inherited the responsibility of the MODIS processing system (Masuoka et al., this volume). Currently, there are several ways to access MODIS data. Tools exist to help users analyze the data and value-added data products and services developed by the Science Team and various data brokers. For example, the MODIS Rapid Response System provides quick access to data, and the Fire Information for Resource Management System (FIRMS) provides Web-GIS capabilities for MODIS fire data. The NASA Distributed Active Archive Center at the USGS EROS Center is the primary source for MODIS land products, which currently distributes over 30 terabytes of data per month. A significant growth in the number of direct readout stations receiving MODIS data has also occurred. The development of shareware code to generate similar land products has allowed ground stations to generate some new products with the cooperation of an international group formed to share their experience and code.

Dr. Vince Salomonson, who was formerly the Project Scientist for Landsat 5, formed and led the NASA MODIS Science Team. The team's success is partly attributed to Dr. Salomonson's two decades of leadership and personal commitment to the MODIS instrument design, its calibration and characterization, the data processing systems, and the Science team. Under his guidance, the MODIS Science team worked closely with the instrument developers and the EOS Data and Information System to overcome the initial obstacles encountered and to identify their solutions. The science discipline sub-teams worked to develop the algorithms and products and provide outreach to the science and applications communities. The discipline sub-team developed to provide the land products (MODLAND) has made a number of important contributions to the field. In addition to growing the number of standard land products available to the science and applications communities, it developed an overarching approach to coarse resolution land product quality assessment and validation (Masuoka et al., this volume). All the MODIS Land products are currently at Stage 2 or 3 validation. MODIS product validation and multiscale research has greatly benefited from the collocation of the ASTER instrument on the Terra platform. The international community now recognizes the need for land product validation, and the Land Product Validation (LPV) Working Group of the Committee on Earth Observation Satellites (CEOS) was established to support this requirement (Townshend et al., this volume).

The chapters in this section represent the status of all the MODIS Land products at the time of writing (close to the completion of Collection 5), which was the fourth major reprocessing (Masuoka et al., this volume). The MODIS Surface Reflectance Product provides state-of-the-art atmospheric correction and takes advantage of the MODIS bands selected for atmospheric characterization and provides a foundation for the higher-order vegetation products (Vermote et al., this volume). The MODIS Albedo and Reflectance Anisotropy Product, championed by Dr. Alan Strahler in the early years of the MODIS program, provides an important product to study the surface energy budget (Schaaf et al., this volume). Relying on multiple observations to characterize the BRDF, this latter product benefits from having two MODIS instruments in orbit. Similarly, the MODIS Land Surface Temperature and Emissivity Product intended for energy balance studies takes advantage of the two instruments (Wan and Li, this volume). The Vegetation Index product builds and expands on the AVHRR NDVI legacy (Huete et al., this volume). The LAI product is designed for the study of fluxes of energy, mass, and momentum between the land source and the atmosphere (Myneni et al., this volume). The MODIS-derived Primary Production products under the direction of Dr. Steve Running were developed for use in both scientific and applied global vegetation studies (Zhao et al., this volume). The MODIS Fire products, developed in partnership with Dr. Yoram Kaufman from the MODIS Atmospheres Team, are used widely by the fire science and management communities around the world (Justice et al., this volume). The MODIS Snow and Ice products were developed for a number of cryospheric and climate science purposes (Riggs and Hall, this volume). The MODIS Land Cover products build on the legacy of the AVHRR 1-km land cover product providing enhancements in a number of

areas associated with the algorithm, the implementation, and additional new information on vegetation dynamics (Friedl et al., this volume). The Vegetation Continuous Fields product pioneered by Drs. John Townshend and Matt Hansen, moves the community beyond land cover classification to direct parameterization of vegetation cover (Carroll et al., this volume). With the free and open access to MODIS data, a number of new and experimental products are being developed within the research community, and are in various stages of maturity. McCabe et al. (this volume) provide an example for evapotranspiration developed within the Science team. Since these chapters were submitted, the Collection 5 reprocessing for the MODIS land products was completed. Collection 6 reprocessing is currently in planning; this reprocessing will include additional improvements to some of the products and is scheduled for completion in early 2011. At that time, the MODIS Collection will consist of 11 years of Terra data and 8 years of Aqua data. This consistent global data record will help detect trends in land surface characteristics, and provide the basis for science quality climate data records. Several geophysical products being derived from MODIS are identified as Essential Climate Variables (ECV) that are required to support the UN Framework Convention on Climate Change.

The MODIS instruments were launched in December 1999 and May 2002, and were designed for a 5-year on-orbit life. Both instruments are continuing to operate, and have shown satisfactory operation and performance. Aqua MODIS has performed somewhat better than Terra MODIS. Calibration monitoring of both instruments continues while the anticipated large-optics degradation is being quantified. Both instruments are subject to a NASA Senior Review every 2 years to determine their continued service. The data record from MODIS extends the AVHRR record, which started in the early 1980s. Developing the long-term record requires an understanding of the relationship between the instruments and benefits from an overlapping operation. The VIIRS instrument on the NPOESS Preparatory Project (NPP), currently slated for launch in January 2011, will continue the legacy of the MODIS land remote sensing in the operational domain (Justice et al., this volume). Overlapping operation of NPP VIIRS with the Aqua MODIS will prove essential to help establish data continuity and the relationship between the land products from the two systems. We hope that the experience gained from MODIS in terms of the instrument characterization, data system, and land products can help the VIIRS mission continue a high quality, long-term data record of coarse resolution data and products for land science and applications.

Chapter 22

MODIS Land Data Products: Generation, Quality Assurance and Validation

Edward Masuoka, David Roy, Robert Wolfe, Jeffery Morisette, Scott Sinno, Michael Teague, Nazmi Saleous, Sadashiva Devadiga, Christopher O. Justice, and Jaime Nickeson

22.1 Introduction

The Moderate Resolution Imaging Spectroradiometer (MODIS) onboard NASA's Earth Observing System (EOS) Terra and Aqua satellites are key instruments that provide data on global land, atmosphere, and ocean dynamics (Salomonson et al. 1989). MODIS acquires data, which covers the entire earth surface on a near-daily basis in 36 spectral bands that span the visible (0.415 μm) to infrared (14.235 μm) spectra at 1-km, 500-m, and 250-m nadir pixel resolutions.

The MODIS land, atmosphere, and ocean products are central to NASA's mission to monitor and understand the Earth system. NASA has developed and generated a suite of MODIS products on a systematic basis. They start with the first Terra MODIS-acquired data on February 22, 2000, and continue with the first Aqua MODIS-acquired data on July 2, 2002.

This chapter describes the production and distribution of the MODIS land products, from initial software delivery by the MODIS Land Science Team, to operational product generation and quality assurance, delivery to EOS archival and distribution centers, and product accuracy assessment and validation. Progress and lessons learned since the first MODIS data were produced in early 2000 are also described.

The MODIS Land Science Team is funded by NASA to develop and maintain the science algorithms and processing software used to generate the MODIS products described in this book. The science team owns responsibility to coordinate, develop, and undertake protocols to evaluate product performance. These tasks are accomplished both on a systematic basis through quality assessment (QA) activities, and on a periodic basis through validation campaigns.

The science team was formed in 1989, 10 years before the launch of EOS/Terra. In this period, the team provided feedback on the design and prelaunch testing of the MODIS instruments and the development of the Earth Observing System Data

E. Masuoka (✉)
Terrestrial Information Systems Branch, NASA Goddard Space Flight Center,
Greenbelt, MD 20771, USA
e-mail: edward.j.masuoka@nasa.gov

and Information System (EOSDIS) elements and its infrastructure, the EOSDIS Core System (ECS) (Asrar and Ramapriyan 1995) which are still used to distribute the MODIS land products (Running et al. 1994). NASA continues to fund the science team to undertake product development but the emphasis has shifted to product maintenance and systematic QA.

22.2 Land Products

The MODIS land products are divided into three product suites: radiation budget products, ecosystem products, and land cover characterization products (Justice et al. 1998). The radiation budget products are used to develop a physical assessment of land surface processes through a better understanding of the surface/atmosphere energy exchange. They are important, for example, in studies of the hydrological cycle, biological productivity, and climate variability. The ecosystem products measure spatial and temporal dynamics of the Earth's terrestrial vegetation and provide inputs for global productivity and biogeochemical models. They are important, for example, in studies of ecosystem functioning and characterization of seasonal vegetation productivity. The land cover characteristics variables measure both anthropogenic and natural changes in the terrestrial landscape, and are used to help understand the causes and impacts of such changes.

All land products are produced on a global basis. They have different spatial and temporal resolutions, which are driven by the MODIS instrument design, and by data storage limitations. The MODIS land product format was developed to satisfy the diverse needs of the user community and the MODIS land product generation algorithms. This format enables data producers to efficiently process and reprocess MODIS land products, and also support flexibility in subsequent data applications.

The MODIS products are produced in a hierarchy of four processing levels: Level 1 (L1) instrument data at full resolution, Level 2 (L2) derived geophysical parameters at the same resolution and location as the L1 products, Level 2G (L2G) and Level 3 (L3) earth-gridded geophysical parameters, and Level 4 (L4) modeled outputs in an earth grid.

All MODIS products are stored in an enhanced Hierarchical Data Format, known as HDF-EOS, composed of multidimensional data arrays and descriptive metadata. Special HDF structures for the L2 and L3 products were mandated by NASA and supported by the National Center for Supercomputing Applications (NCSA) to ensure a compatibility level between products from different instruments on EOS satellites. The metadata conform to the ECS data model, and are used to search the EOS data archives.

The smallest unit of MODIS data processed at any one time at L1 and L2 is a granule. A granule corresponds to 5 min of MODIS swath data covering approximately 2,340 km \times 2,030 km in the across- and along-track directions, respectively. The 5-min granule size was chosen to limit the data volume per file to less than 1 GB, and to enable distributed processing across a large number of processors.

For the gridded products at Levels 2G, 3, and 4, the smallest unit of processing is a tile. Each tile corresponds to a 1,200 km × 1,200 km area defined in a global nonoverlapping grid in the Sinusoidal projection. The snow and sea ice products are defined in the Lambert Azimuthal Equal Area (LAEA) projection. The L2 products acquired day or night are binned into an intermediate tiled data format called L2G, which contains the original MODIS observations and their subpixel geolocation information (Wolfe et al. 1998). Subsequently, in producing the L3 and L4 products, multiple observations for each grid cell are combined using criteria specific to each product.

The MODIS land products are produced by the MODIS Adaptive Processing System (MODAPS) at NASA's Goddard Space Flight Center. The products are electronically transmitted via the Internet to EOS data centers, called Distributed Active Archive Centers (DAACs), where the products are archived and distributed to the user community. Cryospheric products are sent to the National Snow and Ice Data Center (NSIDC) DAAC at the University of Colorado at Boulder, and all other land products are sent to the Land Processes DAAC at the USGS Earth Resources Observation and Science (EROS) Center.

Table 22.1 lists the MODIS land products and provides details on the products and their levels, their archival locations, and spatial and temporal resolutions.

22.3 MODIS Data Production

In 1995, EOSDIS' initial design envisioned a geographically distributed production for MODIS land products among three DAACs. They include GSFC Earth Sciences (GES) DAAC in Greenbelt, Maryland for L1 and L2 products, the NSIDC DAAC in Boulder, Colorado for the snow and sea ice products, and the Land Processes (LP) DAAC at the USGS EROS Center in Sioux Falls, South Dakota for all the other land products (Justice et al. 2002b). EOSDIS development delays led to an alternate approach to science product generation in 1999. The responsibility for producing L2 and L3 science products was shifted from the DAACs to the MODIS science team.

The science team worked closely with the Science Data Support Team (SDST) to develop MODAPS. The science team's control of the processing system offered greater flexibility regarding what new features to incorporate in the system, and reduced the time to incorporate software changes into production from 1 to 2 weeks to 1 to 2 days. Science product archival and distribution to the public remains the responsibility of the three DAACs. However, in 2006, the responsibility to archive and distribute MODIS L1, Atmosphere and Oceans products was transferred from the GES DAAC to MODAPS and the Ocean Color Data Processing System to provide support for these products closer to their science communities. At present, MODAPS distributes land products to the MODIS Land Science Team members, primarily for QA and to a limited number of science and applications users, while the LP and NSIDC DAACs distribute land products to the general user community.

Table 22.1 MODIS land data products and characteristics

| Product | Name | DAAC | Level(s) | Resolution(s) | |
|--------------------------------------------------|------------------------------------|-------|----------|---------------------------|-------------------------------|
| | | | | Spatial | Temporal |
| <i>Radiation balance product suite</i> | | | | | |
| MOD09 | Surface reflectance | LP | L2G, L3 | 250 m, 500 m, 1 km, 0.05° | 1 day, 8 days |
| MOD11 | Surface temperature and emissivity | LP | L2, L3 | 1 km, 5 km, 0.05° | 5 min, 1 day, 8 days, monthly |
| MOD43 | BRDF/Albedo | LP | L3 | 500 m, 0.05° | 16 days |
| MOD10 | Snow cover | NSIDC | L2, L3 | 500 m | 5 min, 1 day, 8 days |
| MOD29 | Sea ice extent | NSIDC | L2, L3 | 500 m | 5 min, 1 day |
| <i>Ecosystem product suite</i> | | | | | |
| MOD13 | Vegetation indices | LP | L3 | 1 km, 500 m, 250 m | 16 days |
| MOD15 | LAI and FPAR | LP | L4 | 1 km | 8 days |
| MOD17 | PSN and GPP | LP | L4 | 1 km | 8 days, 1 year |
| <i>Land cover characterization product suite</i> | | | | | |
| MOD12 | Land cover and vegetation dynamics | LP | L3 | 500 m, 0.05° | 1 year |
| MOD14 | Thermal anomalies and fire | LP | L2, L3 | 1 km | 5 min, 1 day, 8 days |
| MOD44 | Vegetation Cover Change and VCF | LP | L3 | 500 m, 250 m | 96 days, 1 year |

LP land processes DAAC at the USGS EROS Center, NSIDC National Snow and Ice Data Center, BRDF Bidirectional Reflectance Distribution Function, LAI Leaf Area Index, FPAR Fractional Photosynthetically Active Radiation, PSN Net Photosynthesis, GPP Gross Primary Production, VCF Vegetation Continuous Fields

22.3.1 Data Flows

Figure 22.1 summarizes Terra MODIS land data flows from the spacecraft to the end users. The Aqua MODIS data flow is identical to the Terra MODIS flow illustrated in Fig. 22.1 except that the instrument data are sent to ground receiving stations in Alaska and Norway rather than White Sands, New Mexico. The EOS Data and Operations System separates the MODIS instrument data from other spacecraft data streams, orders the data into chronological sequence, and checks for missing or bad data packets, before aggregating the data into 2-h L0 files. Each 2-h file is equivalent to the MODIS-acquired data from approximately 1.2 Earth orbits. Under normal circumstances, most of the MODIS instrument data are delivered to the MODAPS within 8 h of acquisition, and the missing data may take several days to acquire.

Figure 22.2 illustrates the MODAPS processing sequence required to produce the MODIS land products. Ancillary data that include the National Centers for Environmental Prediction (NCEP) meteorological data and Global Modeling and Assimilation Office (GMAO) data are delivered to MODAPS from the GES DAAC soon after acquisition. These ancillary data characterize the atmosphere and are primarily used to generate the MODIS surface reflectance L2 product. Ancillary data delivery lags behind real time by approximately 24 h for NCEP predictions, and by up to 2 weeks for certain GMAO data. The MODIS spacecraft attitude data are measured in real time using onboard gyros and star trackers, and are available for immediate use in the data processing system. Spacecraft ephemeris data (orbit position and velocity) for Terra MODIS are generated from an onboard navigation system that provides accurate real-time measurements of the ephemeris, which are also available for immediate use. However, for Aqua MODIS, only predicted ephemeris with lower accuracy is available in real time. Users must wait up to 24 h to receive ground-based definitive ephemeris to achieve subpixel geolocation accuracies.

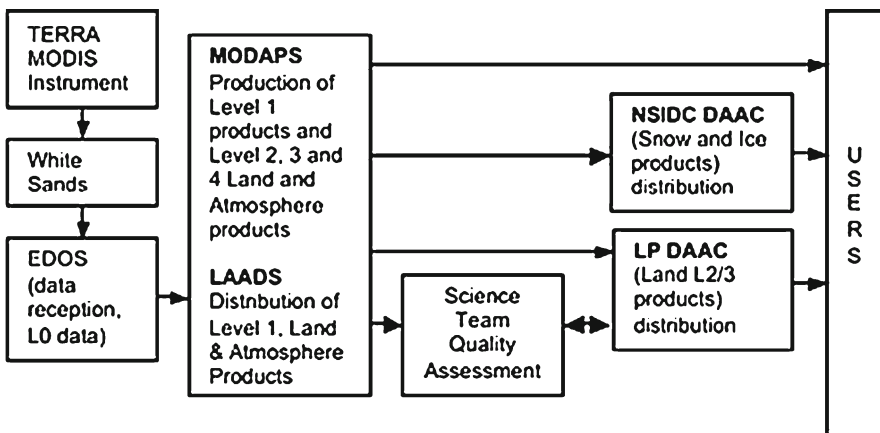


Fig. 22.1 MODIS Terra land product data flows, from spacecraft to end users

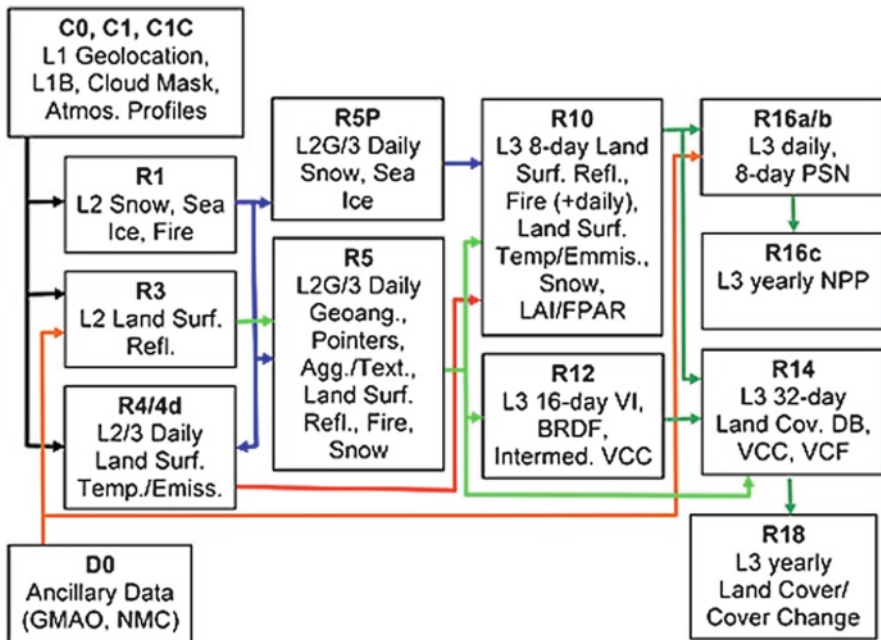


Fig. 22.2 MODIS land production sequence showing the data flow between algorithms running in MODAPS. A letter and a number denote process recipes

Once L0 files are delivered, MODAPS may process them for that current day. Groupable algorithms in a processing chain are collected into recipes denoted by a letter and a number. The MODAPS scheduler launches an instance of a recipe as a job that runs on an individual processor and waits until the recipe completes, and output products are written to disk before launching the next job on the processor. MODAPS can potentially run over 900 processing jobs concurrently.

The L1 products (Level 1B calibrated radiances, geolocation fields, cloud mask, and atmospheric profiles) are generated first and drive the higher-order production streams. Due to differences in input requirements, the L2 processing is split among three different recipes. The first recipe (R1) creates the snow, sea ice, and fire products. It runs independently on each 5-min MODIS granule. The second recipe (R3) is used to create the L2 surface reflectance product. It requires one full orbit’s worth of data as input and generates 19–20 output granules. This recipe runs up to 15 times per day and requires an entire orbit’s data at start time. The third recipe (R4/4d) is used to create the daily land surface temperature products. This recipe divides the globe into six latitudinal zones and runs one processing stream per zone.

The L2 data created by the R1 and R3 recipes are binned into the intermediate daily L2G data products. The L3 daily products use the L2G as their inputs by selecting the best observation or combination of observations in each bin, based on algorithms unique to each L3 product. These operations are performed in the R5 and R5P recipes for equatorial Sinusoidal (most land products) and polar LAEA

Table 22.2 Average daily volume of products produced and archived for each 1× of processing for products from collections 4 and 5

| | MODAPS Production (GB/day) | | Export Volume (GB/day) | | | | |
|---------|-------------------------------|-----|------------------------|-----------|---------------|---------------|------------|
| | | | LP DAAC | | NSIDC DAAC | | MODAPS |
| | C4 | C5 | C4 | C5 | C4 | C5 | |
| Level 1 | 324 | 227 | | | | | 227 |
| L2–L3 | 456 | 140 | 265 | 31 | 7 | < 1 | <i>140</i> |
| Daily | | | | | | | |
| Level 3 | 23 | 26 | 70 | 19 | 1 | < 1 | 19 |
| 8-day> | | | | | | | |
| Total | 803 | 393 | 335 | 50 | 8 | 1 | 524 |

Italicized produced on demand, **Bold** archived on disk or tape, C4 collection 4 products, C5 collection 5 products

projections (snow and sea ice), respectively. The L2G and L3 daily products are temporally composited to create the 8-day products for land surface reflectance, land surface temperature, snow, fire, and LAI/FPAR (recipe R10). The same temporal composites are used to produce the 16-day products for BRDF/Albedo, VI and intermediate land cover conversion products (recipe R12), and 32-day vegetation and intermediate land cover products (recipe R14). Finally, the 32-day products are used to create the Net Primary Production/Photosynthesis (NPP/PSN) and yearly land cover products (recipe R18).

The MODIS data for a current day are processed at the rate of 2 data days per day or 2× (one each Aqua MODIS and Terra MODIS data days). During this time, 34,000 files are staged as input to downstream algorithms or written as output to data archives at the DAACs or in MODAPS. MODAPS has additional capacity to reprocess L1 and land products at the rate of 14× as new science algorithms become available and improvements are deemed significant enough to warrant a full reprocessing of the data record. Table 22.2 summarizes the product volume shipped to the DAACs for each 1× of MODIS production. It illustrates the difference in volume of MODIS products in collection 4, which were not compressed before distribution, and the new MODIS collection 5 products, which use internal HDF compression to facilitate data transfer and to save storage on end-user systems.

22.3.2 The MODIS Adaptive Processing System

In 1999, MODAPS was developed to produce global science products from the twin MODIS instruments, each aboard the Terra and Aqua platforms. Figure 22.3 illustrates the hardware components of the MODAPS production system.

The current MODAPS operates three processing systems, which handle processing, reprocessing, and large-scale testing of science software changes. Each system is based on a Silicon Graphics, Inc. (SGI) Origin 300 or 3000 with 100 TB of disk and 60–100 Intel Xeon-based servers attached through a high-performance network

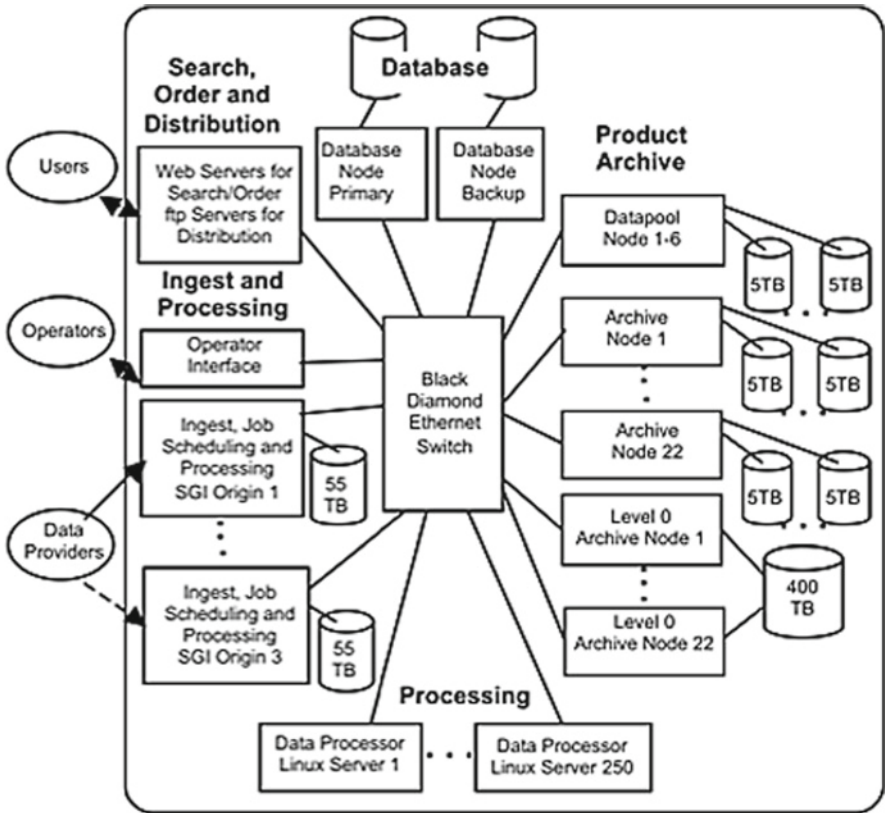


Fig. 22.3 Elements of the MODAPS system

switch. The Intel Xeon-based servers offer higher performance at a lower cost of ownership than SGI Origin servers though not all MODIS science software are ported to run on them. Each production recipe has a dedicated database server, which stores information about the processes running in the system, the location of all the files on the production disks, and relevant metadata associated with each science data product file. Each of the three production strings is capable of generating the equivalent of three to four days of MODIS land products in a single day.

The MODAPS uses File Transfer Protocol (FTP) to transmit land products to the DAACs using an automated process, developed in concert with the DAACs, to ensure that products are re-transmitted if errors occur. In addition, the MODIS land products are made available to the science team and a limited number of science and applications users via FTP servers with a dedicated Web interface that supports search and orders against product temporal and spatial attributes and metadata values. The L0 and calibrated L1 MODIS atmosphere products produced by MODAPS are also made available to the public via a similar dedicated interface. These MODAPS distribution systems are efficient because the distributed products are stored in an online RAID disk rather than on slower tape archives. They are also

robust, as the Web and FTP servers run on redundant Dell servers (currently four dual-processor servers) to ensure high response performance without downtime. Products are stored in the archive in online Serial Advanced Technology Attachment (SATA) disk units. Archive storage includes 400 TB for holding L0 products, and 300 TB to hold L2 and L3 atmosphere and land products. L1 products are excessively large to store for the life of the mission, and once produced, they are placed on a 100-TB disk-based data pool, from which files are deleted after 30 days, with the exception of certain frequently ordered geographical areas such as North America and Western Europe. If a L1 product is ordered following its deletion from the data pool, a processing job is automatically initiated to produce it. During the ordering process, users may also request custom processing of MODIS standard products from the archive to better suit their needs. Users may choose to subset and/or subsample their products, select parameters from a multiparameter product, or choose to change the output map projection. They may also elect a different product format (from HDF-EOS to GIS), create a mosaic of adjacent products, or mask product areas based on political or geographical boundaries.

22.3.3 Software Integration and Testing

The MODIS Land Science Team develops and maintains the science algorithms and processing software used to generate the MODIS products described in this book. Science team-developed software is delivered to the SDST at Goddard Space Flight Center. The SDST members own responsibility to transform the software into MODAPS production-ready executables and to test the production code in the MODAPS processing environment to ensure that it runs efficiently and correctly. The test process involves three test levels: unit tests, chain tests, and science tests.

The science team provides product algorithms, which the SDST staff test to ensure that the software produces the expected results. Following that confirmation, the production-ready software passes unit testing. In the subsequent chain test, the software replaces its predecessor in the production recipe, and runs to ensure output products are free of errors. Once the chain tests are completed, science tests are performed by the science team and the Land Data Operational Product Evaluation (LDOPE) team to ensure that the software updates have met their desired goals, and product quality is maintained or improved by the updates.

22.3.4 Algorithm Improvements

The MODIS processing priorities have evolved since the first terrestrial Earth data were acquired. MODIS's early period was devoted to fix problems in the low-level algorithms and ensure error-free production of higher-order products. The extensive product QA activities in the months that followed the "first light" MODIS data led to a large number of algorithm fixes and code changes.

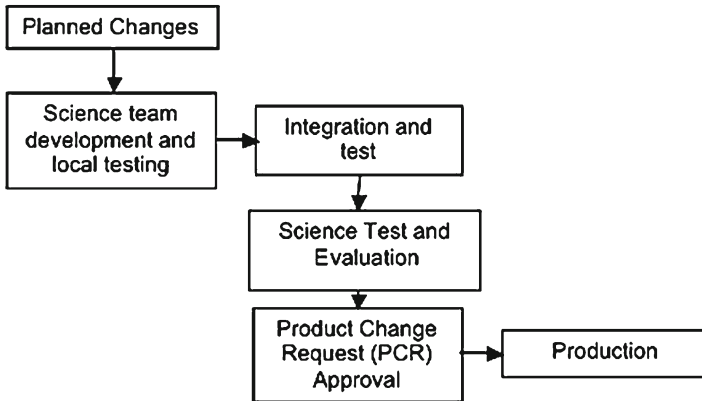


Fig. 22.4 The MODIS land science algorithm update and science test process flow

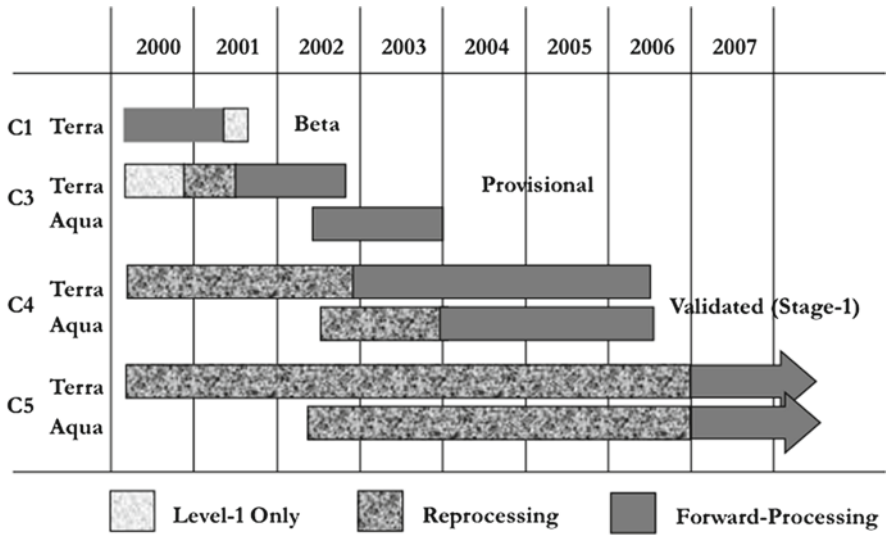
A streamlined approach to accommodate frequent updates and code changes into operational production was adopted to ensure a rapid transition to high quality products. As the algorithms matured, the processing priority shifted from rapid bug fixes and improvements to the creation of consistent datasets. As a result of this change, the approach to promote algorithm updates evolved to a more structured procedure. Figure 22.4 shows the sequence of events used in the current approach.

As the products matured, the extent of the science test process increased. These tests now are extensive, involving production of two 16-day periods globally and/or an entire year of MODIS products over 33 representative tiles. If no problems are identified in the science test, the science team members prepare Product Change Requests (PCRs), which document the rationale for the change and the science test results. Each PCR requires approval by the land science discipline leader and the MODIS science team leader before the software is promoted to operational status and used to generate science products.

22.4 MODIS Reprocessing: Collections

As commonly experienced with a number of satellite-derived datasets, the MODIS land products will undergo several reprocessing runs. A reprocessing task applies the latest version of the science algorithm as well as the calibration and geolocation information to the MODIS instrument data. A collection number is built into the filename for all products to differentiate between different reprocessing runs.

The Terra/MODIS land products derived from the “first light” data were designated beta products, and not deemed appropriate for scientific applications. These products



C*n* – Collection Version *n*

Fig. 22.5 Summary of the different MODIS data collections produced or planned, the range of data included in each collection and its production time

were archived in the appropriate DAACs as collection 1, and were publicly released to allow users to gain familiarity with the new data, their formats, and parameters (see Fig. 22.5). Within the year following the Terra/MODIS launch, most of the land products matured to “provisional” status. Their product quality was deemed sufficient for the general science community’s use, but such users were urged to contact the science team prior to their use in scientific publications. The quality of these products was not optimal, but their improvement over the beta products was substantial, and a reprocessing of the Terra/MODIS record began in July 2001. The provisional products were archived and distributed from the DAACs as collection 3. Further improvements in the algorithms and an ongoing validation effort led many MODIS land products to achieve validated stage 1 maturity in November 2002. These science products had uncertainties defined for a few sites and a limited range of conditions, but were otherwise ready to support scientific publications. The Aqua/MODIS and combined Terra and Aqua MODIS products were not released until they reached provisional status. A reprocessing campaign of both the Terra and Aqua MODIS data started in December 2002 and July 2003, respectively, which helped advance the entire MODIS collections to validated stage 1 level. These products are archived and distributed from the DAACs as collection 4. Extensive validation activities have brought most of the MODIS land products to validated stage 2, where the product accuracies were assessed over a distributed set of locations representative of the range of conditions encountered in the data. An improved dataset is being created as part of a collection 5 forward and reprocessing effort that started in July 2006 and plans to include new products such as burned area (Justice et al. – Chap. 29 in this volume).

22.5 Quality Assessment

Quality Assessment is a necessary part of any systematic production system and is integral to the MODIS land production process (Roy et al. 2002). The purpose of MODIS land QA is to provide the user community with an indication of product quality and to provide feedback to the science team developers. MODIS land QA is undertaken by the science team and by members of the LDOPE facility. The success of the QA process is attested by the incremental refinements to the science algorithms and production code over the four reprocessed MODIS land product collections (see Fig. 22.5).

22.5.1 Rationale for Quality Assessment

Practicality in a large data-intensive mission, such as MODIS, precludes us from distributing the data products until they are completely error-free.

There always remains the potential for introduction of errors during the life of the remote sensing observation system, which may remain unidentified for a considerable time period. Furthermore, certain errors are rectifiable by appropriate user action, which may only benignly impact certain applications. In addition, the user community plays an important role in assessing product quality. For example, the NASA TOMS satellite data failed to reveal the Antarctic ozone hole because abnormally low ozone values were flagged as bad data. The ozone hole was instead discovered by the British Antarctic Survey using Dobson ozone spectrophotometer data. Subsequent reanalysis of 12 years of TOMS data verified the existence of the ozone hole and indicated that it had grown rapidly for that period over most of Antarctica (Farman et al. 1985).

The MODAPS production emphasizes maximizing production efficiency while maintaining the integrity of the data production, transfer, archival, and retrieval processes. The introduction of errors within a product remains a possibility for a variety of reasons, which include the following: instrument errors; incomplete transmission of instrument and ephemeris data from the satellite to ground stations; incomplete instrument characterization and calibration knowledge; geolocation uncertainties; use of inaccurate ancillary datasets; software coding errors; software configuration failures (whereby interdependent products are made with mismatched data formats or scientific content); and algorithm sensitivity to these errors and unmodeled surface, atmospheric, and remote sensing variations.

Satellite-derived product distribution benefits enormously when accompanied by supporting product performance information. Such information is required by users to consider products in their appropriate scientific context, and algorithm developers require that information to identify products that perform poorly so that remedial improvements are implemented.

The MODIS Land Science Team has coordinated and developed protocols to evaluate the performance of their products through QA and validation activities. MODIS land validation is described in Sect. 22.6. Validation and QA results fulfill quite different roles (Roy et al. 2002). Users may consider product validation

results with respect to the general accuracy requirements of their application, but, unlike QA results, validation results do not describe artifacts and issues that may reduce the accuracy of individual pixels or files.

22.5.2 MODIS Land Quality Assessment Roles

The MODIS land QA process is complex, time consuming, and challenging to manage. The reason stems from the large number and volume of data products along with the complex product interdependencies (Fig. 22.2). A centralized QA facility, the LDOPE, was formed in 1998 prior to Terra MODIS launch to coordinate the MODIS land QA process. The LDOPE is supported by a small group of scientific staff; LDOPE is collocated with the MODAPS to enable efficient communication with the production managers and to ensure rapid data access. The LDOPE personnel undertake routine QA of all the MODIS land products, track the quality of input products that are not the responsibility of the land science team (e.g., the MODIS calibrated radiances and cloud mask products), check for the propagation of errors through interdependent products, develop and maintain QA tools, Web sites, and procedures, disseminate QA results and information within the science team, and ensure that the QA results are available to the public.

The science team product developers undertake detailed QA of their own products and collaborate with the LDOPE and other members of the science team responsible for input (upstream) and output (downstream) products. As needed, the science team developers update production codes and/or science algorithms to rectify issues that are discovered. Code updates frequently necessitate subsequent patches to fix bugs introduced by the update. A well-known software life cycle phenomenon, such bugs are complex to diagnose and rectify across the interdependent MODIS land products. For example, bugs and QA issues found in the cloud mask product (Platnick et al. 2003) are passed through the surface reflectance products (Vermote et al. 2002) which in turn propagate into the vegetation index (Huete et al. 2002), LAI/FPAR (Myneni et al. 2002), and BRDF/Albedo (Schaaf et al. 2002) products. The number of code updates was highest in the first 12 months following launch, when for example, the MODIS Terra land surface reflectance code was updated 14 times. The code updates are otherwise generally high in the first several months when the data collection reprocessing is initialized. These periods involve intensive science team and LDOPE QA activity. Outside of these periods, systematic QA is undertaken primarily by the LDOPE personnel.

22.5.3 Product Quality Documentation

The MODIS land product quality information is generated automatically by the algorithm and stored in the products as binary encoded pixel data, and as summary

numerical and textual file metadata. This documentation enables users to consult QA results before they order and/or use the products. In many cases, MODIS land products are meaningfully used only after consulting this information.

The MODIS land per-pixel QA results are generated by the production code for specific science datasets, and are typically stored as separate datasets in each product file. The per-pixel QA information varies among the MODIS land products. Products with meaningful error estimates assigned to them store per-pixel uncertainty estimates and/or ranges. Information on external factors known to affect product quality and consistency is also stored for each product. This information includes atmospheric conditions, surface type, viewing, and solar geometry, and whether dynamic ancillary data or backup estimates were used as input. Additionally, stored metadata fields may include the science code processing history (such as the logical criteria used by the algorithm), the results of different algorithm tests, and whether the input data were useful. To enable consistent interpretation across all the collection 5 MODIS land products, one generic QA bit is used to identify good MODIS land quality pixels (Table 22.3). In previous collections, two generic QA bits were used, with the additional bit describing whether a pixel was not produced due to clouds or other effects (Roy et al. 2002). This additional bit was dropped in collection 5, reflecting the evolution of certain products to attempt to retrieve pixel values regardless of the cloud conditions.

File level QA metadata are stored in the MODIS land products and include product-specific metadata in addition to generic metadata that describe temporal and geographic attributes, version information, input data filenames used to generate the product, and file-level summaries of per-pixel QA information. All MODIS land and NASA EOS products carry metadata summarizing the results of QA procedures performed by the production code following product generation. These metadata were mandated by the ECS (Lutz et al. 2000). Of these, the Science Quality Flag and Science Quality Flag Explanation metadata may receive updated values based on the outcome of QA performed at any time after product generation. The premise for these Science Quality metadata was that an ECS DAAC could update them at the request of the science team, and that users could consult them before they order products. A 3-month time lag may persist between data production and the DAAC's update of the Science QA metadata. Therefore, starting with collection 3, all MODIS land products are generated with a default Science QA flag

Table 22.3 Generic per-pixel QA stored in all collection 5 land products

| Per-Pixel QA code | Meaning |
|-------------------|--------------------------------------------------------------------------------------------------------------------------------------------|
| 0 | Pixel produced, good quality, not necessary to examine more detailed QA |
| 1 | Other quality (produced or not produced, if produced unreliable or unquantifiable quality, examination of more detailed QA is recommended) |

of “Not Investigated.” The Science QA Flag Explanation contains a link which directs the interested user to a public LDOPE Web site for recent quality updates. The LDOPE Web site documents product quality more comprehensively than is possible in the Science Quality metadata, although the LDOPE continues to update and make available the Science Quality Flag metadata on its Web sites. The Science Quality Flag may potentially acquire one of seven valid values (“Passed,” “Failed,” “Suspect,” “Inferred Passed,” “Inferred Failed,” “Being Investigated,” and “Not Investigated”). Users should reject products labeled as “Failed.” After the products are obtained, users should examine the per-pixel QA data to filter pixels deemed unsuitable for their applications.

22.5.4 LDOPE Web Site

The LDOPE Web site at http://landweb.nascom.nasa.gov/QA_WWW/ documents the quality of all the MODIS land products, with the exception of the MODIS sea ice products, and provides a number of Web-enabled services that facilitate product visualization and QA. The Web-enabled services evolved from the need to routinely sample the MODIS land product stream. Standard sampling approaches used in manufacturing were deemed inefficient given the high average daily MODIS land production volume and the nontrivial time required to assess the QA for a single product file. Instead, a number of sampling strategies and Web-enabled tools were developed, which enable representative product sample selections for a detailed and synoptic QA. An average of 150,000 users per month visited the Web site in 2005.

22.5.4.1 Known Issues

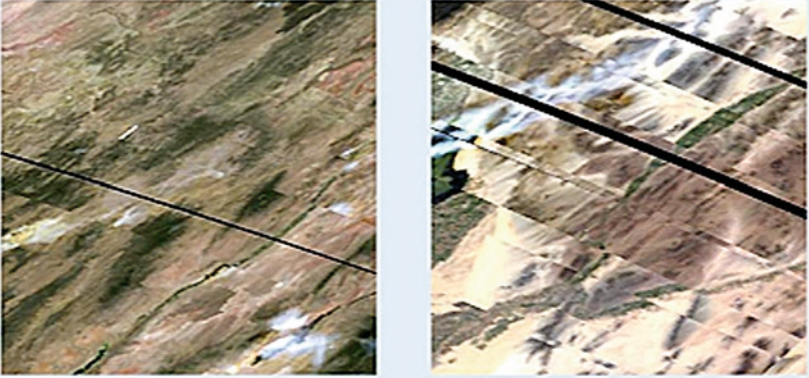
Issues that affect product quality are posted on a Known Issues Web site with example images, algorithm version, and incidence information. Issues are categorized as “pending,” “closed,” “reopened,” or “note,” and are updated as software updates to correct specific problems are promoted in the production system. This provides an effective way to document the propagation of issues through the dependent hierarchy of MODIS land products and to passively communicate product quality information within the science team and to the user community.

Figure 22.6 illustrates an issue posted to communicate the deleterious impact of a MODIS satellite maneuver on the gridded MODIS land products over a 40-day period. This issue arose because the MODIS L1B and geolocation products did not carry the satellite maneuver information and consequently were incorrectly retained in the production system. As described, the impacted MODIS land products were later reprocessed to correct this issue.

Color Key Case pending Case closed Case reopened QA note Small Image

Case #SD_MOD09_04105 Opening date: 05/04/04 Last update: 08/16/04
Status: Note

Several subsets of the data are shifted in the scan direction in some of MOD09 daily and 8-day products due to [geolocation problem](#) caused by an [orbit drag](#) [makeup maneuver](#) performed on data days 2002170 and 2002219. Following example shows RGB composite images of spatial subsets of bands 1, 3, and 4 of daily L2G surface reflectance product for data day 2002170 and 2002219.



MOD09HK_A2002170_10h-05_004_200323713808.hk
SDS RGB of layer 1 of 31, 33, and 34 (spatial subset)

MOD09HK_A200219_10h-05_004_200323211057.hk
SDS RGB of layer 1 of 31, 33, and 34 (spatial subset)

Note: Similar artifact is seen in the 8-day composite Surface Reflectance product made using the bad data. All daily and 8-day products that use the instrument data for day 2002170 and 2002219 will be reprocessed without the bad orbit.

Occurrence: Collection 4 on data day 2002170 and 2002219 (North central Canada, Western Canada, and mid-west of the US).
PGE: v4.0.8

Fig. 22.6 Example of a known issue posted on the LDOPE Web site (see text for details)

22.5.4.2 Global Browse

The MODAPS generates coarse spatial resolution versions of the MODIS land products by aggregation or subsampling to 5 km. These coarse versions are then projected into global images and posted, as they are generated, on a Global Browse Web site. Provided in JPEG format, they contain fixed contrast stretches and color lookup tables to enable consistent temporal comparison. Users may pan and zoom and interactively identify data granules, which enables a synoptic visual inspection and identification of problematic data files. Figure 22.7 illustrates a collection 4 land surface reflectance (Vermote et al. 2002) global browse image.

22.5.4.3 Metadata Database

Every MODAPS-generated MODIS land product's metadata is archived in a database. The database has a Web interface that allows the LDOPE personnel and science team to retrieve any product file metadata by querying against temporal, spatial, and metadata attributes of interest. In the early MODIS land collections, the potential of this system was reduced due to difficulties in maintaining consistent

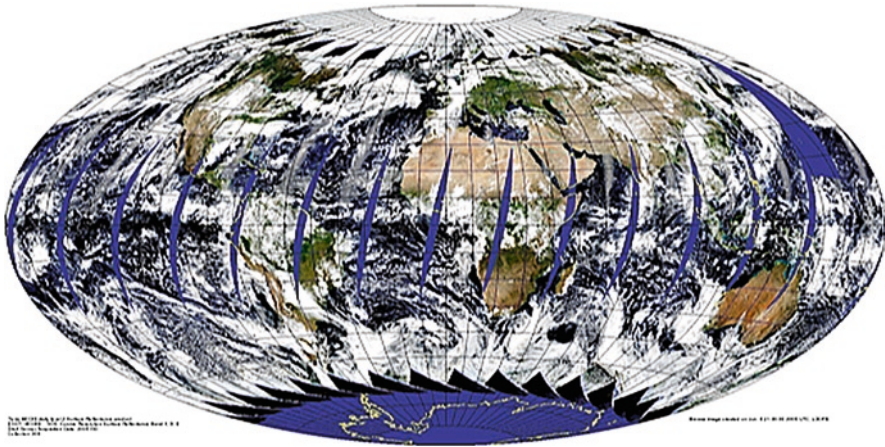


Fig. 22.7 Example of a MODIS surface reflectance global browse image posted on the LDOPE Web site. The MODIS 0.645, 0.555, and 0.469 μm bands are displayed as *red*, *green*, and *blue*, respectively, for MODIS Terra L2 land surface reflectance acquired on Julian day 2005–150

metadata definitions (format and meaning) while the product contents evolved. The database is most frequently used to track product interdependencies, both through the different product levels (2, 2G, 3, and 4) and between products. This enables us to identify all files affected by a known issue or their origin.

22.5.4.4 Time-Series Analysis

A time-series of summary statistics derived from all the gridded MODIS land products at fixed globally distributed locations is maintained and monitored by the LDOPE personnel. Product time-series analyses are important for two reasons: first, they capture algorithm sensitivity to surface (e.g., vegetation phenology), atmospheric (e.g., aerosol loading), and remote sensing (e.g., sun-surface-sensor geometry) conditions that change temporally, and second, they allow us to examine the changes in the MODIS characterization and calibration.

Time-series statistics are extracted at nine MODIS 1,200 km \times 1,200 km areas, which provide representative samples of the expected land product's variability. These datasets are called the land “golden” tiles. A Web interface is provided to enable visualization of time-series plots generated with respect to different land cover and biome types for each golden tile and provides access to browse images in JPEG format over each golden tile. Product files with large deviations from the surrounding time-series values are examined in more detail as they indicate a potential quality-related problem. Figure 22.8 shows time-series extracted from the land surface temperature product (Wan et al. 2002) for the first 5 years of Terra MODIS data. The plot immediately confirms two expected results: the seasonal variation in temperature and the substantial difference between the mean day and night temperatures.

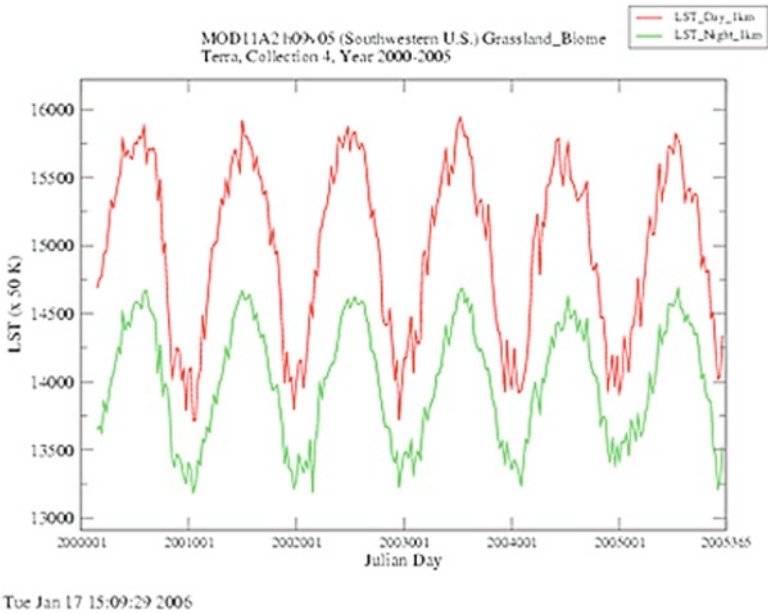


Fig. 22.8 Time-series plot posted on the LDOPE Web site. Time-series of mean 8-day 1-km day and night land surface temperature (LST) computed over approximately 120,000 grassland biome pixels in a southwestern U.S. tile are shown for 2000–2005

22.6 Validation Approach

Building on lessons learned from the previous generation of global land imaging systems (Justice and Townshend 1994; Cihlar et al. 1997), the MODIS land team has committed to quantify the accuracy of the MODIS land product suite (Morisette et al. 2002). Determining the accuracy of the output products is called validation. The validation activities have resulted in online accuracy statements for each of the land products. The MODIS land team maintains and updates the accuracy statements and posts related supporting material on the MODLAND validation page <http://landval.gsfc.nasa.gov> pull-down menu “Val Status.” An example from this site for the LAI/FPAR product is illustrated in Fig. 22.9.

While MODIS land products span a range of spatial scales, accurate validation data are typically derived from point measurements collected on the ground (Gower et al. 1999). Aggregating point data over larger areas (scaling up) is a critical component of validating relatively coarse-resolution global products (Cohen and Justice 1999). To account for differences in scale, the MODLAND validation team (Cohen et al. 2006; Yang et al. 2006; Morisette et al. 2002) and the international community (Yang et al. 2006; Morisette et al. 2006) have emphasized the coupling of field data with fine-resolution airborne or satellite images. Once relationships between field data and high-resolution images are established, it allows us to

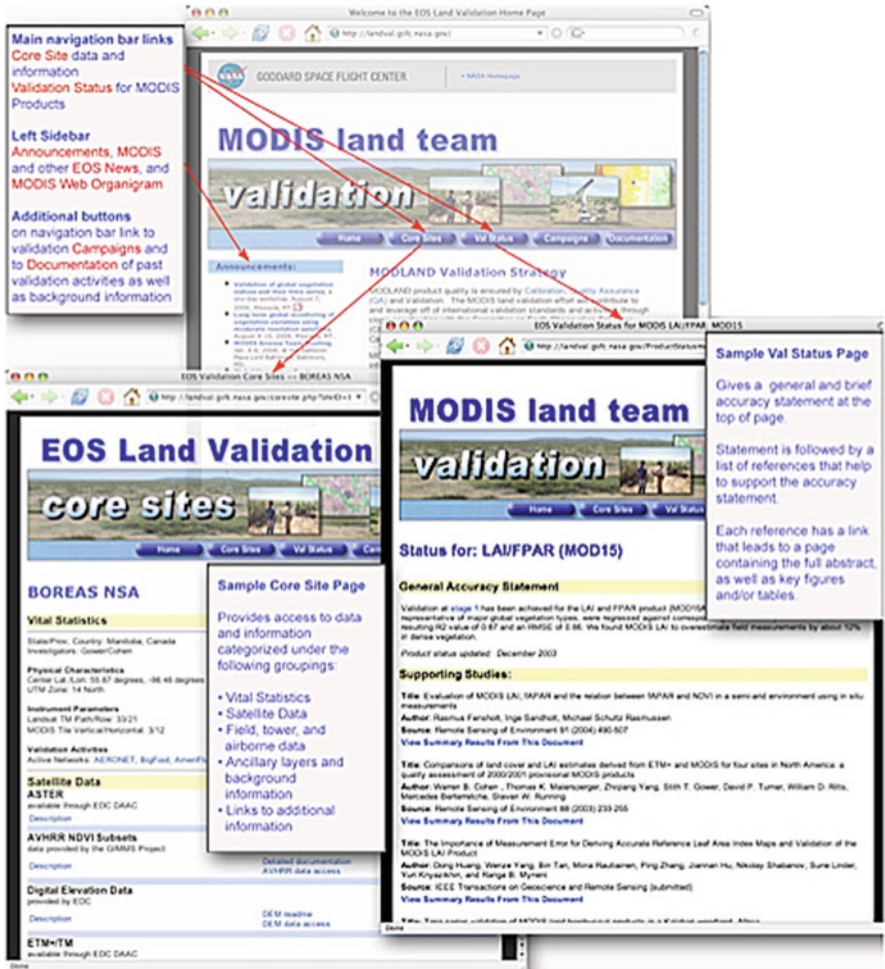


Fig. 22.9 MODIS land validation Web site with accuracy statement and supporting material for LAI/FPAR (MOD15) product

extrapolate the point measurements to the continuous area covered by the images. The images are then aggregated to allow for comparison with the coarse resolution MODIS data. The MODIS validation team has coordinated the acquisition of numerous medium- to fine-resolution datasets since 1999. This facilitates upscaling the ground measurements to digital datasets at resolutions suitable to validate MODIS products as illustrated in Fig. 22.10.

The scaling procedure is greatly enhanced with the ASTER and MODIS sensors' presence onboard the same Terra platform. This enables our validation activities to use ASTER's simultaneous, high spatial and radiometric data to aggregate field measurements to the MODIS scale.

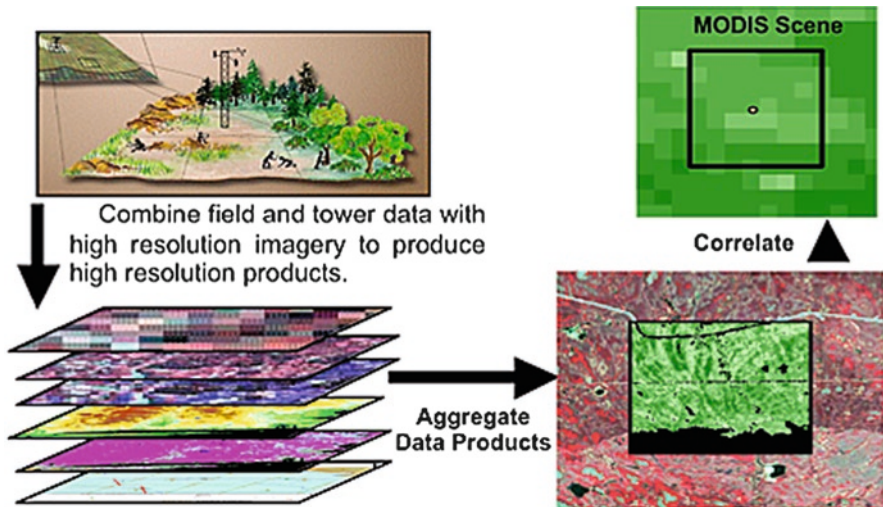


Fig. 22.10 Multitiered validation scheme involves scaling from field measurements and high spatial resolution Earth imaging sensors to the MODIS resolution

Clearly, temporal coincidence among all the comparison datasets (the field, high resolution, and MODIS) is an important goal. The temporal dynamics of the validation product determines how close they are. LAI, for example, will remain fairly stable over several days (Yang et al. 2006). Likewise, field-measured LAI from 1 day is comparable to images acquired within several days of the field data. In contrast, active fires are extremely dynamic. Field data and high-resolution images of fires acquired on different days are not conducive to validate a MODIS fire product. The ability to acquire coincident ASTER/MODIS data provides the primary validation source for the MODIS fire product (Csiszar et al. 2006; Morisette et al. 2005a, b). The Oak Ridge National Laboratory (ORNL) DAAC in Oak Ridge, Tennessee contains archives of combined ASTER and MODIS fire validation data for South Africa (Morisette et al. 2003) and Brazil (Morisette et al. 2004).

Combined field measurements and ASTER high-resolution image data are currently being explored for validating other MODIS products. MODIS subsets and multisensor validation data acquired over the EOS Land Validation Core Sites are available through NASA's EOS Land Validation Core Site infrastructure on the MODLAND validation Web page. These Core Site pages provide links to ground, airborne, and satellite datasets (Nickeson et al. 2007) coordinated for MODIS validation. The Core Sites were established to provide the general community with some of the best and simplest opportunities for multisensor data comparisons and synergistic science. The Core Site philosophy is to collect, archive, and distribute as much EOS and other Earth observing satellite data as possible. Readers interested in exploring product and sensor intercomparison are encouraged to utilize the data available through the EOS Land Validation Core Sites.

Some product intercomparison activities have begun through cooperation with the Committee on Earth Observation Satellites (CEOS) Land Product Validation (LPV) subgroup (<http://lpvs.gsfc.nasa.gov/>) [one of six subgroups of the CEOS Working Group on Calibration and Validation (WGCV)]. The LPV subgroup is leading international efforts on intercomparison of currently available global LAI and Albedo products. As part of these intercomparison efforts, an additional set of sites was established as CEOS LPV Core Sites, some of which overlap with the EOS Core Sites. The Web infrastructure, which currently supports the EOS Land Validation Core Sites, serves as a model for this international effort, and is used to support the coordination of intercomparison datasets.

22.7 Conclusion

This chapter describes how the MODIS land products, their algorithms, and all related processes have evolved since the start of the EOS Terra and Aqua missions. MODAPS has evolved to create a stable environment, which sustains both quality and stability to produce a consistent time-series of validated global products. The efforts of a committed science team are responsible for all the achievements in algorithm development and refinement, and product quality assurance and validation. The science team is complemented by a central support and data processing team, which coordinates all software deliveries, their integration and testing, and provides operational product QA. A close working relationship between these two groups accounts for the success of the MODIS land data production.

Lessons learned from this effort are now being applied to produce datasets from heritage instruments such as AVHRR and Landsat, and to future missions such as the National Polar-Orbiting Operational Environmental Satellite System (NPOESS) Preparatory Project (NPP). The lessons gained from the experiences of the MODIS science and data processing teams are invaluable in all future efforts to produce and assess long-term land data records to study changes in the Earth's climate and ecosystems.

Acknowledgments The authors wish to acknowledge the dedication of the staff of the MODIS SDST and the MODIS Land Science Team. This work was performed in the Terrestrial Information Systems Branch (Code 614.5) of the Hydrospheric and Biospheric Sciences Laboratory (Code 614) at NASA GSFC. The work was funded under NASA contracts NAS5-32350 and NAS5-02041.

References

- Asrar G, Ramapriyan HK (1995) Data and information system for mission to planet Earth. *Remote Sens Rev* 13:1–25
- Cihlar J, Chen J, Li Z (1997) On the validation of satellite-derived products for land applications. *Canadian J Remote Sens* 23(4):381–389

- Cohen WB, Justice CO (1999) Validating MODIS terrestrial ecology products: linking *in situ* and satellite measurements. *Remote Sens Environ* 70(1):1–3
- Cohen WB, Maersperger TK, Turner DP, Ritts WD, Pflugmacher D, Kennedy RE, Kirschbaum A, Running SW, Costa M, Gower ST (2006) MODIS land cover and LAI collection 4 product quality across nine sites in the Western Hemisphere. *IEEE Trans Geosci Remote Sens* 44(7):1843–1857
- Csiszar IA, Morisette JT, Giglio L, (2006). Validation of active fire detection from moderate resolution satellite sensors: the MODIS example in Northern Eurasia. *IEEE Trans Geosci Remote Sens* 44(7):1757–1764
- Farman JC, Gardiner BG, Shanklin JD (1985) Large losses of total ozone in Antarctica reveal seasonal Cl_x/NO_x interaction. *Nature* 315:207–210, May. doi:10.1038/315207a0
- Gower ST, Kucharik CJ, Norman JM (1999) Direct and indirect estimation of leaf area index, fapar, and net primary production of terrestrial ecosystems. *Remote Sens Environ* 70:29–51
- Huete A, Didan K, Miura T, Rodriguez EP, Gao X, Ferreira LG (2002) Overview of the radiometric and biophysical performance of the MODIS vegetation indices. *Remote Sens Environ* 83:195–213
- Justice CO, Townshend JRG (1994) Data sets for global remote sensing: lessons learnt. *Int J Remote Sens* 15(17):3621–3639
- Justice CO, Vermote E, Townshend JRG, Defries R, Roy DP, Hall DK, Salomonson VV, Privette JL, Riggs G, Strahler A, Lucht W, Myneni RB, Wolfe R, Knyazikhin Y, Running SW, Nemani RR, Wan Z, Huete AR, van Leeuwen W, Giglio RE, Muller J-P, Lewis P, Barnsley MJ (1998) The Moderate Resolution Imaging Spectroradiometer (MODIS): Land remote sensing for global change research. *IEEE Trans Geosci Remote Sens* 36(4):1228–1249
- Justice CO, Giglio L, Roy D, Boschetti L, Csiszar I, Davies D, Korontzi S, Schroeder W, O’Neal K MODIS-Derived Global Fire Products (Chapter 29 in this volume)
- Justice CO, Townshend JRG, Vermote EF, Masuoka E, Wolfe RE, Saleous N, Roy DP, Morisette JT (2002b) An overview of MODIS land data processing and product status. *Remote Sens Environ* 83:3–15
- Lutz R, Roy D, Leff C, Lewicki S, Geir E, Ziskin D, Kilpatrick K, Chu A, (2000) A review of EOS Terra quality assessment (QA). Proceedings of IEEE Geoscience and Remote Sensing Symposium (IGARSS), Honolulu, HI, 24–28 July (CD-ROM INT_27_06.pdf, 0-7803-6362-0/00 (c) 2000 IEEE)
- Morisette JT et al. (2006) Validation of global moderate resolution LAI products: a framework proposed within the CEOS Land Product Validation subgroup. *IEEE Trans Geosci Remote Sens* 44(7):1804–1817
- Morisette JT, Giglio L, Csiszar I, Justice CO (2005a) Validation of the MODIS active fire product over Southern Africa with ASTER data. *Int J Remote Sens* 26(19):4239–4264
- Morisette JT, Giglio L, Csiszar I, Setzer A, Schroeder W, Morton D, Justice CO (2005b) Validation of MODIS active fire detection products derived from two algorithms. *Earth Interaction* 9:paper 9.
- Morisette JT, Giglio L, Csiszar I, Setzer A, Schroeder W, Morton D, Justice CO (2004) LBA Eco LC23 ASTER – MODIS Fire Data Comparison – Brazil 2003 & 2004. Data set. Available online <http://www.daac.ornl.gov> Oak Ridge, Tennessee
- Morisette JT, Giglio L, Csiszar I, Justice CO (2003) SAFARI 2000 ASTER and MODIS Fire Data Comparison. Dry Season 2001. (Data set) Available online (<http://www.daac.ornl.gov>) from Oak Ridge National Laboratory Distributed Active Archive Center. Oak Ridge, Tennessee
- Morisette JT, Privette JL, Justice CO (2002) A framework for the validation of MODIS Land products. *Remote Sens Environ* 83:77–96
- Myneni RB, Hoffman S, Knyazikhin Y, Privette JL, Glassy J, Tian Y, Wang Y, Song X, Zhang Y, Smith GR, Lotsch A, Friedl M, Morisette JT, Votava P, Nemani RR, Running SW (2002) Global products of vegetation leaf area and fraction absorbed PAR from year one of MODIS data. *Remote Sens Environ* 83:214–231
- Nickeson JE, Morisette JT, Privette JL, Justice CO, Wickland D, 2007. Coordinating EOS land validation: core site status in 2006. *EOS, Transactions American Geophysical Union* 88(7). doi:10.1029/2007EO070002

- Platnick S, King MD, Ackerman SA, Menzel WP, Baum BA, Riédi JC, Frey RA (2003) The MODIS cloud products: algorithms and examples from Terra. *IEEE Trans Geosci Remote Sens* 41:459–473
- Roy DP, Borak JS, Devadiga S, Wolfe RE, Descloitres J (2002) The MODIS land product quality assessment approach. *Remote Sens Environ* 83:62–76
- Running SW, Justice CO, Salomonson VV, Hall D, Barker J, Kaufman YJ, Strahler AR, Muller J-P, Vanderbilt V, Wan ZM, Teillet P, Carneggie D (1994) Terrestrial remote sensing science and algorithms planned for the MODIS-EOS. *Int J Remote Sens* 15(17):3587–3620
- Salomonson VV, Barnes WL, Maymon PW, Montgomery HE, Ostrow H (1989) MODIS: advanced facility instrument for studies of the Earth as a system. *IEEE Trans Geosci Remote Sens* 27:145–153
- Schaaf CB, Gao F, Strahler AH, Lucht W, Li X, Tsang T, Strugnell NC, Zhang X, Jin Y, Muller J-P, Lewis P, Barnsley M, Hobson P, Disney M, Roberts G, Dunderdale M, Doll C, d'Entremont R, Hu B, Liang S, Privette JL (2002) First operational BRDF, Albedo and Nadir reflectance products from MODIS. *Remote Sens Environ* 83:135–148
- Vermote EF, El Saleous NZ, Justice CO (2002) Atmospheric correction of MODIS data in the visible to middle infrared: first results. *Remote Sens Environ* 83:97–111
- Wan Z, Zhang Y, Zhang Q, Li Z (2002) Validation of the land-surface temperature products retrieved from Terra Moderate Resolution Image Spectroradiometer data. *Remote Sens Environ* 83:163–180
- Wolfe RE, Roy DP, Vermote E (1998) MODIS land data storage, gridding and compositing methodology: Level 2 Grid. *IEEE Trans Geosci Remote Sens* 36:1324–1338
- Yang W, Tan B, Huang D, Rautiainen M, Shabanov NV, Wang Y, Privette JL, Huemmrich KF, Fensholt R, Sandholt I, Weiss M, Ahl DE, Gower ST, Nemani RR, Knyazikhin Y, Myneni RB (2006) MODIS leaf area index products: from validation to algorithm improvement. *IEEE Trans Geosci Remote Sens* 44(7):1885–1898

Chapter 23

MODIS Directional Surface Reflectance Product: Method, Error Estimates and Validation

Eric Vermote and Svetlana Kotchenova

23.1 Introduction

The surface bidirectional reflectance factor (BRF) is the ratio between reflected radiance measured in specific observation geometry (zenith and azimuth) within an infinitely small solid angle and irradiance incident on the surface from a direct source of illumination (zenith and azimuth). The BRF is determined from satellite observations through an atmospheric correction (AC) process. When properly retrieved, the surface BRF is fully decoupled from an atmospheric signal, and thus represents the value as measured by an ideal sensor held at the same view geometry and located just above the Earth's surface assuming an absence of atmosphere.

MODIS Surface Reflectance (MOD09) is a seven-band surface BRF product computed from the MODIS level-1B land bands 1–7 (centered at 648, 858, 470, 555, 1, 240, 1, 640, and 2130 nm, respectively). Surface reflectance is the most basic remotely sensed surface parameter within the MODIS solar reflective bands. It provides the primary input for essentially all higher-level surface geophysical parameters, including Vegetation Indices, Bidirectional Reflectance Distribution Function (BRDF)/Albedo, Leaf Area Index (LAI)/Fraction of Photosynthetically Active Radiation (FPAR), Burned Areas, Land Cover, Thermal Anomalies, and Snow Cover. Besides, the surface reflectance product is also used in various image-based applications to detect and monitor changes on the Earth's surface (e.g., anthropogenic impacts, red-green-blue images).

MOD09's accuracy requirements are typically determined by the higher-level products (e.g., Albedo: 0.02–0.05, NDVI: 0.03, etc.). The MOD09 accuracy is primarily limited by the accuracy of the following: (1) sensor calibration, (2) atmospheric parameter inputs (e.g., aerosol optical depth), (3) a radiative transfer (RT) code used in the forward simulation, and (4) operational implementation of the inverse problem or correction.

E. Vermote (✉)

Department of Geography, University of Maryland, College Park, MD, 20742, USA
e-mail: eric@ltdri.org

This chapter provides a brief overview of the methods and the RT code underlying the MODIS AC algorithm (Sect. 23.2–23.5). It further explores the product’s potential accuracy with the help of a theoretical error budget (Sect. 23.6), and provides a short description of the Collection 5 MOD09 product (Sect. 23.7). It finally describes the MOD09 product validation with 1 year of Terra data for 4,988 cases over 127 AERONET sites (Sect. 23.8).

23.2 Theoretical Basis

The atmospheric “perturbation” of a surface reflectance signal depends on the type and characteristics of atmospheric particles interacting with incident solar radiation and on the surface BRDF via multiple scattering interactions with the surface. Different gas molecules (N_2 , O_2 , O_3 , H_2O , CO_2 , etc.) scatter radiation according to Rayleigh’s law (i.e., molecular scattering) and absorb them within specific spectral bands whose bandwidths vary among species, and depend on the vertical atmospheric pressure and temperature profiles. Atmospheric aerosols presented by suspended particles with the size ranging from $\sim 10^{-3}$ to $\sim 20 \mu m$ scatter and absorb radiation in accordance with the Mie and Geometric Optics theories. The former is used for aerosols with diameters on the order of the radiation wavelength, while the latter is applicable to larger particles, presumed as individual spheres with certain real and imaginary refractive indices.

Atmospheric correction removes or reduces the effects of such atmospheric perturbations. In practice, AC is typically achieved by inverting a highly parameterized model of atmospheric RT coupled to a surface reflectance model. When angular effects are not significant, the underlying surface is often assumed Lambertian (reflecting radiation uniformly in all directions).

Thus, in the idealized case of a Lambertian surface and within narrow spectral bands outside the main absorption features of water vapor, the top-of-atmosphere (TOA) reflectance is simulated as (Vermote et al. 1997):

$$\begin{aligned} \rho_{TOA}(\theta_s, \theta_v, \varphi, P, \overbrace{\tau_A, \omega_0, P_A}^{Aer}, U_{H_2O}, U_{O_3}) \\ = Tg_{OG}(m, P) Tg_{O_3}(m, U_{O_3}) \\ \left[\rho_{atm}(\theta_s, \theta_v, \varphi, P, Aer, U_{H_2O}) + \right. \\ \left. Tr_{atm}(\theta_s, \theta_v, P, Aer) \frac{\rho_s}{1 - S_{atm}(P, Aer)\rho_s} Tg_{H_2O}(m, U_{H_2O}) \right], \end{aligned} \quad (23.1)$$

where, ρ_{TOA} is the reflectance at the top of the atmosphere, ρ_{atm} is the atmosphere-intrinsic reflectance, Tr_{atm} is the total atmosphere transmission (downward and upward), S_{atm} is the atmosphere spherical albedo, and ρ_s is the surface reflectance awaiting retrieval by the AC procedure; the geometrical conditions are described

by the solar zenith angle θ_s , the view zenith angle θ_v , and the relative azimuth ϕ (or the difference between the solar and view azimuth angles); P is the pressure that influences the number of molecules and the concentration of absorbing gases in the atmosphere, Tg designates the gaseous transmission by water vapor (Tg_{H_2O}), ozone (Tg_{O_3}), or other gases (Tg_{OG}), U_{H_2O} is the integrated water vapor content, U_{O_3} is the integrated ozone content, and m is the so-called air-mass computed as $1/\cos(\theta_s)+1/\cos(\theta_v)$.

τ_A , ω_0 , and P_A describe the aerosol properties and are spectrally dependent: τ_a is the aerosol optical thickness (AOT), ω_0 is the aerosol single-scattering albedo, and P_A is the aerosol phase function.

The effect of water vapor on the atmosphere-intrinsic reflectance is approximated as:

$$\rho_{\text{atm}}(\theta_s, \theta_v, \phi, P, Aer, U_{H_2O}) = \rho_R(\theta_s, \theta_v, \phi, P) + (\rho_{R+Aer}(\theta_s, \theta_v, \phi, P, Aer) - \rho_R(\theta_s, \theta_v, \phi, P))Tg_{H_2O}\left(m, \frac{U_{H_2O}}{2}\right), \quad (23.2)$$

where ρ_R represents the atmospheric reflectance due to molecular (Rayleigh) scattering and ρ_{R+Aer} represents the reflectance of the mixture of molecules and aerosol particles. Accounting correctly for the mixing and the so-called coupling effect (Deschamps et al. 1983) is important to achieve highly accurate atmospheric effect modeling. This approximation conserves the correct computation of the coupling and assumes that water vapor is mixed with aerosol particles, and that molecular scattering is not affected by water vapor absorption.

The main challenges to the operational implementation of surface-atmosphere interaction modeling lie in the assignment of input atmospheric parameters and a priori knowledge of surface BRDF (which are strictly necessary for a full inversion). As atmospheric RT modeling is relatively mature, different methods are usable to model such interactions [e.g., successive orders of scattering (SOS), doubling adding, Monte Carlo simulations]. Approaches to operational retrievals of atmospheric parameters have advanced considerably in the last 10 years, as remote sensing instruments capable of retrieving atmospheric properties (aerosol, ozone, water vapor, etc.) are operationally available. In the absence of such operational retrievals, atmospheric climatology or forecasted values are potentially applied, although the product accuracy might degrade considerably. The determination of surface BRDF at the operational level is currently practical only for satellite sensors with a single-pass multi-angular capability, such as MISR or POLDER. MAIAC (Multi-Angle Implementation of AC for MODIS) is a new algorithm, which represents an attempt to retrieve surface BRDF from a sequence of 16 clear-days measurements (Lyapustin and Wang 2007). However, the influence of BRDF effects is probably of second order, and they are not expected to have much impact on an inter-annual variability analysis (Vermote and Vermeulen 1999).

23.3 MODIS AC Input Parameters

As outlined in Sect. 23.2, the key parameters required for AC of level-1B MODIS data include (listed by the order of effect on standard products) (Vermote and Saleous 2006) the following:

- Aerosol optical thickness, size distribution, refractive indices and vertical distribution.
 - AOT requires a spatial resolution of 1 km with values nearly coincident in time with corresponding MODIS observations (± 15 min). For other parameters, a much coarser spatial resolution is acceptable, along with a static model with little loss of accuracy (Remer et al. 2005).
- Atmospheric pressure
 - Obtained from a combination of a coarse-resolution (1° , 6-h time step) Weather Prediction Model (available from NCEP GDAS (NCEP GDAS 2008)) and a Digital Elevation Model at 1-km resolution (USGS 2008).
- Ozone amount
 - Usually determined from a UV ozone sounder (such as NASA's Total Ozone Mapping Spectrometer (TOMS 2008)) at coarse spatial (1°) and temporal (1 day) resolutions.
- Column-integrated water vapor content
 - Derived from the MODIS near-infrared band 18 (931–941 nm) and 19 (915–965 nm) at 1-km spatial resolution (Gao and Kaufman 2003). In the absence of MODIS data, NCEP GDAS meteorological data are a potential substitute.

After retrieval, these atmospheric parameters are input in the RT model, which is used to calculate look-up tables (LUTs) for the MODIS AC algorithm.

23.4 Radiative Transfer Modeling

The MODIS AC algorithm LUTs are calculated with the help of the 6SV (Second Simulation of a Satellite Signal in the Solar Spectrum Vector) code. 6SV is an advanced RT code designed to simulate the reflection of solar radiation by a coupled atmosphere-surface system. This code was developed on the basis of its scalar predecessor 6S, which underlies the MODIS AC algorithm in the past (Vermote et al. 1997). A β -version of 6SV (named 6SV1.0B) was publicly released in May 2005 and has quickly won the recognition of the scientific community. By May 2007, scientists from over 480 different institutions all over the world have started using it for different applications.

The 6SV code covers a wide range of spectral conditions from 350 to 3,750 nm. The input geometric and spectral options include not only a user-defined sun-sensor configuration, but also those specific to 19 major satellites, including ASTER, AVHRR, ETM, MODIS, POLDER, SeaWiFS, VIIRS, VGT, etc. Molecular atmosphere modeling incorporates eight different options, including two user-defined models. Twelve different models can simulate an aerosol atmosphere including a special option to incorporate AERONET measurements. Ground surface modeling includes simulations of homogeneous and nonhomogeneous surfaces with/without a directional effect. A choice exists between ten different BRDF models and one user-defined model. The code operates on the basis of the SOS method, and accounts for the polarization of radiation in the atmosphere through the calculation of the Q and U components of the Stokes vector (Vermote et al. 2006).

The β -version of 6SV was extensively validated since its release by comparison with other commonly used RT codes and valuable benchmarks such as Monte Carlo simulations and Coulson's tabulated values (Coulson et al. 1960). The code's overall theoretical accuracy is within 1%, which conforms to the standard RT code accuracy requirement (Muldashev et al. 1999). The complete validation effort is summarized in two manuscripts (Kotchenova et al. 2006; Kotchenova and Vermote 2007), available on the official 6SV Web site (<http://6s.ltdri.org/>). This site also contains the latest version of the code, information on recent updates, the code manual, and a link to a special Web interface that can help an inexperienced user build necessary input files. In June 2007, the β -version of 6SV was officially transformed into version 1.1 (6SV1.1).

The 6SV validation exercise has also demonstrated the importance of using vector code for AC. In the majority of modeled cases, ignoring the effects of polarization led to the presence of a large relative error (up to 7.2% for a mixed molecular-aerosol atmosphere) in simulated TOA reflectances. The 6SV code was applied to model satellite measurements over AERONET sites with detailed descriptions of atmospheric properties (Holben et al. 1998) for two purposes. The first was to check the importance of accounting for radiation polarization in real conditions. The second was to retrieve very accurate reflectance standards, which include water-leaving reflectances measured by the Marine Optical Buoy System (Kotchenova et al. 2006), and artificial surface tarps (portable brightness targets) measured by high-spatial resolution sensors such as QuickBird and IKONOS (Fig. 23.1).

23.5 Aerosol Inversion

The aerosol inversion stems from a long heritage of algorithms applied to AVHRR, Landsat, and MODIS data, pioneered by Kaufman et al. (1997). These algorithms used the shortest wavelength to estimate aerosol properties when the atmosphere dominated a TOP signal. Most of them were based on the so-called dark and dense vegetation technique, introduced by Holben et al. (1998), which used a fixed linear relationship between reflectances in the red and near-infrared bands, and thus was limited to the scope of dark targets.

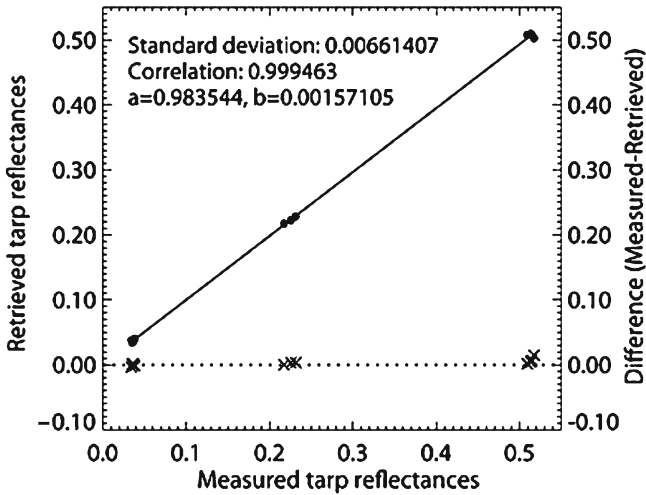


Fig. 23.1 The IKONOS reflectances corrected using AERONET and 6SV (including correction for adjacency effect) versus the reference tarp reflectances. The data were acquired on February 15, 2002 over the Stennis Space Flight Center. *Dark circles* designate reflectance values; *cross symbols* designate the difference between the measured and retrieved reflectance values

Since the beginning of operational application of MODIS data in 2000, the aerosol inversion algorithm was continuously refined, and its current version includes the following:

- All available MODIS bands [land + ocean, e.g., 412 nm as in the deep blue method (Hsu et al. 2004)]
- Improved LUTs
- Improved aerosol models based on the AERONET climatology
- A more robust “dark target inversion scheme” (for vegetated and nonvegetated surfaces), which predicts blue band reflectances based on an empirical relationship with red band reflectances [in tune with the recent finding of the atmosphere group (Levy et al. 2007)]
- Inversion of the aerosol model

The performance of the refined aerosol inversion algorithm is illustrated using example images shown in Figs. 23.2–23.5. Figure 23.2 shows MODIS TOA reflectance and surface reflectance RGB (670, 550, 470 nm) images over the Alta Floresta AERONET site. The MODIS data were acquired on July 16, 2003. The tables above the images show AOT and water vapor parameters provided by AERONET and retrieved from the MODIS data with the help of the refined aerosol inversion algorithm. The retrieved AOT (0.226) is close to the value provided by AERONET (0.299). The retrieved parameters were the same ones used to atmospherically correct the TOA image. Visually, it is clear that even at this average AOT, the atmospheric impact is quite substantial.

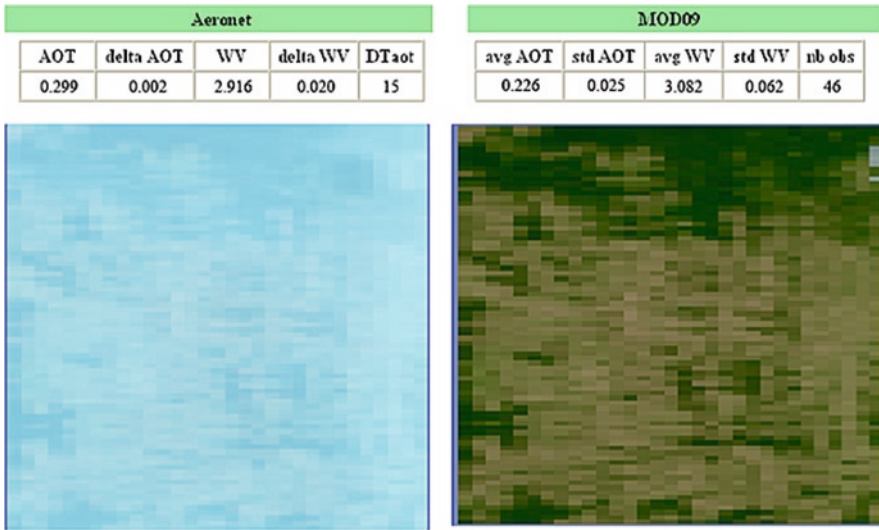


Fig. 23.2 MODIS TOA reflectance (*left*) and surface reflectance (*right*) RGB images over the Alta Floresta AERONET site (2003197 14:30). The tables above the images show AOT and water vapor content with the measured variability (delta AOT, delta WV) and standard deviation (std AOT, std WV). DTaot designates the difference in time between two AERONET observations and nb obs means the number of “good” MODIS observations

Figure 23.3 illustratively explains the principle of the algorithm. MODIS TOA reflectance measured in red (670 nm) is used to estimate TOA reflectances at four blue wavelengths (490, 470, 443, and 412 nm) by assuming a linear correlation between the red and blue wavelengths. The MODIS red band image (Alta Floresta, July 16, 2003) presented in Fig. 23.3 shows a lot of surface information. The cascade of images at the blue wavelengths, presented on the right, shows that the atmospheric influence increases as the wavelength value decreases. We can determine both AOT and the aerosol model with the blue wavelengths. The retrieved AOT (color image) reveals no correlation between the surface signature and AOT values except for some small correlation in the top left corner. Moreover, the AOT displays a lot of small-scale variability, which is important to capture in the AC.

The results of the aerosol model inversion are illustrated in Figs. 23.4 and 23.5. These figures show MODIS TOA reflectance and surface reflectance RGB images over the Alta Floresta (September 10, 2003) and Mongu (September 11, 2003) sites. In both cases, AOT is large and the number of “good” MODIS observations is equal to 0. (The term “good” is explained in Sect. 23.8). Here, we use these images to demonstrate the results of aerosol model inversion.

The AOT value retrieved at 470 nm is input into the aerosol inversion algorithm to simulate TOA reflectances at the other blue wavelengths for four different aerosol atmosphere scenarios: smoke low absorption, smoke high absorption, urban polluted, and urban clean. A residual is then calculated for each aerosol scenario as the average

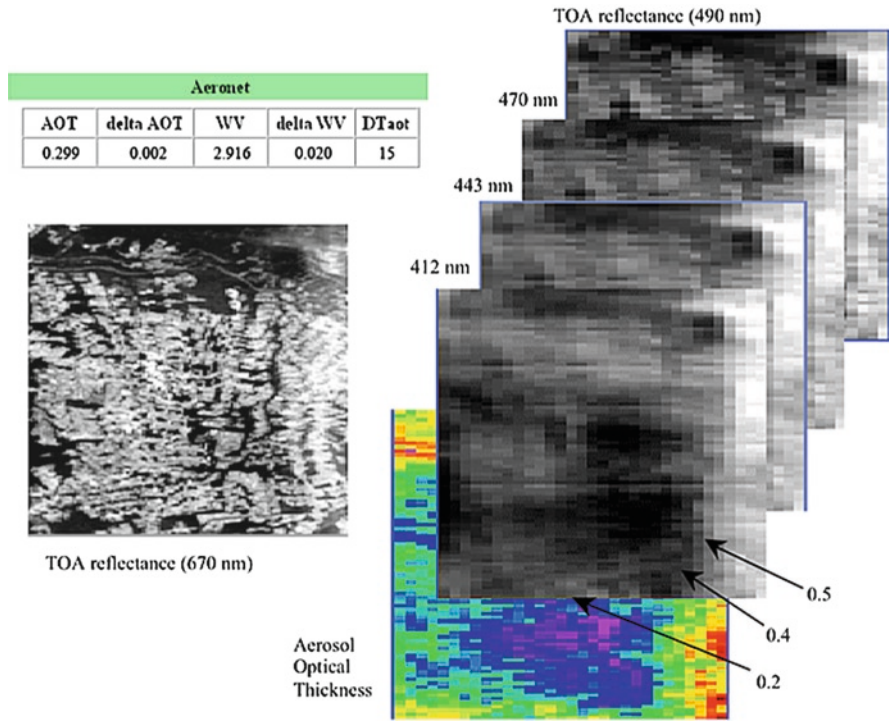


Fig. 23.3 A MODIS TOA reflectance image measured by the *red band* (centered around 670 nm) and estimated surface reflectances at four *blue wavelengths* (490, 470, 443, and 412 nm) over the Alta Floresta site (2003197 14:30) along with the corresponding AERONET data and retrieved AOT. The table parameters are explained in the captions for Fig. 23.2

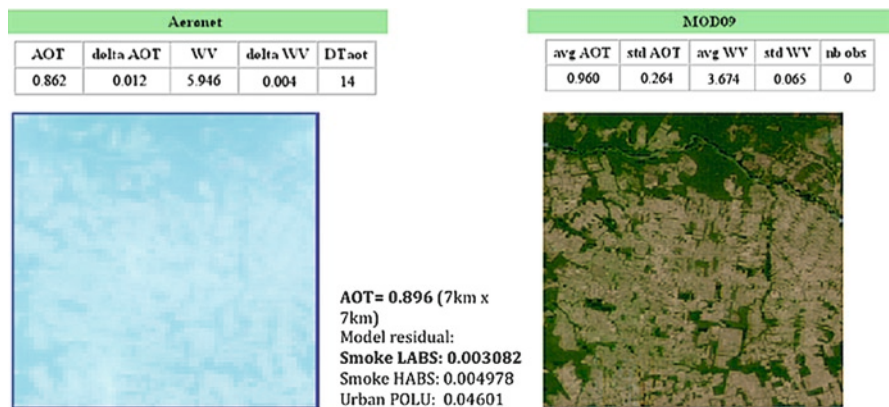


Fig. 23.4 MODIS TOA reflectance (*left*) and surface reflectance (*right*) RGB images over the Alta Floresta AERONET site (2003256 14:10) along with the results of aerosol model inversion. The parameters in the tables above the images are explained in the captions for Fig. 23.2

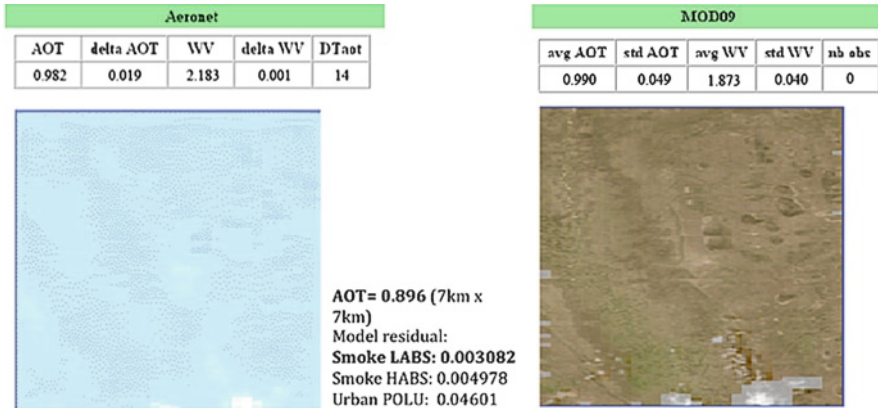


Fig. 23.5 MODIS TOA reflectance (*left*) and surface reflectance (*right*) RGB images over the Mongu AERONET site (2003257 8:20) along with the results of aerosol model inversion. The parameters in the tables above the images are explained in the captions for Fig. 23.2

quadratic difference between the actual estimated and simulated TOA reflectances. The aerosol model is chosen based on the smallest residual value. In Fig. 23.4, the smallest residual corresponds to smoke low absorption, which is quite reasonable, as the site is located in a biomass burning area – one would expect to find low absorption there. In Fig. 23.5, the residual speaks in favor of smoke high absorption, which is reasonable to suggest for this savanna burning area.

23.6 Error Budget

The best way to estimate the sensitivity of surface reflectance to uncertainties in key input atmospheric parameters is to calculate a theoretical error budget, which would provide a realistic estimate of the impact of each uncertainty.

Vermote and Saleous (2006) have made an attempt to calculate such a budget. They simulated TOA reflectances using the 6SV code for a number of atmospheric and geometrical scenarios, and estimated the influence of uncertainties in each input parameter on the final product. In total, they considered uncertainties in the instrument calibration ($\pm 2\%$), atmospheric pressure (± 10 mb), water vapor content (± 0.2 g/cm²), ozone content (± 0.02 cm atm), retrieved AOT values (resulting from the aerosol inversion), and selection of the aerosol model (three additional models, including urban polluted, smoke low absorption, and smoke high absorption, were considered versus the urban clean case). Ten different geometric combinations and three values of AOT (0.05, clear, 0.3, average, 0.5, hazy) were used in the analysis.

Here, we present the summarized results of their work. Table 23.1 shows the overall theoretical accuracy of the AC method considering the influence of all error sources at once. The overall accuracy of surface reflectance varies depending on the

Table 23.1 Overall theoretical accuracy of retrieved surface reflectances and vegetation indices considering the error source on calibration, ancillary data, and aerosol inversion for three values of aerosol optical thickness (0.05, clear; 0.3, average; 0.5, hazy)

| Reflectance/VI | Savanna | | | | | | | | | Semi-arid | | | | | | | | | |
|----------------|---------|-----------------------|-----------------------|---------|-----------------------|-----------------------|-----------|-----------------------|-----------------------|-----------|-----------------------|-----------------------|---------|-----------------------|-----------------------|-----------|-----------------------|-----------------------|--------|
| | Forest | | | Savanna | | | Semi-arid | | | Forest | | | Savanna | | | Semi-arid | | | |
| | Value | Aerosol Optical Depth | Aerosol Optical Depth | Value | Aerosol Optical Depth | Aerosol Optical Depth | Value | Aerosol Optical Depth | Aerosol Optical Depth | Value | Aerosol Optical Depth | Aerosol Optical Depth | Value | Aerosol Optical Depth | Aerosol Optical Depth | Value | Aerosol Optical Depth | Aerosol Optical Depth | |
| p3 (470 nm) | 0.012 | 0.0052 | 0.0051 | 0.0052 | 0.0052 | 0.0052 | 0.04 | 0.0052 | 0.0052 | 0.0052 | 0.0052 | 0.0052 | 0.07 | 0.0051 | 0.0053 | 0.0053 | 0.0055 | 0.0055 | 0.0055 |
| p4 (550 nm) | 0.0375 | 0.0049 | 0.0055 | 0.0064 | 0.0052 | 0.0058 | 0.0636 | 0.0052 | 0.0052 | 0.0058 | 0.0064 | 0.1246 | 0.0051 | 0.0051 | 0.007 | 0.007 | 0.0085 | 0.0085 | 0.0085 |
| p1 (645 nm) | 0.024 | 0.0052 | 0.0059 | 0.0065 | 0.0053 | 0.0062 | 0.08 | 0.0053 | 0.0062 | 0.0067 | 0.14 | 0.0057 | 0.0057 | 0.0074 | 0.0074 | 0.0074 | 0.0085 | 0.0085 | 0.0085 |
| p2 (870 nm) | 0.2931 | 0.004 | 0.0152 | 0.0246 | 0.0035 | 0.0103 | 0.2226 | 0.0035 | 0.0103 | 0.0164 | 0.2324 | 0.0041 | 0.0041 | 0.0095 | 0.0095 | 0.0146 | 0.0146 | 0.0146 | 0.0146 |
| p5 (1240 nm) | 0.3083 | 0.0038 | 0.011 | 0.0179 | 0.0038 | 0.0097 | 0.288 | 0.0038 | 0.0097 | 0.0158 | 0.2929 | 0.0045 | 0.0045 | 0.0093 | 0.0093 | 0.0148 | 0.0148 | 0.0148 | 0.0148 |
| p6 (1650 nm) | 0.1591 | 0.0029 | 0.0052 | 0.0084 | 0.0035 | 0.0066 | 0.2483 | 0.0035 | 0.0066 | 0.0104 | 0.3085 | 0.0055 | 0.0055 | 0.0081 | 0.0081 | 0.0125 | 0.0125 | 0.0125 | 0.0125 |
| p7 (2130 nm) | 0.048 | 0.0041 | 0.0028 | 0.0042 | 0.004 | 0.0036 | 0.16 | 0.004 | 0.0036 | 0.0053 | 0.28 | 0.0056 | 0.0056 | 0.006 | 0.006 | 0.0087 | 0.0087 | 0.0087 | 0.0087 |
| NDVI | 0.849 | 0.03 | 0.034 | 0.04 | 0.022 | 0.028 | 0.471 | 0.022 | 0.028 | 0.033 | 0.248 | 0.011 | 0.011 | 0.015 | 0.015 | 0.019 | 0.019 | 0.019 | 0.019 |
| EVI | 0.399 | 0.005 | 0.006 | 0.007 | 0.003 | 0.005 | 0.203 | 0.003 | 0.005 | 0.005 | 0.119 | 0.002 | 0.002 | 0.004 | 0.004 | 0.004 | 0.004 | 0.004 | 0.004 |

The selected sites are Savanna (Skukuza), Forest (Belterra), and Arid (Sevilleta). The uncertainties are considered independent and summed in quadratic

band and AOT. Under clear atmospheric conditions, it does not exceed 0.006 in reflectance units.

Note that this budget does not account for the impact of correlations between the input parameters. The overall accuracy was estimated by computing the quadratic average of each individual uncertainty.

23.7 Collection-5 MOD09

The Collection-5 MOD09 is produced on the basis of LUTs calculated with the help of the 6SV code. Its content has also been changed in accordance with the user's demand. First, the Daily Surface Reflectance Quality product at 1-km resolution was incorporated into the Daily Surface Reflectance product at 500-m resolution. Second, a new product called Global Daily Surface Reflectance at 0.05° resolution was created (Table 23.2). This new product is applied on a Climate Modeling Grid for use in climate simulation models.

A number of significant improvements have also been introduced in the AC algorithm, which include the modification of LUT format for a more accurate interpolation of atmospheric parameters, and the use of dynamic aerosol models and ocean bands for improved aerosol retrieval over land. A detailed description of these changes is available from the MODIS Land Quality Assessment Web site (MODIS Land Quality Assessment 2008).

In addition, the MODIS AC group has developed its own software called Imager for an easy and sufficient visualization of MOD09 (Imager 2008). This software reads data in the HDF format and displays them either as grayscale or RGB images, together with individual pixel values across all datasets. Imager is also configurable to read GeoTIFF files. The software and its manual are publicly available on the MODIS AC group Web site (<http://modis-sr.ltdri.org/>).

23.8 Performance of the MODIS C5 Algorithms

As part of the Terra MODIS Collection 5 science test activities, the performance of the Collection 5 algorithms was evaluated through the analysis of 1 year of Terra data (2003) collected over 150 AERONET sites (4,498 cases in total). A specific evaluation

Table 23.2 MOD09 Collection 5 product site

| Product name | Terra | Aqua |
|--------------------------------------------------------------|----------|----------|
| Surface Reflectance Daily L2G Global 250 m | MOD09GQ | MYD09GQ |
| Surface Reflectance Daily L2G Global 500 m and 1 km | MOD09GA | MYD09GA |
| Surface Reflectance 8-Day L3 Global 250 m | MOD09Q1 | MYD09Q1 |
| Surface Reflectance 8-Day L3 Global 500 m | MOD09A1 | MYD09A1 |
| Surface Reflectance Daily L3 Global 0.05Deg CMG ^a | MOD09CMG | MYD09CMG |

^aCMG climate modeling grid

approach was developed, which helped analyze a 1-year long time-series in a timely manner to provide the user with a quantitative measure of the surface reflectance code improvement. This approach involves processing subsets of level 1B data over the AERONET sites using an algorithm equivalent to the standard AC algorithm, and compares the obtained results to a reference dataset. The reference dataset was created using the 6SV RT code and AERONET measurements (AOT, distribution of particles, refractive indices, and water vapor content); the underground surface was assumed Lambertian. The accuracy of the reference dataset mainly depended on the accuracy of AERONET measurements, since the accuracy of the code itself was proven as within 1% (Kotchenova et al. 2006; Kotchenova and Vermote 2007). For each case in the study, the difference between the reflectance values obtained by the standard algorithm and the reference dataset was computed. If the difference was less than the theoretical uncertainty of $0.005 + 0.05\rho$, where ρ is the surface reflectance (Vermote and Saleous 2006), the observation was considered “good.” To ensure the use of AERONET measurements that were representative of MODIS acquisition conditions, we did not consider cases where AERONET measurements did not occur within 30 min of the corresponding MODIS acquisition or where the aerosol model inversion was not performed within 1 day of the acquisition.

To facilitate the interpretation of the results, the percentage of “good” observations for each AERONET site was displayed on global maps similar to the one shown in Fig. 23.6. These maps are available on a specially designed Web site (<http://modis-sr.ltdri.org/>). The size and color of the circles centered on AERONET sites indicate the total number of available observations (divided by the cosine of a view zenith angle) and the quality of retrieved surface reflectances, respectively.

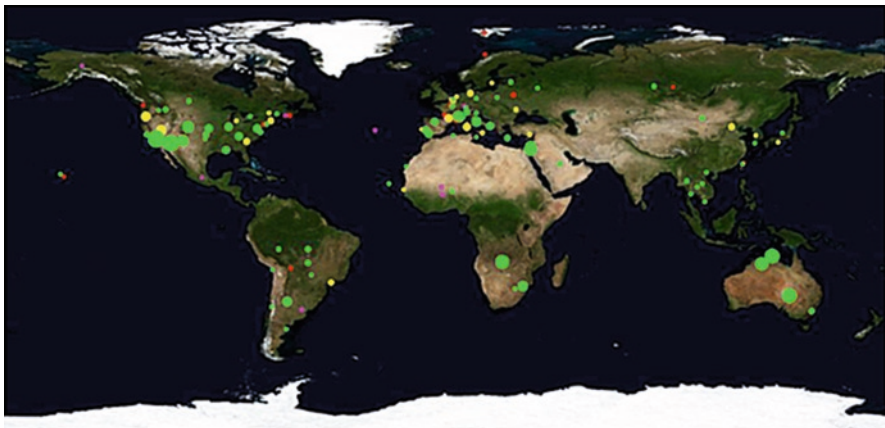


Fig. 23.6 Comparison between the MODIS band 1 surface reflectances and the reference dataset for all available 2003 AERONET data. The *circles* are centered on the AERONET sites. The *circle color* indicates the percentage of comparisons that falls within the theoretical MODIS one-sigma error bar (*green* > 80%, 65% < *yellow* < 80%; 55% < *magenta* < 65%, *red* < 55%). The circle radii are proportional to the number of observations used in the comparison

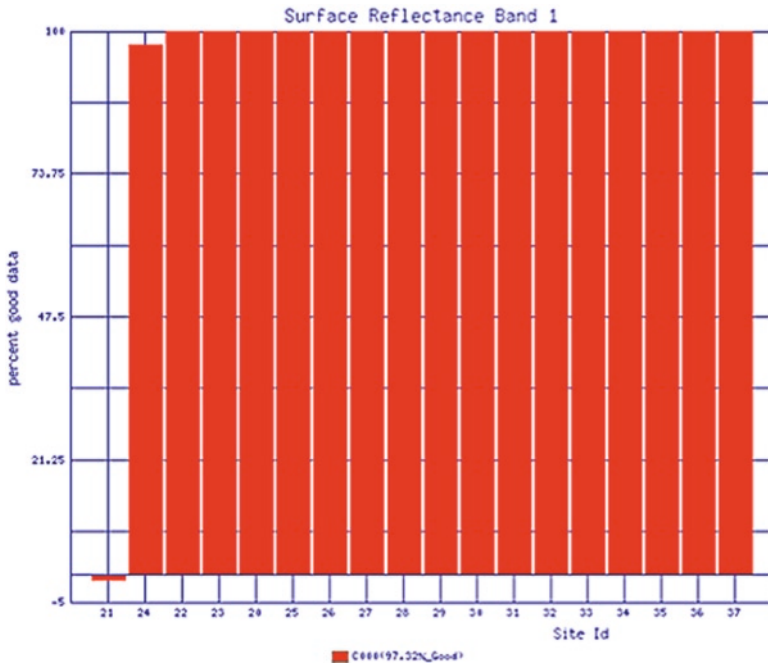


Fig. 23.7 Summary of the results for the Alta Floresta site. Each bar corresponds to a date and time when coincident MODIS and AERONET data are available. The height of a bar indicates the percentage of “good” observations for a given date and time

Clicking the location of a particular site provides more detailed results for this site (Fig. 23.7). The site results are presented as bar graphs, which display the results for all dates analyzed for a site by order of increasing quality. Since the height of each bar designates the percentage of “good” observations for a specific date and time, the graph itself displays the percentage of “good” surface reflectances for all combined time periods.

Clicking a bar in the graph displays a plot of the retrieved surface reflectances versus the reference dataset (Fig. 23.8) along with the linear fit results. In addition to such plots, the Web site shows tables summarizing corresponding AERONET measurements and geometric conditions, and displays browse images of the site before and after AC.

The results shown in Figs. 23.6–23.8 are available for all MODIS surface reflectance product (bands 1–7) of 2003. Globally, the percentage of “good” observations for bands 1–7 are 86.62, 94.13, 51.30, 75.18, 96.36, 97.69, and 98.64%, respectively.

Estimating the impact of the uncertainties in surface reflectance directly on the downstream product is useful because errors are not spectrally independent; for example, the error on NDVI is always lower than the largest possible error related to the uncertainties of individual bands (red and near-infrared). To achieve this goal,

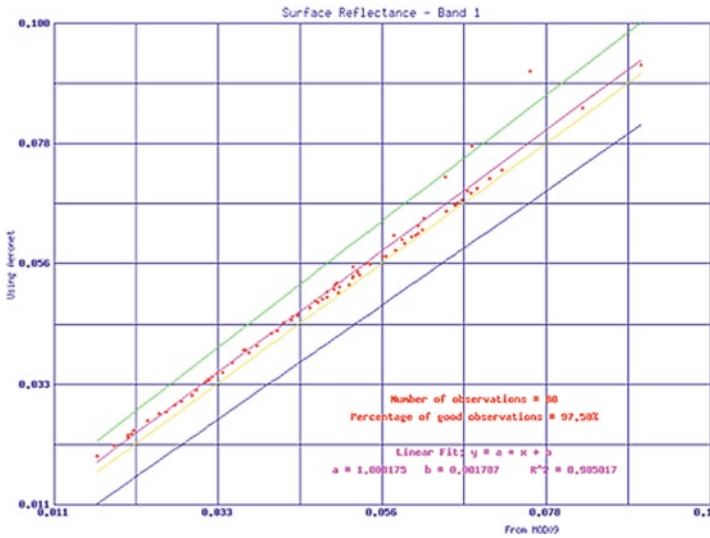


Fig. 23.8 A scatter plot of the surface reflectances retrieved over the Alta Floresta site (2003197 14:30) versus the reference dataset along with the linear fit results. This plot appears on the screen by clicking on the bar corresponding to site id 24 in the Alta Floresta graph bar (Fig. 23.7). The blue and green lines indicate the theoretical uncertainty limits, the yellow line is a one-to-one line, and the magenta line is a linear fit

an analysis similar to that illustrated in Figs. 23.6–23.8 was performed for NDVI and EVI. Globally, 97.11% of retrieved NDVI values and 93.64% of retrieved EVI values fell within the theoretical MODIS one-sigma error bar [$\pm(0.02 + 2\%)$].

23.9 Future Plans

The MOD09 product’s validation of the AC confirms its good quality. Similar validation is required to cover more conditions. In particular, the theoretical error budget requires a re-analysis with better-defined aerosol climatology. As the AC algorithm matures, the error budget needs updating to include nonuniform and non-Lambertian surface cases. Both the remote sensing and climate modeling communities will significantly benefit from the ability to accurately estimate product uncertainties, which will produce more accurate and sophisticated climate models.

References

Coulson KL, Dave JV, Sekera Z (1960) *Tables related to radiation emerging from a planetary atmosphere with Rayleigh scattering*. University of California Press, Berkeley.
 Deschamps PY, Herman M, Tanré D (1983) Modeling of the atmospheric effects and its applications to the remote sensing of ocean color. *Appl Opt* 22(23):3751–3758.

- Gao BC, Kaufman YJ (2003) Water vapor retrievals using Moderate Resolution Imaging Spectroradiometer (MODIS) near-infrared channels. *J Geophys Res* 108(D13):4389, doi:10.1029/2002JD003023.
- Holben BN, Eck TF, Slutsker I, Tanré D, Buis JP, Setzerm A, Vermote EF, Reagan JA, Kaufman Y, Nakajima T, Lavenu F, Jankowiak I, Smirnov A (1998) AERONET – a federated instrument network and data archive for aerosol characterization. *Remote Sens Environ* 66:1–16.
- Hsu NC, Tsay SC, King MD, Herman JR (2004) Aerosol properties over bright reflecting source regions. *IEEE Trans Geosci Remote Sens* 42(3):557–569.
- Imager (2008) <http://modis-sr.ltdri.org> (click on ‘Software’). Accessed 31 Jan 2008.
- Kaufman YJ, Tanré D, Remer L, Vermote EF, Chu A, Holben BN (1997) Operational remote sensing of tropospheric aerosol over land from EOS Moderate Resolution Imaging Spectroradiometer. *J Geophys Res* 102(14):17051–17068.
- Kotchenova SY, Vermote EF (2007) Validation of a vector version of the 6S radiative transfer code for atmospheric correction of satellite data. Part II: Homogeneous Lambertian and anisotropic surfaces. *Appl Opt* 46(20):4455–4464.
- Kotchenova SY, Vermote EF, Matarrese R, Klemm F Jr. (2006) Validation of a vector version of the 6S radiative transfer code for atmospheric correction of satellite data. Part I: Path Radiance. *Appl Opt* 45(26):6726–6774.
- Levy RC, Remer LA, Mattoo S, Vermote EF, Kaufman Y (2007) Second-generation operational algorithm: Retrieval of aerosol properties over land from inversion of MODIS spectral reflectance. *J Geophys Res* 112:D13211, doi:10.1029/2006JD007811.
- Lyapustin A, Wang Y (2007) MAIAC: Multi-Angle implementation of atmospheric correction for MODIS. Algorithm Theoretical Basis Document, 69 <http://neptune.gsfc.nasa.gov/bsb/subpages/index.php?section=Projects&content=MAIAC%20ATDB> Accessed 31 Jan 2008.
- MODIS Land Quality Assessment (2008) Web site http://landweb.nascom.nasa.gov/cgi-bin/QA_WWW/newPage.cgi Accessed 31 Jan 2008.
- Muldashev TZ, Lyapustin AI, Sultangazin UM (1999) Spherical harmonics method in the problem of radiative transfer in the atmosphere-surface system. *J Quant Spectrosc Radiat Transf* 61(3):393–404.
- NASA’s Total Ozone Mapping Spectrometer (TOMS) (2008) Web site <http://toms.gsfc.nasa.gov> Accessed 31 Jan 2008.
- National Center for Environmental Prediction Global Data Assimilation System (NCEP GDAS) (2008) <http://wwwt.emc.ncep.noaa.gov/gmb/gdas/> Accessed 31 Jan 2008.
- Remer LA, Kaufman YJ, Tanré D, Mattoo S, Chu DA, Martins JV, Li R-R, Ichoku C, Levy RC, Kleidman RG, Eck TF, Vermote EF, Holben BN (2005) The MODIS aerosol algorithm, products and validation. *J Atmos Sc* 62(4):947–973.
- Terra MODIS Collection 5 Surface Reflectance Evaluation (2003 time-series science test analysis) http://mod09val.ltdri.org/cgi-bin/mod09_c005_public_allsites_onecollection.cgi Accessed 31 Jan 2008.
- U.S. Geological Survey (2008) <http://edcdaac.usgs.gov/topo30/topo30.asp> Accessed 31 Jan 2008.
- Vermote EF, Saleous NZ (2006) Operational atmospheric correction of MODIS visible to middle infrared land surface data in the case of an infinite Lambertian target. In: Qu JJ, Gao W, Kafatos M, Murphy RE, Salomonson VV (eds) *Earth science satellite remote sensing, science and instruments*, Tsinghua University Press/Springer, Beijing/Berlin 1, ch. 8, pp. 123–153.
- Vermote EF, Vermeulen A (1999) MODIS atmospheric correction over land: surface reflectance. Algorithm Theoretical Background Document, Version 4.0. <http://modis-sr.ltdri.org> (click “Products and User’s Guide”). Accessed 31 Jan 2008.
- Vermote EF, Tanré D, Deuzé JL, Herman M, Morcrette JJ (1997) Second simulation of the satellite signal in the solar spectrum, 6S: an overview. *IEEE Trans Geosci Remote Sens* 35(3):675–686.
- Vermote EF, Tanré D, Deuzé JL, Herman M, Morcrette JJ, Kotchenova SY, Miura T (2006) *Second simulation of the satellite signal in the solar spectrum (6S), 6S User Guide Version 3*, <http://6s.ltdri.org> Accessed 31 Jan 2008.

Chapter 24

Aqua and Terra MODIS Albedo and Reflectance Anisotropy Products

Crystal Barker Schaaf, Jichung Liu, Feng Gao, and Alan H. Strahler

Abstract MODIS albedo and reflectance anisotropy products of the global land surface are routinely available since early 2000. These multiyear satellite-derived measures of surface reflectance anisotropy and albedo are increasingly being used by the modeling community to both evaluate and refine a number of climatological and biogeochemical models. By combining observations from both the Terra and Aqua platforms and easing both the spatial and temporal resolution in the Collection 5 data reprocessing effort, the quality, consistency, and cloud-free coverage of the global land products have increased.

24.1 Introduction

A primary goal of NASA's Earth observation efforts is the long-term monitoring of key biophysical variables and the production of long-term and consistent parameters for modeling studies. Global surface albedo, which controls the land surface radiation energy budget, is required by climate models with an absolute accuracy of 0.02–0.05, and at a range of spatial and temporal scales (Dickinson 1983, 1995; Henderson-Sellers and Wilson 1983; Bonan et al. 2002; Sellers et al. 1996). Therefore, a consistent and accurate global albedo dataset is essential to investigate the sensitivity of climate to various types of forcing, and to identify the effects of human activities. Satellite remote sensing represents the only efficient way to compile such consistent global albedo characterizations.

Early global albedo datasets were derived from the Advanced Very High Resolution Radiometer (AVHRR) (Csiszar and Gutman 1999) and the Earth Radiation Budget Experiment (ERBE) radiometer (Li and Garand 1994), although these efforts assumed a Lambertian surface and did not compensate for surface anisotropy. Now however, routine moderate resolution albedo and reflectance anisotropy products with

C.B. Schaaf (✉)
Department of Geography and Environment,
Boston University, Boston, MA 02215, USA
e-mail: schaaf@bu.edu

spatial resolutions of 500 m–20 km and temporal frequencies of daily to monthly are being derived from various polar orbiting satellites. They include MODIS (Gao et al. 2005; Schaaf et al. 2002; Lucht et al. 2000), MISR (Martonchik et al. 1998a, b, 2002), CERES (Clouds and the Earth's Radiant Energy System) (Rutan et al. 2006), and POLDER (Polarization and Directionality of the Earth's Reflectances) currently on-board PARASOL (Polarization and Anisotropy of Reflectances for Atmospheric Sciences coupled with Observations from a Lidar) (Leroy et al. 1997; Hautrecoeur and Leroy 1998; Bicheron and Leroy 2000; Maignan et al. 2004; Bacour and Bréon 2005). With an assumption of the reciprocity principle, which is generally acceptable for moderate resolution sensors (Lattanzio et al. 2006; Li et al. 1999), similar products from the geosynchronous satellites, Meteosat (Pinty et al. 2000a, b; Govaerts et al. 2004, 2006) and MSG (Meteosat Second Generation) (van Leeuwen and Roujean 2002; Geiger et al. 2005), are also now available. The albedo retrieval from these instruments represents a major advance in sensing the spatial and temporal surface heterogeneity, although issues such as atmospheric correction, directional-to-hemispherical conversion, and spectral interpolation can still introduce small and quantifiable uncertainties into the process. These satellite products rely on sophisticated radiative transfer methods (Vermeote et al. 1997; Kotchenova et al. 2006; Berk et al. 1998; Liang et al. 1999; Liang 2000) and bidirectional anisotropic reflectance modeling (Walthall et al. 1985; Roujean et al. 1992; Rahman et al. 1993; Engelsen et al. 1996; Wanner et al. 1995, 1997; Martonchik et al. 1998b; Pinty et al. 2000a, b; Bréon et al. 2002; Maignan et al. 2004) to obtain accurate surface quantities. The routine retrieval of high quality and consistent global surface Bidirectional Reflectance Distribution Function (BRDF) estimates from flexible and realistic anisotropic models has, therefore, become a necessary and inherently useful by-product of accurate surface albedo product generation.

With more than 8 years of MODIS albedo and reflectance anisotropy data now available, the modeling community is enthusiastically using these global products (Oleson et al. 2003; Zhou et al. 2003; Tian et al. 2004; Roesch et al. 2004; Knorr et al. 2001; Myhre et al. 2005a, b; Lawrence and Chase 2007). Interannual variations are being explored and limited interannual statistics are being prepared that compensate for transient cloudiness or snow cover (Moody et al. 2005, 2007; Gao et al. 2005; Barlage et al. 2005). In addition to the use of the MODIS products, there is a keen interest in generating analogous surface albedo products from the period prior to the deployment of the MODIS sensors when only operational weather satellites were acquiring relevant data (Saleous et al. 2005) and ultimately to link these historical datasets (despite their limitations in terms of accurate sensor characterization, geolocation, and calibration) with the more modern MODIS albedo and anisotropy products.

24.2 MODIS Albedo and Reflectance Anisotropy Algorithm

The operational MODIS albedo and reflectance anisotropy algorithm makes use of a kernel-driven, linear model that relies on the weighted sum of an isotropic parameter and two functions (or kernels) of viewing and illumination geometry (Roujean

et al. 1992) to estimate the BRDF. One kernel is derived from radiative transfer models (Ross 1981) and the other is based on surface scattering and geometric shadow-casting theory (Li and Strahler 1992). The kernel weights selected are those that best fit the cloud-cleared, atmospherically corrected surface reflectances available for each location over a 16-day period (Lucht et al. 2000; Schaaf et al. 2002). This model combination (Ross-Thick/Li-Sparse-Reciprocal or RTLSR) is substantiated as well suited to describe the surface anisotropy of the variety of land covers that are distributed worldwide (Privette et al. 1997; Lucht et al. 2000). RTLSR is similar to the kernel-driven methods used to obtain anisotropy and albedo information by the POLDER satellite sensor (Hautecoeur and Leroy 1998; Bicheron and Leroy 2000; Maignan et al. 2004; Bacour and Bréon 2005) and MSG (van Leeuwen and Roujean 2002; Geiger et al. 2005). The approach assumes that the geophysical system under investigation does not experience significant changes during the period of data accumulation, and the temporal sampling of the radiance field for a given location is interpretable as instantaneous angular sampling (a reasonable assumption except in circumstances of abrupt or catastrophic change such as snow, fire, flood, or harvest).

Once an appropriate anisotropy estimate of the BRDF is retrieved, integration over all view angles results in a Directional Hemispherical Reflectance or a black-sky albedo at any desired solar angle, and a further integration over all illumination angles results in a bihemispherical reflectance under isotropic illumination (BHR_{iso}) or a white-sky albedo (Schaepman-Strub et al. 2006). These quantities are intrinsic to specific locations, and are associated with the structure and optical properties of the land cover. They are combinable with appropriate atmospheric optical depth information to estimate an actual BHR (blue-sky albedo) for a specific time as measured at the surface by field sensors under ambient illumination. The reflectance anisotropy estimates of the BRDF are useful to determine surface reflectances at view or solar angles other than those typically acquired (such as correcting to a nadir view) with uncertainties quantifiable by metrics such as the weight of determination. The spectral acquisitions are also combinable via narrow to broadband conversion coefficients (Liang et al. 1999; Liang 2000) to provide broadband anisotropy information, and thus broadband albedos similar to those routinely collected in the field with pyranometers, and commonly used in large-scale models.

The MODIS instruments on both Aqua and Terra each have a 16-day repeat cycle and provide measurements on a global basis every 1–2 days with multiple overpasses possible at higher latitudes. This 16-day period provides an appropriate tradeoff between the availability of sufficient angular samples and the temporal stability of the surface (Wanner et al. 1997; Gao et al. 2001; Roy et al. 2006). This assumption of stability becomes more tenuous during periods of strong phenological change such as vegetation greenup, senescence, or harvesting. By overlapping data processing such that retrievals are attempted every 8 days (based on all clear observations over the past 16 days), there are more frequent opportunities to obtain high-quality retrievals during periods of intermittent clear sky observations. However, during long periods of clear sky acquisitions, this overlapping technique can result in some autocorrelation between retrievals, as some of the observations may end up being used in more than one retrieval period. Additional occurrences

of rapid change, such as ephemeral snowfall, also provide challenges in surface albedo retrieval. The MODIS algorithm addresses this by determining whether the majority of the clear observations available over a 16-day period represent snow-covered or snow-free situations, and then retrieving the albedo of the majority condition accordingly. The availability of a sufficient number of high-quality clear-sky surface observations of either the snow-covered or snow-free situation will not guarantee a high-quality retrieval, however as an adequate sampling of the angular domain is equally important to establish a model that will accurately estimate the surface reflectance anisotropy (Lucht and Lewis 2000; Barnsley et al. 1994).

Whenever the full anisotropic model described above is not confidently retrievable due to poor sampling or insufficient input observations, a backup algorithm is employed. This method (Strugnell and Lucht 2001; Strugnell et al. 2001) relies on a global database of archetypal anisotropic models based on a land cover classification and historical high-quality full-model MODIS retrievals. This a priori database is then used as a first approximation of the underlying reflectance anisotropy, and any available observations acquired during the 16-day window are used to constrain the model (Li et al. 2001). Although this magnitude inversion is considered and is flagged as a lower quality result, field validation exercises by Jin et al. (2003a, b) and Salomon et al. (2006) have found that this backup method often performs quite well, routinely falling within 5–10% of field-measured albedos.

The MODIS BRDF/Albedo products have now completed their fifth reprocessing. The Collection 5 (C5) standard operational products (Lucht et al. 2000; Schaaf et al. 2002; Gao et al. 2005) include the best-fit, well-sampled RTLSR model parameters describing the surface anisotropy, both black sky and white sky albedo quantities, the nadir (view-angle-corrected) surface reflectance of each location, and extensive quality information. The best-fit RTLSR model parameters are retrieved for the first seven MODIS spectral bands (centered at 648, 858, 470, 555, 1,240, 1,640, and 2,130 nm, respectively) and three additional broadbands (0.3–0.7, 0.7–5, and 0.3–5 μm). These anisotropy models are then integrated to compute white sky albedo and black sky albedo at local solar noon for the same seven spectral bands and three broadbands (Fig. 24.1). Local solar noon was selected both as a compromise geometry between the Terra and Aqua overpasses, and as a value that would ensure maximum illumination at each location worldwide.

While the precomputed albedo values have enjoyed widespread use, users increasingly use the BRDF models directly so that they can generate albedos at any desired illumination angle or under realistic atmospheric conditions. Four common shape factors or structural indices are also operationally computed for the modeling community, including an anisotropic factor, a normalized difference anisotropic index (Sandmeier et al. 1998; Sandmeier and Deering 1999), the structural scattering index (Gao et al. 2003), and the ratio of the white sky albedo to the isotropic model parameter.

As mentioned earlier, users are also interested in using the anisotropy models to directly correct surface reflectances for view-angle effects and provide BRDFs at a common view-angle. The Nadir BRDF-Adjusted Reflectances (NBAR) at local solar noon are operationally computed for the seven spectral bands (Fig. 24.2), and

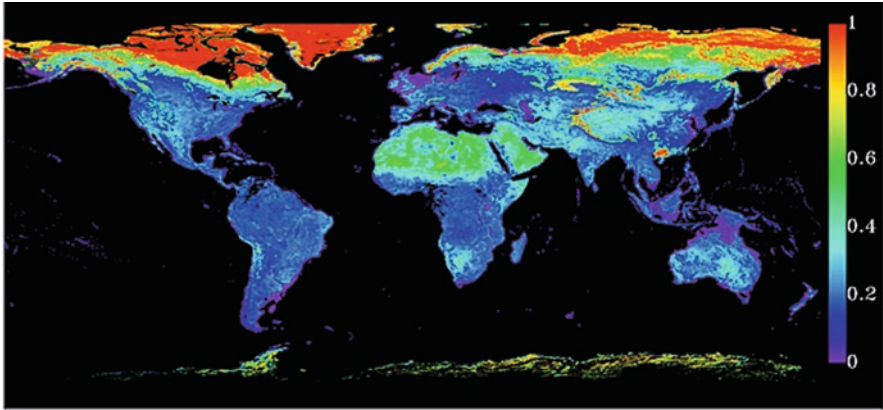


Fig. 24.1 MODIS global white sky albedo Climate Modeling Grid (CMG) 0.05-degree product (April 2003)

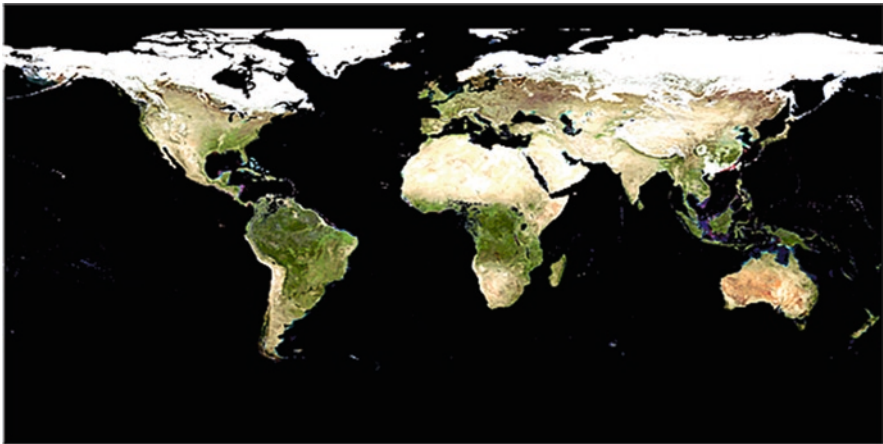


Fig. 24.2 MODIS Nadir BRDF-adjusted Reflectance (NBAR) Climate Modeling Grid (CMG) 0.05-degree product (April 2003)

are used as the primary input for the MODIS Land Cover and Land Cover Dynamics products due to their stability and temporal consistency (Friedl et al. 2002; Zhang et al. 2003, 2006).

The C5 reprocessing retrieves the surface anisotropy models at a 500-m resolution (an improvement over Collection 4 and earlier, where the finest spatial resolution was 1 km). Both the 500-m and 1-km products are retrieved from those observations that fall in or on each spatial bin, and are weighted by their observation coverage. Note, however, that while most of the directional 500-m observations fall fully within a 1-km bin, the off-nadir 500-m observations are obviously sampling beyond each 500-m bin. This means that the 500-m BRDFs really represent the anisotropy of an area somewhat larger than $500 \times 500 \text{ m}^2$. In addition to the standard 500-m and

1-km tiled products provided in a Sinusoidal projection, these same science datasets are also routinely produced at 30-arc-second and 0.05-degree spatial resolutions in global geographic (latitude/longitude) projections specifically for use by global modelers (Gao et al. 2005). In response to user requests, high-quality, snow-free, gap-filled albedo quantities have also been prepared in collaboration with the MODIS Atmosphere Team (Moody et al. 2005). High-quality snow-free retrievals are fit with temporal phenological curves to produce continuous gap-filled annual datasets and multiyear climatologies. More recently, equivalent gap-filled BRDF model parameter datasets have also been prepared.

24.3 Algorithm Quality

In view of the sometimes insufficient angular sampling available from a single polar orbiting sensor, the synergistic use of multisensor observations from both Terra and Aqua has offered an opportunity to improve both the coverage and the quality of global MODIS anisotropy and albedo retrievals. Terra has a descending equatorial crossing time of 10:30 a.m., while Aqua flies in an ascending orbit with a 1:30 p.m. equatorial crossing time. By combining MODIS observations from both Terra and Aqua, more high-quality, cloud-free observations (under varying solar zenith angles) are available to generate better constrained model retrievals (see Fig. 24.3). Since Terra-MODIS and Aqua-MODIS have similar instrument characterizations and use the same atmospheric correction algorithm, the combination of these data is fairly straightforward. However, the calibration and geolocation of both instruments requires continuous monitoring for compatibility and the quality of the

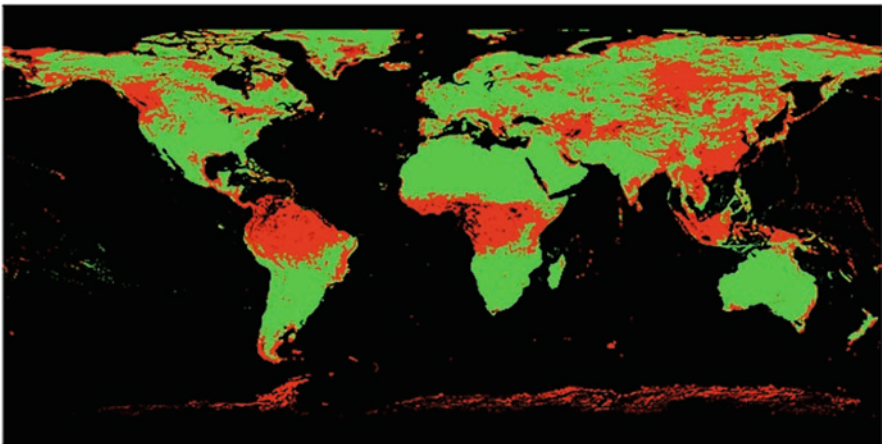


Fig. 24.3 MODIS Terra and Aqua quality flags (*green*, high quality; *red*, lower quality; *black*, fill values), April 2003

aerosol retrieval from each sensor, and its effect on the respective atmospherically corrected surface reflectances also requires accounting.

In general, the combined Terra and Aqua MODIS processing stream begins with a detailed quality check of each atmospherically corrected surface reflectance. Next, various penalty weights are assigned to the individual observations according to the quality flag contained in each surface reflectance product (Schaaf et al. 2002). Thus, the quantified uncertainty of the sensor-specific surface reflectances is directly integrated into the retrieval. Results from the combined Terra-MODIS and Aqua-MODIS algorithm indicate that the increase in the number and angular configuration of observations does result in more higher quality full inversion retrievals (Fig. 24.3), and can decrease the use of the lower quality backup retrievals by as much as 50% (Salomon et al. 2006). A 16-day moving window that attempts retrievals every 8 days also serves to improve the number of high-quality retrievals obtained each month, and the ability of the product to capture phenological changes.

Original plans also called for the use of Multiangle Imaging SpectroRadiometer (MISR) in a joint retrieval algorithm (Diner et al. 1998), since the cross-track scans of Terra-MODIS and along-track multiangular MISR observations complement each other in the azimuthal dimension. Using surface directional reflectances simulated by a canopy radiative transfer model, Lucht and Lewis (2000) demonstrated that combining Terra-MODIS, Aqua-MODIS, and MISR angular samples could further reduce the uncertainty and random noise amplification of anisotropy retrievals. Jin et al. (2002) developed the methodology to incorporate MISR observations obtained close to the principal plane and demonstrated how it was possible to further improve the MODIS retrievals on a regional basis. However, because it is extremely important to minimize the effects of any possible observation bias produced by differing spectral band specifications, geometric co-registration, spatial resolution, and atmospheric correction schemes, a global operational implementation was not undertaken.

The absolute accuracy of the MODIS albedo products has also been established by comparison with field measurements. The products are now validated to a stage 1 level, which indicates that product accuracy was estimated using a small number of independent field measurements obtained from selected locations and time periods (Jin et al. 2003a, b; Salomon et al. 2006). The well-calibrated international Baseline Surface Radiation Network sites, which are represented in the United States by the NOAA-operated Surface Radiation (Surfrad) and DOE-sponsored Atmospheric Radiation Measurement Program (ARM) locations, have provided the primary validation field data for broadband albedo. At each site, black-sky albedo quantities are computed for a range of daily solar zenith angles and coupled with white-sky estimates as a function of the atmospheric optical depth of a location. These actual BHR or blue-sky albedos are compared directly with cloud-free albedometer measurements at the field tower sites. The accuracy of the high-quality MODIS operational albedos at local solar noon are well within 5% of the measured albedos at the validation sites studied thus far, and even those albedo values retrieved with the backup algorithm and thus flagged as low-quality

measures are within 10% of field data. These low-quality values are probably improvable by updating the current a priori database with a pixel-based climatological version that relies on all the years of MODIS reflectance anisotropy model retrievals currently available. In Fig. 24.4, 1-km albedos based on a 16-day retrieval (flagged as v004) are compared with 500-m albedos retrieved every 8 days based on the last 16 days (flagged as v005) and daily tower albedometer data at local solar noon from Extended Facility #15 of the ARM Southern Great Plains site. Furthermore, comparison of high-quality MODIS retrievals with ARM site #15 tower data collected throughout the day (Fig. 24.5) also demonstrates the ability of the MODIS reflectance anisotropy product to consistently produce cloud-free diurnal albedos at solar zenith angles of less than 70°. Although the anisotropy model of the site was only retrieved every 8 days (based on the last 16 days), it was successfully used on a daily basis with the appropriate solar zenith angles to produce hourly albedos. This attribute (of capturing the solar zenith angle depen-

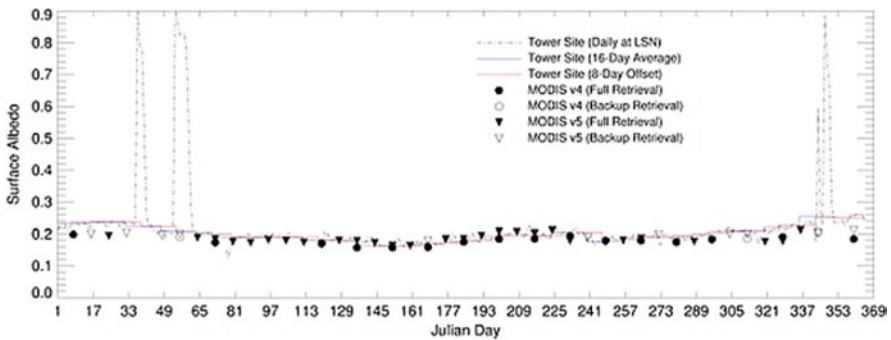


Fig. 24.4 Validation of V005 and V004 MODIS albedo data with daily tower data at local solar noon from the ARM Extended Facility #15 in 2003

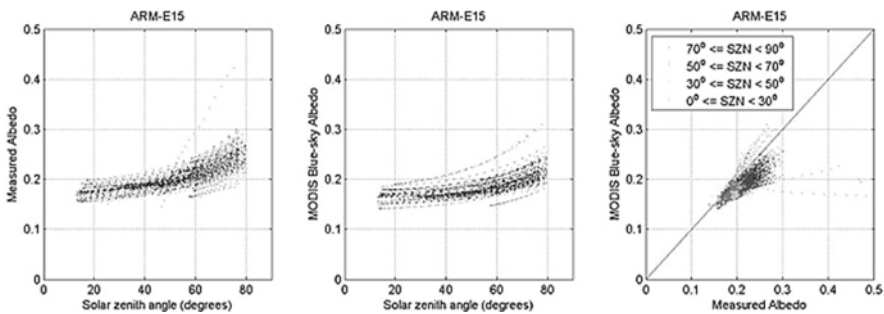


Fig. 24.5 Comparison of MODIS daily albedos for 2003 with tower albedometer data from the ARM Extended Facility #15 (red 0°–30° szn, green 30°–50°, blue 50°–70°, black <70°)

dence of clear sky albedos) is encouraging meteorological modelers to use these satellite-retrieved models directly in their surface energy budget schemes.

24.4 Summary

MODIS remotely sensed observations have helped operationally produce high-quality standard land products since 2000. The production of accurate MODIS surface albedo data depends on the routine retrieval of high-quality and consistent global BRDF estimates of the surface anisotropy. The Collection 5 MODIS data reprocessing implements several refinements. They include the coupled use of both Terra and Aqua MODIS observations, increased spatial and temporal resolutions, and improvements in cloud-clearing and atmospheric correction. This has resulted in a multiyear, consistent, and validated surface reflectance anisotropy models (and thus, surface albedo quantities) for use in a number of modeling and monitoring applications. Historical satellite observations acquired before 2000 do not offer spatial and spectral resolutions of the MODIS kind (not to mention the calibration and geolocation accuracies). Hence, attempts are underway to retrieve consistent broadband anisotropy and albedo products from the operational AVHRR weather sensor, which will produce multidecadal datasets for climate studies (Saleous et al. 2005). Future plans are to continue generating such products with data from similar angular and temporal sampling from the Visible Infrared Imager Radiometer Suite (VIIRS) on-board the next generation of operational weather satellites, the National Polar-orbiting Operational Environmental Satellite System (NPOESS), and its precursor, the NPOESS Preparatory Project (NPP), both of which are slated for launch within the next decade.

References

- Bacour C, Bréon FM (2005) Variability of land Surface BRDFs. *Remote Sens Environ* 98:80–95.
- Barlage M, Zeng X, Mitchell K, Wei H (2005) A global 0.05-deg maximum albedo dataset of snow-covered land based on MODIS observations. *Geophys Res Lett* 32: doi:10.1029/2005GL022881.
- Barnsley MJ, Strahler AH, Morris KP, Muller J-P (1994) Sampling the surface bidirectional reflectance distribution function (BRDF), I, Evaluation of current and future satellite sensors. *Remote Sens Rev* 8:271–311.
- Berk A, Bernstein LS, Anderson GP, Acharya PK, Robertson DC, Chetwynd JH, Adler-Golden SM (1998) MODTRAN cloud and multiple scattering upgrades with application to AVIRIS. *Remote Sens Environ* 65:367–375.
- Bicheron P, Leroy M (2000) Bidirectional reflectance distribution function signatures of major biomes observed from space. *J Geophys Res* 105:26, 669–26, 681.
- Bonan GB, Oleson KW, Vertenstein M, Levis S, Zeng X, Dai RE, Y, Yang Z-L (2002) The land surface climatology of the NCAR community land model coupled to the NCAR Community Climate Model. *J Climate* 15:3123–3149.

- Bréon FM, Maignan F, Leroy M, Grant I (2002) Analysis of hot spot directional signatures measured from space. *J Geophys Res* 107(16):4, 282–284, 296.
- Csiszar I, Gutman G (1999) Mapping global land surface albedo from NOAA/AVHRR. *J Geophys Res* 104:6215–6228.
- Dickinson RE (1995) Land processes in climate models. *Remote Sens Environ* 51:27–38.
- Dickinson RE (1983) Land surface processes and climate-surface albedos and energy balance. *Adv Geophys* 25:305–353.
- Diner DJ, Beckert TH, Reilly JC, Bruegge CJ, Conel JE, Kahn RA, Martonchik JV, Ackerman TP, Davies R, Gerstl SAW, Gordon HR, Muller J-P, Myneni RB, Sellers PJ, Pinty B, Verstraete MM (1998) Multi-angle Imaging SpectroRadiometer (MISR) instrument description and experiment overview. *IEEE Trans Geosci Remote Sens* 36:1072–1087.
- Engelsens O, Pinty B, Verstraete MM, Martonchik JV 1996. Parametric bidirectional reflectance factor models: Evaluation, improvements, and applications. Technical Report EUR 16426 EN. EC Joint Research Centre.
- Friedl MA, McIver DK, Hodges JCF, Zhang XY, Muchoney D, Strahler AH, Woodcock CE, Gopal S, Schneider A, Cooper A, Baccini A, Gao F, Schaaf C (2002) Global land cover mapping from MODIS: algorithms and early results. *Remote Sens Environ* 83(1–2):287–302.
- Gao F, Schaaf C, Strahler AH, Lucht W (2001) Using a multi-kernel least variance approach to retrieve and evaluate albedo from limited BRDF observations. *Remote Sens Environ* 76:57–66.
- Gao F, Schaaf CB, Strahler AH, Jin Y, Li X (2003) Detecting vegetation structure using a Kernel-based BRDF model. *Remote Sens Environ* 86:198–205.
- Gao F, Schaaf C, Strahler A, Roesch A, Lucht W, Dickinson R (2005) The MODIS BRDF/Albedo climate modeling grid products and the variability of albedo for major global vegetation types. *J Geophys Res* 110:D01104, doi:10.1029/2004JD00519.
- Geiger B, Franchistéguy L, Carrer D, Roujean J-L (2005) Land surface analysis satellite application facility (LSA-SAF) product user manual (PUM) on Albedo. Eumetsat p. 41.
- Govaerts Y, Lattanzio A, Pinty B, Schmertz J (2004) Consistent surface albedo retrieved from two adjacent geostationary satellite. *Geophys Res Lett* 31:L15201 10.1029/2004GL020418 03.
- Govaerts Y, Pinty B, Taberner M, Lattanzio A (2006) Spectral conversion of surface albedo derived from Meteosat first generation observations. *IEEE Geosci Remote Sens Lett* 3:23–27, doi: 10.1109/LGRS.2005.854202.
- Henderson-Sellers A, Wilson MF (1983) Surface albedo data for climatic modeling. *Rev Geophys Space Phys* 21:1743–1778.
- Hautecoeur O, Leroy MM (1998) Surface bi-directional reflectance distribution function observed at global scale by POLDER/ADEOS. *Geophys Res Lett* 22:4197–4200.
- Jin Y, Schaaf C, Gao F, Li X, Strahler A, Bruegge C, Martonchik J (2002) Improving MODIS surface BRDF/Albedo retrieval with MISR multi-angle observations. *IEEE Trans Geosci Remote Sens* 40:1593–1604.
- Jin Y, Schaaf CB, Woodcock CE, Gao F, Li X, Strahler AH, Lucht W, Liang S (2003a) Consistency of MODIS surface BRDF/Albedo retrievals: 1. Algorithm performance. *J Geophys Res* 108(D5):4158, doi:10.1029/2002JD002803.
- Jin Y, Schaaf CB, Woodcock CE, Gao F, Li X, Strahler AH, Lucht W, Liang S (2003b) Consistency of MODIS surface BRDF/Albedo retrievals: 2. Validation. *J Geophys Res* 108(D5):4159, doi:10.1029/2002JD002804.
- Knorr W, Schnitzler KG, Govaerts Y (2001) The role of bright desert regions in shaping North African climate. *Geophys Res Lett* 28:3489–3492.
- Kotchenova SY, Vermote EF, Matarrese R, Klemm FJ (2006) Validation of a vector version of the 6S radiative transfer code for atmospheric correction of satellite data. Part I: Path radiance. *Appl Opt* 26:6762–6774.
- Lattanzio A, Govaerts Y, Pinty B (2006) Consistency of surface anisotropy characterization with Meteosat observations. *Adv Space Res* doi:10.1016/j.asr. 2006.02.049.
- Lawrence PJ, Chase TN (2007) Representing a new MODIS consistent land surface in the Community Land Model (CLM 3.0). *J Geophys Res* 112:G01023, doi:10.1029/2006JG000168.

- Leroy M, Deuze JL, Breon FM, Hauteceur O, Herman M, Buriez JC, Tanre D, Bouffies S, Chazette P, Roujean J-L (1997) Retrieval of atmospheric properties and surface bidirectional reflectances over land from POLDER/ADEOS. *J Geophys Res* 102:17023–17037.
- Li Z, Garand L (1994) Estimation of surface albedo from space: A parameterization for global application. *J Geophys Res* 99:8335–8350.
- Li X, Wang J, Strahler AH (1999) Apparent reciprocity failure in BRDF of structured surfaces. *Prog Nat Sci* 9:(10), 747–752.
- Li X, Strahler AH (1992) Geometric-optical bidirectional reflectance modeling of the discrete crown vegetation canopy: Effect of crown shape and mutual shadowing. *IEEE Trans Geosci Remote Sens* 30:276–292.
- Li X, Gao F, Wang J, Strahler AH (2001) A priori knowledge accumulation and its application to linear BRDF model inversions. *J Geophys Res* D106:11925–11935.
- Liang S, Strahler AH, Walthall CW (1999) Retrieval of land surface albedo from satellite observations: A simulation study. *J Appl Meteorol* 38:712–725.
- Liang S (2000) Narrowband to broadband conversions of land surface albedo I: algorithms. *Remote Sens Environ* 76:213–238.
- Lucht W, Schaaf CB, Strahler AH (2000) An Algorithm for the retrieval of albedo from space using semi-empirical BRDF models. *IEEE Trans Geosci Remote Sens* 38:977–998.
- Lucht W, Lewis P (2000) Theoretical noise sensitivity of BRDF and albedo retrieval from the EOS-MODIS and MISR sensors with respect to angular sampling. *Int J Remote Sens* 21:81–98.
- Maignan F, Bréon FM, Lacaze R (2004) Bidirectional reflectance of Earth targets: evaluation of analytical models using a large set of spaceborne measurements with emphasis on the hot spot. *Remote Sens Environ* 90:210–220.
- Martonchik JV, Diner DJ, Kahn RA, Ackerman TP, Verstraete MM, Pinty B, Gordon HR (1998a) Techniques for the retrieval of aerosol properties over land and ocean using multiangle imaging. *IEEE Trans Geosci Remote Sens* 36:1212–1227.
- Martonchik JV, Diner DJ, Pinty B, Verstraete MM, Myneni RB, Knyazikhin Y, Gordon HR (1998b) Determination of land and ocean reflective, radiative, and biophysical properties using multiangle imaging. *IEEE Trans Geosci Remote Sens* 36:1266–1281.
- Martonchik JV, Pinty B, Verstraete MM (2002) Note on an improved model of surface BRDF-atmospheric coupled radiation. *IEEE Trans Geosci Remote Sens* 40:1637–1639.
- Moody EG, King MD, Platnick S, Schaaf CB, Gao F (2005) Spatially complete global spectral surface albedos: Value-added datasets derived from Terra MODIS land products. *IEEE Trans Geosci Remote Sens* 43:144–158.
- Moody EG, King MD, Schaaf CB, Hall DK (2007) Northern Hemisphere five-year average (2000–2004) spectral albedos of surfaces in the presence of snow: Statistics computed from Terra MODIS land products. *Remote Sens Environ* 111:337–345.
- Myhre G, Kvalevåg MM, Schaaf CB (2005a) Radiative forcing due to anthropogenic vegetation change based on MODIS surface albedo data set. *Geophys Res Lett* 32:L21410, doi: 10.1029/2005GL024004.
- Myhre G, Govaerts Y, Haywood JM, Berntsen TK, Lattanzio A (2005b) Radiative effect of surface albedo change from biomass burning. *Geophys Res Lett* 32:L20812, doi: 10.1029/2005GL022897.
- Oleson KW, Bonan GB, Schaaf C, Gao F, Jin Y, Strahler A (2003) Assessment of global climate model land surface albedo using MODIS data. *Geophys Res Lett* 30(8):1443, doi: 10.1029/2002GL016749.
- Pinty B, Roveda F, Verstraete MM, Gobron N, Govaerts Y, Martonchik J, Diner D, Kahn R (2000a) Surface albedo retrieval from METEOSAT – Part 1: Theory. *J Geophys Res* 105:18099–18112.
- Pinty B, Roveda F, Verstraete MM, Gobron N, Govaerts Y, Martonchik J, Diner D, Kahn R (2000b) Surface albedo retrieval from METEOSAT – Part2: Application. *J Geophys Res* 105:18113–18134.
- Privette JL, Eck TF, Deering DW (1997) Estimating spectral albedo and nadir reflectance through inversion of simple BRDF models with AVHRR/MODIS-like data. *J Geophys Res* 102:29529–29542.

- Rahman H, Pinty B, Verstraete MM (1993) Coupled surface-atmosphere reflectance (CSAR) model – 2: Semiempirical surface model usable with NOAA advanced very high resolution radiometer data. *J Geophys Res* 98:20791–20801.
- Roesch A, Schaaf C, Gao F (2004) Use of Moderate-Resolution Imaging Spectroradiometer bidirectional reflectance distribution function products to enhance simulated surface albedos. *J Geophys Res* 109:D12, doi: 10.1029/2004JD004552.
- Ross JK (1981) The radiation regime and architecture of plant stands. Dr. W. Junk Publishers, The Hague, p 392.
- Roujean J-L, Leroy M, Deschamps PY (1992) A bidirectional reflectance model of the Earth's surface for the correction of remote sensing data. *J Geophys Res* 97:20455–20468.
- Roy DP, Lewis P, Schaaf CB, Devadiga S, Boschetti L (2006) The global impact of clouds on the production of MODIS bidirectional reflectance model-based composites for terrestrial monitoring. *IEEE Geosci Remote Sens Lett* 3:452–456.
- Rutan D, Charlock T, Rose F, Kato S, Zentz S, Coleman L (2006) Global surface albedo from CERES/TERRA Surface and Atmospheric Radiation Budget (SARB) data product. Proceedings of 12th Conference on Atmospheric Radiation (AMS), July 10–14, 2006, Madison, Wisconsin.
- Salomon J, Schaaf CB, Strahler AH, Gao F, Jin Y (2006) Validation of the MODIS Bidirectional Reflectance Distribution Function and albedo retrievals using combined observations from the Aqua and Terra Platforms. *IEEE Trans Geosci Remote Sens* 44(6):1555–1565.
- Saleous N, Vermote EF, Masuoka E, Privette J, Roy D, Tucker C, Pinzon J, Prince S (2005). A long term data record from AVHRR, MODIS and VIIRS, Proceedings, American Geophysical Union Fall Meeting, San Francisco, CA.
- Sandmeier S, Müller C, Hosgood B, Andreoli G (1998) Physical mechanisms in hyperspectral BRDF data of grass and watercress. *Remote Sens Environ* 66:222–233.
- Sandmeier, S, and Deering DW (1999) Structure analysis and classification of boreal forest using airborne hyperspectral BRDF data from ASAS. *Remote Sensing of Environment* 69:281–295.
- Sellers PJ, Los SO, Tucker CJ, Justice CO, Dazlich DA, Collatz CJ, Randall DA (1996) A revised land surface parameterization (SiB2) for atmospheric GCMs, part II, The generation of global fields of terrestrial biospheric parameters from satellite data. *J Climate* 9:706–737.
- Schaaf CB, Gao F, Strahler AH, Lucht W, Li X, Tsang T, Strugnell NC, Zhang X, Jin Y, Muller J-P, Lewis P, Barnsley M, Hobson P, Disney M, Roberts G, Dunderdale M, Doll C, d'Entremont R, Hu B, Liang S, Privette JL (2002) First operational BRDF, albedo and nadir reflectance products from MODIS. *Remote Sens Environ* 83:135–148.
- Schaepman-Strub G, Schaepman ME, Painter TH, Dangel S, Martonchik JV (2006) Reflectance quantities in optical remote sensing – definitions and case studies. *Remote Sens Environ* 103:27–42.
- Strugnell N, Lucht W, Schaaf C (2001) A global albedo data set derived from AVHRR data for use in climate simulations. *Geophys Res Lett* 28:191–194.
- Strugnell N, Lucht W (2001) An algorithm to infer continental-scale albedo from AVHRR data, land cover class and field observations of typical BRDFs. *J Climate* 14:1360–1376.
- Tian Y, Dickinson RE, Zhou L, Myneni RB, Friedl M, Schaaf CB, Carroll M, Gao F (2004) Land boundary conditions from MODIS data and consequences for the albedo of a climate model. *Geophys Res Lett* 31:doi:10.1029/2003GL019104, 2004.
- Van Leeuwen W, Roujean J-L (2002) Land surface albedo from the synergistic use of polar (EPS) and geo-stationary (MSG) observing systems: An assessment of physical uncertainties. *Remote Sens Environ* 81(2–3):273–289.
- Vermote EF, Tanre D, Deuze JL, Herman M, Morcette JJ (1997) Second simulation of the satellite signal in the solar spectrum: an overview. *IEEE Trans Geosci Remote Sens* 35:675–686.

- Walthall CL, Norman JM, Welles JM, Campbell G, Blad BL (1985) Simple equation to approximate the bidirectional reflectance from vegetation canopies and bare soil surfaces. *Appl Opt* 24:383–387.
- Wanner W, Li X, Strahler AH (1995) On the derivation of kernels for kernel-driven models of bidirectional reflectance. *J Geophys Res* 100:21077–21090.
- Wanner W, Strahler AH, Hu B, Lewis P, Muller J-P, Li X, Barker Schaaf CL, Barnsley MJ (1997) Global retrieval of bidirectional reflectance and albedo over land from EOS MODIS and MISR data: theory and algorithm. *J Geophys Res* 102:17143–17162.
- Zhang X, Friedl MA, Schaaf CB, Strahler AH, Hodges JCF, Gao F, Reed BC, Huete A (2003) Monitoring vegetation phenology using MODIS. *Remote Sens Environ* 84:471–475.
- Zhang X, Friedl MA, Schaaf CB (2006) Global vegetation phenology from Moderate Resolution Imaging Spectroradiometer (MODIS): evaluation of global patterns and comparison with in situ measurements. *J Geophys Res* 111:G04017, doi:10.1029/2006JG000217.
- Zhou L, Dickinson RE, Tian Y, Zeng X, Dai Y, Yang Z-L, Schaaf CB, Gao F, Jin Y, Strahler A, Myneni RB, Yu H, Wu W, Shaikh M (2003) Comparison of seasonal and spatial variations of albedos from Moderate-Resolution Imaging Spectroradiometer (MODIS) and Common Land Model. *J Geophys Res* 108:D15, 4488, doi:10.1029/2002JD003326.

Chapter 25

MODIS Land Surface Temperature and Emissivity

Zhengming Wan and Zhao-Liang Li

25.1 Introduction

Land surface temperature (LST) is a key parameter in the physics of land surface processes at regional and global scales, combining the results of all surface–atmosphere interactions and energy fluxes between the atmosphere and the ground (Mannstein 1987; Sellers et al. 1988). The Moderate Resolution Imaging Spectroradiometer (MODIS) aboard the Terra and Aqua platforms produce high-quality LST products from data, which possess a number of strengths. They include global coverage, high radiometric resolution and wide dynamic ranges, accurate geolocation (Wolfe et al. 2002), and high-quality thermal infrared (TIR) calibration accuracy used in the LST retrieval (Barnes et al. 1998).

The LST is defined by the thermal radiation emitted by the MODIS-observed land surface at instant viewing angles. Land surface refers to the canopy in vegetated areas or soil surface in bare areas. In TIR remote sensing, accurate atmospheric radiative transfer models such as MODTRAN4 (Berk et al. 1999) provide the spectral infrared radiance $L(\lambda, \mu)$ at the top of the atmosphere (TOA) in clear-sky conditions as surface thermal emittance, thermal path radiance $L_a(\lambda, \mu)$, path radiance resulting from scattering of solar radiation $L_s(\lambda, \mu, \mu_o, \phi_o)$, solar beam and downward solar diffuse radiation and atmospheric thermal radiation reflected by the surface at each wave number, i.e.,

$$\begin{aligned}
 L(\lambda, \mu) = & t_1(\lambda, \mu)\varepsilon(\lambda, \mu)B(\lambda, T_s) + L_a(\lambda, \mu) + L_s(\lambda, \mu, \mu_o, \phi_o) \\
 & + t_2(\lambda, \mu, \mu_o)\mu_o E_o(\lambda)f_r(\mu; \mu_o, \phi_o) + \iint \mu' f_r(\mu; \mu', \phi') \\
 & [t_3(\lambda, \mu)L_d(\lambda', -\mu', \phi') + t_4(\lambda, \mu)L_t(\lambda, -\mu', \phi')]d\mu'd\phi'
 \end{aligned} \tag{25.1}$$

where λ is the wavelength, μ is cosine of the viewing zenith angle, $\varepsilon(\lambda, \mu)$ is the surface spectral emissivity, $B(\lambda, T_s)$ is the radiance emitted by a blackbody at surface temperature T_s given by Planck's function, $E_o(\lambda)$ is the spectral solar irradiance incident on the

Z. Wan (✉)
 ICES, University of California, Santa Barbara, CA 93106, USA
 e-mail: wan@ices.ucsb.edu

TOA (normal to the beam), μ_o is cosine of the solar zenith angle, ϕ_o is the relative azimuth angle between the viewing direction and the solar beam direction, $f_r(\mu; \mu', \phi')$ is the bi-directional reflectance distribution function (BRDF), $L_d(\lambda, -\mu', \phi')$ is the downward solar diffuse radiance, $L_t(\lambda, -\mu', \phi')$ is the atmospheric downward thermal radiance, their incident direction is represented by $-\mu'$ and ϕ' , and $t_i()$, $i = 1, \dots, 4$ are transmission functions for the corresponding terms. Under narrow wavelength intervals, which allow monochromatic approximation, the following relations are assumed:

$$t_3(\lambda, \mu) = t_4(\lambda, \mu) = t_1(\lambda, \mu) \quad \text{and} \quad t_2(\lambda, \mu, \mu_o) = t_1(\lambda, \mu)t_1(\lambda, \mu_o)$$

A Lambertian approximation is used for the reflection of the downward solar diffuse radiance and the atmospheric thermal radiance. The anisotropic factor in (25.2) is defined by the ratio of the surface-reflected solar beam in the radiance view direction that would result if the surface reflects the solar beam isotropically,

$$\alpha = \pi f_r(\mu; \mu_o, \phi_o)/r \quad (25.2)$$

where r is the reflectance of the assumed Lambertian surface.

Equation (25.1) is used to define band-averaged radiance by integrating it over the whole spectral range with its spectral response function as weight, resulting in an approximate expression of the band radiance

$$L(j) = t_1(j)\varepsilon(j)B_j(T_s) + L_a(j) + L_s(j) + [t_2(j)\alpha_j\mu_o E_o(j) + t_3(j)E_d(j) + t_4(j)E_t(j)](1 - \varepsilon)/\pi \quad (25.3)$$

where all terms are band-averaged, $E_d(j)$ and $E_t(j)$ are band-averaged downward solar diffuse and atmospheric thermal irradiances. Uncertainties exist in this band radiance expression (25.3), because the integral of a product of two or more functions do not exactly equal the product of integrals of each individual function. The magnitude of the uncertainty depends on the bandwidth and the relative spectral variations in surface emissivity and atmospheric transmission functions in the whole band. The spectral variations are smaller in narrower MODIS bands; therefore, the uncertainties resulting from using (25.3) are smaller for MODIS TIR bands than for wider AVHRR (Advanced Very High Resolution Radiometer) TIR bands. The maximum uncertainty magnitude in MODIS bands 20–23 in the 3.5–4.2 μm spectral range is approximately 2%, corresponding to a maximum uncertainty of 0.5 K in the brightness temperature of the band radiance. Simpler forms of (25.1) and (25.3) are potentially used for the TIR bands with wavelength range above 8 μm because the solar radiation terms are negligible in the long-wave TIR range. The uncertainties resulting from using (25.3) for MODIS bands 31 and 32 (around 11 and 12 μm , respectively) are very small because the surface emissivities of all terrestrial materials and the atmospheric transmission functions vary a little in these two narrow bands.

As well known, the reflectance/emissivity of natural land surfaces, especially covered with vegetation, are not measurable by laboratory instruments from samples

taken from the field. Preserving the surface structure and roughness in the laboratory instruments is difficult given the variations in the results with the sample preparation procedures and methods. Therefore, Thermal Infrared Multispectral Scanner (TIMS) overflights of deciduous forests in New England failed to show an obvious difference between the apparent emissivity spectra (in the 8–12 μm spectral range) of beech and other species, despite the relatively high spectral contrast of individual beech leaf spectra measured in the laboratory (Salisbury and D’Aria 1992). Similarly, TIMS could not discriminate the apparent emissivity contrasts of harvested winter wheat and pasture, although there was a large contrast (–0.08 vs. 0.36) in their Normalized Difference Vegetation Index (NDVI) values (French et al. 2000). In the measurements of reflectance spectra (in the 2.5–20 μm spectral range) of dry plant materials, Elvidge (1988) prepared samples in powdered form either at leaf level or compound level of plant material constituents, such as cellulose, lignin, starch, and wax, and placed the samples under a 1-mm TIR beam of a Fourier transform interferometer (FTIR) with a biconical reflectance attachment. A common feature of the dry plant materials was that the highest reflectance contrast occurred in the 3–6 μm spectral range. To measure reflectance, transmittance, and emissivity spectra of single leaf samples in green and dry conditions, a series of measurements were made with a specially adapted FTIR with an attached integration sphere. The same leaf sample was measured twice, the first time placed on a gold reference plate and the second on a krylon black-painted plate. The leaf sample was kept at the sample position under the sample port while changing the underlying plates. Because these two plates have very different reflectance values (around 0.95 for the gold plate and around 0.05 for the krylon plate), any significant difference beyond noise in the raw reflectance spectra of the leaf sample from these two measurements is due to the contribution of the TIR signal penetrating through the leaf sample. A fresh ivy leaf (roughly 0.18-mm thickness) was used in the beginning of a series of measurements, which then was baked in an electric oven in steps (5 s each time). The spectral measurements were repeated until the ivy leaf was extremely dry before nearly getting burned. Figure 25.1 shows the results from the spectral measurements of the ivy leaf in fresh and very dry conditions. The noise level in the raw apparent reflectance spectra is about 0.005–0.0075 in the 8–14 μm spectral region and 0.01–0.02 in the 5.7–7 μm region. A running average for the spectral data was computed to increase the signal-to-noise ratio. The transmittance spectra (plot a) calculated from the apparent reflectance differences measured with these two plates are negligibly small (<0.02) for the fresh leaf in the whole spectral region and very small (<0.03) for the dry leaf in the 6–14 μm region considering the noise level in this spectral region. However, the transmittance of the same leaf in dry condition is significant in the 3.5–6 μm spectral region. The single reflectance (in the lower portion of plot b) of the leaf changes significantly only in the 3.5–6 μm region when it changes from fresh (green) to dry (yellow) condition, and is quite low (<0.05) in the whole spectral region for fresh condition. Similarly, the emissivity of the single ivy leaf (in the upper portion of plot b) varies significantly with water content only in the 3.5–6 μm spectral region, and its variation in the 8–14 μm

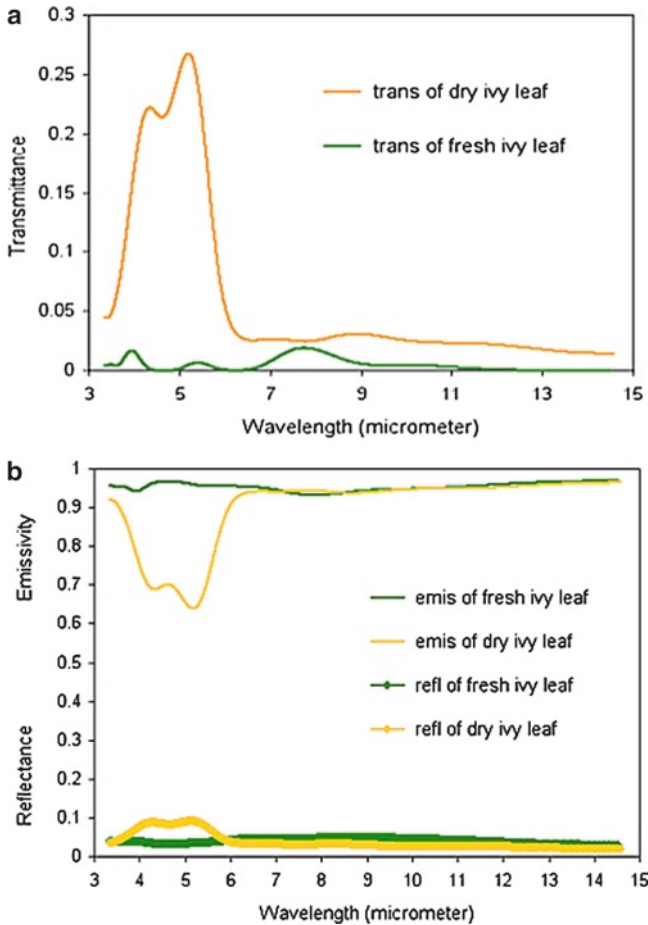


Fig. 25.1 Transmittance (in plot a), reflectance and emissivity (in the lower and upper portions of plot b, respectively) spectra of a single ivy leaf (about 0.18-mm thick) in fresh and extremely dry conditions

region is negligible. This result explains why the TIMS (8–12 μm region) data cannot discriminate a harvested winter wheat field with dry vegetation from a pasture in green condition (French et al. 2000). This indicates that we should not expect any obvious changes in the MODIS day/night algorithm-derived surface emissivities (bands 29 and 31–32) in vegetated areas from wet to dry seasons, unless there are significant changes in vegetation coverage and canopy structures, and soil with a low emissivity (usually in the 8–10 μm) in dry conditions. Note the low emissivity value (<0.75) of the single dry ivy leaf in the 4–5.5 μm region in Fig. 25.1 does not represent the real emissivity of vegetation canopy on the Earth surface because of the following: (1) the emissivity of a stack of multiple dry ivy leaves is predictably larger than 0.9 even in the 4–5.5 μm region; (2) the vegetation is not extremely dry

in normal conditions; and (3) the vegetation canopy structure tends to reduce reflectance and increase emissivity significantly.

The LST in the MODIS LST product is the radiometric (kinetic) temperature derived from the TIR radiation emitted by the land surface, and measured instantaneously by MODIS. Section 25.2 discusses the MODIS LST algorithms and their implementation in the V5 LST Product Generation Executive (PGE) code, test results, validation, and error analysis.

25.2 MODIS LST Algorithms and Their Implementation in the LST PGEs

The MODIS LST suite comprises two algorithms. One is the generalized split-window algorithm (Wan and Dozier 1996), whose formula is similar to the split-window method used for AVHRR data (Becker and Li 1990) to retrieve LSTs of clear-sky pixels by applying classification-based emissivities in the split-window bands (Snyder et al. 1998). Another is the physics-based day/night algorithm (Wan and Li 1997) to retrieve surface spectral emissivity and temperatures at 5 (in V3 and V4) or 6 km (in V5) grids from a pair of daytime and nighttime MODIS data in seven TIR bands. As the theoretical bases and mathematical methods of the two MODIS LST algorithms (Wan and Dozier 1996; Wan and Li 1997) have not changed, and a large number of references are provided in these two papers, details are not repeated here. Wan et al. (2002b, 2004b) describe key points in the implementation of these two algorithms in the V3 and V4 PGE codes, respectively. Wan (2008) describes the major refinements and validation of the V5 LST PGEs. This chapter only highlights some of the main points.

The V4 PGE16 code consists of two parts, the granule-based PGE16A and the tile-based PGE16B. The V5 PGE16 code consists of three parts: revised PGE16A and PGE16B, plus a new PGE16C that removes cloud-contaminated LSTs in the V5 1-km product (MOD11A1 from Terra MODIS data and MYD11A1 from Aqua MODIS data) and the 6-km product (MOD11B1 and MYD11B1) using constraints on the temporal variations in clear-sky LSTs over a 32-day period. The granule-based PGE16A retrieves LSTs for clear-sky land pixels in each granule containing 5 min of MODIS data with the generalized split-window algorithm. PGE16A calculates the coverage of each land pixel on 1-km grid and selectively cumulates the radiance contribution in band 31 at the pixel's retrieved LST to its overlapping 1-km grid in the Sinusoidal projection (Masuoka et al. 1998). This selective radiance accumulation means that the radiance at a higher LST value is selected to avoid a temporal average and possible cloud contamination effects. In the Sinusoidal projection, each tile covers a portion ($10^\circ \times 10^\circ$ at the equator, approximately 1,100 km \times 1,100 km) of the earth's surface, and contains $1,200 \times 1,200$ grids, each of 0.93 km \times 0.93 km size, nominally called a 1-km grid. The Sinusoidal projection is selected as the common projection for the level 3 MODIS land products, because all the grids in this projection have equal areas. Finally, the selectively cumulated radiance values are converted to LST_Day_1 km or LST_Night_1 km in the level-3

1-km LST product (MOD11A1). PGE16A also selectively cumulates the radiance contributions in seven bands, and other related pixel information in 6-km grid, and saves or updates these values in interim updated (UPD) files. The UPD files are used in the daily tile-based PGE16B. PGE16B-derived LSTs and surface emissivities with bands 20, 22, 23, 29, 31, and 32 using the day/night LST algorithm (Wan and Li 1997) is a further development of the temperature-independent spectral index method (Li and Becker 1993). This provides a capability to scale atmospheric parameters to better resolve the nonlinearity problem in LST and emissivity retrievals.

The regression method used to develop the day/night algorithm to assign the initial values is no longer used in the operational processing, because the initial values are provided by the split-window method or estimated from the input MODIS data products. Note that the day/night algorithm is not simply a two-temperature method, as the day and night observation pairs used must meet some special requirements: the daytime observed solar zenith angle is $\leq 75^\circ$, the nighttime observed solar zenith angle needs exceed 90° (in other words, no direct solar beam is seen at the land surface), and the day and night observation dates need fall within 32 days. Given these requirements, the daytime solar radiation in the 3.5–4.2 μm mid-infrared region (MODIS bands 20, 22, and 23) provides active infrared signal to retrieve surface reflectance values in these three bands using a combination of the land-leaving radiance values in the night observation. By applying some realistic assumptions on the surface optical properties, surface emissivities and temperatures from day and night observations are retrievable while treating column water vapor and surface air temperature values in those observations as variables in the nonlinear problem. Given these requirements, the day/night algorithm is usable only in limited time periods during the year in high-latitude regions.

Temporal averaging was applied to generate the V4 1-km LST product, but is discontinued in the V5, as per request of the user community. Following this change, LSTs in 1- and 6-km product are all derived from instantaneous MODIS observations. This change is also necessary to facilitate removal of cloud-contaminated LSTs in the V5 1-km LST product.

The grid size for the day/night algorithm-derived LST/emissivity products was changed to 5.56 km \times 5.56 km (6 km) from 4.63 km \times 4.63 km (5 km) in V4. This matches the Climate Modeling Grid's (CMG) 0.05° grid size used for most CMG land products, and also helps avoid uncertainties from resampling.

The number of viewing angle subranges for the day/night algorithm-derived interim data file (UPD) was increased from 5 and 4 in V4 and V3, respectively, to 16 in V5. We accomplished this without significantly increasing the file size by optimizing the data structure. In the MODIS MOD03 geolocation file, the "Sensor Zenith" attribute provides the Earth surface's view-zenith angle.

The maximum view-zenith angle is about 65° at the swath edges. The UPD file's data structure provides three dimensions: the first defines rows (in latitude direction), the second, columns (in longitude direction), and the third defines bins for the view-zenith angles. Each bin, corresponding to a subrange of view-zenith angles, contains a dataset for one daytime observation (including the brightness

temperatures of radiances in seven bands) and a dataset for one nighttime observation. After increasing the number of subranges, a maximum of 16 sets of daytime and nighttime data are potentially stored for each 6-km grid. This larger dataset reduces the chances for cloud-contamination together with two special procedures in the tile-based PGE16B: one for selecting daytime and nighttime observation pairs with higher brightness temperatures in band 31, and another for setting the initial band emissivity at fixed values rather than assign retrieved values, which are possibly contaminated by cloud effects.

The V5 tile-based PGE16B code fully incorporates the view-angle dependent, generalized split-window method into the day/night algorithm. It uses bands 31 and 32 emissivities, the column water, and low boundary air temperature to iterate the day/night algorithm solution. Therefore, the split-window method is used not only as a constraint, but also as a close component of the day/night algorithm, thus effectively increasing the weights of the highest quality data from bands 31 and 32 for an improved simultaneous retrieval of surface emissivities and temperatures.

Over a period of 8 days, MOD11A1 data are used as input to the 8-day LST PGE31 to composite and average the daily LST values to generate the 8-day LST product (MOD11A2). The logic for the MOD11A2 product is that some applications require spatially distributed LSTs (as complete as possible) at a coarser temporal resolution, and the MODIS instrument repeats its orbit patterns every 16 days.

The daily MOD11B1 data are used as input to the daily CMG PGE32 to generate the LSTs as climate modeling grids (0.05° latitude \times 0.05° longitude) in the daily CMG LST product (MOD11C1). In PGE32, the LST_Day_6 km in MOD11B1 produced by the day/night algorithm is used as the primary source for the LST_Day_CMG. If unavailable, LST_Day_6 km_Aggregated_from_1km, originally from the split-window algorithm, is used as a secondary source. The LST_Night_CMG in the MOD11C1 product is handled similarly. If the LST_Day_CMG and LST_Night_CMG values derive from the aggregated data, the MOD11C1 band emissivities have valid values only in bands 31 and 32, originally estimated from land cover types. The daily MOD11C1 is used as input to CMG PGE58 and PGE59 to generate the 8-day and monthly CMG LST products MOD11C2 and MOD11C3, respectively.

As part of the V5 LST processing, the cloud-contaminated LSTs in the level 2 product (MOD11_L2 and MYD11_L2) are not removed because of the difficulty in dealing with both daily variation and diurnal variation in the clear-sky LSTs. Future reprocessing efforts will resolve this issue.

25.3 Test Results of the V5 PGE16 Code

The V5 PGE16 code was tested with Terra MODIS data in January and July 2003.

Figure 25.2 compares the MOD11B1 images before (on the left side) and after (on the right side) removing the cloud-contaminated LSTs in two tiles, h17v05 and h21v05. The first tile covers Spain and northwest Africa, while the second one covers the Middle East region between latitudes 30° and 40° . On the top are daytime

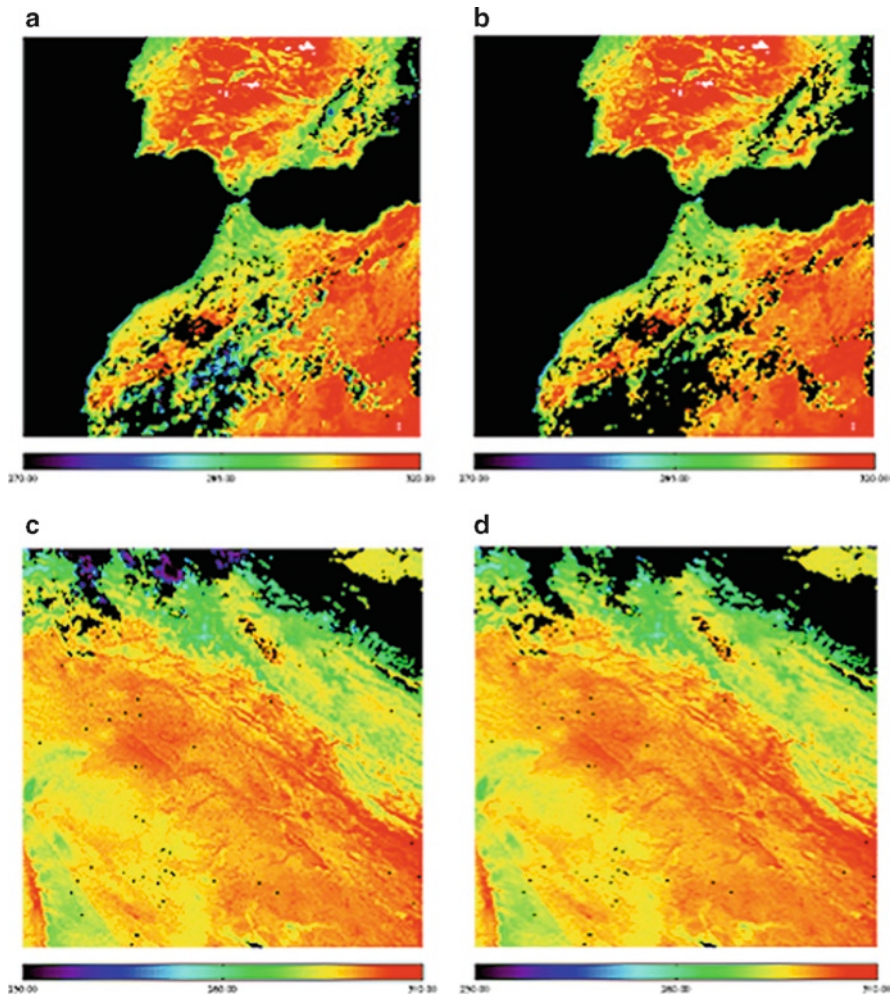


Fig. 25.2 Daytime LSTs (**a** and **b**) in MOD11B1.A2003203.h17v05 (7/22/03) and nighttime LSTs (**c** and **d**) in MOD11B1.A2003204.h21v05 (7/23/03) before (**a** and **c**) and after (**b** and **d**) cloud-contaminated LSTs were removed. Ocean and cloudy areas are in *black*. The minimum daytime LST value in (**a**) is 264.68 K and 284.26 K in (**b**). The minimum nighttime LST value in (**c**) is 247.74 K and 269.98 K in the mountainous area (where surface elevation is more than 3,500 m above sea level) in (**d**)

LST images, and at the bottom are nighttime images. The minimum daytime LST value is 264.7 K before removing the cloud-contaminated LSTs (in image A) or 284.3 K after removal (in image B). The minimum nighttime LST value is 247.7 K (in image C) or 270.0 K in the mountain area, where surface elevation is more than 3,500 m above sea level (in image D). Obviously, such low values for the minimum

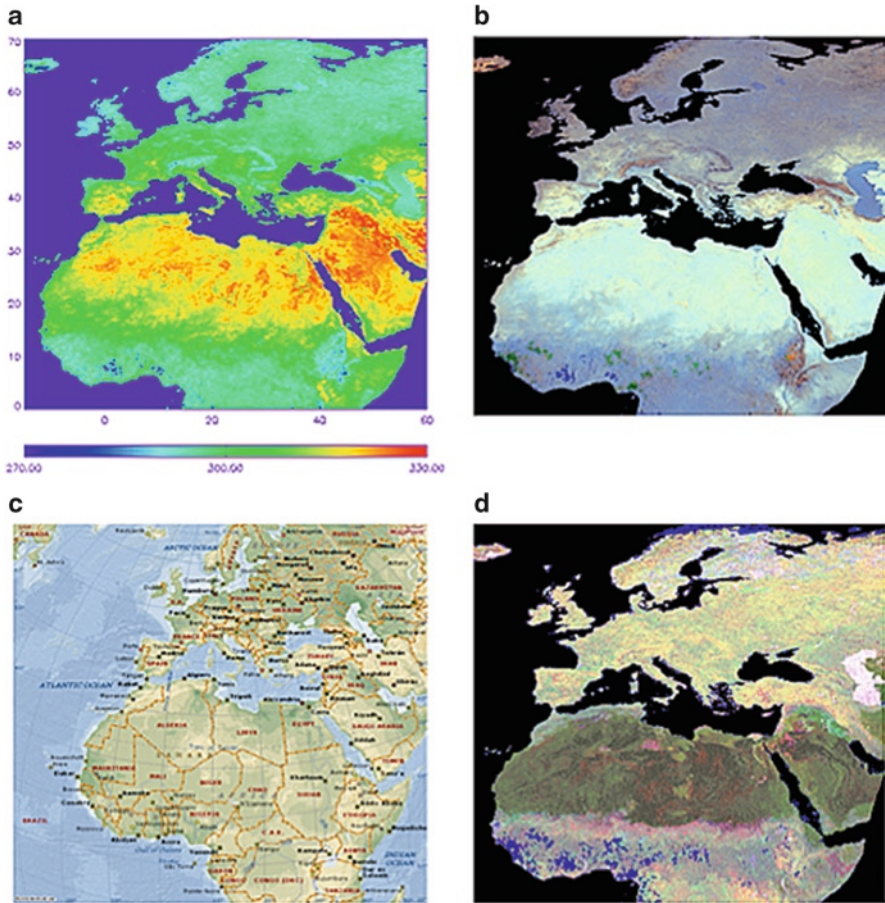


Fig. 25.3 (a) Monthly averaged daytime LSTs in Europe and North Africa from the MODIS CMG LST product (MOD11C3) in July 2003. (b) Color composite generated by using histogram equalization-enhanced day-night differential LSTs, day LSTs, and night LSTs as RGB components. (c) Regional map (Courtesy of Microsoft Mappoint online service). (d) Color composite generated by using histogram equalization-enhanced emissivities in bands 22, 29, and 31 as RGB components

LSTs in images A and C (on the left side) are cloud contaminated, and hence the cloud-contaminated LST removal in PGE16C is necessary.

Figure 25.3 shows monthly averaged daytime LSTs (in plot a) in Europe and North Africa from the MODIS CMG LST product (MOD11C3) in July 2003. Plot b provides a color composite image generated using histogram equalization-enhanced day-night differential LSTs, daytime LSTs, and nighttime LSTs as RGB components. Plot c is a map depicting the region (courtesy of Microsoft MapPoint online service). Plot d is the color composite image generated using histogram-equalization-enhanced emissivities in bands 22, 29, and 31 as RGB components.

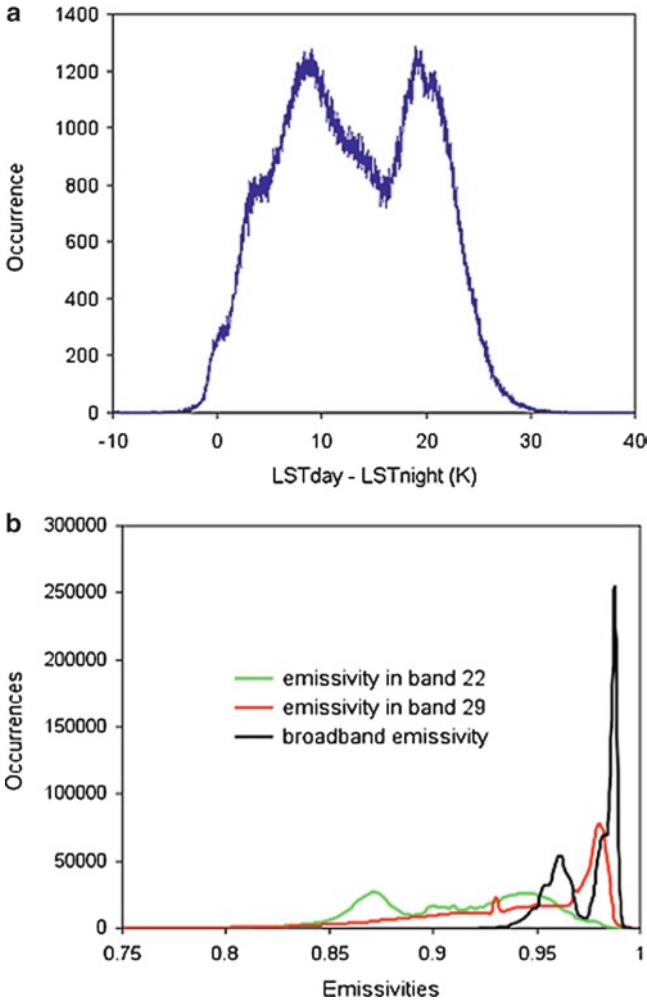


Fig. 25.4 Histograms of the day/night LST differences (a) and emissivities in bands 22 and 29, and broadband emissivity (b) based on the global monthly CMG LST product (MOD11C3) in July 2003. According to Wang et al. (2005), broadband emissivity $\epsilon_{bb} = 0.2122\epsilon_{29} + 0.3859\epsilon_{31} + 0.4029\epsilon_{32}$

Evident are the most obvious features in semiarid and arid regions, especially in northern Africa and Middle East: high daytime LSTs, large day-night LST differences, and low emissivity values in bands 22 and 29.

Figure 25.4 shows histograms of the day-night LST differences (in plot a) and emissivities in bands 22 and 29, and broadband emissivity (in plot b) based on the global monthly CMG LST product (MOD11C3) in July 2003. The cosine of latitude at the land grids in the MOD11C3 product was used as weight to calculate histograms to normalize the equal angle grids to equal area grids.

25.4 Validation and Uncertainty Analysis

Two different methods were used to validate the TIR data-derived LST product: a conventional temperature-based method and an advanced radiance-based method. These two methods were used to validate the V5 LST product (Wan 2008).

Surface emissivity spectra were measured with a sun-shadow method in three field campaigns, one each in Railroad Valley playa, Nevada, in late June 2003, in a grassland (>80% cover) larger than 10 km × 10 km in Dallam County, Texas, in April 2005, and in a bare soil site on the west bank of Salton Sea, California, in June 2006. A TIR interferometric spectroradiometer was deployed in the central portions of the test sites to measure the surface-leaving radiance spectra in the spectral region from 3.5 to 14 μm under sunshine and sun-shadow conditions. Two blackbodies, one at ambient temperature and the other at higher temperatures, were used to calibrate the radiance to an accuracy of better than 0.1 K for the brightness temperature of the radiance. The solar and environmental downward irradiance under sunshine and sun-shadow conditions were measured with a sandblasted aluminum plate placed above the surface target. This aluminum plate reflects the solar radiation like a diffuse reflector as long as the solar incident angle is not far from nadir. The spectral reflectivity of the plate was measured in laboratory.

The averaged radiance values for seven MODIS bands (bands 20, 22, 23, 29, and 31–33) were calculated from the surface target and aluminum plate's measured radiance spectra under sunshine and sun-shadow conditions with the MODIS bands' relative spectral response functions as weights. Based on these averaged radiance values, the surface target's temperature under sunshine and sun-shadow conditions, and the surface band emissivities were extracted using the sun-shadow method, which is similar to but simpler than the day/night method. After the surface temperature in sun-shadow conditions was determined, the surface spectral emissivity was retrieved from the measured surface radiance spectra and aluminum plate under sun-shadow conditions. The quality of the retrieved emissivity spectra depends on the stability of the atmospheric conditions during the whole measurement process, which takes about 10 min. The error in the measured emissivity spectra in the 10.5–12.5 μm range is <0.005 in clear-sky conditions. Radiosonde balloons were launched to measure the temperature and water vapor profiles during the field campaigns. Using the measured atmospheric profiles, the surface emissivity spectrum, and the LST values at the validation sites, MODTRAN4-based radiative transfer simulations were performed to calculate the TOA radiances for the radiance-based validation of the MODIS LST product. The major sources of uncertainties in the radiance-based validation include error ramifications on the following: the surface emissivity spectrum measured by the sun-shadow method; the measured atmospheric temperature and water vapor profiles; the radiative transfer simulations; and in the MODIS calibrated band 31 radiance. The uncertainty effect (about 0.005) on temperature in the surface emissivity spectra is about 0.3 K. In a typical atmospheric profile (column water vapor at 2.2 cm and lower boundary temperature at 310 K), the effects of increasing column water

vapor by 10% and air temperatures by 1 K on band 31's TOA brightness temperature radiance are -0.2 and 0.2 K, respectively.

Comparisons between V5 LSTs and in situ values in 47 clear-sky cases (Wan et al. 2002b, 2004b; Coll et al. 2005) indicate that the MODIS LST product accuracy is better than 1 K in most cases (39 out of 47) in the LST range from -10 to 58°C and atmospheric column water vapor range from 0.4 to 3.5 cm, and the RMS difference is <0.7 K for all 47 cases or 0.5 K for all but eight cases apparently with heavy aerosol loadings (Wan 2008). Emissivities derived by the day/night algorithm compare well to the surface emissivity spectra measured by the sun-shadow method in the three field campaigns.

An analysis of the differences between the day/night algorithm-derived LSTs and those from the independent generalized split-window algorithm produced mean and standard deviation differences of less than 0.2 and 0.5 K, respectively. The temperature source for these differences includes the errors in land cover-dependent classification-based emissivities in bands 31 and 32 errors in both LST algorithms.

The main error sources in the day/night algorithms include four components: (1) Besides bands 31 and 32 used in the split-window algorithm, five more bands (bands 20, 22, 23, 29, and 33) used in the day/night algorithm have larger calibration errors (Wan et al. 2002a) as well as noise-equivalent temperature differences (NE ΔT) (Wan et al. 2004b). (2) The effect of different subpixel temperature components is larger in the mid-infrared bands (bands 20, 22, and 23). (3) Although MODIS achieved a subpixel geolocation accuracy of approximately 50 m (1σ) at nadir (Wolfe et al. 2002), the TIR radiance error at equal-area grids in Sinusoidal projection depends on the spatial variation in LSTs. We account for this dependency thus: one location-fixed grid is possibly covered by variable portions of multiple pixels with dynamic locations and variable sizes that depend on observation time and viewing angles. Therefore, a grid's radiance value is unavoidably affected by contributions from parts outside the grid. (4) The surface emissivity at a given grid may differ at the time of a pair of daytime and nighttime MODIS observations due to high-frequency events such as rains, snow, and dew at night. A quantitative analysis of the last two error sources (3 and 4) without sound knowledge of the LST and surface emissivity distributions at fine subpixel resolutions is difficult. In fact, these two error sources also affect the level-3 1-km LST product (M*D11A1), which derives from the split-window algorithm. The actual spatial resolution of LSTs in M*D11A1 depends on viewing angles of the MODIS observations. It retains the 1-km resolution in the MODIS-observed areas at and near nadir, but is likely much coarser than 1 km at MODIS-observed grids at larger viewing zenith angles near the swath edges. The relative contribution from variable portions outside the grid is smaller because coarser 6 km grids are used in the day/night algorithm-derived temperature and emissivity products. The effect of dew occurrence or changes in the surface moisture condition on surface emissivity is smaller in the 10–13.5 μm spectral range (covered by bands 31–33), because all land cover types in this spectral range already have high emissivities, even under dry conditions.

To reduce the effect of dew occurrence on the performance of the day/night algorithm, smaller weights are assigned to bands 20, 22, 23, and 29 for nighttime observations. An analysis of M*DI1B1 time-series finds that the maximum random error in the retrieved emissivities in bands 20, 22, and 23 is approximately 0.04, which corresponds to 1-K maximum temperature error in these bands. The nighttime LST errors are reducible by using smaller weights in these mid-infrared bands. The split-window method-derived LSTs using the classification-based emissivities in bands 31 and 32 are not far from the day/night algorithm-derived LSTs using MODIS day/night data pairs in seven TIR bands. Although these two algorithms produce compatible LSTs at different spatial resolutions, only the day/night algorithm can retrieve emissivity in the mid-infrared range (covered by bands 20, 22, and 23) and band 29. Land cover types do not help accurately estimate emissivity from these bands because of their high variability.

25.5 Conclusions

The MODIS LST product is used in a growing number of applications. For example, the MODIS LST and NDVI products are used to monitor drought in the U.S. Great Plains (Wan et al. 2004a) and estimate evaporative fraction (Wang et al. 2006). Band 29 emissivity is used in geology studies and to estimate broadband emissivity to calculate long-wave radiation. Wang et al. (2005) estimate broadband emissivity with the retrieved band emissivities in bands 29 and 31–32.

To generate high-quality LSTs from TIR data and also minimize the cloud-contaminated LSTs in an operational product is difficult. New refinements for V5 LST PGE16 were made and tested with Terra and Aqua MODIS data. The V5 PGE16 is used in the Collection 5 (C5) reprocessing since July 2006. The C5 reprocessing completion in mid-2008 will produce an 8-year (2000–2008) record of V5 Terra MODIS LST products and a 6-year (2002–2008) record of V5 Aqua MODIS LST products. These refinements significantly improved the spatial coverage of LSTs, especially in highland regions, and the accuracy and stability of the MODIS LST products. The mean and standard deviation of the differences between the LSTs retrieved from the day/night method and the independent generalized split-window method are less than 0.2 and 0.5 K. Comparisons between V5 LSTs and in situ values in 47 clear-sky cases (LST: -10 to 58°C; and atmospheric column water: 0.4–3.5 cm) indicate that the accuracy of the MODIS LST product is better than 1 K in most cases (39 out of 47) and the RMS difference is <0.7 K for all 47 cases, or 0.5 K for all but eight cases with heavy aerosol loadings. Emissivities retrieved by the day/night algorithm compare favorably to the surface emissivity spectra measured by a sun-shadow method in three field campaigns.

Acknowledgments This work was supported by EOS Program contracts NAS5-31370 and NNG04HZ15C of the National Aeronautics and Space Administration. Dr. Li's work is partly supported by China's National Natural Science Foundation under Grant 40425012, and the

“Hundred Talent” program of the Chinese Academy of Sciences. Larry Zangwill performed the spectral measurements of ivy leaf samples in the laboratory of the UCSB MODIS LST Group and participated in LST validation field campaigns.

References

- Barnes WL, Pagano TS, Salomonson VV (1998) Prelaunch characteristics of the Moderate Resolution Imaging Spectroradiometer (MODIS) on EOS-AM1. *IEEE Trans Geosci Remote Sens* 36:1088–1100
- Becker F, Li Z-L (1990) Toward a local split-window method over land surface. *Int J Remote Sens* 3:369–393
- Berk A, Anderson GP, Bernstein LS, Acharya PK, Dothe H, Matthew MW, Adler-Golden SM, Chetwynd JH Jr, Richtmeier SC, Pukall B, Allred CL, Jeong LS, Hoke ML (1999) MODTRAN4 radiative transfer modeling for atmospheric correction. *Optical Spectroscopic Techniques and Instrumentation for Atmospheric and Space Research III. Proc SPIE* 3756:348–353
- Coll C, Caselles V, Galve JM, Valor E, Nicolòs R, Sánchez JM, Rivas R (2005) Ground measurements for the validation of land surface temperatures derived from AATSR and MODIS data. *Remote Sens Environ* 97:288–300
- Elvidge CD (1988) Thermal infrared reflectance of dry plant materials: 2.5–20.0 μm . *Remote Sens Environ* 26:265–285
- French AN, Schmugge, TJ, Kustas WP (2000) Discrimination of senescent vegetation using thermal emissivity contrast. *Remote Sens Environ* 74:2), 249–254
- Li Z-L, Becker F (1993) Feasibility of land surface temperature and emissivity determination from AVHRR data. *Remote Sens Environ* 43:67–85
- Mannstein H (1987) Surface energy budget, surface temperature and thermal inertia. In: Vaughan RA, Reidel D (eds) *Remote sensing applications in meteorology and climatology*, Reidel, 1987, NATO ASI Ser. C: Math. Phys. Sci., vol. 201. Dordrecht, The Netherlands, pp 391–410
- Masuoka E, Fleig A, Wolfe RE, Patt F (1998) Key characteristics of MODIS data products. *IEEE Trans Geosci Remote Sens* 36:1313–1323
- Salisbury JW, D’Aria DM (1992) Emissivity of terrestrial materials in the 8–14 μm atmospheric window. *Remote Sens Environ* 42:83–106
- Sellers PJ, Hall FG, Asrar G, Strebel, DE, Murphy RE (1988) The first ISLSCP field experiment (FIFE). *Bull Am Meteorol Soc* 69(1):22–27
- Snyder WC, Wan Z, Zhang Y, Feng Y-Z (1998) Classification-based emissivity for land surface temperature measurement from space. *Int J Remote Sens* 19:2753–2574
- Wan Z (2008) New refinements and validation of the MODIS land-surface temperature/emissivity products. *Remote Sens Environ* 112:59–74
- Wan Z, Dozier J (1996) A generalized split-window algorithm for retrieving land-surface temperature from space. *IEEE Trans Geosci Remote Sens* 34:892–905
- Wan Z, Li Z-L (1997) A physics-based algorithm for retrieving land-surface emissivity and temperature from EOS/MODIS data. *IEEE Trans Geosci Remote Sens* 35:980–996
- Wan Z, Wang P, Li X (2004a) Using MODIS land surface temperature and normalized difference vegetation index products for monitoring drought in the Great Plains, USA. *Int J Remote Sens* 25:61–72
- Wan Z, Zhang Y, Li Z-L, Wang R, Salomonson VV, Yves A, Bosseno R, Hanocq JF (2002a) Preliminary estimate of calibration of the Moderate Resolution Imaging Spectroradiometer thermal infrared data using Lake Titicaca. *Remote Sens Environ* 80:497–515

- Wan Z, Zhang Y, Zhang YQ, Li Z-L (2002b) Validation of the land-surface temperature products retrieved from Moderate Resolution Imaging Spectroradiometer data. *Remote Sens Environ* 83:163–180
- Wan Z, Zhang Y, Zhang YQ, Li Z-L (2004b) Quality assessment and validation of the global land surface temperature. *Int J Remote Sens* 25:261–274
- Wang K, Wan Z, Wang P, Sparrow M, Liu J, Zhou X, Haginoya S (2005) Estimation of surface long wave radiation and broadband emissivity using Moderate Resolution Imaging Spectroradiometer (MODIS) land surface temperature/emissivity products. *J Geophys Res* 110:D11109, doi:10.1029/2004JD005566
- Wang K, Li Z, Cribb M (2006) Estimation of evaporative fraction from a combination of day and night land surface temperatures and NDVI: a new method to determine the Priestley-Taylor parameter. *Remote Sens Environ* 102:293–305
- Wolfe RE, Nishihama M, Fleig AJ, Kuyper JA, Roy DP, Storey JC, Patt FS (2002) Achieving sub-pixel geolocation accuracy in support of MODIS land science. *Remote Sens Environ* 83:31–49

Chapter 26

MODIS Vegetation Indices

Alfredo Huete, Kamel Didan, Willem van Leeuwen,
Tomoaki Miura, and Ed Glenn

26.1 Introduction

Assessments of vegetation condition, cover, change, and processes are major components of global change research programs, and are topics of considerable societal relevance. Spectral vegetation indices are among the most widely used satellite data products, which provide key measurements for climate, hydrologic, and biogeochemical studies; phenology, land cover, and land cover change detection; natural resource management and sustainable development. Vegetation indices (VI) are robust and seamless data products computed similarly across all pixels in time and space, regardless of biome type, land cover condition, and soil type, and thus represent true surface measurements. The simplicity of VIs enables their amalgamation across sensor systems, which facilitates an ensured continuity of critical datasets for long-term land surface modeling and climate change studies. Currently, a more than two decades long NOAA Advanced Very High Resolution Radiometer (AVHRR)-derived consistent global normalized difference vegetation index (NDVI) land record exists, which has contributed significantly to global biome, ecosystem, and agricultural studies.

In this chapter, we present the current status of the Moderate Resolution Imaging Spectroradiometer (MODIS) VI products, their algorithm state and heritage, validation, and QA. We highlight some important advances in land remote sensing science, and discuss the full range of applications and societal benefits resulting from the use of MODIS VIs.

A. Huete (✉)
Department Soil, Water & Environmental Science,
University of Arizona, Tucson, AZ 85721, USA
e-mail: ahuete@Ag.arizona.edu

26.2 Definition and Theoretical Basis

Vegetation indices are optical measures of vegetation canopy “greenness,” a *composite* property of leaf chlorophyll, leaf area, canopy cover, and structure. VIs are not “intrinsic physical quantities” but are widely used as proxies to assess canopy biophysical/biochemical variables (leaf area index (LAI), fraction of absorbed photosynthetically active radiation (fPAR), chlorophyll content, green vegetation fraction (Fg), biomass) and canopy biophysical processes (photosynthesis, transpiration) (Choudhury 1987; Tucker 1979). A VI combines the chlorophyll-absorbing red spectral region with the nonabsorbing leaf reflectance signal in the near-infrared (NIR) to depict vegetation “greenness” or area-averaged canopy photosynthetic capacity. A variety of ways exist in which the red and NIR bands are combined to estimate greenness, and this produces a multitude of VI equations, including band ratios and differences (Gallo and Eidenshink 1988), normalized differences (Tucker 1979), linear combinations, and “optimized” band combinations (Huete 1988; Gobron et al. 2000). All VIs are empirically related with various vegetation canopy properties; however, there are significant differences in how they depict “greenness” and multiple VIs are potentially useful and complementary.

The MODIS standard VI products include the NDVI and the enhanced vegetation index (EVI) to more effectively characterize vegetation states and processes, and to better encompass the range of biophysical/biochemical information extractable from vegetated surfaces. The NDVI is a functional variant of the simple ratio (SR = NIR/red) that provides VI values normalized between -1 and +1,

$$\text{NDVI} = (\text{SR} - 1) / (\text{SR} + 1) = (\rho_{\text{NIR}} - \rho_{\text{red}}) / (\rho_{\text{NIR}} + \rho_{\text{red}}) \quad (26.1)$$

Several recent advances in earth science, specific to the global biome and agricultural primary production are attributable to the development and consistency of the AVHRR-NDVI time-series since 1981. They include interannual fluctuations and impacts of El Niño-Southern Oscillation on primary production, phenology, and climate change and variability. The NDVI data record has played a key role in detecting changes in vegetation caused by global temperature increases (Tucker et al. 2005), such as lengthening of the growing season at northern latitudes in response to global temperature increases (Myneni et al. 1997). An important advantage of the NDVI as a ratio, is its ability to normalize and produce stable values across large variations in incoming direct/diffuse irradiances. However, this also results in some disadvantages including the nonlinear nature of ratios, sensitivity to soil background, and saturation at moderate-to-high vegetation densities (Jiang et al. 2006; Huete et al. 2002).

The EVI gains its heritage from the soil adjusted vegetation index (SAVI) and the atmospheric resistance vegetation index, and is an optimized combination of blue, red, and NIR bands, based on Beer’s law of canopy radiative transfer, designed to extract canopy greenness, independent of the underlying soil background and atmospheric aerosol variations (Huete 1988; Kaufman and Tanré 1992),

$$\text{EVI} = 2.5(\rho_N - \rho_R) / (L + \rho_N + C_1\rho_R - C_2\rho_B) \quad (26.2)$$

where $\rho_{N,R,B}$ are reflectances in the NIR, red, and blue bands, respectively; L is the canopy background adjustment factor (Huete 1989); and C_1 and C_2 are the aerosol resistance weights (Liu and Huete 1995). The coefficients of the MODIS EVI equation are $L = 1$; $C_1 = 6$, and $C_2 = 7.5$ (Huete et al. 2002).

The blue band in the EVI is primarily used to stabilize aerosol influences in the red band resulting from residual and aerosol miscorrection (Miura et al. 1998; Xiao et al. 2003). The NDVI is sensitive to the canopy-absorbing “red” band, and has a lower optical penetrating depth in canopies, and thus will saturate more quickly in high biomass areas. The EVI becomes increasingly sensitive to the NIR band at moderate-to-high vegetation amounts with a greater optical depth penetration into canopies. Thus, the EVI will better depict biophysical canopy structural variations, and is less prone to saturate in high biomass areas (Gao et al. 2000).

26.3 Algorithm State and Heritage

Six VI products exist for each of Terra and Aqua MODIS-derived sensors at varying spatial resolutions to best capture the important spatial and temporal complexities associated with vegetation dynamics, biogeochemical and hydrological processes (Table 26.1). This includes moderate resolution, 250 m, 500 m, and 1 km, and coarse resolution, 0.05° (~5.6 km Climate Modeling Grid, CMG) products generated each 16 days, while two standard calendar month products are also generated at 1 km and CMG resolutions to meet the needs of the research and application communities (Fig. 26.1). The products are generated globally over spatial units called tiles that are 10° × 10° (about 1,200 km × 1,200 km at the equator) in the equal-area Sinusoidal projection. No horizontal or vertical tile numbers exist in the global CMG product.

The MODIS science algorithms have undergone several improvements and modifications, including the VIs. The most recent revision, termed “Collection 5” (C5), incorporates changes to known issues and problems identified in the previous Collection 4 (C4). Each new collection supersedes the previous and initiates a complete reprocessing of all MODIS land data products from the first day of data acquisition.

Table 26.1 Terra and Aqua MODIS VI product suites

| Terra MODIS VI products | Aqua MODIS VI products |
|--------------------------|--------------------------|
| MOD13Q1: 16-day 250 m | MYD13Q1: 16-day 250 m |
| MOD13A1: 16-day 500 m | MYD13A1: 16-day 500 m |
| MOD13A2 16-day 1-km VI | MYD13A2 16-day 1-km VI |
| MOD13A3 monthly 1-km VI | MYD13A3 monthly 1-km VI |
| MOD13C1 16-day 0.05° VI | MYD13C1 16-day 0.05° VI |
| MOD13C2 monthly 0.05° VI | MYD13C2 monthly 0.05° VI |

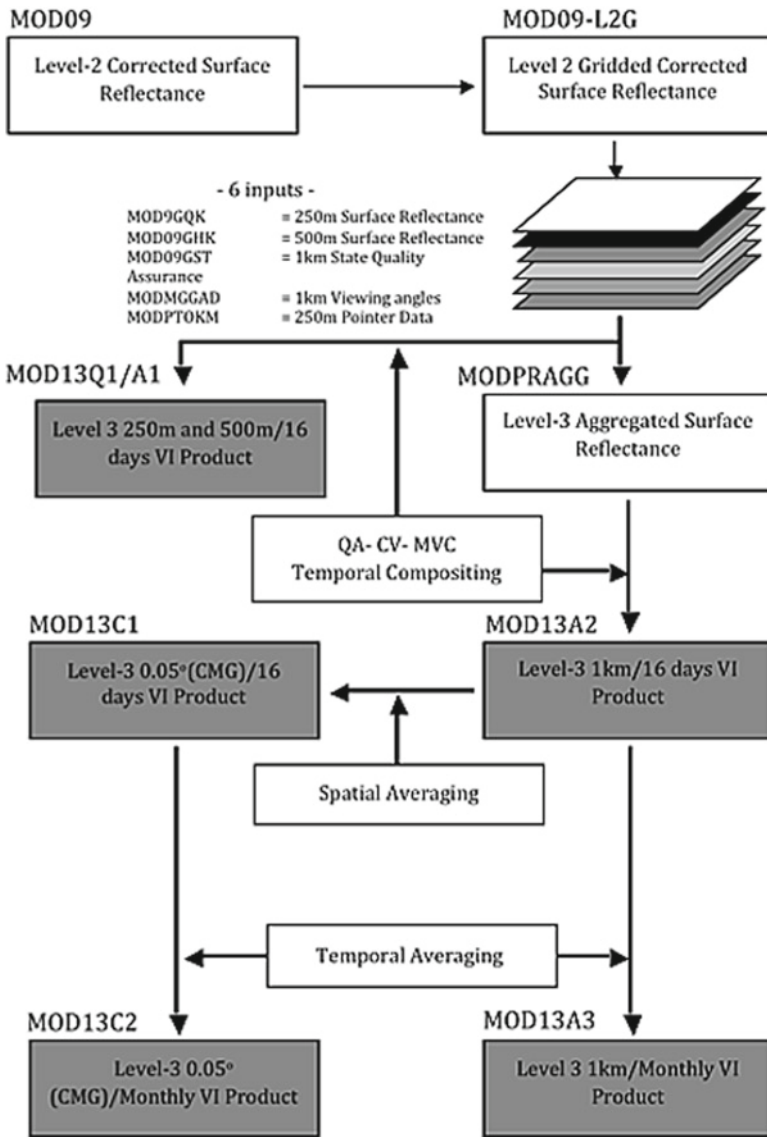


Fig. 26.1 Overview of the Terra MODIS-VI product suite and input dependencies

The MODIS VI product suite contains a set of output parameters known as science datasets (SDS) for each composited, selected pixel, which include the following: (1) composited NDVI and EVI, (2) NDVI/ EVI output quality, (3) reflectances in band 1 (620–670 nm), band 2 (841–876 nm), band 3 (459–479 nm), and band 7 (2,105–2,155 nm), (4) sensor zenith view angle, solar zenith angle, and relative azimuth; (5) day of year, which was added in the C5 product versions, and (6) pixel reliability.

The 500-m and 1-km VI product are computed from aggregated surface reflectances, while the climate modeling grid (CMG, 0.05° resolution) VI product is computed from the averaged reflectance values of good quality 1-km pixel, aggregated to 0.05° using a QA filter scheme that removes lower quality, cloud contaminated pixels. The aggregated CMG VI product includes the following: (1) NDVI and EVI, (2) NDVI and EVI standard deviations of the input 1-km pixel, (3) the number of QA-filtered pixels used to aggregate CMG pixels, and (4) the number of pixels within 30° sensor zenith angle in the CMG pixel.

26.3.1 Compositing Approach

Both the Terra and Aqua MODIS sensors provide nearly complete Earth coverage every day. Due to the ubiquitous presence of clouds and aerosols in daily global imaging sensors, *temporal compositing* of frequent measurements over set time intervals is used to remove clouds, aerosols, and cloud shadow contamination. The composited VIs are produced at 16-day interval from atmospherically corrected (MOD09), surface gridded reflectances with per pixel quality assurance (QA) information that were cloud-filtered. A constrained view angle, maximum value compositing (CV-MVC) method is used to select view angles to within $\pm 30^\circ$. This is carried out with a per-pixel QA-based methodology that selects the closest to nadir value from the two or three highest NDVI values remaining after QA filtering lower quality pixels contaminated by residual clouds, shadows, high aerosol loadings, and large viewing geometries. The selected VI values represent actual, atmospherically corrected VI measurements at local solar zenith angle and close to nadir view geometries while retaining full traceability to the sensor acquisition.

This method is modified from the heritage AVHRR MVC methodology, which selects the highest NDVI value in a compositing cycle to best represent pixel greenness status (Holben 1986). Although maximum NDVI values greatly reduce clouds and aerosols, the highest NDVI value does not necessarily correspond to small sensor viewing angles or to the least-contaminated measurement. The reason stems from the bias resulting from the anisotropic properties of most vegetated surfaces wherein, off-nadir view angles in the forward scatter direction produce the highest NDVI values, even when contaminated by residual clouds and aerosols (Cihlar et al. 1994). With recent advances in atmosphere correction and sensor band-pass avoidance of water vapor and other absorbing gases, surface anisotropic influences are more pronounced and the highest NDVI is increasingly biased toward off-nadir pixel selection.

Potential value-added bidirectional reflectance distribution function (BRDF) applications to further reduce angular variations are possible with the view/sun angle information in the SDSs. For example, Los et al. (2005) adjusted AVHRR-NDVI time-series (Pathfinder AVHRR Land data) to a standard illumination and viewing geometry by applying MODIS-derived kernels, resulting in a 50–85% reduction in BRDF effects.

26.3.2 Dynamic Range of the VI Products

Figure 26.2 depicts the spatial and temporal dynamic range of the MODIS VIs across a range of vegetation cover types, from hyperarid deserts to dense forests. Important vegetation parameters used in climate and hydrological modeling, such as the green vegetation fraction, F_g , are commonly derived through simple linear combinations of high (vegetation) and low (soil) NDVI within a scene or biome.

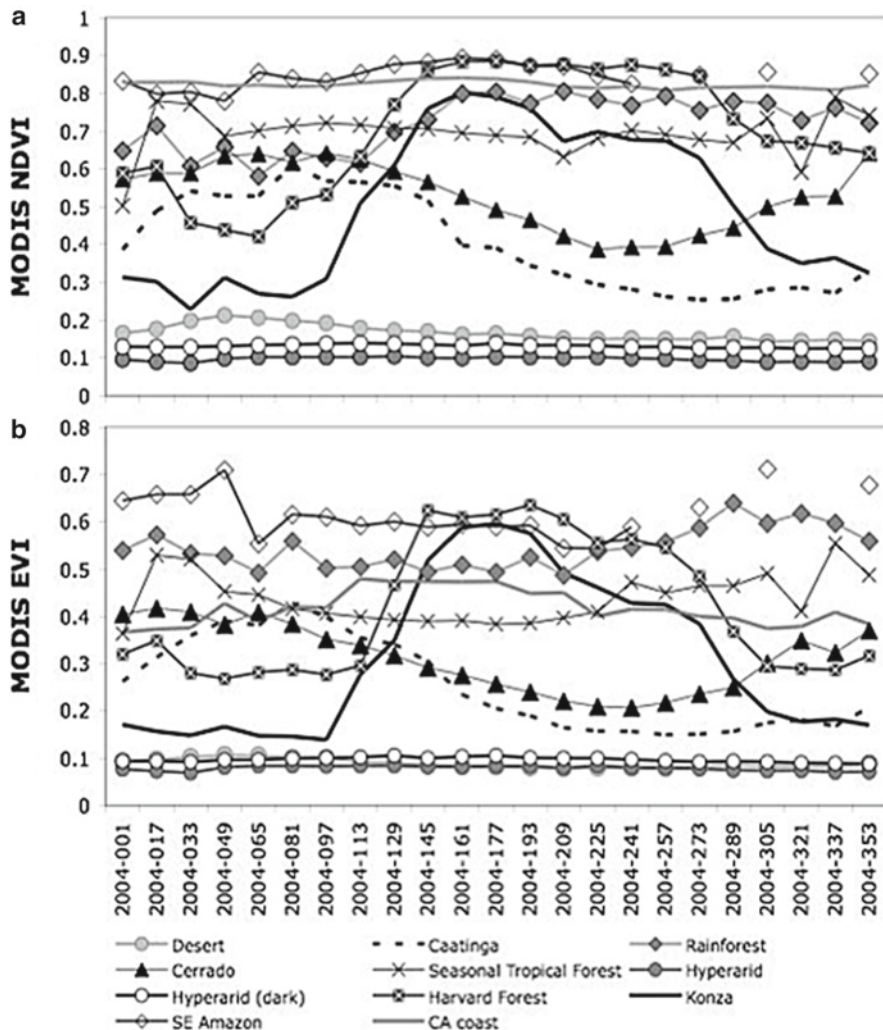


Fig. 26.2 Representative MODIS VI seasonal profiles of major land cover types at 1-km resolution (MOD12A2), depicting dynamic ranges and values

In contrast to the AVHRR-NDVI dynamic range, $NDVI_{soil} = 0.04$ and $NDVI_{dense} = 0.52$ (Gutman and Ignatov 1998), MODIS-NDVI's dynamic range is much greater ($NDVI \sim 0.1-0.90$) due to narrower spectral bandwidths and more complete atmospheric correction (aerosols, water vapor) in the MODIS-NDVI product. The EVI values varied from 0.07 to ~ 0.7 for these same vegetation conditions at 1-km resolution. Several important differences exist between the NDVI- and EVI-based phenology profiles, particularly in the separation of needleleaf and broadleaf forests, the green-up and brown-down patterns of Harvard Forest and the Amazon, and the variation in background values associated with minimum greenness conditions. The EVI has sharper growing season peaks and is sensitive to canopy structure differences, while the NDVI appears more sensitive at the lower range of vegetation conditions while saturating in dense vegetation canopies (Fig. 26.2). The hyperarid desert baseline values are very stable, which suggest radiometrically calibrated bands through approximately 6 years of Terra-MODIS with no aging or degradation effects.

26.4 Validation and Accuracy of the VI Product Suite

The VI product attempts to retrieve cloud-free, near-nadir, top-of-canopy greenness at 16-day interval. Due to the global nature of the algorithm, some problems and uncertainties persist at local scales, mostly associated with residual clouds, shadows, aerosols, atmospheric correction performance, and view sun angle geometries, resulting in nonbiological artifacts and noise in the VI values. The accuracy of the VI product will vary in space and time due to geographical and seasonal variations in cloud persistence, unresolved clouds, the quality of upstream surface reflectance retrievals, sun angle, cross-band (red, NIR) spectral integrity, canopy background (soil, water, snow), topography, and geolocation (Huete and Liu 1994). For example, Miura et al. (2000) noted VI uncertainties due to sensor calibration of 0.01 and 0.02 for the NDVI and EVI, respectively.

Each MODIS VI measurement involves multiple, simultaneous variations in many of these noise sources, making it difficult to assess the influence of individual sources of uncertainty. The MODIS VI product, however, uses a set of QA classes, from best quality observations to fair quality data, to reduce *aggregate uncertainties* in VI values. The selection of the highest QA levels results in the highest confidence of cloud-free, low aerosol, and view angles within 30° of nadir with accuracies and precision within 0.03 and 0.02, respectively. As shown at the Jornada Experimental Range (Gao et al. 2003), VIs are readily computed from field-based, boom-mounted, and aircraft-borne instruments, and from a wide variety of fine and coarse space-based sensors, facilitating the comparison and radiometric validation of MODIS VIs. Light aircraft-mounted sensors, such as MODIS Quick-Airborne Looks (MQUALS), acquire nadir, top-of-canopy reflectance measurements from 150 to 500 m height, that greatly extend locally constrained field measurements to kilometer lengths to aid in validation (Huete et al. 1999).

26.4.1 Angular Sources of Uncertainty

Differences in anisotropic properties between red and NIR reflectances result in unique VI-dependent angular variations that require constraining in the composited VI products for more accurate analysis of vegetation dynamics, including landscape phenology. Fensholt et al. (2006) studied NDVI's dependence on solar and viewing geometries with MODIS and the Meteosat Second Generation (MSG) Spinning Enhanced Visible and Infrared Imager (SEVIRI) sensor. They found higher red reflectances relative to NIR under backscatter conditions, which cause observed NDVI to decrease. In the forward scatter direction, red reflectance data are much more strongly reduced due to shadowing from the highly absorbent vegetated canopies, resulting in higher NDVI. Whereas NDVI is biased positively in forward scatter view directions, the EVI responds more positively to backscatter (sunlit vegetation) view directions; however, since MODIS CV-MVC compositing is based on NDVI values, any positive bias present in NDVI pixel selection will result in a negative bias in EVI values, or underestimation of greenness. In a compositing study of MODIS and AVHRR daily data to map burned area over the Iberian Peninsula, Chuvieco et al. (2005) found the standard MODIS compositing procedure provided close to nadir observation angles and good spatial coherence, while the traditional MVC compositing criterion of maximizing NDVI values provided poor results. A comparison of the MODIS VI compositing algorithm with the heritage MVC technique over an Amazon tile shows significant reductions in view angle influences and improvements in the quality of pixel selection (Fig. 26.3).

An alternative method to assess how well view angle variations are constrained is to compare the VI product with VIs generated with the MODIS Nadir BRDF-Adjusted Reflectance (NBAR) products, MOD43B4 and MCD43A4, which are generated at 1-km/16-day and 500-m/8-day intervals, respectively (Schaaf et al. 2002) (Fig. 26.4). The NBAR product generates nadir reflectances through BRDF model inversions applied to seven or more good QA and cloud-free acquisitions within a 16-day composite cycle. Cross-plots of NBAR VI with the standard VI product over three vegetation types reveal fairly consistent values with relatively small view angle biases (Fig. 26.4b). The MODIS VI and NBAR products are produced at local solar zenith angle, and thus both contain latitudinal and seasonal sun angle influences. Notwithstanding the seasonal significance of the sun angle bias, it is less of a problem in interannual time-series data and trend analyses, provided there is no sensor orbital drift (Los et al. 2005).

26.4.2 Atmosphere and Clouds

The primary inputs to the MODIS compositing algorithm are atmospherically corrected surface reflectances (MOD09), which result in a more accurate and consistent VI product. However, residual effects and artifacts will invariably persist and aerosol miscorrections may occur with high aerosol pixels not corrected to the same

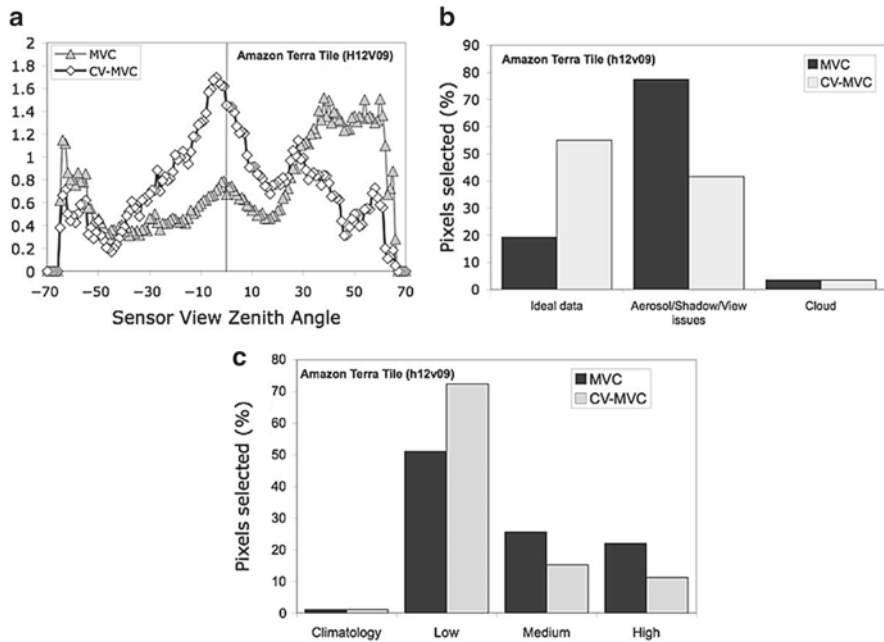


Fig. 26.3 Comparison of view angle distributions for pixels selected using MVC and CV-MVC methods for Amazon Tile (H12V09) (a), and resulting overall QA of output pixels (b), and for aerosol QA (c)

accuracy as low aerosol pixels. Furthermore, uncertainties exist in aerosol correction due to assumptions in the “dark object subtraction” and/or use of aerosol climatology as well as the use of aerosol input parameters at coarser (>10 km) resolution than the 250-m to 1-km VI pixel. Kaufman et al. (2005) found significant problems in aerosol correction attributed to residual cirrus and lower-level cloud contamination, and noted the difficulty of defining cloud contamination vs. aerosol growth. As a result, there likely are significant positive as well as negative error biases associated with atmospheric correction. An overcorrection of aerosols will result in abnormally low red reflectances and very high VI values, especially affecting the red-sensitive NDVI. The VIs are particularly sensitive to any disproportionate correction of the red and NIR bands. The inclusion of the blue band may improve or introduce more uncertainties in the EVI; however, the EVI was found to stabilize atmospheric aerosol effects in the Amazon (Miura et al. 2001) and Northern Asia (Xiao et al. 2003).

26.4.3 Biophysical Validation

An important aspect in validating VIs concerns their ability to capture essential biophysical phenomena with adequate fidelity and with minimal influences from the nongreen component of pixels (soil, nonphotosynthetic vegetation). Numerous

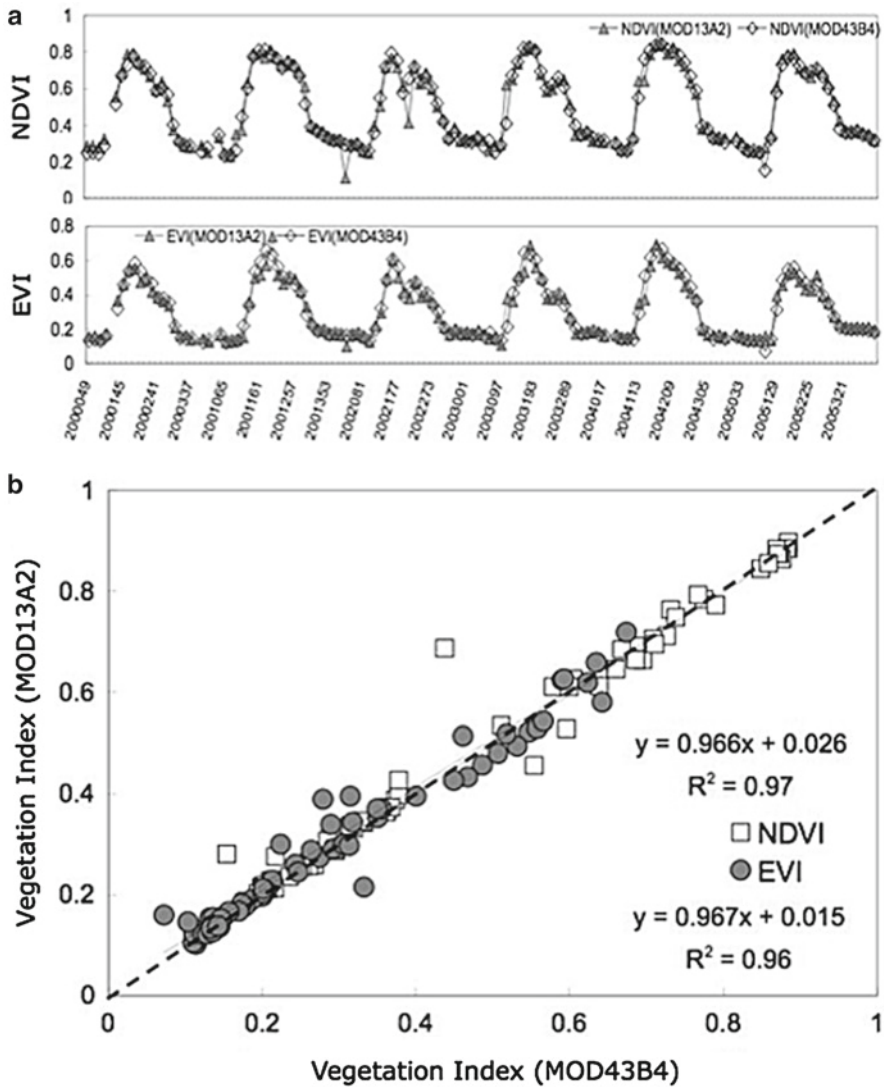


Fig. 26.4 Comparison of MODIS 1-km VI (MOD13A2) with 1-km NBAR generated VI (MOD43B4) for the Konza Prairie site, Kansas, United States over 6 years (a); and linear regression of MOD13A2 with MOD43B4 VIs for Konza Prairie, Lucky Hills shrub site in Arizona, and Harvard Forest in Massachusetts (b)

relationships between VIs and biophysical vegetation properties have been reported over the variable structural assemblages of chlorophyll, vegetation cover, and LAI per plant species or biome type. VI sensitivities and relationships are mostly based on empirical field measurements (Cohen et al. 2003) and canopy radiative transfer models (Huemmrich 2001). Using field-derived LAI values with higher resolution satellite

data, significant albeit nonlinear relationships were found between NDVI and EVI. For example, Chen et al. (2005) studied coniferous forest sites in Siberia with Landsat data. Poorer relationships are common when using coarser MODIS and SPOT-VGT Vis. For example, NDVI-LAI relationships in an European beech deciduous forest varied significantly over different phenology periods, with poor correlations during maximum LAI periods due to NDVI saturation (Wang et al. 2005). Cohen et al. (2003) also showed only weak correlations between field-measured LAI and several MODIS products, including VIs. However, LAI is very difficult to measure on the ground, particularly at scales consistent with MODIS measurements. Evidence shows that EVI enables extended sensitivity over higher LAI/biomass areas whereas the NDVI saturates (Fensholt 2004). Houborg and Soegaard (2004) found MODIS EVI was able to accurately describe the variation in green biomass in agricultural areas in Denmark, up to a maximum green LAI of 5 ($r^2 = 0.91$).

Conversely, the lack of a direct correspondence between VIs and canopy biophysical properties, such as LAI or Fg, does not compromise the utility of VIs in predicting biophysical processes such as photosynthesis or transpiration. Monteith and Unsworth (1990) noted that VIs are legitimately usable to estimate the rate of processes that depend on absorbed light, such as primary production and transpiration, whereas the relationship of LAI or Fg to absorb PAR is strongly nonlinear and depends on leaf architecture and spectral properties. Furthermore, photosynthesis and transpiration are not evenly distributed through the canopy, but are driven mainly by light absorbed by leaves (LAI) at the top of canopy.

Field- and MODIS-based NDVI have demonstrated linear relationships with fPAR across several biome types, and its integral over the growing season was correlated with ecosystem net primary production (NPP) (Asrar et al. 1984; Huemmrich et al. 2005). However, soil background variations introduce noise and uncertainty in NDVI-biophysical relationships on the same order of magnitude as atmospheric contamination (Choudhury 1987; Goward and Huemmrich 1992). Strong, soil-dependent discrepancies in fPAR–NDVI relationships are seen in which, NDVI linearly varies with fPAR in canopies with bright soil backgrounds, while the simple ratio (NIR/red) is linear with fPAR in canopies underlain with darker soil backgrounds (Sellers 1987), hence a nonlinear NDVI relationship with fPAR. The type of soil background not only alters VI-biophysical relationships but affects their degree of linearity with important consequences to scaling (Jiang et al. 2006).

The EVI has proven useful to estimate fPAR in vegetated canopies with relationships that are largely independent of soil background (Gao et al. 2000; Xiao et al. 2004). Zhang et al. (2005) used MODIS data and a coupled leaf-canopy radiative transfer model (PROSAIL-2) and showed significant differences between fPAR absorbed by a canopy ($fPAR_{\text{canopy}}$) and fPAR absorbed by leaf chlorophyll ($fPAR_{\text{chl}}$) in a broadleaf forest canopy, noting that only $fPAR_{\text{chl}}$ is used for photosynthesis and useful to quantify primary production. They found MODIS NDVI approximated $fPAR_{\text{canopy}}$, while EVI was closely coupled with $fPAR_{\text{chl}}$. This was also demonstrated by Xiao et al. (2004, 2005a) with MODIS seasonal analyses in both needleleaf and broadleaf forests, suggesting that EVI is probably more simply related to the chlorophyll content or *canopy greenness*.

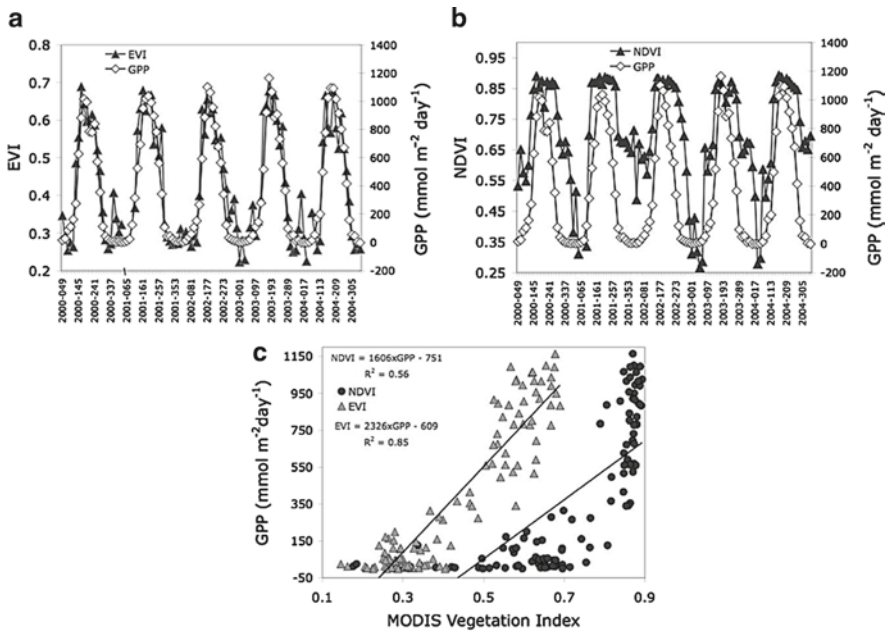


Fig. 26.5 MODIS EVI (a) and NDVI (b) comparisons with 16-day averaged tower flux measurements of gross primary productivity (GPP) for 5 years at Harvard Forest site (3 × 3 MOD13A2 pixels); and linear regression between MODIS VI and Tower GPP (c)

Rahman et al. (2005) and Sims et al. (2006) have shown how MODIS EVI and gross primary productivity (GPP) are highly correlated across a number of North American Ameriflux tower sites. An example of how well seasonal EVI tracks tower-calibrated GPP measurements of carbon fluxes at the Harvard Forest site is shown in Fig. 26.5. In the case of NDVI, there is some saturation and an overestimation of GPP, particularly after the peak growing season, a problem also observed with MODIS NDVI at the Sky Oaks savanna field site (Cheng et al. 2006). The use of tower flux measurements with remote sensing illustrates the power of integrating remote sensing and ground data. The generality of local, single-tower site studies may cast some doubts, and unexpected remote sensing observations are probably attributable to artifacts. For example, from a seasonal interference pattern induced by cloud cover, aerosol, or sun angle, the consistency between the independent VI and tower-derived flux observations lends confidence to both findings.

Each MODIS product revision generates improvements in product quality, and product uncertainties and accuracies are better characterized. To guide the user community in assessing the quality of individual MODIS products, various levels or stages of validation are defined (Morisette et al. 2002). The Collection 5 MODIS VI products are at stage 2 validation, i.e., their performance was assessed over a widely distributed set of locations and time periods with several in situ and validation efforts. The highest, stage 3 validation, will require complete and global product accuracy characterization in a systematic and statistically robust way.

26.5 Science and Applications

26.5.1 Carbon and Water Science

Recent applications of highly calibrated MODIS VIs have demonstrated their utility in studies of ecosystem functioning, which affect net ecosystem CO₂ exchange and water between land and the atmosphere. Huete et al. (2006a) found a strong, linear and consistent relationship between seasonal EVI and tower-calibrated GPP measurements of carbon fluxes in both intact rainforest and forest conversion to pasture and agricultural sites in the Amazon, and suggested that basin-wide carbon fluxes are constrainable by integrating MODIS and local flux measurements. The EVI provides a more direct relationship than NDVI with photosynthesis in high-LAI Amazon forests by relying on the more sensitive NIR canopy reflectance, which is less prone to saturate. Theoretical analyses support this behavior and conclude that spectral indices, which are more functional with NIR best describe area-averaged canopy photosynthetic capacities and GPP (Sellers 1987).

The relationship strength between tower GPP fluxes and MODIS EVI is generally highest in deciduous forests and lower for evergreen sites. However, the EVI is useful to estimate GPP with relatively high accuracy for most sites without direct consideration of light-use efficiency (LUE), thus simplifying carbon balance models over most vegetation types (Rahman et al. 2005; Sims et al. 2006). Yang et al. (2007) developed a continental-scale measure of GPP by integrating MODIS EVI and AmeriFlux data using support vector machines (SVMs).

Most carbon exchange models use a relationship in which LUE is derived and scaled down with available meteorological information, normally, at very coarse resolution. MODIS EVI data were incorporated into the Vegetation Photosynthesis Model to produce tower-calibrated predictions of GPP across a series of biomes, including evergreen and deciduous forest sites in temperate North America, and in seasonally moist tropical evergreen forests in the Amazon (Xiao et al. 2005a, b),

$$\text{GPP} = (\epsilon_0 \times T \times W \times P) \times \text{fPAR}_{\text{PAV}} \times \text{PAR} \quad (26.3)$$

where fPAR_{PAV} is derived from EVI and maximum LUE (ϵ_0) is reduced by the temperature (T), moisture (W), and phenology (P) scalars. NPP was modeled with monthly EVI inputs to the NASA-CASA (Carnegie Ames Stanford Approach) model, and closely resembled both the measured high- and low-seasonal carbon fluxes, enabling prediction of peak growing season uptake rates of CO₂ in irrigated croplands and moist temperate forests (Potter et al. 2007).

Combined remote sensing and in situ tower flux measurements have also yielded close relationships with water fluxes (Glenn et al. 2007). Yang et al. (2006) derived continental-scale estimates of evapotranspiration (ET) by combining MODIS data with eddy covariance flux tower measurements using an inductive machine learning technique called SVM. They found MODIS EVI the most important explanatory factor in their fairly accurate ET estimates (root mean square of 0.62 mm/day).

At regional scales, ET measurements from nine flux towers established in riparian plant communities dominated by five major plant types on the Middle Rio Grande, Upper San Pedro River, and Lower Colorado River were found to correlate strongly with MODIS EVI values. The inclusion of maximum daily air temperatures (T_a) measured at the tower sites further improved this relationship ($r^2 = 0.74$) (Nagler et al. 2005a). ET measured at flux tower sites in semiarid riparian and upland grass and shrub plant communities were also strongly correlated with MODIS EVI ($r = 0.80$ – 0.94) (Nagler et al. 2005b). Examples of MODIS EVI-tower ET relationships at riparian and shrubland sites at the 2004 Soil Moisture Experiment (SMEX04) are depicted in Fig. 26.6. Seasonal EVI profiles track ET fairly well when transpiration

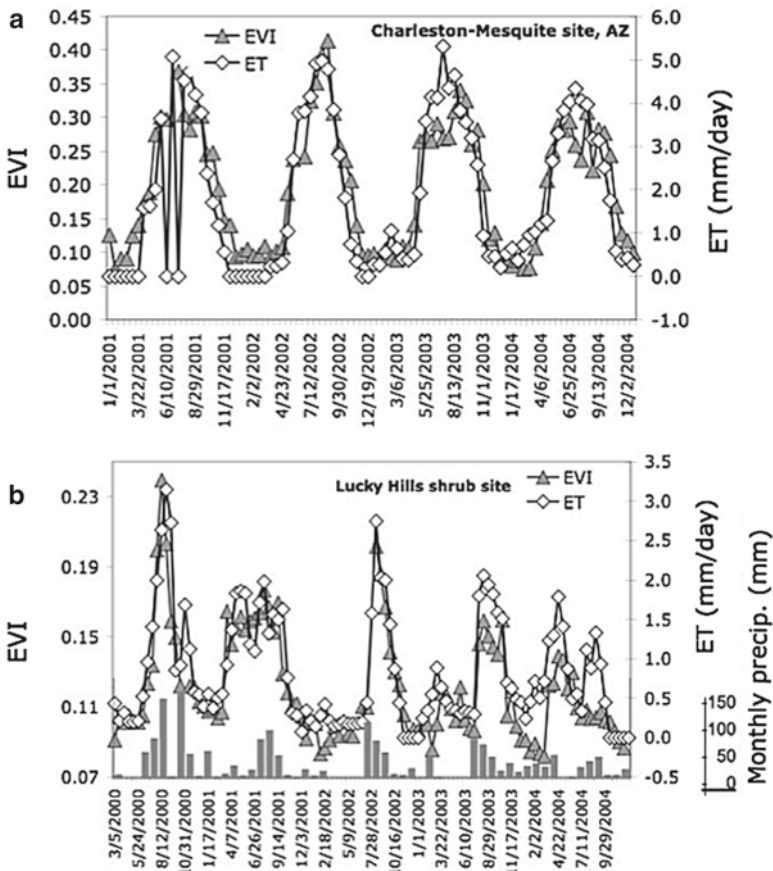


Fig. 26.6 MODIS EVI-eddy covariance tower ET relationships at riparian (a) and upland shrub (b) vegetation communities at the SMEX04 site in southeast Arizona, using MOD13Q1. The strong evaporation component in the upland shrub site during rain events results in significant departures from seasonal EVI values (tower flux data provided by Bill Emmerich and Russell Scott, USDA-ARS Southwest Watershed Research Center, Tucson, AZ)

dominates water fluxes, as found in the riparian site and during inter-storm periods in the upland shrub site with coarse, well-drained soils (Nagler et al. 2007).

The high direct correlation between VIs and GPP and ET in so many different ecosystems may seem surprising since, in theory, CO₂ and water exchanges are related not just to foliage density but to environmental variables (PAR, air temperature, vapor pressure deficit, wind), which can vary considerably over short time periods. However, according to the “resource optimization paradigm,” plants tend to adjust their foliage density over time periods of days to weeks, to match the level of photosynthesis supportable by the environment (Field et al. 1995).

26.5.2 Phenology Studies

The VIs are widely used to characterize vegetation phenology (onset of greening and subsequent browning and dormancy), which is critical to understand ecosystem functioning and associated seasonal patterns of carbon, water, and energy fluxes (Reed et al. 2003). Phenology is also important to quantify ecosystem responses to climate variability, and in coupling land processes into global and regional climate models.

The extended sensitivity of the MODIS EVI has greatly facilitated phenology studies in dense tropical rainforests (Xiao et al. 2005b, 2006a). Using MODIS 250-m and CMG EVI, Huete et al. (2006a) were able to detect phenological variations in greenness, attributed to leaf flushing and leaf exchange, in densely vegetated Amazon tropical rainforests. They found rainforests to green-up by 25% in the dry season in response to the availability of sunlight, a finding confirmed by close couplings to tower-calibrated GPP measurements. Cleared forest areas, on the other hand, showed dry-season declines in EVI, presumably because the more shallow-rooted vegetation had reduced access to deep soil water. Ichii et al. (2007) further combined MODIS EVI with the BIOME-BGC (BioGeochemical Cycles) terrestrial ecosystem model to constrain spatial variability in rooting depths of forest trees over the Amazon and improve the assessments of carbon, water, and energy cycles in tropical forests. They simulated seasonal variations in GPP with different rooting depths (1, 3, 5, and 10 m) at local and regional scales and determined which rooting depths estimated GPP consistent with satellite-based observations. Hence, they were able to map rooting depths across the Amazon with satellite data (Ichii et al. 2007).

MODIS NDVI and EVI were used to characterize the phenology patterns and assess woody plant crown cover across a gradient of physiognomic vegetation classes in the Brazilian cerrado biome (Ratana et al. 2005). Kawamura et al. (2005) monitored short-term phenological changes in rangeland forage conditions with MODIS EVI in the semiarid Xilingol steppe in Inner Mongolia. They were able to estimate forage quantity and derive seasonal changes in live biomass and standing crude protein concentration over areas with different grazing intensities, useful to provide timing information for hay cutting based on nutritive value to

range managers. MODIS NDVI was successfully used to detect varying vegetation conditions caused by locust infestation, and provided a timely monitoring method for locust outbreaks in East China (Zha et al. 2005).

AVHRR-NDVI time-series analysis in high-latitude environments has demonstrated special difficulties due to the dominance of evergreen species with short growing seasons, and long periods of darkness with persistent snow cover in winter. Recently, however, Beck et al. (2006) applied double logistic functions to MODIS NDVI time-series data, and were able to estimate biophysical parameters related to the timing of spring and autumn phenology events in northern Scandinavia.

A MODIS-based algorithm was developed to generate timely and updated geospatial information on paddy rice distributions for irrigation, food security, trace gas emission estimates, and risk assessment of avian flu over South and Southeast Asia (Xiao et al. 2006b). Initial periods of flooding and the phenological growth patterns of paddy rice fields were assessed at regional scales with a three-index algorithm based on NDVI, EVI, and a Land Surface Water Index (Xiao et al. 2006b).

The MODIS vegetation phenology product (MOD12Q2) uses maximum inflections in seasonal NBAR-derived EVI profiles to produce a global set of phenology metrics based on key transition dates related to vegetation growth activity (Zhang et al. 2003). The NBAR-EVI was successfully used to map the phenology of single, double, and triple rice cropping patterns in the Mekong delta, where previously, this was only accomplished with SAR data (Sakamoto et al. 2005, 2006). The NBAR-EVI was also used to show the effect of urban climates on vegetation phenology transition dates in North American cities (Zhang et al. 2004). Strong heat island effects were found in urban areas with increases in the growing season of ~15 days and delays in the onset of dormancy, relative to adjacent nondisturbed ecosystems, a pattern that decays exponentially with distance from urban areas.

26.5.3 Societal Applications

The MODIS VI data are routinely assimilated in a wide variety of different applications, including agriculture, natural resource monitoring and forecasting systems, invasive species, pest and famine early warning systems (FEWS), and diseases in support of scientific and societal purposes. Several priority national application areas, such as agricultural efficiency, carbon management, disaster management, ecological management, homeland security, invasive species, public health and water management, assimilate MODIS VIs as part of their decision support tools of value and benefit to resource management, policy decisions, and resource exploration (NASA 2008).

The MODIS NDVI data are used in interactive monitoring tools for FEWS (USAID 2008), and are assimilated into decision support systems operated by the Production Estimates and Crop Assessment Division (PECAD) of the Foreign Agricultural Service (USDA-FAS) to disseminate global crop conditions and

agricultural production information for selected commodities at a global scale. The MODIS VI product is shared online through Cropexplorer (USDA 2008). The Upper Midwest Aerospace Consortium provides MODIS NDVI data to farmers, ranchers, and foresters living in remote areas of the Upper Midwest, land managers from the Native American Community, and Federal and State Agencies (Seelan et al. 2003; UMAC 2008).

An increasing number of natural resource managers are using Web-based geospatial decision support tools that integrate time-series of both historical and current NDVI data derived from multiple sensors to make better informed planning and management decisions (van Leeuwen et al. 2006). MODIS VI data was used in an operational module, “Integrated Warning Deforestation System for the Amazon” (SIAD), an initiative of the Brazilian government within the scope of the Amazon Protection System (SIPAM) (Ferreira et al. 2007). Jin and Sader (2005) investigated the utility of MODIS NDVI and reflectance products to detect and quantify forest disturbances in northern Maine. MODIS VIs are also utilized as part of the Invasive Species Forecasting System (ISFS), a successful partnership between multilevel agencies (USGS and NASA), academic institutions, and private organizations with the aim of monitoring the introduction and dissemination of invasive species (USGS ISFS 2008). MODIS NDVI time-series are used to predict potential invasive species habitats, so that control or preventative measures are applied before irreversible changes occur (Schnase et al. 2002). Using MODIS NDVI, Franklin et al. (2006) studied the negative impacts of an invasive African grass species, buffelgrass (*Pennisetum ciliare*), on diversity of native rangeland plant communities in Sonora, Mexico.

MODIS VIs contribute to carbon sequestration programs such as the Web-based interface (CASA-CQUEST Carbon Query and Evaluation Support Tools; NASA CASA 2008) to inform land managers about carbon management and sequestration potential. Time-series MODIS VI images are also used for epidemiological purposes (infectious and vector-borne diseases) to address many environment-related health problems by visualizing regions that are either greener (wetter) than average or less green (drier) than normal to aid in assessing outbreaks of Malaria, Rift Valley fever, and other mosquito-borne diseases (Beck et al. 2000).

26.6 Vegetation Index Continuity and Long-Term Data Records

The continuous monitoring of Earth’s vegetation benefits from numerous operational satellite instruments that exist today. Their output is potentially useful to generate a seamless, long-term data record for global change studies. The MODIS VI products will play an important role in extending VI observations from previous AVHRR sensors, and bridge a VI data record into the follow-on operational sensor, the Visible Infrared Imaging Radiometer Suite (VIIRS) slated for launch as part of the National Polar Orbiting Environmental Sensor System (NPOESS) Preparatory

Project (NPP) (Fig. 26.7). The MODIS and VIIRS sensors have similar bandwidths in the red (620–670 and 600–680 nm, respectively) and NIR (841–876 and 845–884 nm, respectively) portions of the spectrum, but differ in their blue channels (459–479 and 478–498 nm, respectively), which may present problems with EVI continuity (Huete et al. 2006b). The VIIRS pixel size is coarser than MODIS (375 m vs. 250 m in the red and NIR) but finer than AVHRR (1.1 km). The bandwidths of both sensors vary considerably from those of the AVHRR, which may present challenges in data continuity and fusion. A greater sensitivity and dynamic range of MODIS-NDVI in comparison with AVHRR-NDVI are known and attributed to the higher spatial resolutions, and narrower red and NIR spectral bandwidths of MODIS, which avoid atmospheric water vapor influences (Huete et al. 2002; Fensholt 2004; van Leeuwen et al. 2006; Miura et al. 2006; Gallo et al. 2005). In a study of NDVI–LAI relationships with NOAA-14 AVHRR, SPOT-4 VGT, and Terra MODIS data, Wang et al. (2005) found significant differences in slope, intercept, and strength of relationships.

However, recent operational water vapor corrections applied to AVHRR/3 data and the narrower bandwidth of AVHRR/3 channel-1 have resulted in near 1:1 linear relationships in 1-km NDVI value derived from overlapping time periods of NOAA-16 and -17 AVHRR/3, and Terra and Aqua MODIS sensors (Gallo et al. 2004, 2005). This suggests that the feasibility to reprocess historical AVHRR datasets to provide continuity of NDVI through the NPOESS era. Brown et al. (2006) demonstrated the consistency of long-term NDVI time-series derived from AVHRR, SPOT-VGT, SeaWiFS, and MODIS sensors. MODIS VI data from Terra and Aqua were shown as interchangeable, despite their overpass time differences (10:30 h vs. 13:30 h) (Gallo et al. 2005). As a result, a MODIS “combined” Terra+Aqua VI product that improves temporal compositing frequency from 16 to 8 days was accomplished in Collection 5, by offsetting the Aqua 16-day composite with an 8-day phase difference so that the two products are merged to generate VIs that are 8 days apart.

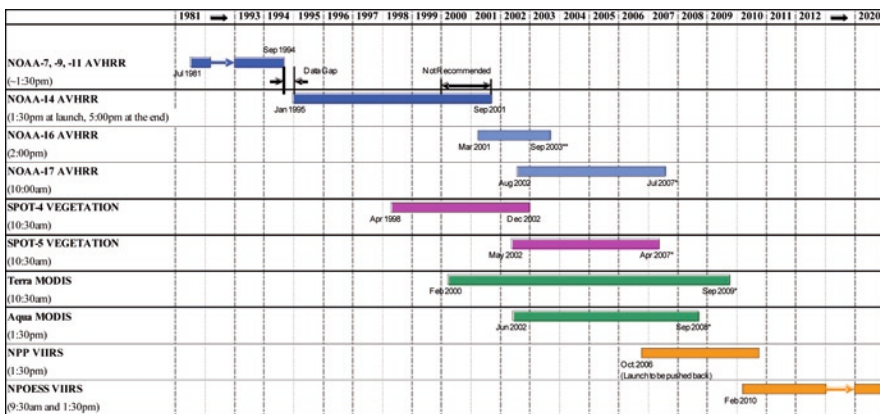


Fig. 26.7 Role of Terra- and Aqua-MODIS sensors within the long-term VI time-series data record

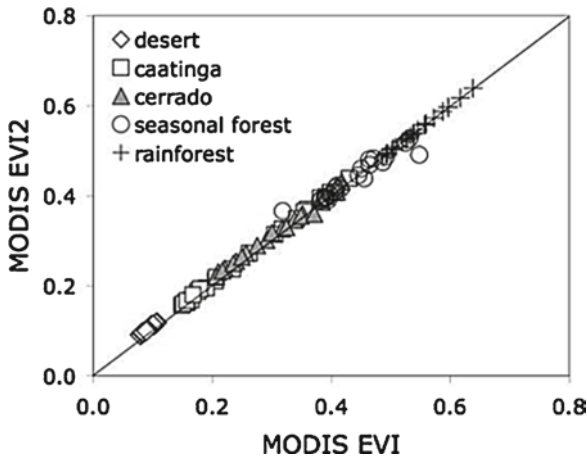


Fig. 26.8 Regression of standard EVI product (MOD13A2) with the two-band EVI2 version for various sites in South America

A backward compatibility of the EVI to the historical AVHRR record to complement the NDVI is also feasible. The EVI uses a blue band to minimize residual atmospheric effects, however, a two-band SAVI-like version is definable when the “blue band” is unavailable, as follows (Jiang et al. 2008):

$$\text{EVI2} = 2.5(\rho_{\text{NIR}} - \rho_{\text{red}}) / (1 + \rho_{\text{NIR}} + 2.4\rho_{\text{red}}) \quad (26.4)$$

Although the EVI2 is computed without a blue band, it remains functionally equivalent to the EVI, although slightly more prone to aerosol noise, which may become less significant with continuing advancements in atmosphere correction (Fig. 26.8). Currently, the EVI2 is used as a backup equation in the MODIS EVI product when snow cover problems render the product unstable. Yoshioka et al. (2003) developed a “bottom-to-top” approach to translate the NDVI from one sensor to another, whereby vegetation isoline equations originally developed to model the behavior of red vs. NIR reflectances were applied to red vs. red and NIR vs. NIR reflectances between two sensors. This theoretical approach provided a better mechanistic understanding and predictive modeling of cross-sensor relationships for the NDVI and input reflectances as well as other VIs, such as EVI.

26.7 Conclusions

Since the respective launches of the Terra and Aqua platforms, MODIS VI products have provided highly calibrated and frequent global measurements of the land surface for monitoring of vegetation dynamics, landscape phenology, and productivity. As outlined in this chapter, new advances in earth system science and in operational applications of satellite data continue with the MODIS VI products. In contrast to

previous satellite observations with AVHRR-NDVI, the MODIS VI products are generated at higher spatial resolution and with negligible water vapor influences and lower-cloud and aerosol contamination. Furthermore, a second index, EVI, offers extended sensitivity into high biomass/LAI canopies, and has provided stronger relationships with canopy biophysical processes, such as photosynthesis and transpiration. The two VIs complement each other and offer a more complete characterization of the entire range of surface biophysical/chemical information and processes taking place in vegetated canopies. Although, the literature has thus far shown the strong utility of both MODIS NDVI and EVI, further research and consensus are valuable in resolving specific VI relationships with canopy properties (chlorophyll content, fPAR, LAI, Fg) and biophysical processes (photosynthesis and transpiration). This will facilitate their inputs to biogeochemical, hydrological, and productivity models, and allow derivation of on-demand biophysical products from the VI data record.

Much of the success in the operational use of VIs resides in their simplicity and ready fusion with data from other sensor systems and platforms. VIs are easily measured on the ground and field-derived biophysical relationships are scaled through finer-grained satellite data or directly to MODIS resolutions. The MODIS VIs are an integral component in the continuing development of long-term time-series applications and climate data records; the proposed AVHRR/MODIS/VIIRS satellite time-series will provide a critical long-term VI data record for Earth studies.

References

- Asrar G, Fuchs M, Kanemasu ET, Hatfield SL (1984) Estimating absorbed photosynthetic radiation and leaf area index from spectral reflectance in wheat. *Agron J* 76:300–306
- Beck LR, Lobitz BM, Wood BL (2000) Remote sensing and human health: new sensors and new opportunities. *Emerg Infect Dis* 6:217–227
- Beck PSA, Atzberger C, Høgda KA, Johansen B, Skidmore AK (2006) Improved monitoring of vegetation dynamics at very high latitudes: A new method using MODIS NDVI. *Remote Sens Environ* 100:321–334
- Brown ME, Pinzon JE, Didan K, Morisette JT, Tucker CJ (2006) Evaluation of the consistency of long-term NDVI time series derived from AVHRR, SPOT-Vegetation, SeaWiFS, MODIS, and Landsat ETM+ sensors. *IEEE Trans Geosci Remote Sens* 44:1787–1793
- Chen X, Vierling L, Deering D, Conley A (2005) Monitoring boreal forest leaf area index across a Siberian burn chronosequence: a MODIS validation study. *Int J Remote Sens* 26:5433–5451
- Cheng Y, Gamon JA, Fuentes DA, Mao Z, Sims DA, Qiu H, Claudio H, Huete A, Rahman AF (2006) A multi-scale analysis of dynamic optical signals in a Southern California chaparral ecosystem: a comparison of field, AVIRIS and MODIS data. *Remote Sens Environ* 103:369–378
- Choudhury BJ (1987) Relationships between vegetation indices, radiation absorption, and net photosynthesis evaluated by a sensitivity analysis. *Remote Sens Environ* 22:209–233
- Chuvieco E, Ventura G, Martin MP, Gomez I (2005) Assessment of multitemporal compositing techniques of MODIS and AVHRR images for burned land mapping. *Remote Sens Environ* 94:450–462
- Cihlar J, Manak D, Voisin N (1994) AVHRR bidirectional reflectance effects and compositing. *Remote Sens Environ* 48:77–88

- Cohen WB, Maieringer TK, Yang Z, Gower ST, Turner DP, Ritts WD, Berterretche M, Running SW (2003) Comparisons of land cover and LAI estimates derived from ETM+ and MODIS for four sites in North America: a quality assessment of 2000/2001 provisional MODIS products. *Remote Sens Environ* 88:233–255
- Fensholt R (2004) Earth observation of vegetation status in the Sahelian and Sudanian West Africa: comparison of terra MODIS and NOAA AVHRR satellite data. *Int J Remote Sens* 25:1641–1659
- Fensholt R, Sandholt I, Stisen S, Tucker C (2006) Analysing NDVI for the African continent using the geostationary Meteosat second generation SEVIRI sensor. *Remote Sens Environ* 101:212–229
- Ferreira NC, Ferreira LG, Huete AR, Ferreira ME (2007) An operational deforestation mapping system using MODIS data and spatial context analysis. *Int J Remote Sens* 28:47–62
- Field CB, Randerson JT, Malmstrom CM (1995) Global net primary production: combining ecology and remote sensing. *Remote Sens Environ* 51:74–88
- Franklin KA, Lyons K, Nagler PL, Lampkin D, Glenn EP, Molina-Freaner F, Markow T, Huete AR (2006) Buffelgrass (*Pennisetum ciliare*) land conversion and productivity in the plains of Sonora, Mexico. *Biol Conserv* 127:62–71
- Gallo KP, Eidenshink JC (1988) Differences in visible and near-IR responses, and derived vegetation indices, for the NOAA-9 and NOAA-10 AVHRRs: a case study. *Photogramm Eng Remote Sens* 54:485–490
- Gallo K, Ji L, Reed B, Dwyer J, Eidenshink J (2004) Comparison of MODIS and AVHRR 16-day normalized difference vegetation index composite data. *Geophys Res Lett* 31:L07502. doi:10.1029/2003GL019385
- Gallo K, Ji L, Reed B, Eidenshink J, Dwyer J (2005) Multi-platform comparisons of MODIS and AVHRR normalized difference vegetation index data. *Remote Sens Environ* 99:221–231
- Gao X, Huete AR, Ni W, Miura T (2000) Optical-biophysical relationships of vegetation spectra without background contamination. *Remote Sens Environ* 74:609–620
- Gao X, Huete AR, Didan K (2003) Multisensor comparisons and validation of MODIS vegetation indices at the semiarid Jornada Experimental Range. *IEEE Trans Geosci Remote Sens* 41:2368–2381
- Glenn EP, Huete AR, Nagler PL, Hirschboeck KK, Brown P (2007) Integrating remote sensing and ground methods to estimate evapotranspiration. *CRC Crit Rev Plant Sci* 26:139–168
- Gobron N, Pinty B, Verstraete MM, Widlowski JL (2000) Advanced vegetation indices optimized for up-coming sensors: design, performance, and applications. *IEEE Trans Geosci Remote Sens* 38:2489–2505
- Goward SN, Huemmrich KF (1992) Vegetation canopy PAR absorptance and the normalized difference vegetation index: an assessment using the SAIL model. *Remote Sens Environ* 39:119–140
- Gutman G, Ignatov A (1998) The derivation of the green vegetation fraction from NOAA/AVHRR data for use in numerical weather prediction models. *Int J Remote Sens* 19:1533–1543
- Holben BN (1986) Characteristics of maximum-value composite images from temporal AVHRR data. *Int J Remote Sens* 7:1417–1434
- Houborg RM, Soegaard H (2004) Regional simulation of ecosystem CO₂ and water vapor exchange for agricultural land using NOAA AVHRR and Terra MODIS satellite data. Application to Zealand, Denmark. *Remote Sens Environ* 93:150–167
- Huemmrich KF (2001) The GeoSail model: a simple addition to the SAIL model to describe discontinuous canopy reflectance. *Remote Sens Environ* 75:423–431
- Huemmrich KF, Privette JL, Mukelabai M, Myneni RB, Knyazikhin Y (2005) Time series validation of MODIS land biophysical products in a Kalahari woodland, Africa. *Int J Remote Sens* 26:4381–4398
- Huete AR (1988) A soil-adjusted vegetation index (SAVI). *Remote Sens Environ* 25:295–309
- Huete AR (1989) Soil influences in remotely sensed vegetation canopy spectra. In: Asrar G (ed) *Theory and applications of optical remote sensing*. Wiley, New York, pp 107–141
- Huete AR, Liu H (1994) An error and sensitivity analysis of the atmospheric- and soil-correcting variants of the NDVI for MODIS-EOS. *IEEE Trans Geosci Remote Sens* 32:897–905

- Huete A, Keita F, Thomé K, Privette J, van Leeuwen WJD, Justice C, Morisette J (1999) A light aircraft radiometric package for MODLAND quick airborne looks (MQUALS). *Earth Obs* 11:22
- Huete A, Didan K, Miura T, Rodriguez EP, Gao X, Ferreira LG (2002) Overview of the radiometric and biophysical performance of the MODIS vegetation indices. *Remote Sens Environ* 83:195–213
- Huete AR, Didan K, Shimabukuro YE, Ratana P, Saleska SR, Hutya LR, Yang W, Nemani RR, Myneni R (2006a) Amazon rainforests green-up with sunlight in dry season. *Geophys Res Lett* 33:L06405. doi:10.1029/2005GL025583
- Huete AR, Miura T, Kim Y, Didan K, Privette J (2006b) Assessments of multisensor vegetation index dependencies with hyperspectral and tower flux data. In: *SPIE proceedings on remote sensing and modeling of ecosystems for sustainability III*, vol 6298-45, San Diego, CA
- Ichii K, Hashimoto H, White MA, Potter C, Hutya LR, Huete AR, Myneni RB, Nemani RR (2007) Constraining rooting depths in tropical rainforests using satellite data and ecosystem modeling for accurate simulation of gross primary production seasonality. *Global Chang Biol* 13:67–77
- Jiang Z, Huete AR, Chen J, Chen Y, Li J, Yan G, Zhang X (2006) Analysis of NDVI and scaled difference vegetation index retrievals of vegetation fraction. *Remote Sens Environ* 101:366–378
- Jiang Z, Huete AR, Didan K, Miura T (2008) Development of a 2-band enhanced vegetation index without a blue band. *Remote Sens Environ* 112:3833–3845
- Jin S, Sader SA (2005) MODIS time-series imagery for forest disturbance detection and quantification of patch size effects. *Remote Sens Environ* 99:462–470
- Kaufman Y, Tanré D (1992) Atmospherically resistant vegetation index (ARVI) for EOS-MODIS. *IEEE Trans Geosci Remote Sens* 30:261–270
- Kaufman YJ, Remer LA, Tanre D, Li R, Kleidman R, Mattoo S, Levy RC, Eck TF, Holben BN, Ichoku C, Martins JV, Koren I (2005) A critical examination of the residual cloud contamination and diurnal sampling effects on MODIS estimates of aerosol over ocean. *IEEE Trans Geosci Remote Sens* 43:2886–2897
- Kawamura K, Akiyama T, Yokota H, Tsutsumi M, Yasuda T, Watanabe O, Wang G, Wang S (2005) Monitoring of forage conditions with MODIS imagery in the Xilingol steppe, Inner Mongolia. *Int J Remote Sens* 26:1423–1436
- Liu H, Huete A (1995) A feedback based modification of the NDVI to minimize canopy background and atmospheric noise. *IEEE Trans Geosci Remote Sens* 33:457–465
- Los SO, North PRJ, Grey WMF, Barnsley MJ (2005) A method to convert AVHRR normalized difference vegetation index time series to a standard viewing and illumination geometry. *Remote Sens Environ* 99:400–411
- Miura T, Huete A, van Leeuwen WJD, Didan K (1998) Vegetation detection through smoke-filled AVIRIS images: an assessment using MODIS band passes. *J Geophys Res* 103:32001–32011
- Miura T, Huete AR, Yoshioka H (2000) Evaluation of sensor calibration uncertainties on vegetation indices for MODIS. *IEEE Trans Geosci Remote Sens* 38:1399–1409
- Miura T, Huete AR, Yoshioka H, Holben BN (2001) An error and sensitivity analysis of atmospheric resistant vegetation indices derived from dark target-based atmospheric correction. *Remote Sens Environ* 78:284–298
- Miura T, Huete A, Yoshioka H (2006) An empirical investigation of cross-sensor relationships of NDVI and red/near-infrared reflectance using EO-1 Hyperion data. *Remote Sens Environ* 100:223–236
- Monteith JL, Unsworth MH (1990) *Principles of environmental physics*, 2nd edn, Arnold, London
- Morisette JT, Privette JL, Justice CO (2002) A framework for the validation of MODIS Land products. *Remote Sens Environ* 83:77–96
- Myneni RB, Keeling CD, Tucker CJ, Asrar G, Nemani RR (1997) Increased plant growth in the northern high latitudes from 1981 to 1991. *Nature* 386:698–702
- Nagler PL, Scott RL, Westenburg C, Cleverly JR, Glenn EP, Huete AR (2005a) Evapotranspiration on western U.S. rivers estimated using the enhanced vegetation index from MODIS and data from eddy covariance and Bowen ratio flux towers. *Remote Sens Environ* 97:337–353

- Nagler PL, Cleverly J, Glenn E, Lampkin D, Huete A, Wan Z (2005b) Predicting riparian evapotranspiration from MODIS vegetation indices and meteorological data. *Remote Sens Environ* 94:17–35
- Nagler PL, Glenn EP, Kim H, Emmerich W, Scott RL, Huxman TE, Huete AR (2007) Relationship between evapotranspiration and precipitation pulses in a semiarid rangeland estimated by moisture flux towers and MODIS vegetation indices. *J Arid Environ* 70:443–462
- NASA CASA Project (2008) <http://geo.arc.nasa.gov/sge/casa/cquestwebsite/index.html> Accessed 27 Feb 2008
- NASA Science Mission Directorate (2008) <http://science.hq.nasa.gov/earth-sun/applications> Accessed 27 Feb 2008
- Potter C, Klooster S, Huete A, Genovese V (2007) Terrestrial carbon sinks for the United States predicted from MODIS satellite data and ecosystem modeling. *Earth Interact* 11:1–21
- Rahman AF, Sims DA, Cordova VD, El-Masri BZ (2005) Potential of MODIS EVI and surface temperature for directly estimating per-pixel ecosystem C fluxes. *Geophys Res Lett* 32:L19404. doi:10.1029/2005GL024127
- Ratana P, Huete AR, Ferreira L (2005) Analysis of cerrado physiognomies and conversion in the MODIS seasonal-temporal domain. *Earth Interact* 8:1–22
- Reed BC, White M, Brown JF (2003). Remote sensing phenology. In: Schwartz MD (ed) *Phenology: an integrative environmental science, Tasks for vegetation science*, vol 39. Kluwer, Dordrecht, The Netherlands, p 569
- Sakamoto T, Yokozawa M, Toritani H, Shibayama M, Ishitsuka N, Ohno H (2005) A crop phenology detection method using time-series MODIS data. *Remote Sens Environ* 96:366–374
- Sakamoto T, Van Nguyen N, Ohno H, Ishitsuka N, Yokozawa M (2006) Spatio-temporal distribution of rice phenology and cropping systems in the Mekong Delta with special reference to the seasonal water flow of the Mekong and Bassac rivers. *Remote Sens Environ* 100:1–16
- Schaaf CB, Gao F, Strahler AH, Lucht W, Li X, Tsang T, Strugnell NC, Zhang X, Jin Y, Muller J-P (2002) First operational BRDF, albedo nadir reflectance products from MODIS. *Remote Sens Environ* 83:135–148
- Schnase JL, Stohlgren TJ, Smith JA (2002) The National Invasive Species Forecasting System: a strategic NASA/USGS partnership to manage biological invasions. *Earth Observing Magazine* August 2002:46–49
- Seelan SK, Laguerre S, Casady GM, Seielstad GA (2003) Remote sensing applications for precision agriculture: a learning community approach. *Remote Sens Environ* 88:157–169
- Sellers PJ (1987) Canopy reflectance, photosynthesis, and transpiration. II. The role of biophysics in the linearity of their interdependence. *Remote Sens Environ* 21:143–183
- Sims DA, Rahman AF, Cordova VD, El-Masri BZ, Baldocchi DD, Flanagan LB, Goldstein AH, Hollinger DY, Misson L, Monson RK, Oechel WC, Schmid HP, Wofsy SC, Xu L (2006) On the use of MODIS EVI to assess gross primary productivity of North American ecosystems. *J Geophys Res* 111:G04015. doi:10.1029/2006JG000162
- Tucker CJ (1979) Red and photographic infrared linear combinations for monitoring vegetation. *Remote Sens Environ* 8:127–150
- Tucker CJ, Pinzon JE, Brown ME, Slayback DA, Pak EW, Mahoney R, Vermote EF, El Saleous N (2005) An extended AVHRR 8-km NDVI dataset compatible with MODIS and SPOT vegetation NDVI data. *Int J Remote Sens* 26:4485–4498
- Upper Midwest Aerospace Consortium (2008) <http://www.umac.org/content/umac/about.shtml> Accessed 27 Feb 2008
- USAID Famine Early Warning Systems (2008) <http://www.fews.net>. Accessed 27 Feb 2008
- Foreign Agriculture Service USDA (2008) Crop explorer. <http://www.pecad.fas.usda.gov/cropexplorer/> Accessed 27 Feb 2008
- USGS Invasive Species Forecasting System (2008) <http://isfs.gsfc.nasa.gov> Accessed 27 Feb 2008
- van Leeuwen WJD, Orr BJ, Marsh SE, Herrmann SM (2006) Multi-sensor NDVI data continuity: uncertainties and implications for vegetation monitoring applications. *Remote Sens Environ* 100:67–81

- Wang Q, Adiku S, Tenhunen J, Granier A (2005) On the relationship of NDVI with leaf area index in a deciduous forest site. *Remote Sens Environ* 94:244–255
- Xiao X, Braswell B, Zhang Q, Boles S, Frolking S, Moore B III (2003) Sensitivity of vegetation indices to atmospheric aerosols: continental-scale observations in Northern Asia. *Remote Sens Environ* 84:385–392
- Xiao X, Zhang Q, Braswell B, Urbanski S, Boles S, Wofsy S, Moore B III, Ojima D (2004) Modeling gross primary production of temperate deciduous broadleaf forest using satellite images and climate data. *Remote Sens Environ* 91:256–270
- Xiao XM, Zhang QY, Hollinger D, Aber J, Moore B III (2005a) Modeling gross primary production of an evergreen needleleaf forest using MODIS and climate data. *Ecol Appl* 15:954–969
- Xiao X, Zhang Q, Saleska S, Hutyrá L, De Camargo P, Wofsy S, Frolking S, Boles S, Keller M, Moore B III (2005b) Satellite-based modeling of gross primary production in a seasonally moist tropical evergreen forest. *Remote Sens Environ* 94:105–122
- Xiao X, Hagen S, Zhang Q, Keller M, Moore B III (2006a) Detecting leaf phenology of seasonally moist tropical forests in South America with multi-temporal MODIS images. *Remote Sens Environ* 103:465–473
- Xiao X, Boles S, Frolking S, Li C, Babu JY, Salas W, Moore B III (2006b) Mapping paddy rice agriculture in south and Southeast Asia using multi-temporal MODIS images. *Remote Sens Environ* 100:95–113
- Yang F, White MA, Michaelis AR, Ichii K, Hashimoto H, Votava P, Zhu AX, Nemani RR (2006) Prediction of continental-scale evapotranspiration by combining MODIS and AmeriFlux data through support vector machine. *IEEE Trans Geosci Remote Sens* 44:3452–3461
- Yang F, Ichii K, White MA, Hashimoto H, Michaelis AR, Votava P, Zhu AX, Huete A, Running SW, Nemani RR (2007) Developing a continental-scale measure of gross primary production by combining MODIS and AmeriFlux data through support vector machine approach. *Remote Sens Environ* 110:109–122
- Yoshioka H, Miura T, Huete AR (2003) An isoline-based translation technique of spectral vegetation index using EO-1 Hyperion data. *IEEE Trans Geosci Remote Sens* 41:1363–1372
- Zha Y, Gao J, Ni S, Shen N (2005) Temporal filtering of successive MODIS data in monitoring a locust outbreak. *Int J Remote Sens* 26:5665–5674
- Zhang X, Friedl MA, Schaaf CB, Strahler AH, Hodges JCF, Gao F, Reed BC, Huete A (2003) Monitoring vegetation phenology using MODIS. *Remote Sens Environ* 84:471–475
- Zhang X, Friedl MA, Schaaf CB, Strahler AH, Schneider A (2004) The footprint of urban climates on vegetation phenology. *Geophys Res Lett* 31:L12209. doi:10.1029/2004GL020137
- Zhang Q, Xiao X, Braswell B, Linder E, Baret F, Moore B III (2005) Estimating light absorption by chlorophyll, leaf and canopy in a deciduous broadleaf forest using MODIS data and a radiative transfer model. *Remote Sens Environ* 99:357–371

Chapter 27

Leaf Area Index and Fraction of Absorbed PAR Products from Terra and Aqua MODIS Sensors: Analysis, Validation, and Refinement

Ranga Myneni, Yuri Knyazikhin, and Nicolay Shabanov

27.1 Introduction

The MODerate resolution Imaging Spectroradiometer (MODIS) onboard NASA's Terra and Aqua platforms is designed to monitor the Earth's atmosphere, oceans, and land surface (Justice et al. 2002). The MODIS Land team (MODLAND) is responsible for the development of algorithms for operationally producing 16 geophysical land data products. In this chapter, we discuss the development of vegetation green leaf area index (LAI) and the fraction of photosynthetically active radiation (400–700 nm) absorbed by vegetation (FPAR) products. LAI is defined as the one-sided green leaf area per unit ground area in broadleaf canopies, and as half the total needle surface area per unit ground area in coniferous canopies. These products are essential for studies of the exchange of fluxes of energy, mass (e.g., water and CO₂), and momentum between the surface and atmosphere (Bonan et al. 2003; Dickinson et al. 1986; Potter et al. 1993; Tian et al. 2003).

MODIS product versions are called Collections. Collection 3 is the first significant processing of Terra MODIS data into products, and covered the period from November 2000 to December 2002. Collection 4 reprocessing delivered improved accuracy and multiyear time-series data both from Terra and Aqua satellites. Terra MODIS data covered from February 2000 to December 2006, while Aqua MODIS spanned from June 2002 to December 2006 timeframe. The next reprocessing (Collection 5) is in progress at the time of this writing. The global Terra and Aqua MODIS LAI/FPAR products are distributed to the public from the Land Processes Distributed Active Archive Center (LP DAAC) (<https://wist.echo.nasa.gov/~wist/api/imswelcome/>). Additionally, the Oak Ridge National Laboratory Distributed Active Archive Center (ORNL DAAC) provides a web-based tool for visualization and distribution of time-series of ASCII subsets (7 × 7 pixels) of LAI/FPAR products over nearly 300 FLUXNET sites over the globe (MODIS ASCII subsets over FLUXNET sites <http://daac.ornl.gov/MODIS/>).

R. Myneni (✉)

Department of Geography and Environment, Boston University, Boston, MA 02215, USA
e-mail: rmyneni@bu.edu

The MODIS LAI and FPAR product development research includes three main components: algorithm development, product analysis, and validation. Algorithm development includes the development of the at-launch algorithm, prototyping of the algorithm, and its refinement. Product analysis includes assessment of algorithm performance and product quality with emphasis on understanding how input data uncertainties propagate into LAI/FPAR retrieval errors. Validation includes comparison of the product to field measurements scaled to MODIS resolution with the goal of quantitatively establishing product accuracy, precision, and uncertainty. The objective of this chapter is to demonstrate incremental development of the MODIS LAI/FPAR products through close interaction between the components of the research. This chapter is organized as follows. [Section 27.2](#) reviews key features of the operational MODIS LAI/FPAR algorithm. [Section 27.3](#) describes results of the analysis of the global time-series of Collection 4 Terra LAI/FPAR products. [Section 27.4](#) summarizes product validation results. [Section 27.5](#) introduces Collection 5 refinements to the algorithm and development of a new product suite from a combination of Terra and Aqua data.

27.2 MODIS LAI/FPAR Algorithm and Products

The MODIS LAI and FPAR products are generated from MODIS daily surface reflectance and view/illumination geometry product (MODAGAGG) (Vermote et al. 2002; Huete et al. 2002). Currently, the red (648 nm) and near-infrared (NIR, 858 nm) bands are used because of high surface reflectance uncertainties in the other MODIS bands (Wang et al. 2001). The Land Cover product (MOD12Q1, LAI/FPAR biomes classification) provides additional input to the algorithm (Friedl et al. 2002). In Collection 4 (and earlier versions) the 6-biome LC was used, in which the global vegetation was stratified into six canopy architectural types, or biomes: (1) grasses and cereal crops, (2) shrubs, (3) broadleaf crops, (4) savannas, (5) broadleaf forests, and (6) needle leaf forests (Friedl et al. 2002). For Collection 5 reprocessing, broadleaf forests and needle leaf forests classes were subdivided into deciduous and evergreen subclasses, resulting in an 8-biome LC map. The biome map reduces the number of unknowns of the inverse problem through the use of simplifying assumptions and standard constants (leaf albedo, soil pattern, etc.) that are assumed to vary with biome types only.

The retrievals are performed with the radiative transfer (RT) algorithm, also called the main algorithm hereafter (Knyazikhin et al. 1998a, b). The approach is implemented with Look-Up Tables (LUTs), which store RT simulations of the surface reflectances (Bidirectional Reflectance Factors, or BRFs) as a function of biome type, view/illumination geometry, LAI/FPAR, canopy structure, leaf optical properties, and soil patterns. During the retrievals, the algorithm selects all canopy/soil patterns for which modeled and observed BRFs differ within specified uncertainties as acceptable solutions. The mean values of LAI/FPAR averaged over all acceptable solutions are reported as the output of the algorithm. The main algorithm, however, may

fail if input reflectance data uncertainties (clouds, aerosols, or snow contamination) are greater than preset threshold values in the algorithm or due to deficiencies in model formulation (BRF simulations errors). In all such cases, the retrievals are generated by the backup algorithm based on biome-specific empirical relationships between the Normalized Difference Vegetation Index (NDVI) and LAI/FPAR (Myneni et al. 1997a, b). The LAI/FPAR algorithm is executed irrespective of MODIS clouds, aerosols, or snow masks to avoid loss of retrievals in view of mask's uncertainties, coarse quantification of contamination conditions or mixed conditions. Thus, data contamination leads to retrievals with varying level of uncertainties; the users are left to select the desirable data quality level to satisfy the application-specific trade-off between data coverage and quality.

The MODIS LAI/FPAR products are generated daily and composited over multiday periods (Fig. 27.1). In Collection 4 separate 8-day Aqua and Terra products were implemented, while in Collection 5, observations from both sensors were combined to generate 8- and 4-day combined Terra and Aqua products. Both single sensor and combined products were generated with single compositing scheme, where Terra and Aqua observations are treated as equivalent. The compositing algorithm is a two-step scheme: (1) the retrievals are selected according to the algorithm path: main algorithm retrievals have the highest priority, if none available, backup algorithm retrievals are selected; (2) the LAI value is selected based on maximum FPAR value from the above subgroup of retrievals. Compositing helps remove contaminated retrievals and minimize the impact of day-to-day variations in surface reflectances that are due to clouds, aerosols, and other residual atmospheric effects. Additional details on algorithm physics are available and found in Huang et al. (2007a), Knyazikhin et al. (1998a, b), Shabanov et al. (2000, 2005), and Wang et al. (2001, 2002).

The products are distributed to the public in HDF format, 1-km spatial resolution, Sinusoidal projection, gridded (18×36 MODIS tiles, each $1,200 \text{ km} \times 1,200 \text{ km}$). The product HDF files contain LAI, FPAR fields, and corresponding Quality Control (QC) flags. The QC bit-fields provide information about the overall quality of the product, algorithm path, cloud state, aerosols, snow, etc. The users are advised to use the QC variables to select reliable retrievals. Examples of global maps of LAI, FPAR, and QC for Collection 3 and 4 products are shown in Fig. 27.2 for composite days, August 5–13, 2002.

27.3 Analysis of Collection 4 Terra LAI/FPAR Global Time-Series

The results of the first component of the MODIS LAI/FPAR research (cf. Sect. 27.1) product analysis are presented here. The analysis focused on understanding product quality as a function of product version (Collection 3 versus Collection 4), algorithm (main versus backup), snow (snow-free versus snow on the ground), and cloud (cloud-free versus cloudy) conditions (Yang et al. 2006a).

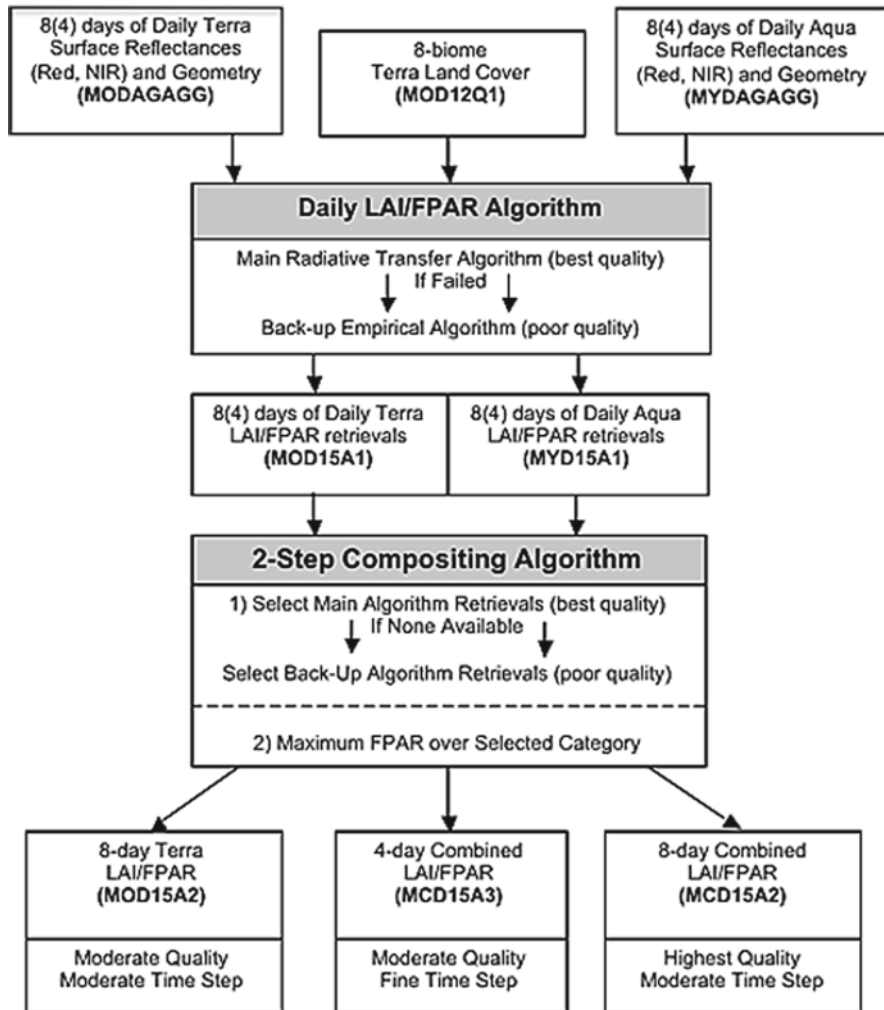


Fig. 27.1 Production stream of Collection 5 MODIS Terra 8-day, Terra and Aqua combined 8- and 4-day LAI/FPAR products

27.3.1 The Collection 4 Algorithm

The Collection 4 reprocessing of LAI and FPAR products benefited from improved inputs and algorithm physics. Refinements to the atmospheric correction algorithm resulted in an increased spatial and temporal coverage of good accuracy surface reflectance data (MODIS Land Surface Product, <http://modis-sr.ltdri.org/>). The at-launch Advanced Very High-Resolution Radiometer (AVHRR) data-based 6-biome LC map used for Collection 3 LAI/FPAR production was replaced in Collection 4 with MODIS

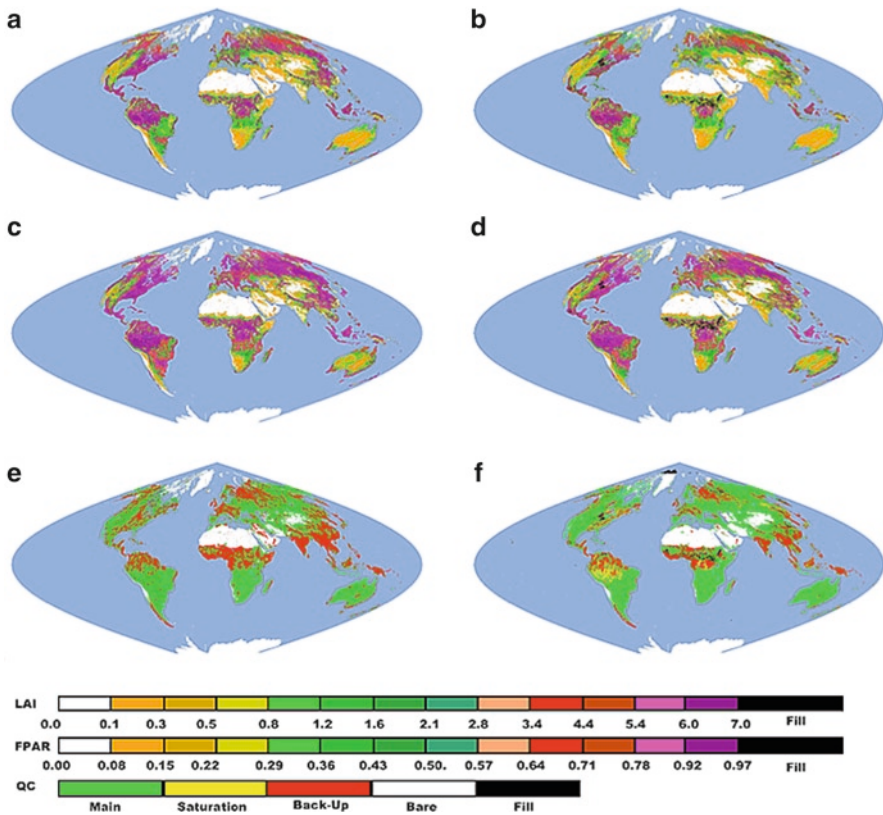


Fig. 27.2 Global maps of LAI, FPAR, and Quality Control (QC) generated from Collection 3 (panels a, c, e) and Collection 4 (panels b, d, f) datasets for Julian date 217–225 in year 2002 (August 5–13, 2002)

data-based biome map (MODIS Land Cover Product, <http://www-modis.bu.edu/landcover/>). The new biome map substantially decreased errors of misclassification especially between cereal crops and broadleaf crops.

The at-launch Sea-Viewing Wide Field-of-view Sensor (SeaWiFS) data-based LUTs used in Collection 3 LAI/FPAR algorithm (Wang et al. 2001) were adjusted in Collection 4 for the MODIS sensor. The new LUTs better simulated the range of MODIS surface reflectance variability, and provided more accurate retrievals over herbaceous vegetation (Tan et al. 2005a, b). The compositing scheme of the algorithm was also revised for Collection 4. In Collection 3, the compositing algorithm selected maximum FPAR value out of eight retrievals regardless of algorithm path, which led in some cases to selection of poor quality backup retrievals, even if main algorithm retrievals were available during the compositing period. In Collection 4, a hierarchical compositing scheme was implemented (cf. Sect. 27.2) which gave preference to main algorithm retrievals. Overall, changes to the Collection 4 LAI/FPAR

algorithm and its inputs resulted in better quality products and helped minimize retrieval anomalies-LAI overestimation over herbaceous vegetation and too few main algorithm retrievals over woody vegetation as detected in product validation studies (cf. Sect. 27.4 for details).

27.3.2 *Data*

Global time-series of Collection 3 (96 datasets from November 2000 to December 2002) and Collection 4 (242 datasets from February 2000 to present) MODIS Terra LAI/FPAR products were analyzed.

27.3.3 *Analysis*

Retrieval Index. The retrieval index (RI) is defined as the ratio of the number of pixels with LAI and FPAR retrieved by the main algorithm to the total number of retrievals by both the main and backup algorithms. This index does not indicate retrieval quality but rather the success rate of the main algorithm. The RI shows a stable but seasonal pattern through 5 years of MODIS operations (Fig. 27.3a). The annual average RI increased from 55% in Collection 3 to 67% in Collection 4 because of the changes discussed in Sect. 27.3.1. The RI is as low as 40–50% during the Northern hemisphere wintertime mainly due to poor quality surface reflectances, and as high as 65–80% during the Northern hemisphere summer time. The points shown off the line in Fig. 27.3a are due to a pause in data collection by the Terra MODIS instrument (Terra MODIS Instrument Performance History, http://www.mcst.ssai.biz/mcstweb/performance/terra_instrument.html).

Biome-by-biome analysis of retrievals is shown in Fig. 27.3b. Grasses and cereal crops have the highest rate of retrievals from the main algorithm (50% in winter and 80–90% in summer). The retrieval rate is lowest in the case of broadleaf forests (40% through the year) because of reflectance saturation in dense canopies, resulting in a high sensitivity of the amount of valid retrievals and its accuracy relative to the surface reflectance accuracy (Knyazikhin et al. 1998a, b). The seasonality in retrieval rate is most pronounced in the high northern latitudes (Fig. 27.3c). The few main algorithm retrievals during the wintertime in this region are due to snow and/or cloudy conditions and fewer measurements (surface reflectances are not generated for solar zenith angle $>70^\circ$). However, the RI for this region is as high as 80% during the summer time. Overall, the main algorithm's retrieval rates increased by 8–16% in all latitudes in Collection 4.

LAI and FPAR Fields. The time-series of LAI and FPAR fields from the Terra MODIS sensor exhibit a seasonal cycle as expected, with a Northern hemisphere wintertime LAI minimum of about 1.5 (1.3) and corresponding summer time maximum of about 2.5 (1.8) for the Collection 3 (Collection 4) processing (Fig. 27.4a, b).

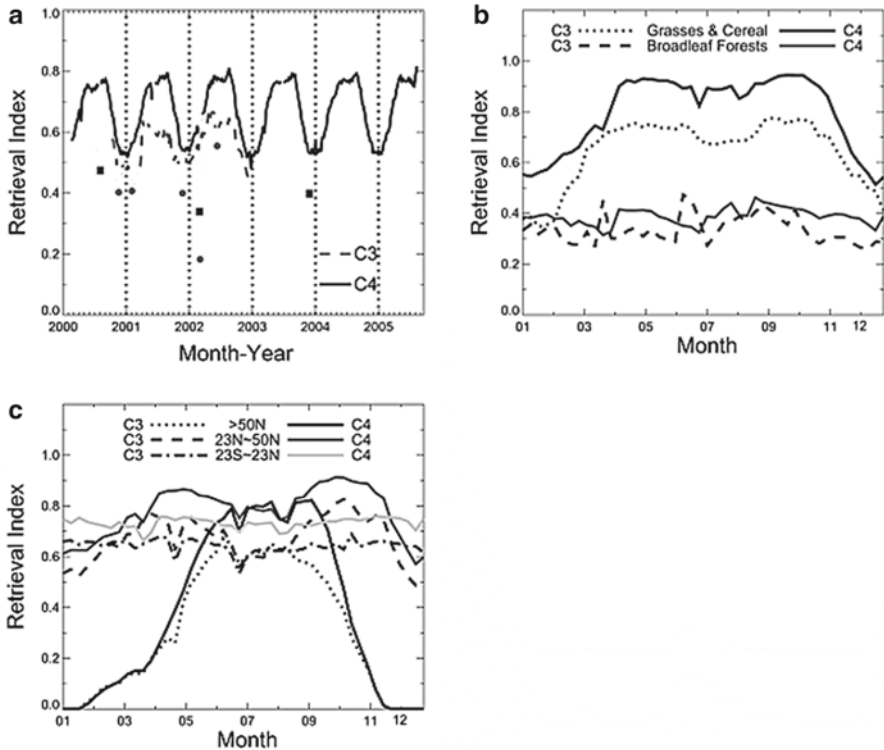


Fig. 27.3 Time-series of the main algorithm retrieval rate, denoted here as the retrieval index (RI) (fraction of main algorithm retrievals) for Collection 3 (dashed lines) and 4 (solid lines) datasets. The global RI is shown in *panel a*. The RI for different biomes (latitudinal bands) is shown in *panel b* (*panel c*). The abbreviations C3 and C4 refer to Collection 3 and 4 products, respectively

The difference between the two collections is mostly due to Collection 3 LAI overestimation in the first four biomes (cf. Sect. 27.3.1), and partially due to Collection 3 input land cover map misclassifications. The global FPAR time-series also show similar seasonality in the range from ~ 0.45 (in winter) to ~ 0.55 (in summer). Thus, on an average, about 50% of the incident photosynthetically active radiation is absorbed by vegetation. This high global rate of absorption is achieved because the vegetated land area is magnified by a factor of 1.3–1.8 through layering of leaves in the canopy.

The LAI and FPAR profiles derived from the main algorithm for individual biomes are shown in Fig. 27.4c, d. The amplitude of seasonal variations for a particular biome type at the global scale is possibly lower or different than the corresponding amplitude at regional scales. The Southern and Northern hemispheres have opposing growing seasons, which dampen the seasonal amplitude at the global scale. Grasses and cereal crops have LAI values of about 1 through the year with negligible seasonal variations. Broadleaf forests indicate some seasonality with LAI varying from about 4 during the Northern hemisphere winter to 5.5 in the summer. This biome class includes both

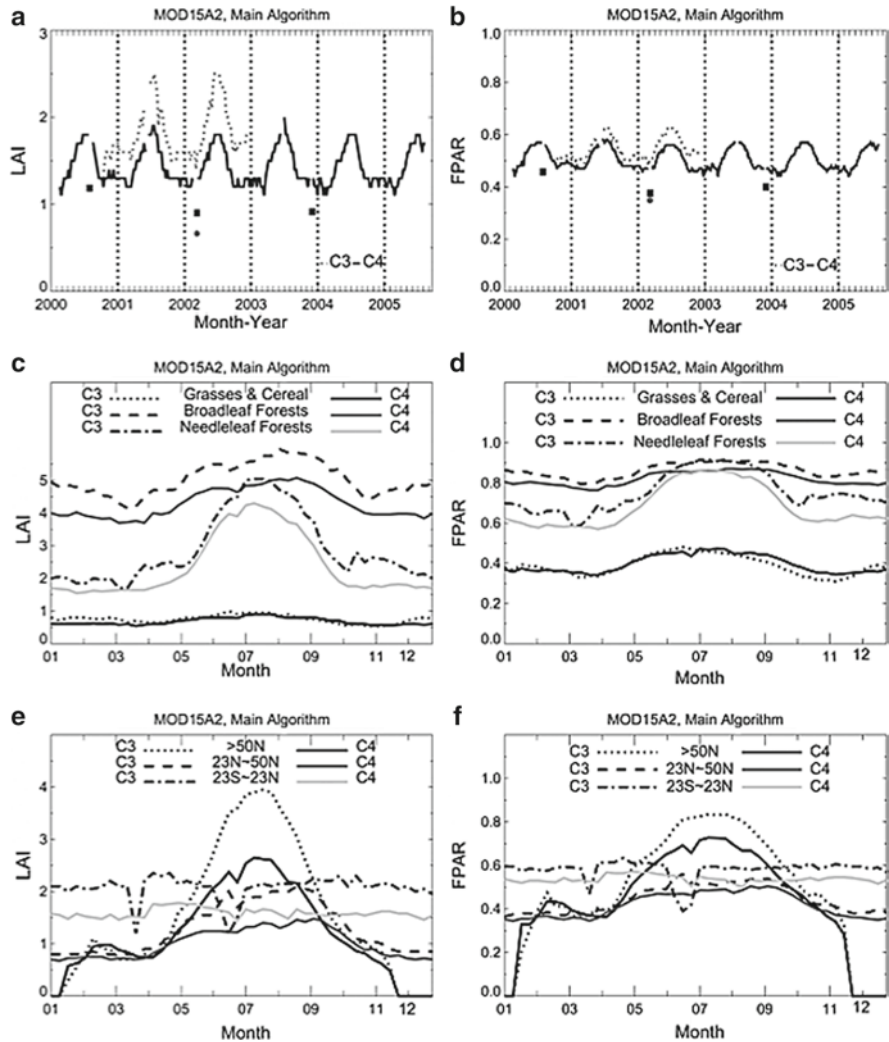


Fig. 27.4 LAI and FPAR for Collection 3 (dashed lines) and 4 (solid lines) datasets. The global LAI and FPAR are shown in panels a and b. The averaged annual profile of LAI and FPAR for different biomes (latitudinal bands) is shown in panels c and d (panels e and f). The abbreviations C3 and C4 refer to Collection 3 and 4 products, respectively

evergreen broadleaf forests from the tropics and deciduous broadleaf forests from the temperate regions. A stronger seasonality is seen in needle leaf forests with LAI varying from about 2 during the Northern hemisphere winter to 4.5 in the summer. Some of this seasonality is an artifact resulting from low data availability during the Northern hemisphere winter due to weak illumination conditions, extreme solar zenith angles, and snow and cloud contamination.

The zonal mean LAI value from the tropics is about 1.5 in Collection 4, which may seem low (Figs. 27.3e and 27.4f). In this band, large areas are under savanna (33%, LAI = 1.6), shrubs (17%, LAI = 0.6), and grasses (10%, LAI = 0.7). The evergreen broadleaf forests occupy 34% of the area in the tropics (23°S–23°N) with a mean LAI value of about 4.2. In the higher northern latitudes (>50°N), the summer time LAI values are about 2.5 in Collection 4. Low wintertime LAI values here are an artifact due to snow and/or cloudy conditions, and the low availability of surface reflectance data. This is further discussed next.

Retrievals under Snow Conditions. The impact of snow cover on algorithm performance is examined here to understand the seasonality observed in LAI and FPAR fields in the high northern latitudes (Fig. 27.5a, c, e). Information on snow cover of each pixel is contained in the product quality flags accompanying the products. According to this information, about 20–30% of the vegetated pixels of 40°N are identified as having snow during the peak winter months (Fig. 27.5a). Under such conditions, the main algorithm retrieval rate is 1.4% in Collection 3 and 2.5% in Collection 4. The high failure rate is due to the fact that snow significantly increases both red and NIR reflectances, such that NDVI is close to 0 (Hall et al. 2002), and the reflectances are not part of the retrieval domain of the main algorithm. The backup NDVI-based algorithm invoked in these cases provides LAI and FPAR retrievals close to 0. Such pixels are tagged as having poor quality in the QA fields.

The Collection 4 LAI retrievals under various snow conditions in the high northern latitudes (>40°N) are shown in Fig. 27.5c, e for needle leaf forests. Total LAI (the sum of LAI values over corresponding pixels), instead of average LAI, is shown in Fig. 27.5e. The total LAI under snow-free conditions is about 100 times greater than that with snow, i.e., LAI retrievals under snow conditions comprise a very small portion of the total retrievals. During the winter months, however, retrievals under snow conditions are considerable, and in fact, there are too few main algorithm retrievals to reliably estimate average LAI values for needle leaf forest pixels (Fig. 27.5c).

Therefore, the LAI and FPAR seasonality in needle leaf forests, seen in Fig. 27.4c, d, is spurious, and worth treating as an artifact resulting from too few reliable retrievals. Also noteworthy is that there are few reliable measurements in the high northern latitudes during the winter period because of low sun angles and weak illumination conditions. This further amplifies the problem of reliably estimating LAI and FPAR in these regions during the winter months.

Retrievals under Cloudy Conditions. The MODIS cloud screening algorithm uses as many as 14 of the 36 MODIS spectral bands to maximize the reliability of cloud detection. Information on cloud optical thickness, effective radius, and cloud-top properties are also used to determine the cloud mask (e.g., single layer, multilayer, clear sky, etc.) (Ackerman et al. 1998). Information on pixel cloud state is contained in quality flags accompanying the products. About 50–65% of the vegetated pixels are identified as cloud-free, 15% as partially cloudy, and the rest as cloud-covered in the Collection 3 dataset. In Collection 4, about 65–75% of the vegetated pixels are identified as cloud-free, 10% as partially cloudy, and the rest as cloud-covered (Fig. 27.5b). These differences are attributable to refinements in the cloud screening

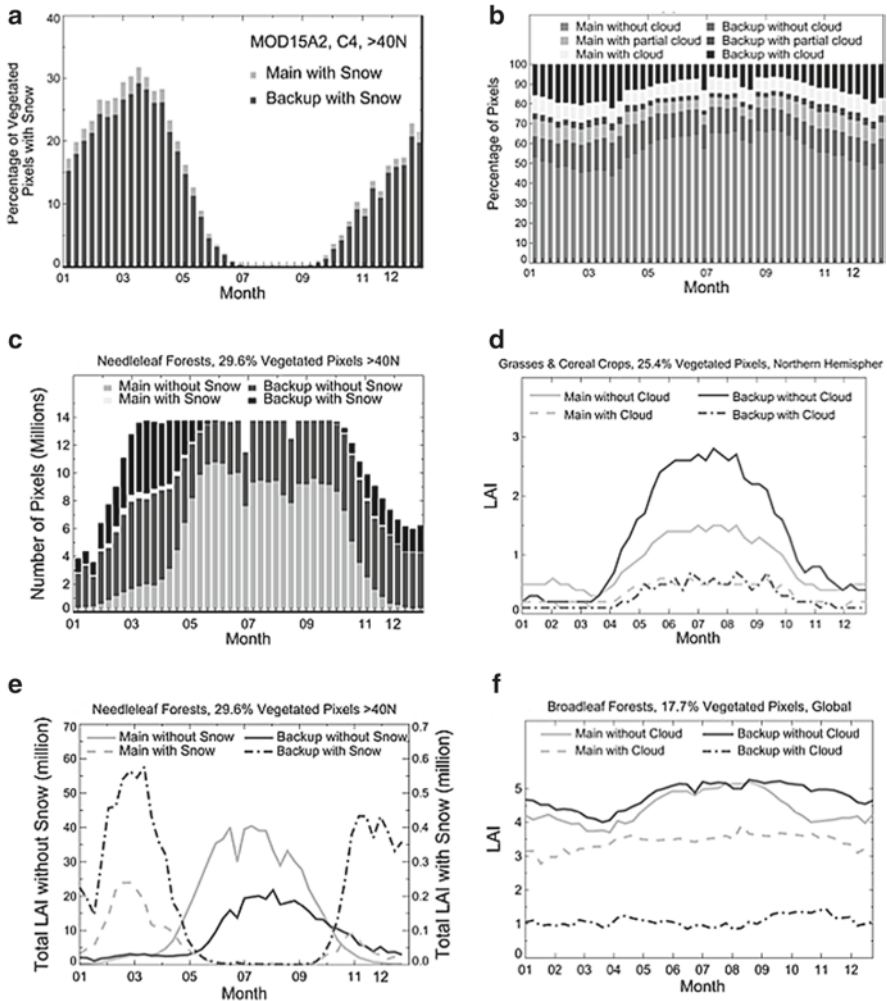


Fig. 27.5 The impact of snow (panels **a**, **c**, **e**) and clouds (panels **b**, **d**, **f**) on the Collection 4 LAI/FPAR retrievals. *Panel (a)*: The annual course of the percentage of snow-covered pixels. *Panel (c)* and *(e)*: The annual course of the pixel counts and total LAI (the sum of LAIs over corresponding pixels) retrieved by main and backup algorithms over needle leaf forests under various snow conditions. *Panel (b)*: The annual course of the percentage of pixels retrieved by the main or the backup algorithms under various cloud conditions. *Panel (d)* and *(f)*: The annual course of LAI retrieved by main and backup algorithms over grasses and cereal crops, and over broadleaf forests under various cloud conditions

algorithm, and an advanced hierarchical compositing scheme implemented for Collection 4 LAI/FPAR algorithm (cf. Sect. 27.2). The increase in the amount of cloud-free pixels in Collection 4 is especially significant during the Northern hemisphere wintertime period.

The annual course of Collection 4 LAI retrieved by the main and backup algorithms under different cloud conditions is shown in Fig. 27.5d, f for two example biomes (grasses and cereal crops, and broadleaf forests). The majority of retrievals under cloudy conditions are performed with the backup algorithm. Main algorithm failure in such cases is expected as the input reflectance data contain large uncertainties. The main algorithm does not fail in some limited cases of cloudiness (Fig. 27.5b). This situation may correspond to a case of cloud cover overestimation by the cloud-screening algorithm. The results shown in Fig. 27.5d, f suggest that the annual course of LAI values retrieved by the main algorithm shows similar patterns, regardless of the degree of cloudiness. However, the differences in LAI magnitudes between the retrievals under cloud-free and cloudy conditions are not negligible, and they depend on the biome type and time of the year. This again reinforces the need to examine the product quality flags accompanying the LAI and FPAR product.

27.4 Validation of MODIS Terra LAI/FPAR Products

This section highlights results of the second component of the MODIS LAI/FPAR research-product validation. Here we review the methodology to validate the coarse resolution LAI/FPAR satellite products, summarize validation results from multiple collaborating investigators and discuss factors, which limit accuracy of product retrievals (Yang et al. 2006b).

27.4.1 Validation Methodology

A direct comparison between ground measurements and corresponding MODIS products is not recommended because of scale-mismatch, geolocation errors, and vegetation heterogeneity at MODIS data resolution. Thus, an intermediate step that involves a fine-resolution map of the variable of interest is introduced. This map is generated with field data and high-resolution satellite data (ETM+, SPOT, ASTER, etc.). When aggregated to the MODIS resolution, this map serves as the ground-truth (Tan et al. 2005a, b; Wang et al. 2001). Therefore, the validation of moderate resolution LAI products includes the following steps (Fig. 27.6): ground sampling of vegetation variables during field campaigns, generation of a fine-resolution map of the variables, and comparison of the aggregated fine-resolution map with MODIS products (Morisette et al. 2002, 2007). Below we detail each step.

To adequately represent the spatial distribution of LAI during ground sampling at a particular site with a minimum of sampling points, existing land cover maps help estimate the spatial distribution of land cover types. For each land cover type, relatively homogeneous patches are defined in order to sample the natural range of the vegetation variables of interest. Patches are identifiable by segmenting high-resolution satellite data (Tan et al. 2005a, b; Wang et al. 2001). Multiple LAI and GPS measurements

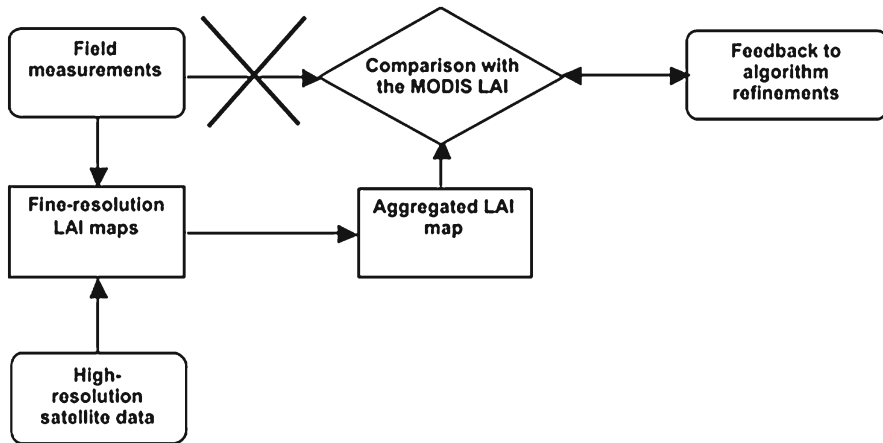


Fig. 27.6 A schematic representation of the validation procedure

are performed in each patch to reduce measurement errors. Measurements are also performed at multiple spatially distributed patches for each land cover class to sample the dynamic range of variation of the variable of interest. LAI measurements are typically performed with optical instruments, such as the LAI-2000 Plant Canopy Analyzer, Tracing Radiation and Architecture of Canopies (TRAC) instrument, and hemispherical fisheye photographs (Jonckheere et al. 2004).

The validation procedure requires generation of a fine-resolution map of the variable of interest from ground measurements, and high-resolution satellite images according to a specific algorithm, also called the *transfer function*. Three broad categories of transfer function exist: empirical methods, physical models, and hybrid approaches (Yang et al. 2006b). Empirical methods are generally implemented with regressions or neural networks. The correlation between high-resolution satellite data-based vegetation indices (VI), such as NDVI, Simple Ratio (SR), Reduced Simple Ratio, Canonical Correlation Analysis Index, and LAI ground measurements, is used to establish an empirical model. The inversion of physical models is an alternative to empirical methods, if generation of a fine-resolution LAI map is required over a large area. Generally, models based on the RT equation are used. In this approach, ground data are mainly used to calibrate model parameters. A hybrid approach that combines physical and empirical methods is useful to generate fine-resolution LAI maps. A training dataset is generated by the physical model, and is used to train a neural network or to calibrate a regression. The trained empirical method is suitably applied to predict LAI values. Regardless of the method used, uncertainties in field measurements and satellite data ultimately limit the accuracy of fine-resolution LAI maps.

The last step in the validation procedure requires aggregation of the fine-resolution LAI map to a moderate-resolution map through averaging (or some other procedure). The comparison between these two fields provides a quantitative accuracy assessment of the moderate resolution LAI products. However, a pixel-by-pixel comparison is not

appropriate for two reasons. First, the actual spatial location of the corresponding pixels in the two LAI maps may not match well because of geolocation uncertainties and pixel-shift errors due to point spread function. Second, the LAI algorithm is not designed to retrieve a deterministic LAI value, but instead generates a mean LAI value from all possible solutions within a specified level of input satellite data and model uncertainties (Knyazikhin et al. 1998a; Tan et al. 2005a, b). Therefore, the retrieved LAI value for a single pixel is likely unreliable, but the mean LAI of multiple similar pixels is likely valid (Wang et al. 2002).

27.4.2 Validation Results

A review of the validation exercises is given below: an example validation work is detailed first, followed by a brief summary of the other validation activities.

An Example Validation at a Cropland Site in France. A field campaign over a 3 km × 3 km agricultural area near Alpillles in France (43.810°N, 4.750°E) was performed from February 26 to March 15, 2001 (Tan et al. 2005a, b). This area is one of the Validation of Land European Remote Sensing Instruments (VALERI) network (Baret et al. 2005). More than 95% of this site was composed of young and mature wheat and grasses on a flat terrain. LAI was measured with a LAI-2000 Plant Canopy Analyzer at 49 distinct locations, 34 of which were concentrated near the center of the site, and the remaining 15 scattered throughout the site to better sample the spatial variability of LAI in fully grown and young wheat (Fig. 27.7a). Measurements at the 15 scattered locations were performed at 4-m interval on two 20-m lines, which formed a regularly shaped cross. An average of 12 measurements was assigned as the LAI value at each of these locations. Standard deviation (STD) values for these 15 sampling locations were taken as the precision of field-measured LAI. The distribution of measured LAI at all 49 locations is shown in Fig. 27.7b.

A subset of an ETM+ image from March 15, 2001 (path 196, row 90) containing the Alpillles site was selected to generate a fine-resolution LAI map of the site. The image was atmospherically corrected using the 6S RT code (Vermote et al. 2002). The MODIS LAI/FPAR algorithm (adjusted for ETM+ data) and the SR relationship ($LAI = 0.2SR - 0.22$, $R^2 = 0.85$) derived from field-measured LAI and atmospherically corrected ETM+ image was used to produce a 30-m LAI map of a 10 km × 10 km area centered on the Alpillles site. The adjustment of the MODIS LAI/FPAR algorithm's LUTs for specific satellite data source (characterized by specific resolution, bandwidths, calibration, etc.) is accomplished by adjusting the configurable parameters (mainly single scattering albedo) to match the simulated retrieval domain in red-NIR spectral space to the observed one (cf. Ganguly et al. (2008) for the theoretical background). The adjusted algorithm was then run with ETM+ red and NIR reflectances. The correlation between LAI retrieved with the fine-resolution algorithm and the SR regression is shown in Fig. 27.7c. Note that at any given value of LAI retrieved by the fine-resolution algorithm, the SR method results in a range of LAI values.

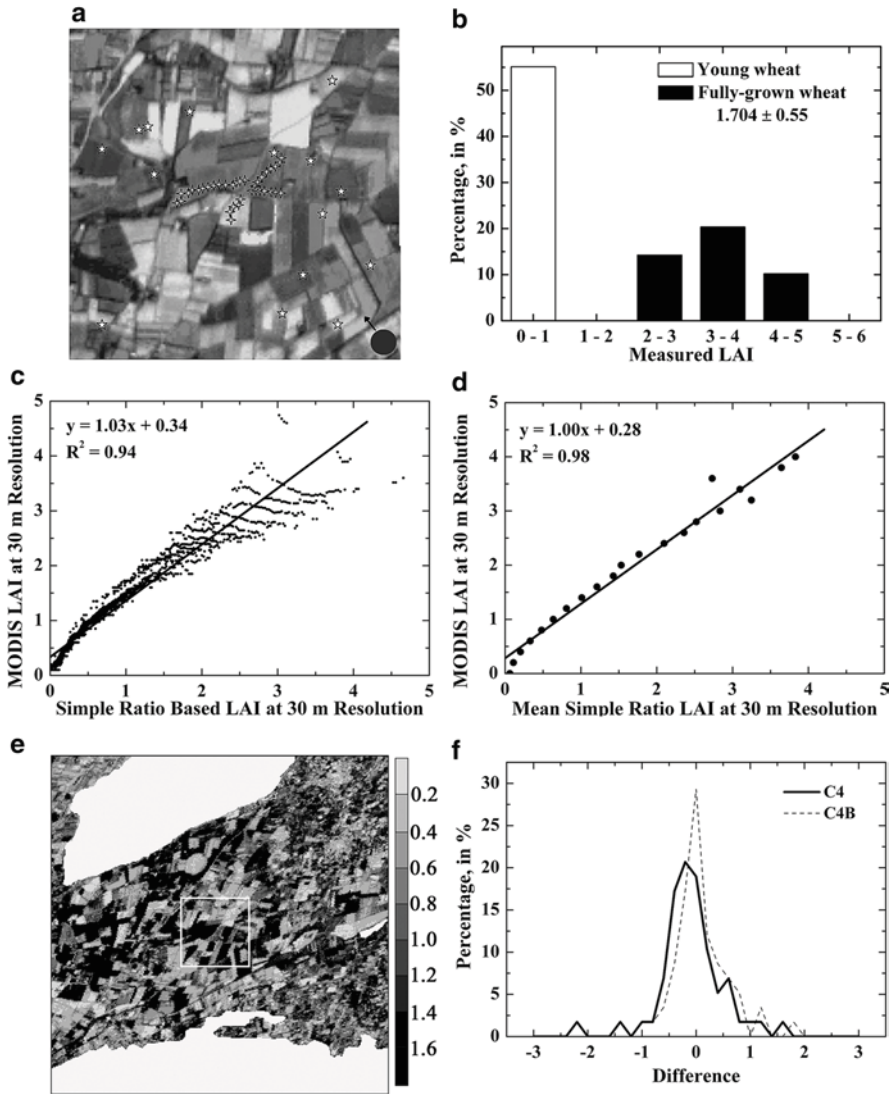


Fig. 27.7 Validation of Collection 4 MODIS LAI product by Tan et al. (2005a) at the Alpilles site in France (croplands). *Panel (a)*: Location of measurements (*stars*) at the 3 km × 3 km site. *Panel (b)*: Distribution of LAI measurements from young wheat and fully grown wheat. *Panel (c)*: LAI retrievals from the fine-resolution MODIS LAI/FPAR algorithm versus retrievals by the simple ratio-based algorithm. *Panel (d)*: Same as in *panel (c)* but retrievals from the simple ratio-based algorithm were averaged at each LAI values retrieved by the fine-resolution MODIS algorithm. *Panel (e)*: Fine-resolution LAI map over the 10 km × 10 km centered at the Alpilles site (*white rectangle*). *Panel (f)*: Histograms of deviations of the Collection 4 LAI product (C4) and LAI product generated with the correct biome map (C4B) from the reference map

This difference stems from the empirical SR approach that is sensitive to the precision of fine resolution satellite observations, which is about 13–20% in this example. The MODIS LAI/FPAR algorithm, however, explicitly accounts for input data uncertainty, and therefore, the retrievals are stable (i.e., do not vary with noise). Variations in surface reflectance due to observation uncertainties, hence, cause horizontal spreads seen in Fig. 27.7c. Thus, the SR-based LAI retrievals require averaging over “indistinguishable” surface reflectances (i.e., reflectances equal within the observation precision) to account for input reflectance uncertainties. The correct LAI values thus obtained with the SR method agree well with the LAI values retrieved by the fine-resolution algorithm (Fig. 27.3d).

A fine-resolution LAI map was derived with both the SR and fine-resolution algorithms (Tan et al. 2005a, b), re-projected to the Sinusoidal projection (Fig. 27.7a), and then degraded to a 1-km resolution. This map was used as a reference. Reference LAI values of cropland and grass (1-km) pixels in the 10 km × 10 km were compared with the Collection 4 MODIS LAI product. Their difference is shown in Fig. 27.7f (legend C4). Note that most of the selected reference LAIs fell in the interval 1 ± 0.3 and formed a relatively homogeneous patch (Tan et al. 2005a, b). The MODIS product is an overestimate compared to the reference values, because most of the pixels in this region were misclassified as broadleaf crops (biome-3) in the biome map used by the Terra MODIS algorithm. A recalculation of the MODIS LAI product with the correct biome map shows a better agreement with the reference values (Fig. 27.7f – C4B).

Related Validation Studies. An early spatial and temporal validation of Collection 1 MODIS LAI product was performed by Privette et al. (2002) in southern Africa along the International Geosphere Biosphere Programme’s Kalahari Transect. This large-scale transect incorporates five sites: Mongu in Zambia (15.438°S, 23.253°E), Pandamatenga in Botswana (18.655°S, 25.500°E), Maun in Botswana (19.92°S, 23.59°E), Okwa River Crossing in Botswana (22.409°S, 21.713°E), and Tshane in Botswana (24.164°S, 21.893°E). From north to south, the sites represent a decreasing annual precipitation trend, decreasing vegetation productivity, and land cover changes from shrubland/woodland in Mongu, open woodland in Pandamatenga to open savanna in Tshane. Field data were collected during March 2000 at four sites in Botswana, and from March through December 2000 at the remaining site in Zambia. At each site, TRAC instruments were used to sample the vegetation overstory LAI along three 750-m transects separated by a distance of 250 m. The direct outcome of TRAC, plant area index, was adjusted with ancillary stem area index data to estimate the LAI. The results indicate that the MODIS LAI products correctly captured the spatially decreasing LAI trend from Mongu, Zambia (LAI ~ 1.7) through Tshane, Botswana (LAI < 0.5) in the wet season, and the temporal phenology in Mongu including the peak during wet season, senescence, peak dry season, and green-up.

Fensholt et al. (2004) performed validation of the seasonal profiles of Collection 4 MODIS LAI and FPAR products at three sites in Senegal (the western Sudano-Sahelian zone) during 2001 and 2002. All sites are closely located: Dahra (15.350°N, 15.480°W), Tessekre North and South (15.817°N, 15.070°W). The land cover types at the sites were similar – dry grasslands with scattered trees and

shrubs. The results show that the seasonal dynamics of in situ LAI were captured well by the MODIS LAI, but the MODIS LAI is a 2–25% overestimate generally, and in low LAI instances, the overestimation was as large as 75%. Similar results for FPAR were found by Fensholt et al. (2004).

Cohen et al. (2003) performed validation of Collections 3 and 4 LAI products at four sites in North America. They include AGRO, a cropland site in Illinois, USA (40.007°N, 88.292°W), KONZ, a prairie grassland site in Kansas, USA (39.089°N, 96.571°W), NOBS, a boreal needle leaf forest site in Manitoba, Canada (55.885°N, 98.477°W), and HARV, a temperate mixed forest site in Massachusetts, USA (42.529°N, 72.173°W). Their results indicate that Collection 3 LAI product overestimates at all four sites. Samples of Collection 4 LAI products were examined and found to consist of improved LAI predictions for KONZ, and to some extent, for the AGRO sites.

The seasonal profiles of Collection 3 MODIS LAI products were validated with 2-year (2000–2002) time-series of monthly ground measurements by Huemmrich et al. (2005) near the flux tower at the Kataba Local Forest, in western Zambia (15.439°S, 23.253°E). The land cover type at the site is Miombo woodland on Kalahari Sand (woody savanna). Comparison of the seasonal profile of the Collection 3 MODIS LAI product and the corresponding ground measurements demonstrated reasonable agreement, however FPAR was overestimated.

Wang et al. (2002) performed a field campaign over Ruokolahti site in Finland (61.320°N, 28.430°E) from June 14 to June 21, 2000. This site is a managed needle leaf forest dominated by Scots pine (*Pinus sylvestris*) with Norway spruce (*Picea abies*) as a subdominant species. The site has a well-developed understory of a mixture of re-growing small pine and spruce trees. A 5 km × 5 km region centered on the validation site was used to compare Collection 4 Terra MODIS LAI product with the aggregated fine-resolution LAI values, derived from field measurements. The patch-by-patch comparison between the MODIS LAI and the reference values was performed. With the exception of one retrieved value, the Collection 4 MODIS LAI product was accurate to within 0.5 LAI.

Table 27.1 summarizes published MODIS Terra LAI/FPAR product validation efforts by multiple international teams. A summary figure, which compares MODIS LAI product with field measurements in all the six biomes referenced by the LAI/FPAR algorithm, indicates that the Collection 4 LAI product overestimates by about 12% (RMSE = 0.66) when all six biomes are taken in account (Fig. 27.8). Overall, according to MODLAND validation methodology, Collections 3 and 4 Terra/Aqua MODIS LAI/FPAR products have stage 1 validation status (i.e., product accuracy was estimated with a small number of independent measurements obtained from selected locations and time periods, and ground-truth/field program effort).

27.4.3 Sources of Retrieval Uncertainties

Validation activities helped detect product deficiencies and feed into assessment of the retrieval technique and its refinement. Three key factors influence the accuracy

Table 27.1 Summary of MODIS LAI/FPAR field campaigns

| Site | Latitude/longitude | Biome type | Date | Measurement | References |
|----------------|--------------------|----------------------|------------------------------------------------------------|-------------|-----------------------------------------------------------------------------------------------------------------------|
| KONZ | 39.089°N/96.571°W | Grasses/cereal crops | June 2000 July 2001 | LAI | Cohen et al. (2003) |
| Alpilles | 43.810°N/4.750°E | Grasses/cereal crops | February 26–March 15, 2001 | LAI | Tan et al. (2005a) |
| Okwa | 22.409°S/21.713°E | Shrubs | March 3–18, 2000 | LAI | Tian et al. (2002) Privette et al. (2002) |
| Mongu | 15.438°S/23.253°E | Shrubland/woodland | April 20, 2000 September 2, 2000 | LAI | Privette et al. (2002) Privette et al. (2002) |
| AGRO | 40.007°N/88.292°W | Broadleaf crops | October 2000–April 2002 | LAI/FPAR | Huemrich et al. (2005) |
| Indore | 22.880°N/75.950°E | Broadleaf crops | July, August 2000 December 2, 2001 December 27, 2001 | LAI | Cohen et al. (2003) |
| Bhopal | 23.170°N/77.470°E | Broadleaf crops | January 21, 2002 December 24, 2001 | LAI | Pandya et al. (2003) |
| Tshane | 24.164°S/21.893°E | Savannas | January 18, 2001 February 12, 2002 | LAI | Tian et al. (2002) Privette et al. (2002) |
| Dahra | 15.350°N/15.480°W | Grasses/savannas | March 3–18, 2000 | LAI | Fensholt et al. (2004) |
| Tessekre North | 15.817°N/15.070°W | Grasses/savannas | August–September 2001 | LAI/FPAR | Fensholt et al. (2004) |
| Tessekre South | 15.817°N/15.070°W | Grasses/savannas | August–September 2002 | LAI/FPAR | Fensholt et al. (2004) |
| Pandamatenga | 18.655°S/25.500°E | Savannas | July–September 2002 | LAI/FPAR | Fensholt et al. (2004) |
| Maun | 19.923°S/23.594°E | Savannas | March 3–18, 2000 | LAI | Tian et al. (2002) Privette et al. (2002) |
| Katiba | 15.439°S/23.253°E | Shrubland/woodland | March 3–18, 2000 February 29, 2000 August 2000 | LAI | Tian et al. (2002) Privette et al. (2002) Tian et al. (2002) Privette et al. (2002) Scholes et al. (2004) |

(continued)

Table 27.1 (continued)

| Site | Latitude/longitude | Biome type | Date | Measurement | References |
|-------------|--------------------|---------------------|------------------------|-------------|----------------------|
| HARV | 42.529°N/72.173°W | Broadleaf forests | July 2000 July 2001 | LAI | Cohen et al. (2003) |
| NOBS | 55.885°N/98.477°W | Needle leaf forests | July 2000 July 2001 | LAI | Cohen et al. (2003) |
| Ruokolahiti | 61.320°N/28.430°E | Needle leaf forests | June 14–21, 2000 | LAI | Wang et al. (2002) |
| Fiakaliden | 64.23°N/19.77°E | Needle leaf forests | June 25–July 4, 2002 | LAI | Huang et al. (2007b) |
| Fundulea | 44.410°N/26.570°E | Broadleaf crops | May 2, 2003 | LAI | Baret et al. (2005) |
| Concepcion | 37.470°S/73.470°W | Broadleaf forests | January 10, 2003 | LAI | Baret et al. (2005) |
| Larose | 45.380°N/75.220°W | Needle leaf forests | August 8, 2003 | LAI | Baret et al. (2005) |
| Haouz | 31.660°N/7.600°W | Grasses | March 11, 2003 | LAI | Baret et al. (2005) |
| Turco | 18.240°S/68.200°W | Grasses | April 16, 2003 | LAI | Baret et al. (2005) |
| Barrax | 39.060°N/2.100°W | Broadleaf crops | July 11, 2003 | LAI | Baret et al. (2005) |
| Hirsikangas | 62.520°N/27.030°E | Needle leaf forests | August 13, 2003 | LAI | Baret et al. (2005) |
| Wisconsin | 45.804°N/90.080°W | Broadleaf forests | May–June 2002 | LAI | Ahl et al. (2006) |

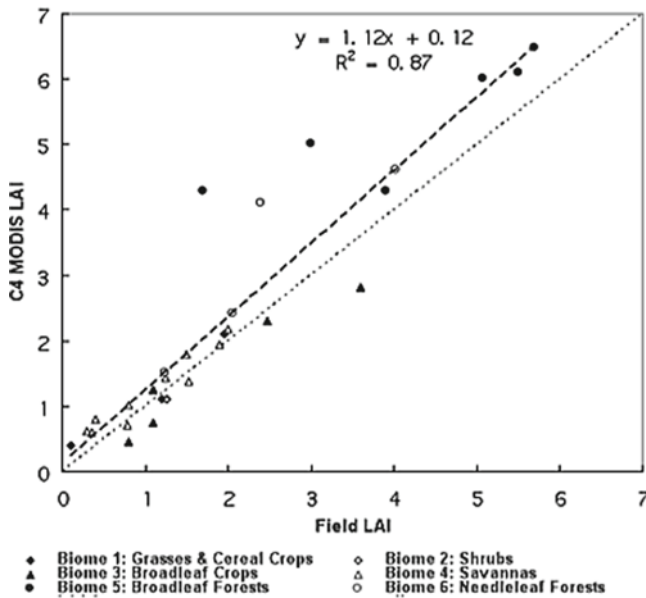


Fig. 27.8 Comparison of Collection 4 MODIS LAI with field measurements in all six biomes referenced by the algorithm. Altogether 29 values are used – the site information, measurement time, and source reference are listed in Table 27.1. The MODIS LAI product is an overestimate by about 12% (RMSE = 0.66) when all six biomes are taken into account

of LAI/FPAR retrievals: (a) uncertainties in input land cover data, (b) uncertainties in input surface reflectances, and (c) uncertainties from the RT model used to build the algorithm’s LUTs. We discuss each type of uncertainty with respect to the validation work of Cohen et al. (2003).

The MODIS LAI/FPAR algorithm references a biome map to select vegetation variables required for LAI retrievals. Biome misclassification may have a twofold effect: directly, whereby a misclassification may result in the selection of a wrong LUT during the retrieval, and indirectly, through the algorithm calibration procedure when the LUTs are developed. For example, consider the 6-biome map for the MODIS tile h10v05 containing the grassland site, KONZ (cf. Sect. 27.4.2). The Collection 3 algorithm referenced the at-launch biome map based on AVHRR data, the accuracy of which was unknown (Fig. 27.9a), while the Collection 4 algorithm referenced a validated biome map based on 1 year of MODIS data (Fig. 27.9b). The at-launch map has significant misclassification between grasses (biome-1) and broadleaf crops (biome-3) both at the site and tile scales, and this clearly impacted the retrievals.

The precision of the surface reflectance product depends on the extent to which atmospheric correction successfully removes the impact of clouds and aerosols on the measurements. While the LAI algorithm was designed to account for uncertainties in the surface reflectance product, the algorithm cannot retrieve LAI values with more precision than its input. Figure 27.9c shows a regression curve of the LAI precision with respect to the precision of the MODIS surface reflectance derived from tile

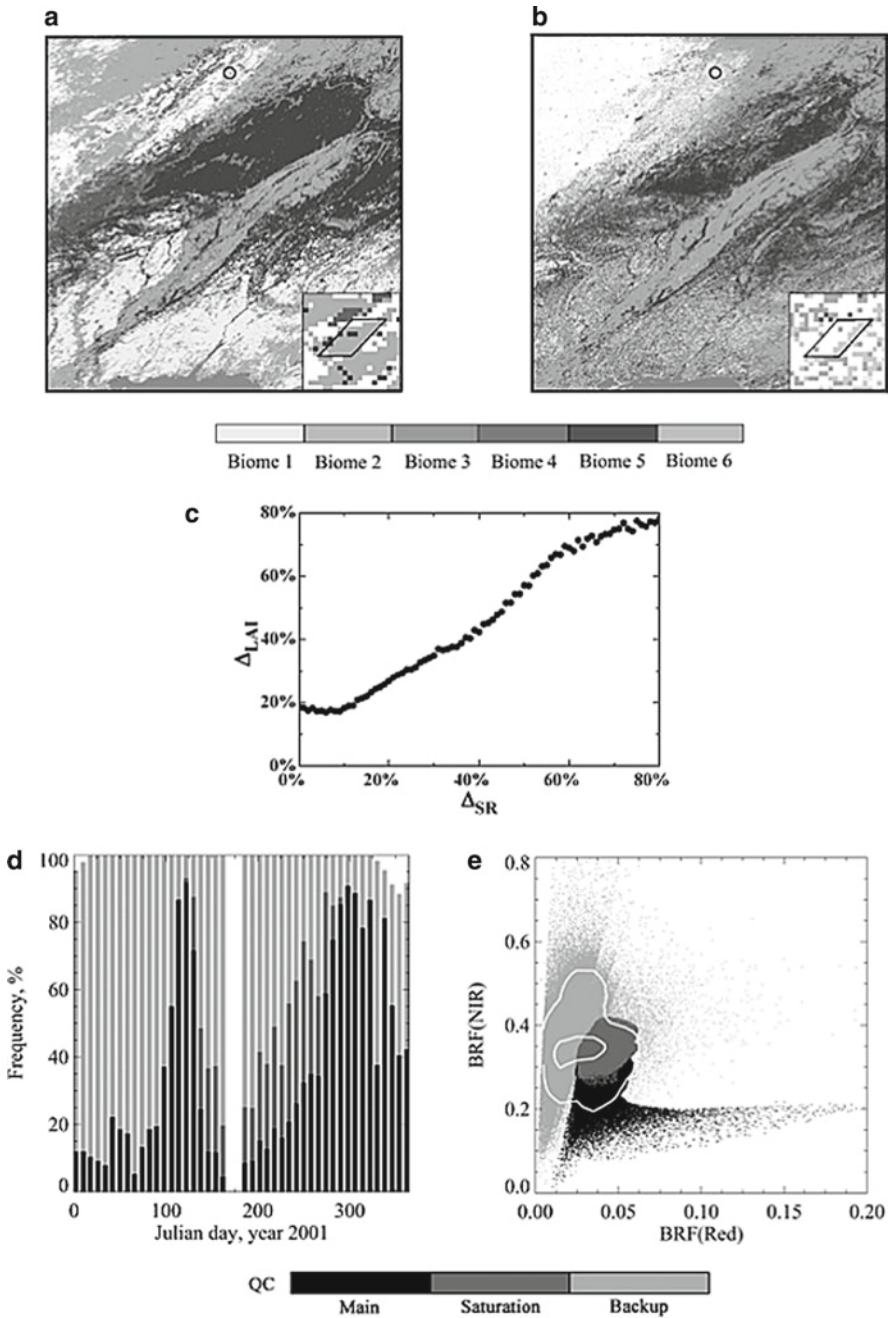


Fig. 27.9 Impact of model and input uncertainties on LAI retrievals. The at-launch AVHRR-based biome map (panel a) and the MODIS-based biome map (panel b) are compared at the tile scale 1,200 km × 1,200 km. The KONZ validation site is marked as a rectangle in this tile (h10v05). The inset shows the biome distribution in a 20 km × 20 km area centered on the site. Panel (c) shows the relationship between precision in surface reflectances and LAI from tile h11v01 containing the

h11v04 containing the AGRO site (cf. Sect. 27.4.2) for the period July 20–27, 2001. Retrieval precision is stable and low when surface reflectance precision is lower than the threshold used by the algorithm. However, when these exceed the threshold, LAI and surface reflectance precisions are linearly related. This example illustrates the connection between the quality of algorithm inputs and outputs.

Finally, we consider the third type of uncertainties: the mismatch between algorithm-simulated reflectances and measured MODIS reflectances, which results in either an inaccurate LAI retrieval or failure of the main RT algorithm. We illustrate this with retrievals from tile h12v04 containing the HARV site (cf. Sect. 27.4.2). The main algorithm mostly fails during the summer period (Julian days 150–250), which is due to the mismatch between simulated and MODIS surface reflectances (Fig. 27.9e). This figure demonstrates the retrieval domain of the main RT algorithm and the backup NDVI-based algorithm in the Red-NIR spectral space and overlaid with a contour plot of MODIS data density. The Collection 4 main algorithm has insufficient ability to simulate a range of observed BRF values in the Red and NIR spectral bands over broadleaf forests, and hence, its rather low retrieval rate.

27.5 Generation of Improved Quality LAI/FPAR Products from Combination of Terra and Aqua Data

This section highlights results of the third component of the MODIS LAI/FPAR research-product refinement. Here we review major changes implemented for the Collection 5 algorithm, and analyze advanced quality products from a combination of Terra and Aqua observations (Yang et al. 2006c).

27.5.1 Collection 5 Algorithm Refinements

The product analysis and validation (Sect. 27.3 and 27.4) provided guidance for algorithm refinements in Collection 5 reprocessing. Earlier versions of the MODIS LAI product overestimated LAI with too few main algorithm retrievals in some areas during the growing season. These anomalies were mostly resolved in Collection 4 over herbaceous vegetation (Tan et al. 2005a, b). In Collection 5, the LUTs for all

← **Fig. 27.9** (continued) AGRO site for the composite period July 20–27, 2001. *Panels (d) and (e)* demonstrate the impact of model uncertainties on LAI retrievals for broadleaf forests pixels in MODIS tile h12v04, containing HARV validation site. *Panel (d)* shows the annual course of main and backup (*light gray bars*) algorithm retrievals for year 2001. Retrievals from the main algorithm are broken down into “best retrievals” (*black bars*) and “LAI values retrieved under a condition of saturation” (*medium gray bars*). *Panel (e)* shows the retrieval domain of the main and the backup algorithm in the red and near-infrared spectral space, overlaid with high density contours of MODIS surface reflectance data for the period July 20–27 in year 2001. The inner and outer contours contain 30 and 50% of observed MODIS BRFs, respectively. The color scheme is the same as in *Panel (d)*

biomes were recalculated based on the stochastic RT model that accounts for effects of spatial heterogeneity of vegetation through the use of the first and second moments of correlation of vegetation structure (Huang et al. 2008; Shabanov et al. 2000, 2005). The LUT parameters were selected to model a majority of MODIS surface reflectances. The main focus of Collection 5 refinements was on woody vegetation: broadleaf and needle leaf forest classes were subdivided into deciduous and evergreen subclasses, and separate LUTs were developed for each subclass (Shabanov et al. 2005). Additionally, biome-dependant uncertainties (i.e., thresholds on allowable discrepancies between simulated and MODIS surface reflectances) were introduced in Collection 5: 20% for Red and 5% for NIR for herbaceous vegetation, 30% for Red and 15% for NIR for woody vegetation. The improved LUTs were used to generate a new suite of Collection 5 MODIS LAI/FPAR products: Terra 8-day, and Terra-Aqua combined 8- and 4-day. All products are generated from a common compositing scheme, where compositing periods are nonoverlapping (cf. Fig. 27.1 and Sect. 27.2). The two new combined products should improve the representation of vegetation in climate studies. In addition, the 4-day product will help address the following objectives of phenological research: (a) to monitor the rapid changes (<1 week) in ecosystems during transition periods of green-up and senescence (Ahl et al. 2006; Chuine et al. 2000); (b) to monitor the spatial variability of greenness onset due to variation in ground temperature and species physiology (Kang et al. 2003; White et al. 2002; Zhang et al. 2005); (c) to monitor the interannual trends in phenology (4–8 days per two recent decades in advance of spring and delay of fall) (Myneni et al. 1997a, b; Schwartz 1998; Sparks and Menzel 2002).

27.5.2 Data

The analysis uses Collection 4 atmospherically corrected surface reflectance products from Terra and Aqua MODIS sensors; and Collection 4 land cover product from the Terra MODIS sensor. A prototype suite of Collection 5 LAI products was generated from the above input data and Collection 5 LAI/FPAR algorithm. Data for 45 MODIS tiles, covering the North American continent during an 8-day composite of Julian days 201–208 (July 20–27) in 2003 were selected to assess spatial variations, while a time-series of data for 2004 for tiles h12v04 (Eastern North America), h11v04 (Mid-western USA), and h12v03 (Central Canada) were chosen to analyze temporal variations through the seasonal cycle.

27.5.3 Analysis

Consistency of Terra, Aqua and Combined LAI Products. The spatial distribution of LAI over North America shown in Fig. 27.10, which is an 8-day composite of Julian days 201–208 (July 20–27) 2003, shows no visibly distinguishable difference between single-sensor and combined products either in pattern or magnitude.

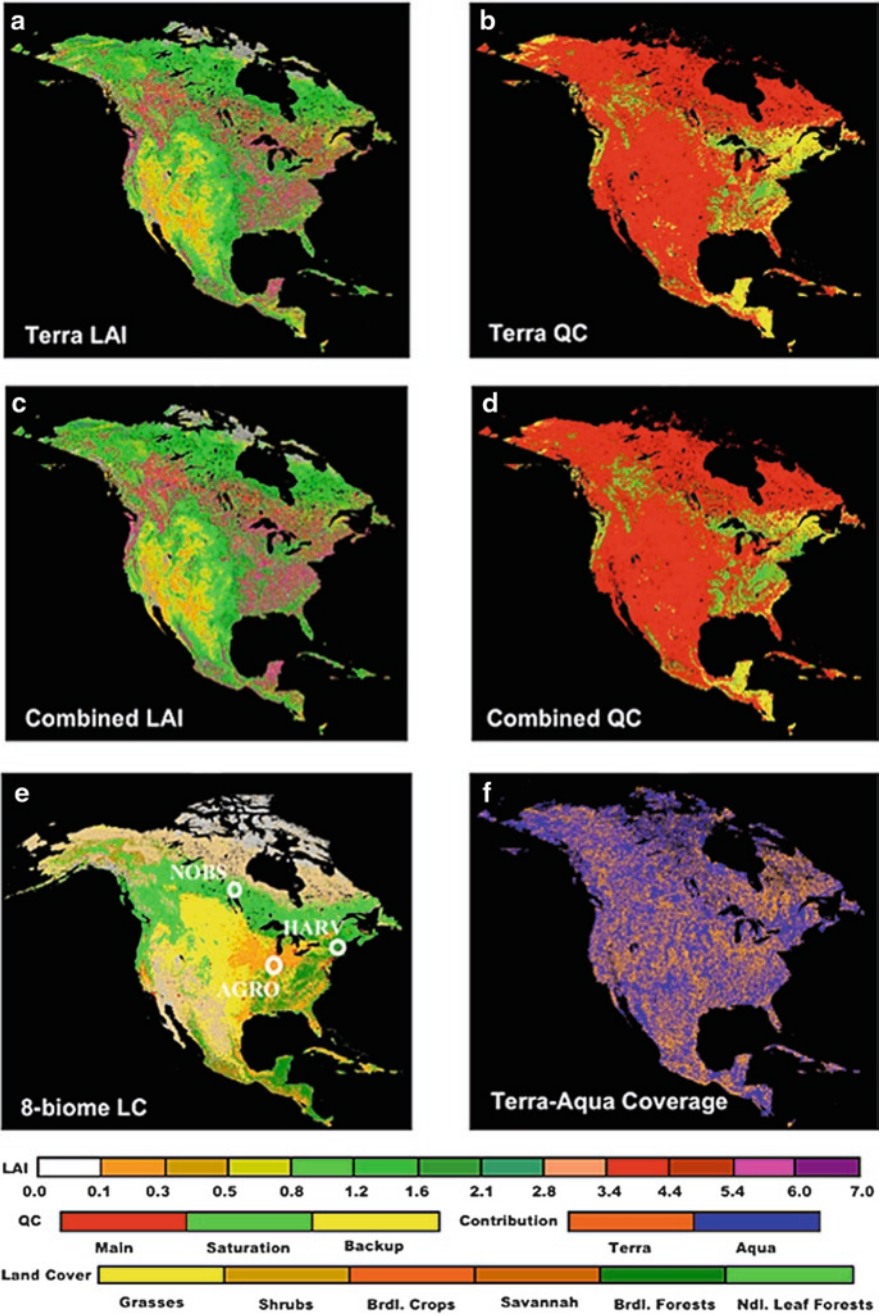


Fig. 27.10 Comparison of Terra MODIS 8-day and Terra-Aqua combined 8-day retrievals at continental scale (North America) during Julian days 201–208 (July 20–27) in year 2003. The spatial distribution of LAI and QC is shown in *panels (a)–(d)*. The spatial distribution of vegetation types according to the 8-biome Terra MODIS land cover product is shown in *panel (e)*. *Circles* on land cover map denote location of three validation sites: AGRO (broadleaf crops), NOBS (needle leaf forests), and HARV (broadleaf forests). The spatial distribution of Terra- and Aqua-MODIS retrievals in combined product (“Coverage”) is shown in *panel (f)*

Namely, more than 88% of all land pixels have a difference less than 0.5 LAI units, and pixels with larger difference are distributed randomly over forested regions. The LAI spatial patterns closely follow the land cover distribution (Figs. 27.10 and 27.11): high LAI over woody vegetation (especially over broadleaf forests) and low LAI over herbaceous vegetation (especially over shrublands). Overall, the main algorithm retrievals constitute 90–95% of retrievals over herbaceous vegetation and 50–75% over woody vegetation. This relatively low retrieval rate of the main algorithm over woody vegetation is due to reflectance saturation. This results in a high sensitivity of the amount of valid retrievals and its accuracy relative to the surface

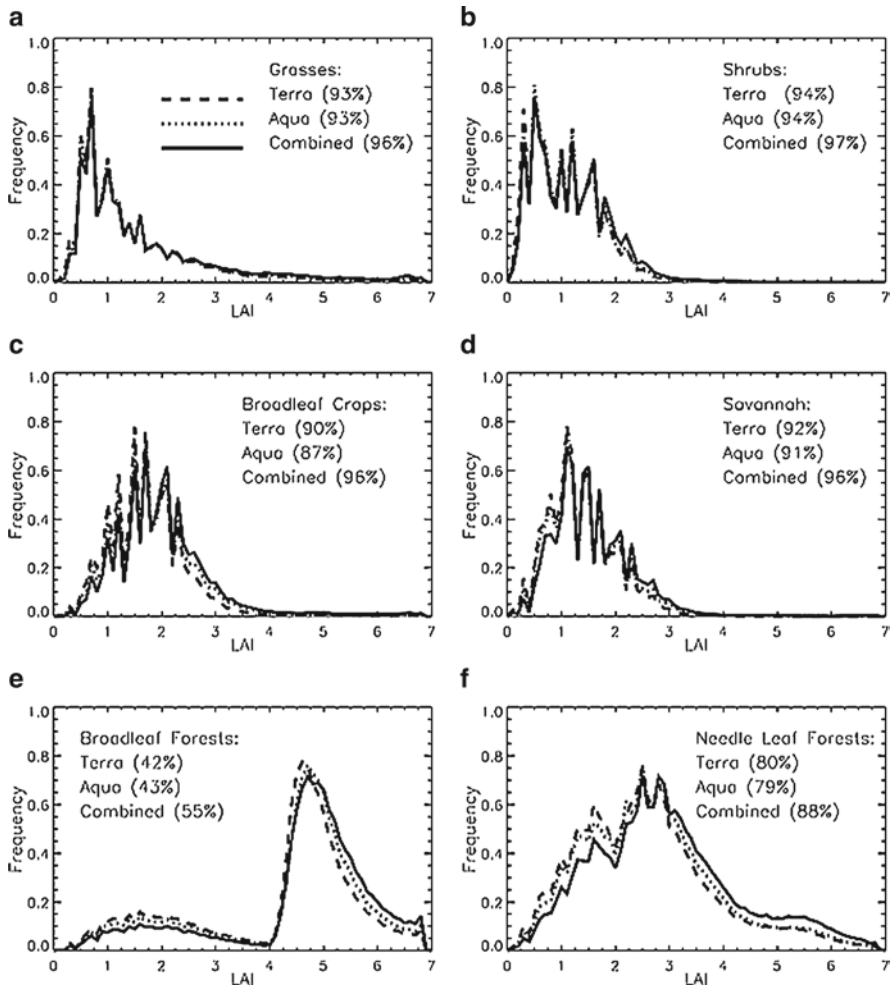


Fig. 27.11 Comparison of Terra MODIS 8-day, Aqua MODIS 8-day, and Terra-Aqua combined 8-day LAI retrievals at continental scale (North America) during Julian days 201–208 (July 20–27) in year 2003. Histograms of LAI retrieved by main algorithm (with or without saturation) are shown as a function of land cover type. Percentages in each panel indicate proportion of main algorithm retrievals in total retrievals

reflectance accuracy (Yang et al. 2006b). When the number of observations is increased from 8 (as in Terra 8-day product) to 16 (as in combined 8-day product), the retrieval rate of the main algorithm is increased by 10–20%. Finally, note that Terra and Aqua observations contribute about equally to the combined product retrievals for all biome types, and the spatial pattern of Terra- and Aqua-based retrievals is apparently random (Fig. 27.10f).

Consistency between Terra, Aqua, and combined Terra-Aqua 8-day products at continental scale is further illustrated in Fig. 27.11, which depicts LAI histograms as a function of land cover type. Good agreement between products exists for all biomes. The sharp variations in LAI histograms at low LAI values (Fig. 27.11) is due to the statistical nature of LAI retrievals – the algorithm reports a single solution, in 0.1 LAI intervals, at low LAI values. Multiple solutions are acceptable at high LAI values, due to low reflectance sensitivity to LAI, and as these solutions are averaged, the histograms likely are smoother at high LAI values.

Seasonal Variations. Seasonal variations in Terra 8-day, Aqua 8-day, and combined 8- and 4-day retrievals during 2004 are shown in Fig. 27.12. The example is

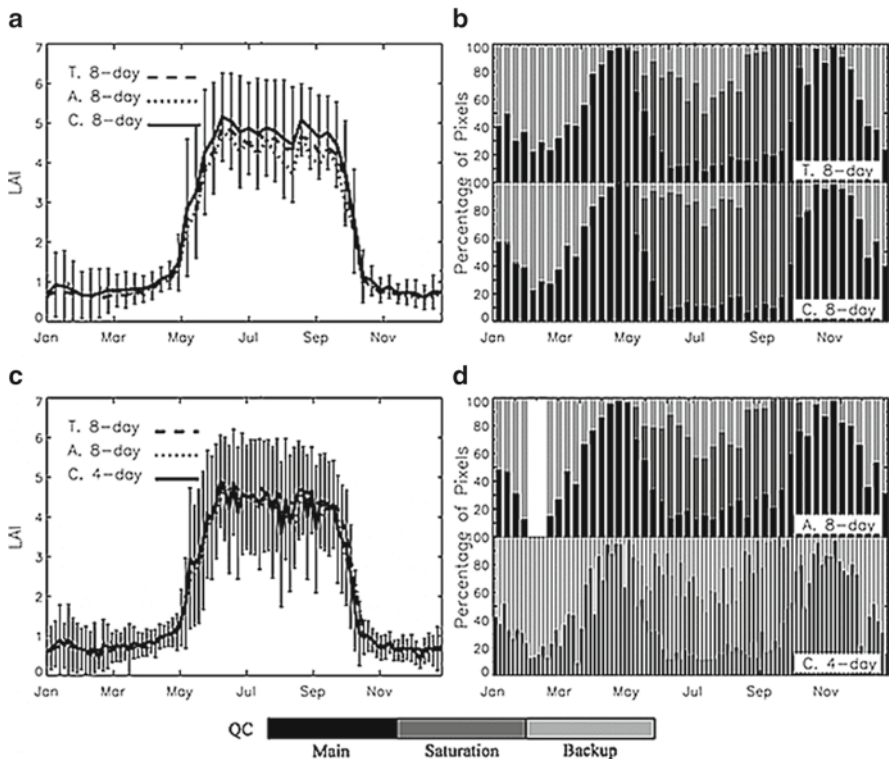


Fig. 27.12 Comparison of LAI and QC from combined 4-day and 8-day retrievals with corresponding single sensor retrievals over broadleaf forests in tile h12v04. *Panels (a) and (b)* show seasonal variations in mean LAI retrieved by the main algorithm (with and without saturation) and QC from Terra-Aqua combined 8-day product and Terra 8-day product. *Panels (c) and (d)* show the same but for Terra-Aqua combined 4-day product and Aqua 8-day product

shown for broadleaf forests in tile h12v04 (Eastern North America) that contain Harvard Forest validation site (cf. Sect. 27.4.3). The retrievals over broadleaf forests (Fig. 27.12a, c) demonstrate expected seasonality in LAI values: from about 1 during winter and about 4.5 during the growing season. Between 70 and 90% of the retrievals are from the main algorithm during the growing season, but most of these are obtained under conditions of reflectance saturation due to high LAI values of these canopies. The combined product helps increase main algorithm retrievals in the product by about 15–20%.

The annual course of combined 4-day LAI product resembles those of the single sensor 8-day products (Fig. 27.12c, d). The combined 4-day product QC shows slightly higher composite-to-composite variability. Decreasing the compositing period, from 8 to 4 days, does not greatly decrease the number of main algorithm retrievals included in the product. The reason derives from environmental conditions (such as clouds), which impact the algorithm path that are only weakly correlated in the 3-h time shift between Terra and Aqua overpasses. Therefore, for compositing purposes, Terra and Aqua MODIS observations acquired in 3-h or 1-day apart are considered to contain equivalent information content.

The impact of aerosol contamination on Terra 8-day, combined 8- and 4-day LAI retrievals is investigated next (Fig. 27.13). Aerosol contamination is quantified by MODIS surface reflectance QC data according to two categories: “no or low atmospheric aerosols levels detected” and “average or high aerosols levels detected.” This QC information was used to define “no aerosols and aerosols” mask. The retrievals were separated into four categories – main or backup algorithm path, and with or without aerosols. Finally, this analysis was restricted to broadleaf forest pixels in tile h12v04.

Surface reflectances, and therefore LAI retrievals under frequent aerosol contamination conditions are seen during winter (with a maximum in February) and a secondary peak in summer (with a maximum in July) (Fig. 27.13a). Conditions of minimum aerosol contamination are seen during spring (May–June) and fall (September–October). The seasonality of aerosol properties was explored with sunphotometer-derived ground measurements, initially, over few sites in the United States (Peterson et al. 1981) and, later, over AERONET global network sites (Holben et al. 2001) (AERONET sunphotometers network, <http://aeronet.gsfc.nasa.gov/>). Significant variability of aerosol regimes was observed over the globe: tropical biomass burning, boreal forest, midlatitude dry or humid climates, desert, oceanic sites, etc. Ground measurements over Eastern North America indicate distinct seasonality in aerosol optical depth with maximum both in the mean and STD observed during summer. This phenomenon was attributed to particular patterns of atmospheric dynamics, caused by dynamic mixture of natural and anthropogenic sources, transported by convection within humid and hot air masses (Holben et al. 2001).

Figure 27.13b–d provide additional details on aerosol impacts on the quality of LAI retrievals. For each composite during the growing season, May–October 2004, broadleaf forests pixels in tile h12v04, two quantities were evaluated: ratio of pixels with retrievals under aerosols to total amount of retrievals (called “aerosol contamination”), and ratio of pixels with retrievals by main algorithm to total retrievals (called “retrievals index,” or RI). The regression of aerosol contamination on RI is shown in Fig. 27.13b.

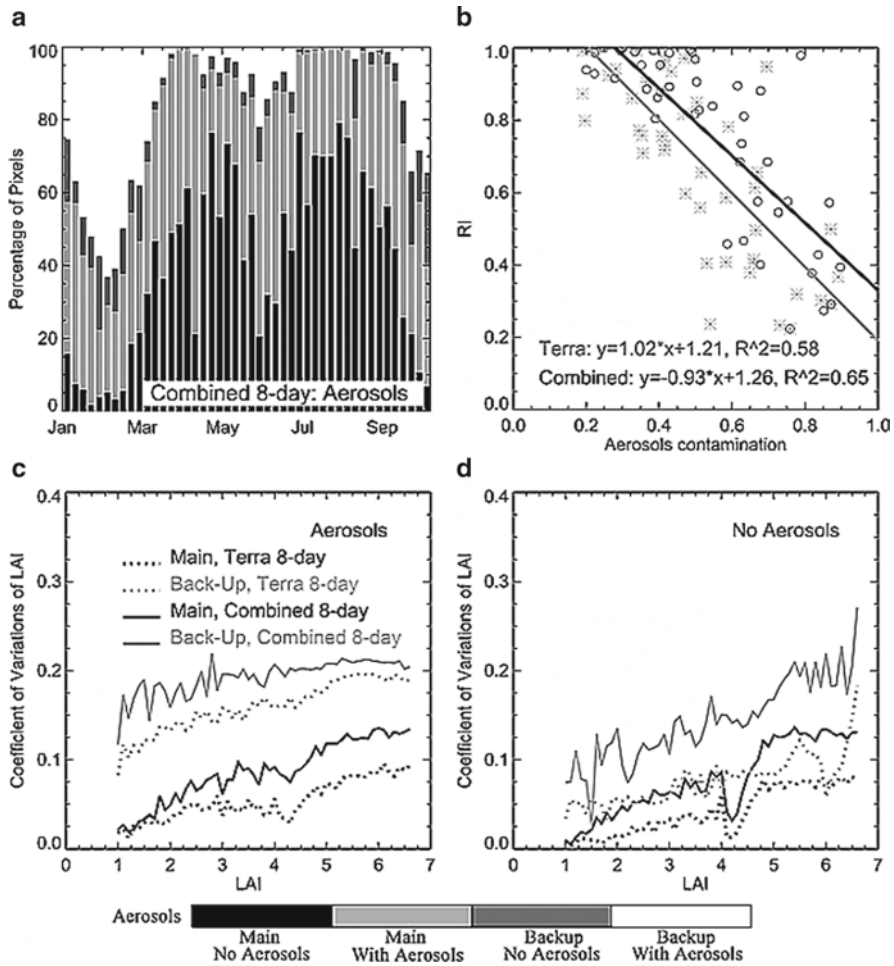


Fig. 27.13 Impact of aerosols on quality of Terra and Terra-Aqua combined 8-day LAI products over broadleaf forests pixels in tile h12v04. *Panel (a)* shows the annual course of the percentages of pixel with retrievals by main and backup algorithms under “aerosol” or “no aerosol” conditions. Data are for January–December in year 2004. *Panel (b)* shows regression of RI with respect to aerosol contamination. Data are for composites during the growing season, May–October in year 2004. *Panels (c)* and *(d)* compare variations in daily LAI, retrieved by main and backup algorithms with and without aerosol contamination, respectively. Data are for composite Julian days 201–208 (July 20–27) in year 2004

These results indicate rapid decrease in RI as aerosol contamination increases, and the correlation is fairly strong: $r^2 = 0.58$ for Terra 8-day and $r^2 = 0.65$ for the combined 8-day products.

Next, consider Fig. 27.13c, d, which show the coefficient of variation (STD/mean) in the retrieved LAI during the 8-day compositing period as a function of LAI values for the two cases: retrievals with and without aerosols contamination. The analysis was

performed for composite Julian days 201–208 (July 20–27) 2004, broadleaf forests pixels in tile h12v04. Aerosols generally increase variations in retrieved LAI, as expressed through coefficient of variations, compared to no-aerosol case. The backup algorithm retrievals have higher variations compared to main algorithm retrievals. Thus, while the combined product does not decrease the total number of retrievals under aerosol contamination, it does increase the number of main algorithm retrievals, which results in a higher precision product. Overall, while a combination of Terra and Aqua observations helps improve quality of retrievals, further product refinement is limited mostly by the MODIS surface reflectance accuracy.

27.6 Conclusions

This chapter presents three main components of the MODIS LAI/FPAR product development research: analysis, validation, and refinement. Interaction between these components enabled incremental improvements to the LAI/FPAR product – from former Collection 3 through current Collection 4 into future Collection 5. The major achievements along each research category are as follows.

Global time-series of Collection 3 and 4 Terra MODIS LAI/FPAR products were analyzed to understand product quality. Retrievals from the main RT algorithm increased from 55% in Collection 3 to 67% in Collection 4. Anomalously high LAI/FPAR values observed in Collection 3 product over herbaceous vegetation were mostly corrected in Collection 4. However, dominance of the backup retrievals over woody vegetation persisted in Collection 4. The spurious seasonality in needle leaf LAI/FPAR fields was detected and traced to fewer reliable input data and retrievals during the Northern hemisphere winter period. Retrievals over snow and cloud-contaminated pixels are performed in the majority of cases with the backup algorithm.

A strategy to validate the MODIS LAI products was formulated and implemented: (1) field sampling representative of LAI spatial distribution and dynamic range at the validation site, (2) development of a transfer function between field LAI measurements and high resolution satellite data to generate a reference LAI map over site, and (3) comparison of MODIS LAI with aggregated reference LAI map. Validation of the MODIS LAI/FPAR products by multiple international teams indicates that the Collection 4 LAI product overestimates by about 12% (RMSE = 0.66) when all biomes are taken into account. Three key factors influence the accuracy of LAI retrievals: (1) uncertainties in input land cover data, (2) uncertainties in input surface reflectances, and (3) uncertainties from the RT model used to build the algorithm's LUTs. Collection 3 and 4 LAI/FPAR products have achieved "Stage 1 validated" status.

In Collection 5 reprocessing, the LUTs of the algorithm for all biomes were recalculated based on the stochastic RT model that accounts for effects of spatial heterogeneity of vegetation with first and second moments of correlation of vegetation structure. The parameters of the LUTs were selected to model a majority of MODIS surface reflectances. Two new products were proposed to fully exploit the MODIS data information content by combining MODIS Terra and Aqua observations.

The Terra-Aqua combined 8-day product helps minimize uncertainties of surface reflectances and increases the number of high quality retrievals by 10–20% over woody vegetation. The Terra-Aqua combined 4-day product doubles the temporal resolution of the seasonal cycle, which facilitates phenology monitoring in application studies during vegetation transition periods. Further LAI/FPAR product refinement is limited mostly by the accuracy of the MODIS surface reflectances.

References

- Ackerman SA, Strabala KI, Menzel PWP, Frey RA, Moeller CC, Gumley LE (1998) Discriminating clear sky from clouds with MODIS. *J Geophys Res* 103(D24):32141–32157
- Ahl DE, Gower ST, Burrows SN, Shabanov NV, Myneni RB, Knyazikhin Y (2006) Monitoring Spring Canopy Phenology of a Deciduous Broadleaf Forest using MODIS. *Remote Sens Environ* 104:88–95
- Baret F, Weiss M, Moreno J, Chen J, Pavageau K, Beal D, Berthelot B, Gonzalez MC (2005) Report on the validation of MERIS TOA_VEG land products. INRA, Avignon, France
- Bonan GB, Oleson KW, Vertenstein M, Levis S (2003) The land surface climatology of the community land model coupled to the NCAR community climate model. *J Clim* 15:3123–3149
- Chuine I, Belmonte J, Mignot A (2000) A modeling analysis of the genetic variation of phenology between tree populations. *J Ecol* 88:561–570
- Cohen WB, Maier-Sperger TK, Yang Z, Gower ST, Turner DP, Ritts WD, Berterretche M, Running SW (2003) Comparisons of land cover and LAI estimates derived from ETM+ and MODIS for four sites in North America: a quality assessment of 2000/2001 provisional MODIS products. *Remote Sens Environ* 88:233–255
- Dickinson RE, Henderson-Sellers A, Kennedy PJ, Wilson MF (1986) Biosphere-Atmosphere Transfer Scheme (BATS) for the NCAR CCM. NCAR Res., Boulder, CO, NCAR/TN-275-STR.
- Fensholt R, Sandholt I, Rasmussen MS (2004) Evaluation of MODIS LAI, fapar and the relation between fapar and NDVI in a semi-arid environment using in situ measurements. *Remote Sens Environ* 91:490–507
- Friedl MA, McIver DK, Hodges JCF, Zhang XYZ, Muchoney D, Strahler AH, Woodcock CE, Gopal S, Schneider A, Cooper A, Baccini A, Gao F, Schaaf C (2002) Global land cover mapping from MODIS: algorithms and early results. *Remote Sens Environ* 83:287–302
- Ganguly S, Schull MA, Samanta A, Shabanov NV, Milesi C, Nemani RR, Knyazikhin Y, Myneni RB (2008) Generating vegetation leaf area index earth system data record from multiple sensors. Part 1: Theory. *Remote Sens Environ* 112:4333–4343
- Hall DK, Riggs GA, Salomonson VV, DiGirolamo NE, Bayr KJ (2002) MODIS snow-cover products. *Remote Sens Environ* 83:181–194
- Holben BN, Tanre D, Smirnov A, Eck TF, Slutsker I, Abuhassan N, Newcomb WW, Schafer JS, Chatenet B, Lavenue F, Kaufman YJ, Castle JV, Setzer A, Markham B, Clark D, Frouin R, Halthore R, Karneli A, O'Neill NT, Piertras C, Pinker RT, Voss K, Zibordi G (2001) An emerging ground-based aerosol climatology: aerosol optical depth from AERONET. *J Geophys Res* 106(D11):12067–12097
- Huang D, Knyazikhin Y, Dickinson RE, Rautiainen M, Stenberg P, Disney M, Lewis P, Cescatti A, Tian Y, Verhoef W, Martonchik JV, Myneni RB (2007a) Canopy spectral invariants for remote sensing and model applications. *Remote Sens Environ* 106(1):106–122
- Huang D, Yang W, Tan B, Rautiainen M, Zhang P, Shabanov NV, Linder S, Knyazikhin Y, Myneni RB (2007b) The importance of measurement errors for deriving accurate reference leaf area index maps for validation of the moderate-resolution satellite LAI product. *IEEE Trans Geosci Remote Sens* 44(7):1866–1871

- Huang D, Knyazikhin Y, Wang W, Deering D, Stenberg P, Shabanov NV, Tan B, Myneni RB (2008) Stochastic transport theory for investigating the three-dimensional canopy structure from space measurements. *Remote Sens Environ* 112:35–50
- Huemmrich KF, Privette JL, Mukelabai M, Myneni RB, Knyazikhin Y (2005) Time-series validation of MODIS land biophysical products in a Kalahari woodland, Africa. *Int J Remote Sens* 26:4381–4398
- Huete A, Didan K, Miura T, Rodriguez EP, Gao X, Ferreira LG (2002) Overview of the radiometric and biophysical performance of the MODIS vegetation indices. *Remote Sens Environ* 83:195–213
- Jonckheere I, Fleck S, Nackaerts K, Muys B, Coppin P, Weis M, Baret F (2004) Methods for leaf area index determination. Part I: theories, techniques and instruments. *Agric Meteorol* 121(1–2):20, 19–35
- Justice CO, Townshend JRG, Vermote EF, Masuoka E, Wolfe RE, El-Saleous N, Roy DP, Morisette JT (2002) An overview of MODIS land data processing and product status. *Remote Sens Environ* 83:3–15
- Kang S, Running SW, Lim JH, Zhao M, Park CR, Loehman R (2003) A regional phenology model for detecting onset of greenness in temperate mixed forests, Korea: an application of MODIS leaf area index. *Remote Sens Environ* 86:232–242
- Knyazikhin Y, Martonchik JV, Myneni RB, Diner DJ, Running S (1998a) Synergistic algorithm for estimating vegetation canopy leaf area index and fraction of absorbed photosynthetically active radiation from MODIS and MISR data. *J Geophys Res* 103:32257–32275
- Knyazikhin Y, Martonchik JV, Diner DJ, Myneni RB, Verstraete M, Pinty B, Gobron N (1998b) Estimation of vegetation leaf area index and fraction of absorbed photosynthetically active radiation from atmosphere-corrected MISR data. *J Geophys Res* 103:32239–32256
- Morisette JT, Privette JL, Justice CO (2002) A framework for the validation of MODIS land products. *Remote Sens Environ* 83:77–96
- Morisette JT, Baret F, Privette JL, Myneni RB, Nickeson JE, Garrigues S, Shabanov NV, Weiss M, Fernandes RA, Leblanc SG, Kalacska M, Sanchez-Azofeifa GA, Chubey M, Rivard B, Stenberg P, Rautiainen M, Voipio P, Manninen T, Pilant AN, Lewis TE, Iiames JS, Colombo R, Meroni M, Busetto L, Cohen WB, Turner DP, Warner ED, Petersen GW, Seufert G, Cook R (2007) *IEEE Trans Geosci Remote Sens* 44(7):1804–1817
- Myneni RB, Nemani RR, Running SW (1997a) Estimation of global leaf area index and absorbed PAR using radiative transfer models. *IEEE Trans Geosci Remote Sens* 35:1380–1393
- Myneni RB, Keeling CD, Tucker CJ, Asrar G, Nemani RR (1997b) Increased plant growth in the northern high latitudes from 1981 to 1991. *Nature* 386:698–702
- Pandya MR, Chaudhari KN, Singh RP, Sehgal VK, Bairag GD, Sharma R, Dadhwal VK (2003) Leaf area index retrieval using IRS LISS-III sensor data and validation of MODIS LAI product over Madhya Pradesh. *Curr Sci* 85:1777–1782
- Peterson JT, Flowers EC, Berri GJ, Reynolds CL, Rudisill JH (1981) Atmospheric turbidity over central North Carolina. *J Appl Meteorol* 20:229–242
- Potter CS, Randerson JT, Field CB, Matson PA, Vitousek PM, Mooney HA, Klooster SA (1993) Terrestrial ecosystem production: A process model based on global satellite and surface data. *Global Biogeochem Cycles* 7(4):811–841
- Privette JL, Myneni RB, Knyazikhin Y, Mukufute M, Roberts G, Tian Y, Wang Y, Leblanc SG (2002) Early spatial and temporal validation of MODIS LAI product in Africa. *Remote Sens Environ* 83:232–243
- Scholes RJ, Frost PGH, Tian Y (2004) Canopy structure in savannas along a moisture gradient on Kalahari sands. *Glob Change Biol* 10:292–302
- Schwartz M (1998) Green-wave phenology. *Nature* 394:839–840
- Shabanov NV, Knyazikhin Y, Baret F, Myneni RB (2000) Stochastic modeling of radiation regime in discontinuous vegetation canopies. *Remote Sens Environ* 74(1):125–144
- Shabanov NV, Huang D, Yang W, Tan B, Knyazikhin Y, Myneni RB, Ahl DE, Gower ST, Huete A, Aragao LEOC, Shimabukuro YE (2005) Analysis and optimization of the MODIS leaf area index algorithm retrievals over broadleaf forests. *IEEE Trans Geosci Remote Sens* 43(8):1855–1865
- Sparks TH, Menzel A (2002) Observed changes in season: an overview. *Int J Climatol* 22:1715–1725

- Tan B, Hu J, Zhang P, Huang D, Shabanov NV, Weiss M, Knyazikhin Y, Myneni RB (2005a) Validation of moderate resolution imaging spectroradiometer leaf area index product in croplands of Alpillles, France. *J Geophys Res.* 110 (D01):107. doi:10.1029/2004JD004860
- Tan B, Hu J, Huang D, Yang W, Zhang P, Shabanov NV, Knyazikhin Y, Nemani RR, Myneni RB (2005b) Assessment of the broadleaf crops leaf area index product from the Terra MODIS instrument. *Agric For Meteorol* 135:124–134
- Tian Y, Woodcock CE, Wang Y, Privette JL, Shabanov NV, Zhou L, Zhang Y, Buermann W, Dong J, Veikkanen B, Hame T, Andersson K, Ozdogan M, Knyazikhin Y, Myneni RB (2002) Multiscale analysis and validation of the MODIS LAI product. I. Uncertainty assessment. *Remote Sens Environ* 83:414–430
- Tian Y, Dickinson RE, Zhou L, Zeng X, Dai Y, Myneni RB, Knyazikhin Y, Zhang X, Friedl M, Yu H, Wu W, Shaikh M (2003) Comparison of seasonal and spatial variations of leaf area index and fraction of absorbed photosynthetically active radiation from moderate resolution imaging Spectroradiometer (MODIS) and Common Land Model. *J Geophys Res* 109(D01):103, doi 10.1029/2003JD003777
- Vermote EF, El-Saleous N, Justice CO (2002) Atmospheric correction of MODIS data in visible to middle infrared: first results. *Remote Sens Environ* 83:97–111
- Wang Y, Tian Y, Zhang Y, El-Saleous N, Knyazikhin Y, Vermote E, Myneni RB (2001) Investigation of product accuracy as a function of input and model uncertainties: Case study with seawifs and MODIS LAI/FPAR Algorithm. *Remote Sens Environ* 78:296–311
- Wang Y, Woodcock CE, Buermann W, Stenberg P, Voipio P, Smolander H, Hame T, Tian Y, Hu J, Knyazikhin Y, Myneni RB (2002) Evaluation of the MODIS LAI algorithm at a coniferous forest site in Finland. *Remote Sens Environ* 91:114–127
- White MA, Nemani RR, Thornton PE, Running SW (2002) Satellite evidence of phenological differences between urbanized and rural areas of the eastern United States deciduous broadleaf forests. *Ecosystems* 5:260–277, doi:10.1007/s10021-001-0070-8
- Yang W, Huang D, Tan B, Stroeve JC, Shabanov NV, Knyazikhin Y, Nemani RR, Myneni RB (2006a) Analysis of leaf area index and fraction of PAR absorbed by vegetation products from the Terra MODIS sensor: 2000–2005. *IEEE Trans Geosci Remote Sens* 44(7):1829–1842
- Yang W, Tan B, Huang D, Rautiainen M, Shabanov NV, Wang Y, Privette JL, Huemmrich KF, Fensholt R, Sandholt I, Weiss M, Ahl DE, Gower ST, Nemani RR, Knyazikhin Y, Myneni RB (2006b) MODIS Leaf Area Index Products: From validation to algorithm improvement. *IEEE Trans Geosci Remote Sens* 44(7):1885–1898
- Yang W, Shabanov NV, Huang D, Wang W, Dickinson R, Nemani R, Knyazikhin Y, Myneni RB (2006c) Analysis of leaf area index products from combination of MODIS Terra and aqua data. *Remote Sens Environ* 104:297–312
- Zhang X, Friedl MA, Schaaf CB, Strahler AH (2005) Monitoring the response of vegetation phenology to precipitation in Africa by coupling MODIS and TRMM instruments. *J Geophys Res* 110:(D12103), doi:10.1029/2004JD005263

Chapter 28

MODIS-Derived Terrestrial Primary Production

Maosheng Zhao, Steven Running, Faith Ann Heinsch,
and Ramakrishna Nemani

Abbreviations

| | |
|--------------|---------------------------------------------------------------------------------------------------------------------------------|
| AmeriFlux | Eddy flux tower network of North America |
| Aqua | NASA's earth observing system satellite with afternoon equatorial crossing time |
| BIOME-BGC | A process-based biogeochemistry model developed by NTSG, University of Montana |
| BPLUT | Biome Properties Lookup Table |
| B_r | Base respiration value |
| C3 | Collection or version 3 of MODIS data |
| C4 | Collection or version 4 of MODIS data |
| C4.8 | Collection or version 4.8 of MODIS GPP/NPP data |
| C5 | Collection or version 5 of MODIS data |
| CDR | Climate data record |
| ENSO | El Niño-Southern Oscillation |
| ERA-40/ECMWF | A 40-year long-term meteorological reanalysis dataset generated by European Center for Medium range Weather Forecasting (ECMWF) |
| ESDR | Earth system data record |
| FAO | Food and Agriculture Organization of the United Nations |
| FLUXNET | Global eddy flux tower network |
| FPAR | Fraction of PAR |
| FTP | File transfer protocol |
| GEOS4 | Name and version of assimilation system of GMAO |
| GMAO | Global modeling and assimilation office belonging to NASA |
| GPP | Gross primary production ($\text{g C/m}^2/\text{d}$) |

M. Zhao (✉)

Numerical Terradynamic Simulation Group, University of Montana,
Missoula, MT 59812 USA
e-mail: zhao@ntsg.umt.edu

| | |
|-----------------|-------------------------------------------------------------------------------------------------------|
| HDF-EOS | An extended Hierarchical Data Format for storing NASA's earth observing system data |
| ITCZ | Intertropical Convergence Zone |
| LAI | Leaf Area Index |
| LP-DAAC | Land Processes Distributed Active Archive Center |
| M_l | Living biomass for leaves and fine roots ($g C/m^2$), derived from LAI |
| MOD12Q1 | MODIS land cover dataset |
| MOD15A2 | 8-day MODIS FPAR/LAI dataset |
| MOD17 | MODIS GPP/NPP dataset |
| MOD17A2 | 8-day MODIS GPP/PsnNet dataset |
| MOD17A3 | Annual MODIS GPP/NPP dataset |
| MODIS | Moderate Resolution Imaging Spectroradiometer, an instrument on board NASA's TERRA and Aqua satellite |
| NARR | North American Regional Reanalysis |
| NASA | The National Aeronautics and Space Administration |
| NCDC | National Climatic Data Center |
| NCEP/NCAR | National Centers for Environmental Prediction/National Center for Atmospheric Research |
| NDVI | Normalized Difference Vegetation Index |
| NH | North hemisphere |
| NPOESS | National Polar-orbiting Operational Environmental Satellite System |
| NPP | Annual net primary production ($g C/m^2/yr$) |
| NTSG | Numerical Terradynamic Simulation Group at University of Montana |
| NU_g | The number of days during the growing season with unreliable or missing MODIS LAI inputs |
| PAR | Photosynthetically active radiation |
| PsnNet | Net photosynthesis, an intermediate variable between GPP and NPP |
| Q_{10} | Respiration quotient, equal to 2.0 |
| QC | Quality control data field for MODIS data |
| R_g | Annual growth respiration ($g C/m^2/yr$) |
| R_{m_lr} | Maintenance respiration from living leaves and fine roots ($g C/m^2/d$) |
| R_{m_w} | Annual maintenance respiration from living wood ($g C/m^2/yr$) |
| R_{plant} | Plant respiration, functionally, it is the summation of maintenance and growth respiration |
| $S\downarrow_s$ | Downward surface solar shortwave radiation ($MJ/m^2/d$) |
| SLA | Specific leaf area |
| SOGS | Surface Observation gridding system |
| T_{avg} | Daily average air temperature ($^{\circ}C$) |
| Terra | NASA's earth observing system satellite with morning equatorial crossing time |

| | |
|--------------------|---------------------------------------------------------|
| T_f | Daily minimum temperature scalar |
| T_{\min} | Daily minimum temperature |
| TOTAL _g | Total number of days in the growing season |
| VIIRS | Visible/Infrared Imager/Radiometer Suite onboard NPOESS |
| VPD _f | Vapor pressure deficits (VPD) scalar |
| ϵ | Light use efficiency parameter (g C /MJ) |
| ϵ_{\max} | Maximum ϵ under optimal conditions (g C /MJ) |

28.1 Introduction

Temporal and spatial changes in terrestrial biological productivity have a large impact on humankind because terrestrial ecosystems not only create environments suitable for human habitation, but also provide materials essential for survival, such as food, fiber and fuel. A recent study estimated that consumption of terrestrial net primary production (NPP; a list of all the acronyms is available in the appendix at the end of the chapter) by the human population accounts for about 14–26% of global NPP (Imhoff et al. 2004). Rapid global climate change is induced by increased atmospheric greenhouse gas concentration, especially CO₂, which results from human activities such as fossil fuel combustion and deforestation. This directly impacts terrestrial NPP, which continues to change in both space and time (Melillo et al. 1993; Prentice et al. 2001; Nemani et al. 2003), and ultimately impacts the well-being of human society (Milesi et al. 2005). Additionally, substantial evidence show that the oceans and the biosphere, especially terrestrial ecosystems, currently play a major role in reducing the rate of the atmospheric CO₂ increase (Prentice et al. 2001; Schimel et al. 2001). NPP is the first step needed to quantify the amount of atmospheric carbon fixed by plants and accumulated as biomass. Continuous and accurate measurements of terrestrial NPP at the global scale are possible using satellite data. Since early 2000, for the first time, the MODIS sensors onboard the Terra and Aqua satellites, have operationally provided scientists with near real-time global terrestrial gross primary production (GPP) and net photosynthesis (PsnNet) data. These data are provided at 1 km spatial resolution and an 8-day interval, and annual NPP covers 109,782,756 km² of vegetated land. These GPP, PsnNet and NPP products are collectively known as MOD17 and are part of a larger suite of MODIS land products (Justice et al. 2002), one of the core Earth System or Climate Data Records (ESDR or CDR).

These products have improved based on extensive validation and calibration activities by the MODIS science team. The Collection-5 (C5) MODIS data are being reprocessed by NASA in 2007 and will have higher quality than the previous collections. In this chapter, we provide a brief description of the global MODIS terrestrial primary production algorithm and data products, and summarize the achievements (i.e., validation, improvements, and applications) and results of a six-year (2000–2005) global MODIS GPP/NPP dataset.

28.2 Description of MODIS GPP/NPP

28.2.1 Theoretical Basis of the Algorithm

MODIS GPP/NPP is the first continuous satellite-derived dataset monitoring global vegetation productivity. The algorithm is based on Monteith's (1972, 1977) original logic, which suggests that NPP under non-stressed conditions is linearly related to the amount of absorbed Photosynthetically Active Radiation (PAR) during the growing season. In reality, vegetation growth is subject to a variety of stresses that tend to reduce the potential growth rate. Especially important are climatic stresses (temperature, radiation, and water) or the interaction of these primary abiotic controls, which impose complex and varying limitations on vegetation activity globally (Churkina and Running 1998; Nemani et al. 2003; Running et al. 2004). Figure 28.1 illustrates the range of three dominant climatic controls on global annual NPP, distributed from arctic tundra to tropical rainforests. Water limits vegetation most strongly on 40% of the land surface. Temperature is most limiting for 33% of the land surface, with annual temperature ranges from -20°C in arctic tundra to $+30^{\circ}\text{C}$ in deserts. Incident solar radiation is the primary limiting factor for 27% of global vegetated areas, mostly in wet tropical regions where temperatures and water availability are usually adequate (Nemani et al. 2003). While it is easy to imagine boreal areas being temperature-limited, and deserts being water-limited, partial constraints limit NPP of temperate regions in a complex fashion at different times of the growing season. A temperate mid-latitude forest is perhaps limited by radiation and temperature in winter, temperature-limited in the spring, and water-limited in mid-summer

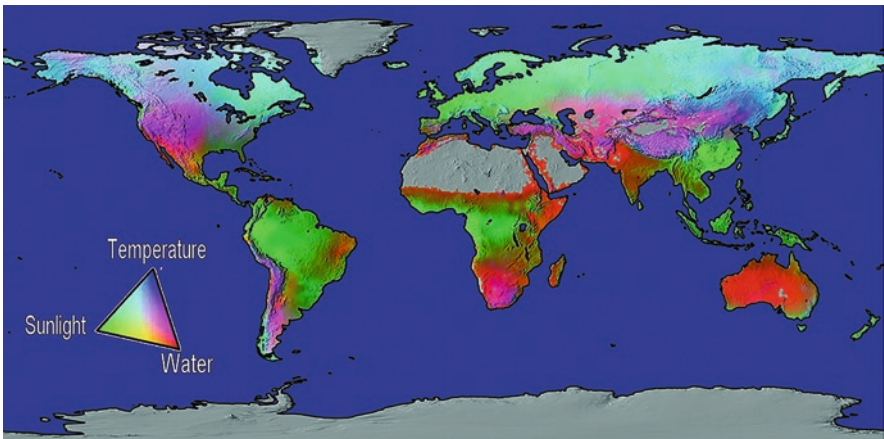


Fig. 28.1 Potential limits to vegetation net primary production based on fundamental physiological limits imposed by solar radiation, water balance, and temperature (from Churkina and Running 1998; Nemani et al. 2003; Running et al. 2004). Land regions with *gray color* are barren, sparsely vegetated and non-vegetated areas

(Jolly et al. 2005a). In addition to the abiotic constraints, another cost associated with the growth and maintenance of vegetation is called autotrophic respiration (Ryan 1991). Combining Monteith's logic, climate control, and some principles of modeling NPP learned from a general process-based ecosystem model, Biome-BGC (Running and Hunt 1993), the MODIS GPP/NPP algorithm was developed with satellite-derived data inputs. They include land cover, the fraction of photosynthetically active radiation absorbed by vegetation (FPAR), and leaf area index (LAI) as surface vegetation inputs (Running et al. 2000). Climate information is obtained from a NASA Goddard Global Modeling and Assimilation Office (GMAO)-developed global climatic data assimilation system.

28.2.2 The Algorithm

The daily GPP in the algorithm is calculated using the equation,

$$\text{GPP} = \text{PAR} \times \text{FPAR} \times \varepsilon \quad (28.1)$$

where ε is the light use efficiency, FPAR is the fraction of absorbed PAR, and PAR accounts for approximately 45% of incident shortwave solar radiation ($S \downarrow_s$), such that

$$\text{PAR} = S \downarrow_s \times 0.45 \quad (28.2)$$

The light use efficiency, ε , is derived by the reduction of the potential maximum, ε_{\max} , as a result of low temperatures (T_f) or limited water availability (VPD_f),

$$\varepsilon = \varepsilon_{\max} \times T_f \times \text{VPD}_f \quad (28.3)$$

The daily *PsnNet* is calculated as what remains once maintenance respiration from leaves and roots (R_{m_lr}) is subtracted from GPP,

$$\text{PsnNet} = \text{GPP} - R_{m_lr} \quad (28.4)$$

The original MODIS algorithm calculated growth respiration (R_g) as a function of annual maximum LAI, which may pose problems for many forests (see details in Sect. 28.5). As a result, for a given forest biome type R_g is invariable across both space and time, which is unreasonable according to plant physiological principles (Ryan 1991; Cannell and Thornley 2000). We have, therefore, modified it by assuming growth respiration is approximately 25% of NPP (Ryan 1991; Cannell and Thornley 2000) for C5 MOD17. Finally, annual NPP is computed as

$$\text{NPP} = 0.8 \times \sum_{i=1}^{365} (\text{PsnNet} - R_{m_w}) \quad (28.5)$$

where R_{m_w} is the maintenance respiration of live wood.

All maintenance respiration terms are calculated according to standard Q_{10} theory, which depends on the average ambient air temperature for leaves (Ryan 1991),

$$R_m = M_r \times B_r \times Q_{10}^{[(T_{avg} - 20)/10]} \quad (28.6)$$

where R_m refers to R_{m_lr} or R_{m_w} ; M_r is the living biomass in units of carbon for leaves, fine roots, or live wood, and B_r is the base respiration value, which is biome type-dependent. Leaf biomass is calculated using specific leaf area (SLA), while fine root biomass is calculated by multiplying the leaf biomass by the ratio of fine root to leaf biomass. This calculation is based on the assumption that the ratio between the fine root mass and leaf mass is constant. The live wood biomass is calculated using the annual maximum leaf biomass, and assumes that the ratio of live wood mass to leaf mass is constant for a given biome. Both these ratios are biome dependent. T_{avg} is daily average temperature. We assume Q_{10} has a constant value of 2.0 for both fine roots and live wood. For leaves, we have adopted a temperature-acclimated Q_{10} equation proposed by Tjoelker et al. (2001),

$$Q_{10} = 3.22 - 0.046 \times T_{avg} \quad (28.7)$$

The parameters for (28.3)–(28.6) are stored in a table called the Biome Properties Lookup Table (BPLUT). More details on the algorithm and data product format for both the 8-day and annual products are available in the MODIS GPP/NPP Users' Guide (Heinsch et al. 2003).

28.2.3 Data Flow and Products

Figure 28.2 provides a flowchart of the logic of the MODIS GPP and NPP algorithm, demonstrating how daily GPP and annual NPP are calculated with MODIS land cover, FPAR, and LAI, as well as the GMAO daily meteorological dataset. The 8-day MODIS GPP and PsnNet values for each pixel are actually the sum of the variables for the 8-day period, which are stored in the 8-day MOD17A2 product. Correspondingly, there is a quality control (QC) variable, which denotes whether the input 8-day FPAR/LAI is contaminated (e.g., by clouds) or reliable. The annual product (MOD17A3) includes annual total (i.e., summation of) GPP and NPP and the accompanying QC (for the definition of the annual QC, please see Sect. 28.5). Both MOD17A2 and MOD17A3 are stored in HDF-EOS format, which is a self-describing data format with ancillary metadata information, such as variable names, units, offset and gain, and other relevant data.

One of the unique features of MODIS GPP and NPP is that they represent the summation of carbon absorbed by vegetation, which differs from other MODIS

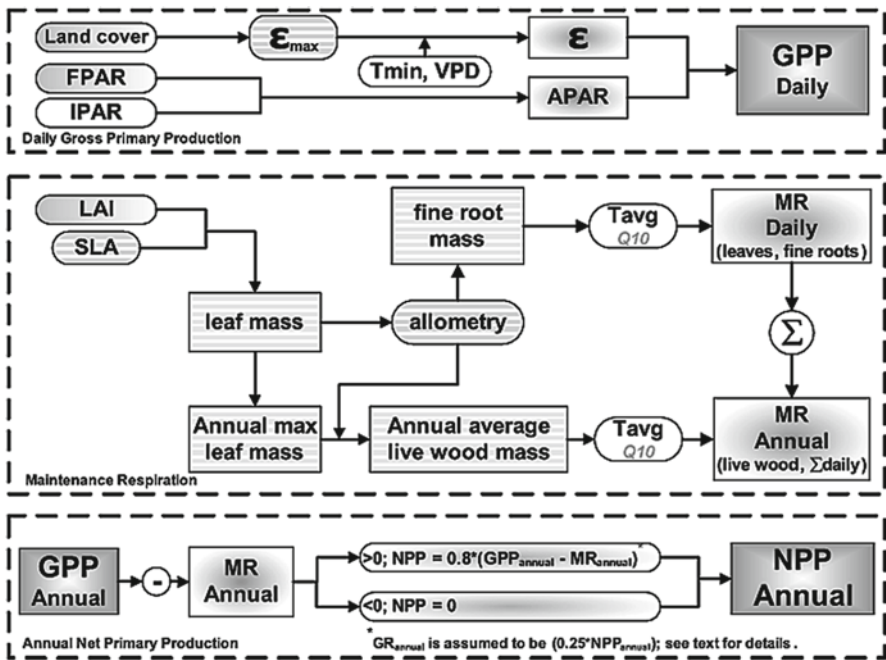


Fig. 28.2 Flowchart showing the logic behind the MOD17 Algorithm used to calculate both 8-day average GPP and annual NPP

vegetation products, such as the vegetation indices, FPAR, and LAI. Vegetation indices and FPAR/LAI are 8-day or 16-day maximum value composited data; there are no associated annual products. If there are missing data or data of poor quality resulting from contamination by cloud cover or severe atmospheric aerosol, users must fill the gaps with a method appropriate to their needs. However, for both 8-day and annual MOD17, if users want to fill the contaminated or missing gaps they must, theoretically, first gap-fill the FPAR and LAI, and then compute the MOD17 products using the MOD17 algorithm and corresponding daily meteorological data. This poses a potentially prohibitive obstacle to users. To solve this problem, we generate an improved MOD17 at the University of Montana and provide the data on our FTP site for users to freely download. The data format is similar to that of the official products to eliminate confusion. As a result, there are several options for users to obtain MOD17, depending on their needs. Users can get the near real-time 8-day MOD17A2, with gaps, through the Land Processes Distributed Active Archive Center (LP-DAAC), or they can get our reprocessed, quality-control filtered, and gap-filled 8-day and annual MOD17 through our FTP site at the end of the processing year. Section 28.5 details the method used to fill gaps in the MODIS FPAR/LAI inputs to reprocess the improved MOD17.

28.3 Input Uncertainties and the Algorithm

Three sources of MOD17 inputs exist (Fig. 28.2). For each pixel, biome type information is derived from MODIS land cover products (MOD12Q1); daily meteorological data are derived from the GMAO dataset; and 8-day FPAR and LAI are obtained from MOD15A2. The uncertainties in GMAO, MOD12Q1, MOD15A2, and the algorithm itself all influence MOD17 results.

The GMAO is an assimilated meteorological dataset, not observed data. As a result, it may contain systematic errors in some regions. At the global scale, we have found that the largest uncertainty for MOD17 derives from the global meteorological re-analysis data. We evaluate uncertainties in the three well-documented global re-analyses, including GMAO/NASA, ERA-40/ECMWF, and NCEP/NCAR, and how these uncertainties propagate to MOD17. To do so, we comprehensively compare the four main surface meteorological variables, surface downward solar radiation ($S\downarrow_s$), air temperature (T_{avg}), air vapor pressure (e_a), and vapor pressure deficit (VPD) from the three re-analyses datasets with surface weather station observations. We evaluated how the uncertainties in these re-analyses affect the MOD17 algorithm-derived NPP estimates (Zhao et al. 2006).

Our study showed that NCEP tends to overestimate $S\downarrow_s$, and underestimate both T_{avg} and VPD . ECMWF has the highest accuracy but its radiation is lower in tropical regions than NCEP, and GMAO's accuracy lies between NCEP and ECMWF. Temperature biases are mainly responsible for the large biases in VPD in the re-analyses data, because of VPD 's dependence on temperature. Figure 28.3 shows the patterns of zonal means and totals of MODIS GPP and NPP estimated by different re-analyses. MODIS NPP contains more uncertainties than GPP. Global total MODIS GPP and NPP driven by GMAO, ECMWF and NCEP show notable differences (>20 Pg C/yr) with the highest estimates from NCEP and the lowest from ECMWF. Again, the GMAO results lie somewhere between the NCEP and ECMWF estimates. Spatially, the larger discrepancies among the re-analyses and their derived MODIS GPP and NPP occur in the tropics. These results reveal that the biases in meteorological re-analyses datasets can introduce substantial error into GPP/NPP estimates, and emphasize the need to minimize these biases to improve the quality of MODIS GPP/NPP products (Zhao et al. 2006).

Land cover (MOD12Q1) accuracies fall in the range of 70–80%, and most “mistakes” are between similar classes (Strahler et al. 2002). A misclassified land cover pixel will likely lead to a misuse of MOD17 BPLUT parameters, which leads to less reliable MOD17 results. In addition, the current 1-km MODIS global land cover classification unit is probably too general for local application. Croplands, for example, are very diverse, yet the same set of parameters is applied indiscriminately to croplands everywhere, introducing large uncertainties for some crops in some regions.

A pixel-by-pixel comparison of MOD15A2 with ground measurements has a poor correlation, and retrieved LAI values have a propensity for overestimation under most conditions (Wang et al. 2004; Abuelgasim et al. 2006; Heinsch et al.

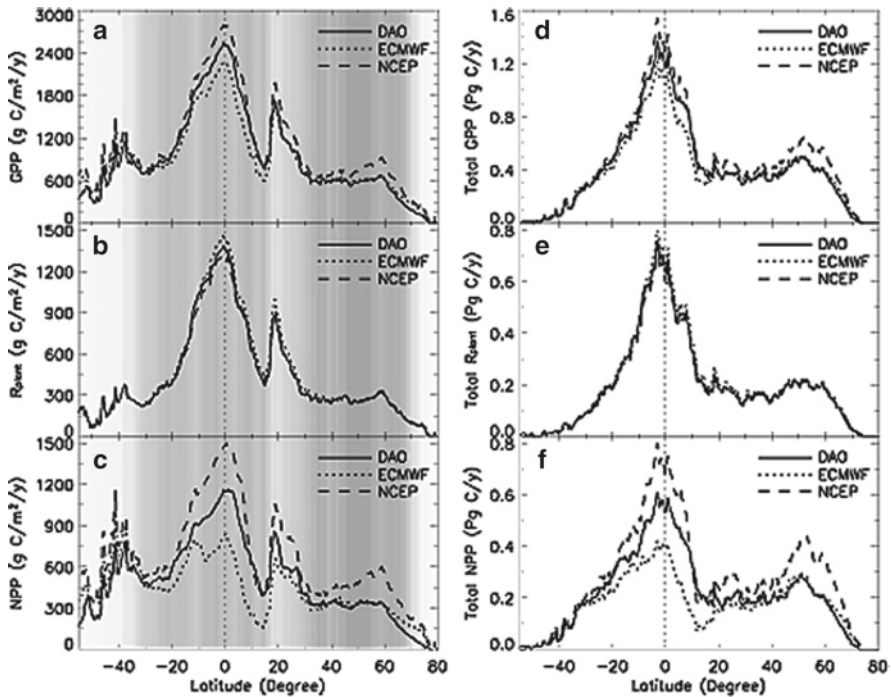


Fig. 28.3 Comparison of the zonal mean of annual GPP, R_{plant} , and NPP (a–c), and corresponding zonal totals (d–f) driven by the three re-analyses for 2000 and 2001 after aggregation into 0.5° intervals. The vegetated land area is shown as a gray scale, where darker shades represent more vegetation (Zhao et al. 2006)

2006; Pandya et al. 2006). Comparison at the patch level can significantly improve the results, but retrieved LAI are still inclined to produce higher values (Wang et al. 2004). In the MOD17 algorithm, FPAR is directly related to photosynthetic assimilation, and LAI is only related to autotrophic respiration. Therefore, an overestimated LAI from MOD15A2 may result in an underestimated NPP even if FPAR is relatively accurate. Although the temporal filling of unreliable FPAR/LAI greatly improves the accuracy of inputs, as discussed in Sect. 28.5, the filled values are artificial and contain uncertainties, and their quality is determined by the accuracy of FPAR/LAI without contamination in the temporal profile.

Finally, weaknesses in the MOD17 algorithm may lead to uncertainties in GPP/NPP. For example, the potential maximum value and realistic value under environmental controls for light use efficiency (ϵ), a key physiological variable, is still difficult to determine globally. GPP estimated from eddy flux towers can provide valuable information on ϵ (Turner et al. 2003a) and is useful to calibrate ϵ in the algorithm (Reichstein et al. 2004; Turner et al. 2005; Zhao et al. 2005). However, current studies are limited to a few sites, and more extensive studies are needed

to conduct the analysis across the global flux network. In addition, we still have little information regarding the actual values of other parameters in the BPLUT, such as fine root maintenance respiration base, and the biomass ratio of fine roots to leaves. Currently, for a given biome type, the same suite of parameters is being used without spatial variation, which may create uncertainties for some regions or specific plant species. Plant respiration algorithms also contain large uncertainties besides those in the input data since we do not yet fully understand plant respiration (Amthor 2000).

28.4 Validation

Validation to identify problems is our first priority because algorithm refinement and BPLUT calibration cannot take place. The BigFoot Project (<http://www.fsl.orst.edu/larse/bigfoot/index.html>) was organized specifically to address MODIS product validation needs for both the MOD15 LAI and the MOD17 GPP/NPP products, and our participation in the Bigfoot project has provided valuable assessment of the MODIS LAI, FPAR, GPP and NPP products. Figure 28.4 shows the logic used for MOD17 validation with AmeriFlux towers, including nine sites in agriculture, temperate mixed forest, semi-arid coniferous forest, boreal needle-leaf forest, Arctic tundra, desert grassland, prairie grassland, southern boreal mixed forest, and moist tropical broadleaf forest (Turner et al. 2006b). Measurements at these sites include field LAI, above-ground NPP, and net ecosystem CO₂ exchange (to estimate GPP) under a carefully-designed sampling scheme for a 7 × 7-km area specifically chosen to allow scaling with geostatistical theory to the MODIS datasets (Cohen et al. 2003). Maximum values, seasonality, and annual total values were estimated for comparison with MODIS data, and a number of papers were published in support of this activity, most recently those by Cohen et al. (2006) and Turner et al. (2005, 2006a, b).

Validation of weekly GPP is important to determine the accuracy of the MOD17 algorithm. As a result, we are developing relationships with researchers who participate in the FLUXNET network of eddy covariance flux towers, which AmeriFlux is a member of for the purpose of comparing MODIS GPP estimates with flux tower estimates (Running et al. 1999; Baldocchi et al. 2001; Falge et al. 2002; Heinsch et al. 2006). Fifteen sites participated fully in the validation effort, and results indicate that MODIS does a reasonable job of predicting GPP over various biomes throughout North America at 1-km resolution ($r = 0.86 \pm 0.17$ [95% confidence limit], Fig. 28.5a), although its accuracy varies by biome type (Heinsch et al. 2006). Much of the variation between tower and MODIS GPP arises from the use of coarse resolution GMAO input data ($28 \pm 45\%$), with much of that error derived from estimates of VPD and incoming shortwave solar radiation. Although the MOD17 GPP algorithm was parameterized specifically for use with

FLUX TOWER-BASED VALIDATION FOR MODIS GPP/NPP

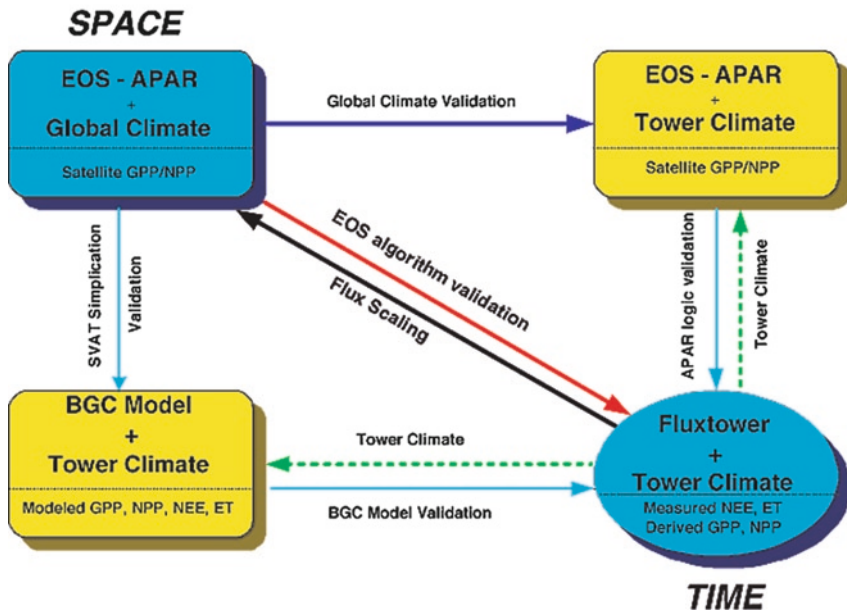


Fig. 28.4 The organizing logic we follow to validate MOD17 GPP with flux tower data, where tower meteorology, ground-measured FPAR, and more rigorous ecosystem models are sequentially substituted to evaluate sources of error and variability in MOD17 (based on Running et al. (1999))

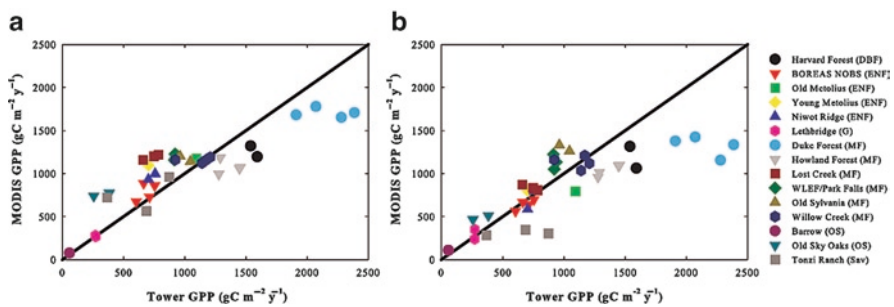


Fig. 28.5 Comparison of the annual MODIS GPP with flux tower-measured GPP for 15 AmeriFlux sites for 2001. These data were created using (a) the global GMAO meteorological data as driver and (b) tower-specific meteorology (Heinsch et al. 2006)

coarse resolution meteorology, using tower meteorology with the MOD17 algorithm suggests the main GPP algorithm is fairly accurate as well ($r = 0.79 \pm 0.21$ [95% confidence limit], Fig. 28.5b).

28.5 Processing Improvements and the Algorithm

Four major issues in the collection-4 (C4) MOD17 reprocessing exist:

1. The C4 MOD17 operational process fails to account for the mismatched spatial resolution between a 1-km MODIS pixel and the corresponding $1.00^\circ \times 1.25^\circ$ GMAO meteorological data.
2. The C4 MOD17 process produces GPP and NPP regardless of the quality of the 8-day FPAR/LAI (MOD15A2) data, which may introduce considerable error in the 8-day MODIS GPP product and, therefore, annual GPP and NPP (Kang et al. 2005).
3. The C4 MOD17 BPLUT was primarily developed and tested before the MODIS launch using upstream inputs that differ from those used operationally (Running et al. 2000).
4. C4 MOD17 uses a fill value for all vegetated pixels rather than a calculated annual quality control (QC) assessment, because there were insufficient data at launch to establish meaningful annual QC values.

To solve the first problem, we have spatially interpolated coarse resolution GMAO data to the resolution of the 1-km MODIS pixel using a non-linear interpolation scheme. Our studies reveal that this spatial interpolation of GMAO can also improve the accuracy of daily meteorological inputs except remove the big GMAO foot print in GPP/NPP images (Zhao et al. 2005). To account for quality control issues in the MODIS FPAR/LAI product, we have temporally filled the missing and contaminated data in the 8-day FPAR/LAI profile for each MODIS pixel. As illustrated in Fig. 28.6, the 8-day MODIS FPAR/LAI data (Myneni et al. 2002) contain some cloud-contaminated or missing data. According to the MOD15A2 quality assessment scheme provided by Myneni et al. (2002), FPAR/LAI values retrieved by the main algorithm (i.e., a Radiation Transfer model, denoted as RT) are most reliable, and those retrieved by the back-up algorithm (i.e., the empirical relationship between FPAR/LAI and NDVI) are less reliable since the backup algorithm is employed mostly when cloud cover, strong atmospheric effects, or snow/ice are detected. The LAI retrievals from the backup algorithm are of lower quality and not suitable for validation and other studies (Yang et al. 2006). For the C4 products, LAI retrievals by the backup algorithm generally have higher values than those derived using the RT model (Yang et al. 2006). This explains why the filled LAI is well below the maxima in some periods, as shown in Fig. 28.6 for the Amazon. The temporal filling process entails two steps. If the first (or last) 8-day FPAR/LAI is unreliable or missing, it is replaced by the closest reliable 8-day (16-day) value during that calendar year. This step ensures that the second step is performed in which, the remaining unreliable FPAR/LAI data are replaced by linear interpolation of the nearest reliable values prior to and after the missing data point.

We have also retuned the BPLUT based on the MODIS GPP validation work on eddy flux towers (Turner et al. 2003b, 2005, 2006a, b; Heinsch et al. 2006), and the synthesized global NPP datasets for different biomes (Clark et al. 2001; Gower et al. 1997, 2001; Zheng et al. 2003) to address the third issue.

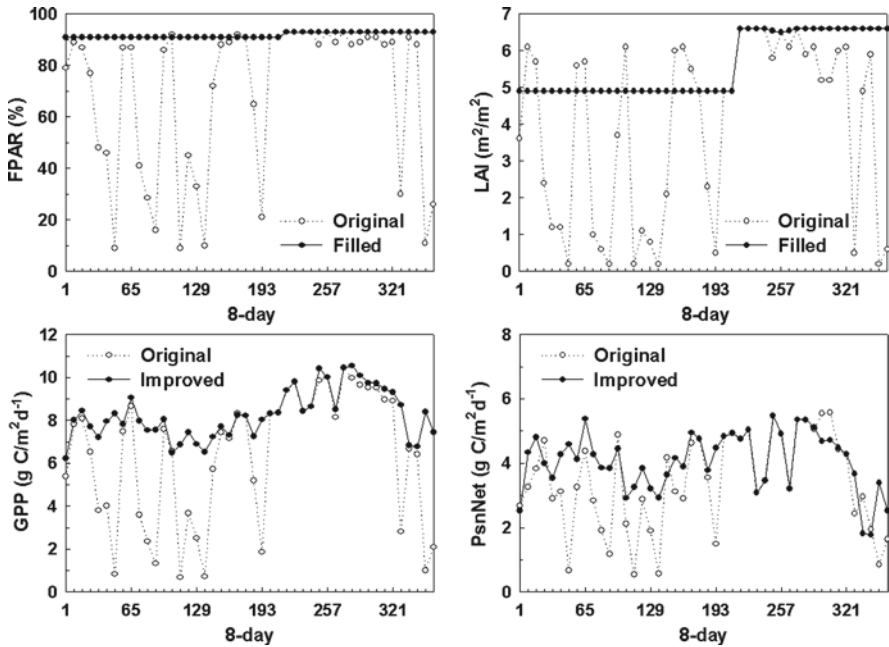


Fig. 28.6 An example depicting temporal filling unreliable 8-day Collection-4 FPAR/LAI, and therefore improved 8-day GPP and PsnNet for one MODIS 1-km pixel located in Amazon basin (lat = -5.0, lon = -65.0) (Zhao et al. 2005)

For the last issue regarding annual QC, we have created a meaningful annual GPP/NPP QC, expressed as:

$$QC = (NU_{\text{g}} / \text{TOTAL}_{\text{g}}) \times 100 \tag{28.8}$$

where NU_{g} is the number of days during the growing season with unreliable or missing MODIS LAI inputs, TOTAL_{g} is total number of days in the growing season. The growing season is defined as all days for which T_{min} is greater than -8°C , which is the minimum temperature control on photosynthesis for all biomes in the BPLUT. Although respiration can occur daily, T_{min} is below -8°C , and both FPAR and LAI are perhaps greater than 0, the GPP magnitude is negligible during the non-growing season. Furthermore, since the annual QC definition is limited to data during the growing season, the number of unreliable LAI values caused by snow cover will contribute less to the QC than those caused by cloud cover. Therefore, the annual MOD17A3 QC reveals the number of growing days (%) when the FPAR/LAI were artificially filled because of cloud cover when calculating the 8-day GPP and annual GPP/NPP (Fig. 28.7). Details of the improvements are available in Zhao et al. (2005).

We have further improved the MOD17 algorithm for C5 based on new knowledge of the MODIS LAI, and plant maintenance respiration. The C4

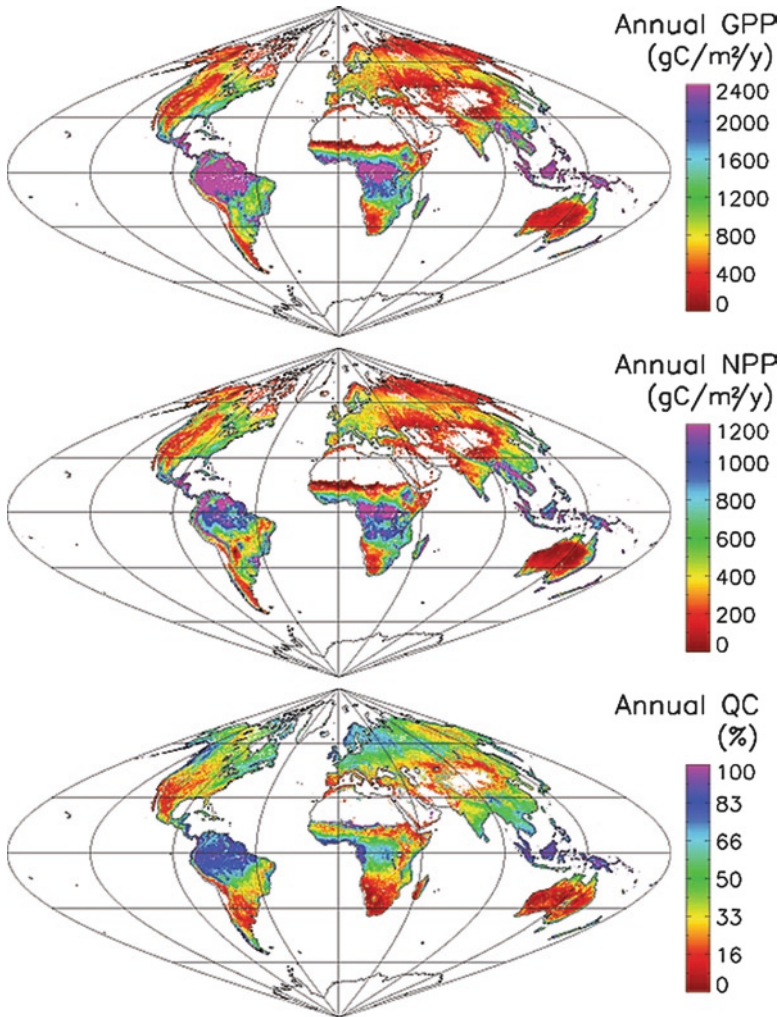


Fig. 28.7 Six-year (2000–2005) mean global 1-km C4.8 improved MODIS annual total GPP, NPP and annual QC images estimated with the C5 MOD17 system but with C4 MODIS FPAR/LAI input (annual QC denotes percent of 8-day with filled MOD15A2 FPAR/LAI as input to the improved MOD17 due to the cloud/aerosol contamination and missing periods. Also see the definition in (28.8) in the text). Land regions with *white color* are barren, sparsely vegetated and non-vegetated areas, including urban, snow and ice, and inland water body

MOD17 algorithm calculates growth respiration (R_g) using the annual maximum LAI (LAI_{max}), and thus, the accuracy of R_g is determined by the accuracy of LAI_{max} . However, when LAI is $>3.0 \text{ m}^2/\text{m}^2$, surface reflectances have lower sensitivity to LAI and the MODIS LAI is retrieved, in most cases, under reflectance saturation conditions (Myneni et al. 2002). Generally, annual MODIS LAI_{max} is calculated as $6.8 \text{ m}^2/\text{m}^2$ for pixels classified as forests. This logic can generate

R_g values that are greater than NPP. R_g is the energy cost for constructing organic compounds fixed by photosynthesis, and it is empirically parameterized as 25% of NPP (Ryan 1991; Cannell and Thornley 2000). To improve the algorithm, we replaced the LAI_{max} dependent R_g with $R_g = 0.25 \times NPP$, and annual MODIS NPP is computed as

$$NPP = GPP - R_m - R_g = GPP - R_m - 0.25 \times NPP \quad (28.9)$$

where R_m is plant maintenance respiration, and therefore,

$$\begin{aligned} NPP &= 0.8 \times (GPP - R_m) && \text{when } GPP - R_m \geq 0, \text{ and} \\ NPP &= 0 && \text{when } GPP - R_m < 0. \end{aligned} \quad (28.10)$$

Until recently, a constant value of 2.0 was widely used for Q_{10} in modelling R_m . Tjoelker et al. (2001) concluded that the Q_{10} for leaves declines linearly with increasing air temperatures in a consistent manner among a range of taxa and climatic conditions (see (28.7)). Wythers et al. (2005) found that the adoption of this temperature-variable Q_{10} may enhance the application of ecosystem models across broad spatial scales, or in climate change scenarios. We have adopted (28.6), replacing the constant Q_{10} for leaves in the algorithm to improve its performance.

28.6 Global Six-Year (2000–2005) Results

Using the improved algorithm and data processing, and the consistent GMAO data (version GEOS4), we reprocessed the global 1-km MOD17 for a six-year period (2000–2005). For this reprocessing, we have again retuned the BPLUT based on recent GPP validation efforts of the Bigfoot project and NTSG, as well as this consistent GMAO dataset. We have named the dataset Collection 4.8 (C4.8) MOD17, even though it was generated with our C5 system, because the input MODIS land cover is Collection-3 (C3) and the input MODIS FPAR/LAI is C4, which form the basis for our C4 processing. The following three sections present the results from the 6-year C4.8 GPP/NPP datasets.

28.6.1 Mean Annual GPP, NPP and QC

Figure 28.7 reveals the spatial pattern of the 6-year mean annual total GPP, NPP, and related QC. As expected, MODIS GPP and NPP have high values in areas covered by forests and woody savannas, especially in tropical regions. Low NPP occurs in areas dominated by adverse environments, such as high latitudes with

Table 28.1 Mean, standard deviation (in parentheses) of annual total GPP and NPP, and ratio of NPP to GPP for different biome types based on the 6-year (2000–2005) 1-km mean annual MODIS GPP and NPP, the corresponding areas for different biome types are derived from MODIS land cover

| | Evergreen needle forests | Evergreen broadleaf forests | Deciduous needle forests | Deciduous broadleaf forests | Mixed forests | Closed shrublands |
|------------------------------|--------------------------------|-----------------------------------|--------------------------------|-----------------------------------|------------------|----------------------|
| Area (M Km ²) | 6.14 | 15.10 | 2.05 | 1.73 | 7.06 | 0.95 |
| GPP (g C/m ² /yr) | 834 (329) | 2668 (342) | 726 (140) | 1276 (376) | 1043 (380) | 809 (359) |
| NPP (g C/m ² /yr) | 464 (152) | 1148 (301) | 305 (64) | 555 (229) | 523 (187) | 387 (190) |
| Ratio (NPP/GPP) | 0.56 | 0.43 | 0.42 | 0.43 | 0.50 | 0.48 |
| | Open shrublands | Woody Savannas | Savannas | Grasslands | Croplands | |
| Area (M Km ²) | 27.49 | 9.28 | 9.74 | 10.70 | 19.53 | |
| GPP (g C/m ² /yr) | 309 (209) | 1368 (533) | 1208 (417) | 392 (262) | 765 (310) | |
| NPP (g C/m ² /yr) | 145 (108) | 670 (276) | 596 (257) | 201 (122) | 419 (150) | |
| Ratio (NPP/GPP) | 0.47 | 0.49 | 0.49 | 0.51 | 0.55 | |

Note: Barren or sparsely vegetated land areas are excluded

short growing seasons constrained by low temperatures, and dry areas with limited water availability. At the global scale, from 2000 to 2005, MODIS estimated a total terrestrial annual GPP of 109.07 Pg C (± 1.66 S.D.), and an annual NPP of 52.03 Pg C (± 1.17 S.D.), ignoring barren land cover as defined by the MODIS land cover product. For vegetated areas, the mean annual GPP and NPP are 996.03 (± 823.67 S.D.) and 475.19 (± 375.44 S.D.) g C/m²/yr, respectively. Table 28.1 lists the mean and standard deviation of annual total GPP, NPP and the ratio between the two for different biome types and their corresponding areas. Evergreen broadleaf forests have the highest GPP and NPP, while open shrublands have the lowest. Generally, NPP is approximately half of GPP, agreeing with the results from field observations (Waring et al. 1998; Gifford 2003). The QC image reflects the percent of filled FPAR/LAI during the growing season as discussed above, and as expected, high values occur in areas of frequent cloud cover (i.e., higher precipitation).

28.6.2 Seasonality

The 8-day composite MOD17 GPP also demonstrates the seasonality of terrestrial ecosystem uptake of carbon from the atmosphere by photosynthesis at the 1-km scale. Figure 28.8 illustrates the seasonality of GPP both spatially and temporally. We have aggregated 8-day values to 3 months (Fig. 28.8a). The spatial seasonal variations clearly demonstrate the expected peak GPP in summer and the low values in winter over the mid- and high-latitudes of the Northern Hemisphere (NH). For Africa, the temporal development of MODIS GPP corresponds spatially to the movements of the Intertropical Convergence Zone (ITCZ). The dry season (approximately July) has lower GPP than the wet periods for the African rain forests south

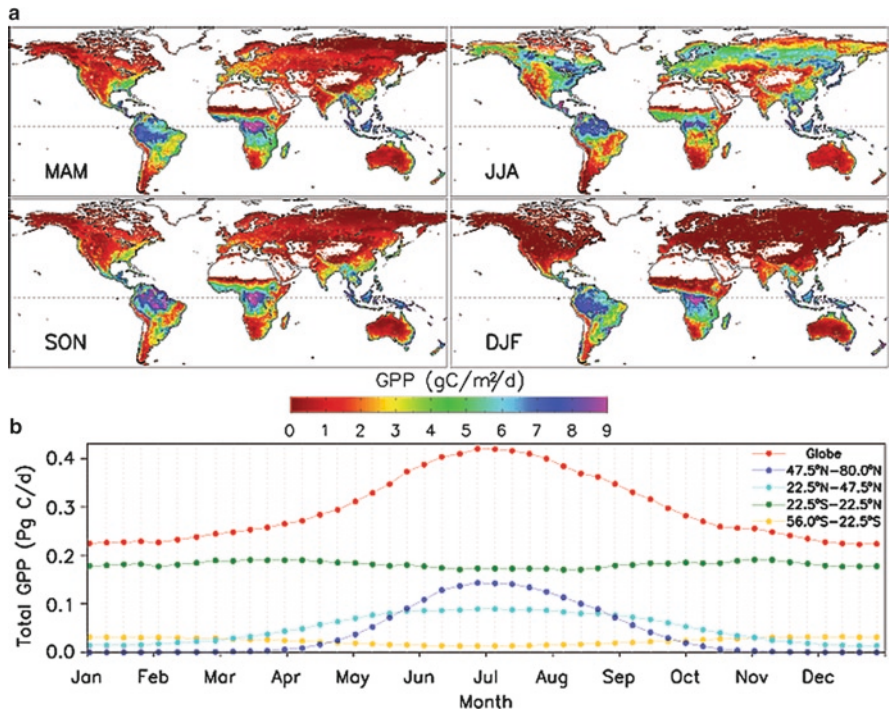


Fig. 28.8 Spatial pattern of (a) the seasonality of MODIS GPP and (b) temporal annual cycle of GPP at 8-day interval for four latitude bands and the globe. Land regions with *white color* are barren, sparsely vegetated and non-vegetated areas, including urban, snow and ice, and inland water bodies

of equator, because, compared with rainforests on other continents, the African tropical rainforest is relatively dry and receives $1,600\text{--}2,000\text{ mm/year}^{-1}$ of rainfall, while areas receiving more than 3,000 mm of rainfall in a given year are largely confined to the coastal areas of Upper and Lower Guinea. Virtually nowhere in the African tropical rainforest is the mean monthly rainfall higher than 100 mm for any month during the year (Tucker et al.). Rainforests of the Amazon basin have higher GPP during the dry season from July to November than during the wet season, which agree with Huete et al. (2006). During the dry season, monthly precipitation in the Amazon basin is approximately 100 mm, making solar radiation, not water, the leading limiting factor in this region. Figure 28.8b shows the annual cycle of total GPP for four latitudinal bands and for the entire globe. Relatively strong seasonal signals occur for the mid- and high-latitudes of the NH (i.e., north of $22.5^\circ N$). The areas south of $22.5^\circ S$ have opposite seasonal profiles relative to the mid- and high-latitudes of NH, and the seasonality for the southern hemisphere is much weaker. For the entire tropical region ($22.5^\circ S\text{--}22.5^\circ N$), there is little to no seasonality, while total GPP is always the highest among the four latitude bands. Therefore, at the global scale, magnitudes of the annual GPP cycle are mostly attributed to the tropical region, while the seasonality is largely determined by areas north of $22.5^\circ N$.

With global warming, the growing season in high latitudes has lengthened (Myneni et al. 1997; Zhou et al. 2001), and the 8-day MOD17 is a valuable dataset to detect the resulting change in the amount of carbon uptake.

28.6.3 Interannual Variability

The improved C4.8 MOD17 also has the ability to capture the response of terrestrial ecosystems to extreme climatic variability at the regional scale, especially widespread drought. During the growing season, water stress is generally the leading control factor on GPP and NPP. Figure 28.9 shows NPP anomalies from 2000 to 2005 as estimated from the 1-km C4.8 improved MODIS NPP, which demonstrates the sensitive responses of terrestrial ecosystem to drought in both China and the southwestern United States during 2000, Europe in 2003, and Australia and the Amazon in 2005. In 2000, the drought occurring in both China and the southwestern USA had negative impacts on NPP. The severe drought in Australia and a large part of the USA in 2002 led to reduced NPP. During 2003 the heat wave in Europe led to drought, and lowered NPP in the region. In 2005, the Amazon experienced the worst drought in 100 years, making water availability the leading limiting factor instead of solar radiation as

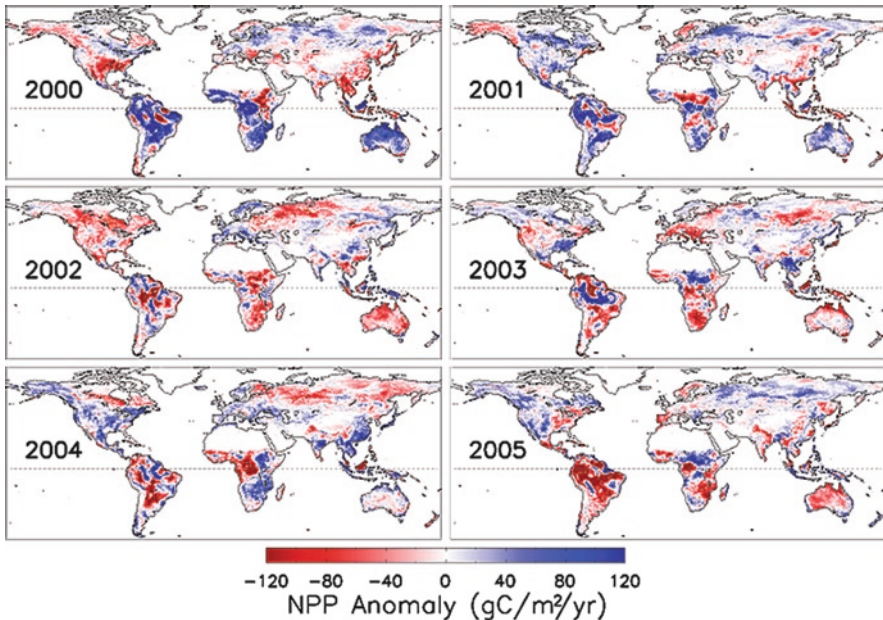


Fig. 28.9 Spatial pattern of C4.8 improved 1-km MODIS NPP anomalies from 2000 to 2005 with same period as the baseline for average. Land regions with *white color* are barren, sparsely vegetated and non-vegetated areas, including urban, snow and ice, and inland water bodies

found by Nemani et al. (2003) and Huete et al. (2006) under normal conditions. Australia also experienced drought in 2005, which is captured by MODIS NPP anomalies. The above-mentioned droughts are reported by different news media and scientific journals. While unable to monitor the impacts of climatic anomaly on ecosystems at the stand or local level, the 1-km resolution MOD17 can measure and track the changes in environment, such as desertification, deforestation, disturbance (e.g., fire and insect outbreak), and the impacts of pollution on a larger scale.

Using AVHRR to calculate NPP, Nemani et al. (2003) found that during the period between 1982 and 1999, the correlation between NPP and inverted anomaly of CO_2 interannual growth rate was 0.70 ($P < 0.001$). For this improved 1-km MOD17, the correlation between MODIS NPP and inverted anomaly of CO_2 interannual growth rate is 0.85 ($P < 0.016$), and 0.91 for the NCEP-driven MODIS NPP with CO_2 growth rate (Fig. 28.10). The high correlation between NPP and CO_2 growth rates may imply terrestrial NPP, rather than heterotrophic respiration or wildfires, is the primary driver of atmospheric CO_2 growth rates. Several potential reasons account for this. First, the similar variations of global rates of changes in $^{13}\text{C}/^{12}\text{C}$ isotopic ratio of CO_2 and CO_2 suggest that exchange of atmospheric CO_2 with terrestrial plants and soil is the dominant cause for both signals (Keeling et al. 2001). Second, tropical NPP values are more highly correlated with CO_2 growth rates than at other latitudes, and NPP and soil respiration are more tightly coupled in tropical areas (Nemani et al. 2003). Third, soil carbon residence times range from less than 4 years in hot, wet tropical areas to greater than 1,000 years in cold boreal or dry desert conditions (Barrett 2002; Mayorga et al. 2005), and furthermore, NPP is the source of soil respiration, and thus, to some extent, NPP exerts control over heterotrophic respiration. More studies are needed to quantify the

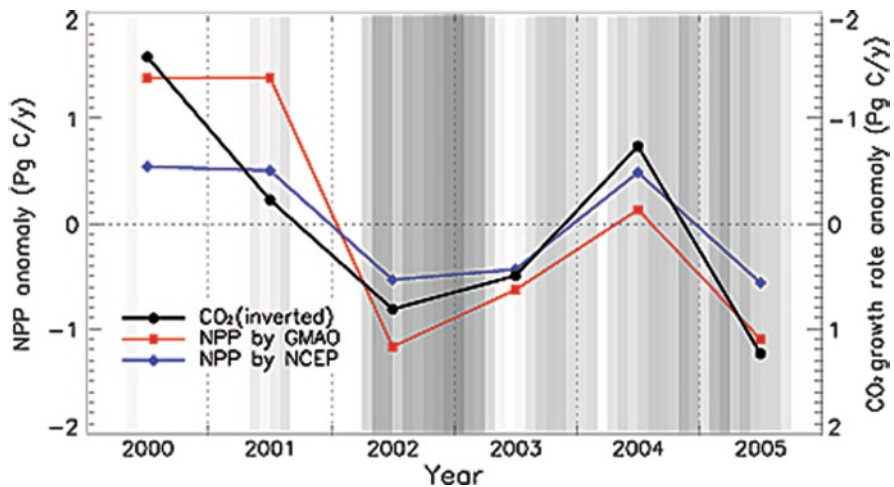


Fig. 28.10 Interannual variations in global total C4.8 MOD17 NPP driven by NCEP and GMAO, respectively, in relation to inverted atmospheric CO_2 interannual growth rate. A Multivariate ENSO Index (MEI) is shown in gray scale, where darker shades represent higher MEI values

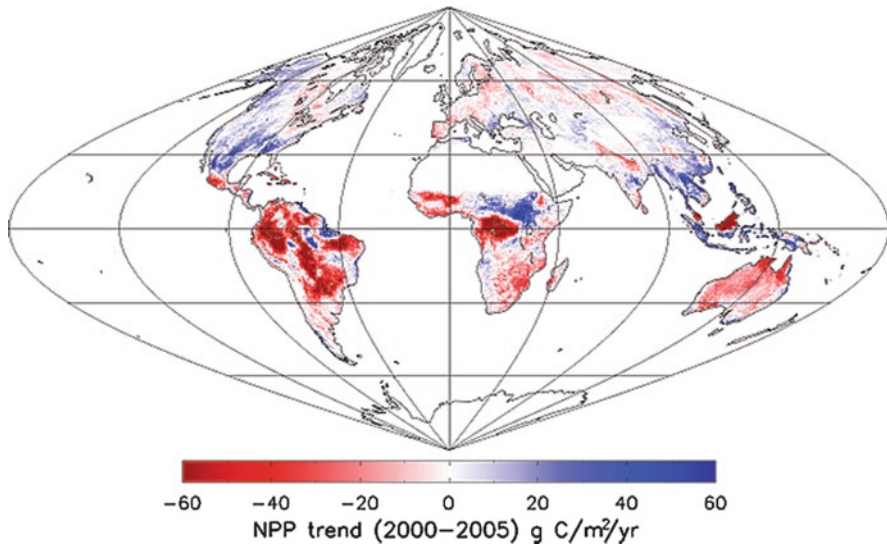


Fig. 28.11 Spatial pattern of 1-km NPP trend from 2000 to 2005 estimated by C4.8 MOD17. Land regions with *white color* are barren, sparsely vegetated and non-vegetated areas, including urban, snow and ice, and in-land water bodies. Some *white color* includes areas with NPP trend close to 0

contribution of terrestrial NPP to the variation in atmospheric CO_2 in the context of the global carbon cycle.

The 6 years of MODIS data, on the other hand, show that global total NPP decreased during 2000–2005 (Fig. 28.10). Spatially, the largest decreasing trends occurred in areas of the tropics and most of Southern Hemisphere, while increasing trends in most of mid-latitudes over the Northern Hemisphere (Fig. 28.11).

28.7 Land Management and Biospheric Monitoring Applications

MODIS NPP is potentially very useful for land management and renewable natural resource estimations. MODIS weekly GPP agreed well with field-observed herbaceous biomass for a grassland in North Dakota (Reeves et al. 2006), and was strongly related to wheat yield for cropland in Montana (Reeves et al. 2005). For forests in the Mid-Atlantic region of the U.S., the regional mean of MODIS NPP was very close to the mean stem and root increment estimated from the US Forest Service Forest Inventory and Analysis (FIA) data (Pan et al. 2006).

MODIS NPP products are also invaluable to measure both changes in the environment, such as desertification, deforestation, disturbances (e.g., fire and insect outbreak), as well as the impacts of pollution and climate change, and to evaluate ecosystem status and service (e.g., ecosystem health, habitat and wildlife, ecological

footprint) (Running et al. 2004). Loehman (2006) used MODIS GPP to study the impacts of resources on rodent populations, especially deer mice, the main reservoir host for the Sin Nombre virus (SNV), a primary disease agent of Hantavirus pulmonary syndrome. Milesi et al. (2003a, b, 2005) have used the global remotely-sensed NPP to analyze the policy relevance of NPP, such as the effects of urbanization on NPP, and identification of human populations that are vulnerable to changes in NPP resulting from interannual climate variability. In addition, MODIS NPP data can provide information to policy makers and stakeholders in evaluating greenhouse gas mitigation (Baisden 2006). Finally, the Heinz Center is considering MODIS annual NPP as a measure of national ecosystem services (Meyerson et al. 2005).

We now use the MODIS GPP and NPP algorithm and data to develop a real-time biospheric monitoring system. The final goal of MOD17 is to generate a regular, real-time monitor of the terrestrial biosphere that provides a meaningful quantification of ecosystem biogeochemistry, of which GPP and NPP are the best current candidates. However, few scientists, and even fewer policy makers can relate intuitively to weekly maps with units of “gC/m²/d”. Departures from a long-term mean condition (similar to weather data) is the most easily understood and interpreted presentation of MODIS GPP and NPP data for policy purposes. With a defined high-quality historical average GPP for each 1-km pixel now complete for 2000–2005, we can compare the most recent 32-day MOD17 GPP against the average GPP for the same period from 2000 to 2005 as an anomaly map. At the global scale (Fig. 28.12), we will use the coarse resolution NCEP/NCAR re-analyses data to generate near real-time GPP. For North America, relatively high resolution, i.e., 32-km, near real-time weather data are available from the regional data assimilation

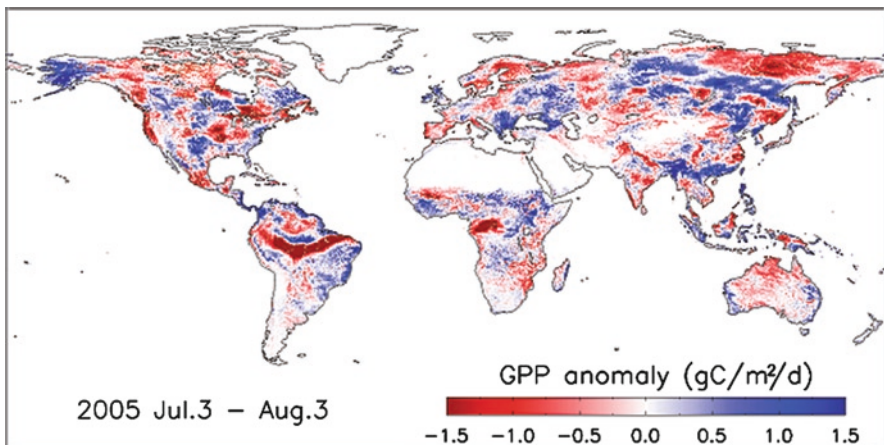


Fig. 28.12 A prototype observed departure from normal for 32-day GPP. When operational, this map updates every 32 days (less than 8 days behind the acquisition date). Land regions with *white color* are barren, sparsely vegetated and non-vegetated areas, including urban, snow and ice, and inland water bodies. Some *white color* includes areas with GPP anomaly close to 0

system for the North American Regional Reanalysis (NARR) (Mesinger et al. 2006), or our own surface observation gridding system (SOGS) (Jolly et al. 2005b) using real-time observations from National Climatic Data Center (NCDC) to produce relatively high resolution real-time MODIS GPP and NPP. Nemani's Ecocasting System (<http://ecocast.arc.nasa.gov/>) will use this real-time GPP for future forecasting.

Anomalies in terrestrial GPP and NPP demonstrate the effects of environmental drivers such as ENSO events, climate change, pollution episodes, land degradation, and agricultural expansion. A regular dataset for global GPP, NPP and their anomalies and trends are useful in biodiversity analysis (Sala et al. 2000; Waring et al. 2006) and as an environmental monitor for policy formulation (Niemeijer 2002). These anomalies delivered in near real-time will provide important information on global agricultural commodity trends. This includes similar yet improved information over what currently are evaluated with AVHRR NDVI by the Foreign Agricultural Service of the U.S. Dept of Agriculture, the FAO, and other agencies. The United Nations FAO is currently considering MODIS GPP anomaly dataset for a new global Drought and Famine warning system. The GEOSS (Global Earth Observation System of Systems) requires quantitative monitoring of the global biosphere with sufficient temporal continuity for change detection, similar to what is offered here with the MODIS NPP and evapotranspiration multi-year datasets. More discussion of MOD17 applications are found in Running et al. (2004).

28.8 Future Directions

Water stress is one of the most important limiting factors controlling terrestrial primary production, and the performance of a primary production model is largely determined by its capacity to capture environmental water stress. The MOD17 GPP and NPP algorithm uses only VPD to express total environmental water stress. In some dry regions where soil water is severely limiting, MOD17 underestimates water stress, thus overestimating GPP, and fails to capture the intra-annual variability of water stress for areas with strong summer monsoons (Mu et al. 2006a; Turner et al. 2005; Leuning et al. 2005; Pan et al. 2006). We have developed a MODIS ET algorithm, validated at 22 AmeriFlux towers, and generated a global MODIS evapotranspiration product (Mu et al. 2006b). Once the MODIS ET has reached Stage-2 validation, we will add ET as an additional modifier to the ϵ calculation at each 8-day time step. Since this index represents a non-linear relationship between soil moisture and leaf water potential, we expect the final relationship will manifest non-linear as well.

With the Terra and Aqua satellites nearing the end of their missions, spectral data from the next-generation radiometer, the Visible-Infrared Imager-Radiometer Suite (VIIRS) flying on the National Polar-orbiting Operational Environmental Satellite System (NPOESS) (Miller et al. 2006), is expected to generate MOD17-like products. The MOD17 algorithm can also use data from other environmental satellites launched by different countries to produce regional or global GPP and NPP. At that point, we

expect these weekly GPP and annual NPP data to routinely become part of land management, environmental policy analysis, agricultural economics, and monitoring of biospheric change. These data products do not meet all the needs and expectations of scientists, managers, policymakers, and the public. However, they are unique tools, which provide global coverage and weekly continuity of key measures of the impacts of environmental changes on terrestrial activity, and ultimately, on humankind.

Acknowledgments This research was funded by the NASA/EOS MODIS Project (NNG04HZ19C) and Natural Resource/Education Training Center (grant NAG5-12540). The improved 1-km MODIS terrestrial GPP and NPP data are available at <http://www.nts.gov.umt.edu/>. We thank Dr. Niall Hanan for his thoughtful and insightful comments on an earlier draft of this paper.

References

- Abuelgasim AA, Fernandes RA, Leblanc SG (2006) Evaluation of national and global LAI products derived from optical remote sensing instruments over Canada. *IEEE Trans Geosci Remote Sens* 44(4):1872–1884
- Amthor JS (2000) The Mccree–de Wit–Penning de Vries–Thornley respiration paradigms: 30 years later. *Ann Bot (Lond)* 86:1–20
- Baisden WT (2006) Agriculture and forest productivity for modelling policy scenarios: evaluating approaches for New Zealand greenhouse gas mitigation. *J R Soc N Z* 36:1–15
- Baldocchi D, 26 co-authors (2001) FLUXNET: A new tool to study the temporal and spatial variability of ecosystem-scale carbon dioxide, water vapor and energy flux densities. *Bull Amer Meteorol Soc* 82:2415–2434
- Barrett DJ (2002) Steady state turnover time of carbon in the Australian terrestrial biosphere. *Global Biogeochem Cycles* 16. doi:10.1029/2002GB001860
- Cannell MGR, Thornley JHM (2000) Modelling the components of plant respiration: some guiding principles. *Ann Bot (Lond)* 85:45–54
- Churkina G, Running SW (1998) Contrasting climatic controls on the estimated productivity of different biomes. *Ecosystems* 1:206–215
- Clark DA, Brown S, Kicklighter D, Chambers J, Thomlinson JR, Ni J, Holland EA (2001) Net Primary Production in tropical forests: an evaluation and synthesis of existing field data. *Ecol Appl* 11:371–384
- Cohen WB, Maersperger TK, Turner DP, Ritts WD, Pflugmacher D, Kennedy RE, Kirschbaum A, Running SW, Costa M, Gower ST (2006) MODIS land cover and LAI Collection 4 product quality across nine sites in the Western Hemisphere. *IEEE Trans Geosci Remote Sens* 44(7):1843–1857
- Cohen WB, Maersperger TK, Yang Z, Gower ST, Turner DP, Ritts WD, Berterretche M, Running SW (2003) Comparisons of land cover and LAI estimates derived from ETM+ and MODIS for four sites in North America: a quality assessment of 2000/2001 provisional MODIS products. *Remote Sens Environ* 88:221–362
- Falge E, 31 co-authors (2002) Seasonality of ecosystem respiration and gross primary production as derived from FLUXNET measurements. *Agric For Meteorol* 113:75–95
- Gower ST, Krankina O, Olson RJ, Apps MJ, Linder S, Wang C (2001) Net primary production and carbon allocation patterns of boreal forest ecosystems. *Ecol Appl* 11:1395–1411
- Gower ST, Vogel JG, Norman JM, Kucharik CJ, Steele SJ, Stow TK (1997) Carbon distribution and aboveground net primary production in aspen, jack pine, and black spruce stands in Saskatchewan and Manitoba, Canada. *J Geophys Res* 104(D22):29029–29041
- Gifford RM (2003) Plant respiration in productivity models: Conceptualisation, representation and issues for global terrestrial carbon-cycle research. *Funct Plant Biol* 30:171–186

- Heinsch FA, 12 co-authors (2003) User's Guide: GPP and NPP (MOD17A2/A3) Products, NASA MODIS Land Algorithm. University of Montana, NTSG, 57
- Heinsch FA, 25 co-authors (2006) Evaluation of remote sensing based terrestrial productivity from MODIS using ameriflux tower eddy flux network observations. *IEEE Trans Geosci Remote Sens* 44:1908–1925
- Huete AR, Didan K, Shimabukuro YE, Ratana P, Saleska SR, Hutrya LR, Yang W, Nemani RR, Myneni R (2006) Amazon rainforests green-up with sunlight in dry season. *Geophys Res Lett* 33:L06405, doi:10.1029/2005GL025583
- Imhoff ML, Bounoua L, Richetts T, Loucks C, Harriss R, Lawrence WT (2004) Global pattern in human consumption of net primary production. *Nature* 429:870–873
- Jolly WM, Nemani R, Running SW (2005a) A generalized, bioclimatic index to predict foliar phenology in response to climate. *Glob Change Biol* 11:619–632
- Jolly WM, Graham JM, Nemani RR, Running SW (2005b) A flexible, integrated system for generating meteorological surfaces derived from point sources across multiple geographic scales. *Environ Model Software* 20:873–882
- Justice CO, Townshend JRG, Vermote EF, Masuoka E, Wolfe RE, Saleous N, Roy DP, Morisette JT (2002) An overview of MODIS Land data processing and product status. *Remote Sens Environ* 83:3–15
- Kang S, Running SW, Zhao M, Kimball JS, Glassy J (2005) Improving continuity of MODIS terrestrial photosynthesis products using an interpolation scheme for cloudy pixels. *Int J Remote Sens* 28:1659–1676
- Keeling CD, Piper SC, Bacastow RB, Wahlen M, Whorf TP, Heimann M, Meijer HA (2001) Exchanges of atmospheric CO₂ and ¹³CO₂ with the terrestrial biosphere and oceans from 1978 to 2000: 1. Global aspects, SIO Reference Series, 01–06 Scripps Institution of Oceanography, San Diego
- Leuning R, Cleugh HA, Zegelin SJ, Hughes DE (2005) Carbon and water fluxes over a temperate Eucalyptus forest and a tropical wet/day savanna in Australia: measurements and comparison with MODIS remote sensing estimates. *Agric For Meteorol* 129:151–173
- Loehman R (2006) Modeling interactions among climate, landscape, and emerging diseases: a hantavirus case study. Ph.D. dissertation, University of Montana
- Mayorga E, Aufdenkampe AK, Masiello CA, Krusche AV, Hedges JI, Quay PD, Richey JE, Brown TA (2005) Young organic matter as a source of carbon dioxide outgassing from Amazonian rivers. *Nature* 436:538–541
- Melillo JM, McGuire AD, Kicklighter DW, Moore B III, Vorosmarty CJ, Schloss AL (1993) Global climate change and terrestrial net primary production. *Nature* 63:234–240
- Mesinger F, 18 co-authors (2006) North American regional reanalysis. *Bull Amer Meteorol Soc* 87:343–360
- Meyerson L, Baron J, Melillo J, Naiman R, O'Malley R, Orians G, Palmer M, Pfaff A, Running S, Sala O (2005) Aggregate measures of ecosystem services: Can we take the pulse of nature? *Front Ecol Environ* 3:56–59
- Milesi C, Elvidge CD, Nemani RR, Running SW (2003a) Assessing the impact of urban land development on net primary productivity in the southeastern United States. *Remote Sens Environ* 86:273–432
- Milesi C, Elvidge CD, Nemani RR, Running SW (2003b) Assessing the environmental impacts of human settlements using satellite data. *Manage Environ Qual* 14:99–107
- Milesi C, Hashimoto H, Running SW, Nemani RR (2005) Climate variability, vegetation productivity and people at risk. *Global Planet Change* 47:221–231
- Miller SD, Hawkins JD, Kent J, Turk FJ, Lee TF, Kuciauskas AP, Richardson K, Wade R, Hoffman C (2006) Nexsat: Previewing NPOESS/VIIRS Imagery Capabilities. *Bull Amer Meteorol Soc* 87:433–446
- Monteith JL (1972) Solar radiation and productivity in tropical ecosystems. *J Appl Ecol* 9: 747–766
- Monteith JL (1977) Climate and efficiency of crop production in Britain. *Philos Trans R Soc Lond B* 281:277–294

- Mu Q, Zhao M, Heinsch FA, Liu M, Tian H, Running SW (2006a) Evaluating water stress controls on primary production in biogeochemical and remote sensing-based models. *J Geophys Res* 112:G01012, doi:10.1029/2006JG000179
- Mu Q, Heinsch FA, Zhao M, Running SW, Cleugh HA, Leuning R (2006b) Development of a global evapotranspiration algorithm based on MODIS and global meteorology data. *Remote Sens Environ* 111(4):519–536
- Myneni RB, Keeling CD, Tucker CJ, Asrar G, Nemani RR (1997) Increased plant growth in the northern high latitudes from 1981–1991. *Nature* 386:698–702
- Myneni RB, 15 co-authors (2002) Global products of vegetation leaf area and fraction absorbed PAR from year one of MODIS data. *Remote Sens Environ* 83:214–231
- Wythers KR, Reich P, Tjoelker MG, Bolstad PB (2005) Foliar respiration acclimation to temperature and temperature variable Q_{10} alter ecosystem carbon balance. *Glob Change Biol* 11:435–449
- Nemani RR, Keeling CD, Hashimoto H, Jolly WM, Piper SC, Tucker CJ, Myneni RB, Running SW (2003) Climate-driven increases in global terrestrial net primary production from 1982 to 1999. *Science* 300:1560–1563
- Niemeijer D (2002) Developing indicators for environmental policy: data-driven and theory-driven approaches examined by example. *Environ Sci Policy* 5:91–103
- Pan Y, Birdsey R, Hom J, McCullough K, Clark K (2006) Improved estimates of net primary productivity from MODIS satellite data at regional and local scales. *Ecol Appl* 16:125–132
- Pandya MR, Singh RP, Chaudhari KN, Bairagi GD, Sharma BR, Dadhwal VK, Parihar JS (2006) Leaf area index retrieval using IRS LISS-III sensor data and validation of the MODIS LAI product over central India. *IEEE Trans Geosci Remote Sens* 44:1858–1865
- Prentice IC, Farquhar GD, Fasham MJR, Goulden ML, Heimann M, Jaramillo VJ, Khashgi HS, Le Quéré C, Scholes RJ, Wallace DWR (2001) The carbon cycle and atmospheric carbon dioxide. In: Ding JY, Griggs DJ, Noguer M, van der Linden PJ, Dai X, Maskell K, Johnson CA (eds) *Climate change 2001: the scientific basis. Contribution of working group I to the third assessment report of the intergovernmental panel on climate change*. Cambridge University Press, Cambridge, United Kingdom and New York, USA, T. Houghton, 182–237
- Reeves MC, Zhao M, Running SW (2005) Usefulness and limits of MODIS GPP for estimating wheat yield. *Int J Remote Sens* 27:1403–1421
- Reeves MC, Zhao M, Running SW (2006) Applying improved estimates of MODIS productivity to characterize grassland vegetation dynamics. *Rangeland Ecol Manage* 59:1–10
- Reichstein M, Valentini R, Running SW, Tenhunen J (2004) Improving remote sensing-based GPP estimates (MODIS-MOD17) through inverse parameter estimation with CARBOEUROPE eddy covariance flux data. *EGU meeting Nice 2004. Geophys Res Abstr* 6:01388
- Running SW, Hunt ER (1993) Generalization of a forest ecosystem process model for other biomes, BIOMEBGC, and an application for global-scale models. In: Ehleringer JR, Field CB (eds) *Scaling physiological processes: leaf to globe*. Academic Press, San Diego, pp 141–158
- Running SW, Nemani RR, Heinsch FA, Zhao M, Reeves M, Hashimoto H (2004) A continuous satellite-derived measure of global terrestrial primary productivity: Future science and applications. *Bioscience* 56:547–560
- Running SW, Baldocchi DD, Turner DP, Gower ST, Bakwin PS, Hibbard KA (1999) A global terrestrial monitoring network integrating tower fluxes, flask sampling, ecosystem modeling and EOS satellite data. *Remote Sens Environ* 70:108–128
- Running SW, Thornton PE, Nemani RR, Glassy JM (2000) Global terrestrial gross and net primary productivity from the earth observing system. In: Sala O, Jackson R, Mooney H (eds) *Methods in Ecosystem Science*. Springer-Verlag, New York, pp 44–57
- Ryan MG (1991) The effects of climate change on plant respiration. *Ecol Appl* 1:157–167
- Sala OE, 18 co-authors (2000) Global biodiversity scenarios for the year 2100. *Science* 287:1770–1774
- Schimel DS, 29 co-authors (2001) Recent patterns and mechanisms of carbon exchange by terrestrial ecosystems. *Nature* 414:169–172

- Strahler AH, Friedl M, Zhang X, Hodges J, Cooper CSA, Baccini A (2002) The MODIS land cover and land cover dynamics products Presentation at Remote Sensing of the Earth's Environment from Terra in L'Aquila, Italy
- Tjoelker MG, Oleksyn J, Reich P (2001) Modelling respiration of vegetation: evidence for a general temperature-dependent Q_{10} . *Glob Change Biol* 7:223–230
- Tucker CJ, Townshend JRG, Goff TE (1985) African land-cover classification using satellite data. *Science* 227:369–375
- Turner DP, Ritts WD, Zhao M, Kurc SA, Dunn AL, Wofsy SC, Small EE, Running SW (2006a) Assessing interannual variation in MODIS-based estimates of gross primary production. *IEEE Trans Geosci Remote Sens* 44:1899–1907
- Turner DP, Ritts WD, Cohen WB, Gower ST, Running SW, Zhao M, Costae MH, Kirschbaum AA, Ham JM, Saleska SS, Ahl DE (2006b) Evaluation of MODIS NPP and GPP products across multiple biomes. *Remote Sens Environ* 102:282–292
- Turner DP, Urbanski S, Bremer D, Wofsy SC, Meyers T, Gower ST, Gregory M (2003a) A cross-biome comparison of daily light use efficiency for gross primary production. *Glob Change Biol* 9:383–395
- Turner DP, Ritts WD, Cohen WB, Gower ST, Zhao M, Running SW, Wofsy SC, Urbanski S, Dunn SA, Munger JW (2003b) Scaling Gross Primary Production (GPP) over boreal and deciduous forest landscapes in support of MODIS GPP product validation. *Remote Sens Environ* 88:256–270
- Turner DP, 17 co-authors (2005) Site-level evaluation of satellite-based global terrestrial gross primary production and net primary production monitoring. *Glob Change Biol* 11:666–684
- Wang Y, Woodcock CE, Buermann W, Stenberg P, Voipio P, Smolander H, Häme T, Tian Y, Hu J, Knyazikhin Y, Myneni RB (2004) Evaluation of the MODIS LAI algorithm at a coniferous forest site in Finland. *Remote Sens Environ* 91:114–127
- Waring RH, Landsberg JJ, Williams M (1998) Net primary production of forests: a constant fraction of gross primary production? *Tree Physiol* 18:129–134
- Waring RH, Coops NC, Fan W, Nightingale JM (2006) MODIS enhanced vegetation index predicts tree species richness across forested ecoregions in the contiguous U.S.A. *Remote Sens Environ* 103:218–226
- Yang W, Huang D, Tan B, Stroeve JC, Shabanov NV, Knyazikhin Y, Nemani RR, Myneni RB (2006) Analysis of leaf area index and fraction of PAR absorbed by vegetation products from the terra MODIS sensor: 2000–2005. *IEEE Trans Geosci Remote Sen* 44:1829–1842
- Zhao M, Heinsch FA, Nemani RR, Running SW (2005) Improvements of the MODIS terrestrial gross and net primary production global dataset. *Remote Sens Environ* 95:164–176
- Zhao M, Running SW, Nemani RR (2006) Sensitivity of Moderate Resolution Imaging Spectroradiometer (MODIS) terrestrial primary production to the accuracy of meteorological reanalyses. *J Geophys Res* 111:G01002. doi:10.1029/2004JG000004
- Zheng D, Prince S, Wright R (2003) Terrestrial net primary production estimates for 0.5° grid cells from field observations – a contribution to global biogeochemical modeling. *Glob Change Biol* 9:46–64
- Zhou L, Tucker CJ, Kaufmann RK, Slayback D, Shabanov NV, Myneni RB (2001) Variations in northern vegetation activity inferred from satellite data of vegetation index during 1981 to 1999. *J Geophys Res* 106:20069–20083

Chapter 29

MODIS-Derived Global Fire Products

Christopher O. Justice, Louis Giglio, David Roy, Luigi Boschetti, Ivan Csiszar, Diane Davies, Stefania Korontzi, W. Schroeder, Kelley O’Neal, and Jeff Morisette

29.1 Introduction

The NASA MODIS global fire data products are digital maps calculated from Terra and Aqua MODIS data, designed primarily to serve the needs of the emissions modeling community. The algorithms were designed to provide a comprehensive global product, and to perform well over the expected range of fire conditions and scene variability. The goal was to maximize product accuracy, and minimize errors of commission and omission. Two products exist, including one, which characterizes actively burning fire locations at satellite overpass time, and two, which depicts the area burned, also called fire-affected areas (URL 1). Since the launch of Terra and Aqua, the user community has expanded to include federal agencies with operational fire monitoring mandates and natural resource managers as well the intended global change researchers.

The two MODIS fire products are produced globally at full resolution as EOS Standard Products. They are independent, using different wavelengths and algorithms. The MODIS Active Fire Product’s (MOD14) methodology builds on the contextual algorithm developed for the AVHRR and TRMM products, which primarily use data from the middle infrared, but also include a fire radiative power parameter (Giglio et al. 1999, 2000, 2003a). The MODIS Burned Area Product (MCD45) is based on bidirectional reflectance distribution function (BRDF) modeling of the surface, and detection of a persistent change in surface response, primarily using visible and shortwave infrared time-series data (Roy et al. 2002, 2005).

The Active Fire Products are generated daily at full resolution, and are summarized and gridded to 0.5° for use by the global modeling community (Giglio et al. 2006). A growing number of MODIS ground stations could also generate them locally aided by publicly-provided product algorithms. To meet the needs of a growing resource management community, the MODIS Rapid Response System (URL 2) was developed to provide near-real-time data (within 2–4 h of acquisition),

C. Justice (✉)
Department of Geography, University of Maryland,
College Park, MD 20742, USA
e-mail: justice@hermes.geog.umd.edu

and a Web Mapping System was developed by the NASA Fire Information for Resource Management System (FIRMS) project to provide data in a flexible web GIS format (URL 3).

The MODIS fire team based the design of the fire products on experience gained with heritage products, with priority given to develop and test the MODIS Active Fire Product. The MODIS Burned Area product emphasized two areas: to develop an automated global algorithm, and to perform validation in different environments with significant biomass burning activity (African and Australian savannas, Siberian boreal forest, Amazon tropical forest) to provide maps of known accuracy. The burned area algorithm is now applied globally, and is part of the MODIS “Collection-5” reprocessing. The Collection-5 burned area product will include all data acquisitions from 2001 onwards (Masuoka et al., this volume).

The fire data from Terra and Aqua MODIS provide an unprecedented record of global fire activity (Csizsar et al. 2005). The MODIS instruments provide an important multi-year record of fire data to monitor seasonal and interannual variability, and long-term trends in fire activity (Korontzi et al. 2006; Giglio et al. 2006). The MODIS fire data will provide a strong foundation for a long-term record as one of NASA’s emerging Earth System Data Records (ESDRs).

29.2 MODIS Active Fire Product (MOD14) Status and Validation

The MODIS active fire products are in continuous production since early 2000 (Justice et al. 2002). At present these products include the following:

- The level-2 fire products, in which active fires and other thermal anomalies such as volcanoes are identified and characterized, and from which, all higher-level MODIS fire products are generated
- The level-3 daily composite fire products, which contain tiled, 1-km gridded composites of daily fire activity
- The level-3 8-day composite fire products, which contain tiled, 1-km gridded, 8-day summary composites of fire activity
- The 0.5° global Climate Modelling Grid (CMG) fire products, available on a monthly and 8-day basis, intended for use in regional and global fire monitoring. An example of a data layer from this product is shown in Fig. 29.1
- The MODIS Rapid Response and FIRMS fire products, which encompass near-real-time global fire images and custom fire subsets and services for various geospatial applications

The MODIS Active Fire Product was validated to Stage 2 (i.e., from a representative sample of locations covering the range of conditions encountered in the global product) (Masuoka et al., this volume). For example, validation was undertaken for representative biomes around the globe, including the Brazilian Amazon (tropical rainforest/deforestation: Morisette et al. 2005b), Southern Africa (tropical savanna/grassland: Morisette et al. 2005a), and Siberia (boreal forest: Csizsar et al. 2006a,b).

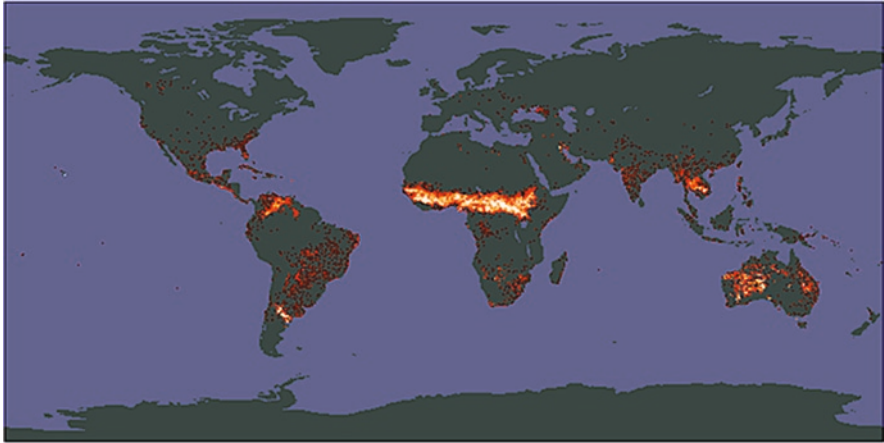


Fig. 29.1 Corrected fire pixel count data layer example for the January 2001 MODIS CMG product. *Brighter shades of red* indicate greater fire activity, while *black areas* indicate no fire activity

Analysis of additional regions is underway. Below, we summarize the approach and show results for three study areas representing distinct ecosystems: Alaska (Boreal Forest), Northwestern Conterminous U.S. (mid-latitude forest), and California (Mediterranean).

Near-nadir active fire detection from Terra MODIS (MOD14) was validated using coincident high-resolution ASTER fire observations. ASTER fire masks were generated for each MODIS 2×1 km pixel by an automated detection algorithm, and were manually checked for commission and omission errors (Morissette et al. 2005a; Giglio et al. 2008). For each MODIS pixel that contained ASTER fire detections, two summary statistics were derived for the ASTER fire pixels: their total number and the mean size of their spatially contiguous clusters.

As the first stage of the validation process, the summary statistics and the MODIS “yes/no” fire flags were included in a logistic regression analysis. This yielded probabilities of MODIS flagging a pixel as “fire” as a function of summary statistics from ASTER. The general formula for the logistic regression model is written thus:

$$\pi(x_i) = \frac{e^{\beta_0 + \sum_{j=1}^p \beta_j x_{ij}}}{1 + e^{\beta_0 + \sum_{j=1}^p \beta_j x_{ij}}}$$

where $\sum_{j=1}^p \beta_j x_{ij}$ represents the linear combination of p ASTER summary statistics within MODIS pixel i , $\pi(x_i)$ is the probability that MODIS pixel i will equal to 1 (i.e., labeled as “fire”) given the values of x_i , and the β_0 and β_j parameters are estimated from the data (Agregsti 1990). In our analysis, we considered only the number

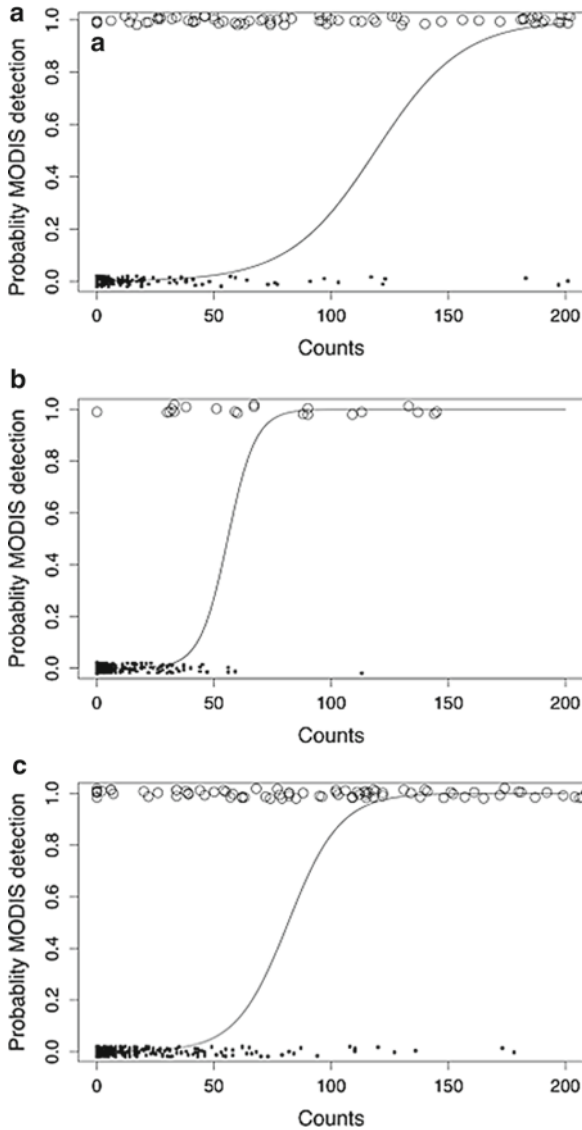


Fig. 29.2 Logistic regression curves showing the probability of MODIS active fire detection as a function of the total number of ASTER fire pixels within the MODIS pixel (“counts,” x-axis). The validation results are shown for Alaska (a), NW CONUS (b), and California (c). The *open circles* and *solid dots* denote detections and no detections by MODIS, respectively

of ASTER fire pixels as the ASTER summary statistic, and therefore $p = 1$ and the regression parameters derived were only β_0 and β_1 .

Figure 29.2 shows logistic regression curves for three study areas in North America: Alaska, Northwestern Conterminous U.S. (“CONUS”) and California.

The curves indicate the lowest detection probabilities in Alaska for a given total number of ASTER fire pixels. Such behavior most probably results from occasional omission of very large fires that are obscured by heavy smoke (Csiszar et al. 2006a,b). In this stage, commission errors were also calculated from MODIS pixels flagged as “fire,” but include no ASTER fire detections. The second stage of the validation process was to determine rates, given the desired lower threshold of the amount of active burning still to detect within the MODIS pixel. As ASTER detects fires that are potentially smaller than those needed for some applications, we derived accuracy assessment curves, which describe the functional relationship between the lower threshold of the number of ASTER fire pixels and the detection probability (Morissette et al. 2005b). For selected thresholds of ASTER fire pixel numbers, we also derived error matrices, including detection rates for fixed values of the lower ASTER classification threshold. We also determined detection probabilities and accuracy assessment curves for contiguous clusters of ASTER fire pixels, regardless of their location relative to the MODIS pixels (Csiszar et al. 2006a,b). In general, the analysis yielded higher detection probabilities than those calculated from summary statistics within the MODIS pixels, probably because multiple, small clusters may exist within the 2×1 km MODIS pixels. Table 29.1 provides sample sizes, coefficients of the logistic regression functions and detection and commission rates for the three study areas in North America. The $N_{th,p}$ and $N_{th,c}$ lower classification thresholds specify the minimum fire sizes to consider. The thresholds are expressed as the total number of ASTER fire counts within the MODIS pixel and the number of ASTER fire counts in the contiguous fire cluster, respectively. The values listed in Table 29.1 for $N_{th,p}$ and $N_{th,c}$ are the rates at which fires greater than those thresholds (i.e., 1 or 50 ASTER fire pixels) are detected by MODIS. We observe an increase in the detection rates for the higher classification threshold as more small fires in fact are omitted by MODIS.

Table 29.1 Results of the statistical analysis of active fires in the three North American study areas. β_0 and β_1 are parameters of the logistic regression curves in Fig. 29.2. $N_{th,p}$ and $N_{th,c}$ are lower classification thresholds of fire sizes expressed in ASTER fire pixel counts for the pixel- and cluster-based analyses, respectively

| | Alaska | NW CONUS | California |
|--------------------------------------------------|--------|----------|------------|
| Number of ASTER scenes | 9 | 14 | 10 |
| Number of MODIS pixels with ASTER fire | 229 | 238 | 395 |
| Logistic regression parameters | | | |
| β_0 | -6.418 | -9.437 | -7.371 |
| β_0 STDE | 0.155 | 0.483 | 0.201 |
| β_1 | 0.054 | 0.169 | 0.090 |
| β_1 STDE | 0.004 | 0.014 | 0.005 |
| Pixel-based detection rate ($N_{th,p} = 1$) | 0.42 | 0.09 | 0.38 |
| Pixel-based detection rate ($N_{th,p} = 50$) | 0.79 | 0.74 | 0.72 |
| Cluster-based detection rate ($N_{th,c} = 1$) | 0.89 | 0.33 | 0.61 |
| Cluster-based detection rate ($N_{th,c} = 50$) | 0.98 | 0.61 | 0.96 |
| Commission rate (pixel-based only) | 0.04 | 0.05 | 0.04 |

The MODIS active fire products include information about the *fire radiative power* (FRP), a measure of fire intensity proposed by Kaufman et al. (1998) and refined by Wooster et al. (2003). By integrating the FRP over the lifetime of a fire, one may compute the *fire radiative energy* (FRE), which is useful to estimate the quantity of biomass combusted, thus potentially permitting improved estimates of pyrogenic gaseous and aerosol emissions. The MODIS fire group is investigating the validation of FRP through collaborations developed with the international Global Observations of Forest Cover/Global Observation of Land cover Dynamics (GOFC/GOLD) program (Csiszar et al. 2006a,b).

29.3 Examples of MODIS Active Fire Studies

29.3.1 *The Fire Information for Resource Management System*

Fire Information for Resource Management System (FIRMS) integrates satellite remote sensing and GIS technology to deliver MODIS active fire data to natural resource managers around the world. Specifically, FIRMS delivers MODIS active fire detection in three main ways: a Web mapping interface, customized e-mail alerts, and short message service (SMS) text messages. FIRMS is used regularly by natural resource managers, scientists, and policy makers from more than 30 countries around the world (URL 3).

FIRMS was developed in response to requests from protected area managers for near-real-time active fire information in a format that is easy to use. FIRMS was developed to provide a simpler and faster means to obtain MODIS active fire locations in a readily usable format relative to downloading standard MODIS Active Fire Products (MOD14) from the Distributed Active Archive Centers (DAACs).

Figure 29.3 illustrates the data flow for FIRMS. Raw MODIS data (Level-0) are taken directly from the EOS Data Operations System (EDOS) and fed to a near-real-time processing system at the Goddard Space Flight Center (GSFC). These data are relayed to the MODIS Rapid Response System, and active fire locations are then generated using the standard NASA (MOD14) Thermal Anomalies algorithm and ingested into the FIRMS database.

The main components of FIRMS are the Web GIS tool and the fire alert notifications: The Web mapping interface (Fig. 29.4) enables users to view, analyze, and query the most up-to-date MODIS active fire information (approximately 2 h after satellite overpass), as well as to search a global database of active fire detections from November 2000 to present, through a series of interactive map services. Each map service allows users to customize maps by selecting from a range of geospatial layers and overlaying them with most recently acquired active fire data. This capacity to integrate fire information with local geospatial information (such as park boundaries, species distributions, roads, and areas already burned) allows natural resource managers to place MODIS active fires in their geographic context.

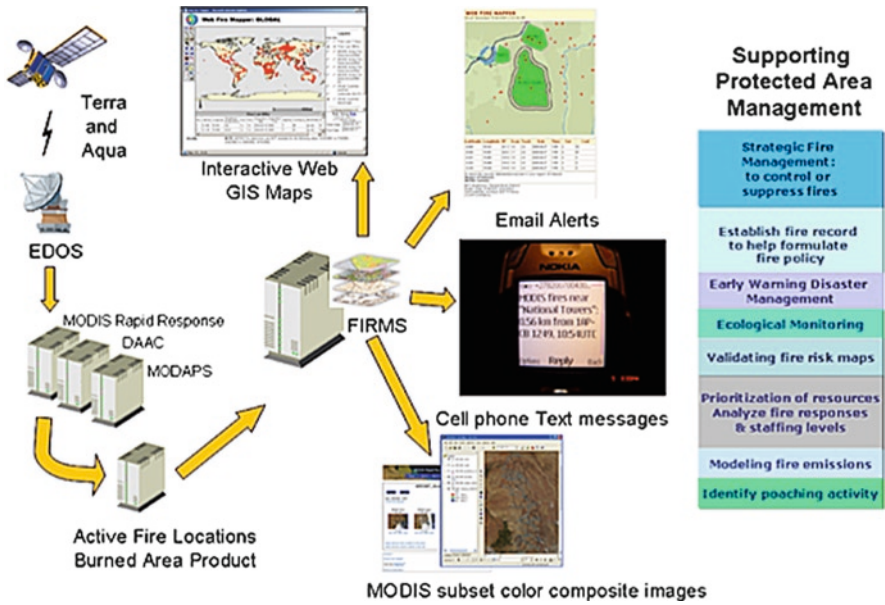


Fig. 29.3 Fire Information for Resource Management System (FIRMS) data flows

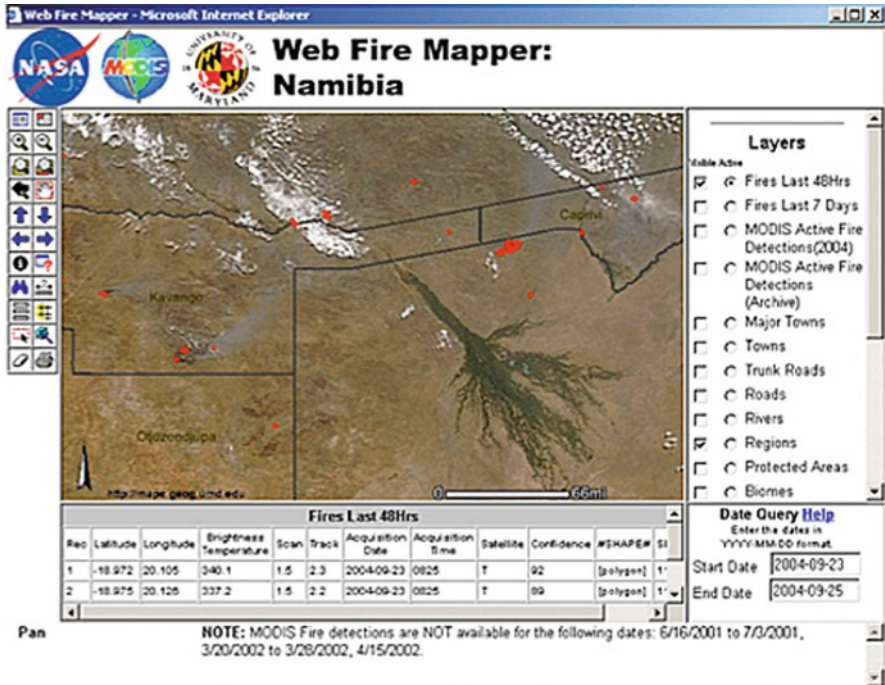


Fig. 29.4 Web GIS interface for the Namibia map service

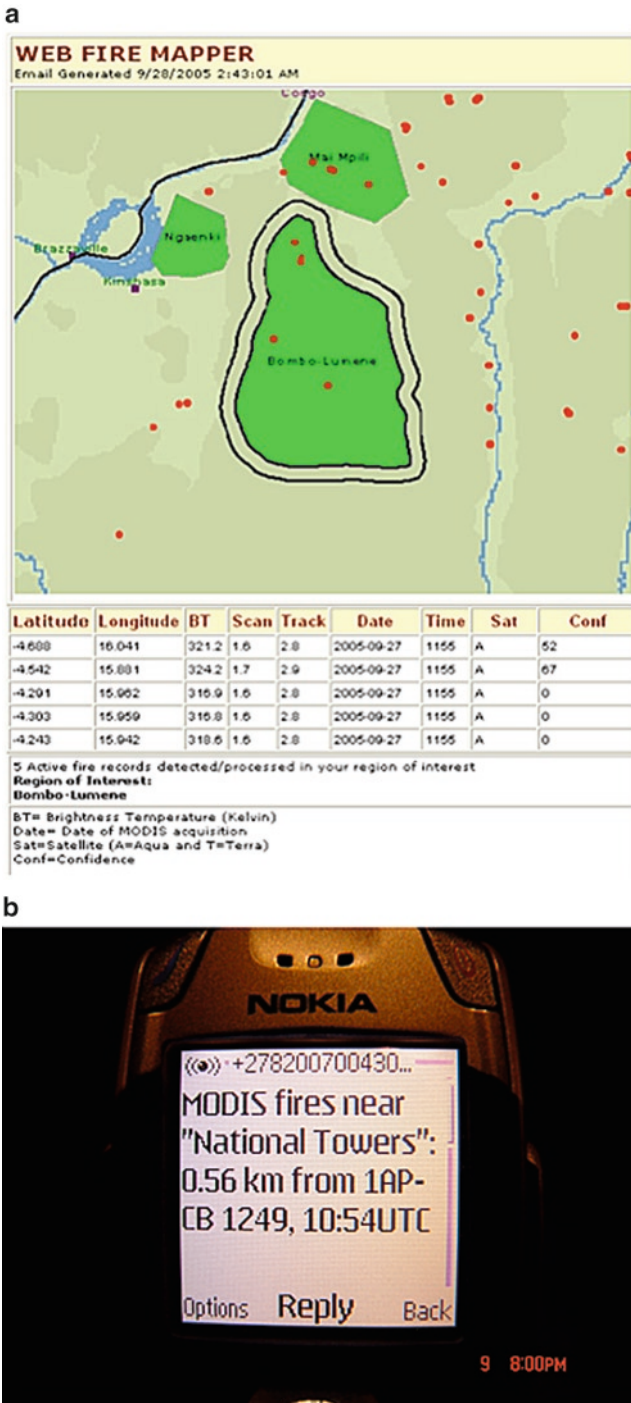


Fig. 29.5 (a) Fire e-mail alert example for Bombo-Lumene Game Reserve in the Democratic Republic of Congo. (b) An SMS text message example

Being notified of a fire occurrence, either by e-mail or cell phone text message (Figs. 29.5a, b) is more efficient than having to continuously check the Internet. SMS fire notifications have become a useful decision support tool for South Africa's largest power company, Eskom. Eskom successfully uses the cell phone alerts to notify staff of fires within 2.5 km of electricity transmission lines. Eskom staff responds to the alerts by investigating the fire; if the fire is likely to affect the power line, Eskom staff will either re-route the electricity through another part of the power grid or take measures to control or suppress the fire. FIRMS is currently being transitioned to an operational system at the United Nations Food and Agricultural Organization (UN FAO) in Rome. Future planned improvements for FIRMS include the addition of the MODIS burned area product.

29.3.2 Amazon Multi-source Fire Integration

Vegetation fires in tropical regions are largely associated with land management practices that tend to exacerbate ecosystem degradation, especially in areas where logging and forest conversion are most pronounced (Cochrane et al. 1999). Fire types vary according to land use with forest-conversion fires normally being replaced by pasture maintenance fires. These fire types possess very distinct characteristics due to differences in fuel load and burning efficiency.

MODIS data are being used operationally to track fire activity in the Brazilian Amazon to monitor rapid land cover change and adherence to fire policies (URL 4). The higher saturation levels and the greater navigation accuracy of the MODIS instrument provide an improved capability to monitor fires over an area that exceeds 5 million km². With a 1-km resolution, the product also supports finer spatial resolution analysis, where deriving important relationships between fire and land-use patterns are possible (Fig. 29.6).

Despite improved fire detection capabilities, the use of Terra and Aqua MODIS active fire data alone may not meet the requirements for vegetation fire monitoring or fire-related studies, given the heterogeneity of Amazon fires in both time and space. Changing conditions between a fire's flaming and smoldering stages, along with the temperature of the background materials, the time of satellite overpass, and variable cloud coverage, can cause the number of fire detections to vary considerably over different products, making data interpretation difficult (Fig. 29.7) (Schroeder et al. 2005, 2007). To characterize vegetation fire dynamics at the local, regional, or global scales, it becomes important to link multiple active fire observations from available satellites. This task is one of the goals identified by the GOF/GOLD Fire program (URL 5). More frequent observations enable a better sampling of the diurnal cycle of fire activity, and provide increased opportunities for cloud-free observations. However, data use from multiple sensors must take into account differences in fire detection accuracy. Schroeder et al. (2008) provide a comprehensive analysis of the MOD14 product's detection performance and the

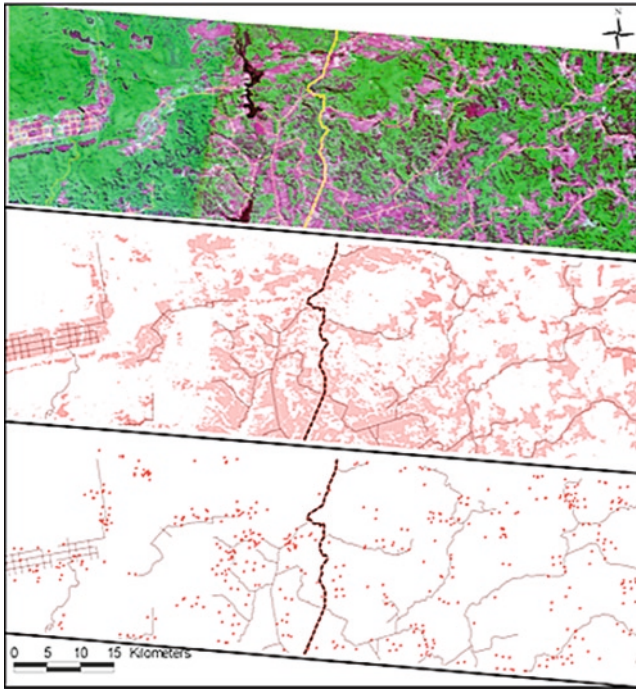


Fig. 29.6 Road network overlaid on top of 2003 20 m resolution China-Brazil Earth Resources Satellite (CBERS-2) subset image from northern Mato Grosso state in Brazil (center coordinates: 9.65S 54.85W) (*top*). The distribution of deforested areas (*center*) with distance from highway BR-163 (*thick line*) is strongly correlated ($r^2 = 0.98$) with that of MODIS/Terra and Aqua 2001–2003 fires (*bottom*). A total of 50% of all fires are closer than 1 km from roads, whereas 85% are closer than 2.5 km

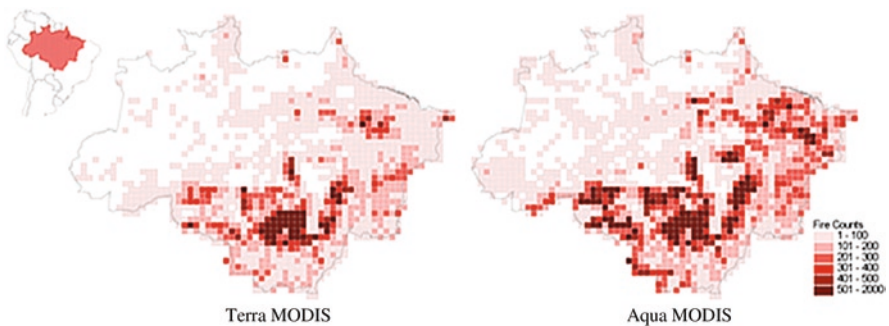


Fig. 29.7 MODIS/Terra (*left*) and Aqua (*right*) 2004 fire detections aggregated into 0.5° grid cells for the Brazilian Amazon region. Differences in density and spatial distribution of fire detections between the two maps are primarily associated with diurnal cycle of fire activity, variable cloud coverage, and unique fire regimes. The combination of these factors often makes the direct comparison of fire products difficult

Wildfire Automated Biomass Burning Algorithm (WFABBA) product derived from the Geostationary Operational Environmental Satellite (GOES) over Brazilian Amazonia.

29.4 The Burned Area Product (MCD45)

29.4.1 Algorithm Overview

Burned areas are characterized by deposits of charcoal and ash, by the removal of vegetation, and by alteration of the vegetation structure (Roy et al. 1999). The MODIS algorithm to map burned areas takes advantage of these spectral, temporal, and structural changes. The algorithm detects the approximate date of burning by locating where rapid changes in daily reflectance time-series (at 500-m resolution) occurs. It improves on previous detection methods through the use of a bidirectional reflectance model to account for angular variations found in the satellite data, and a statistical measure to detect change probability from a previously observed state (Roy et al. 2005). The algorithm exploits the availability of precisely geolocated, calibrated, cloud-screened, and atmospherically corrected MODIS reflectance.

The algorithm is applied independently to geolocated pixels over a long time-series (weeks to months) of reflectance observations. It does not use training data but rather applies a wavelength-independent threshold, and spectral and temporal constraints defined by the noise characteristics of the MODIS reflectance data, together with knowledge of the behavior of burned vegetation and spectrally confusing changes that are not associated with burning. Rather than attempting to minimize the directional information present in wide field-of-view satellite data by compositing, or by the use of spectral indices, the surface reflectance information is used to model the directional dependence of reflectance. The semi-empirical RossThick-LiSparse reciprocal BRDF model is used given its substantial heritage, and is used by the global MODIS BRDF/Albedo product (Schaaf et al. 2002). Similar to other linear kernel-driven models, it allows analytical model inversion, with an estimate of uncertainty in the model parameters and linear combinations thereof (Lucht and Lewis 2000; Schaaf et al. 2002). Reflectance values within a temporal window of a fixed number of days are used to predict the reflectance on a subsequent day. A statistical measure is used to determine whether the difference between the predicted and observed reflectance is a significant spectral change of interest. The algorithm is applied on a temporally overlapping “rolling” basis, which allows for the detection of only persistent changes of interest, and to identify the approximate day of burning.

The algorithm provides a route to use multiple data sources and observations of varying degrees of uncertainty. It was tested extensively not only with Terra MODIS data (Roy et al. 2005) but also with Aqua MODIS data, and both Aqua and

Terra combined data. More reliable results are obtained when Aqua and Terra data are used together for reasons that are similar to those found when comparing the MODIS BRDF/Albedo products derived with different combinations of these data streams (Salomon et al. 2006).

29.4.2 *Product Overview*

The Burned Area product (MCD45) is a monthly level-3 gridded 500-m product. This product is defined in the MODIS land tile format, in the Sinusoidal projection, and in EOS Hierarchical Data Format (Wolfe et al. 1998). Each tile has fixed Earth location and covers an area of approximately $1,200 \times 1,200$ km ($10^\circ \times 10^\circ$ at the equator). The product contains per-pixel burning and quality information and tile-level metadata. Product users are provided with a variety of quality assessment information, and a single, summary quality assessment score for each pixel. The following data are provided for each 500-m gridded pixel:

- “Burndate”: the approximate day of burning from 8 days before the beginning of the month to 8 days after the end of the month, or a unique code indicating no burning detected, or a unique code indicating insufficient observations to enable detection
- “BA pixel QA”: confidence of the detection (high, moderate, low)
- “Number Passed”: number of observations in the time-series after/before “Burndate” that were labeled as burned
- “Number Used”: number of observations in the time-series after/before “Burndate” that were available for consideration (“Number Used” \geq “Number Passed”)
- “Direction”: direction in which burning was detected (forward in time, backward, or both)
- “Surface Type”: information describing the static land cover type, worst data acquisition and aerosol state conditions over the input time-series
- “Gap Range”: information describing the largest and the second largest number of missing/cloudy days (if any) in the time-series; specifically the number of consecutive days with missing observations and the start day of this missing period

Each tile in EOS-HDF format also includes an extensive set of metadata, summarizing these pixel values, and describes the temporal and geographic attributes of the tile. The Burned Area products contain the requisite EOS metadata to facilitate their archival and product orders via the DAAC interfaces. In addition, product-specific tile-level metadata are developed to enable users to select products with specific burning characteristics. For example:

- Percentage of land pixels (in the tile) detected as burned
- Percentage of pixels not processed because of insufficient time-series data

- Percentage of pixels falling in each of the “BA pixel QA” categories
- Number of pixels detected in each direction (forward-processing, backward or both)

29.4.3 Product Examples

Figure 29.8 shows MODIS 500-m burned area mapping results at the continental scale for all southern Africa and Australia. The results exhibit a similar synoptic pattern of burning to previous mapping efforts in southern Africa (Silva et al. 2003) and Australia (Russell-Smith et al. 2003). Comparison of Burned Area products generated recently with contemporaneous time-series MODIS data, the Systeme Pour l’Observation de la Terre (SPOT-VEGETATION) (Tansey et al. 2002) and the Along Track Scanning Radiometer (ATSR-2) (Simon et al. 2004) for southern Africa indicate substantive differences, however, and highlight the need for rigorous product validation (Korontzi et al. 2004).

Figure 29.9 shows a spatial subset of the southern Africa results with contemporaneous MODIS 1-km day and night active fire detections (Giglio et al. 2003b) shown for comparative purposes. These independently-derived fire products exhibit a similar, locally coherent, spatio-temporal progression of burning. Generally, a high correspondence is observed between the locations and dates of the 500-m burned area results, and the cumulative 1-km active fire detections. The MODIS burned area algorithm detects substantially more fire-affected areas than by the cumulative day and night 1-km active fire detections. Such behavior is understandable given that the burned area mapping algorithm takes advantage of the temporal persistence of fire-induced spectral changes, whereas the active fire product only detects fires at the time of satellite overpass. Conversely, however, the active fire detection product may detect very small and hot fires (Giglio et al. 2003b) that do not burn a sufficiently large fraction of the MODIS 500-m observation for potential detection by the fire-affected area mapping algorithm (Roy et al. 2005; Roy and Landmann 2005).

The MODIS burned area mapping algorithm is less reliable when there are periods of frequently missing observations – for example in regions with persistent cloud cover or optically thick smoke. Global cloud analyses indicate that persistent cloud cover may restrict MODIS burned area mapping in parts of equatorial West Africa, equatorial South America, Southern and Southeast Asia, and Boreal regions in Eurasia and Canada (Roy et al. 2006). Active fires are possibly detectable in the cloud-free or smoke-free observations sensed in such periods. We illustrate this in Fig. 29.10, which shows both MODIS fire products for extensive fires in San Diego County, Southern California. Four large fires burned the fire-prone chaparral and coastal sage scrub. The fires were fanned from the east by hot, dry winds, pushing fire and smoke to the west. The lack of burned area detections in the center and western extent of the largest fire was due primarily to the persistent

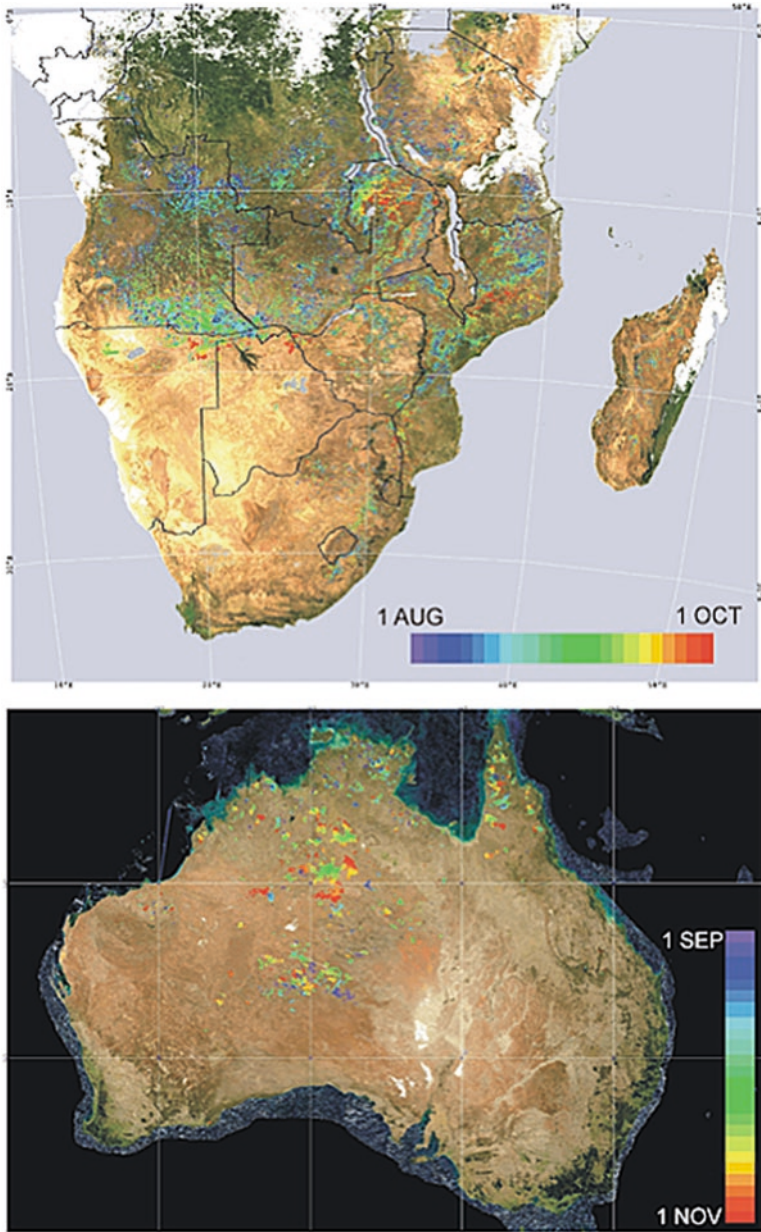


Fig. 29.8 Example of MODIS burned areas at continental scale using MODIS Collection-4 data. On the *top*, burned areas for sub-Saharan Africa produced using MODIS Collection-4 data for the whole sub-equatorial Africa, overlaid on false color mosaic of MODIS bands 6, 5, and 2. The *different colors* indicate the approximate day burning was detected, between August and October 2000. On the *bottom*, mosaic of the MCD45 product over Australia, showing burned areas detected in September and October 2002

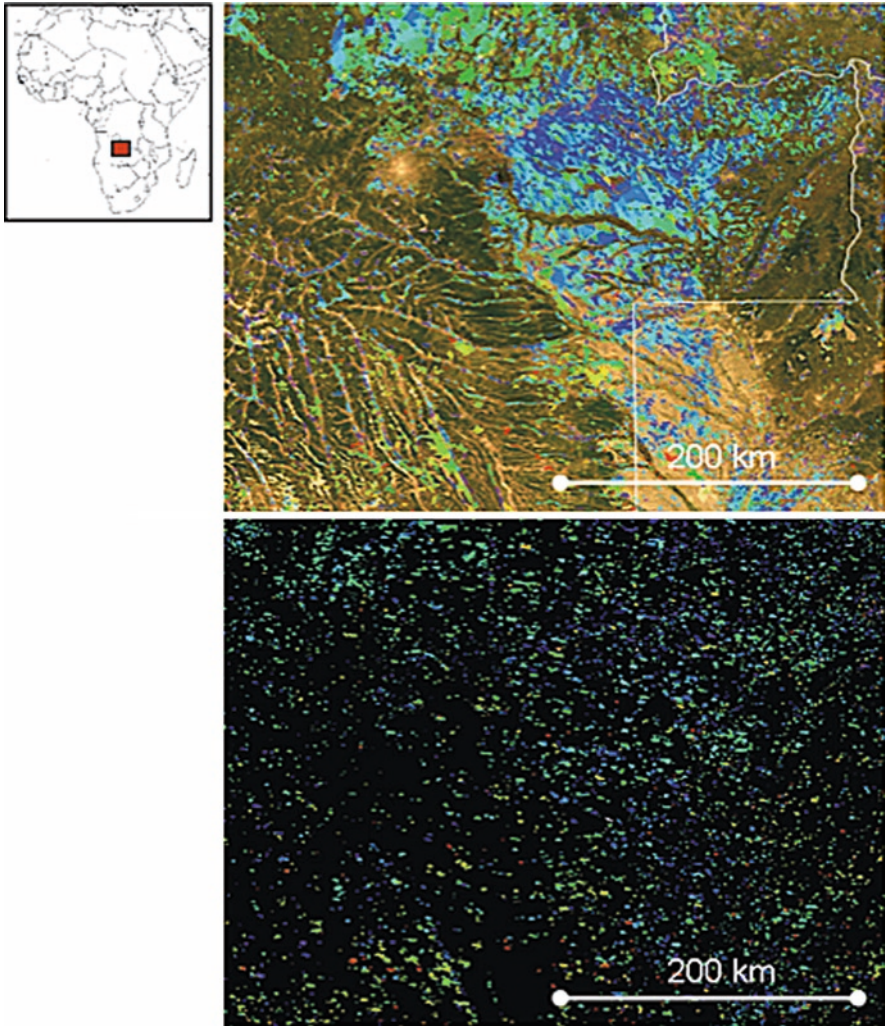


Fig. 29.9 Comparison between MODIS burned areas (*top*) and active fires (*bottom*) over the period 23 June to August 2002. The *colors* indicate the approximate day of burning. The area covered is 450×250 km, encompassing the border between Angola and the Democratic Republic of Congo

smoke, which covered the fire-affected areas not only on the days of burning, but also for many subsequent days. These results support Roy et al.'s finding (2005), regarding the advantage of using the Active Fire and Burned Area products in conjunction. In this context, Giglio et al. (2006) have developed a product, which uses the MODIS active fire to initiate a burned area map for the global modeling community.

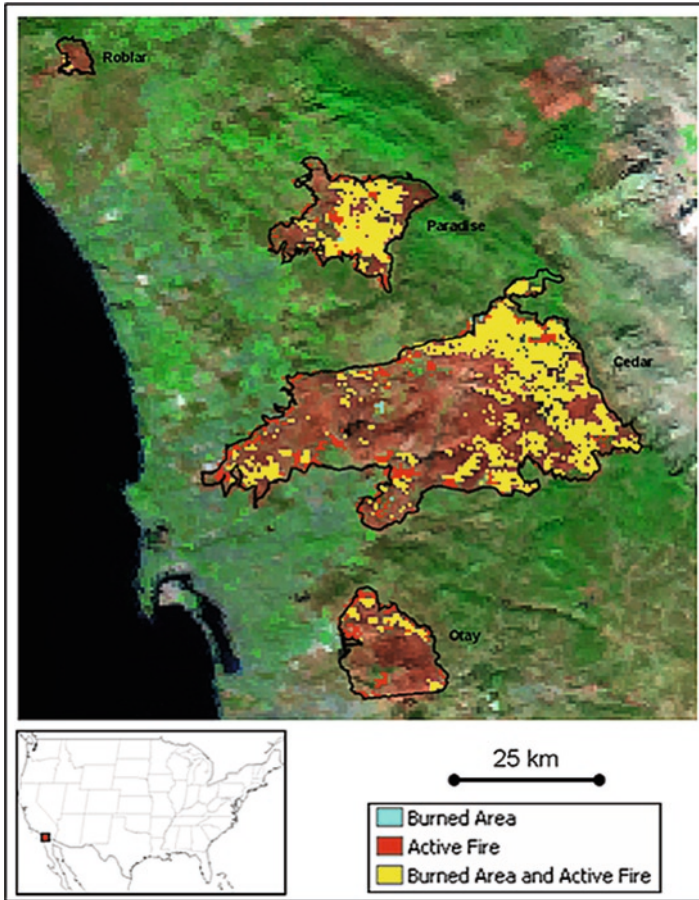


Fig. 29.10 Example of integration between Active Fire and Burned Area products, for an area of approximately 100×100 km around the San Diego County (southern California) fire complex, including four distinct fires that burned in October and November of 2003. The pixels detected only as burned areas are shown in *cyan*, the pixels detected only as active fires are shown in *red*, and the pixels detected both as burned areas and active fires are shown in *yellow*. The perimeter of the fire-affected areas (from a ground survey by San Diego State University (URL 6)) is shown in *black*

29.5 Conclusions

Since the first MODIS-derived fire data were generated in early 2000, we have made substantial progress towards achieving the research objectives identified in the Dahlem Conference on Fire in the Environment, which defined a broad set of global fire research objectives (Justice et al. 1993; Crutzen and Goldammer 1993). Consistent global fire products are now being generated, and NASA has

made a serious commitment towards the following: (i) instrument calibration, (ii) global product validation, (iii) data reprocessing, and (iv) free and unrestricted data distribution. This has helped to establish a consistent time-series record of known accuracy. This time-series is being widely distributed and used. The uptake of the MODIS fire data by the international community remains extensive and provides a good model to apply satellite observations to societal benefit in the framework of the Global Earth Observing System of Systems (GEOSS). The GOCF/GOLD Fire program greatly facilitates this effort (URL 5), through its international fire observation agenda, and promoting the generation and use of fire observations (Justice et al. 2003; Csiszar et al. 2006a,b). UN FAO's adoption of the MODIS fire monitoring capability marks an important step in the transition of global fire monitoring from research to an operational environment.

The MODIS Fire team is committed to improve the Fire product suite. We intend to include an active fire component to capture small fires and non-persistent burned areas in the next incarnation of the Burned Area product in MODIS Collection-6 (Masuoka et al., this volume). In the near term, we plan to emphasize MODIS burned area validation and product refinement, and also develop a long-term NASA Earth System Data Record (ESDR) for Fire.

An evaluation is currently underway on how best to extend the MODIS fire data products with data from the NPOESS VIIRS instrument slated for launch in early 2011. We hope there exists an overlap between the VIIRS and the Aqua MODIS instruments to allow product inter-comparison and performance evaluation. VIIRS data-derived consistent active fire and burned area estimates will provide an important requirement for operational users. In principle, the global Fire ESDR is extensible back in time, using the AVHRR global 1-km data, SPOT-Vegetation, and ATSR nighttime data. The challenge is to characterize the dynamic product continuity from multiple instruments with different sensing characteristics and overpass times. The long-term records will enable scientists to assess how fire regimes are changing as a function of land-use practices and climate. They will help resource managers monitor trends in fire activity, and evaluate efficacy of fire management policies.

Acknowledgments This paper is dedicated to the memory of Yoram Kaufman, who played an important role in developing the MODIS Fire product and the Fire Radiative Power concept. His collaboration with the MODIS Fire Team is truly missed. The work presented here was funded under NASA Grants NNG04HZ18C (EOS), NNS06AA04A (Applications) and NAG513627 (LBA-ECO Phase II).

References

- Agresti A (1990) *Categorical data analysis*. Wiley, New York
- Cochrane MA, Alencar A, Schulze MD Jr, Souza CM, Nepstad DC, Lefebvre P, Davidson EA (1999) Positive feedbacks in the fire dynamic of closed canopy tropical forests. *Science* 284:1832–1835

- Crutzen PA, Goldammer JG (1993) Fire in the environment: the ecological, atmospheric, and climatic importance of vegetation fires. Dahlem Konferenz (15–20 March 1992, Berlin), ES13, Wiley, Chichester, 400 pp
- Csiszar I, Denis L, Giglio L, Justice CO, Hewson J (2005) Global fire distribution from MODIS. *Int J Wildland Fire* 14:117–130
- Csiszar I, Morisette J, Giglio L (2006a) Validation of active fire detection from moderate resolution satellite sensors: the MODIS example in Northern Eurasia. *IEEE Trans Geosci Remote Sens* 44:1757–1764
- Csiszar I, Justice CO, Goldammer JG, Lynham T, de Groot WJ, Prins EM, Elvidge CD, Oertel D, Lorenz E, Bobbe T, Quayle B, Davies D, Roy D, Boschetti L, Korontzi S, Ambrose S, Stephens G (2006b) The GOF/GOLD fire mapping and monitoring theme: assessment and strategic plans. In: *Earth Science Satellite Remote Sensing*. Springer, Dordrecht, The Netherlands
- Giglio L, Kendall JD, Justice CO (1999) Evaluation of global fire detection algorithms using simulated AVHRR infrared data. *Int J Remote Sens* 20:1947–1985
- Giglio L, Kendall JD, Tucker CJ (2000) Remote sensing of fires with the TRMM VIRS. *Int J Remote Sens* 21:203–207
- Giglio L, Kendall JD, Mack R (2003a) A multi-year active fire dataset for the tropics derived from the TRMM VIRS. *Int J Remote Sens* 24:4505–4525
- Giglio L, Descloitres J, Justice CO, Kaufman YJ (2003b) An enhanced contextual fire detection algorithm for MODIS. *Remote Sens Environ* 87:273–382
- Giglio L, Csiszar I, Justice CO (2006) Global distribution and seasonality of active fires as observed with the Terra and Aqua MODIS sensors. *J Geophys Res* 111:G02016. doi:10.1029/2005JG000142
- Giglio L, Csiszar I, Restás Á, Morisette JT, Schroeder W, Morton D, Justice CO (2008) Active fire detection and characterization with the Advanced Spaceborne Thermal Emission and Reflection Radiometer (ASTER). *Remote Sens Environ* 112:3055–3063
- Justice CO, Malingreau JP, Setzer A (1993) Satellite remote sensing of fires: potential and limitation. In: Crutzen P, Goldammer J (eds) *Fire in the environment: its ecological, climatic and atmospheric chemical importance*. Wiley, Chichester, pp 77–87
- Justice CO, Giglio L, Korontzi S, Owens J, Morisette JT, Roy DP, Descloitres J, Alleaume S, Petitcolin F, Kaufman Y (2002) The MODIS fire products. *Remote Sens Environ* 83:244–262
- Justice CO, Smith R, Gill M, Csiszar I (2003) Satellite-based fire monitoring: current capabilities, future directions and applications in Australia. *Int J Wildland Fire* 102:247–258
- Kaufman YJ, Justice CO, Flynn LP, Kendall JD, Prins EM, Giglio L, Ward DE, Menzel WP, Setzer AW (1998) Potential global fire monitoring from EOS-MODIS. *J Geophys Res* 103(D24):32215–32238
- Korontzi S, Roy DP, Justice CO, Ward DE (2004) Modeling and sensitivity analysis of fire emissions in southern African during SAFARI 2000. *Remote Sens Environ* 92:255–275
- Korontzi S, McCarty J, Loboda T, Kumar S, Justice C (2006) Global distribution of agricultural fires in croplands from 3 years of Moderate Resolution Imaging Spectroradiometer (MODIS) data. *Global Biogeochem Cycles* 20:GB2021. doi:10.1029/2005GB002529
- Lucht W, Lewis PE (2000) Theoretical noise sensitivity of BRDF and albedo retrieval from the EOS-MODIS and MISR sensors with respect to angular sampling. *Int J Remote Sens* 21:81–98
- Masuoka E, Wolfe R, Saleous N, Teague M, Roy DP, Devadiga S, Morisette JT, Maieringer T, Justice CO MODIS land data products: generation, quality assurance and validation. (In this volume)
- Morisette JT, Giglio L, Csiszar I, Justice CO (2005a) Validation of the MODIS Active fire product over Southern Africa with ASTER data. *Int J Remote Sens* 26:4239–4264
- Morisette JT, Giglio L, Csiszar I, Setzer A, Schroeder W, Morton D, Justice CO (2005b) Validation of MODIS active fire detection products derived from two algorithms. *Earth Interact* 9:1–23
- Roy DP, Landmann T (2005) Characterizing the surface heterogeneity of fire effects using multi-temporal reflective wavelength data. *Int J Remote Sens* 26:4197–4218
- Roy D, Giglio L, Kendall J, Justice C (1999) Multitemporal active fire-based burn scar detection algorithm. *Int J Remote Sens* 20:1031–1038

- Roy DP, Lewis PE, Justice CO (2002) Burned area mapping using multi-temporal moderate spatial resolution data – a bi-directional reflectance model-based expectation approach. *Remote Sens Environ* 83:263–286
- Roy DP, Jin Y, Lewis PE, Justice CO (2005) Prototyping a global algorithm for systematic fire affected area mapping using MODIS time series data. *Remote Sens Environ* 97:137–162
- Roy DP, Lewis P, Schaaf C, Devadiga S, Boschetti L (2006) The Global impact of cloud on the production of MODIS bi-directional reflectance model based composites for terrestrial monitoring. *IEEE Geosci Remote Sens Lett* 3(4):452–456. doi:10.1109/LGRS.2006.875433
- Russell-Smith J, Yates C, Edwards A, Allan GE, Cook GD, Cooke P, Craig R, Heath D, Smith BR (2003) Contemporary fire regimes of northern Australia, 1997–2001: changes since Aboriginal occupancy, challenges for sustainable management. *Int J Wildland Fire* 12:283–297
- Salomon JG, Schaaf CB, Strahler AH, Gao F, Jin YF (2006) Validation of the MODIS bidirectional reflectance distribution function and albedo retrievals using combined observations from the Aqua and Terra platforms. *IEEE Trans Geosci Remote Sens* 44(6):1555–1565
- Schaaf CB, Gao F, Strahler AH, Lucht W, Li X, Tsang T, Strugnell N, Zhang X, Jin Y, Muller J-P, Lewis PE, Barnsley M, Hobson P, Disney M, Roberts G, Dunderdale M, d’Entremont RP, Hu B, Liang S, Privette J, Roy DP (2002) First operational BRDF, albedo and nadir reflectance products from MODIS. *Remote Sens Environ* 83:135–148
- Schroeder W, Morisette JT, Csiszar I, Giglio L, Morton D, Justice CO (2005) Characterizing vegetation fire dynamics in Brazil through multi-satellite data: common trends and practical issues. *Earth Interact* 9(13):1–26
- Schroeder W, Csiszar I, Morisette JT (2007). Quantifying the impact of cloud obscuration on remote sensing of active fires in the Brazilian Amazon. *Remote Sens Environ*. doi:10.1016/j.rse.2007.05.004
- Schroeder W, Prins E, Giglio L, Csiszar I, Schmidt C, Morisette JT, Morton D (2008) Validation of GOES and MODIS active fire detection products using ASTER and ETM+. *Remote Sens Environ* 112:2711–2726
- Silva JMN, Pereira JMC, Cabral AI, Sá A, Vasconcelos MJP, Mota B, Grégoire J-M (2003) An estimate of the area burned in southern Africa during the 2000 dry season using SPOT-VEGETATION. *J Geophys Res* 108(D13):498. doi:10.1029/2002JD002320
- Simon M, Plummer S, Fierens F, Hoeltzemann JJ, Arino O (2004) Burnt area detection at global scale using ATSR-2: the GLOBSCAR products and their qualification. *J Geophys Res* 109(D14):D14S02. doi:10.1029/2003JD003622
- Tansey K, Binaghi E, Boschetti L, Brivio PA, Cabral A, Ershov D, Flasse S, Fraser R, Gallo I, Graetz D, Grégoire J-M, Maggi M, Peduzzi P, Pereira JM, Sá A, Silva J, Sousa A, Stroppiana D, Vasconcelos MJP (2002) Implementation of regional burnt area algorithms for the GBA-2000 initiative. European Commission Joint Research Centre, EUR 20532 EN. Publications of the European Commission, pp 1–159
- URL 1: <http://modis-fire.umd.edu/> Accessed 27 Nov 2007
- URL 2: <http://rapidfire.sci.gsfc.nasa.gov> Accessed 27 Nov 2007
- URL 3: <http://maps.geog.umd.edu/firms> Accessed 27 Nov 2007
- URL 4: <http://www.cptec.inpe.br/queimadas/> Accessed 27 Nov 2007
- URL 5: <http://gofc-fire.umd.edu/index.asp> Accessed 27 Nov 2007
- URL 6: <http://map.sdsu.edu/> Accessed 27 Nov 2007
- Wolfe R, Roy D, Vermote E (1998) The MODIS land data storage, gridding and compositing methodology: L2 Grid. *IEEE Trans Geosci Remote Sens* 36:1324–1338
- Wooster MJ, Zhukov B, Oertel D (2003) Fire radiative energy for quantitative study of biomass burning: derivation from the BIRD experimental satellite and comparison to MODIS fire products. *Remote Sens Environ* 86:83–107

Chapter 30

MODIS Snow and Ice Products, and Their Assessment and Applications

George Riggs and Dorothy Hall

30.1 Introduction

The Moderate resolution Imaging Spectroradiometer (MODIS) snow cover mapping algorithm provides a snow detection technique that is robust, reliable, and computationally efficient; it generates a daily global snow cover data product without significant bias in errors of commission or omission of snow cover. The products were designed for use by a wide range of users including cryospheric researchers, hydrological and climate modelers, and the general scientific community. A suite of snow products start from the swath (i.e., a 5-min segment of sensor data) at 500-m resolution, to daily global snow maps at 0.05° and 0.25° resolution, and temporal 8-day composited global snow products, and culminate with a monthly snow cover product – all developed to address user community interests (Hall et al. 2006).

MODIS instruments are currently flown on both the Terra and Aqua satellites. At the time of this writing, Terra and Aqua are in their eighth and fifth years, respectively, of their missions. The product algorithms have been revised and the product content (Tables 30.1 and 30.2) has changed over the life of the mission in response to evaluation, validation, and product usage by both the data product developers and users. Reprocessing of the Terra and Aqua MODIS data product collections have generated consistent data collections from first opening of the sensor's Earth-view doors to the present. Data product Collection 5 (C5) is the current collection available to users. C5's operational processing began on 1 January 2007, and its reprocessing, which began in mid-2006 for data from first light to 31 December 2006, was completed in June 2008. Nearly all the literature cited in this chapter used the thematic snow products from Collection 4 (C4), which mapped snow cover as either "snow" or "not snow" (binary mapping). Mapping pixel fractional snow cover (FSC) is new in the C5 swath and daily gridded snow products. Also, new in C5 is a monthly mean snow cover product.

G. Riggs (✉)

Science Systems and Applications Inc., Lanham, MD 20706, USA
e-mail: george.a.riggs@nasa.gov

Table 30.1 MODIS snow data products in Collection 4 (C4) and 5 (C5)

| | |
|------------------------|---------------------------------------------------------------------------------------------------------|
| ESDT – MOD10_L2 | |
| Long name | MODIS/Terra Snow Cover 5-Min L2 Swath 500 m |
| Spatial resolution | 500-m resolution, swath of MODIS data (5 min of data) |
| Datasets V004 | Snow Cover, Snow Cover PixelQA, Snow Cover Reduced Cloud, Latitude, Longitude |
| Datasets V005 | Snow_Cover, Snow_Cover_Pixel_QA, Fractional_Snow_Cover, Latitude, Longitude |
| ESDT – MOD10A1 | |
| Long name | MODIS/Terra Snow Cover Daily L3 Global 500 m SIN Grid (includes daily snow albedo) |
| Spatial resolution | 500-m resolution, Sinusoidal projection, gridded tile data |
| Datasets V004 | Day_Tile_Snow_Cover, Snow_Spatial_QA, Daily_Tile Snow_Albedo |
| Datasets V005 | Snow_Cover_Daily_Tile, Snow_Spatial_QA, Snow_Albedo_Daily_Tile, Fractional_Snow_Cover |
| ESDT – MOD10A2 | |
| Long name | MODIS/Terra Snow Cover 8-Day L3 Global 500°m SIN Grid |
| Spatial resolution | 500-m resolution, Sinusoida projection, gridded tile data |
| Datasets V004 | Maximum_Snow_Extent, Eight_Day_Snow_Cover |
| Datasets V005 | Maximum_Snow_Extent, Eight_Day_Snow_Cover |
| ESDT – MOD10C1 | |
| Long name | MODIS/Terra Snow Cover Daily L3 Global 0.05° CMG |
| Spatial resolution | 0.05° resolution, lat/lon climate modeling grid |
| Datasets V004 | Day_CMG_Snow_Cover, Day_CMG_Confidence_Index, Day_CMG_Cloud_Obscured, Snow_Spatial_QA |
| Datasets V005 | Day_CMG_Snow_Cover, Day_CMG_Confidence_Index, Day_CMG_Cloud_Obscured, Snow_Spatial_QA |
| ESDT – MOD10C2 | |
| Long name | MODIS/Terra Snow Cover 8-Day L3 Global 0.05° CMG |
| Spatial resolution | 0.05° resolution, lat/lon climate modeling grid |
| Datasets V004 | Eight_Day_CMG_Snow_Cover, Eight_Day_CMG_Confidence_Index, Eight_Day_CMG_Cloud_Obscured, Snow_Spatial_QA |
| Datasets V005 | Eight_Day_CMG_Snow_Cover, Eight_Day_CMG_Confidence_Index, Eight_Day_CMG_Cloud_Obscured, Snow_Spatial_QA |
| ESDT – MOD10CM | |
| Long name | MODIS/Terra Snow Cover Monthly L3 Global 0.05° CMG |
| Spatial resolution | 0.05° resolution, lat/lon climate modeling grid |
| Datasets V004 | |
| Datasets V005 | Snow_Cover_Monthly_CMG, Snow_Spatial_QA |
| ESDT – MYD10_L2 | |
| Long name | MODIS/Aqua Snow Cover 5-Min L2 Swath 500 m |
| Spatial resolution | 500-m resolution, swath of MODIS data |
| Datasets V004 | Snow Cover, Snow Cover PixelQA, Snow Cover Reduced Cloud |
| Datasets V005 | Snow_Cover, Snow_Cover_Pixel_QA, Fractional_Snow_Cover, Latitude, Longitude |

(continued)

Table 30.1 (continued)

| | |
|-----------------------|---------------------------------------------------------------------------------------------------------|
| ESDT – MYD10A1 | |
| Long name | MODIS/Aqua Snow Cover Daily L3 Global 500-m SIN Grid (includes daily snow albedo) |
| Spatial resolution | 500-m resolution, projected, gridded tile data |
| Datasets V004 | Day_Tile_Snow_Cover, Snow_Spatial_QA, Daily_Tile_Snow_Albedo |
| Datasets V005 | Snow_Cover_Daily_Tile, Snow_Spatial_QA, Snow_Albedo_Daily_Tile, Fractional_Snow_Cover |
| ESDT – MYD10A2 | |
| Long name | MODIS/Aqua Snow Cover 8-Day L3 Global 0.05° CMG |
| Spatial resolution | 500-m resolution, projected, gridded tile data |
| Datasets V004 | Maximum_Snow_Extent, Eight_Day_Snow_Cover |
| Datasets V005 | Maximum_Snow_Extent, Eight_Day_Snow_Cover |
| ESDT – MYD10C1 | |
| Long name | MODIS/Aqua Snow Cover Daily L3 Global 0.05° CMG |
| Spatial resolution | 0.05° resolution, lat/lon climate modeling grid |
| Datasets V004 | Day_CMG_Snow_Cover, Day_CMG_Confidence_Index, Day_CMG_Cloud_Obscured, Snow_Spatial_QA |
| Datasets V005 | Day_CMG_Snow_Cover, Day_CMG_Confidence_Index, Day_CMG_Cloud_Obscured, Snow_Spatial_QA |
| ESDT – MYD10C2 | |
| Long name | MODIS/Aqua Snow Cover 8-Day L3 Global 0.05° CMG |
| Spatial resolution | 0.05° resolution, lat/lon climate modeling grid |
| Datasets V004 | Eight_Day_CMG_Snow_Cover, Eight_Day_CMG_Confidence_Index, Eight_Day_CMG_Cloud_Obscured, Snow_Spatial_QA |
| Datasets V005 | Eight_Day_CMG_Snow_Cover, Eight_Day_CMG_Confidence_Index, Eight_Day_CMG_Cloud_Obscured, Snow_Spatial_QA |
| ESDT – MYD10CM | |
| Long name | MODIS/Aqua Snow Cover Monthly L3 Global 0.05° CMG |
| Spatial resolution | 0.05° resolution, lat/lon climate modeling grid |
| Datasets V004 | |
| Datasets V005 | Snow_Cover_Monthly_CMG, Snow_Spatial_QA |

Table 30.2 MODIS sea ice data products in Collection 4 (C4) and 5 (C5)

| | |
|---------------------|----------------------------------------------------------------------------------------------------------------------------------------------------|
| ESDT – MOD29 | |
| Long name | MODIS/Terra Sea Ice Extent 5-Min L2 Swath 1 km |
| Spatial resolution | 1-km resolution, swath of MODIS data |
| Datasets V004 | Sea Ice by Reflectance, Sea Ice by Reflectance PixelQA, Ice Surface Temperature, Ice Surface Temperature PixelQA, Sea Ice by IST, Combined Sea Ice |
| Datasets V005 | Sea_Ice_by_Reflectance, Sea_Ice_by_Reflectance_Pixel_QA, Ice_Surface_Temperature, Ice_Surface_Temperature_Pixel_QA |

(continued)

Table 30.2 (continued)

| | |
|------------------------|------------------------------------------------------------------------------------------------------------------------------------------------------------------------------|
| ESDT – MOD29P1D | |
| Long name | MODIS/Terra Sea Ice Extent Daily L3 Global EASE-Grid Day |
| Spatial resolution | 1-km resolution, projected, gridded tile data |
| Datasets V004 | Sea_Ice_by_Reflectance, Sea_Ice_by_Reflectance_Spatial_QA, Ice_Surface_Temperature, Ice_Surface_Temperature_Spatial_QA, Sea_Ice_by_Ice_Surface_Temperature, Combined_Sea_Ice |
| Datasets V005 | Sea_Ice_by_Reflectance, Sea_Ice_by_Reflectance_Spatial_QA, Ice_Surface_Temperature, Ice_Surface_Temperature_Spatial_QA |
| ESDT – MOD29P1N | |
| Long name | MODIS/Terra Sea Ice Extent Daily L3 Global EASE-Grid Night |
| Spatial resolution | 1-km resolution, projected, gridded tile data |
| Datasets V004 | Ice_Surface_Temperature, Ice_Surface_Temperature_Spatial_QA, Sea_Ice_by_Ice_Surface_Temperature |
| Datasets V005 | Ice_Surface_Temperature, Ice_Surface_Temperature_Spatial_QA |
| ESDT – MOD29E1D | |
| Long name | MODIS/Terra Sea Ice Extent and Ice Surface Temperature Daily L3 Global 4-km EASE-Grid Day |
| Spatial resolution | 4-km resolution, global, gridded |
| Datasets V004 | Sea_Ice_by_Reflectance_NP, Ice_Surface_Temperature_N, Sea_Ice_by_Reflectance_SP, Ice_Surface_Temperature_SP |
| Datasets V005 | Sea_Ice_by_Reflectance_NP, Ice_Surface_Temperature_N, Sea_Ice_by_Reflectance_SP, Ice_Surface_Temperature_SP |
| ESDT – MYD29 | |
| Long name | MODIS/Aqua Sea Ice Extent 5-Min L2 Swath 1 km |
| Spatial resolution | 1-km resolution, swath of MODIS data |
| Datasets V004 | Sea_Ice_by_Reflectance, Sea_Ice_by_Reflectance_Spatial_QA, Ice_Surface_Temperature, Ice_Surface_Temperature_Spatial_QA, Sea_Ice_by_Ice_Surface_Temperature, Combined_Sea_Ice |
| Datasets V005 | Sea_Ice_by_Reflectance, Sea_Ice_by_Reflectance_Pixel_QA, Ice_Surface_Temperature, Ice_Surface_Temperature_Pixel_QA |
| ESDT – MYD29P1D | |
| Long name | MODIS/Aqua Sea Ice Extent Daily L3 Global EASE-Grid Day |
| Spatial resolution | 1-km resolution, projected, gridded tile data |
| Datasets V004 | Ice_Surface_Temperature, Ice_Surface_Temperature_Spatial_QA, Sea_Ice_by_Ice_Surface_Temperature |
| Datasets V005 | Sea_Ice_by_Reflectance, Sea_Ice_by_Reflectance_Spatial_QA, Ice_Surface_Temperature, Ice_Surface_Temperature_Spatial_QA |
| ESDT – MYD29P1N | |
| Long name | MODIS/Aqua Sea Ice Extent Daily L3 Global EASE-Grid Night |
| Spatial resolution | 1-km resolution, projected, gridded tile data |
| Datasets V004 | Ice_Surface_Temperature, Ice_Surface_Temperature_Spatial_QA, Sea_Ice_by_Ice_Surface_Temperature |
| Datasets V005 | Ice_Surface_Temperature, Ice_Surface_Temperature_Spatial_QA |

(continued)

Table 30.2 (continued)

| ESDT – MYD29E1D | |
|--------------------|-----------------------------------------------------------------------------------------------------------------|
| Long name | MODIS/Aqua Sea Ice Extent and Ice Surface Temperature Daily L3 Global 4-km EASE-Grid Day |
| Spatial resolution | 4-km Resolution, global, gridded |
| Datasets V004 | Sea_Ice_by_Reflectance_NP, Ice_Surface_Temperature_N, Sea_Ice_ by_Reflectance_SP, Ice_Surface_Temperature_SP |
| Datasets V005 | Sea_Ice_by_Reflectance_NP, Ice_Surface_Temperature_N, Sea_Ice_ by_Reflectance_SP, Ice_Surface_Temperature_SP |

Current literature reports on MODIS snow maps and their evaluation in various regions, their accuracy assessment in various applications, and MODIS snow products as inputs to hydrological modeling and snow climatology studies. Hall and Riggs (2007) review much of that literature through an assessment and discussion of the MODIS snow product's accuracy and errors.

The MODIS snow products are used extensively, and a large collection of literature focuses on the evaluation of the products. The MODIS snow maps' overall accuracy ranges from 80 to 100% according to MODIS snow product-based applications presented in Sect. 30.4.

The snow cover product's overall accuracy reported in the literature is around 90% during the snow season under diverse snow land surface conditions.

The MODIS sea ice product suite includes sea ice extent, and ice surface temperature (IST) (Hall et al. 2006). Frequent and persistent cloud cover, and polar darkness are significant limiting factors to the study of sea ice with MODIS data. However, when cloud cover permits, it is possible to observe sea ice extent, IST, and albedo (although an albedo product is not included in the product suite) at much higher resolutions than is possible with passive microwave sensors with resolutions from approximately 12 to 25 km.

First, we present the data product suite in sequence. Then, we discuss potential errors and how they propagate through the sequence of products to facilitate user-awareness regarding how errors may affect their product use.

30.2 MODIS Snow Products

The MODIS snow product suite (Figs. 30.1–30.7 and Tables 30.1 and 30.2) changes in spatial and temporal resolution through the production sequence; each succeeding product inherits data quality and errors from the preceding product. A brief description of the snow algorithms and products is given in the following sections. The basics of the algorithm are described to highlight their relevance to the quality, accuracy, and use of the product and higher-level products. Detailed descriptions of the algorithms and products are available in the Algorithm Theoretical Basis Document (ATBD) (Hall et al. 2001b), and the Snow User Guide (Riggs et al. 2006a), both available online at the MODIS snow and sea ice global mapping project website <http://modis-snow-ice.gsfc.nasa.gov>. The current suite of snow products begins

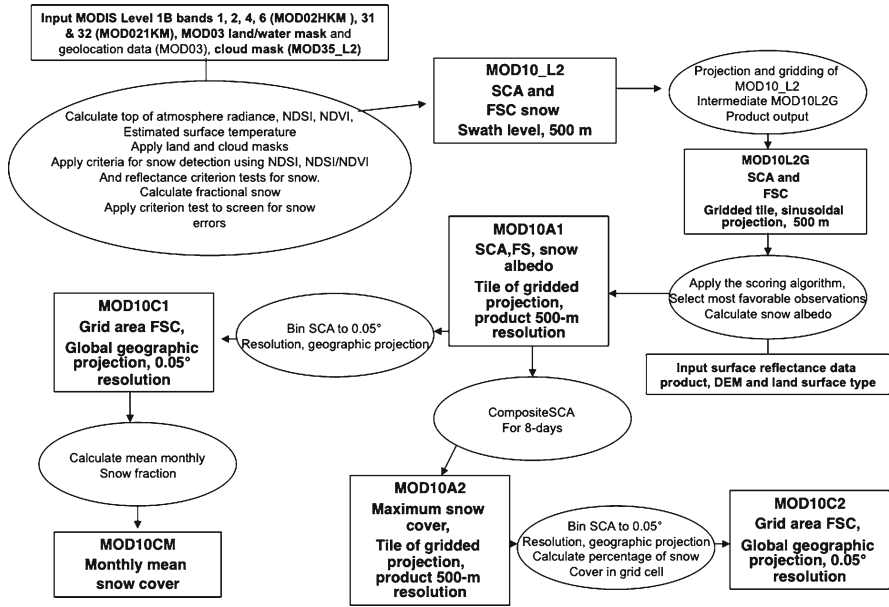


Fig. 30.1 The suite of MODIS snow products. The suite is shown in production sequence with inputs, basic algorithm description and ESDT output

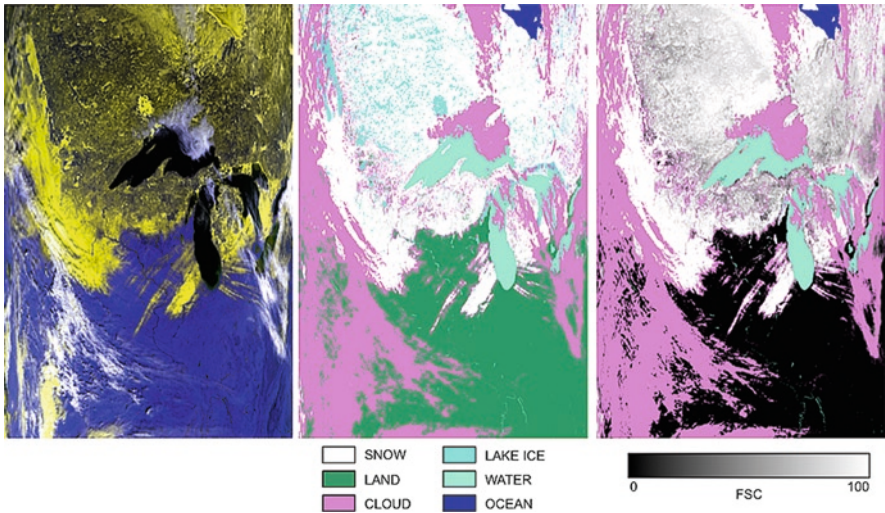


Fig. 30.2 MOD10_L2 product example. False color of MODIS reflectance bands 1, 4, 6 snow is highlighted in yellow in the panel at left. The MOD10_L2 SCA and FSC are shown in center and right, respectively. The image was acquired 26 January 2006, covering the Great Lakes, plains and boreal forest. The image is not projected to a map

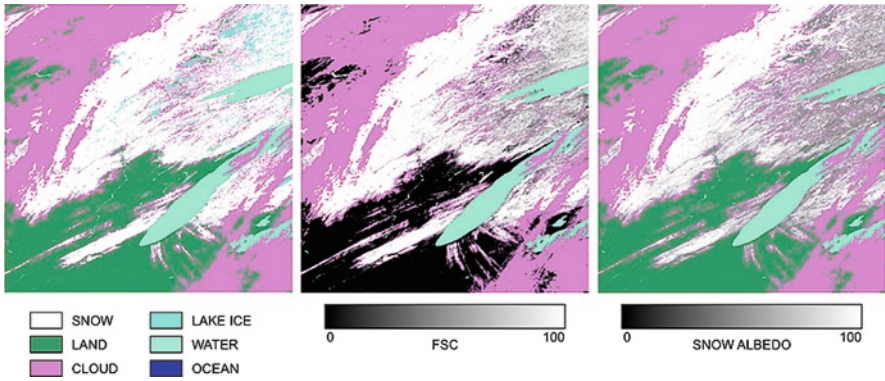


Fig. 30.3 MOD10A1.SCA product example (*left*), FSC (*center*), and snow albedo (*right*). Snow cover for 26 January 2006 is shown for tile h11v04 including the region west of the Great Lakes and lakes Superior and Michigan

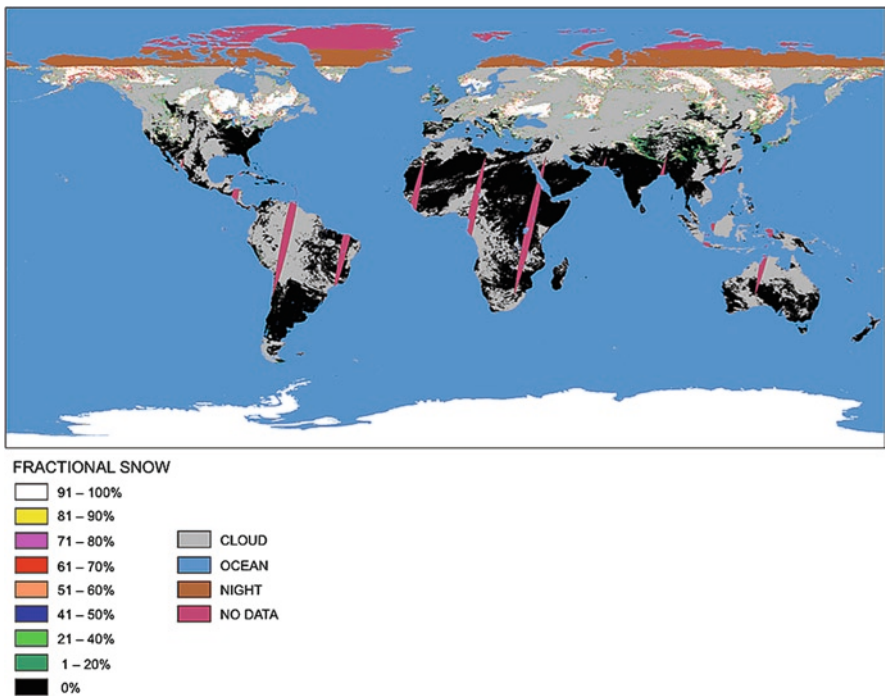


Fig. 30.4 MOD10C1 global FSC product example (acquired 26 January 2006) with the cloud mask applied. The cloud mask was determined from the cloud fraction data array in MOD10C1

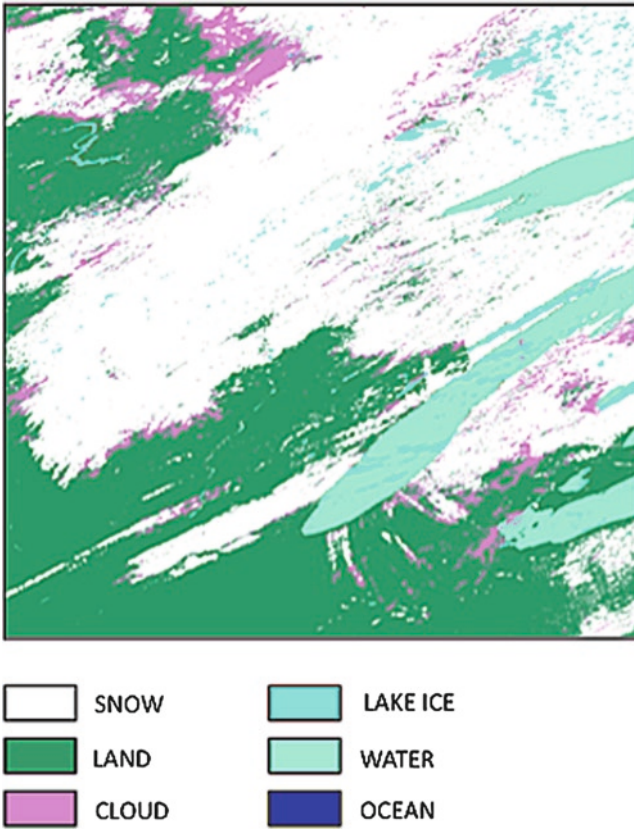


Fig. 30.5 MOD10A2 product example. Maximum SCA is shown for 8-day period from 25 January to 1 February 2006; the image is not projected

with the swath product at 500-m resolution, and then proceeds to a daily global snow map at 0.05° resolution. Eight-day composite global snow products are generated from the daily products. The final product is a 0.5° resolution monthly global mean FSC map derived from the MODIS daily global snow cover product. Except when otherwise noted, the snow algorithms and product descriptions are the same for the Terra and Aqua MODIS instruments.

MODIS data products include a data quality assessment (QA) data array, which provides a user with an indication of the data pixel or grid cell quality. A user may decide on the data quality based on the QA information. In C4, the snow and sea ice products, except for the daily global snow product MOD10C1 (Tables 30.1 and 30.2), store the QA data as a bit flag. For MOD10C1, a confidence index (CI) was calculated and stored as the QA data. To make the QA data more accessible to the user in C5, the QA bit-flagged data were changed to values, which indicate the general quality of an observation.

The most frequently used MODIS snow products, as reported in the literature and through National Snow and Ice Data Center (NSIDC) Distributed Active

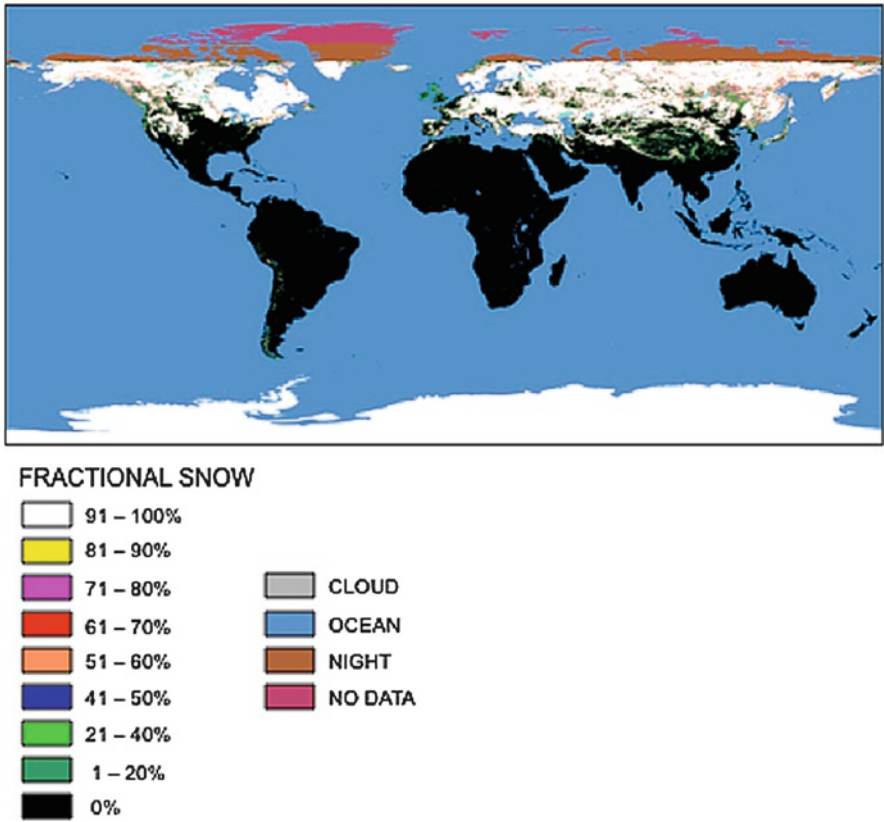


Fig. 30.6 MOD10C2 product example. FCA is shown for 8-day period from 25 January to 1 February 2006

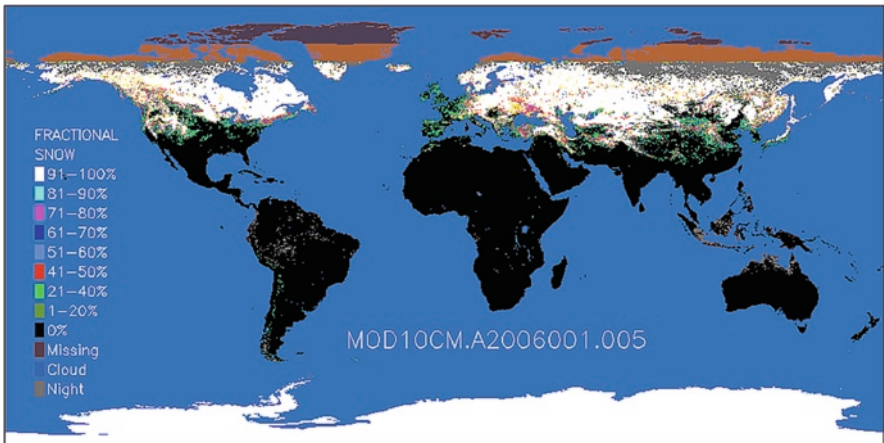


Fig. 30.7 MOD10CM, monthly mean product example. FCA is shown for January 2006

Archive Center (DAAC) distribution statistics, are the daily tiled and 8-day composite tiled products. An advantage of the 8-day products is that snow extent is maximized and cloud obscuration is minimized.

The complete MODIS snow and sea ice product suite is presented in Tables 30.1 and 30.2, respectively. They include the following information: product long name, Earth Science Data Type (ESDT) name, spatial and temporal resolutions, and component datasets. Examples of the products are shown in Figs. 30.2–30.7. The same products are generated for the MODIS Terra and Aqua platforms. The distinction between the two is the ESDT prefix “MOD” for Terra and “MYD” for Aqua. The C4 and C5 datasets are listed in Tables 30.1 and 30.2. Note that some data array names in the products have changed; some data arrays were added and others were deleted. Throughout the chapter, the ESDT is used to refer to the data products.

30.2.1 MODIS/Terra Snow Cover 5-Min L2 Swath 500 m

The MODIS swath-level algorithm, MOD10_L2, includes thematic snow-covered area (SCA) and pixel FSC in C5 at 500-m resolution (Fig. 30.2). The ability to detect snow cover relies on the characteristic of high reflectance across visible wavelengths, and very low reflectance in the near-infrared wavelength at $\sim 1.6 \mu\text{m}$. MODIS-calibrated radiance data converted to top-of-atmosphere reflectance are used as input. The snow algorithm uses the normalized difference snow index (NDSI) to detect snow cover. The NDSI is calculated as $(\text{band-4} - \text{band-6})/(\text{band-4} + \text{band-6})$, with center wavelengths of band-4 at $0.55 \mu\text{m}$ and band-6 at $1.6 \mu\text{m}$.

The NDSI remains in use since the 1980s (or earlier) and viewed as an effective way to map snow cover, especially along with the use of other thresholding techniques (for example, see, Bunting and d’Entremont 1982; Crane and Anderson 1984; Dozier 1989; Hall et al. 1995). Snow is detected by a criterion test of the $\text{NDSI} \geq 0.4$ and minimum reflectance criteria tests using band-2 ($0.86 \mu\text{m}$) ≥ 0.10 and band-4 ($0.55 \mu\text{m}$) ≥ 0.10 . To improve snow detection in dense vegetation, an additional test of the relationship between NDSI and Normalized Difference Vegetation Index (NDVI) is applied. The latter, developed by Klein et al. (1998), enhances the ability to detect snow in dense forests. A surface temperature screen is also applied to prevent warm ($>283 \text{ K}$), bright surfaces from being identified erroneously as snow. An estimated surface temperature is calculated in the algorithm with a split window technique using band-31 ($11.03 \mu\text{m}$) and band-32 ($12.02 \mu\text{m}$). The MODIS cloud mask product, MOD35_L2 (Ackerman et al. 2004), is a cloud “conservative” map (the algorithm tends to label pixels as cloud in situations where uncertainty about a clear view of surface is indicated in the algorithm). Any pixel identified as “certain cloud” in MOD35_L2 is labeled as “cloud” in the snow algorithm; otherwise pixels are processed as “clear” in the snow algorithm. The land/water mask contained in the MODIS geolocation product is used to limit processing to land areas. The land/water mask is also used to map snow- and ice-covered inland water bodies. The snow

algorithm contains very minimal restrictions to allow it to map snow cover globally. No automated QA is performed in the algorithm other than to check for unusable input data, e.g., out of range radiance data. If unusable input data are encountered, the QA is set to “other quality,” otherwise it is set to “good quality.”

The Terra and Aqua snow algorithms differ in the bands used to calculate the NDSI because a majority of band-6 detectors on the Aqua MODIS have remained non-functional since launch. The Aqua snow algorithm was therefore modified to use band-7 (2.1 μm) in place of band-6, which is used for the Terra algorithm (Riggs and Hall 2004). A technique to compensate for the lack of good Aqua MODIS band-6 data is described by Wang et al. (2006), which can potentially help create a band-consistent NDSI between Terra and Aqua.

A pixel FSC algorithm based on a regression with NDSI (Salomonson and Appel 2004, 2006) is given as: $\text{FSC} = -0.01 + 1.45 \times \text{NDSI}$. A modified $\text{FSC} = -0.64 + 1.91 \times \text{NDSI}$ for the Aqua MODIS is given in Salomonson and Appel (2006). The FSC is generated for the full range of NDSI from 0.0 to 1.0, with the same visible reflectance, temperature screens, and cloud mask as applied to thematic snow. The FSC algorithm produces a new FSC (data array) that is included in C5 products: MOD10_L2, MYD10_L2, MOD10A1, and MYD10A1.

30.2.2 MODIS/Terra Snow Cover Daily L3 Global 500-m SIN Grid

Daily snow cover products (MOD10A1, Table 30.1) of SCA and pixel FSC at 500-m resolution are generated from all the MOD10_L2 swaths mapped to the Sinusoidal map projection in gridded tiles of about $10^\circ \times 10^\circ$ in size (Fig. 30.3). An intermediate data processing algorithm maps all the MODIS observations from the swaths into tiles of the map projection, and outputs an intermediate product wherein all the observations for a day in a grid cell (500 m) are “stacked” and available (Wolfe et al. 1998). Daily SCA, FSC (in C5), and QA are selected using a “scoring algorithm” to select an observation of the day based on solar zenith, distance from nadir, and pixel coverage of all observations that were mapped into a grid cell. The objective is to select the observation nearest local noon, closest to nadir, and with maximum grid cell coverage. Details of the scoring algorithm are given in the Snow User Guide (Riggs et al. 2006a). A “best” observation from all the observations for the day is selected based on the score and written into the daily product. The same pixel is used for SCA, FSC, and QA. No other criteria are applied, so errors from MOD10_L2, if present, are propagated to MOD10A1.

Snow albedo is calculated using a method developed by Klein and Stroeve (2002) with the following inputs: MODIS surface reflectance corrected for atmospheric effects, Bidirectional Reflectance Distribution Function (BRDF) land cover product, and a Digital Elevation Model (DEM). Snow is treated as an anisotropic surface except in forests, where it is treated as an isotropic surface. Snow albedo is

calculated only for pixels that are identified as snow in the SCA map. The algorithm details are available in the Snow User Guide (Riggs et al. 2006a).

30.2.3 MODIS/Terra Snow Cover Daily L3 Global 0.05° CMG

The daily global snow product (MOD10C1) in the climate modeling grid (CMG) at 0.05° resolution contains the FSC area calculated by binning the SCA from MOD10A1 (500 m) into CMG cells (Fig. 30.4). A corresponding binned cloud fraction is also generated, from which a cloud mask is extracted and mapped over the FSC (Fig. 30.4). A CI for the FSC is calculated based on the total number of all observations binned into a grid cell, and indicates how much of the data binned in the grid cell contained clear views of the surface. An example of the CI calculations is given in the Snow User Guide.

30.2.4 MODIS/Terra Snow Cover 8-Day L3 Global 500-m SIN Grid

Maximum snow cover occurring in an 8-day period at 500-m resolution is mapped into the MOD10A2 product (Fig. 30.5). Inputs to the algorithm are the SCA maps from the MOD10A1 for the period. If a grid cell was observed as snow-covered on any day in the period, then snow cover is mapped in that grid cell for the 8-day period. Days in which snow was observed are also tracked and mapped in a separate data array in the product. Maximum snow cover extent and minimum cloud obscuration are features of this product.

30.2.5 MODIS/Terra Snow Cover 8-Day L3 Global 0.05° CMG

The 8-day CMG snow product (MOD10C2) at 0.05° resolution represents the maximum SCA in an 8-day period (Fig. 30.6). Eight-day periods are fixed to the calendar; periods are listed in the Snow User Guide. Inputs to the algorithm are the 8-day MOD10A2 for the period. Input data are binned into categories of snow, cloud, night, etc. The percentage of snow, percentage of cloud, and CI are computed based on the binning results for each CMG cell, and written into the appropriate data arrays.

30.2.6 MODIS/Terra Snow Cover Monthly L3 Global 0.05° CMG

A monthly average FSC product, MOD10CM (Figs. 30.1 and 30.7), is computed using 28–31 days of the daily MOD10C1 (Fig. 30.4). Data are filtered so that the

most relevant days with snow cover are used in the average, and the filtered data usually includes monthly snow of low amount and incidence. The latter filter works to remove some occurrences of erroneous snow from the monthly snow average. A daily cell must have a CI of >70% to warrant inclusion in the average. That filter is applied so that only the clearest, i.e., least-cloudy, of the daily observations are included in the average. A daily observation contributes to the monthly average for a cell as follows: daily contribution to monthly mean = $100 \times \text{snow \%}/\text{CI}$.

30.3 Evaluation of Errors in the Snow Products

Results in the literature reveal the usefulness of the snow data products in many applications, and their potential to improve the application capabilities when used as input. Accuracies in the range of 90–94% have been reported primarily for the SCA maps. The FSC, which is new in C5 still awaits extensive study by the community. The snow albedo product was evaluated with surface measurements in a few studies for a few locations, but has not been used as an input to snowmelt modeling or climate change studies. Snow cover product users focus on the utility and accuracy of the snow products as relevant to the application. In this error evaluation section, information on origin and propagation of some snow errors is presented. Aside from potential mapping or geolocation errors, most snow detection errors are associated with non-ideal conditions for snow detection or with snow/cloud discrimination.

In the MODIS snow products processing sequence, the higher-level products are generated from the preceding level, and their accuracy and errors are passed on to the higher-level products. Snow errors of commission and omission, made at the swath level are propagated to the higher-level products. Notable snow errors in MOD10_L2 originate from erroneous snow detection in low illumination conditions at cloud edges in some circumstances. Snow omission errors may occur because of snow/cloud confusion along the periphery of SCAs, and from land/water mask and image geolocation mismatches along some coastlines. These errors are propagated forward to the higher-level products.

Snow errors of commission may occur in cloud shadowed, vegetated land surfaces during the summer. Typically, this error exhibits a few snow pixels on the most intensely cloud-shadowed land in MOD10_L2. When present, this error is typically small, i.e., 0–1% of a swath. However, in some conditions, the error may rise to 1–3% of a scene. For instance, during the summer, broken cloud conditions over the boreal forests may contain more errors.

These situations represent the algorithm's limit to accurately detect snow-free land under cloud shadow illumination conditions. This type of error is highly variable within a swath and from day to day because it is usually associated with broken, scattered cloud cover. These errors are propagated into MOD10A1 if an error-prone observation is selected to represent the day. No screening for snow errors is made in the MOD10A1 algorithm. These types of errors are then composited in the MOD10A2 and appear as erroneous snow in different locations in a tile over an 8-day period.

In MOD10C1, snow commission errors propagated from MOD10_L2 appear as low snow percentages in the binned FSC map. These errors are obvious in regions and seasons where snow is impossible. Typically, the errors occur in the 1–20% range of snow cover; however, if many counts of erroneous snow occur in pixels that are binned into a 0.05° CMG cell, then the error may occur as a higher percentage, e.g., 40% or greater. In regions and seasons where snow is possible, it is more difficult to differentiate between these commission errors and actual snow cover.

Snow errors of commission at edges of clouds, particularly edges shadowed by other parts of the cloud, are associated with the cloud mask not identifying the edge as “certain cloud.” In such cases, the snow algorithm processes the partially cloudy pixel, and because the cloud’s spectral characteristics resemble those of snow with a moderate-to-strong snow signal, i.e., NDSI > 0.4, the pixel is therefore labeled as snow. In addition, in some situations of mixed ice and water cloud types, the cloud mask may not detect the ice cloud types, which are possibly mapped as snow. This results in an error of commission with a tendency for localized (e.g., tens of pixels) occurrence, and is usually observed frequently during the boreal summer.

Long daylight hours during the boreal summer allow several MODIS orbit tracks to occur at times of low solar illumination angles very early in the morning or late in the day. Under such low solar illumination conditions, snow errors of commission may occur because the surface reflectance is very low across the visible and near-infrared bands. Small differences in reflectance between those regions tend to produce high NDSI values even in snow’s absence on the ground. If the visible reflectance amount is just above the threshold tests, the surface is liable for erroneous misinterpretation as “snow.” Such low illumination conditions are at the lower limit of the algorithm’s ability to detect snow accurately. The most accurate MOD10_L2 snow map for a boreal summer day is the one acquired nearest local noon when conditions are considered most favorable for accurate snow mapping. The MOD10A1 algorithm uses a scoring method that selects the most favorable observation (pixel) from several acquired in a day. A major factor in that algorithm is the observation’s solar elevation; observations near solar noon are scored highest. The use of this scoring algorithm greatly minimizes the propagation of snow errors from low solar illumination conditions in MOD10_L2 into MOD10A1.

Cloud commission errors, which identify snow-covered pixels as “cloud” on the edges of snowfields hinder accurate mapping of the snow edge, e.g., note the edge of snow south of Lake Superior in Fig. 30.2. In these situations, the cloud mask algorithm has a low confidence level in cloud-visible spectral tests, and because of its conservative nature, it favors identifying the pixels as cloud in such situations. This error was reported as a problem by investigators using the MODIS SCA products (see applications discussion in Sects. 30.4.1 and 30.4.2). Investigation of these errors indicates a potential to isolate and resolve them with specific cloud spectral test flags stored in the cloud mask products; however, a reliable correction technique still awaits development. Improvements made in the application of cloud spectral tests within the C5 version of the cloud mask algorithm may reduce this problem.

Disagreement between coastline mapping in the MODIS land/water mask at 1-km resolution, and the 500 m level-2 radiance data and the MOD10_L2 product may produce errors along some coastlines, which vary with geographic location. These errors have minimal impact on the quality of the snow maps globally because snow errors along coastlines are uncommon globally, and the temperature screen eliminates many such errors. However, snow mapping problems are obvious in some places during some seasons. For example, the Canadian Arctic Archipelago on the land/water mask is not well-matched with the MODIS swaths, resulting in false “snow” along the coastline in the boreal summer.

Several studies have reported on the accuracy of the snow albedo in MOD10A1. Stroeve et al. (2006) compared the MODIS daily snow albedo to surface measurements at five weather stations on Greenland and reported that, in general, the MODIS snow albedo tracked the seasonal variability in albedo. The daily snow albedo product, however, occasionally had unrealistically high albedos, and there were unexplained differences between the Terra- and Aqua-derived albedos, which suggest that the BRDF is probably poorly modeled. Tekeli et al. (2006) and Sorman et al. (2006) found that the MODIS snow albedo product overestimated albedo by about 10% in the mountains of the Karasu basin when compared with in situ measurements. In general, the snow albedo was consistent in the amount relative to those measured in the in situ locations. Generally, the snow albedo product is considered free of large errors in low relief and deep snow conditions. However, under rugged relief, shallow snow, and anisotropic surfaces, the snow albedo calculations may suffer adverse effects, which may generate unreasonable results. The snow albedo product is also unreliable along coastlines because of discrepancies between the land/water mask and DEM used. Working together with the MODIS albedo product developers, we expect to improve the snow albedo product in the near future.

30.4 Applications of MODIS Snow Products

The MODIS snow products are used in various applications such as SCA mapping, hydrological modeling, data assimilation, operational monitoring, educational projects, and blending with snow data products from other sensors. Herein, we provide an overview of the range of applications, which use the snow products with comments on the utility and reported accuracy.

Collection 4 usage reports from the NSIDC DAAC show that the most-often ordered and distributed product is MOD10A1, followed by MOD10A2 and MOD10C1, and finally MOD10_L2. Terra MODIS products dominate the distribution over their Aqua counterparts. Terra has a longer historical collection when compared with Aqua, and the quality of the Aqua products is less well-known when compared with the Terra, especially because the Aqua MODIS snow algorithm uses band-7 instead of band-6 (because of the non-functional band-6 detectors (Riggs and Hall 2004)). Thus, we generally refer to C4 Terra MODIS products in the remainder of this chapter.

30.4.1 *Determination of Snow-Covered Area*

Many researchers and operational users progressively need accurate SCA estimates.

Therefore, many investigators have evaluated the accuracy of the MODIS snow products to determine its appropriateness for a particular application. Several studies have explored inter-comparisons of other satellite-derived snow maps and/or ground station data networks with the MODIS SCA maps. In general, investigators have reported MODIS SCA accuracy in the 75–100% range, and that cloud obscuration and SCA errors of omission are impediments to overcome. Several researchers reported the accuracy of the MODIS SCA products in the range of 90–95% (see for example, Bitner et al., 2002; Brubaker et al., 2005; Parajka and Blöschl, 2006; Wang et al., 2008). This assumes that the cloud cover limitation is not considered an “error” but a remote sensing limitation in the reflective part of the spectrum. For example, Bitner et al. (2002) reported agreement of the snow maps at 94% in the Pacific Northwest and of 95% in the Great Plains. Differences in snow mapping among the maps were found at the edges of the snowpack where MODIS mapped more snow. In dense forest locations, the MODIS maps showed more snow than did the National Operational Hydrologic Remote Sensing Center (NOHRSC) maps, which was considered good in their work. Furthermore, the higher resolution of the MODIS maps was useful to detect localized snow cover conditions on plains and in forests. Wang et al. (2008) evaluated the MOD10A2 product in Northern Xinjiang China; they found an accuracy of 94% for SCA and snow-free land at 99% accuracy when snow depth ≥ 4 cm, but a very low accuracy of $<39\%$ for patchy or thin snow conditions, and that accuracy varied seasonally.

Klein and Barnett (2003) found $\sim 86\%$ agreement between MODIS and NOHRSC SCA maps. They further determined a 94 and 76% agreement of those SCA maps with Snowpack Telemetry (SNOTEL) measurements in the Upper Rio Grande Basin for the 2000–2001 snow seasons, respectively. A time-series comparison between MODIS snow maps and SNOTEL over the entire snow season revealed an 88% overall classification accuracy for MODIS snow maps. Discrepancies between MODIS and SNOTEL estimated errors of commission at 12% and errors of omission at 15% through the snow season. Most discrepancies occurred during accumulation and dissipation when the snow pack was thin or patchy.

Given the cloud mask’s high error rate, which interferes with snow mapping, researchers have developed techniques to correct such errors to improve the SCA accuracy. For example, Liang et al. (2008) used MOD10A1 and MOD10A2 products and reported accuracies from 98 to 78%, respectively, depending on the season, snow cover characteristics and errors in the cloud mask. They reduced cloud cover problems by using a combination of MOD10A2 and different MOD10A1 compositing periods, thus improving SCA. Maurer et al. (2003) found that MODIS, on average, had less cloud obscuration when compared with the NOHRSC snow maps. In the Columbia River Basin’s complex, forested terrain, that was an advantage of about 15% for MODIS SCA because of a reduction in cloud obscuration resulting

in fewer misclassification errors. That advantage is important in that basin because of the interest in monitoring snow cover for water supply forecasting. In the Missouri River Basin, similar results were found in the forested areas, and over the whole basin, and MODIS SCA maps were more accurate than the NOHRSC SCA maps.

Zhou et al. (2005) highlight the significance of the snow omission error caused by masking snow as cloud. The greatest hindrance to using the daily snow product was cloud obscuration, with errors of misclassifying land or snow as cloud, which greatly impacted the product accuracy. MODIS snow products had low error rates in misclassifying snow as land.

The MODIS snow map's accuracy is affected by the land cover, and shows the lowest accuracy in the boreal coniferous forests. Simic et al. (2004) compared 2001 MODIS daily snow maps over Canada with observations for about 2000 meteorological stations. They found an 80–100% agreement on a monthly basis between the snow maps and station data. Disagreement of about 20% between station data and MODIS was found for all seasons in evergreen forest with errors of commission contributing 15% or more to the error. In other vegetation cover types, deciduous, herb, and lichen, errors ranged from about 2 to 10% and were dominated by errors of commission. Errors of omission, i.e., missing snow, ranged from 1 to 5% in all seasons in all cover types. MODIS was least accurate in dense evergreen forests with an accuracy of about 80%, which is consistent with the findings of Hall et al. (2001a), who reported relatively low accuracy for dense evergreen vegetation.

Several investigators have compared the MODIS SCA to snow maps derived from Special Sensor Microwave Imager (SSM/I) data. The attributes and limitations for snow mapping for the optical and microwave instruments are different, so they are not expected to provide the same results. SSM/I may underestimate snow extent when snow is wet, or thin and dry, but the passive-microwave sensors are useful to map snow through darkness and cloud cover, which optical sensors are not. Furthermore, the spatial resolution of the optical sensors is far better than those of the passive-microwave sensors, so the optical sensors can provide much better detail, especially in mountainous areas and at the edges of SCAs. In general, studies show that later in the snow accumulation season, MODIS and SSM/I SCA results are often very similar. For the most part, the MODIS SCA provides a more accurate areal extent of snow cover, especially early in the season (Hall et al. 2002) when compared with SSM/I-derived SCA. Hall et al. (2002) found differences up to $5.32 \times 10^6 \text{ km}^2$ in the amount of snow mapped with MODIS versus SSM/I, and MODIS data being more accurate. Bussi eres et al. (2002) also compared MODIS and SSM/I-derived snow maps over the prairie and boreal forest region in western Canada, and the taiga region in eastern Canada. They generally found a good correspondence; however, the SSM/I maps were not as accurate as the MODIS results in the fall and spring.

Brubaker et al. (2005) used the CI data in MOD10C1 to construct and apply a triangular probability density function to infer snow cover, when accounting for its uncertainty in a 0.05° cell, which was partially cloud-covered. This embodies an

innovative use of the CI to infer snow cover in situations, where mixed observations of clear and cloud-obscured pixels were mapped in the CMG.

30.4.2 *Hydrological Applications*

Many investigations have used the MODIS snow products in hydrological models to generate “better” SCA maps to model basin snowpack melt and runoff. Daily satellite-derived SCA maps are required to monitor changes in SCA over an entire basin, which is otherwise probably monitored only by a limited network of ground sampling stations. A snow water equivalent (SWE) map, which is obtained from microwave sensors or compiled from station data or surveys, is also needed for hydrological models, and is usable in concert with MODIS SCA. Investigators have used the MODIS SCA products in different models to map SCA or to infer SCA depletion curves to estimate runoff from basins. Most of these models have been applied in small-to-moderate sized basins, where the higher spatial resolution of the daily MODIS snow cover product has the potential to improve estimates of SCA over time to forecast runoff.

The MODIS snow cover products have demonstrated their utility for streamflow prediction with the Snowmelt Runoff Model (SRM), and to generate hydrographs based on climate change scenarios (Rango et al. 2003; Lee et al. 2005). The SRM is a commonly used model in mountainous river basins but still usable for any basin (Martinec et al. 1998). In addition, Lee et al. (2005) used the MODIS snow cover product to simulate stream-flow using the SRM. They ran simulations for two Upper Rio Grande basins: the Rio Grande and the Rio Ojo during the 2001 snowmelt season with both MODIS and NOHRSC SCA maps. Daily snow depletion curves developed from SCA displayed a pattern similar to observations. SRM runoff simulations using the SCA in both watersheds were able to simulate the climbing and falling phases of the hydrograph, although some lesser features of the falling phase were missed. The MODIS SCA showed consistent snow cover retreat with respect to elevation, likely due to the higher spatial resolution, which provides more detailed SCA maps in the high-relief basins studied. MODIS was able to provide SCA information of sufficient quality for stream flow simulation using the SRM in the snowmelt-dominated watersheds.

Zhou et al. (2005) used streamflow and SNOTEL measurements as constraints in an evaluation of the MOD10A1 and MOD10A2 over the Upper Rio Grande Basin. A time-series of snow areal extent (SAE) was constructed for February 2000 to June 2004. They found 84–92% accuracy for the MOD10A2 when compared with the SNOTEL data, and 50–57% accuracy for the MOD10A1 snow map. They established that there was a statistically significant correlation between streamflow and SAE for both the daily and 8-day MODIS snow products. The 8-day product had a better correlation ($r = -0.404$) with streamflow than did the

daily snow product ($r = -0.300$), and is useful to evaluate streamflow response to SAE changes in the long-term perspective.

MODIS provides small-scale variations in snow cover, which is usually assumed as homogeneous over large areas, e.g., grid cells of 1,000 km² in models. Small-scale variations in snow cover have significant effects on energy balance and snow melt in a basin (Déry et al. 2005). MODIS can capture some small-scale variations unlike other coarser resolution products. The MODIS FSC algorithm was used by Déry et al. (2005) to map FSC in the Kuparuk River Basin (KRB) (8,400 km²) on the North Slope of Alaska. FSC maps were used to parameterize the NASA catchment-based land surface model (CLSM) (Koster et al. 2000) to improve the model outputs. They used the MODIS FSC algorithm developed by Salomonson and Appel (2004) to generate the FSC maps. Use of the subgrid-scale snow parameterization from MODIS resulted in significant improvement in the simulation by providing more accurate timing and amount of runoff. A high-level of accuracy was achieved using the MODIS FSC scheme applied to the North Slope of Alaska. Improved simulations and predictions of the global surface energy and water budgets are anticipated by incorporating MODIS snow data into the CLSM.

In the Karasu Basin headwaters of the Euphrates River in Turkey, Tekeli et al. (2005) investigated the use of the MODIS daily and 8-day snow products for SCA mapping and construction of snow depletion curves for snowmelt runoff forecasts using the SRM. They found that the daily MODIS snow maps ranged from 62 to 82% accuracy in the basin. Cloud cover was mainly responsible for the lower accuracy when compared with ground station data. The MODIS 8-day snow products were used to ensure maximum snow cover and minimum cloud cover over a period to construct the snow depletion curves for the SRM. They concluded that operation, which helped improve the water resource management in the basin with MODIS data products and a suitable snowmelt model to forecast magnitude and timing of snowmelt runoff. Sorman et al. (2006) also report on the Tekeli et al. (2005) study.

McGuire et al. (2005, 2006) evaluated the MODIS snow cover data products to improve initial conditions for stream flow forecasts in the Variable Infiltration Capacity (VIF) hydrological model, a grid-based macroscale model that solves the water and energy balances at the land surface in each grid cell in the Snake River basin. The MODIS SCA use in the model improved forecasts during the melt season (March to mid-May), when significant snowpack depletion occurs, and few snow events that could impact the runoff occur.

Shamir and Georgakakos (2006) used the MOD10A1 thematic snow cover as a check on snow cover area estimated in their spatially distributed snow model tested in the American River Basin in the Sierra Nevada.

Lundquist et al. (2005) used the MOD10A2 products to track receding snowlines, and to determine the first snow-free date as part of their research in streamflow timing at different basin scales.

30.4.3 Data Assimilation Model Applications

The daily MODIS CMG snow product was used by Drusch et al. (2004) to support testing of the National Oceanic and Atmospheric Administration (NOAA) National Environmental Satellite, Data and Information Services (NESDIS) operational snow product as input to the European Centre for Medium-Range Weather Forecasts (ECMWF) global snow analysis. A result of that study was the affirmation that daily satellite-derived SCA at high resolution can provide a more realistic SCA, especially the spatial heterogeneity of SCA to the model. The MODIS CMG product was used as an independent dataset as were station data to compare the model analysis outputs.

Rodell et al. (2004) and Rodell and Houser (2004) investigated the utility of the MOD10C1 for SCA assimilation into the Global Land Data Assimilation System (GLDAS). The purpose of assimilating MOD10C1 was to improve model initialization and correct modeled snow output of the land surface state in near-real time. Koster and Suarez (1992) used both Terra MOD10C1 and Aqua MYD10C1 to test a 101-day simulation of the Mosaic land surface model. MOD10C1 was assimilated and used to adjust the simulated snow-water equivalent in the model. The output of the MODIS updated simulation was compared to a control simulation, resulting in more accurate snow coverage (compared to in situ snow time-series). Serious deficiencies were found in some areas, particularly mountainous regions. MOD10C1 was found useful for daily SCA monitoring despite being limited by cloud coverage.

30.4.4 Operational, Educational, and Public Outreach Applications

MODIS snow products are also used in operational applications, and educational projects. For example, the U.S. Agency for International Development (USAID)-funded Famine Early Warning System Network (FEWS NET) (FEWS NET 2006) project uses the MOD10A2 product as part of a system to monitor the snow pack and predict runoff in Afghanistan (Artan et al. 2005; USGS 2006; NASA Earth Observatory story <http://earthobservatory.nasa.gov/Study/Afghanistan/>).

In addition, the daily automated format of the MODIS snow-cover products lend themselves to visualizations, such as one developed by the NASA Goddard Space Flight Center Scientific Visualization Studio, which generated a visualization of snow cover and sea ice cover with the entire time-series of the MODIS snow cover products (Hall and Mitchell 2005) (http://earthobservatory.nasa.gov/Newsroom/NewImages/images.php3?img_id=10274) to monitor snow cover and sea ice changes over the seasons. (Visualization is available at <http://svs.gsfc.nasa.gov/vis/a000000/a002400/a002484/index.html>.)

30.4.5 *Blending MODIS and Passive-Microwave Snow Data Products*

Blending of the MODIS MOD10C1 with the Advanced Microwave Scanning Radiometer for EOS (AMSR-E) SWE product (Kelly et al. 2003; Kelly and Foster 2005) is an active area of research. Blending creates a single product that provides information on SCA and snow volume, e.g., see Hall et al. (2007) and Foster et al. (2007). The blending process maximizes the attributes of each product to adjust for known errors in the other to generate an improved and highly accurate SCA and SWE.

30.5 MODIS Sea Ice Products

Optical, near-infrared, and infrared sensors have a major role in sea ice studies in the Polar Regions. Because of their excellent spatial resolution and their ability to measure albedo and surface temperature, data from these parts of the electromagnetic spectrum provide important information about sea ice conditions that is useful for numerical sea ice modeling (Li et al. 2001; Hall et al. 2004). Surface temperature controls the metamorphism of snow on sea ice and melt, and the rate of sea ice growth. They can also augment the mapping of sea ice with microwave sensors (see for example Parkinson and Cavalieri (2002) for information on passive-microwave remote sensing of sea ice). Together, MODIS and microwave data can provide complementary information about sea ice extent, concentration, age, and temperature.

IST controls the metamorphism of snow on sea ice, melt, and the rate of sea ice growth. Under clear conditions in the Arctic (Advanced Very High Resolution Radiometer (AVHRR)) satellite-derived IST are possibly within 2 K of ice-based drifting buoy measurements (Haggerty et al. 2003). Scambos et al. (2006) found the MODIS IST within $\pm 1.5^\circ\text{C}$ of in situ IST for sea ice off the East Antarctic coast. Hall et al. (2004) showed the MODIS IST as accurate ± 1.3 K under “winter” conditions in the Arctic oceans.

A suite of the MODIS sea ice data products (Table 30.2) is produced in a sequence similar to the MODIS snow products; the sea ice products change in spatial and temporal resolution through the production sequence wherein each succeeding product inherits data quality and errors from the preceding product. The suite begins with the swath-level product at 1-km resolution and ends with a daily global product in polar projection at 4 km for each hemisphere. The MODIS sea ice daily gridded products (MOD29P1D) are the most-often ordered of the sea ice products, followed by the swath and global daily sea ice data products, and lastly, the nighttime sea ice product. Brief descriptions of each product (Table 30.2) are presented in the following sections. An example of the MOD29E1D IST map is shown in Fig. 30.8.

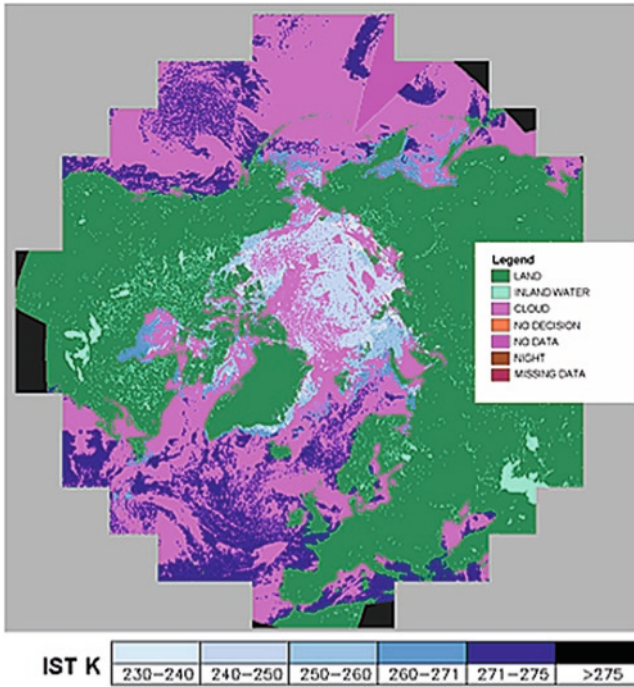


Fig. 30.8 MOD29E1D product example, which depicts the ice surface temperature (IST) map for 1 April 2006 for the Northern Hemisphere.

30.5.1 MODIS/Terra Sea Ice Extent 5-Min L2 Swath 1 km

The sea ice algorithm detects snow-covered sea ice, or sea ice with reflectance features similar to snow. It remains unclear whether the MODIS sea ice algorithm can accurately detect types of sea ice that are blue or clear. The sea ice algorithm is very similar to the snow algorithm in that it relies on the NDSI and visible reflectance criterion tests to detect the presence of sea ice; it also uses the MODIS cloud mask product (MOD35_L2) to mask clouds. A thematic sea ice product is generated that maps the presence of sea ice, open ocean, or cloud cover at 1-km resolution. IST is calculated using band-31 (11.03 μm) and band-32 (12.02 μm) and the split-window technique of Key and Haeffliger (1992) and Key et al. (1997) with coefficients determined for expected temperature ranges, and for the Northern and Southern hemispheres. Details of the sea ice extent and IST algorithms are given in the sea ice User Guide (<http://modis-snow-ice.gsfc.nasa.gov>).

30.5.2 MODIS/Terra Sea Ice Extent Daily L3 Global EASE-Grid Day

Daily gridded sea ice products are generated at 1-km resolution in the polar EASE-Grid projection (Riggs et al. 2006b). An intermediate data processing algorithm

exists that maps all the MODIS observations from the data swaths into the EASE-Grid projection tiles, and outputs an intermediate product in which, all the observations for a day in a grid cell (500 m) are “stacked” and available (Wolfe et al. 1998). Grids are generated for the Northern and Southern hemispheres. A scoring algorithm based on solar zenith, distance from nadir, and pixel coverage in a grid cell is used to select the most favorable observation of the day from the many – 14 or more in boreal summer – observations acquired during a day. The objective is to select the observation nearest local noon, closest to nadir, with the maximum cell coverage. Details of the sea ice extent and IST algorithms are given in the User Guide. The selected observation for sea ice extent and IST is written into the daily product data arrays. No other criteria are applied to screen for potential errors. The products are produced for both daytime and nighttime, with the nighttime containing only the IST data array.

30.5.3 MODIS/Terra Sea Ice Extent and Ice Surface Temperature Daily L3 Global 4-km EASE-Grid Day

Global daily composite sea ice extent and IST products at 4-km resolution for North and South polar EASE-Grid projections are generated by binning and averaging the daily MOD29P1 products from 1 to 4 km. This product is used to create the MOD29E1 (Fig. 30.8) and MYD29E1 sea ice products.

30.6 Summary

MODIS snow products are used to improve mapping of SCA, monitoring SCA for hydrological modeling applications, and for data assimilation models, operational monitoring of SCA, and in educational projects. Evaluations of the MODIS snow products, primarily SCA, by researchers reveal an accuracy of ~93% in near-ideal conditions with a range of 80–100% accuracy over a greater range of conditions. The user may need to interpret or manipulate the SCA for a specific application to compensate for its limitations. Based on the applications reviewed, significant limitations to the utilization of MODIS snow products are cloud cover and snow/cloud discrimination. In some applications, the cloud cover limitations are alleviated by data compositing, as in the 8-day products. Various researchers have devised clever ways to reduce the limitation of cloud cover in the MODIS snow cover products.

The most-often used quality assessment data in the snow and ice products are the CI in the MOD10C1 product. This suggests that investigators desire an index of the data quality over a bit-encoded data quality scheme. Few users reported using the bit-encoded QA data included in the C4 products. In C5, a thematic QA data value has replaced the bit-encoded data with the objective of making the QA data more accessible to the general user community. The concept and technique of reporting on the QA of the data products continues to evolve.

The entire C5 MODIS snow and sea ice product suite is now available for users to order from NSIDC (NSIDC 2008). The major feature of C5 is the inclusion of the pixel FSC map in the MOD10_L2 and MOD10A1 products. In addition, a new monthly mean snow cover product, MOD10CM, is now included. An objective for future revisions of the MODIS snow algorithm is to reduce snow errors of omission and commission by improving the ability to discriminate between clouds and snow. A collaborative effort with other MODIS investigators is being made to improve the snow albedo algorithm. The user community-provided results are likely to guide, at least in part, other anticipated improvements to the MODIS snow and sea ice products.

Acknowledgments The authors thank the reviewers of this chapter – Richard Kelly/University of Waterloo and Andrew Klein/Texas A and M University – for their constructive and detailed comments and suggestions. We also acknowledge current and former members of the MODIS Snow and Ice Team for their many valuable contributions, including Kimberly Casey/Wyle Information Sciences, Janet Y.L. Chien/formerly SSAI, Nick DiGirolamo/SSAI, and Vince Salomonson/University of Utah.

References

- Ackerman SA, Strabala KI, Menzel WP, Frey RA, Moeller CC, Gumley LE, Baum BA, Seaman SW, Zhang H (2004) Discriminating clear-sky from cloud with MODIS. Algorithm Theoretical Basis Document (MOD35). http://modis-atmos.gsfc.nasa.gov/MOD35_L2/atbd.html Accessed 1 June 2006
- Artan G, Dwyer J, Verdin J, Budde M (2005) Monitoring water resources status with distributed snowmelt model. In: Eos Transactions American Geophysical Union, 86(52), Fall Meeting Supplement, Abstract G11A-1191
- Bitner D, Carroll T, Cline D, Romanov P (2002) An assessment of the differences between three satellite snow cover mapping techniques. *Hydrol Process* 16:3723–3733
- Brubaker KL, Pinker RT, Deviatova E (2005) Evaluation and comparison of MODIS and IMS snow-cover estimates for the Continental United States using station data. *J Hydrometeorol* 6:1002–1017
- Bunting JT, d'Entremont RP (1982) Improved cloud detection utilizing defense meteorological satellite program near infrared measurements. Air Force Geophysics Laboratory, Environmental Research, Hanscom Air Force Base, MA. Papers No 765 AFGL-TR-82-0072
- Bussièrès N, De Sève D, Walker A (2002) Evaluation of MODIS snow-cover products over Canadian regions. In: Proceedings of IGARSS'02, 24–28 June 2002, Toronto, Canada, pp 2302–2304
- Crane RG, Anderson MR (1984) Satellite discrimination of snow cloud surfaces. *Int J Remote Sens* 5(1):213–223
- Déry SJ, Salomonson VV, Stieglitz M, Hall DK, Appel I (2005) An approach to using snow areal depletion curves inferred from MODIS and its application to land surface modeling in Alaska. *Hydrol Process* 19:2755–2774
- Dozier J (1989) Spectral signature of alpine snow cover from the Landsat thematic mapper. *Remote Sens Environ* 28:9–22
- Drusch M, Vasiljevic D, Viterbo P (2004) ECMWF's global snow analysis: assessment and revision base on satellite observations. *J Appl Meteorol* 43:1282–1294
- FEWS NET (2006) <http://www.fews.net> Accessed 28 Feb 2006
- Foster J, Hall D, Eylander J, Kim E, Riggs G, Tedesco M, Nghiem S, Kelly R, Choudhury B, Reichle R (2007) Blended visible, passive microwave and scatterometer global snow products. In:

- Proceedings of the 64th annual Eastern snow conference, 29 May–1 June, St. John's, Newfoundland, Canada. http://www.easternsnow.org/proceedings/2007/proceedings_index.html
- Haggerty JA, Maslanik JA, Curry JA (2003) Heterogeneity of sea ice surface temperature at SHEBA from aircraft measurements. *J Geophys Res – Oceans* 108(C10):8052
- Hall D, Mitchell H (2005) MODIS daily global snow cover and sea ice surface temperature. In: International conference on computer graphics and interactive techniques proceedings of the ACM SIGGRAPH 05 electronic art and animation catalog, Los Angeles, California, ACM Press, New York, ISBN ~ ISSN:1098-6154, 1-59593-101-5, pp 234–235
- Hall DK, Riggs GA (2007) Accuracy assessment of the MODIS snow-cover products. *Hydrol Process* 21:1534–1547
- Hall DK, Riggs GA, Salomonson VV (1995) Development of methods for mapping global snow cover using Moderate Resolution Imaging Spectroradiometer (MODIS) data. *Remote Sens Environ* 54:127–140
- Hall DK, Foster JL, Salomonson VV, Klein AG, Chien JYL (2001a) Development of a technique to assess snow-cover mapping accuracy from space. *IEEE Trans Geosci Remote Sens* 39(2):232–238
- Hall DK, Riggs GA, Salomonson VV (2001b) Algorithm Theoretical Basis Document (ATBD) for the MODIS snow and sea ice-mapping algorithms. <http://modis-snow-ice.gsfc.nasa.gov/atbd.html> Accessed June 2008
- Hall DK, Kelly REJ, Riggs GA, Chang ATC, Foster JL (2002) Assessment of the relative accuracy of hemispheric scale snow-cover maps. *Ann Glaciol* 34:24–30
- Hall DK, Key J, Casey KA, Riggs GA, Cavalieri D (2004) Sea ice surface temperature product from the Moderate Resolution Imaging Spectroradiometer (MODIS). *IEEE Trans Geosci Remote Sens* 42(5):1076–1087
- Hall DK, Riggs GA, Salomonson VV (2006) MODIS snow and sea ice products. In: Qu JJ (ed) *Earth science satellite remote sensing – Volume I: Science and instruments*, Springer, Berlin
- Hall DK, Montesano PM, Foster JL, Riggs GA, Kelly REJ, Czajkowski K (2007) Preliminary evaluation of the AFWA-NASA blended snow-cover product over the lower Great Lakes Region. In: Proceedings of the 64th annual Eastern snow conference, 29 May–1 June, 2007, St. John's, Newfoundland, Canada. http://www.easternsnow.org/proceedings/2007/proceedings_index.html
- Kelly RE, Foster JL (2005) The AMSR-E snow water equivalent product: status and future development. In: *Eos Transactions, American Geophysical Union*, 86(52), Fall Meeting Supplement, Abstract C21C-1134
- Kelly REJ, Chang ATC, Tsang L, Foster JL (2003) Development of a prototype AMSR-E global snow area and snow volume algorithm. *IEEE Trans Geosci Remote Sens* 41(2):230–242
- Key J, Haefliger M (1992) Arctic ice surface temperature retrieval from AVHRR thermal channels. *J Geophys Res* 97(D5):5885–5893
- Key JR, Collins JB, Fowler C, Stone RS (1997) High-latitude surface temperature estimates from thermal satellite data. *Remote Sens Environ* 61:302–309
- Klein A, Barnett AC (2003) Validation of daily MODIS snow maps of the Upper Rio Grande River Basin for the 2000–2001 snow year. *Remote Sens Environ* 86:162–176
- Klein AG, Stroeve JC (2002) Development and validation of a snow albedo algorithm for the MODIS instrument. *Ann Glaciol* 34:45–52
- Klein AG, Hall DK, Riggs GA (1998) Improving snow-cover mapping in forests through the use of a canopy reflectance model. *Hydrol Process* 12:1723–1744
- Koster RD, Suarez MJ (1992) Modeling the land surface boundary in climate models as a composite of independent vegetation. *J Geophys Res* 97:2697–2715
- Koster RD, Suarez MJ, Ducharme A, Stieglitz M, Kumar P (2000) A catchment-based approach to modeling land surface processes in a general circulation model, 1 Model structure. *J Geophys Res* 105:24809–24822
- Lee S, Klein AG, Over TM (2005) A comparison of MODIS and NOHRSC snow-cover products for simulating streamflow using the Snowmelt Runoff Model. *Hydrol Process* 19:2951–2972

- Li S, Zhou X, Morris K, Jeffries M (2001) The spatial variability of summer sea ice in the Amundsen Sea seen from MODIS, RADARSAT SCANSAR and Landsat 7 ETM+ images. *Proceedings of IEEE 2001 International Geoscience and Remote Sensing Symposium*, Sydney, Australia, 9–13 July, 2001, pp 160–162, 2001
- Liang TG, Huang XD, Wu CX, Liu XY, Li WL, Guo ZG, Ren JZ (2008) An application of MODIS data to snow cover monitoring in a pastoral area: a case study in Northern Xinjiang, China. *Remote Sens Environ* 112:1514–1526
- Lundquist JD, Dettinger MD, Cayan DR (2005) Snow-fed streamflow timing at different basin scales: case study of the Tuolumne River above Hetch Hetchy, Yosemite, California. *Water Resour Res* 41:W07005. doi:10.1029/2004WR003933
- Martinez J, Rango A, Robert R (1998) Snow runoff model (SRM) user's manual. <http://hydrolab.arsusda.gov/cgi-bin/srmhome> Accessed June 2008
- Maurer EP, Rhoads JD, Dubayah RO, Lettenmaier DP (2003) Evaluation of the snow-covered area data product from MODIS. *Hydrol Process* 17:59–71
- McGuire M, Wood AW, Zeng Q, Lettenmaier DP (2005) Use of MODIS snow cover imagery for streamflow and reservoir storage forecasts in the Snake River basin. In: 85th AMS Annual Meeting, 19th Conference on Hydrology, San Diego, CA
- McGuire M, Wood AW, Hamlet AF, Lettenmaier DP (2006) Use of satellite data for streamflow and reservoir storage forecasts in the Snake River Basin. *J Water Resour Plan Manag* 132(2):97–110
- National Snow and Ice Data Center (NSIDC) (2008) <http://nsidc.org/data/modis/> Accessed June 2008
- Parajka J, Blöschl G (2006) Validation of MODIS snow cover images over Austria. *Hydrol Earth Syst Sci* 10:679–689. <http://www.hydrol-earth-syst-sci.net/10/679/1006/>
- Parkinson CL, Cavalieri DJ (2002) A 21-year record of Arctic sea-ice extents and their regional, seasonal and monthly variability and trends. *Ann Glaciol* 34:441–446
- Rango A, Gomez-Landesa E, Bleiweiss M, Havstad KM, Tanksley K (2003) Improved satellite snow mapping, snowmelt runoff forecasting, and climate change simulations in The Upper Rio Grande Basin. *World Resour Rev* 15(1):25–41
- Riggs G, Hall DK (2004) Snow mapping with the MODIS Aqua instrument. In: *Proceedings of the 61st Eastern snow conference*, 9–11 June 2004, Portland, ME, pp 81–84
- Riggs G, Hall DK, Salomonson VV (2006a) MODIS snow products users guide to Collection 5. <http://modis-snow-ice.gsfc.nasa.gov> Accessed June 2008
- Riggs G, Hall DK, Salomonson VV (2006b) MODIS sea ice products users guide to Collection 5. <http://modis-snow-ice.gsfc.nasa.gov> Accessed June 2008
- Rodell M, Houser PR (2004) Updating a land surface model with MODIS-derived snow cover. *J Hydrometeorol* 5:1064–1075
- Rodell M, Houser PR, Jambor U, Gottschalck J, Mitchell K, Meng CJ, Arsenault K, Cosgrove B, Radakovich J, Bosilovich M, Entin JK, Walker JP, Lohmann D, Toll D (2004) The global land data assimilation system. *Bull Am Meteorol Soc* 85:381–394
- Salomonson VV, Appel I (2004) Estimating fractional snow cover from MODIS using the normalized difference snow index (NDSI). *Remote Sens Environ* 89:351–360
- Salomonson VV, Appel I (2006) Development of the Aqua MODIS NDSI fractional snow cover algorithm and validation results. *IEEE Trans Geosci Remote Sens* 44(7):1747–1756
- Scambos TA, Haran TM, Massom R (2006) Validation of AVHRR and MODIS ice surface temperature products using in situ radiometers. *Ann Glaciol* 44:345–351
- Shamir E, Georgakakos KP (2006) Distributed snow accumulation and ablation modeling in the American River basin. *Adv Water Resour* 29(4):558–570
- Simic A, Fernandes R, Brown R, Romanov P, Park W (2004) Validation of VEGETATION, MODIS, and GOES+SSM/I snow-cover products over Canada based on surface snow depth observations. *Hydrol Process* 18(6):1089–1104
- Sorman AÜ, Akyurek Z, Sensoy A, Sorman AA, Tekeli AE (2006) Commentary on comparison of MODIS snow cover and albedo products with ground observations over the mountainous

- terrain of Turkey. *Hydrol Earth Syst Sci Discuss* 3:3655–3673. <http://www.hydrol-earth-syst-sci-discuss.net/3/3655/2006/>
- Stroeve JC, Box JE, Haran T (2006) Evaluation of the MODIS (MOD10A1) daily snow albedo product over the Greenland ice sheet. *Remote Sens Environ* 105:155–171
- Tekeli AE, Zuhail A, Sorman A, Sensoy A, Sorman AU (2005) Using MODIS snow cover maps in modeling snowmelt runoff process in the eastern part of Turkey. *Remote Sens Environ* 97:216–230
- Tekeli AE, Sensoy A, Sorman A, Zuhail A, Sorman U (2006) Accuracy assessment of MODIS daily snow albedo retrievals with *in situ* measurements in Karasu basin, Turkey. *Hydrol Process* 20:705–721. doi:10.1002/hyp.6114
- USGS Website (2006) <http://earlywarning.usgs.gov/afghan> Accessed 28 Feb 2006
- Wang L, Qu JJ, Xiong J, Hao X, Xie Y, Che N (2006) A preliminary study of Aqua/MODIS snow coverage continuity with simulated band 6. In: Gao W, Ustin SL (eds) *Remote sensing and modeling of ecosystems for sustainability III*. Proceedings of SPIE, vol 6298, p 62981A. doi:10.1117/12.680953
- Wang X, Xie H, Liang T (2008) Evaluation of MODIS snow cover and cloud mask and its application in Northern Xinjiang, China. *Remote Sens Environ* 112:1497–1513. doi:10.1016/j.rse.2007.05.016
- Wolfe RE, Roy DP, Vermote E (1998) MODIS land data storage, gridding, and compositing methodology: Level 2 grid. *IEEE Trans Geosci Remote Sens* 36(4):1324–1338. doi:10.1109/36.701082
- Zhou X, Xie H, Hendrickx JMH (2005) Statistical evaluation of remotely sensed snow-cover products with constraints from streamflow and SNOTEL measurements. *Remote Sens Environ* 94:214–231

Web Resources

- MODIS Snow and Sea Ice Global Mapping Project (2008) <http://modis-snow-ice.gsfc.nasa.gov>
Accessed 9 June 2008
- NASA Earth Observatory (2008) <http://earthobservatory.nasa.gov/> Accessed 9 June 2008

Chapter 31

Characterizing Global Land Cover Type and Seasonal Land Cover Dynamics at Moderate Spatial Resolution With MODIS Data

Mark Friedl, Xiaoyang Zhang, and Alan Strahler

31.1 Introduction

Until recently, the only land cover datasets available with global coverage were compiled from pre-existing maps and atlases based on ground surveys, national mapping programs, and highly generalized biogeographic maps (e.g., Olson and Watts 1982; Matthews 1983; Wilson and Henderson-Sellers 1985). In the 1990s, when Advanced Very High Resolution Radiometer (AVHRR)-derived global remote sensing datasets became available, it was possible to map land cover based on observable land cover properties (DeFries and Townshend 1994; DeFries et al. 1998; Loveland et al. 2000). As newer and better remote sensing data sources have emerged (e.g., MODIS, SPOT, MERIS), global land cover products continue to progress in both methodological maturity and map quality.

This chapter describes the MODIS global land cover product (MOD12). The development of this product began in the mid-1990s (Strahler et al. 1999), and refinements to the MOD12 algorithms still continue. MOD12 product versions, based on Collection 4 MODIS data are currently available for 2001–2004, and Collection 5 processing has just begun at the time of this writing. We focus on the methods and datasets used to create the MODIS land cover product, and also on the properties and status of the product itself.

31.2 Background and Scientific Context

31.2.1 *Significance of Land Cover and Land Cover Dynamics*

Land cover is defined as the biophysical state of the land surface. This definition encompasses both biotic and abiotic properties, but does not strictly include land use

M. Friedl (✉)
Department of Geography and Environment, Center for Remote Sensing,
Boston University, Boston, MA 02215, USA
e-mail: friedl@bu.edu

by humans. That said, humans depend on goods and services provided by terrestrial ecosystems, and reliable information on the state of global land cover is important to the welfare of human society. Land cover is therefore a fundamental component of global ecosystems, one, that humans rely heavily upon (Foley et al. 2005).

Besides providing ecosystem services to humans, land cover information is important to a wide spectrum of global change research. Because land cover strongly influences biosphere–atmosphere interactions, accurate land cover information is essential to parameterize land surface processes in regional to global scale models of the Earth system (e.g., Bonan et al. 2002; Running and Hunt 1993; Sellers et al. 1997). Further, as the Earth’s human population grows, the global footprint of land areas dominated by human use is expanding (Ramankutty and Foley 1998; Sanderson et al. 2002; Vitousek et al. 1997). As a result, human-induced land use and land cover modifications are among the most significant agents of environmental change at local to global scales, and human land use has significant implications for ecosystem health, water quality, and sustainable resource management practices. The state and dynamics of global land cover therefore has significant implications for both the sustainability of the Earth’s ecological systems and the socio-economic stability of current and future generations (Vitousek et al. 1997; Lubchenco 1998; Foley et al. 2005).

Land surface phenology is defined as the seasonal pattern of variation in vegetated land surfaces observed from remote sensing (Reed et al. 1994; White et al. 1997; de Beurs and Henebry 2005). Land surface phenology provides a useful diagnostic related to the nature and magnitude of ecosystem responses to climate variability and change, and vice versa. Moreover, accurate prescription (or prognosis) of land surface phenology is important to calculate key quantities in Earth system models related to surface energy and water fluxes (Arora 2002) and the global carbon cycle (Running and Nemani 1991; Wilson and Baldocchi 2000; Baldocchi et al. 2001). As a result, seasonal variation in land cover (*land cover dynamics*) has recently emerged as an important topic with relevance to a wide array of climate and ecological research areas including regional and global carbon modeling, ecological assessment, and agricultural monitoring, to name a few (Asner and Townsend 2000; Parmesan and Yohe 2003; Lucht et al. 2002).

31.3 The MODIS Land Cover Product

The MODIS land cover product is designed to support scientific investigations that require information on the state and seasonal-to-decadal scale global land cover dynamics. The product consists of two suites of science datasets. *MODIS land cover type* (MOD12Q1) includes five main layers, where land cover is mapped with different classification systems (Fig. 31.1). *MODIS land cover dynamics* (MOD12Q2) includes seven layers, and was developed to support seasonal and interannual variation (phenology) studies in land surface and ecosystem properties (Fig. 31.2). Both products are global. In Collections 1, 3, and 4, MOD12 was produced at a spatial resolution of 1 km. In Collection 5, the spatial resolution was increased to 500 m.

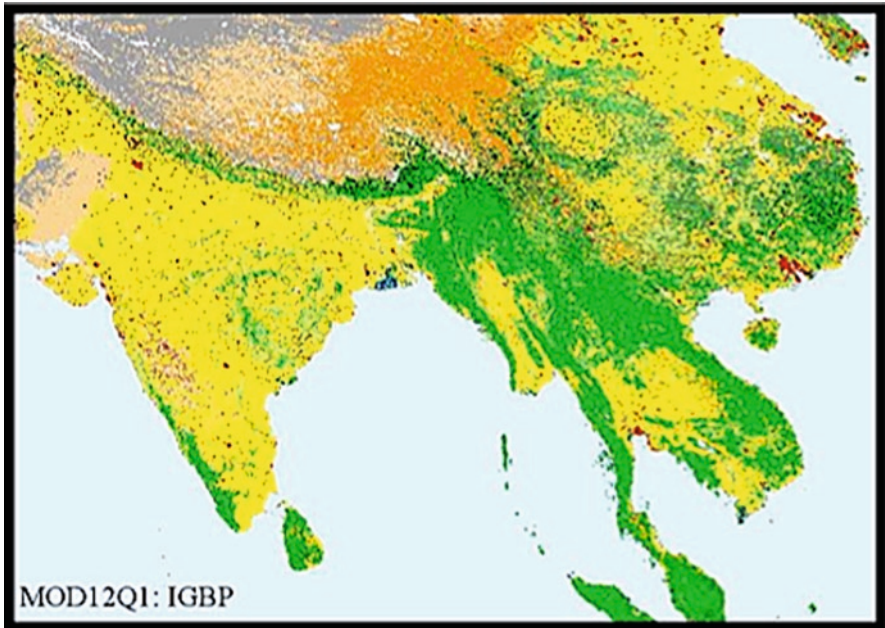


Fig. 31.1 A sample of the MODIS global land cover type product for Southeast Asia. This map shows the International Geosphere-Biosphere Programme layer for the Collection 4 version of MOD12Q1 in 2001 (see Fig. 31.4 for legend)

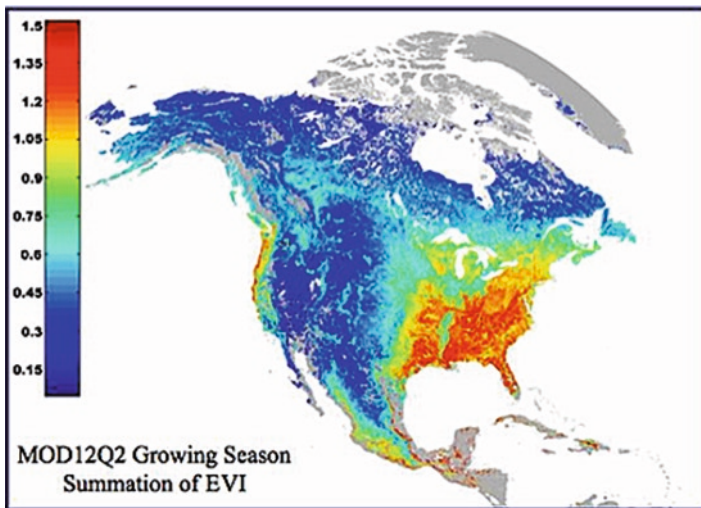


Fig. 31.2 Four-year average for the growing season summation of EVI, which is one of the layers included in the MODIS Land Cover Dynamics Product (MOD12Q2). This figure shows the average computed using Collection 4 data for the period from 2001 to 2004

The MOD12Q1 global land cover product includes a set of internally consistent layers, which depict different land cover classifications (Table 31.1). These layers include the International Geosphere-Biosphere Programme (IGBP; Loveland and Belward 1997) classification; a 14-class system developed at the University of Maryland (UMD; Hansen et al. 2000); a 6-biome system used by the MODIS LAI/FPAR algorithm (Myneni et al. 1997; Lotsch et al. 2001); the biome (BGC) classification proposed by Running et al. (1995); and the plant functional type (PFT) classification described by Bonan et al. (2002). Secondary labels (the most likely alternative IGBP class) and classification confidences (McIver and Friedl 2001) are also provided for each pixel, and a lower spatial resolution climate modeling grid (CMG) is produced for users not requiring the spatial detail afforded by the main land cover product. This grid provides both the dominant land cover type in each cell, as well as the sub-grid scale frequency distribution of land cover classes within each cell.

The MOD12Q2 product provides global maps of seven phenological metrics for all ecosystems exhibiting identifiable annual phenologies (Table 31.2). These metrics include the date of year for the following: (1) the onset of greenness increase (greenup), (2) the onset of greenness maximum (maturity), (3) the onset of greenness decrease (senescence), and (4) the onset of greenness minimum (dormancy). The three remaining metrics comprise the growing season minimum, maximum, and summation of modeled daily-enhanced vegetation index (EVI; Huete et al. 2002) values from MODIS.

Together, the MOD12Q1 and MOD12Q2 products are designed to provide high-quality global datasets, which characterize both the static properties of land cover at annual time scales and their seasonal dynamics.

Table 31.1 The MOD12Q1 product (C4, C5 refers to Collections 4 and 5)

| Science dataset | Descriptor | Spatial resolution (C4, C5) |
|-----------------------------------|---------------------------------------------------------------------------|-----------------------------|
| Land cover type 1–5 | IGBP, UMD, LAI/FPAR, BGC, PFT | 1 km, 500 m |
| Land cover type 1 assessment | Posterior probability (confidence) | 1 km, 500 m |
| Land cover type 1 secondary label | Second most likely class | 1 km, 500 m |
| Climate modeling grid | Majority class and grid proportions for land cover types 1, 2 (IGBP, UMD) | 0.005° |

Table 31.2 The MOD12Q2 product (C4, C5 refers to Collections 4 and 5)

| Science dataset | Descriptor | Spatial resolution (C4, C5) |
|------------------------------------|-------------|-----------------------------|
| Onset of greenness increase | Julian Date | 1 km, 500 m |
| Onset of greenness maximum | Julian Date | 1 km, 500 m |
| Onset of greenness decrease | Julian Date | 1 km, 500 m |
| Onset of greenness minimum | Julian Date | 1 km, 500 m |
| EVI at onset of greenness increase | EVI | 1 km, 500 m |
| EVI at onset of greenness maximum | EVI | 1 km, 500 m |
| Summation of growing season EVI | \sum EVI | 1 km, 500 m |

31.4 Algorithm Descriptions

31.4.1 MODIS Global Land Cover (MOD12Q1)

The classification strategy used by the MODIS land cover product uses a supervised decision tree classification algorithm called C4.5 (Quinlan 1993). This approach is supported by a variety of recent studies, which demonstrate the utility of decision trees for land cover classification problems in remote sensing (DeFries et al. 1998; Friedl and Brodley 1997; Friedl et al. 1999, 2000, 2002; Hansen et al. 1996, 2000; McIver and Friedl 2001, 2002). C4.5 is a univariate decision tree that makes no assumptions about the frequency distribution of the data being classified. This attribute is particularly important at global scales, because virtually all classes of interest exhibit multimodal frequency distributions, and therefore violate assumptions required by parametric supervised approaches such as the maximum likelihood classifier (Schowengerdt 1997).

In addition to being nonparametric (i.e., distribution-independent), C4.5 possesses several other traits that make it particularly useful to classify MODIS data-based land cover. First, C4.5 includes elegant and robust solutions to deal with missing data. This attribute is especially crucial in two geographic locations: high latitudes where low solar zenith angles lead to significant proportions of missing input MODIS data, and the tropics, where cloud cover results in missing data. Second, C4.5 includes mature methods for “pruning” the estimated classifications, thereby avoiding classifications that overfit training data.

A key feature of the MODIS land cover classification algorithm is a technique known as “boosting” (Freund 1995). Boosting is one of numerous ensemble classification methods developed in the mid-to-late 1990s, which widely demonstrate an ability to enhance classification accuracy (Bauer and Kohavi 1999; Dietterich 2000). Boosting also serves to minimize the sensitivity of the classification algorithm to noise in feature data and labeling errors in training data.

31.4.1.1 Training Data

The MOD12Q1 algorithm relies heavily on a land cover exemplars database for classification estimation. A geographically and ecologically comprehensive nature of this database is an essential requirement to capture and reflect the global diversity of land cover. To meet these needs, the System for Terrestrial Ecosystem Parameterization (STEP) was developed (Muchoney et al. 1999). STEP is designed to provide a classification-free and versatile database for site-based characterization of global land cover.

The current STEP database (i.e., for Collection 5) consists of roughly 2,000 sites distributed globally that were selected based on analysis of geographic and ecological sampling criteria (see Friedl et al. 2002). However, the database is dynamic and requires ongoing maintenance and augmentation to meet the needs of the

MODIS global land cover mapping effort. The sites included in the database are derived from manual interpretation of Landsat Thematic Mapper (TM) data, augmented by ancillary map data, as available.

31.4.1.2 Input Features

The input features to C4.5 are designed to exploit two main information dimensions. First, spectral information is provided by the seven MODIS land bands (channels 1–7), supplemented by the EVI product (Huete et al. 2002), and in Collection 5, the MODIS land surface temperature (LST) product (MOD11; Wan et al. 2002). All these input data are cloud-cleared and atmospherically corrected, and are representative of 8-day periods. To minimize artifacts introduced by differences in view geometry, surface reflectance and EVI data from nadir BRDF-adjusted reflectance (NBAR) data provided by the MODIS BRDF/albedo product are used (Schaaf et al. 2002). To exploit temporal information related to land surface phenology, the algorithm ingests a calendar year of monthly time-series of NBAR, LST, and EVI data. Second, a set of “annual metrics” including the annual mean, minimum, and maximum for each of the input features identified above are provided to the algorithm. This provides a total of 135 input features.

31.4.1.3 Decision Tree Classification Theory

C4.5 estimates supervised classifications with training data from the STEP database. To do this, C4.5 recursively partitions the training data using a metric called the information *gain ratio*, which measures the reduction in the data entropy resulting from a split. Formally, for a training dataset D with observations belonging to one of m classes $\{C_1, C_2, \dots, C_m\}$, C4.5 estimates a set of recursive splitting rules. At each node in the tree, a test (T) is estimated that splits D into n mutually exclusive subsets $\{S_1, S_2, \dots, S_n\}$. If $f(C_p, D)$ is defined as the number of cases in D belonging to class C_p , and $|D|$ is defined as equal to the total number of observations in D , then the amount of information required to identify the class for any observation in D is:

$$\text{info}(D) = -\sum_{j=1}^m \frac{f(C_j, D)}{|D|} \times \log_2 \frac{f(C_j, D)}{|D|} \quad (31.1)$$

If a split T partitions D into k outcomes $\{D_1, D_2, \dots, D_k\}$, a similar measure is definable that quantifies the total information content after applying T :

$$\text{info}_T(D) = \sum_{i=1}^k \frac{|D_i|}{|D|} \times \text{info}(D_i) \quad (31.2)$$

This approach is used to quantify the information gained by splitting D using T as:

$$\text{gain}(T) = \text{info}(D) - \text{info}_T(D) \quad (31.3)$$

Using this framework, C4.5 employs the so-called “gain criteria” to select the test for which $\text{gain}(T)$ is maximum. Because the information gain favors tests with large numbers of splits, it is normalized by:

$$\text{split info}(T) = - \sum_{i=1}^n \frac{|D_i|}{|D|} \times \log_2 \left(\frac{|D_i|}{|D|} \right) \quad (31.4)$$

which provides the actual metric used to estimate splits:

$$\text{gain ratio}(T) = \text{gain}(T) / \text{split info}(T) \quad (31.5)$$

Using the gain ratio, D is recursively split until each leaf node contains observations from a single class or further splitting yields no information gain. To minimize over-fitting, C4.5 uses error-based pruning (Mingers 1989), in which a portion of the data is held out during the training phase and used to measure the error rate of nodes based on independent data.

31.4.1.4 Boosting

The goal of boosting is to improve the classification accuracy of a base classification algorithm (in this case C4.5). Studies conducted with remotely sensed data have shown that boosting tends to reduce misclassification error rates by about 25% on average (Friedl et al. 1999; McIver and Friedl 2001). Boosting algorithms operate by estimating multiple classifications in an iterative fashion. At each iteration, each training observation is weighted. Observations misclassified in the previous iteration are assigned a heavier weight in the next iteration, which forces the classification algorithm to concentrate on those more difficult to classify observations. Therefore, each iteration produces a new classification tree with the intent to correct misclassification errors committed in the previous iteration.

The boosting method implemented within the MODIS land cover algorithm is based upon AdaBoost.M1 (Freund and Schapire 1997). More specifically, C4.5 is provided a set of m training examples $X = \{x_1, \dots, x_m\}$, each with an assigned class label (y) in $Y = \{1, \dots, K\}$. Using these data, a set of N decision trees are estimated in an iterative fashion. At each iteration, each training sample is assigned a weight, and the training sample distribution is defined by their weights, which is represented by the set D_n . At the first iteration, each example in the training sample distribution (D_1) is assigned an equal weight of $1/m$. This sample is used to estimate hypothesis h_n (i.e., a classifier; $n = 1$ for the first iteration), which maps $X \rightarrow Y$. The error of hypothesis h_n (the weighted training error) is then calculated as:

$$\varepsilon_n = \sum_{i=1:m; h_n(x_i) \neq y_i} D_n(i) \quad (31.6)$$

along with

$$\beta_n = \frac{\epsilon_n}{(1 - \epsilon_n)} \tag{31.7}$$

where n is the current iteration. The training sample distribution is then modified by updating the weights using:

$$D_{n+1}(i) = \frac{D_n(i)}{Z_n} \times \begin{cases} \beta_n & \text{if } h_n(x_i) = y_i \\ 1 & \text{otherwise} \end{cases} \tag{31.8}$$

where i is an index for each training example and Z_n is a normalization factor such that D_{n+1} is a distribution that sums to 1. After T iterations are completed, the algorithm computes a weighted vote for each class y using:

$$F_y(x) = \sum_{n=1:N} \begin{cases} \log(1/\beta_n) & \text{if } h_n(x) = y \\ 0, & \text{otherwise} \end{cases} \tag{31.9}$$

The final predicted label is then given by:

$$G(x) = \arg \max_{y \in Y} F_y(x) \tag{31.10}$$

In other words, that value of y that produces the largest value from the vote $F_y(x)$ is selected as the predicted class. The system terminates if $\epsilon_n > 0.5$ or if $\epsilon_n = 0$ (i.e., if greater than 50% of cases are misclassified or if all cases are classified correctly).

31.4.1.5 Estimating Class Conditional and Posterior Probabilities

A statistical examination of boosting has shown that the technique minimizes an exponential loss function equivalent to the binomial log-likelihood criteria of additive logistic regression models (Friedman et al. 2000). Using this result, probabilities of class membership are obtained from boosting in the same way that logistic regression provides the probability of a binary response variable based on one or more predictor variables. Given a vector of features x with associated class label y , the probability of membership in class j among K possible classes is provided by:

$$P(y = j | x) = \frac{e^{F_j(x)}}{\sum_{k=1}^K e^{F_k(x)}} \tag{31.11}$$

where $F_y(x)$ is the result from (31.9). This approach is used to compute class-conditional probabilities for the membership of each class at each pixel (e.g., Foody et al. 1992).

The result provided by (31.11) allows us to exploit existing information to improve our final classification result. Specifically, because estimates are available

for the class-conditional probabilities at each pixel, Bayes' rule is potentially useful in association with prior probabilities for specific classes to improve our classification results. The resulting posterior probability associated with the most likely class is included in MOD12Q1 and provides a spatially explicit measure of classification quality at each pixel. See McIver and Friedl (2001, 2002) and Friedl et al. (2002) for details.

31.4.2 MODIS Land Cover Dynamics (MOD12Q2)

The MODIS land cover dynamics algorithm provides a remote sensing-based methodology to identify transition dates that define the key phenological phases of vegetation at annual time scales (Zhang et al. 2003). To estimate these transition dates, EVI values computed from NBAR data are used. Because the presence of snow can significantly affect EVI values, the EVI data are first screened to remove (or at least minimize) snow-contaminated pixels. Specifically, in cases where snow or ice is detected, the EVI value is replaced with the most recent snow-free value. Note that while the MOD12Q1 product is produced annually based on a calendar year of data, the MOD12Q2 algorithm is produced bi-annually to capture differences in the seasonality of phenology in the northern and southern hemispheres.

Figure 31.3 provides a schematic representation of how vegetation phenology is modeled by the MOD12Q2 algorithm using series of piecewise logistic functions. Specifically, temporal variation in satellite-derived EVI data for a single growth or senescence cycle is modeled using a function of the form:

$$y(t) = \frac{c}{1 + e^{a+bt}} + d \quad (31.12)$$

where t is time in days, $y(t)$ is the modeled EVI value at time t , a and b are empirical coefficients, c is the amplitude of variation in EVI, and d is the initial background EVI value. To identify phenological transition dates, the rate of change in the curvature of

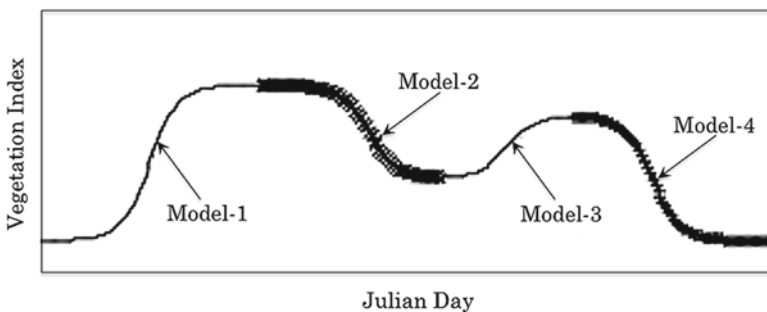


Fig. 31.3 Conceptual representation of the MODIS phenology algorithm, which shows how an annual cycle with two growth cycles is represented using four logistic functions

the fitted logistic models is used. Transition dates correspond to times at which the rate of change in curvature in the EVI data exhibits local minima or maxima. More formally, the curvature (K) for (31.12) at any time t is computed thus:

$$K = \frac{d\alpha}{ds} = -\frac{b^2 cz(1-z)(1+z)^3}{\left[(1+z)^4 + (bcz)^2\right]^{3/2}} \quad (31.13)$$

where $z = e^{a+bt}$, α is the angle (in radians) of the unit tangent vector at time t along a differentiable curve, and s is the unit length of the curve. The rate of change of curvature, K' , is then:

$$K' = b^3 cz \left\{ \frac{3z(1-z)(1+z)^3 \left[2(1+z)^3 + b^2 c^2 z \right]}{\left[(1+z)^4 + (bcz)^2 \right]^{5/2}} - \frac{z^2 (1+2z-5z^2)}{\left[(1+z)^4 + (bcz)^2 \right]^{3/2}} \right\} \quad (31.14)$$

During the growth period when vegetation transitions from a dormant state to maximum leaf area, three extreme points in the modeled EVI curve are inferable from (31.14). These points correspond to the onset of EVI increase (leaf emergence), the onset of EVI maximum (maximum leaf area), and the inflection point between these two events. Transition dates indicating the onset of EVI decrease and the onset of EVI minimum (senescence and dormancy, respectively) are estimated in a similar fashion. Note that before the NBAR EVI data are fit using logistic functions described by (31.12), it is first necessary to identify periods of sustained EVI increase and decrease (i.e., growth and senescence). To do this, a moving window using five 16-day periods is applied to the annual time-series. Transitions from increasing to decreasing EVI trends are identified by a change from positive to negative slope within any given window, and vice versa. This allows us to identify distinct growth cycles within a given annual time-series (e.g. Fig. 31.3).

31.4.2.1 Reprocessing and Current Status

At the time of this writing, the most recent available version of the MOD12 product is based on Collection 4 data, and includes annual maps for 2001 through 2004 (Figs. 31.4 and 31.5). With each reprocessing, the input data have improved, and the resulting maps have improved accordingly. Indeed, the ability to re-process the data has proven invaluable for a variety of reasons. In particular, reprocessing provides twin benefits: it allows implementation of changes to the algorithms, and similar changes to input data based on the previous collection results.

Reprocessing the MODIS land cover type product (MOD12Q1) has resulted in several key improvements to the input data and algorithm. First, the reprocessing has provided opportunity to revise, augment, and improve the quality of the training site database. Maintenance of this database is a very essential and continuous process because it not only plays a key role, the source data is quickly rendered

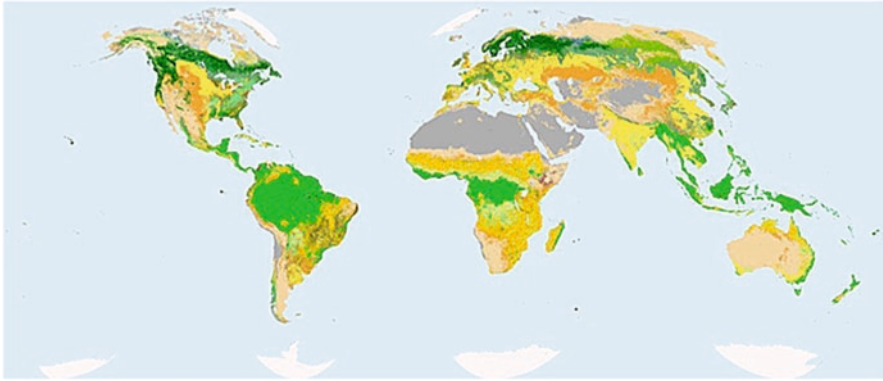


Fig. 31.4 MOD12Q1 IGBP global land cover map showing the IGBP layer for 2001

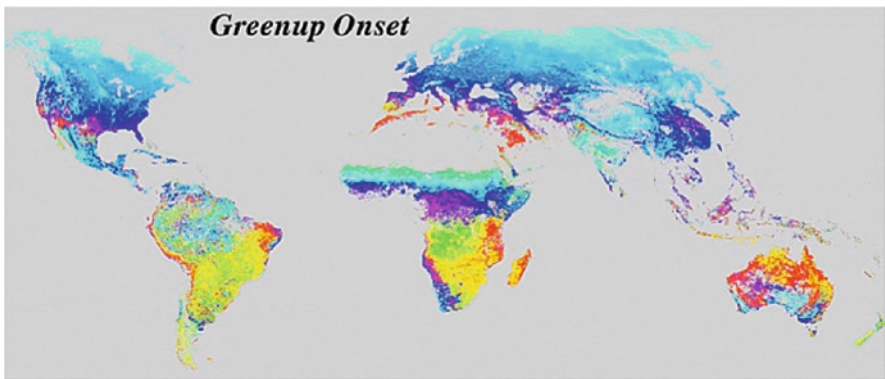


Fig. 31.5 Global onset of greenness derived from MODIS. The color scale progresses from *purple* and *blue* at the beginning of the calendar year, through *green*, *yellow*, and *red* toward the end of the year. The *green wave* in the northern hemisphere is evident

out of date. Therefore, episodic reprocessing affords the ability to update and revise this database, which results in a mature and high-quality land cover training sites database.

In addition to refining the site database, reprocessing has also resulted in a variety of improvements to the classification algorithm itself. One key change in this regard is the inclusion of annual metrics (minimum, maximum, and mean values) for the MODIS land bands and EVI as additional inputs to the classification process. Using these metrics (in addition to the monthly NBAR and EVI data) has improved both the quality of the maps and our ability to map land cover in persistently cloud-covered regions. In a similar fashion, the quality of ancillary information (prior probabilities) used in the classification was updated and improved, and parameters used to weight the influence of these priors in the final classification were tuned. This results in a slow, but steady improvement in the product quality.

Similar to the land cover type product, the current version of the land cover dynamics product is also based on Collection 4 data and includes bi-annual maps for the period from 2001 to 2004. Using these data, climate–vegetation relationships were examined with promising results (e.g., Zhang et al. 2004a, b, 2005). Because the land cover dynamics product is new in Collection 4, it was not revised and refined in a manner similar to most other MODIS land products. The results from Collection 4 are encouraging. For example, Fig. 31.5 shows the global onset of greenness for 2001, which is one of the science datasets included in MOD12Q2. Visual inspection shows spatial patterns that are consistent with known patterns in vegetation phenology at global scales. More importantly, results from comparisons of the MOD12Q2 product with several field datasets indicate that the algorithm performs well (Zhang et al. 2006). However, more work is required to fully assess this product, and understand its properties.

At the time of this writing, the Collection 5 reprocessing effort for both MOD12 products was initiated. Such an effort is significant because the availability of 500-m NBAR data should yield substantial improvements in both products. In particular, the higher spatial resolution provided by these data will reduce the sub-pixel heterogeneity in land cover and land surface phenology. In addition, because the Collection 5 NBAR data are being produced at 8-day intervals, these data provide a much-improved basis to capture phenological phenomena. As a result, significant improvements to the accuracy and precision with which these products characterize global land cover are expected.

31.5 Conclusions and Future Prospects

Since its original conception in the mid-1990s, the MODIS global land cover product (MOD12) has evolved from a prototyping activity based on AVHRR data to a mature operational product generated at regular intervals. In addition to the original product, which provided only thematic information (land cover type), the current version includes complementary information related to seasonal variation in vegetated land cover properties (land cover dynamics). Together, the MOD12Q1 and MOD12Q2 science product suites provide high-quality information related to the state and seasonal variation in land cover properties suitable for studies of regional to global scale land processes. In Collection 5 (which is expected before this chapter is published), the MODIS land cover product is being produced at 500-m spatial resolution. Because spatial heterogeneity is a key challenge that affects the quality of the MOD12 products, this change should lead to significantly improved characterization of both land cover type and land cover dynamics.

Despite the progress made, significant challenges still remain moving forward. Among these challenges, the classification system used for the land cover type product needs updating to reflect growing international community consensus around the FAO Land Cover Classification System (Di Gregorio and Jansen 2000). In addition, our experience over the last decade suggests that several important

classes are extremely difficult to map using the “one-size-fits-all” approach that the MOD12Q1 algorithm currently uses. In particular, agriculture (because of its global extent and diversity), wetlands (because of their ecological importance, diversity and small spatial extent), and deciduous needleleaf forests (because of their heterogeneity and patchiness) may each require more specialized mapping strategies. Similarly, we continue to wrestle with questions of precision for the land cover dynamics product. Specifically, limitations imposed by the temporal sampling afforded by satellites present significant challenges, especially in ecosystems where phenological transitions are rapid or subtle. Development of methods to minimize gaps due to cloud cover, and continued validation efforts for both products remain a priority. Finally, it is improbable that all these and other outstanding issues are solved. However, the existing products and the basic strategies developed to support them provide a sound basis for future operational land cover mapping in the NPOESS era and beyond.

References

- Arora V (2002) Modeling vegetation as dynamic component in soil-vegetation-atmosphere transfer schemes and hydrological models. *Rev Geophys* 40(2):3-1-3-26
- Asner GP, Townsend AR (2000) Satellite observation of El Niño effects on Amazon forest phenology and productivity. *Geophys Res Lett* 27(7):981-984
- Baldocchi D, Falge E, Wilson K (2001) A spectral analysis of biosphere-atmosphere trace gas flux densities and meteorological variables across hour to multi-year time scales. *Agric For Meteorol* 107(1):1-27
- Bauer E, Kohavi R (1999) An empirical comparison of voting classification algorithms: bagging, boosting, and variants. *Mach Learn* 36:105-139
- Bonan GB, Levis S, Kergoat L, Oleson KW (2002) Landscapes of plant functional types: an integrating concept for climate and ecosystem models. *Global Biogeochem Cycles* 16(2):doi:10.1029/2000GB001360
- de Beurs KM, Henebry GM (2005) Land surface phenology and temperature variation in the International Geosphere-Biosphere Programme high latitude transects. *Global Chang Biol* 11(5):779-790
- DeFries RS and Townshend JRG (1994) Global land cover: comparison of ground-based datasets to classifications with AVHRR data. In: *Environmental remote sensing from regional to global scales* (ed. by G Foody and P Curran), John Wiley and Sons, Chichester
- DeFries R, Hansen M, Townshend JGR, Sohlberg R (1998) Global land cover classifications at 8 km resolution: the use of training data derived from Landsat imagery in decision tree classifiers. *Int J Remote Sens* 19:3141-3168
- Dietterich TG (2000) An experimental comparison of three methods for constructing ensembles of decision trees: bagging, boosting, and randomization. *Mach Learn* 40(2):139-158
- Di Gregorio A, Jansen LJM (2000) *Land Cover Classification System Concepts and User Manual*. United Nations Food and Agriculture Organization Publishing Service, Report GCP/RAF/287/ITA, Rome, Italy
- Foley JA, DeFries R, Asner GP, Barford C, Bonan G, Carpenter SR, Chapin FS, Coe MT, Daily GC, Gibbs HK, Helkowski JH, Holloway T, Howard EA, Kucharik CJ, Monfreda C, Patz JA, Prentice IC, Ramankutty N, Snyder PK (2005) Global consequences of land use. *Science* 309:570-574

- Foody GM, Campbell NA, Trodd NM, Wood TF (1992) Derivation and applications of probabilistic measures of class membership from the maximum-likelihood classification. *Photogrammetric Engineering & Remote Sensing* 58:1335–1341
- Freund Y (1995) Boosting a weak learning algorithm by majority. *Inf Comput* 121(2):256–285
- Freund Y, Schapire RE (1997) A decision-theoretic generalization of on-line learning and an application to boosting. *J Comput Syst Sci* 55(1):119–139
- Friedl MA, Brodley CE (1997) Decision tree classification of land cover from remotely sensed data. *Remote Sens Environ* 61:399–409
- Friedl MA, Brodley CE, Strahler AH (1999) Maximizing land cover classification accuracies produced by decision trees at continental to global scales. *IEEE Trans Geosci Remote Sens* 37(2):969–977
- Friedl MA, Muchoney D, McIver DK, Gao F, Hodges JCF, Strahler AH (2000) Characterization of North American land cover from NOAA-AVHRR data using the EOS MODIS land cover classification algorithm. *Geophys Res Lett* 27(7):977–980
- Friedl MA, McIver DK, Hodges JCF, Zhang XY, Muchoney D, Strahler AH, Woodcock CE, Gopal S, Schneider A, Cooper A, Baccini A, Gao F, Schaaf C (2002) Global land cover mapping from MODIS: algorithms and early results. *Remote Sens Environ* 83(1–2):287–302
- Friedman J, Hastie T, Tibshirani R (2000) Additive logistic regression: a statistical view of boosting. *Ann Stat* 28:337–374
- Hansen M, Dubayah R, DeFries R (1996) Classification trees: an alternative to traditional land cover classifiers. *Int J Remote Sens* 17:1075–1081
- Hansen MC, Defries RS, Townshend JRG, Sohlberg R (2000) Global land cover classification at 1 km spatial resolution using a classification tree approach. *Int J Remote Sens* 21(6–7):1331–1364
- Huete A, Didan K, Miura T, Rodriguez EP, Gao X, Ferreira LG (2002) Overview of radiometric and biophysical performance of the MODIS vegetation indices. *Remote Sens Environ* 83(1–2):195–213
- Lotsch A, Tian Y, Friedl MA, Myneni RB (2001) Land cover mapping in support of LAI/FAPAR retrievals from EOS MODIS and MISR: classification methods and sensitivities to errors. *Int J Remote Sens* 24(10):1997–2016
- Loveland TR, Belward AS (1997) The IGBP-DIS global 1-km land cover dataset, DIScover: first results. *Int J Remote Sens* 65(9):1021–1031
- Loveland TR, Reed BC, Brown JF, Ohlen DO, Zhu Z, Yang L, Merchant JW (2000) Development of a global land cover characteristics database and IGBP DIScover from 1 km AVHRR data. *Int J Remote Sens* 21(6–7):1303–1365
- Lubchenco J (1998) Entering the Century of the Environment: a new social contract for science. *Science* 279:491–497
- Lucht W, Prentice IC, Myneni RB, Sitch S, Friedlingstein P, Cramer W, Bousquet P, Buermann W, Smith B (2002) Climatic control of the high-latitude vegetation greening trend and Pinatubo effect. *Science* 296(5573):1687–1689
- Matthews E (1983) Global vegetation and land-use: new-high resolution data bases for climate studies. *J Clim Appl Meteorol* 22:474–487
- McIver DK, Friedl MA (2001) Estimating pixel-scale land cover classification confidence using non-parametric machine learning methods. *IEEE Trans Geosci Remote Sens* 39(9):1959–1968
- McIver DK, Friedl MA (2002) Using prior probabilities in decision tree classification of remotely sensed data. *Remote Sens Environ* 81:253–261
- Mingers J (1989) An empirical comparison of pruning methods for decision tree induction. *Mach Learn* 4:227–243
- Muchoney D, Strahler A, Hodges J, LoCastro J (1999) The IGBP DIScover confidence sites and the system for terrestrial ecosystem parameterization: tools for validating global land-cover data. *Photogramm Eng Remote Sensing* 65(9):1061–1067
- Myneni RB, Nemani RR, Running SW (1997) Estimation of global leaf area index and absorbed par using radiative transfer models. *IEEE Trans Geosci Remote Sens* 35(6):1380–1393

- Olson JS, Watts J (1982) Major world ecosystem complexes. In: Jones DB (ed) *Earth's vegetation and atmospheric carbon dioxide, carbon dioxide review*. Oxford University Press, Oxford, pp 388–399
- Parmesan C, Yohe G (2003) A globally coherent fingerprint of climate change impacts across natural systems. *Nature* 421:37–42
- Quinlan JR (1993) C4.5: Programs for Machine Learning. Morgan Kaufmann, San Mateo, CA
- Ramankutty N, Foley JA (1998) Characterizing patterns of global land use: an analysis of global crop yield data. *Global Biogeochem Cycles* 12(4):667–685
- Reed BC, Brown JF, VanderZee D, Loveland TR, Merchant JW, Ohlen DO (1994) Measuring phenological variability from satellite data. *J Veg Sci* 5:703–714
- Running SW, Hunt ER Jr (1993) Generalization of a forest ecosystem process model for other biomes, BIOME-BGC, an application for global scale models. In: Ehleringer JR, Field CB (eds) *Scaling physiological processes: leaf to globe*. Academic Press, San Diego, pp 141–158
- Running SW, Nemani RR (1991) Regional hydrologic and carbon balance response of forests resulting from potential climate change. *Clim Change* 19(4):349–368
- Running SW, Loveland TR, Pierce LL, Nemani R, Hunt ER Jr (1995) A remote sensing-based classification logic for global land cover analysis. *Remote Sens Environ* 51(1):39–48
- Sanderson EW, Malanding J, Levy MA, Redford KH, Wannebo AV, Woolmer G (2002) The human footprint and the last of the wild. *Bioscience* 52(10):891–904
- Schaaf CB, Gao F, Strahler AH, Lucht W, Li X, Tsang T, Strugnell N, Zhang X, Jin Y, Muller J-P, Lewis PE, Barnsley M, Hobson P, Disney M, Roberts G, Dunderdale M, d'Entremont RP, Hu B, Liang S, Privette J, Roy DP (2002) First operational BRDF, albedo and nadir reflectance products from MODIS. *Remote Sens Environ* 83:135–148
- Schowergerdt RA (1997) *Remote sensing models and methods for image processing*, 2nd edn. Academic Press, San Diego
- Sellers PJ, Dickinson RE, Randall DA, Betts AK, Hall FG, Berry JA, Collatz GJ, Denning AS, Mooney HA, Nobre CA, Sato N, Field CB, Henderson-Sellers A (1997) Modeling the exchanges of energy, water, and carbon between continents and the atmosphere. *Science* 275(5299):502–509
- Strahler A, Muchoney D, Borak J, Gao F, Friedl M, Gopal S, Hodges J, Lambin E, McIver D, Moody A, Schaaf C, Woodcock C (1999) MODIS Land Cover Product, Algorithm Theoretical Basis Document (ATBD), Version 5.0. Center for Remote Sensing, Department of Geography, Boston University, Boston, MA
- Vitousek PM, Mooney HA, Lubchenco J, Melillo JM (1997) Human domination of earth's ecosystems. *Science* 277:494–499
- Wan Z, Zhang Y, Zhang YQ, Li Z-L (2002) Validation of the land-surface temperature products retrieved from Moderate Resolution Imaging Spectroradiometer data. *Remote Sens Environ* 83:163–180
- White MA, Thornton PE, Running SW (1997) A continental phenology model for monitoring vegetation responses to interannual climatic variability. *Global Biogeochem Cycles* 11:217–234
- Wilson KB, Baldocchi DD (2000) Seasonal and interannual variability of energy fluxes over a broadleaved temperate deciduous forest in North America. *Agric For Meteorol* 100(1):1–18
- Wilson M, Henderson-Sellers A (1985) A global archive of land cover and soils data for use in general circulation climate models. *J Climatol* 5:119–143
- Zhang X, Friedl MA, Schaaf CB, Strahler AH, Hodges JCF, Gao F (2003) Monitoring vegetation phenology using MODIS. *Remote Sens Environ* 84:471–575
- Zhang X, Friedl MA, Schaaf CB, Strahler AH, Schneider A (2004a) The footprint of urban climates on vegetation phenology. *Geophys Res Lett* 31:L12209. doi:10.1029/2004GL020137
- Zhang X, Friedl MA, Schaaf CB, Strahler AH (2004b) Climate controls on vegetation phenological patterns in northern mid- and high latitudes inferred from MODIS data. *Global Chang Biol* 10:1133–1145

- Zhang X, Friedl MA, Schaaf CB, Strahler AH, Liu Z (2005) Monitoring the response of vegetation phenology to precipitation in Africa by coupling MODIS and TRMM instruments. *J Geophys Res – Atmospheres* 110:D12103
- Zhang X, Friedl MA, Schaaf CB (2006) Global vegetation phenology from MODIS: evaluation of global patterns and comparison with in-situ measurements. *J Geophys Res – Biogeosciences* 111:G04017. doi:10.1029/2006JG00217

Chapter 32

MODIS Vegetative Cover Conversion and Vegetation Continuous Fields

Mark Carroll, John Townshend, Matthew Hansen,
Charlene DiMiceli, Robert Sohlberg, and Karl Wurster

32.1 Introduction

Land cover change occurs at various spatial and temporal scales. For example, large-scale mechanical removal of forests for agro-industrial activities contrasts with the small-scale clearing of subsistence farmers. Such dynamics vary in spatial extent and rate of land conversion. Such changes are attributable to both natural and anthropogenic factors. For example, lightning- or human-ignited fires burn millions of acres of land surface each year. Further, land cover conversion requires contrasting with the land cover modification. In the first instance, the dynamic represents extensive categorical change between two land cover types. Land cover modification mechanisms such as selective logging and woody encroachment depict changes within a given land cover type rather than a conversion from one land cover type to another. This chapter describes the production of two standard MODIS land products used to document changes in global land cover. The Vegetative Cover Conversion (VCC) product is designed primarily to serve as a global alarm for areas where land cover change occurs rapidly (Zhan et al. 2000). The Vegetation Continuous Fields (VCF) product is designed to continuously represent ground cover as a proportion of basic vegetation traits. Terra's launch in December 1999 afforded a new opportunity to observe the entire Earth every 1.2 days at 250-m spatial resolution. The MODIS instrument's appropriate spatial and temporal resolutions provide the opportunity to substantially improve the characterization of the land surface and changes occurring thereupon (Townshend et al. 1991).

M. Carroll (✉)

Department of Geography, University of Maryland, College Park, MD 20742, USA
e-mail: markc@umd.edu

32.2 Pre-processing

Assembling a coherent global dataset is a prerequisite to generate a global data product. MODIS data are available in three spatial resolutions: 250 m, 500 m and 1 km (Barnes et al. 1998). Band 1 (red 620–670 nm) and band 2 [near-infrared (NIR), 841–876 nm] have a 250-m spatial resolution, and are also averaged to create 500-m resolution products. Bands 3–7 (459–479, 545–565, 1,230–1,250, 1,628–1,652, 2,105–2,155 nm, respectively) have a 500-m spatial resolution. These first seven bands are commonly referred as the ‘land bands’, and are designed primarily for remote sensing of the land surface.

Frequently, the best observations from several days are selected to produce a single output product. This helps optimize data and remove or minimize the inferior variety. This compositing process is carried out for a variety of satellite data products for several years (Holben 1986). The repeat cycle of nadir overpasses for the MODIS instrument is 16 days. Therefore, MODIS’ standard composite periods are multiples of 8 days, exactly the midpoint of the repeat cycle. Thus, MODIS composite products are generated for 8-, 16-, and 32-day periods. Longer compositing time-periods may allow the removal of undesired atmospheric effects, but are potentially disadvantageous in reducing sensitivity to phenological variation.

When MODIS production first began, the 250-m data were produced only for 10% of the global land tiles. They became available globally in the third year of MODIS operations. But it was the fourth year’s end before the entire 250-m global data were processed, which also marked the Collection-4 reprocessing completion. Therefore, all efforts were initially spent in two areas: (1) to develop a global 500-m composite and (2) to build compositing methods to work with the global 250-m data when available.

32.2.1 250-m Composite

The 250-m compositing algorithm (MOD44C) uses the daily surface reflectance product (MOD09) band 1 and 2 at 250-m resolution along with the data quality flags to decide which observations to retain. The MOD44C compositing algorithm rules are described in Table 32.1. The general concept is to choose the most cloud-free observation, which is closest to nadir, and therefore has the highest spatial resolution possible to represent the compositing period. Quality flags in the L2G data are used to eliminate pixels contaminated by clouds, high aerosol concentration, or cloud shadows. Subsequently, the pixel with the lowest sensor zenith angle and highest overlap with the MODIS grid cell is chosen. The “value” in Table 32.1, column 2 refers to the value of the quality flags from the L2G data. A description of the quality flags and their values associated with a given phenomenon is available in the MODIS Surface Reflectance Product’s User Guide (Vermote and Ray 1999). The Normalized Difference Vegetation

Table 32.1 MOD44C compositing rules

| Rule | Value |
|----------------------------------------------------------------------------------------------------------------------------|-------------------------|
| Exclude observations with negative reflectance values | <0 |
| Exclude cloudy observations | 1,2 |
| Exclude observations with cloud shadow | 1 |
| Exclude observations with high solar zenith angle | >85° |
| Exclude observations with highest aerosol correction | 3 |
| Choose observations with low sensor zenith angle | <45° |
| Choose observations with high observation coverage | >25% |
| Choose observations with lowest aerosol correction | 1 |
| Calculate NDVI for all remaining observations. Rank observations from high to low NDVI. Exclude observations with low NDVI | >10% below the max NDVI |
| Choose observations with lowest cirrus clouds detected | 1 |
| Choose observation with the lowest sensor zenith angle | Minimum |

Index (NDVI) is next calculated for the selected pixels. From this pool of pixels, the single pixel with the least contamination from cirrus and aerosol is chosen to represent the given 16-day period. The quality flags for the chosen pixel are retained in a separate layer for use by later processes.

The selected 250-m pixels are used to identify the corresponding observations from bands 3–7, and then used to populate a 250-m data plane. We accomplish this using daily level-2 gridded (L2G) observation pointer files, which store the addresses of the L2 observations that intersect each L2G grid cell. This process enables populating the coarser 500-m observations in the finer resolution 250-m grid output. The resulting enhanced data layers are then available as input for other algorithms such as the VCC and VCF.

32.2.2 500-m Composite

The standard MODIS surface reflectance 8-day composites were used to generate the global 500-m dataset. Four of these 8-day products were combined to produce a cloud-free 32-day composite. The 8-day product (MOD09A1) uses spectral values from the visible bands and the quality flags, and is available from the LP DAAC (Land Processes Distributed Active Archive Center). Details of the MOD09A1 compositing method are described elsewhere (Desloîtres and Vermote 1999) (<http://modis.gsfc.nasa.gov/mod09>).

Several methods to combine these 8-day products into a 32-day product were tested before finally settling on the ranked brightness approach (RBA). The 4-candidate 8-day composite inputs are ranked using a visible brightness measure, and the second darkest value is chosen for the 32-day composite value. Other approaches tested include maximum NDVI and minimum blue reflectance. The former was biased toward the selection of bright objects and the latter toward dark

objects, whereas the RBA showed no noticeable bias to either. Each pixel's brightness was estimated by generating the sum of the reflectance values of the visible bands from the four 8-day MOD09A1 products. This dataset was used to generate the MODIS VCF product (MOD44B) in the absence of a global 250-m dataset for earlier collections.

32.2.3 Future Production

The 250-m data product is spatially and temporally stable and consistent following the fourth MODIS reprocessing (Collection 5). Therefore, avoiding redundancy, Collection 5 provides a single stream 16-day 250-m composite as input to produce the VCC and VCF products. This eliminates the need to generate the 32-day composite described in Sect. 32.2.2.

32.3 Vegetation Continuous Fields

32.3.1 Introduction

The MODIS VCF product provides sub-pixel vegetative cover estimates for the entire globe. VCF describes vegetation characteristics by the proportion of each pixel occupied by a particular property such as tree canopy cover. These types of maps offer many advantages over categorical depictions of the land surface. Continuously varying land cover maps provide improved spatial detail than do discrete classifications. Ecotones and areas undergoing disturbance are more accurately mapped by sub-pixel characterizations that fully exploit the inherent variability found in images. This greater thematic detail enables a better ability to parameterize modeling efforts (DeFries et al. 1995). Continuous cover maps, unlike classifications, are useful to consecutively identify areas experiencing change. They also allow users to define their own thresholds for land cover classes. This avoids the common problem of having a classification scheme forced onto users, without the flexibility to redefine or translate thematic meanings. A significant obstacle in implementing VCF mapping is the need for precise training data at the sub-pixel scale. Also, instead of capturing all thematic content in a single map layer, continuous depictions of sub-pixel cover require data layers for each cover trait of interest. For the VCF standard product, areal proportions of tree cover, herbaceous cover, and bare ground are generated. The MODIS VCF product is available to download through the LP DAAC (<http://edcdaac.usgs.gov>) and through the Global Land Cover Facility at the University of Maryland (<http://glcf.umiacs.umd.edu>).

32.3.2 *Methods*

The VCF products are generated from 32-day composites of Terra/MODIS data at 500-m spatial resolution. These composites are made using the RBA method described in Sect. 32.2. MODIS bands 1–7, derived NDVI and Land Surface Temperature (MOD10), are used as inputs to the VCF algorithm. The MODIS VCF product offers greater mapping accuracy compared to earlier AVHRR (Advanced Very High Resolution Radiometer)-derived versions due to its higher spatial resolution, improved choice of spectral bands with reduced atmospheric effects, and higher radiometric resolution. This produces improved spectral signatures for mapping vegetation cover features.

The MODIS VCF product is generated by an automated procedure, which employs a regression tree algorithm (Hansen et al. 2002a; Venables and Ripley 1994). A regression tree is a non-linear, distribution-free model well-suited to handle the complexities of global land cover spectral signatures. The dependent variable in the algorithm is percent cover, where cover is defined as the amount of skylight orthogonal to the surface that is intercepted by the cover trait of interest. The cover traits are defined in the training data, which include tree, herbaceous or bare ground cover. High-resolution Landsat images are used to develop the percent cover training data. Each high-resolution scene's pixels are classified into dominant cover classes, such as grasslands, woodlands, and forests. Each dominant cover class is assigned a mean cover value and then resampled via averaging to MODIS scales.

The independent variables in the procedure are annual multi-temporal metrics derived from the series of monthly MODIS RBA composites. Metrics are time-integrated means, amplitudes, and ranks of annual composite images that represent salient features of vegetation phenology. The metrics chosen are appropriate for mapping global land cover, as they are independent of the specific timing of vegetation dynamics. They are designed to work generically at the continental and global scale by capturing the phenological traits that are shared by similar land cover types irrespective of specific time of year. The percent cover training data and annual metrics are input to the regression tree to create the global models. The regression outputs are further modified by a stepwise regression and bias adjustment. This derivation of proportional cover allows use of successive products to estimate land cover change. A similar approach was used to detect change based on the long-term AVHRR 8-km Pathfinder dataset by Hansen and DeFries (2004).

The regression tree is generated for each of the three ground cover components: tree canopy cover, herbaceous cover, and bare ground. For the VCF tree cover map, percent tree canopy cover refers to the amount of skylight orthogonal to the surface that is obstructed by tree canopies equal to or greater than 5 m in height, and is different than percent crown cover, which includes both the canopy cover and the within-crown skylight (Hansen et al. 2003). The canopy cover definition is used in vegetation modeling exercises where light availability is an important parameter. Foresters, on the other hand, largely use crown cover to measure forest

density. Crown cover is a better measure when performing aerial surveys, and is used in many forest accounting procedures. Herbaceous cover includes all vegetation less than 5 m in height, and bare ground includes bare soil, rocks, and permanent snow and ice. The 2000 VCF map is shown in Fig. 32.1a. The VCF layers do not account for sub-pixel heterogeneity or fragmentation. For example, a MODIS grid cell covered by 50% dense forest canopy cover and 50% herbaceous cover (a

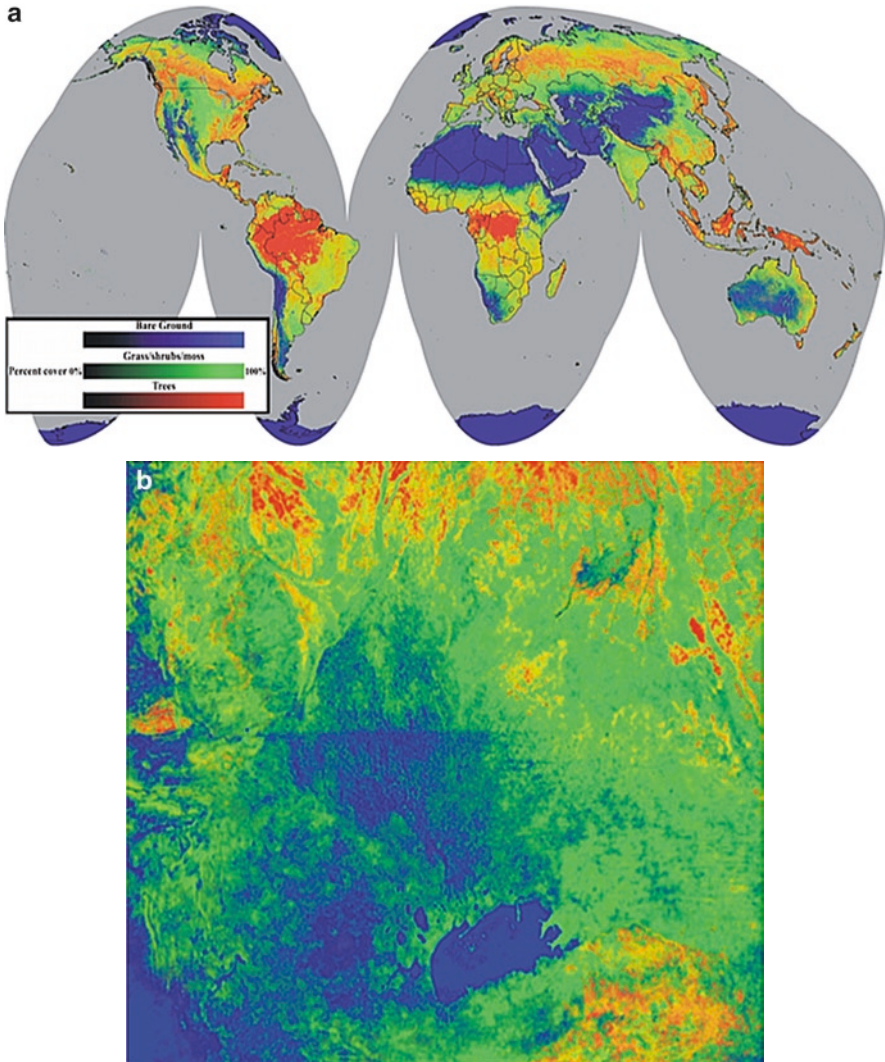


Fig. 32.1 (a) Vegetation Continuous Fields global view of percent cover as a fraction of trees, herbaceous, and bare components. (b) Full resolution view of the border between Namibia and Angola; note the clear line where the bare component (*seen in blue*) begins to dominate is also the administrative boundary

fragmented forest) is not distinguished from a grid cell that consists of 50% woodland canopy cover and 50% herbaceous cover pixel (homogeneous, unfragmented woodland).

32.3.3 Results

VCF maps have substantially increased spatial detail compared to similar previous maps derived from the AVHRR (DeFries et al. 1999). The human imprint on the landscape is more clearly seen in many regions of the world. Discrete breaks in tree cover due to administrative status, such as national parks, government-owned lands, and trans-national variations in land use intensity are clearly evident throughout VCF maps.

The VCF global map is updated annually for all three components. Interannual comparison of the VCF products may potentially mislead, because many changes are merely the consequence of the changing frequency and distribution of clouds and other factors, which obscure the land surface. This leads to isolated errors, which are perhaps beyond the mean validation accuracy. Consequently, simple VCF difference images to synoptically document change are not currently recommended. However, annual product comparisons do reveal real changes in vegetative cover for many regions. For example, changes due to agricultural expansion in the Mato Grosso, Brazil are clearly seen (Fig. 32.1b). Currently, 5-year VCF change products are being created for various regions of the world.

Additionally, on a 5-year time interval, VCF maps are planned for tree-leaf longevity and morphology. More frequent production is unnecessary because of the high degree of inter-annual stability of these properties. These four components are part of the comprehensive depiction of the tree cover component.

32.3.4 Validation

A multi-resolution mapping approach in conjunction with field data was applied at a number of sites to develop validation data for the percent tree cover map. The exercise includes using field data along with IKONOS and Enhanced Thematic Mapper Plus (ETM+) data to create ETM+ image-sized validation test areas. Performing this exercise in a wide variety of biomes helps create a test bed against which successive iterations of the tree cover product are validated. This method was tested for a Western Province, Zambia woodland site (Hansen et al. 2002b), a coniferous forest area in Colorado, USA and a mixed urban environment in Montgomery County, USA. Validation work continues at several other locations across the globe.

Validation results for the VCF tree cover map layer indicate an overall standard error of 11.5% tree crown cover, as shown in Table 32.2. This table compares both training and validation data errors for dominant tree cover strata. The results show

Table 32.2 Standard errors of the estimate for VCF percent tree canopy cover strata for completed validation test areas

| Percent canopy cover | ≤10% | 11–40% | 41–60% | >60% | Overall |
|-----------------------|------|--------|--------|------|---------|
| Training data | 10.3 | 17.6 | 18.3 | 14.5 | 15.6 |
| Validation test areas | 8.1 | 13.1 | 13.8 | 11.9 | 11.5 |

that the training accuracies, or the ability of the VCF algorithm to reproduce the global percent tree cover training data, have higher standard errors than the validation accuracies. The training data are derived at the global scale using disparate ancillary sources. The regression tree algorithm and pruning methods (Hansen et al. 2002a) overcome the apparent noise in the training data to yield mean tree cover estimates per pixel that relate well to the validation data. The validation data are derived through standard protocols that include in situ canopy cover measurements to calibrate the scaling of IKONOS and Landsat-scale data to MODIS spatial resolutions (Hansen et al. 2002b). Errors are relatively low in the extreme ends of low and high canopy cover, with higher standard errors in mid-range canopy cover conditions.

Hansen et al. (2002a; 2003) provide a full description of the MODIS VCF tree cover approach.

32.4 Vegetative Cover Conversion

32.4.1 Introduction

The VCC product was conceived to address the need for global information on changing land cover and land use over time. The 250-m spatial resolution is finer than previously available global datasets, and is better suited to observe more subtle changes in land cover (Townshend et al. 1991). A global alarm product allows targeting of resources, and hence, a better use of finer resolution data in areas where cover change is detected. The quarterly repeat cycle of the alarm product provides a better temporal coverage for resource managers in conservation areas, and in areas with limited resources to find and track change events. The temporal period of change products with fine resolution are usually annual or longer. The VCC alarm product's shorter time horizon allows earlier investigation to determine extent of change.

The VCC method has evolved over time. The original method used five different change detection methods from amongst whose results, a voting system was used to yield a single end-result (Zhan et al. 2002). In addition, the algorithm determined different types of change simultaneously as the data were processed.

In contrast, the current method uses separate techniques to determine deforestation, and forest change due to burning (CDB) and flooding. The differences in

approach are necessitated by the very different space–time characteristics of the changes. For example, extensive flooding typically only lasts for days to weeks, whereas other types of change signals persist for months to years.

The deforestation method is derived from the original space partitioning method (Zhan et al. 2002) and relies on decision tree classification (Breiman et al. 1984) to determine antecedent vegetation condition, which is compared to current vegetation condition. CDB is derived using the normalized burn ratio (NBR), defined as the ratio of near infrared to short wave infrared (van Wagtenonk et al. 2004) from two scenes from alternate years. Flooding is determined similar to deforestation with a decision tree classification to decide where water exists in any given scene, which is then compared to a static water extent map to determine areas that are possibly inundated.

32.4.2 Deforestation

32.4.2.1 Method

Decision trees are derived using a training dataset that relates spectral characteristics to land cover. The decision tree is only as good as the training data used to generate it, so special care is required to ensure the training data are of high quality. For the deforestation method, MODIS data from two different years are classified using the decision tree and then compared to identify changes. Spectral samples from the two MODIS study year’s data are used to generate the training dataset. To minimize potential impacts of spatially variable phenology, the study region (30°N to 30°S) was stratified by month and latitude. Three strata were created: 10°–30°S; 10°N–10°S; 10°–30°N. For each month and stratum, a spectral sample is taken from the input data using the MODIS VCF product to identify classes based on percent tree cover. Two sets of forest cover classes were derived from the VCF product and are shown in Table 32.3. A change dynamic is defined by the

Table 32.3 VCC deforestation class schemes

| | Percent tree cover |
|----------|--------------------|
| Scheme 1 | |
| Class 1 | 0–19 |
| Class 2 | 20–39 |
| Class 3 | 40–59 |
| Class 4 | 60–100 |
| Scheme 2 | |
| Class 1 | 0–18 |
| Class 2 | 19–36 |
| Class 3 | 37–54 |
| Class 4 | 55–72 |
| Class 5 | 73–100 |

Table 32.4 Comparison schemes for VCC deforestation

| |
|-----------------------------------------|
| Year 1 Time 1 compared to Year 2 Time 1 |
| Year 1 Time 2 compared to Year 2 Time 2 |
| Year 1 Time 3 compared to Year 2 Time 3 |
| Year 1 Time 4 compared to Year 2 Time 4 |
| Year 1 Time 5 compared to Year 2 Time 5 |
| Year 1 Time 6 compared to Year 2 Time 6 |

modification from a forest to a non-forest class, where a forest is defined to constitute at least 37% tree canopy cover.

A land/water mask is used to identify an additional water class; this helps limit some confusion in the classifier between water and certain types of forest. A random sample of 20,000 observations per class is then chosen using the data quality flags (Roy et al. 2002) to avoid cloudy observations. This data sample serves as the training dataset, and is used to generate a decision tree. This process is repeated for each month and each stratum to yield 72 decision trees, which are used by the VCC algorithm.

The input data (250-m 16-day surface reflectance composites) are processed on a quarterly basis yielding four data products per year. In each quarter there are six 16-day composites except the fourth quarter, which contains only five 16-day composites. Based on date and location, the algorithm chooses the most appropriate decision tree to classify each image. Each of the input datasets in the quarter is classified under both classification schemes (Table 32.3). Poor quality input data affected by clouds, high view zenith angle, or heavy aerosols are not processed, and a fill value is assigned in the classification. The classifications for the first and second year are then compared as described in Table 32.4.

Each of the above comparisons is determined to have changed in the following manner:

- Scheme 1
 - Observation changed from class 4 to class 2 or 1
 - Observation changed from class 3 to class 1
- Scheme 2
 - Observation changed from class 5 to class 3, 2 or 1
 - Observation changed from class 4 to class 2 or 1
 - Observation changed from class 3 to class 1

Representation in this layer requires change documentation in either scheme in at least two of the six time periods in the quarter. By using both schemes together, up to 30% more actual changes were detected without any substantial increase in errors of commission.

32.4.2.2 Results

The VCC deforestation algorithm was run globally for the humid tropics (between 30°N and 30°S) for the data year 2001–2002. We plan to apply this algorithm to regions outside this range, and for additional years. These results reflect a change in vegetation cover from forest to non-forest for the South American continent north of 30°S latitude. Forest, in this case, is defined as having at least 37% tree canopy cover. This constitutes the lowest percentage of tree cover where change to non-forest is recognizable (Table 32.3). Table 32.5 shows a summary of these results on a per-country basis. Per-pixel data quality assessment is available, and is based on the input data quality.

Figure 32.2a depicts the area of South America that was analyzed, and illustrates how the change observations are distributed north of 30°S. The results show that the vast majority of large-scale deforestation occurring on the South American continent is concentrated in Brazil, Paraguay, and Bolivia. Over 53% of the change observations detected by VCC in all of Brazil were concentrated in Mato Grosso state. In Bolivia, over 80% of all VCC change observations occurred in Santa Cruz state, and in Paraguay, similar observations were concentrated in Alto Paraguay and Chaco states. Using Landsat data, Skole and Tucker (1993) and Steininger et al. (2001) identified these areas to suffer from significant deforestation. Figure 32.2b shows a portion of Mato Grosso state in Brazil, which experienced a significant amount of deforestation.

32.4.2.3 Validation

The 2002 PRODES (*Projeto Desflorestamento*) digital data provide Amazonian deforestation estimates, which are used in the validation. The Instituto Nacional de

Table 32.5 Change observations per country

| Country | Number of change detection observations |
|------------------------|-----------------------------------------|
| Argentina ^a | 8,043 |
| Belize | 127 |
| Bolivia | 10,243 |
| Brazil | 92,073 |
| Chile ^a | 2 |
| Colombia | 249 |
| Ecuador | 6 |
| French Guiana | 15 |
| Guyana | 9 |
| Paraguay | 9,767 |
| Peru | 413 |
| Venezuela | 560 |
| Summary | 121,507 |

^aOnly areas above 30°S latitude in these countries were included

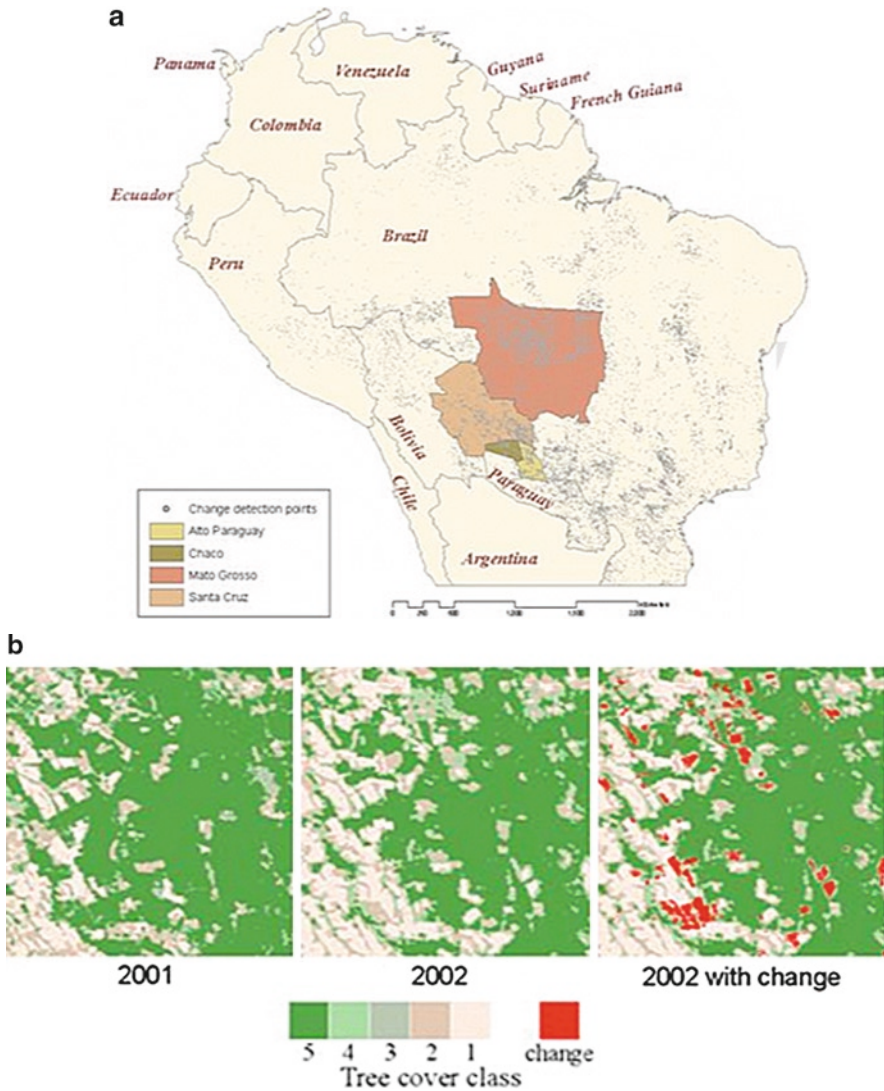


Fig. 32.2 (a) The distribution of change observations detected by VCC in South America in 2002. (b) A visualization of the VCC deforestation result where dense forest is *dark green*; light or no forest is *light tan*, and change is shown in *red*. The image on the *left* is from early 2001, the *center* one is from 2002, and on the *right* is the 2002 image with VCC deforestation result shown in *red*. (c) A visualization of the VCC changes due to burning; change is depicted in *red*, forest is *light green*, and non-forest is *light tan*

Pesquisas Espaciais (INPE) analyzes more than 220 Landsat TM scenes each year to provide annual high-resolution deforestation maps as part of the PRODES (Brazilian Amazonian Forest Monitoring by Satellite) project. The analysis is performed with the most cloud-free scene from the current year's dry season

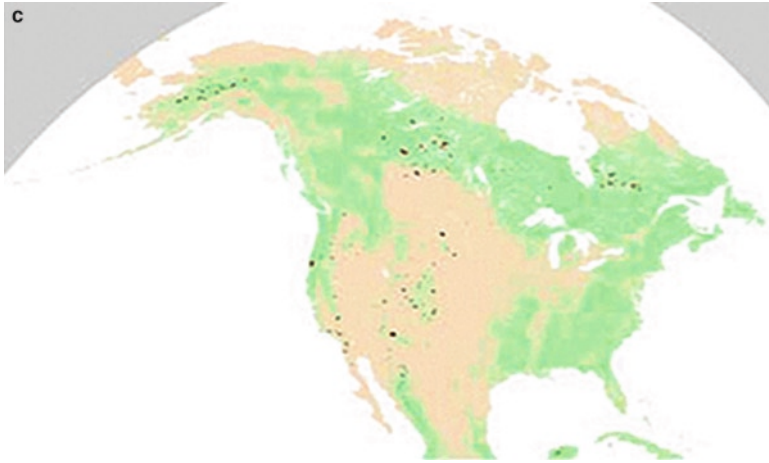


Fig. 32.2 (continued)

(June–August) to derive a forest cover mask. This mask is then compared to the previous year’s forest cover mask, derived from the most cloud-free scene from that year’s dry season.

The VCC method was designed as an alert system and is not expected to fully detect changes with Landsat data at 30 m, or accurately estimate the change area. Therefore, PRODES observations that were less than one 250-m MODIS pixel in size (5.36 ha) were not included in the validation. The Landsat scene (WRS-2 path 226 and row 68) from the Brazilian Mato Grosso state was used in this validation. The PRODES results for this scene represent changes that occurred between June 29, 2001 and August 11, 2002.

Table 32.6 shows the size distribution of PRODES deforestation polygons for the study area in 2002. This table shows that nearly 96% of the total area of deforestation identified by the PRODES data occurs in areas greater than 1 MODIS pixel, and they form 54% of all changes identified by PRODES. If we exclude all observations with an area smaller than 1 MODIS pixel, only around 4% of the deforested area was undetected even though this amounts to over 45% of the total change identified by PRODES. The observations that remain are considered “detectable” PRODES deforestation polygons.

As part of this analysis, the VCC deforestation product was rerun with data deemed closely similar to the Landsat acquisition times used in the PRODES analysis. Five 16-day composites were used with a start date of June 26 and an end date of September 13. This allowed one full composite period after the PRODES 2002 Landsat scene to ensure that any activity that occurred leading up to the August 11th Landsat scene was captured in the composite.

The results comparing the “detectable” PRODES deforestation polygons and the VCC results reveal that as the size of the deforested area increases, the algorithm identifies a greater proportion of the locations correctly. VCC correctly identifies

Table 32.6 Size distribution of PRODES deforestation polygons with respect to a MODIS pixel

| Size of polygons | No. of PRODES polygons | % of total PRODES polygons | Area of PRODES polygons (ha) | % of total area detected |
|----------------------------------------------|------------------------|----------------------------|------------------------------|--------------------------|
| <1 MODIS pixel (<5.36 ha) | 214 | 45.53 | 1,583,144 | 4.26 |
| 1–4 MODIS pixels (5.36–21.44 ha) | 45 | 9.57 | 608,130 | 1.64 |
| 4–8 MODIS pixels (21.44–48.24 ha) | 62 | 13.19 | 2,039,985 | 5.49 |
| >8 MODIS pixels (>48.24 ha) | 149 | 31.70 | 32,941,737 | 88.62 |
| Total of PRODES deforestation | 470 | | 37,172,996 | |
| Total of PRODES deforestation >1 MODIS pixel | 256 | 54.47 | 35,589,852 | 95.74 |

Table 32.7 Distribution of PRODES polygons for scene from path 226 row 68

| | Number | % of polygons |
|------------------------------------------------|--------|---------------|
| Number of polygons w/in 2001 forest mask | 250 | |
| Location of MODIS polygons w/respect to PRODES | | |
| Forested | 6 | 2.40% |
| Deforested in 2002 | 228 | 91.20% |
| Previously deforested | 16 | 6.40% |

62% of all deforestation activity for moderately-sized change areas (> 48 ha). This accounts for 93% of the total area identified by PRODES. VCC correctly identifies only 20% of change for small-sized areas (5–48 ha). However, this represents only 7% of the total change area detected in the PRODES results.

Even though many smaller areas are not identified because of the MODIS pixel size, areas with the most change are correctly labeled for 75% of the deforested area. Table 32.7 shows that MODIS is correct 91% of the time when it identifies change. This translates to a 9% commission error and a 38% omission error for moderate to large-sized change areas (for the 2002 scene 226/68).

32.4.3 Change Due to Burning

32.4.3.1 Method

Burning impacts vegetation in several ways; sufficiently intense burning may convert wooded areas to non-wooded areas at least in the medium term. Fires in grasslands and agricultural areas generally do not cause long-term changes in land

cover or land use, and are not flagged in this product. To identify land cover change in forests, we require knowledge of both the distribution of forests, and a measure of the change intensity. This product uses the MODIS VCF to determine forest distribution, and a NBR algorithm to derive change intensity. The algorithm uses a set of rules described below.

The NBR was previously used to calculate burn extent and severity with Landsat TM and ETM+ data (van Wagtenonk et al. 2004). NBR is calculated thus: $(\text{Near Infrared} - \text{Short Wave Infrared}) / (\text{Near Infrared} + \text{Short Wave Infrared})$. Calculations of both the NBR (with time-series data) and the difference NBR (dNBR) enable us to locate areas of fire occurrence.

The dNBR is initially calculated (with 1-year-apart composites) only for original seed locations, where fires were recorded in the MODIS active fire location points (NASA/University of Maryland 2002), and the dNBR threshold value is greater than 0.2. This threshold was derived by trial and error using a test dataset from the conterminous United States for the 2002–2004 calendar years. The 0.2 threshold is somewhat conservative compared to other studies based on a 0.1 dNBR threshold (van Wagtenonk et al. 2004), which however produced too many false positives with MODIS data. The active fire locations are pre-screened to select only those within or immediately adjacent to a wooded area. Forested areas are determined using the percent tree cover layer from VCF with a threshold of 15% tree cover. This low VCF percent tree cover threshold was used to aggressively represent “forested area.”

To compare two time periods, the observations with dNBR threshold values greater than the 0.2, which fall within a “forested area” and are within an active fire location polygon are considered burns, and function as “burned seed pixels.” These areas are allowed to grow through an iterative process of extending to adjacent pixels with dNBR values higher than the 0.2 threshold. In the first iteration, all pixels adjacent to the “burned seed pixels” are evaluated, and ones with dNBR values greater than the threshold are added to the “seed” to form a new larger burn feature. In the second iteration, the result from the first one is used as the “seed,” and again, all adjacent pixels are evaluated, and those that meet the dNBR threshold are flagged and added to the result.

The number of iterations varies based on initial fire size as determined by the number of active MODIS fire location points. The MODIS active fire location product’s 1-km pixels were used to calculate fires smaller than 1,500 acres, which were ignored. Three fire sizes were identified, and different numbers of iterations were used with each.

- Small fires: 6–18 fire location points (5 iterations)
- Medium fires: 19–62 fire location points (20 iterations)
- Large fires: >62 fire location points (40 iterations).

Exercising a large number of iterations on smaller fires often results in an inaccurate dispersion of the changed area. Processing occurs on a per-fire basis and a composite is selected, which is closest to the fire start time, as determined by the MODIS active fire location points (NASA/University of Maryland 2002). Results from individual composite comparisons are then summarized for the year to yield one product per year.

32.4.3.2 Results

The CDB algorithm was run for North America, Eurasia, and Africa for 2001 through 2004. Future plans include this algorithm's global implementation as processing resources become available, and validation confirms the result's consistency and reliability. The US Forest Service provides a validation dataset to evaluate the North American results presented here. Burned areas are labeled as "changed" if they occurred inside the "wooded area" mask. Figure 32.2c shows synoptic results for each year with changed areas in red. Major concentrations of burns are evident in the western conterminous states, and in Alaska.

32.4.3.3 Validation

The 2003 CDB results for the conterminous US were compared with all available burn intensity polygons from the Burned Area Emergency Rehabilitation (BAER) team within the USDA Forest Service for 2003 (USDA 2006). Table 32.8 shows a comparison of the CDB to the BAER polygons and suggests that CDB represents 100% of the burn occurrences identified by the BAER team. In addition, it shows that the CDB captures ~79% of the total area represented in the BAER polygons. Three fires occurred prior to the dates of composites used in the CDB product. The area affected by these fires is significantly underestimated, but the results would likely improve if the CDB were re-run with image dates corresponding more accurately to their occurrence. CDB frequently labels areas immediately outside of the BAER polygons, which are adjacent to the burned areas. This is likely due to the larger MODIS pixel size as compared to Landsat's 30-m resolution, which captures adjacent pixels, and possibly related to how the BAER polygons are created. This work requires completion within 7 days of fire containment. To do so, they often use Landsat images from before the time the fire was contained. Therefore, some late-runs and breakthroughs are possibly omitted from their final product, but are represented in the MODIS product, which has no such restriction.

32.4.4 Flooding

32.4.4.1 Method

A single decision tree is trained with a global spectral sample of MODIS data to address flooding. The decision tree classifier for water is applied to daily data during the compositing process. The results of this classification are water, no water, or undetermined. Water and land occurrences are recorded in separate data layers in the 16-day composite product. These layers are later compared to a static water mask to determine if water was recorded in areas outside of known water bodies. These areas are then flagged as potential flooded areas. This algorithm requires

Table 32.8 Results of MODIS CDB compared to BAER polygons

| Fire name | Total BAER acres | Total area VCC | VCC acres within BAER polygon | VCC acres outside BAER polygon | % of BAER polygon area covered by VCC polygon |
|--------------------------|------------------|----------------|-------------------------------|--------------------------------|-----------------------------------------------|
| Oct 24 Complex #9 | 109,502 | 76,155 | 60,971 | 15,184 | 55.68 |
| BNB | 91,268 | 104,309 | 80,749 | 23,560 | 88.47 |
| Aspen | 81,981 | 81,591 | 69,614 | 11,977 | 84.91 |
| Fawn Peak | 72,611 | 93,823 | 71,213 | 22,609 | 98.08 |
| Oct 24 Complex #3 | 59,889 | 12,781 | 11,727 | 1,054 | 19.58 |
| Snow | 38,069 | 41,359 | 35,161 | 6,198 | 92.36 |
| Little Salmon Complex #2 | 30,815 | 40,035 | 25,044 | 14,991 | 81.27 |
| Little Salmon Complex #4 | 30,765 | 33,792 | 24,066 | 9,725 | 78.23 |
| Fish Creek | 29,890 | 43,274 | 27,738 | 15,536 | 92.80 |
| Hot #6 | 29,804 | 29,143 | 25,551 | 3,592 | 85.73 |
| Wedge | 27,268 | 51,753 | 25,575 | 26,178 | 93.79 |
| Cooney Ridge | 26,362 | 29,081 | 23,102 | 5,979 | 87.63 |
| Lower Mineral Primm | 19,953 | 27,645 | 19,028 | 8,617 | 95.37 |
| Robert | 19,801 | 53,437 | 19,068 | 34,369 | 96.30 |
| Red Point | 19,226 | 11,830 | 11,697 | 133 | 60.84 |
| Picture | 15,428 | 11,707 | 11,484 | 223 | 74.44 |
| Oct 24 Complex #2 | 13,845 | 14,313 | 9,237 | 5,075 | 66.72 |
| Beaver | 13,176 | 16,649 | 10,778 | 5,870 | 81.80 |
| Slims | 12,197 | 9,807 | 8,904 | 903 | 73.00 |
| Sapp | 11,551 | 15,357 | 10,111 | 5,246 | 87.54 |
| Little Salmon Complex #1 | 11,286 | 12,402 | 9,626 | 2,776 | 85.29 |
| Crazy Horse | 8,869 | 13,683 | 8,665 | 5,018 | 97.70 |
| Black Mountain | 7,950 | 8,649 | 7,115 | 1,534 | 89.49 |
| North Bighorn | 7,858 | 8,880 | 6,696 | 2,185 | 85.22 |
| Oct 24 Complex #4 | 6,708 | 5,328 | 4,809 | 519 | 71.69 |
| Spanish | 6,295 | 12,324 | 5,021 | 7,303 | 79.77 |
| Oct 24 Complex #1 | 6,077 | 2,363 | 1,904 | 459 | 31.32 |
| Oct 24 Complex #7 | 5,753 | 5,900 | 4,692 | 1,208 | 81.55 |
| Oct 24 Complex #10 | 5,688 | 5,869 | 4,409 | 1,460 | 77.52 |
| Lizard | 5,570 | 1,158 | 1,158 | 1 | 20.78 |
| Gold | 5,415 | 10,363 | 5,316 | 5,047 | 98.18 |
| Steeple | 4,930 | 4,571 | 3,702 | 870 | 75.09 |

(continued)

Table 32.8 (continued)

| Fire name | Total BAER acres | Total area VCC | VCC acres within BAER polygon | VCC acres outside BAER polygon | % of BAER polygon area covered by VCC polygon |
|---------------------|------------------|----------------|-------------------------------|--------------------------------|-----------------------------------------------|
| Walker | 4,836 | 1,961 | 1,777 | 184 | 36.75 |
| Togo Mountain | 4,770 | 10,548 | 4,125 | 6,423 | 86.48 |
| Gridstone | 4,728 | 6,795 | 4,135 | 2,660 | 87.47 |
| Complex #7 | | | | | |
| Oct 24 | 4,625 | 2,888 | 2,732 | 157 | 59.07 |
| Complex #6 | | | | | |
| Cherry Creek | 4,221 | 5,606 | 3,881 | 1,725 | 91.95 |
| Mud | 4,091 | 13,622 | 2,957 | 10,665 | 72.26 |
| Pleasant | 3,887 | 5,297 | 3,585 | 1,713 | 92.21 |
| Upper Mineral Primm | 3,878 | 6,378 | 3,725 | 2,654 | 96.06 |
| Little Salmon | 3,785 | 6,452 | 3,607 | 2,845 | 95.29 |
| Complex #6 | | | | | |
| East Table | 3,558 | 7,398 | 3,193 | 4,204 | 89.74 |
| Powell Fire | 3,533 | 4,587 | 3,082 | 1,505 | 87.24 |
| Complex #1 | | | | | |
| Mrytle Creek | 3,498 | 4,633 | 2,886 | 1,748 | 82.50 |
| Powell Fire | 3,445 | 4,819 | 3,021 | 1,797 | 87.70 |
| Complex #3 | | | | | |
| South Fork | 3,424 | 7,676 | 3,373 | 4,303 | 98.49 |
| Oct 24 | 3,379 | 3,398 | 2,464 | 934 | 72.91 |
| Complex #8 | | | | | |
| Fish Lake | 3,106 | 4,510 | 2,758 | 1,752 | 88.79 |
| Mormon | 2,743 | 525 | 504 | 21 | 18.37 |
| Burnt Ridge | 2,490 | 3,629 | 1,464 | 2,166 | 58.79 |
| Largo | 2,308 | 1,807 | 1,573 | 233 | 68.17 |
| Moose | 1,880 | 1,931 | 1,464 | 467 | 77.86 |
| Little Salmon | 1,777 | 7,629 | 1,677 | 5,952 | 94.37 |
| Complex #5 | | | | | |
| Gridstone | 1,528 | 1,514 | 465 | 1,049 | 30.43 |
| Complex #3 | | | | | |

information gathered from daily data during the compositing procedure. Therefore, a global implementation remains unavailable until the fourth reprocessing of MODIS data begins when the compositing algorithm is re-run globally to collect the necessary information. This product is useful for two purposes: to help disaster response teams deal with extensive moderate time-span flooding events, and to assess long-term trends in recurrent seasonal flooding.

32.4.4.2 Results

The algorithm was tested on a limited basis for areas affected by hurricanes in the US in 2005. Figure 32.3 shows the result of applying the VCC flood algorithm for

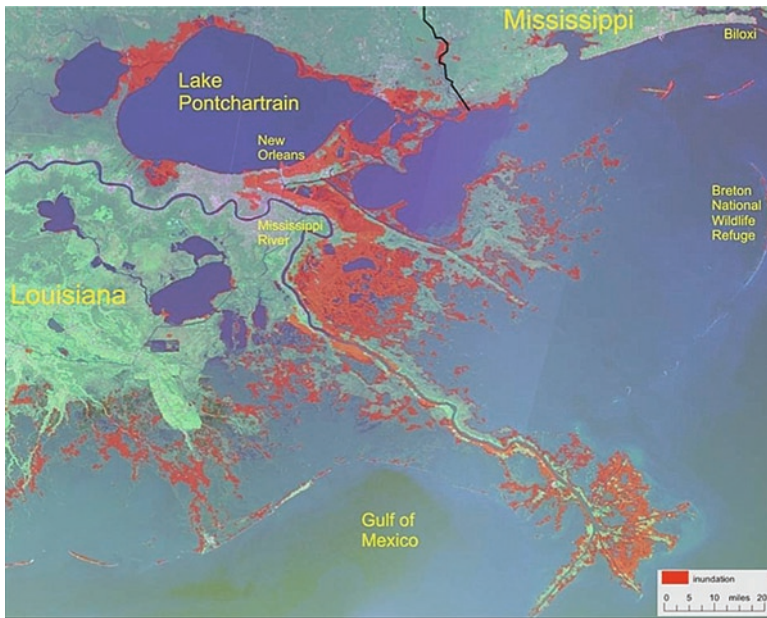


Fig. 32.3 MODIS characterized inundation from Hurricane Katrina in coastal Louisiana, September 2005. The background image is a mosaic of Landsat scenes; inundated areas are shown in *red*.

the area near New Orleans. This result was generated with daily MODIS data from August 27 to September 5, 2005 for the south-central United States. The flood algorithm was applied to the image from each day to identify water and land. Water observations were accumulated over the 10-day period and then compared to a static map of MODIS data-derived water from 2002 and 2003. Areas labeled “water” during the 10-day period in 2005, and not in the static water map were flagged as potentially inundated. The potential flood observations were investigated to ensure that they were not flagged erroneously. The resulting dataset was overlain with a mosaic of Landsat scenes from 2001 and 2002 to yield the image seen in Fig. 32.3. The resulting map shows areas that were inundated for at least 24 h after hurricane Katrina passed through the southern Louisiana and Mississippi region on August 25, 2005.

32.4.4.3 Validation

This product was generated as a time-sensitive product, and hence, no systematic validation was performed. However, anecdotal validation with available datasets from the Dartmouth Flood Observatory and the USGS suggest that the degree of flooding represented is consistent with what occurred on the ground. This provides a basis for future full-scale validation of the method.

32.5 Conclusion

The VCF and VCC products are available at the USGS LP DAAC and represent a comprehensive suite, which depict land cover and land cover change through the MODIS data record. MODIS continues to offer an expansive data record, whose inherent data qualities and limitations are better understood. This portends further advances in the products, especially with the completion of the Collection-5 record. The VCF product provides a proportional representation of land cover, which has been adopted by many in the modeling community to depict ground cover. The VCC product represents a cohesive global attempt to locate areas where forests are being reduced due to human and natural events. Development of new products is currently underway using the complete Collection-5 MODIS data record, and public release of new products is expected in late 2009.

References

- Barnes WL, Pagano TS, Salomonson VV (1998) Prelaunch characteristics of the Moderate Resolution Imaging Spectroradiometer (MODIS) on EOS-AM1. *IEEE Trans Geosci Remote Sens* 36:1088–1100
- Breiman L, Friedman JH, Olshen RA, Stone CJ (1984) *Classification and regression trees*. Chapman & Hall, New York.
- Descloitres J, Vermote E (1999) Operational retrieval of the spectral surface reflectance and vegetation index at global scale from SeaWiFS data. *International Conference on Aerosols, Radiation Budget – Land Surfaces – Ocean Colour: The Contribution of POLDER and New Generation Spaceborne Sensors to Global Change Studies, 18–22 January 1999, Meribel, France*. CNES, Toulouse, France, Land Surfaces-O-02, pp 1–4.
- DeFries R, Field CB, Fung I, Justice CO, Matson PA, Matthews M, Mooney HA, Potter CS, Prentice K, Sellers PJ, Townshend J, Tucker CJ, Ustin SL, Vitousek PM (1995) Mapping the land surface for global atmosphere-biosphere models: toward continuous distributions of vegetation's functional properties. *J Geophys Res* 100(20): 20, 867–820,882
- Defries RS, Hansen M, Townshend JRG, Janetos, A, Loveland T (1999) A new global 1km dataset of percent tree cover derived from remote sensing. *Glob Ecol Biogeogr* 8(5):367–379
- Hansen MC, DeFries RS, Townshend JRG, Sohlberg R, Carroll M, Dimiceli C (2002a) Towards an operational MODIS continuous field of percent tree cover algorithm: examples using AVHRR and MODIS data. *Remote Sens Environ* 83(1/2):303–319
- Hansen MC, DeFries RS, Townshend JRG, Marufu L, Sohlberg R (2002b) Development of a MODIS tree cover validation dataset for Western Province, Zambia. *Remote Sens Environ* 83:320–335
- Hansen MC, DeFries RS, Townshend JRG, Carroll M, Dimiceli C, Sohlberg RA (2003) Global percent tree cover at a spatial resolution of 500 meters: first results of the MODIS Vegetation Continuous Fields Algorithm, 7 (10), 15 p. [Available online at <http://EarthInteractions.org>].
- Hansen MC, DeFries RS (2004) Detecting long term global forest change using continuous fields of tree cover maps from 8km AVHRR data for the years 1982–1999. *Ecosystems* 7:695–722
- Holben BN (1986) Characteristics of maximum-value composite images for temporal AVHRR data. *Int J Remote Sens* 7:1435–1445
- NASA/University of Maryland (2002) MODIS Hotspot/Active Fire Detections. Dataset. MODIS Rapid Response Project, NASA/GSFC [producer], University of Maryland, Fire Information for Resource Management System [distributors]. [Available online at <http://maps.geog.umd.edu>]

- PRODES Digital (2002) <http://www.obt.inpe.br/prodes/> [last accessed June, 2003]
- Roy DP, Borak JS, Devadiga S, Wolfe RE, Zheng M, Desclotres J (2002) The MODIS land product quality assessment approach. *Remote Sens Environ* 83:62–76
- Skole D, Tucker C (1993) Tropical deforestation and habitat fragmentation in the Amazon: satellite data from 1978 to 1988. *Science* 260:1905–1910
- Steininger MK, Tucker CJ, Townshend JRG, Killeen TR, Desch A, Bell V, Ernst P (2001) Tropical deforestation in the Bolivian Amazon. *Environ Conserv* 28:127–134
- Townshend JRG, Justice CO, Li W, Gurney C, McManus J (1991) Global land cover classification by remote sensing: present capacities and future possibilities. *Remote Sens Environ* 35:243–256
- USDA Forest Service Remote Sensing Applications Center – Burned Area Emergency Response Imagery Support Program (2006) Available from <http://www.fs.fed.us/eng/rsac/baer/> [last accessed March 15, 2006]
- Van Wagendonk JW, Root RR, Key CH (2004) Comparison of AVIRIS and Landsat ETM+ detection capabilities for burn severity. *Remote Sens Environ* 92:397–408
- Venables WN, Ripley BD (1994) *Modern applied statistics with S-Plus*. Springer-Verlag, New York
- Vermote E, Ray J (1999) MODIS surface reflectance user's guide. <http://modis-land.gsfc.nasa.gov/MOD09/MOD09ProductInfo/MOD09Level2G250m.htm>
- Zhan X, Defries RS, Townshend JRG, DiMiceli CM, Hansen MC, Huang C, Sohlberg R (2000) The 250 m global land cover change product from the Moderate Resolution Imaging Spectroradiometer of NASA's Earth Observing System. *Int J Remote Sens* 21:1433–1460
- Zhan X, Sohlberg R, Townshend JRG, DiMiceli CM, Carroll ML, Eastman JC, Hansen MC, Defries RS (2002) Detection of land cover changes using MODIS 250 meter data. *Remote Sens Environ* 83:336–350

Chapter 33

Multisensor Global Retrievals of Evapotranspiration for Climate Studies Using the Surface Energy Budget System

Matthew McCabe, Eric Wood, Hongbo Su, Raghuv eer Vinukollu,
Craig Ferguson, and Z. Su

33.1 Introduction

Evaporation from water or soil surfaces and transpiration from plants combine to return available water at the surface layer back to the bulk atmosphere in a process called evapotranspiration. Much of our understanding of the complex feedback mechanisms between the Earth's surface and the surrounding atmosphere is focused on quantifying this process. At its most fundamental level, evapotranspiration is the loss of water from a surface to the atmosphere, achieved through vaporization. The complex nature of the evaporative process, however, includes mechanisms such as turbulent transport, feedback between the surface and atmosphere, and the biophysical nature of transpiration – all of which combine to make both measurement and estimation a difficult task.

Evapotranspiration is one of the most important components of the hydrological cycle, and together with precipitation, also represents the most spatially variable. Combined with rainfall and runoff, it controls the availability and distribution of water at the Earth's surface, and therefore, is significant to a number of research fields. An increased understanding of surface energy interactions broadly contributes to agricultural, hydrological, and climatological investigations. For instance, accurate routine estimation of evapotranspiration provides the following advantages: (a) improve water management practice by estimating recharge in groundwater aquifers or evaporative loss from open water bodies; (b) improve irrigation and water use management for agricultural purposes, particularly in water-intensive farming practice; (c) provide needed constraints in plant growth, carbon and nutrient cycling and production modeling; (d) inform catchment modeling applications; and (e) improve understanding of larger-scale meteorological and climatological applications.

M. McCabe (✉)
Department of Civil and Environmental Engineering,
University of New South Wales,
Sydney, NSW 2052, Australia
e-mail: mmccabe@unsw.edu.au

While evaporation itself is a conceptually simple process, it has proved extremely difficult to accurately describe or characterize for natural surfaces and systems. Apart from difficulties representing aspects of the physical mechanisms mentioned above, heterogeneities at the land surface, and to a lesser extent in the atmosphere (Raupach and Finnigan 1995), the interacting influences and feedbacks in the soil, vegetation and meteorological continuum (Trenberth 1999) and imprecise knowledge of component variables, all contribute to complicate a relatively fundamental theoretical basis. Much effort was directed, over the course of the last three decades, toward developing techniques to quantify evapotranspiration at the land surface using remotely sensed data, in recognition of the critical role they play in many environmental processes. The multitude of techniques subsequently developed to measure or model evapotranspiration vary considerably in the extent of their complexity (see Kalma et al. 2008 for a review).

The variability of evapotranspiration in space and time is influenced by changes in atmospheric condition, land use, vegetation, soils, and topography. Additionally, even where high quality local-scale data may exist, land surface heterogeneity complicates the extrapolation of point source surface flux estimates to larger scales (McCabe and Wood 2006; Li et al. 2008; Brunsell et al. 2008). Currently, it is possible only to accurately measure the latent and sensible heat from the land surface at relatively small spatial scales.

Although evapotranspiration is quantifiable at the small scale using ground-based techniques, larger-scale estimates require alternative measurements and estimation approaches. A lack of such measurements and knowledge hinders the closure of the land surface energy and water balances for regional and larger spatial scales, and impedes the development of suitable land surface parameterizations schemes. Implementing a routine methodology that circumvents the limitations imposed by spatial and temporal heterogeneity necessitates the use of a remote sensing approach to adequately account for such variability. Determining the level of spatial and temporal resolution appropriate for the modeling task is a difficult process, especially because of the lack of a consistent theory to move between scales (Beven and Fisher 1996).

Traditionally, evapotranspiration estimation is limited by the availability of spatially distributed datasets, with analyses subsequently focusing on the field or catchment scale of observation. Remote sensing of the land surface offers a number of unique advantages over conventional field-based data collection. Foremost among these is the spatial extent of data, facilitating observations from local to continental scales. Also, the potential to examine areas at multiple scales due to the array of sensors available, which offer a variety of spatial, spectral, and temporal characteristics exists. There also exist a number of limitations: in particular, the compromise between resolving an appropriate spatial scale and an adequate temporal frequency.

Applications are the primary drivers, which determine the appropriateness of the spatial and temporal scale. For instance, high spatial resolution (sub-100 m)/low temporal frequency (multiweekly) satellites such as Landsat and ASTER offer excellent opportunities to resolve field-scale evapotranspiration for use in agricultural and irrigation applications (Gowda et al. 2007; Glenn et al. 2007), with a

number of approaches being used precisely for this purpose (Bastiaanssen et al. 1998; Allen et al. 2007). In contrast, geostationary satellite platforms (GOES, MeteoSat, FY-2, MTSat) compromise lower spatial resolution (>1 km) with increased temporal frequency (sub-hourly) to provide unparalleled coverage. Recent advances in remote estimation of evapotranspiration with geostationary platforms show considerable promise to provide needed surface retrievals (Norman et al. 2003; Anderson et al. 2007), and partially address the issue of cloud cover influences on infrared surface temperature retrieval through increased temporal frequency.

For climate studies, global coverage using consistent methods and sensors remains a long-term goal of the NASA Energy and Water Cycle Study (NEWS). The Moderate resolution Imaging Spectroradiometer (MODIS) sensor on board the Aqua and Terra satellites, together with other satellites within NASA's Earth Observing System (EOS), offers an excellent compromise between the competing spatial and temporal requirements described above. MODIS contributes moderate resolution (1 km) data at multiple times throughout the diurnal cycle, and therefore remains an extraordinarily valuable resource in the Earth observation.

The focus of the present contribution is a discussion on the application of MODIS and other NASA Earth Observing satellites toward providing consistent global evapotranspiration retrievals. Through a systematic retrieval approach that develops evapotranspiration estimates across local, regional, and continental scales, we illustrate the potential of such products to provide insight and characterization of the land surface for a variety of essential applications.

33.2 Modeling Evapotranspiration

The need to effectively measure regional-, as opposed to point-scale estimates of evapotranspiration, has witnessed the development of a number of modeling approaches. However, the complications mentioned above render the characterization and physical description of evapotranspiration difficult. Of particular interest is the effective representation of the near-surface interaction with the lower atmosphere, especially in the context of generalized circulation models (GCMs). This interest is rendered challenging by land surface schemes, which are commonly inadequate for modelers, who examine such issues as climate prediction or climate change scenarios. A balance between increased model complexity and parsimony of model structure is required, particularly in the light of parameter uncertainty and model validation limitations.

33.2.1 *Surface Energy Balance System: The Interpretive Model*

It is widely accepted that remote sensing has the potential to spatially characterize the evapotranspiration, but it is ineffective on its own, in characterizing the range

of processes operating on the land surface. To effectively use satellite-derived remote sensing data to produce reliable estimates of evapotranspiration, the derived products require incorporation into an interpretive modeling framework.

The approach employed here is based on Su's (2002) Surface Energy Balance System (SEBS) model. SEBS was developed to estimate surface heat fluxes using satellite earth observation data in combination with routinely available meteorological forcing. SEBS is one of a family of similarly constructed models that consider the land surface via electrical analogue; that is, they regard the exchange of heat flux between the surface and atmosphere as driven by a difference in temperature (a potential) with the rate controlled by a number of resistances that depend on local atmospheric conditions, and land surface and vegetation characteristics.

SEBS falls into a general class of micro-meteorological evapotranspiration models that require a near surface and 2-m air temperature gradient, net radiation and other surface meteorology to drive model estimates. A variety of sophisticated approaches are available to estimate evapotranspiration in this manner. For excellent reviews and additional information, refer Kustas and Norman (1996), Quattrochi and Luvall (1999), Kalma et al. (2008) and Verstraeten et al. (2008). Further details on the SEBS model are available in the works of Su (2002), Su et al. (2005) and McCabe and Wood (2006).

33.2.2 Data Sources

Although remote sensing methods cannot measure the evaporative process directly, they do offer a means to extend point measurements to larger scales and also provide information on specific components and variables needed for energy and moisture balance estimation. Coupling remotely sensed information with ground-based data allows much greater insight into the dynamics of larger-scale processes than available from either source alone. The following section details data sources required by SEBS, obtainable from either remote sensing directly or through operational products. Many of the variables required by SEBS are discussed in greater detail elsewhere in this book, so only those data, which require significant modifications are presented.

33.2.2.1 Remote Sensing Variables

1. *Land surface temperature and emissivity*: Land surface temperature estimates are integral in the quantification of energy fluxes, and help estimate evapotranspiration. The MOD11 Surface Temperature product provides the key variable to determine surface fluxes from space. Remotely sensed land surface temperatures are used in a number of applications including monitoring of the surface radiation budget (Nunez and Kalma 1996), modeling of regional scale evapotranspiration (McCabe and Wood 2006), land surface flux estimation (Kustas and Norman 1996; Su et al. 2005), and also assist in moisture availability studies (McVicar and Jupp 2002). SEBS directly uses LST estimates to calculate net

radiation. To determine this value, a broadband emissivity is also needed, which is derived from the daily MODIS (bands 29, 31, and 32) narrow band emissivity estimates (Wan et al. 2002).

2. *Shortwave radiation*: Measuring the individual components which constitute net radiation from space is a difficult task. Due to instrument configuration, many satellites used to derive shortwave radiative fluxes to accurately detect important influences on the radiation budget such as snow cover, cloud and/or aerosol optical properties. The MODIS instrument allows insight into global monitoring of atmospheric profiles, column water vapor amount, aerosol particles, and cloud properties with higher accuracy and consistency than previous Earth observation imagers (King et al. 1992). These simultaneous observations are enormously useful to accurately derive surface radiative fluxes.

Recent experiments using MODIS swath-based shortwave radiation data to estimate flux (Su et al. 2008) indicate much promise. To enable the use of independently derived optical parameters from multispectral satellites such as MODIS, the GEWEX-Surface Radiation Budget (SRB) model (Pinker and Laszlo 1992; Pinker et al. 2003), was modified to use with such observations, and tested with MODIS-based parameterizations. Parameters required to drive the SRB model include the following: viewing geometry, column water vapor, column ozone amount, cloud fraction, cloud optical thickness, aerosol optical depth, and spectral surface albedo – all of which are available from either Terra/Aqua MODIS or the NASA A-Train satellite series. The feasibility to implement this approach with MODIS data at various spatial scales is described in Pinker et al. (2003). Preliminary results on inferring radiative fluxes from MODIS information show that the modified version of GEWEX/SRB is able to use MODIS-derived optical and ancillary information (Su et al. 2008). In previous applications (e.g., Su et al. 2005), the Geostationary Operational Environmental Satellite (GOES) data were used to determine net shortwave. Merging the temporal information available from GOES with the spatial resolution of MODIS data provides a very valuable radiation resource.

3. *Albedo*: Chapter 24 presents a detailed description of the MOD43 Broadband Albedo product (Schaaf et al. 2002). Although a true surface albedo product is not currently available, an average of the black-sky and white-sky albedo available from MOD43 was previously used. Assuming an even distribution between direct (black-sky) and diffuse (white sky) radiation are not likely true under all surface and atmospheric conditions, studies suggest this will provide a reasonable approximation (Wang et al. 2004). To address this shortcoming, a more representative surface albedo requires consideration of atmospheric optical depth and water vapor. Current SEBS applications, which use MOD09 spectral reflectance data, and follow Liang et al. (1999), are expected to provide a more accurate characterization of this variable.
4. *Vegetation indices*: Vegetation indices such as the Normalized Difference Vegetation Index (NDVI), available as part of the MODIS Vegetation Index Product (MOD13) (Chap. 26), and the MODIS Leaf Area Index (LAI) and Fraction of Photosynthetically Active Radiation (fPAR) Product (MOD15)

(Chap. 27), form integral components of the SEBS model. Specifically, LAI and vegetation fraction, which are derived from the NDVI, are used to estimate: (a) the roughness height for heat and momentum transfer; (b) the mixed emissivity when remote sensing data are employed (to derive the surface temperature); and (c) the ground heat flux over a region, if unavailable from measurements.

A number of authors have previously related measured vegetation indices to ground-based records of LAI (Su 2000). Correctly representing the variation of the vegetation is crucial to obtain accurate reproduction of the surface fluxes. Further details of these variables are available in the Chapters listed above.

33.2.2.2 Meteorological Forcing

Coupling remotely sensed information with ground-based data allows much greater insight into the dynamics of larger-scale processes than is available from either source alone. Traditionally, there is a disconnect between the spatially dense nature of remote sensing observation and the sparse distribution of meteorological networks. The North American Land Data Assimilation System (NLDAS) (Mitchell et al. 2004) addresses the lack of spatially and temporally consistent data by gathering best quality, modeled and observed, meteorological fields to produce both real time (1999) and retrospective forcing. NLDAS forcing data are primarily derived from the National Centers for Environmental Prediction (NCEP) Eta Model-based Data Assimilation (EDAS) (Rogers et al. 1996) output.

Meteorological forcing data, such as wind velocity, humidity, pressure, air temperature, and downward longwave radiation, are extracted from the NLDAS to allow SEBS-based estimation of evapotranspiration. NLDAS has a spatial resolution of 0.125° , and provides information at an hourly time step. It is extensively validated and implemented as a dataset for land surface modeling (Luo et al. 2003). The reliance on spatial fields of forcing data clearly restricts broader scale application of SEBS in areas where such data are not available. The recent development of both a Global Land Data Assimilation (GLDAS) (Rodell et al. 2004) and the Land Information System (LIS) (Kumar et al. 2006) offers the possibility to routinely estimate SEBS-derived surface fluxes in data-sparse areas. Additionally, advances in retrieving solar radiation from MODIS (Pinker et al. 2003), and the ability to retrieve atmospheric variables, such as air temperature, from the MODIS Atmospheric profile product (MOD07) (e.g., Bisht et al. 2005) will improve the capacity to globally estimate evapotranspiration by removing the reliance on surface-based meteorological observations.

33.3 Algorithm Validation

SEBS requires evaluation against diverse data to assess its potential to routinely estimate global-scale evapotranspiration. Specifically, the SEBS model requires evaluation across a variety of climate zones and land covers, thereby assessing the

adaptability of the model to climate and land cover variability. To fulfill this goal, a validation dataset satisfying these criteria is required. Here we present two published case studies at different spatial extents that illustrate the progressive nature of validation efforts with SEBS. Good quality surface tower-derived flux data, together with meteorological forcing from both in-situ measurement and operational meteorological datasets are used to assess the model's ability to reproduce flux retrievals.

Further details on the results presented here are available in Su et al. (2005).

33.3.1 Local- and Regional-Scale Flux Validation

An assessment of SEBS' ability to reproduce observed fluxes was performed using independent high-quality data collected during the Soil Moisture Atmospheric Coupling Experiment (SMACEX 02) (Kustas et al. 2005), a crop land-based field campaign in the Walnut Creek catchment in southern Iowa (see Figure 1 of McCabe and Wood 2006). The objectives of this investigation include the following: (1) evaluate SEBS estimates using local-scale (tower) data to determine the accuracy limit at the field scale; and (2) identify the potential to use operational meteorology from the NLDAS coupled with high-resolution Landsat data to predict spatially distributed surface fluxes. Flux measurements from ten eddy covariance systems positioned on towers throughout the catchment were used to evaluate SEBS across both corn and soybean fields.

Independent measurements of the latent and sensible heat fluxes were derived using a 3-D sonic anemometer and a LiCor 7500 water vapor/CO₂ sensor (Kustas et al. 2004). These independent measurements permit a user to make an energy balance closure assessment since the net radiation and soil heat flux are also observed. To address the non-closure problem, a characteristic of much eddy-covariance flux data, a Bowen ratio closure method was employed to correct the sensible and latent heat flux measurements (Twine et al. 2000). Further information on the correction of the eddy covariance data with such closure techniques is provided in the study of Prueger et al. (2005a, b).

33.3.1.1 Results from Local-Scale (Tower Based) Forcing Data

The in-situ measurements required by SEBS are listed in Table 33.1. In addition to tower-based flux measurements, detailed vegetation parameters and hydro-meteorological data were collected during the SMACEX 02 campaign (Kustas et al. 2005). In this analysis, in-situ observations of incoming solar radiation (insolation), downward longwave radiation and soil heat flux were used directly in SEBS to compute the available energy. Meteorological and heat flux data were resampled to 30-min intervals. Standard meteorological forcing data including wind velocity, vapor pressure, air temperature, and atmospheric pressure were used to run the SEBS model.

Table 33.1 SEBS model data requirements

| Data type | Variables | Unit |
|-----------------------------|----------------------------------------------------------|------------------|
| Surface meteorological data | Air temperature | °C |
| | Pressure | kPa |
| | Wind | m/s |
| | Vapor pressure | kPa |
| Radiative energy flux | Incident shortwave radiation | W/m ² |
| | Outgoing shortwave radiation | W/m ² |
| | Incident longwave radiation | W/m ² |
| | Outgoing longwave radiation | W/m ² |
| | Net radiation | W/m ² |
| Surface heat flux | Ground heat flux | W/m ² |
| | Sensible heat flux | W/m ² |
| | Latent heat flux | W/m ² |
| | Evaporative fraction | – |
| Surface temperature | Composite radiometric temperature (soil + vegetation) | °C |
| Vegetation parameters | Vegetation height | M |
| | Vegetation fraction | – |
| | Leaf area index | – |
| | Vegetation type (corn or soybean) | – |

Land surface temperature, a key variable in the SEBS model application, was measured by Apogee infrared thermometers (model IRTS-P) (Jackson and Cosh 2003a). LAI and vegetation fraction were used to estimate the following: (a) the roughness height for heat and momentum transfer; (b) the mixed emissivity when remote sensing data are employed (to derive the surface temperature); and (c) the ground heat flux over a region, if unavailable from measurements. LAI, vegetation fraction and vegetation height were measured on four separate occasions (June 18th, 28th, and July 2nd, 5th). A simple linear interpolation was used to generate daily LAI and vegetation height throughout the study period from the observations. Studies have observed that the relationship between the vegetation fraction and LAI is often nonlinear (Chen and Cihlar 1995), which potentially cause inconsistency between vegetation parameters if a linear interpolation is used. Thus, a nonlinear relationship between LAI and vegetation fraction was formulated to make full use of the vegetation measurements, and maintain consistency between observations (see Su et al. 2005 for further details).

SEBS was run at a temporal resolution of 30 min from 10:00 to 16:00 local solar time, at each of ten flux tower sites for the 20-day duration of SMACEX 02. The SEBS model-estimated evapotranspiration was compared with eddy covariance-based flux observations, which allowed an assessment of the model's accuracy. Figure 33.1 shows the SEBS-derived evapotranspiration scatter plots against the SMACEX-observed latent heat flux. For five corn sites (Fig. 33.1a), an even distribution about the 1:1 line and an r^2 of 0.89 illustrates the consistent agreement between estimates and measured fluxes. A root mean squared error (RMSE) of 46.68 W m⁻² and a mean absolute error (MAE) of 36.14 W m⁻² indicate a performance comparable to an in-situ flux observation technique's error.

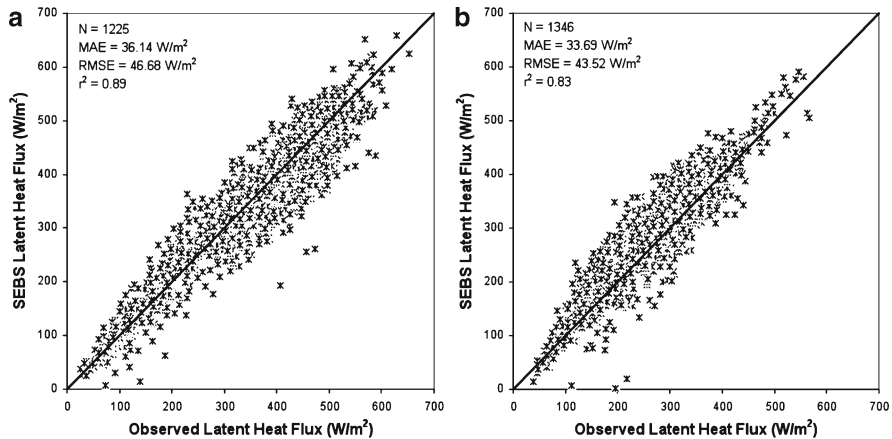


Fig. 33.1 SEBS tower-based predictions of latent heat flux versus eddy covariance observations for (a) corn and (b) soybean field sites. Associated statistics from analysis are included in the plots

During the first 10 days of SMACEX, results indicated that SEBS overestimated the latent heat flux for two of the five soybean sites. Although a number of possible explanations for the inconsistent performance at these locations exist (homogeneity in downward longwave forcing data; variations in energy balance closure; variations in vegetation information or surface temperature), closer examination of the two biased sites indicated that the vegetation fractions were the lowest for all observation locations. A decreased vegetation fraction results in an overestimation of the emissivity. To address this, a new effective emissivity was calculated at these locations by assigning a vegetation emissivity of 0.98 and a soil emissivity of 0.94 (following Chen et al. 2004). Model outputs for the emissivity-corrected sites present improved agreement with an RMSE of 43.52 W m^{-2} , an MAE of 33.69 W m^{-2} and an r^2 of 0.83 (see Fig. 33.2b).

Results of this point scale analysis indicate SEBS can accurately reproduce surface fluxes over varied vegetation and hydrometeorological conditions.

33.3.1.2 Results from the Regional-Scale (NLDAS) Forcing Data

In-situ measurements are not generally available for model forcing to routinely estimate surface fluxes. As a result, data from satellite and operational meteorology offer the best surrogate for local measurements. Table 33.2 shows the outline of the data requirements and sources of the meteorological and satellite products employed in the regional-scale analysis. The data represent a variety of resolutions and interpolation is used where necessary to standardize the measurements. To complement the availability of Landsat-ETM surface temperature data (Li et al. 2004), NLDAS forcing data at 11 AM were used in place of the tower-based meteorology, offering an opportunity to examine a more operationally based estimate of surface fluxes. In addition, high-resolution (30 m) land cover classification and

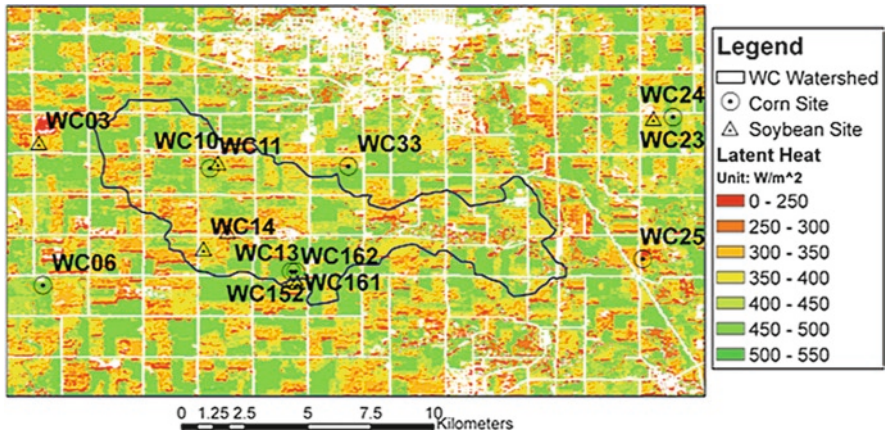


Fig. 33.2 Regional-scale evapotranspiration estimates from SEBS using a combination of Landsat surface temperature, MODIS emissivity, GOES radiation and NLDAS meteorological data

Table 33.2 SEBS data requirements for regional scale estimation of surface fluxes over the Walnut Creek catchment in Iowa, USA

| Data source | Variables | Unit | Resolution |
|---------------|-----------------------------|------------------|------------|
| NLDAS | Air temperature | °C | 0.125° |
| | Pressure | Pa | |
| | Wind | m/s | |
| | Specific humidity | – | |
| | Downward longwave radiation | W/m ² | |
| Landsat7 ETM+ | Brightness temperature | K | 60 m |
| | NDVI | – | 30 m |
| | Land cover | – | 30 m |
| MODIS | Albedo | – | 1 km |
| GOES | Surface insolation | W/m ² | 20 km |

All inputs are based on operational meteorological and satellite data

NDVI data from the Landsat overpass (10:40 AM July 1, 2002 Path 26 Row 31) (Jackson and Cosh 2003b) were used. To maintain consistency, the 60-m surface temperature data were interpolated to 30 m using a nearest neighbor technique. Although interpolating the surface temperature is not strictly correct (due to non-linearity in the Planck function), it is not expected to introduce significant error at this scale (McCabe et al. 2008a). LAI and vegetation fraction were determined from the Landsat NDVI estimates using the experimentally derived nonlinear relationship of Xavier and Vettorazzi (2004).

The emissivity separation approach described above, along with vegetation fraction (f_v) knowledge, was used to calculate an effective emissivity (Chen et al. 2004). It is worth noting that the Landsat-based emissivity’s higher spectral resolution is probably different from the tower surface temperature data, as the bandwidth (10.4–12.5 μm) is generally narrower than that of the infrared thermometer (8–14 μm).

Surface shortwave radiation data were determined from GOES-based estimates. The University of Wisconsin (pers. comm. Dr. M. C. Anderson 2004) provided the data for the study period at hourly time steps and a 20-km spatial resolution.

SEBS-Landsat-based estimates of the surface heat fluxes for July 1 (10:40 AM local time) were calculated for the SMACEX region using operational meteorological and ancillary remote sensing data. Figure 33.2 shows the latent heat flux estimates and the location of the flux tower sites over the catchment. A clear delineation between soybean and corn sites is immediately apparent.

To compare estimates with tower-based flux measurements, a 3×3 pixel box (90 m \times 90 m) centered over each tower was extracted, and the mean latent flux estimate calculated. The results for SEBS-Landsat-based surface fluxes over both corn and soybean sites are presented in Table 33.3, identifying the mean, bias, and RMSE. Evapotranspiration estimates were assessed against eight flux tower sites, which were available for comparison on July 1. Table 33.3 indicates that the mean latent heat flux at corn sites is larger than at soybean sites, consistent with in-situ results. The latent heat flux difference between corn and soybean sites is approximately 120 W m⁻² from in-situ observations and 92.0 W m⁻² from SEBS-Landsat estimates. Individual RMS errors for corn and soybean were calculated as 28.7 and 84.9 W m⁻² respectively, while the combined error for all sites was 60.6 W m⁻². Clearly, the results for soybean are not consistent with those for corn, with a large disparity in the retrieval accuracies. Analysis of the three soybean sites available for comparison reveals the influence of site WC161. WC161 is located adjacent to a cornfield. As a result, the 3×3 spatial averaging performed at this site will inevitably sample from within the higher evaporating corn site.

Comparing mean values of the latent heat fluxes determined from Landsat and those from the tower observations indicate improved agreement. For corn, the difference between the means of the SEBS-Landsat-based 3×3 estimates and the five corresponding tower values is less than 2%, whereas for the three soybean sites, it is approximately 5%. Although the results here indicate considerable agreement, the low number of validation points renders it difficult to draw broad conclusions on their accuracy at the local scale.

Table 33.3 Statistics of the surface energy flux comparison between SEBS-Landsat based estimation and in-situ tower based measurements for July 1, 2002

| | | Corn | Soybean | Corn and soybean |
|----|-----------------------------------|-------|---------|------------------|
| LE | Number of sites | 5 | 3 | 8 |
| | Observed mean (W/m ²) | 459.3 | 339.9 | 414.6 |
| | SEBS mean (W/m ²) | 450.5 | 358.5 | 416.0 |
| | Bias (W/m ²) | -8.8 | 18.6 | 1.4 |
| | RMSE (W/m ²) | 28.7 | 84.9 | 60.6 |
| H | Number of sites | 5 | 3 | 8 |
| | Observed mean (W/m ²) | 95.5 | 172.3 | 124.3 |
| | SEBS mean (W/m ²) | 81.2 | 111.2 | 92.5 |
| | Bias (W/m ²) | -14.2 | -61.0 | -31.8 |
| | RMSE (W/m ²) | 23.8 | 86.3 | 60.0 |

The advantage of using remote sensing data is that spatial variability is analyzable explicitly and compared to point scale measurements. Figure 33.3 shows the results of the mean latent and sensible heat fluxes calculated for corn and soybean sites across the SMACEX domain, as well as the 3×3 pixel averages (see Table 33.3) compared with tower-based observations. To estimate the degree of spatial variability throughout the region, the range in flux tower measurements and the standard deviation of the SEBS-Landsat estimated fluxes across the region are also included. Generally, Fig. 33.3 shows that corn retrievals seem to agree more closely with observations than those for soybean, both for latent and sensible heat fluxes. Interestingly, soybean has an approximately 60% smaller standard deviation relative to corn in both surface fluxes, indicating greater flux consistency within soybean fields. The range of latent heat flux observations is approximately 65 W m^{-2} for corn and 100 W m^{-2} for soybean, although the latter result is again influenced by site WC161. Overall, the observations from the tower sites are seemingly representative of the regional average determined from the SEBS-Landsat results, but particularly so for corn. The variability of soybean results evident in Fig. 33.3 highlights the difficulty in characterizing flux measurements for large areas, even when good validation data are available for this purpose.

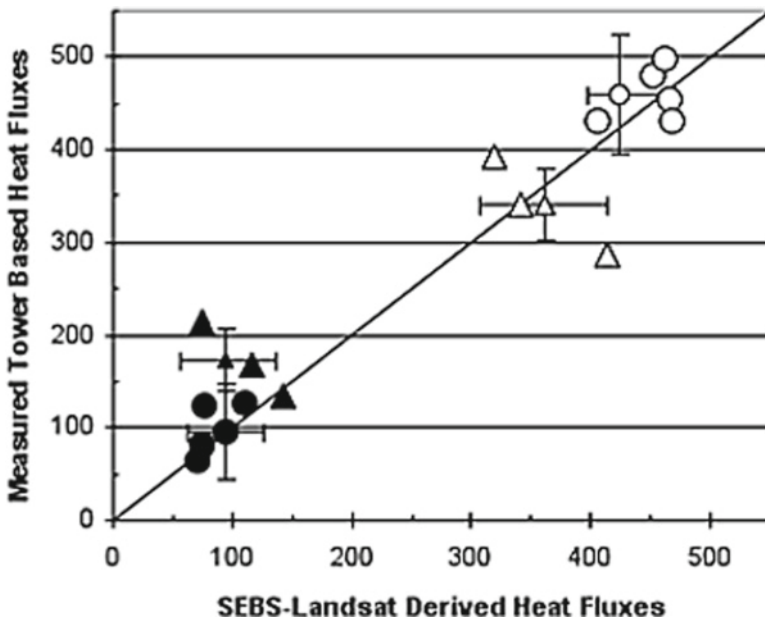


Fig. 33.3 Image is derived from Figure 4 in Su et al. (2005). Comparison of the energy fluxes from SEBS-Landsat-based estimates and in-situ observations at tower sites. *Circles* represent corn sites, while *triangles* signify soybean fields. *Solid symbols* identify the sensible heat flux and *open symbols*, the latent heat flux. The range of results present in tower observations are shown in the *x*-error bars and the standard deviation of satellite based estimates across the region in *y*-error bars. The regional average heat flux (across the domain) is shown at the intersection of these lines

33.3.1.3 Summary of Local- and Regional-Scale Validation

SEBS was evaluated at local and regional scales using both in-situ data and operational meteorology. Results from this analysis indicate that estimation accuracy was strongly related to crop type, with corn estimates showing improved estimates compared to soybean. Although RMSEs were affected by the limited number of samples and one poorly performing soybean site, differences between the mean observation values and SEBS-Landsat-based estimates at the tower sites were approximately 5%. Time-series comparison of the model output and observations also show that SEBS correctly interprets hydrological variability, and is capable of accurately representing the temporal development of evapotranspiration at the local scale. Using operational meteorological forcing data from the NLDAS offers an ideal pathway toward achieving robust estimates of regional-scale surface fluxes when coupled with remote sensing data. While the analysis here offers a retrospective determination of fluxes, the potential exists to employ such data at near real-time, allowing improved characterization of fluxes at time scales suitable for use in weather prediction, water resource management or agricultural applications. MODIS land product-derived surface parameters, GOES radiation information and NLDAS meteorological data form a sufficient database to run the SEBS model at a variety of scales. Combined with meteorological forcing from coarse scale operational data, flux estimates with considerable agreement with in-situ observations were producible.

Overall, these results indicate considerable potential toward routine surface heat flux estimation using remote sensing data and operational meteorology.

33.3.2 Globally Distributed Evapotranspiration Validation

The Coordinated Enhanced Observing Period (CEOP) forms an element of the World Climate Research Program (WCRP). Initiated as part of the Global Energy and Water Cycle Experiment (GEWEX), the CEOP dataset is ideal for SEBS validation requirements by providing continuous, high-quality in-situ measurements at global locations. The purpose of this case study is to assess the adaptability of SEBS to variations in climate and land cover based on the CEOP EOP-1 dataset at both tower and satellite pixel scales. Eight CEOP stations are selected to assess the SEBS model, specifically encompassing a variety of hydro-climatic conditions. An inter-comparison of energy fluxes from SEBS estimates and in-situ eddy correlation-based observations are examined at daily scales for each station.

Spatially representative in-situ data are often only available at a limited number of sites. To broaden the scope of the analysis and encompass a more operational approach to flux estimation, globally distributed forcing data are required. MODIS-based estimates of the land surface temperature and broadband emissivity, leaf area index and vegetation fraction are coupled with meteorology from both the CEOP towers and the Global Land Data Assimilation System (GLDAS) to formulate

additional forcing datasets for SEBS. GLDAS is an integration of observational fields and outputs from the atmospheric data assimilation system (ADAS) component of a weather forecast and analysis system (Rodell et al. 2004), which provides data at 0.25° (spatial) and 3-h (temporal) resolutions. These distinct data sources allow a thorough examination of the impact to evapotranspiration estimates across two scales of meteorological forcing data. Further details of this work are provided in Su et al. (2007).

33.3.2.1 CEOP In-Situ Data and Site Characteristics

The Enhanced Observing Period (EOP-1) of CEOP provides hourly observation of surface meteorological variables and energy fluxes from July 1 through September 30, 2001. CEOP data provide the majority of the forcing variables required by SEBS. Excluding the Southern Great Plains site, eight stations (six sites) from EOP-1 meet the data requirements of the SEBS model, with site names and characteristics (i.e., country, location, land classification and climate type) listed in Table 33.4. The six sites are distributed across five countries and three continents, and fall into three broad climate types and four different vegetation covers. The data include three forested locations within the Boreal Ecosystem Research and Monitoring Sites (BERMS). For CEOP tower-based forcings, surface temperature observations were only available at Bondville and Rondonia. For locations where the surface temperature is not observed directly, it is estimated indirectly from the upward and downward longwave radiation using a correction for the broadband emissivity.

33.3.2.2 Results from the Globally Distributed Tower-Based Flux Data

Daily averages (05:00 through 18:00 local time) and statistics for the energy fluxes at eight globally distributed CEOP stations are presented in Table 33.5. To filter out periods of cloud-affected or rainy days, the daily average is computed only for

Table 33.4 Characteristics of the CEOP-EOP1 reference sites

| Site name | Country | Lat./lon. (°) | Köppen climate | Dominant land cover (DLC) |
|------------------|-------------|----------------|----------------|---------------------------|
| Cabauw | Netherlands | 51.97, 4.93 | C | Grassland |
| Lindenberg | Germany | 52.17, 14.12 | C | Grassland |
| Bondville | USA | 40.01, -88.29 | D | Cropland (corn) |
| Rondonia | Brazil | -10.01, -61.93 | A | Rain forest |
| Manaus | Brazil | -2.61, -60.21 | A | Rain forest |
| BERMS sites | | | | |
| Old Aspen | Canada | 53.63, -106.20 | D | Forest |
| Old Jack Pine | Canada | 53.92, -104.69 | D | Forest |
| Old Black Spruce | Canada | 53.99, -105.12 | D | Forest |

A: tropical; B: dry; C: warm temperate rainy climates and mild winters; D: cold forest climates and severe winters; E: polar; H: highland

Table 33.5 Statistics of the daytime latent heat flux and evaporative fraction at the daily scale for the CEOP globally distributed locations

| Site name | Days | Mean CEOP | | Mean SEBS | | RMSE SEBS | | r-RMSE SEBS | | Mean EF | |
|------------------|------|------------------------|------------------------|------------------------|------------------------|------------------------|--------|-------------|------|---------|------|
| | | LE (W/m ²) | LE (W/m ²) | LE (W/m ²) | LE (W/m ²) | LE (W/m ²) | LE (%) | CEOP | SEBS | CEOP | SEBS |
| Cabauw | 45 | 146.47 | 144.54 | 30.20 | 20.62 | 0.756 | 0.708 | | | | |
| Lindenberg | 70 | 119.49 | 102.70 | 22.61 | 18.92 | 0.741 | 0.625 | | | | |
| Bondville | 23 | 299.68 | 293.85 | 74.17 | 24.75 | 0.602 | 0.582 | | | | |
| Rondonia | 66 | 226.45 | 235.73 | 40.58 | 17.92 | 0.725 | 0.672 | | | | |
| Manaus | 31 | 318.85 | 344.16 | 50.89 | 15.96 | 0.758 | 0.787 | | | | |
| BERMS | | | | | | | | | | | |
| Old Aspen | 84 | 151.09 | 122.80 | 48.25 | 31.93 | 0.548 | 0.576 | | | | |
| Old Jack Pine | 76 | 101.50 | 106.80 | 29.28 | 28.85 | 0.315 | 0.278 | | | | |
| Old Black Spruce | 62 | 134.68 | 118.55 | 56.78 | 42.16 | 0.362 | 0.402 | | | | |

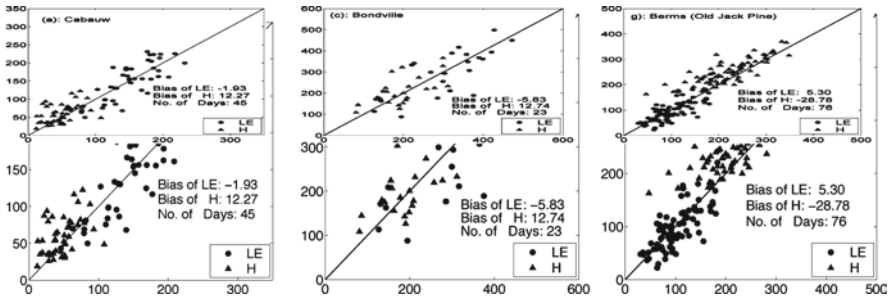


Fig. 33.4 Comparison of daily average SEBS flux estimates using CEOP forcing data and MODIS retrievals compared with measured fluxes at the CEOP observation sites. Both axes represent surface heat flux with units of W m^{-2}

periods when both the observations, and the model estimates are available for more than 4 h/day. Three representative sites are shown for comparison in Fig. 33.4. RMSE estimates of the daily flux indicate a varied level of agreement across the CEOP sites. Considering the range of RMSE and mean flux values, flux results require some normalization to allow intercomparison. The relative RMSE (r-RMSE) was calculated by dividing the RMSE by the mean observed flux as a way to assess the accuracy of SEBS estimates. Based on the relative RMSE, the tropical rain forest sites at Manaus and Rondonia (Brazil) represent the highest accuracy (<20% r-RMSE), followed closely by the two grassland sites at Lindenberg and Cabauw (~20% r-RMSE). The cropland site (corn) at Bondville presents good agreement given the uncertainty in land classification here (~25% r-RMSE), whereas the remaining forested sites illustrate the largest uncertainty and varied levels of agreement (>25% r-RMSE).

The comparison of the mean evaporative fraction (evaporation divided by available energy) shows that estimates from SEBS agree very well with those from observations and exhibit no significant bias. Both model-predicted and observed mean evaporative fractions at the two tropical sites are above 0.65 during the summer of 2001, which is reasonable considering the climatic conditions in the Amazon, where water supply is sufficient for sustained forest growth. Cabauw and Lindenberg also have a high-observed mean evaporative fraction in summer. For the Cabauw grass site, the soil is reported to exist at field capacity for much of the year, thus evaporation is seldom limited by the water supply (Chen et al. 1997). The largest difference in mean EF is 0.111 at Lindenberg. Generally, the SEBS evaporative fraction estimate illustrates a close agreement with that from observations.

These results illustrate that both climate and vegetation type have an important control over the daytime surface heat flux patterns. The SEBS model is observed to reproduce the patterns of the daily surface heat flux under diverse climate conditions and vegetation types. While the SEBS sensible and latent heat flux estimates for the Boreal forests are not as accurately reproduced, such vegetated stands represent some of the most difficult surface types to model evapotranspiration, due to their strong coupling with the atmosphere (Margolis and Ryan 1997) and uncertainties in

retrieving required variables. In the majority of studies cases, estimates of the daytime evapotranspiration agree within an r-RMSE of approximately 30%.

33.3.2.3 Results from MODIS-CEOP and MODIS-GLDAS Derived Fluxes

Evapotranspiration estimates were produced at 1-km resolution using both CEOP and GLDAS forcing data coupled with MODIS land surface temperature (MOD11A1) (Table 33.6). The surface meteorological and radiative data in both CEOP and GLDAS forcing were interpolated to correspond with the overpass time of the MODIS surface temperature data. When remotely sensed data are incorporated, model-predicted evapotranspiration is limited not only by meteorological forcing data, but also by the MODIS surface temperature availability, which is strongly influenced by cloud cover and atmospheric influences. Three sites, which most consistently derive evapotranspiration, are presented for comparison between SEBS-based estimates and tower scale CEOP observations.

Scatter plots comparing MODIS-based retrievals with in-situ flux measurements are shown in Fig. 33.5. As mentioned in the previous section, both meteorological data and surface heat flux measurements were linearly interpolated to correspond

Table 33.6 Forcing data for globally distributed evapotranspiration estimates

| Data source | Variables | Spatial resolution | Temporal resolution |
|-------------|---------------------|--------------------|-----------------------------|
| CEOP | Surface meteorology | Tower scale | Instantaneous, interpolated |
| GLDAS | Surface meteorology | 0.25° | Instantaneous, interpolated |
| MODIS | LST/emissivity | 1 km | Instantaneous |
| | LAI | | 8-day |
| | Land cover | | Yearly |
| | Albedo | | 16-day |

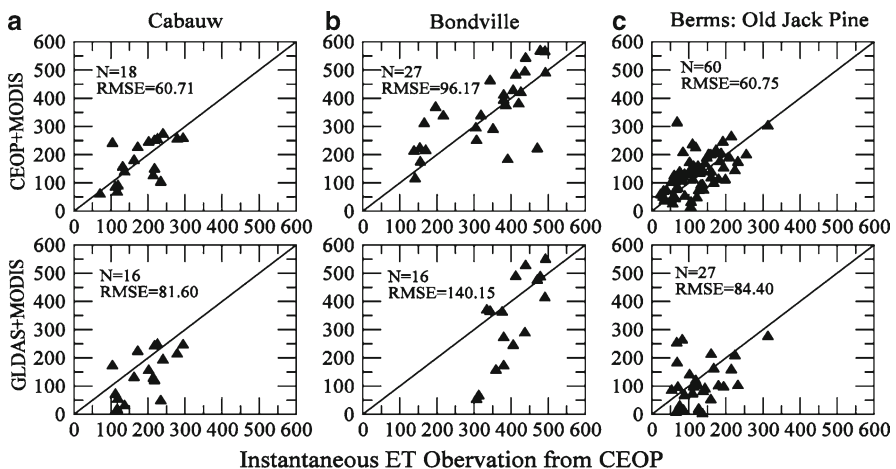


Fig. 33.5 Comparison of instantaneous SEBS evapotranspiration using CEOP meteorological data (*top*) and GLDAS forcing data (*bottom*) together with MODIS retrievals. Values on the *x*-axis are determined from CEOP tower based observations of surface fluxes ($W m^{-2}$)

with the MODIS overpass time at each site. The number of available model estimates and the RMSE are included in each panel. The three sites represent quite different land classifications, including grassland, cropland and cold forest, respectively. A greater number of estimates were obtained from the CEOP+MODIS dataset than from GLDAS+MODIS dataset, although they share the same remotely sensed land surface parameters. Likewise, for all three sites, the evapotranspiration accuracy estimates from CEOP+MODIS dataset are better than those from the GLDAS+MODIS dataset. Specifically, the results from CEOP+MODIS dataset have less bias, less MAE, and less RMSE. This result is not unexpected considering GLDAS meteorological forcing represents a coarser spatial and temporal resolution (0.25° and 3 hourly); however, it is instructive given the option of using global operational forcing.

The RMSE of surface flux estimates at Cabauw and BERMS (old Jack Pine) based on CEOP+MODIS dataset is around 61 W m^{-2} , while results for Bondville indicate an RMSE of 96.17 W m^{-2} . The RMSE of latent heat flux estimates are higher by approximately 33% at Cabauw and BERMS when CEOP forcing is replaced with the GLDAS forcing dataset. For Bondville, the increase in error approaches 45%. These results raise some potential limitations to the broad scale estimation of surface fluxes using globally distributed operational forcing datasets.

33.3.2.4 Summary of Globally Distributed Evapotranspiration Validation

Several factors can potentially affect the accuracy of model-predicted energy fluxes. When combined with remote sensing data, the lack of temporal detail available from measures such as the surface temperature (daily) and LAI (8-day), influence the capacity to capture the dynamics of the evaporating surface, particularly over complex landscapes and growing conditions. From previous analysis, the evaporative fraction was observed to increase from 0.50 to 0.90 within 3 weeks during a period of rapid growth. Figure 1 in Su et al. (2007) demonstrate the variability of LAI during EOP-1 and the subsequent difficulty in effectively capturing these dynamics. Scale issues are another important factor requiring consideration. MODIS land cover classification data at 1-km lacks the degree of variability necessary to correctly parameterize detailed land surface models, or even process models such as SEBS. McCabe and Wood (2006) demonstrated the degree of error resulting from misclassification of known surface types.

The poor performance of the Bondville site is explained to a large degree by land surface heterogeneity effects. Although characterized as a corn crop, Bondville is actually a mixture of corn and soybean within the 1-km MODIS pixel since the two stations at Bondville (which are 400 m apart) were planted with opposite crops (corn and soybean) in 2001 (information from <http://www.fluxnet.ornl.gov/fluxnet/index.cfm>). Su et al. (2005) found that corn routinely exhibits an evapotranspiration up to 100 W m^{-2} greater than for soybean. Thus the heterogeneity within a MODIS pixel would certainly account for the relatively large deviation of evapotranspiration estimates at Bondville evident in all three forcing datasets.

While land surface misclassification may explain aspects of the error, variations in forcing data can potentially contribute much larger sources of inaccuracy. Examination of net radiation from the GLDAS and comparison with CEOP data indicated considerable divergence at all sites presented here. Amongst these, Bondville has the largest negative bias for incoming shortwave (160.1 W m^{-2}), more than twice the bias at the other sites. The poorer surface flux estimates at Bondville and Cabauw are certainly attributable to the large error in the GLDAS downward radiative forcing, given the strong reliance of evapotranspiration on accuracy in available energy (Rn-G).

Forcing data sources such as GLDAS offer immediate advantages, but their use requires prudence especially in areas with limited validation data.

33.4 Application with EOS-Terra and Aqua Data

Techniques which couple land and atmospheric properties' information with remotely sensed variables offer considerable promise to routinely retrieve a number of hydrological variables. Over the last few decades, much effort was directed toward determining evapotranspiration and its spatial variability. Understanding the limitations of remote sensing approaches is as important as identifying their possibilities. Using space-borne remote sensing to estimate surface evapotranspiration at regional to continental scales with algorithms based on micrometeorological approaches present a number of unique challenges. The main challenges include the following: (1) obtaining continuous surface temperature fields uninhibited by clouds; (2) errors in transferring the required surface meteorology from in-situ stations to pixels with retrieved surface temperatures; (3) scale mismatches between the resolution of the remotely sensed observations (insolation, vegetation, surface temperature); (4) natural landscape variability; and (5) aggregating instantaneous surface flux estimates spatially and temporally across large domains.

Despite restrictions associated with atmospheric influences, land surface heterogeneity, the overpass frequency and the development of robust process algorithms, satellite-derived data remain the only viable means to measure evapotranspiration at regional and larger scales on a routine basis. A key concept underpinning the development of a MODIS-based evapotranspiration estimate is to develop a globally distributed product based on local scale evaluation. To achieve this task, a deliberate modeling and evaluation phase is developed, which incorporates multiple sensors, scales and land surface types to assess the feasibility to routinely estimate evapotranspiration. Much of the work and progress toward such a product are available in recent publications, which include Su et al. (2005, 2007), McCabe and Wood (2006), and McCabe et al. (2008b).

The following section describes a recent case study that illustrates an approach using a combination of in-situ and remote sensing datasets to estimate distributed patterns of evapotranspiration across the Oklahoma Mesonet.

33.4.1 Regional- to Continental-Scale Investigations Using the Oklahoma Mesonet

The work presented here uses Terra and Aqua MODIS products, together with a medium spatial resolution (5 km) surface solar insolation product derived from the MODIS sensor (Pinker et al. 2003; Su et al. 2008). The strategies explored in this study form a baseline to assess MODIS-based evapotranspiration at regional to continental scales.

In this study, SEBS is employed to estimate the terrestrial evapotranspiration across Oklahoma state using a combination of remote sensing and in-situ data. The Oklahoma Mesonet (see <http://www.mesonet.org/>) provides an unprecedented level of meteorological detail over portions of the Red-Arkansas basin, a 645,000 km² sub-catchment of the continental-scale Mississippi Basin. The Mesonet consists of over 120 towers that deliver needed surface and atmospheric variables such as air temperature, relative humidity, pressure, wind speed, and downward shortwave radiation (insolation) at 5-min intervals.

A number of strategies are explored to obtain continuous spatial fields of evapotranspiration. An inverse distance weighting interpolation scheme is used to produce spatially continuous fields of surface meteorology based on available tower data. This enables a streamlined integration with grid-based remote sensing data, and provides the necessary spatial forcing data required by SEBS. Comparisons of interpolated in-situ measurements of incoming shortwave (solar) radiation with a MODIS-derived incoming shortwave radiation product are examined, and these data are used for subsequent model simulation. Figure 33.6 presents a spatial comparison of the incoming solar radiation field from interpolated tower data and Aqua MODIS data.

Different combinations of these data fields were inter-compared to assess the evapotranspiration retrieval's fidelity in an operational context. SEBS was also used to predict the evaporative fraction over individual operational meteorological stations, with values then interpolated across the domain to provide a spatial evaporative fraction field. In all, three unique experiments combining the different levels of forcing data (both in-situ and remote) were developed. Table 33.7 shows the experimental design and the forcing combinations.

Scatter plots of Experiments II and III compared with the tower-based retrievals of Experiment I for both Terra and Aqua overpasses are presented in Fig. 33.7. A comparison of these experiment results reveals the following: when the interpolated downward shortwave radiation at the tower sites (Experiment II) is substituted with the corresponding MODIS-based shortwave radiation (Experiment III), the standard deviation of evapotranspiration is 7–0 W m⁻² lower than when compared against the tower-based results in Experiment I. The result is consistent across both Terra and Aqua overpasses, which suggests that incorporating MODIS-based downward shortwave radiation results is beneficial to improve evapotranspiration estimation, particularly when no regional in-situ measurements of this variable are available.

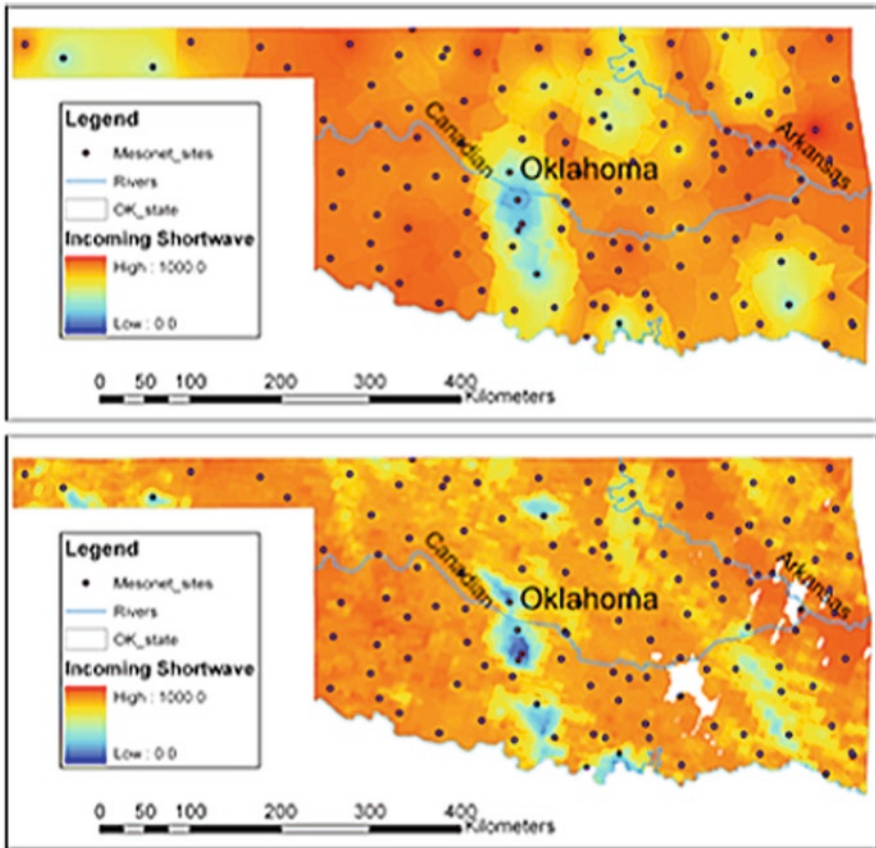


Fig. 33.6 Incoming shortwave radiation in $W\ m^{-2}$ from gridded Oklahoma Mesonet surface meteorology (*upper*) and derived from MODIS-Aqua (*lower*) for August 8, 2003

Table 33.7 Description of the three individual experiments developed for the Oklahoma Mesonet analysis to assess the retrieval of spatially distributed evapotranspiration

| Experiment | Data source and methodology |
|------------|-----------------------------------------------------------------------------------------------------------------------------------------------------------------------------------------------|
| I | Mesonet in-situ tower data (air temperature, relative humidity, pressure, wind speed and downward shortwave radiation) and MODIS derived land surface temperature, leaf area index and albedo |
| II | Interpolated Mesonet in-situ tower data (see Experiment I) and MODIS derived land surface temperature, leaf area index and albedo |
| III | Interpolated Mesonet in-situ tower data (see Experiment I) but using MODIS derived downward shortwave radiation together with MODIS land surface temperature, leaf area index and albedo |

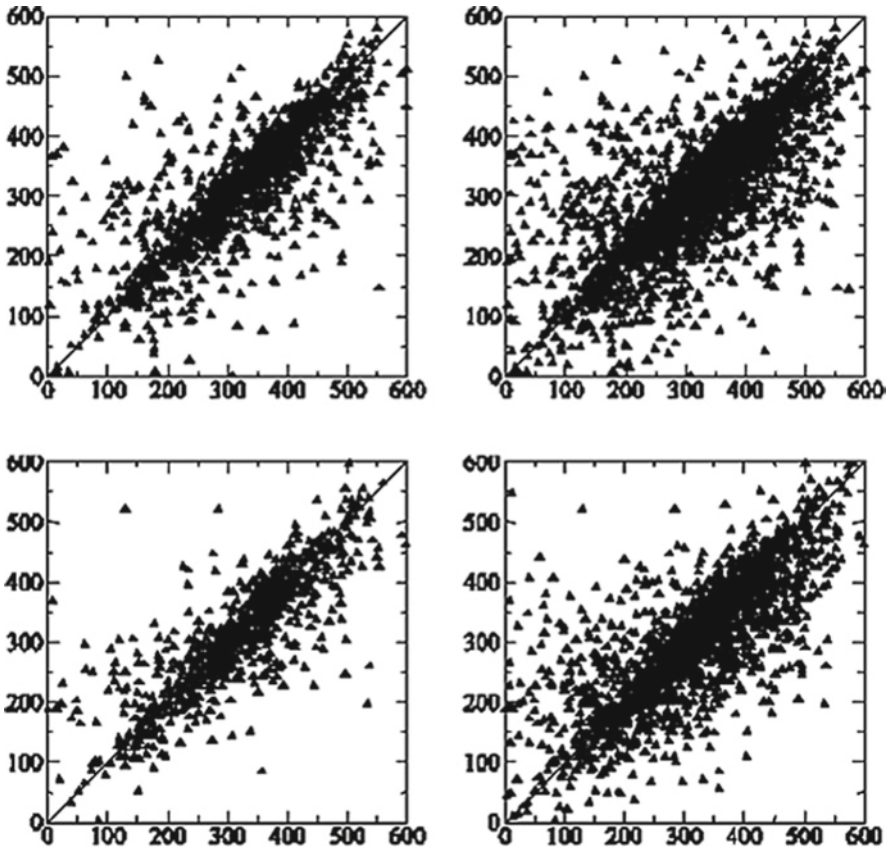


Fig. 33.7 Scatter plots comparing Experiments II and III (refer to Table 33.7) with SEBS latent heat flux derived from Mesonet tower observations (Experiment I) for Terra (*left column*) and Aqua (*right column*)

In both Experiments II and III, Terra results improve when compared against Aqua (and relative to the in-situ tower-based retrievals). Such improvement is likely a function of interpolating meteorological fields at different points in the diurnal cycle. This is explainable thus: the afternoon Aqua overpass will generally exhibit more spatial variability than the earlier morning Terra overpass, purely as a result of solar and atmospheric forcing at those times.

Spatial maps of the evapotranspiration and the evaporative fraction (evapotranspiration divided by the available energy) were determined for a 10-day period over Oklahoma. It was necessary to average daily measurements to the 10-day period due to the relatively poor retrieval rate of surface temperature during the study period. Indeed, this is one of the critical limitations in developing a temperature-based evapotranspiration product: the limitation due to cloud cover variability to produce a continuous spatial field. Composites of spatial evapotranspiration for the first 10 days of August 2003 are shown in Fig. 33.8 for both Terra and Aqua using the results from Experiments II and III.

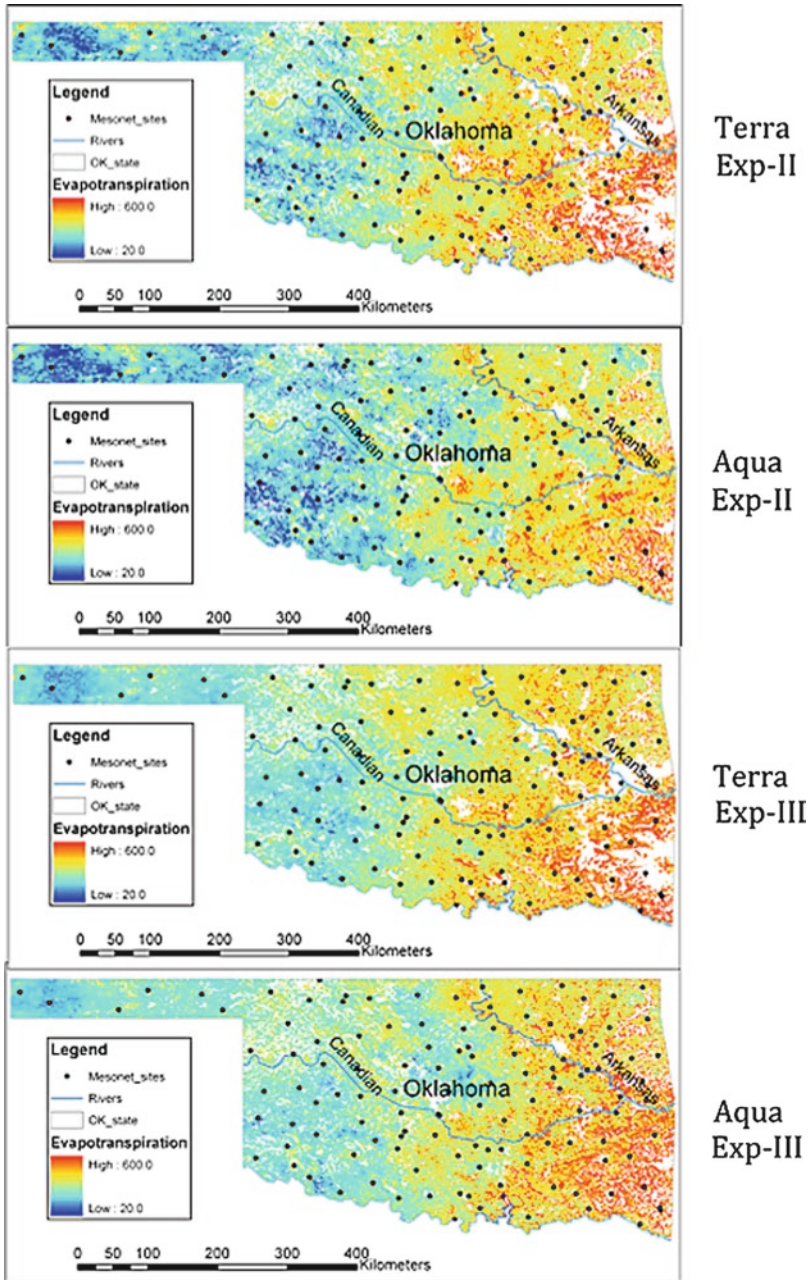


Fig. 33.8 Composite model output for 10-day modeled evapotranspiration between August 1–10, 2003 from the MODIS-Terra and MODIS-Aqua for both Experiment II (*top*) and Experiment III (*bottom*) (refer to Table 33.7 for explanation of forcing data). Flux estimates are in $W m^{-2}$

Evidently, there is a high level of agreement among the spatial maps derived from individual sensor retrievals, indicating a potential to develop a combined Terra+Aqua product to circumvent the cloud contamination issues of the 5-km product. However, the significant surface temperature changes that occur between Terra and Aqua overpasses could potentially affect such a product's accuracy. The 0.05° land surface temperature climate modeling grid (CMG) product shows some improvement in cloud screening, and may provide an alternative approach to temperature retrieval. Further work on this is required.

33.4.2 Developing a Multisensor Approach Toward Global Estimation

In the preliminary stages of developing a MODIS-based evapotranspiration product, the SEBS approach was deemed usable in concert with available surface meteorological fields, supplemented with remote sensing data. As part of this task, the efficacy of using model forcing and ground-based data, as well as the accuracy of retrievals, was undertaken. During the first 2 years of the project, SEBS was evaluated using flux tower data from SMACEX 02 (Iowa) and GEWEX/CEOP EOP-1 tower data. Where good quality data exist, the results were excellent and were reported by Su et al. (2005, 2007). Assessment of the algorithm continues using FLUXNET data (<http://daac.ornl.gov/FLUXNET/>). The project also began testing the SEBS algorithm over two large regional scales: the Red-Arkansas river basin, and over Arizona during the North American Monsoon Experiment (NAME) field campaign period (see McCabe et al. 2008b; Pan et al. 2008).

Through analyses of both the evapotranspiration and SEBS-required forcing data to retrieve evapotranspiration, it was clear that there were deficiencies in predicating the surface flux product solely on MODIS data. Apart from known issues in the surface temperature and vegetation products (retrieval frequency, accuracy, and dynamic response), another primary concern was the lack of a MODIS-based solar radiation product. To address this lack, collaborative work with the University of Maryland (Pinker et al. 2003) helped develop a MODIS-based radiation product, which produced excellent results to assess over Oklahoma (Su et al. 2008).

More recent efforts were directed toward using complementary sensors on-board the Terra and Aqua satellites: in particular, the Cloud and the Earth Radiant Energy System (CERES) for radiation components and surface temperature, and the Atmospheric Infrared Sounder (AIRS) for surface air temperature and humidity. These sensors provide a means to develop a truly global scale product, since the in-situ meteorological variables required by SEBS are not routinely available globally. Figure 33.9 shows some of the swath-based retrievals of the variables used by SEBS to estimate evapotranspiration.

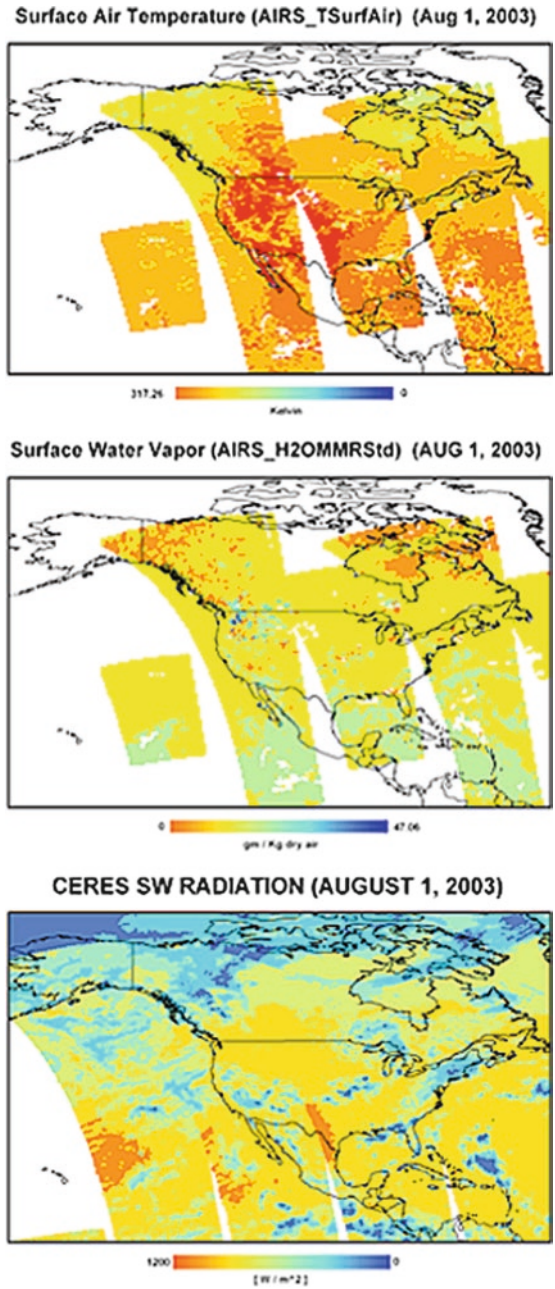


Fig. 33.9 Examples of swath data derived from AIRS and CERES including (from top) AIRS surface air temperature, AIRS surface water vapor and CERES shortwave radiation for August 1, 2003

These efforts to augment the MODIS data with both AIRS and CERES products have produced some positive results, some of which are presented in Fig. 33.10 for Oklahoma using combinations of AIRS meteorology, MODIS-based radiation and surface temperature, and finally, CERES-based radiation and surface temperature. As is evident, there are significant spatial resolution differences in using only MODIS data (1–5 km) in comparison with CERES and AIRS data (20 and 25 km, respectively), but the spatial patterns are well correlated. Table 33.8 shows the list of some of the data sources that drive the current progress to develop a globally distributed evapotranspiration product.

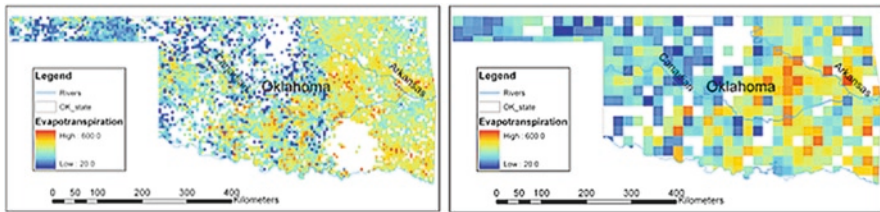


Fig. 33.10 Retrieved evapotranspiration over Oklahoma using (left panel) MODIS land products, MODIS radiation and AIRS meteorology and (right panel) CERES radiation and LST, AIRS meteorology and MODIS land products

Table 33.8 Data types and sources for the development of a multisensor evapotranspiration product

| Data type | Variable | Unit | Source | Platform | Resolution (km) |
|-----------------------------|----------------------------|------------------|--------------|----------|-----------------|
| Surface meteorological data | Air temperature | °C | AIRS | AQUA | 25 ^a |
| | Pressure | kPa | AIRS | AQUA | 25 ^a |
| | U-Wind | m/s | (GMAO/CERES) | AQUA | 20 |
| | V-Wind | m/s | (GMAO/CERES) | AQUA | 20 |
| | Vapor pressure | kPa | AIRS | AQUA | 25 ^a |
| Radiative energy flux | Incident SW | W/m ² | CERES | AQUA | 20 |
| | Incident LW | W/m ² | CERES | AQUA | 20 |
| | Surface temperature | °C | CERES/AIRS | AQUA | 20/25 |
| Vegetation Parameters | Emissivity | – | MODIS | AQUA | 1–5 |
| | Albedo | – | MODIS | AQUA | 5 |
| | LAI | – | MODIS | AQUA | 5 |
| | Veg. type | – | MODIS | AQUA | 1–5 |
| | (MODIS UMD Classification) | – | MODIS | TERRA | 20 |

^aProcessed to 25 km at Princeton

33.5 Current Status and Future Direction

33.5.1 Problems and Issues in Remote Retrievals

General sentiment agrees that remote sensing offers the most amenable means to obtain spatial evapotranspiration patterns. But, there exists little agreement on how best to realize this. While numerous schemes and methodologies were proposed to provide land surface flux estimates with remotely sensed surface temperatures (Diak and Whipple 1995; Anderson et al. 1997; Norman et al. 2000), evapotranspiration estimates derived in such a fashion have achieved varied success levels. Undoubtedly, accurate measurement of surface fluxes with remote sensing techniques would provide a valuable information source, and much progress was made toward achieving this goal (Kustas and Norman 1997; Norman et al. 2003; Kalma et al. 2008).

The SEBS model has demonstrated its ability to produce accurate surface heat flux estimates over agricultural fields using both in-situ and NLDAS-based observational meteorological forcing (Su et al. 2005); globally distributed sites representing disparate land surface types and conditions (Su et al. 2007); and more recently, with MODIS-based radiation and NLDAS forcing over a large basin in the USA. An analysis of scale influence using multisensor remote sensing data was also performed and showed the utility of MODIS retrievals to develop good estimates of the catchment average evapotranspiration (McCabe and Wood 2006). The clearest message from these evaluations is the self-evident conclusion that quality evapotranspiration estimates are only obtained with quality forcing data and remote sensing data.

Excluding the availability of needed forcing data, which is increasingly met by operational meteorological forcing, a critical limitation to routine evapotranspiration estimation is the provision of surface temperature measurements. Accurate retrieval of land surface temperature is difficult due to a number of underlying factors, which combine to provide some interesting challenges. Sea surface temperature retrievals are potentially accurate in the order of 1 K (Prata et al. 1995), but surface temperature estimates are complicated by spatial and temporal resolution, land surface heterogeneity and atmospheric and land surface effects. Coupled with the inability of infrared techniques to penetrate cloud-covered pixels, obtaining spatially continuous surface temperature fields is rare. Cloud presence also increases the radiative flux variations reaching the surface, which renders attempts to extrapolate instantaneous evapotranspiration estimates either spatially (through interpolation) or temporally (through consistency relationships with the evaporative fraction e.g., Crago 1996) difficult.

Another problem in accurate surface flux estimation is the accuracy of land cover classification, fractional vegetation cover and leaf area index – all products derived from MODIS data. Surface flux retrievals are significantly influenced by correct specification of vegetation properties, and issues related to capturing the dynamic response in vegetation systems (particularly LAI) are observed in field and regional-scale analysis. This issue is of particular concern over regions of the globe,

which are not thoroughly validated, or lack the means to perform effective product evaluation. As with surface temperature, the scale issue becomes significant, especially in heterogeneous environments and where mixed land-use occurs.

Characterizing the development of evapotranspiration through time is a difficult task, particularly when using remote sensing data, since retrieved information is often spatially dense, but temporally sparse. Techniques to expand these instantaneous measures are not only limited, they are restricted by the general lack of knowledge to effectively describe the spatial distribution and temporal evolution of evaporative patterns. Although advances in providing accurate evapotranspiration estimates from remote sensing variables are noted and evidenced herein, one of the major shortcomings of such techniques is their basis rooted on essentially instantaneous retrievals. Approaches, which use snapshots of the surface condition to expand surface flux knowledge through time, show much promise. Recent techniques that address this issue include the use of uncertainty modeling (McCabe et al. 2005), multi-objective calibration (Crow et al. 2004) and data assimilation schemes that account for multiple hydrological observations (Pan et al. 2008).

Problems of correct process representation, accounting for uncertainties due to scale and heterogeneity, or characterizing errors in forcing data and their influence on model estimates are not the only issues, which require resolution. Perhaps the key obstacle toward achieving robust and accurate evapotranspiration estimates at globally distributed locations is the lack of quality validation data. Indeed, this leads to a serious shortcoming in remote sensing observations per se; there is a distinct lack of validation data characterizing a wide variety of surface and atmospheric states against which techniques are robustly assessed. Recent efforts addressing the ideas of hydrological consistency (McCabe et al. 2008b) or research to find statistical consistency with land surface model data (Gao et al. 2007) offer some promise toward challenging the current validation–evaluation paradigm.

33.5.2 Future Directions

The development of a global evapotranspiration product demands the successful integration of multiple satellites and sensors. The current availability of EOS represents a rare opportunity to examine the efficacy to incorporate these multiple data into an interpretive process model (SEBS) to allow characterization of needed hydrological and climatological variables. The planned shift in research strategy moves away from a reliance on ground-based meteorology toward a combination of observations from MODIS, CERES and AIRS sensors that will enable global retrievals at mid-level resolution. Preliminary analysis of these data suggests a significant advantage over reliance on single sensor estimation. An initial global-scale evapotranspiration retrieval using these multiple data sources is presented in Fig. 33.11. The result represents the successful evolution of much of the

(SEBS) Instantaneous Latent Heat Flux (Monthly Average)
July 2003

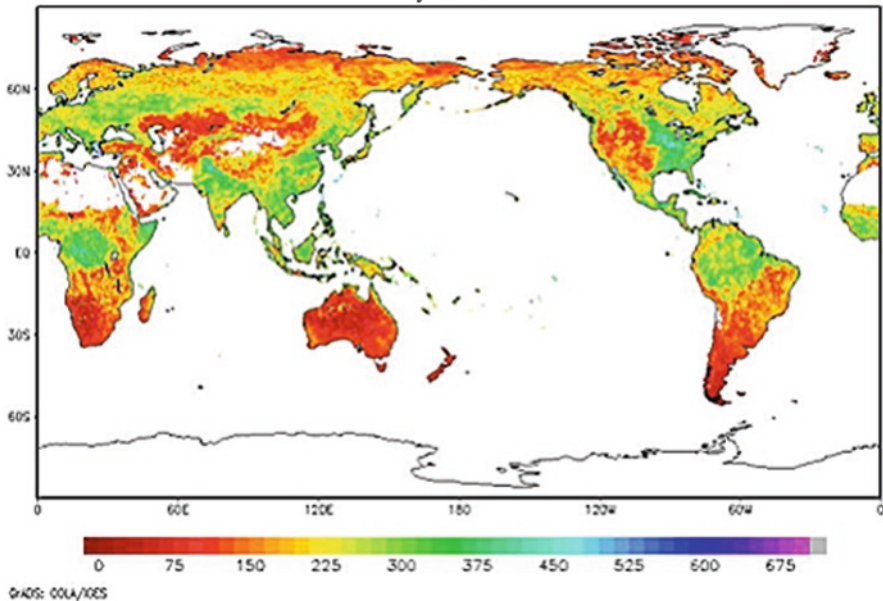


Fig. 33.11 Preliminary results for a new global estimate of evapotranspiration using SEBS and combinations of MODIS, AIRS and CERES data for July 2003 (W m^{-2})

work presented in this chapter and offers a means to produce routine global evapotranspiration estimates.

One of the key issues that require attention is the manner in which evapotranspiration evaluation should proceed. While studies have shown the stability and accuracy of the interpretive model (SEBS) to estimate surface fluxes with good quality data, the different retrieval scales inherent in a global product will demand some innovation in product assessment. Studies examining the hydrological consistency of remotely sensed hydrological variables were undertaken (McCabe et al. 2008b), and work continues over continental scales and longer time periods to examine this approach. Additionally, comparison with land surface model outputs and data assimilation studies to address the added skill from remote observations may also provide a needed means of assessment. Research also continues to examine atmospheric water budgets based on re-analysis divergence fields, and observed precipitation to provide a more accurate characterization of water budget closure. Together with comparison with spatially distributed tower data available at selected locations globally, this represents a comprehensive assessment strategy that should offer some confidence in remote sensing-derived evapotranspiration retrieval.

Acknowledgments NASA supported this work through grant NNG04GQ32G: A Terrestrial Evaporation Product Using MODIS Data. This support is gratefully acknowledged.

References

- Allen RG, Tasumi M, Trezza R (2007) Satellite-based energy balance for mapping evapotranspiration with internalized calibration (METRIC): applications. *ASCE J Irrigation Drainage Eng* 133(4):395–406
- Anderson MC, Norman JM, Diak GR, Kustas WP, Mecikalski JR (1997) A two-source time-integrated model for estimating surface fluxes using thermal infrared remote sensing. *Rem Sens Environ* 60(2):195–216
- Anderson MC, Norman JM, Mecikalski JR, Otkin JA, Kustas WP (2007) A climatological study of evapotranspiration and moisture stress across the continental United States based on thermal remote sensing: 1 Model formulation. *J Geophys Res* 112:D10117, doi:10.1029/2006JD007506
- Bastiaanssen WGM, Pelgrum H, Wang J, Ma Y, Moreno JF, Roerink GJ, Van der Wal T (1998) A remote sensing surface energy balance algorithm for land (SEBAL): 2 Validation. *J Hydrol* 212/213:213–229
- Beven KJ, Fisher J (1996) Remote sensing and scaling in hydrology. In Stewart JB, Engman ET, Feddes RA, Kerr Y (eds) *Scaling up in hydrology using remote sensing*. Wiley, Chichester, UK
- Bisht G, Venturini V, Islam, S, Jiang L (2005) Estimation of net radiation using MODIS-Terra data for clear sky days. *Rem Sens Environ* 97(1):52–67
- Brunsell NA, Ham JM, Owensby CE (2008) Assessing the multi-resolution information content of remotely sensed variables and elevation for evapotranspiration in a tall-grass prairie environment. *Rem Sens Environ* 112:2977–2987
- Chen JM, Cihlar J (1995) Quantifying the effect of canopy architecture on optical measurements of leaf area index using two gap size methods. *IEEE Trans Geosci Remote Sens* 33:777–787
- Chen LF, Li Z-L, Liu S, Tang Y, Zhong B (2004) Definition of component effective emissivity for heterogeneous and non-isothermal surfaces and its approximate calculation. *Int J Remote Sens* 25:231–244
- Chen TH and Coauthors (1997) Cabauw experimental results from the Project for Intercomparison of Land-surface Parameterization Schemes. *J. Climate*, 10:1194–1215
- Crago RD (1996) Conservation and variability of the evaporative fraction during the daytime. *J Hydrology* 180(1–4):173–194
- Crow W, Wood EF, Pan M (2004) Multi-objective calibration of land surface model evapotranspiration predictions using streamflow observations and spaceborne surface radiometric temperature retrievals. *J Geophys Res* 108(D23): 4725, doi:1029/2002JD003292
- Diak GR, Whipple MS (1995) Estimating surface sensible heat fluxes using surface temperatures measured from a geostationary satellite during FIFE 1989 – Note. *J Geophys Res* 100(D12): 25453–25461
- Gao H, Wood EF, Drusch M, McCabe MF (2007) Copula derived observation operators for assimilating TMI and AMSR-E soil moisture into land surface models. *J Hydrometeorol* 8(3): 413–429
- Glenn EP, Huete AR, Nagler PL, Hirschboeck KK, Brown P (2007) Integrating remote sensing and ground methods to estimate evapotranspiration. *Crit Rev Plant Sci* 26(3):139–168
- Gowda PH, Chavez JL, Colaizzi PD, Evett SR, Howell, TA, Tolk JA (2007) Remote sensing based energy balance algorithms for mapping ET: current status and future challenges. *Trans Am Soc Agri Biol Eng (ASABE)* 50(5):1639–1644
- Jackson TJ, Cosh MH (2003a) SMEX02 watershed soil moisture data, Walnut Creek, Iowa. National Snow and Ice Data Center. Digital Media, Boulder, CO
- Jackson TJ, Cosh MH (2003b) SMEX02 Landsat Thematic Mapper Imagery, Iowa. National Snow and Ice Data Center. Digital media, Boulder, CO
- Kalma JD, McVicar TR, McCabe MF (2008) Estimating land surface evaporation: a review of methods using remotely sensed surface temperature data. *Surv Geophys* 29:421–469, doi: 10.1007/s10712-008-9037-z
- King MD, Kaufman YJ, Menzel WP, Tanré D (1992) Remote sensing of cloud, aerosol, and water vapor properties from the Moderate Resolution Imaging Spectrometer (MODIS). *IEEE Trans Geosci Remote Sens* 30:2–27

- Kumar SV, Peters-Lidard CD, Tian Y, Houser PR, Geiger J, Olden S, Lighty L, Eastman JL, Doty B, Dirmeyer P, Adams J, Mitchell K, Wood EF, Sheffield J (2006) Land Information System – An Interoperable Framework for High Resolution Land Surface Modeling. *Environ Model Softw* 21(10):1402–1415, doi:10.1016/j.envsoft.2005.07.004
- Kustas WP, Norman JM (1996) Use of remote sensing for evapotranspiration monitoring over land surface. *Hydrol Sci J* 41(4):495–516
- Kustas WP, Norman JM (1997) A two-source approach for estimating turbulent fluxes using multiple angle thermal infrared observations. *Water Resour Res* 33(6):1495–1508
- Kustas WP, Li F, Jackson TJ, Prueger JH, MacPherson, JI, Wolde M (2004) Effects of remote sensing pixel resolution on modeled energy flux variability of croplands in Iowa. *Remote Sens Environ* 92(4):535–547
- Kustas WP, Hatfield, JL, Prueger JH (2005) The Soil Moisture Atmosphere Coupling Experiment (SMACEX): background, hydrometeorological conditions and preliminary findings. *J Hydrometeorol* 6(6):791–804
- Li, F, Kustas WP, Anderson MC, Prueger JH, Scott RL (2008) Effect of remote sensing spatial resolution on interpreting tower-based flux observations. *Remote Sens Environ* 112:337–349
- Li F, Jackson TJ, Kustas WP, Schmugge TJ, French AN, Cosh, MH, Bindlish R (2004) Deriving land surface temperature from Landsat 5 and 7 during SMEX02/SMACEX. *Remote Sens Environ* 92(4):521–534
- Liang S, Strahler AH, Walthall C (1999) Retrieval of land surface albedo from satellite observations: a simulation study. *J Appl Meteorol* 38(6):712–725
- Luo L, Robock A, Mitchell KE, Houser PR, Wood EF, Schaake JC, Lohmann D, Cosgrove B, Wen F, Sheffield J, Duan Q, Higgins RW, Pinker RT, Tarpley JD (2003) Validation of the North American Land Data Assimilation System (NLDAS) retrospective forcing over the southern Great Plains. *J Geophys Res* 108:8843, doi:10.1029/2002JD003246
- Margolis HA, Ryan MG (1997) A physiological basis for biosphere-atmosphere interactions in the boreal forest: an overview. *Tree Physiol* 17(8–9):491–499
- McCabe MF, Kalma JD, Franks SW (2005) Spatial and temporal patterns of land surface fluxes from remotely sensed surface temperatures within an uncertainty modelling framework. *Hydrol Earth Syst Sci* 9(5):467–480
- McCabe MF, Wood EF (2006) Scale influences on the remote estimation of evapotranspiration using multiple satellite sensors. *Remote Sens Environ* 105(4):271–285
- McCabe MF, Balick LK, Theiler JP, Gillespie AR, Mushkin A (2008a) Forward modeling of linear mixing in thermal IR temperature retrieval. *Int J Remote Sens* 29: 5047–5061.
- McCabe MF, Wood EF, Wójcik R, Pan M, Sheffield J, Su H, Gao H (2008b) Hydrological consistency using multi-sensor remote sensing data for water and energy cycle studies. *Remote Sens Environ* 112(2):430–444, doi:10.1016/j.rse.2007.03.027
- McVicar TR, Jupp DLB (2002) Using covariates to spatially interpolate moisture availability in the Murray–Darling Basin: a novel use of remotely sensed data. *Remote Sens Environ* 79:199–212
- Mitchell KE, Lohmann D, Houser PR, Wood EF, Schaake JC, Robock A, Cosgrove B, Sheffield J, Duan Q, Luo L, Higgins RW, Pinker RT, Tarpley JD, Lettenmaier DP, Marshall CH, Entin JK, Pan M, Shi W, Koren V, Meng J, Ramsay BH, Bailey AA (2004) The multi-institution North American Land Data Assimilation System (NLDAS): utilizing multiple GCIP products and partners in a continental distributed hydrological modeling system. *J Geophys Res* 109(D7): doi:10.1029/2003JD003823
- Norman JM, Anderson MC, Kustas WP, French AN, Mecikalski JR, Torn RD, Diak GR, Schmugge, TJ, Tanner BCW (2003) Remote sensing of surface energy fluxes at 10¹-m resolutions. *Water Resour Res* 39(8):1221, doi:10.1029/2002WR001775
- Norman JM, Kustas WP, Prueger, JH, Diak GR (2000) Surface flux estimation using radiometric temperature: a dual temperature-difference method to minimize measurement errors. *Water Resour Res* 36(8):263–2274
- Nunez M, Kalma JD (1996) Satellite mapping of the surface radiation budget. In: Stanhill G (ed) *Advances in bioclimatology*. Springer-Verlag, Berlin, pp 63–124

- Pan M, Wood EF, Wójcik R, McCabe MF (2008) Estimation of the regional terrestrial water cycle using multi-sensor remote sensing observations and data assimilation. *Remote Sens Environ* 112(4):1282–1294, doi:10.1016/j.rse.2007.02.039
- Pinker RT, Laszlo I (1992) Modelling surface solar irradiance for satellite applications on a global scale. *J Appl Meteorol* 31:194–211
- Pinker RT, Wang H, King MD, Platnick S (2003) The first use of MODIS data to cross-calibrate with GEWEX/SRB datasets. *GEWEX News* 13(4)
- Prata AJ, Caselles V, Coll C, Sobrino JA, Otlle C (1995) Thermal remote sensing of land surface temperature from satellites: current status and future prospects. *Remote Sens Rev* 12:175–224
- Prueger JH, Hatfield JL, Kustas WP, Hipps LE, Li F, Macpherson I, Anderson MC, Parkin TB, Eichinger WE, Cooper DJ (2005a) Spatial and temporal variation of water, energy and carbon fluxes from tower and aircraft measurements. *American Meteorological Society Conference Paper*, 5 p.
- Prueger JH, Hatfield JL, Kustas WP, Hipps LE, MacPherson JI, Neale CMU, Eichinger WE, Cooper DI, Parkin TB (2005b) Tower and aircraft eddy covariance measurements of water vapor, energy, and carbon dioxide fluxes during SMACEX. *J Hydrometeorol* 6(6):954–960
- Quattrochi DA, Luvall FJC (1999) Thermal infrared remote sensing for analysis of landscape ecological processes: methods and applications. *Landscape Ecol* 14:577–598
- Raupach MR, Finnigan JJ (1995) Scale issues in boundary-layer meteorology: surface energy balance in heterogeneous terrain. *Hydrol Processes* 9:589–612
- Rodell M, Houser PR, Jambor U, Gottschalk J, Mitchell K, Meng J, Arsenault K, Cosgrove B, Radakovich J, Bosilovich M, Entin JK, Walker JP, Lohmann D, Toll D (2004) The global land data assimilation system. *Bull Am Meteorological Soc* 85(3):381–394
- Rogers E, Black TL, Deaven DG, Dimego GJ, Zhao Q, Baldwin M, Junker NW, Lin Y (1996) Changes to the operational “Early” Eta analysis/forecast system at the National Centers for Environmental Prediction. *Weather Forecasting* 11:391–413
- Schaaf CB, Gao F, Strahler AH, Lucht W, Li X, Tsang T, Strugnell NC, Zhang X, Jin Y, Muller J-P, Lewis P, Barnsley M, Hobson P, Disney M, Roberts G, Dunderdale M, Doll C, d’Entremont R, Hu B, Liang S, Privette JL (2002) First operational BRDF, albedo and nadir reflectance products from MODIS. *Remote Sens Environ* 83:135–148
- Su Z (2000) Remote sensing of land use and vegetation for mesoscale hydrological studies. *Int J Remote Sens* 21:213–233
- Su Z (2002) The surface energy balance system (SEBS) for the estimation of turbulent heat fluxes. *Hydrol Earth Syst Sci* 6(1):85–99
- Su H, McCabe MF, Wood EF, Su Z, Prueger JH (2005) Modeling evapotranspiration during SMACEX02: comparing two approaches for local and regional scale prediction. *J Hydrometeorol* 6(6):910–922
- Su H, Wood EF, McCabe MF, Su Z (2007) Evaluation of remotely sensed evapotranspiration over the CEOP EOP-1 reference sites. *J Meteorol Soc Jpn* 85A:439–459
- Su H, Wood EF, Wang H, Pinker RT (2008) Spatial and temporal scaling behavior of surface shortwave downward radiation based on MODIS and in-situ measurements. *Geophys Res Lett* 35(3):542–546, doi: 10.1109/LGRS.2008.923209.
- Trenberth KE (1999) Atmospheric moisture recycling: role of advection and local evaporation. *J Climate* 12:1368–1381
- Twine TE, Kustas WP, Norman JM, Cook DR, Houser PR, Meyers TP, Prueger JH, Starks PJ, Wesely ML (2000) Correcting eddy-covariance flux underestimates over a grassland. *Agric For Meteorol* 103(3):279–300
- Verstraeten WW, Veroustraete F, Feyen J (2008) Assessment of evapotranspiration and soil moisture content across different scales of observation. *Sensors* 8:70–117
- Wan Z, Zhang Y, Zhang Q, Li Z-L (2002) Validation of the land-surface temperature products retrieved from Terra Moderate Resolution Imaging Spectroradiometer data. *Remote Sens Environ* 83:163–180
- Wang Z, Heng X, Barlage M, Dickinson RE, Gao F, Schaaf CB (2004) Using MODIS BRDF and albedo data to evaluate global model land surface albedo. *J Hydrometeorol* 5(1):3–14
- Xavier AC, Vettorazzi CA (2004) Mapping leaf area index through spectral vegetation indices in a subtropical watershed. *Int J Remote Sens* 25(9):1661–1672

Part VI

The Future of Land Remote Sensing

While continuing to operate ASTER, Terra and Aqua MODIS, and Landsat-7, NASA is working on three future instruments that will continue systematic acquisition of coarse and mid-resolution data described in this volume. The Landsat Data Continuity Mission (LDCM), which is being developed in cooperation with the USGS, is the eighth in the Landsat series of polar orbiting scanners, and will extend the long history and unparalleled data record of the Landsat series, and more recently, ASTER data record. It will add two new bands to the Landsat-7 configuration: one for detecting cirrus clouds, and another for coastal zone observations. A stand-alone thermal sensor compatible with the Landsat system has been proposed and NASA is currently evaluating options to include this instrument on the LDCM, or flying it separately. LDCM is under construction, and is scheduled for launch in December 2012. The Hyperspectral Infrared Imager (HypIRI) is a 2-instrument package (VSWIR hyperspectral scanner, and multispectral TIR scanner) recommended by the recent National Research Council's Decadal Survey. The mission is at the study stage, and decisions about its funding and schedule will occur in late 2009. The Visible Infrared Imaging Radiometer Suite (VIIRS) is being developed in partnership with DOD and NOAA as part of the NPOESS Preparatory Project due for launch in early 2011. With successful deployment of these instruments, the science and application communities can look forward to several years of continued systematic observations. The challenge facing the nation is how to transition the proven research satellite systems into the operational domain, and secure the long-term data record, which is imperative to study global climate and environmental change.

Chapter 34

The Evolution of U.S. Moderate Resolution Optical Land Remote Sensing from AVHRR to VIIRS

Christopher O. Justice, Eric Vermote, Jeff Privette, and Alain Sei

Abstract Moderate resolution satellite data have become an integral part of land remote sensing, which provide observations to support global and climate change research and applications of societal benefit. Starting with the NOAA Advanced Very High Resolution Radiometer (AVHRR), daily data analysis in the time-domain provided important new insights in vegetation studies at the global scale. Combining the temporal characteristics of the AVHRR and extending the spectral characteristics of the Landsat-5 Thematic Mapper, the NASA Earth Observing System (EOS) Moderate Resolution Imaging Spectroradiometer (MODIS) instruments launched a new era in land remote sensing. The Terra and Aqua MODIS instruments now provide science quality, moderate resolution data with spatial resolutions from 250 m to 1 km. The next generation U.S. moderate resolution sensor, the Visible/Infrared Imager/Radiometer Suite (VIIRS), is scheduled to fly on the National Polar-orbiting Operational Environmental Satellite System (NPOESS) Preparatory Project (NPP), expected to launch in October 2011, and subsequently on successive NPOESS platforms. The VIIRS instrument will transition much of the capability of the experimental MODIS instruments into the operational domain, a critical step for the land remote sensing community. This chapter provides the background to the current state of moderate resolution land remote sensing, and a description of the VIIRS instrument and the associated Environmental Data Records for the land surface. The VIIRS sensor and product similarities and differences with MODIS are described. The challenges in meeting the future needs for moderate resolution land remote sensing are discussed.

34.1 The Origins of Moderate Resolution Land Remote Sensing: The AVHRR

The origins of moderate resolution land remote sensing date back to the early 1980s. The term “moderate resolution” is used here to describe sensors with a nominal spatial resolution between 4 km and 250 m, although recent usage refers

C. Justice (✉)

Department of Geography, University of Maryland, College Park, MD 20742, USA
e-mail: justice@hermes.geog.umd.edu

to such a range as coarse resolution, and 30 m (e.g., Landsat) resolution as moderate. Extending methods developed using ground-based, handheld radiometry to assess total dry matter accumulation, Jim Tucker and colleagues at the NASA Goddard Space Flight Center (GSFC) sought satellite systems with the appropriate temporal resolution and spectral bands for vegetation monitoring. Although not designed for land remote sensing, the NOAA series of operational polar orbiters were the only available sensors with the appropriate temporal resolution at a global scale (4 km Global Area Coverage [GAC]). For some regions 1 km data were collected as Local Area Coverage (LAC) but coverage was constrained by limited capacity of the onboard tape recorders. One-kilometer data were also collected in High Resolution Picture Transmission (HRPT) mode by a number of ground receiving stations. Although Geostationary Operational Environmental Satellite (GOES) data were available with a finer temporal resolution, the coverage was regional, and the near infrared sensors were not available.

Daily NOAA AVHRR vegetation index data were initially investigated to study grassland production (Tucker et al. 1978, 1983). The importance of these time-series data to study global vegetation phenology was recognized by the Global Inventory Monitoring and Modeling Studies (GIMMS) group at GSFC (Justice et al. 1985), and the temporal characteristics of vegetation were used to initiate new approaches to vegetation classification (Townshend et al. 1987, 1991). Other groups evaluated the utility of AVHRR data for vegetation studies and fire detection (e.g. Norwine and Greigor 1983; Muirhead and Cracknell 1985), and investigated various sensor and observation characteristics (e.g. Duggin and Piwinski 1984).

Although there have been some minor modifications to the AVHRR design, the current AVHRR/3 includes two shortwave reflective bands (covering red and NIR spectral space), two thermal infrared (IR) bands (optimized for cloud detection and surface temperature retrieval) and one mid-IR band. The AVHRR samples at 1.1 km resolution at nadir, but pixel size increases markedly with increasing off-nadir view angle over the ~3,400 km ground swath (2,048 samples per scan line). The sensor has an onboard blackbody for thermal IR band calibration, but no onboard calibration system for shortwave or mid-IR bands. Samples are converted to 10-bit data records. Estimated signal-to-noise values are about 38:1 for shortwave bands (Smith and Curran 1996), and about 3:1 (at 0.5% albedo) for thermal IR bands. The latter provides a noise-equivalent change (δ) in temperature (NEDT) of 0.12 K (at 300 K). The sensor flies on both morning (nominally 07:30 h, descending node) and afternoon (nominally between 13:40 and 14:30 h, ascending node) polar orbiters, however traditionally, the land community has relied most on the afternoon data, which provides increased daylight coverage at high latitudes.

As remote sensing science evolved, the limitations imposed by the AVHRR were recognized and the requirements for future moderate resolution land observation became clearer. Earth's land surface heterogeneity requires that sensors have relatively high spatial resolution and a wide swath to provide daily observations, which increase the opportunity for cloud-free observations. A high dynamic range is needed to allow precise radiometry over bright deserts and snowpacks, as well as dark lakes, forests and plowed fields in shortwave bands, and over hot fires and frozen tundra in

the middle and thermal IR bands. Sophisticated retrieval algorithms require sampling of key environmental absorption and scattering features in carefully positioned, narrow spectral band pass instruments. Further, surface topography and vegetation's three-dimensional structure, combined with changing Sun and sensor positions relative to a target, impart significant angular variability in wide-swath observations. Thus, stable satellite platforms and orbits are required for accurate and consistent parameter retrieval. Continuous calibration measurements are needed as sensor degradation increases measurement uncertainty with time. Vicarious field calibration efforts provide some relief, but are costly, episodic, and imperfect. Finally, signal contamination from clouds, atmospheric gases and aerosols varies at high frequency in time and space, and is difficult to quantify without dedicated spectral bands.

NASA initiated a program of moderate resolution research in the late 1980s to address these issues (e.g. Holben 1986; Justice et al. 1991; Vermote and Kaufman 1995). For example, assuming surface characteristics generally change slowly as compared to atmospheric processes, temporal compositing algorithms can provide datasets that are largely cloud-free, atmospherically clear, emphasizing near-nadir view angle geometries, typically within 8–30 days. The term temporal compositing is used to describe the combination of multi-date images into a single composite image. Atmospheric correction procedures were also developed to remove atmospheric contamination of the surface reflectance retrievals (Vermote et al. 1997; Roger and Vermote 1998).

The operational status of the AVHRR was fortuitous, and as a result, long-term data records were developed and refined (Tucker et al. 2005; El Saleous et al. 2000). These records consist of data from the afternoon (c. 2.30 pm) instruments, starting with NOAA-7 in 1981. The afternoon observations permit a greater number of daylight observations during the year. The use of data from multiple satellites in developing a consistent data record created an additional set of problems associated with instrument cross-calibration and the orbital drift of the NOAA satellites (Kaufman et al. 2000). The orbital drift resulted in a progressively later equatorial-crossing time as the satellite aged. Researchers have developed internally consistent long-term records of land variables from the AVHRR through systematic vicarious calibration (Vermote and Kaufman 1995). Processing these calibrated data with customized algorithms has resulted in a number of geophysical products ranging from atmospherically-corrected surface reflectance to broadband albedo, fire and burned area, leaf area index and absorbed radiation, and land surface temperature (LST). Cracknell (2001) provides a comprehensive review of the AVHRR and its uses.

AVHRR data systems were developed in parallel, with NASA providing products to the Earth Systems science community, and NOAA providing products to operational users (Gutman and Ignatov 1995). In addition, "real-time" data needs were met by the direct broadcast capabilities of the NOAA orbiters. These HRPT (or full resolution) data are broadcast continuously from the satellite, and are available to any configured receiving station. Initial experimental stations led to dedicated, low-cost antennas and processing units available from commercial vendors. The success and popularity of direct broadcast technology with the AVHRR led to its implementation for MODIS and inclusion for the VIIRS.

The pioneering developments with the AVHRR, the heightened attention to Earth System science and the advances in space technologies, led NASA to include the MODIS as part of its Earth Observing System (EOS) (Barnes et al. 1998). Although the major improvement of MODIS over the AVHRR was immediately obvious, NOAA continues to operate the AVHRRs, providing service to the operational communities, especially in weather forecasting. Nevertheless, the MODIS–AVHRR measurement overlap is particularly beneficial to the climate community since sensor-to-sensor comparisons allow retroactive AVHRR calibration, product evaluation, and validation. The last AVHRR in the NOAA series is scheduled for launch on NOAA N' in 2009, and should provide afternoon data through 2012. The Initial Joint Polar System developed by NOAA and EUMETSAT adopted the AVHRR to fly on the mid-morning (9.30 am) overpass on the European METOP 1, 2 and 3 (named A, B and C respectively upon launch). The first in this series was launched in late 2006, and its successors are planned for launch in 2010 and 2015. The METOP satellites will acquire global 1 km data. This implies that the AVHRR instrument will continue to provide data through 2020, proving the value of sensors with an operational status.

34.2 Science Quality Data from the EOS MODIS Instrument

34.2.1 *Development of the MODIS*

MODIS was initially planned as one of two hyperspectral spectrometers (moderate and high resolution) each with 128 spectral channels, but as the requirements were refined by the science community, a more practical approach was taken. Incremental improvements over existing observation capabilities were preferred by the land community. The spectral bands of the Landsat Thematic Mapper, which were selected for vegetation mapping, were largely adopted for MODIS with additional bands in the middle and thermal infrared. AVHRR's temporal resolution was approximated with near-daily coverage. The primary MODIS "land" bands were assigned a 500-m resolution, which at the time was considered aggressive in terms of data volume. Two sharpening bands at 250 m for land monitoring were advocated (Townshend and Justice 1990). Ironically, these were accepted only on the grounds that they would enable the identification of sub-pixel clouds in the 1 km bands. In the early design stage, two separate MODIS instruments were planned, a nadir-pointing one for the land community, and a periodically tilting one to avoid sun-glint for the ocean color community. Costs dictated convergence to a single, multidisciplinary instrument designed to meet the needs of the ocean, land, and atmospheric communities (Salomonson et al. 1989). As a result, a number of discipline compromises occurred for band placement, signal-to-noise ratios, and dynamic range. Polarization bands were subsequently removed from the initial

design, and water vapor, cirrus cloud, and fire bands were added to arrive at the final 36-band instrument configuration (Salomonson et al. 2006).

The science quality data requirement meant that calibration was given a high priority (Guenther et al. 2002; Xiong and Barnes 2006). Like the AVHRR, the MODIS contains an onboard blackbody. However, unlike the AVHRR, the MODIS includes two onboard systems for solar reflective band calibration (both an onboard light source system and a passive solar diffuser assembly). Most land remote sensing products rely on solar reflective bands directly or indirectly (e.g. through cloud detection), hence, the MODIS onboard calibration has significantly increased land product accuracy and long-term measurement stability.

The first MODIS was launched into a 10.30 am orbit on the EOS Terra platform in December 1999, followed by its successor on the EOS Aqua platform in May 2002 with a 1.30 pm overpass. Together, these instruments provide at least four observations per day at most earth locations. Unlike the operational NOAA series of satellites, the EOS platforms have advanced orbit and attitude control systems, which have eliminated recessing orbital overpasses, and reduced sub-pixel geolocation errors to sub-pixel values of better than 50 m at nadir for MODIS vs. several km for AVHRR (Wolfe et al. 2002). The MODIS Science Team was selected to develop algorithms to generate MODIS standard products to meet the needs of the NASA science community (Running et al. 1994; Justice et al. 1998). Algorithm Theoretical Basis Documents (ATBD) for each product were peer-reviewed, and provided the basis for the MODIS Standard Land Data Products covering a range of environmental variables (Table 34.1). The MODIS team members were explicitly tasked to determine the accuracy of their products, and a system was developed to characterize the level of product validation (Morisette et al. 2002).

34.2.2 The MODIS Data System

The EOS Data and Information System (EOSDIS) was initially designed as an end-to-end system to provide data from multiple instruments to a wide range of users. The system had a complex set of requirements and data dependencies, with distributed processing and archiving. Problems with the system design and delivery resulted in the rapid development of a science team-led, emergency back-up system for MODIS product generation (MEBS) 1 year before Terra's launch (Masuoka et al. in this volume). This emergency back-up system became the at-launch production system (MODAPS) for level-2 and -3 data products (Justice et al. 2002a). A land data operational product evaluation (LDOPE) system was implemented to undertake routine quality assessment (QA) and coordinate the QA efforts of the science team (Roy et al. 2002). The NASA GSFC Distributed Active Archive Center (DAAC) distributed the MODIS level-1 data (geolocated top-of-atmosphere measurements in physical units). The level-2 and -3 land products

Table 34.1 The MODIS standard products, the land EDRs and their associated performance metrics

| EDR | Horizontal cell size (nadir) (km) | Precision | Accuracy | Uncertainty |
|-------------------------------------|-----------------------------------|-------------------|---------------------------|------------------------------------------------------|
| Land surface temperature | 0.75 | 0.5 K | 2.4 K | N/S |
| Surface type | 1.0 | N/S | N/S | 70% (PCT) |
| Albedo | 0.75 ^a | 0.02 | 0.035 | 0.03 |
| Active fires (ARP) | 0.75 | N/S | N/S | 50 K (sub-pixel temperature) 30% (sub-pixel area) |
| Vegetation index | 0.375 ^b | 0.02 ^b | 0.016 (NDV) 0.11 (EVI) | 0.02 (TOA NDI) 0.11 (TOC EVI) |
| Surface reflectance IP ^c | 0.375 (I), 0.75 (M) | N/S | N/S | <0.01 ^d |
| Snow cover/depth | 0.4 (binary) 0.8 (% cover) | N/S | N/S | 90% (binary PCT) 10% (% cover) |

Note that additional specifications typically apply to each EDR, such as Revisit Time, Coverage, Long-Term Stability and Mapping Uncertainty; for brevity, these are not listed. Further, each EDR has associated Exclusion Conditions (e.g. high solar zenith angles) for which its specifications are relaxed. *N/S*, no value specified; *PCT*, probability of correct typing; *I*, imagery band; *M*, moderate resolution band

^aProduct is reported and delivered at 0.75 km, however the performance is specified at 4 km resolution

^bAccuracy and precision apply to NDVI only. EVI does not have these specifications

^cDerived requirements for intermediate products are not contractually binding

^dSurface reflectance IP requirements are derived as specified in VIIRS Chain Test Report – The VIIRS Land Algorithms Document, Number: D44204: 30 March 2007

(geophysical products in swath and gridded formats, respectively) were sent to the Land Processes (LP) DAAC at the USGS Earth Resources Observation and Science (EROS) Center in South Dakota for distribution, adding complexity to the data flows. The unprecedented data volumes and the dependencies between different production systems for level-0, level-1 and levels-2 and -3 data generation, resulted in a slow flow of data for the first 18 months after launch. Production often lagged acquisition by a couple of months, and up until 2 years after launch, there was insufficient computing capacity for MODAPS to generate global data from the 250 m bands (*c.* 77 GB/day). A standalone system was developed for global 250 m data production and distribution, using simple Web-based access and download tools.

Once the EOSDIS level-1 and MODAPS production had stabilized, and the full data stream was being routinely processed, the 250 m hardware was re-used to develop a MODIS Land Rapid Response System. The Rapid Response system was developed following the catastrophic forest fires in Montana in 2000, to overcome the lag between acquisition and production, and provide near real-time MODIS fire data to the U.S.

Forest Service. Its success, coupled with early challenges to produce and use standard MODIS products (e.g. swaths and tiles in unfamiliar formats and projections), evolved into a system to develop and distribute global, rapidly-produced and simplified MODIS land products, within 2–3 h of the satellite observation, catered primarily to the application-oriented user needs (Justice et al 2002b). The Rapid Response System is a standalone capability whose algorithms suit the Direct Broadcast community, which now comprise more than 100 MODIS ground receiving stations worldwide. As a result, these standalone MODIS algorithms were downloaded more than 1,500 times through 2006. Direct Broadcast stations offer a *c.* 20-min lag between acquisition and data distribution for the area covered by the antennae range, which is an important capability for hazard detection, mapping, and analysis.

The EOS mission, now considered a precursor to NPOESS, offers a number of lessons learned by the MODIS land team, which warrant consideration for future systems. They include the close involvement of the science team in the sensor, data system, and product development, the continuing algorithm improvements, the associated need to reprocess the data record multiple times during the mission life, and the advantages of rigorous QA and product validation (Townshend and Justice 2002).

34.3 NPOESS and the NPOESS Preparatory Project

In May 1994, a Space Technology Council (STC), Presidential Decision Directive was given concerning the convergence of U.S. Polar-Orbiting Operational Environmental Satellite Systems to reduce duplication of efforts in meeting common requirements. The directive stated that “the United States will seek to reduce the cost of acquiring and operating polar-orbiting environmental satellite systems, while continuing to satisfy U.S. operational requirements for data from these systems” (STC 1994). This directive tasked the Department of Commerce and the Department of Defense to integrate their programs into a single, converged, national polar-orbiting operational environmental satellite system, noting that “additional savings may be achieved by incorporating appropriate aspects of NASA’s Earth Observing System.” The Departments of Commerce, Defense and NASA were charged with creating an Integrated Program Office (IPO). In the following years, the EOS program, originally designed to provide three sequential satellites per mission (e.g. AM-1, -2, and -3) was descoped to provide just one satellite per mission. Therefore, to reduce NPOESS development risk and to provide a bridging mission from EOS to NPOESS, the IPO and NASA jointly defined the NPP. The NPP goals include providing continuing observations to study global change after EOS Terra and Aqua, and early user evaluation of NPOESS products. Measurement overlap with EOS and the final afternoon POES platform will allow intercalibration and inter-comparison critical for the development and analysis of accurate long-term records. The Visible/Infrared Imager/Radiometer Suite (VIIRS) instrument is the NPOESS

follow-on to the MODIS instrument, and scheduled for inclusion on the NPP Mission (Murphy et al. 2001).

In 1996, a Joint Agency Requirements Group (JARG) was tasked to define the operational requirements for NPOESS. The resulting Integrated Operational Requirements Document (IORD) defines the types and specifications of both required and desired land, ocean and atmospheric products, known as Environmental Data Records (EDR) for the NPOESS, and thereby helped guide commercial sensor vendors in their designs. In February 1996, a meeting was organized at the University of Maryland by NOAA NESDIS to identify the climate measurement requirements for the NPOESS (Jacobowitz 1997). The workshop reviewed IORD-I and where appropriate, recommended changes to the requirements. The land variables considered were LST, surface soil moisture, normalized difference vegetation index (NDVI), snow cover and depth, and vegetation surface type. Broad recommendations from this workshop included the need to establish science-centered teams to provide research support for the climate mission; institute continuing participation and review by the climate user and research community, develop a strategy to blend current space-based climate information, and perform periodic reprocessing of the entire NPOESS dataset as algorithms are improved. The most recent requirements document IORD-II validated in 2002, identifies 55 EDRs, 25 of which VIIRS will generate, some of which will support EDRs made by other instruments (Murphy 2006). The five VIIRS land EDRs are albedo, land surface type, LST, vegetation index and active fires. Additionally, there are three cryosphere products, namely, ice surface temperature, sea ice characterization, and snow cover/depth. The cryosphere products are not discussed in this chapter.

In reviewing the NPOESS requirements, the National Research Council's, Committee on Earth Sciences recognized that the proposed EDRs, designed primarily for the operational weather community, would not satisfy the needs of the science community, and identified the need for additional climate data records (CDR) to meet the needs of the climate and global change research community (NRC 2000). In 2003, NASA established a NPP Science Team with scientists funded by 3-year research grants initially to evaluate the utility of the EDRs for NASA science, and assist in defining the required data system and climate data products. This team complemented the IPO-formulated Operational Algorithm Teams (OATS), tasked with providing technical advice to the IPO on algorithm and product issues. The IPO further funded Intergovernmental Studies (IGS) for targeted development beyond that of the primary contractors. Nevertheless, these groups function outside of the prime NPOESS contract, and thus their roles are limited to offering advice and analyses.

The VIIRS instrument vendor and design were announced in late 2000, and its Critical Design Review was completed in early 2002. NPP is currently expected to launch in October 2011 and will have a 13:30 (ascending node) overpass. The instrument has 21 bands from 412 to 11.50 nm, distributed on four focal plane assemblies, and a Day-Night Band (broad bandpass) centered at 700 nm on its own assembly (see Table 34.2). The VIIRS instrument and design philosophy are described by Murphy et al. (2006).

Table 34.2 VIIRS spectral bands as compared to other Vis/IR instruments

| VIIRS | | MODIS equivalent | | | AVHRR-3 equivalent | | | OLS equivalent | | | |
|-------|---------------|------------------|------|---------------|--------------------|------|---------------|----------------|------|---------------|-------|
| Band | Range (µm) | HSR (m) | Band | Range | HSR | Band | Range | HSR | Band | Range | HSR |
| DNB | 0.500–0.900 | | | | | | | | HRD | 0.580–0.910 | 550 |
| M1 | 0.402–0.422 | 750 | 8 | 0.405–0.420 | 1,000 | | | | PMT | 0.510–0.860 | 2,700 |
| M2 | 0.436–0.454 | 750 | 9 | 0.438–0.448 | 1,000 | | | | | | |
| M3 | 0.478–0.498 | 750 | 3 | 0.459–0.479 | 500 | | | | | | |
| M4 | 0.545–0.565 | 750 | 10 | 0.483–0.493 | 1,000 | | | | | | |
| | | | 4 | 0.545–0.565 | 500 | | | | | | |
| | | | 12 | 0.546–0.556 | 1,000 | | | | | | |
| I1 | 0.600–0.680 | 375 | 1 | 0.620–0.670 | 250 | 1 | 0.572–0.703 | 1,100 | | | |
| M5 | 0.662–0.682 | 750 | 13 | 0.662–0.672 | 1,000 | 1 | 0.572–0.703 | 1,100 | | | |
| | | | 14 | 0.673–0.683 | 1,000 | | | | | | |
| M6 | 0.739–0.754 | 750 | 15 | 0.743–0.753 | 1,000 | | | | | | |
| I2 | 0.846–0.885 | 375 | 2 | 0.841–0.876 | 250 | 2 | 0.720–1.000 | 1,100 | | | |
| M7 | 0.846–0.885 | 750 | 16 | 0.862–0.877 | 1,000 | 2 | 0.720–1.000 | 1,100 | | | |
| M8 | 1.230–1.250 | 750 | 5 | SAME | 500 | | | | | | |
| M9 | 1.371–1.386 | 750 | 26 | 1.360–1.390 | 1,000 | | | | | | |
| I3 | 1.580–1.640 | 375 | 6 | 1.628–1.652 | 500 | | | | | | |
| M10 | 1.580–1.640 | 750 | 6 | 1.628–1.652 | 500 | 3a | SAME | 1,100 | | | |
| M11 | 2.225–2.275 | 750 | 7 | 2.105–2.155 | 500 | | | | | | |
| I4 | 3.550–3.930 | 375 | 20 | 3.660–3.840 | 1,000 | 3b | SAME | 1,100 | | | |
| M12 | 3.660–3.840 | 750 | 20 | SAME | 1,000 | 3b | 3.550–3.930 | 1,100 | | | |
| M13 | 3.973–4.128 | 750 | 21 | 3.929–3.989 | 1,000 | | | | | | |
| | | | 22 | 3.929–3.989 | 1,000 | | | | | | |
| | | | 23 | 4.020–4.080 | 1,000 | | | | | | |
| M14 | 8.400–8.700 | 750 | 29 | SAME | 1,000 | | | | | | |
| M15 | 10.263–11.263 | 750 | 31 | 10.780–11.280 | 1,000 | 4 | 10.300–11.300 | 1,100 | | | |
| I5 | 10.500–12.400 | 375 | 31 | 10.780–11.280 | 1,000 | 4 | 10.300–11.300 | 1,100 | HRD | 10.300–12.900 | 550 |
| | | | 32 | 11.770–12.270 | 1,000 | 5 | 11.500–12.500 | 1,100 | | | |
| M16 | 11.538–12.488 | 750 | 32 | 11.770–12.270 | 1,000 | 5 | 11.500–12.500 | 1,100 | | | |

34.4 Land Remote Sensing with VIIRS

34.4.1 The Instrument

The VIIRS instrument is considered a hybrid of three existing instruments: the Operational Linescan System (OLS), AVHRR, and MODIS. The OLS is the operational visible/infrared scanner for the Department of Defense, and in non-military, land applications is used to monitor city lights and nighttime fires (Kiran Chand et al. 2006; Small et al. 2005). Its unique strengths are controlled growth in spatial resolution through use of segmented detectors and rotation of the ground instantaneous field of view (GIFOV). The AVHRR and MODIS instruments are described briefly above. These instruments have seen extensive use by their operational user communities.

The VIIRS is intended to provide moderate spatial resolution with controlled off-nadir pixel growth and a sufficient number of spectral bands to satisfy the requirements to generate accurate operational and scientific products. Figure 34.1 illustrates the VIIRS design concept. At its heart is a rotating telescope scanning mechanism that minimizes the effects of solar impingement and scattered light. The VIIRS is essentially a combination of Sea-Viewing Wide Field-of-view Sensor (SeaWiFS) fore optics and an all-reflective modification of MODIS/Thermal Emission Imaging System (THEMIS) aft-optics. Calibration is performed onboard, using a solar diffuser for short wavelengths, and a blackbody source and deep space view for thermal wavelengths. A solar diffuser stability monitor (SDSM) is included to track the performance of the solar diffuser. The VIIRS scan will extend to 56 degrees on either side of nadir, providing a swath width of approximately 3,000 km. The planned nominal altitude for NPOESS is 833 km. This will provide continuous coverage everywhere (in particular in the equatorial region). MODIS in contrast with a swath width of approximately 2,300 km has gaps in

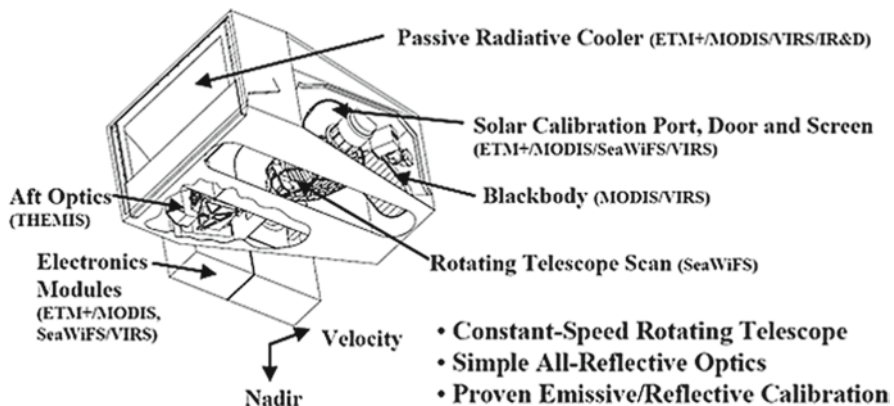


Fig. 34.1 The VIIRS design concept

daily coverage in the equatorial regions. The VIIRS will fly in both NPOESS orbits (05:30 and 13:30 equatorial-crossing times).

The VIIRS Sensor Requirements Document (IPO 2000) placed explicit requirements on spatial resolution for the Imagery EDR. This EDR, primarily designed for manually derived cloud cover mapping and sea ice characterization, provides top-of-atmosphere images for the three solar-reflective bands (both radiance and reflectance) and for the two thermal IR bands (both radiances and brightness temperatures). It also includes a daytime/nighttime visible image product that maintains apparent contrast under daytime, nighttime, and terminator region illumination conditions. Specifically, the horizontal spatial resolution (HSR) of bands used to meet threshold Imagery EDR requirements must not exceed 400 m at nadir and 800 m at the edge of the scan. This requirement led to the development of a unique scanning approach in which detectors sample at a sub-pixel resolution. Three samples are aggregated to form pixels from nadir to 32 degrees in scan angle, two detectors are aggregated to form pixels from 32 to 45 degrees, and a single sample is used per pixel from 45 degrees to the edge of scan. Although the resulting pixel size is discontinuous along a scan, it grows by a factor of only 2, both along track and along scan, compared with a growth factor of 6 along scan, which would materialize without the use of this aggregation scheme (Fig. 34.2a–c). This scanning approach will likely benefit the retrieval of land products since the VIIRS pixel's area at the edge of scan is roughly three times smaller than that of MODIS. A 1 km² nadir MODIS pixel grows to 9.7 km² at the edge of scan, whereas a moderate resolution VIIRS pixel at nadir (0.56 km²) grows to 2.25 km² at the edge of scan. However, saturation issues may pose problems, for example, in fire characterization if saturated and non-saturated pixels are aggregated but not flagged. The remaining 16 spectral bands, referred to as moderate resolution bands, have a spatial resolution of ~750 m at nadir, and likewise, feature constrained pixel growth with scan angle. The full spectral band set used for VIIRS (16 moderate resolution bands and 5 image resolution bands) is similar to MODIS. Table 34.2 provides a synoptic summary of the similarities and differences between the heritage sensors (MODIS, AVHRR, and OLS) and VIIRS. The idealized spectral response of the VIIRS “M” and “I” bands are illustrated in Figs. 34.3–34.6. These figures also illustrate generic spectral characteristics of the atmosphere and surface, which in part explains the location of the VIIRS bands.

34.4.2 The VIIRS Land EDRs and Intermediate Products

Three types of standard products are planned for routine archival by the NPOESS data system, including raw data records (RDR), which consist of the raw instrument observations in sensor count units, sensor data records (SDR), which provide calibrated geolocated values in physical units (e.g. radiance and reflectance), and environmental data records (EDR), which provide higher-level geophysical parameters (e.g. vegetation indices, surface albedo). Non-standard intermediate products (IP) are also generated, and in some limited cases, archived. IPs are usually necessary,

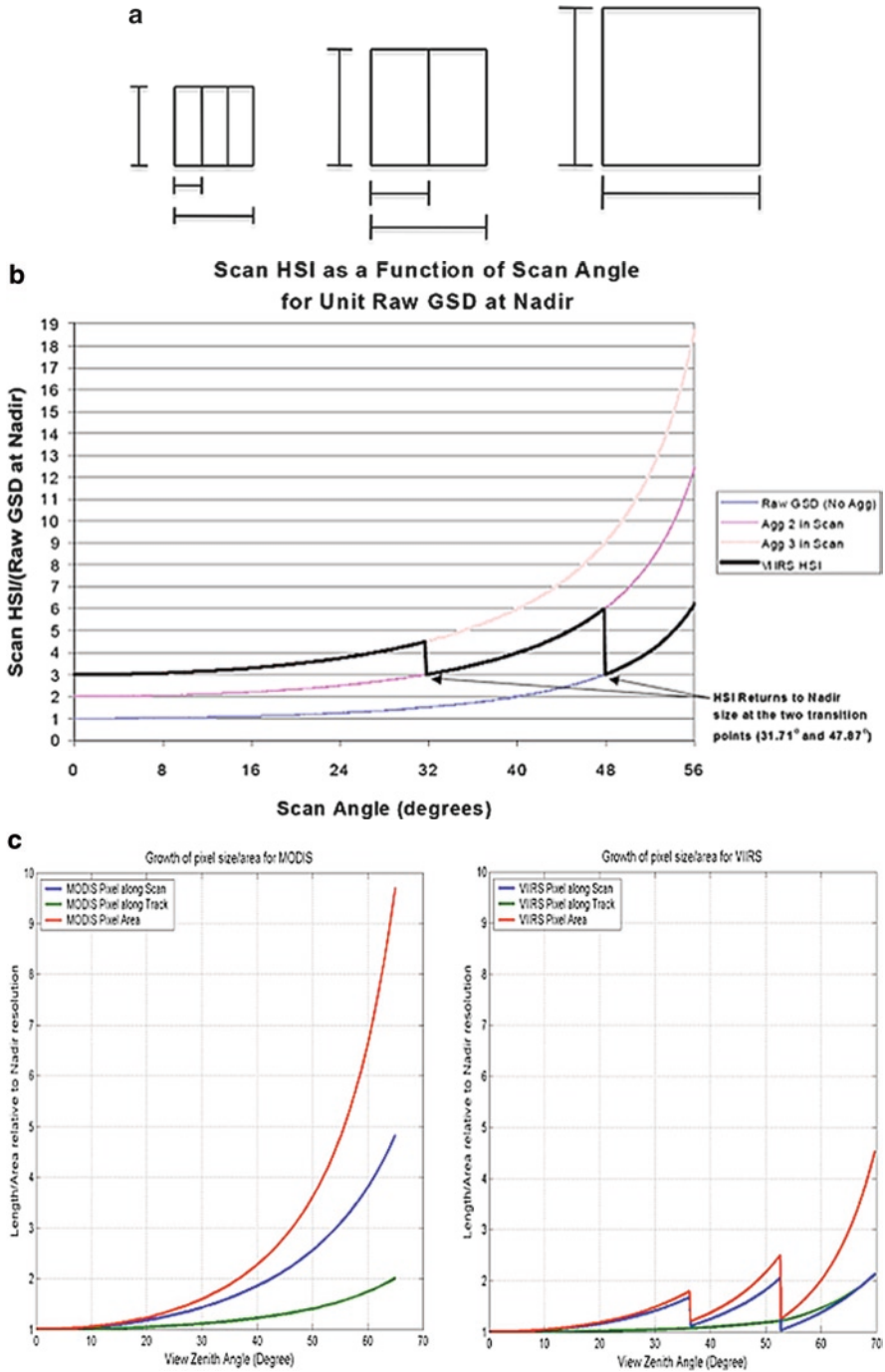


Fig. 34.2 (a) VIIRS detector footprint aggregation scheme for building “pixels.” (b) The VIIRS aggregation scheme. HSI stands for horizontal sampling interval, the distance between centers of aggregated pixels along-scan. GSD is the ground sample distance between individual detector footprints. (c) Comparison of MODIS and VIIRS pixel growth as a function of view zenith angle. VIIRS increased resolution at edge of scan is apparent especially in the along scan direction and in pixel area

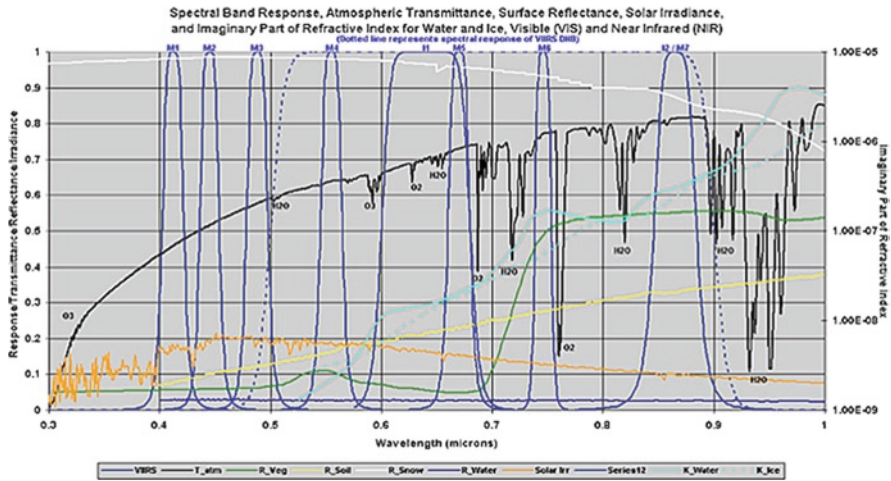


Fig. 34.3 VIIRS spectral bands; visible and near infrared

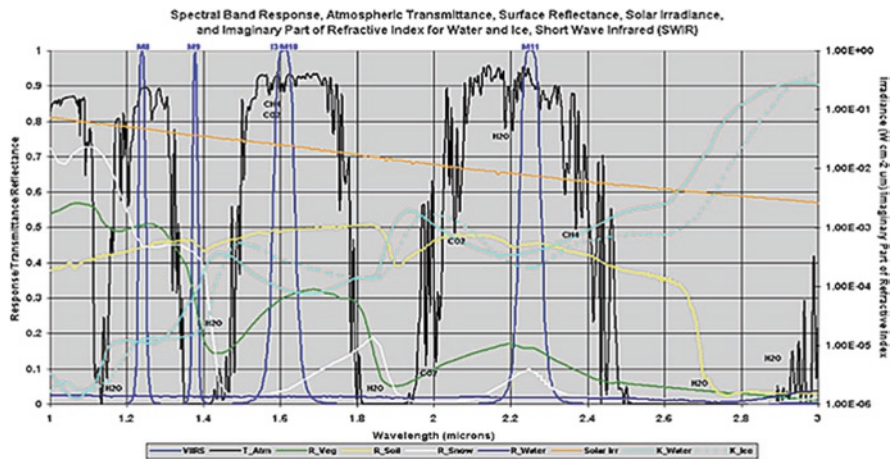


Fig. 34.4 VIIRS spectral bands; shortwave infrared

temporary inputs to produce the land EDRs. For instance, the surface reflectance is required to produce the top-of-canopy enhanced vegetation index (TOC EVI), which is part of the vegetation index EDR. EDRs and IPs will constitute the land parameters, however IPs have no performance requirements, and as a result may have standard documentation, QA, and validation.

The EDR specifications are described in the NPOESS system requirements document. Most NPOESS EDRs are planned for production and archival in the swath format (unlike their AVHRR and MODIS predecessors). Each swath scene (“granule” in MODIS terminology) will equate to 85.7 s of NPP observation, which is roughly equivalent to MODIS level-2 products (Masuoka et al. in this volume).

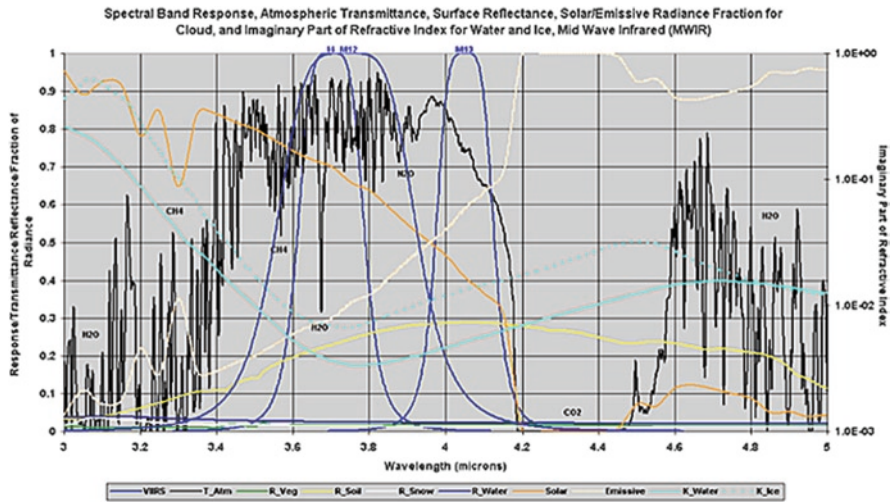


Fig. 34.5 VIIRS spectral bands; midwave infrared

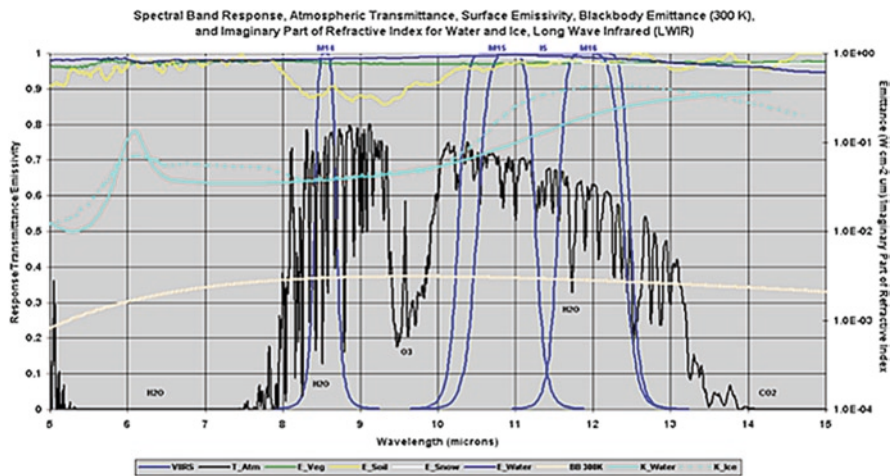


Fig. 34.6 VIIRS spectral bands, longwave infrared

This approach facilitates rapid product generation; however, it adds extra challenges for large area mapping, time-series generation, and most common data usage. As a result, the NOAA CLASS archive and distribution system is being advised to make available VIIRS granules, which are three times larger (257 s in length) and closer to the MODIS granule size.

Each EDR has performance metrics attached to them, such as spatial and temporal resolution, accuracy, precision, uncertainty, or probability of correct typing.

The land EDRs and their associated performance metrics are provided in Table 34.1. Intermediate products are not subjected to such requirements. Also, several land IPs are gridded products needed for various EDRs. For instance, a gridded land surface bidirectional reflectance is needed to produce the albedo EDR. At this time, only the Quarterly Surface Type IP is a so-called “Delivered IP” (i.e., planned for distribution and archiving using the formal NPOESS xDR protocols). The research community is currently exploring options to capture, archive, and distribute a larger set of “Retained IPs” (e.g. surface reflectance, bidirectional reflectance) via other pathways.

Northrop Grumman Space Technology (NGST) developed the algorithms for the EDRs, and at the time of writing, all the land algorithms have been converted into operational code. In most cases for the land EDRs, the early versions of the MODIS land product algorithms were used as a point of departure for algorithm development. A brief description of the land EDRs is provided below.

34.4.2.1 The Albedo EDR

The VIIRS albedo product (750 m) provides an instantaneous broadband surface albedo as collected by a ground-based sensor. This albedo is determined (unlike the standard MODIS-derived version) as the ratio of surface-scattered radiation to the ambient irradiance (i.e. the sum of the direct and diffuse components). Therefore, this albedo is inherently a function of both the surface and atmospheric conditions, and is similar to the blue-sky albedo derived from the MODIS black- and white-sky products (Schaaf et al. 2002). The VIIRS algorithm is based on the linear kernel inversion approach of MODIS for dark pixels, and on a regression formula for bright pixels. In the former approach, a location’s kernel coefficients are updated each 17-day period provided a sufficient set of “good quality” data are collected. This period equates to the orbit repeat cycle of NPP/NPOESS. Spectral albedos are produced as part of the gridded albedo IP, but not archived and distributed.

34.4.2.2 The Land Surface Temperature EDR

The VIIRS LST product (750 m) provides an instantaneous angularly uncorrected estimate of the surface skin radiometric energy. The algorithm uses a unique and relatively untested dual split-window algorithm based on two pairs of adjacent bands in the mid- and thermal-infrared. This approach is intended to minimize atmospheric contamination and slightly different formulations are used for daytime vs. nighttime scenes. In sun-glint regions and as a back-up, the algorithm will utilize a single split window approach similar to heritage AVHRR and MODIS LST products (Yu et al. 2005; Pinheiro et al. 2005). Unlike the MODIS official split window algorithm, the VIIRS algorithm will use unique algorithm coefficients for each IGBP land cover class, where land cover type emissivities from laboratory and other datasets are used to derive the appropriate coefficients a priori.

34.4.2.3 Snow Cover/Depth EDR

The VIIRS snow cover EDR will contain two fields: a 400-m resolution binary map of snow presence and a 750-m resolution data field indicating the fraction of snow cover within a pixel. Following the MODIS heritage, the binary map generation will use the Normalized Difference Snow Index (NDSI) and NDVI ratios. Pixels with at least 50% snow coverage are considered snow-covered. The snow fraction field is determined by the fraction of snow-covered pixels within the coarser resolution pixel. Such an approach cannot meet the 10% uncertainty requirement; therefore, a more sophisticated method based on spectral mixing remains an option. The snow fraction product does not have an AVHRR or MODIS heritage.

34.4.2.4 The Vegetation Index EDR

The NPOESS program presently plans to provide two vegetation indices: a top-of-atmosphere NDVI and a top-of-canopy Enhanced Vegetation Index (EVI). Both are designed to provide continuity with operational NOAA AVHRR and EOS MODIS products, respectively. Both VIs are planned for production at 375 m resolution for each cloud-free pixel. The Surface Type and Cloud mask algorithms will use a 17-day composited NDVI IP. The research community, including the NPP Science Team and VIIRS Operational Algorithm Team (OAT) advocate replacing the NPOESS TOA NDVI with the top-of-canopy equivalent, and replacing the 3-band EVI with a comparable 2-band version (Huete et al. 2006). These desired changes are consistent with EOS technological advances and research findings. In particular, the new 2-band EVI is shown to contain the same biophysical information of its 3-band predecessor, yet more consistent than the 3-band EVI when transitioning from MODIS to VIIRS. Note that the 3-band EVI was designed to correct for residual atmospheric contamination present in the surface reflectance input. Thus, the diminished need for the third band (centered in blue wavelengths) is testimony to the advances in atmospheric correction achieved through the MODIS surface reflectance. Indeed, a third band now appears to add more noise than it removes (e.g. see the 0.47 μm band performance relative to others in Fig. 34.7). Despite these arguments, the final at-launch VIIRS Vegetation Index product configuration is unclear.

34.4.2.5 Surface Type EDR

The surface type EDR consists of a determination of surface types (defined as one of the 17 IGBP classes). It also includes a vegetation fraction product, which indicates the level of “greenness” of a particular pixel as compared to its yearly maximum and minimum NDVI. Precisely, the vegetation fraction F is defined as $F = (\text{NDVI} - \text{NDVI}_{\min}) / (\text{NDVI}_{\max} - \text{NDVI}_{\min})$, where NDVI is the current TOC NDVI, NDVI_{\max} the maximum TOC NDVI over the past year, and NDVI_{\min} the minimum TOC NDVI over the past year. This product has an AVHRR operational heritage,

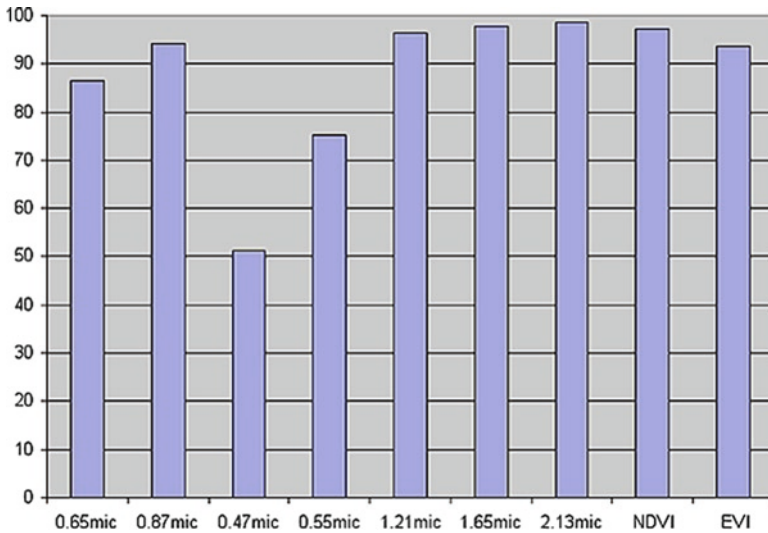


Fig. 34.7 Percentage of pixels (5,000 cases) falling within the announced accuracies (1 sigma) for MODIS Terra Collection-5 surface reflectance and Vegetation indices (statistics from http://mod09val.ltdri.org/cgi-bin/mod09_c005_public_allsites_onecollection.cgi)

but not a MODIS heritage. The VIIRS surface type is based on the quarterly surface type IP, which is similar to the MODIS land cover product (MOD12Q1). The surface type EDR basically consists of the quarterly surface type classification remapped to the swath projection (with snow-covered and fire pixels flagged), and augmented with the vegetation fraction.

The production of the gridded quarterly surface type is based on an AVHRR heritage algorithm, which uses a year's accumulation of gridded monthly values of NDVI, surface reflectance, and brightness temperature to derive the surface type classification. The classification uses a commercial decision tree classifier C5.0 (Quinlan 1993). The current MODIS approach is similar, but relies on annual profiles of raw spectral data.

34.4.2.6 Active Fire EDR

We hope that the VIIRS Active Fire EDR will provide continuity to the MODIS thermal anomalies/fire products (MOD14), which are used extensively in fire monitoring applications, and by the global change research community (Justice et al. 2002a, b; Giglio et al. 2006). The VIIRS fire detection algorithm is currently based on the MODIS version-4 algorithm (Giglio et al. 2003). Ideally, the algorithm output mask will include fire, no fire and cloud values, along with metadata on the detection quality. However, as this chapter is being written, deliberations continue regarding the final form of the VIIRS Fire product. The current specification does not call simply for a fire mask, but a characterization of the active fire by size and temperature. Given

the radiometric characteristics of the available channels, concerns persist regarding the impossibility to extract a reliable fire size and temperature estimate. Such fire characteristics are not readily retrieved from the AVHRR or MODIS (Giglio and Kendall 2001). Instead, the NASA NPP Fire group is recommending the retrieval of fire radiative power as currently generated by MODIS (Giglio et al. 2006). Additional concerns have been raised about the onboard aggregation of saturated fire pixels for the thermal infrared (11 μm) band and discussions are underway regarding the feasibility of downloading full resolution data, which allows ground processing of the fire product or flagging of aggregated pixels. The VIIRS day/night band's capability to replace the OLS for nighttime fire and smoke detection is currently being evaluated (Lee et al. 2006).

34.4.2.7 Directional Surface Reflectance: A Retained IP

The science community has strongly recommended the Directional Surface Reflectance IP, the seminal land product suite output, for formal archival and distribution. Nevertheless, it currently remains a retained IP, and its routine and permanent distribution and archiving are not assured. The availability of this product for downstream applications is crucial, because it conserves the land surface's initial core of full spectral, spatial and directional information, following removal of the atmospheric interference. Directional surface reflectance is defined as the ratio between the radiance measured in specific observation geometry (zenith and azimuth), and a direct source of illumination (zenith and azimuth) in an infinitely small solid angle. The directional surface reflectance is determined from satellite observations through the atmospheric correction process. When properly retrieved, the directional reflectance is fully decoupled from the atmospheric signal, and thus represents the value as measured in the absence of atmosphere.

The VIIRS algorithm is a direct adaptation of the one in the MODIS Collection-5. The principle of the inversion of surface directional reflectance is to rely on accurate vector radiative transfer code, 6SV (Kotchenova et al. 2006) and input atmospheric parameters to perform atmospheric correction of the top-of-the-atmosphere reflectances. Some subsequent adjustments are possible to account for the atmospheric point spread function or adjacency effects, especially for high spatial resolution bands. However, given the operational nature of the VIIRS products, the BRDF atmosphere coupling effect correction was not judged sufficiently mature (i.e., not supported by adequate validation) to include in the algorithm (Sei 2006).

34.4.3 VIIRS Data System and Services

The NPOESS Interface Data Processing Segment (IDPS) will provide pseudo-operational processing of mission data into SDRs, EDRs, and IPs. The civilian community will use records processed at the NOAA Satellite Operations Facility

(NSOF) in Suitland, Maryland. The co-located Data Quality Management (DQM) subsystem will monitor, manage, trend, and resolve data product quality issues. Calibration and validation will occur both in the contractor's NPOESS System Investigator-led Processing System (NSIPS) and the IPO's co-located Government Resource for Validation and Independent Testing and Evaluation (GRAVITE). NOAA will archive and distribute all products at its National Climatic Data Center (NCDC) in Asheville, and its National Geophysical Data Center (NGDC) in Boulder using the Comprehensive Large Array-data Stewardship System (CLASS). The latter is an information technology infrastructure being developed to facilitate data ingest, storage and distribution at the Centers (NESDIS 2005). All products are planned for storage in the Hierarchical Data Format 5 (HDF 5).

The NPOESS operational data record's limited scope and quality has led NOAA and NASA to initiate projects to develop unique and/or superior products for their user and research communities. The NASA Science Data Segment (SDS) is assessing NPOESS sensor and algorithm performance and plans to improve the operational algorithms in cases, where the originals are deemed insufficient to meet NASA's research goals. A distributed set of discipline-specific Product Evaluation and Test System Elements (PEATE) are funded to conduct these evaluations. The Land PEATE is presently an augmentation of the MODIS Adaptive Processing System (MODAPS) at NASA's GSFC, and is being used by the NPP Science Team's land group to evaluate the land-related EDRs. The SDS will support NASA-funded processing centers selected to develop multi-mission, long-term climate-quality data records.

NOAA has initiated the NPOESS Data Exploitation (NDE) project to convert EDRs into tailored products matching the format, content and packaging characteristics, which its operational communities require. The project will both produce new and unique products (e.g. vegetation biophysical products) as well as conduct basic manipulations such as reprojection or gridding of standard EDRs. A demonstration project will likewise help users in the transition from POES to NPOESS, and provide software tools to facilitate NPOESS data manipulation. Its unique products and associated metadata are planned for delivery to the NOAA Long-Term Archives.

34.5 Meeting Future Moderate Resolution Land Data Needs

34.5.1 The Challenge of Transitioning from Research to Operations

In the early 1980s when the GIMMS research group started using AVHRR data, it was impossible to imagine the capabilities of the MODIS mission. Its twin instruments offer global 250 m and multiple bands at 500 m resolution selected for land monitoring. Comprehensive suites of validated global land products are available

over the Internet. It also facilitates near real-time global monitoring. The present challenge is to ensure that these proven MODIS advancements are secured for the long term, and we continue to improve the operational systems to address new scientific and operational applications (Townshend and Justice 2002). The NPP VIIRS provides an opportunity to transition much of the MODIS capability to an operational status.

When the NPP mission was initially announced, the land community heralded the concept of a bridging mission between EOS and NPOESS, with a MODIS-like imager, with considerable enthusiasm and optimism (Townshend and Justice 2002). The tri-agency convergence of the polar orbiters, although appeared a good idea, has unfortunately proven less than optimal. Industry proprietary policies, DOD involvement, and the associated International Traffic in Arms Regulations (ITAR) restrictions have led to limited dissemination of information on the VIIRS and its algorithms. However, the algorithms and codes are posted on the tri-agency servers (CasaNOSA) and available to registered users. Deference to the operational community, especially weather forecasting, has relegated the requirements of the climate and global change science community to a lower priority. Major technical problems with the NPOESS resulted in large cost overruns. As a result, the NPP launch initially planned for 2006 is delayed until October 2011. Also, the Nunn-McCurdy provisions of the DOD acquisition regulatory process were invoked resulting in other cost cutting measures, and the elimination of the mid-morning NPOESS orbit. When appropriate, the 1.1 km resolution global AVHRR data from the EUMETSAT Metop platforms will substitute the mid-morning VIIRS data. Metop-A was launched into a 09:30 orbit in October 2006; Metop-B and -C are scheduled for launch in 2010 and 2015, respectively. As with VIIRS, the Metop mid-morning AVHRR data are scheduled for archival at NOAA Data Centers, and disseminated through CLASS within hours of observation. NOAA will also continue to generate its heritage 4-km resolution NOAA AVHRR products to assure data continuity for its operational users, and will transition to global 1 km resolution datasets over time.

The impact from the planned use of the AVHRR for the morning overpass is still unclear. MODIS studies have demonstrated that superior land products result from fusing mid-morning and mid-afternoon images, both due to lower probability of clouds and the greater diversity of sun-view geometries for albedo algorithms. Further, sampling from both orbits provide insight into land variables with strong diurnal cycles, such as surface temperature, water stress, and fire. It remains uncertain whether the mid-morning AVHRR can adequately combine with afternoon MODIS or VIIRS data. What does emerge clearly is that AVHRR data are not usable in the more sophisticated and accurate geophysical retrieval algorithms. They include the cloud mask and atmospheric correction developed for the EOS land products, and that capability for mid-morning products is potentially lost once the Terra MODIS data stream ceases.

The NPOESS EDRs were originally defined by the operational weather and military agencies, placing a high priority on rapid product generation. Even so, the EDR specifications were sufficiently stringent to initially drive a climate-quality

sensor design (NRC 2000). Indeed, in some cases, the EDR accuracy requirements exceeded previous science product accuracies. As a result, it is hoped that the RDRs and EDR algorithms will satisfy some EOS land product users. For example, the VIIRS land cover map accuracy requirements parallel those currently attained through MODIS. Moreover, EDR analyses may facilitate detection of large-scale episodic and abrupt changes in the Earth's surface (e.g. floods, major droughts, fires, etc.). However, the NASA NPP Science Team and others have largely concluded that more subtle land variability, such as gradual but persistent changes, generally associated with climate change phenomena, will likely require additional research quality calibration and geolocation. The operational and research-oriented agencies, which presently depend on MODIS data, will therefore need to develop alternative ground processing segments for VIIRS that assigns greater emphasis on product quality. We hope that the requirements of the operational land agencies and the climate research community are included in any subsequent system improvements in the future.

For the land science community, the VIIRS will undoubtedly provide extremely useful data, possibly comparable to or better than MODIS. Early attempts to improve the instrument performance specifically for land monitoring, for example by adjusting the saturation level of one of the thermal bands to enable improved fire characterization, were however rejected by competing interests from the traditional operational community. In most cases, the EDR algorithms were based on the MODIS Standard Product algorithms. In some cases, algorithm improvements recommended as a result of EOS findings were deemed unnecessary or prohibitively expensive for the VIIRS operational program.

The VIIRS EDRs are also a subset of the current MODIS land products. For example, leaf area index, net primary productivity, and burned area do not have EDR equivalents. Therefore, it behooves the science agencies, i.e. NASA and NOAA to develop additional products from the VIIRS to meet the needs of the land science community. Also, the demand for science quality data will inevitably require the reprocessing of data, for example, as radiometric calibration is better characterized, or the products are improved based on validation results. Currently, no data reprocessing requirement in NPOESS exists. Based on the MODIS experience, the accuracy assessment of the products (i.e. validation) will also require considerable effort and investment. Although the NPOESS prime contractor is required to show that the specification of the SDRs and EDRs is met, land EDR validation has received little emphasis. The MODIS mission has helped focus considerable efforts to develop and coordinate land product validation, which we hope similarly applies to VIIRS (Morissette et al. 2002; Nickeson et al. 2007).

The science agencies are particularly interested in the development of consistent long-term data records for the study of global change. The rationale for such measurements is found within the US Climate Change Science Plan and the science plans of the various participating agencies (CCSP 2003). Both NASA, through its Climate Analysis Research Systems (CARS), and NOAA, through its Scientific Data Stewardship (SDS) project, have recognized the difference between operational products and climate-quality data records. The two agencies are in the early

stages of cooperatively capturing the requisite heritage knowledge and data to develop climate data records from the early 1980s into the NPOESS era and beyond. WMO's Global Climate Observing System (GCOS 2004), and more recently, the U.S. Climate Change Science Program (CCSP) have formulated sets of essential climate variables for which CDR production is a priority (GCOS).

34.5.2 The International Dimension

Prior to the launch of Metop in 2006, the U.S. was the only provider of operational moderate resolution data, and the international community used AVHRR data widely. Since 2000, there is extensive use of NASA MODIS data and products by the international science and application communities. Other moderate resolution systems have also been launched, for example, by ESA (ATSR, AATSR, MERIS), CNES (VEGETATION) and Japan (GLI). Data from these systems are used to various degrees for land science and applications but different factors have provided obstacles to broad use of these data in the U.S., including difficulty of data access, data cost, limited calibration, lack of product validation, length of data record, and lack of direct broadcast. Over time, the respective agencies have made efforts to reduce these obstacles.

International initiatives to articulate data requirements, such as the IGBP DIS, the Global Observation of Forest Cover/Global Observation of Land Cover Dynamics (GOFC/GOLD), and the Integrated Global Observations of Land (IGOL) have identified the need for continued operational provision of science quality data and better international coordination of the moderate resolution sensing systems (Townshend et al. 1994, 2004, in this volume; Justice et al. 2003). The Global Earth Observing System of Systems (GEOSS) currently provides a focus to coordinate satellite observations, with an emphasis on societal benefits, for example, which accrues from agricultural and disaster monitoring. This could provide an opportunity for the Committee on Earth Observing Systems (CEOS) to better organize the sequence of launches to optimize data continuity, ensure overlap and cross-calibration between systems, and provide some planned redundancy. International coordination of land product validation is already underway by the CEOS Working Group on Calibration and Validation (WGCV) Land Product Validation sub-group (Morissette et al. 2002).

34.5.3 Concluding Remarks

The last two decades have witnessed the emergence and establishment of moderate resolution remote sensing. The AVHRR's operational status has enabled the development of an important long-term record with which to study global land surface changes. However, unlike Landsat, a lack of evolution in AVHRR's design results

in our use of a sensor system designed 30 years ago. In the future, improvements in operational system design should not impair their operational use. Following the recommendation of the NRC Decadal Survey (2007) and other groups, NOAA and NASA are considering reinstating the former Operational Satellite Improvement Program (OSIP) or its equivalent, to address this deficiency. The increasing demand for accurate and timely global environmental information means that moderate resolution data will continue to play an important role in both science and applications, and we need to ensure that the science quality data provided by MODIS are transitioned to NPOESS (NRC 2007). From a land perspective, operational agencies' needs, such as the USDA and USFS, must warrant inclusion in future VIIRS enhancements. The guaranteed flow of calibrated data for operational users, for example, for disaster management, or to monitor global food security, necessitates increased emphasis on operational systems, coordination of international moderate resolution assets, increased attention to timely delivery, interoperable systems, and equitable data policies. If the climate science community is to rely on NPOESS instruments for data and products, we need to emphasize long-term data quality, instrument calibration, and data reprocessing.

New areas of research continue to expand the scope and capabilities of current moderate resolution remote sensing. Development of consistent long-term records from the multi-instrument datasets present a clear challenge for the research community, which requires advances in data fusion, error budgeting, and data homogenization. The combination of moderate- (1 km–250 m) and high-resolution (50–10 m) data will provide the basis for an integrated observing system for the land community. Recent improvement in the spatial resolution of geostationary data has meant that high temporal resolution data are now being investigated for land science and applications. The development of an international network of geostationary systems for disaster management applications is one of the tasks for GEOSS. The increased swath width of the Indian Remote Sensing (IRS) Advanced Wide Field Sensor (AWiFS) operating in three spectral bands in the VNIR and one band in the SWIR with 56-m spatial resolution, results in a more frequent acquisition (several scenes per month). Application of moderate resolution time-series analysis techniques to these high-resolution data will provide a new time-series capability for terrestrial monitoring. Investments in such research and development to enhance moderate resolution sensors, products, and data distribution systems will continue to provide considerable benefits to global change research, and natural resource management applications.

References

- Barnes WL, Pagano TS, Salomonson VV (1998) Prelaunch characteristics of the moderate resolution imaging spectroradiometer (MODIS) on EOS AM1. *IEEE Trans Geosci Remote Sens* 36:1088–1100
- CCSP (2003) Strategic plan for the U.S. Climate Change Science Program. U.S. Climate Change Science Program Office, Washington DC, p 202

- Cracknell AP (2001) The exciting and totally unanticipated success of the AVHRR in applications for which it was never intended. *Adv Space Res* 28:233–240
- Duggin MJ, Piwinski D (1984) Recorded radiance indices for vegetation monitoring using NOAA AVHRR data; atmospheric and other effects in multi-temporal data sets. *Appl Opt* 23:2620
- El Saleous NZ, Vermote EF, Justice CO, Townshend JRG, Tucker CJ, Goward SN (2000) Improvements in the global biospheric record from the Advanced Very High Resolution Radiometer (AVHRR). *Int J Remote Sens* 21(6):1251–1277
- GCOS (2004) Implementation plan for the Global Observing System for Climate in support of UNFCCC. GCOS Report 92, WMO TD 1219
- Giglio L, Kendall JD (2001) Application of the Dozier retrieval to wildfire characterization: a sensitivity analysis. *Remote Sens Environ* 77:34–49
- Giglio L, Descloitres J, Justice CO, Kaufman Y (2003) An enhanced contextual fire detection algorithm for MODIS. *Remote Sens Environ* 87:273–282
- Giglio L, Csizsar I, and Justice CO (2006) Global distribution and seasonality of active fires as observed with the Terra and Aqua MODIS sensors. *J Geophys Res* 111:G02016, doi:10.1029/2005JG000142
- Guenther B, Xiong X, Salomonson VV, Barnes WL, Young J (2002) On-orbit performance of the Earth Observing System Moderate Resolution Imaging Spectroradiometer; first year of data. *Remote Sens Environ* 83:16–30
- Gutman GG, Ignatov A (1995) Global land monitoring from AVHRR: potential and limitations. *Int J Remote Sens* 16:2301–2309
- Holben BN (1986) Characteristics of maximum value composite images from temporal AVHRR data. *Int J Remote Sens* 7:1417–1434
- Huete, AR, Miura T, Kim Y, Didan K, Privette J (2006) Assessments of multisensor vegetation index dependencies with hyperspectral and tower flux data. In: Gao W, Ustin SL (eds) *Remote sensing and modeling of ecosystems for sustainability III*, Proceedings of SPIE, 6298, 1–14 0277–786X/06/\$15 doi: 10.1117/12.681382
- Integrated Program Office (IPO) (2000) Visible/Infrared Image Radiometer Suite (VIIRS) Sensor Requirements Document (SRD) for National Polar-orbiting Operational Environmental Satellite System (NPOESS) Spacecraft and Sensors. Version 2, Rev. D, Silver Spring, Maryland, 20910
- Jacobowitz H (ed) (1997) Climate measurement requirements for the National Polar Orbiting Environmental Satellite System (NPOESS). Workshop Report, February 27–29, (1996) University of Maryland, College Park, NOAA, 71
- Justice CO, Eck T, Holben BN, Tanre D (1991) The effect of water vapor on the NDVI derived for the Sahelian region from NOAA-AVHRR data. *Int J Remote Sens* 12(6):1165–1188
- Justice CO, Vermote E, Townshend JRG, Defries R, Roy DP, Hall DK, Salomonson VV, Privette JL, Riggs G, Strahler A, Lucht W, Myneni RB, Wolfe R, Knyazikhin Y, Running SW, Nemani RR, Wan Z, Huete AR, van Leeuwen W, Giglio RE, Muller J-P, Lewis P, Barnsley MJ (1998) The Moderate Resolution Imaging Spectroradiometer (MODIS): land remote sensing for global change research. *IEEE Trans Geosci Remote Sens* 36(4):1228–1249
- Justice CO, Townshend JRG, Holben BN, Tucker CJ (1985) Analysis of the phenology of global vegetation using meteorological satellite data. *Int J Remote Sens* 6(8):1272–1318
- Justice CO, Eck T, Holben BN, Tanre D (1991) The effect of water vapor on the NDVI derived for the Sahelian region from NOAA-AVHRR data. *Int J Remote Sens* 12(6):1165–1188
- Justice CO, Townshend JRG, Vermote EF, Masuoka E, Wolfe RE, El Saleous N, Roy DP, Morisette JT (2002a) An overview of MODIS Land data processing and product status. *Remote Sens Environ* 83(1–2):3–15
- Justice CO, Giglio L, Korontzi S, Owens J, Morisette JT, Roy D, Descloitres J, Alleaume S, Petitcolin F, Kaufman Y (2002b) The MODIS fire products. *Remote Sens Environ* 83(1–2):244–262
- Justice CO, Smith R, Gill M, Csizsar I (2003) Satellite-based fire monitoring: current capabilities and future directions. *Int J Wildland Fire* 12:247–258
- Kaufman YJ, Tanré D, Remer L, Vermote EF, Chu A, Holben BN (1997a) Operational remote sensing of tropospheric aerosol over land from EOS moderate resolution imaging spectroradiometer. *J Geophys Res* 102(D14):17051–17067

- Kaufman YJ, Wald AE, Remer LA, Gao B, Li R, Flynn L (1997b) The MODIS 2.1- μm channel – correlation with visible reflectance for use in remote sensing of aerosol. *IEEE Trans Geosci Remote Sens* 35(5):1286–1298
- Kaufman RK, Zhou L, Knyazikhin Y, Shabanov V, Myneni RB, Tucker CJ (2000) Effect of orbital drift and sensor changes on the time series of AVHRR vegetation index data. *IEEE Trans Geosci Remote Sens* 38:2484–2597
- Kotchenova SY, Vermote EF, Matarrese R, Klemm F (2006) Validation of a new vector version of the 6S radiative transfer code for atmospheric correction of MODIS data: Part I – Path Radiance. *Appl Opt* 45(26):6762–6774
- Kiran Chand TR, Badarinath KVS, Krishna Prasad V, Murthy MSR, Elvidge CD, Tuttle BT (2006) Monitoring forest fires over the Indian region using Defense Meteorological Satellite Program-Operational Linescan System nighttime satellite data. *Remote Sens Environ* 103(2):165–178
- Lee TE, Miller SD, Turk FJ, Schueler C, Julian R, Deyo S, Dills P, Wang S (2006) The NPOESS VIIRS day/night visible sensor. *Bull Amer Meteorol Soc* 87(2):191–199
- Masuoka E, Wolfe RE, Teague M, Saleous N, Devadiga S, Morisette J, Sinno S, Justice CO, Roy DP (2006) MODIS Land products generation, quality assurance and validation (Chapter 22 in this volume)
- Morisette JT, Privette JL, Justice CO (2002) A framework for the validation of MODIS land products. *Remote Sens Environ* 83(1–2):77–96
- Muirhead K, Cracknell AP (1985) Straw burning over Great Britain detected by AVHRR. *Int J Remote Sens* 6(5):827–833
- Murphy RE (2006) The NPOESS preparatory project. In: Qu JJ et al (eds) *Earth science satellite remote sensing Vol. 1: Science and Instruments*, Chapter 10, pp 183–198. Tsinghua University Press, and Springer, ISBN: 978-3-540-35837-4
- Murphy RE, Ardanuy P, De Luccia FJ, Clement JE, Schueler CF (2006) The visible infrared imaging radiometer suite. In Qu JJ et al (eds) *Earth science satellite remote sensing vol. 1: Science and instruments*, Chapter 3, pp 33–49, Tsinghua University Press, and Springer, ISBN: 978-3-540-35837-4
- Murphy RE, Barnes WL, Lyapustin AI, Privette J, Welsch C, De Luccia F, Swenson H, Schueler CF, Ardanuy PE, Kealey PSM (2001) Using VIIRS to provide data continuity with MODIS. *Proc IEEE Int Geosci Remote Sens Symp (IGARSS '01)* 3:1212–1214
- National Environmental Satellite, Data, and Information Service (NESDIS) (2005) *Comprehensive Large Array-data Stewardship System (CLASS): Master Project Management Plan, CLASS-1028-CLS-PLN-MPMP*. Available at <http://www.osd.noaa.gov/class/>
- National Research Council (NRC) (2000) *Issues in the integration of research and operational satellite systems for climate research. Part I: Science and Design*. National Academies Press, Washington DC, p 124
- National Research Council (NRC) (2007) *Earth Science and Applications from Space: National imperatives for the next decade and beyond*. National Academies Press, Washington DC, p 418
- Nickeson JE, Morisette JT, Privette JL, Justice CO, Wickland DE (2007) Coordinating earth observation system land validation. *EOS Trans* 88:81–82
- Norwine J, Greigor DH (1983) Vegetation classification based on Advanced Very High Resolution Radiometer (AVHRR) satellite imagery. *Remote Sens Environ* 134:69–87
- Pinheiro ACT, Privette JL, Bates JJ, Pedelty J (2005) Satellite retrieval of land surface temperature: challenges and opportunities. 20th Conference on Climate Variability and Change, American Meteorological Society
- Quinlan JR (1993) *C4.5: Programs for Machine Learning*. Morgan Kaufman Publishers Inc., San Mateo, CA
- Roger JC, Vermote EF (1998) A method to retrieve the reflectivity signature at 3.75 μm from AVHRR data. *Remote Sens Environ* 64:103–114
- Roy DP, Borak JS, Devadiga S, Wolfe RE, Descloitres J (2002) The MODIS land product quality assessment approach. *Remote Sens Environ* 83:62–76
- Running SW, Justice CO, Salomonson VV, Hall D, Barker J, Kaufman YJ, Strahler AR, Muller J-P, Vanderbilt V, Wan ZM, Teillet P, Carneggie D (1994) Terrestrial remote sensing science and algorithms planned for the MODIS-EOS. *Int J Remote Sens* 15(17):3587–3620

- Salomonson VV, Barnes WL, Maymon PW, Montgomery HE, Ostrow H (1989) MODIS: advanced facility instrument for studies of the earth as a system. *IEEE Trans Geosci Remote Sens* 27:145–153
- Salomonson VV, Barnes W, Masuoka EJ (2006) Introduction to MODIS and an overview of associated activities. In: Qu JJ et al (eds) *Earth science satellite remote sensing 1: Science and instruments*, Chapter 2, pp 12–31, Tsinghua University Press, and Springer, ISBN: 978-3-540-35837-4
- Sei A (2006) Extension of Chandrasekhar's formula to a homogeneous non-Lambertian surface and comparison with the 6S formulation. *Appl Opt* 45:1010–1022
- Schaaf CB, Gao F, Strahler AH, Lucht W, Li X, Tsang T, Strugnell N, Zhang X, Jin Y, Muller J-P, Lewis PE, Barnsley M, Hobson P, Disney M, Roberts G, Dunderdale M, dEntremont RP, Hu B, Liang S, Privette J, Roy DP (2002) First operational BRDF, Albedo and Nadir reflectance products from MODIS. *Remote Sens Environ* 83:135–148
- Small C, Pozzi F, Elvidge CD (2005) Spatial analysis of global urban extent from DMSP-OLS nighttime lights. *Remote Sens Environ* 96:277–291
- Smith GM, Curran PJ (1996) The signal-to-noise ratio (SNR) required for the estimation of foliar biochemical concentrations. *Int J Remote Sens* 17:1031–1058
- Townshend JRG, Justice CO (1990) The spatial variation of vegetation changes at very coarse scales. *Int J Remote Sens* 11(1):149–157
- Townshend JRG, Justice CO, Skole D, Malingreau JP, Cihlar J, Teilliet P, Sadowski F, Ruttenberg S (1994) The 1-km resolution global data set: needs of the International Geosphere Biosphere Programme. *Int J Remote Sens* 15(17):3417–3442
- Townshend JRG, Justice CO, Skole DL, Belward A, Janetos A, Gunawan I, Goldammer J, Lee B (2004) Meeting the goals of GFOC: an evaluation of progress and steps for the future. In Gutman G et al (eds) *Land Change Science: Observing, Monitoring and Understanding Trajectories of Change on the Earth's Surface*. Kluwer Academic Publishers, Dordrecht, The Netherlands
- Townshend JRG, Latham J, Justice CO, Janetos A, Conant R, Arino O, Balstad R, Belward A, Feuquay J, Liu J, Ojima D, Schmulilius C, Singh A, Tschirley J International coordination of satellite land observations: integrated observations of the land (Chapter 36 in this volume)
- Townshend JRG, Justice CO (2002) Towards operational monitoring of terrestrial systems by moderate-resolution remote sensing. *Remote Sens Environ* 83(1–2):351–359
- Townshend JRG, Justice CO, Kalb V (1987) Characterization and classification of South American land cover types using satellite data. *Int J Remote Sens* 8(8):1189–1207
- Townshend JRG, Justice CO, Li W, Gurney C, McManus J (1991) Global land classification by remote sensing: present capabilities and future prospects. *Remote Sens Environ* 35:243–256
- Tucker CJ (1978) A comparison of satellite sensor bands for vegetation monitoring. *Photogramm Eng Remote Sensing* 44(11):1169–1180
- Tucker CJ, Vanpraet C, Boerwinkel E, Gaston A (1983) Satellite remote sensing of total dry matter production in the Senegalese Sahel. *Remote Sens Environ* 13:461–474
- Tucker CJ, Brown ME, Pinzon JE, Slayback DA, Mahoney R, Saleous NE, Vermote EF (2005) An extended AVHRR 8-km NDVI dataset comparable with MODIS and SPOT Vegetation NDVI data. *Int J Remote Sens* 26:4485–4498
- Vermote EF, Kaufman YJ (1995) Absolute calibration of AVHRR visible and near infrared channels using ocean and cloud views. *Int J Remote Sens* 16(13):2317–2340
- Vermote EF, El Saleous N, Justice CO, Kaufman YK, Privette JL, Remer L, Roger JC, Tanre D (1997) Atmospheric correction of visible to middle infrared EOS MODIS data over land surfaces: background, operational algorithm and validation. *J Geophys Res* 102(D14):17131–17141
- Wolfe R, Nishihama M, Fleig AJ, Kuyper J, Roy DP, Storey JC, Patt F (2002) Achieving sub-pixel geolocation accuracy in support of MODIS land science. *Remote Sens Environ* 83:31–49
- Xiong X, Barnes W (2006) MODIS Calibration and Characterization. In: Qu JJ et al (eds) *Earth science satellite remote sensing Vol. II: data, computational processing and tools*, Chapter 5, pp 77–97, Tsinghua University Press, and Springer, ISBN: 978-3-540-35837-4
- Yu Y, Privette JL, Pinheiro AC (2005) Analysis of the NPOESS VIIRS land surface temperature algorithm using MODIS data. *IEEE Trans Geophys Remote Sens* 43(10):2340–2350. doi:10.1109/TGRS.2005.856114

Chapter 35

The Future of Landsat-Class Remote Sensing

Samuel Goward, Darrel Williams, Terry Arvidson, and James Irons

35.1 Introduction: Importance of Landsat-Class Observations¹

Terrestrial land patterns and processes are unique to Earth in several respects, including human domination of much that we observe (Miller 1978). The Earth's lands, oceans, and atmosphere loosely coincide with matter in solid, liquid, and gaseous states. Whereas matter in the latter two states tends to vigorously mix in the presence of energy, this planet's continents remain in fixed spatial patterns over extended periods of time – although even the continents are known to “drift” over geological time periods. This lack of turbulent mixing of land materials produces detailed patterns, both vertically and horizontally across the continents. Land surface patterns, particularly topography and disturbance processes – driven by weather, fire, and human agents – result in extreme, localized variations in land conditions and cover, at scales of meters to kilometers. Local land variations are just as extreme as one moves from the equator to the poles or from the deserts to tropical rainforest. Remotely observing land patterns and dynamics typically requires remote sensing systems capable of detecting spatial detail at better than 100 m.

At the turn of the nineteenth century a Russian geographer, Vladimir Vernadsky, first coined the term “Noösphere” to describe the pervasive impact that human

¹In this chapter, the 30 m–100 m multispectral observatories are referred to as “Landsat-class” rather than high, moderate, and/or low spatial resolution remote sensing systems. Considerable confusion and disagreement exists in the current remote sensing literature regarding adjectives that describe spatial resolution. This confusion is compounded by sensor descriptions such as the NOAA Advanced Very High Resolution Radiometer (AVHRR – a 1 to 4 km multispectral sensor) and the NASA EOS Moderate-resolution Imaging Spectroradiometer (MODIS – 250 m to 1 km sensor), which renders Landsat, a “high” spatial resolution imaging system at 30 m. In other venues, the term “moderate” spatial resolution is associated with Landsat-class systems to distinguish them from the “commercial” high spatial resolution (1–10 m) multispectral sensors such as those flown by Digital Globe and GeoEye. This latter view is reinforced within the context of the White House Office of Science and Technology Policy (OSTP) initiative to create a National Land Imaging Program NLIP (NSTC, 2007). Given these alternate views, the term Landsat-class seems less ambiguous.

S. Goward (✉)

Department of Geography, University of Maryland, College Park, MD 20742, USA

e-mail: sgoward@umd.edu

populations were beginning to assert on the Earth's land areas (Budyko 1980; Thomas 1954). The progress of the twenty-first century provides clarification that human activities not only dominate the Earth's land areas, but also the entire set of processes, which determine the Earth's dynamics and suitability as a system to support continued presence of life, including human beings (Turner et al. 1990; Foley et al. 2005). Today, as human societies struggle to understand the causes, possible mitigation, and future necessary adaptations to global change, we increasingly turn to Landsat-class observations as a means to evaluate human impacts on the Earth (Woodwell et al. 1987; Townshend et al. 1995; Skole and Tucker 1993; Loveland et al. 1991).

Human impacts-induced acceleration in land cover change necessitates the monitoring of land surface dynamics at spatio-temporal resolutions suitable enough to recognize and characterize anthropogenic actions. Land cover changes now are enhanced to materialize over annual to decadal time periods in contrast to centuries to millennia before human dominance. In addition, most land cover patterns vary seasonally under the influence of solar heating and climate variations, particularly as reflected in vegetation seasonality. Further, as human populations increasingly assert their dominance on land cover attributes, the rates of land cover change are rapidly increasing. Systematic monitoring of terrestrial dynamics requires not only detailed spatial measurements at less than 100 m, but also temporal repetition at weekly, seasonal, and annual repeat cycles. In fact, the more we learn about the temporal dynamics of clouds, the more it becomes clear that a combination of daily observations in the passive optical regions, perhaps combined with regular active microwave imaging, is needed to fully detect the spatio-temporal evolution of the Earth's land cover.

35.2 Background: Origin and Evolution of Landsat-Class Observations

The art and science of land imaging began well over a century ago when photochemical cameras were first taken aloft in hot air balloons (Colwell 1960). These cameras rapidly improved in quality, particularly during World Wars I and II. Also during World War II, new electronic "remote sensing" technologies emerged, which not only expanded the portions of the observable electromagnetic spectrum considerably, but also began to improve the quantitative properties of the acquired observations (Landgrebe 1997). The Space Age advanced land imaging as well, providing new platforms for imaging systems, although initially for intelligence gathering purposes (McDonald 1995). Further, the U.S. astronaut's efforts to photograph the Earth's land areas produced such compelling results that soon, civilian land imaging became a major potential goal of the U.S. space program (Lowman 1998). Finally, and perhaps most important, was the development of electronic – specifically digital – multispectral remote sensing technologies in the research academic community that helped convert visually interpreted imaging concepts to quantitative, multispectral concepts (Landgrebe 2005; Swain and Davis 1978). As reflected in the National

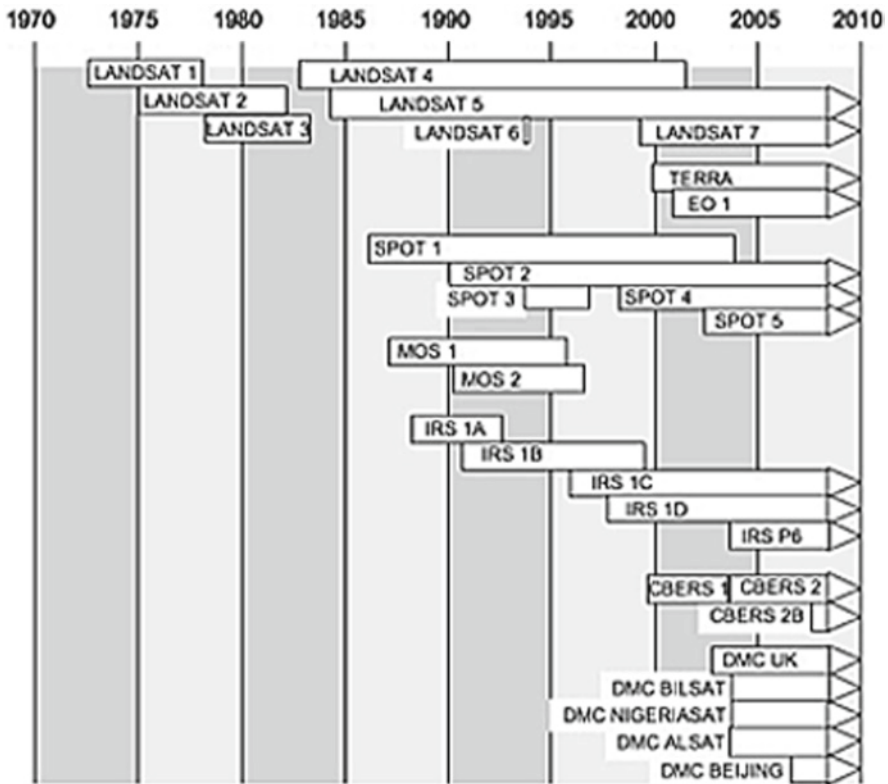


Fig. 35.1 The success of the first three Landsat missions triggered an international dash by other countries to launch their own national missions

Research Council deliberations, this early interest in civilian satellite land imaging blossomed into vigorous remote sensing activities over the last 40 years (Swain and Davis 1978; National Research Council 1969) (Fig. 35.1).

35.2.1 *Origin of Landsat Resolution Observatories*

The Landsat concept emerged from the conflicting views held regarding spaceborne land observatories by the National Aeronautics and Space Administration (NASA), Department of Interior (DOI), the U.S. Intelligence Community, and the U.S. Academic Community (academia). NASA was primarily interested in flying experimental sensor systems, as they did on the Skylab Space Station (Belew 1977). DOI’s U.S. Geological Survey (USGS) wanted a topographic mapping camera (Badgley et al. 1967). The U.S. intelligence community did not want civilian high spatial resolution land imaging (Katz 1976). Academia, along with

the U.S. Department of Agriculture, was becoming increasingly interested in multispectral radiometers (Landgrebe 2005). It was not until William Pecora (then head of the USGS) along with his boss, Interior Secretary, Stewart Udall threatened to develop a DOI-based Earth Resources Observation Satellite, that a convergence of views materialized (Pecora 1966). NASA finally agreed to develop the first experimental system dedicated to land observation – the Earth Resources Technology Satellite (ERTS). To satisfy both the mapping interests of the USGS and the digital, multispectral interests of academia, two sensors were planned for ERTS: the Return Beam Vidicon (RBV) and the Multispectral Scanner System² (MSS).

As a result of the intelligence community's objections, civil land imaging was restricted to spatial resolutions of ~100 m. This explains why many civilian land remote sensing scientists today refer to Landsat 30 m observations as “high” spatial resolution, even when compared to the newer, higher spatial resolution systems (1 m panchromatic and 4 m multispectral) such as IKONOS and Quickbird. An additional outcome of the intelligence community's spatial resolution restrictions may have been the early use of electronic RBV and MSS sensors rather than the film-return camera technology used on CORONA, although the emerging interest in digital multispectral remote sensing may have quickly trumped the persistent interest in high spatial resolution (Landgrebe 2005; McDonald 2002).

35.2.2 *Landsat Evolution*

35.2.2.1 **Sensor Technology**

The original ERTS primary sensor was the RBV, the electronic equivalent of a framing film camera, to meet the mapping requirement of the USGS. Land remote sensing researchers also pushed to include the new multispectral scanner concept, which resulted in the experimental MSS (Mika 1997). The original efforts toward a MSS pursued a six-band concept, similar to today's Thematic Mapper (TM) instrument, which proved impossible to build before the planned launch date for ERTS-1. Eighteen months prior to launch, the six-band MSS was redesigned to a four-band system to meet schedule (Hall 1992). The early successes enjoyed with the MSS – as well as an electrical failure in the RBV – resulted in the MSS quickly becoming the primary sensor on ERTS-1 and later Landsat missions.

Full development of the original MSS six-band design continued during the Landsat 1–3 era. With considerable pressure from the geological community, a seventh band – in the 2.0 μm region – was added late in the sensor development. This sensor ultimately became known as TM, the primary sensor deployed on Landsat 4 and 5. Curiously, late in the Landsat 4–5 development, the user community became so

²The original name of the MSS instrument, as proposed by Hughes Aircraft Company, was the Multispectral Scanner System. Over the years, this name was shortened to Multispectral Scanner (Norwood et al., 1972).

concerned with the increased dimensionality of the TM data stream that a “replicate” four-band MSS sensor was built and comanifested on Landsat 4 and 5 as a safety net.

Slightly more enhanced TM sensors were later developed for Landsat 6 and 7 – the Enhanced Thematic Mapper (ETM) and the Enhanced Thematic Mapper Plus (ETM+).

35.2.2.2 An Experiment in Privatization

From Space Age days, the underlying Landsat selling point was that such Landsat-class observations would have immediate “commercial value” (National Research Council 1969). This Landsat commercialization push culminated around 1979 with the transfer of the Landsat mission from NASA to the National Oceanic and Atmospheric Administration (NOAA). NOAA developed a Landsat “privatization” program and released a request for proposals in 1982. A consortium of General Electric and Hughes – EOSAT Inc. – was selected as the new commercial operator of the Landsat mission. Beginning in late 1985, the Landsat 4 and 5 satellites were operated by EOSAT – subsequently purchased by Space Imaging – under the guidance of NOAA. This government-industry experiment in privatization of government assets failed, for a multitude of reasons, leading to the passage of the Land Remote Sensing Policy Act of 1992 Public Law 102–155 (1992), with responsibility for Landsat 4 and 5 operations returned to the USGS in 2001.

The 1992 law specifically directed the government to develop Landsat 7 and also explore what future directions the U.S. might take for missions beyond 7. The Landsat 7 government management team was a moving target – starting with DoD and NASA, changing to NASA and NOAA, and ultimately changing to NASA and USGS. Fortunately, despite this management chaos, the Landsat 7 ETM+ instrument and mission profile became a stunning success (Goward et al. 2001).

35.2.2.3 Systematic Global Coverage

The ERTS visionaries – notably W. Pecora, W. Nordberg, and A. Park – had a clear sense of the value of systematic global land observations (Logsdon et al. 1998). From Landsat’s early days in 1972, there was continued, if sporadic, commitment to systematic global land monitoring. During the MSS era, early diligent efforts were undertaken – with an active ground crew of operators – to acquire as many cloud-free images on a global basis as possible, until the onboard tape recorders wore out. The tape recorders on Landsat 4 and 5 were replaced by a large Tracking and Data Relay Satellite (TDRS) antenna to relay the downlinked data to the ground. Unfortunately, the first TDRS was not operable until a year after the Landsat 4 launch. The TDRS-West satellite, needed for complete global coverage, was lost in the Challenger accident in 1986. By the time TDRS-West was launched in 1988, the government was charging EOSAT for TDRS use. In response, EOSAT reduced their acquisitions outside the continental United States to only those scenes

for which they had a paying customer. For Landsat 7, a long-term acquisition plan (LTAP) – in concert with an onboard solid-state recorder – has resulted in substantial, systematic global coverage for the first time in Landsat’s mission history (Arvidson et al. 2006). In contrast, most Landsat-class observatories operated by other nations of the world, beginning in the mid- to late 1980s, did not make a similar commitment to global monitoring.

None of these Landsat-class sensors are operated continuously, as are the lower resolution sensors such as the Moderate-resolution Imaging Spectroradiometer (MODIS) and *Système Pour l’Observation de la Terre* (SPOT) Vegetation. Further, carrying out such systematic monitoring is a nontrivial task for Landsat-class observatories. Landsat-class data rates and volumes are high. Demand for on-orbit power and heat dissipation is substantial. Some type of mission operations strategy is needed to achieve systematic monitoring goals. Finally, many of these international Landsat-class systems are frequently pointed off-nadir, to increase local repeat frequency at the expense of systematic global monitoring.

35.2.2.4 National Satellite Land Remote Sensing Data Archive

The USGS established the Earth Resources Observation System (EROS) Data Center³ in Sioux Falls, South Dakota, early in the Landsat mission, to serve as a reception station and archive for the Landsat observation record. This USGS foresight ultimately led to a decision by Congress to formally mandate – in the 1992 Land Remote Sensing Policy Act – a federally-supported national archive dedicated to Landsat and related satellite land observations. Thus, the National Satellite Land Remote Sensing Data Archive (NSLRSDA) was established. As with the Landsat mission dedication to systematic monitoring, this formal U.S. commitment to a national archive of Landsat observations is unique among the nations of the world. This decision – to preserve and maintain access to the Landsat historical record – is becoming increasingly important as our concerns with global change increase.

35.2.2.5 Landsat Spin-Offs in the United States

Two notable Landsat spin-offs flew on other U.S. missions. Japan provided the Advanced Spaceborne Thermal Emission and Reflection Radiometer (ASTER) sensor, with Landsat-class reflective band resolution (15–30 m) and five thermal IR bands at 90 m, onboard the Terra satellite that was launched in late 1999. NASA’s New Millennium Program Earth Observation 1 (EO-1) satellite, launched in 2000, was conceived as a test bed for technologies potentially useful for a future operational Landsat satellite system. In fact, the performance demonstrated by the EO-1

³The EROS Data Center in Sioux Falls, South Dakota was renamed as Earth Resources Observation and Science (EROS) Center in 2005.

Advanced Land Imager (ALI) sensor and the lessons learned from working with ALI data were directly incorporated into the requirements published for the Landsat Data Continuity Mission (LDCM, Landsat 8) Operational Land Imager (OLI) instrument.

35.2.3 *International Contributions*

Soon after Landsat images proved valuable, other nations recognized the potential of Landsat-class remote sensing:

- The French launched the first of the SPOT series of satellites in 1986.
- Japan launched the Multispectral Electronic Self-Scanning Radiometer (MESSR) aboard the first Marine Observation Satellite (MOS-1) series of satellites in 1987.
- India began its Indian Remote Sensing (IRS) series in 1988.
- By 1999, China and Brazil had launched the first of the cosponsored China/Brazil Earth Resources Satellite (CBERS) series of satellites.
- In 2002, the University of Surrey, UK launched the first of the Disaster Monitoring Constellation (DMC) satellites.

All five of these programs include sensors having 10- to 50-m spatial resolution; some also have collocated wide-field imaging sensors for more frequent, lower resolution land coverage.

Implementation policies have varied from fully government-owned to “commercial” with heavy government subsidies. None qualifies as a truly commercial Landsat-class satellite program.

35.3 Current Status of Landsat-Class Observatories

35.3.1 *United States Programs*

Two on-orbit Landsat observatories (Landsat 5 and 7) exist today in October 2008. The next observatory, the LDCM, is currently in development and projected to launch in late 2012. The USGS intends to operate the Landsat 5 and 7 missions such that they overlap, if possible, with the start of the LDCM mission.

35.3.1.1 Landsat 5

Launched in 1984 with two sensors – the MSS and the TM – and a design life of 3 years, Landsat 5 is currently in its 25th year of operations (as of March 2008). The TM sensor continues to return excellent data; however, the MSS was turned off in 1992. Given its extended mission, the satellite has experienced numerous technical problems, and the flight operations team works hard to keep the mission alive.

In 2002, the TM was transitioned to bumper mode – an alternate mode for mirror control to mitigate wear in the mirror assembly that causes calibration signals to obscure parts of the image region (http://landsat.usgs.gov/tools_BumperModeATBDV3.pdf). This wear is expected as the sensor exceeds its design life. Beyond this adjustment, the TM data continues to meet all geometric and radiometric requirements, and the International Cooperator (IC) network of ground receiving stations is actively capturing Landsat 5 TM data.

35.3.1.2 Landsat 7

Launched in 1999 with the ETM+ sensor and a 5-year design life, Landsat 7 is in its 10th year of operations. In 2003, the ETM+ sensor's scan-line corrector failed, introducing wedge-shaped gaps on each side of each image, ranging from 14 pixels at the edge to 1 pixel toward the center, and represents a loss of 22% of each image's data content. The ETM+ sensor has also been transitioned to bumper mode, as of 2007. The spacecraft subsystems are holding up well, with the primary source of concern being the gyroscopes that help maintain attitude control. One of the three gyroscopes was shut down, and implementation is underway to use onboard software to compensate for the loss of a second gyroscope, should it occur. Communications are intact and the solid state recorder is functional, despite the loss of four memory boards as of October 2008; this has reduced overall image storage capacity by 16.7%.

35.3.2 International Efforts

The importance of Landsat-class observations of the Earth is reflected in the current on-orbit assets of the international community (Table 35.1). Currently, seven programs exist with missions comparable to those of Landsat's.

35.3.2.1 Resolution, Swath Width, Spectral Bands

Current international satellite programs represent a wide range of spatial resolutions – 5.8 m (IRS-P6) to 300 m (Small Satellite Constellation for Environment and Disaster Monitoring, HJ-1B) – and swath widths – 60 km (SPOT) to 890 km (CBERS-2, -2B). But they all include the equivalent of some of the Landsat 7/LDCM spectral bands (Table 35.2). Two of the international systems have a thermal infrared (TIR) band, HJ-1B and China and Brazil's CBERS-2, but the latter sensor is currently turned off. The CBERS, SPOT, HJ-1B, and IRS systems include shortwave infrared (SWIR). All other sensors are limited to the visible and near-infrared portions of the spectrum.

Table 35.1 Current international Landsat-class observatories

| Country | China | China-Brazil | France | Germany | India | Japan | Thailand | Various ^a |
|-------------------|------------|-------------------------|---------------------|----------|---------------------|-------|----------|----------------------|
| Satellite | HJ-1A, -1B | CBERS-2,2B (ZY-2,2B) | SPOT-2,4,5 | RapidEye | IRS-1C, 1D, P6 | ALOS | THEOS | DMC |
| Launch year | 2008 | 2003, 2007 | 1990, 1998, 2002 | 2008 | 1995, 1997, 2003 | 2006 | 2008 | 2002-2005 |
| Constellation? | Yes - 2 | No | No | Yes - 5 | No | No | No | Yes - 5 |
| Pointability? | No | Yes | Yes | Yes | Yes | Yes | Yes | Yes |
| Routine pointing? | No | Yes | Yes | Yes | Yes | Yes | Yes | Yes |
| Global survey? | No | No | No | No | No | No | No | No |
| Thermal band? | Yes | Yes ^b | No | No | No | No | No | No |

^aTurkey, Algeria, Nigeria, China, UK

^bCBERS-2 sensor with thermal band is turned off

Table 35.2 Landsat 7 and LDCM spectral band specifications

| # | LDCM band <i>Landsat 7 band</i> | Minimum lower band edge (nm) | Maximum upper band edge (nm) | Center wavelength | Maximum GSD |
|---|------------------------------------|---------------------------------|---------------------------------|----------------------|----------------|
| 1 | Coastal | 433 | 453 | 443 | 30 m |
| 2 | Blue | 450 | 515 | 482 | 30 m |
| 1 | <i>Blue</i> | 450 | 520 | 485 | 30 m |
| 3 | Green | 525 | 600 | 562 | 30 m |
| 2 | <i>Green</i> | 520 | 600 | 560 | 30 m |
| 4 | Red | 630 | 680 | 655 | 30 m |
| 3 | <i>Red</i> | 630 | 680 | 655 | 30 m |
| 5 | NIR | 845 | 885 | 865 | 30 m |
| 4 | <i>NIR</i> | 760 | 900 | 830 | 30 m |
| 6 | SWIR 1 | 1560 | 1660 | 1610 | 30 m |
| 5 | <i>SWIR 1</i> | 1550 | 1750 | 1650 | 30 m |
| 7 | SWIR 2 | 2100 | 2300 | 2200 | 30 m |
| 7 | <i>SWIR 2</i> | 2080 | 2350 | 2215 | 30 m |
| 8 | Panchromatic | 500 | 680 | 590 | 15 m |
| 8 | <i>Panchromatic</i> | 500 | 900 | 700 | 15 m |
| 9 | Cirrus | 1360 | 1390 | 1375 | 30 m |

35.3.2.2 Temporal Repeat Frequency

The temporal revisit frequency of these observatories varies from greater than 46 days to daily. The daily revisits occur with the DMC satellite constellation. Some of the existing systems have been developed as constellations-of-opportunity – a result of long-lived predecessor satellites and judicious orbital placement of a new satellite, reducing the revisit time between them. The revisit time was reduced in this manner throughout the U.S. Landsat and French SPOT programs.

35.3.2.3 Global Survey Mission

In spite of a multiplicity of constellations – planned as well as opportunistic – only Landsat has specified global surveying as a mission goal. The other missions lack onboard resources in terms of storage or duty cycle, or downlink stations for a global survey.

35.3.2.4 Nadir Pointing

The potential for reduced revisit times for specific locations through pointing the sensor or satellite off-nadir has a strong appeal for many operators. However, this capability can compete with the scheduling of data collection for systematic global surveys.

35.4 Near-Future Landsat-Class Imaging Plans

35.4.1 Landsat Data Continuity Mission

The successor to Landsat 7, LDCM is currently in development as a “free-flyer” – a single dedicated satellite – with one Earth-observing sensor dubbed the OLI. The LDCM target launch date is December 2012.

NASA has the responsibility to manage the development and launch of the space segment – the spacecraft and science sensor – and to develop the control center, and systems engineering. USGS holds responsibility to develop the ground system – including a flight operations segment, a data processing, and an archive segment – and procurement of the flight operations team, and will assume responsibility for mission operations following the launch and an initial on-orbit checkout period. NSLRSDA at EROS will archive, process, and distribute OLI data to the general public.

35.4.1.1 Mission Specifications

The overarching LDCM requirement is to collect data sufficiently consistent with Landsat 7 ETM+ data in terms of the following:

- *Acquisition geometry* – Collecting data across a 185-km swath along the same ground paths followed by Landsat 7 with the same ground path repeat period of 16 days and with geolocation accuracy exceeding Landsat 7 requirements.
- *Radiometric performance and accuracy* – Providing improved radiometry in terms of signal-to-noise performance by virtue of linear detector array technology operated in the “push-broom” mode by the OLI. The ETM+, TM, and MSS sensors were all “whisk-broom” scanners. The OLI will maintain the absolute radiometric calibration standard (less than 5% uncertainty in at-aperture spectral radiance) established by ETM+ calibration. Furthermore, the image data are potentially quantized at 12 versus 8 bits for the ETM+.
- *Geographic coverage characteristics* – Achieving systematic seasonal coverage of the global land mass by employing a LTAP to schedule and archive 400 scenes each day. The acquisition plan will likely follow the Landsat 7 model.
- *Spectral and spatial characteristics* – Acquiring multispectral image data for each of the ETM+ spectral bands with the notable exception of the thermal band. In addition, the OLI will collect data for two additional spectral bands: a new blue band, principally for observing ocean color in coastal regions, and a new short-wave infrared band for detecting the presence of cirrus clouds in OLI images (Table 35.2). Spatial characteristics include 30 m for all bands except a 15 m panchromatic band.

- *Data products and product distribution* – Distributing OLI data to the general public on a nondiscriminatory basis consistent with the Landsat 7 data policy. The USGS is rapidly evolving to a policy of distributing orthorectified ETM+ data at no cost to users. The plans include producing orthorectified OLI data products in the same map projection as ETM+ data, and distributed at no cost. *This continuity allows comparisons with* earlier Landsat data to detect and quantitatively characterize changes on the global land surface.

35.4.1.2 Thermal Infrared Measurements

One real loss for LDCM, from the earlier Landsat missions, is TIR sensing. Not only do these measurements have increasing land surface applications – e.g. irrigation monitoring (Allen et al. 2005) – but they are also strongly supportive of cloud assessments. Currently, there are precious few future satellite systems that appear to include a thermal band: China’s HJ-1D with 300 m resolution and CBERS-3/4 in 2008/2010 with 80 m resolution. The primary driver for this lack of thermal capability is not demand, but rather funding. The current costs of effective TIR sensor technology are a significant portion of overall sensor costs. As of late 2008, a considerable pushback by those who routinely use Landsat TIR data has resulted in heightened Congressional interest that may result in direction to build a separate TIR-specific instrument to fly on the LDCM spacecraft. The precedent for such late addition of spectral coverage to a Landsat mission was established in the late 1970s when the geology community successfully lobbied to add band 7, the 2.2 μm band to the TM.

35.4.2 National Land Imaging Program

When ERTS-1 (Landsat-1) was launched in 1972, the proposed concept was to test this observation technology and move toward an operational system within a decade. The Landsat program has followed a tortuous path with respect to program governance since that time. The 1982 commercialization effort – when NOAA solicited private industry interest in “commercializing” the Landsat concept – was the first real effort to move toward an operational Landsat system. For a variety of reasons, the “privatization” effort failed, and in 1992, the Landsat mission was returned to the U.S. Government for continuation. Further failed steps – an additional commercialization effort and the deployment of a Landsat sensor on the NOAA National Polar-orbiting Operational Environmental Satellite System (NPOESS) – have led to a proposal from the National Science and Technology Council (NSTC) to develop a National Land Imaging Program (NLIP) (NSTC 2007). As of this date

(October 2008), the fate of a presidential election and an international financial crisis has the process on hold.

The planned 2012 launch date for the LDCM, more than 8 years past the end of the Landsat 7 design life, is symptomatic of the need to develop an operational Land Observing System. The Director of the U.S. Office of Science and Technology Policy (OSTP) – Dr. John Marburger, III – addressed this persistent challenge in a memorandum dated December 23, 2005 (OSTP 2005). He first stated that “It remains the goal of the U.S. Government to transition the Landsat program from a series of independently planned missions to a sustained operational program ...” and continued by directing that “the National Science and Technology Council, in coordination with NASA, DOI/USGS, and other agencies and EOP offices as appropriate, will lead an effort to develop a long-term plan to achieve technical, financial, and managerial stability for operational land imaging ...”

In response to Dr. Marburger’s direction, the OSTP convened and chaired an interagency working group focused on the future of land imaging. This working group released “A Plan for a National Land Imaging Program” in August 2007 (NSTC 2007). The plan recommends that the U.S. “should maintain a core operational capability to collect moderate-resolution land imagery through the procurement and launch of a series of U.S.-owned satellites” and further recommends the formation of a NLIP led by the U.S. Department of Interior. The proposed role of the NLIP is to “coordinate future civil operational moderate-resolution land imaging programs and activities with other U.S. Federal agencies through the auspices of the U.S. Group on Earth Observations (USGEO).” Note that the references to moderate-resolution images point to Landsat-class images. If the U.S. adopts these recommendations, NLIP is potentially responsible for the next Landsat satellite series.

35.4.3 *International Missions*

Six Landsat-class observatories are planned for launch in the next 5 to 6 years, four of them as new constellations or additions to existing constellations (Table 35.3, for details see Goward et al. 2009). These observatories are not expected to constitute a Global Earth Observation System of Systems (GEOSS) because, at this time, there is no coordination among them regarding data standards, observations, and the like. However, we hope that close attention is paid to any lessons learned in managing these constellations, and to establish the groundwork for future systems in terms of standards, coordination, coverage, and orbital placement. Two of the new systems, CBERS and HJ-1D, will have a thermal imaging capability. Several of the new systems – HJ-1C/-1D, Sentinel 2, CBERS-3/4 – have deliberately planned to construct a constellation, and have obtained funding for their programs based on that premise, although only Sentinel 2 has specified global surveying as a mission goal.

Table 35.3 Future international Landsat-class observatories

| Country | China | China–Brazil | Europe | India | Spain | Various ^a |
|---------------------|---------------|-----------------------|-------------------|--------|---------|----------------------|
| Satellite | HJ-1C, -1D | CBERS-3,4 (ZY-3,4) | Sentinel 2A/2B | IRS-2C | INGENIO | DMC |
| Launch year | Not available | 2008, 2010 | 2012, 2013 | 2009 | 2010 | 2008 |
| Constellation? | Yes – 4 | Yes – 3 | Yes – 2 | No | No | Yes – 8 |
| Pointability? | No | Yes | Yes | Yes | Yes | Yes |
| Routine pointing? | No | Yes | No | Yes | Yes | Yes |
| Global Survey goal? | No | No | Yes; no Antarctic | No | No | No |
| Thermal band? | Yes | Yes | No | No | No | No |

Further details on the spectral bands, swath widths, resolutions etc., are available in Chap. 9 of the SAGE Handbook of Remote Sensing (Goward et al. 2009)

^aSpain, Nigeria, UK

35.4.3.1 CBERS

China and Brazil will continue their successful CBERS series with CBERS-3 and -4, slated for launch in 2008 and 2010. The satellites are likely configured identically, with improvements to the sensors – including a TIR capability – and the ability to record all sensor data on board.

35.4.3.2 HJ-1C, -1D

China will continue to build their constellation of four optical satellites, adding one with CCD cameras and an imaging spectrometer, and one with CCD cameras and an infrared scanner with thermal band coverage; all will have onboard recorders. No announced launch date for these last two satellites of the HJ constellation is available. This program is dubbed either Huan jing-1 (HJ-1) or Environment-1. With the full constellation, equatorial revisit times are 48 h for the imaging spectrometer, and 24 h for the other sensors.

35.4.3.3 Sentinel 2

Europe's constellation, Sentinel 2, is scheduled for launch in 2012 and 2013. The mission for Sentinel 2 is declared as systematic global coverage (not including Antarctica) every 5 days at 10 m resolution. In accordance with this goal, the sensor includes heritage bands from sensors on Landsat, Environmental Satellite (ENVISAT), SPOT, LDCM, EO-1, and Terra. Attention is paid to onboard calibration. ESA has included an off-nadir pointing capability but intends to use it only in emergency situations.

35.4.3.4 IRS-2C

India will extend its IRS program with the launch of IRS-2C in 2009. As with previous IRS satellites, off-nadir pointing is planned for routine use, and global coverage is not a program goal.

35.4.3.5 INGENIO

Spain intends to launch a Landsat-class Earth remote sensing satellite, INGENIO, in 2010. The sensor will provide 10 m data, but with a 25 km swath, it will likely not provide systematic global coverage. ESA will build the satellite for Spain.

35.4.3.6 DMC

The Disaster Monitoring Constellation plans to expand with the launch of three new satellites for Spain, Nigeria, and the UK. Acquisitions are primarily targeted local to the owning country, but may include targets anywhere in response to disaster monitoring requests.

35.4.4 Global Earth Observation System of Systems and the U.S. Group on Earth Observations

A multinational group met in Washington DC in July 2003 for an Earth Observation Summit to discuss international cooperation in global monitoring of the state of our planet. In February 2005, as a result of this summit and subsequent meetings, 55 nations endorsed a 10-year plan to develop and implement a GEOSS. The concept is broad in scope, encompassing the linkage of observations from surface to satellite-borne instruments. In the U.S., a Interagency Working Group of Earth Observations involved 17 federal agencies in developing a strategy for the U.S. contributions to GEOSS, captured in a “Strategic Plan for the U.S. Integrated Earth Observation System” (NSTC 2005). The working group has since been officially established as the USGEO, a subcommittee of the National Science and Technology Council’s Committee on Environment and Natural Resources (CENR). Oversight of an NLIP may become one of the future USGEO responsibilities.

Satellite observations constitute a major component of the GEOSS concept. Those working on the implementation of GEOSS have wisely engaged the Committee on Earth Observation Satellites (CEOS) to address the coordination of Earth observations from space. CEOS is an international organization comprising 26 space agencies and 20 associated organizations that have worked together since 1984 to coordinate Earth observation satellite programs and foster the interactions

between these programs and the satellite data users worldwide. CEOS has conceived for GEOSS, the strategy to coordinate satellite constellations for different components of the Earth system. One of the concepts is called the Land Surface Imaging Constellation (Townshend et al. in this volume). If the national and international strategies come to fruition, then the NLIP will likely define the U.S. contribution to a CEOS Land Surface Imaging Constellation for the international GEOSS on behalf of USGEO.

35.4.4.1 Constellations

The RapidEye constellation, with its five member satellites evenly spaced around the orbit, provides a consistent and frequent revisit time for any point on the Earth (Fig. 35.2a, b). Another example of constellation flying⁴ is the Landsat 5/Landsat 7 constellation of opportunity, in which, the two satellites are spaced in orbit such that the single-satellite revisit time of 16 days is halved to 8 days, yet each remains true to the Landsat Worldwide Reference System. One of the goals of the GEOSS is to increase Landsat-class temporal repeat frequency through internationally-coordinated constellations. Many planned mini-constellations could potentially integrate into a GEOSS. Many nations are actively planning their contributions to the GEOSS, and some have already announced them.

35.4.4.2 Global Systematic Monitoring

The current lack of systematic acquisition capabilities across most Landsat-class observatories makes international coordination toward improved temporal-spatial coverage of Landsat-resolution land observations difficult to achieve.

35.4.4.3 Spectral Coverage

Earliest multispectral studies showed that measurements in the visible, near-infrared, SWIR, and TIR provided primary spectral information on land (Swain and Davis 1978). Maintaining consistency in Landsat-class land measurements over time requires vitally sustaining spectral coverage over extended time periods. Few of the current Landsat-class systems include the TIR portion of the spectrum,

⁴Constellation flying versus formation flying (in which the member satellites' on-orbit positions are closely coordinated) bears differentiation. An example of formation flying is the morning constellation being managed by NASA. The morning constellation satellites – Landsat 7, Terra, EO-1, and SAC-C – are flown in close proximity to each other, on identical orbits, to maximize the simultaneity of their observations. (Note: EO-1 and SAC-C have since left the constellation.) Their orbits are closely controlled, with their respective semimajor axis, eccentricity, and the argument of perigee very closely matched. The satellite control centers exchange ephemeris data, and active control is employed to maintain the formation (Kelly and Case 2004).

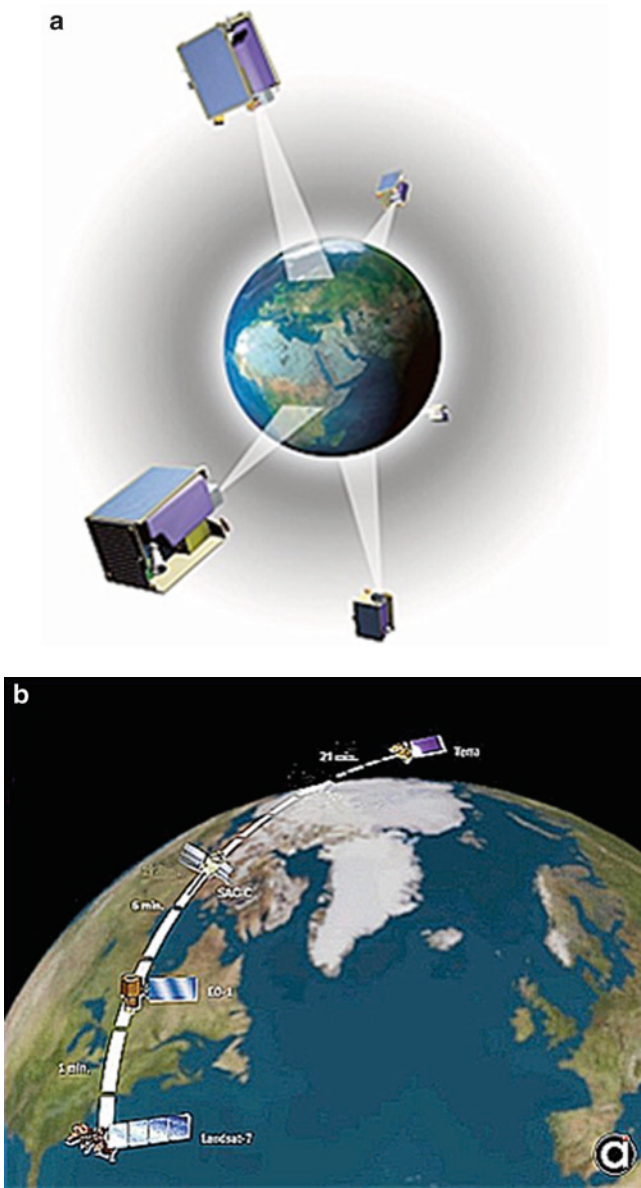


Fig. 35.2 (a) RapidEye is an example of constellation flying, with each satellite evenly spaced around the orbit. (b) NASA’s Morning Constellation is an example of formation flying, with the satellites close together to maximize coincidence of imaging

and only some include the SWIR portion. Related constraints in radiometric performance are also of concern. The best analysis results are only achievable with a 12-bit analog-to-digital signal conversion and gains that prevent saturation from all diffuse targets.

35.4.4.4 Atmospheric Attenuation

Probably the most important unresolved difficulties are in accounting for atmospheric attenuation and identifying clouds and cloud shadows. The band narrowing to avoid atmospheric absorption – introduced in MODIS – is being carried over to LDCM (Table 35.2) and Sentinel-2. In addition, new bands in the blue and SWIR regions are being introduced – again from the MODIS experience – to potentially address aerosols and cirrus contamination.

35.5 From Data to Measurements: Next Phase of Landsat-Class Remote Sensing

After nearly a half-century of experience with Landsat-class systems, there still exist several outstanding issues with these land observatories that need considerable attention. In early Landsat days, during the NASA Large Area Crop Inventory Experiment (LACIE) and the Agriculture and Resource Inventory Surveys through Aerospace and Remote Sensing (AgRISTARS) programs, only small scene subsamples were examined, simply because the computing power at that time could not handle many full scenes (NASA 1982). That constraint no longer exists with contemporary parallel computing systems. Strong evidence of these constraints comes from available statistics concerning Landsat holdings at the USGS EROS. Currently, the NSLRSDA holds over 2.5 million individual Landsat scenes; of these, only ~250 K scenes, or 10%, have ever been ordered by a user. Remaining constraints that impact the data usability include data costs, image mapping standards, and summary information products.

35.5.1 Constraints in Developing Landsat-Class Measurements

35.5.1.1 LDCM and USGS Archive Data Policy

The clear trend in providing access to the Landsat-class data record is to produce more frequent global collections such as the Global Land Survey (GLS) data (Gutman et al. 2008). The basic data policy developed for the LDCM is to provide no-cost access to the standard orthorectified image products as they are generated. This in part originates from the fact that the OLI's pushbroom technology requires processing through orthorectification to generate products with consistent internal geometry and band-to-band registration.

The USGS recently has trumped the LDCM data policy by stating that they will make all nearly cloud-free Landsat images available at no cost via orthorectified products generated to a standard formula (USGS 2008). This implies that interested users can compile local, regional, and global surveys at any annual or seasonal time step they desire. Such compilations are probably easier said than

done. The actual depth of the U.S. archive is, at many times, less than desirable (Goward et al. 2006).

35.5.1.2 Image Mapping Standards

Acquisition of Landsat-class observations is only the first phase in the production of map-quality observations of the Earth's land areas. Moving from data to measurements – getting past the details of data from a specific observatory toward being able to merge observations from various observatories into a common observation pool – is an important goal. This requires that the engineering specifics of a particular sensor do not interfere with our ability to interpret land cover conditions using observations across several sensors. In fact, this is a first step toward producing an Earth System Data Record (ESDR) (ftp://ftp.iluci.org/Land_ESDR/Land_ESDR_Whitepapers_Background.pdf). Factors such as sensor radiometry and geometry need conversion to surface reflectance in a geodetic grid to ease the comparison of observations from differing times and places. Establishing such Image Mapping Standards should remain a near-term, primary goal for satellite land remote sensing, within and beyond the GEOSS.

Image mapping characteristics to address include the following:

- Information goals
 - Spectral coverage
 - Temporal coverage
- Geodetic accuracy
 - Orthorectification
- Radiometric accuracy
 - Measurement precision
- Overall image quality
 - Noise
 - Clouds and shadows
 - Atmospheric attenuation and adjustments

Additional factors not identified here undoubtedly exist. An overall goal should aspire to enable us to produce surface spectral information, free of clouds, shadows, and atmospheric interference at a sufficient temporal repeat frequency to differentiate variations such as vegetation phenology and/or illumination conditions from dynamic long-term land cover changes. As an example, current progress in this direction is being accomplished in the Landsat Ecosystem Disturbance Adaptive Processing System (LEDAPS) and North American Forest Disturbance (NAFD) activities in support of the North American Carbon Program (NACP) (Masek et al. 2008; Goward et al. 2008a).

35.5.2 Steps Toward Landsat-Class Earth System Data Records

Government commitments to establish operational land cover monitoring systems, as defined in NLIP, that provide map-quality observations are a necessary part of capturing the true value of Landsat-class observations. Success in these endeavors moves us to the next phase in Landsat-class information, in which ESDRs of annual and seasonal global summaries of observations, pixel-level mosaicking, and blending of optical and actively-sensed datasets are practical and routine. The end-result will include measurements critical to the monitoring and policy-making required to manage global climate change. Example topics of interest include agricultural production, fresh water supply, forest disturbance and regrowth, urbanization, and glacial dynamics. In each case, accurate ESDRs of annual and seasonal dynamics are needed for accurate assessment. Only recently have efforts begun to produce annual collections of the best – cloud-free, within-season – observations produced by Landsat-class sensors.

35.5.2.1 Development of the First Decadal Datasets

In the late 1990s, Congress allocated funds to NASA in an effort to stimulate scientific use of commercially produced Earth observations data (Goward et al. 2008b). Under this program, the Earth Satellite Corporation (EarthSat) proposed to produce a three-decade, global, orthorectified set of Landsat observations – the GeoCover™ datasets. Each of these global datasets was created primarily from the Landsat sensor in use at the time: the MSS in the 1970s, the TM in 1990, and the ETM+ in 2000. The images chosen to include in these global datasets provided substantially cloud-free, orthorectified coverage, thus enabling land cover and land use change assessment across large regions with minimal preprocessing by a broad and diverse user community (Tucker et al. 2004).

35.5.2.2 Global Land Survey Datasets

Recently, NASA and USGS have undertaken an effort to increase the time density of the original GeoCover™ decadal observations under the Global Land Survey 2005 (GLS2005) activity. GLS2005 will extend the earlier multidecadal Landsat data collection to a 5-year increment rather than the previous 10-year increment. The bulk of this newest GLS dataset consists of images acquired during 2005–2006 by the Landsat 5 TM and the Landsat 7 ETM+, supplemented as needed with images acquired in 2004 and 2007 (Gutman et al. 2008).

One of the major advances under the GLS2005 effort is the revision of the digital terrain elevation data (DTED) base for orthorectification. When the original GeoCover™ sets were produced, the Shuttle Radar Topography Mission (SRTM)

data were not yet available, and older, inconsistent digital terrain models were used instead. Under contract to USGS and NASA, MDA Federal (formerly EarthSat) is now updating the earlier GeoCover™ files to incorporate the SRTM-based DTED data. The resulting datasets are renamed GLS1975, GLS1990, and GLS2000, and provide higher-quality orthorectification for time-series analysis.

35.5.2.3 International Cooperator Archives

To further complicate the compilation of global datasets, at least 50% of all the Landsat acquisitions are held in archives at IC ground stations, where the data products are probably not available at the same processing level as those from USGS, the data policy may not accommodate no-cost data availability, and product formats may differ. Given the bulk of data resident at the IC stations, there is a clear need for a set of further initiatives to capture the full potential of the global Landsat-class historical observation record, and to assure its preservation.

Current assessments reveal that whereas the U.S. archives consist of ~2 million images from 1972 to present, the IC holdings consist of 2–4 million images. The precise dimensions and overlap with the U.S. holdings is currently being assessed. To avoid the loss of the IC holdings, a major initiative to converge the U.S. and IC holdings is needed.

35.5.3 Advanced Data Processing Initiatives

Current Landsat-class data processing approaches are relatively limited when compared to what is done with lower resolution observations such as the Advanced Very-High Resolution Radiometer (AVHRR), MODIS, and SPOT Vegetation. Such a limitation occurs because of the Landsat operations, which predate most other land-focused missions. At the time, the computer processing power was simply not available to carry out second-order data enhancements such as cloud clearing through data merging.

Today, there exists potential for substantial additional processing to enhance the utility of the Landsat-class observation records.

35.5.3.1 Scene Merging with Automated Cloud and Shadow Detection

Unlike lower spatial resolution land observatories, little attention was paid to cloud “clearing” in Landsat-class observations. In part, this is because the image-compositing approach used in AVHRR and MODIS is not well suited for 16-day repeat cycle observatories – there simply are not enough temporally contiguous observations to successfully composite. On the other hand, our recent analyses of 8-day repeat

coverage from Landsat 5 and 7 over the U.S. indicate potential to frequently allow merging two scenes from near time-coincident observation periods to produce near cloud-free surface views.

This “scene merge” approach requires accurate identification of clouds and shadows in specific scenes. Experience with the Landsat 7 automated cloud cover assessment algorithm suggests that this is potentially possible (Irish et al. 2006), although this algorithm is not fully assessed at the per-pixel level – as opposed to the scene quadrant level. This challenge is probably greater in the LDCM era because there is no TIR capability in the OLI. However, this lack of a TIR band is a rather common problem in many Landsat-class observatories. A critical need to find enhanced cloud detection algorithms for all such observations is very important today. One potentially promising approach is the development of a global, seasonal, expected clear view dataset. Differencing a newly acquired scene with the expected view for the same season should highlight the clouds and cloud shadows at the pixel level.

35.5.3.2 Synthesis of Passive Optical and Active Sensor Data

One of the least advanced data processing technologies today involves the merging of Landsat-class optical and related RADAR (radio detection and ranging) and LIDAR (light detection and ranging) observations. Active remote sensing systems provide an added capability to accurately evaluate the third dimension of landscape, including vegetation height, as well as a more accurate mapping of underlying terrain.

Some areas are so persistently cloud-covered that only RADAR observations allow one to observe dynamics such as the clearing of land, and to track these activities between the availability of a cloud-free optical scene. RADAR has the great advantage of “seeing” through clouds. We desperately need methods to relate passive optical and active observations, which allow temporal extrapolation between optical clear surface views.

Much further research is needed to evaluate the relationships of active microwave and laser signals to passive optical signals, and how best to combine them to further enhance land cover research.

35.6 Possible Future Mission Goals

Several things are worth pursuing to improve the information quality extracted from current and planned Landsat-class observatories. However, as we ponder upon global initiatives such as the GEOSS, national initiatives such as the U.S.’s NLIP and China’s HJ-1 constellation, or the commercial RapidEye constellation, the primary goals of such initiatives are essential to consider up front besides the risks and expenses of taking on such endeavors.

35.6.1 *Temporal Resolution*

35.6.1.1 Constellations

As previously noted, there exist today a few observation constellations, including Landsat 5 and 7, and systems such as the DMC and RapidEye. Consider the situation in 2015, with the following planned constellations in orbit: CBERS-3/4, Sentinel 2, and HJ-1A. The data user sees an opportunistic constellation of constellations. At any point in time, potential exists for a member of one, two, or all the constellations to provide coverage of the data user's area of interest. How would a data user know which satellites are potentially in observation view? To whom are acquisition requests sent? From whom are products ordered? Is there a way to layer the products from various satellites to enhance the data user's analysis or provide a more complete characterization of the area of interest? We hope that answers to all these questions lie with GEOSS.

35.6.1.2 How Do Constellations Work?

Flying a constellation is not a trivial undertaking. Many decisions are input into the design and maintenance of the constellation, which include the following:

- *Degree of separation* – near-coincident imaging with different sensors (like train cars) or global survey with frequent revisits (equally spaced around the orbit)
- *Coordination of sensors* – provision of continuity with previous satellites (e.g. Landsat-like) or inclusion of complementary sensors (e.g. optical plus LIDAR)
- *Operational scenario* – Who will lead and dictate station-keeping activities, and who will follow? How do you incrementally build the constellation, adjust positions as new additions are made, or each element is launched into its position in final constellation configuration?
- *Dismemberment plans* – How will a constellation member leave the group? Will the satellite designs incorporate the necessary capabilities?

Management issues may need to consider political realities – crossing national or agency boundaries. Interfaces are critical, especially in formation flying, with clear and open communication lines.

35.6.1.3 Constellation Standards

Accumulating a global archive composed of data derived from various sensors requires global standards in archive access, catalog access, metadata, browse, and archive-level and product-level exchange. Some work in this area was pursued by the Landsat project across Landsat 5 and 7, with plans to extend forward with LDCM, and retrospectively with Landsat 1–4. The CEOS Working Group on

Calibration and Validation (WGCV) is also working on instrumentation standards in anticipation of an international consortium forming a land constellation observatory over the next decade (<http://wgcv.ceos.org/>).

35.6.2 Mission Costs

35.6.2.1 Smallsats

The current smallsat constellation, DMC, demonstrates the concept that small satellites that are flown as a fleet are potentially cost-effective, can provide a desirable revisit frequency, may originate from diverse international sources, and efficiently managed operationally. The recently deployed RapidEye constellation aims to prove that a commercial constellation can flourish in the remote sensing business market.

The smallsat concept engenders both benefits and drawbacks (Table 35.4). The small size that leads to lower costs and better agility may also lead to less stability and less room for recorders, sensors, and calibration equipment. However, advances in miniaturization and more efficient, space-proven storage technologies may minimize these potential drawbacks.

A mitigation approach to deal with less calibration equipment on Smallsats was proposed several years ago by one of the coauthors, Darrel Williams. Cross-calibration methodology has proven successful both within a family of satellites (Landsat 5 and 7) and between satellite families (Landsat 7 and Terra). The proposal is to include in the constellation, a well-calibrated, well-characterized instrument on a stable satellite bus – replete with calibration instrumentation – to which the smallsats are routinely cross-calibrated. This proposal provides the best of both worlds – the first-rate calibration from the larger satellite and the global coverage and frequent revisit of a smallsat constellation.

35.6.2.2 Imaging Spectrometers

One of the more aggressive pushes in Landsat-class remote sensing is to move the sensor technology from broad-band spectral measurements in primary regions of the reflective spectrum to imaging spectrometers that record effectively, continuous

Table 35.4 Potential benefits and drawbacks of Smallsats

| Potential benefits | Potential drawbacks |
|----------------------------------------------|------------------------------------------|
| Lower cost | Less stable platform |
| Shorter manufacturing schedule | Less onboard calibration |
| Easier to be agile | Newer, less mature technology |
| Easier to find manufacturing/test facilities | Harder to work on as more densely packed |
| | Less onboard storage capacity |
| | Less available power |

spectral coverage with numerous narrow spectral bands – that is, hyperspectral data, such as the data collected by the NASA AVIRIS aircraft-based sensor. One advantage of most imaging spectrometers is that the hyperspectral data are intrinsically registered band-to-band unlike data collected by whisk-broom or push-broom sensors. These hyperspectral sensors view the earth through a slit with an element such as a diffraction grating or prism spectrally dispersing the received energy across an array of detectors on a focal plane. To date, however, the optical and focal plane technologies required to collect hyperspectral data over a broad swath have not been demonstrated in space. Only a few imaging spectrometers have flown in space, and all have provided only a narrow swath. The Hyperion imaging spectrometer aboard the EO-1 satellite, for example, provides a 7.6 km swath. Technological advances are required to implement a wide-field-of-view imaging spectrometer for space flight. Beyond the technology, the question regarding the scientific and operational value of producing such a complicated data stream needs more attention.

35.7 Closing Thoughts

Over the last half century, many innovative thinkers and doers have proposed and executed global observatories of the Earth's land areas that now bring us substantial rewards in the form of understanding how the Earth's land areas have changed and continue to change.

Recent efforts under the U.S. GEO program have defined nine societal benefit areas, where remote sensing plays a major role (NSTC 2005) (Table 35.5). Landsat-class observations are critical to at least seven of the nine areas, and most likely will play an important or relevant role in the other two (weather forecasting and ocean resources).

In these early years of the twenty-first century, we are well placed to lay the groundwork for the next 25–100 years of land remote sensing. We need to accept and implement several critical steps to ensure that this observation technology is ready for use by future generations, which include the following:

1. *U.S. NLIP* – The fact that OSTP has released the NLIP planning document is a major step forward. We now need to ensure that NLIP is formulated and executed at the level needed to embrace the successes of the last half century.

Table 35.5 The U.S. Integrated Observing System strategic plan: societal benefit areas

-
1. Improve weather forecasting
 2. Reduce loss of life and property from disasters
 3. Protect and monitor our ocean resource
 4. Understand, assess, predict, mitigate, and adapt to climate variability and change
 5. Support sustainable agriculture and forestry, and combat land degradation
 6. Understand the effect of environmental factors on human health and well-being
 7. Develop the capacity to make ecological forecasts
 8. Protect and monitor water resources
 9. Monitor and manage energy resources
-

A champion for NLIP has been named – the DOI – and now we must provide the budget and the tools.

2. *U.S. GEO and GEOSS* – International collaboration for land imaging clearly remains a major component of a successful global program. No single nation should bear the full expenses of developing a global monitoring system, which benefits all. As a corollary, a critical goal to aspire is for all nations of the world to benefit from such a system. The GEOSS initiative is a critical first step as we find ways to cope with and address global change.
3. *Advanced technologies* – Landsat-class spatial *and* high temporal resolution observatories will require advanced, lower cost technologies – in the form of solid-state sensors, miniaturization, and low-cost satellites – that support the concept of an operational global land monitoring system. Such technologies are now emerging from research and industry laboratories. A supportive environment for the development and use of such technologies is needed.
4. *National mapping standards* – We have yet to apply any mapping standards corresponding to those developed for aerial photography nearly a half-century ago to satellite land observations. We now need to specify what criteria a satellite-acquired dataset must meet, to address discrete mapping goals such as land cover analysis or forest mapping. At a minimum, these standards must consider orthorectification, atmospheric adjustments, cloud and shadow clearing, and spectral consistency. Providing detailed specifications will require serious efforts to reach a consensus.
5. *Robust research program* – A significant portion of the advances that occur over the next 25–100 years will emerge from our successes in learning to exploit not only the observations we have already acquired, but also the improved observations we expect in the future. Achieving such progress requires a robust research program – one that challenges our most skilled scientists and engineers to meet our current and soon-to-evolve methodological and analytical challenges.

Acknowledgments The authors of this chapter were supported from funds provided by the Earth Science Program, Science Mission Directorate, NASA Headquarters, and a U.S. Geological Survey contract number 04CRFS0058, jointly funded by USGS and NASA. The comments from two reviewers were also of considerable assistance and much appreciated.

References

- Allen RG, Tasumi M, Morse AT, Trezza R (2005) A Landsat-based energy balance and evapotranspiration model in western US water rights regulation and planning. *J Irrigation Drainage Syst* 19:251–268
- Arvidson T, Goward SN, Gasch J, Williams DL (2006) Landsat 7 long-term acquisition plan: Development and validation. *Photogramm Eng Remote Sens* 70:1137–1146
- Badgley PC, Centers CD, Colvocoresses AP (1967) Earth resources monitoring by remote sensing from space flights by photography or multichannel scanning. American Society of Photogrammetry Annual Convention, Washington, DC

- Belew LF (ed) (1977) Skylab, our first space station. National Aeronautics and Space Administration, Washington, DC
- Budyko MI (1980) Global ecology. Progress Publishers, Moscow
- Colwell RN (ed) (1960) Manual of photographic interpretation. American Society of Photogrammetry, Washington, DC
- Foley JA, DeFries R, Asner GP, Bradford C, Bonan G, Carpenter DR, Chapin FS, Coe MT, Daily GC, Gibbs HK, Helkowski JH, Holloway T, Howard EA, Kucharik J, Monfreda C, Patz JA, Prentice IC, Ramankutty N, Snyder PK (2005) Global consequences of land use. *Science* 309:570–574
- Goward SN, Masek JG, Williams DL, Irons JR, Thompson RJ (2001) The Landsat 7 mission: Terrestrial research for the 21st century. *Remote Sens Environ* 78:3–12
- Goward SN, Arvidson T, Williams DL, Faundeen J, Irons J, Franks S (2006) Historical record of Landsat global coverage: Mission Operations, NSLRSDA, and international cooperator stations. *Photogramm Eng Remote Sens* 70:1155–1170
- Goward SN, Masek JG, Cohen W, Moisen G, Collatz GJ, Healey S, Houghton R, Huang C, Kennedy R, Law B, Powell S, Turner D, Wulder MA (2008a) Forest disturbance and North American carbon flux. *Eos Trans, AGU* 89(11):105–116
- Goward SN, Underwood LW, Fearson M, Fletcher R, Garvin J, Hurtt GC, Jensen J, Nolan M, Hoekamp K, Pagnutti M, Ryan R, Stanley T, Swearingen W (2008b) NASA's earth science use of commercially available remote sensing datasets. *Photogramm Eng Remote Sens* 74:139–146
- Goward SN, Williams DL, Arvidson T, Irons J, Irish RR (2009) Moderate spatial resolution optical sensors. In: Warner T, Nellis DN, Foody G (eds) *SAGE Handbook of Remote Sensing*, Sage, London
- Gutman G, Byrnes R, Masek J, Covington S, Justice C, Franks S, Headley R (2008) Towards monitoring land-cover and land-use changes at a global scale: The Global Land Survey 2005. *Photogramm Eng Remote Sens* 74:6–10
- Hall SS (1992) Mapping the next millennium: the discovery of new geographies. Random House, New York
- Irish RR, Barker J, Goward SN, Arvidson T (2006) Characterization of the Landsat-7 automatic cloud-cover assessment (ACCA) algorithm. *Photogramm Eng Remote Sens* 70:1179–1188
- Katz A (1976) A retrospective on earth resources surveys: arguments about technology, analysis, politics and bureaucracy. *Photogramm Eng Remote Sens* 42:189–199
- Kelly AC, Case WF (2004) Flying the earth observing constellations. *Space Ops 2004: 8th international conference on space operations*, Montreal, Canada
- Landgrebe D (1997) The evolution of Landsat data analysis. *Photogramm Eng Remote Sens* 63:859–867
- Landgrebe D (2005) Multispectral land sensing: where from, where to? *IEEE Trans Geosci Remote Sens* 43:414–421
- Logsdon JH, Launius RG, Onkst DH, Garber SJ (eds) (1998) Exploring the Unknown: Selected Documents in the History of the U.S. Civilian Space Program, vol. III – Using Space. National Aeronautics and Space Administration, NASA History Division, Washington, DC
- Loveland TR, Merchant JW, Ohlen DO, Brown JF (1991) Development of a land-cover characteristics database for the conterminous U.S. *Photogramm Eng Remote Sens* 57:1453–463
- Lowman PD Jr (1998) Landsat and Apollo: the forgotten legacy. *Photogramm Eng Remote Sens* 65:1143–1147
- Masek JG, Huang CQ, Wolfe R, Cohen W, Hall F, Kutler J, Nelson P (2008) Mapping North American forest disturbance from a Decadal Landsat Record. *Remote Sens Environ* 112:2914–2926
- McDonald RA (ed) (2002) Beyond expectations – building an American national reconnaissance capability. American Society of Photogrammetry and Remote Sensing, Bethesda, MD
- McDonald RA (1995) CORONA – Success for space reconnaissance: a look into the Cold War and a revolution for intelligence. *Photogramm Eng Remote Sens* 61:689–720
- Mika AM (1997) Three decades of Landsat instruments. *Photogramm Eng Remote Sens* 63:839–852

- Miller DH (1978) The factor of scale: Ecosystem, landscape mosaic and region. In: Hammond KA, Macinko G, Fairchild WB (eds) Sourcebook on the environment: a guide to the literature. The University of Chicago Press, Chicago, pp 63–88
- National Aeronautics and Space Administration (1982) The LACIE Symposium. Proceedings of Technical Sessions, NASA Johnson Space Center, Houston, Texas
- National Research Council (1969) Useful Applications of Earth-Oriented Satellites. National Academy of Sciences, Washington, DC
- National Science and Technology Council (2005) Strategic Plan for the U.S. Integrated Earth Observation System. National Science and Technology Council, Washington, DC
- National Science and Technology Council (2007) A Plan for a National Land Imaging Program. Office of Science and Technology Policy, Future of Land Imaging Interagency Working Group, Washington, DC
- Norwood VT, Fermelia LR, Tadler GA (1972) Multispectral Scanner System for ERTS, Four Band Scanner System: Final Report, Volume I, System Description and Performance. Space and Communications Group, Hughes Aircraft Company, Santa Barbara, CA
- OSTP (2005) Landsat Data Continuity Strategy Adjustment. Executive Office of the President, Office of Science and Technology, Washington, DC
- Pecora WT (1966) Earth Resources Observation Satellite (EROS): A Department of Interior program to utilize space-acquired data for natural and human resource management. U.S. Department of Interior, U. S. Geological Survey, Washington, DC
- Public Law (1992) Land Remote Sensing Policy Act, pp.102–555
- Skole DL, Tucker CJ (1993) Tropical deforestation and habitat fragmentation in the Amazon: Satellite data from 1978 to 1988. *Science* 260:1905–1910
- Swain PH, Davis SM (eds) (1978) Remote sensing: the quantitative approach. McGraw-Hill Book Company, New York
- Thomas WL Jr (1954) Man's Role in Changing the Face of the Earth. Univ. Chicago Press, Chicago
- Townshend J, Bell V, Desch A, Havlicek C, Justice C, Lawrence W, Skole D, Chomentowski W, Moore B III, Salas W, Tucker CJ (1995) The NASA Landsat Pathfinder Humid Tropical Deforestation Project. *Proceedings Land Satellite Information in the Next Decade, ASPRS Conference*, Vienna, Virginia
- Townshend J, Latham J, Justice C, Janetos AC, Conant R, Arino O, Balstad R, Belward AS, Feuquay J, Liu J, Ojima D, Schmullius C, Singh A, Tschirley J (2010) International coordination of satellite land observations: Integrated observations of the land. In: Ramachandran B, Justice C, Abrams M (eds) Land Remote Sensing and Global Environmental Change: NASA Earth Observing System and the Science of ASTER and MODIS. Springer, New York (in this volume)
- Tucker CJ, Grant DM, Dykstra JD (2004) NASA's global orthorectified Landsat data set. *Photogramm Eng Remote Sens* 70:313–322
- Turner BL II, Clark WC, Kates RW, Richards JF, Matthews JT, Meyer WB (eds) (1990) The earth transformed by human action: global and regional changes in the biosphere of the last 300 years. Cambridge University Press, Cambridge
- U.S. Geological Survey (2008) Imagery for everyone: Timeline set to release entire Landsat Archive at no charge. Geography Land Remote Sensing Program, Ed.: USGS Office of Communication, p 1
- Woodwell GM, Houghton RA, Stone TA, Nelson RF, Kovalick W (1987) Deforestation in the tropics: New measurements in the Amazon Basin using Landsat and NOAA advanced very high-resolution radiometer imagery. *J Geophys Res* 92:2157–2163

Chapter 36

International Coordination of Satellite Land Observations: Integrated Observations of the Land

John Townshend, John Latham, Christopher O. Justice, Anthony Janetos, Richard Conant, Olivier Arino, Roberta Balstad, Alan Belward, Jay Feuquay, Jiyuan Liu, Dennis Ojima, Christiana Schmullius, Ashbindu Singh, and Jeff Tschirley

36.1 Introduction

Successful and sustainable use of natural resources crucially depends on the continuous assessment and monitoring of the land resource status, their use mechanisms, and their impacts on future resource availability. Remote sensing observations are crucial to all these activities, especially those with finer resolutions in the 30–60 m range, and moderate resolutions in the 250 m to 1 km range. MODIS and ASTER are two key sensors, which provide such data. In this chapter, we consider the comprehensive needs for terrestrial observations including these and many other sensor systems along with in situ observations.

A number of attempts were made to identify terrestrial observation needs and the products derived from them. The early work of the International Geosphere Biosphere Programme (IGBP) in the late 1980s identified the need and assembled several global datasets for the first time (Townshend and Rasool 1993; Townshend et al. 1994). The International Surface Land Climatology Project also identified and created several datasets at regional and global scales (Sellers et al. 1996). The initiation of two global observing systems, the Global Climate Observing System (GCOS) and the Global Terrestrial Observing System (GTOS) also led to improved product specification (e.g., GCOS-GTOS 1995). One of the GTOS Panels, Global Observations of Land and Forest Dynamics (GOFD-GOLD) has specified in some detail the requirements for land cover and fire products (Loveland et al. 1998; Skole et al. 1998; Ahern et al. 2001; Townshend and Brady 2006). Recently, GCOS has specified land products required to understand climate change, and assessed the adequacy of such products (GCOS 2006).

In the early 1990s, the Integrated Global Observation Strategy Partnership was set up to improve the coordination of satellite and in situ observations (Williams and Townshend 1998). It carried out its work within a series of broad themes such

J. Townshend (✉)

Department of Geography, University of Maryland, College Park, MD 20742, USA
e-mail: jtownshend@bsos.umd.edu

as oceans, carbon, water, and geohazards. A land-specific theme called Integrated Global Observations for Land (IGOL) was set up in 2004. IGOL intended to comprehensively define land observation needs, especially those not dealt with by other IGOS themes, such as carbon, coastal, and cryosphere. This chapter provides a current assessment of the state of the international coordination of land observations based on the IGOL report (Townshend et al. 2008).

A major challenge in developing the theme is the enormous variety of land observations that are regularly acquired. Therefore, a filtering process was adopted to include only those observations with the following characteristics. Observation requirements, which benefit from global observations, are justifiable at a global or at a local scale. A case was already made for observations in the documents of the IGOS-Partners and related sources. Considerable efforts were expended to specify land observations at global scales, which warrant consideration while preparing the theme. Observations contribute directly or indirectly to spatially explicit disaggregated data products rather than to country or sub-country units. Finally, there is a realistic chance to implement any of these recommendations in the next 10 years.

36.2 The Need for Land Observations

The IGOL Theme Team identified eleven broad domains, which require land observations: they correspond broadly to the societal benefit areas of the Group on Earth Observations (GEO 2005).

Agriculture: Agriculture's growing challenge is to match food production with an increasing population's needs while also protecting land and water resources (IGOL 2006). A sound knowledge of the spatial extent of major agricultural crops at country-levels is indispensable to major policy decisions on sustainable development planning and food security. Satellite remote sensing-driven monitoring of major food crops facilitates an objective crop condition assessment with more accurate and timely production forecasts. Monitoring the growing conditions of selected food crops in major crop-producing countries help accurately forecast their agricultural product supply. Land observations also help inform strategies for sustainable management of agricultural land and rural development planning, trade, development assistance, humanitarian aid, and environmental protection.

Forestry: Remote sensing provides reliable and timely information on forest cover and its changes, which potentially supports sustainable forest resource management, and strengthens environmental protection. Spatially explicit information on forest change helps judge the effectiveness of forest protection and conservation projects, and helps determine compliance with negotiated terms of commercial timber concessions (including issues associated with illegal logging and non-timber forest products). Such information can help collect national forest cover statistics for use in national resource planning and management. They further provide significant support for national reporting under many green-house gas inventory chapters advocated by the UN Framework Convention on Climate Change (UNFCCC),

especially those linked to agriculture, grasslands, wetlands and forestry. It has the potential to provide a neutral basis to verify carbon trading linked to afforestation, reforestation, and eventually, also avoided-deforestation projects (Defries et al. 2005). Remote sensing-derived forest observations can help early detection of forest cover changes either by natural causes or human activities.

Land degradation: Climate warming, changing rainfall patterns, and agricultural intensification (both agrarian and pastoral) in arid, semi-arid, and sub-humid dry zones result in deterioration of soils, depletion of surface and ground water resources, reduced productivity, loss of biodiversity, food shortages, increased poverty, and forced population migration in affected areas. Land observations help map changes to the boundaries of degrading areas by monitoring changes to the biophysical characteristics of the surface, such as brightness, photosynthetic activity, location, and condition. This information is of immediate value to farmers and range managers attempting to deal with land degradation while maintaining crop production and rangeland productivity. They provide critical information for governments attempting to implement programs to combat desertification in their countries and regions (Van Lynden and Kuhlmann 2002). Systematic global land observations concerning land degradation zones, rates, and dynamics are clearly needed by the Parties to the United Nations Convention to Combat Desertification.

Ecosystem goods and services: Human well-being is directly dependent upon ecosystems for provisioning of food, water, fiber, fuel, and other biological products, for regulation of disease and water supply, for pollination and waste treatment, and for enriching human existence through recreation and inspiration (Millennium Ecosystem Assessment 2003). Land observations are critical for sustainably managing our ecosystems and the services they provide. Knowledge about the location, amount, and condition of resource stocks in water surface-storage units and in agricultural, forest, and grazing land ecosystems is important for decision-making about natural resources. Observations that enable assessment of the propensity of ecosystems to continue to provide services are at least as important. Fundamental to monitoring changes in ecosystem services are such prime variables such as land cover change, but it is clear that many of the services also require intensive sets of in situ observations at sites and in networks that carry out long term terrestrial ecosystem monitoring.

Biodiversity and Conservation: The Millennium Ecosystem Assessment (2005) revealed major declines in biodiversity. Protected areas are one of the primary means to preserve biodiversity and natural environments while providing vital services and goods that support people's livelihoods. Such areas have important intrinsic values as representative of the world's wilderness and as repositories of outstanding areas of living richness (Chape et al. 2005). Much progress was made in establishing protected areas across the globe, so that they currently cover 12.5% of the Earth's surface. Despite the seemingly large proportion of the Earth's surface designated as protected areas, large concerns persist about the adequacy of existing measures to maintain these critical ecosystems (Dudley et al. 1999). Global land observations are vital to meet the goals of the UN Convention on Biological Diversity.

Human health: Human health is influenced by the terrestrial environment through the failure to supply adequate food, the shortage of potable water, and by its impact on diseases and their transmission (Epstein et al. 2005). Disease transmission is often controlled by vectors like rodents and mosquitoes, whose distribution, in turn, is impacted by land variables. Land cover and land use observations are thus important to target disease treatments, and also to optimize efforts to eradicate disease vectors.

Water resource management: The volume of water in surface-storage units such as lakes, reservoirs, rivers, and wetlands is determined by precipitation and evaporation and increasingly, by human water use. The availability of freshwater plays a crucial role in food production and food security (FAO 2003). Water resources control grazing patterns and crop irrigation. Irrigated land comprises about 20% of cropland, but contributes about 40% of total food production. Irrigated agriculture accounts for about 70% of all freshwater consumption worldwide, and more than 80% in developing countries. To obtain improved quantitative information on available water resources and irrigated land, data on their spatial distribution and change over time are essential.

Disasters: The Geohazards Theme Team (2003) and the Global Water Cycle Theme Team (2003) have extensively considered land observations to facilitate forecasting and mitigating disasters. In addition we note the increasing importance of wildland fires especially those near the urban interface. Land use, land cover, and water use also influence land subsidence and landslides. Better information about land use/land cover in relationship to topography will help identify disaster-prone areas. Land cover is also a critical factor in determining flood risk within major river systems, and up to date information on land cover is important in assessments of relief requirements in the aftermath of major disasters, such as the 2004 Indian Ocean tsunami.

Energy: Biofuels including fuel wood, crop residues, and biofuel crops have long been crucial resources and are being increasingly relied upon to provide renewable energy. Land observations are necessary to assess biofuel production and growth, and their environmentally sustainable production. Efficient siting and impact assessments for wind and hydropower generation depend upon land observations. Oil and gas exploration and extraction, refining, and transport also rely upon accurate information about land cover and use, soils, and topography.

Urbanization: Sustainable human settlement. This topic represents a vital area of societal benefit since human population increasingly resides in urban areas. According to UN predictions (United Nations Centre for Human Settlements 2001), by 2030 60% of the world's population will live in cities. Although urban areas occupy only about 3% of the Earth's surface, their impact on surrounding rural areas is rapidly increasing. Urbanization not only concentrates people and therefore demands for social and economic services, it also creates hot spots for energy and natural resource consumption. Consequently, communication and transportation infrastructure development usher in pollution and greenhouse gases, which further increase pressure on the surrounding environment (Satterthwaite 1999).

Climate Change: Climate impacts the distribution of natural vegetation, and their changes provide a way to monitor such impacts. Changes in land cover force climate by modifying water and energy exchanges with the atmosphere, and by changing greenhouse gas and aerosol sources and sinks. Global land observations are used in climate, carbon and ecosystem models, which provide predictions and scenarios for use by the Parties negotiating the UNFCCC development. Many key terrestrial requirements have already been discussed in the Carbon Theme (Ciais et al. 2003) and in the GCOS plans for Essential Climate Variables (GCOS 2005), and hence IGOL did not duplicate these requirement evaluations.

36.3 Stakeholders for Global Land Observations

Stakeholders are grouped into six categories:

- National, regional or local governments who need the information to assist in the development and implementation of their policies, and to help them meet mandatory reporting requirements resulting from such policies
- International initiatives helping countries develop and fund programs linked to all 11 domains from Sect. 36.2, who need the information to develop their policies and operational strategies
- Non-governmental organizations, lobbying for particular policy directions, and directly acting in the various domains
- Scientists, who need the information to improve our understanding of the processes and uncertainties associated with the Earth system
- The individual citizen, who needs access to understandable, reliable information on global environmental trends
- The private sector, which needs information, to help them either partner and directly service the previous five stakeholders

36.4 Products and Observables

On the basis of the needs articulated in Sect. 36.2 and the requirements of serving the range of stakeholders outlined in Sect. 36.3, the following main observation classes are recognized: Land cover, Land use, Biophysical properties relating to ecosystem dynamics, Biodiversity, Agriculture, Forestry, Soils, Human Settlements and Socio-Economic Data, Water Availability and Use, and Topography. Note that the specific needs of terrestrial stakeholders often require multiple observations; hence a simple one-to-one match between user requirements and observation types is nonexistent.

Land cover. Not to confuse with land use, land cover refers to the observed biophysical characteristics on the Earth's surface. Land cover is not only important in its own right, but it vitally helps estimate many other terrestrial characteristics such

as land use, biodiversity, and conservation along with several other ecosystem services. In addition, land cover provides critical information on hydrological and atmospheric drivers.

Two main classes of products are identified (Ahern et al. 1999): Moderate resolution (250 m–1 km) and fine resolution (10–50 m). Moderate resolution data observations are adequate for most modeling purposes, and suitable to detect land cover changes over 5 year periods. However, finer resolution data are essential to reliably monitor most anthropogenic land transformations.

The frequency with which change is monitored also needs establishment. Moderate resolution images are regularly acquired globally by several systems, but except for unusually large land cover changes, such images are inadequate to reliably measure change spatially. Mid-resolution images are sufficient to measure most non-urban changes in land cover and GOF/GOLD originally proposed global monitoring with a 5-year interval (Loveland et al. 1998). However certain areas, such as tropical forests and some temperate ones, require a higher frequency to reliably monitor the dynamics of anthropogenic change. Also, statistics reporting by most countries is on an annual basis – a future goal is annual reporting of land cover change globally. Certain phenomena, such as fires, and some wetlands, may require daily monitoring to fully encapsulate their dynamics.

Currently, confusion persists in the terminology; some refer to Landsat TM data as medium-resolution, while others call it fine-resolution. We have adopted the commonly-used expression “mid-resolution.” More precise resolutions are specified in the text frequently (Table 36.1).

Within the last few years, large volumes of high-quality global remotely-sensed data have become available, provided by instruments such as MODIS (Justice et al. 1998), SPOT-Vegetation (Maisongrande 2004) and MERIS (Curran and Steele 2005). These data are used to create land cover products with resolutions from 500 to 1,000,2000 m. Global land cover maps were constructed using data from AVHRR for the IGBP (Loveland et al. 2000), SPOT-Vegetation for GLC2000 (Bartalev et al. 2003), and MODIS Land Cover since 2000 (Friedl et al. 2002): Future maps are also planned from MERIS (Arino et al. 2005b) and the NPOESS-VIIRS system on a quarterly basis (Townshend and Justice 2002).

Finer resolution data are needed for larger scale products. The most commonly used remote sensing observations are those from Landsat TM and ETM+, ASTER, SPOT-HRV, CBERS (Chinese Brazilian Earth Resources Satellite) and IRS. Latterly reduced coverage of the former has seriously affected our ability to map and monitor land cover. Regional- and continental-scale efforts exist such as Africover (FAO 2007), CORINE in Europe (EEA 1995), and MRLC2001 in the United States (Homer et al. 2004).

Table 36.1 Terminology for optical sensors in terms of spatial resolution as used in this report

| Resolution class | Spatial resolution | Sensor examples |
|-----------------------|--------------------|-----------------------------------------|
| Coarse resolution | >1 km | AVHRR GAC |
| Moderate resolution | 250 m–1 km | MODIS, MERIS, VIIRS |
| Mid-resolution | 10 m–50 m | ASTER, Landsat TM, SPOT-HRV, IRS, CBERS |
| Ultra-fine resolution | <4 m | ALOS, Quickbird, IKONOS |

The main source of ultra-fine resolution data is commercial satellites, though with JAXA's Advanced Land Observing Satellite (ALOS) launch, 2.5 m panchromatic stereoscopic data from its PRISM sensor is more widely available for scientific and other users. Used in land cover mapping, such data are a valuable validation source for coarser resolution products.

The following were identified as the highest priority issues relating to land cover:

- Commitment to continuous 10–30 m resolution optical satellite systems with data acquisition strategies at least equivalent to that of the Landsat-7 mission
- Development of an in situ reference network for land cover validation
- Generation of annual products documenting global land-cover characteristics at resolutions between 250 m and 1 km, according to internationally agreed standards with statistical accuracy assessment
- Generation of products documenting global land cover at resolutions between 10 and 30 m at least every 5 years; a longer-term goal is annual monitoring
- Ensure future continuity of mid-resolution multispectral and SAR L-band data
- Coordinate radar and optical data acquisitions so that radar data are usable to ensure regular, global monitoring of land cover
- Agree upon internationally accepted land cover and use classification systems

36.4.1 Land Use, Land Use Change

Land use is distinct from land cover in that specific use characteristics are associated within a given category, whereas a land cover is possibly used for a variety of activities or purposes (GLP 2005). Land use characterization is needed to evaluate land resource productivity such as wood and crop production, decision-making associated with land management options, and to implement policy.

No definitive universally accepted land use classification exists. The Land Cover Classification System (LCCS) of FAO is increasingly adopted widely (Di Gregorio and Jansen 2000), but even within the FAO, alternatives are used. Currently available maps suffer a number of shortcomings including too few classes, non-standard definitions, and insufficient information on management.

Comprehensive, well-validated global land use maps are currently unavailable. Many products purporting to depict land use in fact predominantly depict land cover. Key land use characteristics are mapped such as cropland extent, grazing land extent, area of built-up land, and the distribution major crops for the early 1990s by the Center for Sustainability and the Environment at the University of Wisconsin. Digital global maps of irrigated areas are available (George and Nachtergaele 2002). Information by country is provided (FAO 2003) and updates created (Siebert et al. 2006).

At a country level, many countries carry out annual and periodic national agricultural surveys, and FAO collects agricultural data, including land use data from all countries, though for many developing countries, the accuracies are probably low.

The FAO's next Global Forest Resource Assessment slated to complete in 2010 plans to generate spatially explicit forest related land use change information. This will involve the establishment of permanent sample plots at each one-by-one degree latitude and longitude intersection, the interpretation of Landsat, and other remote sensing images for each of these for different points in time (1975, 1990, 2000, 2005) supplemented by auxiliary information, including local knowledge and information from field samples for land use classification.

The principal requirements to improve global land use mapping include the following:

- Development of an accepted land use classification system relevant to the viability of short- and long-term land uses, to land potential and sustainability, and stratified by low and high land use intensity
- For intensively used areas, we need maps of mechanized agriculture, pivot irrigation, tropical plantations, deforested areas, and urban areas
- Integration of remotely sensed and in situ information to map crop production, livestock densities, and fertilizer use

36.4.2 Biophysical Properties Relating to Ecosystem Dynamics

Direct observations of the changes in ecosystem characteristics associated with states (i.e., biomass pools) and fluxes (i.e., material exchanges associated with harvest, aerosols, erosion, and gaseous emissions) are observed at multiple scales from in situ (Baldocchi et al. 2001) to coarse resolution remote sensing observations (Running et al. 2000). The spatial and temporal characteristics of ecosystem patterns and development are constantly affected by human activities and climate change, which alter the fragmentation of ecosystems and patterns of succession.

Key observations related to the state ecosystems include: Species composition; vegetation structure, height, and age; net primary productivity; net ecosystem productivity; spatial pattern of ecosystems; biomass estimates of vegetation, soils, and anthropogenic stocks of C and N; and spatial patterns associated with a mixture of land cover types. In addition, multi-temporal observations provide a way to estimate seasonal dynamics of ecosystem properties from which, productivity are inferred (Running et al. 2004), disturbance events associated, periodicity of inundation, frequency of large scale human modification of ecosystem structure, and ecosystem recovery and age from disturbance characterized.

Many aspects of ecosystem dynamics are not directly observable and require estimation by integrating various in situ, survey, and remote sensed information and repeated observations in models to derive these products (Friend et al. 2007). Data model fusion is needed to estimate these derived products from remotely sensed data coupled with in situ observations to provide estimates of ecosystem dynamics useful for agricultural needs, vegetation recovery and succession, and exchanges of key vertical and lateral fluxes.

Vegetation monitoring data are operationally available on a global scale based on NDVI, Leaf Area Index (LAI), and fraction of Absorbed Photosynthetically Active Radiation (fAPAR), with ground resolutions of 250 m to 1 km (Gobron et al. 2005). Multispectral remote sensing data are the main inputs for forest and other land system change mapping and monitoring. SAR data are increasingly used for ecosystem characterization and change monitoring in areas with frequent cloud cover.

Current networks of inventory, biological census, and flux data associated with regular collection of repeated sampling (forest or crop census data) and continuous point sampling (e.g., FLUXNET) (Baldocchi et al. 2001) provide enhanced measurements of ecosystem processes. They relate to information important for forest or grazing land management, net primary and ecosystem productivity, nutrient, and long-term ecosystem and landscape dynamics (Gobron et al. 2005). Most countries with a significant forest industry have information from which key forest parameters are estimated.

Enhanced observations of ecosystem dynamics associated with vegetation and faunal changes are needed from long-term observations. Disturbance events associated with insect and disease outbreaks, storm, droughts, and other events causing structural and flux changes require enhanced ecosystem characteristics measurements.

Several space agencies and other data providers have created global fAPAR products from 1997 onwards. These products are generally available at 1–2 km spatial resolution, and on a daily, weekly, or monthly basis. Finer resolution (250–300 m) products are not available operationally on a global and sustained basis. Such an offering would significantly improve the national or regional scale reporting on the terrestrial carbon sinks.

Given the simplicity of current models using remote sensing data such as the MODIS-Gross Primary Production (GPP) model (Running et al. 2004), and the fact that they are not fitted against flux data, their overall performance in predicting GPP is remarkable under normal conditions (r^2 between 0.7 and 0.95). The assimilated meteorology does not capture all day-to-day variation, but matches the local tower data well on an eight-day scale. However, at some sites the meteorological bias influences GPP estimates significantly. A re-parameterization of parts of the MODIS-GPP algorithm with eddy covariance data would facilitate the synergistic use of MODIS and C Flux data to improve the ability of a global terrestrial observation system (Friend et al. 2007).

Biophysical properties require the following principal improvements:

- Space agencies and data providers should continue to generate gridded fAPAR and LAI
- Reprocessing of available archives of fAPAR and LAI are required to generate and deliver global, coherent and internationally agreed values
- Further efforts are required to re-analyze the historical archives of NOAA's AVHRR instrument, to ensure the long-term consistency of the product with current estimates throughout the entire period.
- The Committee of Earth Observing Satellites (CEOS) Working Group on Calibration/Validation (WGCV) should continue to lead international benchmarking and product inter-comparison and validation exercises including fAPAR and LAI

36.4.3 Fire

Satellite-derived fire information is valuable for improved fire and land management. For instance, hotspots since 1995 are posted in near real time by ESA, and in the World Fire Atlas (Arino et al. 2005a). GOF-C-GOLD Fire Implementation Team (gofc-fire.umd.edu) developed the fire observation requirements at the international level.

Fire early warning requires a combination of recent weather data and information on vegetation composition and condition. Weather data are obtained from a combination of satellite observations and data from in situ weather stations, often through data assimilation models. Time-series satellite vegetation indices at 500 m–1 km provide input for both early warning and vegetation modeling. Some models use satellite-estimated fAPAR and LAI products to help calculate above-ground production, which is allocated into fuel components. Improved characterization of fuels is anticipated from structural information obtained from Vegetation Canopy Lidar (VCL).

Satellite data from the middle and shortwave infrared are used to distinguish burning or active fires from their surrounding conditions (Giglio et al. 2003). Moderate resolution polar orbiters currently provide sub-pixel detection (<1 km) of active fires orbiting twice a day. Geostationary data with coarse-resolutions (>1 km) provide a more frequent half-hourly sampling of the diurnal cycle of fire activity. The channels used to identify fires require a detection capability at 750 K without saturation. Finer resolution sensors (<30 m) provide more complete fire characterization, and help validate moderate resolution-detected fires. Advances in active fire detection include calculation of Fire Radiative Power (FRP), which is related to biomass consumed (Wooster et al. 2005).

Ground surface conditions change following fires. The resultant fire scars are mappable using data from the near-IR and SWIR parts of the spectrum at 500 m–1 km. For rapid post-burn fire assessment impact in ecologically sensitive areas, mid-resolution data (10–30 m) are needed within 48 h of the fire to assess fire extent, severity and ecosystem and hydrological impacts.

Improved monitoring of fires requires considerable enhancements of current capabilities:

- Coordination of data from geostationery imagers, which provide global active fire detection every 15–30 min, and providing these data in near real time for fire alerts and management
- Modifying the NPOESS VIIRS sensor for the non-saturated detection and characterization of active fires. Monthly and near real time burned area products require operational production
- Reprocessing the AVHRR archive with correction for known deficiencies in sensor calibration, and for known directional and atmospheric problems
- Support of a coordinated international effort to validate the current and future global burned area products

- Coordination and target acquisition of data from the international mid-resolution assets to provide finer-resolution images (<20 m) of large and hazardous fire events within 48 h of the event
- Enhancement of access to and utility of their fire products, through the use of near real time delivery systems and Web-GIS

36.4.4 Biodiversity and Conservation

Observations to support biodiversity and conservation deal primarily with the abundance and richness of wild species of plants and animals, their habitat, and threats to the latter. Endemic plants and animals have, by definition, very restricted ranges while other species may have dispersal and migration patterns that are nearly global. As a result, a global framework for monitoring is essential. The major biodiversity data needs are in situ, but require supplementing with remote sensing-based data to monitor changes in the distribution and status of ecosystems (Janetos and Townshend 2005).

Biodiversity threats to conservation are identifiable through regular mid-resolution mapping of human disturbances within and near protected-area boundaries. Combining these data with the active fire products outlined above would provide a near-real-time indicator of major pressures on protected areas. The United Nations Environment Programme's World Conservation Monitoring Centre maintains a global geospatial database of protected areas with attributes describing the level of protection provided.

Habitat maps prepared from high-resolution images must provide the basic floristic and physiognomic characteristics needed for species distribution models. Needed data include trends in land cover, land use, biophysical conditions, fragmentation, and other ecosystem variables. High-resolution, multispectral, and hyperspectral data-derived maps depicting the locations and spread characteristics of specific invasive species are required.

A suite of measures describing habitat patterns are required to understand fragmentation, landscape patch size, and other metrics that relate to habitat condition. Habitat maps showing trends described earlier are key inputs to this work. Trends in species distribution, linked to habitat, are essential to model species ranges, and to evaluate carrying capacities for individual species. This will require a variety of ecosystem-specific models in which, habitat maps and species occurrence data are combined to identify trends in species distribution and abundance. A comparison of species distribution and habitat protection status will help identify conservation gaps and their ecological conditions (e.g., habitats) that require additional protection.

The current availability of biodiversity information is deficient in both content and characteristics, particularly with regards to consistent measurement of trends. Unauthorized land use within protected areas calls for an urgent need to take advantage

of remote sensing-derived data and information on trends in land cover and habitat types. Other needs include the following:

- The conservation community should adopt a consensus ecosystem classification hierarchy and map product
- The World Database of Protected Areas requires regular updating
- Locational coordinates are required to understand biodiversity in a geospatial context, along with time-series data to monitor trends and the effectiveness of interventions
- Georeferenced socio-economic observations are needed to understand the causes and consequences of biodiversity losses

36.4.5 Agriculture

The primary goal of agricultural monitoring systems is to provide information to support decision making, which leads to improved agricultural management, production, and food security. Data observations are required to support four basic aspects of agricultural monitoring:

- The collection of agricultural statistics at the national and sub-national level
- The monitoring of major food crops and crop production
- The forecasting or early warning of harvest shortfalls, for example, due to droughts, pests, or excessive rains
- Long-term monitoring of changes in the extent and productivity of agricultural lands, and their sustainability

Information derived from Earth observations can help reduce risk and increase productivity and efficiency from the global to the farm unit scale. (IGOL 2006).

General requirements for mapping agricultural land and monitoring change in extent are described in the land cover and land use sections. Optical sensor-derived measurements provide the primary input data to map and characterize crop area, type and condition for agriculture. For global scale mapping and monitoring, products derived from daily, moderate resolution (c. 100–500 m) sensors are appropriate. Microwave data helps map and monitor wetland rice, irrigated areas, water impoundments, and areas with persistent clouds. Multi-temporal moderate resolution, tandem SAR data are conducive to detect crop emergence and estimate acreage. SWIR and thermal data facilitate monitoring of plant water regimes and deficits. Vegetation signal anomalies, for example agricultural drought or insect infestation, are identifiable through comparative time-series data analysis from previous growing seasons.

Forecasting of major food crop production in selected countries worldwide remains operational since the mid-1980s; the forecasting objective includes supporting food security in developing countries, and providing information to the global agricultural market. A number of programs use satellite observations for

global agricultural monitoring, traditionally relying upon coarse resolution (8 km) data from the NOAA AVHRR, and more recently on moderate resolution (250 m–1 km) data for example from MODIS, SPOT Vegetation and MERIS.

The U.S. planned NPOESS VIIRS mission is expected to provide operational moderate resolution (375 and 750 m spatial resolution) data over the next decade. This falls somewhat short of the 100–300 m (visible to SWIR) requirement for crop mask and agricultural vegetation monitoring. Agricultural monitoring requires a continuous medium-resolution data record to provide multiple cloud-free observations yearly. The Landsat-7 problems have created a critical gap in global medium-resolution observations for the agricultural monitoring community. An improved replacement is urgently needed for this purpose. A systematic acquisition and near real time delivery of medium-resolution data at critical periods in the growing season (e.g., 5–10 day cloud-free coverage for all agricultural areas) are deemed essential. Equitable and consistent data and pricing policies, and standardized data formats are all important elements.

The principal recommendations for improvements in agricultural monitoring (IGOL 2006) are as follows:

- Provide mid-resolution (10–20 m), cloud-free coverage with a 5–10 day return period
- Ensure continuity of moderate resolution (1 km, 100–300 m) observations
- Improve targeting and reduce costs of ultra-fine resolution (1–3 m) images
- Standardize collection and dissemination of annual national statistical and other in situ data
- Enhance rain gauge data collection network and lower barriers to timely data access
- Provide near real-time access to regularly collected microwave data (10–30 m), which later is potentially fused with optical data

36.4.6 Soils

Global soil resource information is available at 1:5 M scale in paper maps and digital format in the digital FAO/UNESCO Soil Map of the World. This map links to global and regional databases of soil properties, problem soils, and fertility capability classifications. The SOTER (SO: Soil, TER: Terrain) program was initiated to consistently map areas with distinctive landform, morphology, slope, parent material and soil patterns at 1:1 million scale (ISRIC and FAO 2001). SOTER's originally envisioned worldwide scope was not fully implemented. The recent release of the moderate resolution SRTM Digital Elevation Model (90 × 90 m) has enabled the generation of SOTER terrain units globally with continuing efforts to link with soil databases. Geo-referenced and quality-controlled soil profile information is limited to about 6,000 profiles worldwide, though the quality and quantity of the soil information gathered varies greatly from country to country.

The number of controlled georeferenced soil profiles in the public domain is extremely limited (1,100), while the total number of verified georeferenced soil profiles reveals many gaps in terms of soil types for which this information is available. In general, most developing countries have scattered soil surveys only partly correlated with one another, and of variable age and quality.

The following requirements are deemed necessary to deal with fundamental deficiencies in soils observations:

- Harmonized, small-scale (1:1 Million) soil resource information on a global scale
- Finalization of a global soil and terrain database, in particular, information in West Africa and Southeast Asia
- Quality-controlled, geo-referenced soil profile information collection should vastly expand, particularly in areas of paucity (e.g., China, Former Soviet Union)
- Analytical and procedural decisions should remain the purview of a single body (most logically the IUSS), with binding decisions for all organizations involved with soil classification, mapping, and soil analytical methods
- Soil data interpretation needs improvement, which renders them more accessible and intelligible to non-soil scientists

36.4.7 Human Settlements and Socio-Economic Data

Not surprisingly, much socioeconomic data (such as GDP or birth rates) are not directly obtainable through remote sensing data, but they allow integration with socioeconomic data from other sources. Although they are relatively unexploited for urban areas, remote sensing approaches are by far the most systematic means to collect spatial information on human settlements. For example, enumeration or survey data for administrative areas such as countries, provinces, or municipalities when integrated with spatial data from remote sensing are useful as proxies for socio-economic phenomena (Hay et al. 2005).

Censuses and other conventional sources of socioeconomic data remain essential in understanding global socioeconomic patterns and trends, with added remotely sensed data enhancements.

Infrastructure, including road vectors, is mappable with ultra-fine spatial resolution (~1 m resolution) satellite images. The vertical structure of urban cores is derivable from ultra-fine spatial resolution stereo imagery (e.g., the JAXA PRISM). Mid-resolution systems, such as ASTER, Landsat, and SPOT-HRV are potentially useful to map and monitor urban areas.

An alternative approach to global mapping and monitoring of human settlements is through the detection of nocturnal lighting from the U.S. Air Force Defense Meteorological Satellite Program (DMSP). These data have been widely used in applications requiring geographical locations of human settlements and spatial

distribution of economic activity at a kilometer scale (Amaral et al. 2005; Sutton et al. 2006). However, coarse spatial resolution (2.7 km) and a lack of radiometric calibration limit the applications of DMSP lights.

Four major opportunities to improve satellite observations of human settlements are identified:

- Development of improved methods to measure building heights using stereo-optical images; other sensing methods such as LIDAR and microwave warrant consideration
- Direct detection and monitoring of thermal and shortwave infrared emissions from combustion point sources could help improve the spatial distribution models of fossil fuel emissions
- The current and planned systems for low light imaging (DMSP-OLS and VIIRS) are too coarse to delineate intra-urban classes and measurement of annual growth increments. Current technology is capable of creating a satellite sensor dedicated to 30–100 m resolution detection of nighttime lights from sparse rural settings to urban center cores

36.4.8 Water Availability and Use

Several water observation requirements required to address IGOL topics are identified in the 2003 report of the Global Water Cycle Theme Team (2003). In addition, satellite-derived products are essential to characterize water supply, use, extent, quality and quantity, and delivery. In addition, Digital Elevation Models (DEM), land use, land cover, and soils datasets (described in other sections of this chapter) facilitate assessments of water availability and use.

Mid-resolution images are required to categorize and map the extent of wetlands, lakes, and streams. Water bodies require categorizing according to ecological and hydrological processes. Dams, canals, and other infrastructure elements require mapping with a combination of high- and very high-resolution satellite images.

A lake elevation monitoring system will permit understanding hydrologic variability associated with human use, climate change, and other activities and is also useful to estimate water supply. A first step is to determine a sample of lakes that are sensitive to environmental change, or are vital for human survival. The Global Climate Observing System's Global Terrestrial Network on Lakes (GTN-L) has identified 150 key lakes for climate studies. Radar altimetry measurements are a source of lake elevation data. Although there is no current global data archiving capability established, around 1,000 lakes have been monitored by Topex/Poseidon and Jason-1.

Global moderate resolution data are required to produce weekly to biweekly vegetation index products to use to identify vegetation stress, and quantify drought severity. An irrigated area water use observation product is required on a biannual basis. Irrigation consumes a large percentage of the available global water supply;

therefore, frequent global maps at moderate-resolution are essential. Fine-resolution irrigated area maps are required at least on a decadal basis. Monitoring the thermal properties of soils can provide useful input in relation to their energy balance, soil moisture, ET, and hence, irrigation water needs (Anderson et al. 2007). A sedimentation and deposition observation product is required to assess sediment transport. Mid-resolution remote sensing techniques would prove invaluable to map and estimate the sediment quantity in water bodies. Remote sensing-derived land cover is also required to identify erosion sources.

Water clarity and eutrophication measures are mainly derived from field sources, but hyperspectral imaging provides similar potential to derive such measures in a spatially explicit environment.

36.4.9 Topography

A wide range of land-related applications require height information, as highlighted in this chapter, and also by other IGOS themes such as Geohazards, Water, and Cryosphere. Currently available global topographic datasets have relatively coarse resolutions (90 m to 1 km) and were derived from spaceborne observations (SRTM), from ground observations (GTOPO30) or from a combination of ground, airborne and satellite observations. Additionally, accurate topographic information availability facilitates orthorectification of remotely sensed data, which allows geographic intercomparison of various datasets and creation of products, easily assimilated in a GIS without additional processing. This helps data fusion activities. We recommend the industry to generate routine orthorectified products from moderate and finer resolution remote sensing data similar to the Landsat GeoCover products. An explicit need to extend the coverage and resolution of the current 90 m SRTM dataset exists. The ASTER Global DEM, currently in development, should help fulfill that need.

An urgent need exists for higher resolution (1 m) topographic data for coastal zones and flood plains. Local, high quality, standardized topographic data are essential to enable validation of global datasets. In addition, to facilitate the combination of elevation data from different sources, and to incorporate elevation data with other products, a common geodetic reference frame is required. The adoption and implementation of a global datum based on the ITRF (or WGS 84) is essential.

36.5 Concluding Comments

The multiplicity and diversity of uses for land observations means that a complete integrated synthesis is not possible, nor wise. Certain observations are unique to particular stakeholders, and users need to refer to the main document for those. Also, requirements often differ in subtle ways. Demands for medium-resolution

optical data are many. Certain applications require 10 m spatial resolution data, while others are fulfilled by 50 m data. Similarly, temporal frequency also varies from once every 16 days to much higher observation frequencies.

All part of the IGOL Theme Report advocates remote sensing observations to continue existing capabilities, to make incremental additions, and in some cases, calls for new initiatives.

Critical observations that should continue include mid-resolution (10–50 m) optical remote sensing similar to ASTER and Landsat. The decline in mid-resolution data availability due to the Landsat ETM+ problems is a serious concern. But there are an increasing number of countries with systems, which provide mid-resolution data, and the opportunity to develop a distributed global observation capability. Moderate resolution sensors, such as MODIS (250 m–1 km) appear well poised to achieve some continuity, but current plans for sensors like NPOESS VIIRS spell some reductions in capabilities relative to current ones. Several RADAR instruments are currently in operation, and the increasing value of their products calls for their continued development.

Crucial incremental additions: Several applications, including agriculture, require frequent, cloud-free observations. Increasing the observation frequency by coordinating existing and future assets is strongly encouraged as proposed in the CEOS Virtual Land Surface Imaging (LSI) Constellation.

Thermal IR data use for energy balance and hydrological applications is gaining ground, but there currently are no plans for a follow-on ASTER or even an ETM+ (thermal), which identifies a critical need.

The improving spatial resolution of geostationary systems renders them increasingly suitable for land studies and applications, where there is high temporal variability, for example in fire monitoring. The geostationary data providers who traditionally serve mostly the meteorological community need increased awareness of the growing needs of the land community. The complementarity of optical and microwave sensors is long recognized. A improved coordination of optical and microwave acquisition strategies and data fusion tools to enhance their synergistic capabilities are desirable.

Critical new initiatives: Increasing use of hyperspectral data from experimental missions such as EO-1 has called for more observational assets and related research to improve products in areas as diverse as biodiversity, agriculture, and water.

The third dimension of vegetation is important to many users. We note the improvements in estimation of biomass by both microwave and optical sensors. The wide use of laser technology to characterize vegetation structure currently from airborne sensors is noted, and space agencies are encouraged to develop spaceborne instruments for this purpose. Combined short- (X- and C- band) and long-wave (L- and P-band) radar observations in multiple polarizations (including cross-polarized or full-polarized) and in interferometric mode should greatly improve forest mapping of structure, height and biomass, and also augment agricultural monitoring.

In situ observations are dealt with less comprehensively than remote sensing observations. In many fields such as forestry and agriculture, significant benefits

accrue from a greater integration of in situ and satellite observations. Most in situ data are collected with national or local needs, and standardization of collection procedures is often not adhered to, nor is there a tradition of freely exchanging data. The need to improve in situ data collection is almost ubiquitous notably for observations of biodiversity, agriculture, soils and fires. Improved standardization of in situ data is needed for national fire data collection and reporting, and the adoption of international standards for much in situ data is needed for agriculture.

A crucial common ground for in situ data and remote sensing is in product validation. The report stresses, once again, the importance of validating remote sensing-derived products, so that their value is objectively tested, and errors are reliably estimated. Agencies should not distribute unvalidated products. Free and open availability of validation results and their associated validation data are critical.

Central role of land cover products: Throughout this document, most all sub-themes repeatedly advocate the need for reliable land cover products. Many such products were developed for local, national, and regional scales and fine-tuning them to sub-global needs is appropriate. This report identifies several good reasons for global products. Increasingly refined products are created at moderate resolutions, which should continue. No such global products at mid-resolutions exist, despite the availability of observations for this purpose since 1972.

Socio-economic products: The importance of socio-economic variables is apparent in many of the sub-themes including, but not limited to, land use, biodiversity and conservation, agriculture, and human dimensions. We recognize that considerable effort and new initiatives are needed to improve the availability of spatially explicit socio-economic data for large parts of the world.

Key role of improved classification schemes: Converting satellite-derived observations into useful products requires consensus on the characteristics of such products. Such consensus is engendered by improvements in internationally agreed classification schemes for ecosystem hierarchies, land use, and specifically for the built environment and related infrastructure.

Delivering observations and products: Users are obliged to obtain their data from a variety of sources: From space agencies, from government departments, universities, research organizations, and at times, from commercial organizations. While we recognize the desirability and strength of distributed data systems, we believe that providing more coordination in accessing these diverse sources such as portals linking users to multiple related datasets would greatly improve the data consumption. Similarly increased attention by data providers to metadata standards would greatly improve data inter-use.

Data policies: A detailed discussion of the many different data policies for land data is beyond the scope of this chapter. We stress the abundant empirical evidence that making data openly and freely available greatly increases their use and applications.

Capacity building: Disparities in the understanding of what data are available, how to access, process, and apply them remains a major obstacle to broad data use, particularly in developing countries. The demand for capacity building in land observations and their applications is high, and stems primarily from the resource management community.

The role of MODIS and ASTER: MODIS and ASTER observations and those from similar sensors are clearly central to the operational and sustained monitoring of land. Many sensors are planned for the future, which share many of the attributes of these sensors. But in certain key respects future planned systems are inferior to both sensors. In particular, ASTER's multispectral thermal remote sensing capabilities are absent from any known space agencies' plans. NPOESS-VIIRS, which will provide the operational long-term capabilities of MODIS, shares many of the latter's capabilities, but in some respects, is inferior for terrestrial observations. In particular, the absence of a second non-saturating thermal channel, will lead to inferior fire products in the future. Nevertheless, future sensor systems owe much to the success of MODIS and ASTER sensors considered in this volume.

Acknowledgments The support of the following sponsors is gratefully acknowledged: European Space Agency, the UN Food and Agricultural Organization, the National Remote Sensing Center of China, the United Nations Environment Programme, and the United States Geological Survey.

References

- Ahern F, Belward A, Churchill P, Davis R, Janetos A, Justice CO, Loveland T, Malingreau J-P, Maiden M, Skole D, Taylor V, Yasuoka Y, Zhu Z (1999) A Strategy for Global Observations of Forest Cover. CCRS, Ottawa, p 58, GOFCC Report No. 4
- Ahern FJ, Goldammer JG, Justice CO (eds.) (2001) Global and regional vegetation fire monitoring from space: planning a coordinated international effort. Kugler Publications, The Netherlands
- Amaral S, Camara G, Monteiro AMV, Quintanilha JA, Elvidge CD (2005) Estimating population and energy consumption in Brazilian Amazonia using DMSP night-time satellite data. *Comput Environ Urban Syst* 29:179–195
- Arino O, Plummer S, Defrenne D (2005a) Fire disturbance: the ten years time series of the ATSR world fire atlas. Proceedings of the MERIS (A)ATSR Workshop 2005, ESA SP-597
- Arino O, Trebossen H, Achard F, Leroy M, Brockman C, Defourny P, Witt R, Latham J, Schmullius C, Plummer S, Laur H, Goryl P, Houghton N (2005b) The globcover initiative. Proceedings of the MERIS (A)ATSR workshop 2005, ESA SP-597
- Baldocchi D, Falge E, Gu L, Olson R, Hollinger D, Running S, Anthoni P, Bernhofer C, Davis K, Evans R, Fuentes J, Goldstein A, Katul G, Law B, Lee X, Malhi Y, Meyers T, Munger W, Oechel W, Paw UKTPilegaard K, Schmid HP, Valentini R, Verma S, Vesala T, Wilson K, Wofsy S (2001) FLUXNET: a new tool to study the temporal and spatial variability of ecosystem-scale carbon dioxide, water vapor and energy flux densities. *Bull Am Meteorol Soc* 82:2415–2434
- Bartalev SA, Belward AS, Erchov DV, Isaev AS (2003) A new SPOT4-VEGETATION derived land cover map of Northern Eurasia. *Int J Remote Sens* 24(9):1977–1982
- Ciais P, Moore B, Steffen W, Hood M, Quegan S, Cihlar J, Raupach M, Rasool I, Doney S, Heinze C, Sabine C, Hibbard K, Schulze D, Heimann M, Chédin A, Monfray P, Watson A, LeQuéré C, Tans P, Dolman H, Valentini R, Arino O, Townshend J, Seufert G, Field C, Igrashi T, Goodale C, Nobre A, Inoue G, Crisp D, Baldocchi D, Tschirley J, Denning S, Cramer W, Francey R, Wickland D (2003) Integrated Global Carbon Observing: A strategy to build a coordinated operational observing system of the carbon cycle and its future trends. IGOS. <http://www.igospartners.org/Carbon.htm>

- Chape S, Harrison J, Spalding M, Lysenko I (2005) Measuring the extent and effectiveness of protected areas as an indicator for meeting global biodiversity targets. *Philos Trans R Soc B* 360:443–455
- Curran PJ, Steele CM (2005) MERIS: the re-branding of an ocean sensor. *Int J Remote Sens* 26(9):1781–1798
- DeFries R, Asner G, Achard F, Justice C, Laporte N, Price K, Small C, Townshend J (2005) Monitoring tropical deforestation for emerging carbon markets. In: Moutinho P, Schwartzman S (eds) *Tropical Deforestation and Climate Change*. Instituto de Pesquisa Ambiental da Amazonia, Belém, Brazil, pp 35–46
- Di Gregorio A, Jansen LJM (2000) Land cover classification system, concepts and user manual, GCP/RAF/287/ITA Africover, Food and Agriculture Organization, Rome, Italy p 179
- Dudley N, Gujja B, Jackson B, Jeanrenaud JP, Ovedia G, Phillips A, Rosabel P, Stolton S, Wells S (1999) Challenges for protected areas in the 21st century. In: Stolton S, Dudley N (eds) *Partners for protection*. Earthscan, London, pp 3–12
- Epstein PR, Mills E, Frith K, Linden E, Thomas B, Weireter R (2005) *Climate change futures: health, ecological and economic dimensions*. Massachusetts; Center for Health and the Global Environment, p 142
- European Environment Agency (1995) CORINE Land Cover, Commission of the European Communities
- FAO (2003) *Agriculture, food and water*. FAO, Rome
- FAO (2007) Africover. <http://www.africover.org/>. Accessed 27 June 2007
- Friedl MA, McIver DK, Hodges JCF, Zhang XY, Muchoney D, Strahler AH, Woodcock CE, Gopal S, Schneider A, Cooper A, Baccini A, Gao F, Schaaf C (2002) Global land cover mapping from MODIS: algorithms and early results. *Remote Sens Environ* 83(1–2):287–302
- Friend AD, Arneth A, Kiang NY, Lomas M, Ogee J, Rödenbeck C, Running SW, Santaren J, Sitch S, Viovy N, Woodward FI, Zaehle S (2007) FLUXNET and modelling the global carbon cycle. *Glob Chang Biol* 13:610–633
- GCOS (2006) Systematic observation requirements for satellite-based products for climate - Supplemental details to the satellite-based component of the Implementation Plan for the Global Observing System for Climate in Support of the UNFCCC. GCOS Report 107. WMO, Geneva
- GCOS/GTOS (1995) Plan for terrestrial climate-related observations. Version 1.0, November, GCOS Report 21. WMO, Geneva
- Group on Earth Observations (2005) *Global Earth Observation System of Systems (GEOSS). 10-Year Implementation Plan*. Reference Document, GEO 1000R/ESA SP-1284. ESA Publications Division, ESTEC, Noordwijk
- Geohazards Theme Team (2003) IGOS Geohazards Theme Report http://ioc.unesco.org/igospartners/docs/theme_reports/Geohazards.pdf
- George H, Nachtergaele FO (2002) Land use data. In: Tateishi R, Hastings D (eds) *Global environmental databases: present situation; future directions*. ISPRS, pp 53–65
- Giglio L, Descloitres J, Justice CO, Kaufman Y (2003) An enhanced contextual fire detection algorithm for MODIS. *Remote Sens Environ* 87:273–282
- Global Water Cycle Theme Team (2003) A global water cycle theme for the IGOS partnership. <http://ioc.unesco.org/igospartners/Water.htm>
- GLP (2005) Science plan and implementation strategy. IGBP Report No. 53/IHDP Report No. 19. IGBP Secretariat, Stockholm, p 64
- Gobron N, Pinty B, Taberner M, Melin F, Verstraete MM, Widlowski J-L (2005) Monitoring the photosynthetic activity of vegetation from remote sensing data. *Adv Space Res* doi:10.1016/j.asr.2003.07.079
- Hay SI, Noor AM, Nelson A, Tatem AJ (2005) The accuracy of human population maps for public health applications. *Trop Med Int Health* 10(10):1073–1086
- Homer C, Huang C, Yang L, Wylie B, Coan M (2004) Development of a 2001 national land-cover database for the United States. *Photogramm Eng Remote Sens* 70(7):829–840
- IGOL (2006) *Agricultural Monitoring Meeting Convened for the Integrated Global Observations for Land*. (IGOL) Theme, Rome, Italy

- ISRIC and FAO (2001) Guidelines for the Qualitative Assessment of Land Resources and Degradation, International Soil Reference and Information Centre, Food and Agriculture Organization of the United Nations. Rome, AGL/MISC/33/2001
- Janetos AC, Townshend J (2005) Special meeting on observational priorities for conservation and biodiversity. Integrated Global Observations of the Land (IGOL) - an IGOS-P Theme 3–4. H. John Heinz III Center for Science, Economics, and the Environment, Washington DC
- Justice CO, Vermote E, Townshend JRG, Defries R, Roy DP, Hall DK, Salomonson VV, Privette JL, Riggs G, Strahler A, Lucht W, Myneni RB, Wolfe R, Knyazikhin Y, Running SW, Nemani RR, Wan Z, Huete AR, van Leeuwen W, Giglio RE, Muller J-P, Lewis P, Barnsley MJ (1998) The Moderate Resolution Imaging Spectroradiometer (MODIS): Land remote sensing for global change research. *IEEE Trans Geosci Remote Sens* 36(4):1228–1249
- Loveland T, Yasuoka Y, Burgan B, Chen J, Defries R, Lund HG, Lynham T, Mayaux P, Gregoire J-M (1998) Global observations of forest cover: coarse resolution products design strategy. US EROS Data Center, Sioux Falls, South Dakota, GOF-C-GOLD Report No.3, p 23
- Loveland TR, Reed BC, Brown JF, Ohlen DO, Zhu Z, Yang L, Merchant JW (2000) Development of a global land cover characteristics database and IGBP discover from 1 km AVHRR data. *Int J Remote Sens* 21:1303–1330
- Maisongrande P, Duchemin B, Dedieu G (2004) VEGETATION/SPOT: an operational mission for the Earth monitoring; presentation of new standard products. *Int J Remote Sens* 25(1):9–14
- Assessment MillenniumEcosystem (2003) Ecosystems and human well-being: a framework for assessment. Island Press, Washington DC
- Assessment MillenniumEcosystem (2005) Ecosystems and human well-being: synthesis. Island Press, Washington DC
- Running S, Queen L, Thornton M (2000) The earth observing system and forest management. *J For* 98(6):29–31(3)
- Running SW, Nemani RR, Heinsch FA, Zhao M, Reeves M, Hashimoto HA (2004) Continuous satellite-derived measure of global terrestrial primary production. *BioScience* 54(6):547–560
- Satterthwaite D (1999) The Earthscan Reader in Sustainable Cities. Earthscan Publications, London
- Sellers PJ, Meeson BW, Closs J, Collatz J, Corprew F, Dazlich D, Hall FG (1996) The ISLSCP Initiative I global datasets: Surface boundary conditions and atmospheric forcings for land-atmosphere studies. *Bull Am Meteorol Soc* 77:1987–2005
- Siebert S, Hoogeveen J, Frenken K (2006) Irrigation in Africa. Europe and Latin America - Update of the Digital Global Map of Irrigation Areas to Version 4. Frankfurt Hydrology Paper 05. Institute of Physical Geography, University of Frankfurt, Frankfurtam Main, Germany and FAO, Rome, Italy
- Skole DL, Salas WA, Taylor V (1998) Global observation of forest cover: fine resolution data and product design strategy report of a workshop. Paris, France, CNES, GOF-C-GOLD Report No. 4, p 29
- Sutton PC, Cova TJ, Elvidge CD (2006) Mapping “Exurbia” in the Conterminous United States using nighttime satellite imagery. *Geocarto Int* 21(2):39–45
- Townshend JRG, Brady MA (2006) A Revised Strategy for GOF-C-GOLD. GOF-C-GOLD Report No. 24
- Townshend JRG, Justice CO (2002) Towards operational monitoring of terrestrial systems by moderate-resolution remote sensing. *Remote Sens Environ* 83(1–2):351–359
- Townshend JRG, Justice CO, Skole D, Malingreau JP, Cihlar J, Teillet P, Sadowski F, Ruttenberg S (1994) The 1-km resolution global data set: needs of the International Geosphere Biosphere Programme. *Int J Remote Sens* 15(17):3417–3442
- Townshend JRG, Latham J, Arino O, Balstad R, Belward A, Conant R, Elvidge C, Feuquay J, El Hadani D, Herold M, Janetos A, Justice CO, Jiyuan Liu, Loveland T, Nachtergaele F, Ojima D, Maiden M, Palazzo F, Schmillius C, Sessa R, Singh A, Tschirley J, Yamamoto H (2008) Integrated Global Observations of the Land: an IGOS-P Theme. IGOL Report No. 8, GTOS 54
- Townshend JRG, Rasool SI (1993) Global change. *Codata Bull* 24(4) (Special Issue on Data for Global Change):1–14

- United Nations Centre for Human Settlements (2001) *The State of the World's Cities 2001*. Nairobi, United Nations
- Van Lynden GWJ, Kuhlmann T (2002) *Review of degradation assessment methods*. LADA. FAO, Rome, Italy
- Williams D, Townshend JRG (1998) The concept of an integrated global observation strategy 27th International Symposium on Remote Sensing of Environment, Tromso, Norway, (June 1998) pp 95–98
- Wooster MJ, Roberts G, Perry G, Kaufman YJ (2005) Retrieval of biomass combustion rates and totals from fire radiative power observations: calibration relationships between biomass consumption and fire radiative energy release. *J Geophys Res* 110:D21111, doi: 10.1029/2005JD006318

Index

A

- Abiotic, 640, 641, 711
- Absorptance, 385
- ACCESS. *See* Advancing Collaborative Connections for Earth–Sun System Science
- ACORN, 305
- ACSL. *See* Automated cartridge system library software
- Active fire products, 663, 664, 668, 847
- Advanced Industrial Science and Technology (AIST), 32, 89, 96
- Advanced land observing satellite (ALOS), 447, 448, 817, 842, 843
- Advanced microwave scanning radiometer (AMSR), 9, 168, 178, 224, 488, 703
- Advanced microwave scanning radiometer for EOS (AMSR-E), 703
- Advanced microwave sounding unit (AMSU), 9
- Advanced spaceborne thermal emission and reflection radiometer (ASTER), 3–32, 35, 55, 59–114, 117–130, 165–182, 188–196, 203, 208, 215, 218, 221–224, 226, 227, 229–231, 233–270, 273–299, 301–323, 329–373, 379–398, 401–420, 425–440, 443–462, 465–482, 485–503, 508, 529, 530, 539, 615, 665–667, 750, 781, 814, 837, 842, 850, 852, 853, 855
- Advanced very high resolution radiometer (AVHRR), 5, 10, 55, 57, 152, 168, 426, 507–509, 531, 539, 551, 559, 566, 569, 581, 582, 585, 587, 588, 596–600, 608, 623, 624, 655, 658, 663, 679, 703, 711, 722, 731, 733, 783–805, 809, 829, 842, 845, 846, 849
- Advanced wide field sensor (AWiFS), 805
- Advancing Collaborative Connections for Earth–Sun System Science (ACCESS), 186, 199, 200
- Aeolian, 474
- AERONET, 536, 539–543, 545–547, 630
- Aerosol
 - absorption, 111
 - correction, 67, 589, 729
 - optical depth, 112, 535, 544, 630, 753
- Aerosol optical thickness (AOT), 537, 538, 544
- Afforestation, 839
- Africover, 842
- AGFA. *See* Automated global feature analyzer
- Agricultural monitoring, 712, 848, 849, 853
- Agriculture and Resource Inventory Surveys
 - through Aerospace and Remote Sensing (AgRISTARS), 826
- AI. *See* Artificial intelligence
- Airborne visible/infrared imaging spectrometer (AVIRIS), 14, 833
- AIRS. *See* Atmospheric infrared sounder
- AIST. *See* Advanced Industrial Science and Technology
- Alaska SAR facility, 38
- Albedo, 109, 111, 276, 284, 287, 292, 298, 314, 381, 383, 385, 415, 479–481, 508, 514, 517, 523, 531, 535–537, 551–559, 606, 617, 673, 674, 684, 685, 687, 689, 693, 695, 697, 703, 706, 716, 753, 758, 765, 769, 774, 784, 785, 788, 790, 793, 797, 802
- Albedometer, 557, 558
- Algorithm theoretical basis document (ATBD), 31, 238, 240, 450, 456, 687, 787, 816
- Alkali Lake, 122, 123
- Allen glacier, 332
- Along-track (AT), 17, 23, 27, 57, 59–61, 72–74, 76, 100, 104, 106, 107, 109, 110, 124, 125, 136, 137, 140, 152–154, 156, 230, 234, 245, 380, 444–449, 456, 512, 557

- Along track scanning radiometer (ATSR), 675, 679, 804
 ALOS. *See* Advanced land observing satellite
 Altimetry, 38, 357, 358, 443, 851
 Alunite, 304–306, 311, 313–316, 318, 322
 Aluviones, 340, 341, 343–345, 356, 371
 Alyeska pipeline, 336
 AMASS. *See* Archival management and storage system
 Amazon, 30, 587–589, 593, 595, 597, 648, 649, 653, 654, 664, 671–673, 764
 Amberoona formation, 279
 AMeDAS. *See* Automated meteorological data acquisition system
 Ameriflux, 592, 593, 637, 646, 647, 658
 AMSR. *See* Advanced microwave scanning radiometer
 AMSR-E. *See* Advanced microwave scanning radiometer for EOS
 AMSU. *See* Advanced microwave sounding unit
 Anaglyph, 453
 Anisotropic index, 554
 Anisotropy, 508, 551–559, 566, 585, 588, 693, 697
 Anthropocene, x
 Anthropogenic, 6, 379, 380, 385, 387, 388, 392, 397, 398, 414, 512, 630, 727, 810, 842, 844
 Anthropogenic heat discharge, 379, 380, 385, 387, 388, 392, 397
 AOT. *See* Aerosol optical thickness
 APAN. *See* Asia-pacific advanced network
 Application programming interface (API), 53, 166, 194, 201
 Archival management and storage system (AMASS), 169, 177, 181
 Artificial intelligence (AI), 360–363, 371
 Asia-pacific advanced network (APAN), 171, 236, 239
 ASTER. *See* Advanced spaceborne thermal emission and reflection radiometer
 ASTER volcano archive, 266–270
 ATBD. *See* Algorithm theoretical basis document
 Atmospheric correction, 14, 26, 56, 83–114, 117–130, 241, 281, 297, 298, 312, 314, 319, 383, 393, 416, 444, 472–474, 478, 479, 507, 508, 535, 536, 552, 556, 557, 559, 587, 589, 608, 623, 785, 798, 800, 802
 Atmospheric infrared sounder (AIRS), 9, 215, 219, 224, 772–774, 776, 777
 Atmospheric radiation measurement (ARM) program, 557, 558
 Atmospheric resistance vegetation index (ARVI), 582
 Atmospheric thermal radiance, 566
 Atmospheric water vapor, 16, 135, 276, 288, 386, 598
 ATSR. *See* Along track scanning radiometer
 Automated cartridge system library software (ACSLs), 169, 177, 181
 Automated global feature analyzer (AGFA), 359
 Automated meteorological data acquisition system (AMeDAS), 383, 387
 Autotrophic respiration, 641, 645
 AVHRR. *See* Advanced very high resolution radiometer
 AVIRIS. *See* Airborne visible/infrared imaging spectrometer
 AWiFS. *See* Advanced wide field sensor
- B**
 BAER. *See* Burned area emergency rehabilitation
 Balcanoona formation, 278, 279, 286, 287, 298
 Band-pass, 136, 306, 322, 585
 Baseline surface radiation network (BSRN), 557
 Base-to-height ratio, 27, 59–61
 Bayes' rule, 719
 Bayes' theorem, 361
 Bering glacier, 333
 BERMS. *See* Boreal ecosystem research and monitoring sites
 Bidirectional reflectance distribution function (BRDF), 156, 535, 552, 566, 585, 663, 693
 Bidirectional reflectance function (BRF), 113, 114, 138, 139, 142, 151, 535, 554, 606, 607, 625
 Bigfoot project, 646, 651
 Bihemispherical reflectances (BHR), 553
 Biodiversity, 658, 839, 841, 842, 847–848, 853, 854
 Biofuels, 840
 Biogeochemical cycles (BGC), 1, 595
 Biological productivity, 512, 639
 Biomes, 593, 606, 611, 612, 615, 620, 623, 626, 629, 632, 646, 648, 649, 664, 733
 Biotic, 711
 Blackbody, 17, 31, 56, 57, 63, 67, 68, 70, 117–119, 138–140, 143, 144, 160, 241, 246, 565, 784, 787, 792
 Black-sky albedo, 553, 557
 Blue-sky albedo, 553, 557

- BMGT. *See* Bulk metadata generator tool
 Bolometer, 4
 Bondville, 762–764, 766, 767
 Boosting, 715, 717–718
 Boreal ecosystem research and monitoring sites (BERMS), 762, 763, 766
 Bowen ratio, 755
 Bow-tie effect, 57, 152, 154
 BRDF. *See* Bidirectional reflectance distribution function
 BRDF kernel, 157
 BRF. *See* Bidirectional reflectance function
 Broadband anisotropy, 553, 559
 Broadband emissivity, 381, 383, 414, 574, 577, 753, 761, 762
 BSRN. *See* Baseline surface radiation network
 Bulk metadata generator tool (BMGT), 180
 Burned area emergency rehabilitation (BAER), 742–744
 Burned area product, 663, 664, 671, 673–679, 846
- C**
 C4.5 algorithm, 715–717
 Calibration, 9, 11, 12, 14, 17, 24, 26, 31, 32, 56, 57, 63, 70, 76, 77, 83–114, 117–130, 136, 138–151, 156–160, 162, 221, 226, 237, 279, 298, 312, 444, 449, 462, 466, 467, 469–470, 472, 474–479, 481, 482, 491, 507–509, 520, 522, 527, 531, 535, 543, 544, 552, 556, 559, 565, 587, 617, 623, 639, 646, 679, 776, 784–787, 792, 801, 803–805, 816, 819, 832, 845, 846, 851
 Calipso, 8
 Canonical correlation analysis index, 616
 Canopy architectural types, 606
 Carbon, 59, 592–597, 639, 642, 652, 654–656, 712, 749, 838, 839, 841, 845
 Carbonate group, 286
 Carbonates, 109, 273, 274, 277–279, 281, 284–290, 295–298, 302, 304, 311, 313, 322
 Carnegie Ames Stanford approach (CASA), 593, 597
 CARS. *See* Climate analysis research systems
 Catchment-based land surface model (CLSM), 701
 Catchment modeling, 749
 CBERS. *See* China-Brazil Earth Resources Satellite
 CCSDS. *See* Consultative committee on space data systems
 CDF. *See* Common data format
 CDR. *See* Climate data record
 CEOP. *See* Coordinated enhanced observing period
 CEOS. *See* Committee on Earth Observation Satellites
 CERES. *See* Clouds and Earth's Radiant Energy System
 Charge-coupled detector, 445
 Chavez method, 382
 Checksum, 53, 54, 174
 CH₄ flux, 425–427, 429–430, 438–440
 Chikurachki, 262–266
 Chimborazo-Zaldivar, 309–317, 323
 China-Brazil Earth Resources Satellite (CBERS), 447, 672, 815–817, 820–822, 831, 842
 CIRES. *See* Cooperative Institute for Research in Environmental Sciences
 CLASS. *See* Comprehensive large array-data stewardship system
 Climate
 change, 20, 229, 329, 354, 357, 372, 462, 509, 581, 582, 639, 651, 656, 658, 695, 700, 751, 803, 828, 837, 841, 844, 851
 variability, 512, 595, 657, 833
 Climate analysis research systems (CARS), 803
 Climate data record (CDR), 11, 509, 600, 637, 639, 790, 804
 Climate modeling grid (CMG), 545, 555, 570, 571, 583, 585, 684, 685, 694, 714, 772
 Clinometry, 443
 Cloud contamination, 569, 571, 589, 612, 772
 Clouds and Earth's Radiant Energy System (CERES), 9, 552, 772–774, 776, 777
 Cloudsat, 8, 221
 Cloud-screening algorithm, 615
 CLSM. *See* Catchment-based land surface model
 Coastal zone color scanner (CZCS), 4
 Cojup valley, 342, 343, 347
 Cold springs reservoir (CSR), 122, 123
 Commercial off-the-shelf, 50–53, 181, 449, 462
 Committee on Earth Observation Satellites (CEOS), 187, 188, 201, 508, 531, 804, 823, 824, 831, 845, 853
 Common data format (CDF), 204, 206
 Compositing process, 728, 742
 Comprehensive large array-data stewardship system (CLASS), 796, 801, 802
 Confidence index (CI), 684, 685, 690
 Configuration management, 52

Conservation, 734, 838, 839, 842, 847–848, 854
 Constrained view angle, 585
 Consultative committee on space data systems (CCSDS), 205
 Cooperative Institute for Research in Environmental Sciences (CIRES), 166, 168
 Coordinated enhanced observing period (CEOP), 200, 761–767, 772
 Coplanarity, 452
 Copper porphyry, 303, 304, 307, 309, 310
 Copper River, 330–334, 336, 338
 Cordillera Blanca, 330, 331, 333, 334, 336, 338–341, 343, 344, 351, 353, 355, 356, 370, 371
 Cordillera Negra, 340
 CORINE, 842
 CORONA, 812
 COTS. *See* Commercial off-the-shelf
 Crater lakes, 229, 245
 Crosstalk, 56, 83, 84, 96, 98, 99, 101, 104–110, 145, 151, 276–277, 280, 281, 284, 286–295, 298
 Cross-track (CT), 23, 24, 27, 56, 60, 61, 63, 72–74, 76, 100, 107, 110, 124, 125, 152, 156, 230, 298, 446, 557
 Cryocooler, 28, 55, 62, 63
 CSR. *See* Cold springs reservoir
 Cuprite, 307
 Curnamona province, 109, 276
 Custom code, 51, 52, 197
 CV. *See* Constrained view
 CZCS. *See* Coastal zone color scanner

D

DAAC-unique extension (DUE), 52–53
 Dahlem conference on fire in the environment, 678
 Dark and dense vegetation technique, 539
 Data corruption, 53–54
 Data interoperability, 44, 181, 196, 197
 Day/night algorithm, 568–571, 576, 577
 Daytime LST, 272–274
 DB. *See* Direct broadcast
 Death valley, 471, 473, 474, 477–480
 Decision-tree, 381, 715–717, 735, 736, 742, 799
 Deep space calibration (DSC), 99–102, 123, 124
 Deep space maneuver, 144
 Defense Meteorological Satellite Program (DMSP), 850, 851
 Deformation ecosystem structure and dynamics of ice, (DESDynI), x
 Desertification, 440, 655, 656, 839

DHR. *See* Directional hemispherical reflectance
 Digital elevation model (DEM), 23, 26, 56, 113, 114, 155, 160, 170, 172, 222, 223, 226, 230, 239, 240, 242, 243, 245, 253, 254, 263, 269, 274, 283, 292, 294, 301, 302, 319–322, 342, 358, 380, 381, 383, 384, 387, 388, 407, 443–462, 466, 472, 478, 479, 538, 693, 697, 849, 851, 852
 Digital surface model (DSM), 407
 Digital terrain elevation data (DTED), 450, 828, 829
 Direct broadcast (DB), 21, 785, 789, 804
 Directional hemispherical reflectance, 553
 Disaster monitoring constellation (DMC), 403, 815, 817, 818, 822, 823, 831, 832
 DMSP. *See* Defense Meteorological Satellite Program
 Downwelling, 467, 470, 472, 474, 478
 DSC. *See* Deep space calibration
 DSM. *See* Digital surface model
 DTED. *See* Digital terrain elevation data
 DUE. *See* DAAC-unique extension

E

Earth Observing System (EOS), 1, 3, 35, 49, 55, 62, 133, 165, 168, 183, 203, 234, 301, 408, 444, 487, 507, 511, 638, 663, 703, 751, 786, 809
 Earth radiation budget experiment (ERBE), 551
 Earth Remote Sensing Data Analysis Center (ERSDAC), 30, 100, 109, 126, 169, 235, 236, 242, 243, 279, 281–284, 301, 381, 407, 444, 456–461, 488, 493, 498–501
 Earth resources observation and science (EROS), 28, 38, 165, 168, 175, 239, 279, 303, 447, 448, 507, 513, 788, 814, 819, 826
 Earth Satellite Corporation, 828
 Earth science data system working group, 43, 199
 Earth science data types (ESDT), 2, 173–175, 214, 218, 219, 684–688, 692
 Earth system data record (ESDR), 637, 639, 664, 679, 827–829
 Earth systems science, 47, 785
 Earth view (EV), 136, 141, 683
 EASE-grid, 686, 687, 704–705
 ECHO. *See* EOS clearinghouse
 ECMWF. *See* European Centre for Medium-Range Weather Forecasts
 Ecological assessment, 712
 Ecological research, 712

- Ecosystem services, 410, 657, 712, 839, 842
 Ecotones, 730
 ECS. *See* EOSDIS core system
 ECS architecture, 53
 ECV. *See* Essential climate variable
 EDAS. *See* Eta model-based data assimilation
 Eddy covariance flux tower, 593, 646
 EDG. *See* EOS data gateway
 EDOS. *See* EOS data and operations system
 EDR. *See* Environmental data record
 Electromagnetic spectrum, 222, 230, 406,
 703, 810
 Elevation accuracy, 448, 450, 454, 462
 Ellipsoid, 77, 81, 239, 243
 El Niño-Southern Oscillation (ENSO), 582,
 637, 655, 658
 Emissivity, 23, 24, 26, 56, 117, 122, 125, 126,
 128–130, 140, 143, 240–242, 245, 281,
 282, 285, 286, 297–299, 380, 381, 383,
 385, 386, 398, 413–415, 466, 508, 514,
 565–577, 752–753, 756–758, 761, 762,
 765, 774
 Endmember, 279–281, 298, 433, 435–437,
 480, 481
 Energy, 83, 195, 230, 273, 338, 341, 343, 344,
 349, 356, 379, 385, 392–394, 397, 398,
 413, 415, 492, 494, 508, 551, 558, 565,
 595, 605, 651, 701, 712, 749–777, 797,
 809, 833, 840, 852, 853
 Energy exchange, 230, 466, 512
 Enhanced vegetation index (EVI), 544, 548,
 582–585, 587–589, 591–596, 598–600,
 713, 714, 716, 719–721, 788, 795, 798
 ENSO. *See* El Niño-Southern Oscillation
 Environmental data record (EDR), 788, 790,
 793, 795–800, 802, 803
 EOS. *See* Earth Observing System
 EOSAT, 495, 496, 813
 EOS clearing house (ECHO), 2, 166, 175,
 178, 180, 181, 185, 187–190, 192, 194,
 198, 201
 EOS data and information system (EOSDIS),
 1, 2, 28, 35–47, 49–54, 165, 166, 168,
 169, 173, 181, 183, 185–190, 192,
 194–196, 198, 199, 201, 206, 209, 512,
 513, 787, 788
 EOS data and operations system (EDOS), 169,
 170, 173, 236, 237, 243, 668
 EOS data gateway (EDG), 166, 170, 172, 178,
 181, 185, 188–192, 194, 195, 201
 EOSDIS core system (ECS), 2, 40, 41, 45, 46,
 49–54, 169–174, 177–182, 192, 193,
 201, 206, 209, 213, 214, 217, 219, 223,
 512, 524
 EOSDIS evolution, 36, 44, 45, 166
 ERBE. *See* Earth radiation budget experiment
 EROS. *See* Earth resources observation and
 science
 EROS data center, 38, 239, 814
 Errors
 of commission, 417, 663, 683, 695, 696,
 698, 699, 736
 of misclassification, 609
 of omission, 698, 699, 706
 ERSDAC. *See* Earth Remote Sensing Data
 Analysis Center
 ESDR. *See* Earth system data record
 ESDT. *See* Earth science data types
 Essential climate variable (ECV), 509, 841
 Eta model-based data assimilation
 (EDAS), 754
 European Centre for Medium-Range Weather
 Forecasts (ECMWF), 637, 644, 702
 European Space Agency (ESA), 6, 488, 804,
 822, 846
 Eutrophication, 852
 EV. *See* Earth view
 Evaporation, 385, 594, 749, 750, 764
 Evaporative fraction, 577, 756, 763, 764, 766,
 768, 770, 775
 Evapotranspiration (ET), 59, 379, 509,
 593–595, 658, 749–777, 852
 EVI. *See* Enhanced vegetation index
 eXtensible Markup Language (XML), 205,
 214, 218, 223
 External data representation (XDR), 204
- F**
 Famine Early Warning System Network
 (FEWS NET), 702
 FAPAR. *See* Fraction of absorbed
 photosynthetically-active radiation
 Federal Geographic Data Committee (FGDC),
 40, 199, 213
 Fire-affected areas, 663, 675, 678
 Fire information for resource management
 system (FIRMS), 507, 664, 668–671
 Fire monitoring, 663, 664, 671, 679, 853
 Fire radiative energy (FRE), 668
 Fire radiative power (FRP), 663, 668, 800, 846
 FLUXNET, 605, 637, 646, 772, 845
 Focal plane assemblies (FPAs), 14, 56,
 137–138, 140, 144, 148, 149, 151, 790
 Fourier transform, 124
 Fourier transform interferometer (FTIR), 567
 FPAs. *See* Focal plane assemblies
 Fractal, 470
 Fractional snow cover (FSC), 683–685,
 688–690, 692–696, 701, 706

- Fraction of absorbed photosynthetically-active radiation (FAPAR), 582, 845, 846
- FRE. *See* Fire radiative energy
- FRP. *See* Fire radiative power
- Fujitsu, 28
- Fukutoku-Okanoba, 254, 255, 257–260
- Fumaroles, 229, 250, 266
- Fuzzy expert systems, 359, 361–369
- Fuzzy logic, 359–362, 368
- G**
- GAC. *See* Global area coverage
- gaiatsu*, 493
- Gain setting, 68, 69, 85
- GAPHAZ. *See* Glacier and permafrost hazards in mountains
- Gauss–Seidel iteration, 92, 111
- GCM. *See* Generalized circulation model
- GCMD. *See* Global change master directory
- GCOS. *See* Global climate observing system
- GCPs. *See* Ground control points
- GDAS. *See* Global data assimilation system
- GDEM. *See* Global digital elevation model
- GDS. *See* Ground data system
- Generalized circulation model (GCM), 6, 751
- Generalized split-window algorithm, 569, 571, 576
- Geocentric, 77, 222
- GeoCover, 852
- Geodetic, 77, 154, 222, 358, 827, 852
- Geographic information system (GIS), 166, 178, 193, 199, 224–226, 270, 301, 319, 320, 356, 359, 362, 402, 443, 507, 519, 664, 668, 669, 847, 852
- Geohazards, 838, 840, 852
- Geolocation accuracy, 73, 156, 160, 274, 444, 449, 456, 460, 462, 576, 819
- Geological mapping, 273–299
- Geomorphological potential for hazards, 365
- Geomorphology, 283, 329, 340, 355, 360, 365, 367
- Geopositioning, 462
- GEOSS. *See* Global earth observing system of systems
- GeoTIFF, 204, 224, 225, 450, 454, 545
- GEWEX. *See* Global energy and water cycle experiment
- Ghosting, 123
- GIFOV. *See* Ground instantaneous field of view
- GIMMS. *See* Global inventory monitoring and modeling studies
- GIS. *See* Geographic information system
- Glacier and permafrost hazards in mountains (GAPHAZ), 372
- Glacier dynamics, 331, 333, 338, 357, 359, 362, 367, 369
- Glacier lake outburst flood (GLOF), 331–333, 340
- Glacier science, 329
- GLDAS. *See* Global land data assimilation system
- GLI. *See* Global land imager
- GLIMS. *See* Global land ice measurements from space
- Global area coverage (GAC), 784, 842
- Global carbon modeling, 712
- Global change master directory (GCMD), 194–195, 198, 201
- Global climate observing system (GCOS), 804, 837, 841, 851
- Global data assimilation system (GDAS), 127, 128, 538
- Global digital elevation model (GDEM), 113, 230
- Global Earth Observing System of Systems (GEOSS), 2, 231, 658, 679, 804, 805, 821, 823, 824, 827, 830, 831, 834
- Global energy and water cycle experiment (GEWEX), 753, 761, 772
- Global fire products, 663–679
- Global flux network, 646
- Global inventory monitoring and modeling studies (GIMMS), 784, 801
- Global land cover, 482, 644, 711–723, 727, 731, 842, 843
- Global land cover facility, 730
- Global land data assimilation system (GLDAS), 702, 754, 761, 762, 765–767
- Global land ice measurements from space (GLIMS), 30, 229, 340, 351, 462
- Global land imager (GLI), 507, 804
- Global land survey (GLS) 2005, 828
- Global Map, 30, 177, 217, 219, 234, 238, 266, 407, 546, 607, 609, 687, 714, 733, 843, 850, 852
- Global modeling and assimilation office (GMAO), 515, 637, 641, 642, 644, 646–648, 651, 655, 774
- Global observation of land cover dynamics (GOLD), 668, 671, 679, 804, 837, 842, 846
- Global observations of forest cover (GOFC), 668, 671, 679, 804, 837, 842, 846
- Global surface albedo, 551
- Global terrestrial observing system (GTOS), 837

Global visualization (GloVis), 170, 173, 175, 195, 243

Global warming, 334, 344, 345, 352–357, 426, 427, 654

GLOF. *See* Glacier lake outburst flood

GLS2005. *See* Global land survey (GLS) 2005

GMAO. *See* Global modeling and assimilation office

Gobi-Altay strike-slip fault, 479–480

Goddard Space Flight Center (GSFC), 9–12, 38, 39, 44, 50, 70, 133, 141, 151, 165, 170, 172, 173, 196, 200, 201, 213, 224, 227, 236, 432, 486, 513, 519, 528, 531, 630, 668, 687, 702, 704, 729, 784, 787, 801

GOFC. *See* Global observations of forest cover

GOLD. *See* Global observation of land cover dynamics

Google, 47, 269, 270, 369, 401

Government resource for validation and independent testing and evaluation (GRAVITE), 801

GPH. *See* Geomorphological potential for hazards

GRAVITE. *See* Government resource for validation and independent testing and evaluation

Greenhouse gas, 426, 639, 657, 841

Green-up, 587, 595, 619, 626

Green vegetation fraction, 582, 586

Gross primary production (GPP), 514, 592, 593, 595, 637–654, 656–659, 845

Ground control points (GCPs), 73, 155, 160, 211, 239, 314, 444, 449–456, 459, 462

Ground data system (GDS), 28, 30, 100, 165, 169–173, 221, 236–243, 269, 284, 458, 459

Ground instantaneous field of view (GIFOV), 792

Ground sampling distance, 76, 104

Groundwater aquifers, 749

GSFC. *See* Goddard Space Flight Center

GTOPO30, 127, 128, 852

GTOS. *See* Global terrestrial observing system

Gusev crater, 474, 475

H

Hapke parameter, 466

Hierarchical data format (HDF), 54, 76, 77, 165, 166, 178, 193, 203–227, 240, 282, 450, 454, 459, 512, 517, 519, 545, 607, 638, 642, 674, 801

High resolution imaging spectroradiometer (HIRIS), 7, 8, 490, 495

High resolution infrared sounder (HIRS), 5–6

High resolution picture transmission (HRPT), 784, 785

High resolution stereo camera (HRSC), 403, 474

Histogram equalization, 573

Holocene, 267, 471, 473, 480

Home reef, 260–262

HSB. *See* Humidity Sounder for Brazil

Huaraz, 332, 336, 339–343, 345, 349, 351, 352, 355

Huascarán, 341

Hukuzin Kaizan, 255

Human health, 833, 840

Humidity Sounder for Brazil (HSB), 9

Hydrological cycle, 8, 512, 749

Hydrological modeling, 586, 687, 697, 705

HyMap, 274, 275, 278, 279, 282, 283, 285, 288, 290, 292, 293

Hyperion, 88, 278, 305, 833

Hyperspectral, 7, 274

Hyperspectral infrared imager (HyspIRI), 781

I

Ice surface temperature (IST), 685–687, 703–705, 790

IEOS. *See* International Earth Observing System

IGBP. *See* International Geosphere-Biosphere Programme

IGOL. *See* Integrated global observations of land

IJI. *See* Interspersion/juxtaposition index

IKONOS, 403, 406, 447, 448, 539, 540, 733, 734, 812, 842

Illite, 304, 311, 313, 316, 322

Indian Resource Satellite (IRS), 403, 447, 448, 805, 815–817, 822, 823, 842

Information management subsystem (IMS), 166, 186–188, 242

Insolation, 758, 767, 768

Instituto Nacional de Pesquisas Espaciais (INPE), 681, 737–738

Instrument design, 29, 55–57, 59–82, 151, 444, 462, 508, 512, 786

Integrated global observations of land (IGOL), 804, 838, 841, 848, 849, 851, 853

Integrated observations of the land, 837–855

Integrated operational requirements document (IORD), 790

- Integrated program office (IPO), 20, 21, 789, 790, 793, 801
- Integrated Warning Deforestation System for the Amazon (SIAD), 597
- Interferometry, 443
- Intergovernmental panel on climate change (IPCC), 426
- Intermediate thermal infrared radiometer (ITIR), 24–26, 55, 488–498, 502
- International Earth Observing System (IEOS), 42
- International Geosphere-Biosphere Programme (IGBP), 619, 713, 714, 721, 797, 798, 804, 837, 842
- Interspersion/juxtaposition index (IJI), 411, 412
- Intertropical convergence zone (ITCZ), 638, 652
- Invasive species forecasting system (ISFS), 597
- IOR.D. *See* Integrated operational requirements document
- IPCC. *See* Intergovernmental panel on climate change
- IPO. *See* Integrated program office
- Irrigation, 596, 749, 750, 840, 851, 852
- IRS. *See* Indian Resource Satellite
- ISFS. *See* Invasive species forecasting system
- Isotropic, 157, 552–554, 693
- IST. *See* Ice surface temperature
- ITCZ. *See* Intertropical convergence zone
- ITIR. *See* Intermediate thermal infrared radiometer
- Ivanpah playa, 89, 90, 96
- J**
- Japanese Earth Resource Satellite-1 (JERS-1), 23, 24, 55, 93, 444, 447, 449
- Japanese National Space Development Agency, 25
- Japan Resources Observation System Organization (JAROS), 24, 25, 29, 31, 488, 490, 492, 493, 495–497, 499
- JARG. *See* Joint agency requirements group
- JERS-1. *See* Japanese Earth Resource Satellite-1
- Jet propulsion laboratory (JPL), 10, 24–26, 32, 38, 170, 172, 222, 223, 236, 268, 405, 487, 488, 490, 492, 500
- John Marburger, 821
- Joint agency requirements group (JARG), 790
- Jornada experimental range, 587
- Junge distribution, 92
- Just-in-time, 54
- K**
- Kamchatka volcanic eruption response team (KVERT), 263
- Kaolinite, 285, 304–306, 311, 313–316, 322
- Karmadon, 339
- Karman's constant, 387
- Kikai Caldera, 255, 256
- Kolka-Karmadon, 333, 338, 345
- Krylon, 567
- Krypton hygrometer, 395
- KVERT. *See* Kamchatka volcanic eruption response team
- L**
- LAC. *See* Local area coverage
- LACIE. *See* Large area crop inventory experiment
- Lagrangian method, 434
- LAI. *See* Leaf area index
- LAI/FPAR, 517, 523, 528, 529, 605–633, 714
- LAI-2000 plant canopy analyzer, 616, 617
- Lake Kasumigaura, 122, 123
- Lake Tahoe, 122
- Lake Volta, 130
- Lambert azimuthal equal area (LAEA), 213, 513, 516
- Lambertian approximation, 566
- Lambertian surface, 111, 114, 467, 536, 548, 551, 566
- Land cover classification system (LCCS), 722, 843
- Land cover dynamics, 554, 668, 711–723, 804
- Land data operational production evaluation (LDOPE), 180, 519, 522, 523, 525–528, 787
- Land degradation, 658, 833, 839
- Land information system (LIS), 754
- Land Processes Distributed Active Archive Center (LP DAAC), 109, 126, 165, 167–177, 192, 193, 195, 221–224, 227, 236–244, 281–283, 444, 446, 450–456, 458, 513, 517, 605, 638, 643, 729, 730, 746, 788
- Land product validation (LPV), 508, 531, 803, 804
- Land Remote Sensing Commercialization Act, 42
- Land Remote Sensing Policy Act, 813, 814
- Landsat, 1, 4, 6, 22, 27, 28, 30, 38, 55, 59, 88, 98, 165, 168, 188, 195, 234, 255, 273, 302, 305, 306, 308, 314, 380, 381, 398, 403, 406, 407, 420, 426, 447, 448, 479, 495, 507, 508, 531, 539, 591, 716, 731,

- 734, 737–739, 741, 742, 745, 750, 755, 757–761, 781, 784, 786, 804, 842–844, 849, 850, 852, 853
- Landsat-class, 231, 809–834
- Landsat Data Continuity Mission (LDCM), 781, 815, 816, 818–822, 826–827, 830, 831
- Landsat ecosystem disturbance adaptive processing system (LEDAPS), 827
- Land surface heterogeneity, 750, 766, 775, 784
- Land surface imaging (LSI), 824, 853
- Land surface parameterization, 750
- Land surface processes, 512, 565, 712
- Land surface temperature (LST), 145, 380, 414, 415, 461, 508, 516, 517, 527, 528, 565–577, 640, 716, 731, 752–753, 756, 761, 765, 769, 772, 774, 775, 785, 788, 790, 797
- Land surface water index (LSWI), 596
- Land use, 30, 331, 354–357, 382, 393, 394, 406, 408, 412, 416–417, 671, 679, 711, 712, 733, 734, 741, 750, 776, 828, 840–844, 847, 848, 851, 854
- Langley method, 92
- Large area crop inventory experiment (LACIE), 826
- Latent heat, 385, 388
- Latent heat flux, 387, 388, 393–395, 397, 755–757, 759, 760, 763, 764, 766, 770
- Late-Pleistocene, 473, 480
- Lava domes, 229, 249, 250
- LC. *See* Lunar calibration
- LCCS. *See* Land cover classification system
- LDCM. *See* Landsat Data Continuity Mission
- LDOPE. *See* Land data operational production evaluation
- Leaf area index (LAI), 508, 514, 517, 530, 531, 535, 582, 590, 591, 593, 598, 600, 605–633, 638, 641–646, 650, 651, 753, 754, 756, 758, 761, 765, 766, 769, 774, 775, 785, 803, 845, 846
- Leaf chlorophyll, 582, 591
- LEDAPS. *See* Landsat ecosystem disturbance adaptive processing system
- Light detection and ranging (LIDAR), 413, 466, 467, 830, 831, 851
- Light-use efficiency (LUE), 593
- Linear interpolation, 77, 110, 111, 122, 648, 756
- Linear tape-open (LTO), 54, 181
- Line-of-sight, 449
- Line-of-sight vector, 77, 81, 444
- Line spread function (LSF), 103, 104
- LIS. *See* Land information system
- Lithological mapping, 61
- Lithology, 480
- Local area coverage (LAC), 784
- Logistic regression, 665–667, 718
- Long-term acquisition plan (LTAP), 814, 819
- Long-term calibration (LTC), 70, 117–122
- Long-wave infrared (LWIR), 10, 17, 19, 21, 23, 24, 55, 56, 137, 144, 148–151, 301, 302
- Look-up-table (LUT), 110–114, 151, 545, 623, 626
- LP DAAC. *See* Land Processes Distributed Active Archive Center
- LPV. *See* Land product validation
- LSI. *See* Land surface imaging
- LSWI. *See* Land surface water index
- LTAP. *See* Long-term acquisition plan
- LTC. *See* Long-term calibration
- LTO. *See* Linear tape-open
- LUE. *See* Light-use efficiency
- Lunar calibration (LC), 99–102, 104
- Lunar Lake, 122
- LUT. *See* Look-up-table
- LWIR. *See* Long-wave infrared
- M**
- Machine-to-machine gateway (MTMGW), 175, 178, 179
- MAE. *See* Mean absolute error
- MAIAC. *See* Multi-angle implementation of atmospheric correction
- Mamdani-type IF-THEN rules, 364
- Mapsat, 444
- Marine observation satellite, 55, 88
- Marine optical buoy system, 539
- Mars Express (MEx), 474
- Mars Rover, 475
- MASTER, 302, 479
- Mato Grosso, 672, 733, 737, 739
- MAUP. *See* Modifiable areal unit problem
- Maximum-likelihood, 381
- Maximum likelihood classifier, 715
- Maximum value compositing (MVC), 585, 588, 589
- Max-min difference (MMD), 128
- Mean absolute error (MAE), 756, 757
- Measurement of pollution in the troposphere (MOPITT), 9
- MELCO. *See* Mitsubishi Electric Company
- Merapi, 249–253
- MERIS, 711, 804, 842, 849
- MESSR. *See* Multispectral electronic self-scanning radiometer

- Meteorological data, 127, 204, 379, 380, 383–384, 414, 515, 538, 642–644, 647, 648, 755, 756, 758, 761, 765, 774
- Meteorological forcing, 754, 755, 761, 762, 765, 766, 775
- Meteosat second generation (MSG), 552, 553, 588
- Methane, 230, 425–440
- MEx. *See* Mars Express
- Micro-meteorological evapotranspiration models, 752
- Microwave sounding unit (MSU), 6
- Midwave emitted infrared (MWIR), 10, 17, 19, 21, 24, 137, 150
- Midwave infrared, 10, 56, 796
- Millennium ecosystem assessment, 839
- Mineralogy, 274, 286, 298, 302
- Miniaturization, 832, 834
- Mining, 26, 229, 294, 301–323
- Ministry of International Trade and Industry (MITI), 24–26, 28, 31, 485, 486, 488–498, 501
- MISR. *See* Multi-angle imaging spectro radiometer
- Misregistration, 17, 153, 237
- Mission Operations Center (MOC), 236
- Mission to planet earth (MTPE), 1, 7, 183
- MITI. *See* Ministry of International Trade and Industry
- Mitsubishi Electric Company (MELCO), 28
- Miyakejima, 247–248
- MMD. *See* Max-min difference
- MOC. *See* Mission Operations Center
- MODAPS. *See* Modis adaptive processing system
- Mode management, 2, 52
- Moderate resolution, 3–32, 93, 133, 234, 276, 357, 511, 551, 552, 565–578, 581–600, 605, 615, 616, 683, 751, 783–786, 793, 801–805, 809, 814, 821, 837, 842, 846, 848, 849, 851–853
- Moderate resolution imaging spectroradiometer (MODIS), 3, 35, 93, 127, 133, 172, 188–196, 203, 234, 240, 269, 276, 301, 357, 403, 426, 472, 485, 511, 535, 552, 565, 581, 615, 639, 663, 683, 711, 727, 751, 785, 809, 837
- Modifiable areal unit problem (MAUP), 409
- Modis adaptive processing system (MODAPS), 165, 173, 174, 176, 177, 179, 180, 201, 513, 515–519, 522, 523, 526, 531, 787, 788, 801
- MODIS/ASTER airborne simulator, 479
- MODIS land data products, 511–531
- MODIS-N, 8, 10–14
- MODIS quick-airborne looks (MQUALS), 587
- MODIS rapid response system, 507
- MODIS reprojection tool (MRT), 175
- MODIS-T, 8, 10–13, 771
- MODTRAN, 92, 111, 126–128, 248, 472, 474, 478, 479
- Modulation transfer function (MTF), 60, 72, 74, 86, 89, 100, 102–105, 125
- Mohr's Law, 42
- Moisture balance, 752
- Molecular scattering, 111, 436, 437
- Monin-Obukhov length, 387
- Monochromatic, 566
- Monte Carlo simulation, 537, 539
- MOPITT. *See* Measurement of pollution in the troposphere
- Moraines, 330–332, 335, 341, 344, 345, 348, 354, 355, 358, 362
- Mount Saint Helens, 333
- Mount Yatsugatake, 460, 461
- MQUALS. *See* MODIS quick-airborne looks
- MRT. *See* MODIS reprojection tool
- MSG. *See* Meteosat second generation
- MSS. *See* Multispectral scanner
- MSS/ORM, 416
- MSU. *See* Microwave sounding unit
- MTF. *See* Modulation transfer function
- Mt Fitton, 273–299
- MTMGW. *See* Machine-to-machine gateway
- MTPE. *See* Mission to planet earth
- Multi-angle imaging spectro radiometer (MISR), 9, 93, 112, 113, 224, 269, 537, 552, 557
- Multi-angle implementation of atmospheric correction (MAIAC), 537
- Multi-scale segmentation/object-relationship modelling, 416
- Multispectral, 2, 22–24, 234, 247–248, 266, 273, 279, 301, 306, 340, 351, 354, 357, 358, 369, 380, 391, 402, 405, 412, 415, 461, 466, 496, 567, 753, 809, 810, 812, 815, 819, 824, 843, 845, 847, 855
- Multispectral electronic self-scanning radiometer (MESSR), 55, 815
- Multispectral scanner (MSS), 22, 247–249, 279, 306, 567, 812
- Multi-spectrum electronic scanning radiometer, 55
- Muscovite, 278, 285, 304–306, 311, 313, 316, 322
- MVC. *See* Maximum value compositing
- MWIR. *See* Midwave emitted infrared

N

- NACP. *See* North American Carbon Program
- Nadir BRDF-adjusted reflectance (NBAR), 554, 555, 588, 590, 596, 716, 719–722
- NAFD. *See* North American Forest Disturbance
- Nagoya, 104, 106, 379–398, 414
- NAME. *See* North American Monsoon Experiment
- NASA decadal study, 357
- NASA Energy and Water Cycle Study (NEWS), 751
- NASDA. *See* National Space Development Agency
- National Aeronautics and Space Administration (NASA), 3, 35, 49, 70, 109, 133, 167, 183, 203, 234, 301, 351, 432, 444, 470, 486, 511, 538, 551, 593, 605, 639, 663, 701, 741, 751, 784, 809
- National Center for Supercomputing Applications (NCSA), 166, 204, 206, 512
- National Centers for Environmental Prediction (NCEP), 127, 276, 515, 538, 644, 655, 657, 754
- National Environmental Satellite, Data and Information Services (NESDIS), 11, 702, 790, 801
- National Institute of Advanced Industrial Science and Technology, 32
- National Land Imaging Program (NLIP), 231, 809, 820–821, 823, 824, 828, 830, 833, 834
- National Oceanic and Atmospheric Administration (NOAA), 4, 5, 10, 11, 20, 38, 42, 199, 276, 403, 426, 557, 581, 598, 702, 784–787, 790, 796, 798, 800–803, 805, 809, 813, 820, 845, 849
- National Operational Hydrologic Remote Sensing Center (NOHRSC), 698–700
- National Polar Orbiting Environmental Satellite Series (NPOESS), 20, 21, 151, 509, 531, 559, 597, 598, 658, 679, 723, 789–793, 795, 797, 798, 800–805, 820, 842, 846, 849, 853, 855
- National Research and Education Network (NREN), 39
- National Satellite Land Remote Sensing Data Archive (NSLRSDA), 814, 819, 826
- National Science and Technology Council (NSTC), 820, 821, 823
- National Snow and Ice Data Center (NSIDC), 38, 165–182, 192, 193, 196, 513, 514, 517, 690, 697, 706
- National Space Development Agency (NASDA), 25, 28, 488
- Natural hazards, 200, 330, 339
- Naval Research Laboratory (NRL), 3, 70, 127, 128
- NBAR. *See* Nadir BRDF-adjusted reflectance
- NBR. *See* Normalized burn ratio
- NCEP. *See* National Centers for Environmental Prediction
- NCSA. *See* National Center for Supercomputing Applications
- NDSI. *See* Normalized difference snow index
- NDVI. *See* Normalized difference vegetation index
- NE Δ p, 60, 68
- NEC. *See* Nippon Electric Company
- NEDT. *See* Noise-equivalent change (delta) in temperature
- NESDIS. *See* National Environmental Satellite, Data and Information Services
- netCDF, 204, 206
- Net photosynthesis, 639
- Net primary production (NPP), 591, 639, 640, 803, 844
- Neural networks (NNs), 351, 361, 616
- NEWS. *See* NASA Energy and Water Cycle Study
- NGST. *See* Northrop Grumman Space Technology
- Nighttime LST, 572, 573
- Nimbus-7, 4, 7
- Nippon Electric Company (NEC), 28
- Nishinoshima, 254
- NLDAS. *See* North American Land Data Assimilation System
- NLIP. *See* National Land Imaging Program
- NNs. *See* Neural networks
- NOAA. *See* National Oceanic and Atmospheric Administration
- NOAA Satellite Operations Facility (NSOF), 801
- NOHRSC. *See* National Operational Hydrologic Remote Sensing Center
- Noise-equivalent change (delta) in temperature (NEDT), 784
- Noise equivalent delta temperature (NEAT), 15, 16, 19, 21, 24, 60, 68, 70, 124, 133, 135, 145, 146, 266, 576
- Noösphere, 809
- Normalized burn ratio (NBR), 735, 741
- Normalized difference snow index (NDSI), 692, 693, 696, 704

- Normalized difference vegetation index (NDVI), 381, 383, 386, 406, 409, 411, 416, 417, 419, 432, 508, 535, 544, 547, 548, 567, 577, 581–592, 595–600, 607, 613, 616, 625, 648, 658, 692, 728, 729, 753, 754, 758, 788, 790, 798, 799, 845
- North American Carbon Program (NACP), 200, 827
- North American Forest Disturbance (NAFD), 827
- North American Land Data Assimilation System (NLDAS), 754, 755, 757–761, 775
- North American Monsoon Experiment (NAME), 772
- Northrop Grumman Space Technology (NGST), 797
- Noyabrsk, 425–429, 435, 436
- NPOESS. *See* National Polar Orbiting Environmental Satellite Series
- NPOESS preparatory project (NPP), 21, 151, 509, 531, 559, 597, 783, 789–791
- NPOESS system investigator-led processing system (NSIPS), 801
- NREN. *See* National Research and Education Network
- NRL. *See* Naval Research Laboratory
- NSIDC. *See* National Snow and Ice Data Center
- NSIPS. *See* NPOESS system investigator-led processing system
- NSLRSDA. *See* National Satellite Land Remote Sensing Data Archive
- NSTC. *See* National Science and Technology Council
- Nutation, 456
- Nutrient cycling, 749
- Nyquist frequency, 60, 104, 105, 125
- O**
- Oak Ridge National Laboratory (ORNL), 195–196, 530, 605
- OATS. *See* Operational algorithm teams
- OBC. *See* Onboard calibrator
- Object description language (ODL), 214, 218, 223
- Observation geometry, 535, 800
- Ocean data system (ODS), 38
- Office of Science and Technology Policy (OSTP), 809, 821, 833
- Oklahoma Mesonet, 767–772
- OLI. *See* Operational land imager
- OLR. *See* One-level representation
- OLS. *See* Operational linescan system
- Ombrotrophic, 428
- Onboard calibrator (OBC), 84, 86–88, 93–100, 122, 136–141, 143–145, 148, 160
- One-day schedule (ODS), 30, 236
- One-level representation (OLR), 416
- Open-source project for a network data access protocol (OPeNDAP), 198, 200
- Operational algorithm teams (OATS), 790
- Operational land imager (OLI), 815, 816, 819, 820, 830
- Operational linescan system (OLS), 791–793, 800, 851
- Optical sensor (OPS), 23, 55, 59, 61, 93, 406, 699, 842, 848, 853
- Orbview, 403, 406, 447
- ORNL. *See* Oak Ridge National Laboratory
- Orthoimage, 222, 223, 240, 243, 456
- Orthophoto quad, 456
- Orthorectification, 302, 453, 826–829, 852
- OSTP. *See* Office of Science and Technology Policy
- Otto Berg, 3
- Oyu Tolgoi, 317–322
- P**
- PAI. *See* Plant area index
- Palcacocha, 331, 340–352, 369, 370, 372
- Palsa, 426, 429, 435–440
- PAN. *See* Product acceptance notice
- Parallax, 222, 237, 238, 443, 447, 449, 452, 453, 458, 459
- PDPS. *See* Planning and data processing subsystems
- PDR. *See* Product delivery record
- PDRD. *See* Product delivery record discrepancy
- PEATE. *See* Product evaluation and test system elements
- Peat land, 426, 439
- PECAD. *See* Production Estimates and Crop Assessment Division
- Permafrost, 332, 338, 372, 428, 429
- PFM. *See* Proto-flight model
- PFT. *See* Plant functional type
- PGE. *See* Product generation executable
- Phenological variation, 728
- Phenology, 527, 581, 582, 587, 588, 591, 593, 595–596, 599, 619, 626, 712, 716, 719, 722, 731, 735, 784, 827
- Photogrammetry, 443, 444, 449, 451, 455
- Photo-interpretation, 481

Photosynthetic activity, 839
 Photosynthetic assimilation, 645
 Phreato-magmatic, 266
 Phyllosilicate, viii
 Planck equation, 265
 Planck function, 125, 129, 758
 Planimetric, 453, 454
 Planning and data processing subsystems (PDPS), 170, 172
 Plant area index, 619
 Plant functional type (PFT), 714
 Pointing axis vectors, 73, 449
 Pointing knowledge, 73, 136
 Polarimetry, 443
 Polarization, 14, 92, 142, 539, 552, 786, 853
 Polarization and directionality of the Earth's reflectances (POLDER), 88, 537, 539, 552, 553
 Polar orbiting environmental satellites (POES), 20, 789, 801
 Popocatépetl, 332
 Principal component analysis, 415
 PRISM, 447, 448, 843, 850
 PRODES, 737–740
 Product acceptance notice (PAN), 173–175
 Product delivery record (PDR), 173, 174, 177
 Product delivery record discrepancy (PDRD), 174
 Product evaluation and test system elements (PEATE), 801
 Product generation executable (PGE), 214, 218, 569–574, 577
 Production Estimates and Crop Assessment Division (PECAD), 596
 Proto-flight model (PFM), 14, 17, 70, 133
 Prototyping, 43, 49, 187, 368, 606, 722
 Pruning, 715, 717, 734
 Pushbroom, 28, 61, 63, 74
 Pyroclastic flow, 250, 251
 Pyrogenic, 668
 Pyrophyllite, 311, 313, 314, 316, 322

Q

Quadratic, 117, 143, 433, 434, 543–545
 Quality assessment, 180, 455, 508, 511, 522–528, 545, 674, 690, 705, 737, 787
 Quality assurance, 180, 222, 236, 455, 458, 460, 511–531, 581, 585, 587–589, 613, 674, 675, 684, 686, 690, 693, 705, 787, 789, 795
 Quantization, 15, 27, 60, 68, 134, 445
 Quasi-epipolar geometry, 431, 453, 459
 Quickbird, 402–406, 447, 448, 539, 812, 842

R

Radar backscatter, 466
 Radiance, 15, 59, 83, 117, 133, 215, 238, 245, 276, 311, 350, 382, 412, 461, 467, 516, 535, 553, 565, 582, 692, 793, 819
 Radiant flux, 136
 Radiation flux, 383
 Radiative transfer (RT), 56, 89, 92, 96, 111, 114, 122, 126, 472, 535–539, 546, 552, 557, 565, 575, 582, 590, 606, 616, 617, 623, 625, 626, 632, 648, 800
 Radiometric calibration coefficient (RCC), 83, 85–100, 117, 119–122, 237
 Radiosonde, 123, 575
 Railroad Valley Playa, 89, 92, 122, 575
 Ranked brightness approach (RBA), 729–731
 Raphstreng Tsho, 339
 Raw data records (RDR), 793, 803
 Rayleigh scattering, 67
 Rayleigh's law, 536
 RBD. *See* Relative Band Dept
 RBV. *See* Return beam vidicon
 RCC. *See* Radiometric calibration coefficient
 REASoN. *See* Research, education and applications solution network
 Reconnaissance, 302–309, 322, 359, 402
 Reflectance, 10, 56, 68, 83, 125, 136, 240, 248, 273, 304, 358, 381, 405, 432, 461, 466, 508, 514, 535, 551, 582, 606, 650, 663, 685, 716, 728, 785, 827
 Reflectance anisotropy, 508, 551–559
 Reflected solar bands (RSB), 20, 137–139, 141, 142, 144–148, 151, 160, 162
 Regression tree, 731, 734
 Relative azimuth, 157, 537, 566, 584
 Relative Band Dept (RBD), 284–290, 295, 298
 Relative spectral response (RSR), 137, 142, 144, 575
 Remote Sensing Technology Center (RESTEC), 381
 Resampling, 77, 81, 243, 451, 452, 570
 Research, education and applications solution network (REASoN), 186, 199
 Responsivity, 62, 87, 118–119, 122, 148, 150
 Retrieval index (RI), 610, 611, 630, 631
 Return beam vidicon (RBV), 812
 Root mean square error (RMSE), 130, 240, 432, 436, 438, 449, 456, 593, 620, 623, 632, 756, 757, 759, 761, 763–765, 767
 Ross-thick/Li-spares-reciprocal (RTLSR), 157, 553, 554, 673
 RSB. *See* Reflected solar bands
 RSR. *See* Relative spectral response
 RT. *See* Radiative transfer

S

- Safari 2000, 195
- Salton Sea, 122, 123, 128, 575
- SAM. *See* Spectral-angle mapper
- Santa Barbara remote sensing (SBRS), 12, 21, 56, 133, 141
- Santa Barbara Research Center (SBRC), 12
- SAR. *See* Synthetic aperture radar
- Satellite Pour l'Observation de la Terre (SPOT), 23, 59, 88, 358, 371, 402, 403, 426, 447, 448, 451, 495, 591, 598, 615, 675, 679, 711, 814–818, 822, 829, 842, 849, 850
- Satsuma-Iwojima, 253–257, 261
- SAVI. *See* Soil adjusted vegetation index
- SCA. *See* Snow-covered area
- Scanning multichannel microwave radiometer (SMMR), 4, 5
- Scattering, 67, 106, 109–114, 123, 126, 156, 247, 276, 470, 536, 537, 553, 565, 617, 785
- Science data support team (SDST), 513, 519
- Science investigator-led processing system (SIPS), 2, 37, 40–42, 45, 173, 174, 183, 185
- Science Scheduling Support Group (SSSG), 236, 249, 253, 258
- Scientific data sets (SDSs), 206
- Scientific judgment, 230, 485, 486, 497
- SD. *See* Solar diffuser
- SDR. *See* Sensor data records
- SDS. *See* Solar diffuser screen
- SDSM. *See* Solar diffuser stability monitor
- SDST. *See* Science data support team
- Sea ice extent, 514, 685–687, 703–706
- Sea-level change, 329
- Search 'N Order Web Interface (SNOWI), 178–179, 196
- Seasonal land cover, 711–723
- Sea surface temperature (SST), 17, 20, 126, 130, 141, 145, 248, 775
- Sea-viewing wide field-of-view sensor (SeaWiFS), 88, 218, 539, 598, 609, 792
- SEBS. *See* Surface energy balance system
- Second simulation of a satellite signal in the solar spectrum vector, 538
- Senescence, 553, 619, 626, 714, 719, 720
- Sensible heat, 379, 385, 387–392, 394, 395, 397, 414, 750, 755, 756, 760
- Sensor data records (SDR), 793
- Sequestration, 597
- Service-oriented architecture (SOA), 45, 47, 166, 182
- SEVIRI. *See* Spinning enhanced visible and infrared imager
- SFF. *See* Spectral-feature fitting
- Shishmaref, vii
- Short term calibration (STC), 70, 117, 789
- Shortwave infrared (SWIR), 10, 59, 83, 117, 137, 222, 234, 245, 273, 301, 358, 380, 402, 444, 480, 495, 805, 816, 837
- Shuttle Radar Topography Mission (SRTM), 253, 254, 269, 443, 828, 829, 849, 852
- SIAD. *See* Integrated Warning Deforestation System for the Amazon
- Sierra Negra, 251–254
- Signal-to-noise ratio (SNR), 18–21, 68, 86, 96, 102, 133–135, 145, 146, 468, 470, 496, 567, 786
- Silcast, 172, 453, 456
- Silica, 302, 311–314, 318, 322
- Simple, scalable, script-based science processor for missions (S4PM), 172
- Sinusoidal, 155, 213, 513, 516, 555, 569, 583, 607, 619, 674, 684, 693
- SIPS. *See* Science investigator-led processing system
- SIS. *See* Solar integrating sphere
- Sky irradiance, 240, 413, 467, 472
- SLA. *See* Specific leaf area
- SMA. *See* Spectral mixture analysis
- SMACEX. *See* Soil moisture atmospheric coupling experiment
- SMEX04. *See* 2004 Soil moisture experiment
- SMMR. *See* Scanning multichannel microwave radiometer
- Snow albedo, 684, 685, 689, 693, 695, 697
- Snow climatology, 687
- Snow-covered area (SCA), 688, 690, 692–703, 705
- Snow cover mapping, 683
- Snow detection, 683, 695
- SNOWI. *See* Search 'N Order Web Interface
- Snowmelt runoff model (SRM), 700, 701
- Snowpack telemetry (SNOTEL), 698, 700
- Snow water equivalent (SWE), 700, 702, 703
- SNR. *See* Signal-to-noise ratio
- SOA. *See* Service-oriented architecture
- Socompa, 270
- SOGS. *See* Surface observation gridding system
- Soil adjusted vegetation index (SAVI), 409, 582, 599
- Soil moisture atmospheric coupling experiment (SMACEX), 755–757, 759, 760, 772
- Soil moisture experiment, 594

- 2004 Soil moisture experiment (SMEX04), 594
 Solar diffuser (SD), 138–142, 145, 147, 151, 160
 Solar diffuse radiance, 566
 Solar diffuser screen (SDS), 139, 142, 145, 207, 216–218, 584, 801, 803
 Solar diffuser stability monitor (SDSM), 17, 57, 138–142, 160, 792
 Solar incidence angle, 282, 467, 470, 479
 Solar integrating sphere (SIS), 139, 140, 142, 144, 145
 Solar zenith, 67, 68, 111, 112, 114, 141, 154, 157, 537, 556–558, 565, 584, 585, 588, 610, 612, 693, 705, 715, 729, 788
 Solar zenith angle, 67, 68, 111, 112, 114, 141, 154, 157, 537, 556–558, 565, 570, 584, 585, 588, 610, 612, 715, 729, 788
 Solid-state recorders (SSR), 29, 236, 814, 816
 Sonic anemometer, 395, 755
 Sony DTF2, 169
 SOS. *See* Successive orders of scattering
 SOTER, 849
 Space Technology Council (STC), 789
 Space view source (SVS), 144
 Spatial interpolation, 126, 648
 Special sensor microwave imager (SSM/I), 699
 Species physiology, 626
 Specific leaf area (SLA), 642
 Spectral-angle mapper (SAM), 312–314, 319
 Spectral-feature fitting (SFF), 312, 313, 319
 Spectral irradiance, 125
 Spectral mixture analysis (SMA), 230, 414, 427, 433–436, 438, 440, 480, 481
 Spectral signatures, 241, 274, 276, 280, 281, 287, 298, 310, 404, 415, 731
 Spectral transmittance, 125, 247
 Spectral unmixing, 284, 298, 409
 Spectro-radiometric calibration assembly (SRCA), 57, 138–141, 148, 151
 Sphagnum bogs, 428
 Spherical integration source, 140
 Spinning enhanced visible and infrared imager (SEVIRI), 588
 S4PM. *See* Simple, scalable, script-based science processor for missions
 SPOT. *See* Satellite Pour l'Observation de la Terre
 SR. *See* Surface roughness
 SRB. *See* Surface radiation budget
 SRCA. *See* Spectro-radiometric calibration assembly
 SRM. *See* Snowmelt runoff model
 SRR. *See* System requirements review
 SRTM. *See* Shuttle Radar Topography Mission
 SSM/I. *See* Special sensor microwave imager
 SSR. *See* Solid-state recorders
 SSSG. *See* Science Scheduling Support Group
 SST. *See* Sea surface temperature
 SSU. *See* Stratospheric sounding unit
 STC. *See* Short term calibration; Space Technology Council
 Stefan-Boltzmann's law, 385
 STEP. *See* System for terrestrial ecosystem parameterization
 Stereo-matching, 458
 Stereosat, 444
 Stereoscopy, 230, 443–449
 Stewart Udall, 812
 Stokes vector, 539
 Stomatal resistance, 388, 393
 Stratospheric sounding unit (SSU), 6
 Stray light, 65, 86, 100, 104, 106, 107, 109, 110, 123–124
 Streamflow, 700, 701
 Successive orders of scattering (SOS), 537, 539
 Sulfur dioxide, 245, 247–248
 Sunphotometer, 630
 Sun-shadow method, 575, 577
 Sun-synchronous, 8, 15, 67, 137, 152, 234, 446, 471
 Support vector machine (SVM), 593
 Supraglacial lakes, 332
 Surface emissivity, 122, 125, 128, 129, 241, 242, 281, 285, 297–299, 383, 385, 398, 575–577
 Surface energy balance system (SEBS), 751–766, 768, 770, 772, 775–777
 Surface flux, 750, 754, 755, 757, 759–761, 765–767, 772, 775–777
 Surface heat balance, 385, 389
 Surface heat-flux, 379
 Surface kinetic temperature, 122, 125, 241, 242, 263, 265, 413, 414
 Surface observation gridding system (SOGS), 658
 Surface radiation budget (SRB), 752, 753
 Surface reflectance, 83, 84, 89, 92, 93, 96, 112–114, 125, 241, 242, 256, 274, 276, 279–282, 284, 287, 288, 382, 508, 514–517, 523, 526, 527, 535–537, 539–543, 545–548, 553, 554, 556, 557, 559, 570, 585, 587, 588, 606, 607, 609, 610, 613, 619, 623–626, 630, 632, 633, 650, 673, 693, 696, 716, 728, 729, 736, 785, 788, 795, 797–800, 827
 Surface roughness (SR), 465–482
 6SV, 538–540, 543, 545, 546, 800
 SVM. *See* Support vector machine
 SVS. *See* Space view source

- SWE. *See* Snow water equivalent
- SWIR. *See* Shortwave infrared
- SWIR crosstalk, 56, 83, 104, 106–110, 276–277, 284, 295, 298
- Synthetic aperture radar (SAR), 7, 8, 38, 596, 843, 845, 848
- System design, 49, 50, 56, 787, 805
- System for terrestrial ecosystem parameterization (STEP), 715, 716
- System requirements review (SRR), 2, 49, 50
- Systems requirements, 50
- System Z, 7
- T**
- Tagged image file format (TIFF), 204
- TDI. *See* Time-delay and integration
- TDR. *See* Time domain reflectometry
- TDRSS. *See* Tracking data relay satellite system
- TEB. *See* Thermal emissive bands
- Technical decision-making, 230
- Technology infusion, 43, 46, 47, 166, 199
- Technoscientific diplomacy, 230, 485–503
- Telemetry, 143, 237, 698
- Television infrared observation satellite (TIROS), 4, 5
- Television infrared observation satellite-1 (TIROS-1), 4
- Temperature, 6, 56, 61, 87, 117, 133, 221, 240, 245, 281, 312, 345, 379, 412, 428, 461, 508, 514, 536, 565, 582, 626, 640, 671, 685, 716, 731, 751, 784
- Temperature-independent spectral index, 570
- Temperature mapping, 245–246
- Terrestrial dynamics, 810
- Terrestrial primary production, 637–659
- Thematic mapper (TM), 22, 23, 28, 59, 88, 98, 114, 273, 302, 306, 308, 380, 402, 404, 448, 495, 716, 733, 738, 741, 786, 812, 813, 815, 816, 819, 820, 828, 842
- Thermal emission imaging system (THEMIS), 792
- Thermal emissive bands (TEB), 12, 57, 138, 140, 141, 143–148, 151, 160
- Thermal inertia, 23, 28, 392, 466
- Thermal infrared (TIR), 23–28, 56, 59–63, 65, 68, 70, 72–74, 76, 77, 80, 83, 99, 100, 102, 117–128, 222, 230, 234, 239–242, 245–248, 250–254, 263–266, 268, 269, 273, 279, 281, 285, 295, 297–299, 302, 312, 314, 319, 340, 380, 383, 392, 398, 412–415, 417, 444, 445, 466, 479, 487–490, 492, 493, 495–497, 502, 565–567, 569, 575–577, 784, 786, 797, 800, 816, 820, 822, 824, 830
- Thermal infrared ground emission radiometer (TIGER), 24–26, 487–498
- Thermal infrared mapping spectrometer, 23, 24, 278, 279, 489, 495, 567, 568
- Thermal infrared multispectral scanner (TIMS), 23, 24, 247, 249, 278, 279, 489, 495, 567, 568
- Thermistor, 123, 140, 144
- Thorthormi glacier, 339
- TIFF. *See* Tagged image file format
- Time-delay and integration (TDI), 137
- Time domain reflectometry (TDR), 430
- TIN. *See* Triangular irregular network
- TIROS. *See* Television infrared observation satellite
- TIROS-1. *See* Television infrared observation satellite-1
- TIROS operational vertical sounder (TOVS), 5
- TISI. *See* Temperature-independent spectral index
- TM. *See* Thematic mapper
- Topography, 113, 241, 245, 253, 254, 255, 264, 274, 277, 284, 288, 292–295, 02, 314, 318–322, 341, 342, 343, 380, 383, 426, 443, 449, 451, 454, 460, 466, 470, 471, 474, 587, 750, 785, 809, 811, 828, 840, 841, 852
- Total ozone mapping spectrometer (TOMS), 4, 112, 127, 522, 538
- Tower meteorology, 647
- Tracing radiation and architecture of canopies (TRAC), 616, 619
- Tracking data relay satellite system (TDRSS), 173, 235
- Trail Canyon, 472, 473, 477–481
- Transpiration, 379, 385, 388, 393, 394, 582, 591, 594, 600, 749, 768
- Triangular irregular network (TIN), 384
- U**
- UN Framework Convention on Climate Change (UNFCCC), 509, 823
- Unit conversion coefficient (UCC), 78, 80, 81, 84–85, 237, 282
- Universal transverse mercator (UTM), 81, 213, 222, 239, 242, 305, 314, 319, 320, 450, 456
- Upper Atmosphere Research mission (UARS), 8
- Upwelling, 467, 470, 474, 478, 481
- Urban change, 401–420

Urban ecology, 409
 Urban environmental monitoring (UEM), 230, 407, 408, 415, 416, 420
 Urban heat-island, 379, 397
 Urban landscape, 402, 410–412, 419
 Urban vegetation cover index, 410
 U.S. Group on Earth Observations (USGEO), 823–826

V

Validation, 24
 Vaporization, 749
 Vapor pressure deficits (VPD), 595, 639, 641, 644, 646, 658
 Variable infiltration capacity (VIF), 701
 Vegetation continuous fields (VCF), 509, 514, 727–746
 Vegetation cover index (VCI), 410
 Vegetation indices (VI), 406, 409, 508, 514, 523, 535, 544, 567, 581–600, 607, 616, 643, 692, 714, 731, 753, 754, 784, 788, 790, 793, 795, 798, 799, 846, 851
 Vegetation photosynthesis model (VPM), 593
 Vegetative cover conversion (VCC), 727, 729, 730, 734–740, 743, 744, 746
 Verner Suomi, 4
 Vicarious calibration (VC), 83, 84, 86, 88, 96, 97, 101, 122–123, 128, 130
 Vignetting, 142
 Visible and infrared imaging radiometer suite (VIIRS), 20–22, 151, 509, 539, 559, 597, 598, 600, 658, 679, 785, 788–803, 805, 842, 846, 849, 851, 853, 855
 Visible near infrared (VNIR), 17, 59, 83, 117, 222, 234, 246, 273, 301, 358, 380, 402, 444, 466, 487, 805
 Vladimir Vernadsky, 809
 Volcanology, 59, 245–270, 371
 Volumetric water content (VWC), 430, 438, 439
 VPD. *See* Vapor pressure deficits
 VPM. *See* Vegetation photosynthesis model

W

Warehouse inventory search tool (WIST), 166, 175, 178, 181, 185, 188–192, 239, 243, 195, 198
 Waterfall methodology, 40, 49
 Water vapor scaling (WVS), 128–130
 Wavelength, 62–64, 104, 111, 125, 140, 151, 234, 247, 257, 273, 274, 281, 284–286, 292, 311, 313, 340, 409, 467, 489, 490, 492, 496, 536, 539, 541, 565, 566, 673, 692, 818
 WCRP. *See* World Climate Research Program
 West Siberian lowland, 230, 425–440
 Wetlands, 426–428, 439, 723, 839, 840, 842
 Whiskbroom, 28, 63, 72, 74, 136, 152
 White sands, 152, 173, 515
 White-sky albedo, 553, 753
 Wide-field-of-view, 152, 833
 Wildfire automated biomass burning algorithm (WFABBA), 673
 Wildland fires, 840
 William Pecora, 812, 813
 WIST. *See* Warehouse inventory search tool
 Working Group on Calibration and Validation (WGCV), 531, 804, 832, 845
 World Climate Research Program (WCRP), 761
 World Radiation Center (WRC), 89
 WorldView-1, 447
 WVS. *See* Water vapor scaling

X

XDR. *See* External data representation
 Xilingol steppe, 595
 XML. *See* eXtensible Markup Language

Z

Zagros magmatic arc, 303–309